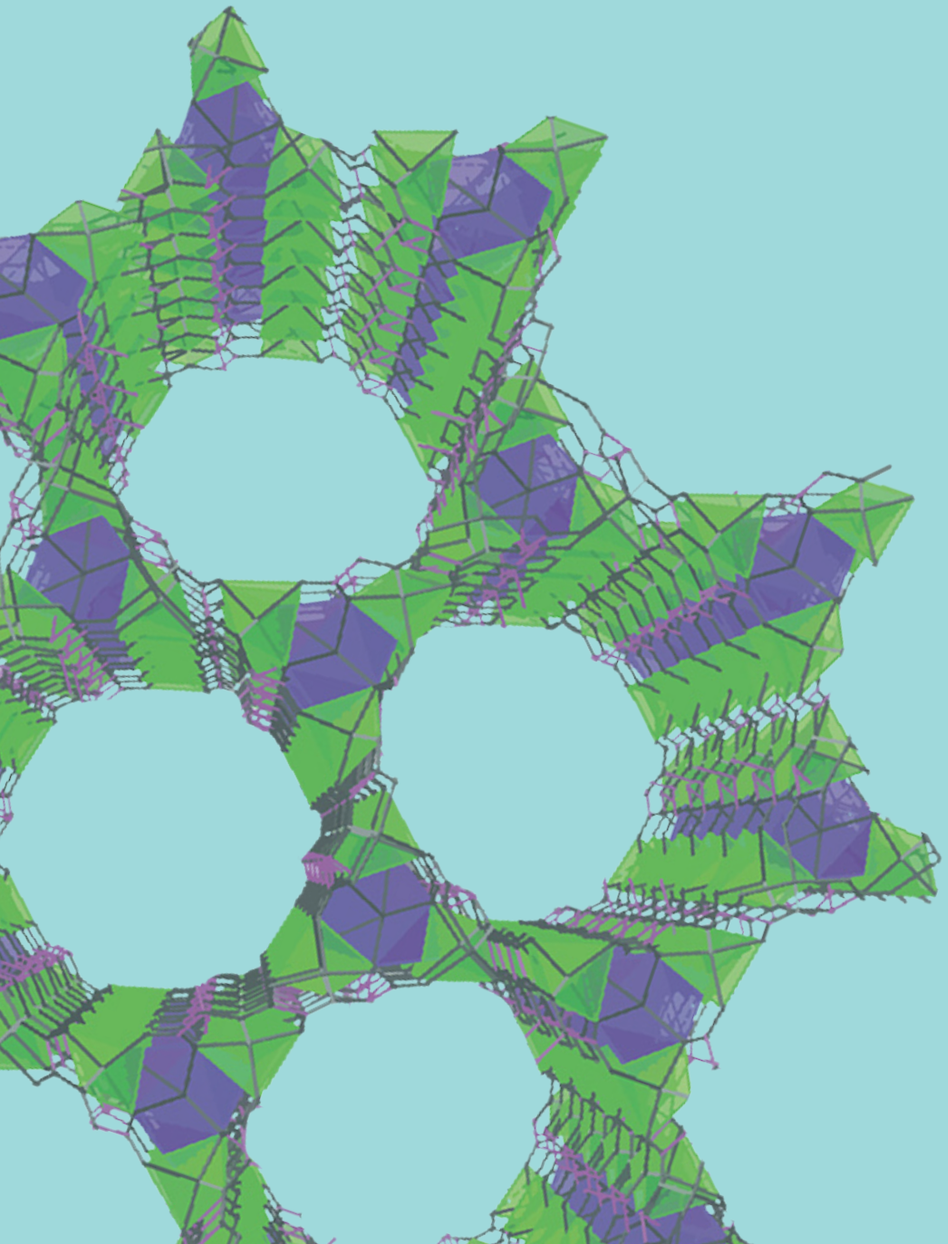

2017

PROGRAMA DE DOCTORADO
NANOCIENCIA Y
NANOTECNOLOGÍA CON
MENCIÓN DE EXCELENCIA

FACULTAD DE QUÍMICA
INSTITUTO DE CIENCIA
MOLECULAR

OXAMATO / OXAMIDATO-BASED MULTIFUNCTIONAL POROUS COORDINATION POLYMERS

TESIS DOCTORAL
THAIS MARÍA GRANCHA MARCO

TESIS DOCTORAL

THAIS MARÍA GRANCHA MARCO

VNIVERSITAT DE VALÈNCIA

DIRIGIDA POR:
PROF. DR. MIGUEL JULVE OLCINA
DR. EMILIO PARDO MARÍN
DR. JESÚS FERRANDO SORIA

MAYO 2017

VNIVERSITAT DE VALÈNCIA

Facultad de Química

Instituto de Ciencia Molecular

Programa de Doctorado Nanociencia y Nanotecnología con Mención de Excelencia

Oxamato/Oxamidato-Based Multifunctional Porous Coordination Polymers

Tesis Doctoral

Thais María Grancha Marco

2017

Dirigida por los Dres. Miguel Julve Olcina, Emilio Pardo Marín y Jesús Ferrando Soria

Miguel Julve Olcina, Doctor en Ciencias Químicas, Catedrático de la Universidad de Valencia, **Emilio Pardo Marín**, Doctor en Ciencias Químicas y **Jesús Ferrando Soria**, Doctor en Ciencias Químicas, todos ellos miembros del Instituto de Ciencia Molecular (ICMol) y del Departamento de Química Inorgánica de la Facultad de Química de la Universidad de Valencia,

CERTIFICAN:

Que el trabajo que presenta Dña. **Thais María Grancha Marco** en esta Memoria, con el título "***Oxamato/Oxamidato-Based Multifunctional Porous Coordination Polymers***", en el marco del programa de doctorado de Nanociencia y Nanotecnología, ha sido realizado bajo nuestra dirección en el Instituto de Ciencia Molecular y el Departamento de Química Inorgánica de la Universidad de Valencia para optar al título de Doctora en Nanociencia y Nanotecnología.

Y para que así conste, firmamos el presente certificado en Burjassot a 22 de mayo de 2017.

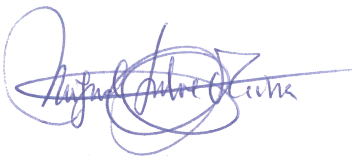

Fdo.: Miguel Julve Olcina

Fdo.: Emilio Pardo Marín

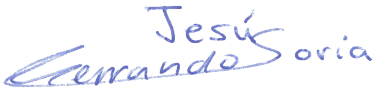

Fdo.: Jesús Ferrando Soria

Dña. **Thais María Grancha Marco**, Licenciada en Ciencias Químicas por la Universidad de Valencia, presenta esta Memoria de título "***Oxamato/Oxamidato-Based Multifunctional Porous Coordination Polymers***", en el marco del programa de doctorado de Nanociencia y Nanotecnología con el fin de optar al grado de Doctora en Nanociencia y Nanotecnología.

Y para que así conste, firma la presente en Burjassot a 22 de mayo de 2017.

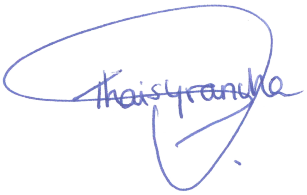

Fdo. Thais María Grancha Marco

A Miguel

Agradecimientos

Para poner en antecedentes al lector diré que no soy mujer de pocas palabras. Sé de sobra que abuso de los adjetivos y de los adverbios de modo y cantidad. Porque cuando se trata de expresarme, todo lo exalto y lo magnifico, porque soy así de sentida (dramática dirían algunos). Precisamente por eso, es para mí una tarea complicada sintetizar en apenas una líneas tanto sentimientos y agradecimientos y quedarme satisfecha (y sin usar emoticonos, lo cual añade dificultad).

Me siento inmensamente afortunada de que en su día, los derroteros me trajeran al grupo de Química de Coordinación por dos motivos principalmente: Miguel y Paco. Haber compartido estos años de mi vida con ellos es un privilegio. Por encima de su bien sabida calidad científica yo admiro su sabiduría, calidad humana, su honestidad, generosidad, honradez y sentido del bien. Son personas excepcionales que me permitieron mostrarme imperfecta y humana, frágil en ocasiones, y que lejos de juzgarme, me tendieron su mano y confiaron en mí. Paco, echaré de menos oírte cantar y a Miguel decir "Si Paco canta, es que hoy está contento". También echaré de menos tus curiosidades científicas y plantearte mis cuestiones e inquietudes. Gracias por tanto.

Miguel, no existen palabras para agradecerte lo que has hecho por mí. Literalmente fuiste Luz cuando no podía ver nada, oxígeno cuando no podía respirar. Fuiste alas, impulso, confianza, esperanza e ilusión. Te quedaste con nosotros, librabas tu lucha y libraste la mía. Caminaste conmigo testigo de mis luces y mis sombras, me sujetaste, me cuidaste. Siempre disponible, agradezco tus horas y deshoras dedicadas a esta Tesis, tus enseñanzas y tus consejos. Tu cariño y comprensión. Siempre te tendré presente, siempre habrá un espacio en mi corazón para ti. Esta Tesis no sería sin ti.

A los dos os agradezco los hermosos valores que me habéis inculcado.

Emilio, te estoy muy agradecida por todo el tiempo (que fue mucho) que invertiste en enseñarme tantísimas cosas y por todo tu esfuerzo y dedicación para que esta investigación y los resultados saliesen adelante. Jesús, te agradezco las veces que amenizaste mis ratos en el Laboratorio, tu alegría, tus enseñanzas y consejos. A ambos os deseo que consigáis todo aquello que soñáis.

Rafa, el mundo se perdió un excelente profesor. Por suerte yo no me lo perdí. Gracias por disfrutar ayudando, por tu altruismo, tu alegría y tu enorme sabiduría. Por arrancarme millones de sonrisas y participar de mis ideas locas. Joan, gracias por tus contribuciones a mis trabajos y por tus anécdotas plagadas de buen humor. Isabel, gracias por llevarme contigo al Sincrotrón. Me diste la oportunidad de visitar un acelerador y acercarme a ti y descubrir una mujer valiente y luchadora. También agradezco al resto del grupo: a Nico, que trajo consigo aire fresco, alegría y buen humor, gracias por preocuparte por mí y por todo tu ánimo y ayuda; a Salah, a Jose Lillo, y a mis compañeros de Laboratorio, especialmente a Marta Mon, que compartió conmigo quebraderos de docencia e investigación.

Agradezco a aquellas personas que sin pertenecer al grupo también contribuyeron al desarrollo de este trabajo. Chema, Gloria, Ale y Ángel, por su amabilidad y disponibilidad para ayudarme. Ben Tama, admiro profundamente tus conocimientos de Química Orgánica, gracias por ayudarme con las síntesis y por ser una excelente persona. Tonino, gracias por tus enseñanzas de Cristalografía. Donatella, siempre te agradeceré el enorme esfuerzo que realizas para resolver nuestras estructuras, así como el entusiasmo y el amor hacia la investigación que desprendes. Gracias por todas las alegrías en forma de estructuras que me has brindado. Así mismo, Jorge, Óscar y Caty, gracias por las estructuras que nos habéis resuelto y que han contribuido enormemente al valor de esta Tesis. Gracias Jorge y Beba por acogerme con los brazos abiertos en Holanda.

Mi estancia en el Laboratorio no habría sido lo mismo sin la presencia de todos aquellos estudiantes pre- y posdoctorales que la vida tuvo a bien de poner en mi camino.

Ellos fueron mi apoyo, me enriquecieron con sus culturas y me regalaron su cariño. Me refiero a mi maravillosa familia brasileña: María Vanda, Tatiana, Wdeson, Lilian y Willian, a mi familia uruguaya: Mario, Lorena y Carlos Rojas. A las polacas Asia y Ania y a las rumanas Mihaela, Diana y Maria. También recuerdo con cariño a Feng, a Hicham y a Laetitia.

Agradezco especialmente a aquellas compañeras que se convirtieron en mis amigas. María, compartimos suficiente como para forjar una amistad que permanece a día de hoy. Gracias por tu bondad, delicadeza y tu fascinante imaginación. Me traes luz y alegría cada vez que me visitas. Tania, encontramos cobijo la una en la otra en el momento adecuado y fuiste y eres un apoyo fundamental para mí. Cris, agradezco los descansos en forma de charlas contigo y que nos apoyáramos la una en la otra. Lucía, tu enorme sensibilidad y sentido del bien hacen que me sienta a gusto y comprendida a tu lado. Gracias por cada conversación, por cada té compartido, por escucharme, por calmarme y aconsejarme, por tus abrazos cargados de energía y por compartir conmigo todas tus inquietudes. Elena, eres una mujer extraordinaria, siempre has tenido palabras y gestos bonitos y altruistas hacia mí. Agradezco todo ese cariño y apoyo. María Jesús, eres un ser de luz que derrocha sensibilidad y cariño. Mari Carmen gracias por tu alegría, por tus broncas, por cuidarme como a una hija, por animarme, por apoyarme y por tenerme siempre presente. Adoro y admiro a todas y cada una de estas mujeres.

A aquellos compañeros del ICMol y del Máster de Nanociencia que alegraron mi día a día: Marta, Lumi, Álvaro, Javi, Dani, Alexandre, Majo, Carlos R., Carlos S., Nely, Juanjo, Juan, Blanca y Bernat. A mis compañeros de Delft y de forma más especial a mis incondicionales Lide, Edu, Mari y Ane.

A mis amigos, que han caminado a mi lado todos estos años, sufriendo cada caída y celebrando cada logro. Por su inagotable paciencia, su amor y su confianza en mí. Diana, Encar y Anita os doy las GRACIAS por haber caminado esta senda conmigo, tirando incansables cuando fue necesario. Porque nunca dudasteis de mí. Porque entre las tres conjugan todo lo que necesito escuchar cuando me hallo perdida. Diana, eres intuición

y sensibilidad, mi *alter ego*. Encar, tu corazón es enorme, eres inocencia y bondad. Anita eres la serenidad, la fuerza y la razón. Agradezco de todo corazón a Loreto y Marcos, Cristy, Nerea, Melanie, Elena, Pablo, Víctor, David, Miralles, Álex, Joan, Adri, a Esther, Cris y Dafne, a Carlos y Bea, a Alba, Patri, Maribel, a Lidia y Sylvia, por los viajes, cenas y celebraciones, escapadas y desconexiones. Por vuestro apoyo y alegría. Me siento muy afortunada de teneros en mi vida.

Gracias a Marisa y a Paola por brindarme las herramientas para crecer y hacerme de guía en este cometido que es la Vida.

Gracias a mi familia, a mi padre, mi madre, mi hermano, María, Rafa y Eva, por caminar a mi lado, por creer en mí aun cuando me vieron flaquear y amarme de manera incondicional.

No quisiera finalizar este apartado sin un último, pero no menos importante agradecimiento. Quiero dirigirme a aquella Thais de hace dos y tres años. Gracias por hacerlo lo mejor que supiste en ese momento, con las herramientas y la perspectiva de que disponías. Gracias por cada decisión que tomaste. Gracias por aguantar, por levantarte todas las veces que te caíste. Gracias por no rendirte. Si no fuera por ti, ahora no estaría escribiendo estas palabras ni materializando todo el trabajo realizado. De no haber sido por ti hoy no sería la mujer que soy ahora.

“Caminante, son tus huellas
el camino, y nada más;
caminante, no hay camino,
se hace camino al andar.
Al andar se hace camino,
y al volver la vista atrás
se ve la senda que nunca
se ha de volver a pisar.
Caminante, no hay camino,
sino estelas en la mar.”

A. Machado

Index

Abstract

0. Introduction

0.1. Porous Coordination Polymers (PCPs) 1

0.1.1. Description 2

0.1.2. Overview of History 8

0.1.3. Synthesis 14

0.1.3.1. Conventional synthesis 14

0.1.3.2. Alternative synthesis 16

0.1.3.3. Post-synthetic methods 16

0.1.4. Applications 19

0.1.4.1. Catalysis 19

0.1.4.2. Gas storage and separation 20

0.1.4.3. Drug Delivery 21

0.1.4.4. Sensing 22

0.2. Oxamato-based CPs: previous results 24

0.2.1. Single-chain magnetic behaviour in linear 1D CPs 27

0.2.2. Long-range magnetic ordering in 2D hexagonal and 3D decagonal CPs 27

0.2.3. Enantiopure SCM 29

0.2.4. Multifunctional switching in a 3D CP with sponge-like dynamic behaviour 30

0.2.5. Selective gas and vapour sorption and magnetic sensing by a 3D CP 31

0.2.6. Luminescence and magnetic sensing in a 2D double-hexagonal CP 33

0.3. References 36

Part 1. Chiral Multifunctional PCPs

1.1. Introduction 45

1.1.1. Synthesis 45

1.1.1.1. Amino acids 46

1.1.1.2. Peptides 49

1.1.1.3. Proteins 51

1.1.1.4. Nucleobases 52

1.1.2. Properties and Applications 54

1.1.2.1. Biocompatibility and biomedical applications 55

1.1.2.2. Storage and delivery of biological gases: NO and H_2S 56

1.1.2.3. Biosensors 58

1.1.2.4. Biodegradability and stability 59

1.1.2.5. Chirality: enantioselective catalysis and separation 60

1.2. Previous work 64

1.3. Objectives 65

1.4. References 67

Part 1.A. Oxamato-based chiral PCPs

1.A.1. Synthetic Route 73

1.A.2. Physico-chemical Characterisation 78

1.A.2.1. Thermo-gravimetric study 78

1.A.2.2. Powder X-ray diffraction 79

1.A.3. Crystal Structures 80

1.A.3.1. Metalloligands 81

1.A.3.2. Porous Coordination Polymers (PCPs) 90

1.A.4. Physical Properties and Applications 106

1.A.4.1. Optical properties 106

1.A.4.2. Magnetic properties 109

1.A.4.3. Gas sorption properties 122

1.A.4.4. Enantiomeric separation 123

1.A.5. Discussion 125

1.A.6. References 127

Part 1.B. Oxamidato-based chiral PCPs

1.B.1. Synthetic Route 129

1.B.2. Physical Characterisation 132

1.B.2.1. Thermo-gravimetric study 132

1.B.2.2. Powder X-ray diffraction 134

1.B.3. Crystal Structures 137

1.B.3.1. Barium(II)-derived PCPs 137

1.B.3.2. Calcium(II)-derived PCPs 150

1.B.3.3. Lanthanide(III)-derived PCPs 155

1.B.4. Physical Properties and Applications 158

1.B.4.1. Optical properties 158

1.B.4.2. Gas sorption properties 160

1.B.4.3. Proton conductivity 169

1.B.4.4. Magnetic properties 179

1.B.5. Discussion 185

1.B.6. References 188

Part 2. Post-Synthetic Modifications

2.1. Introduction 193

2.1.1. Cation Exchange 193

2.1.2. Transmetalation 196

2.2. Previous work 201

2.3. Objectives 205

2.4. References 206

Parte 2.A. MMs obtained by Cation Exchange

2.A.1. Synthesis 209
2.A.2. Crystal Structure and Characterisation 210
2.A.3. Physical Properties 214
2.A.4. Discussion 220
2.A.5. References 221

Part 2.B. MMs obtained by Complex Encapsulation

2.B.1. Synthesis 223
2.B.2. Characterisation 224
2.B.3. Physical properties 227
2.B.4. Discussion 231
2.B.5. References 232

Part 2.C. MMs obtained by Transmetalation

2.C.1. Synthesis 233
2.C.2. Crystal Structure and Characterisation 234
2.C.3. Transmetalation mechanism 238
2.C.4. Physical properties 241
2.C.5. Discussion 247
2.C.6. References 249

3. Conclusions 251

Annex 1 255

Annex 2 289

Resumen 297

Publications

Abstract

The main goal of this Ph.D. Thesis concerns the design and synthesis of multifunctional materials which is one of the most challenging topics for chemists and physicists working together in the multidisciplinary field of Materials Chemistry. In order to do so, we have taken advantage of the new developments of the metallosupramolecular chemistry, in particular the molecular-programmed self-assembly methods that exploit the coordination preferences of the metal ions and the versatility of the tailored ligands. In this sense, we have chosen functionalised oxamato and oxamidato derivatives to build extended architectures which can exhibit interesting features, the control of the porosity being one of them. Our efforts have been devoted to prepare porous coordination polymers (PCPs) and investigate the introduction of new physical properties such as chirality, gas sorption and separation or magnetic properties, among others. In this respect, two separated research lines have been explored whose results are shown in Parts 1 and 2.

Part 1 deals with the development of a synthetic strategy to obtain chiral porous materials in an easy and effective manner. It consists of the functionalisation of enantiopure amino acids (alanine, valine, leucine and phenylglycine) whose encoded chiral information is efficiently transmitted to their derivatives and their different aliphatic residues play a non-negligible role in the self-assembling processes of the extended structures. In turn, Part 1 has been divided into Parts 1.A and 1.B, focusing on oxamate- and oxamidate-based compounds, respectively. Interestingly, both families of ligands gave rise to very different metalloligands and consequently, to a wide variety of fascinating chiral 3D frameworks which display interesting properties. In Part 1.A, we demonstrate that our metalloligand strategy represents an effective synthetic route to rationally prepare chiral PCPs, one of the unprecedented and striking result being the synthesis of a rod-like MOF from a preformed chiral 1D SBU. Among the oxamidato-derived PCPs shown in Part 1.B, we report a family of calcium(II)-derived PCPs which

serves as an excellent platform to study how the gas sorption and selectivity can be tailored by tuning the electron density of the channels of the PCPs, thus achieving an easy manner to separate, for instance, methane from longer hydrocarbons in natural gas.

Part 2 concerns the use of several post-synthetic methods (PSMs) to introduce new physical properties into preformed materials and thus to obtain multifunctional PCPs. In this chapter, we have explored three PSMs which are discussed in Parts 2.A, 2.B and 2.C. Taking advantage of the porous and anionic nature of the preformed PCPs and the resulting presence of counter-balancing cations within their 3D frameworks, we have performed the substitution of such cations and investigated the physical properties that the new materials show. In Part 2.A, we show how the exchange of the sodium(I) ions by lithium(I) and potassium(I) cations affords the derived PCPs which exhibit improved structural stability, gas sorption and magnetic properties. In Part 2.B, we are able to encapsulate a preformed iron(III) cationic complex within the pores of a PCP through cation exchange. This encapsulation results into interesting properties for both, the encapsulated complex and the original PCP. We go a step forward in Part 2.C and explore the substitution of not only the counter-balancing cations but also the metal ions constituting the coordination framework. Hence, we satisfactory exchange the diamagnetic magnesium(II) ions by paramagnetic cations from the first-transition row through transmetallation processes, affording two new magnetic materials which could not be prepared by direct synthesis.

“La actividad más noble de un ser humano es el conocer por conocer,
buscar respuestas a las leyes de la naturaleza”

José Bernabéu.

0. Introduction

0.1. Porous Coordination Polymers (PCPs)

Porous solids, possessing well-defined channels have been proven to be excellent candidates to overcome technological challenges. These materials exhibit fascinating properties and porosity lies at the origin of most of them. The presence of nanometre-sized pores provides with two main advantages. Firstly, the surface area of these materials is much higher than that of non-porous materials. Thus, interactions of the framework with the molecules, ions or atoms occur not only at the external surface but also throughout the whole bulk of the solid. Secondly, controlled porosity with a conscious design in terms of size, shape and functionality, provides with a very rich host-guest chemistry allowing an accurate manipulation of those molecules hosted in these pores. These two advantages clearly contribute to the development of Nanoscience and Nanotechnology, where functional low-density porous materials are increasingly being required to overcome current and future social needs.

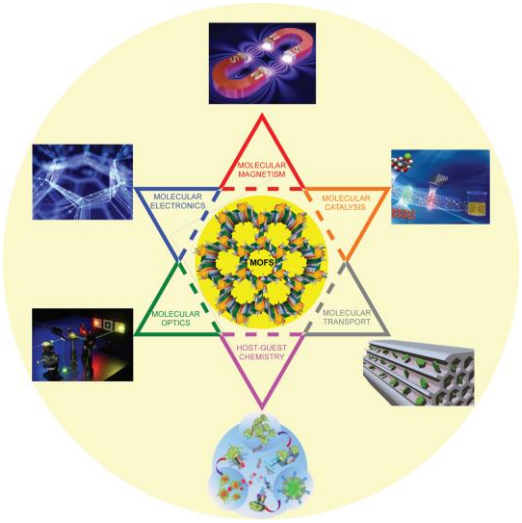

Figure 1. Some of the most relevant disciplines in which MOFs can be placed at the crossing point.

Such technological and scientific interests have motivated the vast efforts devoted during the last few decades to the design and preparation of new porous materials. Among these new materials, porous coordination polymers (PCPs), also termed metal-

organic frameworks (MOFs), are now at the *avant-garde* of current research as a consequence of their fine-tuneable features and properties. Although much work remains to be done in order to introduce MOFs in the industry, they are particularly promising materials in gas storage and separation[1,2], catalysis,[3] drug delivery,[4] sensor technology,[5] molecular recognition,[6] transport[7] and encapsulation,[8] among many others (see Figure 1).

0.1.1. Description

Amongst the different ways of defining a coordination polymer (CP) that can be found in the literature, two of them particularly sound, are highlighted here:

"A coordination polymer is an extended connection of metal and ligand monomers (where the nature of ligand is not defined) through coordination bonds with no regard toward the final structure or morphology".[9]

"A coordination polymer is a compound consisting of multiple units of a basic building block called coordination entity. A coordination entity is an ion or neutral molecule that is composed of a central atom, usually that of a metal, to which is attached a surrounding array of atoms or groups of atoms, each which is called a ligand".[10]

Both definitions share as common point that CPs contain two central components: single metal or metal-complex nodes and organic linkers. Although the main framework is constructed from these two starting reagents, other components such as blocking ligands, counterions and guest molecules, can also play a key role. The presence of both organic and inorganic parts leads to a huge number of advantages. One of the most significant deals with the design and control of the architecture and properties that the final framework will display. For this purpose, not only the right choice of the molecular units (metals and ligands with desirable features and functionalities) is required. Since the network connectivity of the building units will largely determine the properties of the CP, a good foresight as to how the assembling takes place also becomes crucial. In this sense, CPs appear as an excellent playground to study and understand the trends in

connectivity and the principles that govern the assembly of the frameworks. There are many factors influencing the formation of the network that occasionally prevent an accurate prediction of the final structure.

As mentioned above, the combination of both metal nodes and organic linkers, represent a fantastic tool for the design of the desired material. Therefore, after a careful selection of the organic ligand, the physical properties of the CP can, somehow, be modulated. Moreover, organic components provide the chemist with a wide variety of linking sites with tuned binding strength and directionality. The function of the metal node is equally relevant. A great variety of metal cations can participate in the framework. Depending on the metal and its oxidation state, different coordination numbers and geometries can be observed. In addition, when using a metal-complex as a node instead of a naked metal ion, a control of the bond angles and a restriction of coordination sites can be achieved. Besides, the use of blocking ligands (chelating or macrocyclic groups) can be also used to limit the available coordination sites. Overall, the diversity of organic components and metal ions or metal clusters and the many possible combinations between them, give rise to a myriad of CPs showing diverse and fascinating topologies and exhibiting significant properties.

Aiming at establishing a classification for the coordination compounds, one should consider that CPs extend into an infinite array. This definition automatically excludes discrete molecular complexes such as macrocycles ranging from molecular compounds such as rhomboids,[11] helicates,[12] triangles,[13,14] squares[15–17] and rectangles[18] and higher polygons;[19] as well as cages[20,21] and capsules[12,22,23] including cubic,[24,25] tetrahedral[26] and polyhedral structures,[27] among others. Some examples are shown in Figure 2.

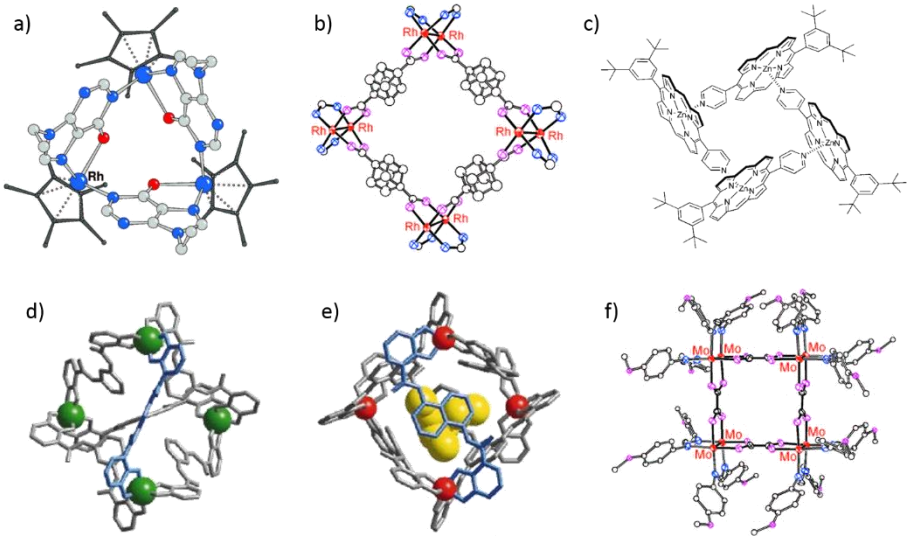

Figure 2. Examples of different metallamacrocycles: (a) trinuclear Rh(III) metallacycle using an hypoxanthine derivative as a linker;[28] (b) Rh_2 cubanedicarboxylate square;[29] (c) tetrameric Zn(II) square from a pyridyl derivative;[30] (d) Ga(III) tetrahedral cluster from a bis(catecholamide) ligand;[31] (e) Fe_4L_6 tetrahedral assembly with encapsulated Et_4N^+ shown in yellow;[32] (f) molecular square showing four Mo_2 units linked by four oxalate anions.[33]

Some of these assemblies display a rich host-guest chemistry, being capable of hosting ions or molecules in their cavities and thus, finding applications as receptors and molecular vessels for trapping reactive intermediates,[34] as well as for stoichiometric[35] and catalytic reactions.[36]

The self-assembly of well-defined and complex molecular clusters, as well as more simple coordination units like monomers, dimers, etc., through the formation of coordination bonds gives raise to infinite extended structures termed CPs that can be classified in one-, two- or three-dimensional entities (nD, n = 1-3). Some examples of the different type of CPs are illustrated in Figure 3.

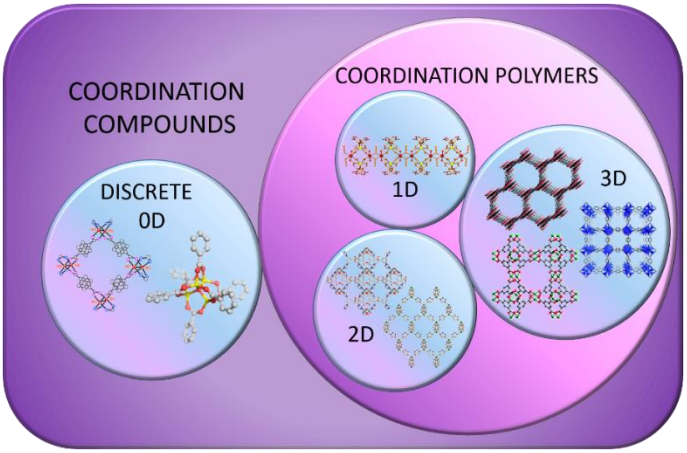

Figure 3. Classification of the CPs after their dimensionality.

CPs must be defined by coordinative bonds. So, multi-dimensional supramolecular architectures of metal complexes, which are linked by hydrogen bonds cannot be considered CPs (see the example of Figure 4). Within the family of CPs, those showing accessible porosity, are often called Metal-Organic Frameworks (MOFs).[37]

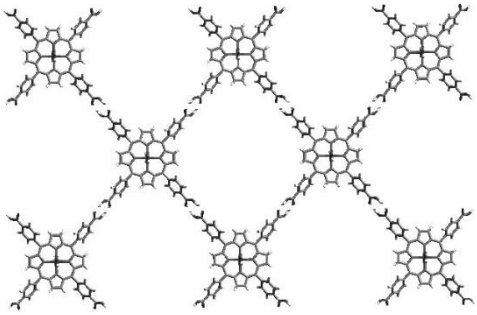

Figure 4. Metal-porphyrins assembling through carboxylic acid pairing, leading to a supramolecular 2D network.[38]

The design and chemistry for the preparation of both 0D coordination compounds and CPs are very similar, the only difference being that the use of the convergent ligands allows for to the former whereas the divergent ones lead to the latter. This approach is illustrated by Figure 5. Nevertheless, it has been observed that the same bridging ligand can generate either a coordination cluster or a CP.

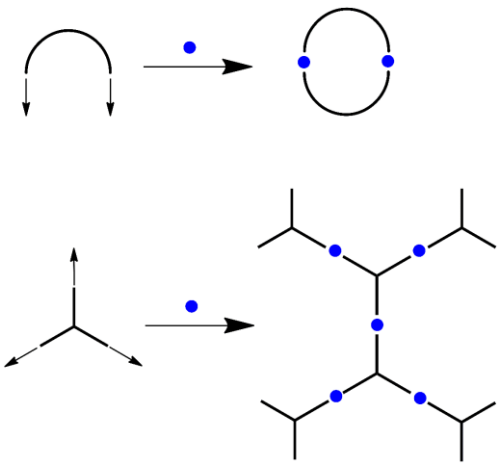

Figure 5. Formation of metallosupramolecules *vs* CPs through the use of convergent or divergent ligands.

In some cases, the formation of polymers is precluded by the use of capping chelating co-ligands on the metals, to restrict the coordination sites and prevent an infinite array extension. For example, the square supramolecule shown in Figure 6 is constructed from 4,4'-bipyridine (4,4'-bipy) and $[Pd^{II}(en)(NO_2)_2]$[39] (en = ethylenediamine) where en acts as blocking ligand. The same square motif is found in the 2D coordination network obtained from the same ligand with $[ZnSiF_6]_n$[40] (which lacks of capping ligand).

In some other cases, discrete polyhedral motifs can be isolated or incorporated into the networks depending on the synthetic conditions. For example, Eddaoudi and co-workers showed that the combination of Ni^{2+} ions and 4,5-imidazoledicarboxylic acid generates a $[M_8L_{12}]$ cube in an edge-directed assembly when a base such as dipiperidine is used to partially deprotonate the carboxylic acid[41] (Figure 7). Xu and co-workers later carried out the self-assembly of the

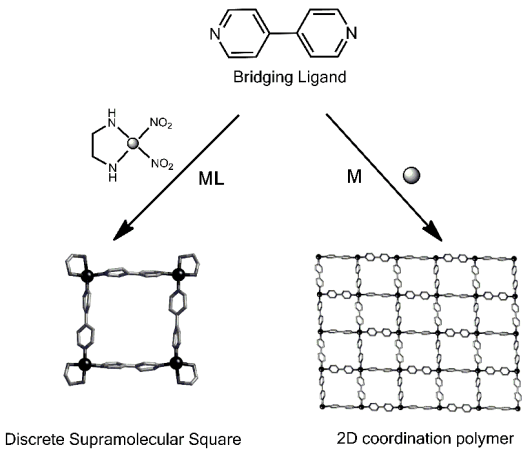

Figure 6. Use of end-cap ligands as an approach for the synthesis of metallosupramolecules (left) instead of polymers (right).

same ligand with Ni^{2+} in the presence of NaOH instead of dipiperidine. Due to the stronger basicity of NaOH, the ligand is totally deprotonated, giving rise to the formation of an extended framework which is also assisted by the coordination of the Na^{+} ions.[42]

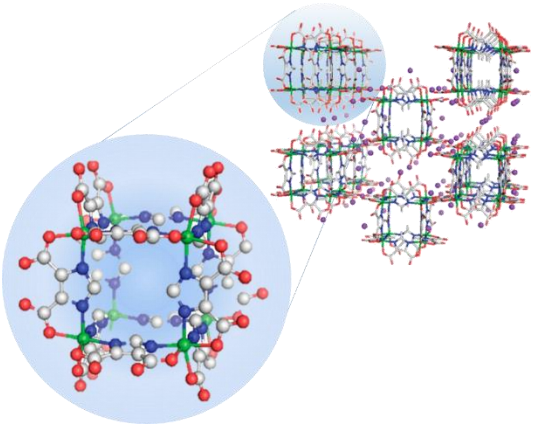

Figure 7. Representation of the discrete $[M_8L_{12}]$ cube synthetized by Eddaoudi and co-workers (left) and the extended cubic network through Na^{+} cations obtained by Xu and coworkers (right).

There is still a third possibility to go from discrete units to polymers. If suitable conditions can be found, capping ligands from the macromolecules could be replaced with bridging ligands to form networks (see Figure 8). Zhou and co-workers reported the synthesis of $[Cu_2(CDC)_2(DMA)(EtOH)]_6$ (CDC = 9H-carbazole-3,6-dicarboxylate and DMA = *N*,*N*-dimethylacetamide) which adopts a supramolecular octahedral topology.[43]

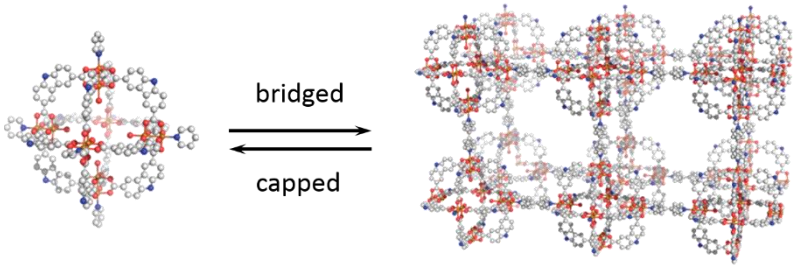

Figure 8. Paddlewheel complex of the type $[Cu_2(CDC)_2(DMA)_2(EtOH)]_6$ may be converted into a pyridine-capped analogue (left) or a 4,4'-bipy-bridged network (right).

When solutions of this paddlewheel precursor were treated with 4,4'-bipy; a two-fold interpenetrated framework was obtained. In addition, the framework could be deconstructed back to discrete polyhedra when dissolved in a DEF/pyridine (DEF = *N*,*N*-diethylformamide) solvent mixture. This last interconversion illustrates a good example of the reversibility of the coordinative bonds, which is a consequence of the lability of these interactions. This feature permits that errors in the assembly of a CP can be readily corrected during the growth. So, a periodic structure with crystallographic order can be obtained, allowing thus the structural determination through X-ray diffraction techniques and a correlation between its structure and properties.

0.1.2. Overview of History

Metal-cyanide compounds are among the earliest reports of CPs. The Prussian Blue pigment can be considered the very first CP of polymeric nature. It has been known and barely used since its first synthesis in the early 1700s,[44] and many investigations concerning its structure, bonding, and the origin of the blue colour were undertaken. It was in 1977 that a correct structure for the Prussian Blue was established by X-ray diffraction techniques[45] (see Figure 9). It is a mixed-valence iron(III) hexacyanoferrate(II) complex. The cubic 3D network is generated by alternating octahedral sites of iron(II) and iron(III) ions linked through cyanide ligands. Due to its intense blue colour, it was firstly used for dye-related[46] and analytical applications, but soon, researchers realised about the potential properties that Prussian

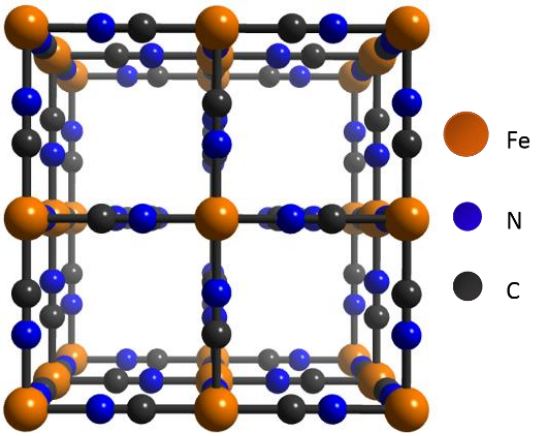

Figure 9. Framework structure of Prussian Blue of formula $Fe_4[Fe(CN)_6]_3 \cdot xH_2O$. Water molecules are omitted for clarity.[45]

Blue may show. The presence of both iron oxidation states leads to interesting applications as semiconductor and in electrochemistry.[47] Moreover, its porous structure affords a rich host-guest chemistry, showing an ability to catalyse reactions like the reduction of molecular oxygen[48] and to trap small molecules, e.g., radioactive thallium(I) and cesium(I) cations.[49] Finally, great attention has been paid since the starting hexacyanometalate complex can be prepared from a wide range of transition metal ions giving rise to an extensive family of metal-organic compounds of general formula $M_x[M_y(CN)_6]_n \cdot mH_2O$. These analogues possess interesting high-temperature magnetic properties, being possible to tune the magnetic ordering (Curie temperature) by a judicious choice of the metal ions.[50]

In 1897, Hoffman and co-workers prepared a coordination network resulting from the addition of benzene to a solution of $Ni(CN)_2$ in the presence of ammonia. However, the seminal work on these polymers could not progress faster due to the lack of structural characterisation techniques. The structure was fully understood fifty years later.[51] It consists of metal nodes linked by cyanide ligands extending into two dimensions and giving rise to benzene-containing channels between the parallel neutral layers. Thanks to this inspiring work and to the improvement of the characterisation techniques, many analogue materials were synthesised throughout the 1950s[51] and 1960s[52,53] by exploring alternative bridging ligands, metal centres and guests. Compounds of Hofmann clathrate type were thoroughly investigated by Iwamoto and co-workers (one of those is shown in Figure 10).[54–56] Moreover the term “coordination polymer” started to be mentioned in the literature during these two decades.[57]

During the next decades, several examples of CPs were reported. A turning point took place when the cyanide ligands started to be replaced by organic ligands leading to a huge variety of compounds.

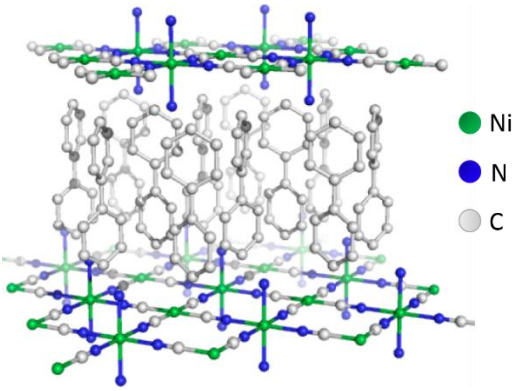

Figure 10. The structure of the Hoffman-type complex *trans*-{[Ni(μ-CN)$_4$Ni(NH$_3$)$_2$] · 2C$_{12}$H$_{10}$}$_n$.[56]

The research concerning this field attracted a great attention from the scientific community thanks to the work of Robson and co-workers in 1989.[58] They described the first example of a 3D framework (shown in Figure 11) consisting of tetrahedral copper(I) centres bridged by polyatomic rod-like segments. The extended network shows a diamond-like topology embracing relatively large adamantane-like cavities.

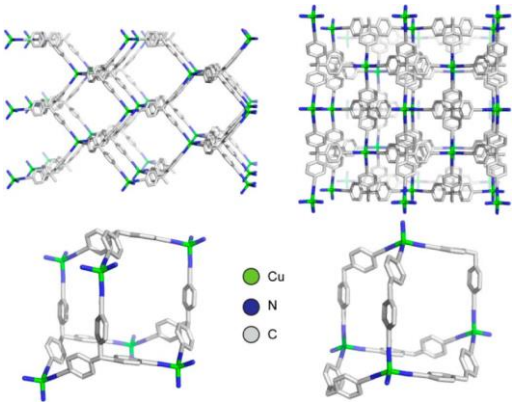

Figure 11. Different views of the 3D network consisting of tetrahedral centres linked together by rod-like units (top) and the repeating adamantanoid units (bottom).

Robson proposed a deliberate design and synthesis of a new class of solid materials showing infinite framework structures resembling scaffolding, which offer remarkable features that are listed here: (i) the relatively large size of the cavities found in the

framework even when using rods of modest length, along with the thermal and chemical stability, may afford unusual low-density materials; (ii) since diffusion of species is allowed throughout the structure, molecular sieve and ion exchange properties may be exhibited; and (iii) the possibility of the chemical functionalisation of the rods should be considered in order to introduce catalytic centres. The open structure should guarantee both an easy access of substrates to the catalytic sites and a ready release of the formed products. Thereby, potential materials for heterogeneous catalysis may be obtained.

Based on the visionary work of Robson on the design of frameworks showing scaffold-type structures and the striking properties that they may display, the exploration of the use of new types of ligands shot up. The choice of the ligand evolved to pyridyl-based donors, being 4,4'-bpy one of the most recurring ligands since it was a rigid linear ditopic donor suitable for a big variety of metals.

In 1995, Robson and co-workers reported a family of CPs prepared from building blocks containing 4-pyridyl ligands as donors.[59] Other teams like Fujita and collaborators also explored the pyridyl-based ligands. The same year, they reported a square grid material using 4,4-bpy (see Figure 12).[60] Moreover, unlike Robson, they studied the discrimination of isomers of aromatic compounds by clathrate formation, achieving the separation of the *orto*-isomers from the *meta*- and *para*-isomers. The catalysis for the cyanosilycation of aldehydes was also tested.

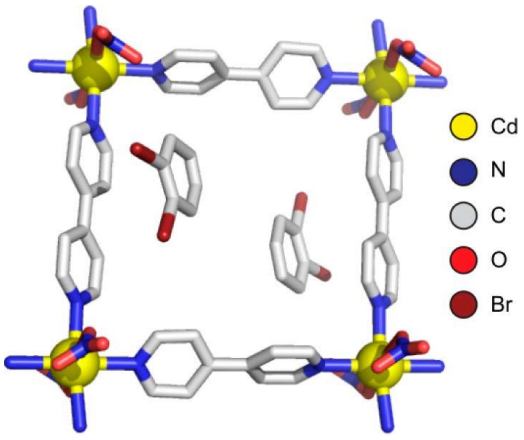

Figure 12. The structure of $[Cd(4,4'\text{-bpy})_2(NO_3)_2]_n$, a square grid displaying channels able to accommodate some aromatic guests with high shape specificity.

Motivated by the successful results so far, great efforts were paid to the search and test for ligands expanded toward polytopic donors, which could afford diverse geometries. Along this line, carboxylate–based materials became especially appealing. Different works by Kitagawa[61] and Yaghi[62] already included gas sorption isotherms and measurements proving the permanent porosity of the pyridyl-based and carboxylate-based CPs, respectively. The research done by these authors paved the way to the design and synthesis of a new class of materials which are "PCPs" and contributed to the understanding of the physical and chemical properties of the cavities and their use for molecular transformations and confinement. As mentioned above, this new type of CPs showing permanent porosity adopts the name "metal-organic framework" or MOF.

Kitagawa established a classification for PCPs based on the stability and dynamic nature of the frameworks (see Figure 13). He distinguished three categories, which he called "generations".

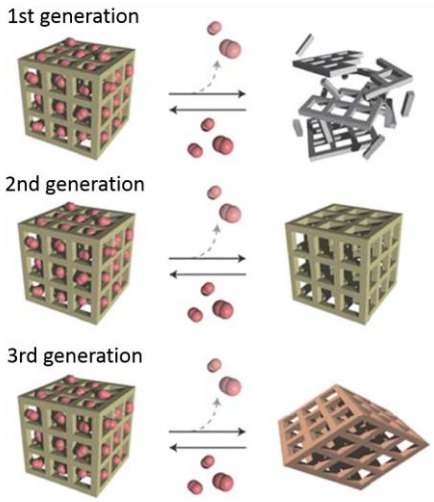

Figure 13. Classification of PCPs in three categories, proposed by Kitagawa.[137]

The first generation of compounds, which show a variety of porous structures, are sustained only with guest molecules and show irreversible framework collapse upon their removal. The second generation corresponds to stable and robust porous frameworks, which reversibly lose and readsorb guest molecules without undergoing any change of phase or morphology. Finally, the third generation refers to flexible and dynamic frameworks, which respond to external stimuli such as light, temperature, electric or magnetic field, pressure, guest molecules, etc., changing their pores reversibly.

The combination of the different dimensionality of the inorganic subnetwork with the concept of "breathing" introduced by Kitagawa (referred to the ability of PCPs to change their shape when responding to external stimuli), led him to distinguish six classes of dynamic frameworks.[63] The voids between the packed chains in the 1D class (Figure 14.I) are occupied by small sized molecules and can they exhibit ion exchange. The way the layers are stacked in the first type of 2D class (Figure 14. II) is strongly dependent on the nature of the guest and on the interaction they have with the layer. The interdigitated layers in the second case of 2D class (Figure 14.III) are superimposed and they form 1D channels which can open in presence of determined guests.

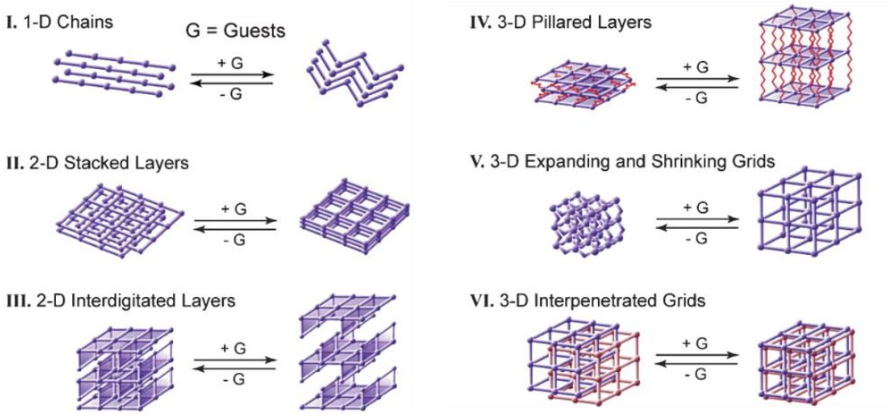

Figure 14. Scheme for dynamic PCPs categorized with structural dimensionalities.

Three situations can be observed in the 3D class: (i) in the first case (Figure 14.IV), pillared layers show channels that are flexible due to the non-rigid nature of the pillars and they may re-form in presence of guests even after their collapse; (ii) in the second type (Figure 14.V), expanding and contracting grids behave as dynamic sponges, reducing dramatically the volume responding to guest evacuation, and increasing it upon guest inclusion; (iii) finally, the third case of 3D concerns the interpenetrated grids, which are densely packed in the absence of guests and the adsorption of molecules causes a sliding of one network (Figure 14.VI)

0.1.3. Synthesis

In order to prepare a PCP, in principle, the only requirement is to react a potentially bridging ligand or a preformed building block with a metal ion. In other words, the PCP will precipitate from a solution of the precursors. Nevertheless, this procedure is more complicated as it could be thought. Many parameters such as the molar ratio and nature of the starting materials, concentration, pH, nature of the solvent, reaction time, temperature and pressure play a fundamental role in the formation of a determined structure. Both, a deep knowledge and a certain control of the reaction conditions are needed in order to induce the desired assembly of the building units precluding also the formation of poor quality crystals, reduced yields or even the formation of entirely new phases.

0.1.3.1. Conventional synthesis

Typically, the term conventional synthesis is applied to reactions which are carried out by conventional heating. The temperature of the reaction is one of the main parameters influencing the synthesis of PCPs, and two techniques are defined according to the temperature range: direct precipitation or non-solvothermal reactions and solvothermal ones. Direct precipitation or non-solvothermal reactions take place below or at the boiling point of the solvent under ambient pressure, feature which simplifies the synthetic requirements. Some very well-known MOFs such as MOF-5,[64] HKUST-1[65] or ZIF-8[66] have been obtained simply by mixing the starting materials at room temperature (see Figure 15). Aiming at obtaining highly crystalline phases, the corresponding building blocks can be slowly introduced to reduce the rate of crystallite nucleation by following different methods such as slow evaporation, layering or slow diffusion on one component solution into another one through a membrane, a gel or a H-shaped tube.

The direct precipitation method displays two advantages. Firstly, the reaction conditions are mild enough to ensure the maintenance of the integrity (functionality and conformation) of the building blocks. Some of them are very susceptible to the hard conditions employed in the solvothermal methods. In this respect, direct precipitation is a more versatile and low-cost technique. This feature directly leads to the second advantage, which is a better control of the final structure. Since the conditions are mild and it is possible to ensure the integrity of the entities, which have been deliberately designed in order to favour a given coordination mode and thus, a determined structure; a certain degree of control is then achieved.

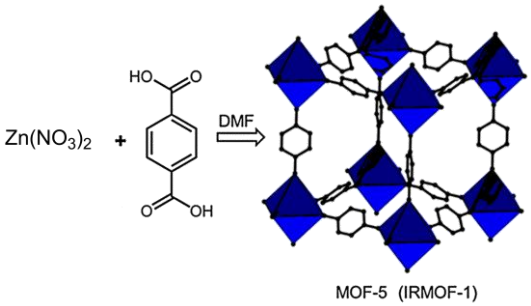

Figure 15. Schematic representation of the synthesis of MOF-5, which can be obtained by direct mixing the starting materials in presence of tetraethylammonium hydroxide and DMF.

The temperature of the reaction has a strong influence on the product formation and often, higher density structures are observed at greater temperatures. Moreover, some systems need an increase of the temperature of reaction in order to attain suitable crystallinity or to increase the reaction rates, especially if kinetically inert ions are used. When the working temperature is above the boiling point of the solvent, one is dealing with solvothermal methods. The precursors are usually combined in diluted conditions in polar solvents such as water, alcohols, acetone or acetonitrile, and heated in sealed vessels such as Teflon-lined stainless steel bombs or glass tubes generating autogenous pressure.

Solvothermal techniques display two main advantages. The need for more robust frameworks requires stronger metal-organic bonds. However, this requirement contrasts with the bond formation reversibility, which in turn, is needed to obtain thermodynamically crystalline stable products. One can overcome this problem when

working at higher temperatures, obtaining so highly stable ordered materials. Moreover, due to the harder conditions, new phases can be obtained. The second advantage implies that solubility of the precursors is not mandatory for the reaction to take place.

0.1.3.2. Alternative synthesis

As described above, the preparation of PCPs usually occur in presence of a solvent and at temperatures ranging from room temperature to *ca.* 200 °C. Commonly, conventional heating is the energy source. Alternatively, energy can also be introduced through other means such as electric potential,[67] ultrasound waves,[68] or microwave radiation.[69] The use of different energy sources can lead to new compounds that could not be obtained otherwise (see Figure 16). In addition, these alternative synthetic routes can afford compounds with different particle size and morphology, which can influence on the material properties. There are also some techniques involving the use of additives like ionic liquids[70] or surfactants.[71]

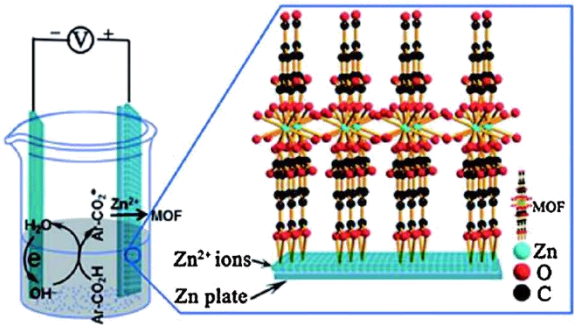

Figure 16. Schematic view of the electrochemical method consisting of applying voltage onto zinc electrodes in a 1,3,5-benzenetricarboxylic acid (H_3BTC) electrolyte affording fluorescent MOF films $[Zn_3(BTC)_2]$.[72]

0.1.3.3. Post-synthetic methods

In some cases, the different routes mentioned above display important limitations for the preparation of highly functionalised PCPs. Issues like limited solubility, thermal

and/or chemical stability of the precursors, functional group incompatibility, undesired reactions between ligand functional groups and metal ions, directly preclude the synthesis or yield unwanted products.

Similarly, adapting an established synthetic pathway to other metal ions is not always successful, since the size, the geometric restrictions at the coordination sphere and the electronic properties considerably differ from one metal ion to another one.

Fortunately, there are alternative approaches for introducing functional groups (and even molecules) into PCPs giving rise to novel functional materials. Post-synthetic methods (PSMs) have been used to achieve the heterogeneous chemical modification of a preassembled PCP affording new materials which could not be produced by direct synthesis. PCPs are excellent candidates to experience such modification since they contain organic ligands which can be easily tuned using the vast range of organic transformations, and metal nodes which offer an excellent platform to investigate the metal substitution and their influence on the final material.

PCPs can be post-synthetically modified in many diverse ways. Considering the many components susceptible of modification (the organic linker, the metal node, a whole building block, the counter ions in the case of charged PCPs and solvent molecules or guests), different classification of the PSMs are described in the literature.[73–75] At the most fundamental level, the desolvation of a PCP can be consider a PSM since the resultant structure differs from the parent one and displays different properties like usually a higher surface area. The exchange of guest molecules inside de pores, including extra-framework cations and anions is also a PSM. It has been demonstrated that these substitutions influence the pore dimensions and metrics, which can be translated into new or improved sorption and separation properties. Moreover, the exchanged molecules can introduce new functions depending on their nature (luminescence, ferroelectricity, catalysis, magnetic properties, etc).[76–79]

The most extensively studied PSM includes the modification of the linkers (*via* covalent modification, deprotection of linker functionality and electron addition or

reduction); and modification of the metal-containing nodes (*via* incorporation of pendant ligands to coordinatively unsaturated metal sites, grafting to oxygen atoms in metal-oxide nodes and attachment of metal ions or complexes at node oxygen sites). Nevertheless, beyond these well-known strategies, an approach consisting of the replacement of key structural components of the PCP is emerging. It is a conceptually different PSM known as *building block replacement* (BBR) involving (i) the solvent-assisted linker exchange (SALE),[80–82] (ii) the non-bridging ligand replacement or incorporation,[83] and (iii) the transmetalation[75,84–86] at the nodes or within the linkers. Examples of these three approaches are illustrated in Figure 17.

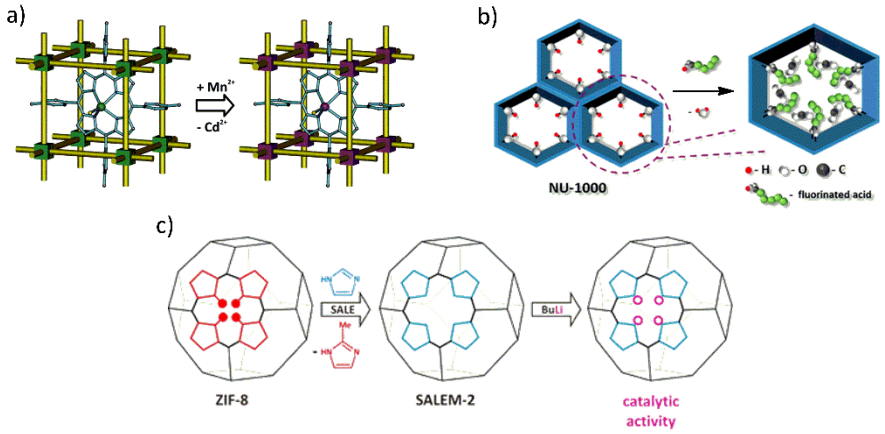

Figure 17. Examples of (a) transmetalation in the PCP porph@MOM-10[87], (b) ligand incorporation in the Zr-based MOF NU-1000[88] and (c) solvent-assisted linker exchange (SALE) of ZIF-8.[82]

Special attention will be paid to the transmetalation process since this technique has been used to synthesise part of the compounds shown in this Thesis. For this reason, this synthetic route will be further described in more detail.

0.1.4. Applications

The wide variety of synthetic methodologies has been crucial not only for the description of new structural motifs and architectures but also for the continuous discovery of new properties. PCPs are potential chemical objects to serve as multifunctional materials since they can combine the classical properties associated to their inherent porosity with the development of novel chemical and physical properties (magnetic, conductivity, catalytic and/or optical properties for instance). For this reason, PCPs are a promise for applications ranging from sensor technology and molecular recognition, proton conductors, magnetic semiconductors, gas storage and separation, drug transport and delivery, catalysis, etc. Among the myriad of applications, some of them have been highlighted and further described.

0.1.4.1. Catalysis

The high surface areas, tuneable pore size and shape, and high density of active sites within the very open structures of the PCPs make them excellent candidates as catalysts.

Three very different strategies have been followed to synthesise catalytically active PCPs. In the first approach, the metal-connecting points with unsaturated coordination environments are used as active sites.[89] These metal sites often have coordinated water or other solvent molecules that can be readily removed without distorting the framework structures. Alternatively, solvent displacement by incoming reactants may be enough to initiate the catalytic reaction at the metal site. In the second approach, catalytic sites are incorporated directly into the bridging ligands since the mild conditions typically used for the synthesis allow the direct incorporation of delicate functionalities.[90] Last but not least, the cavities of the PCP can also serve as the physical space in which catalytic species are encapsulated.[91]

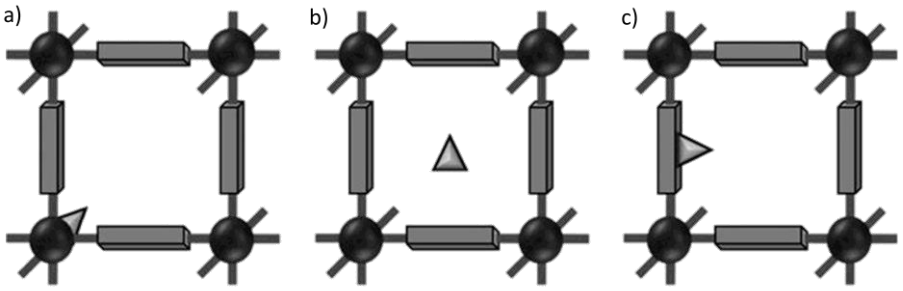

Figure 18. Illustrative examples of some of the strategies used to create MOFs with catalytically active moieties: (a) catalysis occurring at metal nodes; (b) catalysis driven by encapsulated species; (c) catalysis accomplished solely by metal-free organic linkers or facilitated by non-structural metal ions that are coordinated. The spheres, rectangles and triangles are the inorganic nodes, organic linkers and catalytic centres, respectively.

The possibility to introduce more than one active site in the structure (see Figure 18) allows the preparation of multifunctional PCPs. In this way, a material which contains simultaneously various types of functionalities (acid–base, metal–acid, metal–base or metal–metal) can be readily prepared where the catalytic sites are used cooperatively to perform multi-step transformations in one-pot.

0.1.4.2. Gas storage and separation

Among porous materials, PCPs appeal as exceptional candidates when searching for clean energy (hydrogen/methane) carriers[92,93] and greenhouse gas capturers.[1] Moreover, they are also suitable for water adsorption,[94] crucial for the development of industrial processes and for the uptake of hazardous compounds such as NO_x, SO_x, CO, H_2S, NH_3, organothiols, benzene and many others,[95] as well as industry wastes.

The reason because these materials have attracted increasing attention deals with the extraordinary chemical tuneability of the pore geometry and surface functionality, which can facilitate the control over adsorption selectivity, while their high surface areas generally give rise to a large separation working capacity. Due to the pore size and shape or to the presence of open metal or certain functionalisation on the pore surface, selectivity towards certain compounds occurs, and interesting separations apart from

gas separation,[2,96] can be performed. Remarkable examples are hydrocarbon[97,98] or chiral separation,[99] among others.

0.1.4.3. Drug Delivery

PCPs possess several potential advantages over conventional nanomedicines such as their structural and chemical diversity, their high loading capacity, and their intrinsic biodegradability, which have already shown them as a great promise for nanomedicine.[4,100] PCPs can be built up by carefully choosing the metal ions and connectivities chasing two main goals: the first one deals with the use of non-toxic metals and endogenous organic linkers to prepare biodegradable and toxicologically acceptable materials and the second one concerns the incorporation of adequate functions within the framework to carry out the medical application.

Some preliminary biomedical applications of PCPs have focused on their use as delivery vehicles for imaging contrast and therapeutic agents.[101–104] For these purposes, two strategies can be developed. The first approach consists of the direct incorporation of the imaging agent or the drug during the synthesis as a constitutive part of the PCP. Thus, when degradation occurs, the desired molecule could be released into the system. The second strategy is the encapsulation of biological molecules (including anticancer drugs or biogases) inside the pores and their controlled delivery taking advantage of the extremely high drug capacity of some PCP and the possibility to control the release time.[105,106] Moreover, the combination of both approaches could potentially lead to PCP-based theranostics, following drug delivery within the body through the imaging properties.

0.1.4.4. Sensing

Chemical sensors have been long used in many applications including quality controlling, emission and environment monitoring, detecting chemical threats and clinical diagnostics, among others. Ideal chemical sensors should be highly sensitive to analytes of interest and yet remain unperturbed by other molecules that may be present. Besides selectivity, they must exhibit sensitivity, response time, stability and reusability.

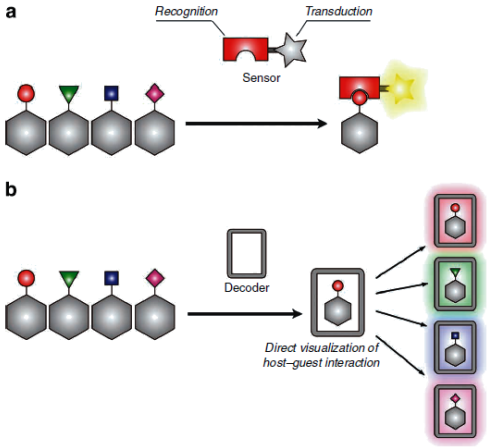

Figure 19. (a) Conventional molecular sensing protocol consisting of a recognition part and a transduction one. (b) Molecular decoding can also differentiate between the analytes by displaying a signal that corresponds to each one.

The excellent properties that PCPs display (e.g., stability, biodegradability, non-toxicity, high loading capacities, luminescence, versatility and facile introduction of specific functional groups *via* post-synthetic methods) make of these materials very promising tools for sensing diverse compounds including small molecules, solvents, pesticides, explosives and biological markers.[107–110] PCPs possess pores and channels which can transport and accommodate the analyte molecules to induce specific recognition due to the channel size and shape exclusion, specific coordination or hydrogen bonding of analytes to the framework, host-guest chemistry in the cavity or the chirality of the framework. The interaction of the analyte with the framework induces changes that can be detected and quantified (see figure 19). Therefore, the greater the interaction of the guest with the framework is, the lower limits of detection can be achieved.

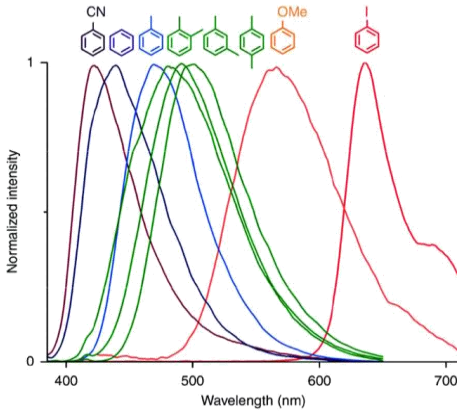

Figure 20. Height-normalized luminescent spectra of guest containing PCP upon excitation at 370 nm.

In particular, there are few PCPs properties which have been exploited for sensing applications such as, electrical-conduction, luminescence or magnetic properties. Thus, interesting examples of electrochemical,[111,112] luminescent [113–116] and magnetic sensors[117,118] are found in the literature. Among all the transduction techniques, luminescence has attracted a great attention because being a well-developed technique, it is highly visible to the naked eye and it exhibits extremely low detection limits.

The luminescence of PCPs can be very sensitive to physical and chemical stimulus such as ions, solvents, small molecules, vapours, pH, etc. The guest analytes interact with the framework altering its luminescence emission intensity and/or colour. Besides, generally the adsorbed species can be easily desorbed, which enables luminescent PCPs for non-destructive and recyclable sensing. The main advantage that PCPs offers among other luminescent materials lays in the possibility of rationally design the PCP with specific functional groups, appropriate pore sizes and tuneable electronic structures, giving rise to the desired luminescence and host-guest properties for the sensing application.

The work presented by Hupp and co-workers illustrates a fascinating example of luminescent PCP sensing.[119] They observe an intense turn-on emission by incorporating a class of aromatic compounds in the framework and the resulting luminescent colour is dependent on the chemical substituent of the aromatic guest (see Figure 20).

0.2. Oxamato-based CPs: previous results

During the last two decades, the field of molecular magnetism has attracted the attention of a large number of research teams worldwide due to its multidisciplinary character.[120] Our group has a large tradition in the design and synthesis of diverse molecule-based magnetic materials. Recently, the addition of another physical property to the magnetic ones has become an outstanding area of research in the field of molecular magnetism and it is at the origin of a new family of compounds, which are referred as multifunctional magnetic materials.[121]

The design and synthesis of this new class of hybrid compounds have largely benefited from the fast development of a well-known branch of coordination chemistry devoted to the study of extended metal-ligand networks, which are CPs. The combination of coordination and organic chemistry provides with the tools to build CPs of variable dimensionality with interesting and predictable structural topologies and properties.

Among the different strategies that can be followed envisioning the preparation of multifunctional magnetic coordination polymers (MMCPs), we used the so-called "complex-as-ligand" strategy, where a complex acts as a ligand (metalloligand) toward fully solvated paramagnetic metal ions or preformed complex whose coordination sphere is unsaturated. This is one of the most promising ways to combine different physical properties in a given material. This is a molecular-programmed method which consists of using a stable preformed metal complex with outer donor groups that can coordinate free metal ions or another preformed complex under "soft" conditions, aiming at controlling the net dimensionality and topology of the resulting CPs.

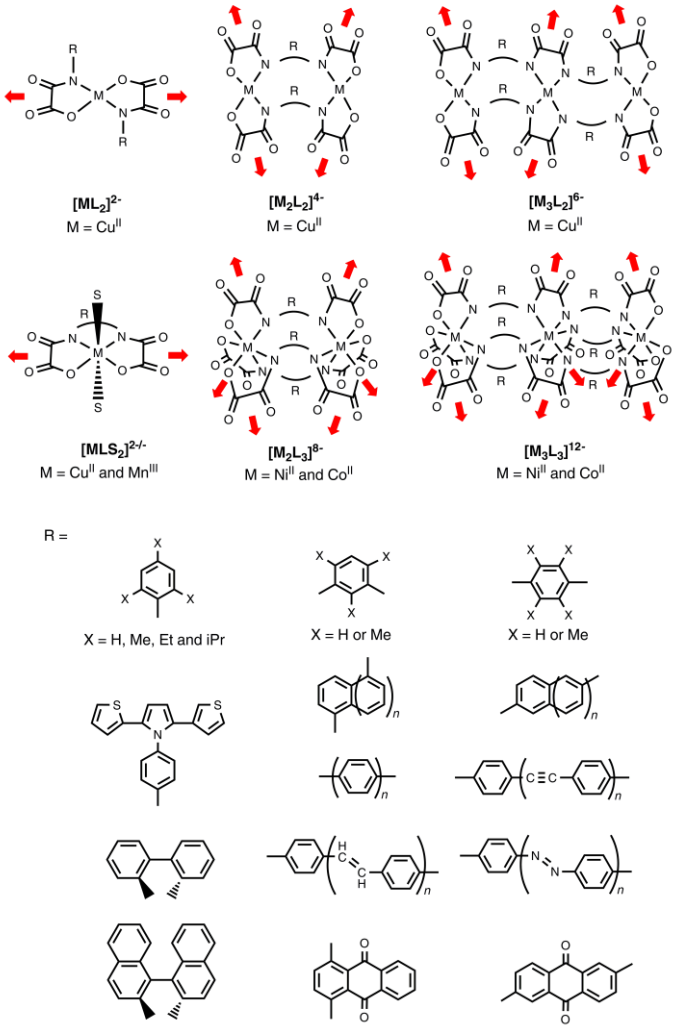

Scheme 1. Molecular libraries of oligonuclear aromatic oxamato complexes used as metalloligands (S stands for labile solvent molecules). The red arrows represent the free coordination sites to build the CPs.

The proper choice of the organic bridging ligand plays a key role for the design of the CPs and the incorporation of the desired properties. In so doing, our group has focused on a family of metalloligands formed by oligonuclear complexes with *N*-substituted aromatic oligo(oxamato) ligands (see Scheme 1). Their potential unique opportunities and advantages are highlighted here under:

(a) Firstly, the *N*,*O*-oxamato and *N*,*N*-oxamidato donor groups show a great coordination affinity toward divalent first-row transition metal ions (such as Cu^{II}, Ni^{II} and Co^{II}) forming very stable complexes in solution (mono-, di- and trinuclear species), the substitution by other divalent metal ions being thus precluded. This allows the formation in solution (and further isolation) of very robust building blocks that have additional binding ability towards other metal ions through the free carbonyl-oxygen atoms directing the synthesis in a programmed manner to afford heterobimetallic CPs with a wide diversity of architectures.

(b) The bis(bidentate) oxamato and oxamidato bridges mediate strong magnetic interactions between the neighbouring metal ions in its homo- and heterobimetallic compounds affording thus, interesting magnetic properties such as long-range 3D magnetic ordering and Single-Molecule Magnet (SMM) or Single-Chain Magnet (SCM) behaviours.

(c) In some cases, the oxamato-based magnets present anionic framework structures. This anionic nature together with the presence of large channels make them suitable candidates to obtain multifunctional materials, since different countercations bearing additional physical properties could be rationally introduced into the pores.

(d) Last but not least, is the fact that the oxamato ligands can be easily functionalised just by choosing the appropriate amine precursor allowing thus, an alternative route to induce new functionalities in the material such as chirality, luminescence, photo-, redox-activity and catalytic activity among others.[122–126]

Therefore, since the pioneering work by Kahn and co-workers in the late 1980s,[127–129] a wide variety of oxamato-based bimetallic compounds, both discrete complexes (0D) as well as extended nD (n = 1-3) CPs with interesting properties have been reported.

In order to illustrate the potential of the oxamato-based heterobimetallic CPs in the field of MMCPs, some examples highlighting not only the interesting magnetic properties that these bridging ligands can afford, but also the additional properties that have been introduced in these systems will be described right after.

0.2.1. Single-chain magnetic behaviour in linear 1D CPs

An oxamato-bridged heterobimetallic cobalt(II)-copper(II) linear chain of formula $\{[Co^{II}Cu^{II}(2,4,6\text{-}Me_3pa)_2(H_2O)_2] \cdot 4H_2O\}_n$, (2,4,6-Me$_3$pa = *N*-2,4,6-trimethylphenyloxamato) was prepared and magnetostructurally characterised (Figure 21).[130–132] The combination in this 1D CP of highly anisotropic *trans*-diaquabis(chelated) octahedral high-spin Co^{II} ions with the presence of the bulky trimethyl-substituted phenyl groups from the $[Cu^{II}(2,4,6\text{-}Me_3pa)_2]^{2-}$ precursor, affords an Ising-type chain magnetic anisotropy and large interchain separations. The minimisation of the though-space between this Ising chain is most likely responsible for the observation of the SCM behaviour at a low blocking temperature ($T_B \approx 2.0$ K) for the first time in a bimetallic ferrimagnetic chain.

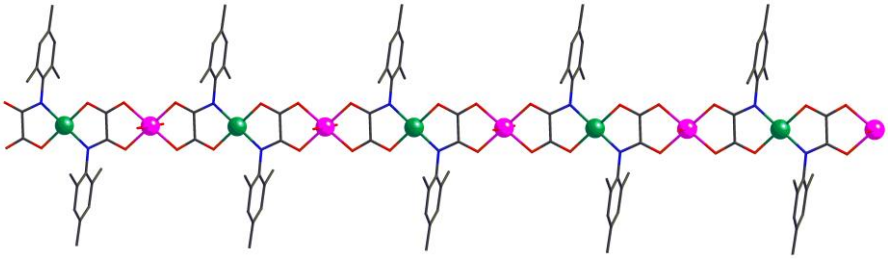

Figure 21. View of a fragment of the chain $\{[Co^{II}Cu^{II}(2,4,6\text{-}Me_3pa)_2(H_2O)_2] \cdot 4H_2O\}_n$ showing the *trans* arrangement of the bulky trimethyl-substituted phenyl groups. The Cu^{II} and Co^{II} atoms are depicted as green and purple spheres, respectively

0.2.2. Long-range magnetic ordering in 2D hexagonal and 3D decagonal CPs

By using the related pair of dianionic mononuclear copper(II) complexes $[Cu^{II}(Me_2pa)_2]^{2-}$ and $[Cu^{II}(Et_2pa)_2]^{2-}$ (2,6-Me$_2$pa = *N*-2,6-dimethylphenyloxamate and 2,6-Et$_2$pa = *N*-2,6-diethylphenyloxamate), as bis(bidentate) metalloligands towards Mn^{II} ions in dimethylsulphoxide (dmso) solution, two novel oxamato-bridged heterobimetallic 2D and 3D CPs of formulas (*n*-Bu$_4$N)$_4$[$Mn^{II}_4Cu^{II}_6$(2,6-Me$_2$pa)$_{12}$] · 2dmso (2D) and (*n*-

$Bu_4N)_4[Mn^{II}_4Cu^{II}_6(2,6\text{-}Et_2pa)_{12}]$ (3D) [*n*-Bu_4N^+ = tetra-*n*-butylammonium cation] were obtained (Figure 22).[133] Upon coordination, the corresponding $[Cu^{II}L_2]^{2-}$ precursor (L = 2,6-Me_2pa and 2,6-Et_2pa) transfers the steric information of its bulky dialkyl-substituted phenyl groups in *trans* arrangement into the stereochemistry of the tris(chelated) Mn^{II} metal centres yielding two coordination polymers of different dimensionality [2D (L = Me_2pa) and 3D (L = Et_2pa)] as a result of the different steric effects introduced by the methyl and ethyl substituents in the phenyl ring.

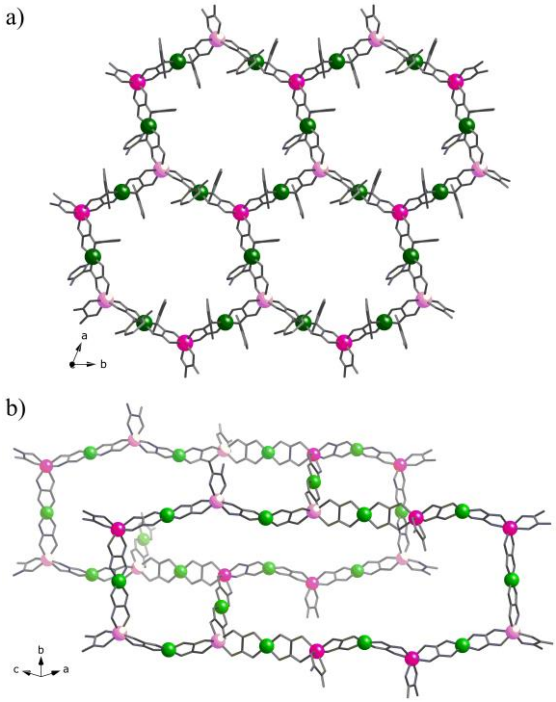

Figure 22. Perspective view of a fragment of (*n*-$Bu_4N)_4[Mn^{II}_4Cu^{II}_6(Me_2pma)_{12}]$· 2dmso (a) and (*n*-$Bu_4N)_4[Mn^{II}_4Cu^{II}_6(Et_2pma)_{12}]$ (b). Metal and ligand atoms are represented by balls and sticks, respectively [Cu, green; (Δ)-Mn, purple; (Λ)-Mn, pink].

As expected from the different dimensionality in these compounds, their magnetic properties drastically differ. Thus, although both 2D and 3D CPs exhibit magnetic ordering, the values of the Curie temperature (T_C) are quite different. So, a long-range ferromagnetic ordering occurs in the compound (*n*-$Bu_4N)_4[Mn^{II}_4Cu^{II}_6(Me_2pma)_{12}]$ ·

2dmso which results from the weak (most likely dipolar) ferromagnetic interactions between the ferrimagnetic $Mn^{II}_2Cu^{II}_3$ layers at T_C = 10 K. In contrast, the intrinsically three-dimensional character of the (*n*-$Bu_4N)_4[Mn^{II}_4Cu^{II}_6(Et_2pma)_{12}]$ complex allows the observation of a long-range ferrimagnetic order of the $Mn^{II}_2Cu^{II}_3$ decagonal net at a higher value of the critical temperature (T_C = 25 K).

0.2.3. Enantiopure SCM

In 2011,[134] our group proposed a rational enantioselective synthetic strategy to obtain chiral heterobimetallic chains based on the use of sterically-hindered, chiral dianionic mononuclear copper(II) complexes with the enantiomerically pure (*M*)-1,1'-binaphtalene-2,2'-bis(oxamato) [(*M*)-binaba] and (*P*)-1,1'-binaphtalene-2,2'-bis(oxamato) [(*P*)-binaba] ligands. This pair of *M* and *P* helical-type mononuclear copper(II) enantiomers, $[Cu[(M/P)\text{-binaba}]]^{2-}$, acting as bis(bidentate) metalloligands towards doubly *cis*-solvated (S = dmso and dmf), divalent transition metal cations like manganese(II) and cobalt(II) (M), transfer their chiral information to the stereochemistry of the octahedral M^{II} metal centres (Δ and Λ propeller-type enantiomers) in a controlled manner and consequently, a

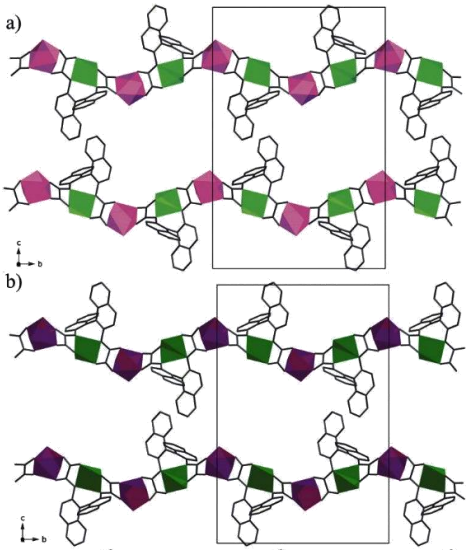

Figure 23. Views of the crystal packing of the chains of $[(M)\text{-}Cu^{II}\text{-}(\Lambda)\text{-}MnII]_n$ (a) and $[(P)\text{-}Cu^{II}\text{-}(\Delta)\text{-}Mn^{II}]_n$ (b) in the crystallographic *bc* plane. Hydrogen atoms and water molecules have been omitted for clarity. The (Λ)-Mn^{II} and (Δ)-Mn^{II} atoms are depicted as pale and dark purple polyhedra respectively, whereas the (*M*)-Cu^{II} and (*P*)-Cu^{II} atoms are drawn as pale and dark green polyhedra.

predetermination of the absolute configuration of the final $Cu^{II}M^{II}$ chain could be achieved.

Indeed, enantiopure chiral chains of general formula $MCuL(S)_m(H_2O)_n \cdot aS \cdot bH_2O$ made up by the repetition of the corresponding neutral chiral (*M*)-Cu^{II}-(Λ)-M^{II} and (*P*)-Cu^{II}-(Δ)-M^{II} units (Fig. 23a,b) were obtained when using the mononuclear (*M*)- and (*P*)-copper(II)-binaba complexes, respectively.

The enantiopure $Co^{II}Cu^{II}$ chains showed slow magnetic relaxation effects that are typical of SCMs, as revealed by the presence of a frequency-dependent peak around T_B = 2.0 K in the out-of-phase alternating current (ac) magnetic susceptibility measurements at very low temperatures. The bulky 1,1'-binaphtalene organic spacer of the (*M*/*P*/*rac*)-binaba ligand allows a good separation between neighbouring chains while the oxamato bridge transmit efficiently the antiferromagnetic interaction between the copper(II) and cobalt(II) ions.

0.2.4. Multifunctional switching in a 3D CP with sponge-like dynamic behaviour

We obtained a novel oxamato-based manganese(II)-copper(II) 3D CP of formula $[Na(H_2O)_4]_4\{Mn_4[Cu_2(mpba)_2(H_2O)_4]_3\} \cdot 56.5H_2O$ by the reaction of $Na_4[Cu_2(mpba)_2] \cdot 10H_2O$ and $Mn(NO_3)_2 \cdot 4H_2O$ in water.[135] This new example of MMCP exhibits a reversible solvent-induced optical, mechanical, and magnetic switching between a high- and a low-temperature ferromagnetic ordered phase upon loss of all the water molecules to give the amorphous dehydrated derivative $Na_4[Mn_4Cu_6(mpba)_6]$.

A crystalline-to-amorphous-like transition from $[Na(H_2O)_4]_4\{Mn_4[Cu_2(mpba)_2(H_2O)_4]_3\} \cdot 56.5H_2O$ to $Na_4[Mn_4Cu_6(mpba)_6]$ occurs upon removal of all crystallisation and weakly coordinated water molecules from by heating at 150 °C. This process is accompanied by a colour change of the crystals from bright to dark green and by a significant crystal contraction with an estimated change of volume of *ca.* 45%. These solvent-induced breathing-type dynamic effects suggest a reversible

collapse/reconstruction of the open-framework structure after water removal and retrieval from the pores, in agreement with the gas sorption studies. In this sense, the CO_2 and N_2 adsorption/desorption isotherms show almost no porosity, suggesting the collapse of the pore system upon dehydration.

In addition to these solvent-triggered mechanical and optical changes, a drastic variation of the temperature of the long-range ferromagnetic ordering was also observed as a function of the water contents. The alternating current (ac) magnetic susceptibility measurements confirm the occurrence of a long-range 3D ferromagnetic ordering at a critical temperature (T_c) of 22.5 K for the hydrated phase, this temperature being shifted to 2.3 K for the dehydrated derivative.

0.2.5. Selective gas and vapour sorption and magnetic sensing by a 3D CP

Porous magnets are very interesting materials which represent an excellent scenario to study the modulation of the magnetic properties of the host open-framework by the inclusion of selected guests such as solvents or gases through physi- or chemisorption processes, opening thus the way for future applications of porous magnets as magnetic sensors for host-guest molecular sensing.

By following the same strategy mentioned in the example above, but using the trimethyl derivative Me_3mpba^{2-} [Me_3mpba = *N,N'*-2,4,6-trimethyl-1,3-phenylenebis(oxamate)] instead, we prepared an isoreticular analogue of formula $[Na(H_2O)_{3.25}]_4\{Mn_4[Cu_2(Me_3mpba)_2(H_2O)_{3.33}]_3\} \cdot 37H_2O$ by the reaction of $Na_4[Cu_2(Me_3mpba)_2] \cdot 4H_2O$ and $Mn(NO_3)_2 \cdot 4H_2O$ in water (see Figure 24).[117]

The anhydrous phase $Na_4\{Mn_4[Cu_2(Me_3mpba)_2]_3\}$ exhibits a selective gas and vapour sorption behaviour together with a drastic variation of the long-range magnetic properties as a function of the adsorbed guest, constituting thus the first example of a genuine 3D porous magnet in the family of the oxamato-based CPs.

The accessible porosity of the anhydrous compound $Na_4\{Mn_4[Cu_2(Me_3mpba)_2]_3\}$ was also estimated by means of gas adsorption measurements, indicating a moderate CO_2/CH_4 gas selectivity. Vapour adsorption/desorption isotherms showed a considerable adsorption of some solvents like water and methanol, whereas under similar conditions, no vapour adsorption was observed for other solvents such as ethanol or acetonitrile. This fact indicated a large selectivity for the sorption of small molecules by this compound and suggested that both the kinetic diameter and the interaction with the network play a key role in the sorption process.

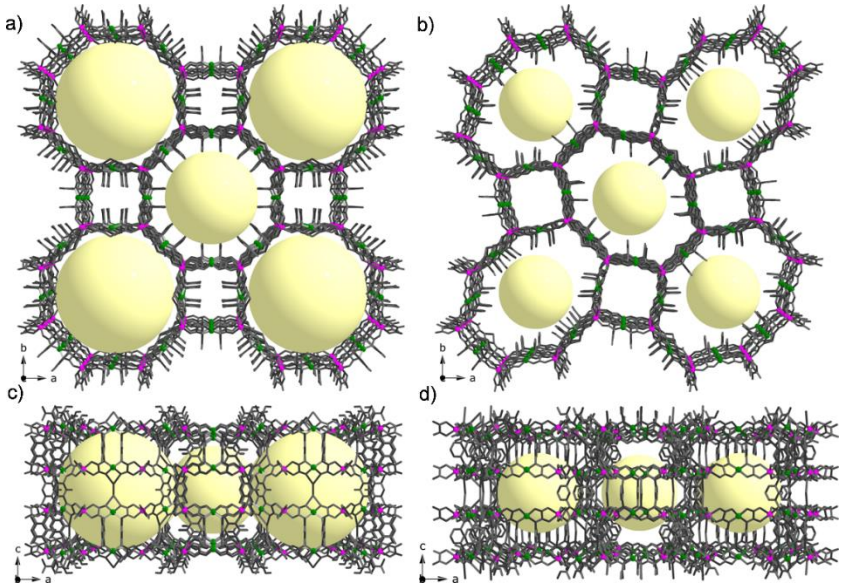

Figure 24. Projection views of the crystal packing of $[Na(H_2O)_{3.25}]_4\{Mn_4[Cu_2(Me_3mpba)_2(H_2O)_{3.33}]_3\} \cdot 37H_2O$ (a and c) and $[Na(H_2O)_4]_4\{Mn_4[Cu_2(mpba)_2(H_2O)_4]_3\} \cdot 56.5H_2O$ (b and d) along the crystallographic *c* and *b* axes emphasising the different pore size distribution of the octagonal pores of the open-framework structure. Metal and ligand atoms are shown as balls and sticks, respectively. The void spaces, copper(II) and manganese(II) are represented by pale yellow, green and purple spheres, respectively.

0.2.6. Luminescence and magnetic sensing in a 2D double-hexagonal CP

A novel manganese(II)-copper(II) 2D compound of formula $MV[Mn_2Cu_3(mpba)_3(H_2O)_3] \cdot 20H_2O$, ($MV^{2+}$ is the methylviologen dicationic dye illustrated in Scheme 2) was prepared and characterised by our group.[136] This compound exhibits highly selective gas sorption ability, luminescence capacity, and long-range magnetic ordering, constituting thus a unique example of luminescent porous magnet with potential applications in host-guest chemical sensing of small molecules. In fact, a unique optical and magnetic switching behaviour is observed accompanying reversible solvation/desolvation and gas sorption/desorption processes.

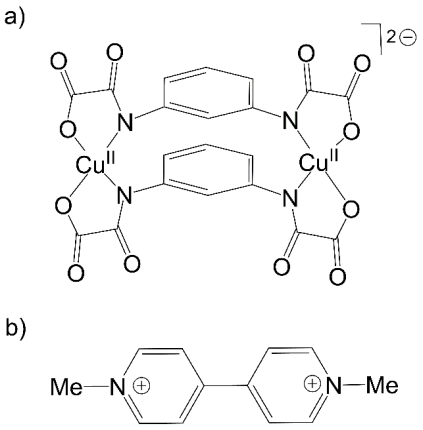

Scheme 2. (a) Tetrakis(bidentate) dicopper(II) anionic unit and (b) templating methylviologen countercation.

The crystal structure reveals an anionic 2D bimetallic network built from tetrakis(bidentate) square pyramidal dicopper(II) anions, $[Cu_2(mpba)_2(H_2O)_2]^{4-}$, and tris(chelated) octahedral manganese(II) ions with alternating opposite chirality (Δ and Λ), together with the methylviologen dye MV^{2+} as templating countercation and water molecules of crystallisation (see Scheme 2). The 2D network consists of double oxamato-bridged Mn^{II}_2-Cu^{II}_3 hexagonal layers interconnected through two *m*-phenylene spacers between Cu^{II} ions (see Figure 25). The double layers grow in the *ac* plane and they are stacked along the crystallographic *b* axis. Overall, this situation leads to small hexagonal nanopores which are occupied by water molecules.

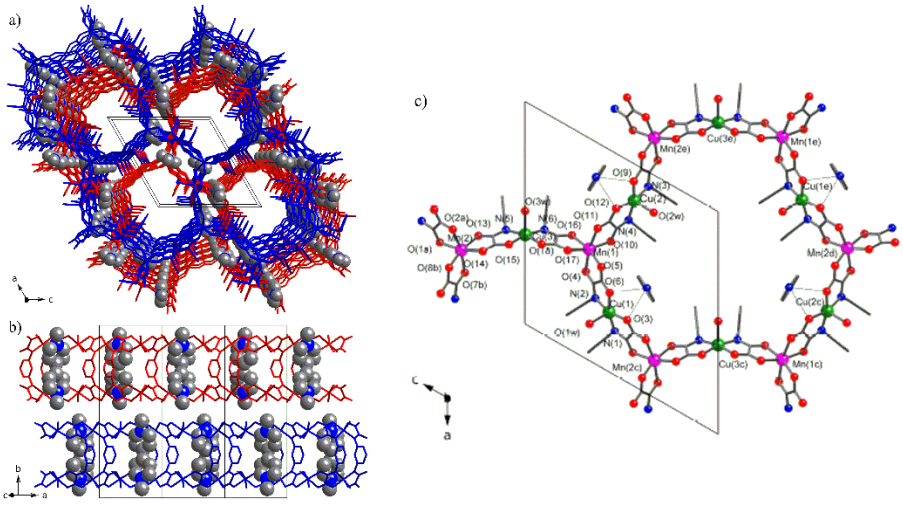

Figure 25. (a) and (b) Perspective views of the crystal packing of the adjacent double layers along the crystallographic *c* and *b* axes, respectively. The MV^{2+} countercations are represented as grey spheres. The water molecules have been omitted for clarity. (c) View of the asymmetric unit of **1** with the atom labelling scheme [symmetry codes: (a) = x, y, z – 1; (b) = x – 1, y, z – 1; (c) = x, y, z + 1; (d) = x + 1, y, z + 2; (e) = x + 1, y, z + 1]. The dashed lines represent the van der Waals and/or electrostatic interactions between the carboxylate-oxygen atoms of the anionic network and the pyridinium-nitrogen atoms of the organic countercations. Hydrogen atoms are omitted for clarity.

The study of the influence of the sorption of small molecules like solvent vapours and gases by this porous material revealed a unique magnetic and luminescent switching behaviour, which can be summarised as follows:

(i) The active anhydrous $MV[Mn_2Cu_3(mpba)_3]$ phase shows a long-range ferromagnetic ordering at a rather low critical temperature (T_C) of 2.0 K. Upon solvent vapour adsorption, the magnetic ordering temperature progressively shifts towards higher values depending on the adsorbed guest molecule: MeOH ($T_C \approx 5.0$ K) and H_2O ($T_C \approx 19.0$ K).

(ii) The active anhydrous phase $MV[Mn_2Cu_3(mpba)_3]$ shows bright UV and visible light emissions at 330 and 586 nm, which make it the first example of an oxamato-based luminescent magnet reported in the literature. The presence of highly ordered MV^{2+} cations filling the nanopores of this material afforded the observed luminescent properties. The most interesting feature, however, lies in the fact that a clear blue-shift

of the lower energy visible emission from 586 to 544 nm occurs upon rehydration at 33% water loading. In addition, a good linear relationship is found between the shift of the emission wavelength and the degree of the framework hydration. The observed solvent-induced variation of the luminescence properties strongly supports the occurrence of small changes in the Cu^{II}-MV^{2+} distance during the adsorption-desorption processes.

(iii) The active anhydrous $MV[Mn^{II}_2Cu^{II}_3(mpba)_3]$ phase shows a relatively large and selective gas adsorption for CO_2 against CH_4. Moreover, a considerable red-shift is observed when CO_2 is adsorbed. For a CO_2/CH_4 mixture, the results are similar to those obtained with pure CO_2 demonstrating that CO_2 can be detected in the presence of non-adsorbing gases (like methane or others). These results highlight the high selectivity of this material as a CO_2 sensor, even in the presence of other analytes. Another relevant feature of this 2D material is that the adsorption of CO_2 results in a clear red-shift emission, whereas the presence of H_2O and CH_3OH in the framework produces a blue-shift emission. This is likely due to the differences in the specific adsorption sites for CO_2, CH_3OH and H_2O and to the different adsorption capacity for these adsorbates. Therefore, this system is not only adsorption loading sensitive but also specific, allowing the identification of adsorbates.

0.3. References

1 G. Férey, C. Serre, T. Devic, G. Maurin, H. Jobic, P. L. Llewellyn, G. De Weireld, A. Vimont, M. Daturi and J.-S. Chang, *Chem. Soc. Rev.*, 2011, **40**, 550–562.

2 J.-R. Li, R. J. Kuppler and H.-C. Zhou, *Chem. Soc. Rev.*, 2009, **38**, 1477–504.

3 A. Corma, H. García and F. X. Llabrés i Xamena, *Chem. Rev.*, 2010, **110**, 4606–4655.

4 P. Horcajada, R. Gref, T. Baati, P. K. Allan, G. Maurin, P. Couvreur, G. Férey, R. E. Morris and C. Serre, *Chem. Rev.*, 2012, **112**, 1232–1268.

5 L. E. Kreno, K. Leong, O. K. Farha, M. Allendorf, R. P. Van Duyne and J. T. Hupp, *Chem. Rev.*, 2012, **112**, 1105–25.

6 Y. Inokuma, M. Kawano and M. Fujita, *Nat. Chem.*, 2011, **3**, 349–358.

7 S. Horike, D. Umeyama and S. Kitagawa, *Acc. Chem. Res.*, 2013, **46**, 2376–2384.

8 G. Lu, S. Li, Z. Guo, O. K. Farha, B. G. Hauser, X. Qi, Y. Wang, X. Wang, S. Han, X. Liu, J. S. DuChene, H. Zhang, Q. Zhang, X. Chen, J. Ma, S. C. J. Loo, W. D. Wei, Y. Yang, J. T. Hupp and F. Huo, *Nat. Chem.*, 2012, **4**, 310–316.

9 J. L. C. Rowsell and O. M. Yaghi, *Microporous Mesoporous Mater.*, 2004, **73**, 3–14.

10 D. T. Connelly Neil G., *Nomenclature of Inorganic Chemistry – IUPAC Recommendations 2005*, 2005, vol. 27.

11 M. Fujita, J. Yazaki and K. Ogura, *J. Am. Chem. Soc.*, 1990, **112**, 5645–5647.

12 M. Fujita, *Chem. Soc. Rev.*, 1998, **27**, 417–425.

13 R.-D. Schnebeck, E. Freisinger and B. Lippert, *Angew. Chemie Int. Ed.*, 1999, **38**, 168–171.

14 E. Zangrando, M. Casanova and E. Alessio, *Chem. Rev.*, 2008, **108**, 4979–5013.

15 R. V Slone, D. I. Yoon, R. M. Calhoun and J. T. Hupp, *J. Am. Chem. Soc.*, 1995, **117**, 11813–11814.

16 P. J. Stang and K. Chen, *J. Am. Chem. Soc.*, 1995, **117**, 1667–1668.

17 P. J. Stang and B. Olenyuk, *Angew. Chemie Int. Ed. English*, 1996, **35**, 732–736.

18 P. Thanasekaran, R.-T. Liao, Y.-H. Liu, T. Rajendran, S. Rajagopal and K.-L. Lu, *Coord. Chem. Rev.*, 2005, **249**, 1085–1110.

19 P. J. Stang, N. E. Persky and J. Manna, *J. Am. Chem. Soc.*, 1997, **119**, 4777–4778.

20 M. Fujita, S. Nagao and K. Ogura, *J. Am. Chem. Soc.*, 1995, **117**, 1649–1650.

21 T. Kusukawa and M. Fujita, *J. Am. Chem. Soc.*, 1999, **121**, 1397–1398.

22 B. Olenyuk, A. Fechtenkötter and P. J. Stang, *J. Chem. Soc. Dalt. Trans.*, 1998, 1707–1728.

23 S. Leininger, B. Olenyuk and P. J. Stang, *Chem. Rev.*, 2000, **100**, 853–908.

24 J. Lang, Q. Xu, Z. Chen and B. F. Abrahams, *J. Am. Chem. Soc.*, 2003, **125**, 12682–12683.

25 K. Suzuki, M. Tominaga, M. Kawano and M. Fujita, *Chem. Commun.*, 2009, 1638–1640.

26 M. D. Ward, *Chem. Commun.*, 2009, 4487–4499.

27 B. Olenyuk, J. A. Whiteford, A. Fechtenkötter and P. J. Stang, *Nature*, 1999, **398**, 796–799.

28 D. P. Smith, E. Baralt, B. Morales, M. M. Olmstead, M. F. Maestre and R. H. Fish, *J. Am. Chem. Soc.*, 1992, **114**, 10647–10649.

29 F. A. Cotton, L. M. Daniels, C. Lin, C. a Murillo and S.-Y. Yu, *J. Chem. Soc. Dalt. Trans.*, 2001, **40**, 502–504.

30 A. Tsuda, T. Nakamura, S. Sakamoto, K. Yamaguchi and A. Osuka, *Angew. Chemie Int. Ed.*, 2002, **41**, 2817–2821.

31 D. L. Caulder, C. Brückner, R. E. Powers, S. König, T. N. Parac, J. A. Leary and K. N. Raymond, *J. Am. Chem. Soc.*, 2001, **123**, 8923–8938.

32 D. L. Caulder, R. E. Powers, T. N. Parac and K. N. Raymond, *Angew. Chemie Int. Ed.*, 1998, **37**, 1840–1843.

33 F. A. Cotton, C. Lin and C. A. Murillo, *Acc. Chem. Res.*, 2001, **34**, 759–771.

34 Y. Nishioka, T. Yamaguchi, M. Yoshizawa and M. Fujita, *J. Am. Chem. Soc.*, 2007, **129**, 7000–7001.

35 M. Yoshizawa, Y. Takeyama, T. Kusukawa and M. Fujita, *Angew. Chemie Int. Ed.*, 2002, **41**, 1347–1349.

36 S. J. Lee, A. Hu and W. Lin, *J. Am. Chem. Soc.*, 2002, **124**, 12948–12949.

37 L. Öhrström, *Crystals*, 2015, **5**, 154–162.

38 C. B. Aakeröy and A. M. Beatty, *Aust. J. Chem.*, 2001, **54**, 409–421.

39 M. Fujita, M. Tominaga, A. Hori and B. Therrien, *Acc. Chem. Res.*, 2005, **38**, 369–378.

40 R. W. Gable, B. F. Hoskins and R. Robson, *J. Chem. Soc., Chem. Commun.*, 1990, **53**, 1677–1678.

41 Y. Liu, V. Kravtsov, R. D. Walsh, P. Poddar, H. Srikanth and M. Eddaoudi, *Chem. Commun.*, 2004, **299**, 2806–2807.

42 R.-Q. Zou, L. Jiang, H. Senoh, N. Takeichi and Q. Xu, *Chem. Commun.*, 2005, **1**, 3526–3528.

43 J.-R. Li, D. J. Timmons and H.-C. Zhou, *J. Am. Chem. Soc.*, 2009, **131**, 6368–6369.

44 *Misc. Berolinensia ad incrementum Sci.*, 1710, **1**, 377–378.

45 H. J. Buser, D. Schwarzenbach, W. Petter and A. Ludi, *Inorg. Chem.*, 1977, **16**, 2704–2710.

46 M. Ware, *Cyanomicon. History, science and art of cyanotype: photographic printing in Prussian blue*, 2014.

47 V. D. Neff, *J. Electrochem. Soc.*, 1978, **125**, 886–887.

48 K. Itaya, N. Shoji and I. Uchida, *J. Am. Chem. Soc.*, 1984, **106**, 3423–3429.

49 D. F. Thompson, *Ann. Pharmacother.*, 2004, **38**, 1509–1514.

50 K. R. Dunbar and R. a Heintz, *Chemistry of Transition Metal Cyanide Compounds: Modern Perspectives*, 1997, vol. 45.

51 J. H. Rayner and H. M. Powell, *J. Chem. Soc.*, 1952, 319–328.

52 S. Block, B. P.; Roth, E. S.; Schaumann, C. W.; Simkin, J.; Rose and H., *J. Am. Chem. Soc.*, 1962, **84**, 3200–3201.

53 T. Iwamoto, T. Nakano, M. Morita, T. Miyoshi, T. Miyamoto and Y. Sasaki, *Inorganica Chim. Acta*, 1968, **2**, 313–316.

54 T. Miyoshi, T. Iwamoto and Y. Sasaki, *Inorg. Nucl. Chem. Lett.*, 1970, **6**, 21–24.

55 T. Miyoshi, T. Iwamoto and Y. Sasaki, *Inorganica Chim. Acta*, 1973, **7**, 97–101.

56 T. Iwamoto, T. Miyoshi and Y. Sasaki, *Acta Crystallogr. Sect. B Struct. Crystallogr. Cryst. Chem.*, 1974, **30**, 292–295.

57 J. C. J. Bailar, *Preparative Inorganic Reactions*, John Wiley & Sons, New York, 1964.

58 B. Hoskins and R. Robson, *J. Am. Chem. Soc.*, 1989, **111**, 5962–5964.

59 S. R. Batten, B. F. Hoskins and R. Robson, *J. Am. Chem. Soc.*, 1995, **117**, 5385–5386.

60 M. Fujita, Y. J. Kwon, S. Washizu and K. Ogura, *J. Am. Chem. Soc.*, 1994, **116**, 1151–1152.

61 M. Kondo, T. Yoshitomi, K. Seki, H. Matsuzaka and S. Kitagawa, *Angew. Chemie Int. Ed. English*, 1997, **36**, 1725–1727.

62 H. Li, M. Eddaoudi, T. L. Groy and O. M. Yaghi, *J. Am. Chem. Soc.*, 1998, **120**, 8571–8572.

63 S. Kitagawa and K. Uemura, *Chem. Soc. Rev.*, 2005, **34**, 109–119.

64 L. Huang, *Microporous Mesoporous Mater.*, 2003, **58**, 105–114.

65 L. H. Wee, M. R. Lohe, N. Janssens, S. Kaskel and J. a. Martens, *J. Mater. Chem.*, 2012, **22**, 13742–13746.

66 S. R. Venna, J. B. Jasinski and M. A. Carreon, *J. Am. Chem. Soc.*, 2010, **132**, 18030–18033.

67 H. Al-Kutubi, J. Gascon, E. J. R. Sudhölter and L. Rassaei, *ChemElectroChem*, 2015, **2**, 462–474.

68 V. Safarifard and A. Morsali, *Coord. Chem. Rev.*, 2015, **292**, 1–14.

69 N. A. Khan and S. H. Jhung, *Coord. Chem. Rev.*, 2015, **285**, 11–23.

70 H. M. Yang, X. L. Song, T. L. Yang, Z. H. Liang, C. M. Fan and X. G. Hao, *RSC Adv.*, 2014, **4**, 15720–15726.

71 T.-Y. Ma, H. Li, Q.-F. Deng, L. Liu, T.-Z. Ren and Z.-Y. Yuan, *Chem. Mater.*, 2012, **24**, 2253–2255.

72 W.-J. Li, J. Lü, S.-Y. Gao, Q.-H. Li and R. Cao, *J. Mater. Chem. A*, 2014, **2**, 19473–19478.

73 A. D. Burrows, in *Metal Organic Frameworks as Heterogeneous Catalysts*, 2013, pp. 31–75.

74 S. M. Cohen, *Chem. Rev.*, 2012, **112**, 970–1000.

75 J. D. Evans, C. J. Sumby and C. J. Doonan, *Chem. Soc. Rev.*, 2014, **43**, 5933–5951.

76 D. Himsl, D. Wallacher and M. Hartmann, *Angew. Chem. Int. Ed. Engl.*, 2009, **48**, 4639–42.

77 J. An and N. L. Rosi, *J. Am. Chem. Soc.*, 2010, **132**, 5578–9.

78 E. Quartapelle Procopio, F. Linares, C. Montoro, V. Colombo, A. Maspero, E. Barea and J. a. R. Navarro, *Angew. Chemie*, 2010, **122**, 7466–7469.

79 Z.-J. Lin, T.-F. Liu, Y.-B. Huang, J. Lü and R. Cao, *Chemistry*, 2012, **18**, 7896–902.

80 O. Karagiaridi, W. Bury, A. a. Sarjeant, C. L. Stern, O. K. Farha and J. T. Hupp, *Chem. Sci.*, 2012, **3**, 3256–3260.

81 O. Karagiaridi, W. Bury, E. Tylianakis, A. A. Sarjeant, J. T. Hupp and O. K. Farha, *Chem. Mater.*, 2013, **25**, 3499–3503.

82 O. Karagiaridi, M. B. Lalonde, W. Bury, A. A. Sarjeant, O. K. Farha and J. T. Hupp, *J. Am. Chem. Soc.*, 2012, **134**, 18790–18796.

83 B. J. Burnett, P. M. Barron, C. Hu and W. Choe, *J. Am. Chem. Soc.*, 2011, **133**, 9984–9987.

84 C. K. Brozek and M. Dincă, *J. Am. Chem. Soc.*, 2013, **135**, 12886–12891.

85 M. Lalonde, W. Bury, O. Karagiaridi, Z. Brown, J. T. Hupp and O. K. Farha, *J. Mater. Chem. A*, 2013, **1**, 5453.

86 L. Bellarosa, C. K. Brozek, M. García-Melchor, M. Dincă and N. López, *Chem. Mater.*, 2015, **27**, 3422–3429.

87 Z. Zhang, L. Zhang, L. Wojtas, P. Nugent, M. Eddaoudi and M. J. Zaworotko, *J. Am. Chem. Soc.*, 2012, **134**, 924–927.

88 P. Deria, J. E. Mondloch, E. Tylianakis, P. Ghosh, W. Bury, R. Q. Snurr, J. T. Hupp and O. K. Farha, *J. Am. Chem. Soc.*, 2013, **135**, 16801–16804.

89 P. Valvekens, F. Vermoortele and D. De Vos, *Catal. Sci. Technol.*, 2013, **3**, 1435–1445.

90 S. Hasegawa, S. Horike, R. Matsuda, S. Furukawa, K. Mochizuki, Y. Kinoshita and S. Kitagawa, *J. Am. Chem. Soc.*, 2007, **129**, 2607–2614.

91 J. Juan-Alcañiz, J. Gascon and F. Kapteijn, *J. Mater. Chem.*, 2012, **22**, 10102–10118.

92 L. J. Murray, M. Dincă and J. R. Long, *Chem. Soc. Rev.*, 2009, **38**, 1294–1314.

93 Y. He, W. Zhou, G. Qian and B. Chen, *Chem. Soc. Rev.*, 2014, **43**, 5657–5678.

94 J. Canivet, A. Fateeva, Y. Guo, B. Coasne and D. Farrusseng, *Chem. Soc. Rev.*, 2014, **43**, 5594–5617.

95 E. Barea, C. Montoro and J. A. R. Navarro, *Chem. Soc. Rev.*, 2014, **43**, 5419–5430.

96 J. Li, J. Sculley and H. Zhou, *Chem. Rev.*, 2012, **112**, 869–932.

97 Z. R. Herm, E. D. Bloch and R. Long, *Chem. Mater.*, 2014, **26**, 323–338.

98 S. Yang, A. J. Ramirez-Cuesta, R. Newby, V. Garcia-Sakai, P. Manuel, S. K. Callear, S. I. Campbell, C. C. Tang and M. Schröder, *Nat. Chem.*, 2014, **7**, 121–129.

99 C.-L. Chang, X.-Y. Qi, J.-W. Zhang, Y.-M. Qiu, X.-J. Li, X. Wang, Y. Bai, J.-L. Sun and H.-W. Liu, *Chem. Commun.*, 2015, **51**, 3566–3569.

100 M. Zhang, Z. Gu, M. Bosch, Z. Perry and H. Zhou, *Coord. Chem. Rev.*, 2015, **293-294**, 327–356.

101 J. Della Rocca, D. Liu and W. Lin, *Acc. Chem. Res.*, 2011, **44**, 957–968.

102 L.-L. Tan, H. Li, Y.-C. Qiu, D.-X. Chen, X. Wang, R.-Y. Pan, Y. Wang, S. X.-A. Zhang, B. Wang and Y.-W. Yang, *Chem. Sci.*, 2015, **6**, 1640–1644.

103 A. Ray Chowdhuri, D. Bhattacharya and S. K. Sahu, *Dalt. Trans.*, 2016, **45**, 2963–2973.

104 P. Horcajada, T. Chalati, C. Serre, B. Gillet, C. Sebrie, T. Baati, J. F. Eubank, D. Heurtaux, P. Clayette, C. Kreuz, J.-S. Chang, Y. K. Hwang, V. Marsaud, P.-N. Bories, L. Cynober, S. Gil, G. Férey, P. Couvreur and R. Gref, *Nat. Mater.*, 2010, **9**, 172–178.

105 S. Rojas, E. Quartapelle-Procopio, F. J. Carmona, M. A. Romero, J. A. R. Navarro and E. Barea, *J. Mater. Chem. B*, 2014, **2**, 2473–2477.

106 J. An, C. M. Shade, D. A. Chengelis-Czegan, S. Petoud and N. L. Rosi, *J. Am. Chem. Soc.*, 2011, **133**, 1220–1223.

107 Z. Hu, B. J. Deibert and J. Li, *Chem. Soc. Rev.*, 2014, **43**, 5815–5840.

108 P. Kumar, A. Deep and K.-H. Kim, *TrAC Trends Anal. Chem.*, 2015, **73**, 39–53.

109 R.-B. Lin, S.-Y. Liu, J.-W. Ye, X.-Y. Li and J.-P. Zhang, *Adv. Sci.*, 2016, **3**, 1500434.

110 D. Liu, K. Lu, C. Poon and W. Lin, *Inorg. Chem.*, 2014, **53**, 1916–1924.

111 Y. Wang, H. Ge, Y. Wu, G. Ye, H. Chen and X. Hu, *Talanta*, 2014, **129**, 100–105.

112 J.-C. Jin, J. Wu, G.-P. Yang, Y. Wu and Y.-Y. Wang, *Chem. Commun.*, 2016, **52**, 8475–8478.

113 R.-X. Yao, X. Cui, X.-X. Jia, F.-Q. Zhang and X.-M. Zhang, *Inorg. Chem.*, 2016, **55**, 9270–9275.

114 B. Wang, X.-L. Lv, D. Feng, L.-H. Xie, J. Zhang, M. Li, Y. Xie, J.-R. Li and H.-C. Zhou, *J. Am. Chem. Soc.*, 2016, **138**, 6204–6216.

115 R. Lv, J. Wang, Y. Zhang, H. Li, L. Yang, S. Liao, W. Gu and X. Liu, *J. Mater. Chem. A*, 2016, **4**, 15494–15500.

116 A. Antonić, M. Marjanović, K. Pripužić and I. Podnar Žarko, *Futur. Gener. Comput. Syst.*, 2016, **56**, 607–622.

117 J. Ferrando-Soria, P. Serra-Crespo, M. de Lange, J. Gascon, F. Kapteijn, M. Julve, J. Cano, F. Lloret, J. Pasán, C. Ruiz-Pérez, Y. Journaux and E. Pardo, *J. Am. Chem. Soc.*, 2012, **134**, 15301–15304.

118 S. Han, H. Kim, J. Kim and Y. Jung, *Phys. Chem. Chem. Phys.*, 2015, **17**, 16977–16982.

119 Y. Takashima, V. M. Martínez, S. Furukawa, M. Kondo, S. Shimomura, H. Uehara, M. Nakahama, K. Sugimoto and S. Kitagawa, *Nat. Commun.*, 2011, **2**, 168.

120 O. Kahn, *Molecular Magnetism*, VCH, New York, 1993.

121 M. Kurmoo, *Chem. Soc. Rev.*, 2009, **38**, 1353–79.

122 J. Ferrando-Soria, M. Castellano, R. Ruiz-García, J. Cano, M. Julve, F. Lloret, J. Pasán, C. Ruiz-Pérez, L. Cañadillas-Delgado, Y. Li, Y. Journaux and E. Pardo, *Chem. Commun.*, 2012, **48**, 8401–8403.

123 M. Castellano, R. Ruiz-García, J. Cano, M. Julve, F. Lloret, Y. Journaux, G. De Munno and D. Armentano, *Chem. Commun.*, 2013, **49**, 3534–3536.

124 M. Castellano, J. Ferrando-Soria, E. Pardo, M. Julve, F. Lloret, C. Mathonière, J. Pasán, C. Ruiz-Pérez, L. Cañadillas-Delgado, R. Ruiz-García and J. Cano, *Chem. Commun.*, 2011, **47**, 11035–11037.

125 F. R. Fortea-Pérez, I. Schlegel, M. Julve, D. Armentano, G. De Munno and S.-E. Stiriba, *J. Organomet. Chem.*, 2013, **743**, 102–108.

126 W. D. do Pim, W. X. C. Oliveira, M. a Ribeiro, É. N. de Faria, I. F. Teixeira, H. O. Stumpf, R. M. Lago, C. L. M. Pereira, C. B. Pinheiro, J. C. D. Figueiredo-Júnior, W. C. Nunes, P. P. de Souza, E. F. Pedroso, M. Castellano, J. Cano and M. Julve, *Chem. Commun.*, 2013, **49**, 10778–10780.

127 O. Kahn, Y. Pei, M. Verdaguer, J. P. Renard and J. Sletten, *J. Am. Chem. Soc.*, 1988, **110**, 782–789.

128 Y. Pei, M. Verdaguer, O. Kahn, J. Sletten and J. P. Renard, *Inorg. Chem.*, 1987, **26**, 138–143.

129 Y. Pei, M. Verdaguer, O. Kahn, J. Sletten and J. P. Renard, *J. Am. Chem. Soc.*, 1986, **108**, 7428–7430.

130 E. Pardo, R. Ruiz-García, F. Lloret, J. Faus, M. Julve, Y. Journaux, F. Delgado and C. Ruiz-Pérez, *Adv. Mater.*, 2004, **16**, 1597–1600.

131 E. Pardo, R. Ruiz-García, F. Lloret, J. Faus, M. Julve, Y. Journaux, M. A. Novak, F. S. Delgado and C. Ruiz-Pérez, *Chem. - A Eur. J.*, 2007, **13**, 2054–2066.

132 J. Ferrando-Soria, E. Pardo, R. Ruiz-García, J. Cano, F. Lloret, M. Julve, Y. Journaux, J. Pasán and C. Ruiz-Pérez, *Chem. - A Eur. J.*, 2011, **17**, 2176–2188.

133 J. Ferrando-Soria, T. Grancha, M. Julve, J. Cano, F. Lloret, Y. Journaux, J. Pasán, C. Ruiz-Pérez and E. Pardo, *Chem. Commun.*, 2012, **48**, 3539–3541.

134 J. Ferrando-Soria, D. Cangussu, M. Eslava, Y. Journaux, R. Lescouëzec, M. Julve, F. Lloret, J. Pasán, C. Ruiz-Pérez, E. Lhotel, C. Paulsen and E. Pardo, *Chem. - A Eur. J.*, 2011, **17**, 12482–12494.

135 J. Ferrando-Soria, R. Ruiz-García, J. Cano, S.-E. Stiriba, J. Vallejo, I. Castro, M. Julve, F. Lloret, P. Amorós, J. Pasán, C. Ruiz-Pérez, Y. Journaux and E. Pardo, *Chem. - A Eur. J.*, 2012, **18**, 1608–1617.

136 J. Ferrando-Soria, H. Khajavi, P. Serra-Crespo, J. Gascon, F. Kapteijn, M. Julve, F. Lloret, J. Pasán, C. Ruiz-Pérez, Y. Journaux and E. Pardo, *Adv. Mater.*, 2012, **24**, 5625–5629.

137 S. Kitagawa and M. Kondo, *Bull. Chem. Soc. Jpn.*, 1998, **71**, 1739–1753.

Part 1

Chiral Multifunctional PCPs

1.1. Introduction

The great number of remarkable features that PCPs may display makes of them suitable candidates for the development of new issues dealing with the term “bio” such as medical applications. Firstly, a large number of PCPs are available and they can be built up from nontoxic metals and low toxicity ligands. Secondly, many PCPs are biodegradable, at least to some degree, upon exposure to aqueous medium. Besides, their hydrophilic–hydrophobic internal microenvironment is adaptable to host a large variety of active molecules with different chemistry. Finally, PCPs are versatile: it should be possible to modulate drug delivery by tuning the host–guest interactions through the introduction of various polar or apolar functional groups within the organic part of the PCPs, and/or by changing the structure of the solid (interconnectivity, pore size, flexibility) to control the diffusion through the porous framework. Moreover, due to the huge library of ligands which can be used to prepare them, they can exhibit some other fascinating features such as chirality, property to which we will pay a special attention.

In order to design novel functional materials compatible with life, researchers have been increasingly looking to nature for inspiration. The idea is to take advantage of the structural and functional diversity of biological molecules, and incorporate such units into PCPs to explore new architectures and applications that normally cannot be achieved using the simple organic linkers traditionally used in the PCPs construction. In such a way, a new generation of materials known as *bio*PCPs has emerged.

1.1.1. Synthesis

As a first approach, one can synthesise biologically compatible PCPs by carefully choosing non-toxic metal centres such as Fe(II), Zn(II), Ca(II), Mg(II), etc. in combination with organic low-toxicity ligands like carboxylate,[1] phosponate[2] and sulfonate[3] derivatives. Nevertheless, a second strategy dealing with the direct incorporation of natural molecules appears as an increasingly attractive alternative to assure biological and environment compatibility. Many biomolecules, such as amino acids, oligopeptides,

proteins, nucleobases, and saccharides, are naturally good ligands and they have already been successfully incorporated into CPs. Some of the advantages they show are: (i) they are readily available in nature in big amounts and relatively low prices; (ii) they lead to biocompatible materials; (iii) they can be either structurally rigid or flexible. Besides, they show many different metal-binding sites, exhibiting multiple possible coordination modes and giving rise to a wide structural diversity; (iv) finally, a good number of biomolecules are chiral and can be used to construct chiral *bio*PCPs, which may have interesting recognition, separation and catalytic properties.

However, some restrictions generally prevent these biomolecules from being good candidates as constituents of PCPs. The symmetry deficiency in many biological building blocks makes the synthesis of ordered materials (PCPs for instance) much more difficult. Additionally, aside from some aromatic and a few cyclic non-aromatic molecules, most biomolecules are too flexible to generate a framework with potential permanent porosity. Some strategies to overcome this problem deal with the synthesis of higher symmetric building units from asymmetric biological ligands or with the use of highly symmetric co-ligands.

Being the use of natural molecules or their functionalized derivatives the most appealing approach to prepare *bio*PCPs, some remarkable examples from the literature have been collected and classified depending on the starting natural molecule.

1.1.1.1. Amino acids

Amino acids (AAs) are promising biomolecules which serve as excellent ligands and may coordinate metal ions through both their carboxylate and amino groups to directly form *bio*PCPs. All natural AAs consist of an α-carbon atom onto which both an amino and a carboxylic groups are attached. Through these metal binding groups, AAs tend to form discrete complexes *via* formation of the typical five-membered glycinate chelate ring. Besides, there are some AAs bearing R side chains with metal binding groups such as β-carboxylate of aspartic (Asp) and glutamic (Glu) acids, the imidazole group of

histidine (His), the thiol group of cysteine (Cys), the thioether group of methionine (Met) or the phenol ring of tyrosine (Tyr) among others (see Scheme 1). These binding sites can be used to increase the dimensionality of the coordination networks.

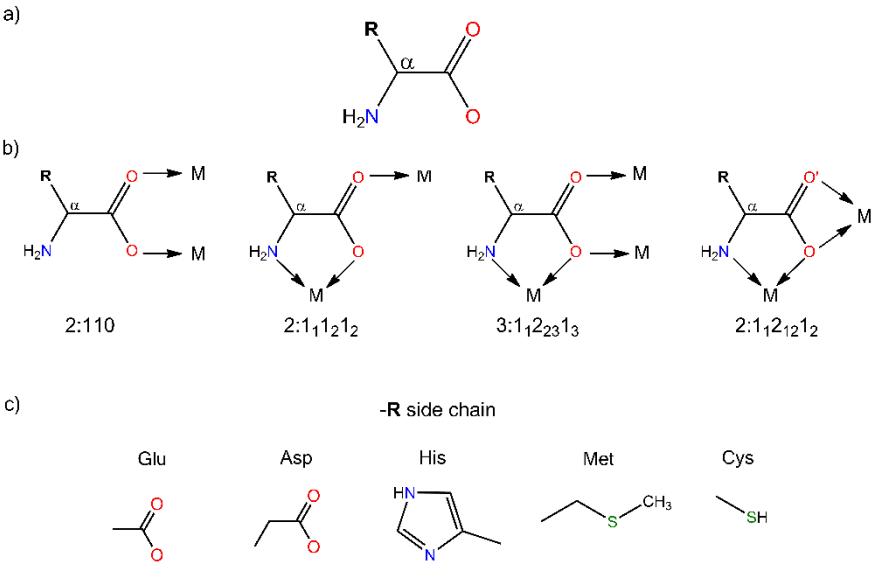

Scheme 1. (a) Illustration of the common skeleton of a natural AA. (b) Some of the potential coordination modes that the skeleton can display through the amino and carboxylate groups and their Harris notation[4,5] (c) Examples of the side arm (R) of some AAs. Note that the potential coordination sites have been highlighted with different colours.

In spite of the fact that examples of 3D CPs built up from pure AAs are scarce, some interesting cases have been reported almost wholly confined to aspartic,[6–8] glutamic,[9–12] methionine[13] and histidine[14] acids (see Figure 1). Nevertheless, aiming at obtaining new topologies of highly porous polymers, chemists usually introduce auxiliary ligands or clusters that can act as linkers within the metal-AA units.

To date, some examples of these *bio*PCPs have been described. One remarkable example is the work carried out by Rosseinsky and co-workers.[16,17] The solvothermal reaction of Ni(*L*-Asp)·3H$_2$O with 4,4'-bipyrdine (4,4'-bipy) affords an homochiral PCP of formula [Ni$_2$(*L*-Asp)$_2$(4,4'-bipy)]·guest. In this framework, neutral chiral Ni(*L*-Asp) layers

are connected by 4,4'-bipy ligands forming a pillared structure with 1D channels (3.8 x 4.7 Å) defined by the length of the 4,4'-bipy spacer.

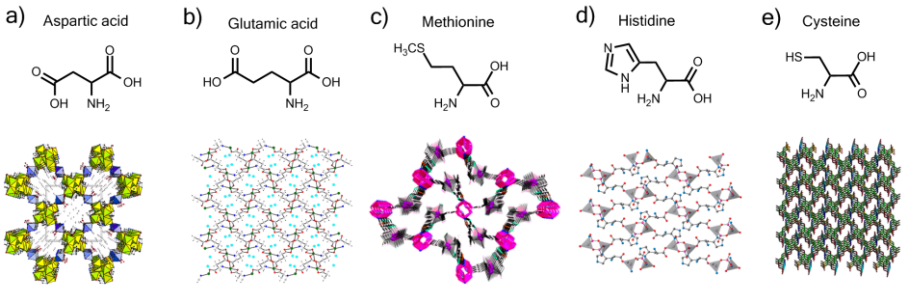

Figure 1. Projection of the metal-AA frameworks along with their AA components of (a) $[Ni_{2.5}(OH)(L\text{-}Asp)_2] \cdot 6.55H_2O$,[6] (b) $[Co(L\text{-}Glu)(H_2O)] \cdot H_2O_\infty$,[10] (c) $[Ag_3Cu_3(L\text{-}Met)_6(NO_3)_3(H_2O)_3] \cdot 7H_2O$,[13] (d) $[Zn(HPO_3)(His)(H_2O)_{0.5}]$,[14] and (e) $[Cu(L\text{-}Cys)(H_2O)]_n$.[15]

Interestingly, this PCP is stable after removal of the guest molecules and the pore characteristics can be controlled by substituting the pillaring ligand with extended bipy-type ligands such as 4,4'-azopyridine (azpy) or 3,5-bis-(4-pyridyl)pyridine (3,5-bpp) among others.[17] The structures of both Ni-Asp derived PCPs with 4,4-bipy and 3,5-bpp as bridging ligands are shown in Figure 2.

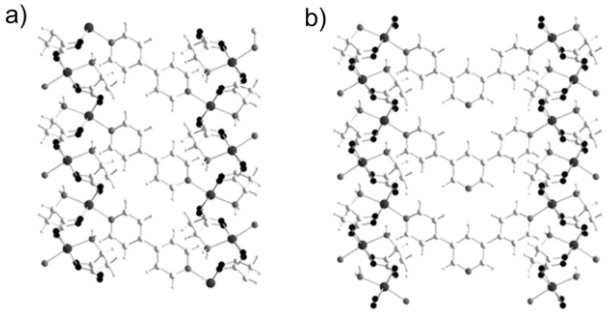

Figure 2. Views of a fragment of the structures of (a) $[Ni_2(L\text{-}Asp)_2(4,4'\text{-}bipy)]$ and (b) $[Ni_2(L\text{-}Asp)_2(3,5\text{-}bpp)]$.

The modification of natural AAs, incorporating thus the desired functional groups, represents another strategy for the preparation of extended frameworks and new architectures.

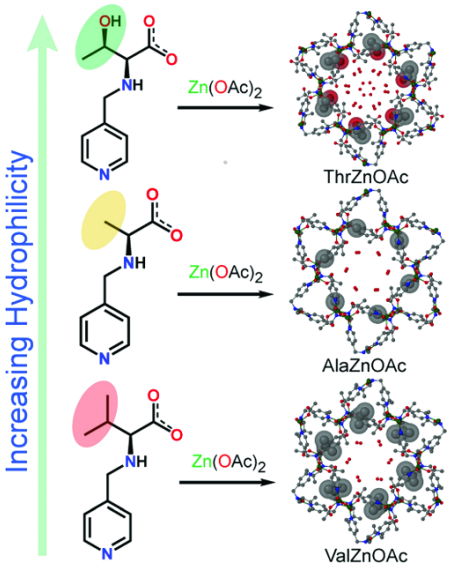

Figure 3. Scheme of the ValOAc, AlaOAc and ThrOAc linkers that react with $Zn(OAc)_2$ to afford the corresponding PCPs architectures. These PCPs possess isostructural integrity along with linker variety (from hydrophobic to hydrophilic). The side arms have been highlighted.

For example, Banerjee and co-workers synthesised a family of Zn(II) based homochiral PCPs using pyridyl functionalised threonine, valine and alanine and $Zn(OAc)_2$ as the metal precursor[18] (see Figure 3). The pyridyl groups, along with the amino and carboxylate groups of the ligand, connect the Zn^{II} ions forming a 3D network, whereas the remaining side arm can act as a functional group for the desired application such as sorption, sensing or catalysis. They carried out solvent sorption measurements on the three PCPs in order to study the role of the amino acid residue and the hydrophilic interactions inside de cavities.

1.1.1.2. Peptides

Peptides are short polymeric biomolecules composed of AAs linked by peptide bonds. Each peptide has a distinctive sequence of AAs, which leads to specific recognition properties and intrinsic chirality that may be useful for a wide range of applications. Peptides have also the ability to act as effective bridging ligands as they have at least one amino and one carboxylic terminal group that can coordinate metal ions in different coordination modes (Scheme 2). Moreover, they provide with an limitless number of flexible polydentate ligands just by tuning the AAs sequence of the peptide. For instance, the incorporation of more carboxylate groups could be achieved by synthesising peptides made from aspartate or glutamine as shown in Scheme 2.

Recently, different works considering peptides as connecting ligands have been published.[19–24] Rosseinsky and co-authors reported two topologically distinct 2D-layered frameworks where the dipeptides Gly-Ala and Gly-Thr connect the Zn^{2+} ions affording the respective compounds [Zn(Gly-Ala)$_2$] and [Zn(Gly-Thr)$_2$].[23,24] The former is a flexible porous material that displays an adaptable pore conformation while the latter is structurally rigid and it exhibits permanent porosity. These examples clearly illustrate how small changes in the peptide unit are translated into different structures and thus, into a strong control of the adsorption properties. The authors further presented a new peptide-based PCP [Zn(Car)]$_n$·xDMF (Figure 4) which is assembled from Zn^{2+} and carnosine (Car), a natural dipeptide with the molecular structure β-alanyl-*L*-histidine.[19] The histidine residue incorporates the imidazole group that serves as an additional binding site. The PCP consists of a flexible 3D framework with 1D permanent porosity upon removal of DMF (*N*,*N*'-dimethylformamide) its specific surface area being 448 $m^2 g^{-1}$ and exhibiting strong binding affinity for small molecules, such as CO_2 and CH_4.

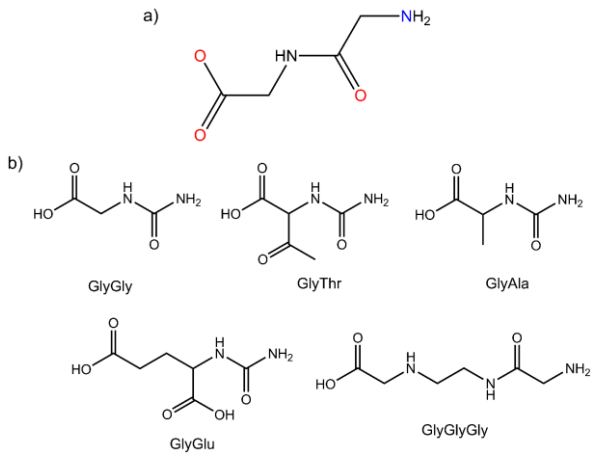

Scheme 2. (a) Illustration of the common skeleton of a peptide. (b) Examples of peptides resulting from different AA combinations.

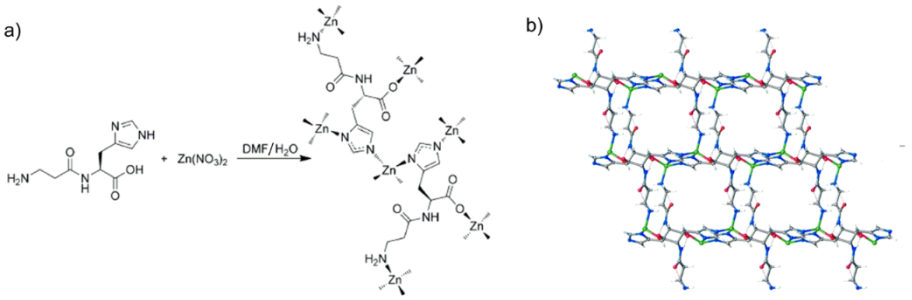

Figure 4. (a) Scheme of the reaction between $Zn(NO_3)_2 \cdot xH_2O$ and carnosine to form the PCP. (b) 3D structure of $[Zn(Car)]_n \cdot xDMF$.

1.1.1.3. Proteins

Proteins are especially attractive building blocks for the synthesis of *bio*PCPs as they provide high chemical and structural diversity and possess inherent functions such as drug delivery, electron transfer, and molecular recognition. Moreover, 3D protein lattices have been proposed as stable porous scaffolds to carry out catalytic reactions. Although a considerable progress toward the understanding of the self-assembly of proteins has been achieved, the ability to predict protein-protein interactions or to engineer new architectures remains a great challenge. Tezcan and co-workers have been thoroughly working on this purpose and they envisioned that the self-assembly of proteins could be controlled by metal coordination. The interesting strategy entailed two complications: (a) proteins display extensive functionalised surfaces that can interact with metal ions in unpredictable ways and (b) the interactions between proteins may not be negligible. Aiming at circumventing this challenge, they developed

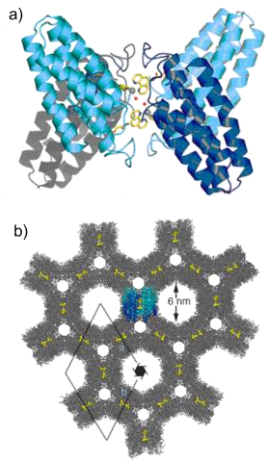

Figure 5. (a) Engineered protein based on the four helix bundle hemeprotein cytochrome cb_{562}. (b) A view of the porous structure resulting from its metal-directed assembly.

the "metal-directed protein self-assembly" strategy,[25,26] taking advantage of the directionality and symmetry inherent to the metal coordination in order to govern the geometry. In early works, they reported how the same protein building block oligomerises in different symmetries depending on the coordination preference of the metal ion.[27,28] After several attempts, Tezcan and co-workers achieved the first porous protein-derived framework (see Figure 5), which consists of an engineered protein that forms porous crystalline frameworks upon metal coordination displaying unsaturated metal centres and hexagonal cavities with dimension of 6 nm.[29]

Recently, they have obtained a 3D, porous, crystalline framework formed by spherical protein nodes.[30] In this work, the 3D lattice is formed *via* coordination of a protein on whose surface, the Zn^{2+} ions have been anchored with asymmetric polytopic organic ligand acting as a linker (see Figure 6).

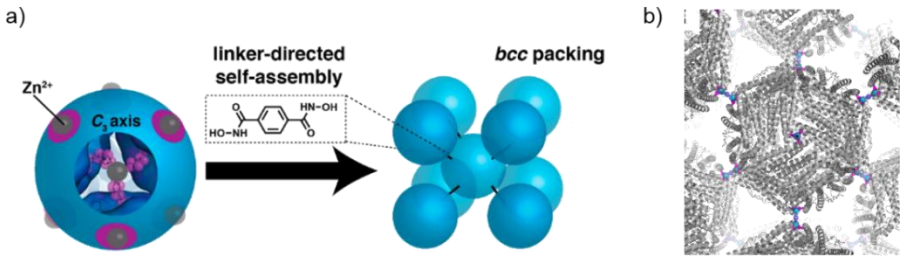

Figure 6. (a) Scheme for the self-assembly of Zn-ferritin through the ditopic organic linker into a *bcc* type lattice. (b) 3D structure of the of the porous bdh-Zn-^{T122H} ferritin lattice.

1.1.1.4. Nucleobases

Nucleobases represent appealing linkers for the synthesis of *bio*PCPs due to their rigidity and the great number of heteroatoms available to coordinate different metal centres. Furthermore, they show a special ability to establish complementary hydrogen bonding interactions, thus increasing the possibilities to obtain porous 3D structures. Nucleobases are classified into double-ringed purines (adenine and guanine) and pyrimidines (cytosine, thymine and uracil).

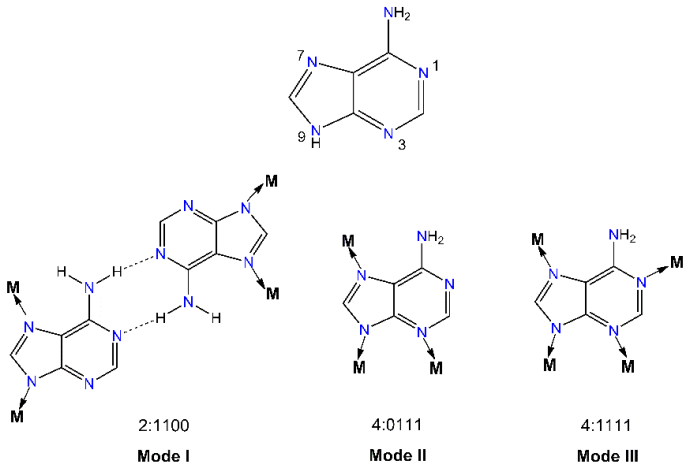

Scheme 3. Coordination modes of adenine. Note that **I** corresponds to a supramolecular dimer where two adenine molecules are linked *via* double hydrogen bond between N1 from an adenine and one H from the amine group of the adjacent adenine.

Thanks to the versatility that nucleobases possess as linkers, they can afford PCPs exclusively based on coordination bonds or emerging supramolecular PCPs,[31] where the hydrogen bonds play an important role in the self-assembly of the porous structure. Here, only a few examples of the former group will be mentioned. The group of Rosi has investigated nucleobases acting as ligands together with different coordination modes (see Scheme 3). Specially, adenine is an ideal linker with multiple Lewis-basic sites that can interact with CO_2, looking into storage and separation properties. In 2009, Rosi and co-authors reported a porous framework named *Bio*-MOF-1 of formula $(Me_2NH_2)_2[Zn_8(\mu_4\text{-adeninato})_4(\mu\text{-BPDC})_6(\mu_4\text{-O})] \cdot 8DMF \cdot 11H_2O$ (BPDC: biphenyldicarboxylate).[32] The anionic network consists of zinc(II)-adeninate columns (formed *via* coordination mode **III**) interconnected through multiple BPDC linkers. This compound exhibits permanent porosity with a BET surface of 1700 $m^2\,g^{-1}$ and it is able to store and release cationic drug molecules.

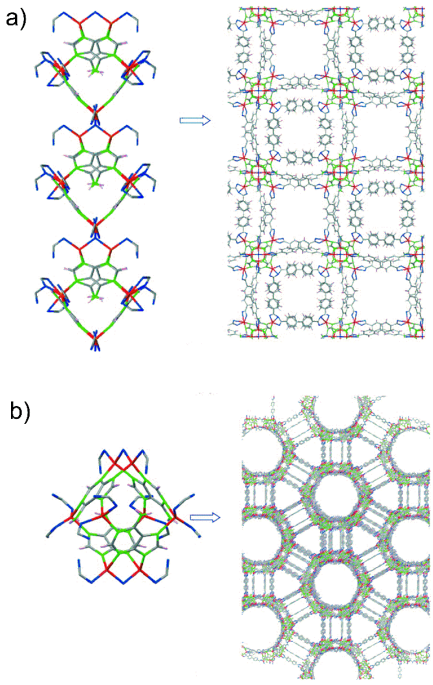

Figure 7. Building blocks and the resulting crystal structures of the compounds (a) $(Me_2NH_2)_2[Zn_8(\mu_4\text{-adeninato})_4(\mu\text{-BPDC})_6(\mu_4\text{-O})] \cdot 8DMF \cdot 11H_2O$ and (b) $(Me_2NH_2)_4[Zn_8(\mu_4\text{-adeninato})_4(\mu\text{-BPDC})_6(\mu\text{-O})] \cdot 49DMF \cdot 31H_2O$.

A few years later (in 2012) the authors reported the *Bio*-MOF-100 of formula $(Me_2NH_2)_4[Zn_8(\mu_4\text{-adeninato})_4(\mu\text{-BPDC})_6(\mu\text{-O})] \cdot 49DMF \cdot 31H_2O$,[33] constructed from the same building blocks than *bio*-MOF-1 but changing the reaction conditions. The resulting material is a mesoporous coordination polymer showing a BET surface area of 4300 $m^2 g^{-1}$. The group also reported an isoreticular series of cobalt-adeninate *bio*PCPs (from *bio*-MOFs-11 to 14)[34]. The porosity and hydrophobicity of these PCPs were modulated by decorating the pores with diverse functions (acetate, propionate, butyrate and valerate). They show that small modifications of the pore space can lead to dramatic changes in the N_2 and CO_2 sorption properties and in the stability in water.

1.1.2. Properties and Applications

*Bio*PCPs display the same properties than PCPs with some additionally advantages. Since the potential applications for PCPs have already been explained in the Introduction, only properties and applications especially concerning *bio*PCPs will be described in this section. The wide chemical versatility together with the presence of tuneable size and shape pores are the main features responsible for the potential applications that have been explored so far.

1.1.2.1. Biocompatibility and biomedical applications

The cavities of PCPs represent a fundamental tool to encapsulate, transport and deliver active molecules through host-guest interactions. However, the use of porous solids for biomedical applications requires additional features such as non-toxic composition and moderate solubility in water. In order to overcome the toxicity issue, *bio*PCPs have been synthesised using the appropriate low-toxic metal ions and preferably endogenous ligands, which could be reused once administrated within the body. One less recommended option can be the use of exogenous linkers. In this case, these molecules should be low toxic and easily degradable to be excreted from the organism as soon as possible. Imaz and co-authors have set out some materials made from endogenous linkers,[35] and more examples of biocompatible porous materials have been covered Section 1.1. Horcajada and co-workers synthesised two Fe-based *bio*PCPs from low toxicity fumarate and trimesate ligands,[36] which acted as nanocarriers for an efficient controlled delivery of challenging antitumoural and retroviral drugs, displaying also imaging properties. Moreover, the non-toxicity of the iron-based *bio*PCPs was proved.

Another remarkable example is the aforementioned *bio*PCP of formula $(Me_2NH_2)_2[Zn_8(\mu_4\text{-adeninato})_4(\mu\text{-BPDC})_6(\mu_4\text{-O})] \cdot 8DMF \cdot 11H_2O$ prepared by Rosi and co-workers.[32] They show that cationic drugs can be loaded into the pores of the anionic framework *via* cation exchange with the dimethylammonium cations to further release the drug molecules from the pores by exchange with exogenous cations from biological fluids.

Sometimes, the encapsulation process cannot be successfully achieved in terms of loading, due to the size and affinity of the biomolecule toward the porous matrix. In these terms, Serre and coauthors developed an excellent strategy for drug delivery (illustrated by Figure 11) where the active molecule is not encapsulated within the pores, but it is a constituent of the framework. They reported a *bio*PCP built up from non-toxic iron and the therapeutically active linker nicotinic acid.[37] The release of the

therapeutic agent, which is a constituent of the framework, is achieved through the degradation of the hybrid phase, under simulated physiological conditions.

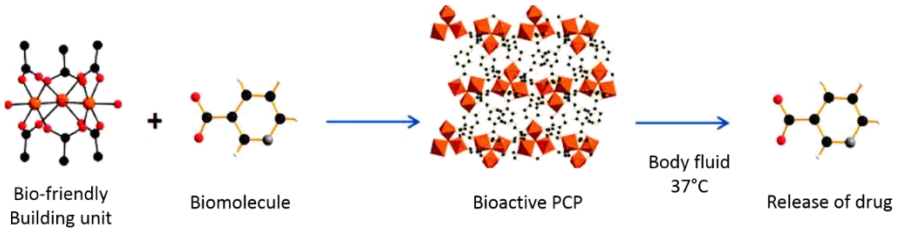

Figure 11. Scheme of the *bio*PCP formation through the direct coupling of the therapeutic biomolecule nicotinic acid as the bridging ligand with a non-toxic metal cluster. The biomolecule is released when the *bio*PCP degrades.

*Bio*PCPs are also excellent candidates to serve as magnetic resonance imaging (MRI) contrast agents because they can carry large amounts of highly paramagnetic metal ions (e.g. Gd^{3+}, Mn^{2+}, etc.). Furthermore, through the incorporation of luminescent or heavy element building blocks, *bio*PCPs also serve as contrast agents for optical imaging or X-ray computed tomography (CT) imaging.[36,38–41]

Interestingly, by conjugating or loading multiple components such as imaging agents, drugs and targeted ligands, *bio*PCPs can display both functions simultaneously, thus releasing and monitoring the active biomolecules within the body. This multifunctionality represents a promising perspective for the so-called “theranostics” or personalised therapy.[36]

1.1.2.2. Storage and delivery of biological gases: NO and H_2S

Gasotransmitter is a term coined to distinguish those biological signaling molecules which are freely permeable to cell membranes. Two of the most important gases encompassed by this term are nitric oxide (NO) and hydrogen sulfide (H_2S). These gases are vital for life and their controlled delivery with a biological/medical target is a growing a research field. NO shows antithrombosis, vasodilatory and antibacterial activity while H_2S has been involved in vasodilatation, neurotransmission and neuroprotection.

The versatility and high porosity of *bio*PCPs have been exploited to adsorb and store bioactive gases. *Bio*PCPs appear as promising materials because most of them show coordinatively unsaturated metal sites on the walls of the pores that are available to bind the gas molecules. For this reason, a previous activation step is required to remove guest molecules inside the pores suggesting that the stability of the framework is an important requirement. Solids with large amount of accessible metal sites lead to strongly NO bonding, which is crucial for stable, long-term storage. However, the cycle illustrated in Figure 12 must be completed and the interactions between the guests and the framework should not be too strong in order to easily recover the gas when required.

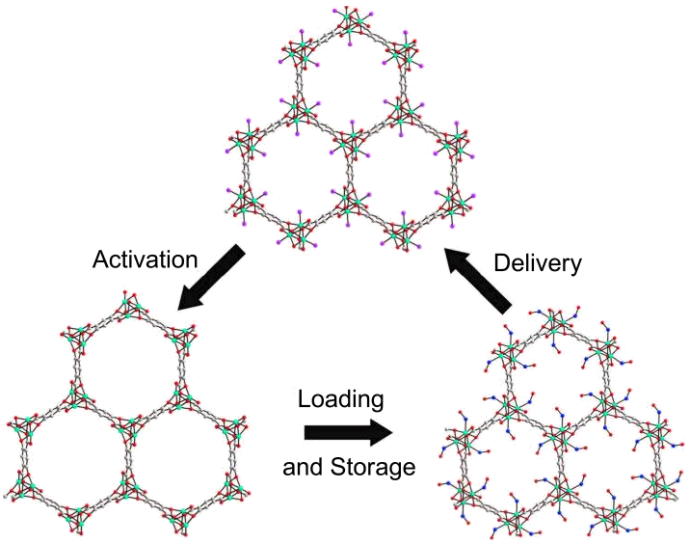

Figure 12. Cycle of activation, loading, storage and delivery illustrated with the Co- and Ni-MOF.

In fact, the control of the rate and dosage of the delivery to achieve beneficial actions from the gas remains the main challenge. Among all the options to desorb the gas (increase of temperature, reduction in pressure, use of a chemical trigger, etc.), the exposure to moisture appeals as the mostly used since this is the simplest method and it works extremely well. Therefore, the porous structures need to be able to interact with water.

Two excellent examples to illustrate this relevant application of *bio*PCPs are represented by the PCPs of formula $[M_2(C_8H_2O_6)(H_2O)_2] \cdot 8H_2O$ with M = Co and Ni, named Co-MOF and Ni-MOF respectively, and synthesised by Morris and coauthors.[42] The solids perform exceptionally well the adsorption, storage and water-triggered delivery of NO. Surprisingly, the entire reservoir of stored gas is available for delivery even after the material has been stored for several months.

*Bio*PCPs show two very attractive properties: i) they deliver only pure gas and ii) the dose and rate of delivery can be controlled by changing the composition and structure of the framework. Anyway, the development of biocompatible PCPs with high loading and controlled release for NO and H_2S still remains challenging.

1.1.2.3. Biosensors

*Bio*PCPs show some advantages that render them promising materials as biosensors. Firstly, they display permanent porous structures and can exhibit high surface areas. Secondly, the interactions between the guest molecules and the pores can induce changes in their physical properties. Thirdly, some biomolecules such as peptides and antibodies which may constitute the framework, have the ability to recognize specific analytes. Despite the appealing potential application, examples of sensors based on *bio*PCPs are still limited.

Rosi and coauthors showed that the porous anionic $(Me_2NH_2)_2[Zn_8(\mu_4\text{-adeninato})_4(\mu\text{-BPDC})_6(\mu_4\text{-O})] \cdot 8DMF \cdot 11H_2O$ framework loaded with lanthanide cations could be potentially used as photostable high surface area sensor for small molecules including O_2.[43] Jiang and coworkers studied two water-stable Fe(III)-based PCPs, MIL-68 [Fe(OH)(BDC)] (BDC = 1,4-bwnzenedicarboxylic acid) and MIL-100 $[Fe_3(\mu_3O)(H_2O)_2(BTC)_2F]$ (H_2BTC = 1,3,5-benzenetricarboxylic acid),[44] which possess intrinsic peroxidase-like activity.

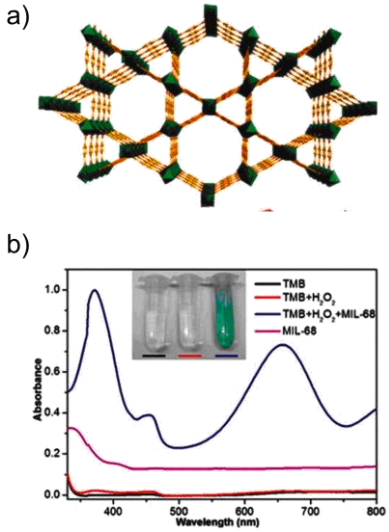

Figure 13. (a) View of the structure of MIL-68 involving two types (hexagonal and trigonal) of channels running through the cristallographic *c* axis. (b) UV-Vis adsorption spectra for TMB, TMB-H_2O_2, TMB-H_2O_2-MIL-68 and MIL-68 solutions. Inset: typical photographs of the three samples corresponding to the lines.

In the presence of H_2O_2 and the peroxidase substrate TMB (3,3',5,5'-tetramethylbenzidine), both PCPs can catalyse the oxidation which can be visually detected due to the appearance of blue color. Hence, providing a colorimetric assay for H_2O_2. Moreover, the influence of ascorbic acid on the oxidation of OPD (o-phenylendiamine) catalysed by the PCPs in the presence of H_2O_2 was investigated. A trace amount of ascorbic acid induces an inhibitory effect on this oxidation leading to a different colour reaction. Thus, a simple colorimetric biosensing system for AA detection is developed.

1.1.2.4. Biodegradability and stability

Stability represents one of the major issues concerning biological applications. The materials should be stable long enough to deliver the therapeutic agent. Nevertheless, a certain degree of solubility is also needed since the body has to clean the system in a reasonable timescale after the achievement of the delivery. Some PCPs are highly unstable in water and thus, in body fluids. In these cases, an external covering with silica can be applied in order to prevent a fast degradation. However, some PCPs like the already mentioned Co-MOF and Ni-MOF[42] (also known as M-CPO-27) can be left in bovine serum for days showing a very small percentage of dissolution.[45] These frameworks degrade slow enough to perform the delivery but still allowing their

removal from the system. One important issue apart from water, which also will determine the delivery performance, is the influence of the pH and composition of the body fluid over the PCP. Overall, a trade-off between stability and solubility is required for a controlled and successful transport and release.

1.1.2.5. Chirality: enantioselective catalysis and separation

Chirality is an important property for current applications. Many substances and drugs, such as pharmaceuticals and agrochemicals are chiral and show two possible enantiomeric forms. Enantiomers of a racemic drug often exhibit different biological and pharmacological responses, as well as different pharmacokinetic and pharmacodynamics effects. Living organisms will interact with each enantiomer in a different manner. Thus, one isomer may produce the desired therapeutic activity while the other one can even produce harmful effects. For this reason, the production and availability of enantiomerically pure drugs are subject of an increasing demand from fine chemical and pharmaceutical industries. On one hand, the separation of enantiomers remains a challenge owing to their identical physical and chemical properties in an achiral environment. On the other hand, the synthesis of enantiomerically pure substances is also a difficult task.

Since many biomolecules are chiral, their use as ligands for the synthesis of CPs represents an excellent tool to obtain homochiral *bio*PCPs. These versatile porous solids showing chiral functions within their cavities possess the ability to enantioselectively interact with molecules and appear as potential materials to separate enantiomers. Due to this chiral recognition feature, one could also think of them as proper heterogeneous catalysts for the asymmetric synthesis.

In order to obtain homochiral PCPs, five different approaches are distinguished. First, chiral open frameworks can be built from achiral components *via* self-resolution. Theoretically, PCPs can crystallise in a chiral space group as a result of a particular spatial disposition of all the building units. However, the bulk samples of the PCPs built from

achiral or racemic components *via* self-resolution tend to contain both enantiomeric crystalline forms and can be racemic even though each single crystal is a single enantiomer. For this reason, examples of chiral porous solids synthesised following this approach are scarce.[46–49]

A second approach is based on the use of an enantiopure auxiliary coligand or template for directing the formation of homochiral porous networks. The strategy is to arrange achiral building blocks in the presence of chiral molecules, charge-balanced ions or even solvents that do not act as constituent ligands but organise the building units into a particular topology around themselves during the crystallisation process by enantiospecific supramolecular interactions.[50–56]

In an unusual discovery, Morris *et al*. demonstrated the homochiral crystallisation of an interesting compound in which the absolute configuration is controllable through the chirality of the chiral ionic liquid solvent 1-butyl-3-methylimidazolium (BMIm) containing *L*-aspartate. Using this chiral ionic liquid as the reaction medium, the organic linker H_3BTC and Ni^{2+} ions, the homochiral $(BMIm)_2[Ni(HBTC)_2(H_2O)_2]$ was obtained.[57] Although containing neither chiral ligands nor chiral anions, the compound crystallises in a chiral space group. Chiral induction was further supported by the fact that substitution of *L*-aspartate with *D*-aspartate yielded crystals with the opposite chirality and that removal of chiral anions in the ionic liquid resulted in the achiral $(BMIm)_2[Ni_3(HBTC)_4(H_2O)_2]$ MOF.

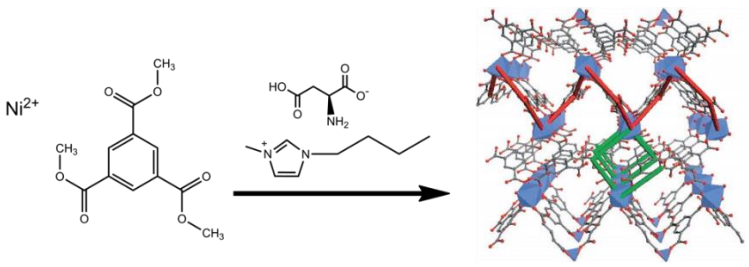

Figure 14. Synthetic strategy which leads to the formation of the homochiral $(BMIm)_2[Ni(HBTC)_2(H_2O)_2]$ PCP.

The third and one of the most reliable approaches to create homochiral PCPs is based on the use of enantiomerically pure polytopic ligands.[22,58–66] These chiral linkers connect the metal nodes into 2D or 3D networks through their primary functional groups. The secondary chiral functionalities that cannot link metal nodes periodically decorate the porous structures and can be used to generate asymmetric active sites that are accessible to the substrates *via* the open channels or cavities. These chiral linkers include ligands derived from natural molecules such as amino acids, nucleotides and carboxylic acids among others. However, sometimes these molecules are not properly equipped with functional groups required for the desired application or they cannot afford the desired 3D structure. For this reason, important research efforts concerning the design and synthesis of chiral multifunctional organic linkers have to be undertaken.

The fourth strategy deals with the synthesis of a homochiral PCP from a parent PCP by synthetic modification of the organic linkers or the metal nodes and/or by guest exchange. An elegant example is illustrated by the work of Kim and co-workers. Starting from the preassembled achiral PCP MIL-101 [$(Cr3(\mu_3\text{-}O)(bdc)_3(H_2O)_2(F,OH)]$, which was chosen due to its chemically and thermally robustness and to the presence of open metal coordination sites, they incorporate pyridine substituted *L*-proline derivatives to the Lewis acidic chromium centres of MIL-101.[67] The postmodification of MIL-101 with two different chiral ligands yielded two new chiral PCPs capable of catalysing asymmetric aldol reactions with a high enantioselectivity.

The last strategy, which provides the most reliable means towards chiral PCPs synthesis, is the use of chiral metalloligands or pre-constructed building blocks to build porous PCPs through the interplay of both metalloligands and organic ligands or metal cations.[68–75]

At first sight, this synthetic approach seems challenging compared with the use of traditional organic ligands, since metalloligands are usually longer and more flexible, thus being much more difficult to stabilise the resulting frameworks. Nevertheless, the metalloligand approach is very appealing to target functional PCPs because of its direct

immobilization of functional sites (both metal and organic functional sites) into the frameworks to introduce their specific functions. Despite this advantage, such promising route has not been extensively explored.

One interesting example is the work done by Cui and co-workers. They have constructed two chiral and robust PCPs of formula $[Cd_4(NiL)_4(DMF)_4] \cdot 4H_2O$ and $[Cd_4(CoL)_4(DMF)_4(OAc)_4] \cdot 4H_2O$ just by heating a mixture of $Cd(NO_3) \cdot 6H_2O$ and the dicarboxylate-functionalised salen (L) complexes with Co^{II} and Ni^{II} ions (metalloligands) in H_2O and DMF respectively.[73] The [Co(salen)] units accessible *via* the open PCP channels were used to generate an efficient heterogeneous asymmetric catalyst for HKR (hydrolytic kinetic resolution) of racemic epoxides to afford the product yielding 99.5% of enantiomeric excess (ee). The MOF catalyst features a high local density of cooperative bis[Co(salen)] motifs, exhibiting improved catalytic performance compared to the monomeric catalyst.

1.2. Previous work

Although an example of homochiral oxamato-based chain was already obtained in our group,[76] the efforts devoted to the synthesis of chiral oxamato-based 3D CPs had been unsuccessful so far. Hence, in order to achieve the first oxamato-based chiral 3D magnet, we explored a new rational synthetic strategy based on the use of the templating chiral (*S*)-trimethyl(1-phenylethyl)ammonium cation, [(*S*)-(1-PhEt)Me_3N^+], together with the oxalate dianion during the self-assembly process of $[Cu^{II}(mpba)_2]^{4-}$ with Mn^{2+} ions (see Scheme 4). This reaction led to a novel chiral manganese(II)-copper(II) 3D compound of formula $[(S)\text{-}(1\text{-}PhEt)Me_3N]_2[Mn^{II}_2(C_2O_4)Cu^{II}_2(mpba)_2(H_2O)_2]\} \cdot 3H_2O$.

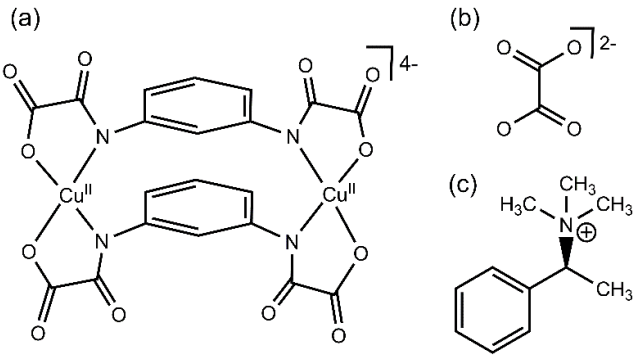

Scheme 4. (a) Dicopper(II) metallacyclophane precursor used as tetrakis(bidentate) metalloligand toward manganese(II) ions. (b) Oxalate dianion. (c) Templating (S)-trimethyl-(1-phenylethyl)ammonium cation.

Its structure consists of a mixed oxalato/oxamato-based heterobimetallic chiral 3D open-framework with a square/octagonal architecture, which is built up from dicopper(II) complex anions, $[Cu^{II}_2(mpba)_2(H_2O)_2]^{4-}$, and dimanganese(II) complex cations, $[Mn^{II}_2(ox)]^{2+}$, together with (*S*)-(1-PhEt)Me_3N^+ countercations and crystallisation water molecules (Figure 15). Interestingly, the presence of the oxalate dianion ox^{2-} in the reaction mixture results crucial to obtain this chiral CP. Indeed, all our previous attempts to construct chiral CPs by using only the templating chiral (*S*)-(1-PhEt)Me_3N^+ cation as a source of chirality in the absence of ox^{2-} failed.

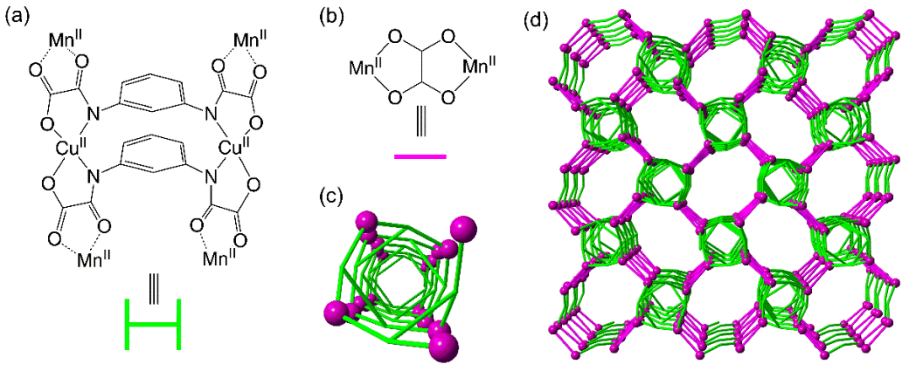

Figure 15. Schematic representation of (a) the double helical chain motif and (b) the oxalate ligand acting as a bridge between two manganese(II) ions of the neighbouring double helical chains. (c) View of the chiral squared pores. (d) A perspective view of the anionic 3D network.

Regardless of our success, we considered that this approach held some degree of serendipity. Indeed, the presence of the chiral (*S*)-(1-PhEt)Me_3N^+ templating cation became mandatory when introducing the negative charged ox^{2-} in the framework, but when using more than one building block (ox^{2-} and $[Cu^{II}_2(mpba)_2(H_2O)_2]^{4-}$), the control over the assembly turns into challenging.

1.3. Objectives

Based on the deep experience of our research group in the oxamato and oxamidato chemistry, we decided to search an alternative synthetic approach which could afford chiral PCPs in easy, controlled and successful ways. For that purpose and having in mind to work with environmentally sustainable materials with possible *bio*-applications, we chose to functionalise natural amino acids. The advantages of these organic molecules are summarised as follows:

a) they are readily and naturally available in big amounts and relatively inexpensive prices,

b) they can lead to biologically-compatible PCPs,

c) they show an amine group which can be easily functionalised into an oxamato group under mild conditions,

d) they show different binding sites, and thus multiple coordination modes giving rise to a rich structural diversity,
e) and they are chiral molecules and consequently, this chirality is expected to be transferred to the final structure.

Taking in account all these issues, the specific objectives for this chapter are listed hereunder:

(i) The design and development of a rational and easy synthetic strategy to prepare chiral MMs which consists of the use of chiral oxamato- and oxamidato-based proligands derived from enantiopure amino acids, aiming at transferring their chiral information to their derivatives.

(ii) The design, synthesis and characterisation of chiral building blocks from the chiral proligands with unoccupied positions, which could coordinate metal ions or metal complexes thus yielding chiral extended frameworks.

(iii) The design, synthesis and characterisation of chiral PCPs making use of the metalloligand approach described in the Introduction.

(iv) The exploration of the properties and applications that those multifunctional materials may display, such as magnetic properties, proton conduction, luminescence, porosity, gas sorption and selectivity, asymmetric catalysis and/or enantiomeric separation.

1.4. References

1 O. M. Yaghi, M. O'Keeffe, N. W. Ockwig, H. K. Chae, M. Eddaoudi and J. Kim, *Nature*, 2003, **423**, 705–714.

2 D. Kong, J. Zoñ, J. McBee and A. Clearfield, *Inorg. Chem.*, 2006, **45**, 977–986.

3 B. D. Chandler, J. O. Yu, D. T. Cramb and G. K. H. Shimizu, *Chem. Mater.*, 2007, **19**, 4467–4473.

4 R. a. Coxall, S. G. Harris, D. K. Henderson, S. Parsons, P. a. Tasker and R. E. P. Winpenny, *J. Chem. Soc. Dalt. Trans.*, 2000, **14**, 2349–2356.

5 S. G. Harris, University of Edinburgh, 1999.

6 E. V Anokhina, Y. B. Go, Y. Lee, T. Vogt and A. J. Jacobson, *J. Am. Chem. Soc.*, 2006, **128**, 9957–9962.

7 P. Zhu, W. Gu, F.-Y. Cheng, X. Liu, J. Chen, S.-P. Yan and D.-Z. Liao, *CrystEngComm*, 2008, **10**, 963–967.

8 B. Ma, D. Zhang, S. Gao and T. Jin, *Angew. …*, 2000, **39**, 3644–3646.

9 C. M. Gramaccioli, *Acta Crystallogr.*, 1966, **21**, 600–605.

10 Y. Zhang, M. K. Saha and I. Bernal, *CrystEngComm*, 2003, **5**, 34–37.

11 R. Wang, H. Liu, M. D. Carducci, T. Jin, C. Zheng and Z. Zheng, *Inorg. Chem.*, 2001, **40**, 2743–2750.

12 A. C. Kathalikkattil, R. Babu, R. K. Roshan, H. Lee, H. Kim, J. Tharun, E. Suresh and D.-W. Park, *J. Mater. Chem. A*, 2015, **3**, 22636–22647.

13 T. Luo, L. Hsu, C. Su, C. Ueng, T. Tsai and K. Lu, *Inorg. Chem.*, 2007, **46**, 1532–1534.

14 L. Chen and X. Bu, *Chem. Mater.*, 2006, **18**, 1857–1860.

15 H.-Y. Li, F.-P. Huang, Y.-M. Jiang and X.-J. Meng, *Inorganica Chim. Acta*, 2009, **362**, 1867–1871.

16 R. Vaidhyanathan, D. Bradshaw, J.-N. Rebilly, J. P. Barrio, J. a Gould, N. G. Berry and M. J. Rosseinsky, *Angew. Chem. Int. Ed. Engl.*, 2006, **45**, 6495–6499.

17 J. P. Barrio, J. N. Rebilly, B. Carter, D. Bradshaw, J. Bacsa, A. Y. Ganin, H. Park, A. Trewin, R. Vaidhyanathan, A. I. Cooper, J. E. Warren and M. J. Rosseinsky, *Chem. - A Eur. J.*, 2008, **14**, 4521–4532.

18 T. Kundu, S. C. Sahoo and R. Banerjee, *CrystEngComm*, 2013, **15**, 9634–9640.

19 A. P. Katsoulidis, K. S. Park, D. Antypov, C. Martí-Gastaldo, G. J. Miller, J. E. Warren, C. M. Robertson, F. Blanc, G. R. Darling, N. G. Berry, J. A. Purton, D. J. Adams and M. J. Rosseinsky, *Angew. Chemie Int. Ed.*, 2014, **53**, 193–198.

20 L. Lin, R. Yu, W. Yang, X. Wu and C. Lu, *Cryst. Growth Des.*, 2012, **12**, 3304–3311.

21 B. Lou, Y. Wei and Q. Lin, *CrystEngComm*, 2012, **14**, 2040–2045.

22 C. Martí-Gastaldo, D. Antypov, J. E. Warren, M. E. Briggs, P. a Chater, P. V Wiper, G. J. Miller, Y. Z. Khimyak, G. R. Darling, N. G. Berry and M. J. Rosseinsky, *Nat. Chem.*, 2014, **6**, 343–351.

23 C. Martí-Gastaldo, J. E. Warren, K. C. Stylianou, N. L. O. Flack and M. J. Rosseinsky, *Angew. Chemie Int. Ed.*, 2012, **51**, 11044–11048.

24 J. Rabone, Y.-F. Yue, S. Y. Chong, K. C. Stylianou, J. Bacsa, D. Bradshaw, G. R. Darling, N. G. Berry, Y. Z. Khimyak, A. Y. Ganin, P. Wiper, J. B. Claridge and M. J. Rosseinsky, *Science (80-.).*, 2010, **329**, 1053–1057.

25 E. N. Salgado, J. Faraone-Mennella and F. A. Tezcan, *J. Am. Chem. Soc.*, 2007, **129**, 13374–13375.

26 R. J. Radford and F. A. Tezcan, *J. Am. Chem. Soc.*, 2009, **131**, 9136–9137.

27 E. N. Salgado, R. A. Lewis, S. Mossin, A. L. Rheingold and F. A. Tezcan, *Inorg. Chem.*, 2009, **48**, 2726–2728.

28 E. N. Salgado, R. J. Radford and F. A. Tezcan, *Acc. Chem. Res.*, 2010, **43**, 661–72.

29 R. J. Radford, M. Lawrenz, P. C. Nguyen, J. A. McCammon and F. A. Tezcan, *Chem. Commun. (Camb).*, 2011, **47**, 313–315.

30 P. A. Sontz, J. B. Bailey, S. Ahn and F. A. Tezcan, *J. Am. Chem. Soc.*, 2015, **137**, 11598–11601.

31 J. Thomas-Gipson, R. Pérez-Aguirre, G. Beobide, O. Castillo, A. Luque, S. Pérez-Yáñez and P. Román, *Cryst. Growth Des.*, 2015, **15**, 975–983.

32 J. An, S. J. Geib and N. L. Rosi, *J. Am. Chem. Soc.*, 2009, **131**, 8376–8377.

33 J. An, O. K. Farha, J. T. Hupp, E. Pohl, J. I. Yeh and N. L. Rosi, *Nat. Commun.*, 2012, **3**, 604.

34 T. Li, D.-L. Chen, J. E. Sullivan, M. T. Kozlowski, J. K. Johnson and N. L. Rosi, *Chem. Sci.*, 2013, **4**, 1746–1755.

35 I. Imaz, M. Rubio-Martínez, J. An, I. Solé-Font, N. L. Rosi and D. Maspoch, *Chem. Commun. (Camb).*, 2011, **47**, 7287–302.

36 P. Horcajada, T. Chalati, C. Serre, B. Gillet, C. Sebrie, T. Baati, J. F. Eubank, D. Heurtaux, P. Clayette, C. Kreuz, J.-S. Chang, Y. K. Hwang, V. Marsaud, P.-N. Bories, L. Cynober, S. Gil, G. Férey, P. Couvreur and R. Gref, *Nat. Mater.*, 2010, **9**, 172–178.

37 S. R. Miller, D. Heurtaux, T. Baati, P. Horcajada, J.-M. Grenèche and C. Serre, *Chem. Commun. (Camb).*, 2010, **46**, 4526–4528.

38 J. Della Rocca, D. Liu and W. Lin, *Acc. Chem. Res.*, 2011, **44**, 957–968.

39 A. Ray Chowdhuri, D. Bhattacharya and S. K. Sahu, *Dalt. Trans.*, 2016, **45**, 2963–2973.

40 R. Liu, T. Yu, Z. Shi and Z. Wang, *Int. J. Nanomedicine*, 2016, **11**, 1187–1200.

41 P. Horcajada, R. Gref, T. Baati, P. K. Allan, G. Maurin, P. Couvreur, G. Férey, R. E. Morris and C. Serre, *Chem. Rev.*, 2012, **112**, 1232–1268.

42 A. C. McKinlay, B. Xiao, D. S. Wragg, P. S. Wheatley, I. L. Megson and R. E. Morris, *J. Am. Chem. Soc.*, 2008, **130**, 10440–10444.

43 J. An, C. M. Shade, D. A. Chengelis-Czegan, S. Petoud and N. L. Rosi, *J. Am. Chem. Soc.*, 2011, **133**, 1220–1223.

44 J.-W. Zhang, H.-T. Zhang, Z.-Y. Du, X. Wang, S.-H. Yu and H.-L. Jiang, *Chem. Commun.*, 2014, **50**, 1092–1094.

45 N. J. Hinks, A. C. McKinlay, B. Xiao, P. S. Wheatley and R. E. Morris, *Microporous Mesoporous Mater.*, 2010, **129**, 330–334.

46 C. J. Kepert and M. J. Rosseinsky, *Chem. Commun.*, 1998, 31–32.

47 M. Du, Y.-M. Guo, S.-T. Chen, X.-H. Bu, S. R. Batten, J. Ribas and S. Kitagawa, *Inorg. Chem.*, 2004, **43**, 1287–1293.

48 B. F. Abrahams, P. A. Jackson and R. Robson, *Angew. Chemie Int. Ed.*, 1998, **37**, 2656–2659.

49 M. Sasa, K. Tanaka, X.-H. Bu, M. Shiro and M. Shionoya, *J. Am. Chem. Soc.*, 2001, **123**, 10750–10751.

50 K. K. Bisht and E. Suresh, *J. Am. Chem. Soc.*, 2013, **135**, 15690–15693.

51 Y.-H. Han, Y.-C. Liu, X.-S. Xing, C.-B. Tian, P. Lin and S.-W. Du, *Chem. Commun.*, 2015, **51**, 14481–14484.

52 X. Jing, C. He, D. Dong, L. Yang and C. Duan, *Angew. Chemie Int. Ed.*, 2012, **51**, 10127–10131.

53 C. J. Kepert, T. J. Prior and M. J. Rosseinsky, *J. Am. Chem. Soc.*, 2000, **122**, 5158–5168.

54 C. Train, R. Gheorghe, V. Krstic, L.-M. Chamoreau, N. S. Ovanesyan, G. L. J. a Rikken, M. Gruselle and M. Verdaguer, *Nat. Mater.*, 2008, **7**, 729–734.

55 J. Zhang, S. Chen, T. Wu, P. Feng and X. Bu, *J. Am. Chem. Soc.*, 2008, **130**, 12882–12883.

56 S.-Y. Zhang, D. Li, D. Guo, H. Zhang, W. Shi, P. Cheng, L. Wojtas and M. J. Zaworotko, *J. Am. Chem. Soc.*, 2015, **137**, 15406–15409.

57 Z. Lin, A. M. Z. Slawin and R. E. Morris, *J. Am. Chem. Soc.*, 2007, **129**, 4880–4881.

58 T. Sawano, N. C. Thacker, Z. Lin, A. R. McIsaac and W. Lin, *J. Am. Chem. Soc.*, 2015, **137**, 12241–12248.

59 A. Hu, H. L. Ngo and W. Lin, *Angew. Chemie Int. Ed.*, 2003, **42**, 6000–6003.

60 A. Hu, H. L. Ngo and W. Lin, *J. Am. Chem. Soc.*, 2003, **125**, 11490–11491.

61 E. Pardo, C. Train, R. Lescouëzec, Y. Journaux, J. Pasán, C. Ruiz-Pérez, F. S. Delgado, R. Ruiz-Garcia, F. Lloret and C. Paulsen, *Chem. Commun.*, 2010, **46**, 2322–2324.

62 X. Zhao, M. Wong, C. Mao, T. X. Trieu, J. Zhang, P. Feng and X. Bu, *J. Am. Chem. Soc.*, 2014, **136**, 12572–12575.

63 M. Sartor, T. Stein, F. Hoffmann and M. Fröba, *Chem. Mater.*, 2016, **28**, 519–528.

64 J. Zhang, S. Chen, A. Zingiryan and X. Bu, *J. Am. Chem. Soc.*, 2008, **130**, 17246–17247.

65 Y. Peng, T. Gong, K. Zhang, X. Lin, Y. Liu, J. Jiang and Y. Cui, *Nat. Commun.*, 2014, **5**, 4406.

66 A. Ferguson, L. Liu, S. J. Tapperwijn, D. Perl, F.-X. Coudert, S. Van Cleuvenbergen, T. Verbiest, M. A. van der Veen and S. G. Telfer, *Nat. Chem.*, 2016, **8**, 250–257.

67 M. Banerjee, S. Das, M. Yoon, H. J. Choi, M. H. Hyun, S. M. Park, G. Seo and K. Kim, *J. Am. Chem. Soc.*, 2009, **131**, 7524–7525.

68 F. Song, C. Wang, J. M. Falkowski, L. Ma and W. Lin, *J. Am. Chem. Soc.*, 2010, **132**, 15390–15398.

69 M. C. Das, Q. Guo, Y. He, J. Kim, C.-G. Zhao, K. Hong, S. Xiang, Z. Zhang, K. M. Thomas, R. Krishna and B. Chen, *J. Am. Chem. Soc.*, 2012, **134**, 8703–8710.

70 F. Song, C. Wang and W. Lin, *Chem. Commun.*, 2011, **47**, 8256–8258.

71 C. Zhu, X. Chen, Z. Yang, X. Du, Y. Liu and Y. Cui, *Chem. Commun.*, 2013, **49**, 7120–7122.

72 Q. Li, S. M. Shin, D. Moon, K. S. Jeong and N. Jeong, *CrystEngComm*, 2013, **15**, 10161–10164.

73 C. Zhu, G. Yuan, X. Chen, Z. Yang and Y. Cui, *J. Am. Chem. Soc.*, 2012, **134**, 8058–8061.

74 Y. Liu, X. Xi, C. Ye, T. Gong, Z. Yang and Y. Cui, *Angew. Chemie Int. Ed.*, 2014, **53**, 13821–13825.

75 S.-C. Xiang, Z. Zhang, C.-G. Zhao, K. Hong, X. Zhao, D.-R. Ding, M.-H. Xie, C.-D. Wu, M. C. Das, R. Gill, K. M. Thomas and B. Chen, *Nat. Commun.*, 2011, **2**, 204–210.

76 J. Ferrando-Soria, D. Cangussu, M. Eslava, Y. Journaux, R. Lescouëzec, M. Julve, F. Lloret, J. Pasán, C. Ruiz-Pérez, E. Lhotel, C. Paulsen and E. Pardo, *Chem. - A Eur. J.*, 2011, **17**, 12482–12494.

Part 1.A

Oxamato-based chiral PCPs

1.A.1. Synthetic Route

Oxamato-based proligands derived from amino acids were prepared by following the same synthetic procedure (shown in Scheme 5): ethyl oxalyl chloride was reacted with the methyl ester derivatives of each enantiopure amino acid in the presence of triethylamine as base and dichloromethane as solvent, at room temperature (for further details on their syntheses see Annex I). The products were finally isolated as methyl ethyl oxamato-derivatives with very good yields (ranging from 80 to 90 %). The whole library of oxamato-based proligands derived from the amino acids alanine, valine, leucine and phenylglycine, which can be obtained by following this synthetic procedure, is illustrated in Scheme 6.

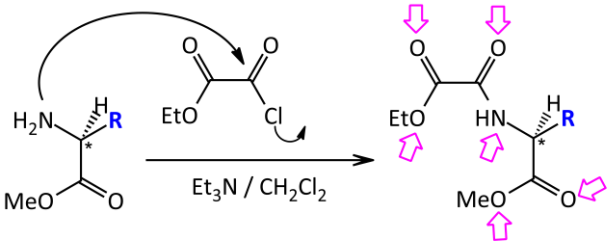

Amino acid	R group	Methyl ethyl derivative
alanine	CH_3	HMeEt-alama
valine	H_3C, H_3C	HMeEt-valma
phenylglycine		HMeEt-pegma
leucine		HMeEt-leuma

Scheme 5. Synthetic route for the preparation of the methyl ethyl derivatives of the chiral (*S*)-*N*-oxalamino acids. The different amino acids with their corresponding R substituent and the nomenclature for the oxamato-based resulting proligands are shown in the Table. HEtMe-alama = *N*-(ethyl oxoacetate)alanine; HEtMe-valma = *N*-(ethyl oxoacetate)valine]; HEtMe-leuma = *N*-(ethyl oxoacetate)leucine] and HEtMe-pegma = *N*-(ethyl oxoacetate)phenylglicine. The asymmetric carbon has been highlighted and the pink arrows indicate the multiple coordinating sites that these ligands have.

These proligands display interesting features. Firstly, they possess multiple coordinating sites (pink arrows in Scheme 5), anticipating a very versatile chemistry and an enormous variety of topological possibilities. Secondly, they are chiral molecules and their chirality can be transferred to their derivate structures. Finally, oxamato ligands are well known to transmit efficiently the magnetic coupling between the neighbouring paramagnetic centres.

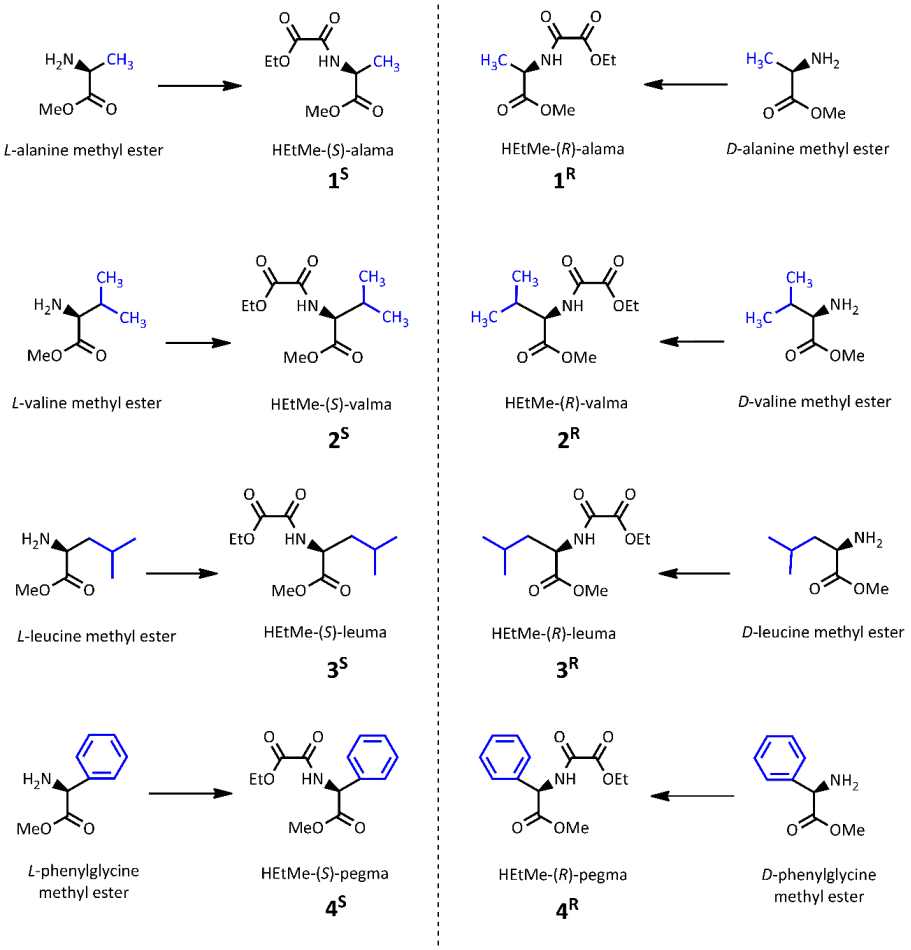

Scheme 6. Library of oxamato-derived proligands synthetised from the starting amino acids derivatives.

The next step consists of the synthesis of the metal complexes from the chiral oxamato-based metalloligands by following the synthetic route illustrated in Scheme 7. The oxamato-containing copper(II) complexes were obtained from the reaction of stoichiometric amounts of $CuCl_2 \cdot 6H_2O$ and the corresponding enantiopure ligands (1:1 metal to ligand molar ratio) in a Me_4NOH methanolic solution. The compounds were isolated as tetramethylammonium salts with general formula $(Me_4N)_x[CuL]_x \cdot nH_2O$ [L = (*S*)-alama^{3-}, (*S*)-valma^{3-}, (*R*)-valma^{3-}, (*S*)-leuma^{3-}, (*S*)-pegma^{3-} and (*R*)-pegma^{3-})] (for further details on their syntheses see Annex I).

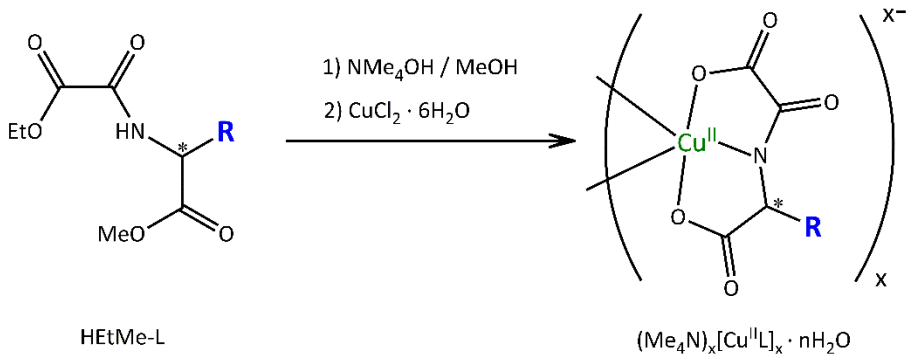

HEtMe-L

$(Me_4N)_x[Cu^{II}L]_x \cdot nH_2O$

Scheme 7. General synthetic route for the preparation of the copper(II) complexes, which will further act as ligands through the free coordinating sites towards a second metal. The chiral centres have been indicated with *.

Different structures were found for the copper(II) complexes depending on the amino acid precursor. In particular, four hexacopper(II) wheels of formulas $(Me_4N)_6\{Cu^{II}_6[(S)\text{-alama}]_6\} \cdot 10H_2O$ (**1a^S**), $(Me_4N)_6\{Cu^{II}_6[(S)\text{-valma}]_6\} \cdot 7H_2O$ (**2a^S**), $(Me_4N)_6\{Cu^{II}_6[(R)\text{-valma}]_6\} \cdot 7H_2O$ (**2a^R**) and $(Me_4N)_6\{Cu^{II}_6[(S)\text{-leuma}]_6\} \cdot 10H_2O$ (**3a^S**) were obtained from (*S*)-alama^{3-}, (*S*)-valma^{3-}, (*R*)-valma^{3-} and (*S*)-leuma^{3-} ligands (see Scheme 8). Alternatively, the synthesis with both enantiomers (*S* and *R*) of the pegma^{3-} ligand does not afford hexacopper(II) rings but copper(II) chains instead. The 1D compounds derived from the (*S*)-pegma^{3-} and (*R*)-pegma^{3-} ligands are $\{Me_4N[Cu^{II}(S)\text{-pegma}] \cdot 2H_2O\}_n$ (**4a^S**) and $\{Me_4N[Cu^{II}(R)\text{-pegma}] \cdot 2H_2O\}_n$, respectively (see Scheme 9).

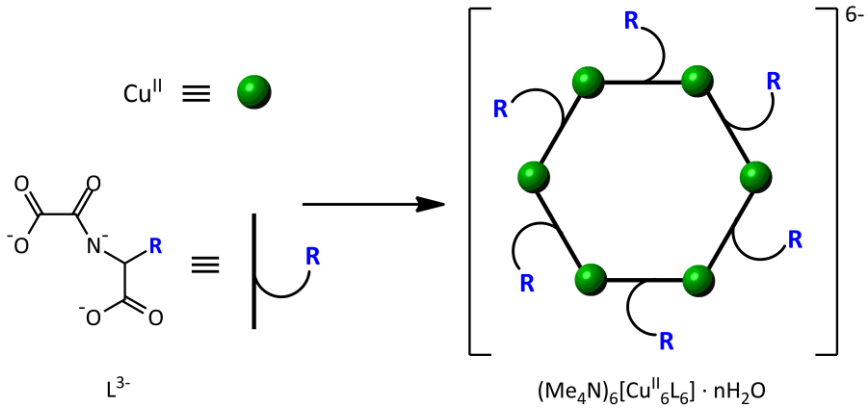

Proligand		R group	Copper(II) complex	
HMeEt-(*S*)-alama	**1^S**	CH_3	$(Me_4N)_6\{Cu^{II}_6[(S)\text{-alama}]_6\} \cdot 10H_2O$	**1a^S**
HMeEt-(*S*)-valma	**2^S**	H_3C H_3C	$(Me_4N)_6\{Cu^{II}_6[(S)\text{-valma}]_6\} \cdot 7H_2O$	**2a^S**
HMeEt-(*R*)-valma	**2^R**		$(Me_4N)_6\{Cu^{II}_6[(R)\text{-valma}]_6\} \cdot 7H_2O$	**2a^R**
HMeEt-(*S*)-leuma	**3^S**		$(Me_4N)_6\{Cu^{II}_6[(S)\text{-leuma}]_6\} \cdot 10H_2O$	**3a^S**

Scheme 8. Synthetic approach illustrating the assembly of the hexacopper(II) wheels. The Table shows the different chiral hexacopper(II) rings which have obtained from the (*S*)-alama^3, (*S*)-valma^{3-}, (*R*)-valma^{3-} and (*S*)-leuma^{3-} ligands.

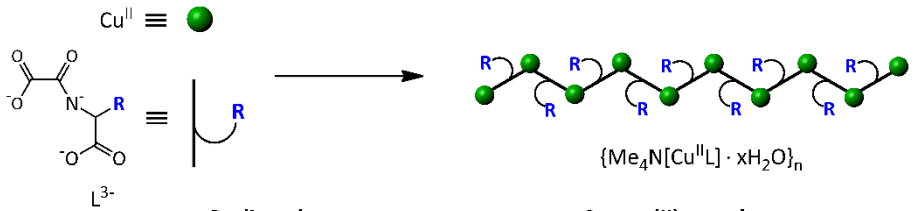

Proligand		R group	Copper(II) complex	
HMeEt-(*S*)-pegma	**4^S**		$\{Me_4N[Cu^{II}(S)\text{-pegma}] \cdot 2H_2O\}_n$	**4a^S**
HMeEt-(*R*)-pegma	**4^R**		$\{Me_4N[Cu^{II}(R)\text{-pegma}] \cdot 2H_2O\}_n$	**4a^R**

Scheme 9. Synthetic approach illustrating the assembly of the copper(II) chains derived from the (*S*)- and (*R*)-pegma^{3-} ligands. The Table shows the two copper(II) 1D compounds that have been synthesised.

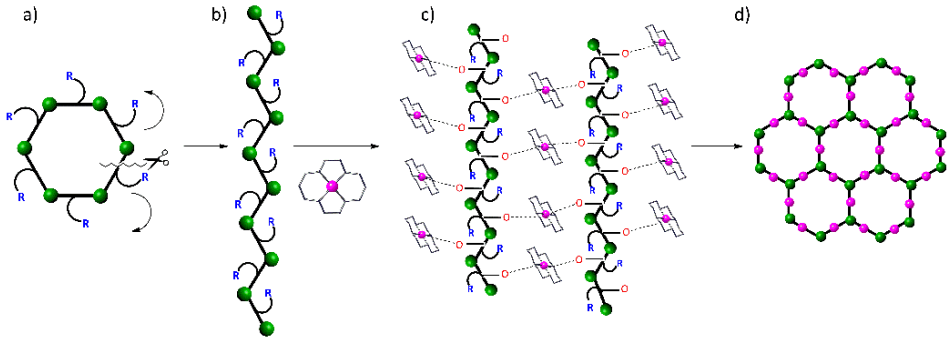

Copper(II) precursor		R group	PCP	
$(MeN_4)_6\{Cu^{II}_6[(S)\text{-alama}]_6\} \cdot 10H_2O$	$\mathbf{1a^S}$	CH_3	$\{[Ni^{II}(cyclam)]_2[Cu^{II}(S)\text{-alama}] \cdot nH_2O\}_n$	$\mathbf{1b^S}$
$(MeN_4)_6\{Cu^{II}_6[(S)\text{-valma}]_6\} \cdot 7H_2O$	$\mathbf{2a^S}$	H_3C, H_3C	$\{[Ni^{II}(cyclam)]_2[Cu^{II}(S)\text{-valma}] \cdot nH_2O\}_n$	$\mathbf{2b^S}$
$(MeN_4)_n\{Cu^{II}[(R)\text{-pegma}]\}_n \cdot 2H_2O$	$\mathbf{4a^R}$		$\{[Ni^{II}(cyclam)]_2[Cu^{II}(R)\text{-pegma}]\} \cdot nH_2O\}_n$	$\mathbf{4b^R}$

Scheme 10. Hypothetic "metalloligand" approach illustrating the assembly of the different chiral 3D porous structures. (a-b) View of the hexacopper(II) wheel and suggestion of its fragmentation-reconstruction process to yield a chain. (c) Suggested self-assembling process consisting of the coordination of the free carbonyl groups from the copper(II) chains towards the $[Ni(cyclam)]^{2+}$ species. (d) Perspective view of the resulting 3D homochiral PCP. The Table shows the different PCPs which have been obtained from the (*S*)-alama^{3-}, (*S*)-valma^{3-} and (*R*)-pegma^{3-} ligands. The whole a-d sequence corresponds to the synthesis of **1b^S** and **2b^S**, being the starting complexes the corresponding hexacopper(II) wheels whilst the b-d sequence illustrates the synthesis of **4b^R**, whose precursor is a chain.

Finally, aiming at building the 3D porous structures, we followed the already mentioned metalloligand strategy and used the copper(II) precursors as ligands towards the preformed square-planar cationic complex $[Ni(cyclam)]^{2+}$ (cyclam = 1,4,8,11-tetraazacyclotetradecane), a complex where the metal ion has only two free axial positions which can be filled by two oxygen atoms from the free carbonyl groups of the copper(II) precursors [see Scheme 10c]. Thus, the $[Ni(cyclam)]^{2+}$ molecules act as linkers between the chains of the copper(II) precursor giving rise to the formation of complex porous structures. From the final structures of the PCPs, we can elucidate that in case of the hexacopper(II) wheels, these may open and change their conformation to

coordinate to the $[Ni(cyclam)]^{2+}$ complexes. This hypothetical mechanism is illustrated in Scheme 10 and will be explained in more detail in the following sections.

1.A.2. Physico-chemical Characterisation

The chemical nature of the proligands, the copper(II) precursors and the oxamato-based copper(II)/nickel(II) PCPs was established through ^{1}H NMR spectroscopy, elemental analysis (C, H, N), FTIR spectroscopy and Scanning Electronic Microscopy (SEM). The obtained data are represented in Tables 1-9 in Annex I.

1.A.2.1. Thermo-gravimetric study

The water contents of **1b^S**, **2b^R** and **4b^R** has been determined by thermogravimetric analysis (TGA) under a dry N_2 atmosphere. A slight mass loss from room temperature to around 150 °C can be observed for all three compounds. It is followed by a *plateau* in the range 150-200 °C, and a further decomposition (Figure 16). The values of the mass loss at 125 °C of *ca*. 7.8 (**1b^S**), 9.0 (**2b^R**) and 9.2 % (**4b^R**), correspond to 9, 15 and 6 water molecules per formula unit, respectively. The reason why the isopropanol molecules in **4b^R** cannot be found in the TGA may be their loss upon the open air during the sample filtration and its further preparation procedure.

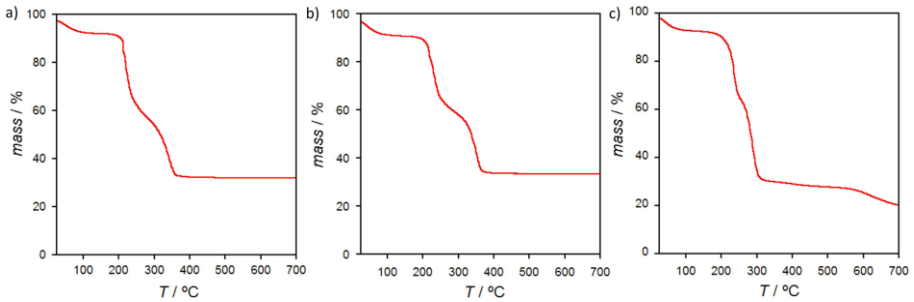

Figure 16. TGA of **1b^S**, **2b^S** and **4b^R** under dry N_2 atmosphere.

1.A.2.2. Powder X-ray diffraction

Powder X-ray diffraction (PXRD) patterns of polycrystalline samples of **1b^S** and **2b^S** at room temperature, prepared from suspensions in water:isopropanol (1:9 v/v) to avoid any loss of water molecules, were measured (see Figure 17). Within each sample, the experimental PXRD pattern profile is consistent with the calculated one, confirming thus that the bulk samples are isostructural to the crystals selected for single-crystal X-ray diffraction. However, the PXRD patterns of the dehydrated samples of **1b^S** and **2b^S** showed a total loss of the crystallinity at room temperature (Figures 17c and f). This situation reveals that the frameworks of **1b^S** and **2b^S** become amorphous upon removal of solvent molecules when they are exposed to the open air.

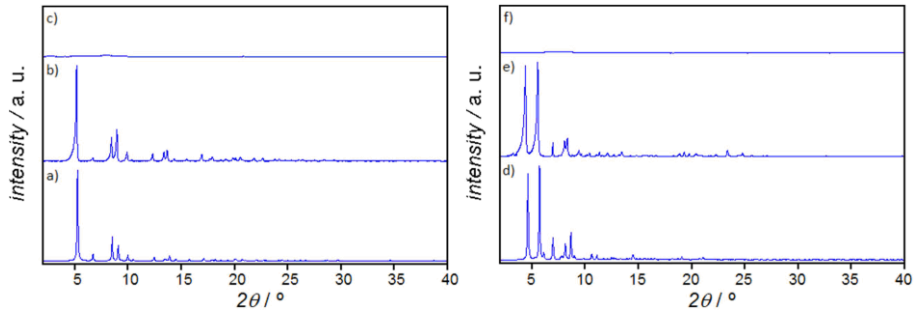

Figure 17. Calculated and experimental PXRD pattern profiles of water:isopropanol (1:9 v/v) suspension and polycrystalline dehydrated samples of **1b^S** (a, b and c) and **2b^S** (d, e and f) measured at r.t.

Powder X-ray diffraction (PXRD) patterns of polycrystalline samples of **4b^R** were also carried out. The experimental PXRD pattern profile measured as a suspension of **4b^R** in water:isopropanol (1:9 v/v) (Figure 18b) is consistent with the calculated one (Figure 18a). Moreover, unlike **1b^S** and **2b^S**, the spectra of the polycrystalline dehydrated sample of **4b^R** reveals a retention of the crystallinity even when exposed to the open air (see Figure 18c). The PXRD pattern of a polycrystalline sample of **4b^R** after gas sorption experiments has also been studied (Figure 18d). The results reveal that the framework remains unaltered despite the activation and sorption processes. The overall situation

suggests that **4b^{R}** exhibits a higher structural stability than **1b^{S}** and **2b^{S}**, as the gas sorption measurements will further demonstrate.

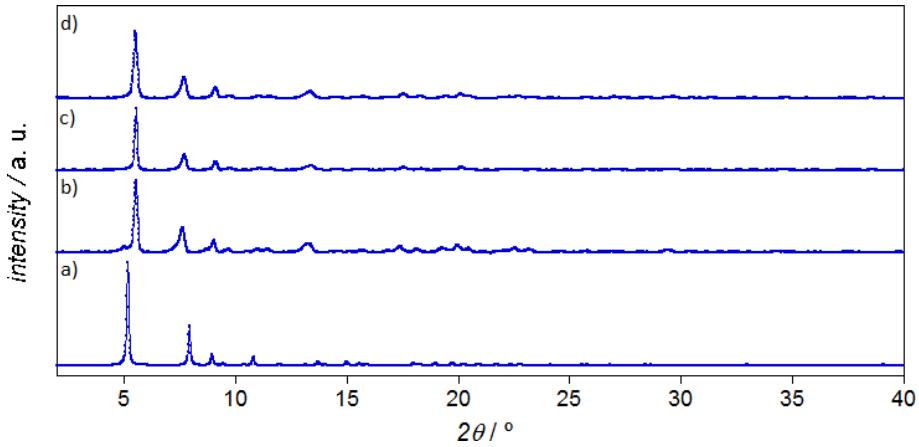

Figure 18. (a) Calculated and experimental PXRD pattern profiles of (b) water:isopropanol (1:9 v/v) suspension and (c) polycrystalline dehydrated samples of **4b^{R}** at r.t. (d) PXRD pattern of **4b^{R}** after sorption experiments.

1.A.3. Crystal Structures

Among the family of the obtained copper(II) compounds, some of them could be crystallised following slow evaporation techniques (see synthetic section, in Annex I, for further information). Their crystal structures could be obtained by using single crystal X-ray diffraction.

Powder samples and X-ray quality crystals of the hexacopper(II) wheels of formula $(Me_4N)_6\{Cu^{II}_6[(S)\text{-alama}]_6\} \cdot 10H_2O$ (**1a^{S}**), $(Me_4N)_6\{Cu^{II}_6[(S)\text{-valma}]_6\} \cdot 7H_2O$ (**2a^{S}**), $(Me_4N)_6\{Cu^{II}_6[(R)\text{-valma}]_6\} \cdot 7H_2O$ (**2a^{R}**) and $(Me_4N)_6\{Cu^{II}_6[(S)\text{-leuma}]_6\} \cdot 10H_2O$ (**3a^{S}**), as well as the copper(II) chains of formula $\{Me_4N[Cu^{II}(S)\text{-pegma}] \cdot 2H_2O\}_n$ (**4a^{S}**) and $\{Me_4N[Cu^{II}(R)\text{-pegma}] \cdot 2H_2O\}_n$ (**4a^{R}**) were obtained (their synthetic procedures being described in Annex I). The well-formed blue hexagonal prisms of **1a^{S}**, **2a^{S}**, **2a^{R}**, **3a^{S}** and blue elongated rectangular prisms of **4a^{S}** and **4a^{R}** allowed us to carry out single crystal

X-ray diffraction measurements. In addition to a thorough structural description (see below) extra data and crystallographic information can be found in Annex I.

These preformed chiral metalloligands of zero- (0D) or one-dimensional (1D) nature exhibiting free coordination sites through the carbonyl groups of the amino acid group are promising SBUs. However, due to the steric hindrance of these copper(II) precursors, we chose the well-known square-planar cationic complex $[Ni(cyclam)]^{2+}$, possessing two available axial positions to be occupied by the carbonyl groups of the SBUs instead of solvated metal ions which cannot accommodate the metalloligands into their environment. In such a way, different 3D porous structures (**1b^{S}**, **2b^{S}** and **4b^{R}**) were obtained.

Noteworthy, all the available copper(II) metalloligands could not yield single crystals of their oxamato-containing copper(II)/nickel(II) PCP derivatives. The complexity of these 3D porous structures lies at the origin of their very laborious and sometimes unsuccessful crystallisation.

1.A.3.1. Metalloligands

1a^{S}, **2a^{S}**, **2a^{R}** and **3a^{S}** crystallise in the same chiral space group $P6_3$ of the hexagonal system and their absolute configuration has been reliably assigned.

The structures of **1a^{S}**, **2a^{S}**, **2a^{R}** and **3a^{S}** consist of cyclic oxamate-bridged hexacopper(II) complex anions, $[Cu^{II}_6L_6]^{6-}$ [L = (*S*)-alama^{3-} (**1a^{S}**), (*S*)-valma^{3-} (**2a^{S}**), (*R*)-valma^{3-} (**2a^{R}**) and (*S*)-leuma^{3-} (**3a^{S}**)] (Figures 19 and 20), together with charge-balancing Me_4N^+ (tetramethylammonium) countercations and free water molecules. These rings show an open calix-type molecular shape which is reminiscent of that found for the well-known α-cyclodextrin.[1] However, the alternating up and down, outward and inward disposition of the six alkyl groups from the amino acid residues results in an approximate S_6 molecular symmetry that differs from that of the C_6-symmetric α-cyclodextrin molecule. That being so, the anionic hexacopper(II) wheels of **1a^{S}**, **2a^{S}**, **2a^{R}** and **3a^{S}** are not exactly planar but they exhibit an overall chair conformation (Figure 19 and 20,

bottom). This conformation leads to a basket-like supramolecular cavity where the Me_4N^+ guest cations are located.

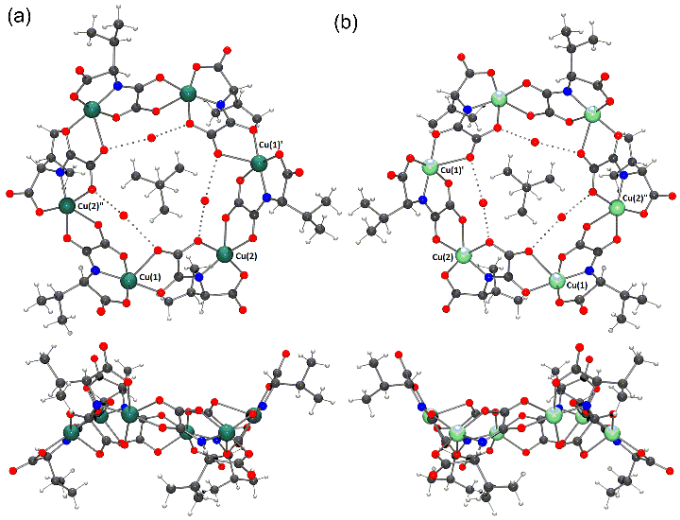

Figure 19. Top and side views of the anionic cyclic hexacopper(II) units of **2a^S** (left) and **2a^R** (right) with the numbering of the metal atom (symmetry code: I = -y, x-y, z; II = -x+y, -x, z) and the templating tetramethylammonium cations. The carbon, copper, hydrogen, nitrogen and oxygen atoms are depicted as grey, green, pale pink, blue and red spheres, respectively.

Interestingly, the degree of distortion of the three different hexacopper(II) wheels **1a^S**, **2a^S**, and **3a^S** is not the same (Figure 21). Compound **1a^S**, where the alkyl substituent is a methyl group, is the one whose structure is closer to a planar conformation whilst the wheel of **2a^S**, where the alkyl substituent is an isopropyl group, displays the higher degree of distortion. Surprisingly, the wheel of **3a^S** exhibits less degree of distortion than that of **2a^S**, despite the bigger size of its isobutyl group. This degree of distortion has been illustrated by Figure 21 and quantified in terms of the distances between two adjacent wheels of **1a^S**, **2a^S**, and **3a^S**, the Cu(1)···Cu(2)^{III} and Cu(2)···Cu(1)^{III} distances being 10.147/10.463 (**1a^S**), 11.476/9.653 (**2a^S**) and 11.371/9.946 Å (**3a^S**). Thus, the ring of **2a^S** is the less planar one.

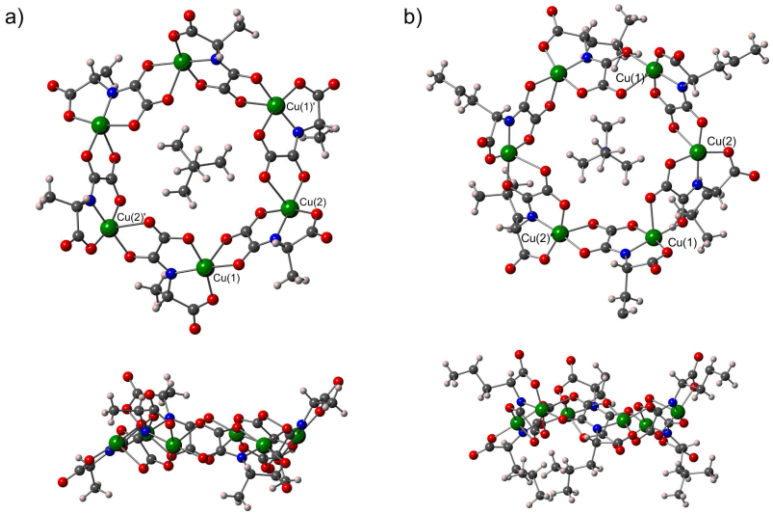

Figure 20. Top and side views of the anionic cyclic hexacopper(II) units of **1a^S** (a) and **3a^S** (b) with the numbering of the metal atoms symmetry code: I = - *y*, *x* - *y*, *z*; II = - *x* + *y*, - *x*, *z*) and the templating tetramethylammonium cations. The carbon, copper, hydrogen, nitrogen and oxygen atoms are depicted as grey, green, pale pink, blue and red spheres, respectively.

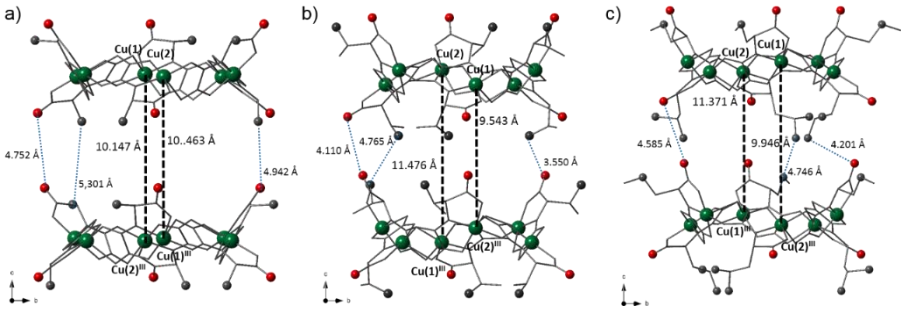

Figure 21. View of two parallel hexacopper(II) wheels from **1a^S** (a), **2a^S** (b) and **3a^S** (c) along the crystallographic *a* axis. The values of the shortest O···O, C···C, O···C and Cu···Cu inter-ring are indicated and shown as dashed lines. The terminal carbon and oxygen atoms and the copper(II) ions are highlighted as grey, red and green spheres, respectively. The countercations and water molecules have been omitted for clarity. (Symmetry code: III = *x* - *y*, -1 + *x*, 0.5 + *z*).

The two crystallography independent Cu(1) and Cu(2) atoms of **1a^S**, **2a^S**, **2a^R** and **3a^S** show a slightly distorted five-coordinate $CuNO_4$ square pyramidal environment, that results from the alternating tridentate/bidentate ($\kappa^3N,O,O':\kappa^2O'',O'''$) bridging mode of

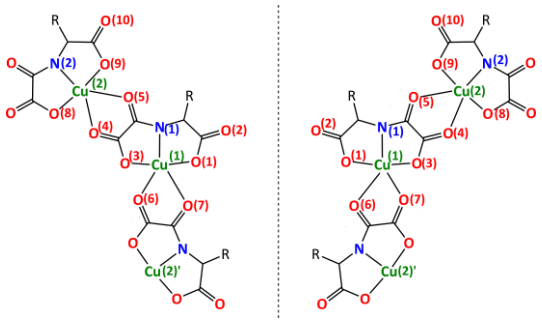

Scheme 10. Drawing of the common asymmetric unit of the four hexacopper(II) wheels in **1a^S**, **2a^S**, **1a^S** and **3a^S**, showing the distorted five-coordinate square pyramidal environment of the Cu(II) atom. The atoms have been labelled according to the data from the tables in Annex I.

the (*S*)-alama^{3-}, (*S*)- and (*R*)-valma^{3-} and (*S*)-leuma^{3-} ligands (see Scheme 10). The bond lengths and interbond bite angles for **1a^S**, **2a^S**, **2a^R** and **3a^S** are collected in Tables 27 and 28 (Annex I).

The intramolecular Cu(1)···Cu(2) / Cu(1)···Cu(2^I) distances are 5.409/5.373 (**1a^S**), 5.391/5.275 (**2a^S**), 5.228/5.343 (**2a^R**) and 5.423/5.301 Å (**3a^S**).

Interestingly, both metal ions in **1a^S**, **2a^S**, **2a^R** and **3a^S** are present as one single enantiomer, A (**1a^S**, **2a^S** and **3a^S**) or C (**2a^R**),[2] confirming thus the effective transmission of the encoded chiral information of the enantiopure ligands (*R* or *S*) to the coordinated metal centres, as expected. Moreover, it is possible to compare the structure of the two hexacopper(II) wheels obtained from the valma^{3-} ligands (**2a^S** and **2a^R**) concluding that each homochiral [AAAAAA-Cu$^{II}_6$ (**2a^S**) and CCCCCC-Cu$^{II}_6$ (**2a^R**)] hexanuclear ring has the opposite metal chirality.

There is a staggered parallel alignment of the anionic hexacopper(II) wheels along the crystallographic *c* axis in the crystal lattice of **1a^S**, **2a^S**, **2a^R** and **3a^S** (Figure 22). This leads to a pseudo-helical supramolecular motif made up by columnar arrays of Cu$^{II}_6$ rings defining a small circular channel with a diameter of *ca*. 0.8 nm which is occupied by some of the Me$_4$N$^+$ cations acting as guests (Figures 19, 20 and 22). There are weak host-guest hydrophobic interactions among the methyl groups from the alkyl residues and the Me$_4$N$^+$ cations located in the centre of the channel [C···C distances of 5.430 (**1a^S**), 4.006 (**2a^S** and **2a^R**) and 4.867 Å (**3a^S**)] (Figure 23).

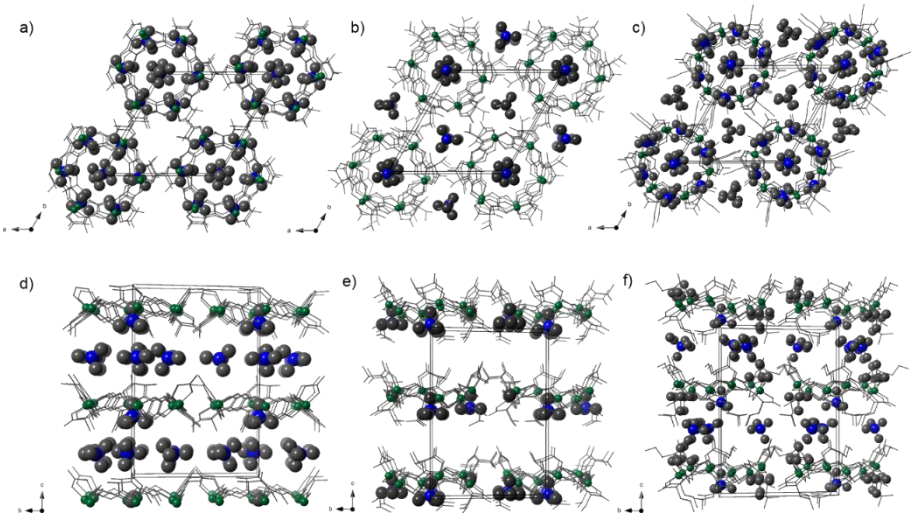

Figure 22. Perspective drawings of the crystal packing along the crystallographic *c* and *a* axis of **1a^S** (a, d), **2a^S** (b, e) and **3a^S** (c, f). The ligand backbones are shown as grey sticks whereas the copper(II) ions, and the carbon and nitrogen atoms of the tetramethylammonium countercations are depicted as green, grey and blue spheres (with an arbitrary radii), respectively. The crystallisation water molecules are omitted for clarity.

The remaining Me_4N^+ cations follow different distributions for each compound. Some of the Me_4N^+ cations in **2a^S**, **2a^R** and **3a^S** are located between two adjacent Cu^{II}_6 rings along the crystallographic *ab* plane the intermolecular Cu···Cu distances being 7.079 (**2a^S** and **2a^R**) and 7.584 Å (**3a^S**). However, the intermolecular Cu···Cu separations in **1a^S** are much more shorter (5.244 Å) due to the minor steric hindrance of the methyl group compared to the isopropyl (**2a^S** and **2a^R**) and isobutyl substituents (**3a^S**), preventing the Me_4N^+ cations from

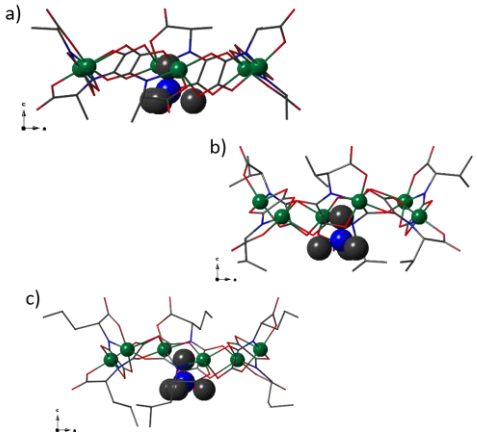

Figure 23. Side views of the Cu^{II}_6 units of **1a^S** (a), **2a^S** (b) and **3a^S** (c). The ligand backbones are shown as coloured sticks whereas the copper, and the carbon and nitrogen atoms of the tetramethylammonium countercations are depicted as green, grey and blue spheres with an arbitrary radii, respectively.

occupying the space between adjacent Cu^{II}_6 wheels on the crystallographic *ab* plane. The Me_4N^+ are also hosted on the crystallographic *bc* plane in **1a^S** and **3a^S**. Interestingly, compounds **2a^S** and **2a^R** do not show cations in such location, since the "interlayer" distance is much shorter (see Figure 21) due to the presence of the isopropyl residue, which is longer than the methyl group from **1a^S** and more rigid than the isobutyl group from **3a^S**. The analysis of the crystal packing of **1a^S**, **2a^S**, **2a^R** and **3a^S** suggests then that the Me_4N^+ cations play a key role in the self-assembling process that leads to formation of the hexacopper(II) rings.

Some of the water molecules of crystallisation are linked to the inner walls of the **1a^S**, **2a^S** and **2a^R** wheels through hydrogen bonds involving the carboxylate-oxygen atoms from the oxamato bridge [O6···O3$_W$ = 2.870 (**1^S**) and O3···O1$_W$ = 2.950 Å (**2a^S** and **2a^R**)] (Figure 24).

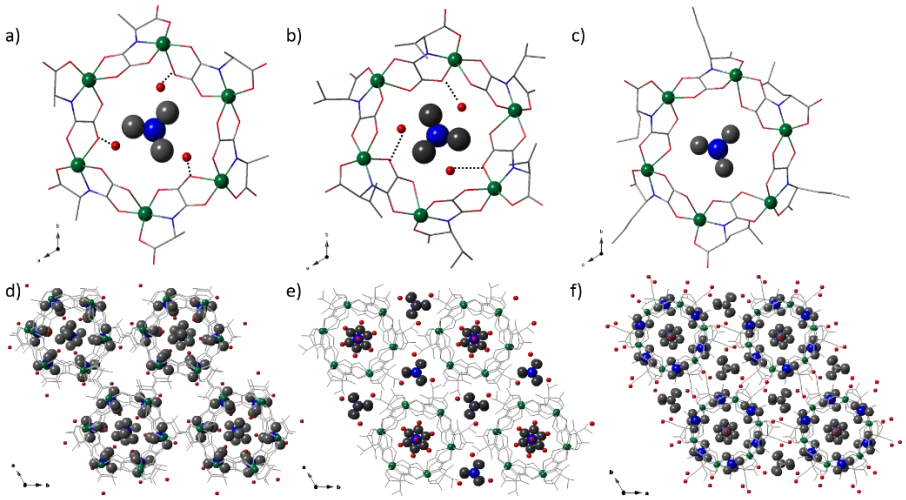

Figure 24. Top views of the Cu^{II}_6 units of (a) **1a^S**, (b) **2a^S** and (c) **3a^S** illustrating the hydrogen bonds (dashed lines) between the crystallisation water molecules and the inner walls of the hexacopper(II) wheels. Views of the crystal packing along the crystallographic *c* axis of (d) **1a^S**, (e) **2a^S** and (f) **3a^S**. The ligand backbones are shown as sticks whereas the copper(II) ions, the carbon and nitrogen atoms of the tetramethylammonium countercations are depicted as green, grey and blue spheres (with an arbitrary radii), respectively. The red spheres stand for the water molecules of crystallisation.

Following the same synthetic route but using the (*S*)-pegma^{3-} (**4^{S}**) and (*R*)-pegma^{3-} (**4^{R}**) ligands instead, powder samples as well as well-formed elongated rectangular blue prisms of **4a^{S}** and **4a^{R}** were obtained (see Annex I for further details).

Their structures could then be determined and their absolute configuration reliably assigned revealing two enantiopure chains of formula $\{Me_4N[Cu^{II}(S)\text{-pegma}] \cdot 2H_2O\}_n$ and $\{Me_4N[Cu^{II}(R)\text{-pegma}] \cdot 2H_2O\}_n$, respectively.

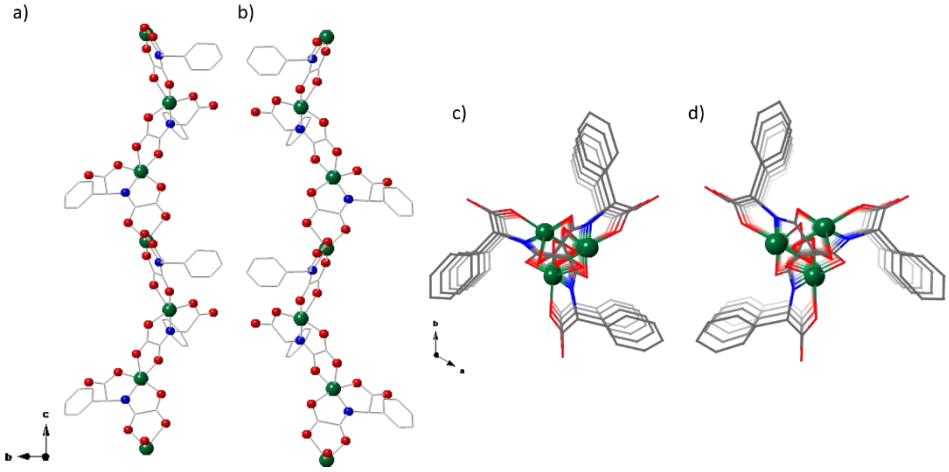

Figure 25. Perspective views along the crystallographic *a* and *c* axis of the left- **4a^{S}** (a and c) and right-handed Cu^{II} helical chain **4a^{R}** (b and d). The carbon atoms are depicted as grey sticks while the copper(II) ions are shown as green spheres. Nitrogen and oxygen atoms are shown as blue and red spheres (a and b) or sticks (c and d). The Me_4N^+ counterbalancing cations and the water molecules of crystallisation have been omitted for clarity.

Both, **4a^{S}** and **4a^{R}**, crystallise in the chiral $P3_1$ space group and they contain enantiomerically pure oxamato-bridged copper(II) helical chains, Me_4N^+ cations and H-bonded lattice water molecules. The single-stranded helices of **4a^{S}** and **4a^{R}** are arranged in a left- (*M*) and right-handed (*P*) fashion respectively, with helical pitches of 14.76 (**4a^{S}**) and 14.43 Å (**4a^{R}**) (Figure 25).

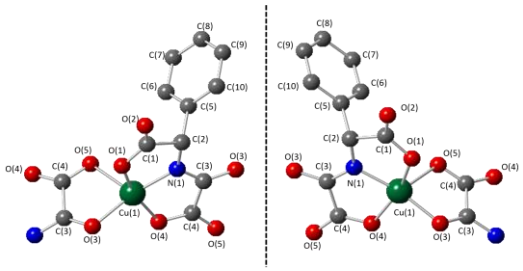

Figure 26. Perspective view of the common asymmetric unit of **4a^{S}** and **4a^{R}** showing the distorted five-coordinate square pyramidal environment of the copper(II) ion. The atoms have been labelled according to the data from the Tables in Annex I.

The (*S*)-pegma^{3-} and (*R*)-pegma^{3-} ligands alternate tridentate/bidentate bridging modes ($\kappa^3N,O,O':\kappa^2O'',O'''$) connecting two copper(II) atoms and constructing chains [shortest intrachain Cu···Cu distances of 5.370 (**4a^{S}**) and 5.322 Å (**4a^{R}**)]. Each copper(II) ion adopts a distorted square pyramidal coordination geometry $CuNO_4$ (see Figures 25 and 26), bonded to one nitrogen and four oxygen atoms from the ligands. The bond distances and the interbond bite angles for **4^{S}** and **4a^{R}** are shown in Tables 29 and 30 in Annex I.

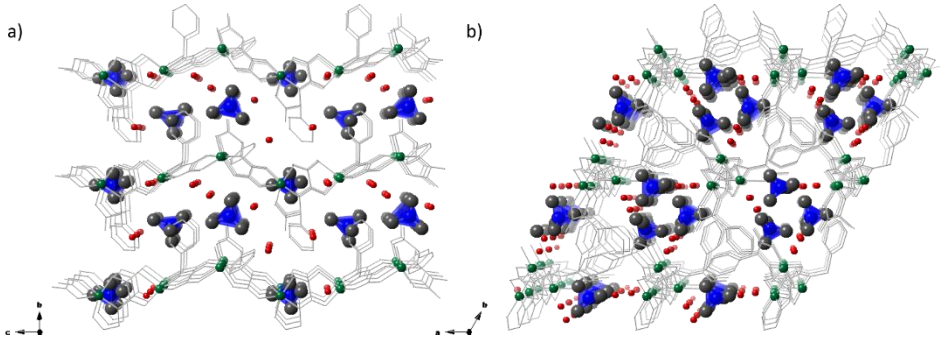

Figure 27. Views of the crystal packing of **4a^{R}** along the crystallographic *a* (a) and *c* axes (b). The ligand backbones are shown as grey sticks whereas the copper(II) ions from the wheels, and the carbon and nitrogen atoms of the tetramethylammonium countercations are depicted as green, grey and blue spheres (with arbitrary radii), respectively. The water molecules of crystallisation are shown as red spheres.

In the crystal lattice of **4a^{S}** and **4a^{R}**, there is a staggered alignment of the anionic copper(II) chains along the crystallographic *c* axis the Me_4N^+ countercations together with the water molecules of crystallisation being confined within the pseudo-channels that are formed (see Figure 27b). The water molecules of crystallisation are hydrogen bonded to the oxygen atoms from the oxamato bridges from one chain [O(1$_W$)···O5 =

2.826 and O(2_W)···O(4) = 2.932 Å) and to the carbonyl-oxygen atom from the amino acid of a neighbouring chain [2.802 and 2.891 Å for O(1_W)···O(2) and O(2_W)···O(2), respectively] (Figure 28), leading thus to a two-dimensional supramolecular arrangement.

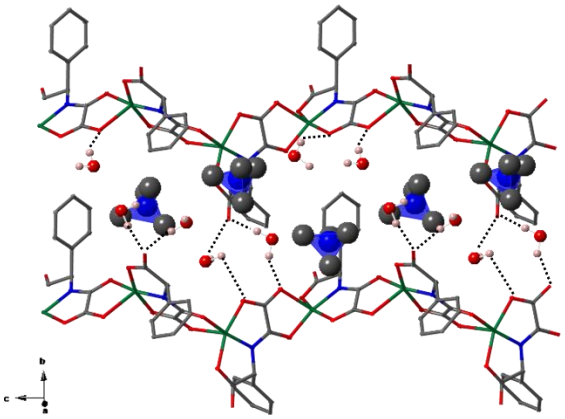

Figure 28. Perspective view of two neighbouring chains of **4a^R** showing the hydrogen bond interactions between the crystallisation water molecules and the oxygen atoms from the ligand (dashed lines). The backbone chain is depicted with sticks for clarity. The nitrogen atoms from the Me_4N^+ cations are shown has blue tetrahedral, whilst the carbon atoms from the Me_4N^+ cations and the hydrogen and oxygen atoms from the water molecules are represented by grey, pale pink and red spheres with arbitrary radii.

1.A.3.2. Porous Coordination Polymers (PCPs)

$\{[Ni^{II}(cyclam)][Cu^{II}(S)\text{-alama}]_2 \cdot 9H_2O\}_n$ (**1b^S**)

Following the related metalloligand strategy, the reaction of the hexacopper(II) wheel **1a^S** with $[Ni(cyclam)]^{2+}$ ions led to the formation of the neutral 3D compound of formula $\{[Ni^{II}(cyclam)][Cu^{II}(S)\text{-alama}]_2 \cdot 9H_2O\}_n$ (**1b^S**) (for further details on their syntheses see Annex I).

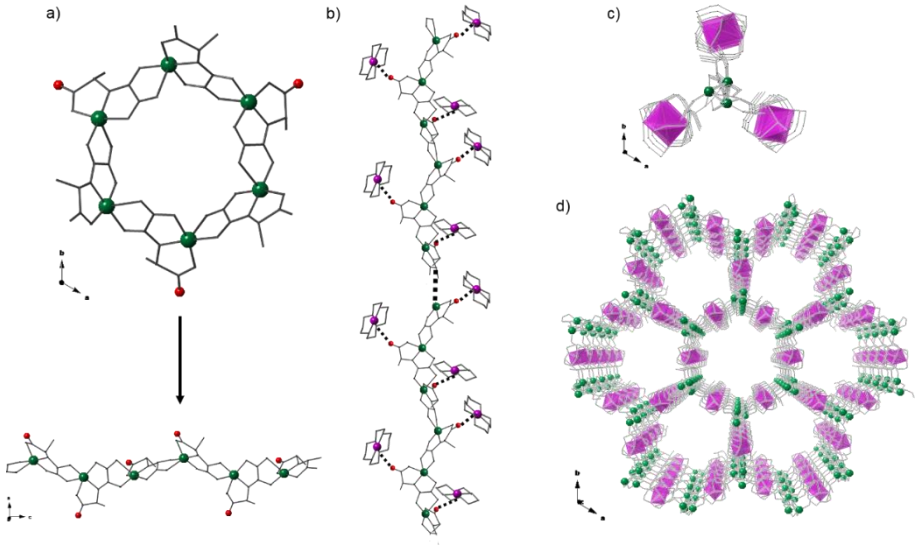

Figure 29. (a) View of the hexacopper(II) (**1a^S**) precursor and its suggested fragmentation-reconstruction process to yield a chain. (b) Proposed self-assembling process consisting of the coordination of the free carbonyl groups of the chain towards the $[Ni(cyclam)]^{2+}$ complex cations. (c) Perspective view of the three-fold helical chains of copper(II) ions along the crystallographic *c* axis and their coordination to the $[Ni(cyclam)]^{2+}$ cations. (d) Perspective view of the resulting 3D homochiral PCP. The copper(II) and nickel(II) ions are depicted as green/purple spheres/polyhedra, respectively. The oxygen atoms of the free carbonyl groups are represented by red spheres. Thin and thick black dashed lines simulate the approach of the $[Ni(cyclam)]^{2+}$ cations to the carbonyl groups and the self-assembly of the copper(II) chains, respectively.

Compound **1b^S** crystallises in the trigonal chiral space group R_3. The fundamental building blocks of **1b^S** consist of helical copper(II) anionic chains (see Figures 29 and 30) interconnected through unsaturated square-planar $[Ni(cyclam)]^{2+}$ ions. These ions are coordinated to the free carbonyl groups from the alanine amino acid residues, which

point outwards, thus holding the chiral chains and generating a neutral 3D non-interpenetrating chiral porous network (see Figure 29).

Based on the crystal structures of the final **1b^{S}** PCP and starting **1a^{S}** wheel we propose a plausible self-assembling approach. Since the building blocks found in the chiral framework are helical chains (see Figures 29 and 30), we suggest that the starting preformed hexanuclear copper(II) wheels in **1a^{S}** may undergo an initial process of disassembly promoted by both the loss of the templating tetramethylammonium cations and the presence of the [Ni(cyclam)]$^{2+}$ complexes (Figure 29a). Subsequently, they may reassembly to yield anionic 1D copper(II) motifs, this feature favouring their coordination to the nickel(II) complexes through their free carbonyl groups and leading to their 3D assembly (see Figure 29b-d).

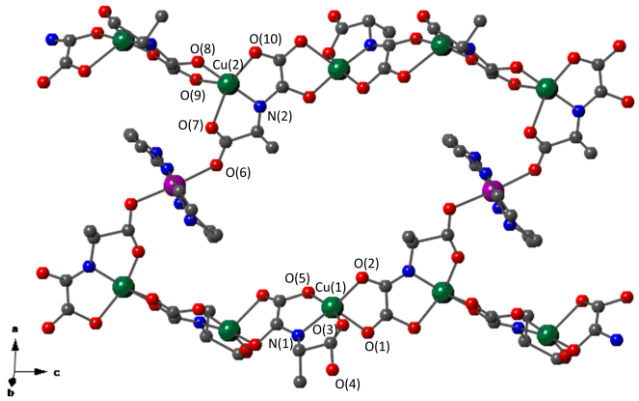

Figure 30. View of the building 1D motifs found in **1b^{S}** connected through [Ni(cyclam)]$^{2+}$ entities. The carbon, copper(II), nickel(II), nitrogen and oxygen atoms are depicted by grey, green, purple, blue and red spheres, respectively. Hydrogen atoms are omitted for clarity. The atoms are labelled according to the Tables included in the Annex I.

The two crystallographically independent Cu(1) and Cu(2) atoms of the helical copper(II) chains constituting **1b^{S}** have a somewhat distorted five-coordinate $CuNO_4$ square pyramidal environment. Within each chain the copper(II) ions are bridged by (*S*)-alama^{3-} ligands adopting the ($\kappa^3N,O,O':\kappa^2O'',O'''$) coordination mode.

The chains of **1b^S** are isostructural with those found in the pegma-derived copper(II) precursors **4a^S** and **4a^R**. Each Ni(II) ion is coordinated to two oxygen atoms from the carbonyl groups of the alanine amino acid residues from two neighbouring chains and to four nitrogen atoms from the cyclam macrocycle in a distorted octahedral geometry (see Figure 30). Noteworthy, the two crystallographic independent Cu(1) and Cu(2) atoms belong to independent chains exhibiting *M* and *P* handedness respectively, the helical pitch being of 14.82 Å (Figure 31). For further details on the bond distances and the interbond bite angles see Tables 31 and 32 (Annex I).

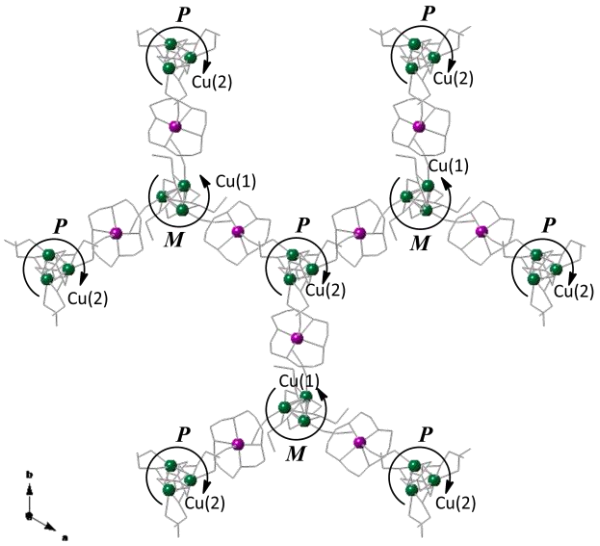

Figure 31. View of the network of alternating left- (*M*) and right-handed (*P*) helical chains along the crystallographic *ab* plane. Copper(II) and nickel (II) atoms have been highlighted as green and purple spheres, respectively.

Since the metal-containing building units of the MOF **1b^S** are infinite in one dimension (generally referred to as rods) we can classify it as a rod-MOF.[3,4] The main advantage of these MOFs is that they do not interpenetrate due to the intrinsic packing arrangement of the rods in the crystal structure, usually leading to porosity.[4,5] Hence, **1b^S** shows the property of forbidden catenation since the periodicity of the rods together with the directionality imposed by the Ni-$O_{carboxylic}$ linkage, build an impenetrable wall, thus any interpenetration being prevented. The resulting chiral architecture displays hexagonal nanotube-like channels with opening size of 15 x 15 Å (Figure 32).

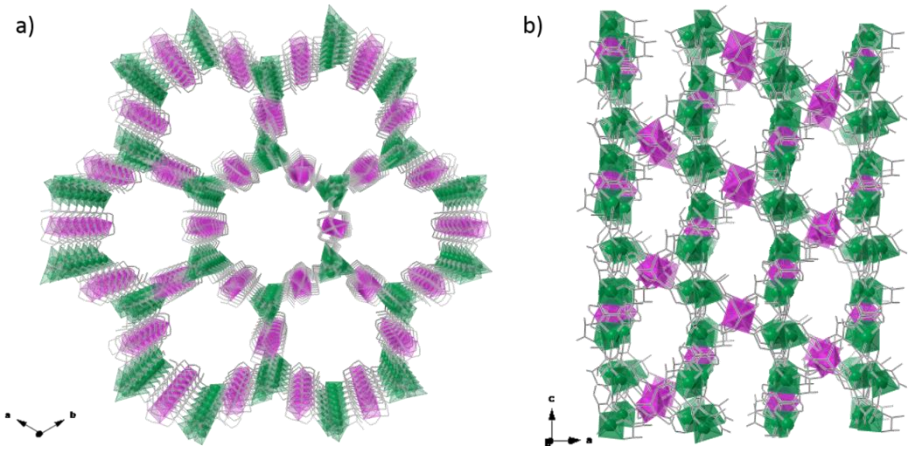

Figure 32. Perspective views of the PCP **1b^S** along the crystallographic *c* (a) and *b* axes (b). The copper and nickel atoms are represented by green and purple polyhedra, respectively. The ligand backbone is depicted by grey sticks.

These pores are filled with nine water molecules per formula unit. The effective free volume of **1b^S**, calculated without the guest molecules, is 9773 Å^3. This value represents *ca*. 66 % of the unit cell volume (14656 Å^3).

By reducing the multidimensional structure of **1b^S**, thus transforming the chains into finite objects, an underlying rod-containing net (whose nodes correspond to the chain nodes) results. The 1D [Cu^{II}(*S*)-alama]$^-$ units in **1b^S** are connected constructing a 3_1 helix. As it is known, there are only two ways for linking 3_1 helices with one kind of vertex: one constituted by helices of one hand and the other by helices of both hands. They are named **eta** and **etb**.[6–8] In **1b^S**, the alternating three-fold helices exhibiting *M* and *P* handedness

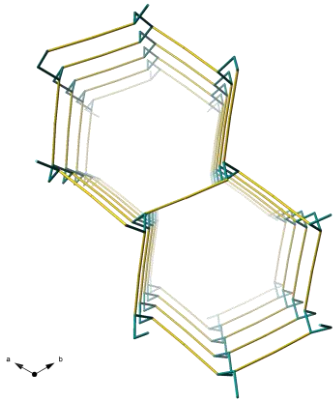

Figure 33. A detail of the resulting underlying net of **1b^S** MOF showing etb topology, formed by rod-like, right- and left-handed helical SBUs. Cu(II) and Ni(II) nodes are shown as cyan and yellow sticks.

held together by the $[Ni(cyclam)]^{2+}$ ions generate an **etb** net (Figure 33).

Considering the sequential copper(II) ions of the rods as three-fold connected nodes of extension and the nickel(II) centres as ditopic *metallolinkers*, the resulting structure of **1b^S** is a three-fold connected 3D chiral network, whose point symbol is 8^3. Each copper atom (node) is 3-c, with two coordination within the three-fold helix and one to the *metallolinker* (Figure 34). Thus, the helical rod axes intersect a perpendicular plane in an **hcb** honeycomb pattern. Moreover, the connections of the $[Ni(cyclam)O_2]$ octahedra through the $[Cu^{II}(S)\text{-alama}]_n^-$ chains define a Kagomé pattern **kgm**,[9] (point symbol 3.6.3.6), made up by hexagonal rings delimited by triangular rings. Overall, **1b^S** can be described as a honeycomb net (**hcb**) built by chiral copper(II) chains interconnected by $[Ni(cyclam)]^{2+}$ ions, exhibiting 1D pseudo-hexagonal channels with a pore's window diameter of *ca*. 1.0 nm taken from the Van der Waals radii, viewed along the crystallographic *c* axis (see Figures 32 and 34).

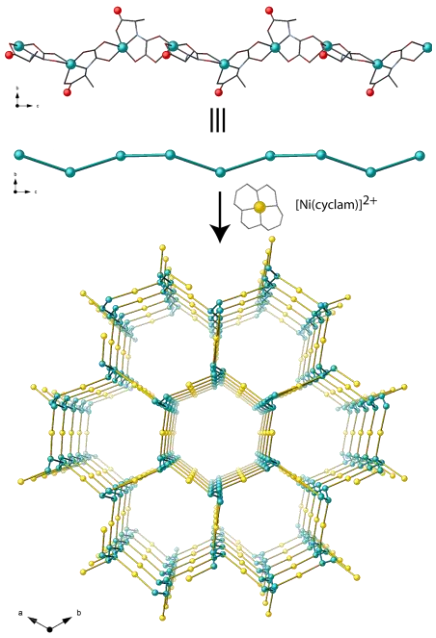

Figure 34. (a) View along the crystallographic *a* axis of the $[Cu^{II}(S)\text{-alama}]_n^-$ helical rod SBU. (b) Schematic representation of the three-fold copper(II) nodes. (c) Schematic view of the net of **1b^S** showing a **hcb** pattern.

$\{[Ni^{II}(cyclam)][Cu^{II}(S)\text{-valma}]_2 \cdot 15H_2O\}_n$ (**2b^S**)

The reaction of the metalloligand **2a^S** with the square-planar $[Ni(cyclam)]^{2+}$ complex leads to the formation of the chiral 3D compound of formula $\{[Ni^{II}(cyclam)][Cu^{II}(S)\text{-valma}]_2 \cdot 15H_2O\}_n$ (**2b^S**) (Figure 35).

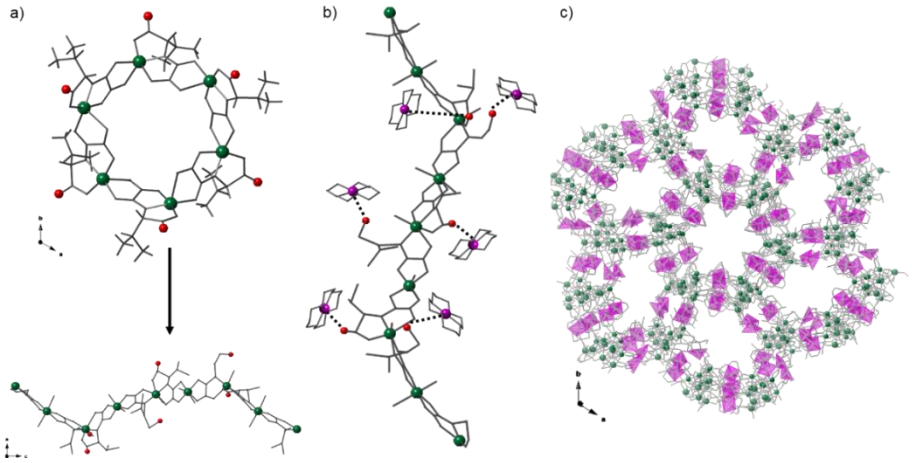

Figure 35. (a) View of the hexacopper(II) precursor (**2a^{S}**) and its suggested fragmentation-reconstruction process to yield a chain. (b) Proposed self-assembling process consisting of the coordination of the free carbonyl groups of the chain towards the $[Ni(cyclam)]^{2+}$ complex cations. (c) Perspective view of the resulting 3D homochiral PCP **2b^{S}**. The copper(II)/nickel(II) ions are depicted as green/purple spheres/polyhedra, respectively. The oxygen atoms from the free carbonyl groups are represented by red spheres. Black dashed lines simulate the approach of the $[Ni(cyclam)]^{2+}$ complex cations to the carbonyl groups.

Compound **2b^{S}** crystallises in the hexagonal chiral space group $P6_5$. The fundamental building blocks of **2b^{S}** consist of anionic left-handed helical copper(II) chains (see Figure 35) interconnected through unsaturated planar-squared $[Ni(cyclam)]^{2+}$ ions which coordinate to the free carbonyl groups from the valine residues pointing at the outer of the chains to afford nanosized tubules (see Figure 35). The neighbouring nanotubules are further connected each other through distinct copper(II) helical chains leading to a very intricate chiral porous 3D framework. The self-assembling process itself plays a crucial role in the topology of the final net (see Figure 35).

Based on the fact that the fundamental building units found in the structure of **2b^{S}** are helical chains, we propose again (as done for the PCP **1b^{S}**) that the starting preformed hexanuclear copper(II) wheels in **2a^{S}** may undergo an initial process of disassembly in the presence of the $[Ni(cyclam)]^{2+}$ complexes (Figure 35a). Subsequently, they may reassembly to yield anionic 1D copper(II) motifs which will be further interconnected by the nickel(II) complexes through their free carbonyl groups (see

Figure 35b) to afford a 3D framework (see Figure 35c). Although both PCPs, **1b^S** and **2b^S**, show 1D motifs as fundamental building units in their final structure, these 1D entities exhibit very different structure and conformation.

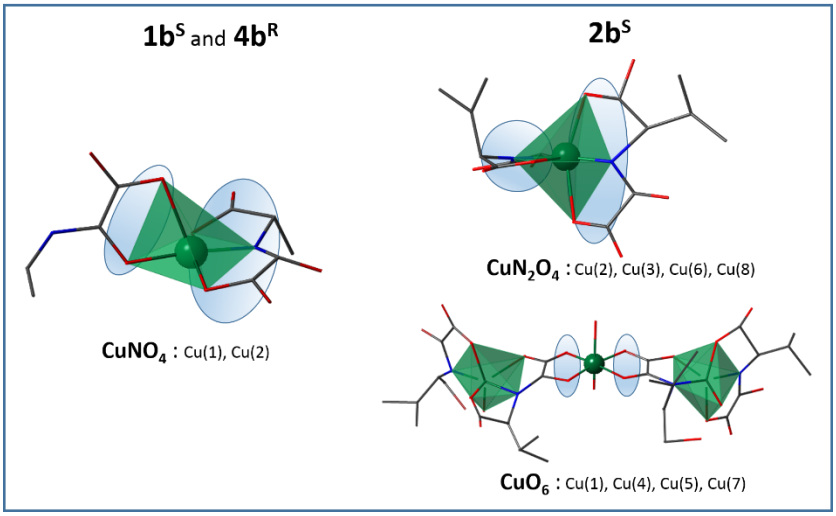

Figure 36. Scheme showing the different environments for the copper(II) ions in **1b^S** and **4b^R** (left) and **2b^S** (right). While in both **1b^S** and **4b^R** the Cu(II) atoms show the same environment than their precursors **1a^S** and **4a^R**, in **2b^S** the disassembly-reassembly process gives rise to two different hexacoordinate modes for the Cu(II) atoms with the (*S*)-valma^{3-} ligands. Despite the copper(II) ions show different environments in **1b^S**, **2b^S** and **4b^R**, their ligands adopt the same ($\kappa^3N,O,O':\kappa^2O'',O'''$) coordination mode.

Although there are two (*S*)-valma^{3-} ligands, one nickel(II) ion and two crystallographic independent copper(II) atoms in the asymmetric unit of **1b^S** with full occupancies, a large number of metal centres and (*S*)-valma^{3-} ligands [eight copper(II) ions, eight (*S*)-valma^{3-} ligands, and four [Ni(cyclam)]$^{2+}$ complex cations] are present in the asymmetric unit of **2b^S**. The copper(II) ions in **2b^S** are six-coordinate and can be classified into two groups depending on their local environment. Four of them [Cu(2), Cu(3), Cu(6) and Cu(8)] exhibit a highly distorted CuN_2O_4 octahedral environment being built by two tridentate (*S*)-valma^{3-} ligands (see Figure 36).

The Cu-N and Cu-O distances vary in the ranges 1.772(9)-1.99(2) and 1.902(14)-2.426(11) Å, respectively. In contrast, Cu(1), Cu(4), Cu(5) and Cu(7) are surrounded by

six oxygen atoms. Two carboxylate- and two amide-oxygen atoms from two (*S*)-valma^{3-} ligands form the basal plane around them (Cu-O bond lengths covering the range 1.734(9)-2.110(7) Å], whereas two *trans*-coordinated water molecules [Cu-O_W bond lengths in the range 2.26(2)-2.350(12) Å] occupy the axial positions (Figures 36 and 37). Noteworthy, the six-coordinate environment for the copper(II) ions occurring in **2b^S** could not be observed in the precursors and the copper(II) ions adopt such an environment only in this MOF.

The nickel(II) ions are six-coordinated: two oxygen atoms from two free carbonyl groups from consecutive valine amino acid residues with Ni-O bond distances ranging from 2.045(12) to 2.233(9) Å and four nitrogen atoms from the cyclam ligand with Ni-N distances in the range 1.873(17) to 2.364(9) describing a distorted octahedral geometry. For further details on the bond distances and the interbond bite angles see Tables 33 and 34 (Annex I).

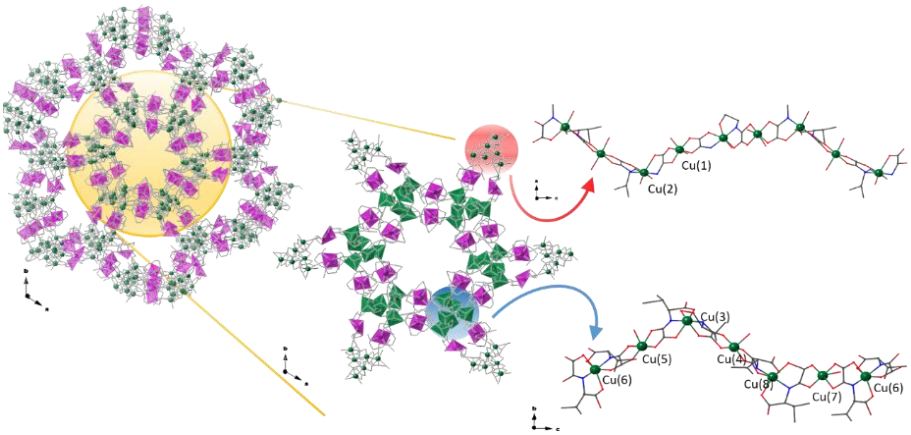

Figure 37. View of one of the nanotubules (highlighted in orange) constituting **2b^S** which grow along the crystallographic *c* axis from the assembly of six left-handed copper(II) chains (highlighted in blue) with the cationic $[Ni(cyclam)]^{2+}$ complexes through the free carbonyl groups from the amino acid residues. The nanotubular channels are further connected with neighbouring ones through Cu(II) chains (highlighted in red) and $[Ni(cyclam)]^{2+}$ complexes.

Overall both groups of non-equivalent copper(II) ions alternate in two independent helical chains, of *M* handedness, their formula being $\{Cu_2[(S)\text{-valma}]_2\}_n$ and growing

along the crystallographic *c* axis (Figure 37). The copper(II) atoms in them are bridged by (*S*)-valma^{3-} ligands adopting the ($\kappa^3N,O'',O''':\kappa^2O,O'$) coordination mode (Figure 36). The alternation of CuN_2O_4 and CuO_6 entities is the feature that makes **2b^S** a different and extraordinarily intricate net (Figure 38).

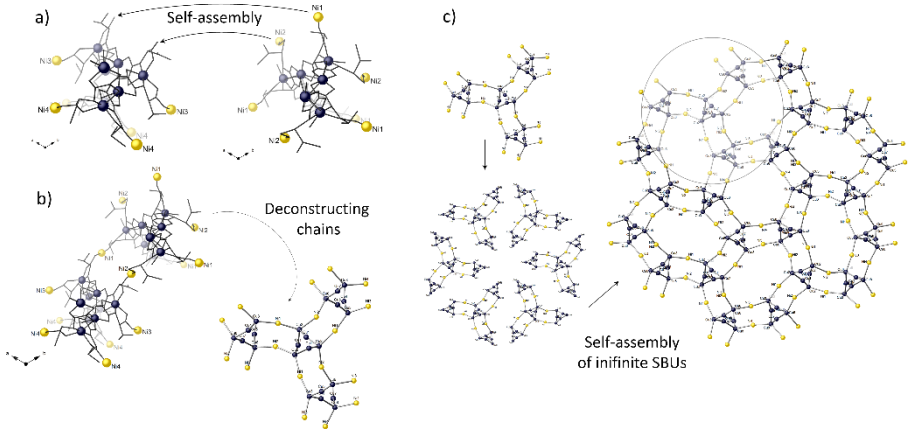

Figure 38. (a) Self-assembly process where the nickel(II) ions from the $[Ni(cyclam)]^{2+}$ complexes coordinate the oxygen atoms from the free carbonyl groups from the valine residues holding together the $[Cu_2(S\text{-valma})_2]_n$ chains. (b) Deconstruction of the copper(II) chains assembly leading to the simplest motif or SBU. (c) Self-assembly of infinite SBUs to construct the chiral PCP **2b^S**.

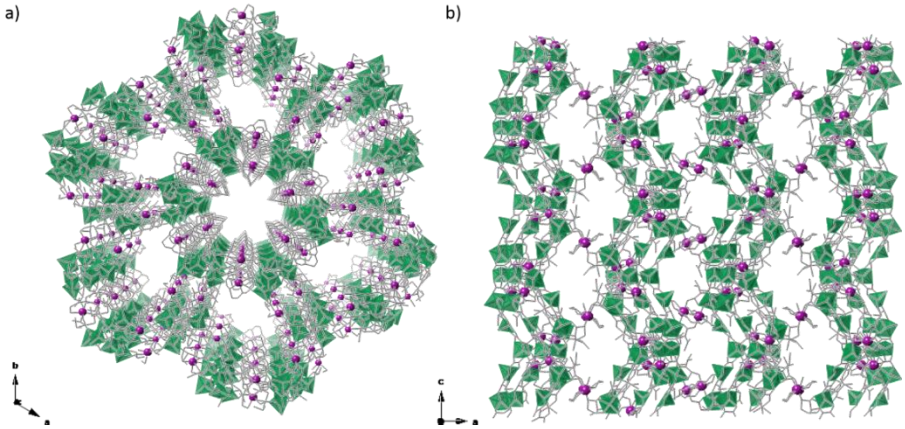

Figure 39. Perspective views of the PCP **2b^S** along the crystallographic *c* (a) and *b* axes (b). The copper(II) and nickel(II) ions are represented as green polyhedra and purple spheres, respectively. The ligand backbones are depicted as grey sticks.

Three types of channels occur in **2b^S** (see Figures 39 and 40). The assembly of six helices generates the inner walls of hexagonal tubules of dimensions of 16.2 x 16.2 Å and a pore window diameter of 0.64 nm (estimated through Van der Waals radii). In turn, each hexagonal tubule is sharing its helices with six elliptical channels with a pore window diameter of *ca*. 0.56 nm (calculated from Van der Waals radii) and dimensions of 18.0 x 14.0 Å. Moreover, small rectangular channels are present in the intricate structure of **2b^S**. The effective free volume of **2b^S**, calculated without the guest molecules, is 30064 Å^3, which represents about 66 % of the unit cell volume (44954 Å^3).

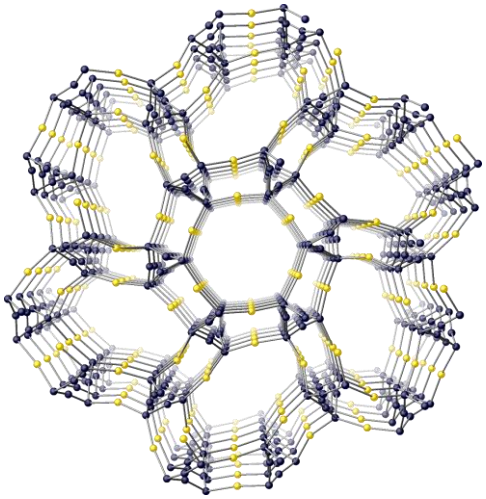

Figure 40. Perspective view of the resulting underlying net of **2b^S** formed by rod, simple right-handed helical SBUs. The copper(II) and nickel(II) atoms are shown as blue and yellow spheres, respectively.

$\{[Ni^{II}(cyclam)][Cu^{II}(R)\text{-pegma}]_2 \cdot 6H_2O \cdot 2C_3H_8O\}_n$ (**4b^R**)

The preformed copper(II) helical chains of **4a^R** serve as a rod-like building blocks towards the square-planar $[Ni(cyclam)]^{2+}$ complexes leading to the formation of the chiral 3D compound of formula $\{[Ni^{II}(cyclam)][Cu^{II}(R)\text{-pegma}]_2 \cdot 6H_2O \cdot 2C_3H_8O\}_n$ (**4b^R**). Unlike in **1b^S** and **2b^S**, the structure of the preformed **4a^R** metalloligand matches up with the building units found in the final structure, ruling out a possible disassembly-reassembly process during the PCP construction (see Figure 41).

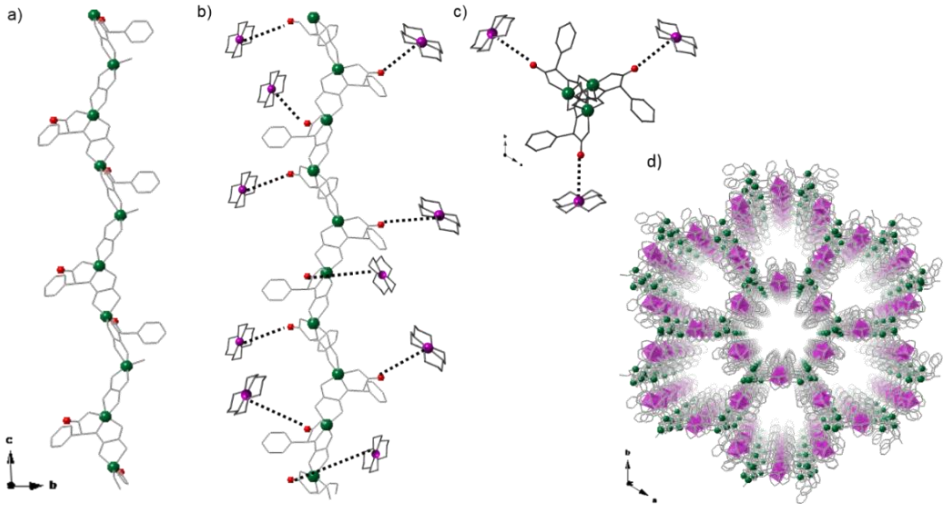

Figure 41. (a) View of the helical 1D precursor **4a^{R}**. (b) Proposed self-assembling process consisting of the coordination of the free carbonyl groups towards the $[Ni(cyclam)]^{2+}$ complex cations. (c) Perspective view of a three-fold helical chain of copper(II) ions along the crystallographic *c* axis and the coordination to the $[Ni(cyclam)]^{2+}$ complex. (d) Perspective view of the resulting 3D homochiral PCP **4b^{R}**. The copper(II) ions and the oxygen atoms from the free carbonyl groups are represented by green and red spheres, respectively. The nickel(II) ions are depicted as purple polyhedra. The dashed lines simulate the approach of the $[Ni(cyclam)]^{2+}$ species to the carbonyl groups.

The homochiral 3D compound **4b^{R}** crystallises in the trigonal chiral space group $P3_221$. The fundamental building units of **4b^{R}** consist of right-handed helical chains of **4a^{R}** interconnected through unsaturated square-planar $[Ni(cyclam)]^{2+}$ entities. These nickel(II) complexes hold the chiral chains by coordinating to the free carbonyl groups from the phenyl-glycine amino acid residues pointing outwards (Figure 41), yielding a 3D non-interpenetrating chiral porous network with 1D pseudo-channels of 13 x 10 Å viewed along the crystallographic *c* axis (see Figures 41 and 42).

The structural parameters of the $[Cu^{II}(R)\text{-pegma}]_n^-$ chains in **4b^{R}** do not display remarkable changes respect to its precursor chain **4a^{R}**. In both 1D compounds, the five-coordinate copper(II) ions have similar Cu-O and Cu-N bond lengths [1.944(7) - 2.263(7) and 1.899(8) Å in **4a^{R}** and 1.928(6) - 2.396(7) and 1.900(7) Å, in **4b^{R}**]. As in **4a^{R}**, both Cu(1)

and Cu(2) atoms are linked by (*R*)-pegma^{3-} ligands adopting the ($\kappa^3N,O'',O''':\kappa^2O,O'$) coordination mode to yield 1D motifs (Figure 43).

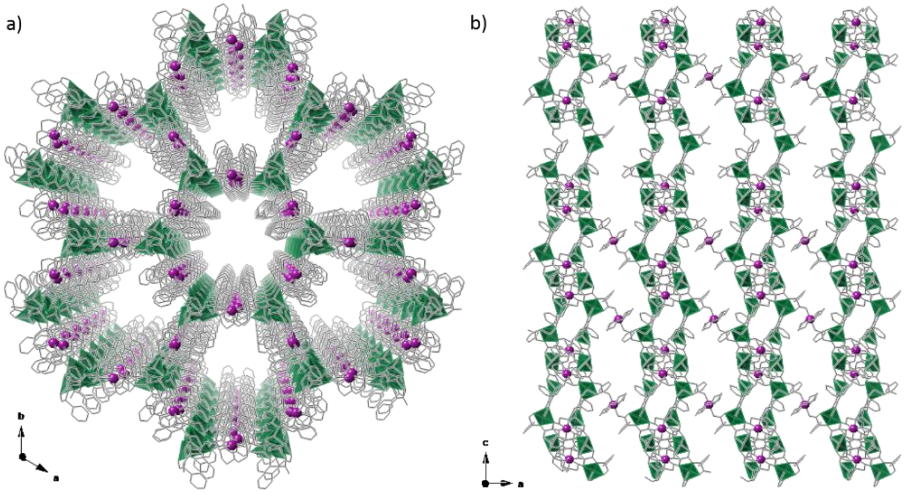

Figure 42 Perspective views of the PCP **4b^R** along the crystallographic *c* (a) and *b* axes (b). The copper(II) and nickel(II) atoms are represented by green polyhedra and purple spheres, respectively. The ligand backbone is depicted as grey sticks.

Moreover, the assembly of the helical chains constituting **4b^R** connected through [Ni(cyclam)]$^{2+}$ complexes was already observed in the PCP **1b^S** (see Figure 30). Thus, the nickel(II) ions are coordinated to two oxygen atoms from two free carbonyl groups from consecutive phenyl-glycine amino acid residues [Ni-O = 2.129(7) and 2.144(7) Å] and four nitrogen atoms from the cyclam ligand [Ni-N = 1.96(2)-2.15(2) Å] in a distorted octahedral geometry. Nevertheless, unlike **1b^S**, in **4b^R** the three-fold helical chains which are connected through [Ni(cyclam)]$^{2+}$ complexes show all the same *P* handedness. For further details on the bond distances and the interbond bite angles see Tables 35 and 36 (Annex I).

Since the metal-containing building units of the MOF **4b^R** are chains as in **1b^S,** we can classify it as a rod-MOF.[3,4] The resulting chiral architecture displays hexagonal nanotube-like channels, their diameter being *ca*. 0.78 nm (estimated through van der Waals radii) (Figures 42a and 43b).

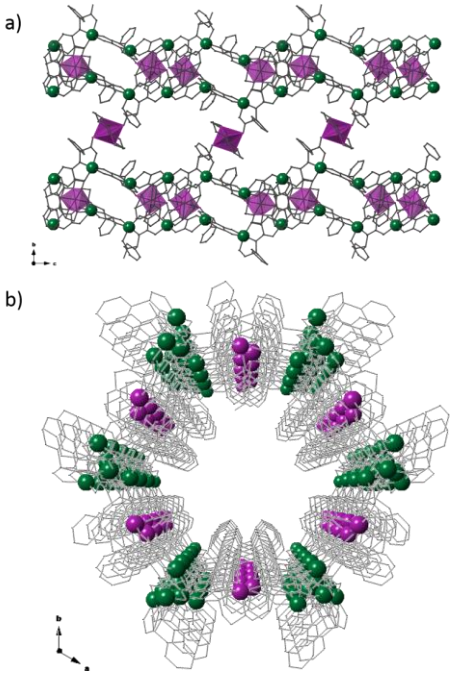

Figure 43. View of a pseudo-hexagonal nanotube-like cannel of **4b^{R}** of dimensions 13 x 10 Å along the crystallographic *a* (a) and *c* (b) crystallographic axes.

These pores are filled with six water and two isopropanol guest molecules per formula unit. The effective free volume of **4b^{R}**, calculated without the guest molecules, is 5692.4 Å^3. This value represents the 57.8 % of the unit cell volume (9846.3 Å^3).

By reducing the multidimensional structure of **4b^{R}**, thus transforming the chains into finite objects, an underlying rod-containing net (whose nodes correspond to the chain nodes) results. The 1D [Cu^{II}(*R*)-pegma]$_n^-$ units in **4b^{R}** , as in its **4a^{R}** precursor, are connected constructing a 3_1 helix. These three-fold helices, all of them being right-handed, are then linearly linked by [Ni(cyclam)]$^{2+}$ complexes to generate a rare **eta** net (Figure 44c),[6–8,10,11] which in fact, is the predicted one by following our rational approach to build enantiopure MOFs.

Considering the sequential copper(II) atoms of the rods as three-fold connected nodes and the nickel(II) ions as ditopic metallolinkers, the resulting structure of **4b^{R}** is a three-fold connected 3D chiral network with 8^3 point symbol.[6–8] Each copper(II) atom is a three-coordinated node, being coordinated to two other ones on the same helix and to one metallolinker (see Figure 43a and 44c). Thus, the helical rod axes intersect a perpendicular plane in a **hcb** honeycomb pattern.[4] On the other hand, the nature of the metallolinker employed to construct **4b^{R}** allows us to consider the {Ni(cyclam)O$_2$} octahedra as nodes.

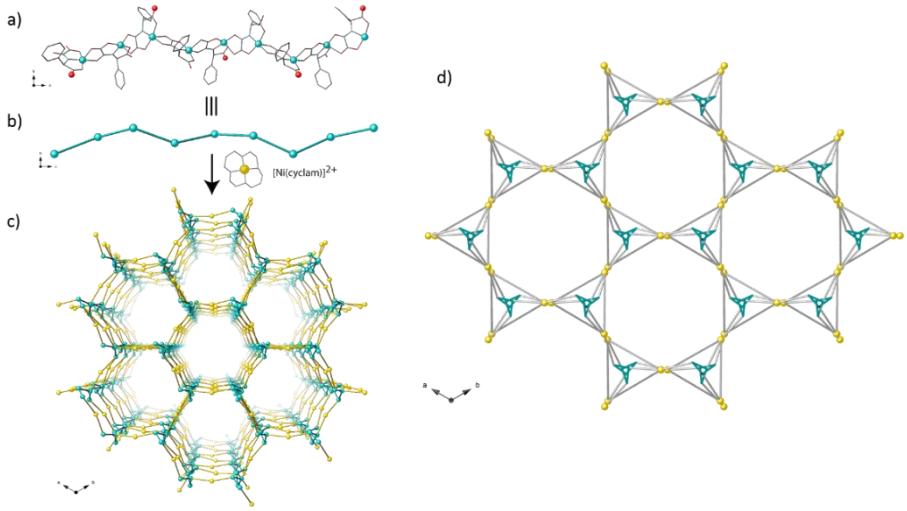

Figure 44. (a) View along the crystallographic *a* axis of a [Cu^{II}(*R*)-pegma]$^{-}$ helical rod SBU. (b) Schematic representation of the three-fold copper nodes. (c) View of the resulting underlying net of **4b^{R}** showing the **eta** topology, formed by rods, simple right-handed helical SBUs. (d) {Ni(cyclam)O_2} octahedra as nodes (gold spheres) in **4b^{R}**, defining a Kagomé pattern, made up of hexagonal rings delimited by six triangular wheels where the [Cu^{II}(*R*)-pegma]$^{-}$ helical rods (green sticks) reside.

In this case, their connections through the [Cu^{II}(*R*)-pegma]$_n^{-}$ chains intersect a perpendicular plane to define a Kangomé pattern **kgm**[9] (point symbol 3.6.3.6), composed of hexagonal rings delimited by six triangular motifs where the [Cu^{II}(*R*)-pegma]$_n^{-}$ helical rods reside (Figure 44d).

In summary, the obtained chiral PCPs **1b^{S}**, **2b^{S}** and **4b^{R}** can be classified as rod-MOFs since the fundamental building units in all of them are helices, but they display different types of network. **1b^{S}** and **4b^{R}** exhibit a very similar honeycomb type network but displaying both-handed and only right-handed helices as fundamental building units, respectively. Nevertheless, **2b^{S}** exhibits a very rare and intricate structure. The origin of this very different architectures probably lies in the singular alternation of copper(II) ions with different environments CuN_2O_4 and CuO_6 (see Figure 36) along the chains constituting **2b^{S}**, where the isopropyl residues from the (*S*)-valma^{3-} ligands arrange in a *syn* conformation (Figure 45b).

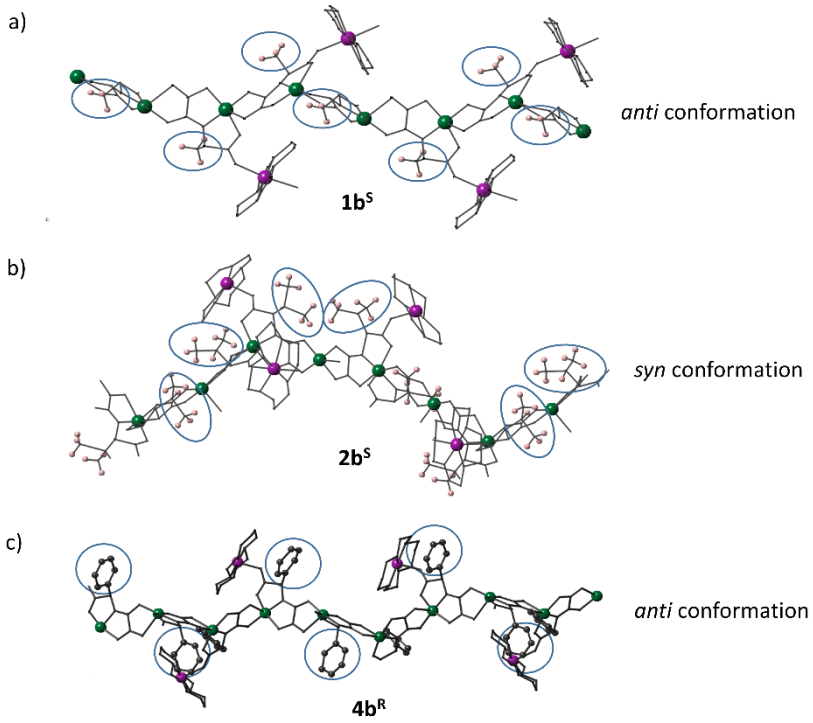

Figure 45. A simplified view of a fragment of the copper(II) helices constituting **1b^S** (a), **2b^S** (b) and **4b^R** (c). The residues of the corresponding amino acids have been highlighted. Noteworthy, the methyl groups from the (*S*)-alama^{3-} as well as the phenyl groups from the (*R*)- pegma^{3-} residues adopt an *anti* conformation in **1b^S** and **4b^R**, respectively, whilst the isopropyl groups from (*S*)-valma^{3-} adopt a *syn* conformation due to the alkyl-alkyl interactions that take place in **2b^S** ($CH_3\cdots CH_3$ distances of 3.212 and 4.024 Å). Some $[Ni(cyclam)]^{2+}$ complexes have been omitted for clarity. The chain framework is depicted as sticks. The copper(II) and nickel(II) ions are shown as green and purple spheres. The hydrogen and carbon atoms from the residues of the amino acids are shown as pale pink and grey spheres.

This feature is likely due to the alkyl-alkyl interactions occurring between the isopropyl groups. Such interactions do not take place in **1b^S** since the less bulky methyl residues from the (*S*)-alama^{3-} ligand are located far from each other, these methyl groups showing thus an *anti* conformation (Figure 45a). The phenyl rings from the (*R*)-pegma^{3-} ligands in compound **4b^R**, also adopt an *anti* conformation (Figure 45c), again due to the lack of alkyl-alkyl interactions playing a stabilising role.

Apparently, these hydrophobic interactions may play an important role in determining the conformational folding of the chains and therefore the self-assembly of the resulting 3D structure. Anyway, there are most likely other subtle factors affecting the self-assembly of the MOFs.

1.A.4. Physical Properties and Applications

1.A.4.1. Optical properties

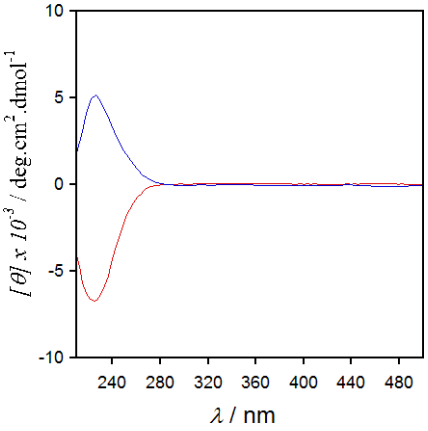

Figure 46. CD spectra of $\mathbf{1^S}$ (red) and $\mathbf{1^R}$ (blue) in MeOH (10^{-4} mol L^{-1}).

Circular dichroism (CD) measurements were performed in order to confirm the enantiopurity of the different compounds. The CD spectra measured for methanol solutions of the HMeEt-(*S*)-alama ($\mathbf{1^S}$) and HMeEt-(*R*)-alama ($\mathbf{1^R}$) proligands are practically mirror images since negative and positive Cotton effects appear at the same wavelength with similar intensity (Figure 46). The intense UV bands at 210 nm can be assigned to intraligand (IL) and metal-to-ligand (ML) charge-transfer transitions, respectively.

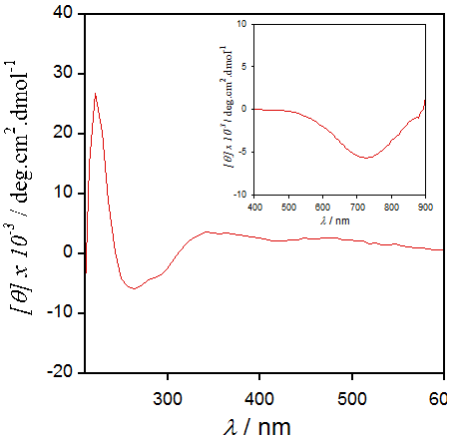

Figure 47. CD spectrum of $\mathbf{1a^S}$ in H_2O (10^{-3} mol L^{-1}) in the 200-600 nm region. The inset shows the CD spectrum in the visible region.

Aiming at confirming the transmission of the chirality from the proligand to the metalloligand, the solution CD spectrum was also performed for the $(Me_4N)_6\{Cu^{II}_6[(S)\text{-alama}])_6\} \cdot 10H_2O$ complex ($\mathbf{1a^S}$). Its CD spectrum in aqueous solution exhibits maximum positive and negative Cotton effects centred at 225 and 280 nm, which are commonly assigned to intraligand (IL) and metal-to-ligand (ML) charge-transfer transitions, respectively

(Figure 47). The weak visible band at 700 nm (which does not appear in the CD spectrum of the proligand), corresponds to the typical d-d transition of the copper(II) ions (see inset of Figure 47). This negative Cotton effect in the visible region obeys to the induction of chirality on the metal centres of the hexacopper(II) wheels in **1a^{S}** by the enantiopure coordinated ligand coming from the **1^{S}** proligand.

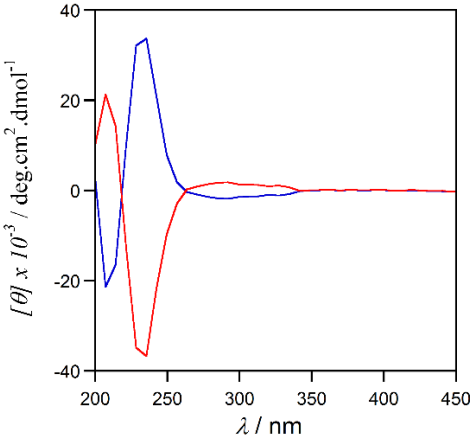

Figure 48. CD spectra of **2^{S}** (red) and **2^{R}** (blue) in MeOH (10^{-4} mol L^{-1}).

CD measurements in solution were also performed in order to confirm the enantiopurity of the HMeEt-(*S*)-valma (**2^{S}**) and HMeEt-(*R*)-valma (**2^{R}**) proligands. The CD solution spectra are practically mirror images since negative and positive Cotton effects appear at the same wavelength with almost equal intensity (Figure 48). As in the previous examples, the intense UV bands at 210 and 235 nm can be assigned to intraligand (IL) and metal-to-ligand (ML) charge-transfer transitions, respectively.

The CD spectra of $(Me_4N)_6\{Cu^{II}_6[(S)\text{-valma}])_6\} \cdot 7H_2O$ (**2a^{S}**) and $(Me_4N)_6\{Cu^{II}_6[(R)\text{-valma}])_6\} \cdot 7H_2O$ (**2a^{R}**) in water solution are again almost mirror images (Figure 49). In fact, they exhibit maximum positive and negative Cotton effects at the same location and with almost identical intensities. The intense UV bands centred at 225 and 300 nm for both **2a^{S}** and **2a^{R}** are commonly assigned to intraligand (IL) and metal-to-ligand (ML) charge-transfer transitions, respectively. The weak visible band at 700 nm for both **2a^{S}** and **2a^{R}**, which does not appear in the CD spectra of the ligands, corresponds to the typical d-d transition of the copper(II) ions (inset of Figure 49). The positive and negative Cotton effects of this visible band obey to the induction of chirality on the metal centres

by the enantiopure coordinated ligands within the anionic hexacopper(II) wheels of **2a^{S}** and **2a^{R}**.

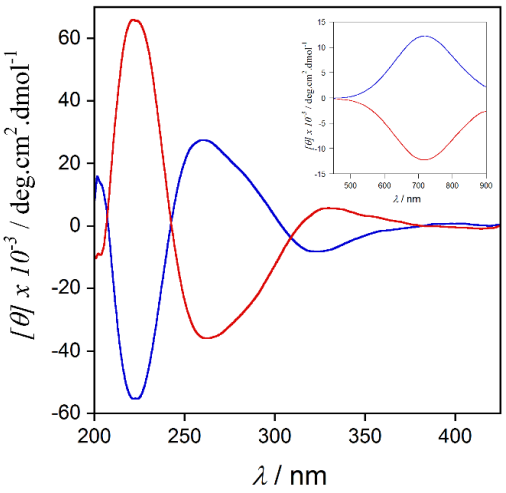

Figure 49. CD spectra of **2a^{S}** (red) and **2a^{R}** (blue) in H_2O (10^{-3} mol L^{-1}) in the 200-450 nm region. The inset shows the CD spectra in the visible region

The CD spectrum of the HMeEt-(*R*)-pegma (**4^{R}**) proligand in methanolic solution shows negative and very slightly positive Cotton effects at 220 and 285 nm that can be assigned to intraligand (IL) and metal-to-ligand (ML) charge-transfer transitions, respectively (see Figure 51a).

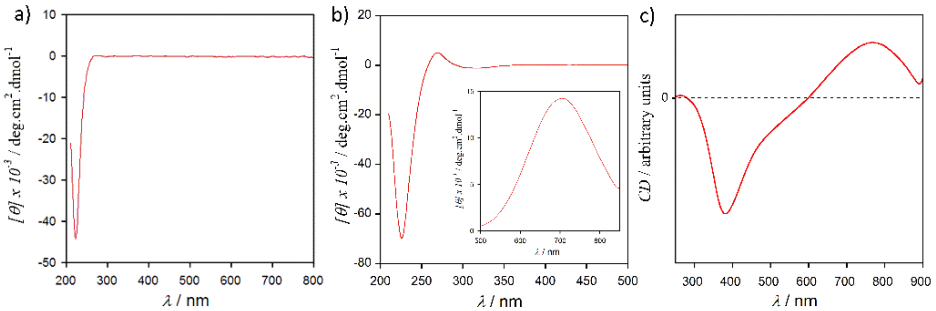

Figure 51. (a) CD spectra of **4^{R}** in MeOH (10^{-4} mol L^{-1}). (b) CD spectra of **4b^{R}** in H_2O (10^{-3} mol L^{-1}). The inset shows the CD spectra in the visible region. (c) CD spectrum of **4b^{R}** as KBr pellets (1 mg MOF in 100 mg of KBr).

Aiming at verifying the transmission of the chirality from the **4^{R}** proligand to the metalloligand {$Me_4N[Cu^{II}$(*R*)-pegma] · $2H_2O\}_n$ (**4a^{R}**) and consequently, to the derived {[Ni^{II}(cyclam)][Cu^{II}(*R*)-pegma]$_2$ · $6H_2O$ · $2C_3H_8O\}_n$ PCP (**4b^{R}**), solution and solid CD spectra were also collected, respectively (Figure 51b,c). The CD solution spectrum of **4a^{R}** exhibits maximum positive and negative Cotton effects centred at 225 and 280 nm which are due to intraligand (IL) and metal-to-ligand (ML) charge-transfer transitions, respectively. The band at 700 nm (which does not appear in the CD spectrum of the ligand), corresponds to the typical d-d transition of the copper(II) ions (see inset of Figure 51b). This negative Cotton effect in the visible region obeys to the induction of chirality on the metal centres of the hexacopper(II) wheels in **4a^{R}** by the enantiopure coordinated ligand derived from the proligand **4^{R}**.

Finally, the CD spectrum of **4b^{R}** exhibits a maximum negative Cotton effect centred at 380 nm which is due to intraligand (IL) and/or metal-to-ligand (ML) charge-transfer transitions (Figure 51c). The positive Cotton effect observed in the visible region, which is very similar with the one exhibited by **4a^{R}**, is attributed to d-d transitions of the copper(II) ions and it is due to the induction of chirality on the metal centres by the enantiopure ligands.

1.A.4.2. Magnetic properties

The magnetic properties of the different hexacopper(II) wheels **2a^{S}**, **2a^{R}** and **3a^{S}** and the copper(II) chain **4a^{R}** were investigated through direct current (dc) magnetic susceptibility measurements in the 1.9-300 K temperature range. The magnetic properties of the hexacopper(II) wheel **1a^{S}** could not be properly measured since we could not collect sufficient amount of crystalline sample and the as-synthesised powder sample showed non-negligible unidentified paramagnetic impurities as well as diamagnetic tetramethylammonium salts that precluded an accurate analysis of its magnetic behaviour.

The χ_M and $\chi_M T$ *versus* T plots for **2a^S**, **2a^R** and **3a^S** [χ_M being the dc molar magnetic susceptibility per six copper(II) ions] are very close (Figures 52 and 53). The values of $\chi_M T$ at room temperature are 2.12 (**2a^S**), 2.09 (**2a^R**) and 2.05 cm^3mol^{-1} K (**3a^S**). They are below the expected value for six magnetically non-interacting copper(II) ions ($\chi_M T$ = 6 x $[(N\beta^2 g_{Cu}^2/3k_B)S_{Cu}(S_{Cu}+1)]$ = 2.40 $cm^3\ mol^{-1}$ K with S_{Cu} = 1/2 and g_{Cu} = 2.1). Upon cooling, $\chi_M T$ continuously decreases for all of them and it vanishes at 5.0 K. This magnetic behaviour is characteristic of a moderate antiferromagnetic coupling within the hexacopper(II) rings. In fact, χ_M exhibits maxima at 60 (**2a^S** and **2a^R**) and 90 K (**3a^S**) (Figures 52 and 53), which unambiguously supports the occurrence of a ground singlet spin state (S = 0) resulting from the intramolecular antiferromagnetic coupling between the six copper(II) ions through the oxamato bridges.

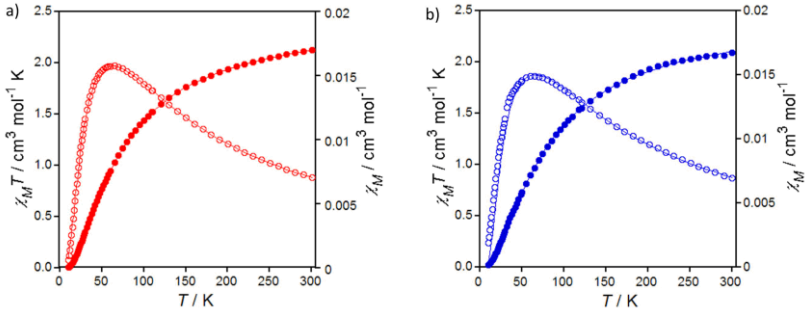

Figure 52. Temperature dependence of χ_M (○) and $\chi_M T$ (●) for **2a^S** (red curves) and **2a^R** (blue curves) under applied dc magnetic fields of 100 G (T < 30 K) and 10 kG (T ≥ 30 K). The solid lines represent the best-fit curves (see text).

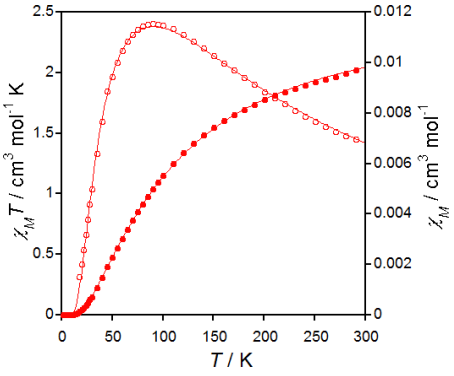

Figure 53. Temperature dependence of χ_M (○) and $\chi_M T$ (●) for **3a^S** under applied dc fields of 100 G (T < 30 K) and 5 kG (T ≥ 30 K). The solid lines represent the best-fit curves.

The analysis of the magnetic susceptibility data of **2a^S**, **2a^R** and **3a^S** was carried out through the appropriate isotropic spin Hamiltonian for a hexanuclear copper(II) ring:

$$\mathbf{H} = -J\sum_{i=1-5}(\mathbf{S}_i \cdot \mathbf{S}_{i+1} + \mathbf{S}_6 \cdot \mathbf{S}_1) + g_i\beta H(\sum_{i=1-6}\mathbf{S}_i)$$

with $S_i = S_{Cu} = 1/2$ and $g_i = g_{Cu}$ for i = 1-6, where J is the magnetic coupling parameter and g is the average Landé factor. Least-squares best-fit parameters through the VPMAG program[12] are: J = −64.2 (**2a^S**), −67.6 (**2a^R**) and −92.6 cm^{-1} (**3a^S**) with g_{Cu} = 2.11 (**2a^S**), 2.11 (**2a^R**) and 2.16 (**3a^S**). The values of the agreement factors R (defined as $\sum[(\chi_M T)_{exp} - (\chi_M T)_{calcd}]^2 / \sum[(\chi_M T)_{exp}]^2$) are 4.0 x 10^{-6} (**2a^S**), 1.8 x 10^{-5} (**2a^R**) and 2.0 x 10^{-6} (**3a^S**). The calculated curves match well the magnetic data in the whole temperature range investigated.

Moreover, aiming at verifying the stability and robustness of the hexacopper(II) wheel in solution, the dc magnetic properties of a frozen methanolic solution of **2a^S** were measured in the low temperature range. χ_M and $\chi_M T$ vs. T plots (Figure 54) show the same qualitative behaviour observed for the polycrystalline solid sample of **2a^S**, with a maximum of χ_M at *ca*. 80 K. The shift in the maximum which is observed for the methanolic solution respect to the measured on the solid sample is mostly due to slight changes of the conformation of the rings in solution. Moreover, there is no evidence of paramagnetic monomeric copper(II) impurities at low temperatures resulting from a putative

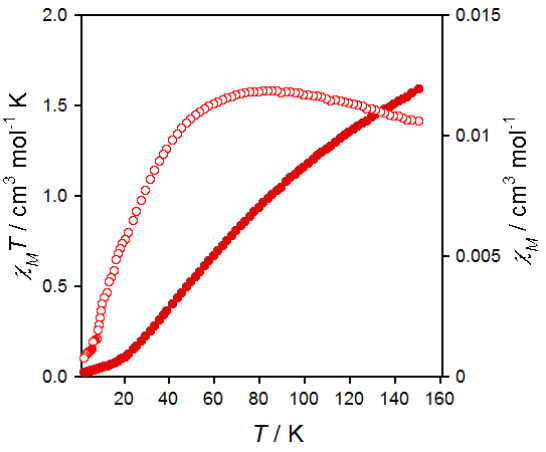

Figure 54. Temperature dependence of χ_M (○) and $\chi_M T$ (●) for a methanolic solution of **2a^S** under applied dc magnetic fields of 100 G (T < 30 K) and 1000 G (T ≥ 30 K). The solid lines represent the best-fit curves (see text).

dissociation process, confirming thus the high stability of **2a^{S}** in solution. This is further confirmed by Q-band EPR spectra.

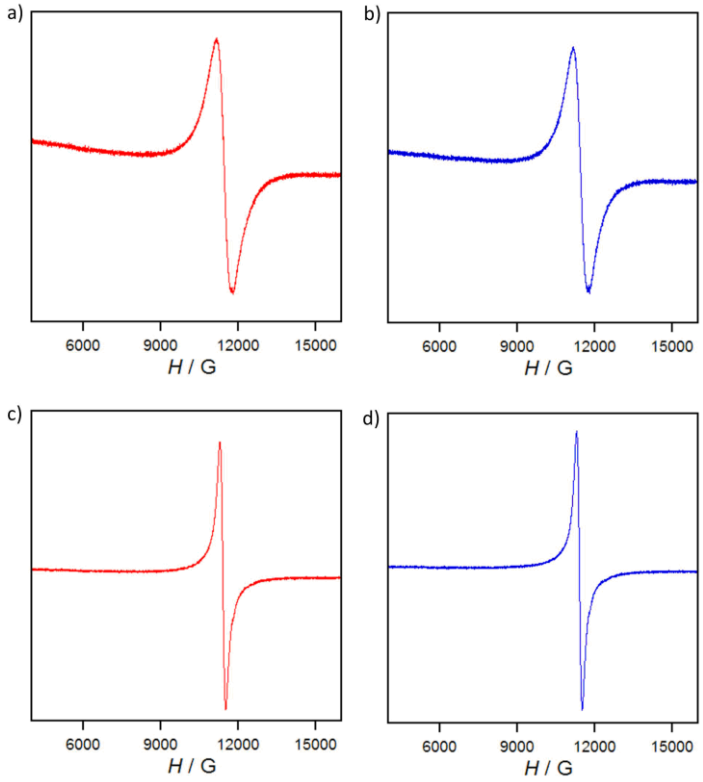

Figure 55. Q-band EPR spectra of polycrystalline samples (top) and frozen methanolic solutions (bottom) of **2a^{S}** (a and c) and **2a^{R}** (b and d) at 60 K.

The Q-band EPR spectra of **2a^{S}** and **2a^{R}** measured in frozen methanolic solutions are identical to those of their polycrystalline powdered samples (Figure 55). All of them show an isotropic signal centred at g = 2.15 (H = 11400 G for ν = 34.277 GHz) at 60 K, which would correspond to the spin-allowed $\Delta M_S = \pm 1$ transitions from the low-lying triplet spin states (S = 1) located above the ground singlet spin state (S = 0).

The magnetic properties of the copper(II) chain **4a^{R}** under the form of χ_M and $\chi_M T$ *versus* *T* plots [χ_M being the dc molar magnetic susceptibility per one copper(II) ion] are shown in Figure 56. The value of $\chi_M T$ at room temperature is 0.30 cm^3 mol^{-1} K. This value is lower than the expected for a magnetically isolated copper(II) ion [$\chi_M T$ = $(N\beta^2 g_{Cu}^2/3k_B)S_{Cu}(S_{Cu} + 1)$ = 0.40 cm^3 mol^{-1} K with S_{Cu} = 1/2 and g_{Cu} = 2.1]. Upon cooling, $\chi_M T$ continuously decreases and it vanishes at 5.0 K. This magnetic behaviour is characteristic of a moderate antiferromagnetic coupling between the copper(II) ions within the chain. In fact, χ_M exhibits a maximum at 82.5 K (Figure 56), which unambiguously supports the occurrence of a ground singlet spin state (S = 0) resulting from the intramolecular antiferromagnetic coupling between the copper(II) ions through the oxamato bridges. The χ_M values decrease after reaching the aforementioned maximum at 82.5 K to further increase due to the presence of an almost negligible paramagnetic impurity.

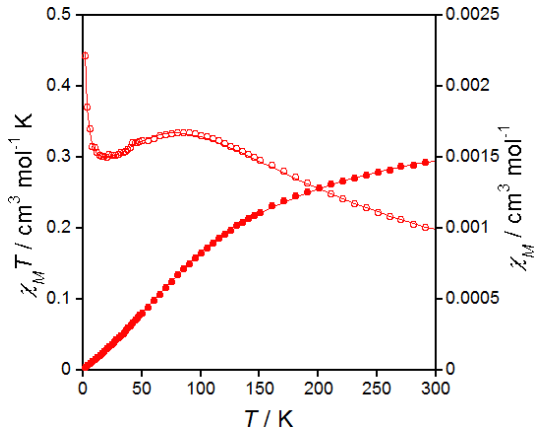

Figure 56. Temperature dependence of χ_M (○) and $\chi_M T$ (●) for **4a^{R}** under applied dc fields of 100 G (T < 30 K) and 5 kG (T ≥ 30 K). The solid lines represent the best-fit curves (see text).

Taking into account the presence of a proportion ρ of noncoupled Cu^{II} (including impurities and ends of chain) the experimental magnetic susceptibility (χ_M) is expressed according to eqn. (1)

$$\chi_M = \chi_C(1-\rho) + \chi_\rho \qquad (1)$$

For the analysis of the magnetic susceptibility of the chain (χ_C) we have used the theoretical expression (the Hamiltonian being $\mathbf{H} = -J\sum_i \mathbf{S}_i \cdot \mathbf{S}_{i+1}$) proposed by Estes *et al.*[13] for a uniform chain of local spins S = 1/2, eqn. (2)

$$\chi_C = \left(\frac{N\beta^2 g^2}{kT}\right)[0.25 + 0.074975x + 0.075235x^2)/(1.0 + 0.9931x + 0.172135x^2 + 0.757825x^3) \quad (2)$$

N, β and *g* have their usual meanings in eqn. (2), $x = |J|/kT$ and *J* is the exchange coupling constant. This expression, which derives from the numerical results from Bonner and Fisher,[14] has been widely used for the treatment of the magnetic data of uniform copper(II) chains. We also assume that the monomeric Cu(II) impurity has the same molecular weight as the building unit of the chain and its magnetic susceptibility follows a Curie law ($\chi_\rho = N\beta^2 g^2 \rho/4kT$). The least-squares best-fit of the magnetic data of **4a^R** through eqn. (1) led to the following set of parameters: *J* = -81.3 cm^{-1}, *g* = 2.09, *ρ* = 0.005 and *R* = 5.2 x 10^{-5} (solid lines in Figure 56). The calculated curves match well the magnetic data in the whole temperature range investigated.

Due to the Jahn-Teller plasticity of the coordination sphere around Cu(II), this ion can show a [4], [4+1] or [4+2] coordination. In these cases, four ligand bonds can be found in a roughly common plane giving square-planar, square pyramidal or pseudooctahedral coordination environments, respectively. The coordination geometry of the copper(II) ions (d^9 electronic configuration) will determine the orientation and symmetry of the molecular orbital describing the unpaired electrons (the so-called magnetic orbital) being dependent of the environment at the metal centre.

Figure 57 shows different possibilities for the relative orientation of the magnetic orbitals when two copper(II) ions are combined in pairs. The first situation (1a), where the magnetic orbitals are located in the plane of the oxamato-bridge, is the most common one. Magnetic measurements of different oxalato-type dicopper(II) compounds exhibiting such orbital topology show that despite the long distance that separates the copper(II) centres (more than 5 Å), an important antiferromagnetic exchange exists as evidenced by the coupling constants which cover the range -300 to -400 cm^{-1}.

The magnetic coupling decreases for the other three possibilities (1b-1d), (see the corresponding values of *J* in Table 1). It is worth noting that the values listed in Table 1 have been measured for oxalato-bridged dicopper(II) compounds. However, the correlation between the orbital topology and the exchange coupling constants can be extended to their analogue oxamato-type compounds, just assuming slightly higher values for the later family because the less electronegativity of the amide-nitrogen donor atom provides a better electron density delocalisation, causing thus an increasing of the magnetic coupling.

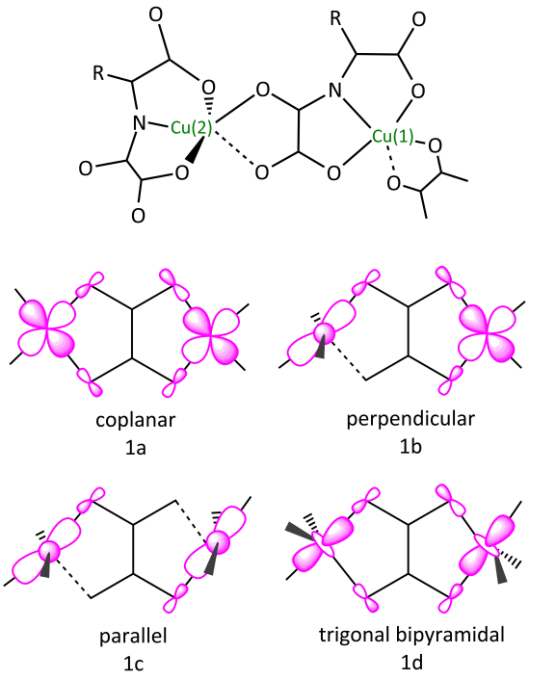

Figure 57. Scheme of the coordination environment of the two copper(II) ions in **2a^S**, **2a^R** and **3a^S** (the long bond distances have been highlighted by dashed lines) (top). Scheme showing four possible orientations of the magnetic orbitals of two coupled copper(II) ions through the oxamato-bridge.

In the three measured hexacopper(II) wheels (**2a^S**, **2a^R** and **3a^S**) the two crystallographic independent atoms [Cu(1) and Cu(2)] are five-coordinate $CuNO_3$, with four short equatorial copper to ligand distances and one longer axial interaction (Cu-O) see [Figure 57 (top)] resulting in a somewhat distorted square pyramidal geometry. The unpaired electron at each copper(II) ion is defined by a magnetic orbital which is delocalised in the basal plane, that of the Cu(2) being coplanar with the oxamato mean plane whereas the one at Cu(1) is practically perpendicular to the oxamato (orbital reversal phenomenon). The net overlay between both magnetic orbitals occurs through

the [Cu(1)-O(4)-C(6)-N(1)-Cu(2)] pathway, given the lack of spin density on the axial O5 atom (see Figure 57 top).

Table 1. Values of the exchange coupling constants *J* (cm^{-1}) for different oxalato-bridged dicopper(II) complexes with different topologies of the two magnetic orbitals

	Orbital topology	*J*
1a	coplanar	-300 to -400[15]
1b	perpendicular	-75[16]
1c	parallel	+1.2 to -37[16–21]
1d	trigonal-bipyramidal	-75[17]

[a]The superscript in square brackets indicates the reference.

The magnetic orbitals of the alternating copper(II) ions (which are also five-coordinate) in the case of the chain **4a^{R}** exhibit the orientation found in **2a^{S}**, **2a^{R}** and **3a^{S}** (Figure 57). Therefore, the value of their coupling constant is expected to be close.

The values of –*J* found in the literature for the antiferromagnetically coupling between the copper(II) centres through the oxamato bridge illustrated in Figure 57a vary in the range 296-420 cm^{-1}.[22–25] In the specific situation of **2a^{S}**, **2a^{R}**, **3a^{S}** and **4a^{R}**, only one magnetic orbital is coplanar with the oxamato-bridge whilst the other shows a perpendicular disposition (see Figure 58). As the exchange involves only the [Cu(1)-O(4)-C(6)-N(1)-Cu(2)] set of atoms,

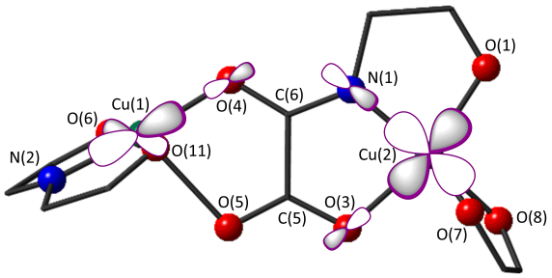

Figure 58. Simplified view of the dimeric moieties of the hexacopper(II) wheels **1a^{S}**- **3a^{S}** and the copper(II) chain **4a^{R}** with the atom numbering scheme. The copper(II) ions show a [4+1] coordination in a distorted square pyramidal geometry with four short equatorial bond distances [Cu(1)-0(6), Cu(1)-O(11), Cu(1)-O(4)and Cu(1)-N(2)] and [Cu(2)-O(3), Cu(2)-0(8), Cu(2)-0(1) and Cu(2)-N(1)];. and one long apical interaction (Cu(1)-0(5) and Cu(2)-0(7)]. The relative orientation of the magnetic orbitals centred on each copper(II) ion is also shown.

the magnetic coupling is supposed to decrease by a factor of 1/4 respect to the coplanar situation (value of –*J* in the range -74 and -105 cm^{-1}).

The variation of the values of *J* observed in the family **2a^S**, **2a^R**, **3a^S** and **4a^R** (Table 2) can be attributed to subtle structural changes in the square pyramidal environment of the copper(II) ions. Relevant factors to be taken into account are: (i) the out-of-plane displacement of the metal centre from the mean basal plane, (ii) the deviation from coplanarity of the base of the pyramid from the oxamato mean plane, (iii) the fact that the four donor atoms on the basal plane are not perfectly planar, showing a tetrahedral distortion and, (iv) the possible trigonal distortion of the square pyramidal geometry.

Table 2. Best-fit values of the exchange coupling constants for **2a^S**, **2a^R**, **3a^S** and **4a^R**

Compound	J^a
2a^S	-64.2
2a^R	-67.6
3a^S	-92.6
4a^R	-81.3

[a]The values of *J* are given in cm^{-1}.

The magnetic properties of the MOF **2b^S** under the form of and its $\chi_M T$ *versus* *T* (χ_M being the dc molar magnetic susceptibility per Cu^{II}_2-Ni^{II} motif) are shown in Figure 59. The value of $\chi_M T$ at room temperature is 1.66 $cm^3\,mol^{-1}$ K, a value which is below the one expected for a set of two magnetically isolated copper(II) ions and one nickel(II) ion [$\chi_M T = 2\cdot(N\beta^2 g_{Cu}^2/3k_B)S_{Cu}(S_{Cu} + 1) + (N\beta^2 g_{Ni}^2/3k_B)S_{Ni}(S_{Ni} + 1) = 0.8112 + 1.1025 = 1.91$ $cm^3\,mol^{-1}$ K (with $S_{Cu} = ½$, $g_{Cu} = 2.08$, $S_{Ni} = ½$ and $g_{Ni} = 2.1$)]. Upon

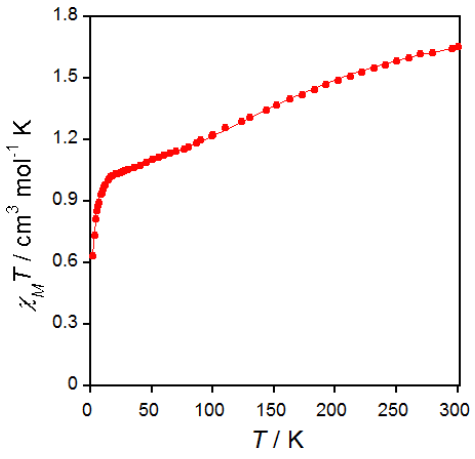

Figure 59. Temperature dependence and $\chi_M T$ **2b^S** under applied dc fields of 100 G (T < 30 K) and 5 kG (T ≥ 30 K). The solid line represents the best-fit curve.

cooling, $\chi_M T$ continuously decreases to reach an incipient pseudo-plateau below 40 K with $\chi_M T$ = 1.05 cm^3 mol^{-1} K, which is consistent with the occurrence of a spin state (S = 1) from the nickel(II) ion. The pseudo-plateau tend to vanish, the values of $\chi_M T$ decreasing until reaching 0.63 cm^3 mol^{-1} K at 2.0 K. This drop is due to the zero-field splitting effects of the nickel(II) ion and/or to the weak intermolecular interactions between the nickel(II) ions. In summary, this overall magnetic behaviour is characteristic of a moderate antiferromagnetic coupling between the copper(II) ions through the oxamato bridges within the copper(II) chains of **2b^S** plus the presence of the magnetically quasi isolated nickel(II) ions.

Having this in mind, the magnetic data of **2b^S** have been fitted considering that they obey to antiferromagnetically coupled alternating copper(II) chains (see Figure 60) interlinked by quasi magnetically isolated Ni(II) ions. Therefore, two exchange coupling parameters, J_1 and J_2, will be considered with $J_2 = \alpha \cdot J_1$ being α the alternation parameter whose values range from 0 to 1 (α = 0 means magnetically isolated dicopper(II) units whereas α = 1 corresponds to a uniform chain).

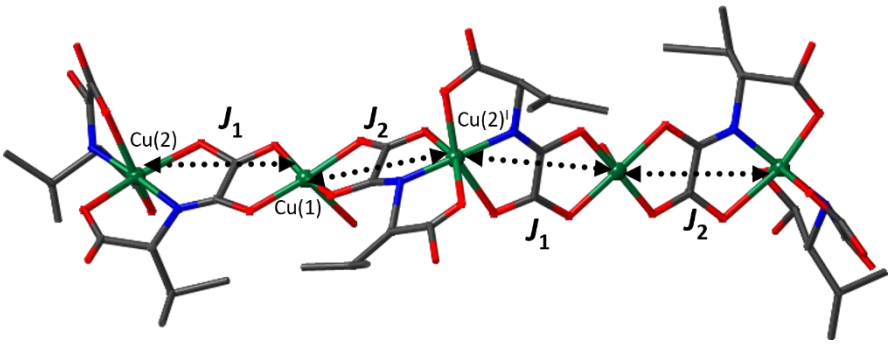

Figure 60. View of a fragment of the chains constituting **2b^S**. Since the magnetic copper(II) centres are not equally spaced along the chain, two different interaction parameters J_1 and J_2 have been considered. The Cu(1)···Cu(2) and Cu(1)···Cu(2)^I distances are 5.290 and 5.381 Å, respectively. [Symmetry code 1-y, x-y+1, z-1/3].

The magnetic susceptibility (χ_M) per $Cu^{II}_2Ni^{II}$ unit of **2b^S** is given by eqn. (3)

$$\chi_M = 2\chi_C + \chi_{Ni} \quad (3)$$

The first term in this equation (χ_C) corresponds to the magnetic susceptibility of an alternating chain with local spins 1/2 proposed by Hatfield,[26,27] eqn. (4)

$$\chi_C = \frac{Ng^2\beta^2}{kT} \frac{A+Bx+Cx^2}{1+Dx+Ex^2+Fx^3} \quad (4)$$

with $x = \frac{|J|}{kT}$

and the A-F coefficients being

$A = 0.25$

$B = -0.068475 + 0.13194\alpha$

$C = 0.0042563 - 0.031670\alpha + 0.12278\alpha^2 - 0.29943\alpha^3 + 0.21814\alpha^4$

$D = 0.035255 + 0.6521\alpha$

$E = -0.00089418 - 0.10290\alpha + 0.87155\alpha^2 - 0.18472\alpha^3$

$F = 0.045230 - 0.0081910\alpha + 0.83234\alpha^2 - 2.6181\alpha^3 + 1.92813\alpha^4$

The second term in eqn. (3) accounts for the magnetic susceptibility of the nickel(II) ions (χ_{Ni}) that can be expressed by eqn. (5)

$$\chi_{Ni} = \frac{N\beta^2 g_{Ni}^2}{3K(T-\theta)} S_{Ni}(S_{Ni}+1) \quad (5)$$

considering a Curie-law behaviour for the nickel(II) ions with the inclusion of intermolecular interactions (θ) between them. In this expression, *N*, β and *g* have their usual meaning and θ is the Weiss factor introduced to take into account the possible weak intermolecular magnetic interactions (*j*) within the mean-field approximation and which is defined as $\theta = \frac{-zjS_{Ni}(S_{Ni}+1)}{3k}$.

Alternatively, the magnetic susceptibility of the nickel(II) ions (χ_{Ni}) can also be calculated according to eqn. (6).

$$\chi_{Ni} = \frac{\chi_{\parallel}+2\chi_{\perp}}{3} \quad (6)$$

with $\chi_{\parallel} = \frac{2N\beta^2 g_{Ni}^2}{kT} \frac{e^{(-\frac{D}{kT})}}{1+2e^{(-\frac{D}{kT})}}$

and $\chi_{\perp} = \frac{2N\beta^2 g_{Ni}^2}{D} \frac{1-e^{(-\frac{D}{kT})}}{1+2e^{(-\frac{D}{kT})}}$

In this case, we discarded the possible intermolecular interactions between nickel(II) ions but we consider the zero-field splitting of their ground state (S = 1) described by the parameter *D*.

Two fits can be done depending on the theoretical expression employed to define χ_{Ni}, either the one that considers weak intermolecular $Ni^{II}\cdots Ni^{II}$ interactions [eqn. (5)] or the other one with zero-field splitting effects [eqn. (6)]. Thus, both fits were performed and they reproduced well the experimental data in the whole temperature range investigated. The least squares best-fit parameters are: J_1 = -94.2 cm^{-1}, α = 0.92, J_2 = -89.5 cm^{-1}, g_{Cu} = 2.08, g_{Ni} = 2.10, θ = -1.45 K [eqn. (3) with eqn. (5)], D = ± 4.2 cm^{-1} [eqn. (3) with eqn. (6)], the values of R being 1.1 x 10^{-5} and 3.5 x 10^{-5}, respectively.

The slightly higher values of J_1 and J_2 (-94.2 and -89.5 cm^{-1}, respectively) found for compound **2b^S** compared to those obtained for the **2a^S**, **2a^R**, **3a^S** and **4a^R** copper(II) metalloligands (see Table 2) could be understood considering the different coordination geometry that the copper(II) ions exhibit within the chains of **2b^S**. As previously described, the Cu(1) atom shows a [4+2] coordination in a Jahn-Teller distorted octahedral geometry with four short equatorial bond distances [Cu(1)-O(1), Cu(1)-O(2), Cu(1)-O(4) and Cu(1)-O(5)] defining the basal plane and two longer bond distances for the axial interactions. Its unpaired electron is delocalised the basal plane which is coplanar with the oxamate mean plane. However, despite the Cu(2) centre also exhibits a [4+2] coordination, in this case there is a compression of the [Cu(2)-N(1) and Cu(2)-N(2)] bonds, the remaining Cu-O bonds being elongated. Consequently, the magnetic orbital of the Cu(2) atom corresponds to a mixture of d_{z^2} and $d_{x^2-y^2}$ orbitals. Figure 61 illustrates the interacting magnetic orbitals for Cu(1) and Cu(2) in **2b^S** considering a pure

d_{z^2} type magnetic orbital for Cu(2). This picture allows the understanding of the somewhat stronger antiferromagnetic coupling between the Cu(1) and Cu(2) ions in **2b^S** respect to **2a^S**, **2a^R**, **3a^S** and **4a^R** since the electronic density in a d_{z^2} type magnetic orbital along the Cu(2)-N(1) axis is greater than that for the $d_{x^2-y^2}$ situation.

The magnetic orbitals topology associated to **2b^S** [based on the geometry of the copper(II) ions] and the consequent magnetic coupling match with its slightly higher value of *J* compared to those of **2a^S**, **2a^R**, **3a^S** and **4a^R**. This might not be the only possible explanation since there are also other subtle factors (mentioned above) which would influence the magnitude of the magnetic coupling.

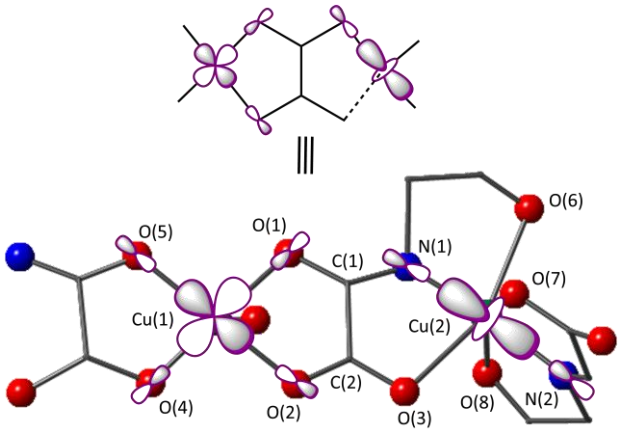

Figure 61. Simplified view of the dimeric moieties of the alternating copper(II) chains in **2b^S** with the atom numbering scheme. Cu(1) shows a [4+2] coordination in a Jahn-Teller distorted octahedral geometry with four short bond distances [Cu(1)-O(1), Cu(1)-O(2), Cu(1)-O(4) and Cu(1)-O(5)] defining the basal plane and two long bond distances (not shown). Cu(2) exhibits a [4+2] coordination in a compressed octahedral geometry with two short bond distances [(Cu2-N1, Cu2-N2), and four long distances [Cu(2)-O(3), Cu(2)-O(6), Cu(2)-O(7) and Cu(2)-O(8)]. The relative orientation of the magnetic orbitals centred on each atom is also represented. It is worth noting that the magnetic orbital of Cu(2) is idealised (read the text).

1.A.4.3. Gas sorption properties

Aiming at investigating the porous nature and gas sorption capacities of **2b^S** and **4b^R**, dinitrogen and carbon dioxide adsorption isotherms were measured.

The compound **2b^S** is essentially nonporous to nitrogen as revealed by the measured isotherm and has a very low estimated BET[28] (Brunauer, Emmett and Teller) surface area of 2.60 $m^2\ g^{-1}$ (Figure 62a). On the other hand, the CO_2 isotherm does not show much better results, reaching a maximum uptake of 1 $mmol\ g^{-1}$ (Figure 62b). The explanation for such low uptakes may be the collapse of the framework of **2b^S** when the solvent molecules are removed during the activation step. This hypothesis is in agreement with the loss of peaks in the PXRD pattern when **2b^S** was measured exposed to the open air (Figure 17f). Despite the collapse of the structure a low uptake of CO_2 has been observed, likely because the smaller and more polarizable CO_2 molecules can accede within the pockets of the framework and interact with the many accessible copper(II) ions.

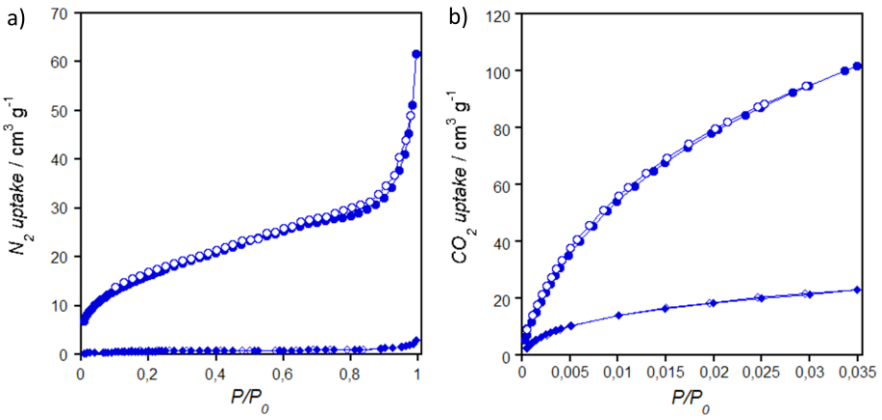

Figure 62. (a) N_2 and (b) CO_2 adsorption isotherms measured at 77 and 273 K respectively for the activated compounds **2b^S** (rhombuses) and **4b^R** (circles). Filled and empty symbols indicate the adsorption and desorption isotherms, respectively.

The N_2 isotherm of **4b^R** shows a very poor uptake of *ca.* 1 $mmol\ g^{-1}$ (Figure 62a), which can be related to concomitant effects of the irregular shape of the pores. In contrast,

the CO_2 isotherm shows a large uptake of 100 $cm^3 g^{-1}$ at 1 atm (Figure 62b) suggesting that the smaller and more polarizable CO_2 molecules can go into the pockets situated between the aromatic rings and interact with the many accessible copper(II) ions. The integrity of the framework was proved by PXRD measurements, thus precluding its collapse after the solvent removal and confirming its stability (see above and Figure 18d).

1.A.4.4. Enantiomeric separation

The incorporation of enantiomerically pure building blocks into our frameworks, giving rise to chiral porous structures, moved us to investigate their capacity for separating mixtures of chiral molecules.

We focused on the homochiral PCP **4b^R** (which showed porosity after solvent removal) as stationary phase for the separation of the chiral guest species methyl lactate and phenyethanol. The choice of acids and amines was discarded since their great reactivity would disassemble the MOF structure. For this purpose, we firstly confirmed that the framework remained stable in the presence of the chiral species. Afterwards we proved that the desired molecules could be effectively adsorbed to finally explore the possible enantioselectivity.

The racemic mixtures of methyl lactate and phenyethanol were artificially prepared (50:50 v/v mixture) from the two resolved enantiomers, and their enantiomeric excess (*ee*) was previously determined through gas chromatography (GC). In order to prepare a stationary phase, a steel stainless column of 10 cm length with an inner diameter of *ca.* 4.6 mm was filled with 228 mg of pellets prepared from the **4b^R** MOF. A 0.1 M racemic mixture of *R*-phenyethanol/*S*-phenylethanol [prepared in water:methanol (1:15 v/v)] was then injected by a syringe pump with a flow rate of 250 μL/min. Several aliquots were collected at the output of the column and further analysed through GC. The results showed that the molecules of the racemic mixture were absorbed by the material until saturation was reached after 7 minutes flowing. Unfortunately, the results

also revealed no *ee* in the samples, reflecting that there was no selective recognition. In a second step, the racemic mixture was desorbed from the MOF by flowing water:methanol. These samples were also analysed and no *ee* was found. The racemic *D*-methyl lactate/*L*-ethyl lactate mixture was also tested in the same conditions with no positive results.

Despite compound **2b^{S}** seemed to become amorphous when exposed to air, we also investigated it since it may transform into crystalline upon suspension in water:methanol solution or even upon reaction with small guest molecules. Unfortunately, nor has this MOF shown any ability to act as separation medium for the tested racemic mixtures.

Since the adsorption of the molecules was confirmed by the GC results, the explanation for the unsuccessful enantiomeric separation is most likely due to the insufficient interactions between the walls of the pores and the chiral molecules. In turn, this could happen because the chiral centres are not readily accessible. It would be a good idea to synthesise a MOF decorated with bigger R groups of the amino acid in order to increase the possible chiral interactions. Another possible strategy relies on the separation of larger chiral molecules capable to interact with the pores of the network and establish host-guest interactions through a chiral recognition process. Moreover, we consider DFT calculations as a very interesting tool for future works in order to get some insights beforehand about the energies of the configurations resulting from the interactions between the two guest enantiomers and the chiral host framework.

1.A.5. Discussion

In this chapter, we have successfully developed an original strategy to rationally design chiral MOFs. This strategy consisted on the use of uncommon enantiopure (such as 1D chains or hexacopper(II) wheels) capable to further coordinate, through their free carbonyl groups, to square-planar complexes yielding high-dimensional enantiopoure MOFs. Overall, the functionalization of natural amino acids derivatives afforded a library of chiral proligands which further reacted with the copper(II) salt to afford a variety of chiral precursors of polymeric nature (surprisingly, monomers could not be obtained but more complex wheels and a chain instead). Interestingly, apart from their use as metalloligands to build chiral 3D structures, they served as an excellent platform to carry out magneto-structural studies

Hence, intriguing and fascinating porous 3D structures were synthesised and characterised, and their crystal structures could be successfully determined from X-ray diffraction despite the complex unit cell that these compounds possess. This hard and detailed work allowed us to carry out a structural and topological study of the chiral frameworks, one of the most impressive results being the preparation for the first time of a Rod-like MOF (**4b^{R}**) where the fundamental building unit from the framework exactly matches with the chain used as precursor to build the MOF. The transmission of the chirality from the starting amino acids to the final 3D frameworks, which was the main goal of our approach, was achieved and demonstrated through both crystallographic data and chiral dichroism measurements.

The main disadvantage of this family of chiral MOFs is the lack of stability that they show in water. This fact may be due to the weak bond that the [Ni(cylam)]$^{2+}$ complex form with the carbonyl oxygen from the amino acid residues. This lack of stability in water precluded many asymmetric catalysis experiments. On the other hand, their lack of structural stability when exposed to the solvent removal made difficult, or even precluded in some cases, the possibility of displaying gas sorption properties. Although the experiments involving separation of chiral molecules (methyl lactate and

phenylglycine) were carried out without positive results, the fundamental knowledge has been established to come back to these experiments through subtle structural modifications. Moreover, separation of larger chiral molecules is still planned and we think that these chiral MOFs, showing large chiral pores, could be useful for these types of separations through chiral recognition processes. In any case, the results collected in this chapter showed novel and very original methodologies for the design of chiral MOFs which is still a synthetic challenge.

1.A.6. References

1 A. A. Bagabas, M. Frasconi, J. Iehl, B. Hauser, O. K. Farha, J. T. Hupp, K. J. Hartlieb, Y. Y. Botros and J. F. Stoddart, *Inorg. Chem.*, 2013, **52**, 2854–2861.

2 A. von Zelewsky, *Stereochemistry of Coordination Compounds*, 1996.

3 V. A. Blatov, *Struct. Chem.*, 2016, **27**, 1605–1611.

4 A. Schoedel, M. Li, D. Li, M. O'Keeffe and O. M. Yaghi, *Chem. Rev.*, 2016, **116**, 12466–12535.

5 N. L. Rosi, M. Eddaoudi, J. Kim, M. O'Keeffe and O. M. Yaghi, *Angew. Chemie Int. Ed.*, 2002, **41**, 284–287.

6 E. V. Alexandrov, V. a. Blatov, a. V. Kochetkov and D. M. Proserpio, *CrystEngComm*, 2011, **13**, 3947–3958.

7 M. O'Keeffe and O. M. Yaghi, *Chem. Rev.*, 2012, **112**, 675–702.

8 N. L. Rosi, J. Kim, M. Eddaoudi, B. Chen, M. O'Keeffe and O. M. Yaghi, *J. Am. Chem. Soc.*, 2005, **127**, 1504–1518.

9 K. Barthelet, J. Marrot, G. Férey and D. Riou, *Chem. Commun.*, 2004, 520–521.

10 B. S. Luisi, V. C. Kravtsov and B. D. Moulton, *Cryst. Growth Des.*, 2006, **6**, 2207–2209.

11 M. Tiliakos, E. Katsoulakou, A. Terzis, C. Raptopoulou, P. Cordopatis and E. Manessi-Zoupa, *Inorg. Chem. Commun.*, 2005, **8**, 1085–1089.

12 J. Cano, VPMAG *package,* Univeristy of Valencia, Valencia, Spain, 2003.

13 W. E. Estes, D. P. Gavel, W. E. Hatfield and D. J. Hodgson, *Inorg. Chem.*, 1978, **17**, 1415–1421.

14 J. C. Bonner and M. E. Fisher, *Phys. Rev.*, 1964, **135**, A640–A658.

15 J. Cano, P. Alemany, S. Alvarez, M. Verdaguer and E. Ruiz, *Chem. - A Eur. J.*, 1998, **4**, 476–484.

16 M. Julve, M. Verdaguer, A. Gleizes, M. Philoche-Levisalles and O. Kahn, *Inorg. Chem.*, 1984, **23**, 3808–3818.

17 T. R. Felthouse, E. J. Laskowski and D. N. Hendrickson, *Inorg. Chem.*, 1977, **16**, 1077–1089.

18 O. Kahn, *Angew. Chemie Int. Ed. English*, 1985, **24**, 834–850.

19 A. Escuer, R. Vicente, J. Ribas, J. Jaud and B. Raynaud, *Inorganica Chim. Acta*, 1994, **216**, 139–145.

20 P. Román, C. Guzmán-Miralles, A. Luque, J. I. Beitia, J. Cano, F. Lloret, M. Julve and S. Alvarez, *Inorg. Chem.*, 1996, **35**, 3741–3751.

21 E. Ruiz, P. Alemany, S. Alvarez and J. Cano, *Inorg. Chem.*, 1997, **36**, 3683–3688.

22 W. P. Barros, B. C. da Silva, N. V Reis, C. L. M. Pereira, A. C. Doriguetto, J. Cano, K. R. Pirota, E. F. Pedroso, M. Julve and H. O. Stumpf, *Dalt. Trans.*, 2014, **43**, 14586–14595.

23 T. R. G. Simões, R. V Mambrini, D. O. Reis, M. V Marinho, M. a Ribeiro, C. B. Pinheiro, J. Ferrando-Soria, M. Déniz, C. Ruiz-Pérez, D. Cangussu, H. O. Stumpf, F. Lloret and M. Julve, *Dalt. Trans.*, 2013, **42**, 5778–5795.

24 A. Bencini, C. Benelli, D. Gatteschi, C. Zanchini, A. C. Fabretti and G. C. Franchini, *Inorganica Chim. Acta*, 1984, **86**, 169–172.

25 Verdaguer M.; Kahn O.; Julve M.; Gleizes A., *Nouv. J. Chim.*, 1985, **9**, 325–334.

26 J. W. Hall, W. E. Marsh, R. R. Weller and W. E. Hatfield, *Inorg. Chem.*, 1981, **20**, 1033–1037.

27 W. Duffy and K. P. Barr, *Phys. Rev.*, 1968, **165**, 647–654.

28 M. F. De Lange, T. J. H. Vlugt, J. Gascon and F. Kapteijn, *Microporous Mesoporous Mater.*, 2014, **200**, 199–215.

Part 1.B

Oxamidato-based chiral PCPs

1.B.1. Synthetic Route

Oxamidato-based proligands derived from amino acids were prepared by following the same synthetic procedure (see Scheme 11): oxalyl chloride was condensated with the methyl ester derivative of the corresponding enantiopure amino acid in the presence of trimethylamine and dichloromethane as base and solvent respectively, at room temperature (for further details on their syntheses see Annex I). The products were finally isolated as methyloxamidato-derivatives with very good yields (ranging from 80 to 90 %). The whole library of proligands obtained by following this preparative route is illustrated in Scheme 12.

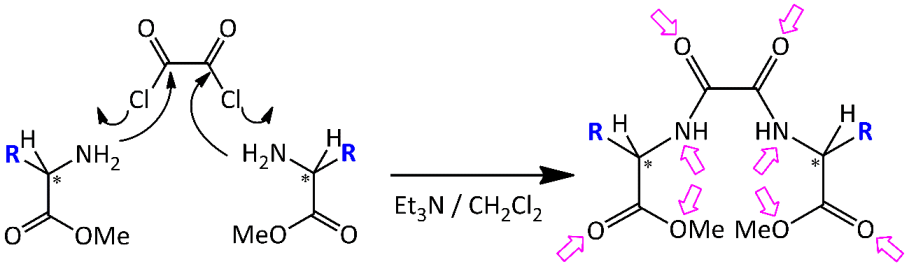

Amino acid	-R group	Methyl derivative proligand
Alanine	CH_3	H_2Me_2alamox
Valine	H_3C, H_3C	H_2Me_2valmox
Leucine		H_2Me_2leumox

Scheme 11. Synthetic route for the preparation of the methyl derivatives of the chiral *N*-oxalamide acids. The different amino acids with their corresponding R substituent and the nomenclature for the resulting oxamidato-based proligands are shown in the Table. H_4alamox = *N*,*N*'-bis(alanine)oxalyl diamide; H_4valmox = *N*,*N*'-bis(valine)oxalyl diamide and H_4leumox = *N*,*N*'-bis(leucine)oxalyl diamide. The asymmetric carbon has been marked with an asterisc and the pink arrows indicate the multiple coordinating sites that these proligands (and the corresponding ligands) have.

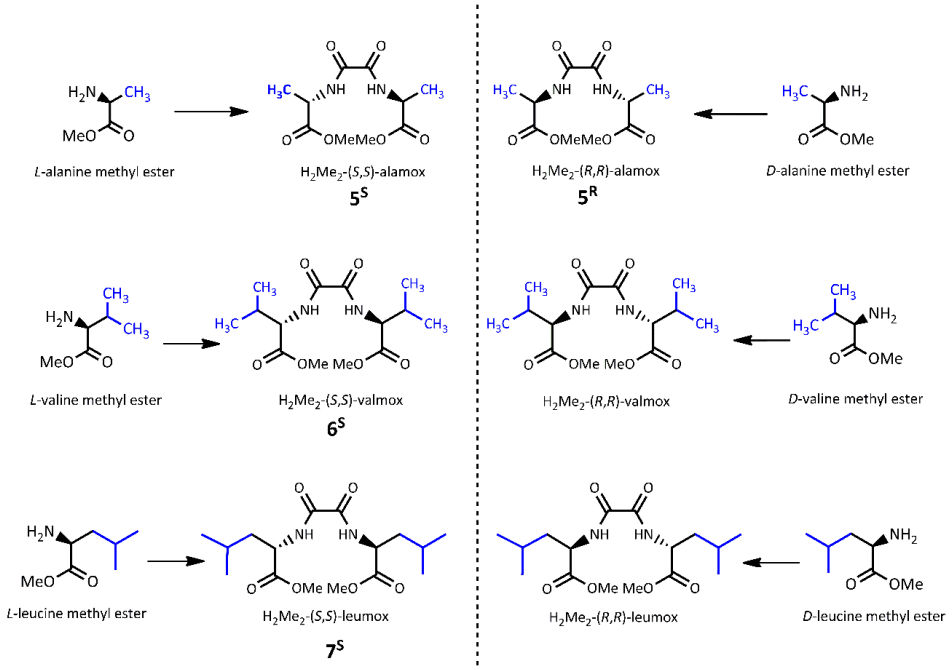

Scheme 12. Library of oxamidato-based proligands synthetised from the starting amino acids derivatives.

The next step consists of the synthesis of the metal complexes from the chiral oxamidato-based proligands by following the synthetic route illustrated in Scheme 13 (detailed in Annex I). The oxamidato-containing copper(II) complexes were obtained from the reaction of stoichiometric amounts of $CuCl_2 \cdot 6H_2O$ and the corresponding enantiopure proligands (2:1 metal to ligand molar ratio) with Me_4NOH in a methanolic solution. The resulting compounds were isolated as tetramethylammonium salts of general formula $(Me_4N)_2[Cu^{II}_2L(OH)_2] \cdot nH_2O$.

Following the corresponding syntheses described in detail in Annex I, copper(II) oxalamido-containing complexes of formulas $(Me_4N)_2\{Cu^{II}_2[(S,S)\text{-alamox}](OH)_2\} \cdot 6H_2O$ (**5a^S**), $(Me_4N)_2\{Cu^{II}_2[(R,R)\text{-alamox}](OH)_2\} \cdot 6H_2O$ (**5a^R**), $(Me_4N)_2\{Cu^{II}_2[(S,S)\text{-valmox}](OH)_2\} \cdot 2H_2O$ (**6a^S**), $(Me_4N)_2\{Cu^{II}_2[(R,R)\text{-valmox}](OH)_2\} \cdot 2H_2O$ (**6a^R**) and $(Me_4N)_2\{Cu^{II}_2[(S,S)\text{-leumox}](OH)_2\} \cdot 2H_2O$ (**7a^S**) were obtained. Unfortunately, the high hygroscopic

character of these compounds prevented the obtaining of crystals suitable for X-ray diffraction.

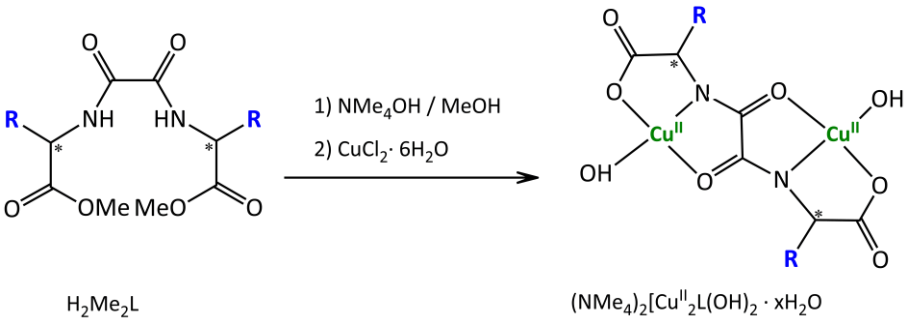

Scheme 13. Synthetic route for the preparation of the copper(II) complexes, which will be further used as ligands through the free coordination sites towards a second metal ion. The chiral centres have been marked with *.

Finally, aiming at building the 3D porous structures, we followed the already mentioned metalloligand strategy consisting of using the copper(II) precursors as metalloligands towards alkaline-earth [calcium(II) and barium(II)] and lanthanide [dysprosium(III) and terbium(III)] ions through their available coordination sites (see Scheme 14). This preparative route provided with a family of chiral PCPs which is listed in Table 3. Detailed synthetic procedures are given for all of them in Annex I.

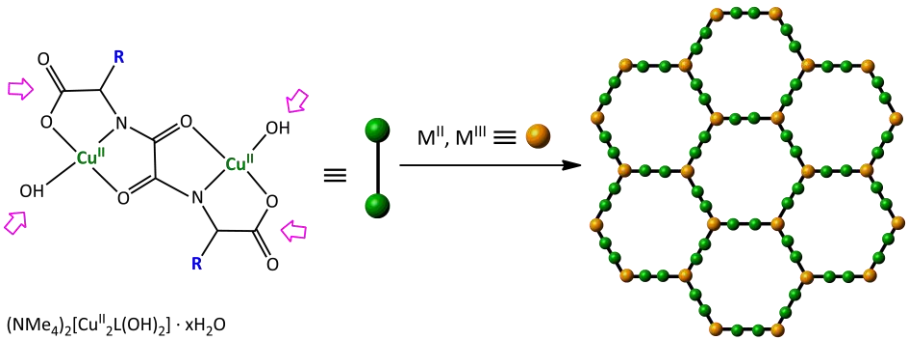

Scheme 14. Hypothetic "metalloligand" approach illustrating the assembling process of the dicopper(II) precursors acting as metalloligands through their hydroxo and carboxylate potential coordination sites (indicated with pink arrows) towards M^{II} (M = Ca, Ba and Sr) and M^{III} ions (M = Dy and Tb) affording the 3D porous structures.

Table 3. List of the obtained PCPs

Compound	Formula
5b^{S}	$\{Ba^{II}Cu^{II}_6[(S,S)\text{-alamox}]_3(OH)_2(H_2O) \cdot 30H_2O\}_n$
5c^{S}	$\{Ca^{II}Cu^{II}_6[(S,S)\text{-alamox}]_3(OH)_2(H_2O) \cdot 32H_2O\}_n$
5c^{R}	$\{Ca^{II}Cu^{II}_6[(R,R)\text{-alamox}]_3(OH)_2(H_2O) \cdot 32H_2O\}_n$
5d^{S}	$\{Dy^{III}Cu^{II}_6[(S,S)\text{-alamox}]_3(OH)_3 \cdot 21H_2O\}_n$
5e^{S}	$\{Tb^{III}Cu^{II}_6[(S,S)\text{-alamox}]_3(OH)_3 \cdot 21H_2O\}_n$
6b^{S}	$\{Ba^{II}Cu^{II}_6[(S,S)\text{-valmox}]_3(OH)_2(CH_3OH)_6 \cdot 6H_2O\}_n$
6c^{S}	$\{Ca^{II}Cu^{II}_6[(S,S)\text{-valmox}]_3(OH)_2(H_2O) \cdot 13H_2O\}_n$
7b^{S}	$\{Ba^{II}Cu^{II}_4[(S,S)\text{-leumox}]_3(OH)_2(H_2O)_2 \cdot 14H_2O\}_n$
7c^{S}	$\{Ca^{II}Cu^{II}_6[(S,S)\text{-leumox}]_3(OH)_2(H_2O) \cdot 11H_2O\}_n$

1.B.2. Physical Characterisation

The chemical nature of the proligands, the *trans*-oxamidato dicopper(II) precursors and the oxamidato-based PCPs was established through ^{1}H NMR spectroscopy, elemental analysis (C, H, N), FTIR spectroscopy and Scanning Electronic Microscopy (SEM). All these data are gathered in Tables 10-19 in Annex I.

1.B.2.1. Thermo-gravimetric study

The water contents of the oxamidato-based PCPs has been determined by thermogravimetric analyses (TGA) under a dry N_2 atmosphere. The mass loss *vs*. temperature plots of **5b^{S}**, **6b^{S}** and **7b^{S}** are shown in Figure 63a. Values of mass loss of *ca*. 27.1 (**5b^{S}**), 12.8 (**6b^{S}**) and 15.0 % (**7b^{S}**) at 150 °C correspond to 30 (**5b^{S}**) and 12 (**7b^{S}**) water molecules per formula unit, and 6 water and 4 methanol molecules (**6b^{S}**).

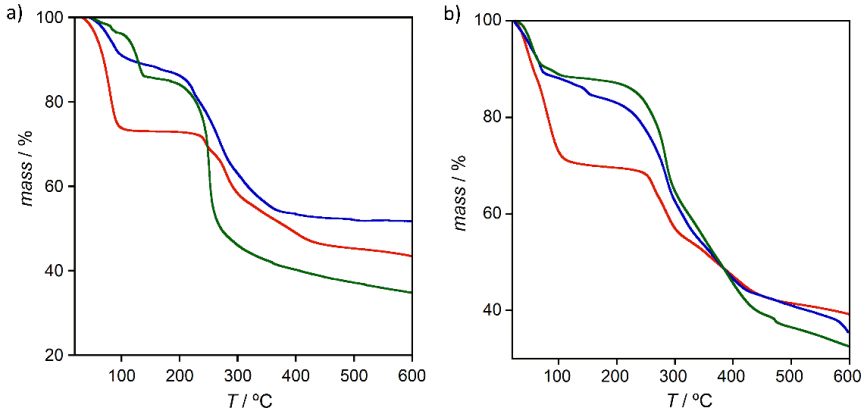

Figure 63. (a) TGA of **5b^S** (red), **6b^S** (blue) and **7b^S** (green) under a dry N_2 atmosphere. (b) TGA of **5c^S** (red), **6c^S** (blue) and **7c^S** (green) under a dry N_2 atmosphere.

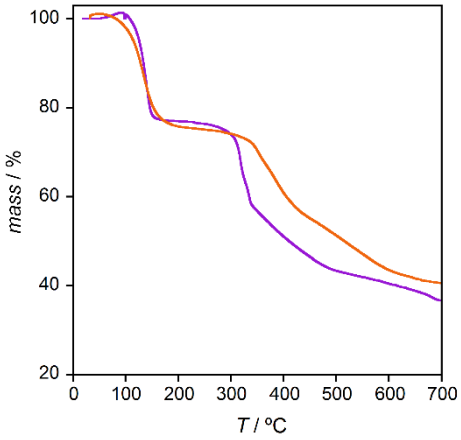

Figure 64. (b) TGA of **5d^S** (purple) and **5e^S** (orange) under dry N_2 atmosphere.

Values of mass loss about 31.5 (**5c^S**), 15.0 (**6c^S**) and 12.0 % (**7c^S**) at *ca*. 150 °C (Figure 63b) are consistent with 32, 13 and 11 water molecules per formula unit, respectively. Even if the larger pores of **5c^S** undoubtedly influence the very large number of water molecules that can be accommodated in its channels, these results allow to envisage the very different hydrophobicity of the compounds of this copper(II)-calcium(II) family. So, the number of water molecules of crystallisation filling the pores of **6c^S** and **7c^S** is drastically reduced compared to **5c^S** as a consequence of their much bulkier alkyl chains and the resulting stronger hydrophobic environment. Percentages of mass loss about 24.3 (**5d^S**) and 23.1 % (**5e^S**) at *ca*. 150 °C (Figure 64) are consistent with 21 water molecules per formula unit for both compounds.

1.B.2.2. Powder X-ray diffraction

Powder X-ray diffraction (PXRD) patterns of polycrystalline samples of the barium(II)-based subfamily **5b^S**, **6b^S**, and **7b^S** at room temperature are shown in Figure 65.

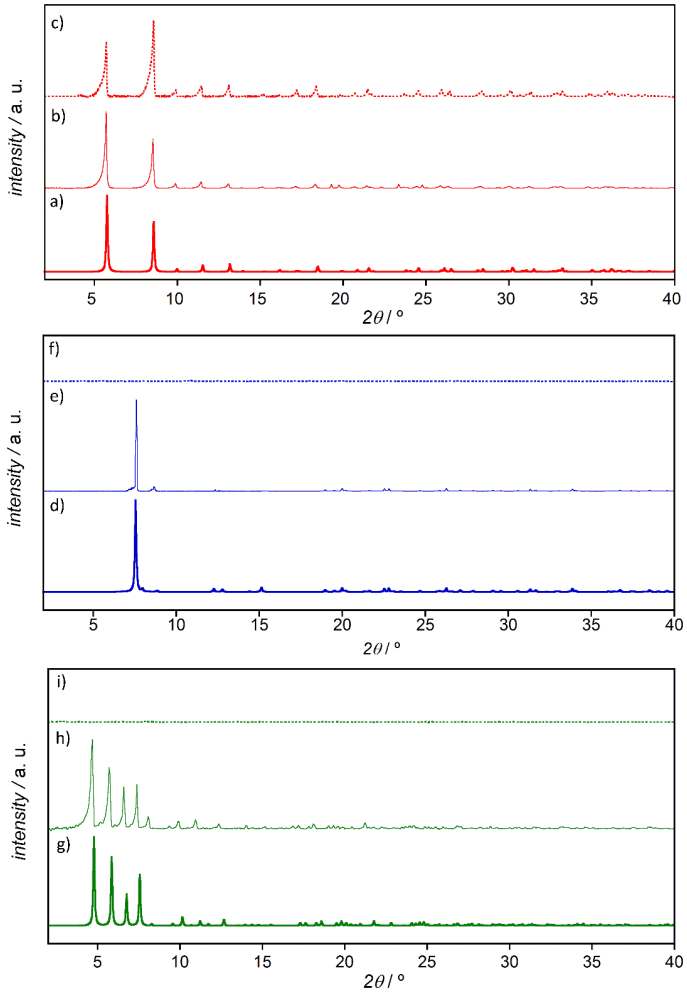

Figure 65. Calculated (a, d and g) and experimental PXRD pattern profiles of samples of **5b^S** (red), **6b^S** (blue) and **7b^S** (green) at r.t. as (b, e and h) aqueous-suspensions and (c, f and i) dehydrated.

These patterns reveal a total loss of crystallinity for **6b^S** and **7b^S** indicating that they become amorphous when exposed to the open air (Figures 65f,i). These results were not surprising since both the structures of **6b^S** and **7b^S** contain solvent molecules acting

as bridging nodes supporting the whole system and their removal leads to the collapse of the framework (especially for **6b^{S}**, whose bridging methanol molecules are much more volatile). On the contrary, the more stable structure of **5b^{S}** whose bridging nodes are mainly hydroxo molecules, remains crystalline (Figure 65c).

Therefore, in order to prevent the partial loss of solvent molecules at room temperature and the corresponding collapse of some of the frameworks, the PXRD patterns of **5b^{S}**, **6b^{S}** and **7b^{S}** were then measured in water suspensions (Figures 65b,d,h). Within each sample, the experimental PXRD pattern profile is consistent with the calculated one, confirming thus that the bulk samples are isostructural with the crystals selected for single-crystal X-ray diffraction.

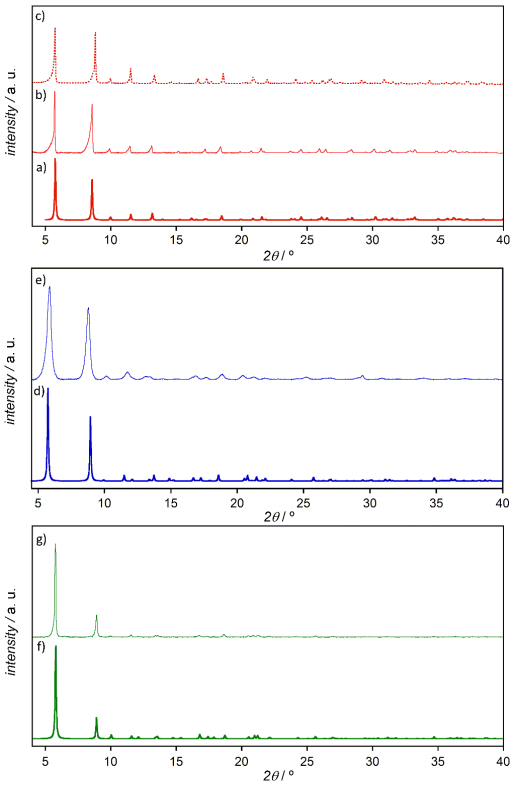

Figure 66. Calculated PXRD pattern profiles of (a) **5c^{S}**, (d) **6c^{S}** and (f) **7c^{S}**. Experimental PXRD pattern profiles of dehydrated polycrystalline samples of (b) **5c^{S}**, (c) **5c^{R}**, (e) **6c^{S}** and (g) **7c^{S}** at r.t.

PXRD patterns of polycrystalline samples of the calcium(II)-based subfamily **5c^{S}**, **5c^{R}**, **6c^{S}**, and **7c^{S}** at room temperature were measured (see Figure 66).

For all the samples, the experimental PXRD pattern profiles match well the simulated ones, confirming thus that the bulk samples are isostructural with the crystals selected for single-crystal X-ray diffraction. Moreover, the presence of peaks under solvent loss shows the structural stability that this calcium(II)-derived subfamily of PCPs exhibits, a feature that makes them good candidates for further gas sorption experiments.

Finally, PXRD measurements were carried out for polycrystalline samples of the dysprosium(III)- (**5d^{S}**) and terbium(III)-based (**5e^{S}**) compounds at room temperature and then compared to the theoretical pattern of **5e^{S}** (since only this last structure could be determined through single-crystal X-ray diffraction). The presence of well-defined peaks in the PXRD patterns of **5d^{S}** and **5e^{S}** reveals that both compounds show structural stability upon solvent removal (Figure 67). Moreover, a good match is observed between the experimental and simulated patterns of **5e^{S}** (Figure 67a,b). In turn, the PXRD pattern of **5d^{S}** (Figure 67c) seems quite consistent with the one of **5e^{S}** indicating that they are most likely isostructural compounds.

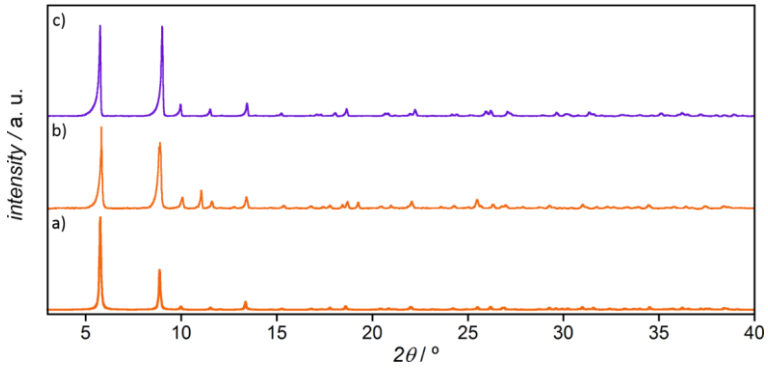

Figure 67. (a) Calculated PXRD pattern profile of **5e^{S}** and (b and c) experimental PXRD pattern profiles of polycrystalline samples of **5e^{S}** (orange), and **5d^{S}** (purple) at r.t.

1.B.3. Crystal Structures

Previous work from Lloret *et al*.[1–3] on oxamidato-containing copper(II) complexes revealed that the oxamidato-type bridging ligands usually exhibit a *trans* configuration the *cis* one being less stable due to steric hindrance between their substituents. This leads to dinuclear copper(II) species and the consequent formation of five- or six-membered chelate rings (see Scheme 13).

Therefore, based on their studies and supported by the physical characterisation, we assume that the precursors synthesised from (*S*,*S*)-alamox^{4-}, (*R*,*R*)-alamox^{4-}, (*S*,*S*)-valmox^{4-} and (*S*,*S*)-leumox^{4} proligands (**5a^{S}**, **5a^{R}**, **6a^{S}** and **7a^{S}**) are dicopper(II) complexes where the equatorial positions at each copper(II) ion are occupied by one nitrogen and two oxygen atoms from the bis(tridentate) bridging ligand and a water molecule or a hydroxo group depending on the value of the pH of the medium (see Scheme 13).

Hence, we decided to use the properly characterised polycrystalline samples of the copper(II) complexes **5a^{S}**, **5a^{R}**, **6a^{S}** and **7a^{S}** as metalloligands towards metal cations in order to build 3D chiral structures. The first attempts to build extended structures upon coordination of such dinuclear copper(II) precursors towards fully solvated first-row metal ions were unsuccessful. Thus, we tried with larger alkaline-earth and lanthanide metal ions achieving interesting compounds. The reason is likely to be the relative bigger sizes of the alkaline-earth and lanthanide metal-ions compared to those of the first-row metal ions (they can easily accommodate more SBUs into their coordination environment), together with their intrinsic coordinating nature.

1.B.3.1. Barium(II)-derived PCPs

Following the synthetic route described in the Annex I, polycrystalline powder samples as well as single crystals of $\{Ba^{II}Cu^{II}_6[(S,S)\text{-alamox}]_3(OH)_2(H_2O) \cdot 30H_2O\}_n$ (**5b^{S}**), $\{Ba^{II}Cu^{II}_6[(S,S)\text{-valmox}]_3(OH)_2(CH_3OH)_6 \cdot 6H_2O\}_n$ (**6b^{S}**) and $\{Ba^{II}Cu^{II}_4[(S,S)\text{-leumox}]_3(OH)_2(H_2O)_2 \cdot 14H_2O\}_n$ (**7b^{S}**) were obtained (Scheme 14). This novel family of

chiral PCPs arises as the perfect playground to study both how the encoded chiral information of the enantiopure proligands is ultimately translated into the 3D structure and the influence of the nature (size, shape and hydrophobicity) of the aliphatic residue of the amino acid on the final architecture of the resulting PCP. For further crystallographic details of **5b^{S}**, **6b^{S}** and **7b^{S}** see Table 23 in the Annex I.

Compound **5b^{S}** crystallises in the *P*6$_3$ space group of the hexagonal system. Its structure consists of a chiral 3D barium(II)-copper(II) network, which is built up from *trans*-oxamidato-bridged dicopper(II) units, {Cu$^{II}_2$[(*S*,*S*)-alamox]}, acting as linkers between the barium(II) ions through the carboxylate group. Additionally, aqua/hydroxo groups (1:2 statistical distribution) acting as additional bridges between two neighbouring dicopper(II) units and coordinated in a μ_3 fashion, support the whole system, unfolding an uninodal six-connected net (Figure 68).

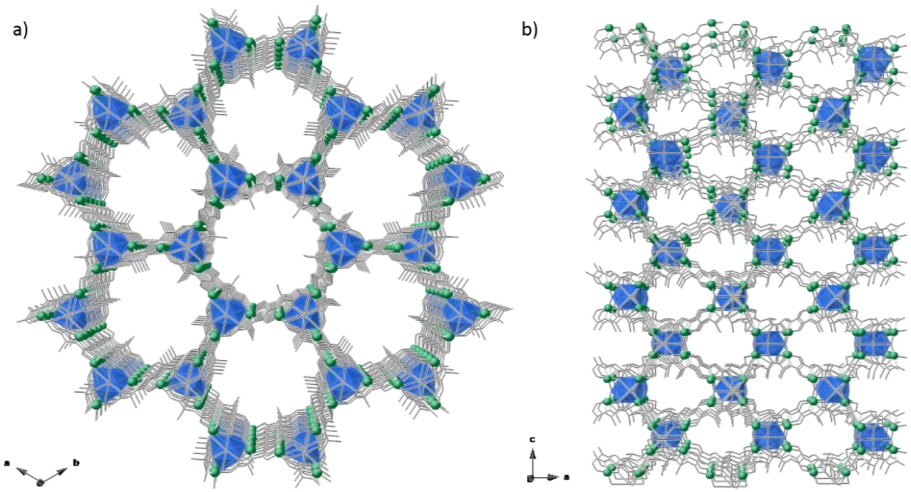

Figure 68. Perspective view of the structure of **5b^{S}** along the crystallographic *c* (a) and *b* (b) axes. The ligands are shown as sticks. The copper(II) and barium(II) ions are depicted as green spheres and blue polyhedra, respectively. Hydrogen atoms and water molecules are omitted for clarity.

The crystallographically independent copper(II) ions [Cu(1) and Cu(2)] are located at the edges of each hexagon (Figure 68). They are five-coordinate in an elongated square pyramidal geometry ($CuNO_3O_{OH}$): one nitrogen and two oxygen atoms from the

bis(tridentate) bridging oxamide ligand and one oxygen atom from one aqua/hydroxo group define the equatorial plane whereas the axial position is occupied by a carboxylate-oxygen atom from a neighbouring dicopper(II) entity [average values Cu-N = 1.915(10) Å, Cu-O_{OH} = 1.917(9) Å and Cu-O = 2.003(8) Å] (Figure 69). For further details on the interbond bite angles see Table 37, Annex I.

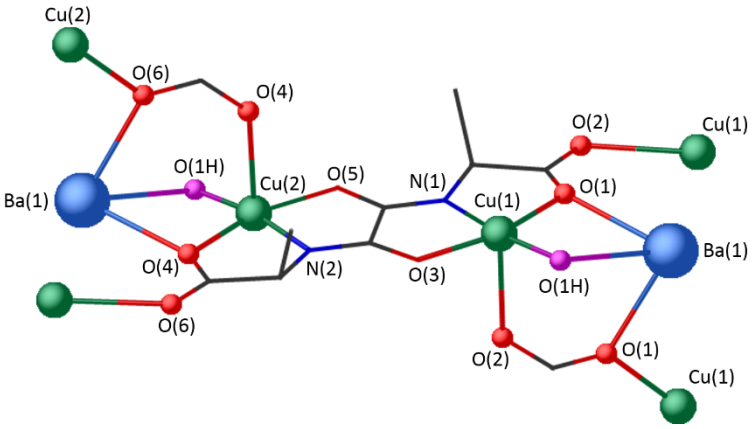

Figure 69. View of a fragment of the structure of **5b**[5] showing the oxamidate-bridged dicopper(II) unit and its coordination towards the neighbouring copper(II) and barium(II) ions with the numbering of the metal atoms (arbitrary radii).

The barium(II) ions, Ba(1), regularly occupy the corners of each hexagon (Figure 68) being the Ba···Ba distance 12.365(3) Å. They are nine-coordinate and exhibit a distorted monocapped square antriprismatic geometry (BaO_9) which is built by six carboxylate-oxygen atoms from six oxamidate groups and three aqua/hydroxo molecules (Figure 70) [Ba-O = 2.662(9) Å and Ba-O_{OH} = 2.835(4) Å].

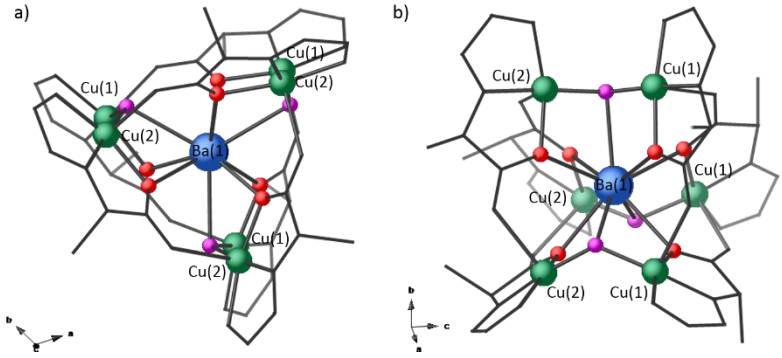

Figure 70. (a) View of the nine-coordinate environment of the barium(II) ion in **5b^{S}** along the crystallographic *c* axis. b) View illustrating the monocapped square antriprismatic geometry of the barium(II) ion. The ligand backbones are shown as grey sticks for clarity. Barium(II) and copper(II) ions, oxygen and hydroxylic oxygen atoms are depicted by blue, green, red and purple spheres (with arbitrary radii), respectively.

Overall, **5b^{S}** can be described as a mixed oxamidate- and carboxylate(aqua/hydroxo)-bridged, honeycomb-like hexagonal 3D $Ba^{II}Cu^{II}_{6}$ open-framework showing relatively large hexagonal channels along the crystallographic *c* axis (Figure 68), which are occupied by crystallisation water molecules (Figure 71). These channels have a virtual diameter of *ca.* 1.0 nm resulting from the alternating orientation of the methyl residues from the *trans*-(*S*,*S*)-alamox^{4-} bridging ligands within adjacent channels (Figures 68 and 71). The estimated empty volume without the crystallisation water molecules is 2209.2 Å^3, a value that represents up to *ca*. the 58.5 % of the potential void per unit cell volume (V = 3777.1 Å^3).

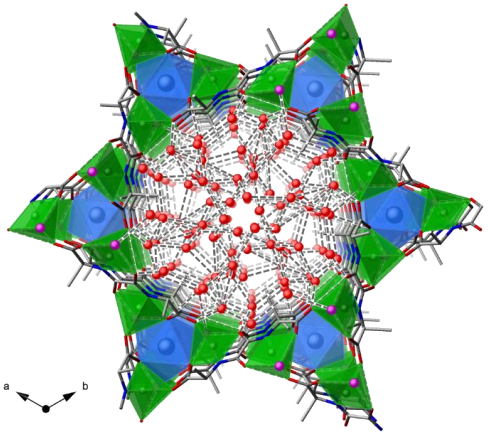

Figure 71. View of a pore of **5b^{S}** along the crystallographic *c* axis showing the net of hydrogen bonded water molecules (red spheres connected through dashed lines). Barium(II) and copper(II) are depicted as blue and green polyhedra, respectively. Hydrogen atoms have been omitted for clarity.

Compound **6b^{S}** crystallises in the chiral R_3 space group of the trigonal system. Its structure consists of a chiral 3D barium(II)-copper(II) network (Figure 72), which is built up from *trans*-oxamidato-bridged dicopper(II) units, {Cu^{II}_2[(*S*,*S*)-valmox]}, acting as linkers between the barium(II) ions through the carboxylate groups. The dicopper(II) units are further interconnected through methanol and hydroxo groups coordinating in μ and μ_3 modes, respectively, affording a fascinating triangular node (Figures 72 and 73).

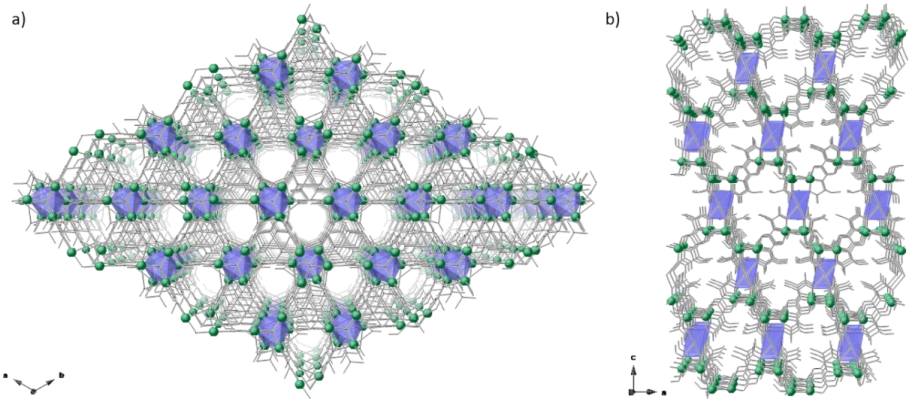

Figure 72. Perspective view of the structure of **6b^{S}** along the crystallographic *c* (a) and *b* (b) axes. The ligands are shown as sticks. The copper(II) and barium(II) atoms are depicted as green spheres and blue polyhedra, respectively. Hydrogen atoms and water molecules are omitted for clarity.

The two crystallographic independent copper(II) ions [Cu(1) and Cu(2)] are six-coordinate ($CuNO_2O_{OH}O_{2,MeOH}$) exhibiting an elongated distorted octahedral geometry. The basal plane is formed by one amidate-nitrogen, one carbonyl-oxygen atom, one carboxylate-oxygen and one hydroxo group, whilst two molecules of methanol occupy the axial positions (Figure 73) [average values Cu-N = 1.939(7), Cu-O = 2.007(8), Cu-O_{OH} = 1.982(3) and Cu-O_{MeOH} = 2.55(3) Å]. For further details on the interbond bite angles see Table 37, Annex I.

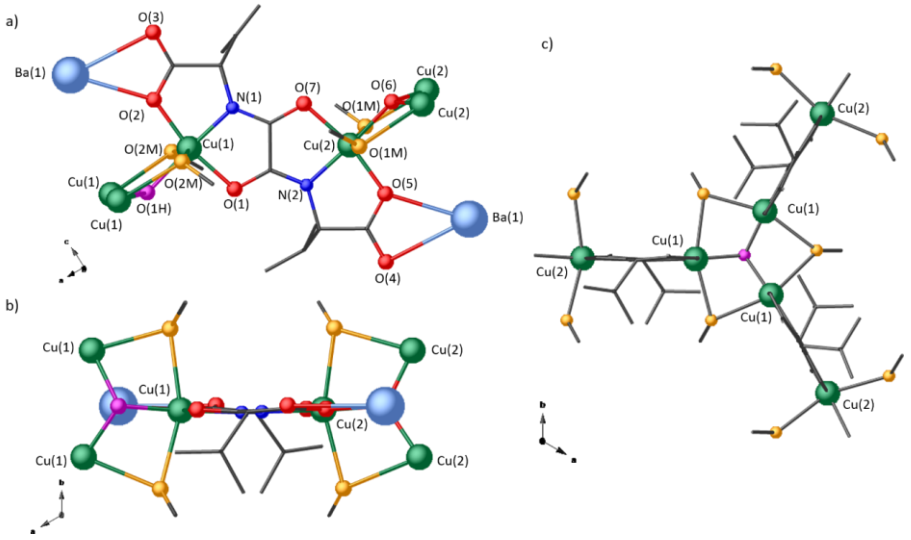

Figure 73. View of one dicopper(II) unit constituting **6b^S** (atoms drawn with arbitrary radii) along the crystallographic *b* (a) and *c* (b) axes and details of the coordination mode and environment of the copper(II) ions. The carbon atoms are shown as grey sticks, the copper(II) and barium(II) ions and the nitrogen and oxygen atoms are depicted by green, pale blue, blue and red spheres, respectively. The oxygen atoms from hydroxo groups and those from methanol are shown as purple and orange spheres, respectively. (c) A view of the hydroxo groups coordinating in a μ_3 mode connecting three dicopper(II) units.

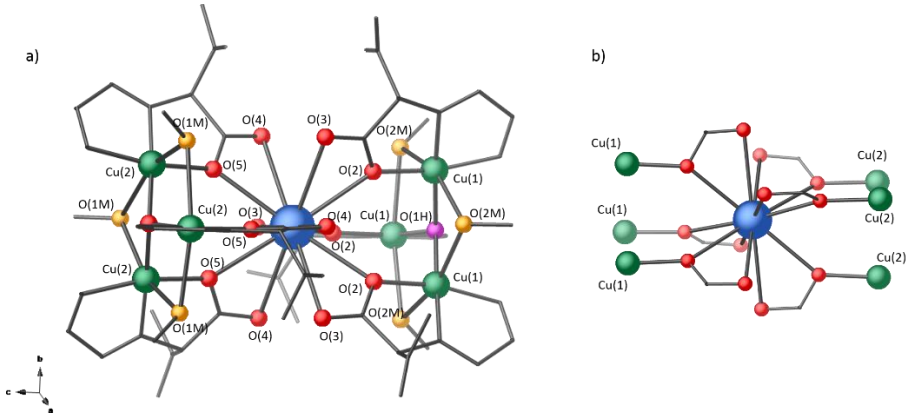

Figure 74. (a) View of the twelve-coordinate environment of the barium(II) ion in **6b^S** with the numbering of the donor atoms and metal ions (arbitrary radii). (b) View illustrating the bicapped pentagonal antiprismatic geometry of the barium(II) ion. The ligand backbones are shown as grey sticks for clarity. Barium(II) and copper(II) ions and oxygen atoms are depicted as pale blue, green and red spheres, respectively. The oxygen atoms from the hydroxo groups and methanol molecules are shown as purple and orange spheres, respectively.

Each barium(II) ion [Ba(1)] is twelve-coordinated (BaO_{12}) and exhibit a distorted bicapped pentagonal antiprismatic geometry, being bonded to twelve oxygen atoms from the six chelating carboxylate groups of the (*S*,*S*)-valmox^{4-} ligands from six dicopper(II) units (Figures 73a and 74).

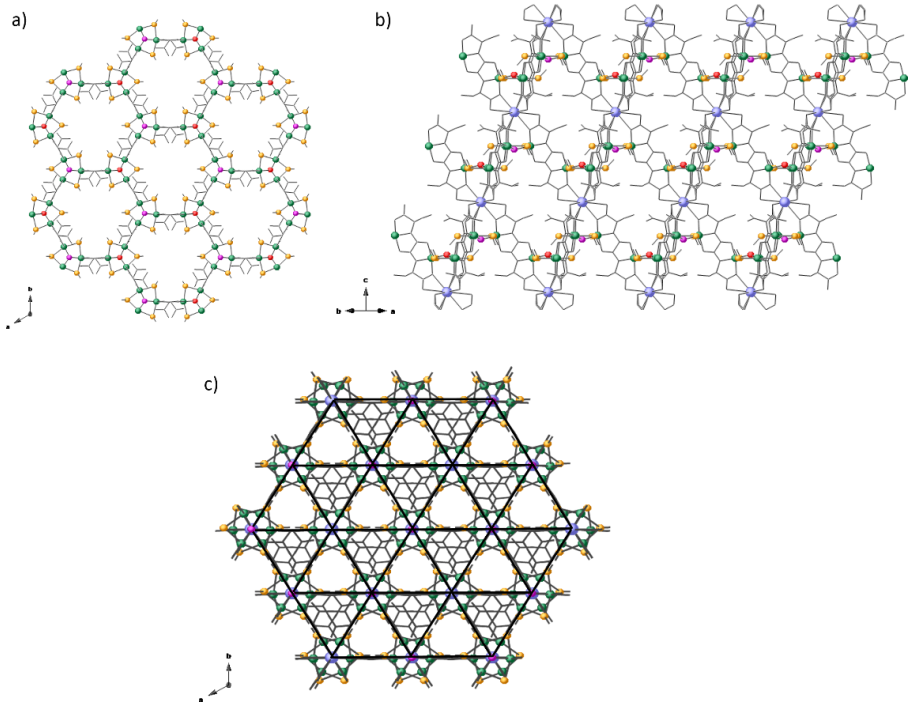

Figure 75. (a) View of a fragment of the extended array of anionic oxamidato-bridged Cu^{II}_3O layers of **6b^S** with a hexagonal net topology growing in the crystalographic *ab* plane and detail of the triangular nodes made up by the dicopper(II) units interconnected through oxygen atoms from methanol molecules (orange spheres) and hydroxo groups (purple spheres) which adopt μ and μ_3 bridging modes, respectively [the barium(II) ions have been omitted for clarity)]. (b) View of the adjacent layers displaced along the [110] direction leading to an *ABAB* pattern along the crystallographic *c* axis, which are further interconnected through the barium(II) ions acting as pillars in an up and down disposition. (c) View of the resulting uninodal six-connected net in the crystallographic *ab* plane. The ligand backbones are depicted as sticks. Barium(II) and copper(II) ions as well as oxygen atoms are shown as blue, green and red spheres. The water molecules of crystallisation have been omitted for clarity.

As shown in Figures 72a and 75c, this $Ba^{II}Cu^{II}_6$ open-framework show two types of small corrugated hexagonal channels: the hydrophilic ones along the crystallographic *c*

axis which are occupied by crystallisation water molecules (Figure 76) and the hydrophobic ones along the crystallographic *b* axis where the aliphatic chains (isopropyl valine residue) of the ligands are confined. In comparison with **5b^{S}**, the empty volume of these channels have been reduced as a consequence of the spatial orientation of the larger isopropyl residues and the carbonyl groups of the acidic part from the *trans*-(*S*,*S*)-valmox^{4-} bridging ligands (Figure 76). In this respect, the estimated empty volume without the crystallisation solvent molecules is 2822.7 Å^3, a value which represents up to *ca*. 47.2 % of the potential void per unit cell volume [V = 5974.2 Å^3].

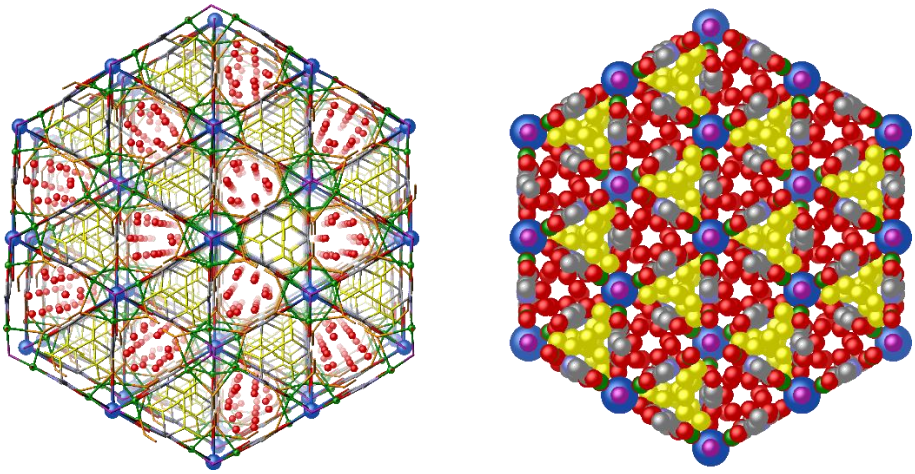

Figure 76. Perspective view of the porous structure of **7b^{S}**, using ball and sticks (left) and space filling (right) models, along the crystallographic *c* axis showing the pore window filled by hydrogen bonded water molecules (red spheres) and the hydrophobic channels where the isopropyl groups from the amino acid residues of (*S*,*S*)-valmox^{4-} ligands are confined (isopropyl groups are shown in yellow). Hydrogen atoms have been omitted for clarity.

Compound **7b^{S}** crystallises in the chiral $P2_13$ space group of the cubic system. Its structure consist of a chiral 3D barium(II)-copper(II) network (Figure 77) built up from *trans*-oxamidato-bridged dicopper(II) units, {Cu$^{II}_2$[(*S*,*S*)-leumox]}, acting as linkers between two of the three crystallographically independent barium(II) ions [Ba(1) and Ba(2)] through the carboxylate group. The other barium(II) ions [Ba(3)] are further grasped through a triple water bridge in fascinating terminal -Ba$^{II}_2$(μ-H_2O)$_3$- clusters. Additionally, hydroxo groups acting as supplementary bridges between two

neighbouring dicopper(II) units and coordinated in a μ_3 fashion keep the framework (Figure 78).

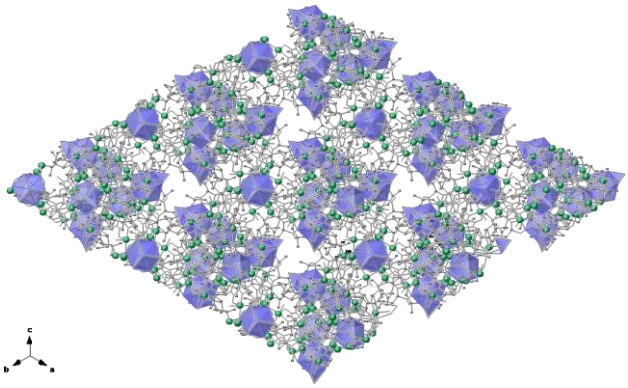

Figure 77. Perspective view of the structure of **7b^S** along the crystallographic [111] direction. The ligand backbones are depicted as grey sticks. The copper(II) and barium(II) ions are shown as green spheres and blue polyhedra, respectively.

The four crystallographically independent copper(II) ions [Cu(1), Cu(2), Cu(3) and Cu(4)] are five-coordinate ($CuNO_4$) in square pyramidal geometries. One amidate-

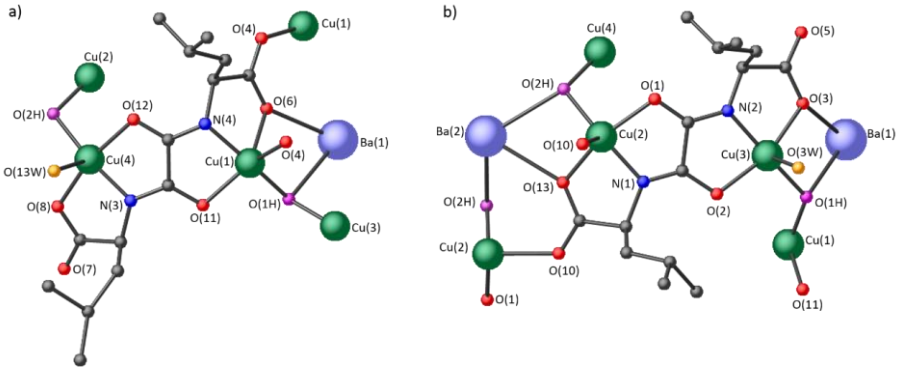

Figure 78. Details of the coordination mode and environment of the four non-equivalent copper(II) ions [Cu(1), Cu(2), Cu(3) and Cu(4)] in **7b^S** with the numbering of the non-carbon atoms. Noteworthy, the hydroxo groups act as supplementary bridges between two neighbouring dicopper(II) units and a barium(II) ion in a μ_3 fashion. Barium(II) and copper(II) ions and nitrogen and oxygen atoms are depicted as pale blue, green, blue and red spheres, respectively. The oxygen atoms from the hydroxo group and methanol molecule are shown as purple and orange spheres, respectively.

nitrogen atom, a carbonyl-oxygen atom, one carboxylate-oxygen atom and a hydroxo group build the basal plane, and one carboxylate-oxygen atom from the neighbouring dicopper(II) unit for Cu(1) and Cu(2), or one water molecule for Cu(3) and Cu(4), occupy the apical positions (Figure 79) [average values: Cu-N = 1.915(9), Cu-O_{OH} = 1.929(9), Cu-O_{eq} = 2.017(8), Cu-O_{ax} = 2.220(8) and Cu-O_{water} = 2.392(7) and 2.550(8) Å]. For further details on the interbond bite angles see Table 37, Annex I.

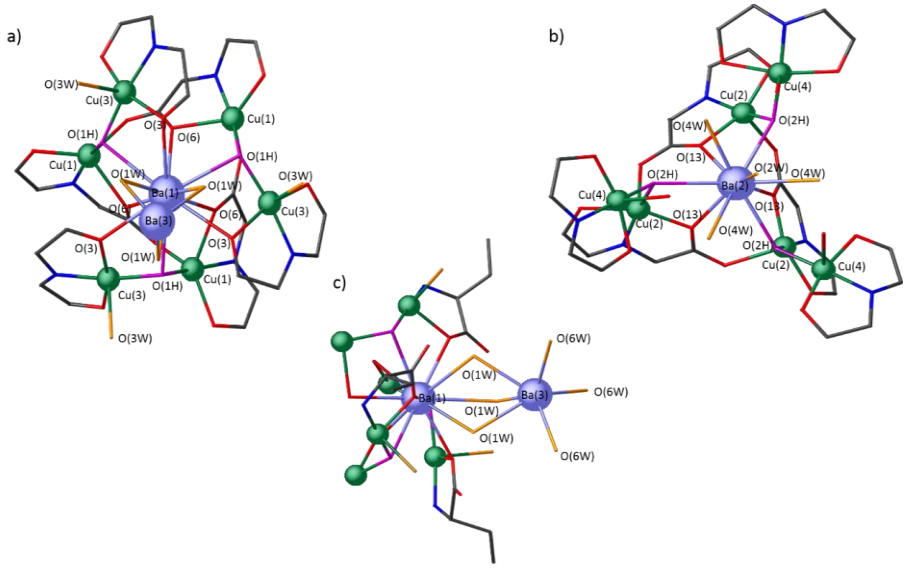

Figure 79. Views of the environment of Ba(1), Ba(2) and Ba(3) atoms in **7b^S** (arbitrary radii for the labelled atoms). (a) The Ba(1) atom is coordinate by six carboxylate-oxygen atoms [O(3) and O(6)], three hydroxo groups [O(1H)] and three water molecules [O(1W)], in a distorted bicapped pentagonal antiprismatic geometry. (b) The Ba(2) atom is coordinate by three carboxylate-oxygen atoms [O(13)], three hydroxo groups [O(2H)] and four water molecules [O(4W) and O(2W)] in a bicapped square prismatic geometry. (c) The Ba(3) atom is surrounded by three terminal [O(6W)] and three bridging O(1W) water molecules. Set of colours [green (copper), pale blue (barium), blue (nitrogen), red (oxygen), orange (oxygen from water), purple (oxygen from hydroxo group) and grey (carbon)].

The asymmetric coordination mode of the (*S*,*S*)-leumox^{4-} ligand employing only one of the two available carbonyl-oxygen atoms as donor generates an intricate framework, where each crystallographically independent barium(II) ion adopts a different coordination geometry with Ba-O bond distances varying in the range 2.740(8)-

3.030(14) Å. Their connectivities in the overall network have been represented in Figure 79. The Ba(1) atom is twelve-coordinate (BaO_{12}) in a distorted bicapped pentagonal antiprismatic geometry, made by six carboxylate-oxygen atoms, three hydroxo groups and three water molecules (Figure 79a). The Ba(2) atom is ten-coordinate (BaO_{10}) in a bicapped square prismatic geometry built by three carboxylate-oxygen atoms, three hydroxo groups and four water molecules (Figure 79b). The Ba(3) atom is only six-coordinate (BaO_6) being surrounded by six water molecules [three of them shared with Ba(2) atoms] in a highly distorted trigonal prismatic geometry (Figure 79c).

The structure of **7b^S** can be described as a 3D copper(II) network, which is built up by tetracopper(II) rings, {Cu^{II}_4[(*S*,*S*)-leumox]$_2$}, in which two neighbouring dicopper(II) units are linked through a hydroxo group acting as bridge together with a carbonyl-oxygen atom from the oxamidate ligand coordinated in a μ_3 fashion (Figure 80). Partially solvated barium(II) ions are grasped by the net to ensure electroneutrality.

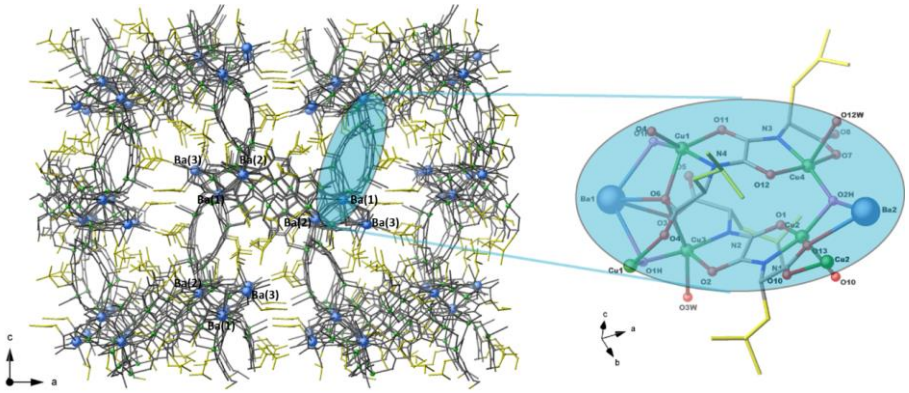

Figure 80. Perspective view of the 3D net structure of **7b^S** along the crystallographic *b* axis showing the distribution of the barium(II) ions. The inset shows a detail of the tetracopper(II) units regularly alternating in the structure.

In comparison to **5b^S** and **6b^S**, the empty volume of the channels of **7b^S** has been reduced because of the spatial orientation of the larger isobutyl residues and the carbonyl groups of the acidic part from the *trans*-(*S*,*S*)-leumox^{4-} bridging ligands even if not as much as expected (Figure 81). In fact, the estimated empty volume without the

crystallisation solvent molecules is 7997.9 Å^3, a value which represents up to *ca*. 44.9 % of the potential void per unit cell volume [V = 17825 Å^3].

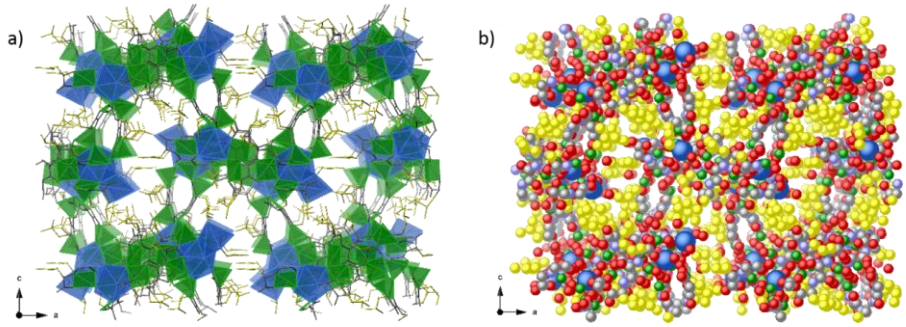

Figure 81. Perspective views of the structure of **7b^S** along the crystallographic *b* axis as (a) polyhedra and (b) space filling models exhibiting isobutyl chains buried inside the hydrophobic channels.

We have simplified the underlying nets[4–9] of **5b^S**, **6b^S** and **7b^S** to make easier the analysis of their different topologies through the computer program TOPOSPRO.[10] Moreover, their structures have been checked against the Reticular Chemistry Structural Resource (RCSR)[11] and EPINET databases.[12,13]

Thus, the network analysis of **5b^S** reveals a uninodal six-connected hexagonal **acs** net[14] made up by aligned, corner-sharing trigonal prisms (Figure 82a) with a point symbol of ($4^9{\cdot}6^6$). Despite this net is among the twenty most frequent 3D underlying nets, a search using the TOPOS database shows that there are only a few examples of **acs** nets involving alkaline-earth metal ions.[15–18] In particular, they all report structures of Mg^{2+} ions and formate as ligand exhibiting chiral space groups. Interestingly, no examples with amino acid derivative ligands are known.

The topological analysis of **6b^S** reveals the most common **pcu** network,[9,11] with a point symbol of ($4^{12}{\cdot}6^3$). Figure 82b illustrates the underlying uninodal six-connected net, obtained by applying simplification procedures. Only one example of **pcu** net containing alanine as ligand [with Pb(II) ions] has been reported,[19] whereas no examples with valine or leucine amino acids are known. Finally, the underlying net of **7b^S** is a

uninodal 3-connected one (Figure 82c) with a 10^3 point symbol featuring a **srs** ($SrSi_2$) topology according to the RCSR classification.[20] Despite it is a quite common net, only very few examples of 3D nets built up by Cu(II),[21] Ni(II)[22] and Cd(II) ions[23] and amino acid derivate ligands can be found in the literature.

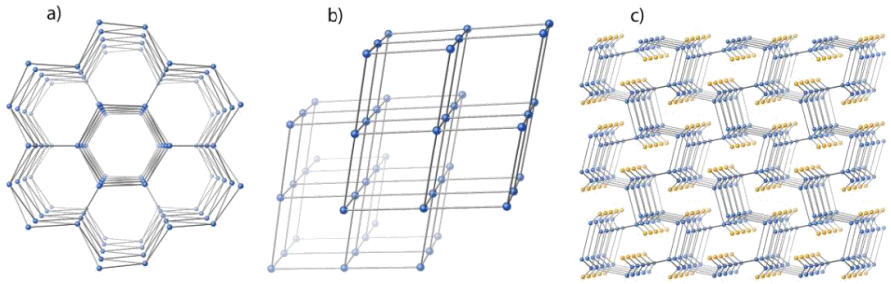

Figure 82. Schematic representation of the underlying **acs** (a) **pcu** (b) and **srs** (c) nets for **5b^S**, **6b^S** and **7b^S**, respectively. The barium(II) ions depicted in orange, not being nodes of the nets, have been represented to underline the fascinating grasping of simply solvated ions, as reported in the main text.

The unifying theme of the ligands used to build **5b^S**, **6b^S** and **7b^S** is that they contain non-reactive and flexible side chains that are ideally suited for the packing in the large structure. Furthermore, strictly speaking, the amino acids employed to prepare our ligands possessing aliphatic side chains (alanine, valine, and leucine) can be all classified as hydrophobic amino acids. Anyway, the alanine side chain being very short (a methyl group), is not particularly hydrophobic. In our opinion, this must be at the origin of the porous structure of compound **5b^S** where either many water molecules or methyl group share the same channels. In contrast, the more hydrophobic valine side chain rules the self-assembly in **6b^S** in order to confine solvent and isopropyl groups in diverse pores. Leucine residues being hydrophobic, longer and so more hindered than others, prefers (as the valine ones) to be buried in the hydrophobic cores of the network implying thus larger space to reach the more stable folding. In this situation, even expected metal ions bound by a bis(amino acid)oxalamide ligand may be affected and driven toward the more kinetically stable compound. In fact, side-chain packing may also be important to the kinetics of folding.

1.B.3.2. Calcium(II)-derived PCPs

Following the synthetic route described in detail in the Annex I, polycrystalline powder samples as well as single crystals of $\{Ca^{II}Cu^{II}_6[(S,S)\text{-alamox}]_3(OH)_2(H_2O) \cdot 32H_2O\}_n$ (**5c^S**), $\{Ca^{II}Cu^{II}_6[(S,S)\text{-valmox}]_3(OH)_2(H_2O) \cdot 13H_2O\}_n$ (**6c^S**) and $\{Ca^{II}Cu^{II}_6[(S,S)\text{-leumox}]_3(OH)_2(H_2O) \cdot 11H_2O\}_n$ (**7c^S**) were obtained (Scheme 14). In addition, in order to further confirm the validity of this chiral strategy, the corresponding MOF prepared from the other enantiomer of the alamox ligand $[(R,R)\text{-alamox}]^{4-}$ was also prepared and named $\{Ca^{II}Cu^{II}_6[(R,R)\text{-alamox}]_3(OH)_2(H_2O) \cdot 33H_2O\}_n$ (**5c^R**). This novel family of chiral PCPs arises as the perfect playground to study how the charge density of the channels can be tuned by increasing the length of the alkyl residue of the amino acid the, affording thus with different adsorption properties for all the four compounds. For further crystallographic details of **5c^S**, **5c^R**, **6c^S** and **7c^S** see Tables 24 and 25 in the Annex I.

The structures of **5c^S**, **5c^R**, **6c^S** and **7c^S** could be determined by X-ray diffraction on single crystals. The four compounds were found to be isostructural with the previously described $Ba^{II}Cu^{II}_6$ PCP (**5b^S**). They crystallise in the same chiral $P6_3$ space group of the hexagonal system. Their structures consist of chiral 3D calcium(II)-copper(II) networks which are built up by the corresponding *trans*-oxamidato-bridged dicopper(II) units $[\{Cu^{II}_2L(OH)_2\}$ with L = (*S*,*S*)-alamox^{4-}, (*R*,*R*)-alamox^{4-} , (*S*,*S*)-valmox^{4-} and (*S*,*S*)-leumox^{4-}], acting as linkers between the calcium(II) ions through their carboxylate groups. Three bridging aqua/hydroxo molecules (1:2 statistical distribution) acting as additional bridges between two neighbouring dicopper(II) units and a calcium(II) ion in a μ_3 fashion, support the entire system, unfolding an uninodal six-connected net topology with $(4^9 \cdot 6^6)$ Schläfli symbol (see Figure 83).

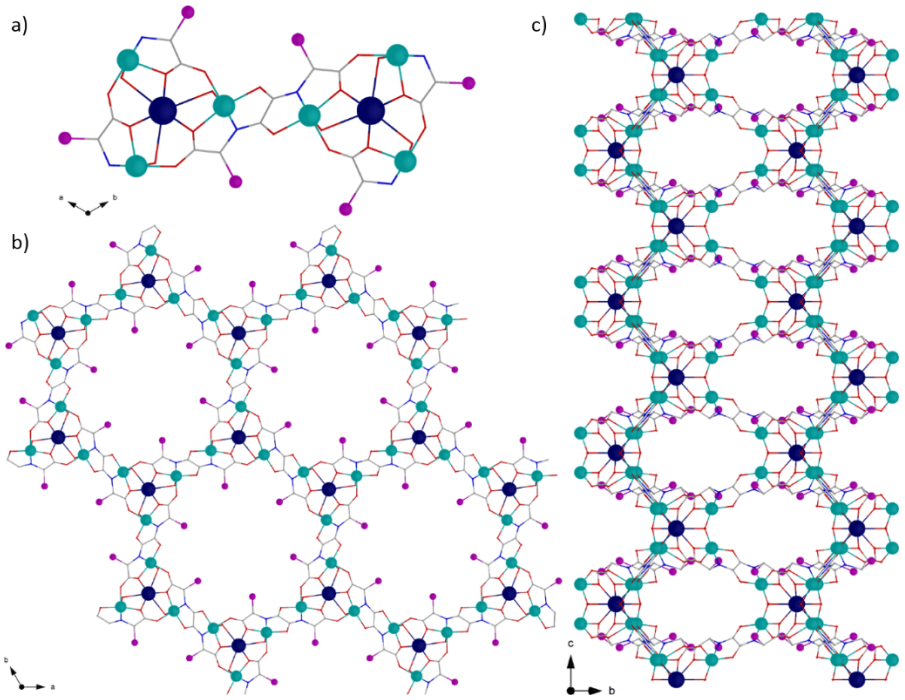

Figure 83. (a) Common dicopper(II) building blocks in **5c^S**, **5c^R**, **6c^S** and **7c^S**. Views of the fragments of the structures of **5c^S**, **5c^R**, **6c^S** and **7c^S** in the crystallographic *ab* (b) and *bc* (c) planes, respectively. Copper(II) and calcium(II) ions are represented by green and dark blue spheres respectively, whereas the carbon, oxygen and nitrogen atoms from the ligand are shown as grey, red and pale blue sticks. The purple spheres represent the methyl (**5c^S** and **5c^R**), isopropyl (**6c^S**) and isobutyl (**7c^S**) amino acid residues.

The two crystallographic independent copper(II) ions [Cu(1) and Cu(2)] are five-coordinate ($CuNO_3O_{OH}$) exhibiting a somewhat distorted square pyramidal geometry (Figure 84a). The basal plane is formed by one amidate-nitrogen, one carbonyl-oxygen atom, one carboxylate-oxygen and one hydroxo group, whilst one carboxylate-oxygen from a neighbouring dicopper(II) unit occupy the apical positions (Figure 84). [Average values of Cu-N = 1.920(6), Cu-O_{eq} = 2.025(4), Cu-O_{ax} = 2.297(5), Cu-O_{OH} = 1.911(5) Å (**5c^S**), Cu-N = 1.929(4), Cu-O_{eq} = 2.036(3), Cu-O_{ax} = 2.300(3), Cu-O_{OH} = 1.922(4) Å (**5c^R**), Cu-N = 1.915(4), Cu-O_{eq} = 2.005(3), Cu-O_{ax} = 2.285(3), Cu-O_{OH} = 1.930(3) Å (**6c^S**) and Cu-N = 1.880(16), Cu-O_{eq} = 1.998(12), Cu-O_{ax} = 2.280(14), Cu-O_{OH} = 1.922(13) Å (**7c^S**)]; (further information about interbond bite angles is gathered in Table 40, annex I). Each

calcium(II) ion [Ca(1)] is nine-coordinate in a distorted monocapped square antriprismatic geometry (CaO_9) built by six carboxylate-oxygen atoms from six oxamidato groups and three hydroxo groups (Figure 84b) [average distances Ca-O = 2.497(5) and Ca-O_{OH} = 2.633(3) Å (**5c^S**), Ca-O = 2.501(4) and Ca-O_{OH} = 2.649(2) Å (**5c^R**), Ca-O = 2.495(3) and Ca-O_{OH} = 2.600(12) Å (**6c^S**), and Ca-O = 2.470(13) and Ca-O_{OH} = 2.631(6) Å (**7c^S**)].

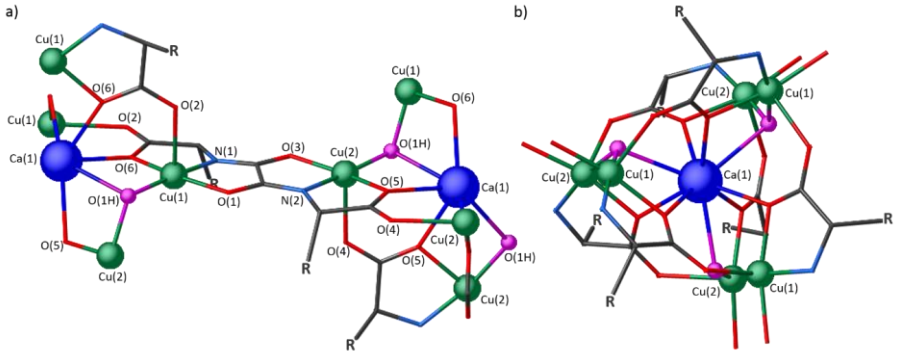

Figure 84. (a) Detail of the coordination mode and environment of the Cu(1) and Cu(2) atoms in **5c^S**, **5c^R**, **6c^S** and **7c^S** with the numbering of the non-carbon atoms. Noteworthy, the hydroxo groups [O(1H)] act as supplementary bridges between two neighbouring dicopper(II) units and a calcium(II) ion coordinating in a μ_3 fashion. (b) View of the environment and details of the coordination of the calcium(II) ion in **5c^S**, **5c^R**, **6c^S** and **7c^S**. (a) The Ca(1) atom is coordinate to six carboxylate-oxygen atoms [O(5) and O(6)] and three hydroxo groups [O(1H)] in a monocapped square antriprismatic geometry. Calcium(II) and copper(II) ions are depicted as dark blue and green spheres with arbitrary radii, respectively. The carbon, nitrogen and oxygen atoms from the ligands are depicted as grey, pale blue and red sticks. The oxygen atoms from the hydroxo group have been highlighted as purple spheres.

Overall, the 3D $Ca^{II}Cu^{II}_6$ networks of **5c^S**, **5c^R**, **6c^S** and **7c^S** exhibit a honeycomb-like hexagonal architecture, giving rise to relatively large hexagonal channels along the crystallographic *c* axis (Figure 85). The calcium(II) ions occupy the vertices of each hexagonal channel, the adjacent Ca···Ca distance constituting the edge of each hexagonal ring being 12.187(1), 12.251(1), 12.122(4) and 12.076(4) Å for **5c^S**, **5c^R**, **6c^S** and **7c^S**, respectively. In turn, the dicopper(II) oxamidato units are located along the edges of the channels.

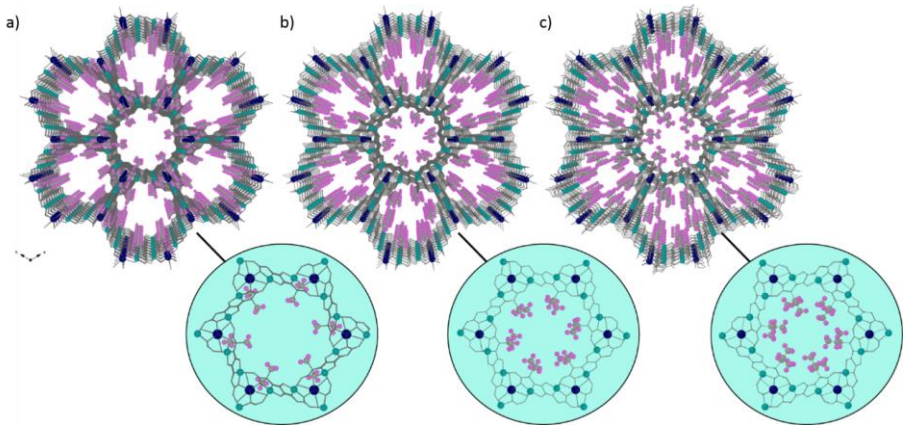

Figure 85. Perspective views along the crystallographic *c* axis of the porous structures of **5c^{S}** (a) **6c^{S}** (b) and **7c^{S}** (c) emphasising the different alkyl groups in the boxed structures. Copper(II) and calcium(II) ions are represented by cyan and dark blue spheres, respectively. The alkyl residues of the amino acids are shown as balls and sticks whereas the remaining carbon, nitrogen and oxygen atoms from the ligand are represented as sticks. The water molecules of crystallisation are omitted for clarity.

The most striking structural feature of this series of isoreticular compounds arises from the orientation of the amino acid residues pointing inwards the hexagonal channels and the interstitial voids (Figures 85 and 87). As observed for the two methyl groups in **5c^{S}** and **5c^{R}**, the two isopropyl chains from the ligands in **6c^{S}** show a medium to regular distended conformation, pointing inwards the pores. In contrast, only one of the two isobutyl residues exhibits a distended conformation inwards the pores in **7c^{S}**. The isobutyl residues of leucine, being more hydrophobic and longer and so more hindered than the ones from the other amino acids, most likely prefer to be buried in large space to reach the more stable folding, forcing one of the flexible isobutyl chains to adopt a highly bent conformation with their methyl groups pointing outward the pores (Figure 86c). The great framework flexibility specially shown by **6c^{S}** and **7c^{S}**, due to the presence of the longer isopropyl and isobutyl amino acid side chains respectively, will further influence the diffusion of gases through the pores. Therefore, this must be one of the factors to take into account when aiming at achieving a fine control on the selectivity and separation of gases.

In particular, the high thermal motion of the carbon atoms belonging to the leucine amino acid residues in **7c^{S}**, revealed by its X-ray structure, let us to suppose a further optimization of the more stable side chains conformation, thus enhancing efficient host-guest interactions or allowing also opportunistic hopping of these gases along the pores.

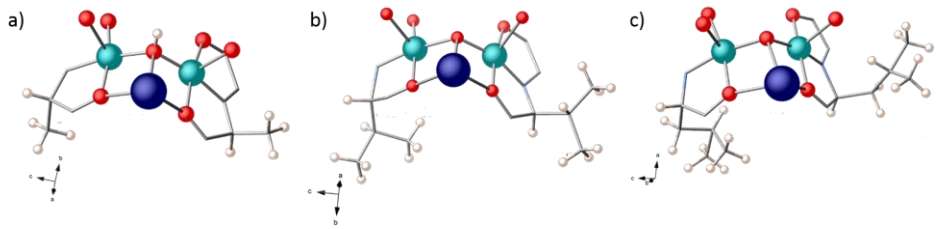

Figure 86. Asymmetric units without solvent molecules of (a) **5c^{S}** and **5c^{R}**, (b) **6c^{S}** and (c) **7c^{S}** featuring highly flexible side chains of the amino acids, which show different conformations of the hydrophobic methyl (**5c^{S}** and **5c^{R}**), isopropyl (**6c^{S}**) and isobutyl (**7c^{S}**) groups depending on the steric hindrance. [Colour code: calcium(II), dark blue; copper(II), green; oxygen, red; nitrogen, pale blue; hydrogen, white; carbon atoms, grey sticks].

Because of the different size of the hydrophobic methyl (**5c^{S}** and **5c^{R}**), isopropyl (**6c^{S}**) and isobutyl (**7c^{S}**) groups, the resulting channels possess varying virtual diameters of *ca.* 1.0 (**5c^{S}** and **5c^{R}**), 0.8 (**6c^{S}**) and 0.6 (**7c^{S}**) nm, respectively (Figure 87). The increasing degree of hydrophobicity together with the decreasing size of the pores account for the contents of free water molecules [32 (**5c^{S}**), 33 (**5c^{R}**), 13 (**6c^{S}**) and 11 (**7c^{S}**)] (see Figure 88). This increasing charge density at the channels from **5c^{S}** to **7c^{S}** also suggest a different functionality of the channels and will be further reflected in their gas adsorption properties. Finally, the estimated empty volumes for **5c^{S}**, **5c^{R}**, **6c^{S}** and **7c^{S}** without the water molecules of crystallisation are 2089.1 (**5c^{S}**), 2140.8 (**5c^{R}**), 1532.6 (**6c^{S}**) and 1312.0 (**7c^{S}**) Å^{3}. These values represent *ca*. 58.0, 58.4, 43.4 and 37.5 % respectively, of the potential void per unit cell volume [V = 3604.1(5) (**5c^{S}**), 3665.5(5) (**5c^{R}**), 3529.7(11) (**6c^{S}**) and 3501(3) (**7c^{S}**) Å^{3}] (Figure 87).

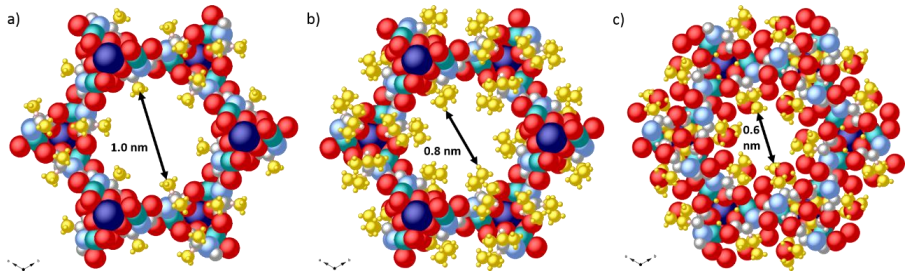

Figure 87. View along the crystallographic *c* axis of the hexagonal pores of (a) **5c^S**, (b) **6c^S** and (c) **7c^S** using a space filling mode (Van der Waals radii). The calcium(II) and copper(II) ions are shown as dark blue and green spheres whilst the oxygen, nitrogen, hydrogen and carbon atoms are depicted as red, pale blue, white and grey spheres. The aliphatic groups of the amino acid residues are highlighted in yellow.

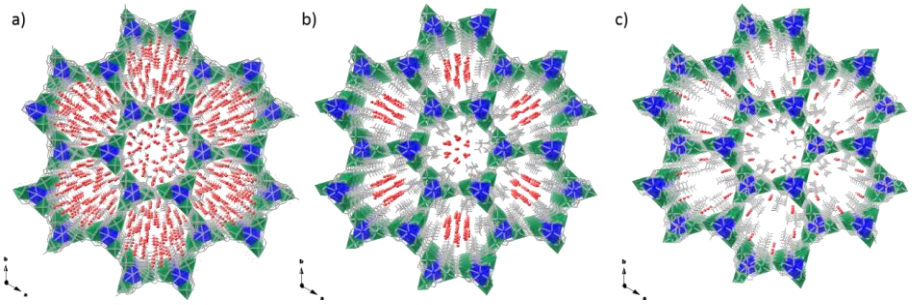

Figure 88. View of the porous structures of (a) **5c^S**, (b) **6c^S** and (c) **7c^S** along the crystallographic *c* axis showing the different contents of water molecules of crystallisation inside the pores (red spheres). Calcium(II) and copper(II) ions are depicted as blue and green polyhedra, respectively.

1.B.3.3. Lanthanide(III)-derived PCPs

Aiming at introducing also interesting magnetic properties to these families of PCPs, we reacted the precursor complex $(Me_4N)_2\{Cu^{II}_2[(S,S)\text{-alamox}](OH)_2\} \cdot 6H_2O$ (**5a^S**) towards the highly anisotropic Dy(III) and Tb(III) ions. Thus, by following the synthetic route detailed in the Annex I, two novel PCPs named $\{Dy^{III}Cu^{II}_6[(S,S)\text{-alamox}]_3(OH)_3 \cdot 21H_2O\}_n$ (**5d^S**) and $\{Tb^{III}Cu^{II}_6[(S,S)\text{-alamox}]_3(OH)_3 \cdot 21H_2O\}_n$ (**5e^S**) were obtained in the form of polycrystalline powder samples. The use of paramagnetic lanthanide(III) ions as nodes instead of diamagnetic alkaline-earth cations provides a new family of multifunctional PCPs which arises as the perfect playground to study how the magnetic

behaviour of the lanthanide(III) ions can be influenced by their confinement inside the framework.

Although highly pure polycrystalline samples of **5d^S** and **5e^S** could be synthesised, only single crystals of **5e^S** were obtained, allowing its structural determination by X-ray diffraction. **5e^S** was found to be isostructural with the previously described $Ba^{II}Cu^{II}_6$ PCP (**5b^S**), and the calcium(II)-derived PCPs family (**5c^S**, **5c^R**, **6c^S** and **7c^S**). Moreover, **5d^S** is also isostructural with all the aforementioned PCPs as revealed by the PXRD measurements. For further crystallographic details of **5e^S** see Table 26 in the Annex I.

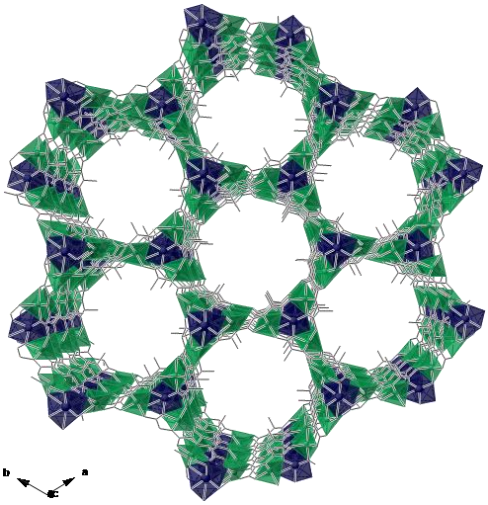

Figure 89. Perspective view along the crystallographic *c* axis of the porous structure of **5e^S**. Copper(II) and terbium(III) ions are represented by green and dark blue polyhedra, respectively. The ligand backbones are shown as sticks. The water molecules of crystallisation are omitted for clarity.

5e^S crystallises in the chiral $P6_3$ space group of the hexagonal system. Its structure consists of a chiral terbium(III)-copper(II) 3D network built up from the *trans*-oxamidato-bridged dicopper(II) units [{$Cu^{II}_2L(OH)_2$}, with L = (*S*,*S*)-alamox^{4-}, acting as linkers between the terbium(III) ions through their carboxylate groups. Three bridging hydroxo molecules acting as additional bridges between two neighbouring dicopper(II) units and a lanthanide(III) ion in a μ_3 fashion, support the entire system, unfolding an uninodal six-connected net topology with ($4^9 \cdot 6^6$) Schläfli symbol (see Figures 89 and 90).

The environments of the two crystallographic independent copper(II) ions in **5e^S** [Cu(1) and Cu(2)] is the same than the one exhibited by **5b^S** and **5c^S**. They are five-coordinate ($CuNO_3O_{OH}$) in a somewhat distorted square pyramidal geometry (Figure

90a). Again, the basal plane is formed by one amidate-nitrogen, a carbonyl-oxygen atom, one carboxylate-oxygen and a hydroxo group which acts as a μ_3 bridge linking one terbium(II) and two copper(II) ions. The apical position at each copper(II) ion is occupied by one carboxylate-oxygen from a neighbouring dicopper(II) unit (Figure 90a) [average bond lengths are: Cu-N = 1.905(19), Cu-O_{eq} = 2.027(17), Cu-O_{ax} = 2.303(18) and Cu-O_{OH} = 1.937(19) Å]; (the interbond bite angles are gathered in Table 41, Annex I). The terbium(III) ions are nine-coordinate in a distorted monocapped square antriprismatic geometry (TbO_9) which is defined by six carboxylate-oxygen atoms from six oxamidate groups and three hydroxo groups (Figure 90b,c) [average Tb-O and Tb-OH bond distances are 2.442(17) and 2.523(6) Å, respectively].

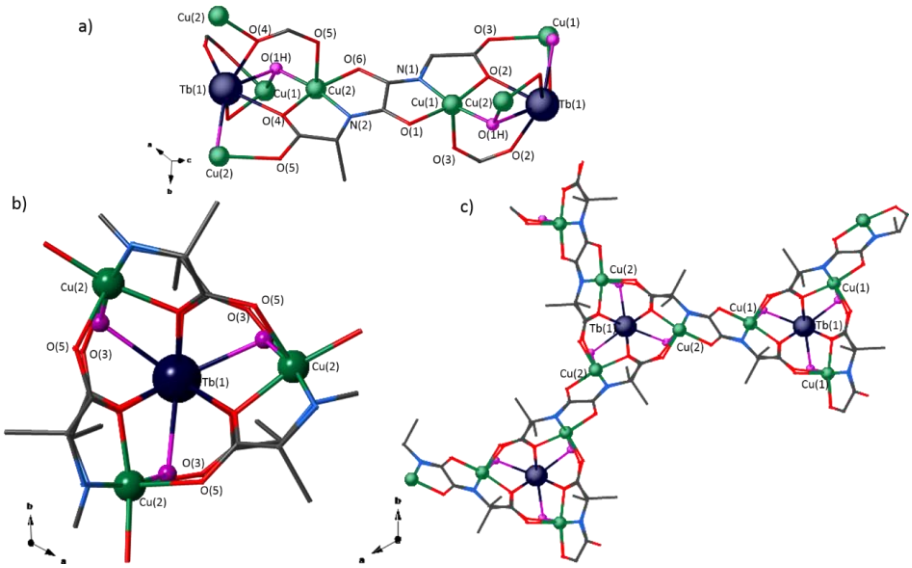

Figure 90. Detail of the environment of (a) the two copper(II) ions [Cu(1) and Cu(2)] and (b) the barium(II) ions in **5e^S**. (c) View of a fragment of the structure of **5e^S** for a better understanding of the connectivities. Terbium(III) and copper(II) ions are depicted as dark blue and green spheres of arbitrary radi, respectively. The carbon, nitrogen and oxygen atoms of the ligands are depicted as grey, pale blue and red sticks. The oxygen atoms from the hydroxo group are highlighted as purple spheres.

Overall, the 3D $Tb^{II}Cu^{II}_6$ network of **5e^S** exhibits a honeycomb-like hexagonal architecture, giving rise to relatively large hexagonal channels along the crystallographic

c axis of *ca*. 1 nm of virtual diameter (Figure 89) which are occupied by water molecules of crystallisation. The terbium(II) ions occupy the vertices of each hexagonal channel, the edge of each hexagonal ring corresponding to the adjacent Tb···Tb distance and being of 12.15 Å. In turn, the dicopper(II) oxamidate units are arranged along the edges of the channels. The estimated empty volume for **5e^{S}** without the water molecules of crystallisation is 2140.8 Å^3, a value which represents *ca*. 58.4 % of the potential void per unit cell volume [*V* = 3563.5(7) Å].

1.B.4. Physical Properties and Applications

1.B.4.1. Optical properties

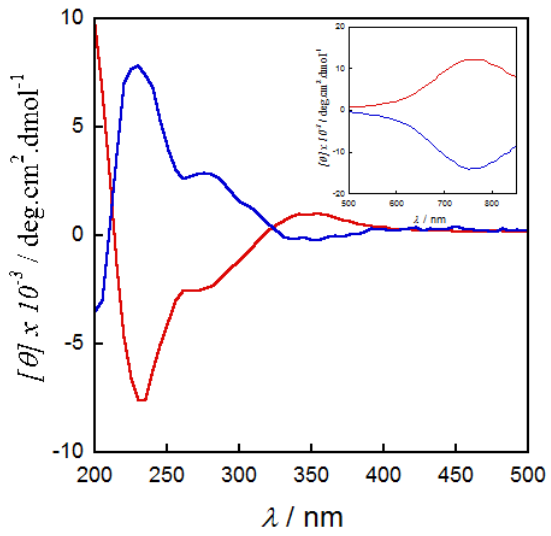

Figure 91. CD spectra of aqueous solutions of **5a^{S}** (red) and **5a^{R}** (blue) (10^{-3} mol L^{-1}) in the 200-500 nm region. The inset shows the CD spectra in the visible region (10^{-4} mol L^{-1}).

Circular dichroism (CD) spectra were collected to check the enantiopurity of the copper(II) complexes derived from (*S*,*S*)- and (*R*,*R*)-alamox^{4-} ligands, $(Me_4N)_2\{Cu^{II}_2[(S,S)\text{-alamox}](OH)_2\} \cdot 6H_2O$ (**5a^{S}**) and $(Me_4N)_2\{Cu^{II}_2[(R,R)\text{-alamox}](OH)_2\} \cdot 6H_2O$ (**5a^{R}**) (see Figure 91). The CD solution spectra of **5a^{S}** and **5a^{R}** in aqueous solution are almost mirror images. In fact, they exhibit maximum positive and negative Cotton effects at the same location and with almost identical intensities. The intense UV bands centred at 225 and 275 nm for **5a^{S}** and **5a^{R}** can be assigned to intraligand (IL) and metal-to-ligand (ML) charge-transfer transitions,

respectively. The visible band at 750 nm for **5a^S** and **5a^R**, corresponds to the typical d-d transition of the copper(II) ions (see inset of Figure 91). The positive and negative Cotton effects of this visible band obey to the induction of chirality at the metal centres by the enantiopure coordinated amino acid derived ligands and, ultimately, confirms the validity of the synthetic strategy.

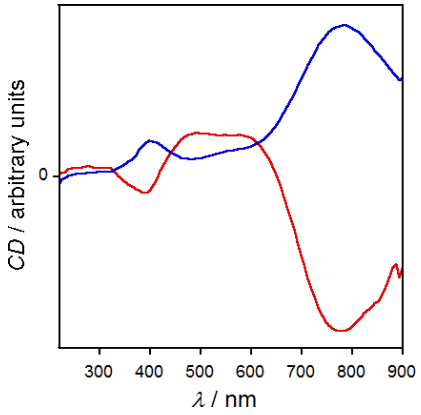

Figure 92. CD spectrum of **5c^S** and **5c^R** as KBr pellets (1 mg MOF in 100 mg of KBr).

Finally, solid CD spectra were also collected for the PCPs **5c^S** and **5c^R** to confirm that this enantiopure character is maintained in the final high-dimensional compounds. Even if the quality of the solid CD measurements is not as good as those in solution, Figure 92 clearly shows that the spectra of **5c^S** and **5c^R** are almost mirror images. They exhibit maximum positive and negative Cotton effects at practically the same location. The bands centred at 380 nm are due to intraligand (IL) and/or metal-to-ligand (ML) charge-transfer transitions. Again, the positive and negative Cotton effects observed in the visible region are attributed to d-d transitions of the copper(II) ions and they are due to the induction of chirality on the metal centres by the enantiopure ligands.

1.B.4.2. Gas sorption properties

Among all the oxamidato-derived PCPs that have been obtained, the isoreticular calcium-based subfamily (**5c^S**, **6c^S** and **7c^S**) represents an outstanding platform for the study of their gas sorption and separation properties. The reasons are two-fold: (i) they are isostructural frameworks exhibiting different size and functionality of their pores depending on the amino acid residue and (ii) they show high stability upon solvent removal. As mentioned before, the difference between these isostructural PCPs relies on the length of the alkyl substituents from the metalloligand, which are pointing inwards the hexagonal channels. Hence, by increasing the length of the aliphatic residue and consequently reducing the pore size, the functionality and the charge density of the channels can be tuned leading to different sorption and separation capacities.

The strategy based on the enhancement of the sorption performance of the PCPs (uptake and selectivity) by subtle modifications of both the pore size and shape has given interesting results so far.[24–28] Moreover, the purification of methane has attracted an intense research activity due to its fundamental importance from industrial and ecological viewpoints.[29] Therefore, we decided to use our series of copper(II)-calcium(II) PCPs to achieve a fine control on the selectivity and separation of methane towards other light hydrocarbons present in natural gas.

In principle, the pore-limiting diameters from the crystal structures of **5c^S**, **6c^S** and **7c^S** of *ca*. 10, 8 and 6 Å respectively, are large enough to allow the diffusion of different light hydrocarbons such as methane (CH_4), ethane (C_2H_6), ethylene (C_2H_4), propane (C_3H_8), propylene (C_3H_6) and butane (*n*-C_4H_{10}), which have related estimated kinetic diameters increasing from 3.8 Å for CH_4 up to 4.3 Å for *n*-C_4H_{10}.[30]

Firstly, aiming at proving the permanent porosity of **5c^S**, **6c^S** and **7c^S**, we measured nitrogen adsorption isotherms at 77 K. Noteworthy, prior to the sorption measurements, all samples were activated by immersion in methanol and then desolvated at 80 °C under reduced pressure for 24 h. The N_2 adsorption plots for **5c^S**, **6c^S** and **7c^S** (bearing methyl, isopropyl and isobutyl amino acid residues, respectively) show

fully reversible type I isotherms, characteristic of microporous materials with permanent porosity, with estimated[31] BET surface areas [1015 (**5c^S**), 561 (**6c^S**) and 312 $m^2\ g^{-1}$ (**7c^S**)] following the trend **5c^S** > **6c^S** > **7c^S**, as expected from their decreasing pore size (Figure 93a).

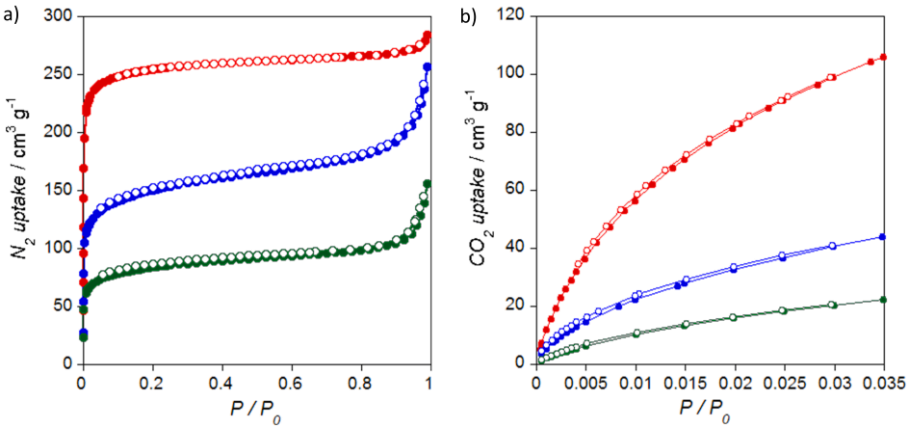

Figure 93. (a) N_2 and (b) CO_2 adsorption isotherms measured at 77 and 273 K respectively for the activated compounds **5c^S** (red), **6c^S** (blue) and **7c^S** (green). Filled and empty circles indicate the adsorption and desorption isotherms, respectively.

The CO_2 adsorption isotherms measured at 1 bar and 273 K followed the same behaviour (Figure 93b), showing a decrease of the gas uptake [106.0 (**5c^S**), 44.1 (**6c^S**) and 22.3 $cm^3\ g^{-1}$ (**7c^S**)] with the increase of the length of the amino acid residue.

Once demonstrated the permanent microporosity of **5c^S**, **6c^S** and **7c^S** as well as their different pore windows depending on the amino acid residue filling the cavities, we investigated the performance of this family in the adsorption of different light hydrocarbons such as methane (CH_4), ethane (C_2H_6), ethylene (C_2H_4), propane (C_3H_8), propylene (C_3H_6) and butane (*n*-C_4H_{10}). In so doing, single-component adsorption measurements of the different gases as well as breakthrough experiments of binary CH_4/C_2H_6 and CH_4/C_3H_8 mixtures were carried out.

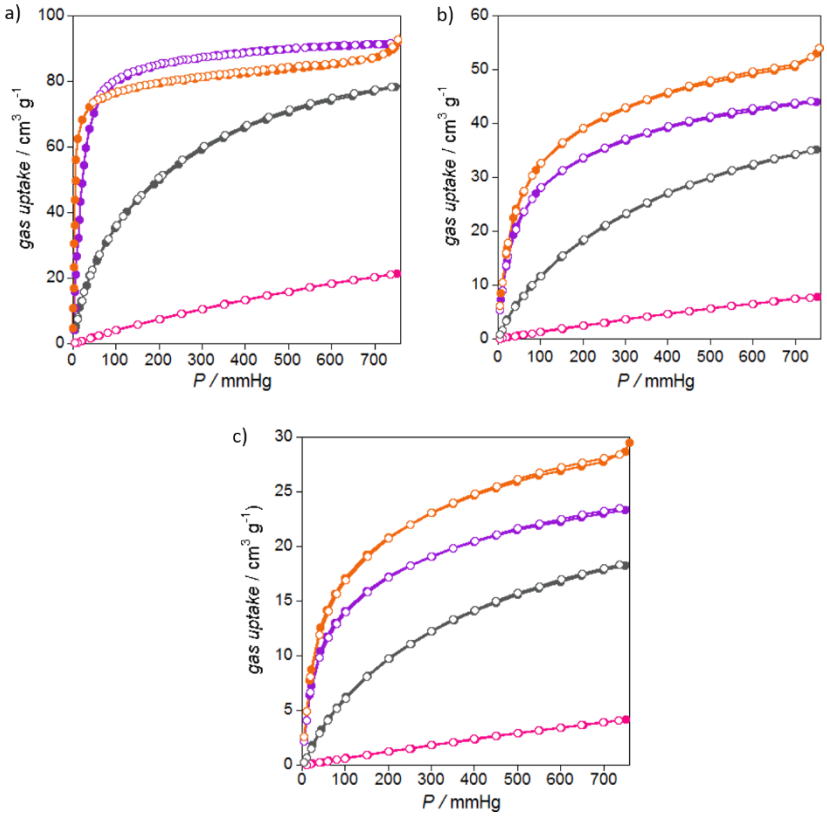

Figure 94. CH_4 (pink), C_2H_6 (grey), C_3H_8 (purple) and *n*-C_4H_{10} (orange) adsorption isotherms for **5c^S** (a), **6c^S** (b), and **7c^S** (c) at 273 K. Filled and empty circles indicate the adsorption and desorption isotherms, respectively.

Adsorption isotherms of light paraffins, CH_4, C_2H_6, C_3H_8 and *n*-C_4H_{10} were firstly measured for **5c^S**, **6c^S** and **7c^S** at 1 bar and 273 K (Figure 94). The adsorption capacities follow the same overall trend for all the three compounds. Hence, the uptake increases with the length of the carbon chain of the paraffin, following the sequence $CH_4 << C_2H_6 < C_3H_8 <$ *n*-C_4H_{10}, as a result of the enhancement of the interactions with the side chain of the MOF. However, the slightly higher C_3H_8 uptake compared to the *n*-C_4H_{10} one observed for compound **5c^S** remains an exception. This could be likely due to the bigger kinetic diameter of the *n*-C_4H_{10} molecules respect to the C_3H_8 ones together with less efficient interactions between the methyl groups of the walls of **5c^S** and the alkyl chains of the gas.

In addition, the slope in the C_2H_6, C_3H_8 and *n*-C_4H_{10} adsorption isotherms (in particular the two last ones) becomes much steeper (Figure 94), clearly indicating a stronger affinity between the larger hydrocarbons and the pore surface of **5c^S**, **6c^S** and **7c^S**. Interestingly, the C_2H_6/CH_4 and C_3H_8/CH_4 adsorption ratios (Figure 94), follow the sequence **5c^S** (3.69 and 4.29) < **6c^S** (4.45 and 5.57) < **7c^S** (4.51 and 5.64), suggesting that the larger the alkyl group decorating the MOF (**5c^S** < **6c^S** < **7c^S**), the larger is the separation equilibrium between methane and the other hydrocarbon in the binary mixture.

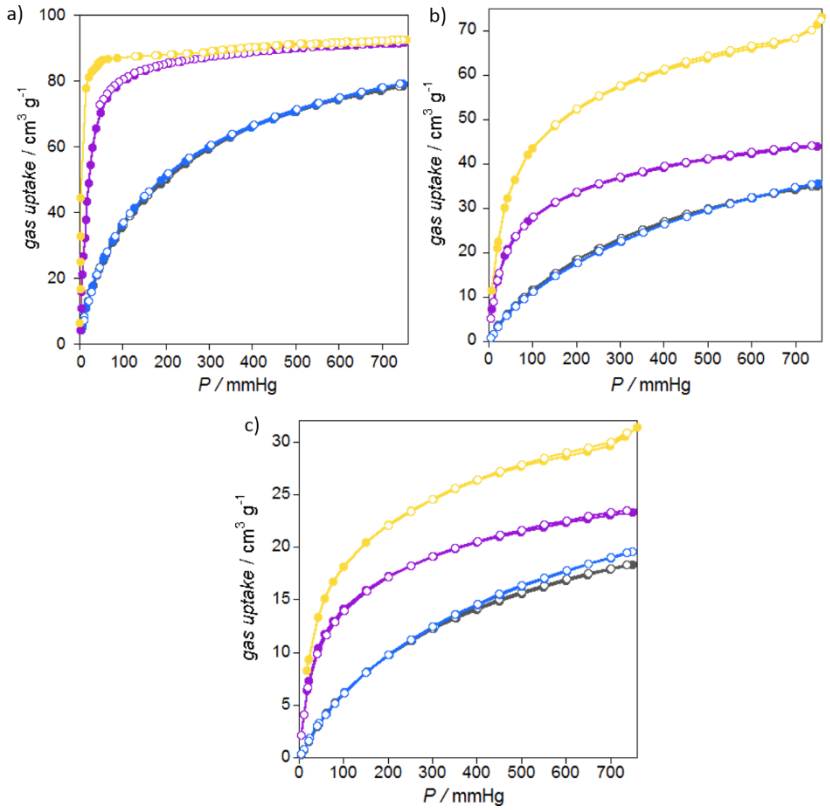

Figure 95. C_2H_6 (grey), C_2H_4 (blue), C_3H_8 (purple) and C_3H_6 (yellow) adsorption isotherms for **5c^S** (a), **6c^S** (b), and **7c^S** (c) at 273 K. Filled and empty circles indicate the adsorption and desorption isotherms, respectively.

The adsorption capabilities of **5c^S**, **6c^S** and **7c^S** for the olefins C_2H_4 and C_3H_6 were also evaluated and are shown in Figure 95 together with the ones of the paraffins. The C_2H_4 adsorption isotherms for all three compounds are identical to the C_2H_6 ones. In turn, the amounts of C_3H_6 adsorbed by **5c^S**, **6c^S** and **7c^S** are significantly higher than those observed in the case of C_3H_8, which may be due to the stronger interaction of the π-bonding orbital of C_3H_6 with the open metal sites and to its smaller kinetic diameter.[32]

In view of the results shown in Figure 94 and aiming at further confirming the effect of the increasing size of the alkyl chains for this new family of isoreticular MOFs on the adsorptive properties, kinetics adsorption of CH_4, C_2H_6, C_3H_8 and *n*-C_4H_{10} were performed (Figure 96), which assess how fast hydrocarbons are adsorbed. A non-negligible impact on the kinetics adsorption was observed for the different adsorbates as one moves from **5c^S** to **7c^S**.

The adsorbed amount of *n*-C_4H_{10} with respect to C_3H_8 changes from being almost equal for **5c^S**, to be significantly higher in **6c^S**, as a consequence of the higher number of aliphatic carbons which are able to interact with *n*-C_4H_{10}. However, these amounts tend to be similar in the case of **7c^S**, due to the bigger size of *n*-C_4H_{10} respect to C_3H_8 and to the smaller pore size of the MOF, factors which hinder the gas uptake. Noteworthy, the adsorbed amount of C_2H_6 with respect to CH_4 shows a considerable increase as one moves in the series **5c^S** - **7c^S**. Thus, the larger the alkyl side chain in the surface of the pores (**5c^S** < **6c^S** < **7c^S**), the lower is the amount of CH_4 adsorbed by the MOF. This is especially relevant for **7c^S**, where the CH_4 is hardly adsorbed. These results further confirm the trend observed in the single-component isotherms (Figure 94) and even suggest higher mixture selectivities.

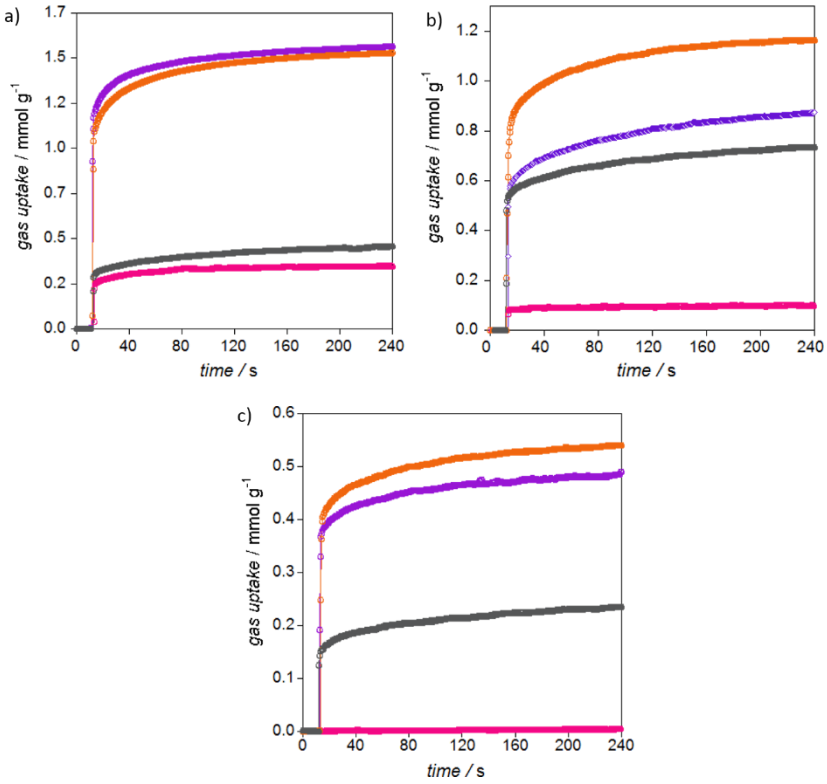

Figure 96. Adsorption kinetic profiles of CH_4 (pink), C_2H_6 (grey), C_3H_8 (purple) and C_4H_{10} (orange) for **5c^S** (a), **6c^S** (b) and **7c^S** (c) at 273 K.

Finally, since the adsorption isotherm measurements collected in Figure 95 also showed a certain selectivity for C_3H_6 *vs*. C_3H_8, the kinetic adsorption of C_3H_6 was also evaluated and compared with that of C_3H_8 (Figure 97). However, even if Figure 95 shows a higher adsorption of C_3H_6 respect to C_3H_8 (especially for compound **6c^S**), this small selectivity is not reflected in the kinetic experiments and does not allow to predict a successful separation. This is why breakthrough experiments have not been carried out for these gases.

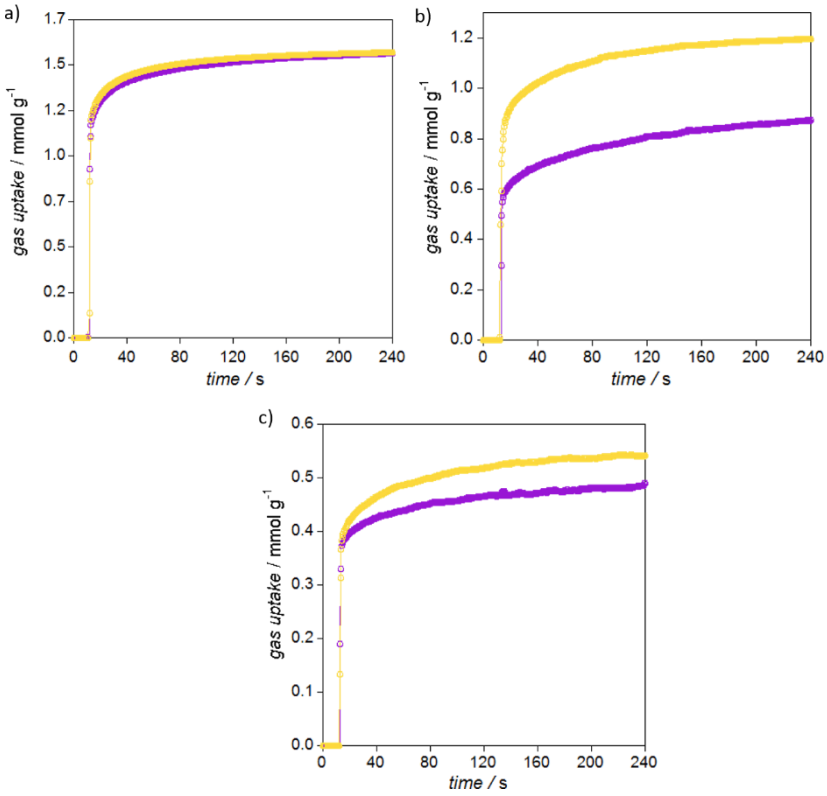

Figure 97. Adsorption kinetic profiles of C_3H_8 (purple) and C_3H_6 (yellow) for **5c^S** (a), **6c^S** (b) and **7c^S** (c) at 273 K.

In the light of the results shown above and aiming at investigating the practical separation performance of this subfamily of PCPs, breakthrough experiments were carried out at 298 K and 1 bar for binary mixtures of CH_4/C_2H_6 (75:25, v/v) and CH_4/C_3H_8 (75:25 v/v). For this purpose, packed columns (*ca*. 1 g) of **5c^S** and **7c^S** as stationary phases and a total gas flow of 1 $cm^3\ min^{-1}$ were used (Figure 98).

H_2, being the reference gas which is not adsorbed under these conditions,[33] breaks at the same time as CH_4 for the sample **7c^S** (Figure 98a, bottom), indicating an almost negligible CH_4 uptake on this material. On the other side, C_2H_6 (Figure 98a, bottom) and C_3H_8 (Figure 98b, bottom) break much later, suggesting an almost infinite selectivity for the C_2H_6/CH_4 and C_3H_8/CH_4 separations. In contrast,

CH_4 breaks later than H_2 for **5c^S**, (Figure 98a, top), suggesting some CH_4 adsorption and thus, pointing towards a reduction of the selectivity for separating C_2H_6/CH_4 and C_3H_8/CH_4 mixtures when using this material.

Therefore, as expected from the kinetic measurements, better separations of CH_4 from C_3H_8 and C_2H_6 were observed for **7c^S**. Overall, when using **5c^S** as stationary phase, the CH_4 was absorbed for a short time in the packed column bed (*ca*. 5 min) whereas C_2H_6 and C_3H_8 were retained for *ca*. 54 and 198 min, respectively. In turn, when working with **7c^S**, no adsorption of CH_4 was detected and C_2H_6 and C_3H_8 were retained for *ca*. 71 and 246 min, respectively.

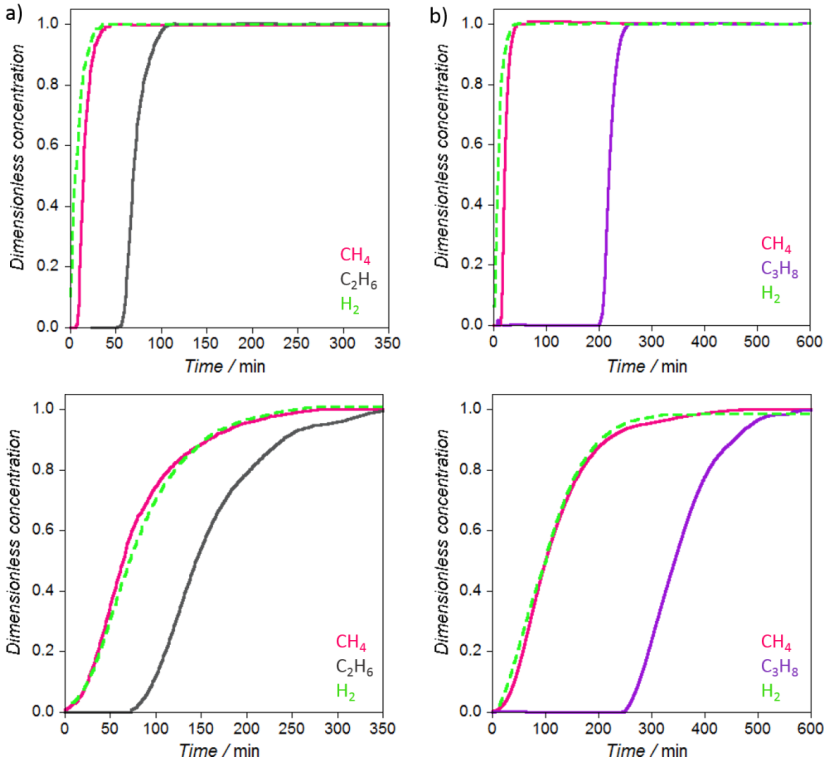

Figure 98. Experimental column breakthrough curves for (a) CH_4/C_2H_6 (75:25, v/v) and CH_4/C_3H_8 (75:25 v/v) gas mixtures measured at 298 K and 1 bar in a column using **5c^S** (top) and **7c^S** (bottom) as stationary phases.

In summary, the results indicate that even if the pore window plays a key role to explain the trend **5c^S** > **6c^S** > **7c^S** in the adsorption capacities of this family, side-chain interactions between alkyl groups from both, gases and MOF's walls, lie at the origin of their different selectivities. The very different uptake results for **5c^S**, **6c^S** and **7c^S** clearly evidence that playing with the 'pore-limiting diameter' concept, through the increase of the length of aliphatic side chains residing in the pores, does not only modify the sorption capacity of a given material but, more importantly, it may also affect the kinetics of the adsorption. A fine-tuning of these two related factors may enable a control of the selectivity and separation of methane from other hydrocarbons present in natural gas.

1.B.4.3. Proton conductivity

Among the different subfamilies of amino acid-derivative PCPs that have been synthesised, compound **5c^{S}** shows a considerably larger number of hydrogen-bonded water molecules embedded into its pores, being the water contents of 31.5 % (30 molecules per formula unit) as revealed by the TGA measurements (Figure 63). This value is very close to the one determined by the single-crystal X-ray diffraction (32 molecules). Interestingly, the array of water molecules hosted in the pores are hydrogen-bonded, forming 1D ribbons along the hexagonal channels that also involve the aqua/hydroxo bridges of the network. Remarkably, this array of hydrogen-bonded water molecules in **5c^{S}** has been precisely determined due to the high-quality refinement of its crystal structure (showing the positions of the water molecules including their hydrogen atoms), (Figures 99 and 100). Details on the hydrogen bonds and on the O···O distances of the hydrogen-bonded water/hydroxo molecules involved in the proton conduction mechanism are gathered in Tables 38 and 39, Annex I.

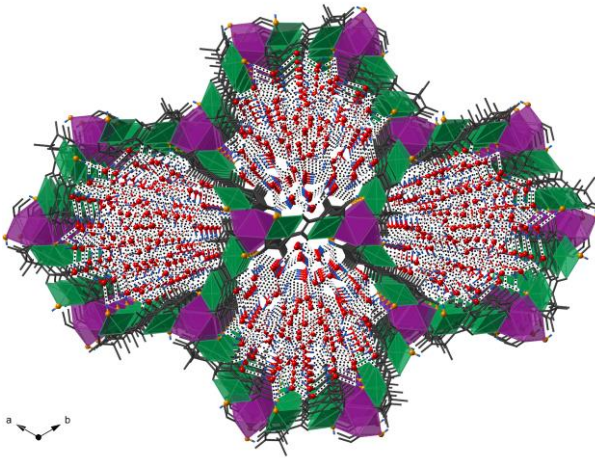

Figure 99. Projection view of the crystal packing of **5c^{S}** along the crystallographic *c* axis showing the filling of the hexagonal pores by the water molecules of crystallisation (red spheres). The dotted lines represent the hydrogen bonds which also involve the hydroxide anions (orange spheres). Copper and calcium atoms are represented by green and purple polyhedra respectively, whereas the ligands are depicted as sticks. The hydrogen atoms of the water molecules and the hydroxo groups are represented by blue sticks.

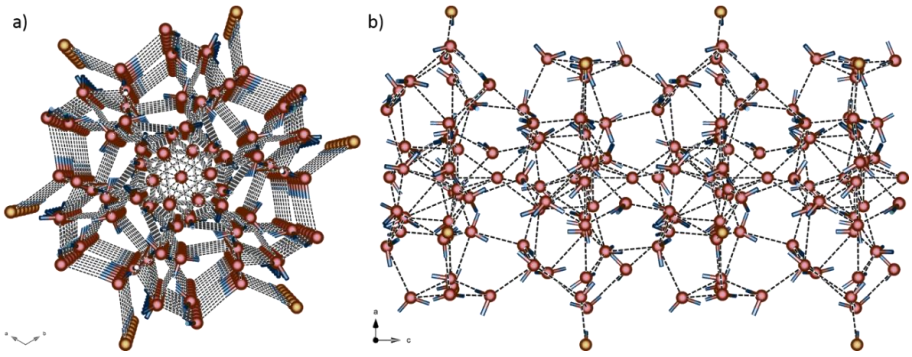

Figure 100. Views along the crystallographic *c* (a) and *b* axes (b) of the array of hydrogen-bonded guest water molecules and hydroxide anions located in each hexagonal channel. The hydrogen atoms are represented as blue sticks whereas the oxygen atoms and hydroxide anions are depicted as red and orange spheres, respectively. The hydrogen bonds are represented by dotted lines.

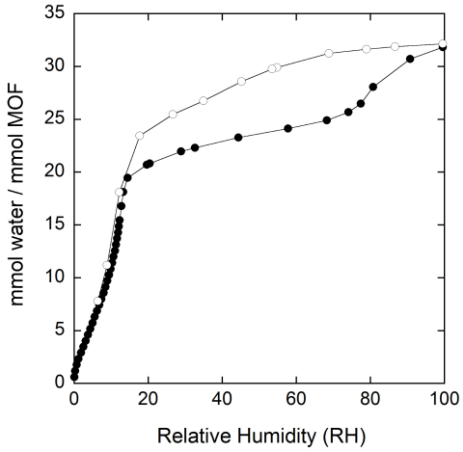

Figure 101. Water vapour adsorption isotherm at 298 K for the activated compound **5c^{S}**. Filled and open circles indicate the adsorption and desorption isotherms, respectively.

In order to have some insights about the dehydration and rehydration process in **5c^{S}**, we carried out water adsorption measurements (Figure 101). The vapour water isotherm at 25 °C shows that the complete rehydration process, with the recovery of 32 mmol of water per mmol of PCP, can be achieved only under maximum relative humidity. This is an interesting information to further perform proton conductivity experiments.

Aiming at confirming the robustness of the material upon the water loss, we took additional temperature-variable PXRD patterns for **5c^S**. As shown in Figure 102, the retention of crystallinity occurs over the entire range of temperatures studied. In addition, the structural stability of **5c^S** was further verified both after proton conductivity experiments (Figure 102f) and in basic aqueous media by immersion in a pH = 14 aqueous solution for one month (Figure 102g).

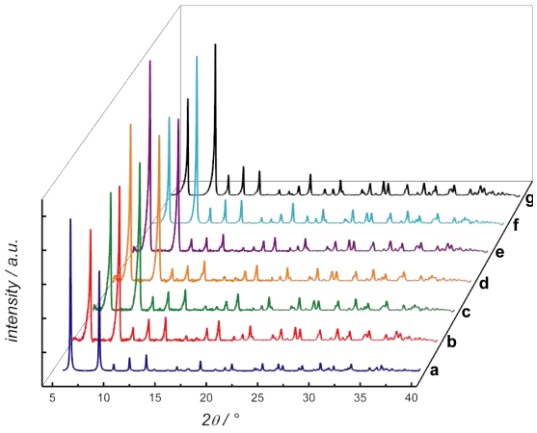

Figure 102. Calculated (a) and variable-temperature PXRD patterns of the activated phase of **5c^S** at (b) 298, (c) 343, (d) 353, and (e) 370 K. PXRD pattern profiles of **5c^S** (f) after proton conduction measurements and (g) after 1 month immersed in a pH = 14 aqueous solution at RT.

Once its proper characterisation was done, and considering the strong interest observed recently in proton conductors together with the presence of an extended net of hydrogen-bonded water molecules and hydroxide anions in **5c^S**, we decided to perform ionic conductivity measurements on this water-stable material aiming at shedding some light concerning the transport mechanism involved in the proton-hopping dynamics.

Impedance data in the form of a complex plane plot for **5c^S** at 353 K and different relative humidity values (RH) are shown in Figure 103. The data show an overlapped/deformed broad arc at high frequencies/low RH with an associated capacitance of ~ 2-3·10^{-11} F cm^{-1}. With increasing RH, lower frequency effects are seen, in the form of an inclined spike with an associated capacitance of ~ 8-10 μF cm^{-1}, what indicates a partial-blocking electrode response consistent with proton migration. The structural stability of **5c^S** after post-impedance measurements was confirmed by X-ray diffraction (Figure 102f).

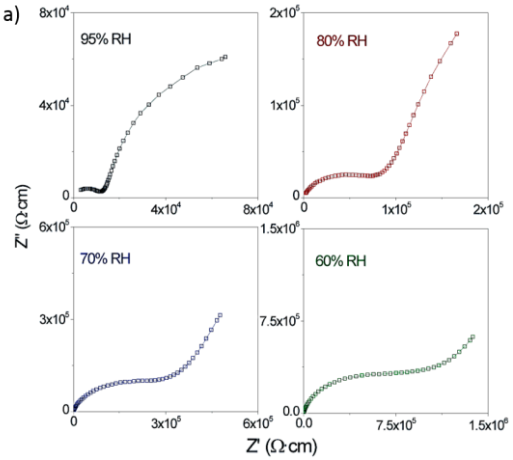

Figure 103. Nyquist plots for **5c^S** at 353 K under four different relative humidity values. Solid lines indicate the fitting to the equivalent circuit (RbQb)(RgbQgb)(Qe).

The conductivity of **5c^S** increases with the relative humidity (Figure 103), a feature which is characteristic of many water-mediated proton conductors. For instance, the conductivity at 353 K increases from 1.1×10^{-6} S cm^{-1} at 60 % RH up to 8.6×10^{-4} S cm^{-1} at 95 % RH. The proton conductivity for **5c^S** measured at 297 K and 95 % RH, 1.0×10^{-5} S cm^{-1}, is comparable with other carboxylate-based MOFs.[34]

Figure 104 shows the overall pellet conductivities in the shape of traditional Arrhenius plots as a function of RH. These plots show a linear behaviour with activation energies (E_a) of 0.42, 0.43, 0.42, and 0.34 eV for RH values of 60, 70, 80, and 95 %, respectively. Such relatively small numbers are within the range typically attributed to a Grotthuss transfer mechanism *via* water molecules, 0.1–0.5 eV.[35–39]

These results suggest that, even in the absence of free acid or basic groups in the framework, the presence of a hydrogen-bonded intricate chain involving both the free water and the hydroxo/water ligands is enough to develop moderate ionic conductivity. Although a vehicle mechanism[40] contribution cannot be discarded, this conductivity most-likely arises from the proton hopping through the hydrogen-bonded array of water molecules, as expected for a structure diffusion mechanism[41,42] in agreement with previous theoretical-experimental studies in pure water[43–45] or acid aqueous solutions.[46]

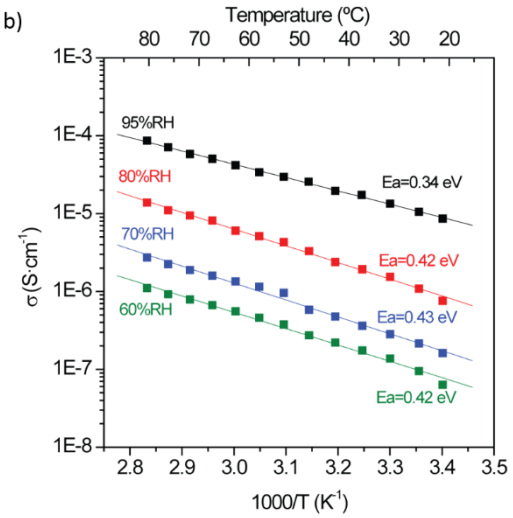

Figure 104. Protonic conductivity data of **5c^{S}** *vs.* reciprocal temperature (Arrhenius plot) at four selected relative humidity values. The corresponding activation energies (E_a) are indicated.

Proton transport mechanisms in solids has attracted great interest because of its relation to many natural processes[47] and its potential application in a wide variety of electrochemical and energy-conversion devices.[48] However, the vast majority of the theoretical studies, with regard to the mechanism of proton conduction (most of them of theoretical nature), could only be carried out so far in non-porous solids.[49–53] In contrast, despite the fact that MOFs show excellent results as proton conducting materials (since they exhibit large pores which allow the movement of ions as well as the presence of guest carrier molecules),[54,55] the first joint experimental/theoretical study dealing with the proton-conduction mechanism in a MOF was published only very recently.[56] This outstanding feature is undoubtedly related to the high disorder that the solvent molecules display.

Therefore, in spite of the large pores that **5c^{S}** exhibits, the water molecules hosted in its channels are particularly ordered and their positions (including those of their hydrogen atoms and thus, the directionality of the H-bond) could be accurately allocated. With this information in mind, we are able to propose a clear conduction

mechanism for the proton conductive **5c^{S}** MOF in agreement with the recent findings shown by Damasceno *et al.*[56]

Figure 100 shows the hydrogen-bonded pathways developing inside one hexagonal channel in **5c^{S}**. At first sight, it is reasonable to suppose that a number of concerted tautomeric equilibria should be followed in the channels (and in other proton conducting MOFs). Aiming at suggesting a model consistent with the experimentally located hydrogen atoms, we have focused just on a few of them. The observed pattern of atomic positions in the water branched chain is reliable with a hopping of protons between neighbouring and H-bonded water molecules being consistent with a Grotthuss-like mechanism.[41] The distances crossed by the H atoms in the hopping process range from 0.73(4) to 1.14(1) with corresponding O···O separations varying in the range 2.686(10)-2.957(9) Å (see the detailed values in Tables 38 and 39, Annex I).

The proposed mechanism is as follows: the starting situation found in the crystal structure would correspond to Figure 105a whereas Figures 105b and c show the proposed intermediate stages with the proton hopping between neighbouring molecules and their consecutive reorientation to finally recover the original situation (Figure 105d). Their orientations represent always a valid structure for the water net. We choose O2W as the proton transfer starting point which can initiate two different pathways toward O9W (path 1) or O1W (path 2). Afterwards, the two pathways must follow the labelled way of path 1/path 2 or exhibit a possible deviation (path 1' or path 2'), which is logical, given that an efficient concerted pathway requires multiple ways. Another important point is the occurrence of a hydrogen bond between hydroxo/water (O1H) and the water molecule O2W. The O2W···OH distance of 2.908(5) Å and the quite perfect directionality of the H-bond [(O-H···O2W angle of 171(14)°] seem to suggest that a proton transfer from O1H to the "initiator" O2W happens, indicating that a hydrogen of the hydroxo/water bridged molecule in **5c^{S}** plays a role, as proton injector, in the proposed mechanism.

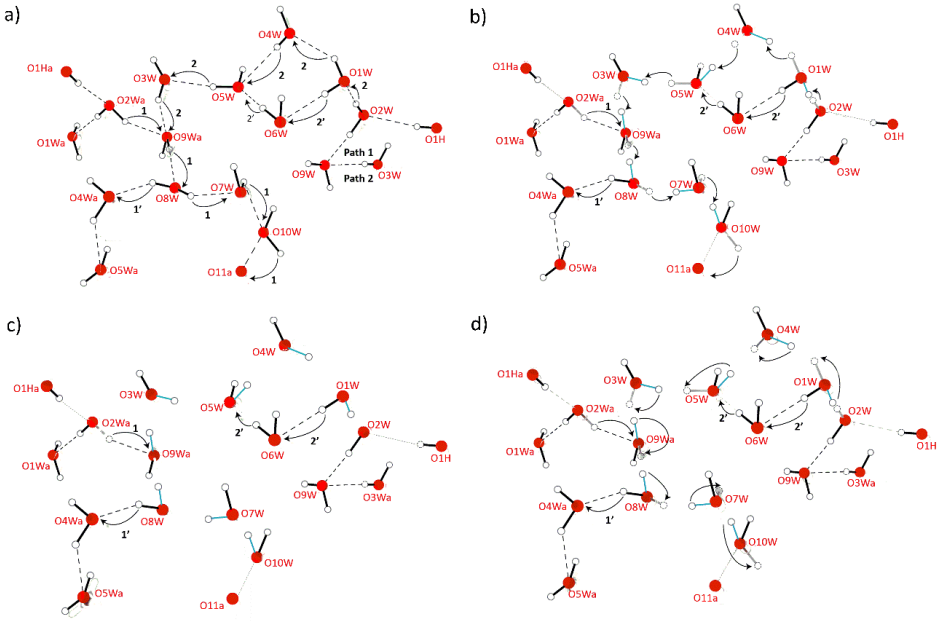

Figure 105. Complete cycle of the proton conduction showing the proton hopping between the hydrogen-bonded water/hydroxo groups and the sequential reorientation: (a) starting real situation (data shown from crystal structure); (b and c) intermediate proposed stages where the proton hopping and the water molecules reorientation occur; and (d) recovery of the starting situation. The water molecules are represented by red filled spheres. The black, grey and blue solid lines represent the initial (observed), broken and formed O-H bonds, respectively. The dotted and the continuous circles represent initial and final hydrogen positions, respectively. The dotted lines represent the hydrogen bonds (for details on the O···O distances see Table 39 in Annex I).

As shown in Figure 106, the proton transfer extents to the O10W and O11 disordered water molecules located in the centre of the channels, suggesting that the whole network of water molecules participates in the conduction. We suggest that the translation movement of the O10w and O11 water molecules along the crystallographic *c* axis around the centre of the hexagonal voids, (see structure refinement and Figure 106) is consistent with proton transfer along the 1D channels and could be the key point for the proton conductivity. It is obvious to suggest that the insertion of acidic molecules, acting as proton injectors, would increase the value of the proton conductivity dramatically.

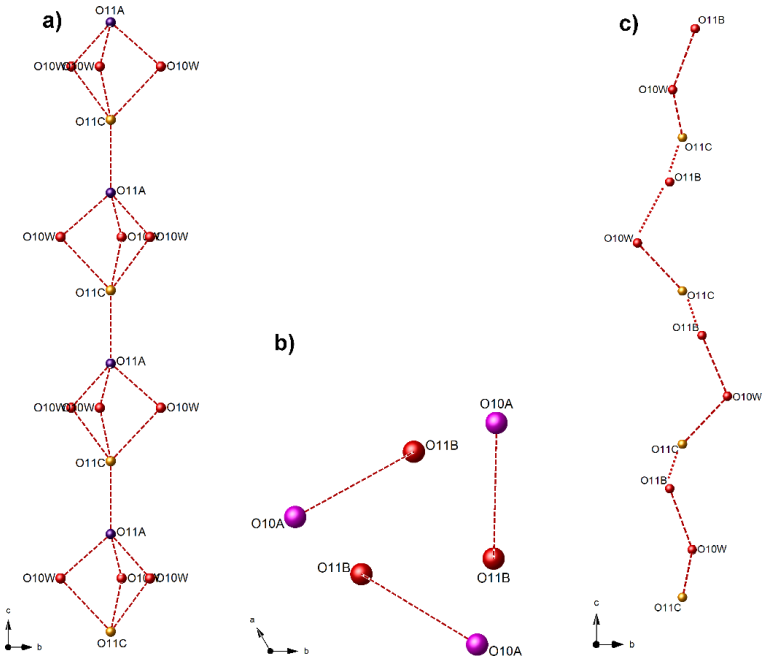

Figure 106. Perspective view of the three possible dispositions of the disordered water molecules (O10 and O11) along the water chain located closer and in the centre of the channels averaged over the whole crystal and captured at the data collection temperature: separate pattern formed by (a) O10W, O11A and O11C along the crystallographic *a* axis, (b) O10A and O11B along the crystallographic *c* axis and (c) O10W, O11B and O11C along the crystallographic *a* axis. (O10W and O11B water molecules of crystallisation are depicted as red spheres, while O10A, O11A and O11C are drawn as purple, violet and yellow spheres, respectively). The dotted lines represent the plausible pathways of the hydrogen bonds.

A detailed study of this type of material is not an easy task. Although some computational schemes, such as *ab initio* and density functional theory (DFT) methods, could offer a more realistic picture of this process, they have not been considered because of the complexity and high CPU time consumption that it would take.

We have found that quantum molecular dynamics simulations are an excellent compromise alternative. This methodology has been used to contrast the proposed structure diffusion mechanism on the basis of the experimental data. This simplified

model provide us with a visual and dynamic picture of the proton hopping between neighbouring water molecules within the hydrogen-bonded 1D arrays of water molecules hosted in the channels. Two different simulations were done on a fragment of the water channel, where O2W is considered as the starting point and therefore, an additional hydrogen (coming from the 1/3 water-bridged molecule O1H) was added.

In the first simulation, the O11A water molecule was replaced by a hydroxo group in order to include, in a way, the attractive effect of the anode on the extra proton (see computational details and Videos 1-4 in Annex I). In the second one, no replacement was done to verify that the proton hopping occurs in a spontaneous manner (Videos 5 and 6). Overall, the optimised structures shown in the videos are in agreement with the proposed structure diffusion (Grotthuss-type) mechanism[41] involving the cleavage and formation of O–H bonds, together with the hopping of the protons followed by the reorientation of the water molecules.

Even the limitations of the simplified model used, the dynamics simulation shown in Videos 1-6 shed light on the same direction and contrast the possibility of the proposed pathways on the basis of the experimental data. In this sense, several remarkable features are clearly observed:

(*i*) the hopping of the protons occurs through a process of cleavage and formation of covalent O–H bonds involving the formation of relatively small charged water clusters ($H_5O_2^+$, $H_7O_3^+$ and $H_9O_4^+$) followed by a solvent reorganisation process;[43]

(*ii*) the transfer of a hydrogen atom from the O2W *initiator* to the O10W *terminal*, after successive proton transfers and water molecules reorientation, follows the sequence: "O2W-O9W-O8W-O7W-O10W", as predicted in the proposed mechanism (path 1 in Figure 105);

(*iii*) and the proton, upon arriving to the *terminal* O10W, continues on his way towards O11A along the crystallographic *c* axis, suggesting that the proton hopping

continues along the disordered water molecules through the centre of the channels (Figure 106). The process takes 200 and 300 femtoseconds (fs) to finish in the two theoretical simulations.

1.B.4.4. Magnetic properties

The magnetic properties of two dicopper(II) oxamidato-containing precursors, $(Me_4N)_2\{Cu^{II}_2[(S,S)\text{-alamox}](OH)_2\} \cdot 6H_2O$ (**5a^S**) and $(Me_4N)_2\{Cu^{II}_2[(S,S)\text{-valmox}](OH)_2\} \cdot 6H_2O$ (**6a^S**), were investigated through direct current (dc) magnetic susceptibility measurements as a function of the temperature.

The $\chi_M T$ *versus* T plots for **5a^S** and **6a^S** [χ_M being the dc molar magnetic susceptibility per two copper(II) ions] are shown in Figure 107. The values of $\chi_M T$ at room temperature are 0.33 (**5a^S**) and 0.40 $cm^3\ mol^{-1}\ K$ (**6a^S**). They are below the expected value for two magnetically non-interacting copper(II) ions ($\chi_M T = 2 \times [(N\beta^2 g_{Cu}^2/3k_B)S_{Cu}(S_{Cu}+1)] \approx 0.80\ cm^3\ mol^{-1}\ K$ with $S_{Cu} = 1/2$ and $g_{Cu} = 2.1$). Upon cooling, the values of $\chi_M T$ continuously decrease for both compounds and they vanish at *ca*. 90 K. This magnetic behaviour is characteristic of a moderately strong antiferromagnetic coupling within the two copper(II) centres through the oxamidato bridge.[57]

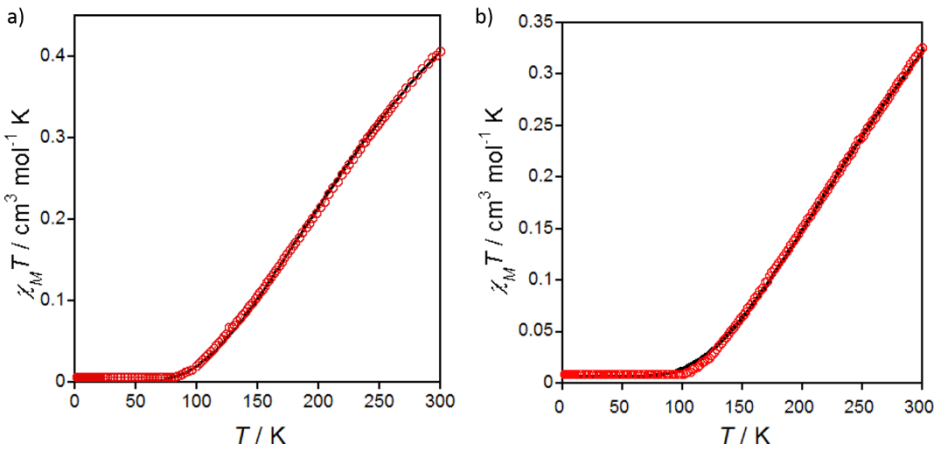

Figure 107. Temperature dependence of $\chi_M T$ for (a) **5a^S** and (b) **6a^S** under applied dc magnetic fields of 10 kG. The solid black lines represent the best-fit curves (see text).

The analysis of the magnetic susceptibility data of **5a^S** and **6a^S** was carried out according to the Bleaney-Bowers expression for a pair of magnetically interacting spin doublets [eqn. (1)][58]

$$\chi_M T_{Cu} = \frac{2N\beta^2 g_{Cu}^2}{k_B T}\left[3 + \exp\left(\frac{-J}{kT}\right)\right]^{-1} \quad (1)$$

where N, β and k have their usual meanings, *J* is the magnetic coupling parameter and *g* is the average Landé factor. The best-fit values are: *J* = -359 (1) (**5a^S**) and −412 cm^{-1} (**6a^S**) with g_{Cu} = 2.15 (**5a^S**) and 2.10 (**6a^S**). The values of the agreement factors *R* are 2.0 x 10^{-5} (**5a^S**) and 3.0 x 10^{-5} (**6a^S**), which are defined as $\sum[(\chi_M T)_{exp} - (\chi_M T)_{calcd}]^2 / \sum[(\chi_M T)_{exp}]^2$. The calculated curves match well the magnetic data in the temperature range investigated (Figure 107). The calculated *J* are in agreement with those found in the literature for oxamidato-bridged dicopper(II) complexes which vary in the range -305 to -591 cm^{-1}.[57]

Among the families of PCPs that have been obtained, the lanthanide(III)-based one deserves a special attention from the magnetic point of view since the lanthanide(III) nodes distributed within the framework have a square-antiprismatic geometry which is suitable for exhibiting single-ion magnet (SIM) behaviour.[59–61] Therefore, the magnetic properties of the two Dy(III)- and Tb(III)-containing PCPs (**5d^S** and **5e^S**, respectively) were firstly investigated through direct current (dc) magnetic susceptibility measurements in the temperature range 2.0 - 300 K. $\chi_M T$ *versus T* plots [χ_M being the dc molar magnetic susceptibility per one lanthanide(III) and six copper(II) ions] are shown in Figure 108. The values of $\chi_M T$ at room temperature are 16.3 (**5d^S**) and 13.6 cm^3 mol^{-1} K (**5e^S**). They are lower than those expected for a set of six magnetically isolated copper(II) ions and one lanthanide(III) ion, the $\chi_M T$ value for one copper(II) ion and that for a trivalent lanthanide cation being given by eqns (2) and (3), respectively:

$$\chi_M T_{Cu} = \frac{N\beta^2 g_{Cu}^2}{3k_B} S_{Cu}(S_{Cu} + 1) \quad (2)$$

$$\chi_M T_{Ln} = \frac{N\beta^2 g_{Ln}^2 J_{Ln}(J_{Ln}+1)}{3k_B} + \frac{2N\beta^2 (g_{Ln}-1)(g_{Ln}-2)}{3\lambda} \quad (3)$$

In eqn. (3) we consider that the free-ion ground state is well separated in energy from the first excited state, the ground state being the only one thermally populated at room temperature. g_{Ln} is the Zeeman factor which obeys the expression [eqn(4)]:

$$g = \frac{3}{2} + [S(S+1) - L(L+1)]/2J(J+1) \quad (4)$$

Finally, L is the orbital quantum number and λ is the spin-orbit coupling parameter. Therefore, the expected $\chi_M T$ value for a set of six magnetically isolated copper(II) ions and one lanthanide(III) ion is 16.58 $cm^3\ mol^{-1}\ K$ for dysprosium(III) [with S_{Cu} = 1/2, g_{Cu} = 2.08, S_{Dy} = 5/2, g_{Dy} = 4/3, J_{Dy} = 15/2 and L_{Dy} = 5] and 14.24 $cm^3\ mol^{-1}\ K$ for terbium(III) [with S_{Cu} = 1/2, g_{Cu} = 2.08, S_{Tb} = 3, g_{Tb} = 3/2, J_{Tb} = 6 and L_{Tb} = 3].

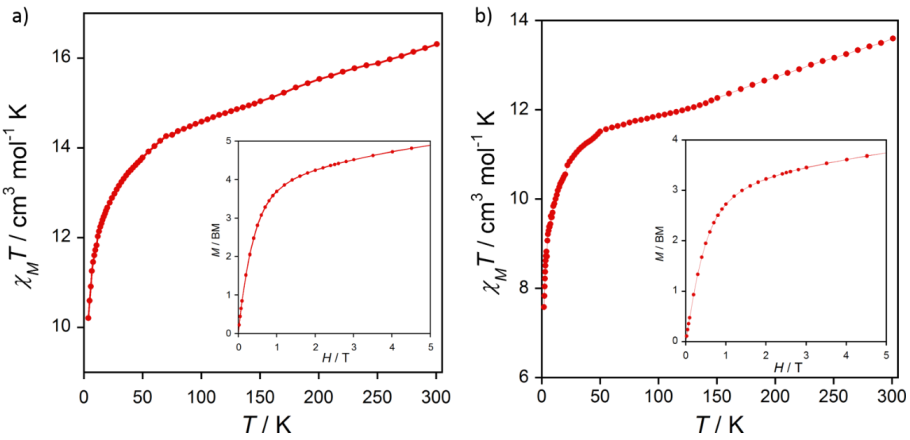

Figure 108. Temperature dependence of $\chi_M T$ for (a) **5d^S** and (b) **5e^S** under applied dc magnetic fields of 250 G (T < 30 K) and 5 kG (T ≥ 30 K). The insets show the field dependence of the magnetization (M) of **5d^S** (a) and **5e^S** (b) at T = 2.0 K. The solid lines are only eye-guides.

Upon cooling, $\chi_M T$ continuously decreases most likely due to the antiferromagnetic coupling between the copper(II) centres through the *trans*-oxamidato and hydroxide bridges to further reach an incipient pseudo-plateau [at *ca*. 100 K (more evidenced for **5e^S**) with $\chi_M T$ values of 14.2 (**5d^S**) and 11.8 $cm^3\ mol^{-1}\ K$ (**5e^S**)] which is consistent with the free-ion ground state from the dysprosium(III) and terbium(III) ions in **5d^S** and **5e^S**. A strong decrease $\chi_M T$ occurs in the low temperature range due to the thermal

depopulation of the Stark levels of the lanthanide(III) ions until reaching 10.1 (**5e^{S}**) at 7.6 $cm^3\ mol^{-1}\ K$ (**5f^{S}**) at 2.0 K.

The presence of non-interacting lanthanide(III) ions within the PCPs is supported by the *M vs*. *H* plots at 2.0 K (insets of Figure 108), where *M* is de magnetization per $Cu^{II}_6Ln^{III}$ unit and *H* is the applied dc magnetic field. The magnetization curves show maximum values of *M* at 5 T of 4.88 (**5d^{S}**) and 3.75 μ_B (**5e^{S}**) that are far from reaching the saturation. They are both below the calculated values for the dysprosium(III) (10.0 μ_B) and terbium(III) (9.0 μ_B) free ions (without the influence of any ligand field).

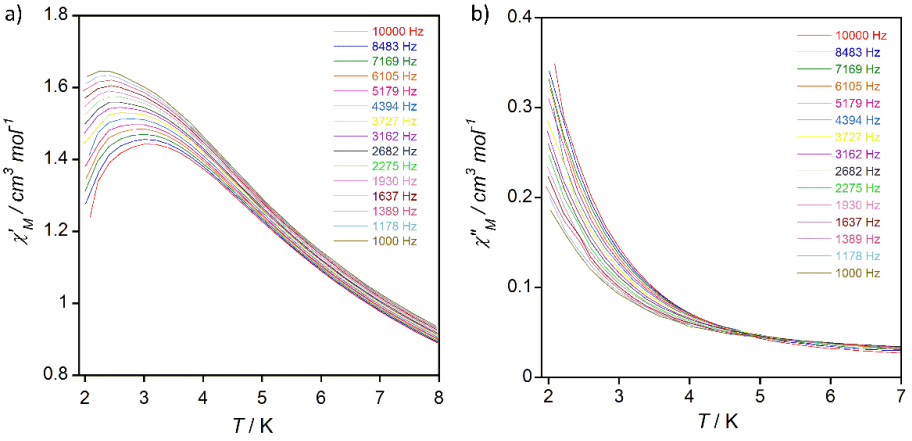

Figure 109. Frequency and temperature dependence of the (a) in-phase (χ_M') and (b) the out-of-phase (χ_M'') component of the ac susceptibility for **5d^{S}** under an applied dc magnetic field of 2500 G and a ±4.0 G oscillating field at various frequencies.

Alternating current (ac) measurements were then carried out in order to investigate the possible slow relaxation of the magnetization of the dysprosium(III)-based PCP (**5d^{S}**). The χ_M' and χ_M'' *vs*. *T* plots (Figure 109) [χ_M' and χ_M'' being the in-phase and the out-of-phase magnetic susceptibilities measured per $Cu^{II}_6Dy^{III}$ unit] show an incipient frequency dependence under an applied field of 2500 G below 8.0 K down to the lowest temperature 2.0 K. This feature indicates the occurrence of slow relaxation of the magnetization, reminiscent of a SIM behaviour.[62–66]

However, the expected maxima in the curves due to the blocking could not be observed in the temperature range investigated (2.0 - 8.0 K), even by applying a dc magnetic field in order to suppress the quantum tunnelling of the magnetization (Figure 109b). Hence, assuming a relaxation process driven by one activation energy (E_a) and exhibiting a single relaxation time (τ), this can be expressed in terms of the Arrhenius law [eqn. (5)].

$$\tau = \tau_0 \exp\left(\frac{E_a}{k_B T}\right) \quad (5)$$

where E_a is the activation energy and τ_0 is the relaxation time. Taking into account that $\chi_M''/\chi_M' = \ln(2\pi\nu\tau_0)$ where ν is the experimental ac field exciting frequency, one obtains eqn. (6),

$$\ln\left(\frac{\chi_M''}{\chi_M'}\right) = \ln(2\pi\nu\tau_0) + \frac{E_a}{k_B T} \quad (6)$$

which has been successfully applied in other examples of SIM and single-molecule magnets (SMM) systems to roughly evaluate the values of E_a and τ_0.[67,68] By applying this methodology (Figure 110), the calculated values for E_a and τ_0 are 4.3 (3) cm^{-1} and 2.8 (2) x 10^{-7} s, respectively. These values are within the range expected for a SIM behaviour.

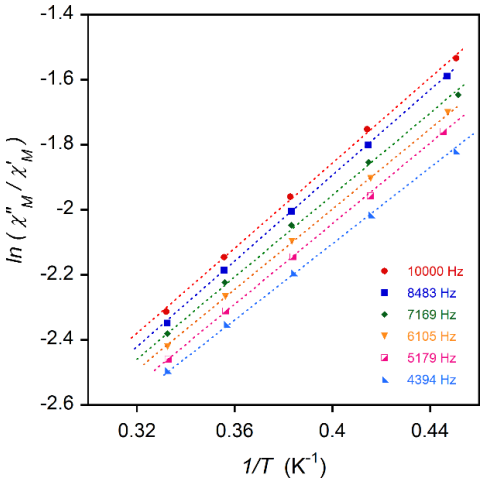

Figure 110. Natural logarithm of the χ_M''/χ_M' ratio *vs*. 1/*T* under a dc magnetic field of 2500 G and a 4 G oscillating field at diverse frequencies.

Alternating current (ac) measurements were also carried out for the terbium(III)-based PCP (**5e^{S}**). The χ_M' and χ_M'' *vs*. *T* plots (Figure 111) [χ_M' and χ_M'' being the in-phase and the out-of-phase magnetic susceptibilities measured per $Cu^{II}_6Tb^{III}$ unit] show an very incipient frequency dependence under an applied dc field of 2500 G which is better appreciated at very low temperatures in the χ_M'' *vs*. *T* plot (Figure 111b). This frequency dependence indicates a possible slow relaxation of the magnetization for the terbium(III) ions in **5e^{S}**; however, the blocking temperatures, as maxima, would be found well below 2.0 K and the very few available data (far from such maxima) prevent any treatment to calculate the relaxation time and the activation energy.

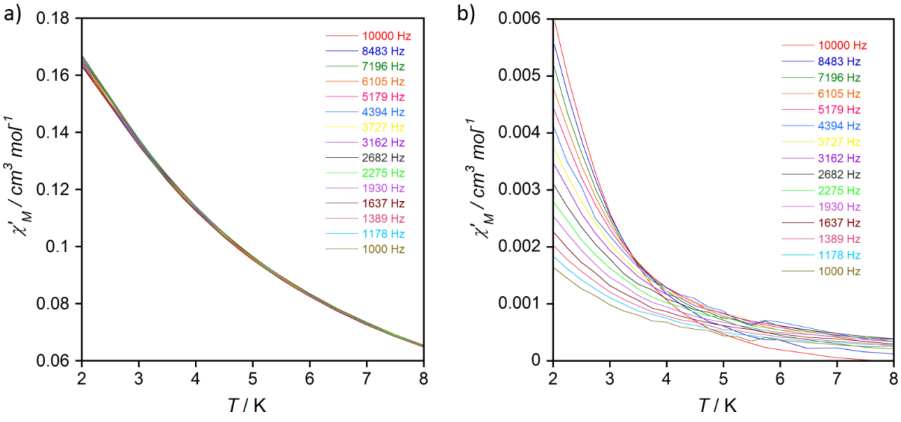

Figure 111. Frequency and temperature dependence of the (a) in-phase (χ_M') and the (b) out-of-phase (χ_M'') component of the ac susceptibility for **5e^{S}** under an applied dc magnetic field of 2500 G and a ±4.0 G oscillating field at various frequencies.

1.B.5. Discussion

Encouraged by the results obtained in the section 1.A, where a family of PCPs was synthesised from a series of amino acid derivative oxamato-based ligands, we decided to functionalise the library of amino acids derivatives with the oxamidato group instead, aiming at synthesising a new family of chiral materials which could exhibit interesting physicochemical properties.

Hence, the effectiveness of the metalloligand design strategy has been demonstrated by the synthesis of a series of chiral subfamilies of PCPs exhibiting different architectures and properties, being their encoded chiral information efficiently transferred from the starting amino acids by means of a metallosupramolecular design strategy. Three subfamilies of PCPs have been obtained depending on the metal ion used as node to link the trans-oxamidato dicopper(II) precursors: barium(II)-, calcium(II)- and lanthanide(III)-derived ones.

The subfamily of barium(II)-derived PCPs (**5b^{S}**, **6b^{S}** and **7b^{S}**) exhibit very different structures depending on the ligand used. Although the three [(*S*,*S*)-alamox^{4}, (*S*,*S*)-valmox^{4-} and (*S*,*S*)-leumox^{4-}] ligands are in principle very similar, the different length of their hydrophobic aliphatic chains determine the metal ion organisation. The thorough study of their crystal structures has revealed a close relationship between the length and shape of the aliphatic residue and the complexity of the resulting 3D open-framework. This phenomenon resembles the process of molecular recognition that takes place in polypeptides chains, where each amino acid residue is identified by different ligand connections acting as fingerprints.

The isoreticular subfamily of calcium(II)-derived chiral PCPs (**5c^{S}**, **6c^{S}** and **7c^{S}**) offered a unique possibility regarding the evaluation of the impact of the length of the alkyl side-chains from the ligand decorating the walls of the pores on the adsorption of different light hydrocarbons. As far as we know, this is the first experimental study in which a family of isoreticular PCPs exhibiting different alkyl-functionalised pores is used to rationalise the adsorptive properties. The systematic variation of the length of the

aliphatic residue has allowed to investigate at the same time the influence of other parameters such as the pore window, the hydrophobicity, the kinetics and alkyl interactions on the adsorption and consequently, the selectivity.

The overall trend observed in their adsorption capacities (**5c^S** > **6c^S** > **7c^S**) is consistent with their decreasing pore size. Moreover, the three compounds exhibit higher adsorption abilities for those hydrocarbons with longer chain (CH_4 << C_2H_6 < C_3H_8 < *n*-C_4H_{10}) as result of the enhancement of interactions with the side chain of the MOF. In addition, the slope of the isotherms for C_3H_8 and *n*-C_4H_{10} are much steeper, reflecting a stronger affinity for these gases.

The study of the adsorption capabilities of **5c^S**, **6c^S** and **7c^S** for olefins showed no distinction between the C_2H_6 and the C_2H_4 uptake, but a significantly higher uptake of C_3H_6 respect to C_3H_8, most likely due to the stronger interaction of the π-bonding orbital of C_3H_6 with the open metal sites and its smaller kinetic diameter. The kinetics study further confirmed the trend observed above, even revealing an enhancement of the selectivities of **5c^S**, **6c^S** and **7c^S** towards the higher hydrocarbons, the adsorbed amount of CH_4 being almost negligible especially for **7c^S**. Breakthrough experiments were also carried out showing very interesting results for **7c^S**, where the methane is not adsorbed at all and the values of retention time for ethane/methane and propane/methane are 71 and 246 min, respectively.

In summary, the use of amino acids with smaller residues leads to PCPs with bigger pore windows which is translated into higher gas uptakes but less selectivity since the carbon-carbon hydrophobic interactions are less effective. Thus, by the rational choice of the amino acid derivative ligand, we are capable to control the kinetic adsorption selectivity of methane towards other light hydrocarbons present in the natural gas, offering a new way for its purification.

Furthermore, compound **5c^S** hosting a large number of water molecules into its pores, exhibited proton conductivity properties (its humidity-dependent conductivity at 353 K ranging from 1.1 x 10^6 at 60 % RH to 8.6 x 10^4 S cm^{-1} at 95 % RH). The good quality

single crystal X-ray diffraction data showed an ordered net of water molecules, their positions (including the hydrogen atoms) being accurately determined in such a way that, the directionality of the hydrogen bonds could be then established. This allowed us to propose the involved pathways in the hopping of protons between neighbouring water molecules, which are in agreement with a Grotthuss-like mechanism and that have been further supported by quantum molecular dynamics simulations.

Finally, two isoreticular PCPs were obtained when we explored the use of lanthanide instead of alkaline-earth ions for acting as nodes between the *trans*-oxamidato copper(II) complexes. Thus, using the (*S*,*S*)-alamox^{4-} ligand, we obtained both dysprosium(III)- and terbium(III)-based PCPs **5d^{S}** and **5e^{S}**, respectively. Their magnetic properties were investigated through both direct (dc) and alternating current (ac) magnetic susceptibility measurements. The plots of the out-of-phase magnetic susceptibility *vs*. temperature of **5d^{S}** and **5e^{S}** showed incipient maxima which are indicative of a SIM behaviour of the lanthanide(III) ions embedded within their open-frameworks, more evidenced in the case of the dysprosium(III)-derivative (**5d^{S}**), where we could calculate the relaxation time and activation energy of the magnetization. The relatively fast relaxation time and thus the lack of maxima exhibited by **5d^{S}** and **5e^{S}** could be explained because both the dysprosium(III) and terbium(III) ions are not effectively isolated from a magnetic viewpoint and dipolar interactions may occur. Further works will include the use of a magnetic diluted sample with variable dysprosium(III)/yttrium(III) and terbium(III)/yttrium(III) molar ratio to minimise the possible quenching in the magnet-like properties of the dysprosium(III) nodes. In any case, these compounds expand the still very limited family of lanthanide-based SIM-MOFs[60] published so far.

1.B.6. References

1 F. Lloret, M. Julve, J. Faus, R. Ruiz, I. Castro, M. Mollar and M. Philoche-Levisalles, *Inorg. Chem.*, 1992, **31**, 784–791.

2 F. Lloret, M. Julve, B. J. Faus and C. Boisb, *Inorg. Chem.*, 1992, **31**, 2956–2961.

3 R. Ruiz, J. Faus, F. Lloret, M. Julve and Y. Journaux, *Coord. Chem. Rev.*, 1999, **193-195**, 1069–1117.

4 E. V. Alexandrov, V. a. Blatov, a. V. Kochetkov and D. M. Proserpio, *CrystEngComm*, 2011, **13**, 3947–3958.

5 V. A. Blatov and D. M. Proserpio, *Modern Methods of Crystal Structure Prediction*, Wiley-VCH Verlag GmbH&Co. KGaA, 2010.

6 V. A. Blatov, M. O'Keeffe and D. M. Proserpio, *CrystEngComm*, 2010, **12**, 44–48.

7 L. Carlucci, G. Ciani and D. M. Proserpio, *Making Crystals by Design*, KGaA, Wiley-VCH Verlag GmbH&Co., Weinheim, Germany, 2007.

8 F. Hoffman and M. Fröba, *The Chemistry of Metal-Organic Frameworks: Synthesis, Characterization and Applications*, Wiley-VCH Verlag GmbH&Co. KGaA, Weinheim, Germany, 2016.

9 M. O'Keeffe and O. M. Yaghi, *Chem. Rev.*, 2012, **112**, 675–702.

10 V. A. Blatov, A. P. Shevchenko and D. M. Proserpio, *Cryst. Growth Des.*, 2014, **14**, 3576–3586.

11 M. O'Keeffe, M. A. Peskov, S. J. Ramsden and O. M. Yaghi, *Acc. Chem. Res.*, 2008, **41**, 1782–1789.

12 V. A. Blatov, *Multipurpose crystallochemical analysis with the program package TOPOS*, 2006, vol. 7.

13 V. A. Blatov and D. M. Proserpio, *Acta Crystallogr. Sect. A Found. Crystallogr.*, 2009, **65**, 202–212.

14 A. C. Sudik, A. P. Côté and O. M. Yaghi, *Inorg. Chem.*, 2005, **44**, 2998–3000.

15 B. Liu, R. Shang, K. Hu, Z. Wang and S. Gao, *Inorg. Chem.*, 2012, **51**, 13363–13372.

16 S. Chen, R. Shang, K.-L. Hu, Z.-M. Wang and S. Gao, *Inorg. Chem. Front.*, 2014, **1**, 83–98.

17 M. Mączka, A. Pietraszko, B. Macalik and K. Hermanowicz, *Inorg. Chem.*, 2014, **53**, 787–794.

18 R. Shang, G.-C. Xu, Z.-M. Wang and S. Gao, *Chem. - A Eur. J.*, 2014, **20**, 1146–1158.

19 K. Reynolds, R. D. Willett and B. Twamley, *Acta Crystallogr. Sect. E Struct. Reports Online*, 2003, **59**, m402–m404.

20 S. T. Hyde, M. O'Keeffe and D. M. Proserpio, *Angew. Chemie Int. Ed.*, 2008, **47**, 7996–8000.

21 L. Lin, R. Yu, W. Yang, X. Wu and C. Lu, *Cryst. Growth Des.*, 2012, **12**, 3304–3311.

22 H.-Y. Li, F.-P. Huang and Y.-M. Jiang, *Inorganica Chim. Acta*, 2011, **377**, 91–98.

23 T. Kundu, S. C. Sahoo and R. Banerjee, *Cryst. Growth Des.*, 2012, **12**, 4633–4640.

24 M. Eddaoudi, *Science (80-.).*, 2002, **295**, 469–472.

25 R.-B. Lin, T.-Y. Li, H.-L. Zhou, C.-T. He, J.-P. Zhang and X.-M. Chen, *Chem. Sci.*, 2015, **6**, 2516–2521.

26 M. Kobalz, J. Lincke, K. Kobalz, O. Erhart, J. Bergmann, D. Lässig, M. Lange, J. Möllmer, R. Gläser, R. Staudt and H. Krautscheid, *Inorg. Chem.*, 2016, **55**, 3030–3039.

27 H. Furukawa, Y. B. Go, N. Ko, Y. K. Park, F. J. Uribe-Romo, J. Kim, M. O'Keeffe and O. M. Yaghi, *Inorg. Chem.*, 2011, **50**, 9147–9152.

28 I. Spanopoulos, C. Tsangarakis, E. Klontzas, E. Tylianakis, G. Froudakis, K. Adil, Y. Belmabkhout, M. Eddaoudi and P. N. Trikalitis, *J. Am. Chem. Soc.*, 2016, **138**, 1568–1574.

29 G. A. Olah and A. Molnár, *Hydrocarbon Chemistry*, Inc., Hoboken, NJ, USA, 2003.

30 Z. R. Herm, E. D. Bloch and R. Long, *Chem. Mater.*, 2014, **26**, 323–338.

31 M. F. De Lange, T. J. H. Vlugt, J. Gascon and F. Kapteijn, *Microporous Mesoporous Mater.*, 2014, **200**, 199–215.

32 Y.-S. Bae, C. Y. Lee, K. C. Kim, O. K. Farha, P. Nickias, J. T. Hupp, S. T. Nguyen and R. Q. Snurr, *Angew. Chemie Int. Ed.*, 2012, **51**, 1857–1860.

33 V. Safarifard, S. Rodríguez-Hermida, V. Guillerm, I. Imaz, M. Bigdeli, A. Azhdari Tehrani, J. Juanhuix, A. Morsali, M. E. Casco, J. Silvestre-Albero, E. V. Ramos-Fernandez and D. Maspoch, *Cryst. Growth Des.*, 2016, **16**, 6016–6023.

34 S. Horike, D. Umeyama and S. Kitagawa, *Acc. Chem. Res.*, 2013, **46**, 2376–2384.

35 P. Colomban and A. Novak, *J. Mol. Struct.*, 1988, **177**, 277–308.

36 C.-A. Dai, C.-P. Liu, Y.-H. Lee, C.-J. Chang, C.-Y. Chao and Y.-Y. Cheng, *J. Power Sources*, 2008, **177**, 262–272.

37 R. GOSALAWIT, S. CHIRACHANCHAI, S. SHISHATSKIY and S. NUNES, *Solid State Ionics*, 2007, **178**, 1627–1635.

38 N. Hara, H. Ohashi, T. Ito and T. Yamaguchi, *J. Phys. Chem. B*, 2009, **113**, 4656–4663.

39 H. Munakata, H. Chiba and K. Kanamura, *Solid State Ionics*, 2005, **176**, 2445–2450.

40 K. Kreuer, A. Rabenau and W. Weppner, *Angew. Chemie Int. Ed. English*, 1982, **21**, 208–209.

41 N. Agmon, *Chem. Phys. Lett.*, 1995, **244**, 456–462.

42 D. Marx, *ChemPhysChem*, 2006, **7**, 1848–1870.

43 A. Hassanali, F. Giberti, J. Cuny, T. D. Kühne and M. Parrinello, *Proc. Natl. Acad. Sci.*, 2013, **110**, 13723–13728.

44 D. Marx, M. E. Tuckerman, J. Hutter and M. Parrinello, *Nature*, 1999, **397**, 601–604.

45 M. E. Tuckerman, *Science (80-.).*, 1997, **275**, 817–820.

46 L. Vilčiauskas, M. E. Tuckerman, G. Bester, S. J. Paddison and K.-D. Kreuer, *Nat. Chem.*, 2012, **4**, 461–466.

47 Y. Fujiyoshi, K. Murata, K. Mitsuoka, T. Hirai, T. Walz, P. Agre, J. B. Heymann and A. Engel, *Nature*, 2000, **407**, 599–605.

48 J. a Hurd, R. Vaidhyanathan, V. Thangadurai, C. I. Ratcliffe, I. L. Moudrakovski and G. K. H. Shimizu, *Nat. Chem.*, 2009, **1**, 705–10.

49 S. C. Capelli, L. R. Falvello, E. Forcén-Vázquez, G. J. McIntyre, F. Palacio, S. Sanz and M. Tomás, *Angew. Chemie*, 2013, **125**, 13705–13709.

50 R. E. Gordon, J. H. Strange and T. K. Halstead, *Solid State Commun.*, 1979, **31**, 995–997.

51 K. D. Kreuer, A. Rabenau and R. Messer, *Appl. Phys. A Solids Surf.*, 1983, **32**, 45–53.

52 T. Ogawa, T. Aonuma, T. Tamaki, H. Ohashi, H. Ushiyama, K. Yamashita and T. Yamaguchi, *Chem. Sci.*, 2014, **5**, 4878–4887.

53 T. Ogawa, K. Kamiguchi, T. Tamaki, H. Imai and T. Yamaguchi, *Anal. Chem.*, 2014, **86**, 9362–9366.

54 X. Liang, F. Zhang, W. Feng, X. Zou, C. Zhao, H. Na, C. Liu, F. Sun and G. Zhu, *Chem. Sci.*, 2013, **4**, 983–992.

55 M. Tadokoro, Y. Ohhata, Y. Shimazaki, S. Ishimaru, T. Yamada, Y. Nagao, T. Sugaya, K. Isoda, Y. Suzuki, H. Kitagawa and H. Matsui, *Chem. - A Eur. J.*, 2014, **20**, 13698–13709.

56 D. D. Borges, S. Devautour-Vinot, H. Jobic, J. Ollivier, F. Nouar, R. Semino, T. Devic, C. Serre, F. Paesani and G. Maurin, *Angew. Chemie*, 2016, **128**, 3987–3992.

57 J. Cano, E. Ruiz, P. Alemany, F. Lloret and S. Alvarez, *J. Chem. Soc. Dalt. Trans.*, 1999, **1**, 1669–1676.

58 B. Bleaney and K. D. Bowers, *Proc. R. Soc. Lond. A. Math. Phys. Sci.*, 1952, **214**, 451–465.

59 M. A. AlDamen, J. M. Clemente-Juan, E. Coronado, C. Martí-Gastaldo and A. Gaita-Ariño, *J. Am. Chem. Soc.*, 2008, **130**, 8874–8875.

60 J. J. Baldoví, E. Coronado, A. Gaita-Ariño, C. Gamer, M. Giménez-Marqués and G. Mínguez Espallargas, *Chemistry*, 2014, **20**, 10695–702.

61 N. Ishikawa, M. Sugita, T. Ishikawa, S. Koshihara and Y. Kaizu, *J. Am. Chem. Soc.*, 2003, **125**, 8694–8695.

62 G. A. Craig and M. Murrie, *Chem. Soc. Rev.*, 2015, **44**, 2135–2147.

63 J. M. Frost, K. L. M. Harriman and M. Murugesu, *Chem. Sci.*, 2016, **7**, 2470–2491.

64 S.-D. Jiang, B.-W. Wang and S. Gao, in *Struct Bond (2015)*, Springer-Verlag Berlin Heidelberg 2014, 2015, pp. 111–141.

65 Y.-S. Meng, S.-D. Jiang, B.-W. Wang and S. Gao, *Acc. Chem. Res.*, 2016, **49**, 2381–2389.

66 C. J. Milios and R. E. P. Winpenny, in *Struct Bond (2015)*, Springer-Verlag Berlin Heidelberg 2014, 2014, pp. 1–110.

67 A. S. Dinca, J. Vallejo, S. Shova, F. Lloret, M. Julve and M. Andruh, *Polyhedron*, 2013, **65**, 238–243.

68 J. Martínez-Lillo, T. F. Mastropietro, E. Lhotel, C. Paulsen, J. Cano, G. De Munno, J. Faus, F. Lloret, M. Julve, S. Nellutla and J. Krzystek, *J. Am. Chem. Soc.*, 2013, **135**, 13737–13748.

Part 2

Post-Synthetic Modifications

2.1. Introduction

The use of post-synthetic methods (PSM) leads to the heterogeneous chemical modification of a preassembled PCP, affording a new material that could not be synthesised *de novo*. Among all the possible post-modification routes which have been described previously in the main introduction, the so-called cation exchange and transmetalation techniques have been particularly useful in this Thesis and thus, they are described in detail.

2.1.1. Cation Exchange

In general, the term "cation exchange" refers to the replacement of the extra-framework cations that can be attached to the framework structure or located within its pores. They include metal ions, cationic metal complexes and organic cations; so, a distinction from the metal-ion exchange described in the next section (where the metal ions susceptible to be exchanged are contained in the building blocks and constitute the framework) has been done (see Figure 1). Note that the term "cation exchange" can be found in the literature referring to the transmetalation as well.[1–4]

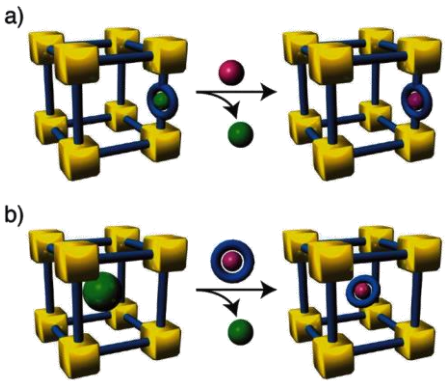

Figure 1. PSM by exchange of (a) metal ions of the secondary building units of the framework (transmetalation) and (b) charge-balancing cations within the pores (cation exchange).

The vast family of anionic PCPs that has been described to date represents an outstanding platform for the study of the exchange of their charge-balancing cations by metal cations, cationic metal complexes or organic cations and for the investigation of their influence on the final properties of

the material. Cation exchange methods have been proven to be successful in order to tune the PCP features enhancing and/or introducing new functionalities such as magnetic properties, luminescence, gas sorption, catalysis, etc.

The ion substitution phenomena have been long observed in zeolites,[5] molecular cages[6] and more recently in PCPs.[7] One of the first reports concerning cation exchange in PCPs is the work done by Liu and Eddaoudi.[8] They synthesised a series of anionic zeolite-like MOFs (ZMOFs) which exhibit and easy ionic exchange capacity retaining their morphology and crystallinity and affording thus, a novel strategy to encapsulate cationic chromophores which could serve as sensor units.

Dincă and collaborators performed the substitution of the extra-framework Mn^{2+} ions in $Mn_3[(Mn_4Cl)_3(btt)_8(CH_3OH)_{10}]_2$ [btt = 1,3,5-benzenetris(tetrazolate)] with Li^+, Cu^+, Fe^{2+}, Co^{2+}, Ni^{2+}, Cu^{2+} and Zn^{2+} yielding a series of isostructural compounds and they studied their influence on the H_2 adsorption enthalpy.[9] The results revealed a large cation-dependent variation of this adsorption enthalpy. Many other illustrative examples of the enhancement of the H_2 sorption properties *via* cation exchange, usually with Li^+ cations, can be found in the literature.[10–13]

Besides the improvement of the sorption properties of the PCPs, cation exchange also represents a useful strategy in order to introduce catalytic functionalities into a preformed material as demonstrated by the work carried out by Sanford and co-workers.[14] They incorporated a variety of cationic complexes of Pd(II), Fe(II), Ir(I), Rh(I) and Ru(II) into the ZJU-28 MOF affording a new family of materials (see Figure 2). Interestingly, the Rh(I)-based ZJU-28 MOF catalyses the hydrogenation of 1-octene to *n*-octane.

Intensive studies on lanthanide(III)-loaded luminescent PCPs revealed that the post-synthetic encapsulation of lanthanide(III) ions *via* cation exchange provides a promising method to achieve tuneable luminescence of application in sensing.[15,16]

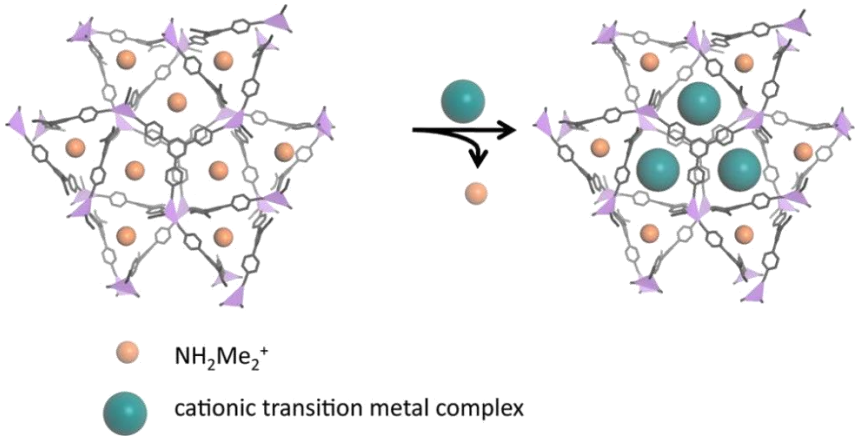

Figure 2. Strategy for supporting molecular transition metal catalysts in the ZJU-28 MOF.

The Zhang team carried out the post-synthetic cation exchange of the dimethylammonium cations in the MOF $\{[Me_2NH_2]_{0.125}[In_{0.125}(H_2L)_{0.25}] \cdot xDMF\}_n$ with lanthanide(III) cations such as Eu^{3+}, Tb^{3+}, Dy^{3+} and Sm^{3+}.[17] Moreover, this MOF could also be loaded with different dyes such as rhodamine B affording a material which is sensitive to organic solvent molecules and shows a potential application in the fabrication of luminescent sensors. The success of this technique resides on three basic factors: (i) usually mild conditions are required for the post-modification step, (ii) the sensitisation that luminescent ions may undergo within de framework and (iii) PCPs provide a rigid scaffold that can serve to protect lanthanide cations from solvent quenching.

Drug delivery is another very interesting application of the cation exchange approach. Special attention deserves the smart work reported by Rosi *et al.*[18] where they illustrate that cationic drugs can be loaded into the pores of a PCP through cation exchange. The authors exchanged the dimethylammonium cations residing in the pores of their *bio*MOF-1 with procainamide·HCl.[18] Aiming at proving that exogenous cations in biological fluids could then affect the release of the drugs *via* alternative cation replacement, they soaked the drug loaded material in a phosphate-buffered saline solution and monitored the drug release in competition with buffer cations.

2.1.2. Transmetalation

Early studies in cation exchange demonstrated that the metal substitution in PCPs was not only achieved for charge-balancing metals but also for intra-framework, strongly bound nodes. Long and Dincă wanted to exchange the Mn^{2+} counter-balancing cations in their $Mn_3[(Mn_4Cl)_3(BTT)_8(CH_3OH)_{10}]_2$ material by Li^+, Cu^+, Fe^{2+}, Co^{2+}, Ni^{2+}, Cu^{2+} and Zn^{2+} aiming at improving the H_2 sorption.[9] The metal cation exchange resulted into the formation of isostructural compounds with different exchange ratio depending on the size and charge of the exchanged metal ion. Surprisingly, they observed that not only the expected substitution of extra-framework Mn^{2+} cations took place for the Cu^{2+} and Zn^{2+} ions, but also a significant degree of intra-framework cation substitution occurred. In such a way, they demonstrated that even the metal ions from the framework could be exchanged.

The transmetalation process, also referred as “metal metathesis”, entails the partial or complete replacement of the SBU or metal nodes of a PCP with a metal precursor (usually a solution of a metal salt), without compromising the structure, preferably in a single crystal-to-single crystal (SC to SC) transformation.

Sometimes, the conventional synthetic path for a PCP turns to be unsuccessful when working with different metal ions. This is not surprising since the variation in size, geometric restriction on the coordination sphere and electronic properties of the different metal ions may interfere with the PCP structure assembly. Moreover, certain metal ions (Ti^{3+}, V^{2+}, Cr^{2+}, Co^{2+}, etc.) can be oxidised under standard solvothermal conditions (high temperature and dioxygen atmosphere). Some small metals ions such as Ti^{4+} show difficulties to be incorporated into structures which demand high coordination numbers. Conversely, it is not a trivial task to introduce metals that favour high coordination numbers such as lanthanides into an octahedral geometry. Therefore, transmetalation methods may help to overcome some of these problems until a certain extent, expanding the synthetic possibilities in the PCPs chemistry.

Nevertheless, attaining a complete and controlled exchange can sometimes be a challenging task. Metal nodes substitution requires overcoming large kinetic barriers, diffusion problems due to the limited pore sizes, steric hindrances imposed by the ligand and framework and confinement into unusual geometries. If one wants to make of transmetalation a rational tool to prepare new materials with prefixed properties, a proper understanding of the factors which govern the metal exchange and its mechanism becomes pivotal.

Firstly, one must be able to predict, to some extent, which metal ions will replace the others from the framework. In so doing, one must take into account the features of the leaving and inserting metal ions such as the size, geometric restriction on the coordination sphere and electronic properties, as well as the role of the ligand field strength. As a very general approach, metal sites having high coordination numbers will undergo less degree of exchange than those containing open metal sites unless their weak field ligands dissociate readily. Those ions with greater charge or smaller radius are incorporated easier because they form stronger bonds. The majority of studies about transmetalation reported so far, claim that Cu^{2+} typically inserts to the greatest extent and is the least reversible since it forms more covalent and thermodynamically stable bonds.[19–24] However, less electronegative cations like Pb^{2+}, Cd^{2+} or Mn^{2+} form more labile bonds, allowing them to undergo a faster metal substitution.[25,26] Therefore, information about the kinetics and thermodynamics of the process is required, especially for the preparation of heterometallic species, which can be achieved by carefully choosing the initial concentration of the solution of the inserting ion.

Yao and co-workers reported an example of metal ion exchange process which illustrates the metal ion preferences mentioned above. They synthesised a material called SUMOF-1-Zn with formula $[Zn_6(BTB)_4(bpy)_3] \cdot (sol)_x$ (H_3BTB = 4,4',4''-benzene-1,3,5-triyl-benzoic acid), containing the commonly used paddle-wheel entity $[M_2(RCOO)_4]$ as SBU. The study of the exchange of the Zn^{2+} ions from the SBU with different transition metal ions revealed interesting conclusions.[23] Scheme 1 summarizes the transmetalation reactions that take place.

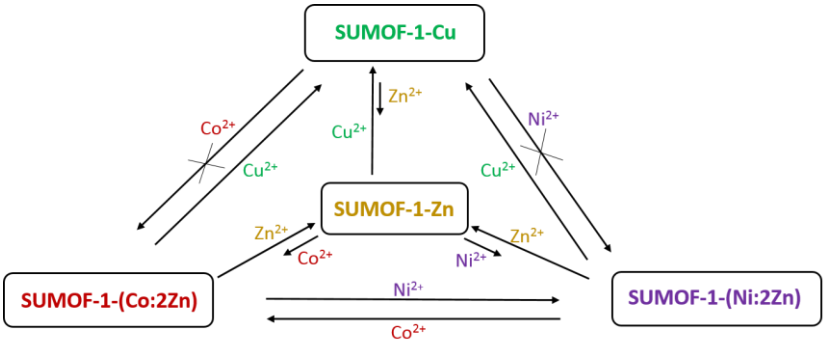

Scheme 1. Total and partial substitution processes of the intra-framework metal ions at the paddle-wheel motif in SUMOF-1.

They show a complete exchange of the Zn^{2+} by the Cu^{2+} metal ions in SUMOF-1-Zn. Interestingly, the reverse ion exchange only takes place up to 38 % yield. The parent material SUMOF-1-Zn can also show a partial exchange of the Zn^{2+} by Ni^{2+} and Co^{2+} ions, (38 and 35 % of the Zn^{2+} ions being substituted, respectively). These two exchange reactions are reversible and the Ni^{2+} and Co^{2+} atoms can be completely substituted with Zn^{2+} ions. Overall, the relative stabilities of the metal-carboxylate paddle-wheel motifs within this SUMOF-1 family follow the trend Co ≈ Ni < Zn < Cu which is consistent with the Irving-Willian series.[27]

However, the metal exchange processes neither necessary obey the observed trend above nor the general metal-ion considerations explained before since the framework itself also plays a key role. The metal nodes are embedded in the lattice of the PCP so they do not possess the degrees of freedom that molecules in solution do. Considering that the lattice limits the geometrical distortions, a certain degree of flexibility is needed. Moreover, the process is likely influenced by diffusion and size effects, because the exchange mainly occurs within the pores.

An illustrative example is the work done by Song and co-workers[28] where the authors demonstrate that the transmetalation process is not only influenced by the chemical nature of the exchanged ion but also by the flexibility of the framework. They use the two MOFs, Zn-HKUST-1 and Zn-PMOF-2 having the same $Zn_2(RCOO)_4$ paddle-wheel SBUs but linked through ligands of different size and flexibility (see Figure 3) to investigate their transmetalation with Cu(II) ions. While the complete transmetalation could be accomplished in a flexible Zn-PMOF-2 framework made with large organic linkers, only up to 56 % of the framework Zn(II) ions were replaced from the rigid Zn-HKUST-1 system consisting of small and rigid organic linkers.

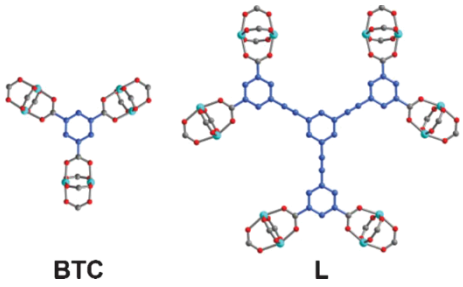

Figure 3. BTC and L ligands interlinking three Zn(II) paddle-wheel SBUs within the MOF Zn-HKUST-1 and six Zn(II) paddle-wheel SBUs within the MOF Zn-PMOF-2, respectively.

The proper choice of the solvent also becomes a fundamental factor to take in account. Solvents are involved in the metal exchange mechanisms in diverse manners: solvating the inserting metal ions, coordinating the leaving metal ions and/or stabilising the intermediate species. Therefore, the consideration of the solvent properties (dielectric constant, molecular size or ligand field strength) might become a powerful handle in order to target the exchange. For instance, Song and co-workers reported in their aforementioned work (see above) that the substitution of Zn^{2+} ions in their MOF Zn-HKUST-1 with Cu^{2+} ions occurs more slowly in DMF than in methanol, a solvent with a stronger field ligand.[28]

The metal exchange processes look into the improvement of the PCPs properties such as thermal stability, robustness, permanent porosity, etc. and/or into de incorporation of new properties such as magnetic, catalytic and luminescent, selective sorption, etc.[3,29–32]

The most usual application for cation exchanged PCPs is gas storage since inserting cations with open coordination sites and open shell electronic structures can enhance the adsorption interactions between the framework and the guest molecules. Besides, some metal substitutions led to more stable materials. Continuing with the work by Song *et al.*,[28] they illustrate how by replacing the Zn^{2+} metal nodes from their Zn-HKUST-1 material by Cu^{2+} ions, an improvement in the stability and thus, in the adsorption properties of the MOF, can be achieved. The Cu-exchanged material exhibits a BET (Brunauer–Emmett–Teller) surface area of 3550 $m^2\ g^{-1}$ and a N_2 uptake of 942 $cm^3\ g^{-1}$, while the original Zn-HKUST-1 is not stable and loses its crystallinity during the activation step and shows no significant N_2 sorption (see Figure 4).

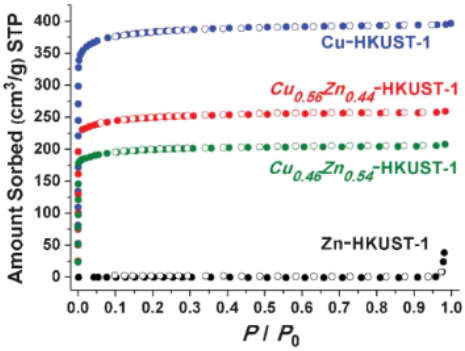

Figure 4. The N_2 sorption isotherms of Zn-HKUST-1, Cu-HKUST-1 and two partially transmetalated Zn-HKUST-1 materials.

This technique has been also explored for the improvement of the CO_2 sorption affording successful results such as the work done by Lau *et al*. where they partially replace the Zr(IV) ions by Ti(IV) ions in the MOF UiO-66.[33] The smaller Ti(IV) ions may decrease the pore sizes within the framework to be closer to the ideal pore sizes for CO_2 adsorption, enhancing thus the CO_2 uptake of Ti-exchanged UiO-66.

Transmetalation also offers an attractive strategy for the incorporation of catalytic sites. Eddaoudi and coauthors applied metal-ion exchange to their material porph@MOM-10 consisting of a [*meso*-tetra(*N*-methyl-4-pyridyl)porphine tetratosylate] encapsulated in the $[Cd_6(bpt)_4Cl_4(H_2O)_4]$ (bpt = biphenyl-3,4',5-tricarboxylate) (see Figure 5).[26] By replacing the Cd(II) atoms by Mn(II) and Cu(II) *via* SC to SC processes, the resulting derivatives are permanently porous and exhibit catalytic activity for the epoxidation of *trans*-stilbene affording a 75 and 79 % percentages of

conversion, respectively (compared to only a 7% conversion provided by the original Cd(II) material).

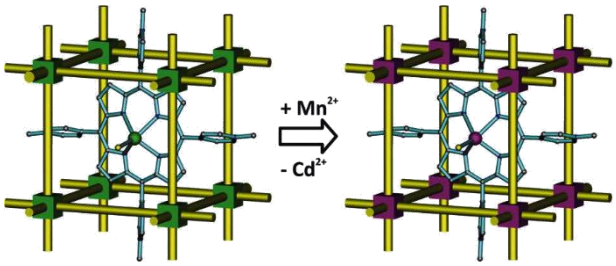

Figure 5. Schematic representation of the transmetalation process in the porph@MOM-10 framework.

Last, but not least, exchanged materials represent an excellent platform for reactivity studies, since some of the resulting metal assemblies within the frameworks cannot be achieved in the traditional molecular chemistry. For instance, a ligand field analysis of Ni-MOF-5 indicates that the tripodal ligand $Zn_3O(COO)_6$ is by far the strongest ligand to stabilise a Ni^{2+} ion in a pseudo-tetrahedral geometry (see Figure 6). This is remarkable because ligand fields of similar strength coerce the Ni^{2+} ion to assume a square planar configuration.[34]

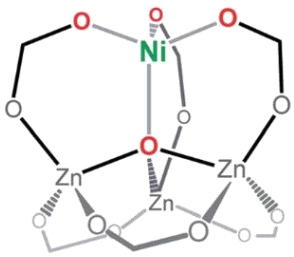

Figure 6. Illustration of the $Zn_3O(COO)_6$ SBU of MOF-5 as a tripodal support that reinforces a tetrahedral oxygen ligand field.

2.2. Previous work

Although some preliminary attempts of cation exchange have been performed in our group, the corresponding studies were not sufficiently developed and the results have not been reported. Herein, in order to investigate the diverse post-modification approaches, we have chosen the well-known three-dimensional PCP of formula $Na^{I}_4\{Mn^{II}_4[Cu^{II}_2(Me_3mpba)_2]_3\} \cdot 60H_2O$ (**8**) [Me_3mpba^{4-}= *N,N'*-2,4,6-trimethyl-1,3-

phenylenebis(oxamate)] for several reasons. Firstly, it is a well-known system in our group and both its synthesis and its characterisation are well established; secondly, it is a robust and water stable material which facilitates the SC to SC transformations; in addition, its anionic framework provides an outstanding platform to carry out the cation substitution experiments. Finally, the combination of porosity and long-range magnetic ordering in the same material makes **8** a promising candidate for the preparation of multifunctional magnetic materials.

The anionic compound **8** is prepared following the metalloligand approach reacting the dicopper(II) complex $Na_4[Cu_2(Me_3mpba)_2] \cdot 4H_2O$ with $Mn(NO_3)_2 \cdot 4H_2O$ (see Schemes 2 and 3).

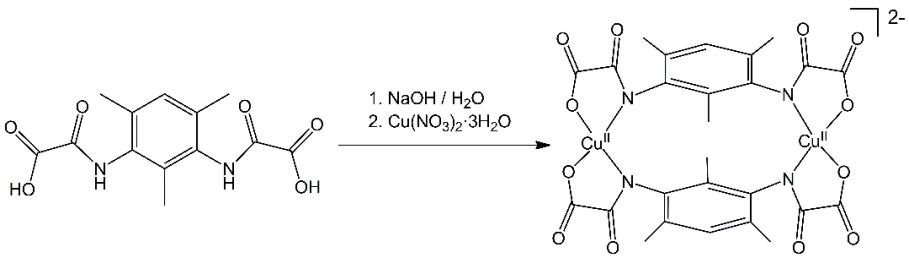

Scheme 2. Synthetic route for the preparation of the dicopper(II) metalloligand $Na_4[Cu_2(Me_3mpba)_2] \cdot 4H_2O$.

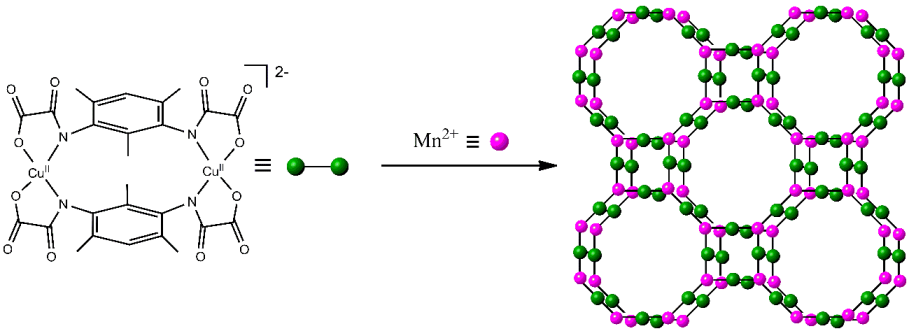

Scheme 3. Metalloligand strategy fot the construction of the PCP $Na^{I}_4\{Mn^{II}_4[Cu^{II}_2(Me_3mpba)_2]_3\} \cdot 60H_2O$ using the dinuclear metallacyclophane $[Cu_2(Me_3mpba)_2]^{4-}$ toward tris-chelated Mn(II) ions.

Compound **8** crystallises in the *P4/mmm* space group of the tetragonal system. It consists of an anionic 3D open-framework structure with hydrated Na^+ countercations occupying its cavities together with crystallisation water molecules. The 3D network can be described as an extended parallel array of anionic oxamato-bridged $Mn^{II}_4Cu^{II}_6$ layers growing in the *ab* plane with a mixed square/octagonal ($4{\cdot}8^2$) net topology that are further interconnected through the two *m*-phenylene spacers among the Cu(II) ions in an up-and-down disposition to yield a trinodal (3,4,4) net with a $(6^3)(6^4{\cdot}8^2)(6^4{\cdot}8{\cdot}10)$ symbol.

The resulting open-framework structure presents a trimodal pore size distribution along the crystallographic *c* axis with small square pores and two types of large octagonal pores. These two types of wide octagonal channels result from the distinct orientation of the trimethyl-substituted phenylene spacers pointing inward or outward of the channels (see Figure 7). Thus, the channels where the aliphatic groups point inward are hydrophobic while those where the aliphatic groups point outward are hydrophilic. This situation is reflected both in their relative diameters of 1.5 and 2.2 nm for the hydrophobic and hydrophilic pores, respectively, and in their different occupation by the crystallisation water molecules and the hydrated Na^+ countercations.

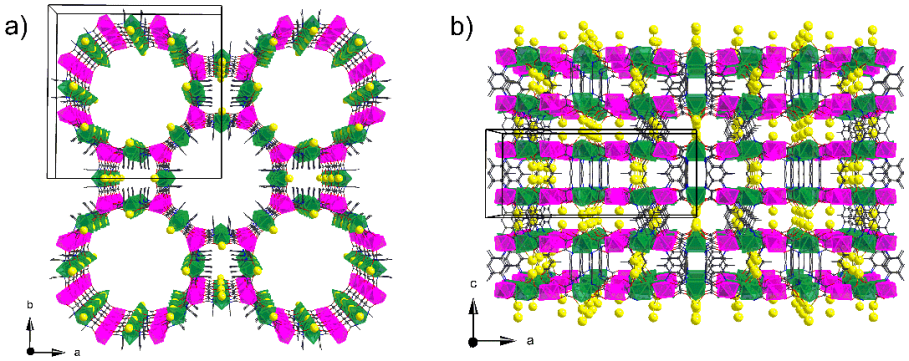

Figure 7. Perspective view of the 3D anionic network of **8** (a) along the crystallographic *c* and (b) *b* axes. Cu(II) and Mn(II) atoms from the coordination network are represented as green and purple polyhedral, respectively, whereas the Na(I) atoms occupying the channels are depicted as yellow spheres. Water molecules are omitted for clarity.

Therefore, the free water molecules are unequally hosted within both types of octagonal channels, whereas the tetraaquasodium(I) motifs which are weakly bounded to the carboxylate and carbonyl oxygen atoms from the oxamato groups ocuppy the hydrophilic channels. The estimated empty volume without the crystallisation water molecules is 11997 Å^3, a value which represents up to *ca*. 60 % of the potential void space per unit cell volume (V = 20075 Å^3).

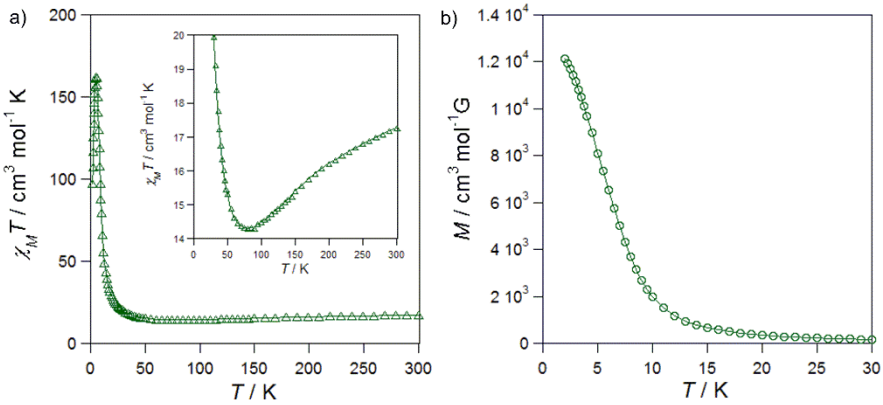

Figure 8. (a) Temperature dependence of the product of the direct current (dc) molar magnetic susceptibility by the temperature ($\chi_M T$) of **8** (the inset shows the minimum of $\chi_M T$ in detail). (b) Field-Cooled Magnetization of **8**. The solid lines are only eye-guides.

The magnetic properties of **8** have also been previously reported. The presence of a minimum in the $\chi_M T$ vs. T plot (Figure 8a) is characteristic of an overall ferrimagnetic behaviour resulting from the moderately strong antiferromagnetic interaction between the Mn^{II} and the Cu^{II} ions through the oxamato bridge. The long-range magnetic ordering that **5** exhibits (Figure 8b), arises from the occurrence of an effective interlayer ferromagnetic interaction resulting from the weak ferromagnetic coupling between the Cu^{II} ions across the double 2,4,6-trimethylphenylenebis(amidate) bridges within the dinuclear metallacyclophane pillaring units.

2.3. Objectives

The first objective is to synthesise and characterise a new series of multifunctional materials derived from the already well-known anionic PCP **8**, which serves as a platform to test the cation exchange approach. The Na^+ countercations will be exchanged with other alkali cations leading to a new family of analogue PCPs aiming at investigating the effect of the alkaline countercation replacement on the structure stability and the final properties of the material.

Following this vein, the second objective deals with the substitution of the extra-framework cations of the porous magnet **8** with a cationic metal complex displaying magnetic properties as well. Thus, we will investigate the incorporation of new properties through cation exchange and the possible interaction between both magnetic behaviours.

The third objective concerns the design and performance of SC to SC metal-exchange experiments in order to substitute the extra- and/or intra-framework metal ions of a parent PCP to get a new family of multifunctional PCPs which cannot be obtained *via* direct synthesis. They will be thoroughly characterised in order to prove their isostructurality and their physical properties will be deeply studied. We want to demonstrate that the post-modification techniques constitute an efficient approach for the introduction of new physical properties in a preformed PCP. The possible substitution of the different metal sites within the PCP will be investigated, aiming at shedding some light on the exchange mechanism.

2.4. References

1 M. Kim, J. F. Cahill, H. Fei, K. A. Prather and S. M. Cohen, *J. Am. Chem. Soc.*, 2012, **134**, 18082–18088.

2 C. K. Brozek, A. F. Cozzolino, S. J. Teat, Y. Chen and M. Dincă, *Chem. Mater.*, 2013, **25**, 2998–3002.

3 C. K. Brozek, L. Bellarosa, T. Soejima, T. V. Clark, N. Lõpez and M. Dincă, *Chem. - A Eur. J.*, 2014, **20**, 6871–6874.

4 C. K. Brozek and M. Dincă, *Chem. Soc. Rev.*, 2014, **43**, 5456–5467.

5 M. Huang, A. Adnot and S. Kaliaguine, *J. Am. Chem. Soc.*, 1992, **114**, 10005–10010.

6 O. M. Yaghi, Z. Sun, D. A. Richardson and T. L. Groy, *J. Am. Chem. Soc.*, 1994, **116**, 807–808.

7 O. M. Yaghi, H. Li, C. Davis, D. Richardson and T. L. Groy, *Acc. Chem. Res.*, 1998, **31**, 474–484.

8 Y. Liu, V. C. Kravtsov, R. Larsen and M. Eddaoudi, *Chem. Commun.*, 2006, 1488–1490.

9 M. Dinca and J. R. Long, *J. Am. Chem. Soc.*, 2007, **129**, 11172–11176.

10 S. Yang, X. Lin, A. J. Blake, K. M. Thomas, P. Hubberstey, N. R. Champness and M. Schröder, *Chem. Commun. (Camb).*, 2008, **7345**, 6108–6110.

11 D. Himsl, D. Wallacher and M. Hartmann, *Angew. Chem. Int. Ed. Engl.*, 2009, **48**, 4639–4642.

12 S. Yang, X. Lin, A. J. Blake, G. S. Walker, P. Hubberstey, N. R. Champness and M. Schröder, *Nat. Chem.*, 2009, **1**, 487–493.

13 S. Yang, G. S. B. Martin, J. J. Titman, A. J. Blake, D. R. Allan, N. R. Champness and M. Schröder, *Inorg. Chem.*, 2011, **50**, 9374–9384.

14 D. T. Genna, A. G. Wong-Foy, A. J. Matzger and M. S. Sanford, *J. Am. Chem. Soc.*, 2013, **135**, 10586–10589.

15 J. An, C. M. Shade, D. A. Chengelis-Czegan, S. Petoud and N. L. Rosi, *J. Am. Chem. Soc.*, 2011, **133**, 1220–1223.

16 J.-S. Qin, S.-R. Zhang, D.-Y. Du, P. Shen, S.-J. Bao, Y.-Q. Lan and Z.-M. Su, *Chemistry*, 2014, **20**, 5625–5630.

17 S.-N. Zhao, X.-Z. Song, M. Zhu, X. Meng, L.-L. Wu, J. Feng, S.-Y. Song and H.-J. Zhang, *Chem. - A Eur. J.*, 2015, **21**, 9748–9752.

18 J. An, S. J. Geib and N. L. Rosi, *J. Am. Chem. Soc.*, 2009, **131**, 8376–8377.

19 T. K. Prasad, D. H. Hong and M. P. Suh, *Chem. - A Eur. J.*, 2010, **16**, 14043–14050.

20 Z.-J. Zhang, W. Shi, Z. Niu, H.-H. Li, B. Zhao, P. Cheng, D.-Z. Liao and S.-P. Yan, *Chem. Commun. (Camb).*, 2011, **47**, 6425–6427.

21 G. Mukherjee and K. Biradha, *Chem. Commun. (Camb).*, 2012, **48**, 4293–4295.

22 X.-J. Wang, P.-Z. Li, L. Liu, Q. Zhang, P. Borah, J. D. Wong, X. X. Chan, G. Rakesh, Y. Li and Y. Zhao, *Chem. Commun. (Camb).*, 2012, **48**, 10286–10288.

23 Q. Yao, J. Sun, K. Li, J. Su, M. V. Peskov and X. Zou, *Dalt. Trans.*, 2012, **41**, 3953–3955.

24 Z. Wei, W. Lu, H. Jiang and H. Zhou, *Inorg. Chem.*, 2013, **52**, 1164–1166.

25 J. Li, L. Li, H. Hou and Y. Fan, *Cryst. Growth Des.*, 2009, **9**, 4504–4513.

26 Z. Zhang, L. Zhang, L. Wojtas, P. Nugent, M. Eddaoudi and M. J. Zaworotko, *J. Am. Chem. Soc.*, 2012, **134**, 924–927.

27 H. Irving and R. J. P. Williams, *J. Chem. Soc.*, 1953, 3192–3210.

28 X. Song, S. Jeong, D. Kim and M. S. Lah, *CrystEngComm*, 2012, **14**, 5753–5756.

29 Y. Kim, S. Das, S. Bhattacharya, S. Hong, M. G. Kim, M. Yoon, S. Natarajan and K. Kim, *Chem. - A Eur. J.*, 2012, **18**, 16642–16648.

30 C. K. Brozek and M. Dincă, *J. Am. Chem. Soc.*, 2013, **135**, 12886–12891.

31 O. Karagiaridi, W. Bury, D. Fairen-Jimenez, C. E. Wilmer, A. A. Sarjeant, J. T. Hupp and O. K. Farha, *Inorg. Chem.*, 2014, **53**, 10432–10436.

32 C. K. Brozek, J. T. Miller, S. A. Stoian and M. Dinca, *J. Am. Chem. Soc.*, 2015, **137**, 7495–7501.

33 C. Hon Lau, R. Babarao and M. R. Hill, *Chem. Commun.*, 2013, **49**, 3634–3636.

34 C. K. Brozek and M. Dincă, *Chem. Sci.*, 2012, **3**, 2110–2113.

Part 2.A

MMs obtained by Cation Exchange

The sodium(I) cations of the compound $Na^{I}_4\{Mn^{II}_4[Cu^{II}_2(Me_3mpba)_2]_3 \cdot 60H_2O\}_n$ can be exchanged with other alkaline cations affording two new isostructural materials. Their physical properties are then studied to determine the possible influence of the different cations on the structure and properties.

2.A.1. Synthesis

Crystals of the ancestor MOF **8** were immersed into saturated aqueous solutions of $LiCl \cdot 6H_2O$ and $KCl \cdot 6H_2O$ and the alkaline cation exchange *via* SC to SC transformation occurred to afford the new MOFs $Li^{I}_4\{Mn^{II}_4[Cu^{II}_2(Me_3mpba)_2]_3 \cdot 68H_2O\}_n$ (**9**) and $K^{I}_4\{Mn^{II}_4[Cu^{II}_2(Me_3mpba)_2]_3 \cdot 69H_2O\}_n$ (**10**), respectively (Scheme 4).

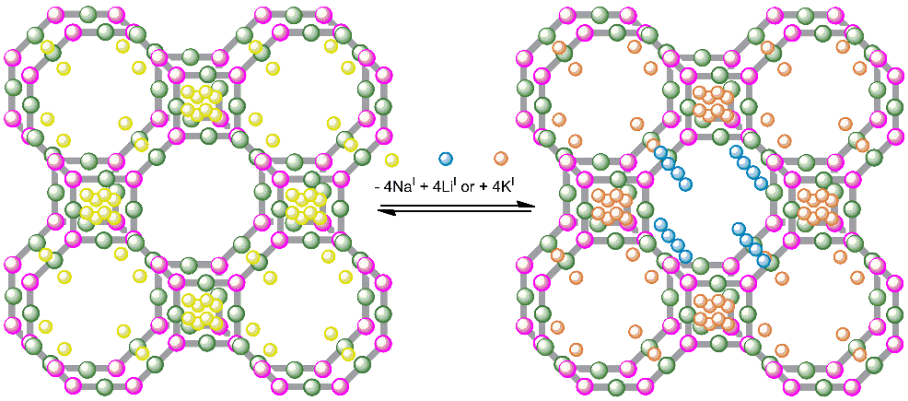

Scheme 4. Cation exchange approach for the replacement of the sodium(I) ions in the anionic framework of **8** with lithium(I) or potassium(I) cations affording the new MOFs **9** and **10**. The pink and green spheres represent the Mn(II) and Cu(II) atoms from the covalent framework respectively, whilst the yellow, blue and orange spheres stand for the sodium(I), lithium(I) and potassium(I) counterions, respectively.

Although inductively coupled plasma atomic absorption spectroscopy (ICP-AES) and scanning electron microscopy (SEM) measurements indicate that the most of the cations are exchanged in a few minutes (preventing any possible kinetic analysis), the crystals were left into the saturated solutions for 24 hours to ensure the complete replacement. Moreover, preliminary results pointed out the reversibility of the cation substitution.

2.A.2. Crystal Structure and Characterisation

Compounds **8**-**10** are isostructural and they crystallise in the *P4/mmm* space group of the tetragonal system. Their structure consist of an anionic 3D Mn_4Cu_6 open-framework exhibiting a pillared square/octagonal layer structural architecture containing either small square channels or two types of large octagonal pores along the crystallographic *c* axis. The presence of these two types of narrow and wide octagonal pores (relative diameters of ca. 1.5 and 2.0 nm) arises from the different disposition of the trimethyl-substituted phenylene spacers directing inward or outward of the voids, respectively. The estimated empty volumes without the highly disordered crystallisation water molecules are slightly different in the three isostructural compounds [11997 (**8**), 13109 (**9**) and 12204 $Å^3$ (**10**)], and they correspond to 60.0 (**8**), 63.1 (**9**) and 55.8 % (**10**) of potential void per unit cell volume [V = 20075 (**8**), 20770 (**9**) and 21868 $Å^3$ (**10**)].

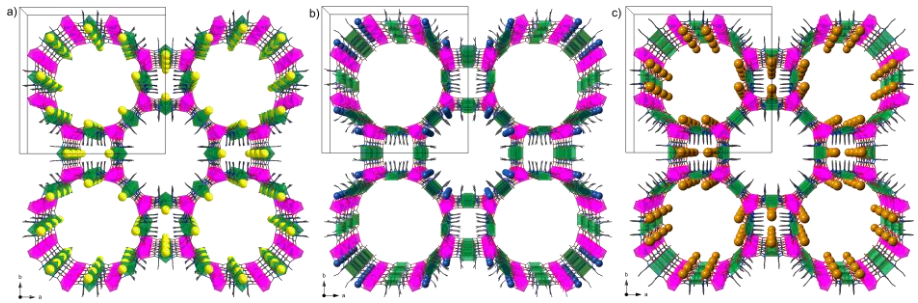

Figure 9. Perspective view of the 3D anionic network of **8** (a), **9** (b) and **10** (c) along the crystallographic *c* axis. Copper and manganese atoms from the covalent network are represented by green and purple polyhedra, respectively, whereas the sodium (**8**), lithium (**9**) and potassium (**10**) atoms occupying the channels are depicted as yellow, blue and orange spheres, respectively (free and coordinated water molecules are omitted for clarity).

The hydrated charge-counterbalancing alkaline M^+ cations [M = Na (**8**), Li (**9**) and (**10**)] exhibit a different distribution within the channels along both the parallel and perpendicular directions, most likely due to the variation in the ionic radii of these cations [0.68 (Li^+), 0.95 (Na^+) and 1.33 Å (K^+)]. While the small-sized Li^+ ions occupy only the narrow octagonal channels in **9**, the bigger Na^+ and K^+ are hosted in the square and

wide octagonal channels in **8** and **10**, respectively. Moreover, Li^+ ions are located in the intralayer space in **9**, whereas Na^+ and K^+ occupy the interlayer space in **8** and **10**, respectively (see Figure 9 and 10).

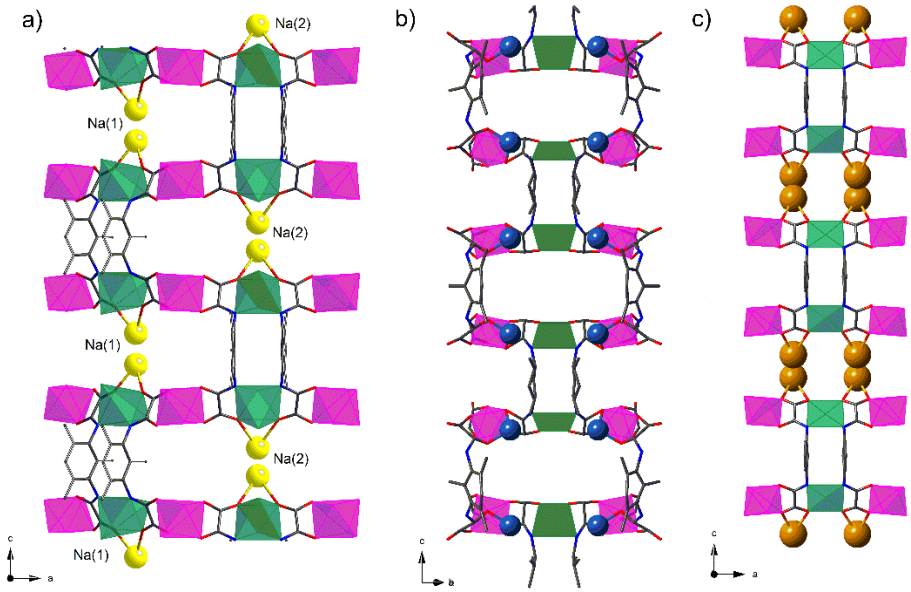

Figure 10. Perspective views fragments of the coordination network of **8** (a), **9** (b) and **10** (c) emphasising the coordinative interactions of the alkaline cations. Copper and manganese atoms from the covalent network are represented by green and purple polyhedra, respectively, whereas the sodium (**8**), lithium (**9**) and potassium (**10**) atoms occupying the channels are depicted as yellow, blue and orange spheres respectively.

Figure 10 shows that both type of Na^+ ions in **8**, (Na1 and Na2), which are located in the larger octagonal pores also full with water molecules, are simultaneously coordinated to the carboxylate-oxygen atoms from the two Me_3mpba ligands, forming the copper(II) basal plane. In contrast, Li^+ and K^+ ions in **9** and **10** respectively, are coordinated to the carbonyl-oxygen atoms that form the coordination environment of the octahedral manganese(II) ions (see Figures 9 and 10).

The water contents of **8**-**10** has been determined by thermogravimetric analysis (TGA) under a dry N_2 atmosphere. A fast mass loss from room temperature to around 150 °C can be observed for all three compounds. It is followed by a *plateau* in the range *ca*. 150-300 °C, and then its decomposition starts (Figure 11). The values of the mass loss *ca*. 31 (**8**), 34 (**9**) and 35 % (**10**) at 125 °C, correspond to 60, 68 and 69 water molecules per formula unit, respectively.

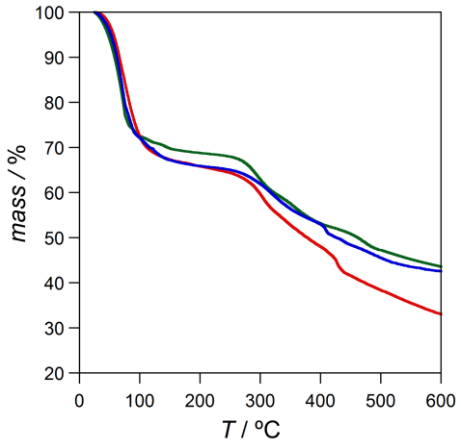

Figure 11. TGA of **8** (green), **9** (red) and **10** (blue) under a dry N_2 atmosphere.

Powder X-ray diffraction (PXRD) patterns of polycrystalline samples of **8**-**10** have been measured in water suspensions to prevent the partial loss of water at room temperature. Within each sample, the experimental PXRD pattern profile is consistent with the calculated one (see Figure 12) confirming the purity of the bulk samples. Moreover the comparison of the PXRD patterns of **8**-**10** further confirms that all three compounds are isostructural and thus, that the exchange process of the alkaline cations does not modify the

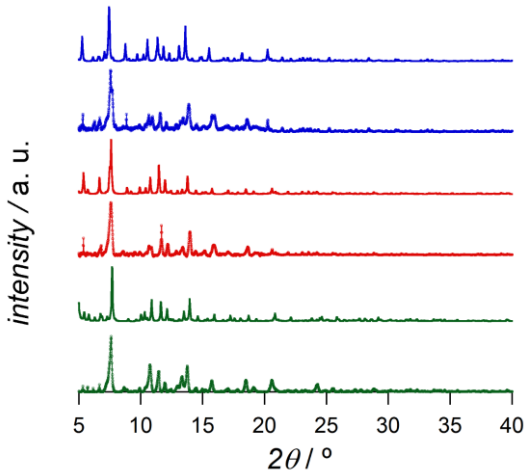

Figure 12. Experimental (—) and calculated (-o-) PXRD pattern profiles of the hydrated phases of **8** (green), **9** (red) and **10** (blue) measured as water suspensions in the 2θ range 5.0–40.0° at r.t.

open-framework structures, as revealed by the X-ray diffraction results on single crystals of the samples.

PXRD studies were then carried out for **8**-**10** under heating from 298 up to 370 K in order to analyse the relative structural stability of each compound upon water loss (Figure 13). The variable-temperature PXRD pattern shows a total loss of the crystallinity for the starting material **8**, even at room temperature (Figure 13). In contrast, the PXRD patterns of **9** and **10** reveal a retention of the crystallinity over the whole temperature range investigated. The overall situation reveals that **8** seems to become amorphous upon removal of water whereas the frameworks of **9** and **10** remain crystalline. The different locations of the alkaline cations within the open-frameworks must lie at the origin of the enhanced structural stability of **9** and **10** compared to **8.**

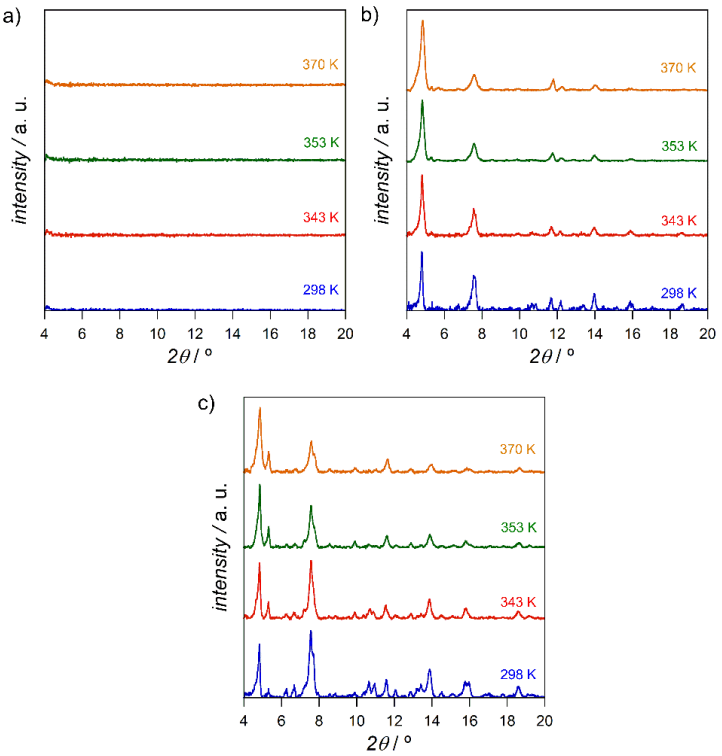

Figure 13. Variable temperature PXRD patterns of dehydrated **8** (a), **9** (b) and **10** (c) at 298 (blue), 343 (red), 353 (green), and 370 K (orange).

The analysis of the crystal structure of **8** shows that both Na1 and Na2 atoms are located inside the larger octagonal pores simultaneously coordinated to the carboxylate-atoms from the two Me_3mpba ligands which constitute the copper(II) basal plane (see Figure 10). Upon water removal, this feature can originate a reorientation of the organic linkers, ultimately leading to the structural collapse. This tetrahedral distortion of the copper(II) ions has already been reported for other oxamato-based PCPs.[1] In contrast, the Li and K atoms in **9** and **10** respectively, are coordinated to the carbonyl-oxygen atoms that build the coordination environment of the octahedral manganese(II) ions (see Figure 10). The possible distortions in the Mn(II) octahedral geometry that are caused by displacements of the coordinated Li or K atoms when losing the water molecules would be much softer than those predicted for a square to tetrahedral distortion and would not lead to a final structural collapse. Therefore, the behaviour predicted through the analysis of the crystal structures of **8**-**10**, matches with the observed behaviour illustrated by the PXRD patterns.

2.A.3. Physical Properties

The stability of **8**-**10** was also proven in terms of gas sorption properties. All samples were dehydrated at 80 °C under reduced pressure for 16 h prior to the sorption measurements to afford the corresponding dehydrated phases **8'**-**10'**.

The low-pressure N_2 adsorption isotherms at 77 K for **8'**-**10'** show remarkable differences. While the original **8'** displays hardly any adsorption of N_2, its lithium(I) (**9'**) and potassium(I) (**10'**) derivatives exhibit a much greater uptake (Figure 14a). For compounds **9'** and **10'**, the calculated BET surface areas [270 (**9'**) and 200 m^2g^{-1} (**10'**)] follow the trend expected according to the estimated volumes [13109 (**9**) and 12204 $Å^3$ (**10**)].

A similar trend to that of N_2 adsorption is observed for the high-pressure H_2 isotherms measured at 77 K. In contrast, the adsorption isotherms of CO_2 and CH_4 (both measured at 273 K) indicate that **8'** and **9'** have comparable uptakes since especially

their CO_2 isotherms almost overlap (Figure 14c). The results for **8'** can be attributed to its loss of structural stability upon dehydration, which obviously leads to slightly smaller and less homogeneous pores and this is translated into less uptakes. Even so, its channels are accessible to smaller molecules such as CO_2.

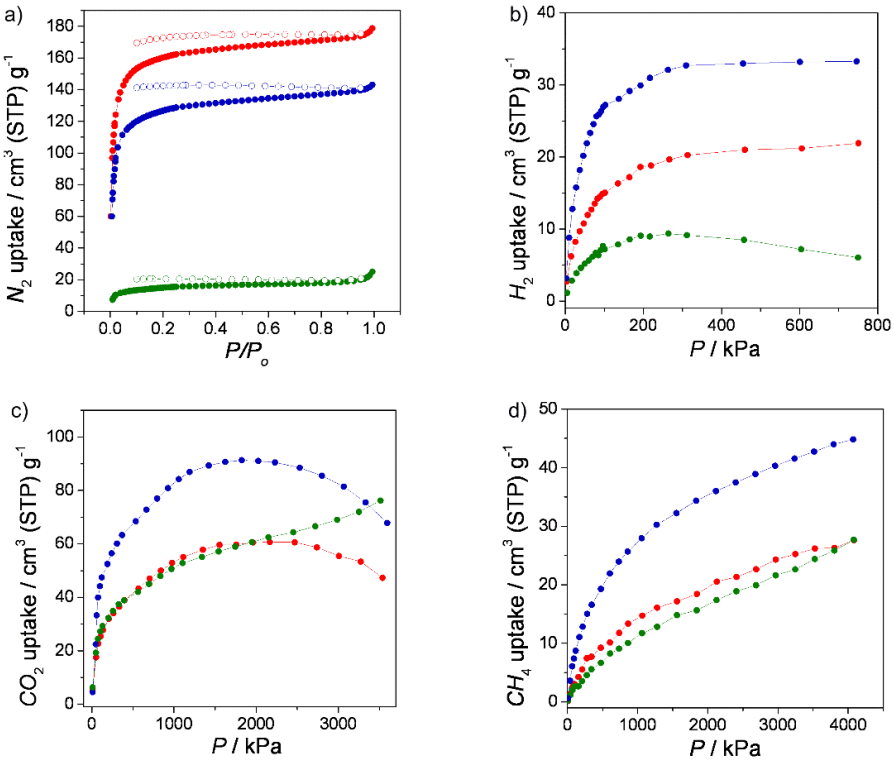

Figure 14. (a) Low-pressure N_2 at 77 K, high-pressure (b) H_2 at 77 K, (c) CO_2 at 273 K and (d) CH_4 at 273 K sorption isotherms for **8'** (green), **6'** (red), and **7'** (blue). Filled and empty symbols indicate the adsorption and desorption isotherms, respectively.

When comparing the adsorptive behaviour for **9'** and **10'**, it is striking to observe that while the Li(I)-containing sample displays a larger BET area, the K(I)-containing sample shows a much higher affinity for H_2, CO_2 and CH_4 (see Figure 14). These results demonstrate that both the nature and location of the cation within the framework are of fundamental importance in the adsorptive properties of the material. Interestingly, these different uptake results for different adsorbates evidence that we are not only

able to achieve an important increase in the sorption capacity in a given material *via* cation exchange but, more importantly, they reveal that we can also modify the gas selectivity.

Aiming at studying the effect of the alkaline countercation replacement and the water loss along this series on the magnetic properties, we measured them in both the direct current (dc) and alternating current (ac) regimes, for both the hydrated (**8**-**10**) and dehydrated phases (**8'**-**10'**).

The $\chi_M T$ *vs.* *T* plots (χ_M being the dc molar magnetic susceptibility per $Cu^{II}_6Mn^{II}_4$ unit and *T* the temperature) for both **8**-**10** and **8'**-**10**, show the same qualitative general behaviour (Figure 15). They exhibit a characteristic minimum which is indicative of a ferrimagnetic behaviour resulting from the intralayer antiferromagnetic interactions between the Cu^{II} and high-spin Mn^{II} ions through the oxamato bridge, as previously found in other oxamate-based manganese(II)-copper(II) layered compounds.[2,3]

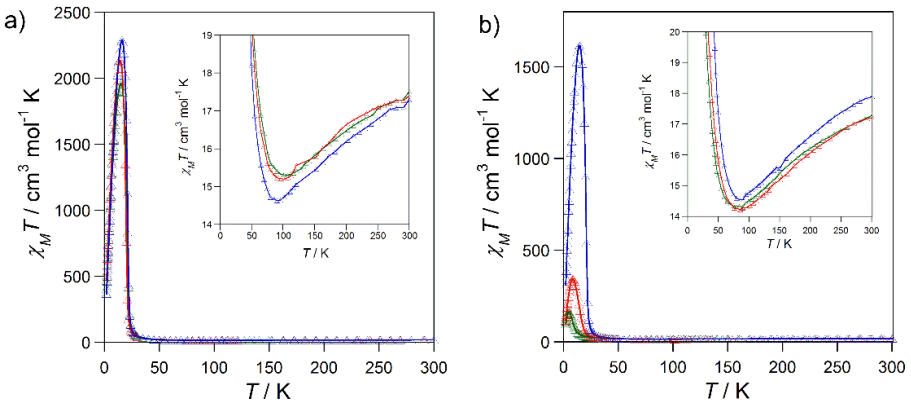

Figure 15. Temperature dependence of the product of the direct current (dc) molar magnetic susceptibility by the temperature ($\chi_M T$) of the (a) hydrated and (b) dehydrated phases of **8** (green), **9** (red) and **10** (blue). The inset shows the minima of $\chi_M T$ for **8**-**10** in detail. The solid lines are only eye-guides.

This common ferrimagnetic behaviour of **8**-**10** was also suggested by the *M vs*. *H* plots at 2.0 K (where *M* is de magnetization per $Cu^{II}_6Mn^{II}_4$ unit and *H* is the applied dc

magnetic field), which reveal, however non-negligible differences between the hydrated and the dehydrated phases (see Figure 16).

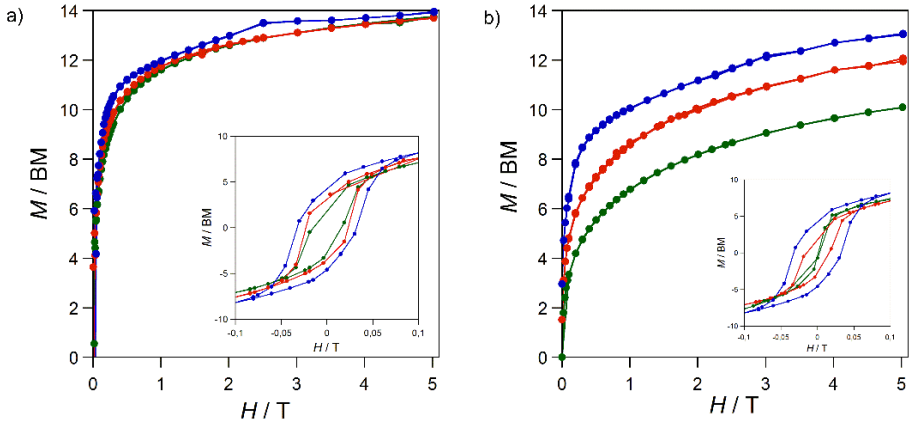

Figure 16. Field dependence of the magnetization (*M*) of the (a) hydrated and (b) dehydrated phases of **8** (green), **9** (red) and **10** (blue) at $T = 2.0$ K. The insets show the hysteresis loops in detail. The solid lines are only eye-guides.

The isothermal magnetization curves for **8**-**10** rapidly saturate at low field values, exhibiting maximum values of *M* at 5 T, which are close to the calculated value of the saturation magnetization for the antiparallel spin alignment of the high-spin Mn^{II} (S_{Mn} = 5/2) and Cu^{II} (S_{Cu} = 1/2) ions [$M_S = (4g_{Mn}S_{Mn} - 6g_{Cu}S_{Cu})N\beta = 13.90\ N\beta$ with g_{Mn} = 2.0 and g_{Cu} = 2.1] (Figure 16a).

In contrast, the isothermal magnetization curves for the dehydrated phases **8'**-**10'** do not saturate even at high fields, the maximum values of *M* at 5 T being lower than the calculate saturation magnetization and also dependent on the nature of the alkaline counteraction (see Figure 16b). In addition, the hydrated phases of **8**-**10** show magnetic hysteresis loops with rather similar but low values of the coercive magnetic field around 400 G that are typical of soft magnets (inset of Figure 16a), whereas those almost negligible of the dehydrated phases increase from **8** to **10** (inset of Figure 16b).

These differences in the magnetic behaviour between the hydrated and dehydrated phases of **8**-**10** are also shown in the field-cooled magnetization (FCM) *vs*. *T* plots (see Figure 17).

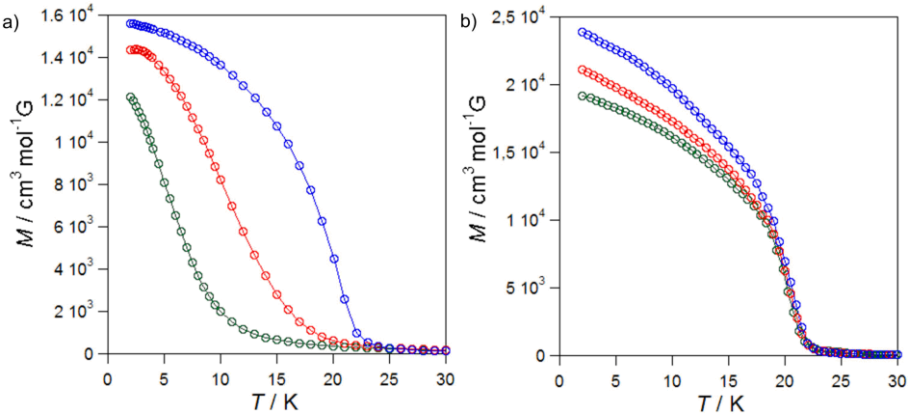

Figure 17. Field-cooled magnetization (FCM) of the (a) dehydrated and (b) hydrated phases of **8** (green), **9** (red) and **10** (blue). The solid lines are only eye-guides.

While the FCM curves of the hydrated phases show an abrupt increase indicating a long-range magnetic ordering at around 20.0 K for all three compounds (Figure 17b), those of the dehydrated phases continuously shift to lower temperatures following the trend **10'** > **9'** > **8'** (Figure 17a). The long-range magnetic ordering is consistent with the occurrence of an effective interlayer ferromagnetic interaction resulting from the weak ferromagnetic coupling between the Cu^{II} ions across the double 2,4,6-trimethylphenylenbis(amidate) bridges within the dinuclear metallacyclophane pillaring units.

This is further confirmed by the χ_M" *vs. T* plots (χ_M" being the out-of-phase ac molar magnetic susceptibility per formula unit) of **8**-**10** (Figure 18). Hence, a sharp frequency-independent peak occurs for the hydrated phases of all three compounds at a common value of the critical temperature (T_C) of 20.0 K (Figure 18a). Instead, the values of T_C for the dehydrated phases decrease from 20.0 (**10**) to 12.0 (**9**) and then to below 2.0 K (**8**) (Figure 18b).

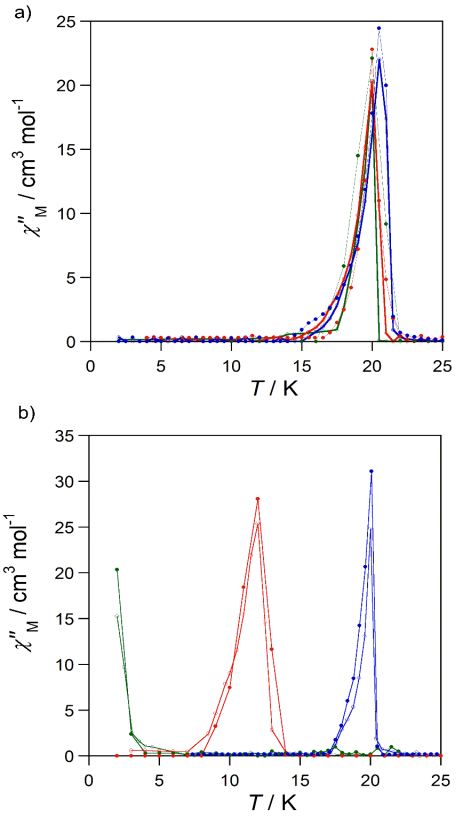

Figure 18. Temperature dependence of the out-of-phase ac signal (χ_M'') of the (a) hydrated and (b) dehydrated phases of **8** (green), **9** (red) and **10** (blue) with a ±4.0 G field oscillating at 1000 (-●-) and 100 (-○-) Hz, respectively.

Interestingly, the variation found in the long-range 3D magnetic ordering between the hydrated and dehydrated phases of **8**-**10** reflects the observed differences in the robustness of each compound upon water loss, as revealed by the PXRD studies. So, the value of T_C is shifted from 20.0 to below 2.0 K for the sodium(I) derivative (**8**), a feature which is probably related to the aforementioned partial collapse of the network structure upon water removal. In contrast, the lithium(I) derivative (**9**) exhibits a much softer decrease of the value of T_C from 20.0 to 12.0 K while the one for the potassium(I) derivative (**10**) remains unaltered, confirming thus the robustness of the network structure upon water removal.

2.A.4. Discussion

We have demonstrated that the cation exchange is a straightforward and successful post-modification approach to modulate the physical properties of a given PCP without altering its structure. The parent framework undergoes a total exchange of its countercations in a fast and easy manner leading to two novel isostructural PCPs as revealed by both single-crystal and powder X-ray diffraction data.

The exchange of the sodium(I) countercations hosted in the channels of the framework with lithium(I) and potassium(I) ions results into two more robust materials and influences dramatically their physical properties. On the one hand, an increase of the long-range 3D magnetic ordering temperature for both novel PCPs has been observed. Hence, the K^+ and Li^+ derivatives possess a relatively high value of T_C compared to that of the Na^+ ancestor (20.0, 12.0 and 2.0 K respectively). The K^+ derivative is the most robust framework since its T_C does not decrease when dehydrating the sample unlike the Li^+ and Na^+ derivatives. These last compounds must undergo some distortions affecting the bridging ligands [oxamate and/or the 2,4,6-trimethylphenylenbis(amidate)] as well as the Cu(II) environment upon water removal. In this way, the magnetic exchange decreases and consequently the long-range magnetic order is less effectively transmitted.

On the other hand, the nature and location of the cations within the framework influence the gas sorption properties of the PCP. Thus, the different size and position of the counter-cations inside the pores determine the different estimated empty volumes of the frameworks. These estimated volumes match with the BET areas calculated from the N_2 isotherms measured at 77 K. Nevertheless, the ancestor PCP generally displays lower uptakes than expected for all the gases tested because of the structural collapse of its framework during the activation process. This trend is less significant for the CO_2 and CH_4 uptakes since the smaller size of these gases allows them to enter into the pores. Moreover, the K^+ derivative shows higher uptakes for H_2, CO_2 and CH_4 despite displaying lower BET than the Li^+ derivative. This fact is most likely due to their different

affinity for these gases. In summary, apart from the increase in the sorption capacitiy, a gas selectivity can be also achieved by cation exchange.

2.A.5. References

1 J. Ferrando-Soria, M. T. M. Rood, M. Julve, F. Lloret, Y. Journaux, J. Pasán, C. Ruiz-Pérez, O. Fabelo and E. Pardo, *CrystEngComm*, 2012, **14**, 761–764.

2 J. Ferrando-Soria, D. Cangussu, M. Eslava, Y. Journaux, R. Lescouëzec, M. Julve, F. Lloret, J. Pasán, C. Ruiz-Pérez, E. Lhotel, C. Paulsen and E. Pardo, *Chem. - A Eur. J.*, 2011, **17**, 12482–12494.

3 J. Ferrando-Soria, R. Ruiz-García, J. Cano, S.-E. Stiriba, J. Vallejo, I. Castro, M. Julve, F. Lloret, P. Amorós, J. Pasán, C. Ruiz-Pérez, Y. Journaux and E. Pardo, *Chem. - A Eur. J.*, 2012, **18**, 1608–1617.

Part 2.B

MMS obtained by Complex Encapsulation

Post-synthetic methods have been proven to be effective for the insertion of a type of Single-Molecule Magnets (SMMs), the so-called Single-Ion Magnets (SIMs), within the channels of a 3D magnetic MOF, affording with a new class of advanced magnetic materials and allowing an unprecedented study of the interplay between the SIM behaviour and the long-range magnetic ordering.[1] In this work, we plan to extend the use of post-synthetic methods to other areas of molecular magnetism. For this purpose, we incorporate a cationic complex which could undergo a spin-crossover (SCO) transition inside the pores of the already reported anionic MOF $Na^{I}_4\{Mn^{II}_4[Cu^{II}_2(Me_3mpba)_2]_3\} \cdot 60H_2O$ (**8**) through cation exchange techniques *via* SC to SC transformation.

2.B.1. Synthesis

$[Fe^{III}(sal_2\text{-trien})]NO_3 \cdot H_2O$ (H_2sal_2-trien = *N*,*N*'-disalicylidenetriethylenetetramine)[2] is the cationic complex displaying SCO properties (see Figure 19). It was prepared by following the synthetic procedure described in the Annex II.

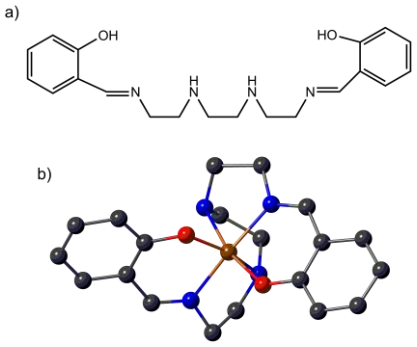

Figure 19. (a) Schematic view of the H_2sal_2-trien ligand. (b) View of the cationic complex $[Fe^{III}(sal_2\text{-trien})]^+$. Carbon, oxygen, nitrogen and iron(III) atoms are represented by grey, red, blue and brown spheres, respectively. Hydrogen atoms are omitted for clarity.

Crystals of **8** were immersed into a saturated aqueous solution of $Fe^{III}(sal_2\text{-trien})]NO_3 \cdot H_2O$ for seven days to afford the new hybrid material $[Fe^{III}(sal_2\text{-trien})]Na_3\{Mn_4[Cu_2(Me_3mpba)_2]_3\} \cdot 43H_2O$ [**Fe(sal$_2$-trien)@8**]. The cation-exchanged crystals had the same size and shape as those of the original ones, ruling out a possible dissolution-recrystallization mechanism for this system and strongly suggesting a solid-state process.[3] Figure 20 illustrates a schematic view of the cation substitution process.

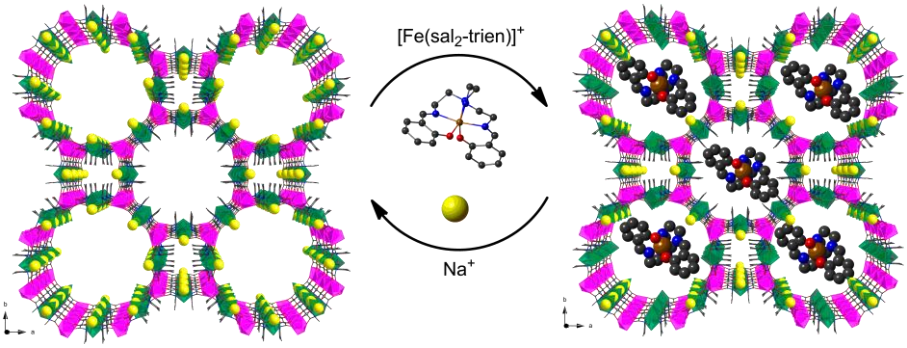

Figure 20. Schematic representation of the SC to SC cation exchange approach leading to the hybrid **Fe(sal$_2$-trien)@8**.

2.B.2. Characterisation

The partial exchange of Na^+ ions by the cationic $[Fe^{III}(sal_2\text{-trien})]^+$ complex was monitored through SEM and ICP-AES. After 7 days of immersion, only one of the four Na(I) atoms per formula unit is replaced by one $[Fe^{III}(sal_2\text{-trien})]^+$ unit, shown Table 1.

Table 1. ICP-AES and SEM analyses of **Fe(sal$_2$-trien)@8**.

Atom (M)	% atomic ICP-AES	% atomic SEM	Cu/M molar ratio
Cu	1.583	1.57	1
Mn	1.051	1.04	1.5
Fe	0.264	0.26	6
Na	0.789	-	2

Aiming at verifying the effective encapsulation of the cationic $[Fe^{III}(sal_2\text{-trien})]^+$ complex within the pores of **8**, infrared spectroscopy (IR) measurements (see Figure 21) were carried out. The IR spectrum of **Fe(sal$_2$-trien)@8** matches the spectrum of **8**. The IR spectrum of both isostructural compounds show the characteristic peak corresponding to the ν(C=O) vibration from the Me$_3$mpba ligands at 1591 cm^{-1}.

Moreover, the spectrum of **Fe(sal$_2$-trien)@8** shows the ν(N-H) and the ν(C=N) vibrations at 3319 and 1622 cm^{-1}, respectively, which are due to the presence of the [Fe^{III}(sal$_2$-trien)]$^+$ complex.

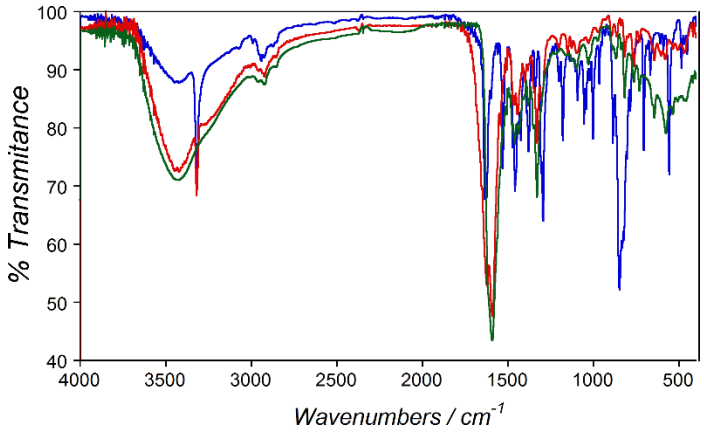

Figure 21. IR spectra of [Fe^{III}(sal$_2$-trien)]$NO_3 \cdot H_2O$ (blue), **8** (green) and **Fe(sal$_2$-trien)@8** (red) in the range of 400-4000 cm^{-1}.

The retention of crystallinity during the SC to SC process was further confirmed by single-crystal X-ray diffraction. According to the unit cell measurements, the crystals of **Fe(sal$_2$-trien)@8** appear to be stable upon dehydration. Besides, a small increase in the size of the unit cell is observed for the single crystals of **Fe(sal$_2$-trien)@8** compared with the crystal data of **8**. Unfortunately, the structure could not be solved due to the crystallographic disorder displayed by the encapsulated Fe^{III}(sal$_2$-trien)]$^+$ motifs.

PXRD patterns were carried out to check the isostructurality of **8** and **Fe(sal$_2$-trien)@8** (see Figure 22). Firstly, suspended samples of **8** in water (Figure 22b) and **Fe(sal$_2$-trien)@8** (Figure 22c) were measured. Their experimental PXRD patterns are very similar and consistent with the calculated one of **8** (Figure 22a). Only small differences can be appreciated for **Fe(sal$_2$-trien)@8** at higher values of 2θ due to the bigger size of its unit cell.

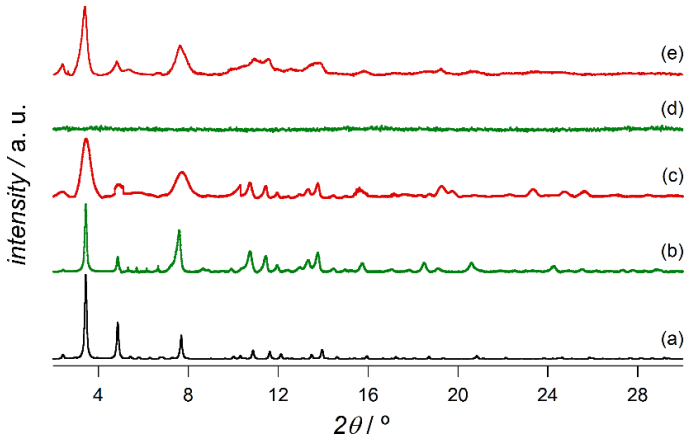

Figure 22. (a) Calculated PXRD pattern profile of **8**. Experimental PXRD pattern profiles of water-suspended and filtered polycrystalline samples of **8** (b and d, respectively) and **Fe(sal$_2$-trien)@8** (c and e, respectively) in the 2θ range 2.0-30.0° at room temperature.

Interestingly, both compounds show very different structural stabilities when they are exposed to air. Thus, **8** exhibits no sign of crystallinity (Figure 22d), indicating a complete collapse of the original hydrated phase upon water loss. On the contrary, the PXRD pattern of the filtered sample of **Fe(sal$_2$-trien)@8** shows well-resolved peaks indicating that the structure does not collapse upon solvent removal (Figure 22e). This fact suggests that the presence of the Fe(III) complexes inside the pores of **8** confers structural stability to the open-framework.

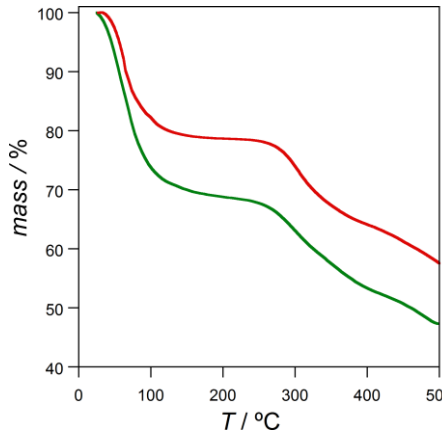

Figure 23. TGA of **8** (green) and **Fe(sal$_2$-trien)@8** (red) under dry N_2 atmosphere.

The water contents of **8** and **Fe(sal$_2$-trien)@8** was determined through TGA under a dry N_2 atmosphere (Figure 23). Both compounds show a fast mass loss from room temperature to *ca*. 125 °C which is followed by a *plateau* until the decomposition starts. Estimated values of weight loss of 31 (**8**) and 22 % (**Fe(sal$_2$-trien)@8**) at 180 °C correspond to 60 and 43 water

molecules, respectively. The lower contents of water molecules for **Fe(sal$_2$-trien)@8** compared to its precursor **8** is in complete agreement with the occupation of the channels by the Fe^{III}(sal$_2$-trien)]$^+$ cations.

2.B.3. Physical properties

On one hand, the magnetic properties of **8** were subject of a previous report[4] and they were summarised in section 2.A. On the other hand, we knew that the precursor Fe^{III}(sal$_2$-trien)]NO$_3$ · H$_2$O employed for the cation exchange is a low-spin (LS) iron(III) species at room temperature (S_{Fe} = 1/2) and does not transit in the temperature range 2-300 K unlike other salts of the same complex, which have shown SCO behaviours.[2,5] Hence, in order to study the possible SCO transition of the Fe^{III}(sal$_2$-trien)]$^+$ cations hosted in the channels of the MOF and its possible interaction with the framework, the magnetic properties of **8** and the hybrid system **Fe(sal$_2$-trien)@8** were investigated in both the direct (dc) and alternating current (ac) regimes. The $\chi_M T$ *vs.* *T* plots (χ_M being the dc molar magnetic susceptibility per Cu$^{II}_6$Mn$^{II}_4$ unit and *T* the temperature) for both compounds are shown in Figure 24. **Fe(sal$_2$-trien)@8** shows a similar qualitative behaviour in the low-temperature region to that of **8**, but having slightly higher $\chi_M T$ values due to the presence of one LS Fe^{III} centre per formula unit. Overall, they exhibit the same characteristic minimum indicative of a ferrimagnetic behaviour of the 3D network

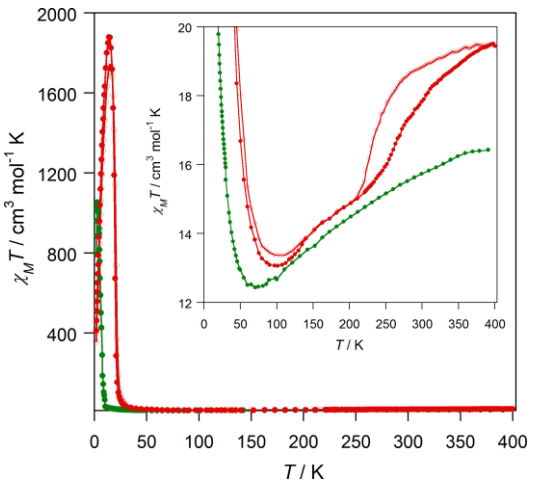

Figure 24. $\chi_M T$ *vs.* *T* plot for **8** (green) and **Fe(sal$_2$-trien)@8** (red). The inset shows the minima and the high temperature region in detail, emphasising the thermal hysteresis loop. The full and empty circles represent the **Fe(sal$_2$-trien)@8** data recorded in the heating and cooling modes, respectively.

resulting from the antiferromagnetic coupling between the four high-spin sextuplets [Mn^{II}, (S_{Mn} = 5/2)] and the six doublets [Cu^{II}, (S_{Cu} = 1/2)] through the oxamato bridge, as previously found in other oxamato-based manganese(II)-copper(II) MOFs. Interestingly, the value of the temperature of the minimum (T_{min}) for **Fe(sal$_2$-trien)@8** (see inset of Figure 24) increases respect to that of **8**. This observation suggests a strengthening of the antiferromagnetic coupling, which is likely associated with the enhanced structural stability after the inclusion of the Fe(III) complexes inside the pores (feature which is supported by the PXRD measurements). The improvement of the magnetic exchange due to the enhanced structural stability has been already mentioned in previous sections as well as reported in other works.[1]

The observed common ferrimagnetic behaviour is further confirmed by the *M vs. T* plots (*M* being the molar magnetization per formula unit and *H* is the applied dc magnetic field) at 2.0 K (see Figure 25a). The isothermal magnetization curves exhibit a fast saturation in both compounds (slightly slower for **8**), and reach the maximum values of *M* at 5.0 T of 13.5 $N\beta$ (**8**) and 14.3 $N\beta$ (**Fe(sal$_2$-trien)@8**).

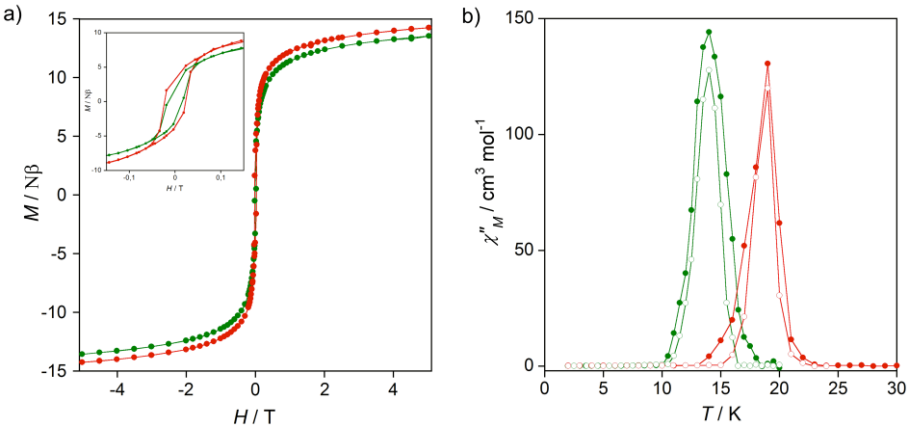

Figure 25. (a) Field dependence of the magnetization (*M*) of **8** (green) and **Fe(sal$_2$-trien)@8** (red) at *T* = 2.0 K. The inset shows their hysteresis loops in detail. (b) Temperature dependence of the out-of-phase ac molar susceptibility (χ_M'') under ± 4.0 G field oscillating at 1000 (-●-) and 10 Hz (-○-) for **8** (green) and **Fe(sal$_2$-trien)@8** (red).

These values are consistent with the expected ones considering the antiparallel alignment of the spins of four HS manganese(II) (S_{Mn} = 5/2) and six copper(II) (S_{Cu} = 1/2) ions for **8** [$M_S = (4g_{Mn}S_{Mn} - 6g_{Cu}S_{Cu})\ N\beta = 13.90\ N\beta$ with g_{Mn} = 2.0 and g_{Cu} = 2.1] plus the spin of one LS iron(III) (S_{Fe} = 1/2) ion for **Fe(sal$_2$-trien)@8** [$M_S = 13.90\ N\beta + 1.10\ N\beta = 15.0\ N\beta$].

Moreover, magnetic susceptibility measurements for both compounds in the alternating current (ac) regime in the form of the χ_M'' *vs*. *T* plots (χ_M'' being the out-of-phase ac molar magnetic susceptibility per formula unit) were carried out. Figure 25b shows the presence of a frequency-independent sharp χ_M'' maximum at the critical temperatures of 14 (**8**) and 19 K (**Fe(sal$_2$-trien)@8**) at the two different frequencies used, confirming the occurrence of a long-range 3D magnetic ordering in both compounds. In addition, the higher value of T_C for **Fe(sal$_2$-trien)@8** compared to that observed for **8**, supports the aforementioned increase of the intra-network magnetic coupling through the oxamato bridges induced by the presence of the iron(III) complex within the pores of the MOF (see above).

The inset of Figure 24 shows the high temperature region in detail. In contrast to what is seen in the low-temperature region, considerable discrepancies in the temperature range 200-400 K are found between both compounds. The value of $\chi_M T$ for **Fe(sal$_2$-trien)@8** at room temperature (17.82 cm^3 K mol^{-1}) is well above the one expected for the sum of one LS Fe^{III} ion (values ranging from 0.7 to 1.1 cm^3 K mol^{-1} depending on the orbital contribution) plus the $\chi_M T$ value of **8** (15.73 cm^3 K mol^{-1}). This fact could indicate that a HS $\leftrightarrow$ LS transition for the Fe^{III} centres occurs. Moreover, the values of $\chi_M T$ for **Fe(sal$_2$-trien)@8** corresponding to the cooling mode (empty circles in the inset of Figure 22) decrease very slowly down to *ca*. 250 K to further decrease very sharply to 200 K, a feature which is characteristic of a $S = 5/2 \leftrightarrow S = 1/2$ SCO transition. In contrast, compound **8** does not show any remarkable change in the slope of the $\chi_M T$ *vs*. *T* plot when cooling down from 400 to 200 K. The different behaviour of the heating

and cooling modes of **Fe(sal$_2$-trien)@8** could be due to the loss of solvent molecules and/or to subtle hysteresis effects.

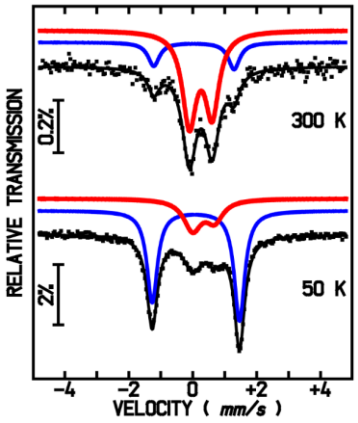

Figure 26. Mössbauer spectra of **Fe(sal$_2$-trien)@8** measured at 300 and 50 K. The lines over the experimental points are the sum of two doublets shown slightly shifted for clarity, corresponding to HS (red) and LS (blue) Fe^{III}.

Since the evidence so far suggests a partial HS ↔ LS SCO, Mössbauer spectroscopy measurements at 50 and 300 K were performed for **Fe(sal$_2$-trien)@8** aiming at finding the HS:LS molar ratio at these temperatures. The spectrum taken at 300 K [Figure 26, (top)] of a sample prepared at room temperature shows four absorption peaks corresponding to two doublets. The estimated parameters (see Table 2) of the most intense doublet , values of the isomer shift and quadrupole splitting of 0.36 mm and 0.71 mm s^{-1}, respectively) are consistent with a HS Fe^{III} ion (S = 5/2), whereas the other doublet (IS = 0.14 mm s^{-1} and QS = 2.53 mm s^{-1}) is consistent with a LS Fe^{III} ion (S = 1/2).[6,7] The estimated relative areas clearly show that Fe^{III} in the HS is predominant showing a fraction equal to 80 % at 300 K.

The spectrum taken at 50 K also shows four absorption peaks corresponding to both HS and LS Fe^{III} doublets [Figure 26, (bottom)]. The parameters listed in Table 2 undoubtedly reveal that the fraction of Fe^{III} in the LS state at 50 K is predominant (71 %) whilst the fraction of Fe^{III} in the HS state has decreased down to roughly 29 %, thus evidencing the spin transition of the Fe^{III} complex inside the pores of the MOF.

Table 2. Estimated parameters from the Mössbauer spectra taken at different temperatures of a **Fe(sal$_2$-trien)@8** sample prepared at 300 K, not pre-heated to 400 K.

	LS Fe^{III}			HS Fe^{III}		
T	**IS[a]**	**QS[b]**	**I[c]**	**IS[a]**	**QS[b]**	**I[c]**
300 K	0.14	2.53	**20 %**	0.36	0.71	**80 %**
50 K	0.21	2.74	**71 %**	0.45	0.70	**29 %**

[a]IS (mm/s) isomer shift relative to metallic α-Fe at room temperature. [b]QS (mm/s) quadrupole splitting. [c]I relative area. Estimated errors are $\leq$ 0.02 mm s^{-1} (IS and QS) and <2% (I).

2.B.4. Discussion

We have successfully encapsulated the cationic complex $[Fe^{III}(sal_2\text{-trien})]NO_3 \cdot H_2O$ within the channels of the anionic 3D PCP $Na^{I}_4\{Mn^{II}_4[Cu^{II}_2(Me_3mpba)_2]_3\} \cdot 60H_2O$ through a SC to SC cation exchange process, affording the novel hybrid compound Fe(sal$_2$-trien)@**8**. Despite the encapsulated cations are disordered thus preventing the crystal structure of Fe(sal$_2$-trien)@**8** from being determined, different characterisation techniques such as IR, ICP-AES, SEM, elemental, PXRD and TGA analyses unambiguously confirm its isostructurality with **8** and the presence of the mononuclear Fe(III) cationic complexes inside its pores.

Interestingly, this post-synthetic process affords a novel material with enhanced structural stability, which is supported by the PXRD patterns and it lies at the origin of the strengthening of the ferrimagnetic behaviour of the Fe(sal$_2$-trien)-exchanged framework, therefore exhibiting a higher value of the temperature of the magnetic ordering. Moreover, the magnetic susceptibility and Mössbauer measurements have further confirmed that indeed, the $[Fe^{III}(sal_2\text{-trien})]^+$ complexes are hosted within the pores of **8** and they exhibit a HS $\leftrightarrow$ LS transition behaviour unlike the starting precursor salt, which does not transit.

Overall, the results demonstrate the encapsulation of a SCO complex within the pores of a magnetic 3D PCP for the first time and they evidence that post-synthetic methods are a valid tool to obtain multifunctional materials with rationally predetermined architectures and to tune their physical properties.

2.B.5. References

1 M. Mon, A. Pascual-Álvarez, T. Grancha, J. Cano, J. Ferrando-Soria, F. Lloret, J. Gascon, J. Pasán, D. Armentano and E. Pardo, *Chem. - A Eur. J.*, 2016, **22**, 539–545.

2 E. Sinn, G. Sim, E. V Dose, M. F. Tweedle and L. J. Wilson, *J. Am. Chem. Soc.*, 1978, **100**, 3375–3390.

3 X. Cui, A. N. Khlobystov, X. Chen, D. H. Marsh, A. J. Blake, W. Lewis, N. R. Champness, C. J. Roberts and M. Schröder, *Chemistry*, 2009, **15**, 8861–8873.

4 J. Ferrando-Soria, P. Serra-Crespo, M. de Lange, J. Gascon, F. Kapteijn, M. Julve, J. Cano, F. Lloret, J. Pasán, C. Ruiz-Pérez, Y. Journaux and E. Pardo, *J. Am. Chem. Soc.*, 2012, **134**, 15301–15304.

5 S. Dorbes, L. Valade, J. a Real and C. Faulmann, *Chem. Commun.*, 2005, 69-71.

6 M. Clemente-León, E. Coronado, M. C. Giménez-López, A. Soriano-Portillo, J. C. Waerenborgh, F. S. Delgado and C. Ruiz-Pérez, *Inorg. Chem.*, 2008, **47**, 9111–9120.

7 S. Floquet, S. Salunke, M.-L. Boillot, R. Clément, F. Varret, K. Boukheddaden and E. Rivière, *Chem. Mater.*, 2002, **14**, 4164–4171.

Part 2.C

MMs obtained by Transmetalation

In this section, we will try to rationalise the mechanisms operating in the so-called transmetalation processes as well as to design novel materials with improved or even new properties by applying these methods. So, a novel anionic $Cu^{II}Mg^{II}$-based PCP have been firstly synthesised, by following traditional self-assembling methods. Then, magnesium(II) metal cations have been exchanged by cobalt(II) and nickel(II) ones, in a SC to SC transformation, yielding two materials which could not be synthesised *de novo*. Interestingly, new physical properties have been incorporated (magnetic properties) and those already existing have been improved as a consequence of the enhanced structural stability (gas sorption properties). Moreover, from the study of the different metal-exchange processes, some insights about the mechanism can be drawn in the light of the obtained results.

2.C.1. Synthesis

The novel PCP of formula $Mg^{II}_2\{Mg^{II}_4[Cu^{II}_2(Me_3mpba)_2]_3\} \cdot 45H_2O$ (**11**) has been obtained by following the already mentioned metalloligand synthetic approach. Similarly to the preparation of the PCP $Na^{I}_4\{Mn^{II}_4[Cu^{II}_2(Me_3mpba)_2]_3\} \cdot 60H_2O$ (**8**), **11** has been obtained by the direct reaction of aqueous solutions of the dicopper(II) complex $Na_4[Cu_2(Me_3mpba)_2] \cdot 4H_2O$ and $Mg(NO_3)_2 \cdot 4H_2O$ (1:2 molar ratio) at room temperature *via* slow diffusion in an H-shaped tube.

Crystals of **11** were immersed into saturated aqueous solutions of $M^{II}(NO_3)_2 \cdot 6H_2O$ [M = Co (**12**) and Ni (**13**)] for several weeks. After the complete replacement of the Mg^{II} ions within the coordination network and those hosted in the channels by either Co^{II} and Ni^{II} ions, two analogue PCPs of formulas $Co^{II}_2\{Co^{II}_4[Cu^{II}_2(Me_3mpba)_2]_3\} \cdot 56H_2O$ (**12**) and $Ni^{II}_2\{Ni^{II}_4[Cu^{II}_2(Me_3mpba)_2]_3\} \cdot 54H_2O$ (**13**) respectively, resulted. The attempts to directly synthesise crystals of **12** and **13** were unsuccessful.

2.C.2. Crystal structure and characterisation

The crystal structures of **11**-**13** could be determined by single-crystal X-ray diffraction using synchrotron radiation. The **11**-**13** series crystallises in the same *P4*/*mmm* space group of the tetragonal system (see Table 4 in the Annex II). All three isostructural compounds are made up of anionic 3D $M^{II}_4Cu^{II}_6$ [M = Mg (**11**), Co (**12**) and Ni (**13**)] open-framework structures with hydrated M^{II} countercations occupying their cavities together with a varying amount of crystallisation water molecules. The anionic 3D network of **11**-**13** can be described as an extended parallel array of oxamato-bridged $M^{II}_4Cu^{II}_6$ layers growing in the *ab* plane with a mixed square/octagonal ($4{\cdot}8^2$) net topology (Figure 27). The layers are further interconnected through the two trimethyl-substituted *m*-phenylene spacers among the Cu^{II} ions, as found earlier in the aforementioned manganese(II) derivative (**8**).

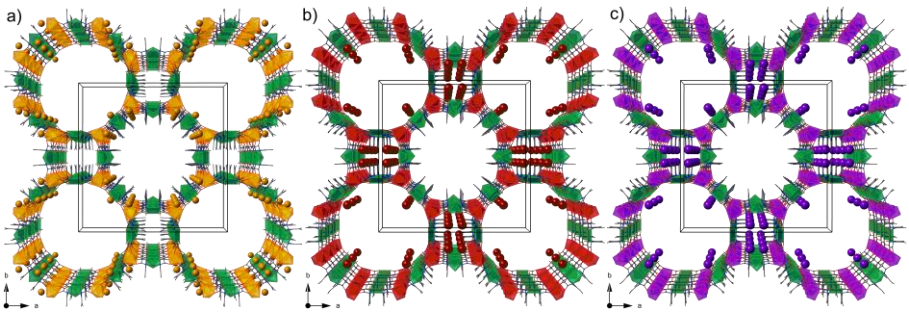

Figure 27. Perspective views of the anionic 3D $M^{II}_4Cu^{II}_6$ networks of **11** (a), **12** (b) and **13** (c) along the crystallographic *c* axis, showing the different site occupation of the channels by the M^{II} countercations (the coordinated and crystallisation water molecules are omitted for clarity). The green, orange, red and purple polyhedra represent the Cu, Mg (**11**), Co(**12**) and Ni(**13**) atoms in the coordination network and the orange, red and purple spheres stand for the Mg(**11**), Co(**12**) and Ni(**13**) atoms occupying the channels.

The compounds **11**-**13** have in common a porous structure with a trimodal pore-size distribution along the crystallographic *c* axis made up of one single type of square pores but two types of octagonal pores depending on the distinct orientation of the trimethyl-substituted phenylene spacers, which point inwards or outwards the channels and

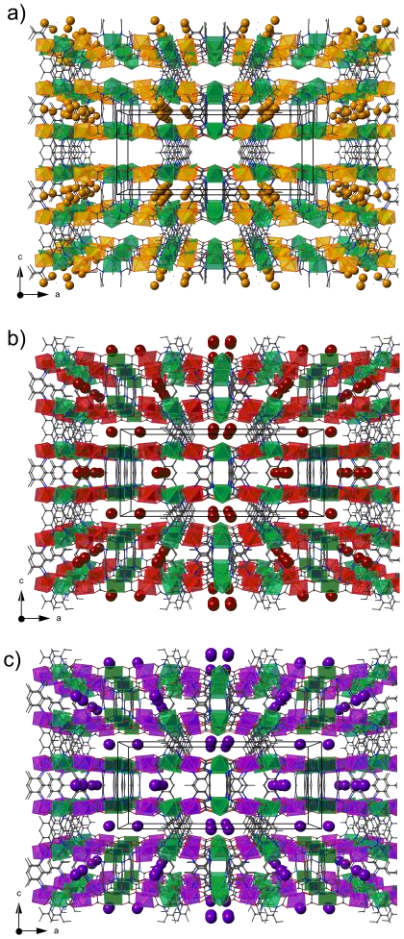

Figure 28. Perspective views of the anionic 3D $M^{II}_4Cu^{II}_6$ networks of **11** (a), **12** (b) and **13** (c) along the crystallographic *b* axis, showing the different site occupation of the channels by the M^{II} countercations. The coordinated and crystallization water molecules are omitted for clarity, (see the caption of Figure 27).

having relative diameters of *ca*. 1.5 and 2.0 nm (see Figure 27). However, the occupation of the channels by the corresponding countercations is very different for the starting compound **11** and the transmetalated species **12** and **13**. The hydrated Mg^{II} counterions in **11** are alternatively located in both the narrow and wide octagonal channels: half of them (Mg2) are weakly bound to the carboxylate oxygen atoms from the anionic network (Figure 29). In contrast, in **12** and **13**, the hydrated M^{II} countercations coming from the metal-ion exchange process [M = Co (**12**) and Ni (**13**)] can be found in the wide octagonal channels (being hydrogen bonded to the coordination network) (Figure 29), and in the square ones (see Figures 27-29). The estimated values of the empty volume without the crystallisation water molecules are 11,074 (**11**), 11,073 (**12**) and 11,023 $Å^3$ (**13**), which represent up to ca. 54.7 (**11**), 54.8 (**12**) and 55.4 % (**13**) of the potential empty space per unit cell volume [V = 20,262 (**11**), 20,216 (**12**) and 19,911 $Å^3$ (**13**)].

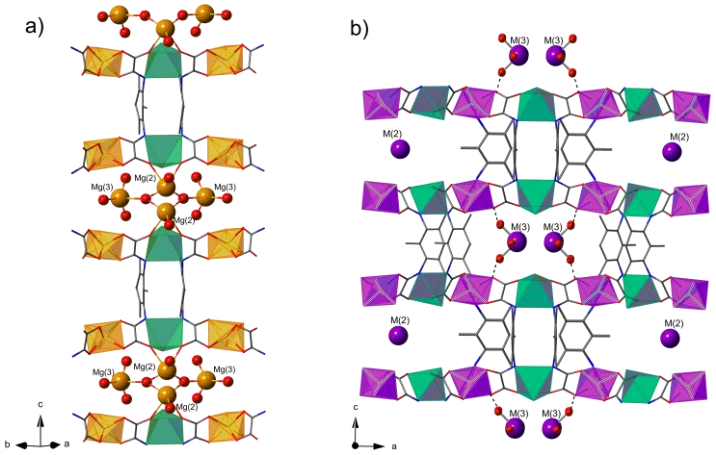

Figure 29. View of a fragment of **11** (a) and **12**/**13** (b) to show the connectivities of the Mg(II) (orange) and Co(II)/Ni(II) (purple) countercations occupying the channels in the coordination network. The dashed lines represent the hydrogen bonds.

The water contents of **11**-**13** was determined by TGA analysis under a dry N_2 atmosphere (Figure 30). All three compounds present a qualitatively similar behaviour with a first fast mass loss from room temperature which is followed by a *plateau* until the decomposition starts. The estimated percentage of the weight loss values of 26 (**11**), 29 (**12**) and 28 % (**13**) at 130 °C. They correspond to ca. 45 (**11**), 56 (**12**) and 54 (**13**) water molecules, respectively.

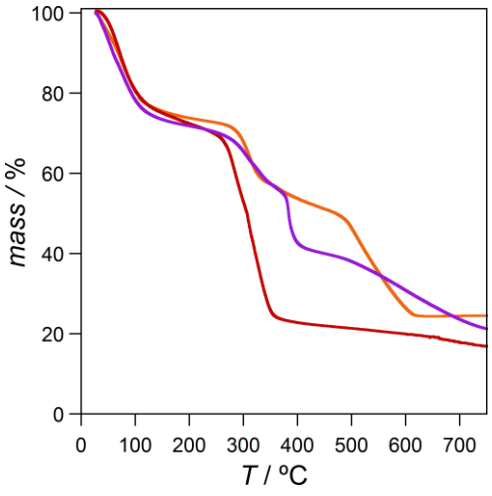

Figure 30. TGA of **11** (orange), **12** (red) and **13** (purple) under a dry N_2 atmosphere.

The PXRD patterns of freshly prepared samples of **11**-**13** (prepared from suspensions in water to avoid any loss of water molecules) are almost identical and they are consistent with the simulated ones (see Figure 31). The correspondence of the experimental and calculated patterns confirms that the bulk samples are isostructural to the crystals selected for single-crystal X-ray diffraction, and that the open-framework structures remain unchanged after the transmetalation reaction.

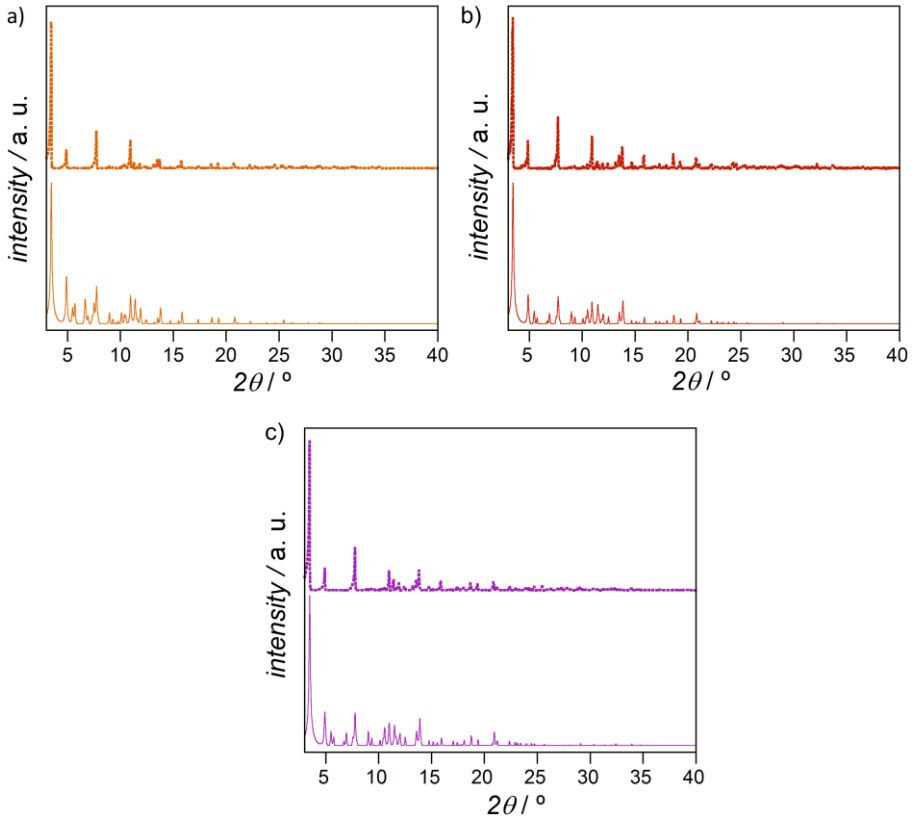

Figure 31. Calculated (—) and experimental (····) PXRD pattern profiles of polycrystalline samples of **11** (a), **12** (b) and **13** (c) measured as water suspensions at r.t.

2.C.3. Transmetalation mechanism

We prepared two different vials with concentrated aqueous solutions of $Co(NO_3)_2 \cdot 6H_2O$ and $Ni(NO_3)_2 \cdot 6H_2O$ to further immerse single-crystals of **11**. The complete SC to SC exchange processes were visually followed and no crystal dissolution was detected.[1] Moreover, the final crystals had the same shape and size as those of the original ones. Searching to elucidate the mechanism of the transmetalation process, we monitored the exchange of Mg^{II} ions in **11** with M^{II} ions [M = Co (**12**) and Ni (**13**)] by analysing the single crystals through ICP-AES and SEM.

We designed two different experiments aiming at clarifying the metal-ion exchange thermodynamics and kinetics. In order to study the thermodynamics, we monitored the variation in metal stoichiometry within the PCP (Mg^{II}:Cu^{II} and M^{II}:Cu^{II}) for different concentrations of M^{II} [M = Co (**12**) and Ni (**13**)] at long exchange times (14 days).

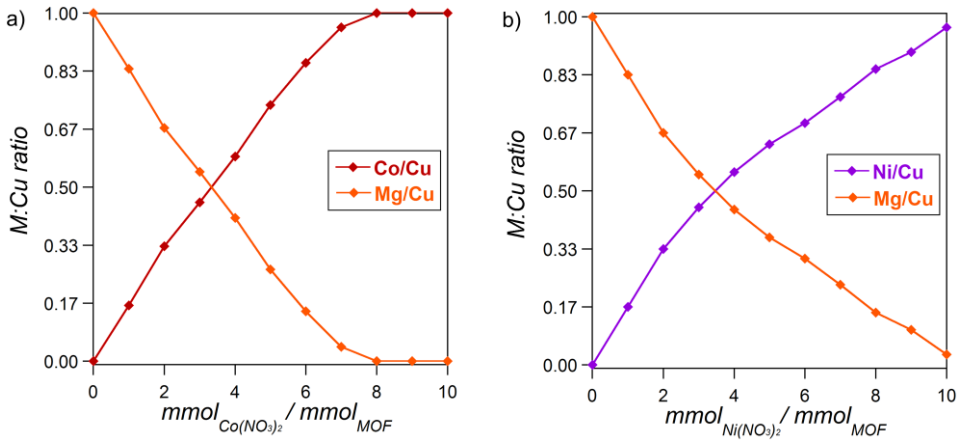

Figure 32. Variation of the M^{II}:Cu^{II} ratio within the MOF after 14 days of immersion of **11** in aqueous solutions of variable concentrations of $Co(NO_3)_2 \cdot 6H_2O$ (a) and $Ni(NO_3)_2 \cdot 6H_2O$ (b).

Both transmetalation processes in **11** with Co^{II} and Ni^{II} show a very similar ion-exchange thermodynamics. Figure 32 illustrates essentially the same substitution patterns consisting of a continuous decrease of the Mg^{II} occupancy and a concomitant increase of the M^{II} (M = Co, Ni) occupancy up to reaching the saturation, which occurs

when all Mg^{II} ions have been replaced. However, this saturation takes place at lower M^{II} concentration for the Co^{II} exchange than for the Ni^{II} one (see Figure 32). The two first mmol of M^{II} completely replace two mmol of Mg^{II}, which most probably are the extra-framework ones located inside the pores. In contrast, the substitution of the four remaining Mg^{II} atoms from the coordination network follows a different thermodynamic equilibrium, which is not completely shifted.

Table 3. Experimental SEM and ICP-AES data of the thermodynamic transmetalation equilibriums.

$[Co^{II}]_0$	$[Mg^{II}]_{aq}$	$[Co^{II}]_{aq}$	$[Ni^{II}]_0$	$[Mg^{II}]_{aq}$	$[Ni^{II}]_{aq}$
1	0.70	0.30	1	0.73	0.27
2	1.60	0.40	2	1.30	0.70
3	2.40	0.60	3	1.80	1.20
4	3.14	0.86	4	2.20	1.80
5	3.80	1.20	5	2.62	2.38
6	4.00	2.00	6	3.10	2.90
			7	3.40	3.60
			8	3.80	4.20

$[Mg^{II}]_{aq}$, $[Co^{II}]_{aq}$ and $[Ni^{II}]_{aq}$ are the experimental concentrations measured in the equilibrium conditions. $[Co^{II}]_0$ and $[Ni^{II}]_0$ are the initial concentrations in solution. The concentrations are given in $mmol_{M(II)}/mmol_{MOF}$.

Therefore, searching for a comparison between the cation exchange thermodynamics of the Mg^{II} intra-framework sites with Co^{II} and Ni^{II} formulated in eqn (1), we decided to calculate the equilibrium constant k for both Co^{II} and Ni^{II} exchange processes according to the eqn (2). We have excluded the data corresponding to the countercations substitution, which occurs in a first and fast step, since this exchange follows a different regime.

$$Mg^{II}\text{-MOF (sol)} + M^{II}\,(aq) \leftrightarrow M^{II}\text{-MOF (sol)} + Mg^{II}\,(aq) \qquad (1)$$

$$k = \frac{[Mg^{II}]_{aq}}{[M^{II}]_{aq}} \quad (2)$$

Figure 33 shows the plots of $[Mg^{II}]_{aq}$ vs. $[M^{II}]_{aq}$ (M = Co, Ni) (data taken from Table 3). The value of the thermodynamic constant (k) is equal to the slope, which can be extracted from eqn (2) by the least squares fitting of the data. In so doing, the values obtained for the thermodynamic constants are 2.71 and 0.70 for the Co^{II} and Ni^{II} transmetalations, respectively.

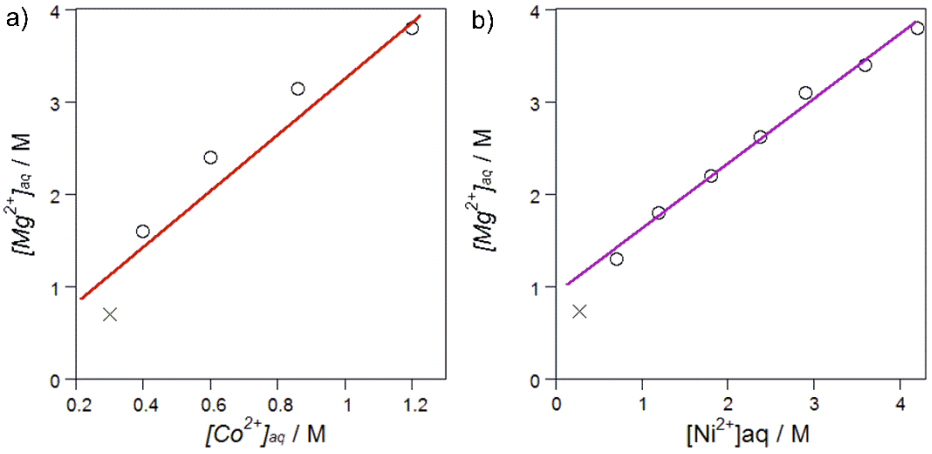

Figure 33. Plot of the $[Mg^{II}]_{aq}$ vs. $[M^{II}]_{aq}$, [M = Co (a) and Ni (b)], according to the eqn (2). The corresponding equations obtained from the least squares method are (a) y = 0.66351 + 2.7078x (R^2 = 0.975) and (b) y = 0.91354 + 0.70472x (R^2 = 0.991).

The fact that the values of k are of the same order of magnitude suggests a rather similar thermodynamics stability for Co^{II} and Ni^{II} transmetalations, the Co-derivative being slightly more stable.

Aiming at studying the metal-ion exchange kinetics, we immersed crystals of **11** in saturated aqueous solutions of M^{II} and followed the increase of the M^{II}:Cu^{II} molar ratio within the MOF by analysing samples at specific time intervals (0-10 days).

Figure 34 shows a very fast exchange of around two of the six Mg^{II} ions, which takes places in less than five minutes of exposure. This identical behaviour for both Co^{II} and Ni^{II} substitutions, together with reaching the same M^{II}:Cu^{II} ratio (*ca*. 0.33), strongly suggest that this first step corresponds to the substitution of those metal ions hosted in the pores being the charge counter-balancing ions. Afterwards, a slower substitution of the remaining four Mg^{II} ions from the coordination network by M^{II} ions occurs over the course of five (M = Co) and seven days (M = Ni), respectively, leading to the complete transmetalation of the network.

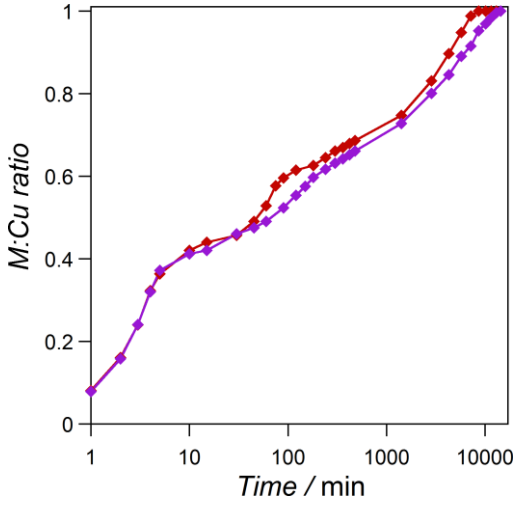

Figure 34. Kinetic profile of the ion exchange process represented as the M^{II}:Cu^{II} ratio [M = Co(red) and Ni (purple)] *vs*. time (in logarithmic scale).

Interestingly, an intermediate saturation step (which is more obvious in the case of the Co^{II} derivative) can be observed at a M^{II}:Cu^{II} molar ratio of around 0.66 (Figure 34), which is likely related to cooperative effects in the occupation of the coordination network.

2.C.4. Physical properties

In order to study the structural stability of the family of compounds **11**-**13** upon removal of water molecules, variable-temperature PXRD measurements were also carried out at 25, 70, 80 and 97 °C (see Figure 35). Compound **11** loses crystallinity very fast when it is removed from the mother liquor and further deteriorates when heating.

Thus, its dehydrated phase shows a very poor crystallinity, suggesting a great collapse of the open-framework structure of **11** upon water removal as illustrated in Figure 35a.

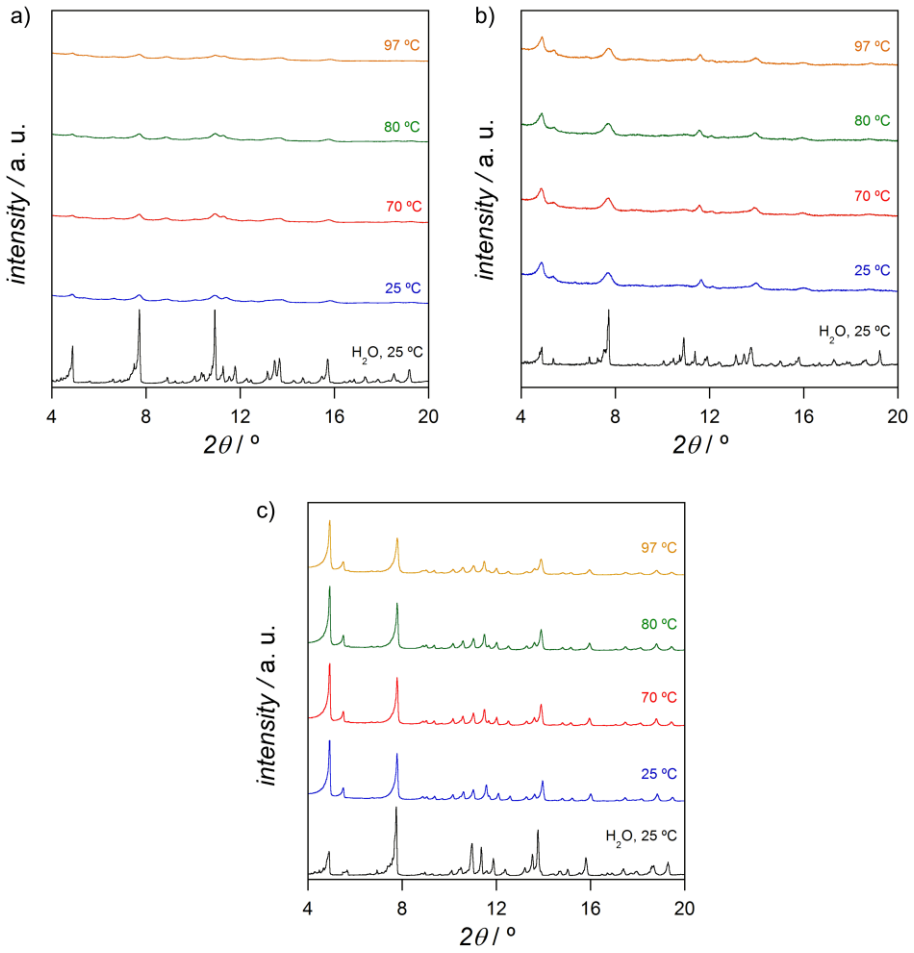

Figure 35. Variable temperature XRD patterns of polycrystalline samples of **11** (a), **12** (b) and **13** (c) in the temperature range 25-97 °C compared with that of water suspended samples at 25 °C.

Compound **12**, also loses crystallinity when exposed to air but the intensity of the peaks does not appreciably decrease when heated up to 97 °C (see Figure 35b). In contrast, the variable-temperature patterns of **13** show well-resolved peaks, which are located at the same positions and with similar intensities to those of the original

hydrated phase, confirming the robustness of the MOF upon water removal (see Figure 35c).

The results obtained from the study of the structural stability of **11**-**13** through PXRD measurements, suggest that very different gas sorption properties are expected for the three isostructural compounds. Figure 36a shows the N_2 adsorption isotherms at 77K of **11**-**13**, a type I sorption behaviour being observed for all of them which is characteristic of microporous compounds.[2] Their N_2 uptake follows the trend **11** < **12** < **13**, which is in correlation with the results deduced from the variable-temperature PXRD studies, where **11** was demonstrated to show a lack of structural stability upon activation, i.e. upon water removal. The calculated BET surface areas for compounds **11**-**13** are 444, 613 and 905 $m^2\ g^{-1}$, respectively.[3]

In order to further confirm the results shown by the N_2 adsorption isotherms, that reveal the effect of the metal substitution on the gas sorption capacity of the MOF, some other gases were also tested. Thus, high-pressure H_2 (77 K), CO_2 (273 K) and CH_4 (273 K) adsorption isotherms for **11**-**13** were measured (Figures 36b-d). Overall, a significant increase of the sorption capacities can be observed for the transmetalated species **12** and **13** (with a larger increase for the Ni^{II}-derivative, **13**). The greater sorption capacity of **12** and specially **13**, not only can be attributed to the aforementioned increase of their structural stability (more remarkably in **13**), but also to the larger ion-quadrupole interactions because of the presence of Co^{II} and Ni^{II} ions.

Although the gas uptakes follow, for all of the gases, the general trend **11** < **12** < **13**, the adsorption capacity ratio between its Co^{II}- (**12**) and Ni^{II}-derivatives (**13**) and the ancestor MOF are quite different depending on the measured gas. Hence, whilst the **12** respect to **11** and the **13** respect to **11** adsorption ratios are quite similar for CO_2 and CH_4, the **13** respect to **11** adsorption ratio is much higher for H_2.

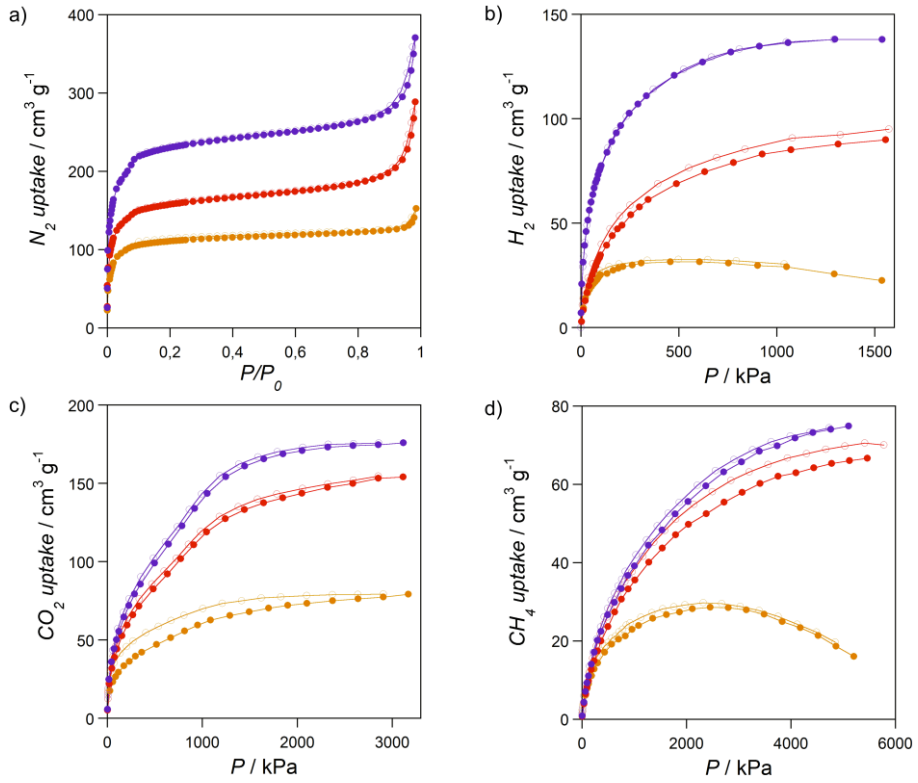

Figure 36. (a) Low pressure N_2 (77 K) and high pressure (b) H_2 (77 K), (c) CO_2 (273 K) and (d) CH_4 (273 K) sorption isotherms for the activated (dehydrated) compounds **11** (orange), **12** (red) and **13** (purple). Filled and empty symbols indicate the adsorption and desorption isotherms, respectively.

The analysis of these results proposes that this post-synthetic method for the preparation of MOFs is not only able to improve the adsorption capacity of a given material but also to tune its gas selectivity.

The magnetic behaviour of **11**-**13** was investigated through magnetic susceptibility measurements in both the direct (dc) and the alternating current (ac) fields. As expected, the exchange of the diamagnetic Mg^{II} ions in **11** by paramagnetic Co^{II} (**12**) and Ni^{II} ions (**13**) (being S_{Co} = 3/2 and S_{Ni} = 1), has a dramatic influence in the magnetic properties.

The $\chi_M T$ *vs.* T plots [χ_M being the dc molar magnetic susceptibility per $Cu^{II}_6M^{II}_4$ unit (M = Mg, Co and Ni) and T the temperature] for **11**-**13** illustrate their different magnetic behaviour (see Figure 37). Compound **11** contains three crystallographically independent dicopper units which are magnetically isolated from each other by the diamagnetic magnesium(II) cations. These dicopper(II) units exhibit a moderate ferromagnetic coupling (J = +14.0 cm^{-1}, the spin Hamiltonian being defined as $H = -JS1 \cdot S2$ with $S_1 = S_2 = S_{Cu} = ½$) through the trimehtyl-substituted phenylendiamidate bridges [copper(II)-copper(II) distances of 7.052, 6.862 and 7.035 Å]. This magnetic coupling agrees both in sign and magnitude with the previously reported for the dicopper(II) complex $Na_4[Cu_2(mpba)_2] \cdot 10H_2O$ with mpba = N,N'-1,3-phenylenebis(oxamato) [J = +16.8 cm^{-1}, copper(II)-copper(II) distance of 6.822 Å].[4]

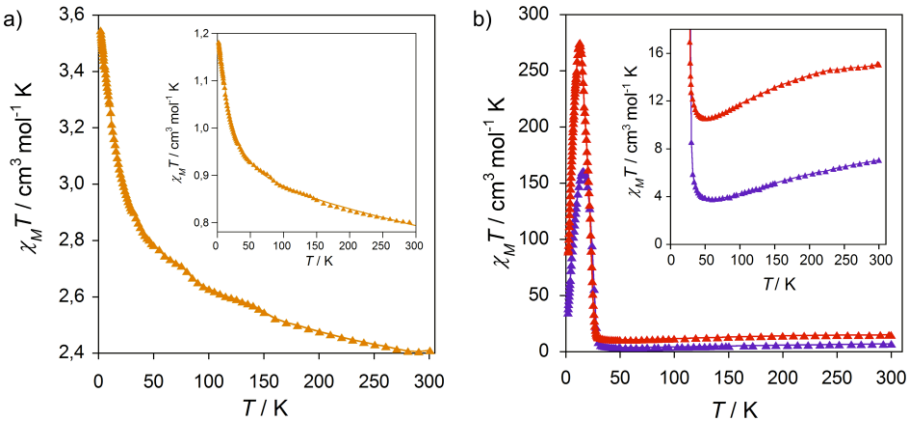

Figure 37. Temperature dependence of the product of the direct current (dc) molar magnetic susceptibility ($\chi_M T$) by the temperature (T) of (a) **11** [the inset shows the best-fit curve for a dinuclear copper(II) model],[4] and (b) **12** (red) and **13** (purple). The inset in (b) shows a magnification of the minimum and the solid lines are only eye-guides.

In contrast, **12** and **13** exhibit a typical ferrimagnetic behaviour resulting from the strong antiferromagnetic coupling between the Cu^{II} and M^{II} ions through the oxamato bridge within each $M^{II}_4Cu^{II}_6$ layer [M = Co (**12**) and Ni (**13**)], as previously found for the

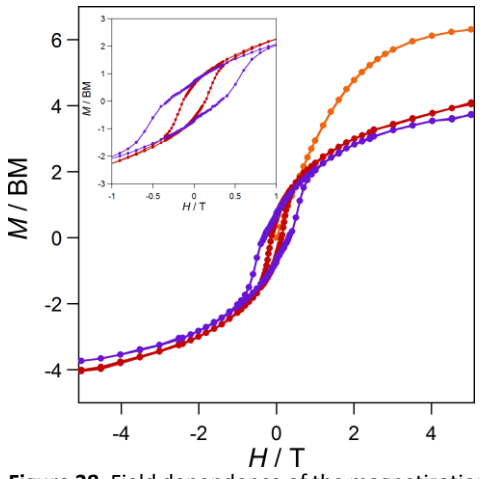

Figure 38. Field dependence of the magnetization (*M*) of **8** (orange), **9** (red) and **10** (purple) at 2.0 K. The inset shows the hysteresis loops for **9** and **10** in detail.

manganese(II) derivative.[5] These overall ferro- (**11**) and ferrimagnetic (**12** and **13**) behaviours are further confirmed by the magnetization per formula unit (*M*) *vs*. applied dc magnetic field (*H*) plots at 2.0 K (see Figure 38).

Moreover, a magnetic hysteresis loop is observed (see inset of Figure 36) for both **12** and **13** at 2.0 K, with values of the coercive field of H_C = 150 (**12**) and 300 G (**13**) which are typical of soft magnets.

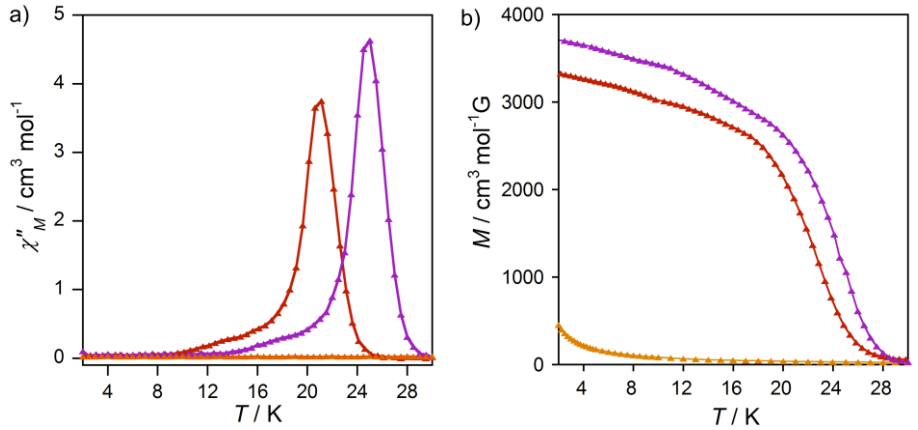

Figure 39. (a) Temperature dependence of the out-of-phase ac molar magnetic susceptibility (χ_M'') of **11** (orange), **12** (red) and **13** (purple) with a ±4.0 G field oscillating at 1000 Hz. (b) Temperature dependence of the magnetization (*M*) of **11** (orange), **12** (red) and **13** (purple).

The occurrence of a long-range 3D magnetic ordering in **12** and **13** is evidenced by the presence of a sharp frequency-independent maximum in the χ_M'' *vs*. *T* plots (χ_M'' being the out-of-phase ac molar magnetic susceptibility per formula unit) at critical temperatures of 21.5 (**12**) and 25.0 K (**13**) (see Figure 39a). This is further confirmed by

the *M* vs. *T* plots (see Figure 39b) which show an abrupt increase below *ca*. 21.5 (**12**) and 25.0 K (**13**). These values of T_C are somewhat higher than that earlier reported for the aforementioned manganese(II)-derivative (21.0 K).

Overall, the analysis of all the measurements that have been performed supports the occurrence of an effective ferromagnetic interaction between the oxamato-bridged $M^{II}_4Cu^{II}_6$ ferrimagnetic layers. This interaction results from the weak ferromagnetic coupling between the Cu^{II} ions across the double 2,4,6-trimethyl-phenylenediamidate bridge within the Cu^{II}_2 pillaring units, as revealed by the magnetic behaviour of **11**. Besides these "through-bond" interlayer interactions, the dipolar interactions with the paramagnetic high-spin M^{II} ions [M = Co (**12**) and Ni (**13**)] hosted in the channels of the MOF also may play a non-negligible role on the long-range 3D magnetic ordering. This idea is supported by the higher values of T_C for **12** and **13** when compared to the related manganese(II) derivative with the hosted diamagnetic sodium(I) ions.

2.C.5. Discussion

The PCP of formula $Mg^{II}_2\{Mg^{II}_4[Cu^{II}_2(Me_3mpba)_2]_3\} \cdot 45H_2O$ (**11**) undergoes a complete metal ion exchange, replacing both the extra and intra-framework Mg^{II} cations by Co(II) and Ni(II) ions, yielding two novel PCPs of formulas $Co^{II}_2\{Co^{II}_4[Cu^{II}_2(Me_3mpba)_2]_3\} \cdot 56H_2O$ (**12**) and $Ni^{II}_2\{Ni^{II}_4[Cu^{II}_2(Me_3mpba)_2]_3\} \cdot 54H_2O$ (**13**) respectively, which could not be obtained by common self-assembly methods.

The two new materials **12** and **13** show enhanced structural stability as demonstrated by the variable-temperature PXRD measurements. Whilst compound **11** loses crystallinity very fast when it is removed from the mother liquor, **12** and specially **13** show well-resolved peaks, confirming the robustness of these PCPs upon water removal. It is worth noting, that this enhanced robustness is probably due to the replacement of the magnesium(II) cations in their anionic coordination networks and also in the pores, which undoubtedly contributes to the stabilisation of the 3D network.

Some conclusions can be drawn from the kinetic studies. The substitution of the Mg(II) cations located inside the pores readily occurs in a first step and no differences are shown between the Co(II) and Ni(II) exchanged cations. Contrary, the substitution of the four remaining intra-framework Mg(II) ions follows a slower kinetics, being slightly faster for the Co(II) exchanged cations. The analysis of the thermodynamic data supports that the extra-framework Mg(II) ions undergo a different substitution regime compared to the intra-framework ones. Furthermore, the Co-derivative is a bit more thermodynamically stable than the Ni-derivative.

The enhanced structural stability that these derivatives show, leads to an improvement of the gas adsorption properties. The calculated BET surface areas for the compounds **11**-**13** (444, 613 and 905 $m^2 g^{-1}$, respectively) are in agreement with the trends of the structural stability obtained from the variable-temperature PXRD patterns, corroborating that the structure of **11** collapses after activation unlike **12** and **13** which exhibit a remarkably higher gas uptake, being more drastic for **13**. Moreover, the sorption measurements for the different gases suggest some differences in the selectivity of the three compounds. Hence, **13** seems to show more affinity for H_2.

The substitution of the diamagnetic Mg^{II} ions in **11** with paramagnetic Co^{II} and Ni^{II} cations is responsible for the occurrence of a long-range magnetic ordering in **12** and **13**. Compound **11** behaves as a well-isolated ferromagnetically coupled dicopper(II) units, while **12** and **13** show a typically ferrimagnetic behaviour resulting from the strong antiferromagnetic coupling between the Cu^{II} and M^{II} ions through the oxamato bridge within each $M^{II}{}_4Cu^{II}{}_6$ layer [M = Co (**12**) and Ni (**13**)]. The magnetic long range ordering of **12** and **13** results from the weak ferromagnetic coupling between the Cu^{II} ions across the double 2,4,6-trimethyl-phenylenediamidate bridge and the dipolar interactions with the paramagnetic high-spin M^{II} ions [M = Co (**12**) and Ni (**13**)] hosted in the channels of the PCP. These last dipolar interactions could account for the slightly higher value of T_C in **13**.

Overall, our work has demonstrated that the metal ion exchange is a valid post-synthetic method for the insertion of magnetic properties on a preformed PCP. Moreover, this approach provides materials with enhanced robustness which exhibit improved gas sorption properties and it offers the possibility to tune them.

2.C.6. References

1 X. Cui, A. N. Khlobystov, X. Chen, D. H. Marsh, A. J. Blake, W. Lewis, N. R. Champness, C. J. Roberts and M. Schröder, *Chemistry*, 2009, **15**, 8861–8873.

2 J. Rouquerol, D. Avnir, C. W. Fairbridge, D. H. Everett, J. M. Haynes, N. Pernicone, J. D. F. Ramsay, K. S. W. Sing and K. K. Unger, *Pure Appl. Chem.*, 1994, **66**, 1739–1758.

3 M. F. De Lange, T. J. H. Vlugt, J. Gascon and F. Kapteijn, *Microporous Mesoporous Mater.*, 2014, **200**, 199–215.

4 I. Fernández, R. Ruiz, J. Faus, M. Julve, F. Lloret, J. Cano, X. Ottenwaelder, Y. Journaux and M. C. Muñoz, *Angew. Chemie Int. Ed.*, 2001, **40**, 3039–3042.

5 J. Ferrando-Soria, P. Serra-Crespo, M. de Lange, J. Gascon, F. Kapteijn, M. Julve, J. Cano, F. Lloret, J. Pasán, C. Ruiz-Pérez, Y. Journaux and E. Pardo, *J. Am. Chem. Soc.*, 2012, **134**, 15301–15304.

3. Conclusions

The goals described for this Thesis have been investigated and the most of them successfully achieved. Overall, the results collected in Part 1 have shown novel and very original methodologies for the design of chiral MOFs which still remains a synthetic challenge. Moreover, additional physical properties have been introduced into the chiral structures giving rise to the so-called multifunctional materials (MMs) which constitute the main aim of the present work.

We have successfully developed an original strategy to rationally prepare chiral PCPs. This synthetic approach consists of using uncommon enantiopure precursors [such as copper(II) chains, dicopper(II) species and hexacopper(II) rings] derived from natural amino acids, which are capable to further coordinate to metal ions or metal complexes through their free carbonyl groups, yielding high-dimensional enantiopoure MOFs. We have proven that the encoded chiral information is efficiently transferred from the starting amino acids by means of the matallosupramolecular design strategy.

Hence, intriguing and fascinating porous 3D structures have been synthesised and characterised, and their crystal structures could be successfully determined by X-ray diffraction on single-crystals despite the complex unit cell that they possess. Noteworthy, apart from their chiral information, the amino acids bear aliphatic residues which also play a fundamental role due the hydrophobic interactions that they establish.

We have investigated how the different size and shape of these carbon chains affect the metallosupramolecular assembly. The oxamato-based series of precursors afforded, by following the metalloligand strategy, rod-like MOFs (described in Part 1.A) being the fundamental building units in all of them are helices but exhibiting different types of network. The reason of such a diversity is likely the non-negligible role that the hydrophobic interactions between the aliphatic residues play in determining the conformational folding of the 1D building units and therefore, the self-assembly of the resulting 3D structure. One of the most remarkable results concerning the synthesis of chiral PCPs is the preparation for the first time of a rod-like MOF (**4b^{R}**) where the fundamental building unit from the framework exactly matches with the chain used as

precursor to build the MOF. The main disadvantage of this family of chiral MOFs is the lack of stability that they show in water as well as upon solvent removal. These features preclude to carry out many asymmetric catalysis experiments and the possibility of displaying gas sorption properties.

We have also studied the impact of the length of the alkyl side-chains from the ligands decorating the walls of the pores of a calcium(II)-derived family of PCPs on their adsorption of different light hydrocarbons. As far as we know, this is the first experimental study in which a family of isoreticular PCPs exhibiting different alkyl-functionalised pores is used to rationalise the adsorptive properties. We have demonstrated that the use of amino acids with smaller residues leads to PCPs with bigger pore windows which is translated into higher gas uptakes but smaller selectivity since the carbon-carbon hydrophobic interactions are less effective. Thus, by the rational choice of the amino acid derivative ligand, we are capable to control the kinetic adsorption selectivity of methane towards other light hydrocarbons which occur in the natural gas, offering a new way for its purification.

Furthermore, compound **5c^{S}** hosting a large number of water molecules into its pores, exhibited proton conductivity properties. The accurately established knowledge of the hydrogen-bonded net of water molecules, allowed us to propose the involved pathways in the hopping of protons between neighbouring water molecules. These processes are in agreement with a Grotthuss-like mechanism and have been further supported by quantum molecular dynamics simulations.

Magnetic properties have been also implemented into our chiral materials by using trivalent lanthanide ions to act as nodes between the dicopper(II)-oxamidate precursors. In so doing, dysprosium(III)- and terbium(III)-based PCPs were obtained and the SIM behaviour of the lanthanide(III) ions embedded within their open-frameworks was investigated.

The results collected in Part 2 prove that the use of the post-synthetic methods is a straightforward and successful alternative tool to prepare MMs.

We have achieved the replacement of the cations of the MOF without altering its structure, by means of an easy methodology which consists of immersing single-crystals of the parent MOF into saturated aqueous solutions containing the metal ions or complexes that we want to exchange. As a result, improved isostructural materials have been prepared.

Based on the well-known dicopper(II)-bis(oxamato) derived MOF **8** (already studied in our group), we have successfully exchanged the sodium(I) countercations hosted in its channels by lithium(I) and potassium(I) ions affording two novel and more robust materials. Their improved structural stability influences the magnetic properties, the derivatives exhibiting higher long-range 3D magnetic ordering temperatures. Moreover, the gas sorption studies revealed that the more robust derivatives also show higher gas uptakes and that the nature and location of the cations within the framework modify the gas selectivity.

Encouraged by the success of the cationic exchange, we investigated the substitution of the sodium(I) countercations by the cationic complex of the compound $[Fe^{III}(sal_2\text{-trien})]NO_3 \cdot H_2O$. This post-synthetic process afforded again a novel material with enhanced structural stability which lies at the origin of the strengthening of the ferrimagnetic behaviour of the parent MOF, the derivative exhibiting a higher value of the temperature of the magnetic ordering. In addition, the magnetic susceptibility measurements and the Mössbauer spectroscopy have further confirmed that indeed, the $[Fe^{III}(sal_2\text{-trien})]^+$ entity has been encapsulated within the pores of **8** and it undergoes a HS $\leftrightarrow$ LS transition unlike the starting precursor salt, where this phenomenon does not occur. Hence, the post-synthetic modification not only enhances the magnetic properties of the MOF, but also causes the spin crossover behaviour of the iron(III) complex.

Finally, we went a step further and investigated the substitution of both the countercations located in the pores and the metal ions constituting the coordination framework of a diamagnetic magnesium(II)-bis(oxamato) based MOF. The magnesium(II) ions underwent a total exchange by cobalt(II) and nickel(II) ions yielding two novel materials which, interestingly, cannot been synthesised in a conventional manner. Some conclusions can be drawn from the kinetic studies. The substitution of the magnesium(II) cations located inside the pores readily occurs in a first step and no differences are shown between the cobalt(II) and nickel(II) exchanged cations. However, the substitution of the four remaining intra-framework magnesium(II) ions follows a slower kinetics, being slightly faster for the cobalt(II) exchanged cations. The analysis of the thermodynamic data supports that the extra-framework magnesium(II) ions undergo a different substitution regime compared to those of the intra-framework.

These two novel derived frameworks show enhanced structural stability which leads to an improvement of the gas adsorption properties. Moreover, the sorption measurements for different gases suggest some differences in the selectivity of the three compounds.

The most striking result is the occurrence of a long-range magnetic ordering due to the substitution of the diamagnetic magnesium(II) ions in the parent MOF by the paramagnetic cobalt(II) and nickel(II) ions.

Overall, our work has demonstrated that the cation exchange, complex encapsulation and transmetalation are useful post-synthetic approaches to provide materials with enhanced physical properties such as robustness, gas sorption or magnetic properties. In addition, they also represent a powerful tool for the insertion of new physical properties on a preformed PCP, thus giving rise to examples of the so-called MMs that could not be isolated through conventional synthetic routes.

Annex I

I.1. Experimental Section

Materials. All chemicals were of reagent grade quality. They were purchased from commercial sources and used as received.

Physical Techniques. Elemental (C, H, N) analyses were performed at the Microanalytical Service of the Universitat de València. ^{1}H NMR spectra were recorded at room temperature on a Bruker AC 200 (200.1 MHz) spectrometer. FT–IR spectra were recorded on a Perkin-Elmer 882 spectrophotometer as KBr pellets. Thermogravimetric analysis (TGA) were carried out on an SDT-Q600 analyser from TA instruments. The samples were placed in open platinum crucibles and the measurements were done in the temperature range 25-800 °C at a heating rate of 10 °C min^{-1} under a flow of N_2.

Magnetic measurements. Variable-temperature (2.0 – 400 K) direct current (dc) magnetic susceptibility measurements under an applied field of 100 G (T < 30 K) and 5.0 kG (T ≥ 30 K), and magnetization measurements at 2.0 K were carried out with a Quantum Design SQUID magnetometer. Variable-temperature (2.0 – 30 K) alternating current (ac) magnetic susceptibility measurements under ± 5.0 G oscillating field at frequencies in the range of 1.0 – 10.0 kHz were performed under different applied static fields in the range 0 – 5.0 kG with a Quantum Design Physical Property Measurement System (PPMS). The magnetic susceptibility data were corrected for the diamagnetism of the constituent atoms and the sample holder. Dc and ac magnetic measurements were done on powdered microcrystals and, when necessary, restraining the sample with *n*-eicosane in order to avoid any field induced torqueing as well as to prevent any solvent loss.

Gas sorption measurements. N_2 physical adsorption measurements were performed at 77 K on crystalline samples with a Tristar II 3020 Micrometrics instrument.

The CO_2 adsorption-desorption isotherms at 273 K were carried out on polycrystalline samples with a Micromeritics ASAP2020 instrument. Vapour adsorption isotherms were acquired using a Quantachrome Autosorb 1C volumetric adsorption analyser equipped with a vapor-dosing system. All samples were evacuated at 348 K during 19 h under 10^{-6} Torr prior to their analysis, for both nitrogen and vapour measurements. The Brunauer-Emmett-Teller (BET) surface areas were calculated from the N_2 adsorption isotherm according to the criteria reported by Rouquerol *et al*. and de Lange *et al*.[1,2]

Hydrocarbon adsorption isotherms at 273 K were performed through a home-made fully automated manometric equipment designed and constructed by the Advanced Materials Group (LMA), and now commercialized as N2GSorb-6 (Gas to Materials Technologies; www.g2mtech.com). Before the adsorption experiments, the samples were outgassed at 348 K for 16 hours under vacuum.

Kinetics of adsorption. Kinetic evaluation of the sorbents was performed at 273 K in a glassmade manometric adsorption equipment using pure gas components. Prior to the adsorption experiment, the samples were degassed under vacuum at the activation temperature. The initial pressure in the manifold was defined at 750 mbar for all adsorbates. Once equilibrated, the manifold was expanded to the sample holder, pressure readings being recorded every second and lasting for ten minutes. The dead volume of the sample cell was measured by expansion of helium from the manifold to the sample cell.

Breakthrough measurements. Breakthrough curve experiments for different mixtures of gases were carried out using a column at 298 K. The sample powder (1.0 g) was packed in the middle part of the column. Breakthrough allows *in situ* activation of the sample under a helium flow. Mass flow controllers regulated the flow rates of all gases. Before each measurement, the sample was activated at the desired temperature for 19 hours. The gas stream from the outlet of the column was analysed online with a mass spectrometer. In order to have into account the bed dispersion and its effect on the breakthrough curve shape, we used as internal standard H_2. In others words, we co-

feed a H_2 flow (H_2 is not adsorbed by these materials at this conditions) together with the gases we want to separate.

X-ray crystallographic data collection and structure refinement. Suitable crystals were selected and mounted on a MITIGEN holder in Paratone oil and very quickly placed on a liquid nitrogen stream cooled at 90 K to avoid any possible degradation upon dehydration. Diffraction data were collected on a Bruker-Nonius X8APEXII CCD area detector diffractometer using graphite-monochromated Mo-Kα radiation (λ = 0.71073 Å). The data were processed through the SAINT[3] reduction and SADABS[4] multi-scan absorption software. The structures were solved with the ShelXS structure solution program, using the Direct Methods solution method. The model were refined with the version 2013/4 of ShelXL against F^2 on all data by full-matrix least squares.[5,6] The final geometrical calculations on free voids and the graphical manipulations were carried out with PLATON[7] implemented in WinGX,[8] and CRYSTAL MAKER[9] programs, respectively.

X-ray Powder Diffraction Measurements. The polycrystalline samples were introduced into 0.5 mm borosilicate capillaries prior to being mounted and aligned on a Empyrean PANalytical powder diffractometer, using Cu Kα radiation (λ = 1.54056 Å). Five repeated measurements were collected for each sample, at room temperature (2θ = 2 – 40°) and merged in a single diffractogram. Variable temperature PXRD studies were also carried out following the same procedure. In this specific case, three repeated measurements were collected for each sample with 2θ = 4 – 40° at different temperatures (298, 343, 353 and 370 K) and merged in a single diffractogram.

Proton conductivity studies. All measurements were controlled by the winDETA package of programs.[10] The total pellet resistances (R_T) were obtained from the intercept of the spike and/or the arc (low-frequency end) on the Z' axis. All impedance spectra show three overlapped contributions ascribed to grain interior, grain boundary and electrode processes. The resistance and capacitance values corresponding to the different processes were obtained by fitting the data with the ZView program[11] using

the equivalent circuit $(R_bQ_b)(R_{gb}Q_{gb})Q_e$, where the subscripts b, gb and e denote grain interior, grain boundary and electrode processes, respectively.

Computational details. The GGA exchange-correlation functional proposed by Perdew, Burke and Erzernhof (PBE)[12] with a DZP basis set was employed for the external electrons and pseudopotentials generated following the approach proposed by Trouiller and Martins for the internal electrons.[13] The cut-off radii for O and H atoms were 1.47 and 1.31 Å, respectively. Values of 50 meV for the energy shift, 400 Ry for mesh cut-off and 10.7 Å for the k-grid cut-off were used. Atmospheric pressure and *T* = 298 K, which were controlled by Parrinello-Rahman[14] and Nose[15] methods, respectively, were considered during the simulation employing 1000 steps at a rate of 1 fs per step. The first (Videos 1-4) and second simulations (Videos 5 and 6) took 200 and 300 fs to finish, respectively.

I.2. Synthetic Procedures

I.2.1. Oxamato/oxamidato-based proligands (**1^S**/**1^R** - **7^S**)

HMeEt-(*S*)-alama (**1^S**) **and HMeEt-(*R*)-alama** (**1^R**) were prepared by following the same synthetic procedure: 8.37 g (60 mmol) of the hydrochloride forms of the methyl ester derivatives of the corresponding enantiopure amino acids (*L*)- (**1^S**) or (*D*)-Alanine (**1^R**) were dissolved in 150.0 mL of dichloromethane and charged with 17.6 mL (126 mmol) of trimethylamine. The mixtures were cooled down to 0 °C on an ice-bath under vigorous stirring. After 10 minutes, 7.4 mL (66 mmol) of ethyl oxalyl chloride ester were added dropwise under vigorous stirring and the resulting solutions were further stirred during four hours. The solutions were then washed three times with water (3 x 50.0 mL) and the organic solutions were dried with Na_2SO_4. After 15 minutes stirring, the solids were filtered off and the organic solvents were removed in a rotatory evaporator to afford yellow oils, which were further purified in a silica column using a mixture of hexane:ethyl acetate (2:1, v/v) as eluent. Amounts of 10.2 (**1^S**) and 10.9 g (**1^R**) of colourless oils were finally obtained which represent yields of 84.0 (**1^S**) and 89.5 % (**1^R**).

HMeEt-(*S*)-valma (**2^S**) **and HMeEt-(*R*)-valma** (**2^R**) were prepared by following the same synthetic procedure: 10.1 g (60 mmol) of the hydrochloride forms of the methyl ester derivatives of the corresponding enantiopure amino acids (*L*)- (**2^S**) or (*D*)-Valine (**2^R**) were dissolved in 150.0 mL of dichloromethane and charged with 17.6 mL (126 mmol) of trimethylamine. The mixtures were cooled down to 0 °C on an ice-bath under vigorous stirring. After 10 minutes, 7.4 mL (66 mmol) of ethyl oxalyl chloride ester were added dropwise under vigorous stirring and the resulting solutions were further stirred during four hours. The solution were then washed three times with water (3 x 50.0 mL) and the organic solutions were dried with Na_2SO_4. After 15 minutes stirring, the solids were filtered off and the organic solvents were removed in a rotatory evaporator to afford yellow oils, which were further purified in a silica column using a mixture of hexane:ethyl acetate (2:1, v/v) as eluent. Amounts of 11.5 (**2^S**) and 11.2 g (**2^R**) of colourless oils were finally obtained which correspond to yields of 83.0 (**2^S**) and 80.7 % (**2^R**).

HMeEt-(*S*)-leuma (**3^S**) **and HMeEt-(*R*)-leuma** (**3^R**) were prepared by following the same synthetic procedure: 10.9 g (60 mmol) of the hydrochloride forms of the methyl ester derivatives of the corresponding enantiopure amino acids (*L*)- (**3^S**) or (*D*)-Leucine (**3^R**) were dissolved in 150.0 mL of dichloromethane and charged with 17.6 mL (126 mmol) of triethylamine. The mixtures were cooled down to 0 °C on an ice-bath under vigorous stirring. After 10 minutes, 7.4 mL (66 mmol) of ethyl oxalyl chloride ester were added dropwise under vigorous stirring and the resulting solutions were further stirred during four hours. The solutions were then washed three times with water (3 x 50.0 mL) and the organic solutions were dried with Na_2SO_4. After 15 minutes stirring, the solids were filtered off and the organic solvents were removed in a rotatory evaporator to afford yellow oils, which were further purified in a silica column using a mixture of hexane:ethyl acetate (2:1, v/v) as eluent. Amounts of 12.3 (**3^S**) and 12.1 g (**2^R**) of colourless oils were finally obtained which represent yields of 83.7 (**3^S**) and 82.3 % (**3^R**).

HMeEt-(*S*)-pegma (**4^S**) **and HMeEt-(*R*)-pegma** (**4^R**) were prepared by following the same synthetic procedure: 12.1 g (60 mmol) of the hydrochloride forms of the methyl

ester derivatives of the corresponding enantiopure amino acids (*L*)- (**4^{S}**) or (*D*)-Phenylglycine (**4^{R}**) were dissolved in 150.0 mL of dichloromethane and charged with 17.6 mL (126 mmol) of trimethylamine. The mixtures were cooled down to 0 °C on an ice-bath under vigorous stirring. After 10 minutes, 7.4 mL (66 mmol) of ethyl oxalyl chloride ester were added dropwise under vigorous stirring and the resulting solutions were further stirred during four hours. The solutions were then washed three times with water (3 x 50.0 mL) and the organic solutions were dried with Na_2SO_4. After 15 minutes stirring, the solids were filtered off and the organic solvents were removed in a rotatory evaporator to afford white powders which were then collected and dried under vacuum. Amounts of 13.6 (**4^{S}**) and 14.2 g (**4^{R}**) were finally obtained which correspond to yields of 85.4 (**4^{S}**) and 89.0 % (**4^{R}**).

HMeEt-(*S*,*S*)-alamox (**5^{S}**), **HMeEt-(*R*,*R*)-alamox** (**5^{R}**), **HMeEt-(*S*,*S*)-valmox** (**6^{S}**) **and HMeEt-(*S*,*S*)-leumox** (**7^{S}**): 60 mmol of the hydrochloride form of the methyl ester derivatives of the corresponding enantiopure amino acids [(*L*)- (**5^{S}**), (*D*)-Alanine (**5^{R}**), (L)-Valine (**6^{S}**) or (L)-Leucine (**7^{S}**)] were dissolved in 100.0 mL of dichloromethane and charged with triethylamine (17.6 mL, 126 mmol). Solutions containing 2.6 mL (30 mmol) of oxalyl chloride in 50.0 mL of diclorometane were added dropwise to the resulting colourless reaction mixtures under vigorous stirring at 0 °C on an ice-bath. After further stirring during three hours, the small amount of white solid (Et_3NHCl) formed was filtered off and the resulting colourless solutions were then concentrated in a rotatory evaporator to a final volume of 50.0 mL. The pale yellow solutions were washed three times with water (3 x 25 mL) and finally, the solvents were removed in a rotatory evaporator to afford white solids which were dried under vacuum. Yields: 13.3 g, 85.0 % (**5^{S}**), 12.9 g, 82.7 % (**5^{R}**), 15.6 g, 82.3 % (**6^{S}**) and 16.4 g, 80.0 % (**7^{S}**).

I.2.2. Oxamato/oxamidato-based copper(II) complexes (**1a^{S} – 7a^{S}**)

$(Me_4N)_6\{Cu^{II}_6[(S)\text{-alama}])_6\} \cdot 10H_2O$ (**1a^{S}**). A methanolic solution (50.0 mL) of the corresponding proligand HMeEt-(*S*)-alama (5.1 g, 25 mmol) was treated with a 25 %

methanolic solution of Me_4NOH (33.7 mL, 80 mmol). Another methanolic solution (10.0 mL) of $CuCl_2 \cdot 6H_2O$ (4.26 g, 25 mmol) was then added dropwise under continuous stirring. The resulting deep blue solution was filtered off to remove the small amount of solid particles and then concentrated to dryness in a rotary evaporator. The obtained blue powder was gently washed with acetone to remove the excess of Me_4NOH and dried under vacuum. The resulting powder was dissolved in 5.0 mL of ethanol and left overnight at 0 °C in order to precipitate the impurity. The colourless impurities were then separated by filtration and the deep blue solution was concentrated to dryness in a rotatory evaporator. Well-formed hexagonal prisms of **1a^S** were grown after several weeks of slow evaporation of a water:methanol solution (1:1, v/v) containing the deep blue solid. Yield: 2.0 g, 24.6 %.

$(Me_4N)_6\{Cu^{II}_6[(S)\text{-valma}])_6\} \cdot 7H_2O$ (2a^S) and $(Me_4N)_6\{Cu^{II}_6[(R)\text{-valma}])_6\} \cdot 7H_2O$ (2a^R). Methanolic solutions (50.0 mL) of the corresponding proligands HMeEt-(*S*)-valma or HMeEt-(*R*)-valma (5.8 g, 25 mmol) were treated with 25 % methanolic solutions of Me_4NOH (33.7 mL, 80 mmol). Then, methanolic solutions (10.0 mL) of $CuCl_2 \cdot 6H_2O$ (4.26 g, 25 mmol) were added dropwise under continuous stirring. The resulting deep blue solutions were filtered off to remove the small amount of solid particles and then concentrated to dryness in a rotary evaporator. The obtained blue powders were gently washed with acetone to remove the excess of Me_4NOH and dried under vacuum. The resulting powders were dissolved in 5.0 mL of ethanol and left overnight at 0 °C in order to precipitate the impurity. The colourless crystals were separated by filtration and the deep blue solutions were concentrated to dryness in a rotatory evaporator. Well-formed hexagonal prisms of **2a^S** and **2a^R** were grown after several weeks of slow evaporation of water:methanol solutions (1:1, v/v) containing the solids. Yields: 3.1 g, 36.0 % (**2a^S**) and 2.7 g 31.5 % (**2a^R**).

$(Me_4N)_6\{Cu^{II}_6[(S)\text{-leuma}])_6\} \cdot 10H_2O$ (**3a^S**). A methanolic solution (50.0 mL) of the HMeEt-(*S*)-leuma proligand (6.13 g, 25 mmol) was treated with a 25 % methanolic solution of Me_4NOH (33.7 mL, 80 mmol). Another methanolic solution (10.0 mL) of $CuCl_2 \cdot 6H_2O$ (4.26 g, 25 mmol) was then added dropwise under continuous stirring. The

resulting deep blue solution was filtered off to remove the small amount of solid particles and then concentrated to dryness in a rotary evaporator. The obtained blue powder was gently washed with acetone to remove the excess of Me_4NOH and dried under vacuum. The resulting powder was dissolved in 5.0 mL of ethanol and left overnight at 0 °C in order to precipitate the impurity. The colourless crystals were then filtered off and the deep blue solution was concentrated to dryness in a rotatory evaporator. Well-formed hexagonal prisms of **3a^S** were grown after several weeks of slow evaporation of a water:methanol solution (1:1, v/v) containing the solid. Yield: 2.5 g, 27.2 %.

{Me$_4$N[Cu^{II}(*S*)-pegma] · 2H$_2$O}$_n$ (4a^S) and {Me$_4$N[Cu^{II}(*R*)-pegma] · 2H$_2$O}$_n$ (4a^R). Methanolic solutions (50.0 mL) of the corresponding proligands HMeEt-(*S*)-pegma or HMeEt-(*R*)-pegma (6.63 g, 25 mmol) were treated with 25 % methanolic solutions of Me_4NOH (33.7 mL, 80 mmol). Methanolic solutions (10.0 mL) of $CuCl_2 \cdot 6H_2O$ (4.26 g, 25 mmol) were then added dropwise under continuous stirring. The resulting deep blue solutions were filtered off to remove the small amount of solid particles and then concentrated to dryness in a rotary evaporator. The obtained blue powders were gently washed with acetone to remove the excess of Me_4NOH and dried under vacuum. The resulting powders were dissolved in 5.0 mL of ethanol and left overnight at 0 °C in order to precipitate the impuritiy. The colourless crystals were removed by filtration and the deep blue solutions were concentrated to dryness in a rotatory evaporator. Well-formed elongated rectangular prisms of **4a^S** and **4a^R** were grown after several weeks of slow evaporation of water:methanol solutions (1:1, v/v) containing the solids. Yields: 3.4 g, 34.5 % (**4a^S**) and 3.8 g, 38.6 % (**4a^R**).

(Me$_4$N)$_2${Cu$_2$[(*S*,*S*)-alamox](OH)$_2$} . 6H$_2$O (**5a^S**), **(Me$_4$N)$_2${Cu$_2$[(*R*,*R*)-alamox](OH)$_2$} . 6H$_2$O** (**5a^R**), **(Me$_4$N)$_2${Cu$_2$[(*S*,*S*)-valmox](OH)$_2$} . 2H$_2$O** (**6a^S**) **and (Me$_4$N)$_2${Cu$_2$[(*S*,*S*)-leumox](OH)$_2$} . 2H$_2$O** (**7a^S**): the corresponding HMeEt-(*S*,*S*)-alamox, HMeEt-(*R*,*R*)-alamox, HMeEt-(*S*,*S*)-valmox or HMeEt-(*S*,*S*)-leumox proligands (20 mmol) were treated with 25% methanolic solutions of Me_4NOH (35.4 mL, 84 mmol). Then, methanolic

solutions (25.0 mL) of $CuCl_2 \cdot 6H_2O$ (6.82 g, 40 mmol) were added dropwise under continuous stirring. The resulting deep green solutions were filtered to remove any solid particles and concentrated in a rotary evaporator. The mixtures were then allowed to stand overnight at 0 °C on an ice-bath, and finally they were filtered to remove the precipitate. The solvent of the resulting deep green solutions was removed in a rotatory evaporator to afford green polycrystalline solids that were gently washed with acetone and dried under vacuum. Afterwards, they were recrystallized in 10 mL of ethanol. Yields: 7.10 g, 55.0 (**5a^S**), 6.72 g, 52.0 (**5a^R**), 6.9 g, 54.8 (**6a^S**) and 7.45 g, 56.4 % (**7a^S**).

I.2.3. Oxamato-based copper(II)/nickel(II) PCPs (**1b^S – 4b^R**)

{[Ni(cyclam)][Cu^{II}(*S*)-alama]$_2$ · 9H$_2$O}$_n$ (**1b^S**): A multigram scale synthesis was carried out by direct reaction of water:methanol solutions (1:9, v/v) of $(Me_4N)_6\{Cu^{II}_6[(S)\text{-alama}])_6\} \cdot 10H_2O$ (**1a^S**) (1.96 g, 1 mmol) and [Ni(cyclam)Cl$_2$] (0.996 g, 3 mmol). [Ni(cyclam)Cl$_2$] was synthesised according to the procedure described in the literature.[16] The mixture was stirred at r.t. for 48 h. The resulting pale green polycrystalline powder was filtered, gently washed with water or water:methanol (1:9, v/v) and dried under vacuum. Yield: 1.27 g, 65 %. Well-formed green cubic prisms of **1b^S**, suitable for X-ray diffraction, were obtained by slow diffusion in an H-shaped tube of water:methanol solutions (1:9, v/v) containing stoichiometric amounts of **1a^S** in one arm and [Ni(cyclam)Cl$_2$] in the other one. The crystals were collected by filtration and air-dried.

{[Ni(cyclam)][Cu^{II}(*S*)-valma]$_2$ · 15H$_2$O}$_n$ (**2b^S**): A multigram scale synthesis was carried out by direct reaction of water/methanol solutions (1:9, v/v) of $(Me_4N)_6\{Cu^{II}_6[(S)\text{-valma}])_6\} \cdot 7H_2O$ (**2a^S**) (2.07 g, 1 mmol) and [Ni(cyclam)Cl$_2$] (0.996 g, 3 mmol). The mixture was stirred at r.t. for 48 h. The resulting pale green polycrystalline powder was filtered, gently washed with water or water:methanol (1:9, v/v) and dried under vacuum. Yield: 1.45 g, 70 %. X-ray quality cubic prisms of **2b^S** were obtained by slow diffusion in an H-shaped tube of water:methanol solutions (1:9, v/v) containing stoichiometric amounts of **2a^S** in one arm and [Ni(cyclam)Cl$_2$] in the other one. The crystals were collected by filtration and air-dried.

{[Ni^{II}(cyclam)][Cu^{II}(*R*)-pegma]$_2$ · 6H$_2$O · 2C$_3$H$_8$O}$_n$ (**4b^R**): A multigram scale synthesis was carried out by direct reaction of water/isopropanol solutions (1:1, v/v) of {Me$_4$N[Cu^{II}(*R*)-pegma] · 2H$_2$O}$_n$ (**4a^R**) (0.98 g, 2.5 mmol) and [Ni(cyclam)Cl$_2$] (0.415 g, 1.25 mmol). The mixture was stirred at r.t. for 48 h. The resulting pale green polycrystalline powder was filtered, gently washed with water or water:isopropanol (1:1, v/v) and dried under vacuum. Yield: 1.9 g, 72 %. Well-formed green cubic prisms of **4b^R**, suitable for X-ray diffraction, were obtained by slow diffusion in an H-shaped tube of water:isopropanol solutions (1:1, v/v) containing stoichiometric amounts of **4a^R** in one arm and [Ni(cyclam)Cl$_2$] in the other one. The crystals were collected by filtration and air-dried.

I.2.4. Oxamidato-based copper(II)/M(II) PCPs (**5b^S – 5e^S**, **6b^S – 6c^S** and **7b^S – 7c^S**)

{Cu$^{II}_6$Ba[(*S*,*S*)-alamox]$_3$(OH)$_2$(H$_2$O) · 30H$_2$O}$_n$ (**5b^S**), **{Cu$^{II}_6$Ba[(*S*,*S*)-valmox]$_3$(OH)$_2$(CH$_3$OH)$_6$ · 6H$_2$O}$_n$** (**6b^S**) **and {Cu$^{II}_4$Ba[(*S*,*S*)-leumox]$_3$(OH)$_2$(H$_2$O)$_2$ · 11H$_2$O}$_n$** (**7b^S**): Multigram scale syntheses were carried out by direct reaction of water (**5b^S** and **7b^S**) and water:methanol (1:1, v/v, **6b^S**) solutions of the dicopper(II) precursors **5a^S**, **6a^S** or **7a^S** (6 mmol) and BaCl$_2$ (0.42 g, 2 mmol). The mixtures were stirred at r.t. for 48 h. The resulting blue polycrystalline powders were removed by filtration, gently washed with water or water:methanol (1:1, v/v) and dried under vacuum. Yields: 2.94 g, 82 (**5b^S**), 2.52 g, 74 (**6b^S**) and 2.06 g, 77 % (**7b^S**). X-ray suitable well-shaped blue hexagonal prisms of **5b^S**, **6b^S** and **7b^S** were obtained by slow diffusion in an H-shaped tube of water:methanol mixtures (1:1, v/v) containing stoichiometric amounts of **5a^S**, **6a^S** or **7a^S** (0.18 mmol) in an arm and BaCl$_2$ (0.013 g, 0.06 mmol) in the other one. After several weeks, the crystals were formed and they were collected by filtration on filter paper and air-dried.

{Cu^{II}_6Ca[(*S*,*S*)-alamox]$_3$(OH)$_2$(H_2O) · 32H_2O}$_n$ (**5c^S**), **{Cu^{II}_6Ca[(*R*,*R*)-alamox]$_3$(OH)$_2$(H_2O) · 32H_2O}$_n$** (**5c^R**), **{Cu^{II}_6Ca[(*S*,*S*)-valmox]$_3$(OH)$_2$(H_2O) · 13H_2O}$_n$** (**6c^S**) **and {Cu^{II}_6Ca[(*S*,*S*)-leumox]$_3$(OH)$_2$(H_2O) · 11H_2O}$_n$** (**7c^S**): Multigram scale syntheses were carried out by direct reaction of water (**5c^S** and **5c^R**) and water:methanol (1:1, v/v, **6c^S** and **7c^S**) solutions of the dicopper(II) precursors **5a^S**, **5a^R**, **6a^S** or **7a^S** (6 mmol) and $CaCl_2$ (0.22 g, 2 mmol). The mixtures were stirred at r.t. for 48 h. The resulting blue polycrystalline powders were filtered, gently washed with water or water:methanol (1:1, v/v) and dried under vacuum. Yields: 2.49 g, 72.0 (**5c^S**), 2.36 g, 68.0 (**5c^R**), 1.59 g, 51.0 (**6c^S**) and 2.09 g, 65.0 % (**7c^S**). Well-formed blue cubic prisms of **5c^S**, **5c^R**, **6c^S** and **7c^S** suitable for X-ray diffraction, were obtained by slow diffusion in an H-shaped tube of water:methanol mixtures (1:1, v/v) containing stoichiometric amounts of **5a^S**, **5a^R**, **6a^S** or **7a^S** (0.18 mmol) in an arm and $CaCl_2$ (0.01 g, 0.06 mmol) in the other one. After several weeks, the crystals were separated and collected by filtration on filter paper and air-dried.

{Cu^{II}_6Dy[(*S*,*S*)-alamox]$_3$(OH)$_3$ · 21H_2O}$_n$ (**5d^S**) **and {Cu^{II}_6Tb[(*S*,*S*)-alamox]$_3$(OH)$_3$ · 21H_2O}$_n$** (**5e^S**): Multigram scale syntheses were performed by direct reaction of aqueous solutions of the dicopper(II) precursor **5a^S** (3.87 g, 6 mmol) and $DyCl_3 \cdot 6H_2O$ or $TbCl_3 \cdot 6H_2O$ (2 mmol). The mixtures were stirred at r.t. for 48 h. The blue polycrystalline powders which were formed, were filtered, gently washed with water and dried under vacuum. Yield: 2.52 g, 76 (**5d^S**) and 2.32 g, 70 % (**5e**). X-ray quality, well-shaped blue hexagonal prisms of **5e^S** were obtained by slow diffusion in an H-shaped tube of water/methanol mixed solvents (1:1, v/v) containing stoichiometric amounts of **5a^S** (0.18 mmol) in an arm and $TbCl_3 \cdot 6H_2O$ (0.06 mmol) in the other one. The crystals, which were grown after several weeks, appeared and were collected by filtration on filter paper and air-dried.

I.3. Physicochemical Characterisation

Table 1. ^{1}H RMN data of HMeEt-(*S*)-alama and HMeEt-(*R*)-alama in deuterated CH_2Cl_2[a]

1^{S} δ (ppm)	**1^{R}** δ (ppm)	H-type[b]
7.62 (d)	7.60(d)	-NH
4.61 (m)	4.60 (m)	-CH
4.35 (q)	4.33 (q)	-OCH_2CH_3
3.77 (s)	3.75 (s)	-OCH_3
1.48 (d)	1.47 (d)	CH_3-CH-
1.38 (dt)	1.35 (dt)	-OCH$_2$CH_3

[a]Chemical shifts are given in δ (ppm) against TMS. [b]Highlighted in blue.

Table 2. ^{1}H RMN data of HMeEt-(*S*)-valma and HMeEt-(*R*)-valma in deuterated CH_2Cl_2[a]

2^{S} δ (ppm)	**2^{R}** δ (ppm)	H-type[b]
7.48 (d)	7.48 (d)	-NH
4.47 (m)	4.45 (m)	-CH
4.28 (q)	4.28 (q)	-OCH_2CH_3
3.67 (s)	3.65 (s)	-OCH_3
2.17 (m)	2.16 (m)	-CH
1.32 (dt)	1.32 (td)	-OCH$_2$CH_3
0.88 (td)	0.88 (td)	CH_3-CH-CH_3

[a]Chemical shifts are given in δ (ppm) against TMS. [b]Highlighted in blue.

Table 3. ^{1}H RMN data of HMeEt-(*S*)-leuma and HMeEt-(*R*)-leuma in deuterated DMSO[a]

3^{S} δ (ppm)	**3^{R}** δ (ppm)	H-type[b]
9.20 (d)	9.22 (d)	-NH
4.36 (m)	4.39 (m)	-CH
4.26 (m)	4.26 (m)	-OCH_2CH_3
3.64 (s)	3.65 (s)	-OCH_3
1.78 (t)	1.79 (t)	CH_3-CH-CH_3
1.55 (m)	1.56 (m)	CH-CH_2-CH
1.27 (m)	1.29 (m)	-OCH_2CH_3
0.86 (td)	0.86 (td)	CH_3-CH-CH_3

[a]Chemical shifts are given in δ (ppm) against TMS. [b]Highlighted in blue.

Table 4. ^{1}H RMN data of HMeEt-(*S*)-pegma and HMeEt-(*R*)-pegma in deuterated DMSO[a]

4^{S} δ (ppm)	**4^{R}** δ (ppm)	H-type[b]
9.61 (d)	9.59 (d)	-NH
7.38 (m)	7.41 (m)	-C$_6$H$_5$
5.57 (d)	5.53 (d)	-CH
4.26 (q)	4.24 (q)	-OCH_2CH_3
3.66 (s)	3.65 (s)	-OCH_3
1.27 (t)	1.24 (t)	-OCH_2CH_3

[a]Chemical shifts are given in δ (ppm) against TMS. [b]Highlighted in blue.

Table 5. Elemental analysis of the proligands[a]

Compound	C (%)	H (%)	N (%)
1^{S}	47.01 (47.28)	6.32 (6.45)	6.92 (6.89)
1^{R}	47.10 (47.28)	6.37 (6.45)	6.93 (6.89)
2^{S}	51.87 (51.94)	7.29 (7.41)	6.06 (6.06)
2^{R}	51.93 (51.94)	7.33 (7.41)	6.09 (6.06)
3^{S}	52.98 (53.86)	7.64 (7.81)	5.90 (5.71)
4^{S}	58.87 (58.86)	5.49 (5.70)	5.33 (5.28)
4^{R}	58.85 (58.86)	5.47 (5.70)	5.34 (5.28)

[a]Calculated data are given in parentheses.

Table 6. Elemental analysis of the oxamato-containing copper(II) precursors[a]

Compound	C (%)	H (%)	N (%)
1a^{S}	33.72 (33.80)	5.62 (5.88)	8.70 (8.76)
2a^{S}	38.42 (38.31)	6.33 (6.53)	8.13 (8.13)
2a^{R}	38.29 (38.31)	6.40 (6.53)	8.09 (8.13)
3a^{S}	39.09 (39.17)	6.78 (6.94)	7.51 (7.62)
4a^{S}	42.62 (42.69)	5.50 (5.63)	7.13 (7.11)
4a^{R}	42.63 (42.69)	5.51 (5.63)	7.14 (7.11)

[a]Calculated data are given in parentheses.

Table 7. Selected FTIR data of the oxamato-containing copper(II) precursors[a]

Compound	$\nu_{C=O}$ (cm^{-1})	ν_{C-H} (cm^{-1})
1a^{S}	1650, 1616	2940, 2917
2a^{S}	1637, 1615	2963, 2935, 2877
2a^{R}	1639, 1618	2963, 2933, 2874
3a^{S}	1653, 1609	2961, 2926, 2868
4a^{S}	1640, 1608	2961, 2918
4a^{R}	1643, 1610	2962, 2918

[a]KBr disk.

Table 8. Elemental analysis[a] and SEM data of the oxamato-based copper(II)/nickel(II) PCPs

Compound	C (%)	H (%)	N (%)	Cu:Ni[b]
1b^{S}	34.11 (34.30)	4.24 (4.32)	11.87 (12.00)	2.00
2b^{S}	36.35 (36.67)	4.01 (4.07)	10.82 (10.70)	2.02
4b^{R}	41.11 (41.00)	6.03 (6.12)	7.84 (7.97)	1.97

[a]Calculated data are given in parentheses. [b]Values determined by SEM.

Table 9. Selected FTIR data of the oxamato-based copper(II)/nickel(II) PCPs[a]

Compound	$\nu_{C=O}$ (cm^{-1})	ν_{C-H} (cm^{-1})
1b^{S}	1653, 1602	2930, 2870
2b^{S}	1638, 1595	2958, 2928, 2870
4b^{R}	1642, 1593	2929, 2871

[a]KBr disk.

Table 10. ^{1}H RMN data of HMeEt-(*S*)-alamox and HMeEt-(*R*)-alamox in deuterated CH_2Cl_2[a]

5^{S} δ (ppm)	**5^{R}** δ (ppm)	H-type[b]
9.12 (d)	9.11 (d)	-NH
4.38 (m)	4.38 (m)	-CH
3.64 (s)	3.64 (s)	-OCH$_3$
1.35 (d)	1.36 (d)	-CH$_3$

[a]Chemical shifts are given in δ (ppm) against TMS. [b]Highlighted in blue.

Table 11. ^{1}H RMN data of H_2Me_2-(*S*,*S*)-valmox and H_2Me_2-(*R*,*R*)-valmox in deuterated DMSO[a]

6^{S} δ (ppm)	**6^{R}** δ (ppm)	H-type[b]
8.74 (d)	8.74 (d)	-NH
4.16 (m)	4.15 (m)	-CH-NH
3.66 (s)	3.66 (s)	-OCH$_3$
2.19 (m)	2.20 (m)	CH$_3$-CH-CH$_3$
0.88 (dd)	0.88 (dd)	CH$_3$-CH-CH$_3$

[a]Chemical shifts are given in δ (ppm) against TMS. [b]Highlighted in blue.

Table 12. ^{1}H RMN data of H_2Me_2-(*S*,*S*)-leumox in deuterated DMSO[a]

7^{S} δ (ppm)	H-type[b]
9.05 (d)	-NH
4.37 (m)	-CH-NH
3.69 (s)	-OCH$_3$
1.80 (q)	-CH$_3$-CH-CH$_3$
1.57 (m)	CH-CH$_2$-CH
0.89 (t)	-CH$_3$-CH-CH$_3$

[a]Chemical shifts are given in δ (ppm) against TMS. [b]Highlighted in blue.

Table 13. Elemental analysis of the proligands[a]

Compound	C (%)	H (%)	N (%)
5^{S}	46.01 (46.15)	6.29 (6.20)	10.73 (10.76)
5^{R}	46.03 (46.15)	6.25 (6.20)	10.69 (10.76)
6^{S}	53.11 (53.21)	7.53 (7.65)	8.82 (8.91)
6^{R}	53.14 (53.21)	7.58 (7.65)	8.84 (8.91)
7^{S}	55.66 (55.80)	8.09 (8.19)	8.08 (8.13)

[a]Calculated data are given in parentheses.

Table 14. Selected FTIR data of the oxamidato-derivative proligands[a]

Compound	$\nu_{C=O}$ (cm^{-1})[b]	ν_{C-H} (cm^{-1})[b]
5^{S}	1708, 1623	2980, 2933
5^{R}	1709, 1623	2981, 2933
6^{S}	1735, 1657	2964 ,2933, 2872
6^{R}	1733, 1653	2962 ,2933, 2870
7^{S}	1735, 1656	2957, 2926, 2870

[a]KBr disk.

The different dicopper(II) precursors were characterised through elemental analysis and FTIR spectroscopy. The obtained data are represented in Tables 15 and 16.

Table 15. Elemental analysis data[a] of the oxamidato-containing dicopper(II) precursors[a]

Compound	C (%)	H (%)	N (%)
5a^S	30.08 (29.76)	7.37 (7.18)	8.72 (8.68)
5a^R	30.14 (29.76)	7.28 (7.18)	8.75 (8.68)
6a^S	34.11 (34.23)	7.71 (7.76)	7.91 (7.98)
6a^R	34.13 (34.23)	7.69 (7.76)	7.90 (7.98)
7a^S	37.95 (38.09)	7.77 (7.85)	7.99 (8.08)

[a]Calculated data are given in parentheses.

Table 16. Selected FTIR data of the oxamidato-containing dicopper(II) precursors[a]

Compound	ν_{O-H} (cm^{-1})	ν_{C-H} (cm^{-1})	$\nu_{C=O}$ (cm^{-1})
5a^S	3430	2960, 2940, 2911	1710, 1653, 1618
5a^R	3435	2958 ,2941, 2911	1718, 1658, 1618
6a^S	3448	2961, 2933, 2874	1701, 1634, 1618
6a^R	3440	2964, 2934, 2877	1701, 1640, 1620
7a^S	3639	2957, 2926, 2870	1701, 1653, 1618

[a]KBr disk.

The different oxamidato-based bimetallic PCPs were characterised through elemental analysis, SEM and FTIR. The obtained data are represented in Tables 17 and 18.

Table 17. Elemental analysis and SEM data of the copper(II) oxamidato-derivative PCPs [a]

Compound	C (%)	H (%)	N (%)	Cu:M[b]
5b^S	16.03 (16.07)	5.00 (4.94)	4.59 (4.69)	6.01
5c^S	16.87 (16.62)	5.15 (5.35)	4.65 (4.85)	5.97
5c^R	16.70 (16.62)	5.21 (5.35)	4.69 (4.85)	5.95
5d^S	17.31 (17.20)	4.92 (5.01)	4.35 (4.27)	5.91
5e^S	17.40 (17.43)	4.11 (5.08)	4.32 (4.20)	5.98
6b^S	29.87 (29.61)	5.01 (5.09)	4.91 (4.93)	6.01
6c^S	27.67 (27.71)	5.01 (5.04)	5.49 (5.39)	6.05
7b^S	25.17 (25.12)	5.61 (5.57)	4.11 (4.18)	5.99
7c^S	31.22 (31.36)	5.11 (5.39)	5.23 (5.22)	5.97

[a]Calculated data are given in parentheses. [b]Values determined by SEM.

Table 18. Selected FTIR data of the copper(II)-oxamidato PCPs [a]

Compound	ν_{O-H} (cm^{-1})	ν_{C-H} (cm^{-1})	$\nu_{C=O}$ (cm^{-1})
5b^S	3422	2990, 2936	1718, 1663, 1605
5c^S	3420	2986, 2941	1701, 1663, 1605
5c^R	3420	2988, 2940	1702, 1665, 1605
5d^S	3420	2990, 2940	1701, 1656 ,1600
5e^S	3420	2987, 2941	1701, 1660, 1603
6b^S	3448	2963, 2933, 2872	1701, 1647, 1603
6c^S	3440	2960, 2937, 2873	1702, 1650, 1606
7b^S	3448	2957, 2929, 2872	1701, 1647, 1602
7c^S	3440	2960, 2929, 2870	1703, 1645 ,1604

[a]KBr disk.

I.4. Summary of the Crystallographic Data and Refinement Conditions

Table 19. Summary of Crystallographic Data and Refinement Conditions for $(Me_4N)_6\{Cu_6^{II}[(S)\text{-alama}]_6)\} \cdot 10H_2O$ (**1a^S**) and $\{[Ni(cyclam)][Cu^{II}(S)\text{-alama}]_2 \cdot 9H_2O\}_n$ (**1b^S**)

Compound	**1a^S**	**1b^S**
Formula	$C_{54}Cu_6H_{116}N_{12}O_{54}$	$C_{20}Cu_2NiH_{50}N_6O_{19}$
M (g mol^{-1})	1954.82	864.45
λ (Å)	0.71073	0.71073
Crystal system	Hexagonal	Trigonal
Space group	$P6_3$	$R3$
a (Å)	15.8175(15)	33.792(6)
b (Å)	15.8175(15)	33.792(6)
c (Å)	20.608(2)	14.820(2)
V (Å^3)	4465.1(10)	14656(5)
α (°)	90	90
β (°)	90	90
γ (°)	120	120
Z	2	9
ρ_{calc} (g cm^{-3})	1.454	0.882
μ (mm^{-1})	1.491	0.978
T (K)	296	100
θ range for data collection (°)	1.487 to 26.419	1.205 to 25.242
Completeness to θ = 21.0°	100 %	100 %
Completeness to θ = 25.0	100 %	58.4 %
Measured reflections	51973	39207
Unique reflections (R_{int})	6030 (0.0809)	6864 (0.16)
Observed reflections [$I > 2\sigma(I)$]	3676	2822
[c]Goodness-of-fit on F^2	1.046	1.176
Absolute structure parameter (Flack)	0.042(14)	0.46(4)
R^a [$I > 2\sigma(I)$] (all data)	0.0590 (0.1130)	0.1160 (0.1940)
wR^b [$I > 2\sigma(I)$] (all data)	0.1463 (0.1793)	0.2628 (0.2899)

$^aR_1 = \sum(||F_o| - |F_c||)/\sum|F_o|$. $^bwR_2 = [\sum w(F_o^2 - F_c^2)^2/\sum w(F_o^2)^2]^{1/2}$. $^cS = [\sum w(|F_o| - |F_c|)^2/(N_o - N_p)]^{1/2}$.

Table 20. Summary of Crystallographic Data and Refinement Conditions for $(Me_4N)_6\{Cu_6^{II}[(S)\text{-valma}]_6)\} \cdot 7H_2O$ (**2a^S**), $(Me_4N)_6\{Cu_6^{II}[(R)\text{-valma}]_6) \cdot 7H_2O$ (**2a^R**) and $\{[Ni(cyclam)][Cu^{II}(S)\text{-valma}]_2 \cdot 15H_2O\}_n$ (**2b^S**)

Compound	**2a^S**	**2a^R**	**2b^S**
Formula	$C_{66}Cu_6H_{134}N_{12}O_{37}$	$C_{66}Cu_6H_{134}N_{12}O_{37}$	$C_{24}Cu_2NiH_{70}N_6O_{25}$
M (g mol^{-1})	2069.69	2069.69	1028.65
λ (Å)	0.71073	0.71073	0.71073
Crystal system	Hexagonal	Hexagonal	Hexagonal
Space group	$P6_3$	$P6_3$	$P6_5$
a (Å)	16.8745(7)	16.7208(4)	44.286(3)
b (Å)	16.8745(7)	16.7208(4)	44.286(3)
c (Å)	21.0124(14)	20.8549(8)	26.4667(17)
V (Å^3)	5181.6(5)	5049.5(3)	44954(6)
α (°)	90	90	90
β (°)	90	90	90
γ (°)	120	120	120
Z	2	2	24
ρ_{calc} (g cm^{-3})	1.326	1.361	0.912
μ (mm^{-1})	1.288	1.321	0.864
T (K)	293	296	100
θ range for data collection (°)	1.39 to 23.06	1.41 to 23.30	0.920 to 26.373
Completeness to θ max	100 %	100 %	99.1 %
Completeness to θ full	100 %	100 %	96.5 %
Measured reflections	61429	60872	316854
Unique reflections (R_{int})	4858 (0.0365)	4882 (0.0285)	50728 (0.1224)
Observed reflections [$I > 2\sigma(I)$]	4343	4368	17526
[c]Goodness-of-fit on F^2	1.157	1.148	0.912
Absolute structure parameter (Flack)	-0.02(2)	0.00(2)	0.338(12)
R^a [$I > 2\sigma(I)$] (all data)	0.0595 (0.0731)	0.0613 (0.0746)	0.0911 (0.1940)
wR^b [$I > 2\sigma(I)$] (all data)	0.1628 (0.1842)	0.1644 (0.1837)	0.2226 (0.2399)

$^aR_1 = \sum(||F_o| - |F_c||)/\sum|F_o|$. $^bwR_2 = [\sum w(F_o^2 - F_c^2)^2/\sum w(F_o^2)^2]^{1/2}$. $^cS = [\sum w(|F_o| - |F_c|)^2/(N_o - N_p)]^{1/2}$.

Table 21. Summary of Crystallographic Data and Refinement Conditions for $(Me_4N)_6\{Cu_6^{II}[(S)\text{-leuma}]_6)\} \cdot 10H_2O$ (**3a^S**)

Compound	**3a^S**
Formula	$C_{72}Cu_6H_{152}N_{12}O_{40}$
M (g mol^{-1})	2207.29
λ (Å)	0.71073
Crystal system	Hexagonal
Space group	$P6_3$
a (Å)	17.3468(10)
b (Å)	17.3468(10)
c (Å)	21.3108(14)
V (Å^3)	90
α (°)	90
β (°)	120
γ (°)	5553.5(7)
Z	2
ρ_{calc} (g cm^{-3})	1.320
μ (mm^{-1})	1.208
T (K)	296
θ range for data collection (°)	1.355 to 25.242
Completeness to θ max	100 %
Completeness to θ full	80 %
Measured reflections	79848
Unique reflections (R_{int})	5211 (0.0485)
Observed reflections [$I > 2\sigma(I)$]	4007
[c]Goodness-of-fit on F^2	1.076
Absolute structure parameter (Flack)	0.025(7)
R^a [$I > 2\sigma(I)$] (all data)	0.0578 (0.0888)
wR^b [$I > 2\sigma(I)$] (all data)	0.1655 (0.1960)

[a]$R_1 = \sum(|F_o| - |F_c|)/\sum|F_o|$. [b]$wR_2 = [\sum w(F_o^2 - F_c^2)^2/\sum w(F_o^2)^2]^{1/2}$. [c]$S = [\sum w(|F_o| - |F_c|)^2/(N_o - N_p)]^{1/2}$.

Table 22. Summary of Crystallographic Data and Refinement Conditions for {$Me_4N[Cu^{II}(R)$-pegma] · $2H_2O\}_n$ (**4a^R**), {$Me_4N[Cu^{II}(S)$-pegma] · $2H_2O\}_n$ (**4a^S**) and {[Ni(cyclam)][$Cu^{II}(R)$-pegma]$_2$ · $6H_2O$ · $2C_3H_8O\}_n$ (**4b^R**)

Compound	**4a^R**	**4a^S**	**4b^R**
Formula	$C_{14}CuH_{22}N_2O_7$	$C_{14}CuH_{22}N_2O_7$	$C_{36}Cu_2NiH_{64}N_6O_{18}$
M (g mol^{-1})	393.87	393.87	1054.72
λ (Å)	0.71073	0.71073	0.71073
Crystal system	Trigonal	Trigonal	Trigonal
Space group	$P3_1$	$P3_1$	$P3_221$
a (Å)	10.143(1)	10.2528(6)	19.699(1)
b (Å)	10.143(1)	10.2528(6)	19.699(1)
c (Å)	14.428(2)	14.7602 (8)	29.298(2)
α (°)	90	90	90
β (°)	90	90	90
γ (°)	120	120	120
V (Å^3)	1285.5(4)	1343.72(13)	9846.3(14)
Z	3	3	6
ρ_{calc} (g cm^{-3})	1.526	1.460	1.067
μ (mm^{-1})	1.312	1.255	0.980
T (K)	90	296	90
θ range for data collection (°)	2.319 to 26.321	2.29 to 30.62	1.38 to 25.242
Completeness to θ max°	100 %	100 %	100 %
Completeness to θ full	100 %	100 %	58.3 %
Measured reflections	14310	56461	74812
Unique reflections (R_{int})	3451 (0.0531)	5022 (0.0418)	6823 (0.0583)
Observed reflections [$I > 2\sigma(I)$]	2947	4621	4985
[c]Goodness-of-fit on F^2	1.236	0.793	0.937
Absolute structure parameter (Flack)	0.050(10)	-0.008(9)	0.050(12)
R^a [$I > 2\sigma(I)$] (all data)	0.0653 (0.0796)	0.0299 (0.0342)	0.0480 (0.0679)
wR^b [$I > 2\sigma(I)$] (all data)	0.1682 (0.1772)	0.0888 (0.0942)	0.1140 (0.1201)

[a]$R_1 = \sum(||F_o| - |F_c||)/\sum|F_o|$. [b]$wR_2 = [\sum w(F_o^2 - F_c^2)^2/\sum w(F_o^2)^2]^{1/2}$. [c]$S = [\sum w(|F_o| - |F_c|)^2/(N_o - N_p)]^{1/2}$.

Table 23. Summary of Crystallographic Data and Refinement Conditions for $\{Cu^{II}_6Ba[(S,S)\text{-alamox}]_3(OH)_2(H_2O) \cdot 30H_2O\}_n$ (**5b^S**), $\{Cu^{II}_6Ba[(S,S)\text{-valmox}]_3(OH)_2(CH_3OH)_6 \cdot 6H_2O\}_n$ (**6b^S**) and $\{Cu^{II}_4Ba[(S,S)\text{-leumox}]_3(OH)_2(H_2O)_2 \cdot 11H_2O\}_n$ (**7b^S**)

Compound	**5b^S**	**6b^S**	**7b^S**
Formula	$C_{24}H_{88}BaCu_6N_6O_{51}$	$C_{42}H_{86}BaCu_6N_6O_{32}$	$C_{84}H_{222}Ba_3Cu_{12}N_{12}O_{90}$
M (g mol^{-1})	1794.58	1705.74	4015.22
λ (Å)	0.71073	0.71073	0.71073
Crystal system	Hexagonal	Trigonal	Cubic
Space group	$P6_3$	$R3$	$P2_13$
a (Å)	17.7003(7)	14.4099(15)	26.1224(5)
b (Å)	17.7003(7)	14.4099(15)	26.1224(5)
c (Å)	13.9208(5)	32.222(4)	26.1224(5)
α (°)	90	90	90
β (°)	90	90	90
γ (°)	120	120	90
V (Å^3)	3777.1(3)	5974.2(14)	17825.4(10)
Z	2	3	4
ρ_{calc} (g cm^{-3})	1.579	1.422	1.496
μ (mm^{-1})	2.268	2.130	2.140
T (K)	100(2)	100(2)	90(2)
θ range for data collection (°)	1.328 to 28.945	1.743 to 27.954	1.102 to 26.370
Completeness to θ = 25.0	100 %	100 %	100 %
Measured reflections	49832	38348	87668
Unique reflections (R_{int})	6178 (0.0358)	6170 (0.0382)	12163 (0.0425)
Observed reflections [$I > 2\sigma(I)$]	5375	5646	10077
[c]Goodness-of-fit on F^2	1.058	1.103	1.090
R^a [$I > 2\sigma(I)$] (all data)	0.0418 (0.0522)	0.0418 (0.0493)	0.0698 (0.0927)
wR^b [$I > 2\sigma(I)$] (all data)	0.1178 (0.1277)	0.1230 (0.1332)	0.2007 (0.2260)
Flack parameter	0.21(2)	0.011(9)	0.031(6)

[a]$R_1 = \sum(||F_o| - |F_c||)/\sum|F_o|$. [b]$wR_2 = [\sum w(F_o^2 - F_c^2)^2/\sum w(F_o^2)^2]^{1/2}$. [c]$S = [\sum w(|F_o| - |F_c|)^2/(N_o - N_p)]^{1/2}$.

Table 24. Summary of Crystallographic Data and Refinement Conditions for $\{Cu^{II}_6Ca[(S,S)\text{-alamox}]_3(OH)_2(H_2O) \cdot 32H_2O\}_n$ (**5c^S**) and $\{Cu^{II}_6Ca[(R,R)\text{-alamox}]_3(OH)_2(H_2O) \cdot 33H_2O\}_n$ (**5c^R**)

Compound	**5c^S**	**5c^R**
Formula	$C_{24}H_{92}CaCu_6N_6O_{53}$	$C_{24}H_{98}CaCu_6N_6O_{54}$
M (g mol^{-1})	1734.35	1756.40
λ (Å)	0.71073	0.71073
Crystal system	Hexagonal	Hexagonal
Space group	$P6_3$	$P6_3$
a (Å)	17.6943(10)	17.724(3)
b (Å)	17.6943(10)	17.724(3)
c (Å)	13.2921(8)	13.474(3)
α (°)	90	90
β (°)	90	90
γ (°)	120	120
V (Å^3)	3604.0(5)	3665.5(15)
Z	2	2
ρ_{calc} (Mg m^{-3})	1.598	1.591
μ (mm^{-1})	1.916	1.887
T (K)	90(2)	90(2)
θ range for data collection (°)	2.658 to 27.979	1.327 to 28.582
Completeness to θ 25.242°	99.9 %	99.9 %
Measured reflections	34464	85614
Unique reflections (R_{int})	5790 (0.0411)	6226 (0.0373)
Observed reflections [$I > 2\sigma(I)$]	4983	5796
[c]Goodness-of-fit on F^2	1.062	1.177
Absolute structure parameter (Flack)	0.025(11)	0.049(7)
R^a [$I > 2\sigma(I)$] (all data)	0.0367 (0.0452)	0.0344 (0.0388)
wR^b [$I > 2\sigma(I)$] (all data)	0.0966 (0.1017)	0.1290 (0.1354)
Largest diff. peak and hole (e Å^{-3})	1.416 and -0.530	1.796 and -0.672

$^aR_1 = \sum(||F_o| - |F_c||)/\sum|F_o|$. $^bwR_2 = [\sum w(F_o^2 - F_c^2)^2/\sum w(F_o^2)^2]^{1/2}$. $S = [\sum w(|F_o| - |F_c|)^2/(N_o - N_p)]^{1/2}$.

Table 25. Summary of Crystallographic Data and Refinement Conditions for $\{Cu^{II}_6Ca[(S,S)\text{-valmox}]_3(OH)_2(H_2O) \cdot 13H_2O\}_n$ (**6c^S**) and $\{Cu^{II}_6Ca[(S,S)\text{-leumox}]_3(OH)_2(H_2O) \cdot 11H_2O\}_n$ (**7c^S**)

Compound	**6c^S**	**7c^S**
Formula	$C_{36}Cu_6CaH_{78}N_6O_{34}$	$C_{42}Cu_6CaH_{86}N_6O_{32}$
M (g mol^{-1})	1560.36	1608.48
λ (Å)	0.71073	0.71073
Crystal system	hexagonal	hexagonal
Space group	$P6_3$	$P6_3$
a (Å)	17.783(3)	17.603(6)
b (Å)	17.783(3)	17.603(6)
c (Å)	12.889(2)	13.045(4)
α (°)	90	90
β (°)	90	90
γ (°)	120	120
V (Å^3)	3530(1)	3501(3)
Z	2	2
ρ_{calc} (g cm^{-3})	1.468	1.526
μ (mm^{-1})	1.930	1.946
T (K)	90(2)	90(2)
θ range for data collection (°)	1.32 to 26.0	1.33 to 26.0
Completeness to θ = 25.0	100 %	100 %
Measured reflections	20336	47764
Unique reflections (R_{int})	4076 (0.21)	4777 (0.10)
Observed reflections [$I > 2\sigma(I)$]	1687	2505
[c]Goodness-of-fit on F^2	1.008	0.959
Absolute structure parameter (Flack)	0.37(18)	0.36(9)
R^a [$I > 2\sigma(I)$] (all data)	0.0960 (0.2383)	0.0710 (0.1175)
wR^b [$I > 2\sigma(I)$] (all data)	0.2290 (0.3194)	0.1810 (0.2043)
Largest diff. peak and hole (e.Å^{-3})	1.101 and -1.018	0.835 and -0.767

[a]$R_1 = \sum(||F_o| - |F_c||)/\sum|F_o|$. [b]$wR_2 = [\sum w(F_o^2 - F_c^2)^2/\sum w(F_o^2)^2]^{1/2}$. [c]$S = [\sum w(|F_o| - |F_c|)^2/(N_o - N_p)]^{1/2}$.

Table 26. Summary of Crystallographic Data and Refinement Conditions for $\{Cu^{II}_6Tb[(S,S)\text{-alamox}]_3(OH)_3 \cdot 21H_2O\}_n$ (**5e^S**)

Compound	**5e^S**
Formula	$C_8Cu_2Tb_{0.33}H_{23}N_2O_{14}$
M (g mol^{-1})	551.34
λ (Å)	0.71073
Crystal system	hexagonal
Space group	$P6_3$
a (Å)	17.7181(14)
b (Å)	17.7181(14)
c (Å)	13.1074(12)
α (°)	90
β (°)	90
γ (°)	120
V (Å^3)	3564(7)
Z	6
ρ_{calc} (g cm^{-3})	1.541
μ (mm^{-1})	2.822
T (K)	100(2)
θ range for data collection (°)	1.32 to 26.0
Completeness to θ = 25.0	100 %
Measured reflections	80943
Unique reflections (R_{int})	4780 (0.0429)
Observed reflections [$I > 2\sigma(I)$]	3910
[c]Goodness-of-fit on F^2	1.042
Absolute structure parameter (Flack)	0.63(6)
R^a [$I > 2\sigma(I)$] (all data)	0.0471 (0.0670)
wR^b [$I > 2\sigma(I)$] (all data)	0.1268 (0.1436)

[a]$R_1 = \sum(||F_o| - |F_c||)/\sum|F_o|$. $wR_2 = [\sum w(F_o^2 - F_c^2)^2/\sum w(F_o^2)^2]^{1/2}$. [c]$S = [\sum w(|F_o| - |F_c|)^2/(N_o - N_p)]^{1/2}$.

Table 27. Bond distances for $(Me_4N)_6\{Cu^{II}_6[(S)\text{-alama}]_6\} \cdot 10H_2O$ (**1a^S**), $(Me_4N)_6\{Cu^{II}_6[(S)\text{-valma}]_6\} \cdot 7H_2O$ (**2a^S**), $(Me_4N)_6\{Cu^{II}_6[(R)\text{-valma}]_6\} \cdot 7H_2O$ (**2a^R**) and $(Me_4N)_6\{Cu^{II}_6[(S)\text{-leuma}]_6\} \cdot 10H_2O$ (**3a^S**)

Bond distance / Å	**1^S**	**2^S**	**2^R**	**3^S**
Cu(1)-N(1)	1.921(8)	1.905(5)	1.891(5)	1.915(8)
$Cu(1)\text{-}O(1)_{eq}$	1.977(8)	1.957(5)	1.956(5)	1.973(10)
$Cu(1)\text{-}O(3)_{eq}$	2.002(8)	2.055(4)	2.011(4)	2.042(8)
$Cu(1)\text{-}O(7)_{eq}$	1.962(7)	1.992(4)	1.940(4)	1.939(7)
$Cu(1)\text{-}O(6)_{ax}$	2.405(8)	2.260(5)	2.367(5)	2.440(8)
Cu(2)-N(2)	1.906(8)	1.912(5)	1.894(5)	1.902(8)
$Cu(2)\text{-}O(5)_{eq}$	1.964(6)	1.959(4)	1.980(4)	1.977(7)
$Cu(2)\text{-}O(8)_{eq}$	2.018(7)	2.036(5)	2.034(4)	2.052(7)
$Cu(2)\text{-}O(9)_{eq}$	1.954(8)	1.965(5)	1.937(5)	1.980(8)
$Cu(2)\text{-}O(4)_{ax}$	2.338(7)	2.398(5)	2.241(4)	2.298(8)

The standard deviation values are given in parentheses.

Table 28. Selected interbond bite angles for $(Me_4N)_6\{Cu^{II}_6[(S)\text{-alama}]_6\} \cdot 10H_2O$ (**1a^S**), $(Me_4N)_6\{Cu^{II}_6[(S)\text{-valma}]_6\} \cdot 7H_2O$ (**2a^S**), $(Me_4N)_6\{Cu^{II}_6[(R)\text{-valma}]_6\} \cdot 7H_2O$ (**2a^R**) and $(Me_4N)_6\{Cu^{II}_6[(S)\text{-leuma}]_6\} \cdot 10H_2O$ (**3a^S**)[a]

Bite angle / °	**1^S**	**2^S**	**2^R**	**3^S**
$N(1)\text{-}Cu(1)\text{-}O(1)_{eq}$	83.0(4)	82.9(2)	83.4(2)	83.8(4)
$N(1)\text{-}Cu(1)\text{-}O(3)_{eq}$	82.8(3)	82.7(2)	83.4 19)	82.9(4)
$N(1)\text{-}Cu(1)\text{-}O(7)_{eq}$	176.8(4)	160.5(2)	174.2(2)	176.7(4)
$O(1)_{eq}\text{-}Cu(1)\text{-}O(6)_{ax}$	98.8(4)	101.6(2)	96.7(2)	94.9(4)
$O(3)_{eq}\text{-}Cu(1)\text{-}O(6)_{ax}$	88.7(3)	90.83(19)	86.80(17)	87.0(3)
$O(7)_{eq}\text{-}Cu(1)\text{-}O(6)_{ax}$	78.1(3)	80.64(16)	78.01(16)	77.7(3)
$N(2)\text{-}Cu(2)\text{-}O(5)_{eq}$	171.0(4)	174.2(2)	160.5(2)	166.4(4)
$N(2)\text{-}Cu(2)\text{-}O(8)_{eq}$	82.8(3)	83.5(2)	82.8(2)	81.8(3)
$N(2)\text{-}Cu(2)\text{-}O(9)_{eq}$	83.9(3)	83.8(2)	82.7(2)	82.4(3)
$O(5)_{eq}\text{-}Cu(2)\text{-}O(4)_{ax}$	78.8(3)	78.01(16)	80.60(16)	79.8(3)
$O(8)_{eq}\text{-}Cu(2)\text{-}O(4)_{ax}$	91.8(3)	86.33(18)	91.35(18)	92.2(3)
$O(9)_{eq}\text{-}Cu(2)\text{-}O(4)_{ax}$	98.4(3)	96.5(2)	101.3(2)	103.7(4)

[a]The values of the standard deviation are given in parentheses.

Table 29. Selected bond distances for {$Me_4N[Cu^{II}(S)$-pegma] · $2H_2O\}_n$ (**4a^S**) and {$Me_4N[Cu^{II}(R)$-pegma] · $2H_2O\}_n$ (**4a^R**)[a]

Bond distance / Å	**4^S**	**4^R**
Cu(1)-N(1)	1.9044(16)	1.889(8)
$Cu(1)-O(1)_{eq}$	1.9915(17)	1.985(7)
$Cu(1)-O(3)_{eq}$	1.9654(14)	1.945(7)
$Cu(1)-O(4)_{eq}$	2.0146(16)	2.017(7)
$Cu(1)-O(5)_{ax}$	2.3083(16)	2.284(7)

[a]The values of the standard deviation are given in parentheses.

Table 30. Interbond bite angles for {$Me_4N[Cu^{II}(S)$-pegma] · $2H_2O\}_n$ (**4a^S**) and {$Me_4N[Cu^{II}(R)$-pegma] · $2H_2O\}_n$ (**4a^R**)[a]

Bite angle / °	**4^S**	**4^R**
$N(1)-Cu(1)-O(1)_{eq}$	82.69(7)	82.0(4)
$N(1)-Cu(1)-O(4)_{eq}$	82.89(6)	83.2(3)
$O(3)_{eq}-Cu(1)-O(5)_{ax}$	79.73(6)	80.5(3)

[a]The values of the standard deviation are given in parentheses.

Table 31. Selected bond distances for {[Ni(cyclam)][$Cu^{II}(S)$-alama]$_2$ · $9H_2O\}_n$ (**1b^S**)[a]

Bond distance / Å	**1b^S**
Cu(1)-N(1)	2.02(3)
$Cu(1)-O(2)_{eq}$	1.947(19)
$Cu(1)-O(3)_{eq}$	1.78(2)
$Cu(1)-O(5)_{eq}$	2.11(2)
$Cu(1)-O(1)_{ax}$	2.27(2)
Cu(2)-N(2)	1.88(2)
$Cu(2)-O(7)_{eq}$	2.17(2)
$Cu(2)-O(8)_{eq}$	1.90(2)
$Cu(2)-O(10)_{eq}$	1.93(2)
$Cu(2)-O9_{ax}$	2.31 (2)
Ni(1)-N(3)	1.778(9)
Ni(1)-N(4)	2.241(9)
Ni(1)-N(5)	2.017(9)
Ni(1)-N(4)	2.241(9)
Ni(1)-O(4)	2.22(2)
Ni(1)-O(6)	2.16(3)

[a]The values of the standard deviation are given in parentheses.

Table 32. Interbond bite angles for {[Ni(cyclam)][Cu^{II}(*S*)-alama]$_2$ · 9H$_2$O}$_n$ (**1b^S**)[a]

Bite angle / °	**1b^S**
N(1)-Cu(1)- O(5)$_{eq}$	82.7(11)
N(1)-Cu(1)-O(3)$_{eq}$	81.9(12)
O(1)$_{ax}$-Cu(1)- O(2)$_{eq}$	82.1(8)
N(2)-Cu(2)- O(7)$_{eq}$	78.9(9)
N(2)-Cu(2)-O(10)$_{eq}$	86.7(10)
O(9)$_{ax}$-Cu(2)- O(8)$_{eq}$	77.3(9)

[a]The values of the standard deviation are given in parentheses.

Table 33. Average bond distances for {[Ni(cyclam)][Cu^{II}(*S*)-valma]$_2$ · 15H$_2$O}$_n$ (**2b^S**).[a] The copper(II) ions have been divided into two groups according to their environment. Cu(2), Cu(3), Cu(6) and Cu(8) atoms (with a CuN$_2$O$_4$ environment) will be noted as Cu* whereas Cu(1), Cu(4), Cu(5) and Cu(7) atoms (with a CuO$_6$ environment) will be noted as Cu$^{\#}$.

Bond distance / Å	**2b^S**
Cu*-N$_{eq}$	1.895(10)
Cu*-O$_{eq}$	2.122(10)
Cu*-O$_{ax}$	2.305(12)
Cu$^{\#}$-O$_{eq}$	1.94(12)
Cu$^{\#}$-O$_{ax}$	2.267(14)
Ni-N	2.147(19)
Ni-O	2.151(12)

[a]The values of the standard deviation are given in parentheses.

Table 34. Average values of the interbond bite angles for Cu(2), Cu(3), Cu(6) and Cu(8) atoms in {[Ni(cyclam)][Cu^{II}(*S*)-valma]$_2$ · 15H$_2$O}$_n$ (**2b^S**)[a]

Bite angle / °	**2b^S**
O'-Cu(2)-N	79.0(6)
N-Cu(2)-O	73.7(6)
O'-Cu(3)-N	83.2(4)
N-Cu(3)-O	77.3(4)
O'-Cu(6)-N	80.2(5)
N-Cu(6)-O	76.4(5)
O'-Cu(8)-N	82.8(5)
N-Cu(8)-O	73.4(5)

[a]The values of the standard deviation are given in parentheses.

Table 35. Selected bond lengths for {[Ni^{II}(cyclam)][Cu^{II}(*R*)-pegma]$_2$ · 6H_2O · 2C_3H_8O}$_n$ (**4b^R**)[a]

Bond distance / Å	**4b^R**
Cu(1)-N(1)	1.904(7)
Cu(1)-O(1)$_{eq}$	1.979(5)
Cu(1)-O(4)$_{eq}$	1.998(6)
Cu(1)-O(7)$_{eq}$	1.933(6)
Cu(1)-O(8)$_{ax}$	2.310(5)
Cu(2)-N(2)	1.910(7)
Cu(2)-O(6)$_{eq}$	2.022(6)
Cu2-O(9)$_{eq}$	1.941(7)
Cu2-O(3)$_{eq}$	1.969(5)
Cu(2)-O(2)$_{ax}$	2.396(6)
Ni(1)-N(1N)	2.083(11)
Ni(1)-N(2N)	1.957(15)
Ni(1)-N(3N)	2.027(13)
Ni(1)-N(4N)	2.147(15)
Ni(1)-O(10)	2.145(6)
Ni(1)-O(5)	2.131(6)

[a]The values of the standard deviation are given in parentheses.

Table 36. Interbond bite angles for {[Ni^{II}(cyclam)][Cu^{II}(*R*)-pegma]$_2$ · 6H_2O · 2C_3H_8O}$_n$ (**4b^R**)[a]

Bite angles / °	**4b^R**
N(1)-Cu(1)- O(1)$_{eq}$	83.3(3)
N(1)-Cu(1)-O(4)$_{eq}$	82.6(3)
O(8)$_{ax}$-Cu(1)- O(7)$_{eq}$	80.5(2)
N(2)-Cu(2)- O(6)$_{eq}$	84.0(3)
N(2)-Cu(2)-O(9)$_{eq}$	82.8(3)
O(2)$_{ax}$-Cu(2)- O(3)$_{eq}$	79.3(2)

[a]The values of the standard deviation are given in parentheses.

Table 37. Values of the average interbond bite angles for $\{Cu^{II}_6Ba[(S,S)\text{-alamox}]_3(OH)_2(H_2O) \cdot 30H_2O\}_n$ (**5b^S**), $\{Cu^{II}_6Ba[(S,S)\text{-valmox}]_3(OH)_2(CH_3OH)_6 \cdot 6H_2O\}_n$ (**6b^S**) and $\{Cu^{II}_4Ba[(S,S)\text{-leumox}]_3(OH)_2(H_2O)_2 \cdot 11H_2O\}_n$ (**7b^S**)[a]

Bite angle / °	**5b^S**	**6b^S**	**7b^S**
O-Cu-N	83.6(4)	84.9(3)	83.7(5)
O'-Cu -N	80.9(4)	82.8(3)	80.7(5)

[a]The values of the standard deviation are given in parentheses.

Table 38. Hydrogen bonds for **5c^S** [a,b]

D-H···A[c]	D-H / Å	H-A / Å	D···A / Å	< D-H···A / °
O(1H)-H(1H)···O(2W)#9	0.78(4)	2.13(4)	2.908(5)	171(14)
O(1W)-H(1W)···O(6W)	0.95(4)	2.02(4)	2.957(9)	173(9)
O(1W)-H(2W)···O(4W)	0.93(4)	2.06(7)	2.870(8)	145(8)
O(2W)-H(3W)···O(9W)	0.95(4)	1.86(5)	2.752(9)	156(7)
O(2W)-H(4W)···O(1W)	0.95(4)	1.92(4)	2.866(6)	175(8)
O(3W)-H(5W)···O(3)#3	0.91(4)	1.92(5)	2.781(7)	156(8)
O(3W)-H(6W)···O(9W)#8	0.96(4)	1.92(5)	2.825(10)	156(7)
O(4W)-H(7W)···O(2)#2	0.98(4)	1.80(5)	2.778(8)	175(8)
O(4W)-H(8W)···O(5W)	1.00	2.14	2.801 (9)	122.0
O(5W)-H(9W)···O(3W)	0.95(4)	1.84(4)	2.776(6)	167(8)
O(5W)-H(10W)···O(4W)	0.92(4)	2.28(8)	2.801(9)	115(7)
O(6W)-H(11W)···O(5W)	1.02(4)	1.73(4)	2.740(9)	174(8)
O(7W)-H(13W)···O(6W)	1.03(4)	2.29(9)	2.910(11)	117(6)
O(8W)-H(15W)···O(7W)	1.03(4)	1.91(5)	2.780(11)	140(6)
O(8W)-H(16W)···O(4W)#6	1.01	1.84	2.775(12)	152.8
O(9W)-H(18W)···O(8W)#7	0.93	1.87	2.754(12)	159.3
O(10W)-H(20W)···O(10A)#11	1.03	1.85	2.77(3)	146.5
O(10W)···O(11A)	/	/	2.686(10)	/
O(10A)···O(11B)#12	/	/	2.518(10)	/
O(10W)···O(11B)	/	/	2.909(10)	/
O(10W)···O(11C)	/	/	2.922(10)	/
O(11C)···O(11A)#13	/	/	2.850(10)	/

[a]The values of the standard deviation are given in parentheses. [b]Symmetry transformations used to generate equivalent atoms: #1 *-x+y,-x+1,z* #2 *-y+1,x-y+1,z* #3 *-x,-y+1,z+1/2* #4 *-x,-y+1,z-1/2* #5 *y,-x+y,z-1/2* #6 *x-y,x,z+1/2* #7 *-x+y,-x,z* #8 *-y,x-y,z* #9 *y,-x+y+1,z-1/2* #10 *-y+1,x-y+1,z+1* #11 *y,-x+y,z+1/2* #12 *x-y,x,z-1/2* #13- *x,-y,z-1/2.* [c]D = donnor, A = aceptor.

Table 39. Values of the O···O distance for the hydrogen-bonded water/hydroxo groups involved in the proton conduction mechanism of **5c^{S}** [a,b]

O···O	Distance / Å
O1W···O4W	2.870(8)
O1W···O6W	2.957(9)
O2W···O9W	2.752(9)
O2W···O1W	2.866(6)
O2W···O1H	2.908(5)
O3W···O5W	2.776(6)
O3W···O9Wa	2.825(10)
O4W···O5W	2.801(9)
O4Wa···O8W	2.775(12)
O5W···O6W	2.740(9)
O7W···O8W	2.780(11)
O7W···O10W	2.885(10)
O8W···O9Wa	2.754(12)
O10W···O11A	2.686(10)

[a]The values of the standard deviation are given in parentheses. [b]Symmetry code: (a) = -*y*, *x*-*y*, *z*.

Table 40. Average values of the interbond bite angle for $\{Cu^{II}_6Ca[(S,S)\text{-alamox}]_3(OH)_2(H_2O) \cdot 32H_2O\}_n$ (**5c^{S}**), $\{Cu^{II}_6Ca[(R,R)\text{-alamox}]_3(OH)_2(H_2O) \cdot 33H_2O\}_n$ (**5c^{R}**), $\{Cu^{II}_6Ca[(S,S)\text{-valmo}]_3(OH)_2(H_2O) \cdot 13H_2O\}_n$ (**6c^{S}**) and $\{Cu^{II}_6Ca[(S,S)\text{-leumox}]_3(OH)_2(H_2O) \cdot 11H_2O\}_n$ (**7c^{S}**)[a]

Bite angle / °	**5c^{S}**	**5c^{R}**	**6c^{S}**	**7c^{S}**
O-Cu-N	83.4(2)	83.4(2)	84.6(6)	84.0(6)
O'-Cu -N	82.2(2)	82.1(2)	82.2(6)	82.7(6)

[a]The values of the standard deviation are given in parentheses.

Table 41. Average values of the interbond bite angles for for $\{Cu^{II}_6Tb[(S,S)\text{-alamox}]_3(OH)_3 \cdot 21H_2O\}_n$ (**5e^{S}**)[a]

Bite angle / °	**5e^{S}**
O-Cu-N	84.1(8)
O'-Cu -N	82.5(8)

[a]The values of the standard deviation are given in parentheses.

I.5. References

1 M. F. De Lange, T. J. H. Vlugt, J. Gascon and F. Kapteijn, *Microporous Mesoporous Mater.*, 2014, **200**, 199–215.

2 J. Rouquerol, D. Avnir, C. W. Fairbridge, D. H. Everett, J. M. Haynes, N. Pernicone, J. D. F. Ramsay, K. S. W. Sing and K. K. Unger, *Pure Appl. Chem.*, 1994, **66**, 1739–1758.

3 SAINT, version 6.45, Bruker Analytical X-ray Systems, Madison, WI, 2003.

4 G. M. Sheldrick, SADABS Program for Absorption Correction, version 2.10, Analytical X-ray Systems, Madison, WI, 2003.

5 G. M. Sheldrick, *Acta Crystallogr. Sect. A Found. Crystallogr.*, 2008, **64**, 112–122.

6 SHELXTL-2013/4, Bruker Analytical X-ray Instruments, Madison, WI, 2003.

7 A. L. Spek, *Acta Crystallogr. Sect. D Biol. Crystallogr.*, 2009, **65**, 148–155.

8 L. J. Farrugia, *J. Appl. Crystallogr.*, 1999, **32**, 837–838.

9 D. Palmer, CRYSTAL MAKER, Cambridge University Technical Services, C. No Title, 1996.

10 WinDETA, Novocontrol GmbH, Hundsangen, Germany, 1995.

11 D. Johnson and Z. View, A software Program for IES Analysis, version 2.8, Scribner Associates, Inc., Southern Pines, NC, 2002.

12 J. P. Perdew, K. Burke and M. Ernzerhof, *Phys. Rev. Lett.*, 1996, **77**, 3865–3868.

13 N. Troullier and J. L. Martins, *Phys. Rev. B*, 1991, **43**, 1993–2006.

14 M. Parrinello and A. Rahman, *Phys. Rev. Lett.*, 1980, **45**, 1196–1199.

15 S. Nosé, *J. Chem. Phys.*, 1984, **81**, 511–519.

16 T. Ito, M. Kato and H. Ito, *Bull. Chem. Soc. Jpn.*, 1984, **57**, 2641–2649.

Annex II

II.1. Experimental Section

Mössbauer measurements. The Mössbauer spectra were collected between 300 and 50 K in transmission mode using a conventional constant-acceleration spectrometer and a 25 mCi ^{57}Co source in a Rh matrix. The velocity scale was calibrated using α-Fe foil. Isomer shifts (IS) are given relative to this standard at room temperature. The absorbers were obtained by packing the powdered samples (approximately 2 mg of natural Fe/cm^2) into a perspex holder. Absorber thicknesses were calculated on the basis of the corresponding electronic mass-absorption coefficients for the 14.4 keV radiation, according to Long *et al*.[1] Low-temperature measurements were performed with the sample in He exchange gas in a bath cryostat. The spectra were fitted to Lorentzian lines using a non-linear least-squares method.

Crystal Structure Data Collection and Refinement. The X-ray diffraction data collection on single crystals were performed on the CRISTAL beamline at SOLEIL synchrotron (Saclay, France) with λ = 0.66951 Å at 45 K. A special care was taken to prevent the degradation upon dehydration, and the crystal was mounted in a grease drop and immediately frozen. Due to the poor diffraction of the samples, 2θ was limited to 23.68 °. The data were indexed, integrated and scaled with the CrysalisPro[2] software program. The structure was solved by direct methods and refined with full-matrix least-squares technique on F^2 using the SHELXS-97 and SHELXL-97 programs by Sheldrick.[3] A good model for the solvent molecules cannot be achieved because of the severe disorder. Thus, to obtain a good refinement of the structures, the SQUEEZE subroutine in the PLATON software package[4] was applied to mask the electron density allocated in the cavities with the exception of those related with the counter cations and the coordinated water molecules, which were kept in the final model. This subroutine was applied on an anisotropic model of the framework.

II.2. Synthetic Procedures

2,4,6-trimethyl-*N*,*N*'-1,3-phenylenebis(oxamate). The $H_2Et_2Me_3mpba$ proligand was prepared by following a previously reported method.[5] Ethyl oxalyl chloride ester (14.0 mL, 120 mmol) was added to a solution of the corresponding diamine (2,4,6-trimethyl-1,3-phenylenediamine, 60 mmol) in THF (250 mL) under vigorous stirring at 0 °C. Finally, the reaction mixture was brought up to reflux for 1 h. $H_2Et_2Me_3mpba$ was obtained from the removal of the THF with a rotatory evaporator and it was further washed with diethyl ether, and dried under vacuum. Analysis calculated for $H_2Et_2Me_3mpba$ ($C_{17}H_{22}N_2O_6$; 350.4) C, 58.27; H, 6.33; N, 8.00. Found: C, 57.92; H, 5.88; N, 8.01. Yield: 20.2 g (96%). ^{1}H NMR (300 MHz, DMSO-d_6, 25 °C, TMS): δ 1.34 (t, 6 H; 2 CH3 from the ethyl groups), 1.95 (s, 3 H; 2–CH3 from the phenylene group), 2.10 (s, 6 H; 4–CH3 and 6–CH3 from the phenylene group), 4.32 (q, 4 H; 2 CH2 from the ethyl groups), 7.04 (s, 1 H; 5–H from the phenylene group), 10.383 (s, 2 H; 2 NH). IR (KBr in cm^{-1}) 3237 (NH), 1751, 1733 and 1692 (CO).

$Na_4[Cu_2(Me_3mpba)_2] \cdot 4H_2O$. The dicopper(II) precursor was prepared by following a previously reported method.[5] An aqueous solution (5 mL) of NaOH (0.16 g, 4.0 mmol) was added to a suspension of the $H_2Et_2Me_3mpba$ proligand (1 mmol) in water (15 mL) under continuous stirring. After its complete dissolution, an aqueous solution (5 mL) of $Cu(NO3)_2 . 3H_2O$ (0.24 g, 1 mmol) was added dropwise under stirring. The resulting deep green solution was filtered on paper to remove any small amount of solid particles. Solvent reduction under vacuum of the filtered solution afforded a green polycrystalline solid that was collected by filtration, washed with ethanol and diethyl ether, and air-dried. Yield: 0.76 g (87.4 %). Elemental analysis calculated for $C_{26}H_{28}Cu_2Na_4N_4O_{16}$ (870): C, 35.86; H, 3.21; N, 6.37. Found: C, 35.12; H, 3.30; N, 6.25 %; IR (KBr in cm^{-1}) 1654 (C=O).

$Na^I_4\{Mn^{II}_4[Cu^{II}_2(Me_3mpba)_2]_3\} \cdot 60H_2O$ (**8**): This compound was prepared by following a previously reported method.[6] X-ray quality bright green tiny prisms of **8** were grown by slow diffusion of aqueous solutions containing stoichiometric amounts of the preformed $Na_4[Cu_2(mpba)_2] \cdot 10H_2O$ (0.011 g, 0.015 mmol) species and $Mn(NO_3)_2 \cdot 4H_2O$

(0.005 g, 0.020 mmol) in an H-shaped tube on standing at room temperature for four weeks. Yield: 0.010 g, 54 %.

$M_4\{Mn_4[Cu_2(Me_3mpba)_2]_3\} \cdot nH_2O$ (**9**, M = Li and n = 68; **10**, M = K and n = 69): Well-formed pale green prisms of **9** and **10**, which were suitable for X-ray diffraction, were obtained by immersing crystals of **8** in saturated aqueous solutions of $LiCl \cdot 6H_2O$ and $KCl \cdot 6H_2O$ respectively, during 24 h. The crystals were collected by filtration and air-dried.

$[Fe^{III}(sal_2\text{-trien})]Na_3\{Mn^{II}_4[Cu^{II}_2(Me_3mpba)_2]_3\} \cdot 43H_2O$ [Fe(sal_2-trien)@8]: Well-formed dark green prisms of **Fe(sal_2-trien)@8** were obtained by immersing *ca.* 50 mg of crystals of **8** in a water solution containing 35 mg of $[Fe^{III}(sal_2\text{-trien})]NO_3 \cdot H_2O$ (synthesised according to literature methods[7]) for six days and then, gently washed with water to remove any trace of the mononuclear complex. The exchange of the Na^+ cation by the cationic $[Fe^{III}(sal_2\text{-trien})]^+$ species was monitored through SEM every 24 hours to ensure the maximum loading. Unfortunately, crystals of **Fe(sal_2-trien)@8** were not suitable for X-ray diffraction but they were characterized by SEM microscopy, Elemental Analysis, IR, ICP-AES and TGA and PXRD studies. Elemental analysis calculated for $C_{98}H_{170}Cu_6FeMn_4N_{16}Na_3O_{81}$ (3589.2): C 32.76, H 4.77, N 6.24 %. Found: C 32.75, H 4.62, N 6.31 %. IR (KBr in cm^{-1}) 3319 [NH from Fe(sal_2-trien)], 1622 [CN from Fe(sal_2-trien)] and 1591 cm^{-1} (CO from **8**).

$Mg^{II}_2\{Mg^{II}_4[Cu^{II}_2(Me_3mpba)_2]_3\} \cdot 45\ H_2O$ (11): X-ray quality bright green tiny prisms of **11** were grown by slow diffusion of aqueous solutions containing stoichiometric amounts of $Na_4[Cu_2(Me_3mpba)_2] \cdot 4H_2O$ (0.011 g, 0.015 mmol) and $Mg(NO_3)_2 \cdot 6H_2O$ (0.008 g, 0.030 mmol) in an H-shaped tube on standing at 18 °C after several weeks. Yield: 0.013 g, 67%.

$M^{II}_2\{M^{II}_4[Cu^{II}_2(Me_3mpba)_2]_3\} \cdot nH_2O$ (**12**, M = Co and n = 56; **13**, M = Ni and n = 54): Well-formed pale green prisms of **12** and **13**, which were suitable for X-ray diffraction, were obtained by immersing crystals of **11** for 3 weeks in saturated aqueous solutions of $Co(NO_3)_2 \cdot 6H_2O$ and $Ni(NO_3)_2 \cdot 6H_2O$, respectively. The crystals were collected by filtration and air-dried.

II.3. Physicochemical Characterisation

Table 1. Elemental analysis[a] and selected FTIR data[b] of $Na^{I}_4\{Mn^{II}_4[Cu^{II}_2(Me_3mpba)_2]_3\} \cdot 60H_2O$ (**8**), $Li^{I}_4\{Mn^{II}_4[Cu^{II}_2(Me_3mpba)_2]_3\} \cdot 68H_2O$ (**9**) and $K^{I}_4\{Mn^{II}_4[Cu^{II}_2(Me_3mpba)_2]_3\} \cdot 69H_2O$ (**10**)

Compound	C (%)	H (%)	N (%)	$\nu_{C=O}$ (cm^{-1})
8	26.59(26.65)	5.11(5.16)	4.78(4.78)	1602
9	26.19(26.06)	5.71(5.49)	4.66(4.67)	1599
10	25.01(25.04)	5.42(5.33)	4.47(4.49)	1600

[a]Calculated data are given in parentheses. [b]KBr disk.

Table 2. Elemental analysis[a] and selected FTIR data[b] of $Mg^{II}_2\{Mg^{II}_4[Cu^{II}_2(Me_3mpba)_2]_3\} \cdot 45\ H_2O$ (**11**), $Co^{II}_2\{M^{II}_4[Cu^{II}_2(Me_3mpba)_2]_3\} \cdot 56H_2O$ (**12**) and $Ni^{II}_2\{Ni^{II}_4[Cu^{II}_2(Me_3mpba)_2]_3\} \cdot 54H_2O$ (**13**)

Compound	C (%)	H (%)	N (%)	$\nu_{C=O}$ (cm^{-1})
11	29.91(30.42)	4.89(4.91)	5.42(5.45)	1609
12	27.01(26.88)	4.91(4.97)	4.83(4.83)	1603
13	27.19(27.17)	4.82(4.91)	4.91(4.87)	1605

[a]Calculated data are given in parentheses. [b]KBr disk.

II.4. Summary of the Crystallographic Data and Refinement Conditions

Table 3. Summary of Crystallographic Data and Refinement Conditions for $Na^{I}_4\{Mn^{II}_4[Cu^{II}_2(Me_3mpba)_2]_3\} \cdot 60H_2O$ (**8**), $Li^{I}_4\{Mn^{II}_4[Cu^{II}_2(Me_3mpba)_2]_3\} \cdot 68H_2O$ (**9**) and $K^{I}_4\{Mn^{II}_4[Cu^{II}_2(Me_3mpba)_2]_3\} \cdot 69H_2O$ (**10**)

Compound	**8**	**9**	**10**
formula	$C_{78}H_{180}Cu_6Mn_4N_{12}Na_4O_{96}$	$C_{78}H_{196}Cu_6Mn_4N_{12}Li_4O_{104}$	$C_{78}H_{198}Cu_6Mn_4N_{12}K_4O_{105}$
M (g mol^{-1})	3515.27	3595.22	3741.87
crystal system	tetragonal	tetragonal	tetragonal
space group	*P*4/*mmm*	*P*4/*mmm*	*P*4/*mmm*
a (Å)	36.332(5)	36.71(2)	37.492(8)
b (Å)	36.332(5)	36.71(2)	37.492(8)
c (Å)	15.208(3)	15.414(9)	15.557(3)
α = β = γ (°)	90	90	90
V (Å^3)	20075(6)	20770(29)	21868(10)
Z	4	4	4
ρ_{calc} (g cm^{-3})	1.123	1.150	1.137
μ (mm^{-1})	1.057	0.921	0.952
T (K)	100(2)	100(2)	100(2)
Unique reflections	9434	3677	8826
Observed reflections [$I > 2\sigma(I)$]	9389	2625	3628
R^a [$I > 2\sigma(I)$] (all data)	0.1906	0.2077	0.1699
wR^b [$I > 2\sigma(I)$] (all data)	0.5535	0.4780	0.3939

$^aR = \sum(||F_o| - |F_c||)/\sum|F_o|$. $^bwR = [\sum w(|F_o| - |F_c|)^2/\sum w|F_o|2]^{1/2}$.

Table 4. Summary of Crystallographic Data and Refinement Conditions for $Mg^{II}_2\{Mg^{II}_4[Cu^{II}_2(Me_3mpba)_2]_3\} \cdot 45\ H_2O$ (**11**), $Co^{II}_2\{M^{II}_4[Cu^{II}_2(Me_3mpba)_2]_3\} \cdot 56H_2O$ (**12**) and $Ni^{II}_2\{Ni^{II}_4[Cu^{II}_2(Me_3mpba)_2]_3\} \cdot 54H_2O$ (**13**)

Compound	**11**	**12**	**13**
Formula	$C_{39}H_{30}Cu_3Mg_3N_6O_{25}$	$C_{39}H_{50}Cu_3Co_3N_6O_{28}$	$C_{78}H_{90}Cu_6Ni_6N_{12}O_{53}$
M (g mol^{-1})	1260.24	1418.10	2780.82
Crystal system	Tetragonal	Tetragonal	Tetragonal
Space group	*P*4/*mmm*	*P*4/*mmm*	*P*4/*mmm*
a (Å)	35.9863(3)	36.0882(4)	36.1886(6)
b (Å)	35.9863(3)	36.0882(4)	36.1886(6)
c (Å)	15.1020(2)	15.0225(4)	14.8134(2)
α = β = γ (°)	90	90	90
V (Å^3)	19557.3(4)	19564.7(5)	19399.8(7)
Z	8	8	4
ρ_{calc} (g cm^{-3})	0.847	0.949	0.940
μ (mm^{-1})	0.713	1.008	1.073
T (K)	45.0	45.0	45.0
Measured reflections	272916	274464	126621
Unique reflections (Rint)	22121 (0.0853)	22218 (0.0985)	8917 (0.1140)
Observed reflections [$I > 2\sigma(I)$]	10731	9275	5545
[c]Goodness-of-fit on F^2	1.249	1.264	1.415
R^a [$I > 2\sigma(I)$] (all data)	0.0962 (0.1589)	0.1241 (0.2486)	0.1173 (0.1533)
wR^b [$I > 2\sigma(I)$] (all data)	0.3476 (0.3914)	0.4014 (0.4525)	0.3673 (0.3936)

$^aR = \sum(|F_o| - |F_c|)/\sum|F_o|$. $^bwR = [\sum w(|F_o| - |F_c|)^2/\sum w|F_o|2]^{1/2}$. $^cS = [\sum w(|F_o| - |F_c|)^2/(N_o - N_p)]^{1/2}$.

II.5. References

1 G. J. Long, T. E. Cranshaw and G. Longworth, *Mossb. Eff. Ref. Data J.*, 1983, **6**, 42–49.

2 Agilent, CrysAlis PRO. Agilent Technologies UK Ltd, Yarnton, England, 2011.

3 G. M. Sheldrick, *Acta Crystallogr. Sect. A Found. Crystallogr.*, 2008, **64**, 112–122.

4 A. L. Spek, *J. Appl. Cryst.*, 2003, **36**, 7–13.

5 J. Ferrando-Soria, J. Pasán, C. Ruiz-Pérez, Y. Journaux, M. Julve, F. Lloret, J. Cano and E. Pardo, *Inorg. Chem.*, 2011, **50**, 8694–8696.

6 J. Ferrando-Soria, R. Ruiz-García, J. Cano, S.-E. Stiriba, J. Vallejo, I. Castro, M. Julve, F. Lloret, P. Amorós, J. Pasán, C. Ruiz-Pérez, Y. Journaux and E. Pardo, *Chem. - A Eur. J.*, 2012, **18**, 1608–1617.

7 E. Sinn, G. Sim, E. V Dose, M. F. Tweedle and L. J. Wilson, *J. Am. Chem. Soc.*, 1978, **100**, 3375–3390.

Resumen

1. Introducción

De entre las diferentes áreas de investigación que conciernen al campo de la Química, el diseño y síntesis de MOFs (Metal Organic Frameworks)[1–5] ha experimentado uno de los crecimientos más pronunciados durante las últimas décadas como consecuencia no sólo de la gran variedad de topologías que pueden adoptar dichos sistemas, sino también por las interesantes propiedades físico-químicas que pueden presentar y que son de gran importancia para campos de investigación estratégicos como la Nanociencia y la Nanotecnología.

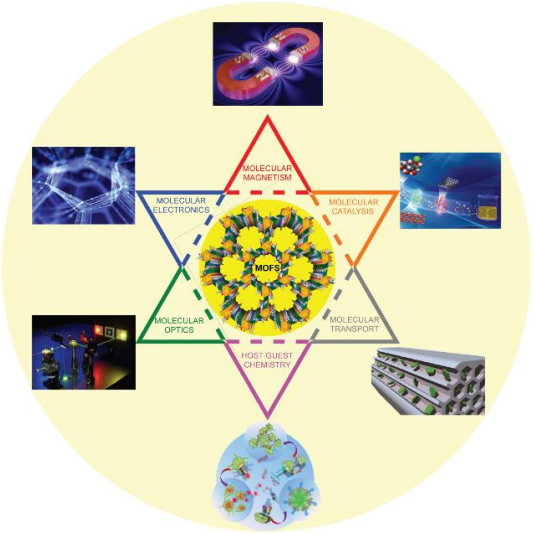

Figura 1. MOFs como punto de encuentro pluridisciplinar.

Estos materiales híbridos constituidos por iones metálicos (o pequeños clústeres metálicos) conectados a través de una gran diversidad de espaciadores de naturaleza orgánica, han sido objeto de estudio exhaustivo debido a la gran diversidad de propiedades que poseen. Los MOFs pueden ser empleados en la preparación de sensores,[6] captura y separación selectiva de gases,[7] en el transporte y liberación de fármacos,[8,9] reconocimiento molecular[10] y catálisis,[11] conducción protónica,[12] etc. Además, de manera más específica, sus poros pueden ser empleados como plantillas

donde llevar a cabo el crecimiento controlado de nanopartículas así como para encapsular una gran variedad de moléculas orgánicas y complejos.[13] Debido a su porosidad y a la presencia de determinados grupos funcionales, presentan una química huésped-anfitrión muy variada,[14,15] lo que convierte a estos materiales en candidatos idóneos para preparar Materiales Multifuncionales (MMs),[16–20] o sea aquéllos que combinan más de una propiedad física o química, siendo posible la sinergia entre ellas. Por todo ello, los MOFs representan el punto de cruce de diversos campos de la ciencia como el Magnetismo y la Electrónica Molecular, la Electroquímica y la Fotoquímica Molecular así como la Química huésped-anfitrión también a nivel molecular (ver Figura 1).

De entre las características que presentan los MOFs, la porosidad se encuentra en el origen de la mayoría de las propiedades y las aplicaciones tan fascinantes que estos materiales ofrecen. Es por ello, que en esta Tesis nos hemos centrado principalmente en el diseño, síntesis y caracterización de polímeros de coordinación porosos (PCPs) teniendo como objetivo la incorporación de nuevas propiedades físico-químicas, que puedan o no presentar sinergia entre ellas y que den lugar a los mencionados MMs.

En algunos casos, el diseño y síntesis de PCPs altamente funcionalizados no resulta una tarea obvia debido a factores como la limitada solubilidad o la escasa estabilidad térmica de los precursores, la incompatibilidad entre los grupos funcionales, las reacciones no deseadas de los centros metálicos con otros grupos dadores, etc. Por todo ello, en ocasiones, la síntesis directa mediante métodos convencionales de un material no se puede llevar a cabo. Afortunadamente, existe una alternativa útil y sencilla para modificar los constituyentes (centros metálicos, contraiones, ligandos y/o moléculas de disolvente) de materiales que ya están preformados sin alterar la integridad de la estructura: los métodos post-sintéticos (MPSs). Además, en un gran número de trabajos publicados al respecto, se ha comprobado que mediante la modificación de los constituyentes del MOF, se pueden mejorar las propiedades físicas ya existentes y/o introducir otras nuevas.

Durante el transcurso de esta Tesis, se han diferenciado dos líneas de investigación (Partes 1 y 2). En la primera, nuestro interés se ha localizado en la incorporación de quiralidad en materiales porosos. Por ello, esta línea se basa en el uso de aminoácidos como moléculas de partida, las cuales convenientemente funcionalizadas, puedan dar lugar a estructuras de mayor complejidad y cuya quiralidad se pueda transmitir a todas ellas. De este modo, se pueden obtener PCPs quirales cuyas características de poro (tamaño y funcionalidad) puedan ser moduladas de manera intencionada para ser empleados en diferentes aplicaciones como separación de gases y/o de mezclas quirales o bien catálisis asimétrica. La segunda línea de investigación se ha centrado en el estudio de los métodos MPSs como herramientas factibles para modificar materiales a la carta de manera sencilla y obtener así compuestos derivados nuevos que muestren propiedades interesantes que no estaban presentes en el material de partida o incluso consigan mejorar las ya existentes.

2. Metodología

Para la síntesis de los diferentes materiales hemos utilizado las herramientas que nos proporcionan tanto la Química de Coordinación como la Química Orgánica, al hilo de la línea que se lleva desarrollando en nuestro grupo de investigación durante los últimos años. Los grupos funcionales con los que hemos modificado los ligandos, así como la estrategia sintética seguida para su obtención, constituyen el nexo común que comparten ambas familias de compuestos (PCPs quirales y PCPs obtenidos mediante MPSs).

La estrategia preparativa empleada para la obtención de PCPs se basa en la síntesis inicial del proligando adecuado (basado en las propiedades que se pretenden incorporar al material final; ver Figura 2), la síntesis de un metaloligando con carga, obtenido a partir de la coordinación del proligando con un ion (generalmente de la segunda serie de transición) y por último la coordinación de este metaloligando con un segundo ion metálico (alcalino o de la segunda serie de transición) o un complejo metálico, para

obtener estructuras de dimensionalidad elevada. Las propiedades finales del material dependen, por tanto, de la naturaleza del ligando orgánico, de las propiedades de los diferentes iones metálicos utilizados y de la propia topología y estructura de la red tridimensional.

En una primera etapa, se funcionalizan las moléculas de partida (aminoderivados) para obtener los proligandos de tipo oxamato $(C_2O_3NR\text{-})^{2-}$ y oxamidato $(C_2O_2N_2R_2)^{4-}$, ya que éstos ofrecen diversas ventajas: (i) los grupos dadores *N*,*O*-oxamato y los *N*,*N'*-oxamidato muestran una gran afinidad hacia los iones metálicos de la primera serie de transición (M = Cu^{II}, Ni^{II} and Co^{II}) formando complejos muy estables en disolución (especies mono-, di- y/o trinucleares), lo que permite la formación de metaloligandos robustos con capacidad de coordinarse a otros iones metálicos a través de los átomos de oxígeno de los grupos carbonilo libres, conduciendo a la síntesis de polímeros de coordinación heterobimetálicos de manera programada; (ii) los ligandos puente bis-bidentados oxamato y oxamidato transmiten de manera efectiva las interacciones magnéticas entre centros metálicos paramagnéticos, permitiendo la incorporación de propiedades magnéticas de interés; (iii) en algunos casos, los ligandos aniónicos de tipo oxamato y oxamidato dan lugar a estructuras tridimensionales aniónicas, cuya carga negativa se compensa con la presencia de cationes que suelen ubicarse en los poros del material (esta característica les convierte en excelentes candidatos para ser MMs ya que dichos cationes pueden aportar propiedades físicas adicionales y además representan una plataforma interesante para el estudio del intercambio catiónico como posible MPS); (iv) por último, los ligandos oxamato y oxamidato se pueden funcionalizar con facilidad seleccionando el precursor amino adecuado, hecho que se traduce en otra herramienta para introducir nuevas propiedades en el material.

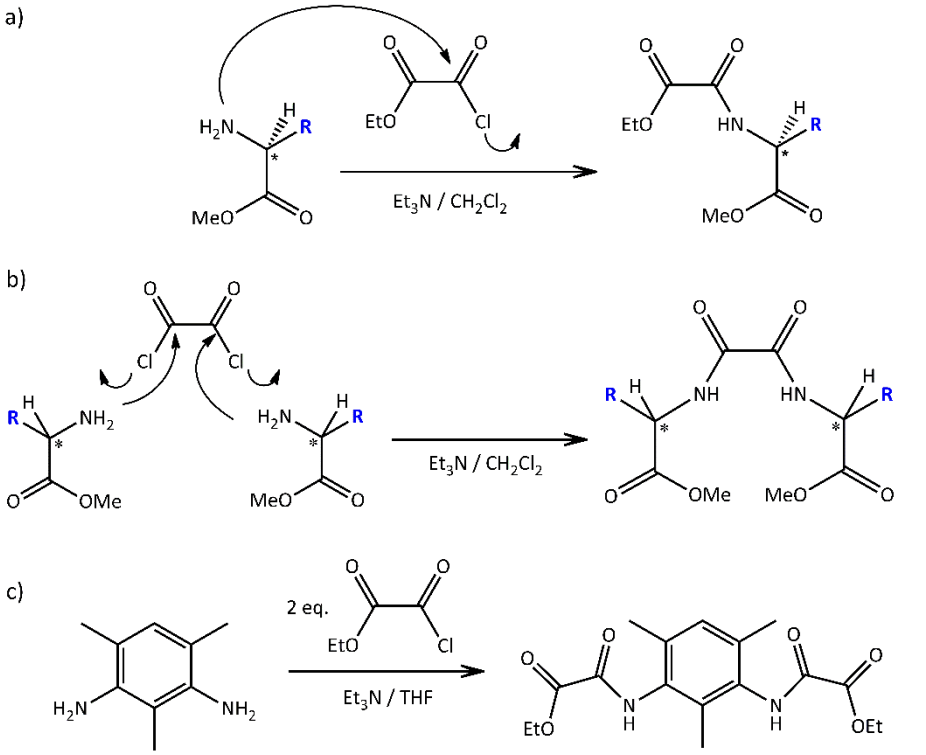

Figura 2. Esquemas sintéticos para la preparación de los proligandos de tipo (a) mono-oxamato y (b) bis-oxamidato a partir de los aminoácidos quirales y (c) bis-oxamato a partir de diaminas aromáticas sustituidas.

En una segunda etapa, se obtienen sales precursoras de cobre(II) mediante la desprotonación e hidrólisis de los proligandos de tipo oxamato y oxamidato y su posterior complejación con cobre(II), en disolución y a temperatura ambiente. Estos compuestos de cobre(II) de diversa naturaleza se hacen reaccionar en una tercera etapa, a través de sus átomos dadores disponibles, con complejos o iones metálicos dando lugar a estructuras de dimensionalidad elevada.

2.1. PCPs multifuncionales quirales

En esta parte de la Tesis, nuestro interés se ha focalizado en la síntesis y caracterización de MOFs quirales. Estos materiales se obtienen a partir de proligandos derivados de aminoácidos (ver Figuras 2a,b y 3).

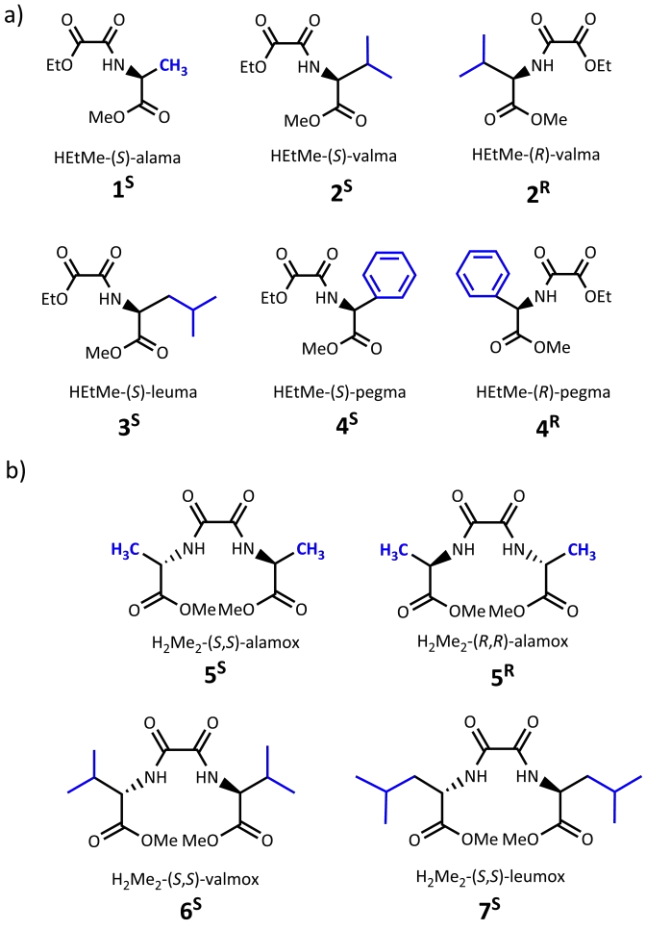

Figura 3. Conjunto de proligandos oxamato- (a) y oxamidato-derivados (b) que se han obtenido a partir de aminoácidos siguiendo la estrategia sintética definida. HEtMealama = *N*-(etil oxoacetato)alanina; HEtMevalma = *N*-(etil oxoacetato)valina]; HEtMeleuma = *N*-(etil oxoacetato)leucina] y HEtMepegma = *N*-(etil oxoacetato)fenilglicina, H_4alamox = *N*,*N*'-bis(alanina)oxalildiamida; H_4valmox = *N*,*N*'-bis(valina)oxalildiamida and H_4leumox = *N*,*N*'-bis(leucina)oxalildiamida.

Algunas de las ventajas de estos materiales se enumeran a continuación: (i) son materiales mucho más apropiados para aplicaciones biocompatibles; (ii) presentan quiralidad gracias a la estrategia sintética mediante la cual las propiedades ópticas de los aminoácidos de partida se transmiten a los compuestos resultantes de una manera racional y dirigida y (iii) presentan una gran compatibilidad con el agua como disolvente, lo que facilita estudios posteriores como por ejemplo la conducción protónica o de iones hidróxido, así como la realización de experimentos de intercambio iónico o transmetalación.

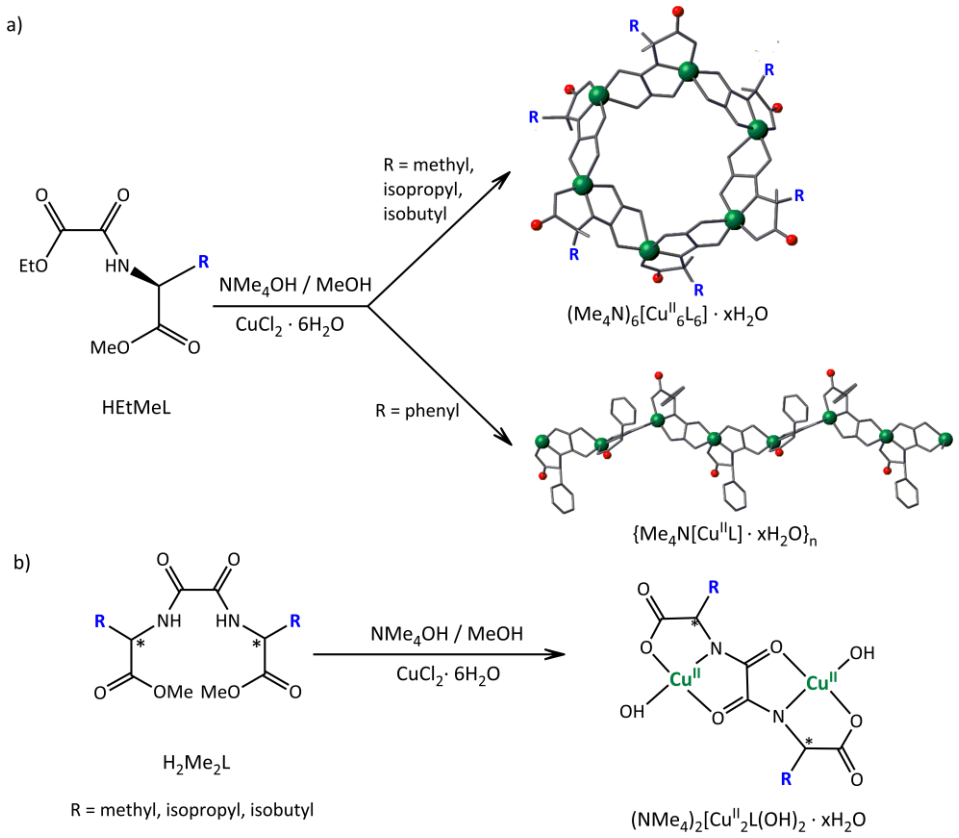

Figura 4. Rutas de síntesis para la obtención de los metaloligandos quirales: (a) anillos hexanucleares de cobre(II) derivados de los proligandos (*S*)-alama^{3-} (R = metil), (*S*)- y (*R*)-valma^{3-} (R = isopropil) y (*S*)-leuma^{3-} (R = isobutil) y de cadenas de cobre(II) a partir de los proligandos (*S*)- y (*R*)-pegma^{3-} (R = fenil); (b) complejos *trans*-oxamidato de cobre(II) derivados de los proligandos (*S*,*S*)-alamox^{4-}, (*S*,*S*)-valmox^{4-} y (*S*,*S*)-leumox^{4-}.

Siguiendo la estrategia sintética previamente definida, hemos funcionalizado diferentes aminoácidos con grupos oxamato $(C_2O_3NR-)^{2-}$ y oxamidato $(C_2O_2N_2R_2)^{2-}$ y hemos obtenido una amplia librería de proligandos que se muestran en la Figura 3. A continuación se han hecho reaccionar estos proligandos con iones cobre(II) en medio metánolico y en presencia de una base para la preparación de los diferentes complejos aniónicos precursores (metaloligandos), tal como se muestra en la Figura 4 y se han obtenido complejos aniónicos de diferente naturaleza (dímeros, anillos hexanucleares 0D y compuestos 1D). Todos ellos han sido aislados y caracterizados (incluidas medidas de dicroísmo circular para comprobar que la quiralidad ha sido transmitida de manera efectiva) y posteriormente empleados como metaloligandos para coordinar o iones alcalino-térreos y lantánidos (caso de los precursores de tipo oxamidato) o bien complejos metálicos (caso de los precursores de tipo oxamato) a través de sus grupos carbonilo libres, dando lugar a estructuras porosas quirales tridimensionales (3D) de muy diversa naturaleza.

2.2. PCPs multifuncionales obtenidos a partir de métodos post-sintéticos (MPSs)

De entre todos los MPSs posibles que se conocen, hemos sacado provecho de la naturaleza aniónica de algunos de nuestros PCPs para intercambiar los cationes que actúan compensando la carga (intercambio catiónico) así como los iones metálicos de la red de coordinación (transmetalación) (ver Figura 5), siempre en procesos en fase sólida preferiblemente en transformaciones de cristal a cristal.

Los intercambios de iones metálicos de cristal a cristal se producen introduciendo cristales del MOF preformado en una disolución saturada de la sal del ion metálico o complejo metálico que se desea incorporar. La cinética y la termodinámica de estos intercambios se pueden estudiar analizando los equilibrios de sustitución mediante Microscopía Electrónica de Barrido o Espectroscopía de Absorción Atómica de Plasma. Una vez caracterizados los nuevos materiales para comprobar el grado de sustitución y su isoestructuralidad con el material de partida, se procede a medir sus propiedades físicas con el fin de obtener alguna información acerca de la influencia del intercambio de los iones metálicos en las propiedades finales del MOF.

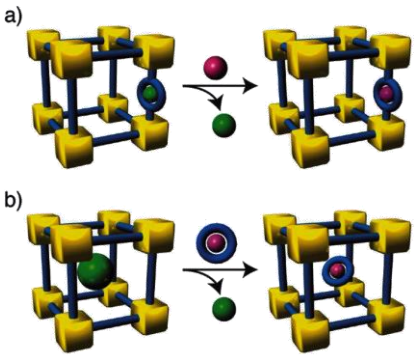

Figura 5. Ejemplos de MPSs por intercambio de (a) iones metálicos que forman parte de la red de coordinación más fuertemente enlazados (transmetalación) y (b) contracationes ubicados en los poros del MOF (intercambio catiónico).

3. Objetivos

Para la línea de investigación que tiene que ver con los PCPs multifuncionales de naturaleza quiral se marcan los siguientes objetivos:

(i) Diseñar e implementar una ruta sintética efectiva para incorporar la quiralidad en nuestros materiales basada en el uso de aminoácidos enantiopuros. Para ello se empezará por funcionalizar dichos aminoácidos con grupos oxamato y oxamidato para obtener los correspondientes proligandos enantiopuros.

(ii) Sintetizar complejos precursores quirales de cobre(II) que presenten posiciones vacantes para, posteriormente, llevar a cabo la estrategia sintética del metaloligando mediante su coordinación a un segundo ion metálico o complejo que actúe de nexo

entre ellos; de esa manera se pretende obtener estructuras de alta dimensionalidad quirales, que además presenten propiedades físico-químicas adicionales.

(iii) Explorar las posibles propiedades físico-químicas y las aplicaciones que los MMs sintetizados puedan tener, tales como porosidad, quiralidad, propiedades magnéticas, conducción protónica, adsorción selectiva de gases, catálisis asimétrica y/o separación de enantiómeros.

Para la línea de investigación centrada en el uso de los MPSs para la obtención de PCPs multifuncionales, se establecen los siguientes objetivos:

(i) Diseñar los procedimientos adecuados para llevar a cabo transformaciones post-sintéticas con MOFs preformados que pueden haber sido aislados en trabajos anteriores o bien que se puedan preparar específicamente para utilizarlos como plataforma en el estudio de los MPSs.

(ii) Explorar los diferentes mecanismos de sustitución, ya sea de aquellos iones metálicos presentes en la propia red de coordinación del material cuyos enlaces tienen un carácter más fuerte (y en principio resulta un reto su sustitución manteniendo la integridad del PCP) o bien de los cationes que están en los poros.

(iii) Estudiar las propiedades de los materiales nuevos obtenidos para establecer la posible influencia de los iones metálicos en las mismas así como en la estabilidad estructural. Pretendemos demostrar que las técnicas post-sintéticas constituyen una herramienta eficaz para introducir nuevas propiedades físico-químicas en materiales preformados, o bien mejorar aquéllas que ya estaban presentes.

(iv) Investigar la encapsulación de complejos metálicos con propiedades interesantes en los poros del material mediante intercambio catiónico y estudiar las propiedades introducidas mediante dicho proceso así como su posible sinergia con las propiedades del material de partida.

4. Resultados

4.1. PCPs multifuncionales quirales

Partiendo de los isómeros *R* y S de los aminoácidos alanina, valina, leucina y fenilglicina, se sintetizaron los correspondientes proligandos de tipo oxamato mostrados en la Figura 3a. Haciendo uso de estos proligandos se prepararon los correspondientes metaloligandos de cobre(II) (Figura 4). Una vez aislados y caracterizados estos precursores, se hicieron reaccionar con el complejo cuadrado $[Ni(cyclam)]^{2+}$ (cyclam = 1,4,8,11-tetraazacicloteradecano) obteniéndose diferentes estructuras porosas tridimensionales. La estrategia mediante la cual los diferentes complejos de cobre(II) son empleados como metaloligandos y cómo se van ensamblando mediante su coordinación con el complejo de níquel(II) formando estructuras ordenadas se visualiza en la Figura 6.

Los tres MOFs así obtenidos (ver Figura 6) son quirales y además presentan canales cuyo tamaño viene determinado por el del residuo alquílico del aminoácido de partida. En principio son un ejemplo de MMs con varias propiedades (porosidad y quiralidad). Sin embargo, su escasa estabilidad en agua representó una limitación importante a la hora de llevar a cabo experimentos de catálisis enantioselectiva así como experimentos de separación quiral. No obstante, la propia complejidad estructural de los mismos, los convierte en una plataforma interesante para el estudio del ensamblaje de PCPs quirales. De la misma manera se confirma la ruta sintética propuesta como una herramienta efectiva para la preparación a la carta de PCPs quirales.

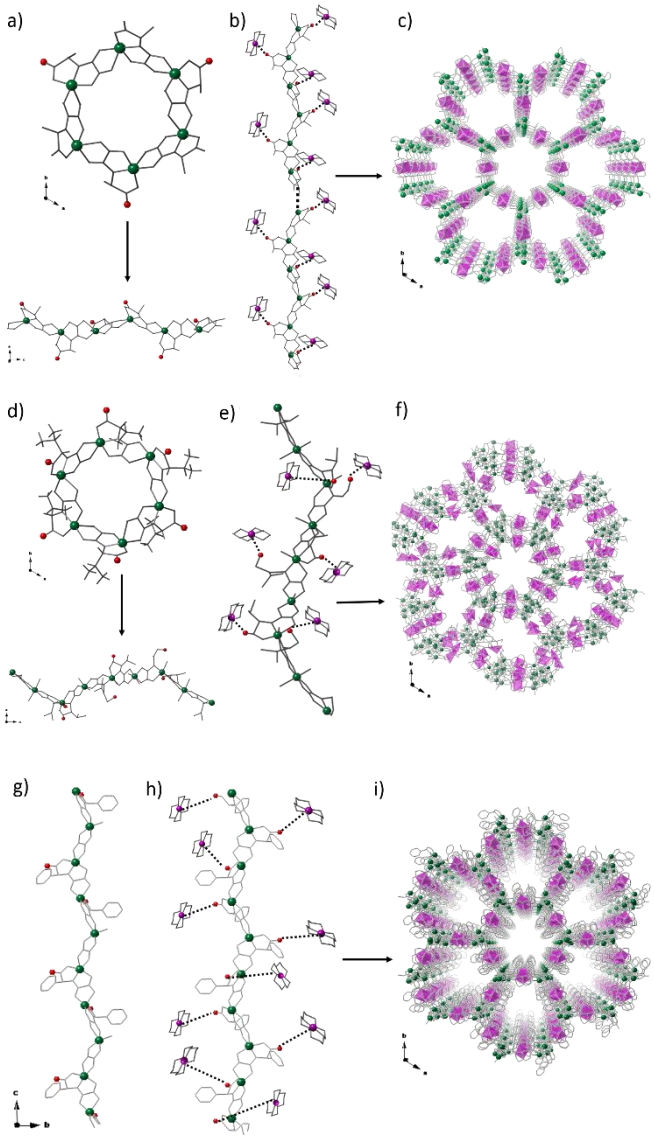

Figura 6. Vista en perspectiva de los compuestos precursores derivados de (a) (*L*)-alanina, (d) (*L*)-valina y (g) (*D*)-fenilglicina. (b, e y h) Procesos de ensamblaje propuestos donde los grupos carbonilo libres (esferas rojas) de los precursores coordinan a los cationes $[Ni(cyclam)]^{2+}$. Vista en perspectiva de los PCPs quirales derivados de (c) *L*-alanina, (f) *L*-valina e (i) *D*-fenilglicina. Los iones cobre(II) y níquel(II) están representados mediante esferas verdes y fucsias, respectivamente, mientras que las varillas representan a los ligandos. Las líneas discontinuas simulan la aproximación de los cationes $[Ni(cyclam)]^{2+}$ a los grupos carbonilo del metaloligando y el correspondiente ensamblaje.

La misma estrategia sintética también proporcionó resultados interesantes para los compuestos de tipo oxamidato derivados de aminoácidos (Figura 3b). Al hacer reaccionar los ligandos (*S*,*S*)-alamox^{4-}, (*S*,*S*)-valmox^{4-} y (S,*S*)-leumox^{4-} con una sal de cobre(II) en medio básico y en metanol como disolvente, se obtuvieron dímeros aniónicos de cobre(II) que presentan posiciones libres para extender su coordinación y formar así compuestos de dimensionalidad elevada (ver Figura 4b). Estos compuestos dinucleares de cobre(II) se hicieron reaccionar en medio acuoso con iones calcio(II), bario(II), disprosio(III) y terbio(III) para obtener las correspondientes subfamilias de PCPs que presentan un tamaño de poro distinto en función del residuo alquílico del aminoácido de partida.

Haciendo reaccionar los dímeros precursores $[(Me_4N)_2\{Cu^{II}_2(S,S)\text{-}L(OH)_2\} \cdot nH_2O$ (L = alamox^{4-}, valmox^{4-}, leumox^{4-}) con iones bario(II) se obtuvieron tres PCPs de fórmulas $\{Ba^{II}Cu^{II}_6[(S,S)\text{-alamox}]_3(OH)_2(H_2O) \cdot 30H_2O\}_n$ (**5b^S**), $\{Ba^{II}Cu^{II}_6[(S,S)\text{-valmox}]_3(OH)_2(CH_3OH)_6 \cdot 6H_2O\}_n$ (**6b^S**) and $\{Ba^{II}Cu^{II}_4[(S,S)\text{-leumox}]_3(OH)_2(H_2O)_2 \cdot 14H_2O\}_n$ (**7b^S**) (Figura 7).

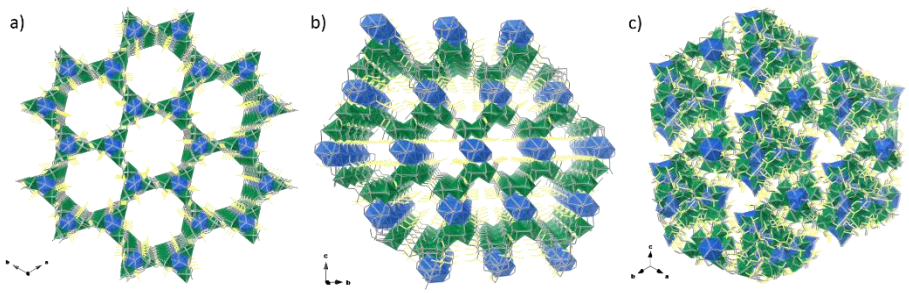

Figura 7. Vista en perspectiva de los MOFs de bario(II) derivados de (a) (*S*,*S*)-alamox, (b) (*S*,*S*)-valmox and (c) (*S*,*S*)-leumox ilustrando la reducción de porosidad a lo largo de la serie. Los átomos metálicos y los ligandos están representados como poliedros y varillas, respectivamente (Cu, verde; Ba, azul). Los residuos alquílicos (a) R = -CH_3 (alanina), (b) -$CH(CH_3)_2$ (valina) and (c) -$CH_2CH(CH_3)_2$ (leucina) se han dibujado como varillas amarillas. Las moléculas de agua de cristalización se han omitido para mayor claridad.

Esta nueva familia de PCPs quirales representa un interesante escenario para estudiar, en primer lugar, como la información quiral intrínseca de los ligandos enantiopuros se puede transmitir a las estructuras 3D resultantes; y en segundo lugar,

la influencia de la naturaleza (tamaño, forma e hidrofobicidad) de los residuos alifáticos de los aminoácidos en el ensamblaje y la topología final del material 3D.

Mediante la reacción de los dímeros precursores de cobre(II) con iones calcio(II) se obtuvo una subfamilia de estructuras porosas 3D idénticas de fórmula general $\{Ca^{II}Cu^{II}_6[(S,S)\text{-L}]_3(OH)_2(H_2O)\}_n \cdot xH_2O$ [L = alamox^{4-} (x = 32; **5c^S**), valmox^{4-} (x = 13; **6c^S**) y leumox^{4-} (x = 11; **7c^S**), tal como se puede observar en la Figura 8. Estos derivados de calcio(II) resultan especialmente interesantes por dos motivos: (i) son materiales isoestructurales cuya diferencia radica en el tamaño y funcionalidad de los residuos alifáticos de los aminoácidos que decoran las paredes de sus poros y, por tanto, dichos canales presentan diferente densidad de carga, y (ii) sus estructuras permanecen inalteradas cuando se eliminan las moléculas de disolvente. Ambas características los convierten en candidatos idóneos para estudiar sus propiedades de adsorción y de separación de gases.

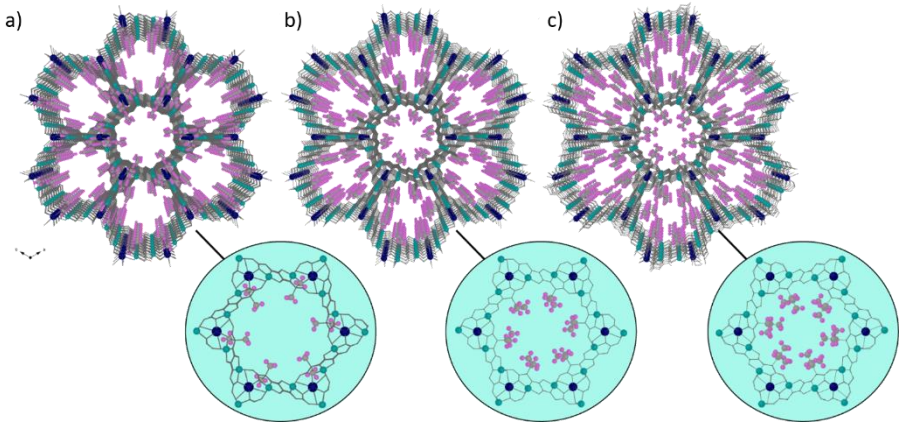

Figura 8. Vistas a lo largo del eje cristalográfico *c* de las estructuras porosas de (a) **5c^S**, (b) **6c^S** and (c) **7c^S** con detalle de los diferentes grupos alquilo en una vista ampliada del poro. Los iones cobre(II) y calcio(II) están representados por esferas cian y azules, respectivamente. Los residuos alquílicos de los aminoácidos se muestran como bolas y varillas, mientras que el resto de los ligandos se representan con varillas. Las moléculas de agua de cristalización se han omitido para mayor claridad.

Previa comprobación de su porosidad permanente mediante medidas de adsorción de N_2 a 77 K y las adicionales de CO_2 a 1 bar y 273 K (ambas mostraron una tendencia

5c^S > 6c^S > 7c^S, de acuerdo con su decreciente tamaño de poro), nos propusimos estudiar la posible selectividad de estos materiales frente a diferentes hidrocarburos ligeros. Para ello, se midieron las isotermas de adsorción de metano (CH_4), etano (C_2H_6), etileno (C_2H_4), propano (C_3H_8), propileno (C_3H_6) y butano (*n*-C_4H_{10}).

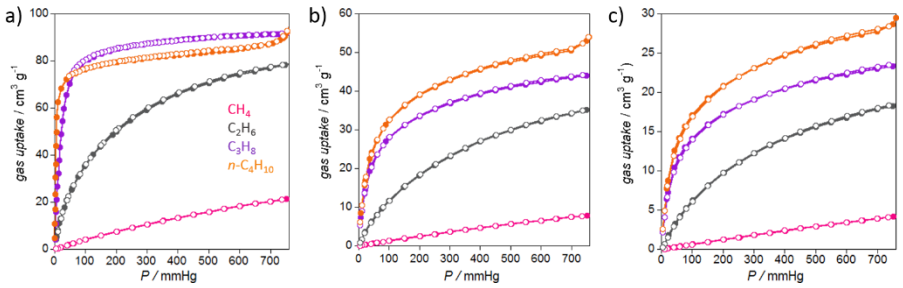

Figura 9. Isotermas de adsorción de CH_4 (rosa), C_2H_6 (gris), C_3H_8 (morado) y *n*-C_4H_{10} (naranja) para (a) **5c^S**, (b) **6c^S** y (c) **7c^S** a 273 K. Los círculos rellenos y vacíos indican la adsorción y desorción, respectivamente.

Las capacidades de adsorción de parafinas para los tres PCPs (Figura 9) muestran en general la misma tendencia, de manera que aquéllas cuya cadena carbonada es mayor, se adsorben en mayor cantidad (CH_4 << C_2H_6 < C_3H_8 < *n*-C_4H_{10}). Este resultado tiene su origen en las interacciones carbono-carbono que se establecen entre los hidrocarburos y los residuos alifáticos de los aminoácidos que decoran las paredes de los poros de los MOFs y que se ven intensificadas con la longitud de la cadena carbonada de la parafina. De hecho, las pendientes de las isotermas de propano y butano son visiblemente más abruptas, indicando una mayor selectividad hacia ellos.

Cuando se midieron las isotermas de adsorción de las olefinas C_2H_4 and C_3H_6 se encontró que la cantidad adsorbida de propeno era bastante mayor que la de propano, probablemente debido a las interacciones del orbital π-enlazante del propeno con los centros metálicos de los MOFs y al menor diámetro cinético del propeno respecto al propano. Por otro lado, la adsorción de eteno respecto a etano no mostró una diferencia significativa.

También se estudió la cinética de adsorción de las parafinas en los tres compuestos para obtener información acerca de la velocidad a la que eran adsorbidas y por tanto, de la selectividad. En general, las cinéticas de adsorción arrojaron los mismos resultados que las medidas de las isotermas. De nuevo, al avanzar en la serie de los derivados de calcio(II), cuanto mayor es la cadena del residuo aminoácido, mayor es la selectividad hacia las parafinas de mayor longitud. Resulta especialmente interesante que la cantidad de metano adsorbida es cada vez menor al avanzar en la serie (**5c^S > 6c^S > 7c^S**), de modo que el derivado de (*S*,*S*)-leumox^{4-} (cuyo residuo es isobutil), apenas adsorbe metano.

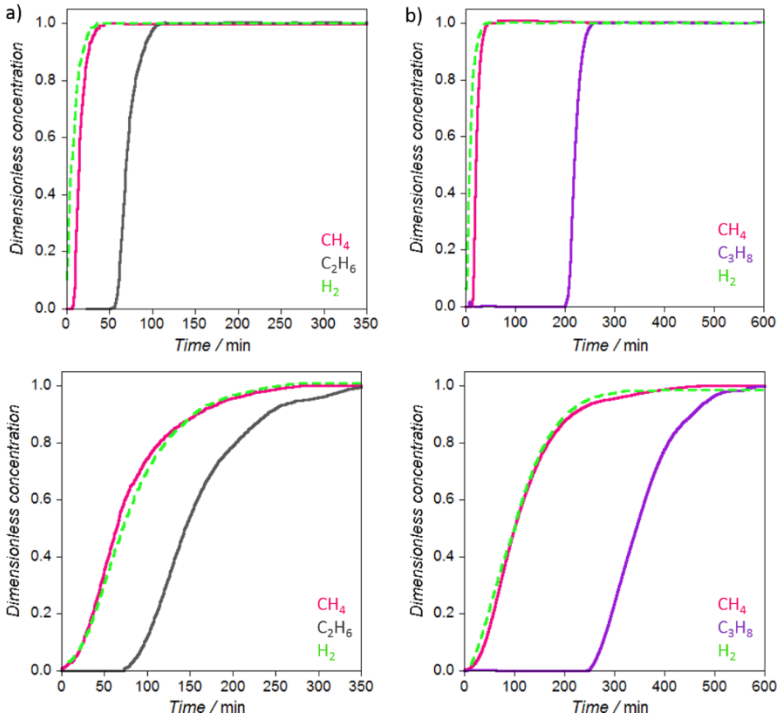

Figura 10. Curvas de ruptura de separación de las mezclas de gases (a) CH_4/C_2H_6 (75:25, v/v) y (b) CH_4/C_3H_8 (75:25 v/v) medidas a 298 K y 1 bar empleando columnas cuya fase estacionaria es **5c^S** (arriba) y **7c^S** (abajo).

En vista de los resultados, se pudo prever que los materiales podrían funcionar bien en la separación de metano del resto de hidrocarburos más pesados y se llevaron a cabo experimentos de ruptura de separación para los MOFs **5c^{S}** y **7c^{S}** (Figura 10).

El hecho que la curva del metano en el caso de **5c^{S}** (Figura 10, arriba) rompa después que la del gas de referencia (H_2) indica que una pequeña cantidad de metano está siendo adsorbida. Sin embargo, para el MOF **7c^{S}** (Figura 10, abajo), que el metano y el H_2 rompan a la vez, indican que el metano no está siendo adsorbido en esas condiciones y que hay una mayor selectividad hacia la parafina de mayor tamaño.

Mientras que usando **5c^{S}**, el etano y propano se retuvieron durante 54 and 198 min respectivamente, cuando se utilizó **7c^{S}**, no se detectó ninguna adsorción de metano y además el etano y propano se retuvieron durante 71 and 246 min, respectivamente. Por todo ello, como ya preveían las isotermas de adsorción de parafinas medidas por separado, se observan mejores separaciones CH_4/C_2H_6 y CH_4/C_3H_8 cuando se emplea **7c^{S}** como fase estacionaria en la columna.

Además, uno de los compuestos que forman parte de la subfamilia de derivados de calcio(II), el MOF $\{Ca^{II}Cu^{II}_6[(S,S)\text{-alamox}]_3(OH)_2(H_2O)\cdot 32H_2O\}_n$ (**5c^{S}**), atrajo especialmente nuestro interés debido a la extensa red de moléculas de agua alojada en sus poros (32 moléculas) que además, gracias a la precisa resolución de su estructura cristalina, se pudo establecer con exactitud incluyendo los átomos de hidrógeno de las moléculas de agua y la direccionalidad de los enlaces de hidrógeno (Figura 11). Todo ello, nos indujo a medir las propiedades de conducción protónica y a establecer un mecanismo para dicha conducción.

El material mostró valores de conductividad crecientes con la humedad relativa (HR) en función de la temperatura. Este hecho es típico de conductores protónicos cuya conducción está mediada por la presencia de agua. Por ejemplo, los valores a 353 K aumentan desde 1.1×10^{-6} S cm^{-1} al 60 % HR hasta 8.6×10^{-4} S cm^{-1} al 95 % HR. La conductividad protónica de **5c^{S}** medida a 297 K y con 95 % HR es de 1.0×10^{-5} S cm^{-1}, un valor comparable con la de otros MOFs sintetizados con ligandos derivados de carboxilatos. Además, se obtuvieron valores para las energías de activación a las diferentes HR a partir de los datos experimentales. Los valores obtenidos relativamente bajos (0.42, 0.43, 0.42, y 0.34 eV para HR 60, 70, 80, and 95 %, respectivamente), se encuentran dentro del intervalo típicamente atribuido a un mecanismo de transferencia de tipo Grotthuss (0.1−0.5 eV).

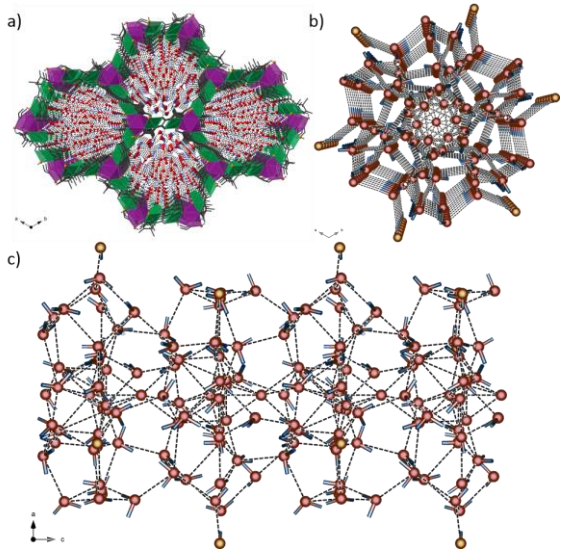

Figura 11. (a) Vista del empaquetamiento cristalino de **5c^{S}** a lo largo del eje cristalográfico *c* mostrando la red de moléculas de agua contenidas en sus canales hexagonales como esferas rojas. Vistas a lo largo de los ejes cristalográficos *c* (b) and *b* (c) de la red de moléculas de agua conectadas a través de enlaces de hidrógeno dentro de cada canal hexagonal. Los enlaces de hidrógeno se muestran como líneas con puntos.

Por ello, basándonos en dichos resultados experimentales, conociendo las posiciones de las moléculas de agua (incluidos los átomos de hidrógeno) y teniendo en cuenta distancias y ángulos, hemos establecido un mecanismo plausible por el cual los protones se desplazarían de una molécula a otra a lo largo de la red de moléculas de aguas conectadas a través de enlaces de hidrógeno. Adicionalmente, hemos realizado simulaciones cuánticas de dinámica molecular que corroboran el mecanismo propuesto.

Al reaccionar el dímero precursor de cobre(II)-(*S*,*S*)-alamox^{4-} con los iones disprosio(III) y terbio(III) se obtuvo una subfamilia de MOFs (**5d^{S}** and **5e^{S}**, respectivamente), siendo materiales isoestructurales con la subfamilia de calcio(II).

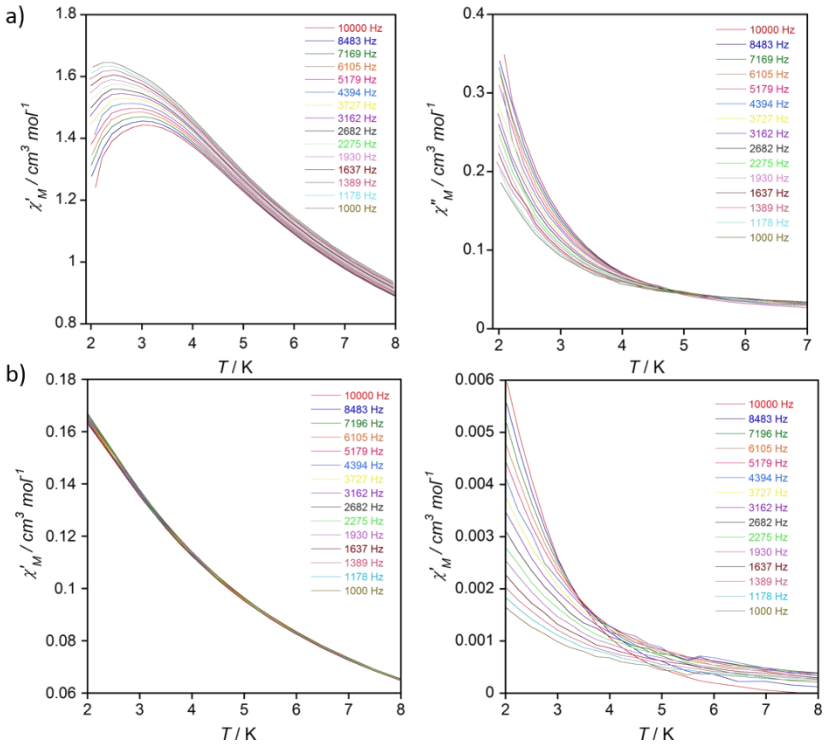

Figura 12. Dependencia con la frecuencia y la temperatura de la susceptibilidad molar magnética en corriente alterna en fase (χ_M', izquierda) y fuera de fase (χ_M'', derecha) de (a) **5d^{S}** y (b) **5e^{S}** bajo un campo magnético en corriente directa de 2500 G y un campo oscilante de ±4.0 G aplicado a varias frecuencias.

Estos compuestos son interesantes desde un punto de vista magnético, ya que los iones lantánido(III) anisotrópicos, que actúan de nexo entre los dímeros de cobre(II), presentan una geometría antiprisma cuadrada pudiendo exhibir un comportamiento de "single-ion magnet" (SIM). Por ello, se estudiaron las propiedades magnéticas de ambos compuestos a través de medidas de susceptibilidad magnética tanto en corriente directa como alterna, en el intervalo de temperatura 2.0 - 300 K.

La dependencia de χ_M' y χ_M'' (susceptibilidad molar magnética real e imaginaria, respectivamente) con la frecuencia, aunque de manera incipiente, indica la existencia del fenómeno de lenta relajación de la magnetización de los iones lantánido(III) en **5d^S** and **5e^S** (Figura 12). Además, en el caso de **5d^S**, donde el máximo en las curvas de χ_M'' frente a la temperatura no se prevé a tan bajas temperaturas, se pudo calcular de manera aproximada tanto la energía de activación como el tiempo de relajación del fenómeno obteniéndose valores de 4.3(3) cm^{-1} and 2.8(2) x 10^{-7} s, respectivamente.

4.2. PCPs multifuncionales obtenidos a partir de métodos post-sintéticos (MPSs)

Se eligió como producto de partida un PCP de carácter aniónico, bien conocido y empleado con anterioridad en nuestro grupo de investigación, de fórmula $Na^{I}_4\{Mn^{II}_4[Cu^{II}_2(Me_3mpba)_2]_3\} \cdot 60H_2O$ (**8**) [Me_3mpba^{4-}= *N,N'*-2,4,6-trimetil-1,3-phenilenbis(oxamato)]. Este PCP presenta un orden magnético de largo alcance y una capacidad de adsorción de gases prácticamente nula. Hemos investigado cómo se afectan ambas propiedades cuando se produce el intercambio de los cationes metálicos que están ubicados en los poros (Na^+) por otros iones alcalinos (K^+ y Li^+) (Figura 13) o bien por un complejo metálico catiónico con determinadas propiedades magnéticas $\{[Fe^{III}(sal_2\text{-trien})]^+$ [H_2sal_2-trien = *N,N'*-disalicylidenetriethylenetetramine)] (Figura 15).

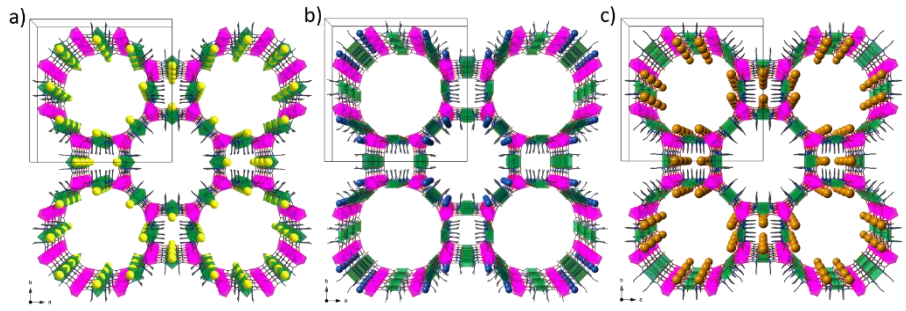

Figura 13. Vista en perspectiva de las redes 3D del PCP (a) $Na^{I}_4\{Mn^{II}_4[Cu^{II}_2(Me_3mpba)_2]_3 \cdot 60H_2O\}_n$ y sus análogos sustituidos de (b) Li^+ y (c) K^+ a lo largo del eje cristalográfico *c*. Los iones Cu(II) y Mn(II) de la red de coordinación se muestran como poliedros verdes y morados respectivamente,

mientras que los iones Na^+, Li^+ y K^+ que ocupan los poros se muestran como esferas de color amarillo, azul y naranja, respectivamente.

La estabilidad estructural de los derivados de Li^+ y K^+ [$Li^I_4\{Mn^{II}_4[Cu^{II}_2(Me_3mpba)_2]_3\} \cdot 68H_2O$ (**9**) y $K^I_4\{Mn^{II}_4[Cu^{II}_2(Me_3mpba)_2]_3\} \cdot 69H_2O$ (**10**)], mejora respecto a la del precursor de Na^+ (**8**). Dicha estabilidad estructural repercute directamente en las propiedades de adsorción de gases, donde el derivado de Li^+ presenta la mayor superficie, calculada a partir de las isotermas de N_2 a 77 K. El derivado de K^+ presenta un área algo menor mientras que el compuesto original de Na^+ apenas adsorbe, ya que su estructura colapsa en la fase de activación. Sin embargo, cuando se midieron las isotermas de H_2, CO_2 y CH_4, fue el derivado de K^+ el que exhibió mayor afinidad por dichos gases a pesar de no poseer la mayor superficie.

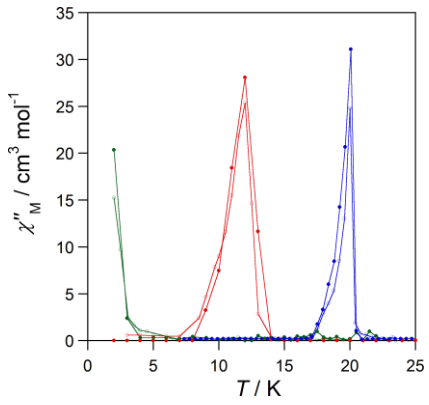

Figura 14. Susceptibilidad molar magnética fuera de fase (χ_M'') frente a *T* de las fases deshidratadas de **8** (verde), **9** (rojo) and **10** (azul) con un campo de ±4.0 G oscilando a 1000 (–●–) y 100 (–○–) Hz, respectivamente.

La mejorada estabilidad estructural de los derivados de Li^+ y K^+ también afecta a las propiedades magnéticas de los PCPs deshidratados, como refleja la tendencia de valores de T_C : 20.0 (K^+), 12.0 (Li^+) y 2.0 K (Na^+) (Figura 14), concluyendo que una mayor estabilidad estructural se traduce en una mayor eficiencia del canje magnético entre centros metálicos.

Motivados por el éxito del intercambio de los iones Na^+ por K^+ y Li^+ que produce una mejora en las propiedades del MOF, decidimos emplear la misma estrategia para encapsular el complejo catiónico $[Fe^{III}(sal_2\text{-trien})]^+$, el cual podría presentar transición de espín, fenómeno que está ausente en su sal de partida. De esta manera, la encapsulación

dentro de los poros del MOF magnético podría por un lado provocar dicha transición y por otro lado influir en las propiedades magnéticas propias del MOF (Figura 15).

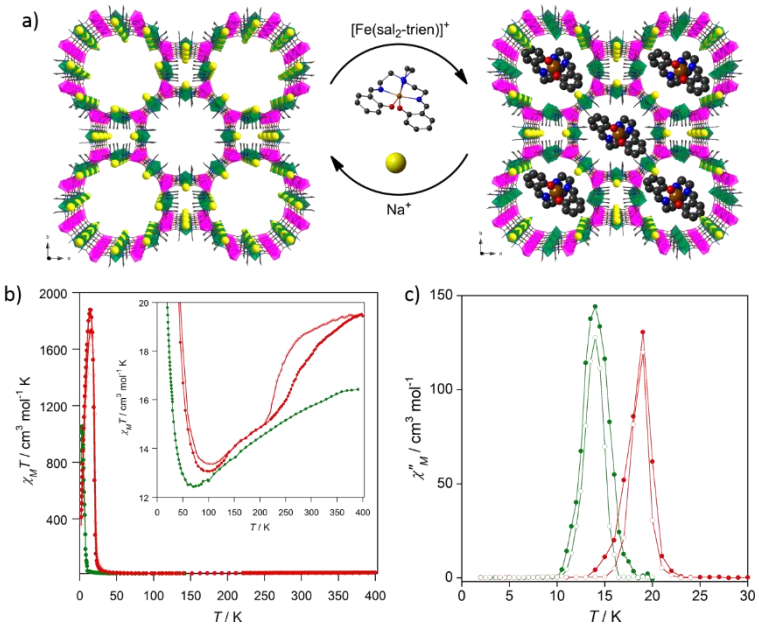

Figura 15. (a) Esquema ilustrando el proceso de encapsulación del complejo $[Fe^{III}(sal_2\text{-trien})]^+$ en los poros del MOF mediante intercambio con los iones Na^+. (b) Gráfico mostrando el producto de la susceptibilidad molar y la temperatura frente a *T* para el precursor de Na^+ (verde) y el derivado de $[Fe^{III}(sal_2\text{-trien})]^+$ (rojo). El recuadro muestra el mínimo y la región de alta temperatura con detalle. (c) Gráfico mostrando la susceptibilidad molar fuera de fase (χ_M'') en función de *T* bajo un campo de ±4.0 G oscilando a 1000 (-●-) and 10 Hz (-o-) para el derivado de Na^+ (verde) y el de $[Fe^{III}(sal_2\text{-trien})]^+$ (rojo).

La inclusión de los complejos catiónicos de Fe(III) en los poros del MOF conlleva una mejora en la estabilidad estructural del mismo, que de nuevo se ve traducida en una transmisión del canje magnético más efectiva como refleja el aumento de la T_C para el derivado de $[Fe(sal_2\text{-trien})]^+$ (ver Figura 15c). Además, resulta interesante que el complejo $[Fe(sal_2\text{-trien})]^+$ sí presenta transición de alto a bajo espín cuando se halla confinado en los canales del MOF, prueba de ello es la pendiente pronunciada que se observa en la gráfica de $\chi_M T$ en función de *T* en el intervalo de temperaturas 200 - 400

K (ver recuadro de la Figura 15b). Esta transición de alto a bajo espín del complejo de hierro(III) fue corroborada mediante espectroscopía Mössbauer.

Por último, hemos hecho uso de los MPSs para implementar propiedades magnéticas en un MOF diamagnético y mejorar la estabilidad estructural del mismo, viéndose a su vez incrementada su capacidad de adsorción de gases. Para ello partimos del MOF aniónico diamagnético de fórmula $Mg^{II}_2\{Mg^{II}_4[Cu^{II}_2(Me_3mpba)_2]_3\} \cdot 45H_2O$ (**11**) cuya estructura es análoga al previamente descrito $Na^{I}_4\{Mn^{II}_4[Cu^{II}_2(Me_3mpba)_2]_3\} \cdot 60H_2O$ (**8**). Al cabo de varias semanas de haber adicionado cristales del MOF de magnesio(II) a disoluciones acuosas saturadas de $M^{II}(NO_3)_2 \cdot 6H_2O$ [M = Co and Ni], se obtuvieron dos análogos de fórmulas $Co^{II}_2\{Co^{II}_4[Cu^{II}_2(Me_3mpba)_2]_3\} \cdot 56H_2O$ (**12**) y $Ni^{II}_2\{Ni^{II}_4[Cu^{II}_2(Me_3mpba)_2]_3\} \cdot 54H_2O$ (**13**), respectivamente. Cabe reseñar que dichos compuestos no pudieron ser aislados mediante síntesis directa.

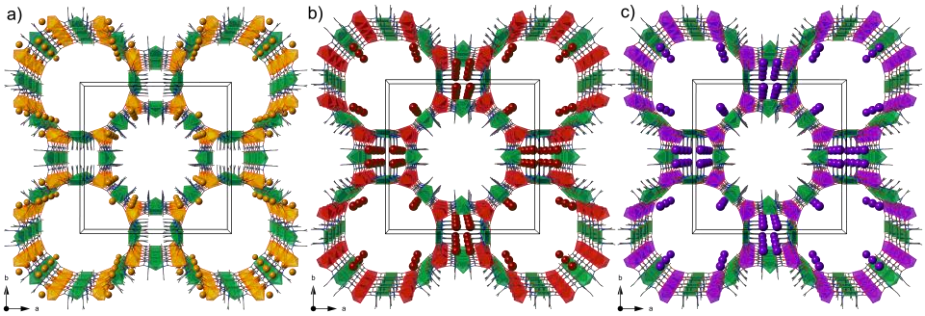

Figura 16. Vistas en perspectiva del MOF aniónico (a) $Mg^{II}_2\{Mg^{II}_4[Cu^{II}_2(Me_3mpba)_2]_3 \cdot 45H_2O$ y sus derivados de (b) Co(II) y (c) Ni(II) mostrando la diferente ocupación de los contracationes en el interior de los poros. Los iones cobre(II), magnesio(II), cobalto(II) y níquel(II) de la red de coordinación están representados mediante poliedros verdes, naranjas, rojos y morados, respectivamente. Los contracationes magnesio(II), cobalto(II) y níquel(II) que se hallan en los poros se muestran como esferas naranjas, rojas y moradas, respectivamente.

Se han diseñado experimentos para estudiar la cinética y la termodinámica de ambas sustituciones [tanto la de los iones magnesio(II) que actúan como contracationes situados en los poros como la de los magnesio(II) que forman parte de la red de coordinación] con iones cobalto(II) y níquel(II). Los seis iones magnesio(II) por celda unidad se sustituyen de manera rápida y efectiva tanto con cobalto (II) como con

níquel(II). De los resultados de la cinética y termodinámica se deduce que los dos primeros moles de magnesio(II), los situados en los poros, se sustituyen más rápidamente y en una primera fase, mientras que los cuatro iones magnesio(II) restantes, que forman parte de la red, presentan una cinética más lenta (Figura 17a).

La sustitución de los iones magnesio(II) por iones cobalto(II) y níquel(II) da lugar a dos PCPs que presentan una mayor estabilidad estructural, hecho que se ve reflejado en las diferentes capacidades de adsorción de gases, siendo concretamente el derivado de níquel(II) el que mayor adsorción presenta para los gases medidos (N_2, H_2, CO_2 y CH_4) (Figura 17b-d).

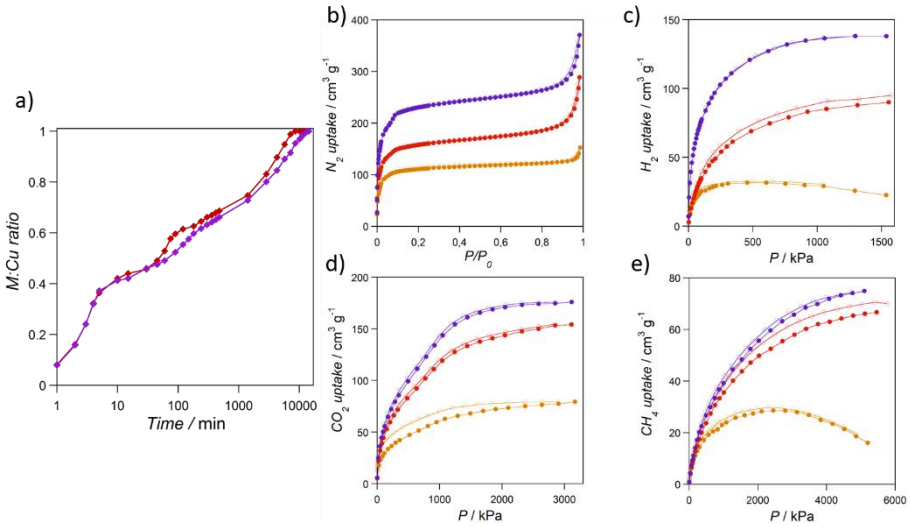

Figura 17. (a) Perfil cinético del proceso de intercambio iónico representado como la relación molar M^{II}:Cu^{II} [M = Co (rojo) and Ni (morado)] frente al tiempo en escala logarítmica. Isotermas de adsorción a baja presión de (b) N_2 (77 K) y de alta presión de (c) H_2 (77 K), (d) CO_2 (273 K) and (e) CH_4 (273 K) para el derivado de Mg(II) (naranja), el de Co(II) (rojo) y el de Ni(II) (morado). Los círculos rellenos y vacíos de las isotermas corresponden a los procesos de adsorción y desorción, respectivamente.

El intercambio de los iones magnesio(II) diamagnéticos por iones cobalto(II) y níquel(II) paramagnéticos ejerce una influencia importante en las propiedades magnéticas del MOF. Mientras que en el MOF de Mg(II) los dímeros de cobre (II) se acoplan de manera ferromagnética y están aislados magnéticamente unos de otros, los

MOFs de Co(II) y Ni(II) exhiben un carácter ferrimagnético debido al acoplamiento de carácter antiferromagnético entre los iones cobre(II) y los metales M(II) (M = Co y Ni) a través del puente oxamato. La aparición de un momento magnético de largo alcance debe su origen tanto al acoplamiento ferromagnético de los dímeros de cobre(II) como a las interacciones dipolares que se establecen con los átomos paramagnéticos M(II) (M = Co y Ni) situados en los canales.

5. Conclusiones

5.1. PCPs multifuncionales quirales

Hemos desarrollado una estrategia original para el diseño y obtención de MOFs quirales de manera racional. La estrategia consiste en el uso de precursores nuevos enantiopuros [como cadenas o anillos hexanucleares de cobre(II)] capaces de actuar como ligandos a través de sus grupos carbonilo libres frente a complejos cuadrados de níquel(II) dando lugar a compuestos enantiopuros de dimensionalidad elevada. Todos los compuestos fueron caracterizados y sus propiedades ópticas y magnéticas investigadas.

La funcionalización de aminoácidos (alanina, valina, leucina y fenilglicina) con grupos oxamato nos proporcionó una librería de proligandos quirales que transmitieron de forma efectiva su información quiral a sus derivados. Los MOFs resultantes presentan estructuras porosas complejas y fascinantes, que pudieron ser obtenidas a pesar de la complicación que entraña la resolución de estructuras con un gran número de átomos en la celda unidad. Uno de los resultados más relevantes consiste en la obtención de un MOF (**4b^{R}**) donde la unidad fundamental que lo compone (una cadena) coincide exactamente con la cadena que se empleó como especie precursora. En general, el estudio topológico de esta familia de MOFs quirales aporta información interesante acerca del ensamblaje de estructuras quirales de dimensionalidad elevada. Los experimentos de separación de enantiómeros o los de catálisis enantioselectiva no

ofrecieron los resultados esperados, siendo su inestabilidad en agua uno de los factores limitantes.

La funcionalización de diferentes aminoácidos (alanina, valina, leucina) con grupos oxamidato nos proporcionó una librería de proligandos quirales que transfieren de forma efectiva su información quiral a sus derivados. Se llevó a cabo la misma estrategia sintética obteniéndose especies dinucleares de cobre(II) que se usaron como metaloligandos frente a diferentes cationes alcalino-térreos y lantánidos. De esta manera se aislaron diferentes subfamilias de PCPs derivadas de iones calcio(II), bario(II) o lantánidos(III) dependiendo del catión que actúa de nexo.

Los PCPs derivados de bario(II) (**5b^{S}**, **6b^{S}** and **7b^{S}**) muestran estructuras cristalinas muy diferentes a pesar de que, en principio, derivan de ligandos muy similares [(*S*,*S*)-alamox^{4}, (*S*,*S*)-valmox^{4-} and (*S*,*S*)-leumox^{4-}]. La forma y la longitud de los residuos alifáticos hidrofóbicos de los aminoácidos, determinan la organización y ensamblaje de los metaloligandos y los iones bario(II) que actúan de nexo.

Por otro lado, los PCPs derivados de calcio(II) (**5c^{S}**, **6c^{S}** and **7c^{S}**) son todos ellos isoestructurales. Su única diferencia reside en la forma y longitud del residuo alifático del aminoácido que decora las paredes de las redes 3D y por tanto, en el tamaño y densidad de carga del poro. Con dichas características, esta familia nos proporcionó la oportunidad para comprender su capacidad de adsorción de gases así como su selectividad. Se midieron isotermas adsorción de N_2, CO_2, parafinas (CH_4, C_2H_6, C_3H_8, *n*-C_4H_{10}) y olefinas (C_2H_4 y C_3H_6), así como cinéticas de adsorción y experimentos de ruptura de separación. De todo ello se pudo concluir que existen dos factores antagónicos, ya que cuanto menor es el residuo alifático del aminoácido, mayor es el tamaño de poro y por tanto mayor es la capacidad de adsorción (**5c^{S} > 6c^{S} > 7c^{S}**); sin embargo, a mayor longitud del residuo alifático (aunque el poro es menor) se establecen interacciones más efectivas con aquellos hidrocarburos de mayor cadena y por tanto la selectividad aumenta (CH_4 << C_2H_6 < C_3H_8 < *n*-C_4H_{10}). Concretamente, **7c^{S}** mostró resultados muy interesantes en los experimentos de ruptura de separación

metano/etano y metano/propano, siendo la adsorción de metano nula en ambos casos, y reteniendo el etano y el propano 71 y 246 min, respectivamente.

Además el PCP derivado de calcio(II) **5c^{S}**, que alberga una amplia red de moléculas de agua conectadas mediante puentes de hidrógeno en sus canales, presenta conductividad protónica dependiente de la humedad relativa (valores que van desde 1.1 x 10^{6} con 60 % HR hasta 8.6 x 10^{4} S cm^{-1} con 95 % HR, medidos a 353 K). La calidad de los datos obtenidos de la difracción de rayos X sobre monocristal permitió determinar con exactitud las posiciones de las moléculas de agua (incluidos los átomos de hidrógeno) involucradas en el proceso de transmisión de protones. Ello nos llevó a proponer los posibles caminos que siguen los protones en su desplazamiento de unas moléculas de agua a otras durante la conducción protónica, que a su vez están de acuerdo con un mecanismo de tipo Grotthuss y que fue confirmado a través de simulaciones cuánticas de dinámica molecular.

Por último, se estudiaron las propiedades magnéticas de los MOFs derivados del ligando (*S*,*S*)-alamox^{4-} utilizando iones disprosio(III) y terbio(III) para conectar los dímeros de cobre(II). Los datos de susceptibilidad molar fuera de fase (χ_M'') en función de *T* muestran máximos incipientes indicando un posible fenómeno de lenta relajación de los iones disprosio(III) y terbio(III) comportándose así como "Single Ion Magnets" (SIMs) insertados en la estructura del MOF, ampliando así la escasa lista de ejemplos de SIM-MOFs que existen actualmente en la bibliografía.

5.2. PCPs multifuncionales obtenidos a partir de métodos post-sintéticos (MPSs)

Hemos desarrollado con éxito el intercambio catiónico como MPs. La total sustitución de los contracationes Na^{+} por iones Li^{+} y K^{+} del MOF original **8** ha dado lugar a dos nuevas redes 3D sin alterar su estructura. Estos nuevos derivados son más robustos que el MOF original, lo que se ve traducido en una mejora de sus propiedades físicas. Por un lado, los derivados de Li^{+} (**9**) y K^{+} (**10**), presentan una temperatura de

orden magnético de largo alcance mayor que su precursor de Na^+, indicando que el canje magnético se transmite de manera más efectiva en aquellos derivados. Por otro lado, se ha comprobado que la naturaleza y posición concreta de los cationes dentro de la red 3D tienen una influencia no despreciable en las propiedades de adsorción de gases puesto que **9** y **10** exhiben mayores capacidades de adsorción, y el derivado de K^+, concretamente, posee una mayor afinidad hacia H_2, CO_2 and CH_4.

Hemos llevado a cabo de manera satisfactoria la sustitución de los cationes Na^+ en **8** por el complejo catiónico $[Fe(sal_2\text{-trien})]^+$. Resulta interesante que, de manera sencilla, esta técnica post-sintética permite obtener un nuevo material más robusto que su precursor cuyas propiedades magnéticas se han visto mejoradas. Así, Fe(sal_2-trien)@**8** presenta una temperatura de orden mayor que la de **8**. Además, tanto las medidas de susceptibilidad magnética como las de espectroscopía Mössbauer confirman que los complejos de $[Fe^{III}(sal_2\text{-trien})]^+$ que se localizan en el interior de los poros del MOF experimentan transición de espín por el hecho de estar alojados en la estructura, ya que la sal precursora del complejo no transita.

Por último se estudió la transmetalación como posible MPS para la obtención de nuevos materiales. Se partió de un derivado de magnesio(II) análogo a **8** (compuesto **11**) y se investigó la sustitución con iones cobalto(II) y níquel(II) tanto de los contracationes de magnesio(II) situados en los poros como de los que forman parte de la red de coordinación de **11**. Las sustituciones se llevaron a cabo satisfactoriamente, estando más favorecidas aquéllas que implican los iones magnesio(II) que actúan como contracationes. Como resultado se obtuvieron monocristales de dos nuevos materiales [el derivado de cobalto(II) (**12**) y el derivado de níquel(II) (**13**)] que no pudieron ser obtenidos mediante síntesis directa. Ambos mostraron una estabilidad estructural reforzada que se vio traducida a su vez, en una mejora de las propiedades de adsorción de gases. El intercambio de los iones magnesio(II) diamagnéticos por iones cobalto(II) y níquel(II) paramagnéticos dotó de interesantes propiedades magnéticas a los materiales intercambiados.

6. Referencias

1 H. Furukawa, K. E. Cordova, M. O'Keeffe and O. M. Yaghi, *Science*, 2013, **341**, 1230444.

2 J. R. Long and O. M. Yaghi, *Chem. Soc. Rev.*, 2009, **38**, 1213–1214.

3 G. Férey, *Chem. Soc. Rev.*, 2008, **37**, 191–214.

4 S. KITAGAWA and R. MATSUDA, *Coord. Chem. Rev.*, 2007, **251**, 2490–2509.

5 D. Bradshaw, J. B. Claridge, E. J. Cussen, T. J. Prior and M. J. Rosseinsky, *Acc. Chem. Res.*, 2005, **38**, 273–282.

6 L. E. Kreno, K. Leong, O. K. Farha, M. Allendorf, R. P. Van Duyne and J. T. Hupp, *Chem. Rev.*, 2012, **112**, 1105–1125.

7 J.-R. Li, R. J. Kuppler and H.-C. Zhou, *Chem. Soc. Rev.*, 2009, **38**, 1477–1504.

8 S. Horike, D. Umeyama and S. Kitagawa, *Acc. Chem. Res.*, 2013, **46**, 2376–2384.

9 A. C. McKinlay, R. E. Morris, P. Horcajada, G. Férey, R. Gref, P. Couvreur and C. Serre, *Angew. Chemie Int. Ed.*, 2010, **49**, 6260–6266.

10 Y. Inokuma, T. Arai and M. Fujita, *Nat. Chem.*, 2010, **2**, 780–783.

11 J. Lee, O. K. Farha, J. Roberts, K. a Scheidt, S. T. Nguyen and J. T. Hupp, *Chem. Soc. Rev.*, 2009, **38**, 1450–1459.

12 M. Sadakiyo, T. Yamada and H. Kitagawa, *J. Am. Chem. Soc.*, 2009, **131**, 9906–9907.

13 G. Lu, S. Li, Z. Guo, O. K. Farha, B. G. Hauser, X. Qi, Y. Wang, X. Wang, S. Han, X. Liu, J. S. DuChene, H. Zhang, Q. Zhang, X. Chen, J. Ma, S. C. J. Loo, W. D. Wei, Y. Yang, J. T. Hupp and F. Huo, *Nat. Chem.*, 2012, **4**, 310–316.

14 S. Kitagawa, R. Kitaura and S. Noro, *Angew. Chemie-International Ed.*, 2004, **43**, 2334–2375.

15 O. M. Yaghi, M. O'Keeffe, N. W. Ockwig, H. K. Chae, M. Eddaoudi and J. Kim, *Nature*, 2003, **423**, 705–714.

16 C. Train, M. Gruselle and M. Verdaguer, *Chem. Soc. Rev.*, 2011, **40**, 3297–3312.

17 S.-I. Ohkoshi, K. Imoto, Y. Tsunobuchi, S. Takano and H. Tokoro, *Nat. Chem.*, 2011, **3**, 564–569.

18 C. Train, R. Gheorghe, V. Krstic, L.-M. Chamoreau, N. S. Ovanesyan, G. L. J. a Rikken, M. Gruselle and M. Verdaguer, *Nat. Mater.*, 2008, **7**, 729–734.

19 D. Maspoch, D. Ruiz-Molina and J. Veciana, *Chem. Soc. Rev.*, 2007, **36**, 770–818.

20 E. Coronado, J. R. Galán-Mascarós, C. J. Gómez-García and J. M. MartínezAgudo, *Inorg. Chem.*, 2001, **40**, 113–1

El filósofo Aristipo cortejaba el poder
de la corte de Dionisio, tirano de Siracusa.

Una tarde encontró a Diógenes preparándose un
pequeño plato de lentejas.

-Si halagases a Dionisio, no te verías forzado a
comer lentejas- dijo Aristipo.

-Si tú supieras comer lentejas, no te verías
forzado a halagar a Dionisio- respondió
Diógenes.

Maktub

ChemComm

View Online / Journal Homepage / Table of Contents for this issue
Dynamic Article Links

Cite this: *Chem. Commun.*, 2012, **48**, 3539–3541

www.rsc.org/chemcomm

COMMUNICATION

Ligand effects on the dimensionality of oxamato-bridged mixed-metal open-framework magnets†

Jesús Ferrando-Soria,[a] Thais Grancha,[a] Miguel Julve,[a] Joan Cano,[a] Francesc Lloret,*[a] Yves Journaux,*[b] Jorge Pasán,[c] Catalina Ruiz-Pérez[c] and Emilio Pardo*[a]

Received 12th December 2011, Accepted 14th February 2012
DOI: 10.1039/c2cc17767f

Increasing dimensionality [from 2D (1) to 3D (2)] and T_C [from 10 (1) to 20 K (2)] in two new oxamato-bridged heterobimetallic $Mn^{II}_2Cu^{II}_3$ open-frameworks result from the steric hindrance provided by the different alkyl substituents of the *N*-phenyloxamate bridging ligands.

Extended multidimensional coordination polymers, also known as Metal–Organic Frameworks (MOFs),[1] have become an outstanding area of research in modern supramolecular coordination chemistry and crystal engineering.[2] Besides their fascinating structures, MOFs can exhibit a wide range of physical and chemical properties. For example, when paramagnetic ions[3] are incorporated into MOFs, a variety of magnetic materials can be obtained.[4] In this respect, an accurate control of the coordination network structure is needed to get the desired interesting magnetic properties. This task is still exceedingly difficult because of the many subtle factors that may affect the assembly process.[5]

Among the different synthetic routes to obtain MOFs with a long-range magnetic ordering that coordination chemistry offers, the rational self-assembly methods based on the metalloligand approach are the prominent ones.[6] The validity of this strategy was demonstrated by the work of Okawa, Decurtins, Coronado and others on heterobimetallic 2D and 3D MOFs built upon oxalato and related dithiooxalato metal building blocks.[7] The rational synthesis of new examples of magnetic MOFs can serve as valuable candidates for experimental and theoretical studies in the field of molecule-based magnets.[8]

In this contribution, we present a rational synthetic strategy to obtain new 2D and 3D MOFs that is based on the use of dianionic mononuclear copper(II) complexes $[Cu^{II}L_2]^{2-}$, where L = *N*-2,6-dimethylphenyloxamate (Me_2pma) and *N*-2,6-diethylphenyloxamate (Et_2pma) (Scheme 1a), as bisbidentate metalloligands toward solvated manganese(II) cations.[9] A key point is the use of a large excess of the mononuclear copper(II) precursors (5 : 1 stoichiometry) as it prevents the formation of the corresponding one-dimensional (1D) compounds reported earlier (1 : 1 stoichiometry).[9a,b] This approach would afford high dimensionality oxamato-based compounds with a variety of possible structures that are reminiscent of those earlier observed in oxalato-bridged heterobimetallic MOFs. In fact, molecular model considerations indicate that the spatial arrangement of the chiral tris(chelated) octahedral Mn^{II} ions can produce both 2D and 3D structures (Scheme 1b–d).

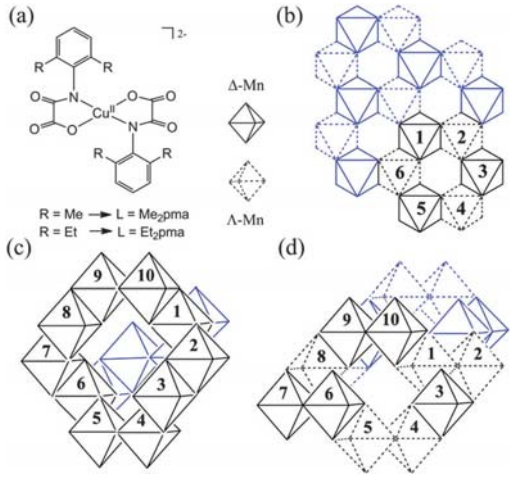

Scheme 1 Metalloligand strategy for the molecular-programmed self-assembly of oxamato-bridged heterobimetallic MOFs: (a) copper(II) starting bis(bidentate) metalloligand. (b–d) Postulated structures of the resulting 2D and 3D MOFs. The tris(chelated) Mn^{II} cations of different propeller chiralities (Δ and Λ) are shown as solid and dotted octahedra, where the shared edges represent the bridging Cu^{II} complex anions.

Hence, achiral 2D extended networks of hexagonal symmetry containing alternating octahedral (Λ)-Mn and (Δ)-Mn units are the most evident possibility (Scheme 1b). On the contrary, a chiral 3D framework of decagonal symmetry would be obtained

[a] *Depto. de Química Inorgànica, Instituto de Ciencia Molecular (ICMOL), Universitat de València, 46980 Paterna, València, Spain. E-mail: Emilio.Pardo@upmc.fr; Fax: +34 963543273; Tel: +34 963544440*
[b] *Institut Parisien de Chimie Moléculaire, Université Pierre et Marie Curie-Paris 6, UMR 7201, F-75252 Paris, France. E-mail: Yves.Journaux@upmc.fr; Fax: +33 144273841; Tel: +33 144275562*
[c] *Laboratorio de Rayos X y Materiales Moleculares, Depto. de Fisica Fundamental II, Universidad de La Laguna, 38201 Tenerife, Spain*

† Electronic supplementary information (ESI) available: Experimental preparation, analytical and spectroscopic characterization of ligands, copper(II) complexes and **1** and **2**. Quantum Monte Carlo calculations, additional Fig. S1–S6. Crystallographic refinement details for **1** and **2**. CCDC 852495 (**1**) and 852496 (**2**). For ESI and crystallographic data in CIF or other electronic format see DOI: 10.1039/c2cc17767f

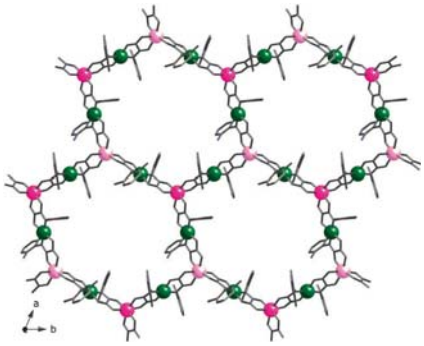

Fig. 1 Perspective view of a fragment of **1** in the *ab* plane. Metal and ligand atoms are represented by balls and sticks, respectively [Cu, green; (*Δ*)-Mn, purple; (*Λ*)-Mn, pink]. Hydrogen atoms are omitted for clarity.

when all the Mn centres have the same absolute configuration (*Λ* or *Δ*) (Scheme 1c). Finally, a third and more elusive possibility is the alternating alignment of pairs of manganese centres with identical configuration (*ΛΛ* and *ΔΔ*) which would lead to an achiral 3D compound of decagonal symmetry as well (Scheme 1d). Herein we report the syntheses, crystal structures, magnetic properties and Quantum Monte Carlo simulations of two new oxamato-bridged heterobimetallic 2D and 3D $Mn^{II}_2Cu^{II}_3$ networks of formula $(n\text{-}Bu_4N)_4[Mn_4Cu_6(Me_2pma)_{12}(DMSO)_2]\cdot 8DMSO\cdot 2H_2O$ (**1**) and $(n\text{-}Bu_4N)_4[Mn_4Cu_6(Et_2pma)_{12}]\cdot DMSO\cdot 10H_2O$ (**2**). The relationship between the structure and magnetic properties in **1** and **2** and the influence of the steric effects on the dimensionality are analysed and discussed.

The structure of **1** consists of oxamato-bridged $Mn^{II}_2Cu^{II}_3$ bimetallic hexagonal layers of 6^3-**hcb** net topology growing in the *ab* plane (Fig. 1), which are interleaved by layers formed by the $n\text{-}Bu_4N^+$ cations and free water and DMSO molecules (Fig. S1, ESI†). Within each $Mn^{II}_2Cu^{II}_3$ hexagonal layer, two five-coordinated, square pyramidal and four four-coordinated square bis(oxamato)copper(II) units [the coordination environment containing two amidate-nitrogen and two carboxylate-oxygen atoms from the two oxamate ligands in all cases and a DMSO molecule occupying the apical position only for Cu(1) and Cu(4)] (Fig. S2, ESI†) act as bisbidentate bridging metalloligands through the *cis* carbonyl oxygen atoms toward six-coordinated, trigonally distorted octahedral manganese(II) ions in such a way that each Mn atom is surrounded by three Cu atoms and each Cu atom by two Mn atoms. In the crystal lattice of **1**, the adjacent anionic $Mn^{II}_2Cu^{II}_3$ flat hexagonal layers are not eclipsed but they are displaced along the [100] direction leading thus to an *ABAB* disposition pattern along the *c* axis (Fig. S3, ESI†).

The structure of **2** consists of an oxamato-bridged $Mn^{II}_2Cu^{II}_3$ anionic 3D network with a 10^3-**ths** net topology (Fig. 2), together with $n\text{-}Bu_4N^+$ cations and free water and DMSO molecules (Fig. S4, ESI†). The three crystallographically independent copper(II) ions are all four coordinate in square planar [Cu(1) and Cu(2)] and flattened tetrahedral [Cu(3)] geometries, with two amidate-nitrogen and two carboxylate-oxygen atoms from the oxamato groups (Fig. S5, ESI†). The manganese(II) ions have a trigonally distorted six-coordinate octahedral geometry formed by six carbonyl-oxygen atoms

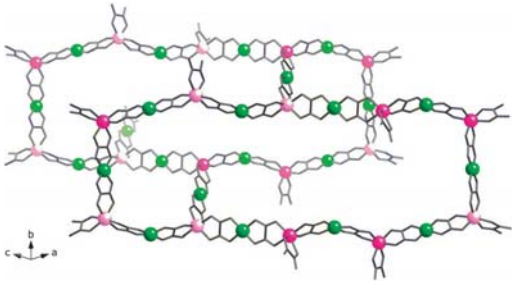

Fig. 2 Perspective view of the anionic 2D network of **2** along the [111] direction. Metal and ligand atoms are represented by balls and sticks, respectively (Cu, green; (*Δ*)-Mn, purple; (*Λ*)-Mn, pink). The aromatic rings of the oxamate ligand have been omitted for clarity.

from the oxamato groups. There are two different types of oxamatocopper(II) units: the Cu(3) atoms connect Mn^{II} centers of the same chirality (*Δ*-Mn–*Δ*-Mn and *Λ*-Mn–*Λ*-Mn subunits, Fig. S5c (ESI†)) while the Cu(1) and Cu(2) atoms link Mn^{II} centres of opposite chirality (*Δ*-Mn–*Λ*-Mn subunits, Fig. S5a and b (ESI†)). Overall, this leads to a global achiral 3D decagonal net (Fig. 2), and large nanopores along the *c* axis which are occupied by $n\text{-}Bu_4N^+$ cations and solvent molecules (Fig. S4b, ESI†).

The 2D network of **1** can be best described as an extended parallel array of oxamato-bridged manganese(II)–copper(II) chains running along the [010] direction with a *ΔΛ* sequence for the chirality of the manganese(II) ions (Fig. 1). The adjacent zigzag chains are further interconnected through oxamatocopper(II) complexes acting as bisbidentate bridges between the manganese(II) ions of opposite *Δ* and *Λ* chiralities in an alternately up and down disposition to give an hexagonal layer (Fig. 1). On the contrary, the 3D network of **2** can be described as an extended parallel array of oxamato-bridged manganese(II)–copper(II) chains running along the $[10\bar{1}]$ direction with a *ΔΔΛΛ* sequence for the chirality of the manganese(II) ions (Fig. 2). The adjacent mesohelical chains of opposite chirality (*P* and *M*) are further interconnected through oxamatocopper(II) units acting as bisbidentate bridges between the manganese(II) ions of opposite *Δ* and *Λ* chiralities in an alternately up and down disposition to give a decagonal net (Fig. 2). This structural variability for **1** and **2** is controlled in an almost unpredictable way by the size of the alkyl substituents that are located in the positions 2 and 6 of the aromatic phenyl ring of the oxamate ligand. Upon coordination, the $[Cu^{II}L_2]^{2-}$ precursors transfer the steric information of their bulky dimethyl- or diethyl-substituted phenyl groups in *trans* arrangement into the stereochemistries of the tris(chelated) octahedral Mn^{II} centres (Fig. S2 and S5, ESI†).

The magnetic properties of **1** and **2** are drastically different as expected from the different dimensionality observed for both systems. Their $\chi_M T$ *versus* *T* plots (χ_M being the molar magnetic susceptibility per Cu_3Mn_2 unit and *T* the temperature) are depicted in Fig. S6a (ESI†). They show minima at *ca.* 132 and 136 K for **1** and **2**, respectively, suggesting the occurrence of a moderate *intra*molecular antiferromagnetic interaction between the Cu^{II} and Mn^{II} ions through the oxamate bridges.

The magnetic susceptibility data of **1** and **2** were analysed through Quantum Monte Carlo (QMC) calculations (see ESI†). The theoretical curves obtained reproduce quite well the observed

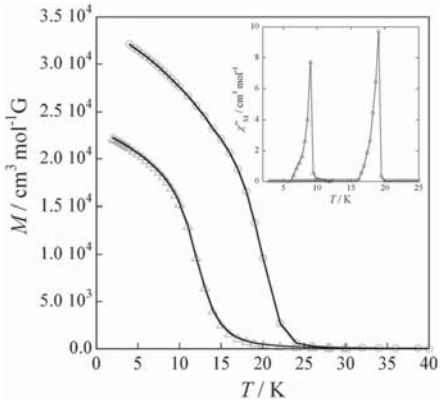

Fig. 3 Temperature dependence of the magnetization under an applied dc field of 100 G for **1** (Δ) and **2** (○). The field-cooled magnetization (FCM) was measured upon cooling within the field. The inset shows the temperature dependence of the out-of-phase susceptibility for **1** (Δ) and **2** (○) with a 1.0 G oscillating field at a frequency of 1000 Hz. The solid lines are eye-guides.

minimum of the $\chi_M T$ *vs.* T plots (solid lines in the inset of Fig. S6a (ESI†)). The values of the best-fit parameters are: $J = -35.1(5)$ (**1**) and $-36.1(4)$ cm^{-1} (**2**), $g_{Cu} = 2.140(40)$ (**1**) and 2.105(22) (**2**), and $g_{Mn} = 2.000(4)$ (**1**) and 2.000(2) (**2**) with $F = 5.5 \times 10^{-5}$ (**1**) and 2.2×10^{-5} (**2**), where J is the intralayer magnetic coupling, g_{Cu} and g_{Mn} are the Zeeman factors of the Cu^{II} and Mn^{II} ions respectively (F is the agreement factor defined as $F = \sum[(\chi_M T)_{exp} - (\chi_M T)_{calcd}]^2/\sum[(\chi_M T)_{exp}]^2$).

Both MOFs undergo abrupt paramagnetic-to-ferri- or ferromagnetic phase transitions at $T_C = 10$ (**1**) and 20 (**2**) K. These 3D magnetic orderings are revealed by the temperature dependence of the field-cooled magnetization (FCM) (Fig. 3). The FCM curves increase sharply below 15 (**1**) and 25 K (**2**), thereby suggesting the onset of a long range ferro- or ferrimagnetic transition. Indeed, the magnetic ordering is confirmed for **1** and **2** by the χ_M'' *versus* T plots at different frequencies (ν) of the 1 G oscillating field: χ_M'' becomes nonzero below 15 (**1**) and 25 K (**2**) and non-frequency-dependent maxima are observed at 10 (**1**) and 20 (**2**) K for the different explored frequencies (inset of Fig. 3).

In conclusion, the use of a series of preformed oxamatocopper(II) complexes, $[Cu^{II}(L)_2]^{2-}$ (L = Me_2pma and Et_2pma) toward tris(chelated) Mn^{II} ions, yielded two very different structures a 2D hexagonal structure (**1**) when the aromatic ring is dimethyl-substituted, or an unprecedented 3D decagonal open-framework structure (**2**) when that ring was diethylsubstituted. The magnetic properties of **1** and **2** differ drastically as expected from their very different architectures (a long-range ferromagnetic ordering at $T_C = 10$ K in **1** and a 3D ferrimagnetic ordering at $T_C = 20$ K in **2**). Therefore, we can modify the dimensionality of the resulting open-framework and, more interestingly, the magnetic properties of each compound by controlling the length of the alkyl-substituents present in the aromatic ring of the oxamate ligands. Future work will focus on the preparation of similar 2D and 3D networks with the substitution of n-Bu_4N^+ cations by functionalized ones that could provide new physical properties in addition to the magnetic ones to obtain the so-called multifunctional magnetic materials.

This work was supported by the MICINN (Spain) (Projects CTQ2010-15364, MAT2010-16981, CSD2007-00010, CSD2006-00015, and DPI2010-21103-C04-03), the Generalitat Valenciana (Spain) (Project PROMETEO/2009/108), the ACIISI-Gobierno Autónomo de Canarias (Spain) (Project PIL-2070901), the ESRF (France) (Projects HS3902 and 25-01-783), the MFR and the CNRS (France). We acknowledge the staff in charge of the BM16-CRG and BM25-CRG beamlines for their assistance and help in data collection. J. F.-S. thanks the Generalitat Valenciana for a doctoral grant. E. P. and J. P. thank the "Juan de la Cierva" (MICINN), and NANOMAC projects (ACIISI-Gobierno Autónomo de Canarias), respectively, for contracts.

Notes and references

1 (*a*) S. R. Batten and R. Robson, *Angew. Chem., Int. Ed.*, 1998, **37**, 1460; (*b*) C. Janiak, *Dalton Trans.*, 2003, 2781; (*c*) D. Maspoch, D. Ruiz-Molina and J. Veciana, *Chem. Soc. Rev.*, 2007, **36**, 770; (*d*) G. Férey, *Chem. Soc. Rev.*, 2008, **37**, 191; (*e*) J. R. Long and O. M. Yaghi, *Chem. Soc. Rev.*, 2009, **38**, 1213.
2 (*a*) J. M. Lehn, *Supramolecular Chemistry: Concepts and Perspectives*, VCH, Weinheim, 1995; (*b*) J. W. Steed and J. L. Atwood, *Supramolecular Chemistry*, Wiley and Sons, New York, 2000.
3 O. Kahn, *Adv. Inorg. Chem.*, 1995, **43**, 179.
4 (*a*) S.-I. Ohkoshi, K.-I. Arai, Y. Sato and K. Hashimoto, *Nat. Mater.*, 2003, **2**, 190; (*b*) E. Coronado, J. R. Galán-Mascarós, C. J. Gomez-García and V. Laukhin, *Nature*, 2000, **408**, 447; (*c*) E. Pardo, C. Train, G. Gontard, K. Boubekeur, O. Fabelo, H. Liu, B. Dkhil, F. Lloret, K. Nakagawa, H. Tokoro, S. I. Ohkoshi and M. Verdaguer, *J. Am. Chem. Soc.*, 2011, **133**, 15328; (*d*) C. Train, R. Gheorghe, V. Krstic, L. M. Chamoreau, N. S. Ovanesyan, L. J. A. Rikken, M. Gruselle and M. Verdaguer, *Nat. Mater.*, 2008, **9**, 729.
5 (*a*) F. M. Tabellion, S. R. Seidel, A. M. Ari and P. J. Stang, *J. Am. Chem. Soc.*, 2001, **123**, 7740; (*b*) J. Ferrando-Soria, M. T. M. Rood, M. Julve, F. Lloret, Y. Journaux, J. Pasán, C. Ruiz-Pérez, O. Fabelo and E. Pardo, *CrystEngComm*, 2012, **14**, 761.
6 (*a*) M. Pilkington, M. Gross, P. Franz, M. Biner, S. Decurtins, H. Stoeckli-Evans and A. Neels, *J. Solid State Chem.*, 2001, **159**, 262; (*b*) M. Pilkington and S. Decurtins, in *Comprehensive Coordination Chemistry II: From Biology to Nanotechnology*, ed. J. A. McCleverty and T. J. Meyer, Elsevier, Oxford, USA, 2004, vol. 7, p. 177.
7 (*a*) H. Tamaki, Z. J. Zhong, N. Matsumoto, S. Kida, M. Koikawa, N. Achiwa, Y. Hashimoto and H. Okawa, *J. Am. Chem. Soc.*, 1992, **114**, 6974; (*b*) R. Pellau, H. W. Schmalle, R. Huber, P. Fischer, T. Hauss, B. Ouladdiaf and S. Decurtins, *Inorg. Chem.*, 1997, **36**, 2301; (*c*) E. Coronado, J. R. Galán-Mascarós, C. J. Gómez-García and J. M. Martínez-Agudo, *Inorg. Chem.*, 2001, **40**, 113; (*d*) G. Ballester, E. Coronado, C. Giménez-Saiz and F. M. Romero, *Angew. Chem., Int. Ed.*, 2001, **40**, 792.
8 (*a*) E. Pardo, D. Cangussu, M.-C. Dul, R. Lescouëzec, P. Herson, Y. Journaux, E. F. Pedroso, C. L. M. Pereira, M. C. Muñoz, R. Ruiz-García, J. Cano, P. Amorós, M. Julve and F. Lloret, *Angew. Chem., Int. Ed.*, 2008, **47**, 4211; (*b*) D. Cangussu, E. Pardo, M.-C. Dul, R. Lescouëzec, P. Herson, Y. Journaux, E. F. Pedroso, C. L. M. Pereira, H. O. Stumpf, M. C. Muñoz, R. Ruiz-García, J. Cano, M. Julve and F. Lloret, *Inorg. Chim. Acta*, 2008, **361**, 3394; (*c*) J. Ferrando-Soria, J. Pasán, C. Ruiz-Pérez, Y. Journaux, M. Julve, F. Lloret, J. Cano and E. Pardo, *Inorg. Chem.*, 2011, **50**, 8694.
9 (*a*) E. Pardo, R. Ruiz-García, F. Lloret, J. Faus, M. Julve, Y. Journaux, M. A. Novak, F. S. Delgado and C. Ruiz-Pérez, *Chem.–Eur. J.*, 2007, **13**, 2054; (*b*) J. Ferrando-Soria, E. Pardo, R. Ruiz-García, J. Cano, F. Lloret, M. Julve, Y. Journaux, J. Pasán and C. Ruiz-Pérez, *Chem.–Eur. J.*, 2011, **17**, 2176; (*c*) J. Ferrando-Soria, D. Cangussu, M. Eslava, Y. Journaux, R. Lescouëzec, M. Julve, F. Lloret, J. Pasán, C. Ruiz-Pérez, E. Lhotel, C. Paulsen and E. Pardo, *Chem.–Eur. J.*, 2011, **17**, 12482.

Inorganic Chemistry

Communication

pubs.acs.org/IC

Solid-State Aggregation of Metallacyclophane-Based $Mn^{II}Cu^{II}$ One-Dimensional Ladders

Jesús Ferrando-Soria,[†] Thais Grancha,[†] Jorge Pasán,[‡] Catalina Ruiz-Pérez,[‡] Laura Cañadillas-Delgado,[§] Yves Journaux,[⊥] Miguel Julve,[‡] Joan Cano,[‡] Francesc Lloret,*[,‡] and Emilio Pardo*[,†]

[†]Departament de Química Inorgànica, Instituto de Ciencia Molecular (ICMOL), Universitat de València, 46980 Paterna, València, Spain

[‡]Laboratorio de Rayos X y Materiales Moleculares, Departamento de Física Fundamental II, Universidad de La Laguna, 38201 La Laguna, Tenerife, Spain

[§]Institut Laue Langevin, 38042 Grenoble, France

[⊥]Institut Parisien de Chimie Moléculaire, Université Pierre et Marie Curie-Paris 6, UMR 7201, F-75252 Paris, France

Supporting Information

ABSTRACT: Two distinct one-dimensional (**1**) and two-dimensional (**2**) mixed-metal−organic polymers have been synthesized by using the "complex-as-ligand" strategy. The structure of **1** consists of isolated ladderlike $Mn^{II}_2Cu^{II}_2$ chains separated from each other by neutral Mn^{II}_2 dimers, whereas **2** possesses an overall corrugated layer structure built from additional coordinative interactions between adjacent $Mn^{II}_2Cu^{II}_2$ ladders. Interestingly, **1** and **2** show overall ferri- and antiferromagnetic behavior, respectively, as a result of their distinct crystalline aggregation in the solid state.

The design and synthesis of metal−organic polymers (MOPs)[1] with interesting and predictable magnetic properties has been a subject of great interest for inorganic chemists interested in molecular magnetism during the last 3 decades.[2−4] One- (1D), two- (2D), and three-dimensional (3D) MOPs are also relevant from a crystal-engineering point of view[5] because of the wide range of structural motifs and intriguing topologies that can be found. In the search for rationally designed *n*D (*n* = 1−3) MOPs,[1c,d] the molecular-programmed self-assembling methods show clear advantages over the so-called serendipitous self-assembling ones.[1a,b] However, total control of the final structure is still a challenge even when following these rational synthetic strategies. In fact, there are many subtle factors that may affect the self-assembly process, both intrinsic (stereochemical and steric requirements of the metal and ligand, respectively) and extrinsic (metal−ligand ratio, solvent, and temperature),[6] and then influence the final structure of the MOPs.

Our strategy in this field is based on the use of oxamato-based homodinuclear copper(II), nickel(II), and cobalt(II) metallacyclic complexes as ligands (metalloligands) toward fully solvated divalent first-row transition-metal ions like manganese(II) and cobalt(II) to afford mixed-metal−organic polymers, abbreviated as M′MOPs, of varying dimensionality.[7,1c,d] So, for instance, the double-stranded dicopper(II) metallacyclophanes of the general formula $[Cu_2L_2]^{4-}$ [L = *N*,*N*′-1,3-phenylenebis(oxamate) (mpba), 2-methyl-*N*,*N*′-1,3-phenylenebis(oxamate) (Mempba), and 2,4,6-trimethyl-*N*,*N*′-1,3-phenylenebis(oxamate) (Me_3mpba)][7] can be advantageously used as a tetrakis(bidentate) metalloligand toward bis(chelated) M^{II} ions (M = Mn and Co) to render neutral M′MOPs with different 1D or 2D architectures (Scheme 1). In follow-up works,[7a,b] some of us reported two examples of 2D M′MOPs possessing a "brick-wall" rectangular layer structure of (6, 3) net topology that were obtained through the self-assembly of the anionic dicopper(II) complexes $[Cu_2(mpba)_2]^{4-}$ and $[Cu_2(Me_3mpba)_2]^{4-}$ with Co^{II} or Mn^{II} ions, respectively (Scheme 1b).[7a,b]

Scheme 1. Self-Assembly of 1D (b) and 2D (c and d) M′MOPs Resulting from the Use of a Dicopper(II) Metallacyclophane Anion (a) as the Tetrakis(bidentate) Metalloligand toward Bis(chelated) Mn^{II} Ions

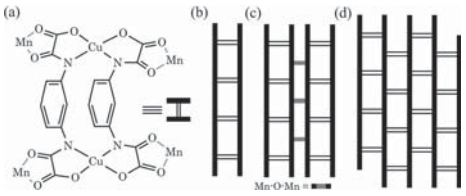

In this Communication, we show that 1D (**1**) and 2D (**2**) M′MOPs with a basic "ladderlike" structural motif but different degrees of aggregation in the solid state (Scheme 1b,c), can be alternatively obtained under different experimental conditions. Herein we report the syntheses, crystal structures, and magnetic properties of these new examples of M′MOPs of formulas $[Mn_4(H_2mpba)_4(H_2O)_{12}]\{[Mn_8Cu_8(mpba)_8(H_2O)_{24}]\}\cdot 29.5H_2O$ (**1**) and $[Mn_4Cu_4(mpba)_4(H_2O)_9]\cdot 14H_2O$ (**2**).

Compounds **1** and **2** were both obtained as pale-green rectangular and cubic crystals, respectively, by slow diffusion in an H-shaped tube of aqueous solutions of $Na_4[Cu_2(mpba)_2]\cdot 8H_2O$[7a] and $Mn(NO_3)_2\cdot 4H_2O$ at 16 °C.

Received: May 9, 2012
Published: June 18, 2012

   dx.doi.org/10.1021/ic300953n | *Inorg. Chem.* 2012, 51, 7019−7021

Interestingly, control of the temperature is crucial to avoid formation of the MOP with the "brick-wall" structure.[7a,b] Moreover, the dicopper(II) complex/manganese(II) molar ratio also plays a key role in the self-assembling process. Thus, a 2D network with a Cu/Mn ratio of 1:1 (**2**) crystallized when using the stoichiometric relation (1:2). However, when this molar ratio was increased to 1:6 in the double H-shaped tube, a double-chain 1D compound (**1**) results with a final Cu/Mn ratio of 2:3. Their crystal structures were solved by single-crystal X-ray diffraction using synchrotron radiation at the BM16 beamline in the ESRF. They crystallize in the $P2_1cn$ (**1**) and $P2_1/c$ (**2**) space groups.

Complex **1** consists of neutral oxamato-bridged double copper(II)/manganese(II) chains, $[Mn_2Cu_2(mpba)_2(H_2O)_6]$ (Figures 1a and S1a in the Supporting Information, SI),

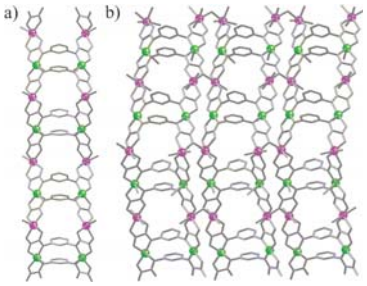

Figure 1. Perspective views of the fragments of two double chains of **1** (a) and the 2D neutral network of **2** (b). Metal and ligand atoms are represented by balls and sticks, respectively [Cu, green; Mn, purple].

cocrystallized $[Mn(H_2mpba)(H_2O)_3]$ chains, and free water molecules (Figure S1b in the SI). Each bis(oxamato)copper(II) entity acts as a bis(bidentate) ligand through the carbonyl oxygen atoms toward *cis*-diaquamanganese(II) units, affording zigzag double bimetallic chains that run parallel to the *c* axis (Figure 1a). These one-dimensional motifs possess a ladderlike architecture,[7c,d] where two phenylenediamidate bridges act as "rungs" between the two oxamate-bridged zigzag CuMn chains, which then serve as "rods". The shortest intrachain Cu···Cu and Cu···Mn distances are in the ranges 6.654(2)−6.656(2) and 5.4532(14)−5.4865(15) Å, respectively.

The four crystallographically independent copper atoms in **1** [Cu(1)−Cu(4)] have five-coordinated square-pyramidal CuN_2O_3 surroundings, with two amide nitrogen atoms [Cu−N = 1.940(5)−2.061(6) Å] and two carboxylate oxygen atoms [Cu−O = 1.962(5)−2.052(4) Å] from the two oxamate ligands in a trans arrangement building the basal plane and the apical position being occupied by a water molecule [Cu−Ow = 2.322(5)−2.369(7) Å]. The four crystallographically independent manganese atoms of the double chains [Mn(1)−Mn(4)] are six-coordinate with two water molecules in cis positions [Mn−Ow = 2.096(6)−2.178(7) Å] and four oxygen atoms [Mn−O = 2.129(4)−2.258(7) Å] from two oxamate ligands, forming distorted octahedral surroundings.

In the crystal lattice of **1**, the zigzag CuMn double chains run along the [001] direction (Figure S2b in the SI). Moreover, they are displaced along the [010] direction, leading thus to an ABAB disposition pattern in the *ab* plane. Overall, this situation leads to large channels along the *c* axis that are occupied by the cocrystallized $[Mn(H_2mpba)(H_2O)_3]$ chains that situate perpendicularly to the CuMn double chains (Figure S2 in the SI). Interestingly, there is a regular alternation of these highly disordered enantiopure Mn^{II} chains of opposite chiralities (Δ and Λ) along the *b* axis. The shortest interchain Cu···Cu, Cu···Mn, and Mn···Mn distances are 8.327(2), 5.150(2), and 5.761(4) Å, respectively.

The structure of **2** consists of neutral oxamato-bridged copper(II)/manganese(II) 2D networks, $[Mn_4Cu_4(mpba)_4(H_2O)_9]$ (Figure 1b) and crystallization water molecules. It can be alternatively described as a series of Cu_2Mn_2 double chains linked by coordinative interactions, giving rise to a corrugated 2D network. Each double chain has the same ladderlike structure of **1**; however, two carbonyl oxygen atoms from the oxamato ligands, which are coordinated to manganese(II) ions along the zigzag chain [O(1) and O(16)], also coordinate to manganese(II) ions of a neighboring double chain, giving rise to the final layered 2D structure (Figure 1b). The intrachain Cu···Cu and Cu···Mn distances through the oxamate and *m*-phenylene bridges are within the ranges of 6.7954(14)−6.8461(14) and 5.3328(11)−5.5510(11) Å, respectively. Along the 2D network, the shortest interchain Mn···Mn distance is 4.0399(12) Å and the Mn−O−Mn angle varies in the range 122.43(15)−122.51(15)°.

There are four crystallographically independent copper atoms in **2**. Three of them [Cu(1), Cu(2), and Cu(4)] have five-coordinated square-pyramidal CuN_2O_3 surroundings (Figure S3a in the SI), with two amidate nitrogen atoms [Cu−N = 1.960(3)−1.984(3) Å] and two carboxylate oxygen atoms [Cu−O = 1.969(3)−2.018(3)] Å) from the oxamate groups of the ligands building the basal plane and the apical positions being occupied by a water molecule [Cu−Ow = 2.360(3)−2.600(4) Å]. The fourth copper atom [Cu(3)] has a square-planar CuN_2O_3 environment [Cu−N = 1.956(3)−1.965(3) Å and Cu−O = 1.956(3)−1.978(3) Å]. There are also four crystallographically independent manganese atoms [Mn(1)−Mn(4)] that exhibit very distorted octahedral geometries, MnO_6, formed by four carbonyl oxygen atoms from two oxamato groups in all cases [Mn−O = 2.089(3)−2.397(3) Å] and two coordinated water molecules in trans and cis dispositions for Mn(1) and Mn(4), respectively [Mn−Ow = 2.127(3)−2.259(3) Å], and one coordinated water molecule and one carbonyl oxygen atom from the oxamate group of a neighboring double chain in trans and cis dispositions for Mn(2) and Mn(3), respectively [Mn−O = 2.249(3)−2.313(3) Å and Mn−Ow = 2.126(3)−2.278(4) Å]. This coordination mode is rare when looking at other similar oxamato-bridged copper(II)/metal(II) MOPs.[1c,d,8]

In the crystal lattice of **2**, the corrugated layers are slightly shifted from the neighboring ones, avoiding a perfect stacking along the *c* axis (Figure S3b in the SI). The shortest Cu−Cu, Cu−Mn, and Mn−Mn interlayer separations are 5.9958(11), 4.5757(10), and 5.1642(11) Å, respectively. In addition, intermolecular hydrogen bonds [Ow···Ow = 2.668(5)−3.112(8) Å] involving coordinated [either to manganese(II) and to copper(II) atoms] and crystallization water molecules build a three-dimensional motif (Figure S3b in the SI).

The magnetic properties of **1** and **2** in the form of $\chi_M T$ versus *T* plots [with χ_M being the molar magnetic susceptibility per Cu_2Mn_2 (**1**) and Cu_2Mn_2 (**2**) units] are very different (Figure 2). At room temperature, $\chi_M T$ values for **1** and **2** (12.46 and 9.03 cm^3 K mol^{-1}, respectively) are slightly lower than those expected for the sum of two square/square-pyramidal copper(II) ions (**1** and **2**) and three (**1**) or two (**2**) octahedral manganese(II) ions [$\chi_M T$ = 13.91 (**1**) and 9.54 (**2**) cm^3 mol^{-1}

dx.doi.org/10.1021/ic300953n | *Inorg. Chem.* 2012, 51, 7019−7021

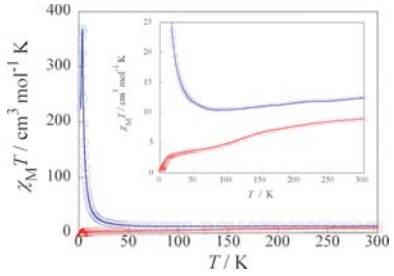

Figure 2. Temperature dependence of $\chi_M T$ of **1** (○, blue) and **2** (△, red) [under an applied magnetic field of 1 T ($T \geq 50$ K) and 250 G ($T < 50$ K]. The inset shows in detail the different behavior of **1** and **2**. The solid lines are eye guides.

K with $g_{Mn} = 2.0$, $g_{Cu} = 2.1$, $S_{Mn} = {}^5/_2$, and $S_{Cu} = {}^1/_2$]. Upon cooling, $\chi_M T$ for **1** decreases, attains a minimum around 95 K (inset of Figure 2), and then rapidly increases to reach a maximum at about 4.0 K with $\chi_M T = 375$ cm^3 K mol^{-1} because of saturation effects. The presence of a minimum of $\chi_M T$ for **1** is characteristic of an overall ferrimagnetic behavior, as was previously observed in related oxamato-bridged manganese(II)/copper(II) chains.[8] More likely, the moderate ferromagnetic interaction between copper(II) ions through the double *m*-phenylene bridge that occurs by means of a spin-polarization mechanism[7c,d] is masked by the more important antiferromagnetic interaction between copper(II) and manganese(II) ions through the oxamate bridge.

On the contrary, $\chi_M T$ for **2** continuously decreases upon cooling to reach an incipient *plateau* in the range 75−15 K and then rapidly decreases and almost vanishes at 2.0 K ($\chi_M T$ = 0.58 cm^3 K mol^{-1}; inset of Figure 2). This overall antiferromagnetic behavior results from the nonnegligible antiferromagnetic coupling between neighboring double chains through the monatomic carboxylate−oxo bridge.[9] The observed *plateau* is thus a consequence of the two different competitive magnetic interactions mediated by the oxamate− and carboxylate−oxo bridges, respectively.

In conclusion, a binuclear copper(II) precursor complex has been used as the metalloligand toward manganese(II) ions to afford two new M′MOPs with a common ladderlike chain motif. Yet, their distinct crystalline aggregation in the solid state leads to dramatically different magnetic properties. Thus, **1** behaves as a ferrimagnetic double chain with moderately strong antiferromagnetic intrachain coupling between copper(II) and manganese(II) ions through the oxamato bridge. In contrast, the antiferromagnetic interchain interactions between neighboring ferrimagnetic double chains dominate in **2**, giving rise to a $S = 0$ ground spin state.

■ ASSOCIATED CONTENT

Ⓢ Supporting Information

X-ray data in CIF format, experimental preparation, analytical and spectroscopic characterization (**1**/**2**), and additional figures (Figures S1−S3). This material is available free of charge via the Internet at http://pubs.acs.org.

■ AUTHOR INFORMATION

Corresponding Author

*E-mail: Emilio.Pardo@uv.es (E.P.), Francisco.Lloret@uv.es (F.L.).

Notes

The authors declare no competing financial interest.

■ ACKNOWLEDGMENTS

This work was supported by the MICINN (Spain; Projects CTQ2010-15364, MAT2010-19681, DPI2010-21103-C04-03, CSD2007-00010, and CSD2006-00015), the Generalitat Valenciana (Spain; Projects PROMETEO/2009/108 and ISIC/2012/002), the ACIISI-Gobierno Autónomo de Canarias (Spain; Project PIL-2070901 and structuring project NANOMAC), and the MFR and CNRS (France). We also acknowledge the Long Term Project HS3902 of the ESRF, Grenoble, France, for the beamtime assigned. J.F.-S. thanks the Generalitat Valenciana for a doctoral grant. E.P. and J.P. thank the "Juan de la Cierva" (MICINN) and the structuring project NANOMAC, respectively, for postdoctoral contracts.

■ REFERENCES

(1) (a) Batten, S. R.; Robson, R. *Angew. Chem., Int. Ed.* **1998**, *37*, 1460. (b) Maspoch, D.; Ruiz-Molina, D.; Veciana, J. *Chem. Soc. Rev.* **2007**, *36*, 770. (c) Pardo, E.; Ruiz-García, R.; Cano, J.; Ottenwaelder, X.; Lescoüezec, R.; Journaux, Y.; Lloret, F.; Julve, M. *Dalton Trans.* **2008**, 2780. (d) Dul, M.-C.; Pardo, E.; Lescouëzec, R.; Journaux, Y.; Ferrando-Soria, J.; Ruiz-García, R.; Cano, J.; Julve, M.; Lloret, F.; Cangussu, D.; Pereira, C. L. M.; Stumpf, H. O.; Pasán, J.; Ruiz-Pérez, C. *Coord. Chem. Rev.* **2010**, *254*, 2281.

(2) Pilkington, M.; Decurtins, S. In *Comprehensive Coordination Chemistry II: From Biology to Nanotechnology*; McCleverty, J. A., Meyer, T. J., Eds.; Elsevier: Oxford, U.K., 2004; Vol. 7, p 177.

(3) Verdaguer, M.; Bleuzen, A.; Marvaud, V.; Vaissermann, J.; Seuleiman, M.; Desplanches, C.; Scuiller, A.; Train, C.; Garde, R.; Gelly, G.; Lomenech, C.; Rosenman, I.; Veillet, P.; Cartier, C.; Villain, F. *Coord. Chem. Rev.* **1999**, *190*, 1023.

(4) (a) Kahn, O. *Struct. Bonding (Berlin)* **1987**, *68*, 89. (b) Kahn, O. *Acc. Chem. Res.* **2000**, *33*, 647.

(5) (a) Lehn, J. M. *Supramolecular Chemistry: Concepts and Perspectives*; VCH: Weinheim, Germany, 1995. (b) Leininger, S.; Olenyuk, B.; Stang, P. J. *Chem. Rev.* **2000**, *100*, 853.

(6) (a) Tabellion, F. M.; Seidel, S. R.; Ari, A. M.; Stang, P. J. *J. Am. Chem. Soc.* **2001**, *123*, 7740. (b) Janiak, C. *Dalton Trans.* **2003**, 2781. (c) Biradha, K.; Sarkar, M.; Rajput, L. *Chem. Commun.* **2006**, 4169.

(7) (a) Pereira, C. L. M.; Pedroso, E. F.; Stumpf, H. O.; Novak, M. A.; Ricard, L.; Ruiz-García, R.; Rivière, E.; Journaux, Y. *Angew. Chem., Int. Ed.* **2004**, *43*, 956. (b) Ferrando-Soria, J.; Pasán, J.; Ruiz-Pérez, C.; Journaux, Y.; Julve, M.; Lloret, F.; Cano, J.; Pardo, E. *Inorg. Chem.* **2011**, *50*, 8694. (c) Pardo, E.; Bernot, K.; Julve, M.; Lloret, F.; Cano, J.; Ruiz-García, R.; Delgado, F. S.; Ruiz-Pérez, C.; Ottenwaelder, X.; Journaux, Y. *Inorg. Chem.* **2004**, *43*, 2768. (d) Pardo, E.; Ruiz-García, R.; Lloret, F.; Julve, M.; Cano, J.; Pasán, J.; Ruiz-Pérez, C.; Filali, Y.; Chamoreau, L. M.; Journaux, Y. *Inorg. Chem.* **2007**, *46*, 4504. (e) Pardo, E.; Ferrando-Soria, J.; Dul, M.-C.; Lescouëzec, R.; Journaux, Y.; Ruiz-García, R.; Cano, J.; Julve, M.; Lloret, F.; Cañadillas-Delgado, L.; Pasán, J.; Ruiz-Pérez, C. *Chem.—Eur. J.* **2010**, *16*, 12838.

(8) (a) Pardo, E.; Ruiz-García, R.; Lloret, F.; Faus, J.; Julve, M.; Journaux, Y.; Novak, M. A.; Delgado, F. S.; Ruiz-Pérez, C. *Chem.—Eur. J.* **2007**, *13*, 2054. (b) Ferrando-Soria, J.; Pardo, E.; Ruiz-García, R.; Cano, J.; Lloret, F.; Julve, M.; Journaux, Y.; Pasán, J.; Ruiz-Pérez, C. *Chem.—Eur. J.* **2011**, *17*, 2176. (c) Ferrando-Soria, J.; Cangussu, D.; Eslava, M.; Journaux, Y.; Lescouëzec, R.; Julve, M.; Lloret, F.; Pasán, J.; Ruiz-Pérez, C.; Lhotel, E.; Paulsen, C.; Pardo, E. *Chem.—Eur. J.* **2011**, *17*, 12482.

(9) Milios, C. J.; Kefalloniti, E.; Raptopoulou, C. P.; Terzis, A.; Escuer, A.; Vicente, R.; Perlepes, S. P. *Polyhedron* **2004**, 83.

ADVANCED ENERGY MATERIALS
www.advenergymat.de

Efficient, Cyanine Dye Based Bilayer Solar Cells

*Olga Malinkiewicz, Thais Grancha, Agustin Molina-Ontoria, Alejandra Soriano, Hicham Brine, and Henk J. Bolink**

Simple bilayer solar cells, using commercially available cationic cyanine dyes as donors and evaporated C_{60} layer as an acceptor are prepared. Cyanine dyes with absorption maxima of 578, 615 and 697 nm having either perchlorate or hexafluorophosphate counter-ions are evaluated. The perchlorate dye leads to cells with S-shape current-voltage curves; only the dyes with the hexafluorophosphate counter-ions lead to efficient solar cells. When the wide bandgap dyes are employed, S-shape current-voltage curves are obtained when the conductive polymer PEDOT:PSS is used as hole transport layer. Substitution of PEDOT:PSS with MoO_3 leads to cells with more rectangular current–voltage curves and high fill factors. Additionally, the cells using the MoO_3 layer for hole extraction lead to high open circuit voltages of 0.9 V. In the case that a low bandgap hexafluorophosphate dye is used with the HOMO above that of the PEDOT:PSS the cell performance is independent on the type of hole transport layer employed. Using this approach, bilayer solar cells are obtained with power efficiencies ranging from 1.8 to 2.9% depending on the particular dye employed. These are impressive numbers for bilayer solar cell that are partially solution processed in ambient conditions.

1. Introduction

Organic photovoltaic cells (OPVs) have attracted a lot of attention in the last years not least due to significant breakthroughs in device efficiencies.[1] Most of the best performing cells rely on bulk heterojuctions, optimized for maximum light absorption and efficient charge generation. Less attention has been paid to the much simpler planar heterojunctions in bilayer OPVs as first described by Tang.[2] Although bilayer cells have lower efficiencies as a consequence of the use of thinner active layers (determined by the limited exciton diffusion lengths), they still possess very interesting features which make them an excellent platform for the screening of new materials and for fundamental studies.[3] Thanks to the planar structure (one organic layer on top of another) the charges generated at the interface are spatially separated which means that holes are confined within the donor layer while the electrons are confined within the acceptor layer. Since recombination between free charges is practically eliminated it is possible to obtain information on physical phenomena in such cells.[3] Cyanine dyes are interesting molecules for use in photovoltaic applications, in particular in bilayer solar cells.[4] This is because they have very high absorption coefficients (~10^5 M^{-1} cm^{-1}) and their absorption spectra cover a wide range of wavelengths, from the blue to the near infrared.[5] Additionally, it was demonstrated that excitons generated in a thin film of cyanine dyes exhibit relatively long exciton diffusion lengths (aprox. 30 nm).[6] Hence, in principle, all excitons generated in a film with a thickness up to 30 nm can reach the interface. Furthermore, cyanine dyes are used in various applications and are therefore commercially available in high purity and quantities at low cost. In previously reported cyanine based solar cells, S-shaped current-voltage (I–V) curves were frequently reported.[4,7] The origin of the S-shaped I–V curves is not yet understood, but has been shown to be influenced by the type of counter-ion, partial oxidation, and the type of hole transporting material employed. Recently, an interesting hole injection/extraction material, MoO_3, has been successfully implemented as hole injection layer (HIL) in many OLEDs and recently also in some BHJ OPVs.[8] Additionally, it was shown that the MoO_3 layers can be obtained by solution processing.[9]

In this work we present planar heterojunctions using a solution processed cyanine dye donor layer and an evaporated fullerene layer. Also we demonstrate how the S-shape current density vs. voltage (J–V) curves can be avoided. Four cyanine dyes are used with different absorption spectra, three with a hexafluorophosphate (PF_6) and one with a perchlorate (ClO_4) counter-ion. The dye with the ClO_4 counter-ion leads to cells with low fill factors due to S-shaped J–V curves. Whereas the cells using the dyes having a PF_6 counter-ion have high fill factors and good device performances. The device performances can be increased when a MoO_3 hole transporting layer is used. This leads to an increase of the V_{oc} and the shape of the current density vs. voltage (J–V) curve which results in an increased fill factor. The best devices reach a power conversion efficiency (PCE) of 2.9%.

O. Malinkiewicz, T. Grancha, Dr. A. Soriano, H. Brine, Dr. H. J. Bolink
Instituto de Ciencia Molecular
Universidad de Valencia
C/Catedrático J. Beltrán 2
ES-46980 Paterna (Valencia), Spain
E-mail: henk.bolink@uv.es
Dr. A. Molina-Ontoria
Departamento de Química Orgánica
Facultad de Química
Universidad Complutense
28040 Madrid, Spain

DOI: 10.1002/aenm.201200764

ADVANCED ENERGY MATERIALS
www.advenergymat.de

Materials Views
www.MaterialsViews.com

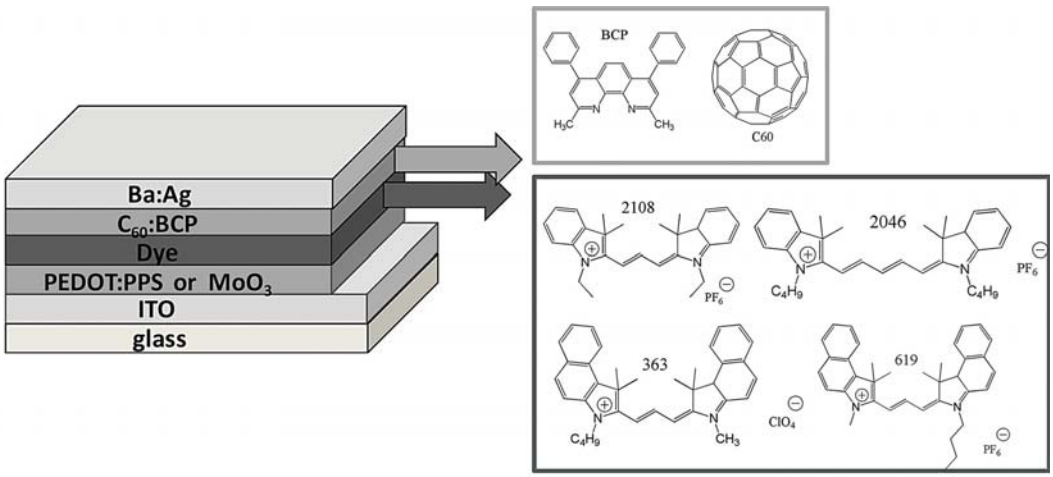

Figure 1. Schematic of the device layout and the chemical structures of the materials employed.

2. Results and Discussion

Four cyanine dyes were studied as donors: 1-ethyl-2-[3-[1-ethyl-3,3-dimethyl-1,3-dihydro-indol-2-ylidene]-propenyl]-3,3-dimethyl-3H-indolium hexafluorophosphate (**2108**), 3-butyl-1,1-dimethyl-2-[3-(1,1,3-trimethyl-1,3-dihydro-benzo[e]indol-2-ylidene)-propenyl]-1H-benzo[e]indolium hexafluorophosphate (**619**), 3-butyl-2-[3-(1,3-dihydro-1,3,3-trimethyl-2H-indol-2-ylidene)-propenyl]-1,1-dimethyl-1H-benzo[e]indolium perchlorate (**363**) and 1-butyl-2-[5-(1-butyl-1,3-dihydro-3,3-dimethyl-2H-indol-2-ylidene)-penta-1,3-dienyl]-3,3-dimethyl-3H-indolium hexafluorophosphate (**2046**) (**Figure 1**). The dye **2108** has been used before in this type of solar cells and the dyes **619** and **2046** have a similarly high extension coefficient but with a red shifted absorption spectrum. In addition to these hexafluorophosphate salts the perchlorate dye, **363** with the organic part similar to **619** was also evaluated.

Bilayer cells were prepared according to the layout shown in Figure 1. The dye layer is deposited on top of a hole transporting layer (HTL). This is either poly-(3,4-ethylenedioxythiophene)-poly-(styrenesulfonate), PEDOT:PSS (Clevios AI4083, from Hereaus) or MoO_3. The PEDOT:PSS layer was prepared by spincoating in ambient conditions. The MoO_3 was prepared by thermal evaporation in a high vacuum environment. Independently of this, HTL was employed the dye layer was prepared using spincoating from a chlorobenzene solution (7 mg/ml) in ambient conditions. The acceptor layer consisted of C_{60} which was thermally evaporated under a high vacuum. Prior to the deposition of the Ba/Ag cathode, a thin layer of (bathocuproine) BCP was evaporated. This layer of BCP is evaporated in between the C_{60} layer and the cathode to ensure a proper ohmic contact and hence an efficient charge extraction.[10] More detailed information regarding device preparation can be found in the Experimental Section.

The absorption spectra of 30 nm thin films of the dyes and C_{60} are depicted in **Figure 2**. Dye **2108** shows a maximum absorption at 578 nm, dye **619** and **363** both have a maximum absorbance at 615 nm and dye **2046** has the maximum at 697 nm. The absorption of the dyes **619**, **363** and **2046** is shifted towards longer wavelength with respect to that of dye **2108** which is due to an increase in the effective conjugation length of the dye. At similar film thicknesses the absorbance of the cyanine dyes in the visible part of the spectrum is approximately twice that of C_{60} as expected from their high extinction coefficients. However, due to the narrow width of the absorption spectra of the dyes the absorption of C_{60} at wavelengths below 500 nm is stronger than that of the dyes.

First we evaluated the 363 and 619 dyes that have a very similar organic cation, yet with a perchlorate and a hexafluorophosphate counterion, respectively. The effect of the counterion is not very well known but can play a significant role if it diffuses into the C_{60} layer. In **Figure 3**, the current density (J) to voltage

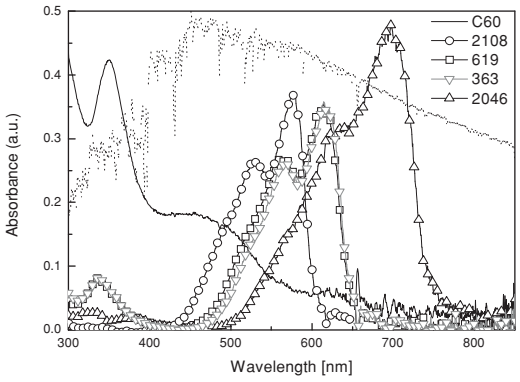

Figure 2. Absorption spectra of thin films of C_{60} (solid black line) and the cyanine dyes **2108**, **619**, **363** and **2046**. The dotted line represents the AM1.5 solar spectrum.

DOI: 10.1002/aenm.201200764

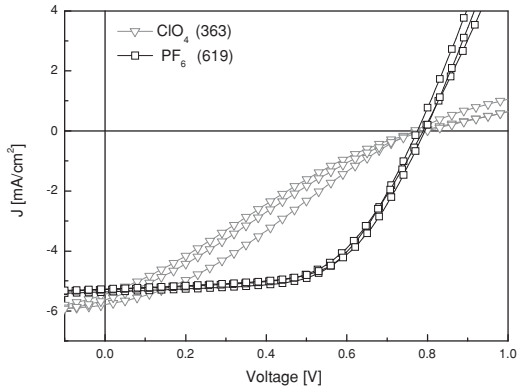

Figure 3. Current density vs voltage for cells using either dye **363** or **619** under an illumination of 1000 W/m^2 simulated AM1.5 solar light.

(V) characteristics are shown for cells using either the dye 363 or 619 under an illumination of 1000 W/m^2 simulated AM1.5 solar light. The J–V curve of cells using the ClO_4^- containing dye (363) has a very clear S-shape which leads to a very low fill factor. This is in sharp contrast with the J–V curve obtained from the devices employing the PF_6 dye (619), which has a rectangular shape, leading to a fill factor of 60%. The open circuit voltage (V_{oc}) and the short-circuit current (J_{sc}) are rather similar for both type of cells. Similar results were reported previously in two reports.[7] Notice also that the reproducibility of the results in these devices is rather good. This large change in performance is most likely not a result of a different absorbance or exciton formation process since the absorption spectra for both dyes are identical. The hole mobility in the dye layer is primarily determined by the organic cation of the dye, which, as mentioned, is the same in both cases. The type of counterion may influence the hole mobility as it may reorient to stabilize/trap a hole. This effect would be stronger for a more mobile counterion, such as the ClO_4^- ion. However, a more plausible explanation can be derived from a previous report by the group of Nuesch that mentions that ion migration from the dye layer to the acceptor layer can occur.[11] This leads to a strong interface dipole over the donor acceptor interface, which changes the energy off-set between donor LUMO and acceptor LUMO. Migration of ions is likely to depend strongly on the ion size, hence it is possible that the smaller ClO_4^- ions migrate more rapidly into the C_{60} layer, causing the poor photovoltaic performance. To identify the origin of this effect detailed studies are required.

In view of the results obtained the PF_6^- dyes (**619**, **2108** and **2046**) were selected to compare the effect of the hole injection material and the bandgap of the dye on the device performances. The incident photon-to-current conversion efficiencies (IPCE) for cells using the **619** dye with either an PEDOT:PSS or a MoO_3 HTL is depicted in **Figure 4**a. Figure 4b shows the typical J–V curves for both type of devices. The IPCE indicates that light absorption in the dye and C_{60} layer contribute both to the photovoltaic effect (Figure 4). This implies that the energy off-set between the lowest unoccupied molecular orbital (LUMO) of the dye is sufficiently above that of the LUMO of C_{60} and that the highest occupied molecular orbital (HOMO) of the C_{60} is sufficiently below that of the HOMO of the dye. The IPCE of the cells using PEDOT:PSS is slightly higher than that of the cells using MoO_3. This higher IPCE for the cells with PEDOT;PSS is reflected in a higher J_{sc} (see Figure 4 and **Table 1**). The reason for this difference may be related to a lower light transmission due to the absorbance of the MoO_3 layer. This was also observed for bulk-heterojunction solar cells using such layers.[9] The device absorption spectrum which contains the contribution from the C_{60} and the **619** dye shows a higher absorption in the wavelength range from 550 to 650 nm, demonstrating that the dye film is absorbing more light than the C_{60} film nm (Figure S5). Therefore, one might expect the IPCE to be higher in the wavelength range from 550 to 650 nm. The IPCEs of the PEDOT:PSS containing cells do show higher values in that wavelength range, yet those of the MoO_3-containing cells

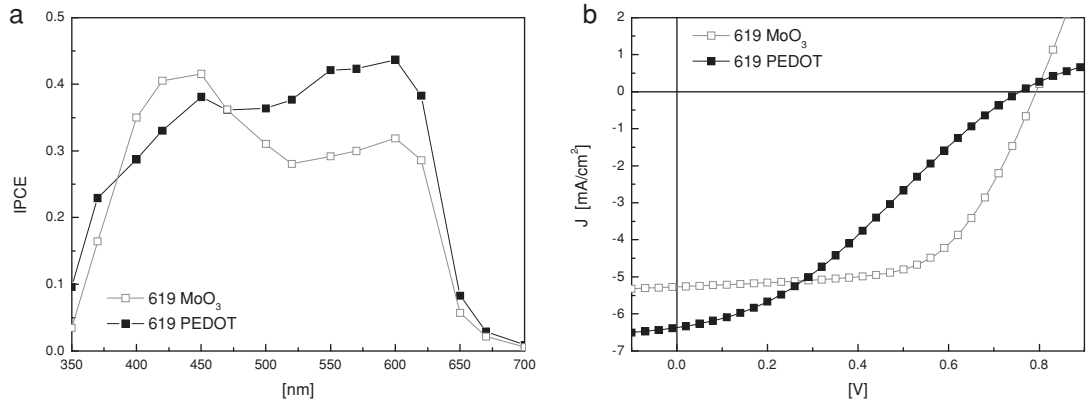

Figure 4. Left: IPCE of the solar cells based on dye **619** with a PEDOT:PSS (full squares) or a MoO_3 (open squares) anode. Right: Current density vs voltage for these two devices.

Table 1. Overview of the characteristics for the different cells described. Values displayed are average values from more than 10 cells. For an indication of the reproducibility of the cells see Figures (S1, S2 and S3) in the Supporting Information.

DYE	[nm]	HTL	[nm]	IPCE $_{max}$ [%]	PCE [%]	FF [%]	V_{OC} [V]	J_{SC} [mA/cm^2]
2108	30	MoO_3	30	41	2.4	55	0.92	4.6
2108[a)]	23	MoO_3	30	45	2.9	62	0.92	5.1
2108	30	PEDOT	70	54	1.9	44	0.77	5.7
0619	30	MoO_3	30	41	2.5	60	0.79	5.3
0619	30	PEDOT	70	44	1.4	30	0.76	6.3
0363	30	MoO_3	30	48	1.1	24	0.79	5.6
2046	30	MoO_3	20	35	1.8	50	0.62	5.8
2046	30	PEDOT	70	28	1.7	49	0.62	5.7

[a)] Best device.

do not. Hence in this case it appears that the lower IPCE is caused by an extraction barrier for holes when MoO_3 is used as the HTL (**Figure 5**). More striking is the different shape of the J–V curves. The MoO_3-containing cells show a rectangular curve leading to a fill factor of 60%. Whereas the cells using PEDOT:PSS have an S-shaped J–V curve. The S-shape for the PEDOT:PSS-containing devices is related to the lower build-in voltage for these devices. As shown by Uhrich et al., S-shape J–V curves are expected for bilayer solar cells when the build-in voltage is lower than the V_{oc}.[3] As shown in Figure 5 the energy level of the PEDOT:PSS layer is higher (less deep) than for the MoO_3 layer and therefore the built-in voltage is reduced when PEDOT:PSS is used. These results were also obtained for cells using dye **2108** (**Figure 6**). This implies that both dyes have a similar behaviour in the solar cells. The V_{oc} of the cells containing the MoO_3 layer is significantly higher (reaching 0.92 V) than what is obtained with the PEDOT:PSS layer. The higher V_{oc} for the cell based on this dye is in part due to the larger bandgap and to the larger built-in voltage when MoO_3 is used as the HTL. Also for these cells (like in those using dye **619**) the IPCE does not resemble the absorption spectrum of the device (Figure S6). The higher contribution of the dye layer to the device absorption is not reflected in a higher IPCE for the cells using the MoO_3 layer. When PEDOT:PSS is used as the HTL, a peak in the IPCE is observed in the wavelength range where the dye absorbs.

There is therefore a trade-off between an increase in the V_{oc} and the reduction of the J_{sc} when using MoO_3 as the HTL. Yet the good fill factors (FF) observed for the cells using MoO_3 leads to superior power conversion efficiencies (PCE) for these cells when compared with those using PEDOT:PSS as the HTL. Quite good PCE values are obtained for devices employing dyes with a PF_6 counterion and that use the MoO_3 as the HTL. They are very similar for both dyes, leading to average PCE values of 2.4 and 2.5% for cells using **2108** and **619**, respectively. Best devices showed even a sligthly higher value of 2.9%.

If the S-shape observed for the above described cells is indeed caused by an insufficient difference between the V_{oc} and the V_{bi}, when PEDOT:PSS is used as the HTL, it should be absent for cells using lower bandgap dyes. To verify this hypothesis, cells were prepared analogous to those mentioned above, yet using dye **2046**. Indeed, virtually no difference is observed in the J–V curves for cells using PEDOT:PSS or those using MoO_3 as the HTL (**Figure 7**). Both devices have very similar fill factors, 49 and 50%. Therefore, it appears plausible that the reason for the S-shapes observed for the cells uing the wider bandgap dyes is due to an insufficient V_{bi} when PEDOT:PSS is used as the HTL. The cells using **2046** also show more clearly the two distinct regions in the IPCE; one region due to the absorption in the fullerene layer (in the 400–500 nm range) and another due to the absorption in the dye layer (in the 550–750 range). This shows clearly that both layers contribute the photocurrent generation. The absorption spectrum of these devices (Figure S7) shows that the dye layer leads to an absorption that is almost twice as high as that

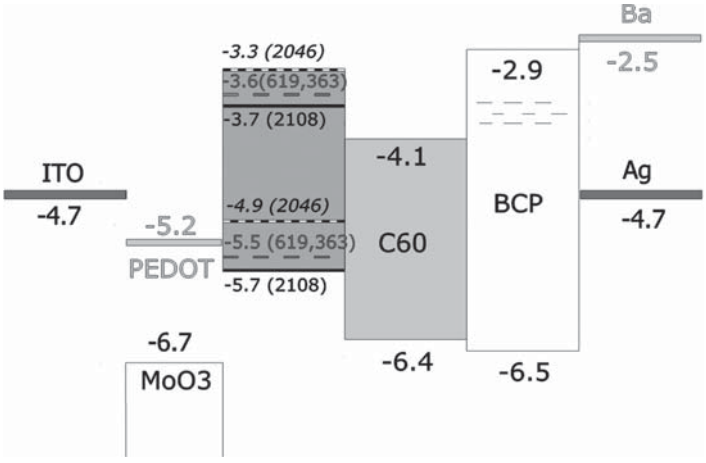

Figure 5. Energy levels of the different materials used in these solar cells.

DOI: 10.1002/aenm.201200764

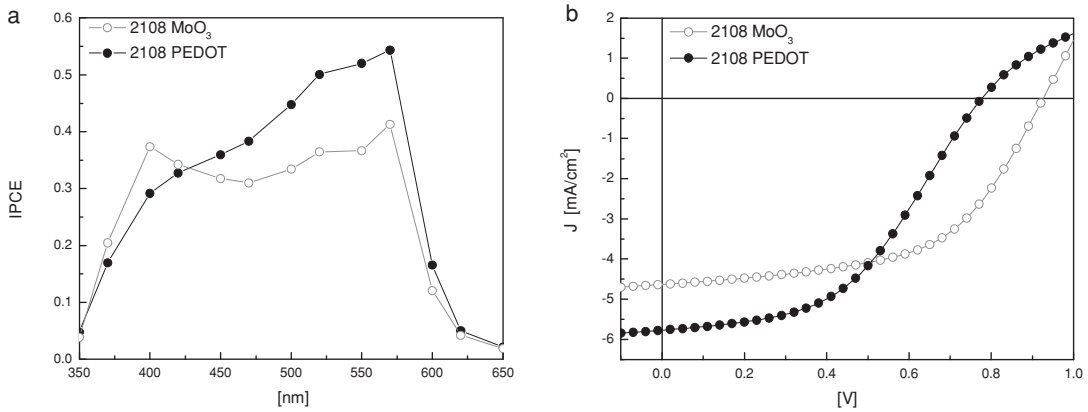

Figure 6. Left, IPCE of the solar cells based on dye **2108** with a PEDOT:PSS (full circles) or a MoO_3 (open circles) anode anode. Right, current density vs voltage for these two devices.

caused by the C_{60} layer. Yet, like in the previously described devices, the IPCE shows an approximately equal contribution from both layers. For this dye no difference is observed for PEDOT:PSS- or MoO_3-based devices, hence the extraction barrier for holes is the same in both cases. The lower IPCE in the wavelength region where the dye absorbs must therefore be related to a lower exciton diffusion/seperation in the dye layer compared to the C_{60} layer, or alternatively is caused by poorer charge carrier mobilities in the dye layer.

3. Conclusions

Simple bilayer solar cells, using commercially available cationic cyanine dyes as donors and evaporated C_{60} layer as an acceptor are prepared. Cyanine dyes with absorption maxima of 578, 615 and 697 nm having either perchlorate or hexafluorophosphate counter-ions were evaluated. Only the dyes with the hexafluorophosphate counter-ions lead to efficient solar cells. When the wide bandgap dyes are employed, S-shape current–voltage curves are obtained when the conductive polymer PEDOT:PSS is used as hole transport layer. Substitution of PEDOT:PSS with MoO_3 leads to cells with more rectangular current–voltage curves and high fill factors. Additionally, the cells using the MoO_3 layer for hole extraction lead to high open circuit voltages of 0.9 V. The performance of the cells employing the lower bandgap dye is independent on the type of hole transport layer employed. Using this approach, bilayer solar cells are obtained with power efficiencies ranging from 1.8 to 2.9% depending on the particular dye employed. These are impressive numbers for bilayer solar cells that are partially solution processed in ambient conditions.

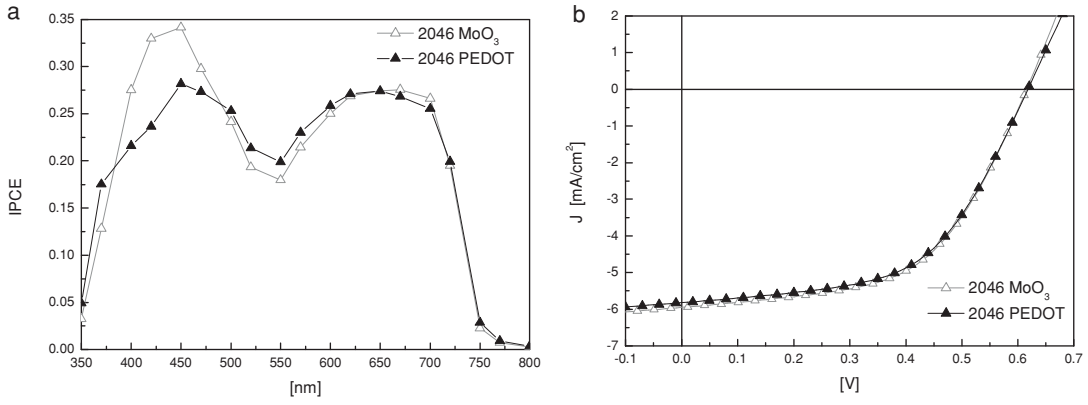

Figure 7. Left, IPCE of the solar cells based on dye **2108** with a PEDOT:PSS (full triangles) or a MoO_3 (open triangles) anode. Right, current density vs voltage for these two devices.

4. Experimental Section

Pre-patterned ITO-covered glass substrates (www.naranjosubstrates.com) where first pre-cleaned using a standard procedure involving a 5 min ultrasonication in detergent, deionized water and isopropanol respectively. UV-ozone treatment was applied for 15 min, after which the samples were immediately transferred in to the metal evaporator. 30nm layers of MoO_3 (ALDRICH) were there evaporated at 0.1 nm/s rate at 2×10^{-6} mbar. The thickness of molybdenum was both checked by profilometer and absorption spectra. In case of the samples without MoO_3 layer, 70nm of PEDOT:PSS (Clevios AI4083, from Hereaus) was spin-coated instead. The PEDOT:PSS was dried by 10 min annealing at 150°C in ambient atmosphere. Cyanine dyes, purchased from Few Chemicals were used as received and were spin coated (1000 rpm) from a chlorobenzene solution (7 mg/ml) in ambient atmosphere resulting in a layer thicknesses of around 30nm. After spin coating of the dye, the substrates were transferred to a nitrogen filled glove box (1 ppm O_2 and <0.1 ppm H_2O) for further processing. 30 nm layer of C_{60} (ALDRICH) and 10 nm of BCP (LUMTEC) were thermally evaporated in a molecular evaporator (7×10^{-7} mbar) followed by thermal evaporation of 5 nm barium and 70 nm silver in a separate vacuum system (2×10^{-6} mbar). Solar cells (with different active areas ranging from 9, 15, 35 to 95 mm^2) were illuminated by a white light halogen lamp in combination with interference filters for the EQE and J–V measurements (MiniSun simulator by ECN the Netherlands). An estimation of the short-circuit current density (J_{sc}) under standard test conditions was calculated by convolving the EQE spectrum with the AM1.5G reference spectrum, using the premise of a linear dependence of J_{sc} on light intensity. Current-voltage (J–V) characteristics were measured using a Keithley 2400 source measure unit. All characterisation was done in a nitrogen filled glove box (<0.1 ppm O_2 and <0.1 ppm H_2O) without exposure to ambient atmosphere. The reproducibility of the device performance is good as can be observed from Figure 3 and S1, S2 and S3 (see supporting information).

Supporting Information

Supporting Information is available from the Wiley Online Library or from the author.

Acknowledgements

This work has been supported by the European Union FP7 program (ORION, 229036), the Spanish Ministry of Science and Innovation (MICINN) (MAT2011-24594, CSD2007-00010) and the Generalitat Valenciana (Prometeo/2012/053).

Received: September 24, 2012
Published onlne:

[1] a) G. Dennler, M. Scharber, C. J. Brabec, *Adv. Mater.* **2009**, *21*, 1323; b) P. Heremans, D. Cheyns, B. P. Rand, *Acc. Chem. Res.* **2009**, *42*, 1740; c) M. A. Green, K. Emery, Y. Hishikawa, W. Warta, E. D. Dunlup, *Prog. Photovolt. Res. Appl.* **2012**, *20*, 12; d) G. Li, R. Zhu, Y. Yang, *Nature Photon.* **2012**, *6*, 153.
[2] C. W. Tang, *Appl. Phys. Lett.* **1986**, *48*, 183.
[3] C. Uhrich, D. Wynands, S. Olthof, M. K. Riede, K. Leo, S. Sonntag, B. Maenning, M. Pfeiffer, *J. Appl. Phys.* **2008**, *104*, 43107.
[4] a) F. Meng, K. Chen, H. Tian, L. Zuppiroli, F. Nuesch, *Appl. Phys. Lett.* **2003**, *82*, 3788; b) H. Bürckstümmer, N. M. Kronenberg, M. Gsänger, M. Stolte, K. Meerholz, F. Würthner, *J. Mater. Chem.* **2010**, *20*, 240; b) B. Fan, R. Hany, J. Moser, F. Nuesch, *Org. Electr.* **2008**, *9*, 85; c) X. Ma, J. Hua, W. Wu, Y. Jin, F. Meng, W. Zhan, H. Tian, *Tetrahedron* **2008**, *64*, 345; d) M. Lenes, H. J. Bolink, *ACS Appl. Mater. & Inter.* **2010**, *2*, 3664; e) O. Malinkiewicz, M. Lenes, H. Brine, H. J. Bolink, *RSC Adv.* **2012**, *2*, 3335.
[5] T. H. James, *The Theory of the Photographic Process*, Macmillan, Collier Macmillan, New York, London **1977**.
[6] R. Hany, B. Fan, F. Araujo de Castro, J. Heier, W. Kylberg, F. Nuesch, *Prog. Photovolt. Res. Appl.* **2011**, *19*, 851.
[7] a) B. Fan, F. A. Castro, J. Heier, R. Hany, F. Nuesch, *Org. Electr.* **2010**, *11*, 583; b) B. Fan, F. Araujo de Castro, B. T. Chu, J. Heier, D. Opris, R. Hany, F. Nuesch, *J. Mater. Chem* **2010**, *20*, 2952.
[8] a) V. Shrotriya, G. Li, Y. Yao, C.-W. Chu, Y. Yang, *Appl. Phys. Lett.* **2006**, *88*, 073508; b) S. Tokito, K. Noda, Y. Taga, *J. Phys. D: Appl. Phys.* **1996**, *29*; c) T. Matsushima, Y. Kinoshita, H. Murata, *Appl. Phys. Lett.* **2007**, *91*, 253504; d) H. Kanno, R. J. Holmes, Y. Sun, S. Kena-Cohen, S. R. Forrest, *Adv. Funct. Mater.* **2006**, *18*, 339; e) J. Meyer, A. Shu, M. Kröger, A. Kahn, *Appl. Phys. Lett.* **2010**, *96*, 133308; f) M. Sessolo, H. J. Bolink, *Adv. Mater.* **2011**, *23*, 1829.
[9] a) S. R. Hammond, J. Meyer, N. E. Widjonarko, P. F. Ndione, A. K. Sigdel, A. Garcia, A. Meidaner, M. T. Lloyd, A. Kahn, D. S. Ginley, J. J. Berry, D. C. Olson, *J. Mater. Chem 22*, 3249; b) K. Zilberberg, H. Gharbi, A. Behrendt, S. Trost, T. Riedl, *ACS Appl. Mater. Interfaces* **2012**, *4*, 1164; c) C. Girotto, E. Voroshazi, D. Cheyns, P. Heremans, B. P. Rand, *ACS Appl. Mater. Interfaces* **2011**, *3*, 3244.
[10] H. Gommans, B. Verreet, B. P. Rand, T. Muller, J. Poortmans, P. Heremans, J. Genoe, *Adv. Funct. Mater.* **2008**, *18*, 3686.
[11] H. Benmansour, F. A. Castro, M. Nagel, J. Heier, R. Hany, F. Nuesch, *Chimia* **2007**, *61*, 787.

ChemComm

RSC Publishing

COMMUNICATION

View Article Online
View Journal | View Issue

Cite this: *Chem. Commun.*, 2013, **49**, 5942

Received 15th April 2013,
Accepted 14th May 2013

DOI: 10.1039/c3cc42776e

www.rsc.org/chemcomm

Enantioselective self-assembly of antiferromagnetic hexacopper(II) wheels with chiral amino acid oxamates†

Thais Grancha,[a] Jesús Ferrando-Soria,‡[a] Joan Cano,[a] Francesc Lloret,[a] Miguel Julve,[a] Giovanni De Munno,*[b] Donatella Armentano[b] and Emilio Pardo*[a]

The Cu^{2+}-mediated self-assembly of oxamato-based ligands derived from either the (*S*)- or (*R*)-enantiomers of the amino acid valine leads to the formation of two antiferromagnetically coupled homochiral anionic hexacopper(II) wheels in the presence of templating tetramethylammonium countercations.

Supramolecular coordination chemistry (termed metallosupramolecular chemistry) provides tools for the synthesis of a large variety of polynuclear metallacyclic complexes which are based on metal–ligand coordinative interactions.[1] The rational introduction of additional physicochemical functionalities into this class of metallosupramolecular systems has been studied in recent years.[2] In particular, chiroptical and/or magnetic properties are of great interest due to the supramolecular chiral recognition processes that take place in enantioselective catalysis and biological transformations but also for the development of new classes of chiroptical probes and magnetic sensors.[3]

Among this type of metallacyclic complex, self-assembling polymetallic wheels are very attractive motifs because they can exhibit interesting functionalities with application in different fields such as bioinorganic chemistry and molecular magnetism.[4] So, Winpenny *et al.* have proposed antiferromagnetically coupled heterobimetallic $Cr^{III}_7M^{II}$ wheels (M = Mn, Fe, Co, Ni and Cd) as candidates for high-density magnetic memories or quantum computing devices.[5] Although some examples of chiral magnetic wheels have been recently reported,[6] they remain a challenge from a synthetic point of view.

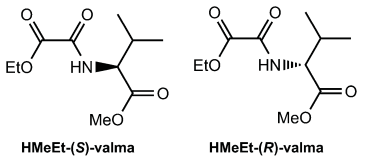

As part of our recent work on chiral magnetic materials,[7] we have undertaken exploratory studies on the coordination chemistry of paramagnetic 3d metal ions with a new family of enantiopure, oxamato-based ligands derived from natural amino acids. Herein we report the synthesis and structural characterization, spectroscopic and magnetic properties of two new examples of homochiral hexanuclear copper(II) wheels of general formula $(Me_4N)_6[Cu^{II}_6L_6]\cdot 7H_2O$ [L = (*S*)-valma ($\mathbf{1^S}$) and (*R*)-valma ($\mathbf{1^R}$)]. As far as we know, $\mathbf{1^S}$ and $\mathbf{1^R}$ are the first examples of countercation-templated enantioselective self-assembly of two antiferromagnetically coupled metal wheels.

The methyl ester derivatives of the (*S*)- and (*R*)-*N*-(ethyl oxoacetate)valine, HMeEt-(*S*)-valma and HMeEt-(*R*)-valma, were easily obtained in an enantiopure form from the reaction of the commercially available methyl ester derivatives of the corresponding (*S*)- and (*R*)-enantiomers of the valine amino acid with ethyl oxalyl chloride. The hexacopper(II) wheel complexes $\mathbf{1^S}$ and $\mathbf{1^R}$ were then prepared in very good yields from the reaction of stoichiometric amounts of $CuCl_2\cdot 6H_2O$ and the corresponding enantiopure proligands (1 : 1 metal to ligand molar ratio) in a Me_4NOH methanolic solution. X-ray quality hexagonal prisms of $\mathbf{1^S}$ and $\mathbf{1^R}$ were obtained by slow evaporation of H_2O–MeOH (1 : 1 v/v) mixtures. They both crystallize in the same chiral space group *P*6(3) of the hexagonal system, their absolute configuration being reliably assigned.

The structures of $\mathbf{1^S}$ and $\mathbf{1^R}$ consist of cyclic oxamato-bridged hexacopper(II) complex anions, $[Cu^{II}_6L_6]^{6-}$ [L = (*S*)-valma ($\mathbf{1^S}$) and (*R*)-valma ($\mathbf{1^R}$)] (Fig. 1), together with charge-balancing tetramethylammonium countercations and free water molecules (Fig. 2 and Fig. S1–S5, ESI†). The intramolecular Cu(1)···Cu(2) and Cu(1)···Cu(2)^{I} distances across the oxamato bridge are 5.391(1) ($\mathbf{1^S}$)/5.228(1) ($\mathbf{1^R}$) and 5.275(1) ($\mathbf{1^S}$)/5.343(1) Å ($\mathbf{1^R}$), respectively.

The two crystallography independent Cu(1) and Cu(2) atoms of $\mathbf{1^S}$ and $\mathbf{1^R}$ have a somewhat distorted five-coordinate square pyramidal environment ($CuNO_4$) with rather similar average bond lengths and

[a] *Departament de Química Inorgánica, Instituto de Ciencia Molecular (ICMOL), Universitat de València, 46980 Paterna, València, Spain. E-mail: Emilio.Pardo@uv.es; Fax: +34 3543273; Tel: +34 3544442*

[b] *Dipartimento di Chimica e Tecnologie Chimiche, Universitá della Calabria, 87036, Cosenza, Italy. E-mail: demunno@unical.it*

† Electronic supplementary information (ESI) available: Synthesis and selected data for the proligands and complexes $\mathbf{1^S}$ and $\mathbf{1^R}$, crystallographic details of $\mathbf{1^S}$ and $\mathbf{1^R}$ (Fig. S1–S9). CCDC 931371 ($\mathbf{1^R}$) and 931372 ($\mathbf{1^S}$). For ESI and crystallographic data in CIF or other electronic format see DOI: 10.1039/c3cc42776e

‡ Present address: Department of Chemistry, Texas A&M University College Station, TX 77843, USA.

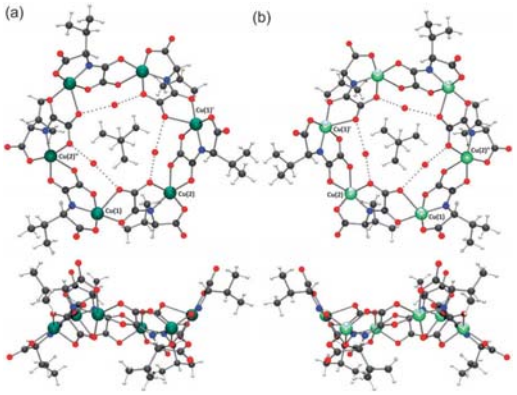

Fig. 1 Top and side views of the anionic cyclic hexacopper(II) units of $\mathbf{1^S}$ (a) and $\mathbf{1^R}$ (b) with the metal atom numbering scheme (symmetry code: I = $-y, x-y, z$; II = $-x+y, -x, z$). The metal atoms of A or C chirality are shown in deep and pale green colours, respectively.

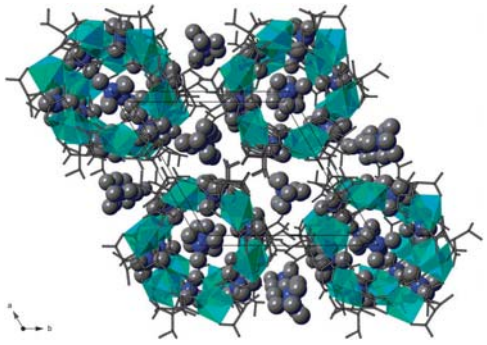

Fig. 2 Crystal packing view of $\mathbf{1^S}$ along the crystallographic *c* axis. The ligand backbones are shown as grey sticks whereas the copper atoms of C chirality are depicted as deep green polyhedra. The carbon and nitrogen atoms of the tetramethylammonium countercations are shown as spheres with an arbitrary radius. The free water molecules have been omitted for clarity.

interbond bite angles (Fig. S1, ESI†). Interestingly, both metal ions in $\mathbf{1^S}$ and $\mathbf{1^R}$ are present as one single enantiomer, A ($\mathbf{1^S}$) or C ($\mathbf{1^R}$),[8] thus confirming the transmission of the chiral properties from the enantiopure ligand counterpart to the coordinated metal center. Each homochiral hexanuclear ring [AAAAAA-Cu^{II}_6 ($\mathbf{1^S}$) and CCCCCC-Cu^{II}_6 ($\mathbf{1^R}$)] has then opposite metal chirality, which results from the alternating tridentate–bidentate bridging mode of the disymmetric (*S*)- and (*R*)-valma^{3-} ligands (Fig. 1a and b, top). Overall, they both have an open calix-type molecular shape which is reminiscent of that found for the well-known α-cyclodextrin (Fig. 1).[9] However, the alternating up and down, outward and inward disposition of the six iso-propyl groups from the valine residues results in an approximate S_6 molecular symmetry that differs from that of the C_6-symmetric α-cyclodextrin molecule. That being so, the anionic hexacopper(II) wheels of $\mathbf{1^S}$ and $\mathbf{1^R}$ are not exactly planar but they exhibit an overall chair conformation (Fig. 1a and b, bottom).

In the crystal lattice of $\mathbf{1^S}$ and $\mathbf{1^R}$, there is a staggered parallel alignment of the anionic hexacopper(II) wheels along the crystallographic *c* axis (Fig. 2 and Fig. S3, ESI†). This leads to a pseudo-helical supramolecular motif designed by columnar arrays of Cu^{II}_6 rings defining a small circular channel with a diameter of *ca.* 1.0 nm which is occupied by some of the Me_4N^+ cations acting as guests (Fig. S4, ESI†). There are weak host–guest hydrophobic interactions among the methyl groups from the iso-propyl residues and the Me_4N^+ cations located in the center of the channel [C···C = 4.00(1) Å]. The remaining Me_4N^+ cations are differently located between two adjacent Cu^{II}_6 rings along each column or in the void space between three neighbouring columns (Fig. 2 and Fig. S3, ESI†). Crystallisation water molecules are linked to the wall of the wheel through hydrogen bonds involving the carboxylate-oxygen atoms of the oxamato bridge [O···O = 2.95] (Fig. 1a and b, top). This leads to a basket-like supramolecular cavity where the Me_4N^+ guest cations reside (Fig. S3, ESI†). The analysis of the crystal packing features of $\mathbf{1^S}$ and $\mathbf{1^R}$ suggests that the Me_4N^+ cations play a key role in the self-assembly process that leads to the wheel formation in the solid state.[4h]

The direct current (dc) magnetic properties of $\mathbf{1^S}$ and $\mathbf{1^R}$ in the form of the χ_M and $\chi_M T$ *versus* *T* plots (χ_M being the dc molar magnetic susceptibility per hexanuclear unit) are almost identical (Fig. 3 and Fig. S6, ESI†). The $\chi_M T$ values of 2.12 ($\mathbf{1^S}$) and 2.09 cm^3 mol^{-1} K ($\mathbf{1^R}$) at room temperature are below that expected for six non-interacting Cu^{II} ions [$\chi_M T = 6 \times (N\beta^2 g_{Cu}{}^2/3k_B)S_{Cu}(S_{Cu}+1) = 2.40$ cm^3 mol^{-1} K with $S_{Cu} = 1/2$ and $g_{Cu} = 2.1$]. Upon cooling, $\chi_M T$ continuously decreases and it vanishes at 5.0 K. This magnetic behaviour is characteristic of moderately strong antiferromagnetic coupling within the Cu^{II}_6 rings. In fact, χ_M exhibits a maximum at 60 K for both $\mathbf{1^S}$ and $\mathbf{1^R}$ (inset of Fig. 3 and Fig. S6, ESI†), which unambiguously supports the occurrence of a ground singlet spin state ($S = 0$) resulting from the intramolecular antiferromagnetic coupling between the six copper(II) ions through the oxamato bridges.

The analysis of the magnetic susceptibility data of $\mathbf{1^S}$ and $\mathbf{1^R}$ was carried out through the appropriate spin hamiltonian for a hexanuclear copper(II) ring [$\boldsymbol{H} = -J\sum_{i=1-5}(\boldsymbol{S}_i\boldsymbol{S}_{i+1} + \boldsymbol{S}_6\boldsymbol{S}_1) + g_i\beta H\left(\sum_{i=1-6}\boldsymbol{S}_i\right)$ with $S_i = S_{Cu} = 1/2$ and $g_i = g_{Cu}$ for $i = 1$–6]. The least-squares fit of the experimental data by using the VPMAG program[10] gave $J = -64.2$ ($\mathbf{1^S}$)/-67.6 cm^{-1} ($\mathbf{1^R}$), $g_{Cu} = 2.11$ ($\mathbf{1^S}$)/2.11 ($\mathbf{1^R}$), and $R = 4 \times 10^{-6}$ ($\mathbf{1^S}$)/1.8×10^{-5} ($\mathbf{1^R}$), where *J* is the average magnetic coupling parameter, g_{Cu} is the Landé factor of the Cu^{II} ions and *R* is the agreement factor defined as

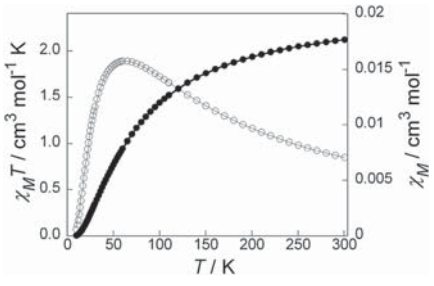

Fig. 3 Temperature dependence of χ_M (○) and $\chi_M T$ (●) for $\mathbf{1^S}$ under applied dc fields of 100 G ($T < 30$ K) and 10 kG ($T \geq 30$ K). The solid lines correspond to the best-fit curves (see the text).

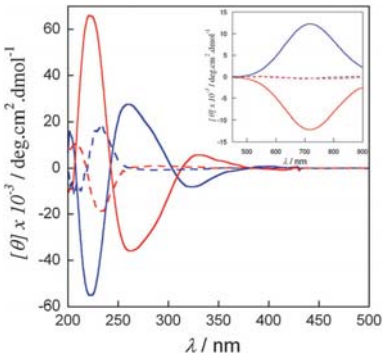

Fig. 4 CD spectra of $\mathbf{1^S}$ (red —) and $\mathbf{1^R}$ (blue —) in H_2O ([$\mathbf{1^S}$] = [$\mathbf{1^R}$] = 10^{-5} mol L^{-1}) compared to those of HMeEt-(*S*)-valma (red ···) and HMeEt-(*R*)-valma (blue ···) in MeOH ([HMeEt-(*S*)-valma] = [HMeEt-(*R*)-valma] = 10^{-4} mol L^{-1}). The inset shows the CD spectra in the visible region.

$\sum\left[(\chi_M T)_{exp}-(\chi_M T)_{calcd}\right]^2 \Big/ \sum\left[(\chi_M T)_{exp}\right]^2$ (solid lines in Fig. 3 and Fig. S6, ESI†).

In order to verify the stability and robustness of the hexacopper(II) ring in solution, the dc magnetic properties of a frozen methanolic solution of $\mathbf{1^S}$ were measured in the low temperature range. χ_M (the molar magnetic susceptibility) and $\chi_M T$ *vs.* *T* plots (Fig. S7, ESI†) show the same qualitative behaviour observed for the polycrystalline powdered sample of $\mathbf{1^S}$, with a maximum of χ_M at *ca.* 80 K (inset of Fig. S7, ESI†). Moreover, there is no evidence of paramagnetic monomeric Cu^{II} impurities at low temperatures resulting from a putative dissociation process, thus confirming the high stability of $\mathbf{1^S}$ in solution. This is further confirmed by both Q-band EPR spectra and circular dichroism (CD) measurements in solution.

Hence, the Q-band EPR spectra of $\mathbf{1^S}$ and $\mathbf{1^R}$ in frozen methanolic solutions are identical to those of their polycrystalline powdered samples (Fig. S8 and S9, ESI†). They both show an isotropic signal centred at g = 2.15 (H = 11 400 G for ν = 34.277 GHz) at 60 K, which would correspond to the spin-allowed $\Delta M_S = \pm 1$ transitions from the low-lying triplet spin states (S = 1) located above the ground singlet spin state (S = 0).

On the other hand, the CD solution spectra of $\mathbf{1^S}$ and $\mathbf{1^R}$ and the corresponding HMeEt-(*S*)-valma and HMeEt-(*R*)-valma proligands are almost mirror images of each other (Fig. 4). In fact, they exhibit maximum positive and negative Cotton effects at the same location with almost identical intensities. The intense UV bands centred at 225 and 300 nm for both $\mathbf{1^S}$ and $\mathbf{1^R}$ are commonly assigned to intraligand (IL) and metal-to-ligand (ML) charge-transfer transitions, respectively. The weak visible band at 700 nm for both $\mathbf{1^S}$ and $\mathbf{1^R}$, which does not appear in the CD spectra of the proligands, is the typical d–d transition of the Cu^{II} ions (inset of Fig. 4). The positive and negative Cotton effects of this visible band obey the induction of chirality at the metal centres by the enantiopure coordinated ligand within the anionic hexacopper(II) wheels of $\mathbf{1^S}$ and $\mathbf{1^R}$.

In conclusion, a unique pair of homochiral, antiferromagnetically coupled hexacopper(II) wheels has been successfully prepared through a ligand design strategy allowing the transfer of the chiral information from each enantiopure amino acid-functionalized oxamate ligand (*chiragen*-type ligand) to the stereochemistries of the Cu^{II} metal centres. Current efforts are devoted firstly to investigating the putative templating role of the organic tetraalkylammonium countercations in the self-assembly process of this metalloorganic analogue of α-cyclodextrin to obtain larger polynuclear wheels for potential applications in magnetic sensing of small guest molecules, and secondly to exploring the coordination ability of the six free carbonyl groups from the valine residues to yield chiral Metal–Organic Frameworks (MOFs) with possible application in gas storage and separation.

This work was supported by the MICINN (Spain) (Project CTQ2010-15364), the University of Valencia (Project UV-INV-AE11-38904), the Generalitat Valenciana (Spain) (Projects PROMETEO/2009/108, GV/2012/051 and ISIC/2012/002) and the MiUR (Italy) through the Centro di Eccellenza CEMIF.CAL (Grant CLAB01TYEF). T. G. thanks the Universitat de Valéncia for a predoctoral contract. J. F.-S. and E. P. thank the MICINN for contracts.

Notes and references

1 S. Lenninger, B. Olenyuk and J. Stang, *Chem. Rev.*, 2000, **100**, 853.
2 (*a*) M. Fujita, *Chem. Soc. Rev.*, 1998, **27**, 417; (*b*) J. M. Lehn, *Angew. Chem., Int. Ed.*, 2004, **43**, 3644; (*c*) L. K. Thompson and O. Waldman, *Coord. Chem. Rev.*, 2005, **249**, 2677; (*d*) D. Fiedler, D. H. Leung, R. G. Bergman and K. N. Raymond, *Acc. Chem. Res.*, 2005, **38**, 351; (*e*) G. A. Timco, T. B. Faust, F. Tuna and R. E. P. Winpenny, *Chem. Soc. Rev.*, 2011, **40**, 3067.
3 (*a*) C. P. Montgomery, B. S. Murray, E. J. New, R. Pal and D. Parker, *Acc. Chem. Res.*, 2009, **42**, 925; (*b*) G. Muller, *Dalton Trans.*, 2009, 9692; (*c*) J. Crassous, *Chem. Soc. Rev.*, 2009, **38**, 830.
4 (*a*) K. L. Taft, C. D. Delfs, G. C. Papaefthymiou, S. Foner, D. Gatteschi and S. J. Lippard, *J. Am. Chem. Soc.*, 1994, **116**, 823; (*b*) A. Caneschi, A. Cornia, A. C. Fabretti, S. Foner, D. Gatteschi, R. Grandi and L. Schenetti, *Chem.–Eur. J.*, 1996, **2**, 1379; (*c*) M. Murugesu, K. A. Abboud and G. Christou, *Dalton Trans.*, 2003, 4552; (*d*) E. M. Rumberger, L. N. Zakharov, A. L. Rheingold and D. N. Hendrickson, *Inorg. Chem.*, 2004, **43**, 6531; (*e*) R. W. Saalfrank, T. Nakajima, N. Mooren, A. Scheurer, H. Maid, F. Hampel, C. Trieflinger and J. Daub, *Eur. J. Inorg. Chem.*, 2005, 1149; (*f*) S. Koizumi, M. Nihei, M. Nakano and H. Oshio, *Inorg. Chem.*, 2005, **44**, 1208; (*g*) D. Armentano, T. F. Mastropietro, M. Julve, R. Rossi, P. Rossi and G. De Munno, *J. Am. Chem. Soc.*, 2007, **129**, 2740; (*h*) E. Colacio, H. Aouryaghal, A. J. Mota, J. Cano, R. Sillanpää and A. Rodríguez-Diéguez, *CrystEngComm*, 2009, **11**, 2054.
5 (*a*) F. K. Larsen, E. J. L. McInnes, H. El Mkami, J. Overgaard, S. Piligkos, G. Rajaraman, E. Rentschler, A. A. Smith, G. M. Smith, V. Boote, M. Jennings, G. A. Timco and R. E. P. Winpenny, *Angew. Chem., Int. Ed.*, 2003, **42**, 101; (*b*) M. L. Baker, G. A. Timco, S. Piligkos, J. S. Mathieson, H. Mutka, F. Tuna, P. Kozłowski, M. Antkowiak, T. Guidi, T. Gupta, H. Rath, R. J. Woolfson, G. Kamieniarz, R. G. Pritchard, H. Weihe, L. Cronin, G. Rajaraman, D. Collison, E. J. L. McInnes and R. E. P. Winpenny, *Proc. Natl. Acad. Sci. U. S. A.*, 2012, **109**, 19113.
6 (*a*) Z.-M. Zhang, Y.-G. Li, S. Yao, E.-B. Wang, Y.-H. Wang and R. Clérac, *Angew. Chem., Int. Ed.*, 2009, **48**, 1581; (*b*) J. Fielden, M. Speldrich, C. Besson and P. Kögerler, *Inorg. Chem.*, 2012, **51**, 2734; (*c*) G. Bozoklu, C. Gateau, D. Imbert, J. Pécaut, K. Robeyns, Y. Filinchuk, F. Memon, G. Muller and M. Mazzanti, *J. Am. Chem. Soc.*, 2012, **134**, 8372.
7 (*a*) E. Pardo, C. Train, R. Lescouëzec, Y. Journaux, J. Pasán, C. Ruiz-Pérez, F. S. Delgado, R. Ruiz-García, F. Lloret and C. Paulsen, *Chem. Commun.*, 2010, **46**, 2322; (*b*) J. Ferrando-Soria, D. Cangussu, M. Eslava, Y. Journaux, R. Lescouëzec, M. Julve, F. Lloret, J. Pasán, C. Ruiz-Pérez, E. Lhotel, C. Paulsen and E. Pardo, *Chem.–Eur. J.*, 2011, **17**, 12482.
8 A. von Zelewsky, *Stereochemistry of Coordination Compounds*, Wiley, 1996, p. 68.
9 A. A. Bagabas, M. Frasconi, J. Iehl, B. Hauser, O. K. Farha, J. T. Hupp, K. J. Hartlieb, Y. Y. Botros and J. F. Stoddart, *Inorg. Chem.*, 2013, **52**, 2854, and references therein.
10 J. Cano, *VPMAG package*, University of Valencia, Valencia, Spain, 2003.

CrystEngComm

RSC Publishing

COMMUNICATION

View Article Online
View Journal | View Issue

Cite this: *CrystEngComm*, 2013, **15**, 9312

Received 5th June 2013,
Accepted 8th July 2013

DOI: 10.1039/c3ce41022f

www.rsc.org/crystengcomm

Self-assembly of a chiral three-dimensional manganese(II)–copper(II) coordination polymer with a double helical architecture†

Thais Grancha,[a] Clarisse Tourbillon,‡[a] Jesús Ferrando-Soria,*[b] Miguel Julve,[a] Francesc Lloret,[a] Jorge Pasán,[c] Catalina Ruiz-Pérez,[c] Oscar Fabelo[cd] and Emilio Pardo*[a]

The use of the anionic dicopper(II) complex, $[Cu^{II}(mpba)_2]^{4-}$ [mpba = *N*,*N*′-1,3-phenylenebis(oxamate)], as tetrakis(bidentate) metalloligand toward Mn^{II} ions in the presence of oxalate and the chiral (*S*)-trimethyl-(1-phenylethyl)ammonium cation affords the first example of a mixed oxalato/oxamato-based chiral 3D metal–organic polymer.

The design and synthesis of extended metal–organic polymers (MOPs)[1] has been a subject of intense research during the last decades in supramolecular coordination chemistry and crystal engineering.[2] Due to their large variety of structural motifs and intriguing topologies, MOPs can exhibit a wide range of interesting physical and chemical properties. For instance, a variety of molecule-based magnetic materials[3a] can be obtained when incorporating paramagnetic ions into MOPs with the appropriate organic linker capable of efficiently transmitting the magnetic coupling.[3b] More recently, the incorporation of other physical properties in addition to magnetic ones (chirality,[4a] ferroelectricity,[4b] or proton and electron conduction,[4c,d]) has become relevant in order to obtain the so-called multifunctional magnetic molecular materials (M_4).[4]

An accurate control of the final structure of the MOP is a key point in order to obtain the desired physical properties. However, it is still a challenge from a synthetic point of view because of the many subtle factors that may affect the assembly process of metal ions and organic ligands. This issue is especially true when using the widespread hydro(solvo)thermal reaction conditions. Molecular programmed self-assembling methods[5] show clear advantages over the aforementioned serendipitous self-assembling ones.[1] Yet, ever in that case, a total control of the final structure is almost impossible to be ensured. In particular, some of us have shown recently that the use of preformed oxamato-based dicopper(II) complexes as metalloligands towards first-row transition metals is a straightforward rational preparative route to produce a family of MOPs of varying dimensionality with interesting magnetic as well as adsorption and/or luminescence properties.[6] Even though some examples of M_4 have been reported in this way,[6d–f] all the efforts devoted to the synthesis of chiral oxamato-based 3D MOPs have been unsuccessful so far.

In previous works,[6a–c] the double-stranded dicopper(II) complex $[Cu_2(mpba)_2]^{4-}$ [mpba = *N*,*N*′-1,3-phenylenebis(oxamate)] was used as tetrakis(bidentate) metalloligand towards bis(chelated) M^{2+} ions (M = Mn and Co) to render neutral achiral oxamato-based 1D or 2D MOPs with either "ladderlike" or "brickwall" topologies, respectively. In this communication, we explore a new rational synthetic strategy towards chiral MOPs that is based on the use of the bis(bidentate) oxalate dianion (ox^{2-}) and the templating chiral (*S*)-trimethyl-(1-phenylethyl)ammonium cation $[(S)\text{-}(1\text{-PhEt})Me_3N^+]$ during the self-assembly process of $[Cu^{II}(mpba)_2]^{4-}$ with Mn^{2+} ions (Scheme 1). Herein we report the synthesis, crystal structure, spectroscopic and magnetic properties of the novel compound of formula $[(S)\text{-}(1\text{-PhEt})Me_3N]_2[Mn_2(ox)Cu_2(mpba)_2(H_2O)_2]\cdot 3H_2O$ (**1**). Although a few examples of neutral oxamato-based chiral 1D MOPs have been recently reported by some of us,[7] **1** is the very first example of an anionic mixed oxalato/oxamato-based chiral 3D MOP.

[a] *Departament de Química Inorgànica, Instituto de Ciencia Molecular (ICMOL). Universitat de València, 46980 Paterna, València, Spain. E-mail: Emilio.Pardo@uv.es; Fax: +343543273; Tel: +343544442*
[b] *Department of Chemistry, Texas A&M University College Station, TX 77843, USA. E-mail: jesus.ferrando@chem.tamu.edu*
[c] *Laboratorio de Rayos X y Materiales Moleculares, Depto. de Fisica Fundamental II. Universidad de La Laguna, 38201 Tenerife, Spain*
[d] *Instituto de Ciencia de Materiales de Aragón, CSIC-Universidad de Zaragoza, Zaragoza, 50009, Spain*

† Electronic supplementary information (ESI) available: Preparation and physical characterization data of **1**, additional Table S1 and Fig. S1–S3. Crystallographic refinement details for **1** (Table S1). CCDC 941373 (**1**). For ESI and crystallographic data in CIF or other electronic format see DOI: 10.1039/c3ce41022f

‡ Present address: Département de Chimie, Université de Sherbrooke, Quebec J1K 2R1, Canada.

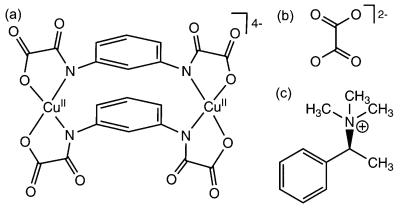

Scheme 1 (a) Dicopper(II) metallacyclophane precursor used as tetrakis(bidentate) metalloligand toward manganese(II) ions. (b) Oxalate dianion. (c) Templating (*S*)-trimethyl-(1-phenylethyl)ammonium cation.

Green rectangular prisms of **1** were grown by slow diffusion in an H-shaped tube of aqueous solutions of $[(S)\text{-(1-PhEt)Me}_3\text{N}]_4[\text{Cu}_2(\text{mpba})_2]\cdot 8\text{H}_2\text{O}$/$[(S)\text{-(1-PhEt)Me}_3\text{N}]_2(\text{ox})$ (2 : 1 molar ratio) and $\text{Mn}(\text{NO}_3)_2\cdot 4\text{H}_2\text{O}$ on each side of the tube at 16 °C (Scheme 1, ESI†). Interestingly, the presence of ox^{2-} in the reaction mixture is crucial to obtain this chiral MOP. Indeed, all our previous attempts to construct chiral MOPs by using only the templating chiral $(S)\text{-(1-PhEt)Me}_3\text{N}^+$ cation as a source of chirality in the absence of ox^{2-} failed. So, the reaction of $[(S)\text{-(1-PhEt)Me}_3\text{N}]_4[\text{Cu}_2(\text{mpba})_2]\cdot 8\text{H}_2\text{O}$ and $\text{Mn}(\text{NO}_3)_2\cdot 4\text{H}_2\text{O}$ yielded the previously reported achiral neutral compound of formula $[\text{Mn}_4\text{Cu}_4(\text{mpba})_4(\text{H}_2\text{O})_9]\cdot 14\text{H}_2\text{O}$.[6c]

The crystal structure of **1** was solved by single-crystal X-ray diffraction using synchrotron radiation at the BM16 beamline at the ESRF.§ It crystallizes in the chiral $P4_12_12$ space group of the tetragonal system and the absolute configuration could be reliably assigned (Table S1, ESI†). Its structure consists of a mixed oxalato/oxamato-based heterobimetallic chiral 3D open-framework with a square/octagonal architecture, which is built up from dicopper(II) complex anions, $[\text{Cu}^{\text{II}}_2(\text{mpba})_2(\text{H}_2\text{O})_2]^{4-}$, and dimanganese(II) complex cations, $[\text{Mn}^{\text{II}}_2(\text{ox})]^{2+}$, together with $(S)\text{-(1-PhEt)Me}_3\text{N}^+$ countercations and crystallisation water molecules (Fig. 1, 2 and S1, ESI†). The topology found is unprecedented and consists of a binodal 3,4-connected

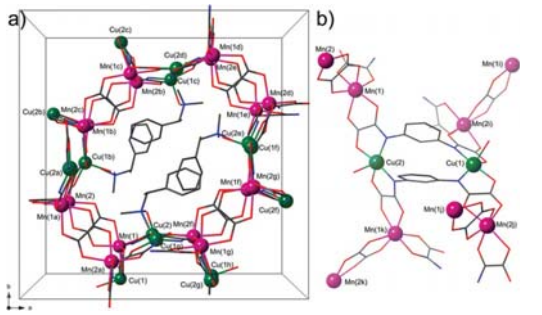

Fig. 1 (a) Perspective view of a unit cell of **1** with the metal atom labelling showing the filling of the octagonal pores by the countercations. (b) View of a fragment of **1** with the metal atom labeling [symmetry code: (a) = *x*, *y*, −*z* + 1/4; (b) = −*x* + 1/2, *y* + 1/2, −*z* + 1/4; (c) = *x* + 1/2, −*y* + 1/2, *z* + 1/4; (d) = −*x* + 1, −*y* + 1, *z* + 1/2; (e) = −*x* + 1, −*y* + 1, −*z* + 1/2; (f) = *x* + 1/2, −*y* + 1/2, −*z* + 3/4; (g) = −*x* + 1/2, *y* + 1/2, *z* + 3/4; (h) = −*x* + 1, −*y*, *z* + 1/2; (i) = −*x* + 1/2, *y* − 1/2, −*z* + 1/4; (j) = *x*, *y*, −*z*; (k) = −*x* + 1/2, *y* + 1/2, *z* − 1/4].

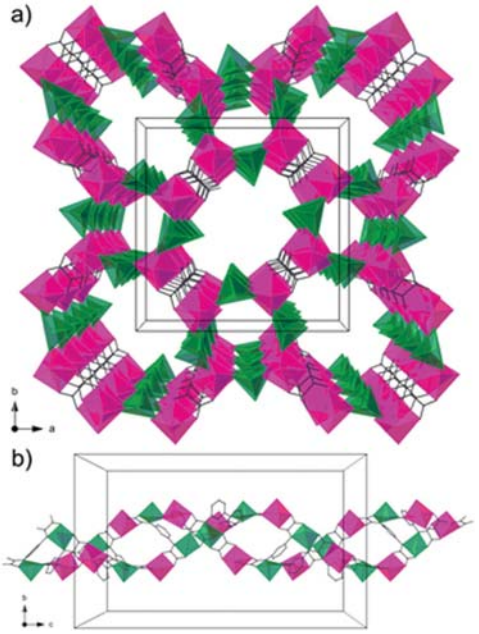

Fig. 2 (a) Perspective view of the anionic 3D network of **1** along the crystallographic *c* axis. (b) View of a fragment of the double helical chain motif of **1** along the crystallographic *c* axis. Metal and ligand atoms are represented by polyhedra and sticks, respectively (Cu, green; Mn, purple). Hydrogen atoms, countercations and crystallization water molecules are omitted for clarity.

$[(4.6.8)_2(4^2.6.8^2.10)]$-net considering the dicopper(II) $[\text{Cu}^{\text{II}}_2(\text{mpba})_2(\text{H}_2\text{O})_2]^{4-}$ units and the manganese(II) ions as four- and three-fold nodes, respectively.[8]

The Cu(1) and Cu(2) atoms are located at the middle of the edges of each square. They adopt a trigonally distorted square pyramidal geometry, $\text{Cu}_2\text{N}_2\text{O}_2\text{O}_w$, formed by two amidate nitrogen and two carboxylate oxygen atoms from the oxamato groups in the equatorial plane and an axially coordinated water molecule [Cu–N = 1.977(5)–1.988(4) Å, Cu–O = 1.971(4)–2.039(4) Å, and Cu–O_w = 2.229(5)–2.302(5) Å] (Fig. 1b and S2, ESI†). The values of the trigonality parameter (τ) at Cu(1) and Cu(2) are 0.41 and 0.31 respectively, reflecting thus a large distortion of the square pyramidal metal environment towards trigonal bipyramidal, so-called Berry pseudorotation (τ = 0 and 1 for ideal square pyramid and trigonal bipyramid, respectively).[9a]

The tris(chelated) Mn(1) and Mn(2) atoms have the same absolute configuration (Λ) and they occupy the corners of each square. They exhibit a trigonally distorted octahedral geometry, MnO_6, built by six carbonyl oxygen atoms from the two oxamato groups and the oxalate group [Mn–O = 2.128(4)–2.214(4) Å] (Fig. S2, ESI†). The values of the trigonal twist angle (ϕ) at Mn(1) and Mn(2) are 58.4(1)° and 45.3(2)° respectively, while the average values of the compression ratio (s/h) are 1.31(1) and 1.36(1), respectively (ϕ = 60° and s/h = 1.22 for an ideal octahedron).[9b]

The anionic 3D network of **1** can be alternately described as an extended array of neutral oxamato-bridged manganese(II)–copper(II) double helical chains running parallel to the crystallographic *c* axis (Fig. 2b and S3, ESI†), which are further interconnected by the oxalate ligands acting as bridges between two manganese(II) ions of the neighbouring double helical chains (Fig. 2). Within each double helix, the pair of $Mn^{II}Cu^{II}$ chains related by a 4_1 axis are interconnected through the two *m*-phenylenediamidate bridges between the Cu^{II} ions, which would act as "bridge tights" (Fig. 2b). The shape of these right-handed double-stranded helices is reminiscent of that found for the well-known A-DNA double helix, where the two *m*-phenylene spacers stack each other in a similar way to that observed for the nucleobases in the DNA double helix. The shortest values of the intrachain Cu···Cu and Cu···Mn distances are 7.0046(13) and 5.4107(12) Å, respectively.

Overall, this situation leads to a bimodal pore size distribution along the crystallographic *c* axis (Fig. 2a), with small square and large octagonal pores of approximate dimensions 0.70 × 0.70 nm and 1.75 × 1.75 nm respectively, defined as the distances between directly opposed manganese atoms of each polygon, which are occupied by counterbalancing (*S*)-trimethyl-(1-phenylethyl)ammonium cations and both coordinated and free water molecules (Fig. S1, ESI†).

The magnetic properties of **1** in the form of the $\chi_M T$ *vs. T* plot (χ_M being the molar magnetic susceptibility per $Cu^{II}_2Mn^{II}_2$ unit) are shown in Fig. 3. At room temperature, the $\chi_M T$ value of 8.97 cm^3 K mol^{-1} for **1** is slightly lower than that expected for the sum of two square pyramidal Cu^{II} ions and two octahedral Mn^{II} ions ($\chi_M T$ = 9.54 cm^3 mol^{-1} K with g_{Mn} = 2.0, g_{Cu} = 2.1, S_{Mn} = 5/2 and S_{Cu} = 1/2). Upon cooling, $\chi_M T$ decreases and it attains a rounded minimum at around 80 K (inset of Fig. 3). Then, $\chi_M T$ increases to reach a sharp maximum at about 18.4 K with $\chi_M T$ = 9.05 cm^3 K mol^{-1}, and finally decreases abruptly to a $\chi_M T$ value of 2.08 cm^3 K mol^{-1} at 2.0 K (Fig. 3). The presence of the minimum of $\chi_M T$ is characteristic of an overall ferrimagnetic behaviour resulting from the strong antiferromagnetic interactions between the Mn^{II} and Cu^{II} ions through the oxamato bridge, as previously observed in similar oxamato-bridged manganese(II)–copper(II) chains.[7b] Finally, the abrupt decrease of $\chi_M T$ below the maximum is due to the moderately strong antiferromagnetic interaction between the Mn^{II} ions of neighbouring chains through the oxalate bridge, which becomes dominant over the weak ferromagnetic interaction between the Cu^{II} ions through the double *m*-phenylene bridge at low temperatures.

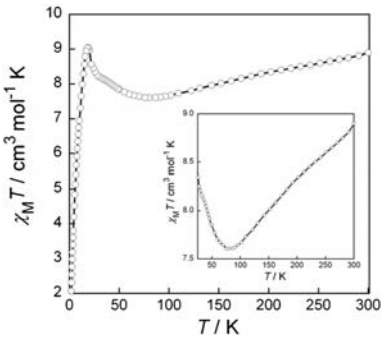

Fig. 3 Temperature dependence of $\chi_M T$ for **1** (○) under an applied magnetic field of 1 T ($T \geq 50$ K) and 100 G ($T < 50$ K). The inset shows a detail of the minimum of $\chi_M T$. The solid lines are only guides for the eye.

In conclusion, the use of the anionic dicopper(II) complex, $[Cu^{II}(mpba)_2]^{4-}$, as metalloligand toward Mn^{II} ions in the presence of the bis(bidentate) oxalate dianion and the chiral (*S*)-trimethyl-(1-phenylethyl)ammonium cation yielded the very first example of an anionic mixed oxalato/oxamato-based chiral 3D MOP. Indeed, a template effect of the chiral cation takes place for the construction of this anionic 3D MOP because attempts to construct other chiral MOPs by using chiral cations as a source of chirality in the absence of ox^{2-} were unsuccessful. Future work will focus on the (i) post-modification of this chiral MOP by replacing the large (*S*)-(1-PhEt)Me_3N^+ cations by smaller alkaline ones and (ii) the substitution of the small ox^{2-} bridging ligand by larger bis(bidentate) mononuclear bis(oxamato)copper(II) anionic complexes to get the first example of chiral porous magnet of the bimetallic oxamate family with additional new interesting features (gas storage, chiral discrimination, long-range ferromagnetic ordering, *etc.*).

This work was supported by the MICINN (Spain) (Project CTQ2010-15364), the University of Valencia (Project UV-INV-AE11-38904) and the Generalitat Valenciana (Spain) (Projects PROMETEO/2009/108, GV/2012/051 and ISIC/2012/002). T. G. thanks the Universitat de València for a predoctoral contract. J. F.-S. and E. P. thank the MICINN for contracts. J. P. thanks 'La Factoría' Consolider Project CSD2006-00015 for a contract.

Notes and references

§ Crystal data for $C_{44}H_{58}N_6O_{24}Cu_2Mn_2$ (**1**), Fw = 1291.92 g mol^{-1}, *a* = 20.467(3) Å, *c* = 34.344(7) Å, *V* = 14 387(4) $Å^3$, tetragonal, $P4_12_12$, *Z* = 8, λ = 0.7379 Å, *T* = 100(2) K, 127 126 reflections measured, 15 896 unique and 14 262 with $I > 2\sigma(I)$, R_{int} = 0.1041, *R* (all) = 0.0842, w*R* (all) = 0.2274.

1 (*a*) S. R. Batten and R. Robson, *Angew. Chem., Int. Ed.*, 1998, **37**, 1460; (*b*) C. Janiak, *Dalton Trans.*, 2003, 2781; (*c*) G. Férey, *Chem. Soc. Rev.*, 2008, **37**, 191; (*d*) J. R. Long and O. M. Yaghi, *Chem. Soc. Rev.*, 2009, **38**, 1213 and references therein.

2 (*a*) J. M. Lehn, *Supramolecular Chemistry: Concepts and Perspectives*, VCH, Weinheim, 1995; (*b*) J. W. Steed and J. L. Atwood, *Supramolecular Chemistry*, Wiley and Sons, New York, 2000.

3 (*a*) O. Kahn, *Adv. Inorg. Chem.*, 1995, **43**, 179; (*b*) H. O. Stumpf, L. Ouahab, Y. Pei, D. Grandjean and O. Kahn, *Science*, 1993, **261**, 447.

4 (*a*) C. Train, R. Gheorghe, V. Krstic, L. M. Chamoreau, N. S. Ovanesyan, L. J. A. Rikken, M. Gruselle and M. Verdaguer, *Nat. Mater.*, 2008, **7**, 729; (*b*) E. Pardo, C. Train, H. Liu, L.-M. Chamoreau, B. Dkhil, K. Boubekeur, F. Lloret, K. Nakatani, H. Tokoro, S. Ohkoshi and

M. Verdaguer, *Angew. Chem., Int. Ed.*, 2012, **51**, 8356; (*c*) E. Pardo, C. Train, G. Gontard, K. Boubekeur, O. Fabelo, H. Liu, B. Dkhil, F. Lloret, K. Nakagawa, H. Tokoro, S. I. Ohkoshi and M. Verdaguer, *J. Am. Chem. Soc.*, 2011, **133**, 15328; (*d*) E. Coronado, J. R. Galán-Mascarós, C. J. Gomez-García and V. Laukhin, *Nature*, 2000, **408**, 447.

5 (*a*) M. Pilkington, M. Gross, P. Franz, M. Biner, S. Decurtins, H. Stoeckli-Evans and A. Neels, *J. Solid State Chem.*, 2001, **159**, 262; (*b*) M. Pilkington and S. Decurtins, in *Comprehensive Coordination Chemistry II: From Biology to Nanotechnology*, ed. J. A. McCleverty and T. J. Meyer, Elsevier, Oxford, USA, 2004, vol. 7, p. 177.

6 (*a*) C. L. M. Pereira, E. F. Pedroso, H. O. Stumpf, M. A. Novak, L. Ricard, R. Ruiz-García, E. Rivière and Y. Journaux, *Angew. Chem., Int. Ed.*, 2004, **43**, 956; (*b*) J. Ferrando-Soria, J. Pasán, C. Ruiz-Pérez, Y. Journaux, M. Julve, F. Lloret, J. Cano and E. Pardo, *Inorg. Chem.*, 2011, **50**, 8694; (*c*) J. Ferrando-Soria, T. Grancha, J. Pasán, C. Ruiz-Pérez, L. Cañadillas-Delgado, Y. Journaux, M. Julve, J. Cano, F. Lloret and E. Pardo, *Inorg. Chem.*, 2012, **51**, 7019; (*d*) J. Ferrando-Soria, R. Ruiz-García, J. Cano, S.-E. Stiriba, J. Vallejo, I. Castro, M. Julve, F. Lloret, P. Amorós, J. Pasán, C. Ruiz-Pérez, Y. Journaux and E. Pardo, *Chem.–Eur. J.*, 2012, **18**, 1608; (*e*) J. Ferrando-Soria, P. Serra-Crespo, M. de Lange, J. Gascon, F. Kapteijn, M. Julve, J. Cano, F. Lloret, J. Pasán, C. Ruiz-Pérez, Y. Journaux and E. Pardo, *J. Am. Chem. Soc.*, 2012, **134**, 15301; (*f*) J. Ferrando-Soria, H. Khajavi, P. Serra-Crespo, J. Gascon, F. Kapteijn, M. Julve, F. Lloret, C. Ruiz-Pérez, Y. Journaux and E. Pardo, *Adv. Mater.*, 2012, **24**, 5625.

7 (*a*) E. Pardo, C. Train, R. Lescouëzec, Y. Journaux, J. Pasán, C. Ruiz-Pérez, F. S. Delgado, R. Ruiz-García, F. Lloret and C. Paulsen, *Chem. Commun.*, 2010, **46**, 2322; (*b*) J. Ferrando-Soria, D. Cangussu, M. Eslava, Y. Journaux, R. Lescouëzec, M. Julve, F. Lloret, J. Pasán, C. Ruiz-Pérez, E. Lhotel, C. Paulsen and E. Pardo, *Chem.–Eur. J.*, 2011, **17**, 12482.

8 V. A. Blatov, Nanocluster analysis of intermetallic structures with the program package TOPOS *Struct. Chem.*, 2012, **23**, 955.

9 (*a*) D. Casanova, J. Cirera, M. Llunell, P. Alemany, D. Avnir and S. Alvarez, *J. Am. Chem. Soc.*, 2004, **126**, 1755; (*b*) E. I. Stiefel and G. F. Brown, *Inorg. Chem.*, 1972, **11**, 434.

Dalton Transactions

PAPER

View Article Online
View Journal | View Issue

Cite this: *Dalton Trans.*, 2014, **43**, 15359

A triple-bridged azido-Cu(II) chain compound fine-tuned by mixed carboxylate/ethanol linkers displays slow-relaxation and ferromagnetic order: synthesis, crystal structure, magnetic properties and DFT calculations†

Xiangyu Liu,[a,b] Sanping Chen,*[a] Thais Grancha,[c] Emilio Pardo,*[c] Hongshan Ke,[a] Bing Yin,[a] Qing Wei,[a] Gang Xie[a] and Shengli Gao[a]

Received 21st July 2014,
Accepted 13th August 2014

DOI: 10.1039/c4dt02195a

www.rsc.org/dalton

A new azido-Cu(II) compound, [Cu(4-fba)(N_3)(C_2H_5OH)] (4-fba = 4-fluorobenzoic acid) (**1**), has been synthesized and characterized. The X-ray crystal structure analysis demonstrates that only one crystallographically independent Cu(II) ion in the asymmetric unit of **1** exhibits a stretched octahedral geometry in which two azido N atoms and two carboxylic O atoms locate in the equatorial square, while two ethanol O atoms occupy the apical positions, forming a 1D Cu(II) chain with an alternating triple-bridge of EO-azido, *syn*,*syn*-carboxylate, and μ2-ethanol. The title compound consists of ferromagnetically interacting ferromagnetic chains, which exhibit ferromagnetic order (T_c = 7.0 K). The strong ferromagnetic coupling between adjacent Cu(II) ions within each chain is due to the countercomplementarity of the superexchange pathways, whereas the ferromagnetic interchain interactions – responsible for the long-range magnetic ordering – are most likely due to the presence of coordinated ethanol molecules establishing hydrogen bonds with neighboring chains. DFT calculations have been performed on compound **1** to offer a qualitative theoretical explanation of the magnetic behavior.

Introduction

The synthesis of novel examples of one-dimensional (1D) chain compounds attracts interest from both a crystal engineering point of view[1] – because of the wide range of structural motifs and topologies that can be found – and also because of the intriguing, and sometimes predictable magnetic properties that they can exhibit. Both factors have equally contributed to the special attention that scientists working in the field of molecular magnetism[2] have focused on this class of materials during the last three decades.[3] Among the wide plethora of magnetic properties that a given 1D compound can exhibit, those related to the slow-relaxation of the magnetization are especially appealing. In this sense, both the so-called single-chain-magnets (SCMs)[4] and those compounds exhibiting a spontaneous magnetization below a critical temperature (T_c),[5] are significant from the perspectives of basic and applied research, and have rich potential applications such as in quantum computation and information storage.[6]

A popular approach for constructing these types of materials is to employ short ligands capable of efficiently transmitting the magnetic coupling.[7] In this sense, the azido ligand has attracted a lot of attention for its inherent advantages for obtaining magnetic materials.[8] The two typical coordination modes of azido ligands – μ-1,3 (end-to-end, EE) and μ-1,1 (end-on, EO) modes – usually correspond to antiferromagnetic and ferromagnetic exchanges,[9] respectively (Scheme 1).

A large number of azido-bridged metal compounds with alternating 1D chain structures and diverse magnetic properties have been demonstrated in the past decades.[10] For example, azido-Cu(II) systems are considered as ideal candidates for understanding the fundamental science of magnetic

[a]*Key Laboratory of Synthetic and Natural Functional Molecule Chemistry of Ministry of Education, College of Chemistry and Materials Science, Northwest University, Xi'an 710069, China. E-mail: sanpingchen@126.com; Fax: +86-029-88302604; Tel: +86-029-88302604*

[b]*School of Chemistry and Chemical Engineering, Ningxia University, Yinchuan 750021, China*

[c]*Departament de Química Inorgànica/Instituto de Ciencia Molecular (ICMol), Universitat de València, 46980 Paterna, València, Spain. E-mail: Emilio.Pardo@uv.es; Fax: +34 3543273; Tel: +34 3544442*

† Electronic supplementary information (ESI) available: Fig. S1 and Table S1, crystal structure of compound **1** in CIF format. CCDC number for **1**, 980967. For ESI and crystallographic data in CIF or other electronic format see DOI: 10.1039/c4dt02195a

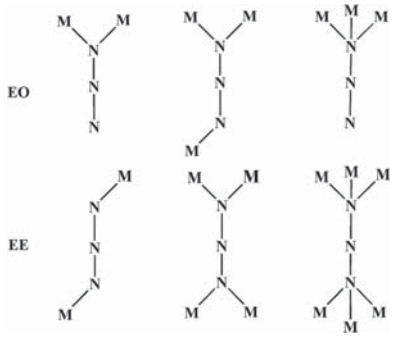

Scheme 1 Coordination modes of bridging azido ligands.

interactions and magneto-structural correlations in molecular systems,[11] and exhibit various structures and interesting magnetic properties with the assistance of secondary bridging ligands. For azido-Cu(II) compounds, it has been suggested that the strongest ferromagnetic coupling in the EO-azido linker occurs at a Cu–N–Cu bond angle close to 108°, and so an antiferromagnetic interaction would probably be found for larger Cu–N–Cu bond angles.[12] Consequently, an effective strategy for tuning the structures of azido-Cu(II) compounds with notable magnetic properties is to introduce carboxylates as coligands into the systems, as the μ-1,1-azido and *syn*,*syn*-carboxylate ligands usually bridge the Cu(II) ions to form a tetra-coordinated quadrangular geometry in previous reports.[13] In particular, molecular orbital calculations dramatically support the countercomplementary effect enforced by the carboxylate ligand, which weakens the effect of the antiferromagnetic azido ligand to the point where dominant ferromagnetic behavior is obtained.[14] A series of azido/carboxylate/Cu(II) compounds with isolated ferromagnetic chains involving the combinations of μ-1,1-azido ligands and *syn*,*syn*-carboxylates[15] have been previously prepared. However, to our knowledge only rare examples of them have shown long-range magnetic ordering.[16]

The scenario which captures our attention involves numerous solvents such as dimethylsulfoxide and alcoholic solvents, as well as aqueous solutions, which could coordinate to the Cu(II) ions as triple bridging ligands in the azido/carboxylate/Cu(II) systems,[16a,17] regulating the intrachain or interchain structures and thus the magnetic properties, for the following reasons: (i) the bridging solvent molecules between the Cu(II) ions do not only change the coordination geometry and orbital exchange of the Cu(II) ions, but also fine-tune the structural parameters including the Cu–Cu distances and the Cu–N–Cu angles; (ii) the solvent molecules would provide a higher possibility of forming weak interchain interactions like hydrogen-bonding and π–π stacking, which are known to be an effective pathway for magnetic transmission, contributing to the long-range magnetic order.[18]

Herein, we report the synthesis, structure, and magnetic properties of a new 1D chain-like azido-Cu(II) compound, $[Cu(4\text{-fba})(N_3)(C_2H_5OH)]$ (4-fba = 4-fluorobenzoic acid) (**1**), in which the Cu(II) ions are connected by a triple-bridge of a μ-1,1-azido ligand, a *syn*,*syn*-carboxylate and a μ2-ethanol molecule. The integration of intrachain and interchain magnetic exchanges from the alternating ferromagnetic chains leads to slow relaxation and long-range order which are rarely observed in most of the known azido/carboxylate-Cu(II) systems with well-isolated 1D chains. Moreover, the strong ferromagnetic coupling between adjacent Cu(II) ions was also confirmed using density functional theory (DFT) calculations.

Experimental section

Physical measurements

Elemental analysis (C, H, N) was performed on a Perkin-Elmer 2400 CHN elemental analyzer. The FT-IR spectra were recorded in the range 400–4000 cm^{-1} using KBr pellets on an EQUINOX55 FT/IR spectrophotometer. The phase purity of the bulk or polycrystalline samples was verified by powder X-ray diffraction (PXRD) measurements performed on a Rigaku RU200 diffractometer at 60 kV, 300 mA and CuKα radiation (λ = 1.5406 Å), with a scan speed of 5° min^{-1} and a step size of 0.02° in 2θ. Variable-temperature (2.0–300 K) direct current (dc) magnetic susceptibility measurements under an applied field of 50 G (T < 20 K) and 5 kG ($T \geq$ 20 K), and variable-field (0–5 T) magnetization measurements at 2.0 K were carried out with a Quantum Design SQUID magnetometer. Variable-temperature (2.0–10 K) alternating current (ac) magnetic susceptibility measurements under a zero applied static field were carried out with a Quantum Design Physical Property Measurement System (PPMS). The magnetic susceptibility data were corrected for the diamagnetism of the constituent atoms and the sample holder. Dc and ac magnetic measurements were carried out by powdering and restraining the sample in order to prevent any displacement.

Synthesis

All reagents and solvents employed were commercially available and used as received without further purification.

CAUTION! Azido compounds of metal ions are potentially explosive. Only a small amount of the materials should be prepared, and they should be handled with care.

$[Cu(4\text{-fba})(N_3)(C_2H_5OH)]$ (1)

An ethanol solution (10 mL) of NaN_3 (0.013 g, 0.2 mmol) and 4-Hfba (0.056 g, 0.4 mmol) in a tube was layered with aqueous ethanol (50%, 5 mL), and an aqueous solution (10 mL) of $Cu(NO_3)_2{\cdot}3H_2O$ (0.048 g, 0.2 mmol) was carefully added. Slow diffusion at room temperature yielded green crystals of **1** within three weeks (yield: 80%, based on Cu). Anal. calcd for $CuC_9H_{10}FN_3O_3$ (290.74): C, 37.15; H, 3.44; N, 14.45%. Found: C, 37.12; H, 3.39; N, 14.40%. Main IR (KBr, cm^{-1}): 2987 (w), 2088 (s), 1606 (s), 1544 (s), 1415 (s), 1238 (m), 852 (w), 777 (m), 634 (m).

Table 1 Crystal data and structure refinement details for compound **1**

	1
Empirical formula	$C_9H_{10}CuFN_3O_3$
Formula weight	290.74
Crystal system	Monoclinic
Space group	$P2_{(1)}/n$
a (Å)	7.6404(15)
b (Å)	6.3146(12)
c (Å)	24.268(5)
α (°)	90
β (°)	93.497(4)
γ (°)	90
V (Å^3)	1168.7(4)
Z	4
$D_{(calcd)}$ (g cm^{-3})	1.652
μ (mm^{-1})	1.882
F(000)	588
Θ range (°)	1.68–26.19
Unique reflections	2331
Observed reflections	6021
R_{int}	0.0750
Goodness of fit (F^2)	1.001
Parameters refined	155
Final R indices [$I > 2\sigma(I)$]	R_1 = 0.0567, wR_2 = 0.1235
R indices (all data)	R_1 = 0.1176, wR_2 = 0.1542
Residuals (e Å^{-3})	0.438, −0.692

Crystallographic data collection and refinement

Single-crystal diffraction data for **1** was collected on a Rigaku SCX mini CCD diffractometer using graphite-mono-chromatized MoKα radiation (λ = 0.71073 Å) at room temperature. The data integration and reduction were processed with SAINT software. Absorption correction based on multi-scan was performed using the SADABS program.[19a] The structure was solved by the direct method using SHELXTL and refined by a full-matrix least-squares method on F^2 with the SHELXL-97 program.[19b] All non-hydrogen atoms were refined anisotropically. A summary of the crystallographic data and data collection, and the refinement parameters are listed in Table 1, and selected bond lengths and angles are listed in Table S1.†

Computational methodology

The following computational methodology was used to calculate the coupling constant in the title compound.[20] The spin Hamiltonian suggested originally by Heisenberg can be written as $\hat{H} = -\sum_{(i>j)} J S_i S_j$ (where S_i and S_j are the spin operators of the paramagnetic centers, $S_i = S_j = 1/2$ for Cu(II) ion; and the J constant is the coupling constant between the paramagnetic spin carriers), which can be employed to express the exchange coupling between two transition metal ions, and the full Hamiltonian matrix for the entire system can be established.

The DFT calculations were implemented with the ORCA 3.0 package.[21] The BP86 functional proposed by Becke[22] and Perdew[23] was applied in all calculations. The polarized triple-ζ quality basis set def2-TZVP proposed by Ahlrichs and coworkers was used for all atoms.[24] The calculation model for the compound was built from the experimental results.

Results and discussion

Crystal structures

The single crystal X-ray analysis revealed that compound **1** is composed of isolated 1D azido-copper chains. The Cu(II) ions located at the inverse centers adopt a hexa-coordinated environment through an N_2O_4 chromophore in which two nitrogen atoms from two azido anions and two oxygen atoms from two carboxylates [Cu–N1 = 1.988 Å, Cu–O1 = 1.950 Å, Cu–N1A = 1.988 Å and Cu–O2 = 1.943 Å] lie on the equatorial region, while two oxygen atoms from two ethanol molecules occupy apical positions [Cu–O3 = 2.528 Å, Cu–O3B = 2.419 Å] (Fig. 1a). All of the Cu(II) ions have an elongated octahedral geometry resulting from the typical Jahn–Teller effect. The single EO-azido ligand can be considered as a bridge between neighboring copper atoms in the μ2-1,1 coordination mode, in which all of the bridging nitrogen atoms are coordinated in equatorial positions. The azido groups are quasi linear with N(3)–N(2)–N(1) angles of 179.1(8)°, and exhibit unsymmetric N–N bond lengths, with the bonds involving the donor atoms (N(1)–N(2) = 1.208(7) Å) being relatively longer than N(2)–N(3) = 1.131(7) Å. The *syn*,*syn*-carboxylato bridges of the deprotonated 4-fluorobenzoic acids are pseudosymmetrically bound to the copper centers with a slight difference in the Cu–O distances [Cu–O1 = 1.950 Å, Cu–O2 = 1.943 Å]. Moreover, the oxygen atoms in the ethanol molecules adopt a μ2 mode to bridge the adjacent Cu(II) ions. Then, adjacent metal ions are simultaneously linked by an μ-1,1 (EO)-azido bridge and a *syn*, *syn*-carboxylate bridge, as well as an μ2-ethanol bridge, yielding a formal 1D chain along the a axis (Fig. 1b). The coordination of ethanol shortens the distance between the intrachain copper ions [Cu1–Cu1A = 3.160 Å]. As shown in Table S1,† the bond lengths between one Cu(II) ion and two ethanol bridging-oxygen atoms are slightly different [Cu–O = 2.528 Å or 2.419 Å], while the Cu–N–Cu angle (105.2°) is in the normal range of the EO-azido bridging mode. The interchain hydrogen-bonding between the oxygen atom in the coordinated ethanol molecule and the terminal nitrogen atom in the azido ligand [O3–H1···N3 = 2.918 Å] might induce magnetic transmission, which integrates all of the Cu(II) chains, constructing the supramolecular framework of **1** (Fig. 1c). The shortest distance between interchain Cu(II) ions is 7.640 Å.

Magnetic properties

Magnetic measurements were carried out on a polycrystalline sample **1**, the phase purity of which was confirmed by PXRD (see Fig. S1†).

The $\chi_M T$ *vs.* T plot of **1**, (χ_M being the molar magnetic susceptibility per Cu(II) atom and T the temperature, under applied magnetic fields H of 5000 G (T > 30 K) and 100 G ($T \leq$ 30)), is shown in Fig. 2a. At room temperature, the $\chi_M T$ is equal to 0.51 cm^3 mol^{-1} K, a value which is somewhat larger than that expected for a magnetically isolated copper(II) ion [$\chi_M T = (N\beta^2 g_{Cu}{}^2/3k) S_{Cu}(S_{Cu} + 1)$ = 0.41 cm^3 mol^{-1} K with g_{Cu} = 2.1 and S_{Cu} = 1/2]. Upon cooling, $\chi_M T$ continuously increases to reach a maximum with a $\chi_M T$ value of 6.11 cm^3 mol^{-1} K at

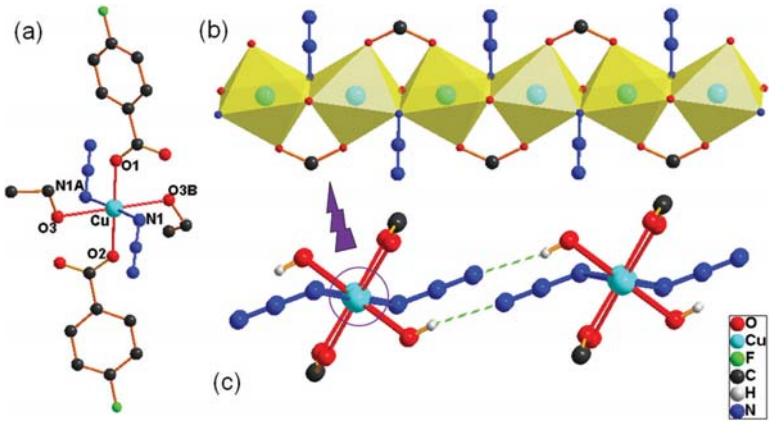

Fig. 1 (a) The coordination environment of the Cu ions in **1**. (Hydrogen atoms are omitted for clarity.) (b) The 1D chain with mixed ethanol oxygen, carboxylate and azido bridges for **1**. (Hydrogen atoms and benzene rings are omitted for clarity.) (c) Hydrogen bonding formed by azido and ethanol molecules between adjacent chains in **1**.

7.54 K (Fig. 2a). Below this temperature, $\chi_M T$ decreases rapidly to reach a $\chi_M T$ value of 2.02 $cm^3\ mol^{-1}$ K at 1.90 K. This behavior is consistent with a ferromagnetic coupling between the Cu(II) ions along the chain. Such parallel alignment of the neighboring local spins when the bridging ligands are different is well documented and is due to orbital counter-complementarity.[25] The *M vs. H* plot at 2.0 K, (*M* being the molar magnetization per Cu(II) atom and *H* the applied field) is shown in Fig. 2b. The maximum *M* value at $H = 5.0$ T is very close to $1N\beta$ ($0.98N\beta$), a value which confirms that all of the $S_{Cu} = 1/2$ centers are aligned along the same direction. Interestingly, the χ_M *vs. T* plot of **1** (inset of Fig. 2a), reveals that below 15 K, χ_M shows a sharp increase and also an incipient saturation below *ca.* 7.5 K. These features suggest the onset of a long-range ferromagnetic ordering which must be the result of interchain ferromagnetic interactions. This saturation also accounts for the rapid decrease of $\chi_M T$ below 7.54 K (Fig. 2a).

The presence of this ferromagnetic ordering is revealed by the coalescence of the field-cooled magnetization (FCM) and the zero-field-cooled magnetization (ZFCM) curves at 7.0 K (Fig. 3). In order to further confirm the presence of the magnetic ordering, ac susceptibility measurements were performed. Fig. 4 shows how the out-of-phase magnetic susceptibility becomes nonzero below 12 K and exhibits frequency-independent maxima in the narrow range 7.0–6.0 K. Ferromagnetic ordering is more often observed in high-dimensional (two- and three-dimensional) compounds, however, examples of ferromagnetic chains exhibiting interchain ferromagnetic interactions and long-range magnetic ordering have already been reported.[5,16] The presence of this ferromagnetic ordering indicates the presence of long-range ferromagnetic interchain magnetic interactions at low temperature. An intriguing remaining question concerns the frequency dependence of χ''_M (Fig. 4), which is reminiscent of that observed in so-called single-chain magnets (SCMs).[4] However, this dependence is very weak and the values for the relaxation time (τ_0) and the activation energy (E_a) are physically meaningless. This very weak dependence is commonly observed in spin-glasses,[26] and can be due to the occurrence of competitive ferromagnetic (F) and antiferromagnetic (AF) interactions yielding a spin-frustrated system with a vitrification process.[27]

The temperature dependence of the magnetic susceptibility data of **1** was analyzed with the expression proposed by Baker *et al.*[28] for a ferromagnetic $S = 1/2$ chain (eqn (1)) which was obtained from a high-temperature series expansion.

$$\chi_M = \frac{N\beta^2 g^2}{4kT}\left(\frac{A}{B}\right)^{2/3} \quad (1)$$

$A = 1.0 + 5.7980x + 16.9027x^2 + 29.3769x^3 + 29.8329x^4 + 14.0369x^5$, $B = 1.0 + 2.7980x + 7.0087x^2 + 8.6538x^3 + 4.5743x^4$, $x = J/2kT$.

The fitting of the experimental data in the 300–20 K range (solid line in Fig. 2a) gave: $g = 2.20$, $J = +36.2$ cm^{-1} and $R = 2.4 \times 10^{-7}$, where J is the intrachain magnetic coupling, g_{Cu} is the Zeeman factor of the Cu(II) ions and R is the agreement factor defined as $R = \sum[(\chi_M T)_{exp} - (\chi_M T)_{calcd}]^2/\sum[(\chi_M T)_{exp}]^2)$. Further attempts to fit the magnetic data below $T = 20$ K were unsuccessful due to the spin-frustrating interactions at low temperatures but also because of the limitations of a law derived from a high-temperature series expansion. In addition, we also tried to include a term that took into account the interchain magnetic interactions (θ). However, interchain magnetic interactions are only relevant at low temperatures. Thus, the fitting of the experimental data in the 300–20 K range, gave always negligible values for θ.

Theoretical study

In order to further demonstrate the ferromagnetic nature of the exchange interaction in compound **1**, we performed a

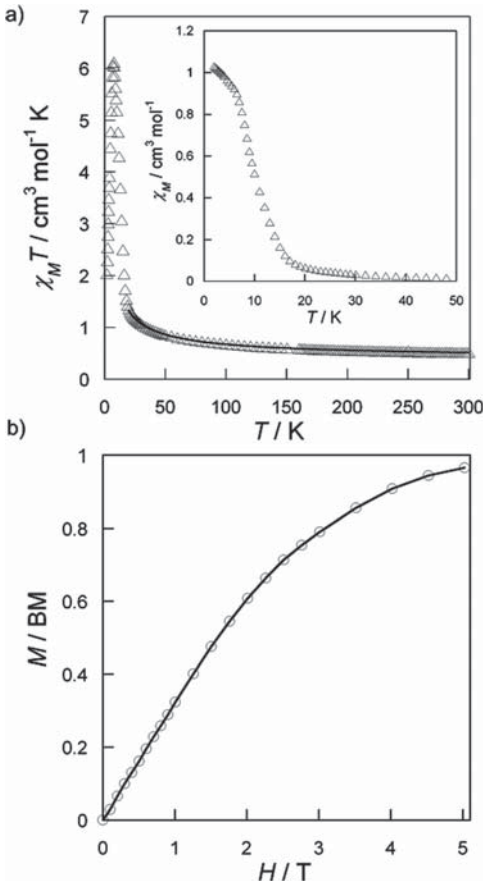

Fig. 2 (a) Temperature dependence of $\chi_M T$ under applied dc fields of 50 G (T < 30 K) and 5 kG ($T \geq 30$ K). The solid lines correspond to the best-fit curves (see text). The inset shows the thermal dependence of χ_M for **1**. (b) Field dependence of the M of **1** at 2.0 K. The solid line is an eye-guide.

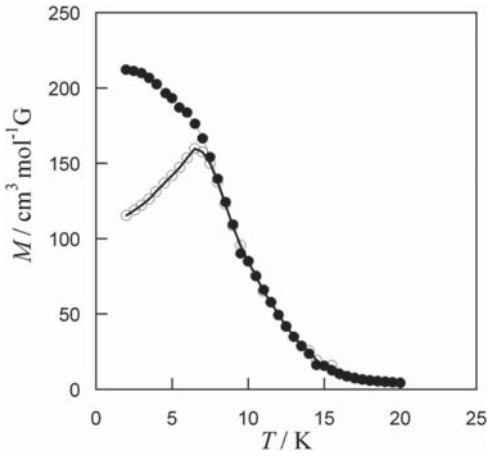

Fig. 3 Field-cooled magnetization (FCM, ●) and the zero-field-cooled magnetization (ZFCM, ○) of **1**. The solid lines are only eye-guides.

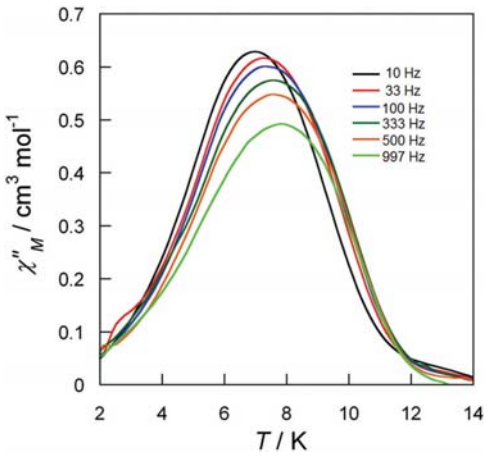

Fig. 4 Temperature dependence of the ac out-of-phase magnetic susceptibility of **1** at frequencies in the range 10–997 Hz.

theoretical study of the isotropic coupling constants J between the Cu(II) ions based on DFT calculations at the B3LYP level with the aid of ORCA. Considering the structure of **1** and supposing that the dominant magnetic exchange is mediated between adjacent Cu(II) ions through azido, carboxylate and ethanol ligands. The calculation was carried out with the model (for comparison) applied to the magnetic fitting by filling-in all the coordination sites of the Cu(II) ions (Fig. 5).

The results of the theoretical calculations and the experimental fitting in terms of the coupling constants are listed in Table 2. The calculated coupling constant is J = 61.0 cm^{-1}, which verifies that the strong ferromagnetic coupling is prevailing in compound **1**. Although the calculated value shows a certain deviation from the fitting value, the sign and the relative magnitude of the coupling constant agrees well with the experimental value. It is difficult to estimate the accuracy of the theoretical calculation, but the work is only qualitative. This may result from the fact that the real compound is not made up of scattered entities as it has been modeled, but is very complicated across the whole structure.

Magneto-structural correlation

The magnetic exchanges between the Cu(II) ions depend on three paths in **1** (Fig. 6): the *syn*,*syn*-carboxylate and the μ-1,1-azido ligands (Cu–N = 1.99 Å, Cu–N–Cu = 105.2°), as well as the ethanol molecule coordinate to the Cu(II) ions, forming the hexa-coordinated geometry (Cu–O = 2.42–2.53 Å). Additionally, the intrachain and interchain Cu–Cu bond lengths are determined to be 3.160 Å and 7.640 Å, respectively. Undoubtedly,

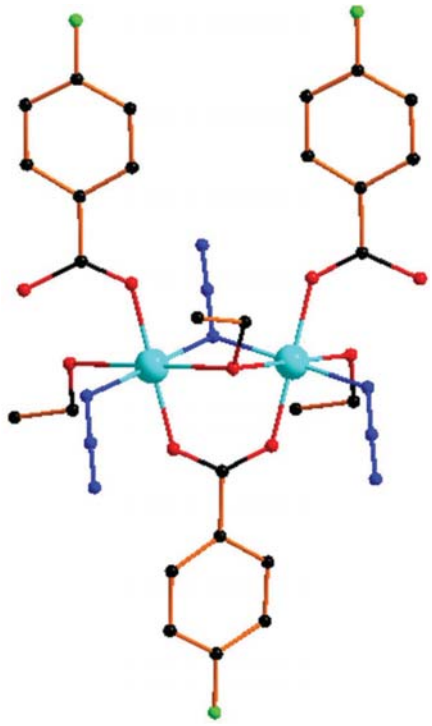

Fig. 5 The magnetic core of **1** used for the computational study.

Table 2 Comparison of the results of the experimental (from fitting) and DFT studies

Compound	J/cm^{-1}	Expt	DFT(TZVP)
1	J	36.2	61.0

the coordination of ethanol oxygen atoms could reduce the distance of the intrachain Cu(II) ions, by comparison with a dual-bridging 1D Cu(II) chain reported previously. As observed, the counter complementarity effect resulting from the three different ligands may explain the occurrence of the intrachain ferromagnetic exchange. The interchain hydrogen-bonding derived form the ethanol oxygen atom and the terminal nitrogen atom of the azido group affords an additional pathway to transmit the interaction between the well-isolated ferromagnetic chains. This feature can explain the long-range magnetic ordering observed, which is rarely observed in 1D chain-like Cu(II) compounds containing EO-azido and carboxylate ligands.

Conclusions

In the present work, an azido-Cu(II) compound with 4-fluorobenzoic acid as a coligand was obtained using a slow diffusion method. Structural analyses show that compound **1** is a 1D Cu(II) chain with a μ-1,1 (EO)-azido ligand, a *syn–syn*-carboxylate and μ2-ethanol connecting the copper(II) ions. Compared with previously reported 1D Cu(II) chain compounds, which were bridged only by (EO)-azido and carboxylate ligands, **1** exhibits different intrachain and interchain structures due to the coordination of ethanol molecules which also influence the magnetic properties. Magnetic investigations show that compound **1** behaves as a ferromagnet composed of ferromagnetically interacting ferromagnetic chains. The intrachain behavior reflects how the countercomplementary effect imposed by the carboxylate bridge overcomes the antiferromagnetic effect of the azido bridge resulting in an overall ferromagnetic interaction. In addition, the long-range ferromagnetic interchain interactions afford the observation of a ferromagnetic order at 7 K. DFT calculations qualitatively confirm the strong ferromagnetic coupling between the Cu(II) ions.

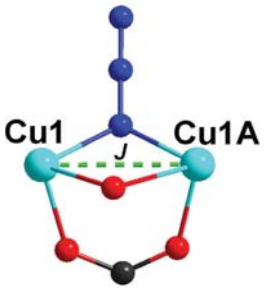

Fig. 6 Magnetic exchange between Cu(II) ions in compound **1**.

Acknowledgements

The present work was supported by the National Natural Science Foundation of China (21173168, 21073142, 21373162 and 21463020), and the Nature Science Foundation of Shanxi Province (FF10091, SJ08B09 and 11JS110). E. P. thanks the MINECO for a "Ramón y Cajal" contract.

References

1 E. Pardo, C. Train, K. Boubekeur, G. Gontard, J. Cano, F. Lloret, K. Nakatani and M. Verdaguer, *Inorg. Chem.*, 2012, **51**, 11582–11593.
2 J.-P. Launay and M. Verdaguer, *Electrons in Molecules: From Basic Principles to Molecular Electronics*, Oxford Scholarship Online, 2013.
3 (*a*) D.-S. Li, J. Zhao, Y.-P. Wu, B. Liu, L. Bai, K. Zou and M. Du, *Inorg. Chem.*, 2013, **52**, 8091–8098; (*b*) I. Castro, M. L. Calatayud, W. P. Barros, J. Carranza, M. Julve, F. Lloret, N. Marino and G. De Munno, *Inorg. Chem.*, 2014, **53**, 5759–5771, and references therein.

4 (*a*) E. Pardo, R. Ruiz-García, F. Lloret, J. Faus, M. Julve, Y. Journaux, F. S. Delgado and C. Ruiz-Pérez, *Adv. Mater.*, 2004, **16**, 1597–1600; (*b*) E. Pardo, R. Ruiz-García, F. Lloret, J. Faus, M. Julve, Y. Journaux, M. A. Novak, F. S. Delgado and C. Ruiz-Pérez, *Chem. – Eur. J.*, 2007, **13**, 2054–2066; (*c*) J. Ferrando-Soria, E. Pardo, R. Ruiz-García, J. Cano, F. Lloret, M. Julve, Y. Journaux, J. Pasán and C. Ruiz-Pérez, *Chem. – Eur. J.*, 2011, **17**, 2176–2188.

5 E. Coronado, J. R. Galán-Mascarós, C. J. Gómez-García and C. Martí-Gastaldo, *Inorg. Chem.*, 2005, **44**, 6197–6202.

6 (*a*) D. Gatteschi, R. Sessoli and J. Villain, *Molecular Nanomagnets*, Oxford University Press, 2006; (*b*) C. Coulon, H. Miyasaka and R. Clérac, in *Structure and Bonding*, ed. R. Winpenny, Springer, 2006, pp. 163–206; (*c*) H. L. Sun, Z. M. Wang and S. Gao, *Chem. – Eur. J.*, 2009, **15**, 1757–1764; (*d*) Y.-Z. Zheng, M.-L. Tong, W.-X. Zhang and X.-M. Chen, *Angew. Chem., Int. Ed.*, 2006, **45**, 6310–6314; (*e*) Y.-Z. Zheng, W. Xue, M.-L. Tong, X.-M. Chen and S.-L. Zheng, *Inorg. Chem.*, 2008, **47**, 11202–11211; (*f*) D.-S. Li, J. Zhao, Y.-P. Wu, B. Liu, L. Bai, K. Zou and M. Du, *Inorg. Chem.*, 2013, **52**, 8091–8098.

7 (*a*) R. Lescouëzec, L.-M. Toma, J. Vaissermann, M. Verdaguer, F.-S. Delgado, C. Ruiz-Pérez and M. Julve, *Coord. Chem. Rev.*, 2005, **249**, 2691–2729; (*b*) H. Miyasaka, M. Julve, M. Yamashita and R. Clerac, *Inorg. Chem.*, 2009, **48**, 3420–3437; (*c*) K. Bernot, J. Luzon, R. Sessoli, A. Vindigni, J. Thion, S. Richeter and A. Van Der Lee, *J. Am. Chem. Soc.*, 2008, **130**, 1619–1627; (*d*) M. Ding, B. Wang, Z. Wang, J. Zhang, O. Fuhr, D. Fenske and S. Gao, *Chem. – Eur. J.*, 2012, **18**, 915–924.

8 (*a*) T.-F. Liu, D. Fu, S. Gao, Y.-Z. Zhang, H.-L. Sun, G. Su and Y.-J. Liu, *J. Am. Chem. Soc.*, 2003, **125**, 13976–13977; (*b*) A.-H. Fu, X.-Y. Huang, J. Li, T. Yuen and C.-L. Lin, *Chem. – Eur. J.*, 2002, **8**, 2239–2247; (*c*) U. Ray, S. Jasimuddin, B. K. Ghosh, M. Monfort, J. Ribas, G. Mostafa, T.-H. Lu and C. Sinha, *Eur. J. Inorg. Chem.*, 2004, **2004**, 250–259.

9 (*a*) A. Escuer, J. Cano, M. A. S. Goher, Y. Journaux, F. Lloret, F. A. Mautner and R. Vicente, *Inorg. Chem.*, 2000, **39**, 4688–4695; (*b*) C. Adhikary and S. Koner, *Coord. Chem. Rev.*, 2010, **254**, 2933–2958.

10 (*a*) X.-Y. Wang, Z.-M. Wang and S. Gao, *Chem. Commun.*, 2008, 281–294; (*b*) Y.-F. Zeng, X. Hu, F.-C. Liu and X.-H. Bu, *Chem. Soc. Rev.*, 2009, **38**, 469–480; (*c*) K. S. Lim, D. W. Ryu, W. R. Lee, E. K. Koh, H. C. Kim and C. S. Hong, *Chem. – Eur. J.*, 2012, **18**, 11541–11544; (*d*) S. Mukherjee and P. S. Mukherhee, *Acc. Chem. Res.*, 2013, **46**, 2556–2566; (*e*) C. I. Yang, W. Wernsdorfer, G. H. Lee and H. L. Tsai, *J. Am. Chem. Soc.*, 2007, **129**, 456–457.

11 (*a*) *Magnetism: Molecules to Materials*, ed. J. S. Miller and M. Drillon, Wiley-VCH, Weinheim, 2002; (*b*) O. Kahn, *Molecular Magnetism*, VCH, New York, 1993; (*c*) J. Liu, Y.-L. Qin, M. Qu, R. Clérac and X.-M. Zhang, *Dalton Trans.*, 2013, **42**, 11571–11575.

12 (*a*) E. Ruiz, J. Cano, S. Alvarez and P. Alemany, *J. Am. Chem. Soc.*, 1998, **120**, 11122–11129; (*b*) J. Cabrero, C. Graaf, E. Bordas, R. Caballol and J. P. Malrieu, *Chem. – Eur. J.*, 2003, **9**, 2307–2315; (*c*) S. Triki, C. J. G. García, E. Ruiz and J. S. Pala, *Inorg. Chem.*, 2005, **44**, 5501–5508; (*d*) P. Mialane, A. Dolbecq, J. Marrot, E. Riviére and F. Sécheresse, *Chem. – Eur. J.*, 2005, **11**, 1771–1778; (*e*) P. K. Nanda, G. Aromí and D. Ray, *Chem. Commun.*, 2006, 3181–3183; (*f*) J.-P. Zhao, B.-W. Hu, E. C. Sañudo, Q. Yang, Y.-F. Zeng and X.-H. Bu, *Inorg. Chem.*, 2009, **48**, 2482–2489.

13 (*a*) D. Visinescu, A. M. Madalan, M. Andruh, C. Duhayon, J. P. Sutter, L. Ungur, W. V. Heuvel and L. F. Chibotaru, *Chem. – Eur. J.*, 2009, **15**, 11808–11814; (*b*) X.-T. Wang, X.-H. Wang, Z.-M. Wang and S. Gao, *Inorg. Chem.*, 2009, **48**, 1301–1308; (*c*) T. Liu, Y.-J. Zhang, Z.-M. Wang and S. Gao, *Inorg. Chem.*, 2006, **45**, 2782–2784; (*d*) Q. Yang, J.-P. Zhao, B.-W. Hu, X.-F. Zhang and X.-H. Bu, *Inorg. Chem.*, 2010, **49**, 3746–3751; (*e*) Y. Ma, K. Wang, E.-Q. Gao and Y. Song, *Dalton Trans.*, 2010, **39**, 7714–7772.

14 (*a*) L. K. Thompson, S. S. Tandon, F. Lloret, J. Cano and M. Julve, *Inorg. Chem.*, 1997, **36**, 3301–3306; (*b*) A. Escuer, R. Vicente, F. A. Mautner and M. A. Goher, *Inorg. Chem.*, 1997, **36**, 1233–1236.

15 (*a*) L. Yang, S. Zhang, X.-Y. Liu, Q. Yang, Q. Wei, G. Xie and S.-P. Chen, *CrystEngComm*, 2014, **16**, 4194–4201; (*b*) T. C. Stamatatos, G. Vlahopoulou, C. P. Raptopoulou, V. Psycharis, A. Escuer, G. Christou and S. P. Perlepes, *Eur. J. Inorg. Chem.*, 2012, **2012**, 3121–3131; (*c*) V. Tangoulis, D. Panagoulis, C. P. Raptopoulou and C. Dendrinou-Samara, *Dalton Trans.*, 2008, 1752–1760.

16 (*a*) Q. Gao, Y.-B. Xie, M. Thorstad, J.-H. Sun, Y. Cui and H.-C. Zhou, *CrystEngComm*, 2011, **13**, 6787–6793; (*b*) Y.-F. Zeng, J.-P. Zhao, B.-W. Hu, X. Hu, F.-C. Liu, J. Ribas and X.-H. Bu, *Chem. – Eur. J.*, 2007, **13**, 9924–9930.

17 Q.-J. Su, S.-H. Li, L. Wang, C.-Z. Xie, Y. Ouyang and J.-Y. Xu, *Inorg. Chem. Commun.*, 2010, **13**, 1210–1212.

18 (*a*) K. Awaga and Y. Maruyama, *Chem. Phys. Lett.*, 1989, **158**, 556–558; (*b*) H. Oshio, T. Watanabe, A. Ohto, T. Ito and H. Masuda, *Inorg. Chem.*, 1996, **35**, 472–479; (*c*) W. A. Alves, R. H. Santos, A. Paduan-Filho, C. C. Becerra, A. C. Borin and A. M. Ferreira, *Inorg. Chim. Acta*, 2004, **357**, 2269–2278; (*d*) H. Andres, R. Basler, A. J. Blake, C. Cadiou, G. Chaboussant, C. M. Grant and R. E. Winpenny, *Chem. – Eur. J.*, 2002, **8**, 4867–4876.

19 (*a*) G. M. Sheldrick, *SADABS, Program for Empirical Absorption Correction*, University of Göttingen, Göttingen, Germany, 1996; (*b*) G. Sheldrick, *M. SHELXTL*, Bruker Analytical X-ray Instruments Inc., Madison, WI, 1998.

20 (*a*) E. Ruiz, P. Alemany, S. Alvarez and J. Cano, *J. Am. Chem. Soc.*, 1997, **119**, 1297–1303; (*b*) E. Ruiz, A. Rodríguez-Fortea, J. Cano, S. Alvarez and P. Alemany, *J. Comput. Chem.*, 2003, **24**, 982–989; (*c*) E. Ruiz, J. Cano, S. Alvarez and P. Alemany, *J. Comput. Chem.*, 1999, **20**, 1391–1400; (*d*) E. Ruiz, *Struct. Bonding*, 2004, **113**, 71–102.

21 (*a*) F. Neese, *ORCA-an ab initio, Density Functional and Semiempirical Program Package, 3.0.1*, University of Bonn, Bonn, Germany, 2013, http://www.thch.uni-bonn.de/tc/orca/; (*b*) F. Neese, *WIREs Comput. Mol. Sci.*, 2012, **2**, 73–78.

22 A. D. Becke, *Phys. Rev. A*, 1988, **38**, 3098–3100.
23 J. P. Perdew, *Phys. Rev. B*, 1986, **33**, 8822–8824.
24 A. Schäfer, C. Huber and R. J. Ahlrichs, *Chem. Phys.*, 1994, **100**, 5829–5835.
25 L. K. Thompson, S. S. Tandon, F. Lloret, J. Cano and M. Julve, *Inorg. Chem.*, 1997, **36**, 3301–3306.
26 J. A. Mydosh, *Spin Glasses: An Experimental Introduction*, Taylor & Francis, London, 1993.
27 R. Y. N. Gengler, L. M. Toma, E. Pardo, F. Lloret, X. Ke, G. Van Tendeloo, D. Gournis and P. Rudolf, *Small*, 2012, **8**, 2532–2540.
28 G. A. Baker and G. S. Rushbrooke, *Phys. Rev.*, 1964, **135**, 1272–1277.

ChemComm

FEATURE ARTICLE

View Article Online
View Journal | View Issue

Cite this: *Chem. Commun.*, 2014, **50**, 7569

Oxamato-based coordination polymers: recent advances in multifunctional magnetic materials

Thais Grancha,[a] Jesús Ferrando-Soria,*[a] María Castellano,[a] Miguel Julve,[a] Jorge Pasán,[b] Donatella Armentano[c] and Emilio Pardo*[a]

Received 7th March 2014,
Accepted 28th March 2014

DOI: 10.1039/c4cc01734j

www.rsc.org/chemcomm

The design and synthesis of novel examples of multifunctional magnetic materials based on the so-called coordination polymers (CPs) have become very attractive for chemists and physicists due to their potential applications in nanoscience and nanotechnology. However, their preparation is still an experimental challenge, which requires a deep knowledge of coordination chemistry and large skills in organic chemistry. The recent advances in this field using a molecular-programmed approach based on rational self-assembly methods which fully exploit the versatility of the coordination chemistry of the barely explored and evergreen family of *N*-substituted aromatic oligo(oxamato) ligands are presented in this feature article. These exploratory studies have revealed a wide variety of interesting multifunctional magnetic materials such as optically-active chiral and luminescent magnets or dynamic porous magnets as candidates for chemical sensing. Our feeling, however, is that we have only scratched the surface of the topic and that there are many more exciting brand-new molecule-based materials waiting to be discovered.

1. Introduction

During the last two decades, the field of molecular magnetism has attracted a large number of research teams worldwide due to its multidisciplinary character.[1,2] In fact, it lies at the crossing point of several disciplines such as chemistry (inorganic and organic chemistry as well as physical chemistry), physics (solid state and applied physics as well as theoretical physics), and materials science. The convergence of research in this field by scientists with specific backgrounds in such different domains has resulted in a fast and significant progress due to the complementarity between the knowledge that they possess and the techniques they use.

In relation to this multidisciplinary character, the addition of another physical property to the magnetic ones to build the so-called multifunctional magnetic materials has recently become an outstanding area of research in the field of molecular magnetism, opening new possibilities in molecule-based magnetic materials.[3] The main goal of this research is to synthesize and explore new classes of compounds that exhibit several properties of fundamental importance in nanoscience and nanotechnology.[3a] In so doing, molecular magnetism meets other fields of molecular sciences, such as molecular electronics and photonics, molecular electrochemistry and photochemistry, and molecular host–guest chemistry (including aspects of both molecular recognition and catalysis).

The design and synthesis of this new class of materials have largely benefited from the rapid development of a well-known branch of coordination chemistry devoted to the study of extended metal–ligand networks, which are named coordination polymers (CPs) or Metal–Organic Frameworks (MOFs).[4–8] They consist of hybrid materials where metal ions or small metal clusters are linked into one-, two-, or three-dimensions (*n*D with $n = 1$ to 3) by a wide diversity of organic bridging ligands, giving rise to putative open-framework (porous) structures. Since the seminal work by Hoskins and Robson[5] and others[6,7] on the chemistry and magnetic properties of CPs, the interest in this field has rapidly grown following the O'Keeffe and Yaghi's pioneering work on the sorption properties of MOFs.[8]

The design and synthesis of multifunctional magnetic coordination polymers (MMCPs) showing at least one physical property in addition to the magnetic ones, are formidable tasks which require a deep knowledge of both coordination chemistry and organic chemistry. On the one hand, proper choices of the organic linkers and metal ions are required in order to build CPs of variable dimensionality with interesting and predictable structural topologies and magnetic properties. On the other hand, the introduction of an additional physical property can be achieved, either by functionalizing the organic bridging ligand and/or by inserting a specific organic guest molecule into the channels of the open-framework, its properties being

[a] *Departament de Química Inorgànica/Instituto de Ciencia Molecular (ICMol), Universitat de València, 46980 Paterna, València, Spain. E-mail: Emilio.Pardo@uv.es; Fax: +34 3543273; Tel: +34 3544442*
[b] *Laboratorio de Rayos X y Materiales Moleculares, Departamento de Física Fundamental II, Universidad de La Laguna, E–38201 Tenerife, Spain*
[c] *Dipartimento di Chimica e Tecnologie Chimiche, Università della Calabria, 87036, Cosenza, Italy*

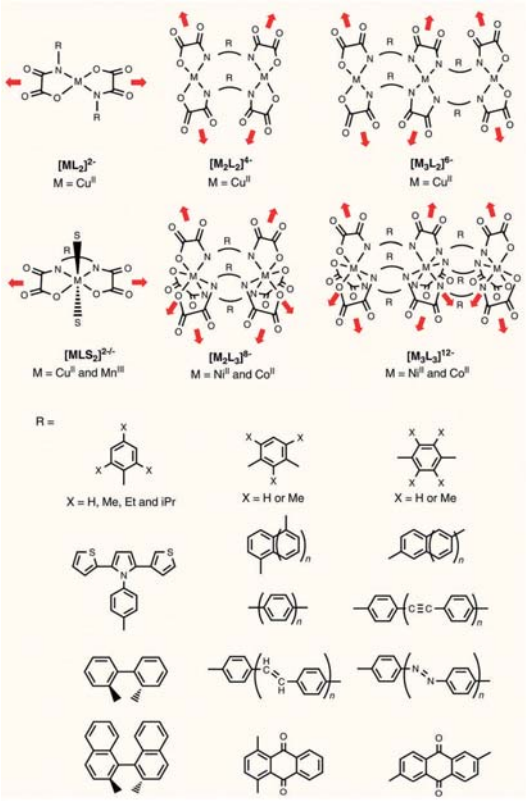

Scheme 1 Molecular libraries of oligonuclear aromatic oxamato complexes used as metalloligands (S stands for labile solvent molecules). The red arrows represent the free coordination sites to build the CPs.

incorporated into the resulting hybrid inorganic–organic material (Scheme 1).

When multifunctionality arises from the presence of guest molecules present in the voids of the CPs, it is more than evident that porosity is required. However, the combination of porosity and long-range magnetic ordering in the same material is an intellectual challenge. In general, porosity requires bridging ligands with long organic spacers connecting the individual metal ions or the polymetallic units that lead to an open-framework structure.[8] However, the long organic spacers do not facilitate the magnetic interactions between the distant metal centres. This apparent paradox with which synthetic chemists working in the field of MMCPs are faced, accounts for the small number of reports on porous magnets based on CPs.[9]

2. Molecular-programmed approach to heterobimetallic *n*D (*n* = 1 to 3) CPs

Coordination chemistry offers the basic tools to build MMCPs.[10,11] Two main different strategies can be chosen in this respect: (i) the largely spread, serendipitous self-assembly methods (often employing hydro(solvo)thermal reaction conditions),[12] and (ii) the use of the so-called "complex-as-ligand" strategy, where a preformed complex acts as a ligand (metalloligand) toward fully solvated paramagnetic metal ions. The second rational approach shows clear advantages over the first one. These molecular-programmed methods consist of using a stable preformed metal complex with additional coordination sites, which can coordinate free metal ions (or coordinatively-unsaturated metal complexes) under "soft" conditions. They constitute one of the most efficient ways to gain control over the net dimensionality and topology of the CPs, allowing thus a step further to get the desired properties in a given material. However, a total control of the final architecture and properties is still exceedingly difficult in spite of these clear advantages because of the subtle factors that may affect the assembly process of metalloligands and metal ions/preformed complexes.

Two representative examples of the richness of this metalloligand design strategy are represented by the use of cyanide- and oxalate-bearing mononuclear precursors such as $[M^{III}(CN)_6]^{3-}$ and $[M^{III}(C_2O_4)_3]^{3-}$ (M = Cr or Fe) as ligands towards different divalent metal ions.[10,11] So, the host–guest chemistry and sorption properties of the well-known families of bimetallic cyanide (Prussian blue)[10] and oxalato[11] magnets have been extensively explored affording a large variety of examples of MMCPs when incorporating guest molecules with additional properties of interest (*e.g.*, chirality, electrical and protonic conductivity, non-linear optics, photomagnetism).[10,11]

Another family of related metalloligands concerns the oligonuclear complexes with *N*-substituted aromatic oligo(oxamate) ligands, as depicted in Scheme 1. They have received a comparatively less attention in spite of their potentially unique opportunities to design novel multifunctional magnetic materials that they offer.[13] The main advantages provided by this type of ligand envisaging the construction of MMCPs are highlighted here:

(a) Firstly, the *N*,*O*-oxamato donor group shows a great coordination affinity toward divalent first-row transition metal ions (M = Cu^{II}, Ni^{II} and Co^{II}) with a high stability in solutions of the resulting oligonuclear complexes, from mono-, to di-, and trinuclear species (Scheme 1, top), the substitution by other divalent ions being thus precluded. This allows the formation in solution (and further isolation) of very stable and robust building blocks that have additional binding ability towards other divalent metal ions (M = Ni^{II}, Co^{II} and Mn^{II}) through the free carbonyl-oxygen atoms offering the possibility of obtaining heterobimetallic CPs with a wide diversity of architectures.

(b) The bis(bidentate) oxamate bridge mediates a strong magnetic coupling between the neighbouring metal ions in homo- and heterobimetallic compounds affording thus, interesting magnetic properties such as long-range 3D magnetic ordering[14,15] and tentatively Single-Molecule Magnet (SMM)[16] or Single-Chain Magnet (SCM)[17] behaviours.

(c) In some cases, oxamato-based magnets present anionic open-framework structures,[14e,f,18] instead of the more common neutral ones.[14b–d] The anionic nature of the networks together with the presence of large channels make these systems suitable

candidates to obtain multifunctional materials. Indeed, different countercations could be rationally introduced into their pores, affording the required additional physical property.

(d) Last but not least, is the fact that oxamate ligands can be easily functionalised just by choosing the appropriate amine precursor (Scheme 1, bottom), allowing thus, an alternative route to induce new functionalities in the material such as chirality, luminescence, photo- or redox-activity, pH-triggered switches for the reversible formation of emulsions, and catalysts for environmentally friendly organic reactions.[19]

Therefore, since the pioneering work of Kahn and coworkers in the late 1980s,[20] a wide variety of oxamato-based bimetallic compounds, both discrete zero-dimensional (0D) high-nuclearity complexes[21] as well as extended one- (1D),[22] two- (2D),[14b–g] or three-dimensional (3D)[15] coordination polymers with interesting and predictable magnetic properties have been reported. This is impressively demonstrated by the family of heterobimetallic CPs built from mononuclear copper(II) precursors containing polyalkyl-substituted *N*-phenyloxamate as ligands. Hereafter, we briefly develop our results on this topic in order to nicely illustrate some of the aforementioned advantages of the metalloligand strategy towards oxamate-based magnetic coordination polymers.

2.1 Single-chain magnetic behaviour in linear 1D CPs

The observation of slow magnetic relaxation and hysteresis effects in a cobalt(II)-nitronyl nitroxide radical chain[23a] which was not associated with a 3D ordering but having a purely 1D origin, the so-called Single-Chain Magnet behaviour (SCM)[23] has provided an experimental confirmation of the Glaubers' prediction[24] and opened exciting new perspectives for storing information in low-dimensional magnetic materials (see discussion below).

In order to prepare novel examples of SCMs, we designed an alternative synthetic strategy based on the use of sterically hindered dianionic oxamato-containing copper(II) mononuclear complexes (Scheme 1) as bis(bidentate) metalloligands (instead of the organic nitronyl nitroxide radicals) towards Co^{II} ions in aqueous solution. This approach resulted in an oxamato-bridged heterobimetallic cobalt(II)–copper(II) linear chain of formula $[CoCu(2,4,6\text{-}Me_3pa)_2(H_2O)_2]_n\cdot 4nH_2O$, where 2,4,6-$Me_3$pa = *N*-2,4,6-trimethylphenyloxamate (Fig. 1).[17] The combination in this 1D CP of highly anisotropic, *trans*-diaquabis(chelated) octahedral high-spin Co^{II} ions in the presence of the bulky trimethyl-substituted phenyl groups from the $[Cu^{II}(2,4,6\text{-}Me_3pa)_2]^{2-}$ precursor affords an Ising-type chain magnetic anisotropy and a large separations between adjacent chains. The minimisation of the interchain interactions in this Ising chain is most likely responsible for the observation of the SCM behaviour at a low blocking temperature ($T_B \approx 2$ K) for the first time in a bimetallic ferrimagnetic chain.

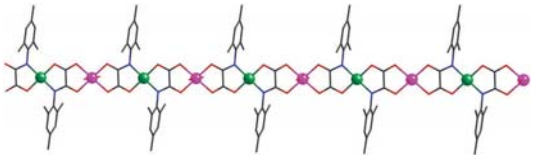

Fig. 1 View of a fragment of the chain $[CoCu(2,4,6\text{-}Me_3pa)_2(H_2O)_2]_n\cdot 4nH_2O$ showing the *trans* arrangement of the bulky trimethyl-substituted phenyl groups. The Cu^{II} and Co^{II} atoms are depicted as green and purple spheres, respectively.

2.2 Long-range magnetic ordering in 2D hexagonal and 3D decagonal CPs

By using the related pair of dianionic mononuclear copper(II) complexes $[Cu^{II}(Me_2pa)_2]^{2-}$ and $[Cu^{II}(Et_2pa)_2]^{2-}$ (2,6-Me_2pa = *N*-2,6-dimethylphenyloxamate and 2,6-Et_2pa = *N*-2,6-diethylphenyloxamate), as bis(bidentate) metalloligands towards Mn^{II} ions in dimethylsulphoxide (dmso) solution, two novel oxamato-bridged heterobimetallic 2D and 3D CPs of formulae $(n\text{-}Bu_4N)_4[Mn_4Cu_6(2,6\text{-}Me_2pa)_{12}]\cdot 2dmso$ (2D) and $(n\text{-}Bu_4N)_4[Mn_4Cu_6(2,6\text{-}Et_2pa)_{12}]$ (3D) [n-Bu_4N^+ = tetra-*n*-butylammonium cation] were obtained (Fig. 2).[15] Upon coordination, the corresponding $[Cu^{II}L_2]^{2-}$ precursor (L = 2,6-Me_2pa and 2,6-Et_2pa) transfers the steric information of its bulky dialkyl-substituted phenyl groups in a *trans* arrangement into the stereochemistries of the tris(chelated) Mn^{II} metal centres yielding two coordination polymers of different dimensionality [2D (L = 2,6-Me_2pa) and 3D (L = 2,6-Et_2pa)] as a result of the different steric effects introduced by the methyl and ethyl substituents in the phenyl ring.

The structure of the compound $(n\text{-}Bu_4N)_4[Mn_4Cu_6(2,6\text{-}Me_2pa)_{12}]\cdot 2dmso$ consists of anionic oxamato-bridged $Mn^{II}_2Cu^{II}_3$ hexagonal layers of 6^3 net topology growing in the crystallographic *ab* plane (Fig. 2a). Within each bimetallic hexagonal ring, the chirality of the tris(chelated) octahedral Mn^{II} ions follows the '$\Delta\Lambda$' sequence.

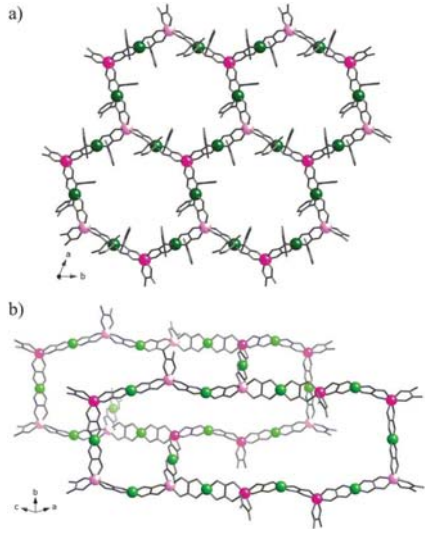

Fig. 2 Perspective view of a fragment of $(n\text{-}Bu_4N)_4[Mn_4Cu_6(Me_2pma)_{12}]\cdot 2dmso$ (a) and $(n\text{-}Bu_4N)_4[Mn_4Cu_6(Et_2pma)_{12}]$ (b). Metal and ligand atoms are represented by balls and sticks, respectively [Cu, green; (Δ)-Mn, purple; (Λ)-Mn, pink].

Each $Mn^{II}_2Cu^{II}_3$ hexagonal layer can be alternatively described as an extended parallel array of oxamato-bridged manganese(II)–copper(II) chains which are further connected by additional bis(bidentate) copper(II) precursors.

In contrast, the structure of $(n\text{-}Bu_4N)_4[Mn_4Cu_6(Et_2pma)_{12}]$ is made up of an anionic oxamato-bridged $Mn^{II}_2Cu^{II}_3$ 3D decagonal network with a 10^3-ths net topology (Fig. 2b). Within each $Mn^{II}_2Cu^{II}_3$ decagonal ring, the chirality of the tris(chelated) octahedral Mn^{II} ions follows the '*ΔΔΔΔ*' sequence. This unprecedented situation leads to an overall achiral $Mn^{II}_2Cu^{II}_3$ decagonal framework which results from the existence of two different bis(bidentate) copper(II) precursors connecting the Mn^{II} centres of the same (*Δ*-Mn-*Δ*-Mn and *Λ*-Mn-*Λ*-Mn) and opposite (*Δ*-Mn-*Λ*-Mn) chiralities.

As expected from the different dimensionality in these compounds, their magnetic properties differ drastically. However, although both 2D and 3D CPs exhibit magnetic ordering, the values of the Curie temperature (T_C) are quite different. So, a long-range ferromagnetic ordering occurs in the compound $(n\text{-}Bu_4N)_4[Mn_4Cu_6(Me_2pma)_{12}]\cdot 2dmso$ which results from the weak (most likely dipolar) ferromagnetic interactions between the ferrimagnetic $Mn^{II}_2Cu^{II}_3$ hexagonal layers at T_C = 10 K. In contrast, the intrinsically three-dimensional character of the complex $(n\text{-}Bu_4N)_4[Mn_4Cu_6(Et_2pma)_{12}]$ allows the observation of a long-range ferrimagnetic order of the $Mn^{II}_2Cu^{II}_3$ decagonal net at a somewhat greater value of the critical temperature (T_C = 25 K).

In summary, we have shown some previous results of oxamato-based CPs that highlight the interesting magnetic properties that these bridging ligands can afford. It deserves to be noted that additional physical properties have been rationally introduced in these systems only very recently providing the first examples of oxamato-based MMCPs.[25–29] Indeed, the variety of multifunctional magnetic behaviours reported in this review, ranging from optically-active chiral and luminescent magnets to porous magnets, illustrates the potential of oxamato-based heterobimetallic coordination polymers in the field of MMCPs. Let us briefly develop all these topics in the following sections by including a proposal of the main objectives and application domains for each type of oxamato-based MMCPs.

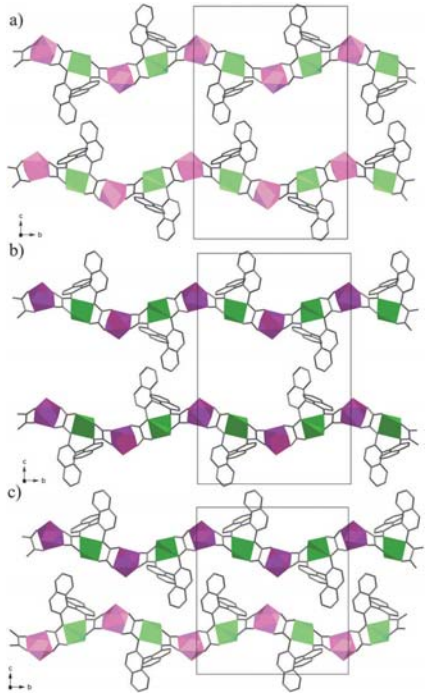

Fig. 3 Views of the crystal packing of the chains of $[(M)\text{-}Cu^{II}\text{-}(\Lambda)\text{-}Mn^{II}]_n$ (a), $[(P)\text{-}Cu^{II}\text{-}(\Delta)\text{-}Mn^{II}]_n$ (b) and the racemic compound (c) in the crystallographic *bc* plane. Hydrogen atoms and crystallization solvent molecules have been omitted for clarity. The $(\Lambda)\text{-}Mn^{II}$ and $(\Delta)\text{-}Mn^{II}$ atoms are depicted as pale and dark purple polyhedra respectively, whereas the $(M)\text{-}Cu^{II}$ and $(P)\text{-}Cu^{II}$ atoms are drawn as pale and dark green polyhedra.

3. Optically-active chiral magnets

3.1 Single-chain magnetic behaviour in enantiopure zigzag 1D CPs

Among the molecule-based low-dimensional magnetic materials, the aforementioned 1D coordination polymers exhibiting slow magnetic relaxation below a blocking temperature (T_B) are particularly appealing to get MMCPs. These compounds, which are called Single Chain Magnets (SCMs)[17,23] by analogy to the single molecule magnets (SMMs),[16,30] offer the great advantage of achieving information storage at higher temperatures. In fact, SMMs have a high-spin (S) ground state with an important Ising-type magnetic anisotropy (D) that results in a large activation energy (E_a) for the magnetisation reversal, given by $E_a = |D|S^2$ (for an integer S). In the case of SCMs, the activation energy also depends upon the intrachain magnetic coupling (J) according to the expression $E_a = (4|J|+|D|)S^2$. That being so, many groups have focused their efforts on the search for SCMs instead of SMMs because of the possibility of increasing the value of T_B by enhancing the intrachain interactions and thus opening the way to future applications of molecular nanomagnets in nanoscience and nanotechnology.[31]

After the publication in 2001 of the first example reported by Gatteschi *et al.*,[23a] which still exhibits the highest blocking temperature observed so far ($T_B \approx 15$ K), some additional examples of SCMs were published during the following years because of the possibility of storing information in these low-dimensional magnetic materials. However, regarding the relatively wide variety of examples of SCMs published until 2010,[17,23] none of them showed another physical property in addition to the magnetic one. So, for instance, the combination of slow magnetization relaxation effects (characteristic of SCMs) and optical properties (typical of chiral organic compounds) opens new exciting perspectives for storing information in the domain of MMCPs.

In a recent work,[25] we proposed for the first time a rational enantioselective synthetic strategy to obtain chiral heterobimetallic chains based on the use of sterically-hindered, chiral dianionic mononuclear copper(II) complexes with the enantiomerically pure (*M*)-1,1′-binaphtalene-2,2′-bis(oxamate)

[(*M*)-binaba] and (*P*)-1,1′-binaphtalene-2,2′-bis(oxamate) [(*P*)-binaba] ligands (Scheme 1). This pair of *M* and *P* helical-type mononuclear copper(II) enantiomers, [Cu[(*M*/*P*)-binaba]]$^{2-}$ (Scheme 1), acting as bis(bidentate) metalloligands towards doubly *cis*-solvated (S = dmso and dmf), divalent transition metal cations like manganese(II) and cobalt(II), transfer their chiral information to the stereochemistry of the octahedral M^{II} metal centres (*Λ* and *Δ* propeller-type enantiomers) in a controlled manner and consequently, a predetermination of the absolute configuration of the final $Cu^{II}M^{II}$ chain could be achieved.[32] Indeed, enantiopure chiral chains of general formula $MCuL(S)_m(H_2O)_n{\cdot}aS{\cdot}bH_2O$ made up by the repetition of the corresponding neutral chiral (*M*)-Cu^{II}-(*Λ*)-M^{II} and (*P*)-Cu^{II}-(*Δ*)-M^{II} units (Fig. 3a and b) were obtained when using the mononuclear (*M*)- and (*P*)-copper(II)–binaba complexes, respectively. In contrast, when using the racemic mononuclear copper(II)–binaba complex, an achiral zigzag $Cu^{II}M^{II}$ chain was obtained, consisting of alternating (*M*)-Cu^{II}-(*Λ*)-M^{II}-(*P*)-Cu^{II}-(*Δ*)-M^{II} units (Fig. 3c). Therefore, this molecular-programmed approach allowed the rational preparation of enantiopure chiral and racemic achiral, oxamato-bridged heterobimetallic chains. CD spectra of the heterobimetallic chain compounds confirmed the absolute configuration of the chiral metal centres in each case, by the occurrence of large, either negative or positive Cotton effects for the enantiopure chains of opposite chirality and conversely, by their absence in the racemic achiral ones (Fig. 4a).

Indeed, the enantiopure $Co^{II}Cu^{II}$ chains showed slow magnetic relaxation effects that are typical of SCMs, as revealed by the presence of a frequency-dependent peak around T_B = 2.0 K in the out-of-phase alternating current (ac) magnetic susceptibility measurements at very low temperatures (Fig. 4b). Certain structural (steric) as well as electronic (magnetic anisotropy) requirements on both the organic ligand and the divalent metal ion respectively, must be fulfilled in order to observe this phenomenon. So, the bulky 1,1′-binaphtalene organic spacer of the (*M*/*P*/*rac*)-binaba ligand allows a good separation between neighbouring chains while the oxamato bridge transmit efficiently the antiferromagnetic interaction between the copper(II) and cobalt(II) ions. Moreover, the large local magnetic anisotropy of the orbitally degenerate octahedral high-spin Co^{II} ions is ultimately responsible for the occurrence of a large Ising-type magnetic anisotropy along the chain. In the case of the racemic $Co^{II}Cu^{II}$ analogue, the interchain magnetic interactions preclude the observation of the SCM behaviour.

Hence, slow relaxation of the magnetisation was observed in the chiral $Co^{II}Cu^{II}$ derivatives for the first time in enantiopure magnetic chain compounds, constituting thus the first examples of a new class of MMCPs, referred to as chiral single chain magnets (CSCMs). Interestingly, the presence of an additional frequency-independent peak below the blocking temperature suggests the occurrence of a long-range 3D antiferromagnetic order of the chains, which are not perfectly isolated in the crystal lattice (Fig. 4b). However, the greater magnitude of the interchain magnetic interactions precludes the observation of slow magnetic relaxation effects in the case of the racemic $Co^{II}Cu^{II}$ chain. The large magnetic moment due to the CSCM behaviour of the one-dimensional array of magnetic ions, which are also

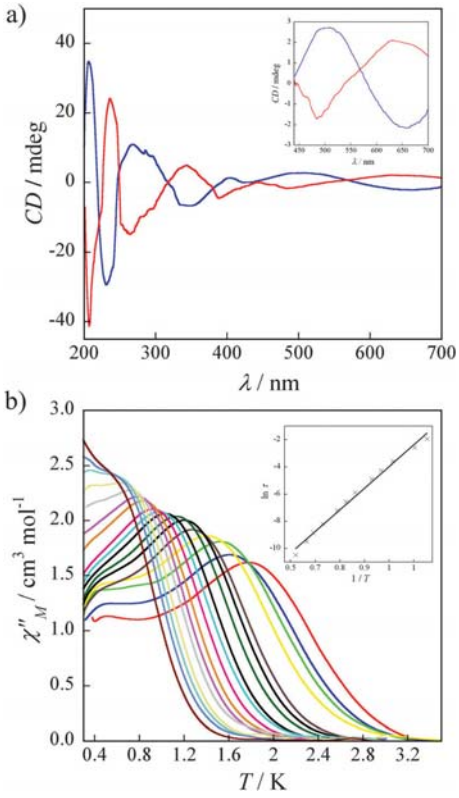

Fig. 4 (a) Solid CD spectra of the $[(M)\text{-}Cu^{II}\text{-}(\Lambda)\text{-}Co^{II}]_n$ (blue) and $[(P)\text{-}Cu^{II}\text{-}(\Delta)\text{-}M^{II}]_n$ (red) chains. The inset shows the CD spectra in the visible region. (b) Temperature dependence of the out-of-phase magnetic susceptibility of the $[(M)\text{-}Cu^{II}\text{-}(\Lambda)\text{-}Co^{II}]_n$ chain under zero applied static field at different frequencies (0.021–5700 Hz) of the ±1 G oscillating field. The inset shows the Arrhenius plot.

the chiral centres, ensures a strong coupling effect between the two physical properties, thus opening excellent perspectives to study for the first time the magnetochiral dichroism effect (see discussion below) in enantiopure 1D compounds with a higher T_B.[33]

3.2 Chiral cation-templated solid-state aggregation of enantiopure 1D double-helical CPs

Optically active, chiral magnets have given rise to interesting magneto-chiral dichroic effects[11c,33] because of the coexistence of asymmetry and magnetic ordering. In addition, the presence of non-centrosymmetric space groups can lead to interesting ferroelectric properties[11b,34] as well as non-linear optics (NLO).[35] However, it is not always possible to obtain the desired chiral magnets when using chiral templating cations because of the problems related to the fact that a chiral induction from the cation to the stereochemistries of the metal ions from the covalent framework is not always guaranteed. By the way, all the efforts devoted to the synthesis of chiral oxamato-based 3D CPs had been unsuccessful until very recently.

In that sense, the use of the anionic double-stranded dicopper(II) complex, $[Cu_2(mpba)_2]^{4-}$ [mpba = *N*,*N*′-1,3-phenylenebis(oxamate)] (Scheme 1), as tetrakis(bidentate) metalloligand towards bis(chelated) M^{2+} ions (M = Mn and Co) yields neutral achiral oxamato-based 1D or 2D CPs with either "ladderlike" or "brick-wall" topologies,[14b–g] respectively, even in the presence of chiral templating cations.

In order to achieve the first oxamato-based chiral 3D magnet, we explored a new rational synthetic strategy based on the use of the templating chiral (*S*)-trimethyl(1-phenyl-ethyl)ammonium cation, [(*S*)-(1-PhEt)Me_3N^+], together with the oxalate dianion during the self-assembly process of $[Cu^{II}(mpba)_2]^{4-}$ with Mn^{2+} ions. This reaction led to a novel chiral manganese(II)–copper(II) 3D compound of formula [(*S*)-(1-PhEt)Me_3N]$_2$[$Mn_2(C_2O_4)Cu_2(mpba)_2(H_2O)_2$]·3$H_2O$ (Fig. 5).[26] Its crystal structure consists of a mixed oxalato/oxamato-based heterobimetallic chiral 3D open-framework with small square and large octagonal pores of approximate dimensions 0.70 × 0.70 nm and 1.75 × 1.75 nm respectively, which are occupied by the (*S*)-(1-PhEt)Me_3N^+ countercations and crystallisation water molecules (Fig. 5). Interestingly, the anionic 3D network possesses a unprecedented binodal 3,4-connected [$(4{\cdot}6{\cdot}8)_2(4^2{\cdot}6{\cdot}8^2{\cdot}10)$]-net topology when considering the dicopper(II) units and the manganese(II) ions as four- and three-fold nodes, respectively (Fig. 6).

The anionic 3D network of the compound [(*S*)-(1-PhEt)Me_3N]$_2$-[Mn_2(ox)Cu_2(mpba)$_2$(H_2O)$_2$]·3H_2O can be alternatively described as an extended array of neutral oxamato-bridged manganese(II)–copper(II) double helical chains running parallel to the crystallographic *c* axis, which are further interconnected by the oxalate group acting as a bis-bidentate linker between two manganese(II) ions of the neighbouring double helical chains (Fig. 6a). Within each double helix, the pair of $Mn^{II}Cu^{II}$ chains related by a 4_1 axis is interconnected through the two *m*-phenylenediamidate bridges between the Cu^{II} ions, which would act as "bridge tights" (Fig. 6b). The shape of these right-handed double-stranded helices is reminiscent of that found for the well-known A-DNA double helix, where the two *m*-phenylene spacers stack each other in a similar way to that observed for the nucleobases in the DNA double helix. Most likely, the weak intermolecular (van der Waals and/or electrostatic) interactions between the (*S*)-(1-PhEt)Me_3N^+ guest cations and the anionic 3D host network (Fig. 5a) account for the right-handness chirality of the constituting double helices, so that the use of (*R*)-(1-PhEt)Me_3N^+ guest cations would lead to an identical anionic 3D host network but having double helices of left-handness chirality. These chiral cation templating effects would be also responsible for the formation of chiral double helices instead of the aforementioned achiral ladders[14b–g] as constituting units of the anionic 3D network.

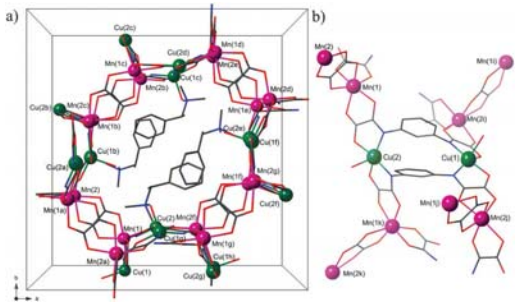

Fig. 5 (a) Perspective view of the unit cell of [(*S*)-(1-PhEt)Me_3N]$_2$[Mn_2(ox)Cu_2-(mpba)$_2$(H_2O)$_2$]·3H_2O with the metal atom labelling showing the filling of the octagonal pores by the countercations. (b) View of a fragment of [(*S*)-(1-PhEt)Me_3N]$_2$[Mn_2(ox)Cu_2(mpba)$_2$(H_2O)$_2$]·3H_2O with the numbering of the metal ions.

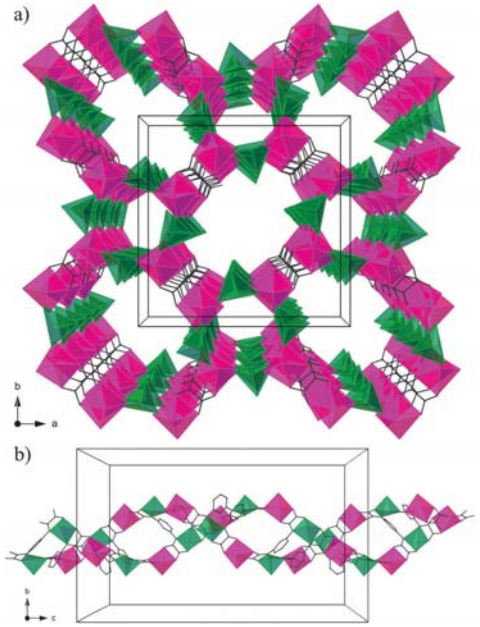

Fig. 6 (a) Perspective view of the anionic 3D network of [(*S*)-(1-PhEt)Me_3N]$_2$[Mn_2(ox)Cu_2(mpba)$_2$(H_2O)$_2$]·3H_2O along the crystallographic *c* axis. (b) View of a fragment of the double helical chain motif of [(*S*)-(1-PhEt)Me_3N]$_2$[Mn_2(ox)Cu_2(mpba)$_2$(H_2O)$_2$]·3H_2O along the crystallographic *c* axis. Metal and ligand atoms are represented by polyhedra and sticks, respectively (Cu, green; Mn, purple). Hydrogen atoms, countercations and crystallization water molecules are omitted for clarity.

The direct current (dc) magnetic susceptibility measurements of [(*S*)-(1-PhEt)Me_3N]$_2$[Mn_2(ox)Cu_2(mpba)$_2$(H_2O)$_2$]·3H_2O revealed a typical 1D ferrimagnetic behaviour at high temperatures resulting from the strong antiferromagnetic intrachain interactions between the Mn^{II} and Cu^{II} ions through the oxamato bridge within the double helical chain. At low temperatures, however, the moderately strong antiferromagnetic interchain interaction between the Mn^{II} ions of neighbouring double helical chains through the oxalate bridge dominates over the weak ferromagnetic intrachain interactions between the Cu^{II} ions through the double *m*-phenylene bridge within the double helical chains. Nevertheless, no evidence of long-range 3D magnetic ordering above 2.0 K was found from the low-temperature heat capacity measurements.

4. Dynamic porous magnets

4.1 Multifunctional switching in a 3D square/octagonal coordination polymer with sponge-like dynamic behaviour

The concept of "molecular magnetic sponges", referring to the exotic sponge-like behaviour of certain molecule-based materials that undergo a dramatic change of their magnetic properties upon reversible dehydration–rehydration processes, was introduced for the first time in 1999 by Olivier Kahn.[36a] This was exemplified by the compound of formula $[CoCu(obbz)(H_2O)_4]\cdot 2H_2O$[36b] [obbz = oxamidato-*N*,*N*′-bis(2-benzoate)], which is able to reversibly release and uptake five water molecules, switching from a non-magnetic ground state in the hydrated phase to as a hard magnet in the dehydrated one.

In a recent work, we obtained a novel oxamato-based manganese(II)–copper(II) 3D CP of formula $[Na(H_2O)_4]_4\{Mn_4[Cu_2(mpba)_2(H_2O)_4]_3\}\cdot 56.5H_2O$ by the reaction of $Na_4[Cu_2(mpba)_2]\cdot 10H_2O$ and $Mn(NO_3)_2\cdot 4H_2O$ in water.[27] This new example of MMCP exhibits a reversible solvent-induced optical, mechanical, and magnetic switching between a high- and a low-temperature ferromagnetic ordered phase upon loss of all the water molecules to give the amorphous dehydrated derivative of formula $Na_4[Mn_4Cu_6(mpba)_6]$. Under identical conditions, however, the reaction of $Na_4[Cu_2(mpba)_2]\cdot 10H_2O$ and $Co(NO_3)_2\cdot 4H_2O$ in water gave the oxamato-based cobalt(II)–copper(II) 2D CP of formula $[Co_2Cu_2(mpba)_2(H_2O)_4]$, which exhibits a metamagnetic behaviour with a field-induced transition from an antiferro- to a ferromagnetic ordered state.[14b]

The anionic 3D network of $[Na(H_2O)_4]_4\{Mn_4[Cu_2(mpba)_2(H_2O)_4]_3\}\cdot 56.5H_2O$ can be best described as an extended parallel array of oxamato-bridged manganese(II)–copper(II) layers with a mixed square/octogonal ($4\cdot 8^2$) net topology, which are further interconnected through two *m*-phenylene spacers between the copper(II) ions, acting as pillars in an alternately up and down disposition, to give a trinodal (3,4,4) net with a $(6^3)(6^4\cdot 8^2)(6^4\cdot 8\cdot 10)$ topology (Fig. 7a). Overall, this situation leads to a bimodal pore size distribution, with small square and large octagonal pores of approximate dimensions 1.2 × 1.2 nm and 2.1 × 3.0 nm respectively, which are occupied by the coordinated Na^I countercations and a large amount of both coordinated and hydrogen-bonded water molecules (Fig. 7b). The estimated empty volume without the crystallization water molecules is 13 580 Å^3, a value which represents up to *ca.* 70% of potential void per unit cell volume [V = 19 746(6) Å^3].

A crystalline-to-amorphous-like transition from $[Na(H_2O)_4]_4\{Mn_4[Cu_2(mpba)_2(H_2O)_4]_3\}\cdot 56.5H_2O$ to $Na_4[Mn_4Cu_6(mpba)_6]$ occurs upon removal of all crystallisation and weakly coordinated water molecules by heating at 150 °C. This process is accompanied by a colour change of the crystals from bright to dark green and by a significant crystal contraction with an estimated change of volume of *ca.* 45% (Fig. 8a). This transformation is reversible as evidenced by the recovery of the original volume and bright green colour of the crystals under rehydration. This dynamic behaviour in flexible MOFs is a well-established phenomenon since the pioneering work of Kitagawa and Férey.[37,38] So, for instance, the well-known family of iron(III) or chromium(III) frameworks with aliphatic and aromatic dicarboxylates as organic bridging ligands (MIL-88A–D) undergoes a volume change of up to *ca.* 300% upon desolvation.[39]

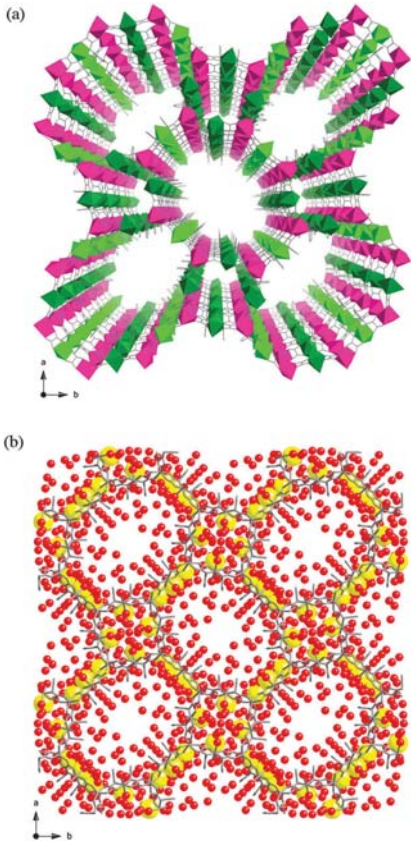

Fig. 7 (a) Perspective view of $Na_4[Mn_4Cu_6(mpba)_6(H_2O)_{12}]\cdot 72.65H_2O$ along the crystallographic *c* axis. Cu and Mn atoms are represented by green and purple octahedra, respectively. (b) Projection view of the crystal packing along the crystallographic *c* axis showing the filling of the small square and large octogonal pores of the open-framework structure by solvated sodium countercations (yellow spheres) as well as coordinated and free water molecules (red spheres).

Indeed, the combination of reversible optical and mechanical switching behaviours in this compound is a rare phenomenon, which was earlier observed in a 2D honeycomb copper(II) framework with polychlorinated triphenylmethyl tricarboxylate radicals as paramagnetic organic bridging ligands (MOROF-1).[40] The simultaneous and gradual colour change and volume expansion of the crystal during the rehydration process have been followed by optical microscopy (Fig. 8b). These solvent-induced breathing-type dynamic effects suggest a reversible collapse/reconstruction of the open-framework structure after water removal and retrieval from the pores, in agreement with the gas sorption studies. In this sense, the CO_2 and N_2 adsorption–desorption isotherms show almost no porosity, suggesting the collapse of the pore system upon dehydration.[41] On the other hand, the reversible colour change from bright to dark green is likely attributed to the

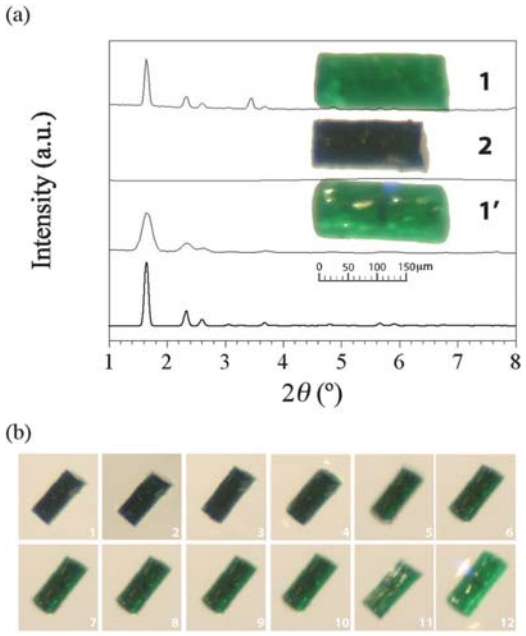

Fig. 8 (a) XRPD patterns of the hydrated (**1**), dehydrated (**2**), and rehydrated species (**1′**) at 25 °C along with the corresponding single-crystal optical microscopy images. The bold line corresponds to the calculated XRPD pattern of **1**. (b) Optical microscopy images of one single crystal of **2** taken every minute after immersion into water showing the colour and volume changes that accompany the rehydration process.

variation in the copper(II) surrounding from six- ($CuN_2O_2Ow_2$) to four-coordination (CuN_2O_2) upon removal of the two weakly bound axial water molecules, while the six-coordinate manganese(II) environment remains unchanged (MnO_6).

In addition to these solvent-triggered mechanical and optical changes, a drastic variation of the long-range ferromagnetic ordering temperature was also observed as a function of the water contents, as expected for a magnetic sponge. The alternating current (ac) magnetic susceptibility measurements confirm the occurrence of a long-range 3D ferromagnetic ordering at a critical temperature (T_c) of 22.5 K for the hydrated phase, this temperature being shifted to 2.3 K for the dehydrated derivative (Fig. 9). Moreover, a complete recovering of the long-range 3D ferromagnetic ordering is observed when rehydrating, thus confirming the reversible nature of the dehydration–rehydration processes. The drastic variation of the long-range ferromagnetic ordering temperature as a function of the water contents in this novel class of oxamato-based porous magnets with open metal sites and pore spaces offers fascinating possibilities in chemical sensing of small guest molecules (such as other coordinating solvents and gases), as we will show hereafter.

4.2 Selective gas and vapour sorption and magnetic sensing by a 3D square/octagonal coordination polymer

Among the variety of MMOPs, porous magnets – where the sorption properties coexist with a long-range magnetic ordering – have become one of the most challenging research fields for a great number of chemists, physicists, and materials scientists. The main goal with these materials is the modulation of the magnetic properties of the host open-framework by the inclusion of selected guests such as solvents or gases through physi- or chemisorption processes, opening thus the way for future applications of porous magnets as magnetic sensors for host–guest molecular sensing.[42]

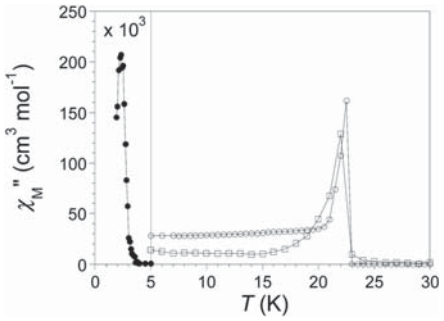

Fig. 9 Temperature dependence of the alternating current (ac) out-of-phase (χ'') magnetic susceptibility of the hydrated (○), dehydrated (●) and rehydrated (□) species.

By following the same preparative route described above to synthesize the magnetic sponge of formula $[Na(H_2O)_4]_4\{Mn_4[Cu_2(mpba)_2(H_2O)_4]_3\}\cdot 56.5H_2O$, we recently prepared an isoreticular analogue of formula $[Na(H_2O)_{3.25}]_4\{Mn_4[Cu_2(Me_3mpba)_2(H_2O)_{3.33}]_3\}\cdot 37H_2O$ [Me_3mpba = *N*,*N*′-2,4,6-trimethyl-1,3-phenylenebis(oxamate)] by the reaction of $Na_4[Cu_2(Me_3mpba)_2]\cdot 4H_2O$ and $Mn(NO_3)_2\cdot 4H_2O$ in water.[28] Unlike the related compound of formula $Na_4\{Mn_4[Cu_2(mpba)_2]_3\}$, the anhydrous phase $Na_4\{Mn_4[Cu_2(Me_3mpba)_2]_3\}$ exhibits selective gas and vapour sorption behaviour together with a drastic variation of the long-range magnetic properties as a function of the adsorbed guest, constituting thus the first example of a genuine 3D porous magnet in the family of the oxamato-based CPs.[14,15]

The anionic 3D pillared, square/octagonal networks of $[Na(H_2O)_{3.25}]_4\{Mn_4[Cu_2(Me_3mpba)_2(H_2O)_{3.33}]_3\}\cdot 37H_2O$ and $[Na(H_2O)_4]_4\{Mn_4[Cu_2(mpba)_2(H_2O)_4]_3\}\cdot 56.5H_2O$ are topologically identical but they have different shapes because of the regular or flattened nature respectively, of the octagonal circuits in each case, as nicely illustrated by Fig. 10. Moreover, the resulting open-framework structure in this novel analogue presents a trimodal pore size distribution with small square pores but two types of large octagonal pores (Fig. 10a), instead of the bimodal one found in the parent compound (Fig. 10b). These medium and wide octagonal channels with approximate diameters of 1.5 and 2.2 nm respectively, result from the distinct orientation of the trimethyl-substituted phenylene spacers pointing inwards or outwards of the channels (steric size effect).

The percentage of potential void space per unit cell volume in $[Na(H_2O)_{3.25}]_4\{Mn_4[Cu_2(Me_3mpba)_2(H_2O)_{3.33}]_3\}\cdot 37H_2O$ is lower than in $[Na(H_2O)_4]_4\{Mn_4[Cu_2(mpba)_2(H_2O)_4]_3\}\cdot 56.5H_2O$ (60 *vs.* 70%), as expected because of the additional presence of methyl group substituents and further supported by the

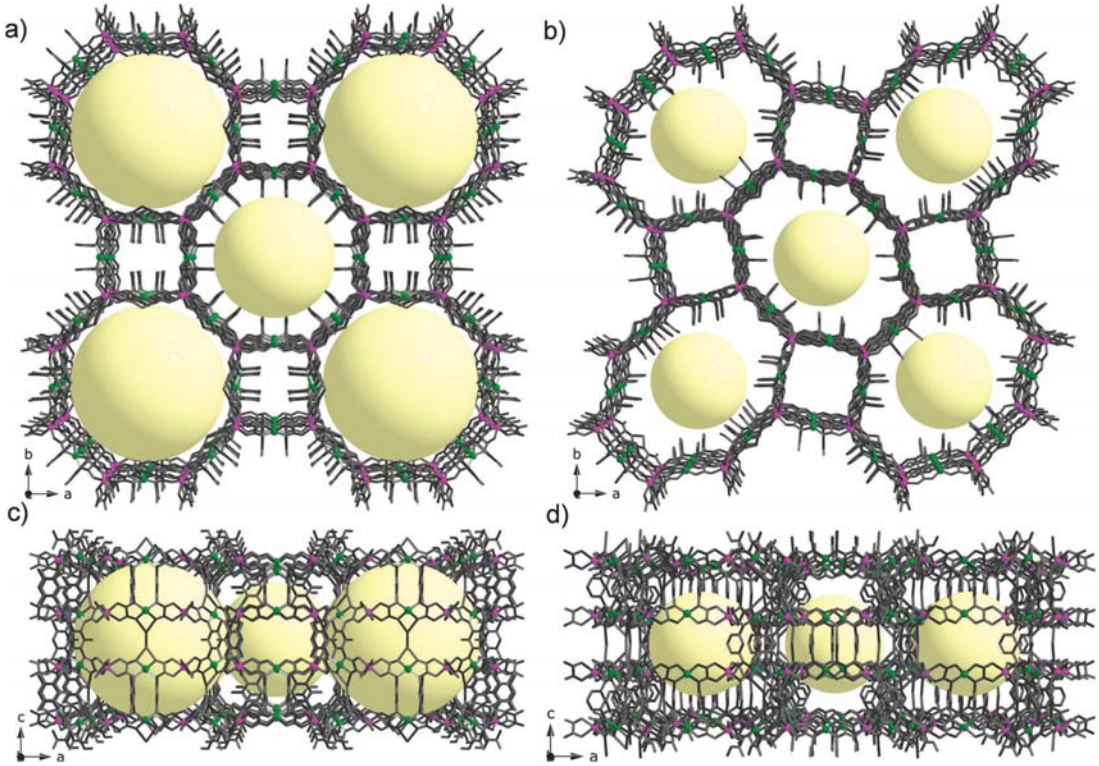

Fig. 10 Projection views of the crystal packing of $[Na(H_2O)_{3.25}]_4\{Mn_4[Cu_2(Me_3mpba)_2(H_2O)_{3.33}]_3\}\cdot 37H_2O$ (a and c) and $[Na(H_2O)_4]_4\{Mn_4[Cu_2(mpba)_2(H_2O)_4]_3\}\cdot 56.5H_2O$ (b and d) along the crystallographic *c* and *b* axes emphasizing the different pore size distribution of the octagonal pores of the open-framework structure (the void spaces are represented by pale yellow spheres). Metal and ligand atoms are represented by balls and sticks, respectively (Cu, green; Mn, purple).

smaller amount of crystallisation water molecules. However, the trimethyl-substituted derivative presents two clear differences with respect to the non-substituted one that can have a strong influence on their relative adsorptive properties: (i) larger diameters for the wide octagonal pores as a consequence of the different orientations of the phenylene spacers (which would be reflected in an increase of the accessible surface area of the MOF), and (ii) easier accessibility for the guest molecules to interact with the copper(II) ions within the wide octagonal channels since the phenylene spacers are pointing inwards the medium octagonal channels (Fig. 10a).

The accessible porosity of the anhydrous compound $Na_4\{Mn_4[Cu_2(Me_3mpba)_2]_3\}$ was also estimated by means of gas adsorption measurements, indicating a moderate CO_2–CH_4 gas selectivity.[28] This situation clearly contrasts with that previously found for $Na_4\{Mn_4[Cu_2(mpba)_2]_3\}$, where no gas or vapour sorption loadings were observed.[27] This dramatically different sorption behaviour was attributed to the larger accessible surface area present in $Na_4\{Mn_4[Cu_2(Me_3mpba)_2]_3\}$ and/or the possible collapse of the structure in $Na_4Mn_4[Cu_2(mpba)_2]_3$ under removal of the solvent water molecules. Other gas molecules like H_2 or N_2 were not adsorbed by $Na_4Mn_4[Cu_2(Me_3mpba)_2]_3$ at room temperature, suggesting that they do not interact with the host network and confirming thus the large selectivity of this system for the separation of small molecules.

Vapour adsorption-desorption isotherms showed a considerable adsorption of some solvents like water and methanol, whereas under similar conditions, no vapour adsorption was observed for other solvents such as ethanol or acetonitrile. This fact indicated a large selectivity for the sorption of small molecules by this compound and suggested that both the kinetic diameter and the interaction with the network play a key role in the sorption process. This large selectivity for small molecules and the growing interest in the development of energy efficient methods for the separation of azeotropic mixtures, led us to perform breakthrough experiments in a column packed with $Na_4\{Mn_4[Cu_2(Me_3mpba)_2]_3\}$. The results obtained in the separation of a liquid azeotropic CH_3CN/CH_3OH solvent mixture (79 : 21 v/v) revealed that CH_3CN eluted very fast from the column (retention time close to zero), while CH_3OH was strongly retained (retention time of 12.70 min) (Fig. 11).[28]

Finally, we also studied the influence of the sorption of small molecules in the overall magnetic behaviour. A paramagnetic to ferromagnetic phase transition was observed for the anhydrous phase $Na_4\{Mn_4[Cu_2(Me_3mpba)_2]_3\}$ at a rather low critical

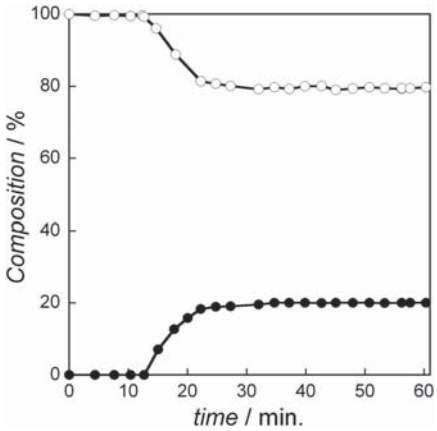

Fig. 11 Evolution of the CH_3OH (●) and CH_3CN (○) concentrations after feeding of a liquid azeotropic CH_3CN/CH_3OH mixture (79 : 21 v/v) through a column packed with the compound $Na_4\{Mn_4[Cu_2(Me_3mpba)_2]_3\}$.

temperature (T_C) of *ca.* 2.0 K, as revealed by both the alternating current (ac) magnetic susceptibility and direct current (dc) magnetisation measurements (Fig. 12). Interestingly, the value of the magnetic ordering temperature progressively shifts to higher values when solvents like methanol (T_C = 6.5 K) or water (T_C = 21 K) are adsorbed within the host framework. The observed variation in the magnetic behaviour for the different adsorbates was repeated for several cycles of solvent adsorption–desorption with identical results, thus supporting the reversible nature of the adsorption–desorption processes and the fast interconversion between the different adsorbates. The differences observed in the magnetic properties of the different adsorbates are likely related to the axial binding and their removal of the solvent molecules (H_2O or CH_3OH) from the first coordination sphere of the Cu^{II} ions.

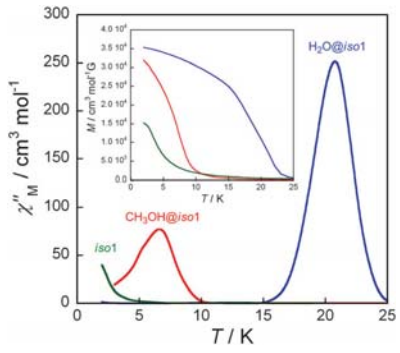

Fig. 12 Temperature dependence of the ac out-of-phase molar magnetic susceptibility (χ_M'') of ***iso1*** (green), **CH_3OH@*iso1*** (red), and **H_2O@*iso1*** (blue) with a ±4.0 G field oscillating at 1000 Hz. The inset shows the temperature dependence of the magnetization (M) of the three adsorbates.

The coexistence of a selective vapour and gas sorption behaviour and a solvent-dependent enhancement of the long-range magnetic ordering temperature allows for potential applications in magnetic sensing of small guest molecules for this new member of the family of porous magnets.[42,43]

5. Luminescent porous magnets

Among the wide variety of properties of interest that a given material can exhibit, luminescence attracts much attention due to its potential application in optical devices for lighting equipment and optical storage,[44a–c] optical switching,[44d,e] and sensing.[44f–i] In this respect, many groups are directing their effort towards the preparation of luminescent materials with potential sensing applications. For instance, sensitive and selective detection of gas and vapour phase analytes can be particularly interesting because of their variety of applications in many different fields.

5.1 Luminescence and magnetic sensing in a 2D double-hexagonal CP

In a recent work,[29] we synthesized a novel manganese(II)–copper(II) 2D compound of formula $MV[Mn_2Cu_3(mpba)_3(H_2O)_3]\cdot 20H_2O$, where MV^{2+} is the methylviologen dicationic dye.[45] This compound exhibits highly selective gas sorption ability, luminescence capacity, and long-range magnetic ordering, constituting thus a unique example of a luminescent porous magnet with potential applications in host–guest chemical sensing of small molecules. In fact, a unique optical and magnetic switching behaviour is observed accompanying reversible solvation–desolvation and gas sorption-desorption processes.

Its crystal structure consists of anionic 2D bimetallic networks made up of two adjacent oxamato-bridged $Mn^{II}_2Cu^{II}_3$ flat irregular hexagonal layers of [6^3] hcb topology that are interconnected through two *m*-phenylene spacers between the Cu^{II} ions along the crystallographic *b* axis (Fig. 13). These adjacent double hexagonal layers closely stack above each other yielding small nanopores, which are occupied by hydrogen-bonded arrays of crystallization water molecules and the methylviologen cations (Fig. 13). The estimated empty volume without the crystallization water molecules is 3179 Å^3, a value that represents up to *ca.* 43% of potential void per unit cell volume [V = 7414.7(18) Å^3]. The MV^{2+} cations are situated very close to the anionic heterobimetallic double layers, establishing weak intermolecular (van der Waals and/or electrostatic) interactions between their pyridinium–nitrogen and the carboxylate–oxygen atoms which are coordinated to the Cu^{II} ions (Fig. 13b). This situation results in an effective approach between the anionic metal–organic network and the organic cations which are responsible for the cation templating effects that lead to the adoption of a lower symmetry ('non-default') double layer 2D hexagonal architecture instead of the highest symmetry ('default') pillared 3D hexagonal one, where the two *m*-phenylene spacers between the Cu^{II} ions would act as pillars in an alternately up and down disposition. Moreover, these weak interactions between the anionic metal–organic network

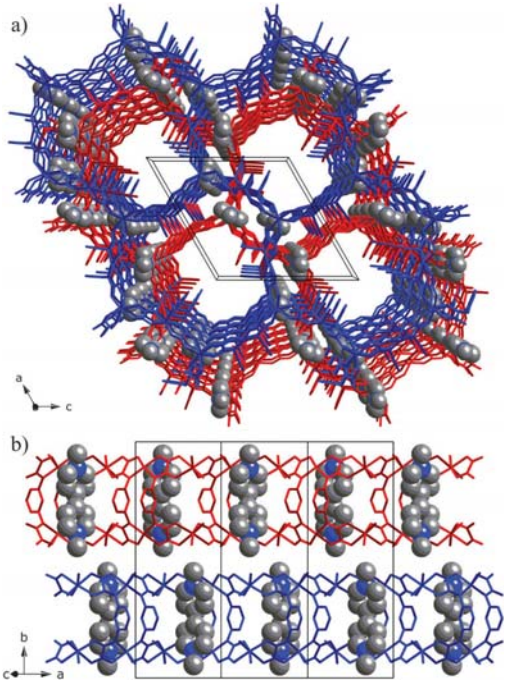

Fig. 13 Perspective views of the crystal packing of adjacent double layers of $MV[Mn_2Cu_3(mpba)_3(H_2O)_3]\cdot 20H_2O$ along the crystallographic *b* (a) and in the *ab* plane (b). The alternating A and B double layers are in red and blue colours, respectively. The MV^{2+} countercations are represented as space filling spheres. The solvent water molecules have been omitted for clarity.

and the organic cations would be ultimately responsible for the intriguing magnetic and luminescent sensing properties.

In fact, the study of the influence of the sorption of small molecules like solvent vapours and gases by this porous material revealed a unique magnetic and luminescent switching behaviour, which can be summarised as follows:

(i) The active anhydrous phase $MV[Mn_2Cu_3(mpba)_3]$ shows a long-range ferromagnetic ordering at a rather low critical temperature (T_C) of 2.0 K, as found earlier for related oxamato-based heterobimetallic manganese(II)–copper(II) magnets with a single layer hexagonal structure (see Section 2.2).[15] Upon solvent vapour adsorption, the magnetic ordering temperature progressively shifts towards higher values depending on the adsorbed guest molecule: MeOH ($T_C \approx 5.0$ K) and H_2O ($T_C \approx 19.0$ K). The observed variation in the magnetic behaviour along this series of adsorbates can be repeated for several cycles of solvent adsorption–desorption with identical results. This supports the reversible nature of the adsorption–desorption processes and the fast interconversion between the dehydrated phase and the two different adsorbates. The differences observed in their magnetic properties would be related to the presence of weak dipolar ("through-space") and/or hydrogen-bonded ("through-bond") magnetic interactions between adjacent double layers through the solvent molecules, as revealed by the crystal structure of the hydrated phase $MV[Mn_2Cu_3(mpba)_3(H_2O)_3]\cdot 20H_2O$, which are ultimately responsible for the long-range 3D ferromagnetic order of the weakly-interacting ferrimagnetic heterobimetallic double layers.[27–29]

(ii) The active anhydrous phase $MV[Mn_2Cu_3(mpba)_3]$ shows a bright UV and visible light emission at 330 and 586 nm (upon excitation at 225 and 400 nm, respectively), which makes it the first example of an oxamato-based luminescent magnet reported in the literature. The presence of highly ordered MV^{2+} cations filling the nanopores of this material afforded the observed luminescent properties. In fact, although MV^{2+} in solution does not fluoresce, a bright UV light emission at around 330 nm had been already reported when encapsulated in porous solids.[45] Herein, the dual UV and visible light emission is attributed to the MV^{2+} species interacting with the Cu^{II} ions.[45a] The most interesting feature, however, lies in the fact that a clear blue-shift of the lower energy visible emission from 586 to 544 nm occurs upon rehydration at 33% water loading (Fig. 14a). In addition, a good linear relationship is found between the shift in the emission wavelength and the degree of framework hydration. Similarly, a smaller but non-negligible blue-shift of the lower energy visible emission from 586 to 580 nm was observed when loading the anhydrous compound with methanol (data not shown). The observed solvent-induced variation of the luminescence properties strongly supports the occurrence of small changes in the Cu^{II}–MV^{2+} distance during the adsorption–desorption processes.

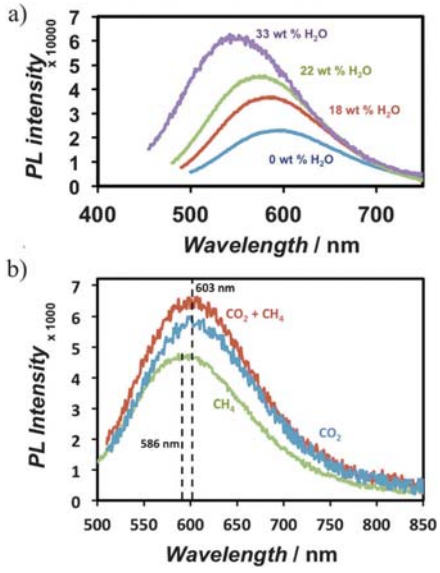

Fig. 14 (a) Emission spectra of **1** (λ_{exc} = 400 nm) during adsorption at different water loadings. (b) Emission spectra of the anhydrous derivative of $MV[Mn_2Cu_3(mpba)_3]$ in CH_4, CO_2 and an equimolar CO_2:CH_4 mixture at 1 bar.

(iii) The active anhydrous phase $MV[Mn_2Cu_3(mpba)_3]$ shows a relatively large and selective gas adsorption for CO_2 against CH_4, constituting thus a unique example of luminescent porous magnet. Challenged by these surprising results, additional emission studies were performed under different pure and mixture gas atmospheres. The corresponding emission spectra of the anhydrous phase $MV[Mn_2Cu_3(mpba)_3]$ under 1 bar of pure CH_4, 1 bar of pure CO_2, and 1.5 bar of a 1 : 1 CO_2/CH_4 mixture can be seen in Fig. 14b. The emission spectrum after CH_4 treatment still corresponds with that of the dehydrated framework, further demonstrating that CH_4 does not adsorb. In contrast, a considerable red-shift is observed when CO_2 is adsorbed. For a CO_2–CH_4 mixture, the results are similar to those obtained with pure CO_2. Since CH_4 does not adsorb on the dehydrated framework, the luminescence response to CO_2 is similar as for the single gas experiment, demonstrating that CO_2 can be detected in the presence of non-adsorbing gases (like methane or others). These results highlight the high selectivity of this material as a CO_2 sensor, even in the presence of other analytes. Another relevant feature of **1** is that the adsorption of CO_2 results in a clear red-shift emission, whereas the presence of H_2O and CH_3OH in the framework produces a blue-shift emission. This is likely due to the differences in the specific adsorption sites for CO_2, CH_3OH and H_2O and to the different adsorption capacity for these adsorbates. This difference in the response is very important, since it probes that this system is not only adsorption loading sensitive but also specific, allowing the identification of adsorbates and fulfilling thus, some of the key principles which were outlined by Kitagawa for its use in chemical sensing.[43b]

In summary, by combining the well-known emitting properties of the MV^{2+} cation guest with the magnetic properties of the oxamato-bridged bimetallic open-framework host with shape selective sorption behaviour, identification of small molecules is possible by direct observation of the host–guest interactions. The combination of these thrilling porous, optical, and magnetic properties makes it an ideal molecule-based multifunctional material for specific chemical sensing applications.[42,43]

6. Conclusions and outlook

The advantages that the well-known but barely used *N*-substituted aromatic oligo(oxamato) ligands can offer for the construction of MMCPs have been outlined in this feature article. Oxamato-based oligonuclear metal complexes, from mono- to di- and trinuclear species (see Scheme 1), can be used as metal–organic ligands (metalloligands) for the preparation of multidimensional *n*D (*n* = 1–3) coordination polymers (CPs) or metal–organic frameworks (MOFs) with interesting magnetic properties.

Additional physical properties can be introduced in these materials by means of either the ligand design or the appropriate choice of the required countercation, affording the first examples of oxamato-based multifunctional magnetic coordination polymers (MMCPs) which include: (i) optically-active chiral magnets (including the first example of enantiopure 1D chiral single-chain magnets); (ii) dynamic porous magnets; and (iii) luminescent porous magnets. Overall, these results show that the oxamate ligands constitute a rational and suitable alternative route to prepare molecule-based multifunctional magnetic materials, an avenue that inexplicably was rarely explored in the widespread field of porous coordination polymers (PCPs) or metal–organic frameworks (MOFs).[4–8]

Indeed, we feel that only a small fraction of the potentialities of oxamato-based MMCPs (those presented in this contribution) has been explored, most of the iceberg being still hidden beneath the surface. In an attempt to highlight the vast perspectives for the near future, let us briefly advance some of the very recent results issued from our two current research avenues in this area.

6.1 Electro- and photoactive CPs as magnetic sensors

PCPs are well-recognised for their use in gas storage and separation but, however, their applications for drug delivery, detoxification of radioactive and heavy metals and pesticides are much less explored. Moreover, there are relatively fewer reports on their capacity for tentatively acting as *magnetic sensors* through adsorption–desorption of specific guest molecules with reversible and dynamic changes of their open-framework structures and magnetic properties. In fact, the preparation of this type of dynamic porous magnets with a wide range of miscellaneous sensing applications presents some major challenges.

Our strategy for the design of a new family of dynamic porous magnets with potential applications as magnetic sensors is based on the use of oxamate-containing dicopper(II) complexes with π-conjugated aromatic spacers such as oligophenylene (OPs), oligophenyleneethyne (OPEs), oligoacenes (OAs), oligoacenoquinones (OAQs), oligophenylenevinylenes (OPVs), and oligoazobenzenes (OABs) (see Scheme 1), which can act as metalloligands toward first-row transition metal ions such as manganese(II), cobalt(II) and nickel(II) leading to the corresponding PCPs.

The strategy for the rational design of this new family of dynamic porous magnets for magnetic sensing is based on two advantages that the oxamate-based dicopper(II) metallacyclophane precursors may show, as mentioned in Section 2.1. On the one hand, we have demonstrated the unique ability of OPs and OPEs to act as ''molecular magnetic wires'' (MMWs), being efficient in the transmission of magnetic exchange interactions between the two metal centres separated by very long intermetallic distances in the corresponding oxamato-based dicopper(II) oligophenylenophanes and oligophenyleneethynophanes.[19b,e] On the other hand, the oxamato-based dicopper(II) oligoacenophanes and oligoacenoquinophanes act as ''molecular magnetic switches'' (MMSs), because of the non-innocent character of the aromatic spacers as regarding their photo- or electroactive character.[19d,g] Thus, they would present two metastable states ('ON/OFF') with totally different magnetic properties which can be reached in a reversible manner through photochemical or redox processes. The spins of the magnetic centres are ferromagnetically coupled in one of the states ('ON'),

whereas they are antiferromagnetically coupled or magnetically isolated in the other state ('OFF').

Indeed, the design and synthesis of exchange-coupled, oxamato-based dicopper(II) complexes exhibiting a magnetic bistable behaviour is a corner stone in the building of dynamic porous magnets for chemical sensing because the changes in the magnetic properties of the host framework can be used to monitor the binding and/or transformation of the organic guest. Several points should be considered in order to obtain a new family of magnetic sensors of the host–guest type depending on the nature of the target chemical sensing application.

Firstly, we plan the synthesis of neutral oxamato-bridged heterobimetallic 2D CPs with rod-like OP and OPE spacers as dynamic porous magnets for gas storage and separation, as those reported earlier for the permethylated derivative of the shorter dicopper(II) paracyclophane possessing a brick-wall architecture (Fig. 15a).[14b,c] So, the systematic variation of the length of the aromatic spacers of the oxamate-containing dicopper(II) precursors can modulate the size of the channels which in the last term, would afford a selective gas separation (Fig. 11). Moreover, the longer OP and OPE spacers, like 1,4-di(4-phenyl)phenylene and 1,4-di(4-phenylethynyl)phenylene, are suitable candidates to afford quite big channels with large storage capacity for gases with potential oxidising (O_2) or reducing (H_2) power.

So, for instance, our preliminary studies on the sorption properties of the oxamato-based manganese(II)–copper(II) 2D CPs with permethylated dicopper(II) paracyclophane cores show a unique magnetic switching behaviour after bromine gas adsorption. So a change from non-magnetic to magnetic layer ground state occurs upon Br_2 oxidation of the tetramethyl-substituted

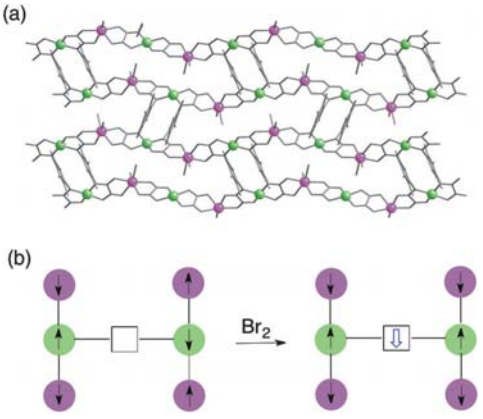

Fig. 15 (a) Crystal structure of $[Mn_2Cu_2(Me_4ppba)_2(H_2O)_4]_n \cdot nH_2O$ showing the neutral 2D rectangular layer of brick-wall architecture. Metal and ligand atoms are represented by balls and sticks, respectively (Cu, green; Mn, purple). (b) Proposed magnetic electroswitching in neutral oxamato-bridged 2D CPs built from redox-active, antiferromagnetically coupled dicopper(II) precursors acting as magnetic sensors of the 'host–guest' type for gas storage and separation.

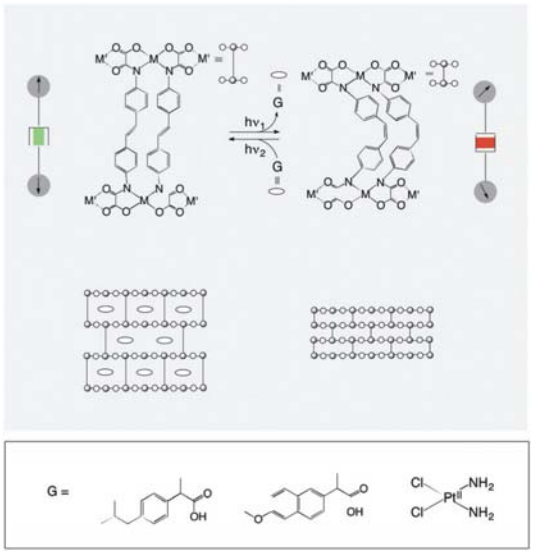

Fig. 16 Proposed photomagnetic switching in neutral oxamato-bridged 2D CPs built from photo-active, antiferromagnetically coupled dicopper(II) precursors acting as magnetic sensors of the 'host–guest' type for drug delivery.

p-phenylene spacers (Fig. 15b), as reported earlier for the dicopper(II) precursor itself,[19f] constituting thus a unique example of electroactive porous magnet which can be used as magnetic sensor.

Secondly, we also plan the synthesis of neutral oxamato-bridged heterometallic 2D coordination polymers with photo-active OPVs and OABs spacers as dynamic porous magnets for drug delivery, as depicted by Fig. 16. In this sense, the shorter OPV and OAB spacers such as stilbene and azobenzene are interesting candidates for small drugs storage and delivery by taking advantage of their well-known *cis–trans* photoisomerization to modulate the pore size upon irradiation ('photo-gated pores'). These include either non-steroidal anti-inflammatory organic drugs (ibuprofen, naproxen, aspirin, *etc.*) or metallo-organic molecules with pharmacological potential (*cis*-platine). In both cases, the spins of the metal centers are antiferromagnetically coupled in the planar *trans* isomer ('ON' state), whereas they are magnetically isolated in the non-planar *cis* one ('OFF' state). Indeed, these changes in the magnetic properties of the host framework can be used to monitor the binding of the organic guest (magnetic sensing).

Thirdly, we plan to investigate the ability of anionic oxamate-bridged heterobimetallic 3D CPs, as those earlier reported for the permethylated derivative of the shorter dicopper(II) metacyclophane possessing a pillared square/octagonal architecture (Fig. 10a and c) to act as selective ion exchangers for detoxification of radioactive (Cs, U and Th) and heavy metal (Pb and Hg) atoms, as depicted by Fig. 17. In fact, we have recently shown that the weakly coordinated Na^+ cations in the oxamate-bridged porous magnet of formula

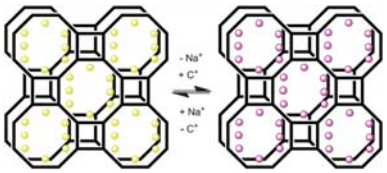

Fig. 17 Cation exchange approach for the replacement of sodium cations in the anionic oxamato-bridged 3D CPs built from ferromagnetically coupled dicopper(II) precursors with pollutant agents such as radioactive isotopes and heavy metals.

$[Na(H_2O)_4]_4\{Mn_4[Cu_2(Me_3mpba)_2(H_2O)_4]_3\}\cdot 56.5H_2O$ (Fig. 12) can be easily replaced by other alkaline (Li^+ or K^+) and alkaline-earth cations (Mg^{2+} or Ca^{2+}) as well as transition metal ions (Ni^{2+} or Co^{2+}) or lanthanide cations, with a concomitant change in the long-range magnetic ordering temperature.

6.2 Multifunctional chiral bio-coordination polymers

This last point, describing our current work with a novel family of bio-inspired carboxylate-functionalised oxamato ligands, deserves especial attention. Among the wide variety of physical properties that a MMCP can exhibit, those involving spatial asymmetry are especially appealing because of the intriguing properties associated to chirality. In this sense, MMCPs exhibiting chiro-optical and/or magnetic properties are a potentially new generation of chiral separation materials but have also relevant in the development of new classes of chiro-optical probes and magnetic sensors. Although we have already successfully prepared the first example of oxamato-based optically-active chiral 3D magnetic polymers (see Section 3.1.2), an accurate control of the final structure of the CP, and thus, of the chiral and magnetic properties, is still a challenge. This is particularly true from a synthetic point of view, since we cannot completely ensure the chiral induction from the cation to the stereochemistries of the metal ions by following the cation-assisted chiral-induction.[32]

In order to overcome these severe limitations, we are following the same synthetic strategy used in Section 3.1.1 which is based on the use of a new family of enantiopure, oxamato-based ligands derived from natural and non-natural amino acids (Scheme 2). The resultant anionic coordination networks could tentatively exhibit chirality and host a wide variety of functional cations in their channels giving rise to new classes of hybrid materials and multifunctional molecule-based magnets presenting new physical properties such as second-order optical nonlinearities, magnetochiral-dichroism or ferroelectricity.[33–35]

The methyl ethyl derivatives of the (*S*)- and (*R*)-*N*-oxalamino acids can be easily obtained in an enantiopure form from the reaction of the methyl ester derivatives of the corresponding amino acids with ethyl oxalyl chloride as shown in Scheme 2. The most remarkable point of this new generation of ligands together with their intrinsic chiral nature, lies in their great versatility as well as large variety of coordination modes they can adopt. For example, as a part of our preliminary work, we

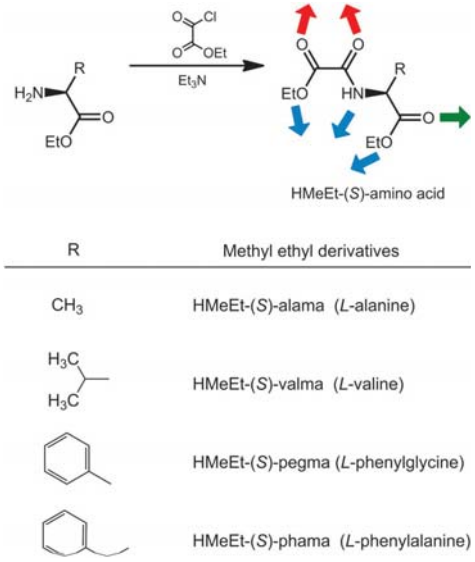

Scheme 2 Synthetic route for the preparation of the methyl ethyl derivatives of the chiral (*S*)-*N*-oxalamino acids as a function of the starting natural or not aminoacid precursors. The red, blue and green arrows represent the three different coordination modes of these versatile ligands.

reported how the Cu^{2+}-mediated self-assembly of the putative tridentate HMeEt-(*S*)- and HMeEt-(*R*)-valma proligands in basic aqueous solutions leads to the formation of two homochiral

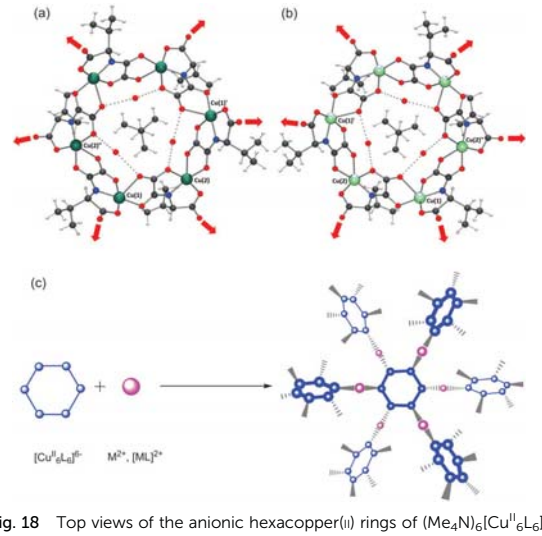

Fig. 18 Top views of the anionic hexacopper(II) rings of $(Me_4N)_6[Cu^{II}_6L_6]\cdot 7H_2O$ [L = (*S*)-valma (a) and (*R*)-valma (b)]. The metal atoms of A or C chirality are shown in deep and pale green colours, respectively. (c) Proposed structure of the 3D CP resulting from the self-assembly of the hexacopper(II) chiral rings and M^{2+} ions or square metal–organic cationic complexes.

anionic hexacopper(II) wheels of general formula $(Me_4N)_6[Cu^{II}_6L_6]\cdot 7H_2O$ [Me_4N^+ = tetramethylammonium cation; L = (*S*)-valma and (*R*)-valma] that crystallize in the same chiral space group *P*6(3) of the hexagonal system (Fig. 18).[46]

These polymetallic wheels present up to six free carbonyl groups from the valine residues at the outer rim (red arrows in Fig. 18) that can coordinate to other metal ions or coordinatively unsaturated metal complexes to afford high-dimensional PCPs. (Fig. 18). In addition, the chiral nature of the ligand itself which is transferred to the coordination spheres of the metal ions, allow us to predict that chiral CPs, with large chiral channels, could be obtained. This original two-step programmed method affords a better control of both the final architecture and the enantiopure nature of the resulting bio-CP.[47] Finally, these new chiral materials would provide fascinating possibilities in enantiomeric separation and could exhibit NLO and/or ferroelectric properties when a polar guest molecule is introduced.[33–35]

Acknowledgements

This work was supported by the MICINN (Spain) (Project CTQ2010-15364) and the Generalitat Valenciana (Spain) (Projects PROMETEO/2009/108, GV/2012/051 and ISIC/2012/002). T. G. thanks the Universitat de València for a predoctoral contract. Thanks are also extended to the MICINN Ramón y Cajal Program (E. P.) and 'Factoría de Cristalización' Consolider-Ingenio Project CSD2006-00015 (J. P.) for postdoctoral contracts. We acknowledge all the coworkers who have collaborated in this area and whose names appear in the reference list below. Particular thanks go to our colleagues from the groups of Drs Yves Journaux (Université Pierre et Marie Curie) and Jorge Gascon (Delft University of Technology), whose contributions and enthusiasm have been essential to the birth and further development of our research on oxamato-based multifunctional magnetic coordination polymers. We are especially thankful to Drs Rafael Ruiz-García and Joan Cano (Universitat de València) for unselfish help and continuous interest in this work.

Notes and references

1 O. Kahn, *Molecular Magnetism*, VCH, New York, USA, 1993.
2 (*a*) *Magnetism: A Supramolecular Function*, ed. O. Kahn, NATO ASI Series C, Kluwer, Dordrecht, Germany, 1995, vol. 484; (*b*) *Molecular Magnetism: From Molecular Assemblies to the Devices*, ed. E. Coronado, P. Delhaès, D. Gatteschi and J. S. Miller, NATO ASI Series E, Kluwer, Dordrecht, Germany, 1995, vol. 321; (*c*) *Supramolecular Engineering of Synthetic Metallic Materials*, ed. J. Veciana, C. Rovira and D. Amabilino, NATO ASI Series C, Kluwer, Dordrecht, Germany, 1999, vol. 518; (*d*) *Magnetism Molecules to Materials*, ed. J. S. Miller and M. Drillon, Wiley-VCH, Weinheim, Germany, 2001, vol. I–V; (*e*) *Multifunctional Molecular Materials*, ed. L. Ouahab, Pan Standford Publishing, Singapore, 2013; (*f*) *Electrons in Molecules. From Basic Principles to Molecular Electronics*, ed. J. P. Launay and M. Verdaguer, Oxford University Press, Oxford, United Kingdom, 2014.
3 (*a*) M. M. Turnbull, T. Sugimoto and L. K. Thompson, *Molecule-Based Magnetic Materials*, American Chemical Society, Washington, DC, 1996; (*b*) E. Coronado, F. Palacio and J. Veciana, *Angew. Chem., Int. Ed.*, 2003, **42**, 2570 and references therein.
4 C. Janiak and J. K. Vieth, *New J. Chem.*, 2010, **34**, 2366, and references therein.
5 B. F. Abrahams, B. F. Hoskins, D. M. Michail and R. Robson, *Nature*, 1994, **369**, 727.
6 S. Decurtins, H. W. Schmalle, P. Schneuwly and H. R. Oswald, *Inorg. Chem.*, 1993, **32**, 1888.
7 (*a*) G. De Munno, M. Julve, F. Nicolo, F. Lloret, J. Faus, R. Ruiz and E. Sin, *Angew. Chem., Int. Ed. Engl.*, 1993, **32**, 613; (*b*) G. De Munno, M. Julve, G. Viau, F. Lloret, J. Faus and D. Viterbo, *Angew. Chem., Int. Ed. Engl.*, 1996, **35**, 1748; (*c*) F. Lloret, G. De Munno, M. Julve, J. Cano, R. Ruiz and A. Caneschi, *Angew. Chem., Int. Ed.*, 1998, **37**, 135.
8 O. M. Yaghi, M. O'Keeffe, N. W. Ockwig, H. K. Chae, M. Eddaoudi and J. Kim, *Nature*, 2003, **423**, 705.
9 (*a*) D. Maspoch, D. Ruiz-Molina and J. Veciana, *Chem. Soc. Rev.*, 2007, **36**, 770; (*b*) M. Kurmoo, *Chem. Soc. Rev.*, 2009, **38**, 1353; (*c*) P. Dechambenoit and J. R. Long, *Chem. Soc. Rev.*, 2011, **40**, 3249.
10 (*a*) L. G. Beauvais and J. R. Long, *J. Am. Chem. Soc.*, 2002, **124**, 12096; (*b*) S. S. Kaye and J. R. Long, *J. Am. Chem. Soc.*, 2005, **127**, 6506; (*c*) S. S. Kaye, H. J. Choi and J. R. Long, *J. Am. Chem. Soc.*, 2008, **130**, 16921; (*d*) L. J. Murray, M. Dinca and J. R. Long, *Chem. Soc. Rev.*, 2009, **38**, 1294; (*e*) H. Tokoro and S.-I. Ohkoshi, *Dalton Trans.*, 2011, **40**, 6825; (*f*) S.-I. Ohkoshi and H. Tokoro, *Acc. Chem. Res.*, 2012, **45**, 1749.
11 (*a*) E. Pardo, C. Train, G. Gontard, K. Boubekeur, O. Fabelo, H. Liu, B. Dkhil, F. Lloret, K. Nakagawa, H. Tokoro, S.-I. Ohkoshi and M. Verdaguer, *J. Am. Chem. Soc.*, 2011, **133**, 15328; (*b*) E. Pardo, C. Train, H. Liu, L. M. Chamoreau, B. Dkhil, K. Boubekeur, F. Lloret, K. Nakatani, H. Tokoro, S.-I. Ohkoshi and M. Verdaguer, *Angew. Chem., Int. Ed.*, 2012, **51**, 8356; (*c*) C. Train, R. Gheorghe, V. Krstic, L. M. Chamoreau, N. S. Ovanesyan, G. L. J. A. Rikken, M. Gruselle and M. Verdaguer, *Nat. Mater.*, 2008, **9**, 729; (*d*) E. Coronado, J. R. Galán-Mascarós, C. J. Gómez-García and V. Laukhin, *Nature*, 2000, **408**, 447.
12 (*a*) S. R. Batten and R. Robson, *Angew. Chem., Int. Ed.*, 1998, **37**, 1460; (*b*) G. Férey, *Chem. Soc. Rev.*, 2008, **37**, 191; (*c*) N. L. Rosi, M. Eddaoudi, J. Kim, M. O'Keeffe and O. M. Yaghi, *CrystEngComm*, 2002, **4**, 401; (*d*) J. R. Long and O. M. Yaghi, *Chem. Soc. Rev.*, 2009, **38**, 1213, and references therein; (*e*) S. Kitagawa and R. Matsuda, *Coord. Chem. Rev.*, 2007, **251**, 2490; (*f*) D. Bradshaw, J. B. Claridhe, E. J. Cussen, T. J. Prior and M. J. Rosseinsky, *Acc. Chem. Res.*, 2005, **38**, 273.
13 (*a*) E. Pardo, R. Ruiz-García, J. Cano, X. Ottenwaelder, R. Lescouëzec, Y. Journaux, F. Lloret and M. Julve, *Dalton Trans.*, 2008, 2780; (*b*) M.-C. Dul, E. Pardo, R. Lescouëzec, Y. Journaux, J. Ferrando-Soria, R. Ruiz-García, J. Cano, M. Julve, F. Lloret, D. Cangussu, C. L. M. Pereira, H. O. Stumpf, J. Pasán and C. Ruiz-Pérez, *Coord. Chem. Rev.*, 2010, **254**, 2281.
14 (*a*) M. Verdaguer, O. Kahn, M. Julve and A. Gleizes, *Nouv. J. Chim.*, 1985, **9**, 325; (*b*) C. L. M. Pereira, E. F. Pedroso, H. O. Stumpf, M. A. Novak, L. Ricard, R. Ruiz-García, E. Rivière and Y. Journaux, *Angew. Chem., Int. Ed.*, 2004, **43**, 956; (*c*) J. Ferrando-Soria, J. Pasán, C. Ruiz-Pérez, Y. Journaux, M. Julve, F. Lloret, J. Cano and E. Pardo, *Inorg. Chem.*, 2011, **50**, 8694; (*d*) J. Ferrando-Soria, T. Grancha, J. Pasán, C. Ruiz-Pérez, L. Cañadillas-Delgado, Y. Journaux, M. Julve, J. Cano, F. Lloret and E. Pardo, *Inorg. Chem.*, 2012, **51**, 7019; (*e*) E. Pardo, D. Cangussu, M.-C. Dul, R. Lescouëzec, P. Herson, Y. Journaux, E. F. Pedroso, C. L. M. Pereira, M. C. Muñoz, R. Ruiz-García, J. Cano, P. Amorós, M. Julve and F. Lloret, *Angew. Chem., Int. Ed.*, 2008, **47**, 4211; (*f*) D. Cangussu, E. Pardo, M.-C. Dul, R. Lescouézec, P. Herson, Y. Journaux, E. F. Pedroso, C. L. M. Pereira, H. O. Stumpf, M. C. Muñoz, R. Ruiz-García, J. Cano, M. Julve and F. Lloret, *Inorg. Chim. Acta*, 2008, **361**, 3394; (*g*) H. O. Stumpf, L. Ouahab, Y. Pei, D. Grandjean and O. Kahn, *Science*, 1993, **261**, 447.
15 J. Ferrando-Soria, T. Grancha, M. Julve, J. Cano, F. Lloret, Y. Journaux, J. Pasán, C. Ruiz-Pérez and E. Pardo, *Chem. Commun.*, 2012, **48**, 3539.
16 E. Pardo, I. Morales-Osorio, M. Julve, F. Lloret, J. Cano, R. Ruiz-García, J. Pasán, C. Ruiz-Pérez, X. Ottenwaelder and Y. Journaux, *Inorg. Chem.*, 2004, **43**, 7594.
17 (*a*) E. Pardo, R. Ruiz-García, F. Lloret, J. Faus, M. Julve, Y. Journaux, F. S. Delgado and C. Ruiz-Pérez, *Adv. Mater.*, 2004, **16**, 1597;

(*b*) E. Pardo, R. Ruiz-García, F. Lloret, J. Faus, M. Julve, Y. Journaux, M. A. Novak, F. S. Delgado and C. Ruiz-Pérez, *Chem. – Eur. J.*, 2007, **13**, 2054; (*c*) J. Ferrando-Soria, E. Pardo, R. Ruiz-García, J. Cano, F. Lloret, M. Julve, Y. Journaux, J. Pasán and C. Ruiz-Pérez, *Chem. – Eur. J.*, 2011, **17**, 2176.

18 M.-C. Dul, R. Lezcouëzec, L. M. Chamoreau, Y. Journaux, R. Carrasco, M. Castellano, R. Ruiz-García, J. Cano, F. Lloret, M. Julve, C. Ruiz-Pérez, O. Fabelo and E. Pardo, *CrystEngComm*, 2012, **14**, 5639.

19 (*a*) I. Fernández, R. Ruiz, J. Faus, M. Julve, F. Lloret, J. Cano, X. Ottenwaelder, Y. Journaux and M. C. Muñoz, *Angew. Chem., Int. Ed.*, 2001, **40**, 3039; (*b*) E. Pardo, J. Faus, M. Julve, F. Lloret, M. C. Muñoz, J. Cano, X. Ottenwaelder, Y. Journaux, R. Carrasco, G. Blay, I. Fernández and R. Ruiz-García, *J. Am. Chem. Soc.*, 2003, **125**, 10770; (*c*) E. Pardo, R. Carrasco, R. Ruiz-García, M. Julve, F. Lloret, M. C. Muñoz, Y. Journaux, E. Ruiz and J. Cano, *J. Am. Chem. Soc.*, 2008, **130**, 576; (*d*) M. Castellano, J. Ferrando-Soria, E. Pardo, M. Julve, F. Lloret, C. Mathonière, J. Pasán, C. Ruiz-Pérez, L. Cañadillas-Delgado, R. Ruiz-García and J. Cano, *Chem. Commun.*, 2011, **47**, 11035; (*e*) J. Ferrando-Soria, M. Castellano, R. Ruiz-García, J. Cano, M. Julve, F. Lloret, J. Pasán, C. Ruiz-Pérez, L. Cañadillas-Delgado, Y. Li, Y. Journaux and E. Pardo, *Chem. Commun.*, 2012, **48**, 8401; (*f*) M. Castellano, R. Ruiz-García, J. Cano, M. Julve, F. Lloret, Y. Journaux, G. De Munno and D. Armentano, *Chem. Commun.*, 2013, **49**, 3534; (*g*) W. D. do Prim, W. X. C. Oliveira, M. A. Ribeiro, E. N. de Faria, I. F. Teixeira, H. O. Stumpf, R. M. Lago, C. L. M. Pereira, C. B. Pinheiro, J. C. D. Figueiredo-Júnior, W. C. Nunes, P. P. de Souza, E. F. Pedroso, M. Castellano, J. Cano and M. Julve, *Chem. Commun.*, 2013, **49**, 10778; (*h*) F. R. Fortea-Pérez, I. Schlegel, M. Julve, D. Armentano, G. De Munno and S. E. Stiriba, *J. Organomet. Chem.*, 2013, **743**, 102.

20 (*a*) Y. Pei, M. Verdaguer, O. Kahn, J. Sletten and J. P. Renard, *J. Am. Chem. Soc.*, 1986, **108**, 7428; (*b*) Y. Pei, M. Verdaguer, O. Kahn, J. Sletten and J. P. Renard, *Inorg. Chem.*, 1987, **26**, 138; (*c*) O. Kahn, Y. Pei, M. Verdaguer, J. P. Renard and J. Sletten, *J. Am. Chem. Soc.*, 1988, **110**, 782.

21 (*a*) B. Cervera, J. L. Sanz, M. J. Ibáñez, G. Vila, F. Lloret, M. Julve, R. Ruiz, X. Ottenwaelder, A. Aukauloo, S. Poussereau, Y. Journaux and M. C. Muñoz, *J. Chem. Soc., Dalton Trans.*, 1998, 781; (*b*) A. Aukauloo, X. Ottenwaelder, R. Ruiz, Y. Journaux, Y. Pei, E. Rivière, B. Cervera and M. C. Muñoz, *Eur. J. Inorg. Chem.*, 1999, 209; (*c*) A. Aukauloo, X. Ottenwaelder, R. Ruiz, S. Poussereau, Y. Pei, Y. Journaux, P. Fleurat, F. Volatron, B. Cervera and M. C. Muñoz, *Eur. J. Inorg. Chem.*, 1999, 1067; (*d*) K. E. Berg, Y. Pellegrin, G. Blondin, X. Ottenwaelder, Y. Journaux, M. M. Canovas, T. Mallah, S. Parsons and A. Aukauloo, *Eur. J. Inorg. Chem.*, 2002, 323; (*e*) X. Ottenwaelder, R. Ruiz-García, G. Blondin, R. Carrasco, J. Cano, D. Lexa, Y. Journaux and A. Aukauloo, *Chem. Commun.*, 2004, 504.

22 (*a*) Y. Pei, Y. Journaux, A. Dei, O. Kahn and D. Gatteschi, *J. Chem. Soc., Chem. Commun.*, 1986, 1300; (*b*) Y. Pei, Y. Journaux and O. Kahn, *Inorg. Chem.*, 1988, **27**, 399.

23 (*a*) A. Caneschi, D. Gatteschi, N. Lalioti, C. Sangregorio, R. Sessoli, G. Venturi, A. Vindigni, A. Rettori, M. G. Pini and M. Novak, *Angew. Chem., Int. Ed.*, 2001, **40**, 1760; (*b*) R. Clérac, H. Miyasaka, M. Yamashita and C. Coulon, *J. Am. Chem. Soc.*, 2002, **124**, 12837; (*c*) R. Lescouëzec, J. Vaissermann, C. Ruiz-Pérez, F. Lloret, R. Carrasco, M. Julve, M. Verdaguer, Y. Dromzée, D. Gatteschi and W. Wernsdorfer, *Angew. Chem., Int. Ed.*, 2003, **42**, 1483; (*d*) S. Wang, J.-L. Zuo, S. Gao, Y. Song, H.-C. Zhou, Y.-Z. Zhang and X.-Z. You, *J. Am. Chem. Soc.*, 2004, **126**, 8900; (*e*) R. Lescouëzec, L. M. Toma, J. Vaisermann, M. Verdaguer, F. S. Delgado, C. Ruiz-Pérez, F. Lloret and M. Julve, *Coord. Chem. Rev.*, 2005, **249**, 2691; (*f*) L. M. Toma, R. Lescouëzec, J. Pasán, C. Ruiz-Pérez, J. Pasán, J. Vaissermann, J. Cano, R. Carrasco, W. Wernsdorfer, F. Lloret and M. Julve, *J. Am. Chem. Soc.*, 2006, **128**, 4842; (*g*) E. Coronado, J. R. Galán-Mascarós and C. Martí-Gastaldo, *J. Am. Chem. Soc.*, 2008, **130**, 14987; (*h*) L. Bogani, A. Vindigni, R. Sessoli and D. Gatteschi, *J. Mater. Chem.*, 2008, **18**, 4750; (*i*) H. Miyasaka, M. Julve, M. Yamashita and R. Clérac, *Inorg. Chem.*, 2009, **48**, 3420; (*j*) H. L. Sun, Z. M. Wang and S. Gao, *Coord. Chem. Rev.*, 2010, **254**, 1081; (*k*) T. D. Harris, M. V. Bennett, R. Clérac and J. R. Long, *J. Am. Chem. Soc.*, 2010, **132**, 3980; (*l*) X. Feng, T. D. Harris and J. R. Long, *Chem. Sci.*, 2011, **2**, 1688; (*m*) D. P. Dong, T. Liu, S. Kanegawa, S. Kang, O. Sato, C. He and C. Y. Duan, *Angew. Chem., Int. Ed.*, 2012, **51**, 5119; (*n*) L. M. Toma, J. Pasán, C. Ruiz-Pérez, F. Lloret and M. Julve, *Dalton Trans.*, 2012, **41**, 13716; (*o*) H. Miyasaka, T. Madanbashi, A. Saitoh, N. Motokawa, R. Ishikawa, M. yamashita, S. Bahr, W. Wernsdorfer and R. Clérac, *Chem. – Eur. J.*, 2012, **18**, 3942; (*p*) L. M. Toma, C. Ruiz-Pérez, J. Pasán, W. Wernsdorfer, F. Lloret and M. Julve, *J. Am. Chem. Soc.*, 2012, **134**, 15265.

24 R. J. Glauber, *J. Math. Phys.*, 1963, **4**, 294.

25 (*a*) E. Pardo, C. Train, R. Lescouëzec, Y. Journaux, J. Pasán, C. Ruíz-Pérez, F. S. Delgado, R. Ruiz-García, F. Lloret and C. Paulsen, *Chem. Commun.*, 2010, **46**, 2322; (*b*) J. Ferrando-Soria, D. Cangussu, M. Eslava, Y. Journaux, R. Lescouëzec, M. Julve, F. Lloret, J. Pasán, C. Ruiz-Pérez, E. Lhotel, C. Paulsen and E. Pardo, *Chem. – Eur. J.*, 2011, **17**, 12482.

26 T. Grancha, C. Tourbillon, J. Ferrando-Soria, M. Julve, F. Lloret, J. Pasán, C. Ruíz-Pérez, O. Fabelo and E. Pardo, *CrystEngComm*, 2013, **15**, 9312.

27 J. Ferrando-Soria, R. Ruiz-García, J. Cano, S.-E. Stiriba, J. Vallejo, I. Castro, M. Julve, F. Lloret, P. Amorós, J. Pasán, C. Ruiz-Pérez, Y. Journaux and E. Pardo, *Chem. – Eur. J.*, 2012, **18**, 1608.

28 J. Ferrando-Soria, P. Serra-Crespo, M. de Lange, J. Gascon, F. Kapteijn, M. Julve, J. Cano, F. Lloret, J. Pasán, C. Ruiz-Pérez, Y. Journaux and E. Pardo, *J. Am. Chem. Soc.*, 2012, **134**, 15301.

29 J. Ferrando-Soria, H. Khajavi, P. Serra-Crespo, J. Gascon, F. Kapteijn, M. Julve, F. Lloret, J. Pasán, C. Ruiz-Pérez, Y. Journaux and E. Pardo, *Adv. Mater.*, 2012, **24**, 5625.

30 (*a*) R. E. P. Winpenny, *Adv. Inorg. Chem.*, 2001, **52**, 1; (*b*) D. Gatteschi and R. Sessoli, *Angew. Chem., Int. Ed.*, 2003, **42**, 268; (*c*) L. Thomas, F. Lionti, R. Ballou, D. Gatteschi, R. Sessoli and B. Barbara, *Nature*, 1996, **383**, 145; (*d*) J. R. Friedman, M. P. Sarachik, J. Tejada and R. Ziolo, *Phys. Rev. Lett.*, 1996, **76**, 3830; (*e*) C. Coulon, R. Clérac, L. Lecren, W. Wernsdorfer and H. Miyasaka, *Phys. Rev. B: Condens. Matter Mater. Phys.*, 2004, **69**, 132408.

31 D. Gatteschi, R. Sessoli and J. Villain, *Molecular Nanomagnets*, Oxford University Press, 2006.

32 J. Crassous, *Chem. Commun.*, 2012, **48**, 9687.

33 G. L. J. A. Rikken and E. Raupach, *Nature*, 1997, **390**, 493.

34 (*a*) K. Hashimoto, *Angew. Chem., Int. Ed.*, 2007, **46**, 3238; (*b*) P. Jain, V. Ramachandran, R. J. Clark, H. D. Zhou, B. H. Toby, N. S. Dalal, H. W. Kroto and A. K. Cheetham, *J. Am. Chem. Soc.*, 2009, **131**, 13625; (*c*) G.-C. Xu, W. Zhang, X.-M. Ma, Y.-H. Chen, L. Zhang, H.-L. Cai, Z.-M. Wang, R.-G. Xiong and S. Gao, *J. Am. Chem. Soc.*, 2011, **133**, 14948; (*d*) A. O. Polyakov, A. H. Arkenbout, J. Baas, G. R. Blake, A. Meetsma, A. Caretta, P. H. M. Loosdrecht and T. T. M. Palstra, *Chem. Mater.*, 2012, **24**, 133.

35 (*a*) S. Bénard, P. Yu, J. P. Audiere, E. Riviere, R. Clément, J. Guilhem, L. Tchertanov and K. Nakatani, *J. Am. Chem. Soc.*, 2000, **122**, 9444; (*b*) J. S. O. Evans, S. Bénard, Y. Pei and R. Clément, *Chem. Mater.*, 2001, **13**, 3813; (*c*) M. Gruselle, B. Malézieux, S. Bénard, C. Train, C. Guyard-Duhayon, P. Gredin, K. Tonsuaadu and R. Clément, *Tetrahedron: Asymmetry*, 2004, **15**, 3103; (*d*) E. Cariati, R. Macchi, D. Roberto, R. Ugo, S. Galli, N. Casati, P. Macchi, A. Sironi, L. Bogani, A. Caneschi and D. Gatteschi, *J. Am. Chem. Soc.*, 2007, **129**, 9410; (*e*) E. Cariati, R. Ugo, G. Santoro, E. Tordin, L. Sorace, A. Caneschi, A. Sironi, P. Macchi and N. Casati, *Inorg. Chem.*, 2010, **49**, 10894.

36 (*a*) O. Kahn, J. Larianova and J. V. Yakhmi, *Chem. – Eur. J.*, 1999, **5**, 3443; (*b*) J. Larionova, S. A. Chavan, J. V. Yakhmi, A. Gulbrandsen Froystein, J. Sletten, C. Sourisseau and O. Kahn, *Inorg. Chem.*, 1997, **36**, 6374.

37 (*a*) S. Kitagawa, R. Kitaura and S.-I. Noro, *Angew. Chem., Int. Ed.*, 2004, **43**, 2334; (*b*) S. Kitagawa and K. Uemura, *Chem. Soc. Rev.*, 2005, **34**, 109; (*c*) S. Kitagawa and R. Matsuda, *Coord. Chem. Rev.*, 2007, **251**, 2490.

38 (*a*) G. Férey, C. Mellot-Draznieks, C. Serre and F. Millange, *Acc. Chem. Res.*, 2005, **38**, 217; (*b*) G. Férey, *Chem. Soc. Rev.*, 2008, **37**, 191; (*c*) G. Férey and C. Serre, *Chem. Soc. Rev.*, 2009, **38**, 130.

39 C. Serre, C. Mellot-Draznieks, S. Surblé, N. Audebrand, Y. Filinchuk and G. Férey, *Science*, 2007, **315**, 1828.

40 D. Maspoch, D. Ruiz-Molina, K. Wurst, N. Domingo, M. Cavallini, F. Biscarini, J. Tejada, C. Rovira and J. Veciana, *Nat. Mater.*, 2003, **2**, 190.

41 N. W. Ockwig, O. Delgado-Friedrichs, M. O'Keeffe and O. M. Yaghi, *Acc. Chem. Res.*, 2005, **38**, 176.

42 (*a*) G. J. Halder, C. J. Kepert, B. Moubaraki, K. S. Murray and J. D. Cashion, *Science*, 2002, **29**, 1762; (*b*) M. Ohba, K. Yoneda, G. Agustí, M. C. Muñoz, A. B. Gaspar, J. A. Real, M. Yamasaki, H. Ando, Y. Nakao, S. Sasaki and S. Kitagawa, *Angew. Chem., Int. Ed.*, 2009, **48**, 4652.

43 (*a*) H.-L. Jiang, Y. Tatsu, Z.-H. Lu and Q. Xu, *J. Am. Chem. Soc.*, 2010, **132**, 5586; (*b*) Y. Takashima, V. M. Martínez, S. Furukawa, M. Kondo, S. Shimomura, H. Uehara, M. Nakahama, K. Sugimoto and S. Kitagawa, *Nat. Commun.*, 2011, **2**, 168.

44 (*a*) T. C. Chao, Y. T. Lin, C. Y. Yang, T. S. Hung, H. C. Chou, C. C. Wu and K. T. Wong, *Adv. Mater.*, 2005, **17**, 992; (*b*) X. Hu, J. Deng, J. P. Zhang, A. Lunev, Y. Bilenko, T. Katona, M. S. Shur, R. Gaska, M. Shatalov and A. Khan, *Phys. Status Solidi A*, 2006, **203**, 1815; (*c*) S. Mochizuki, S. Minami and F. Fujishiro, *J. Lumin.*, 2005, **112**, 267; (*d*) C. D. Müller, A. Falcou, N. Reckefuss, M. Rojahn, V. Wiederhirn, P. Rudati, H. Frohne, O. Nuyken, H. Becker and K. Meerholz, *Nature*, 2003, **421**, 829; (*e*) M. Q. Zhu, L. Zhu, J. J. Han, W. Wu, J. K. Hurst and A. D. Q. Li, *J. Am. Chem. Soc.*, 2006, **128**, 4303; (*f*) K. Binnemans, *Chem. Rev.*, 2009, **109**, 4283; (*g*) S. H. Hwang, C. N. Moorefield and G. R. Newkome, *Chem. Soc. Rev.*, 2008, **37**, 2543; (*h*) S. V. Eliseeva and J. C. G. Bunzli, *Chem. Soc. Rev.*, 2010, **39**, 189; (*i*) M. D. Allendorf, A. Schwartzberg, V. Stavila and A. A. Talin, *Chem. – Eur. J.*, 2011, **17**, 11372.

45 (*a*) M. Alvaro, G. A. Facey, H. García, S. García and J. C. Scaiano, *J. Phys. Chem.*, 1996, **100**, 18173; (*b*) M. Alvaro, H. García, S. García, F. Márquez and J. C. Scaiano, *J. Phys. Chem. B*, 1997, **101**, 3043.

46 T. Grancha, J. Ferrando-Soria, J. Cano, F. Lloret, M. Julve, G. De Munno, D. Armentano and E. Pardo, *Chem. Commun.*, 2013, **49**, 5942.

47 I. Imaz, M. Rubio-Martinez, J. An, I. Solé-Font, N. L. Rosi and D. Maspoch, *Chem. Commun.*, 2011, **47**, 7287, and references therein.

Inorganic Chemistry

Communication

pubs.acs.org/IC

High-Temperature Spin Crossover in a Mononuclear Six-Coordinate Cobalt(II) Complex

Joanna Palion-Gazda,[†] Anna Świtlicka-Olszewska,[†] Barbara Machura,*[,†] Thais Grancha,[‡] Emilio Pardo,[‡] Francesc Lloret,[‡] and Miguel Julve*[,‡]

[†]Department of Crystallography, Institute of Chemistry, University of Silesia, 9th Szkolna Street, 40006 Katowice, Poland

[‡]Departament de Química Inorgànica, Instituto de Ciencia Molecular (ICMol), Universitat de València, 46980 Paterna, València, Spain

Supporting Information

ABSTRACT: The six-coordinate cobalt(II) complex of formula $[Co(tppz)_2](tcm)_2$ exhibits a thermally induced spin-crossover behavior from a high spin ($S = {}^3/_2$) at higher temperatures to a low spin ($S = {}^1/_2$) at lower temperatures, with the low-spin phase being achieved at $T \leq 200$ K.

Although the preparation of the 2,3,5,6-tetrakis(2-pyridyl)-pyrazine ligand (hereafter denoted as tppz) was first reported in 1959 by Goodwin and Lions,[1] the first structural report of a tppz-containing metal complex appeared only 20 years ago.[2] The apparent lack of interest in the investigation of the coordination chemistry of such a prototype of a ligand with two 2,2′:6′,2″-terpyridine (terpy) domains was based the assumption that tppz would coordinate to only one metal ion because the four pendant 2-pyridyl rings could not be coplanar with the central pyrazine ring. In spite of confirmation of this lack of coplanarity,[3] several studies have revealed the great versatility of this ligand in complex formation, adopting a variety of terminal (bidentate α or γ and tridentate) and bridging [bis(bidentate) α or γ, bis(bidentate) α and γ, and bis(tridentate)] coordination modes.[4] Applications of its metal complexes as sensors,[5] molecular wires,[6] biochemical and DNA binding properties,[7] supramolecular films,[8] precursors to synthesize carbon-supported catalysts ($Fe-N_x/C$),[9] and builders for the rational design of extended structures containing $[Mo_5O_{15}(HOPO_3)_2]^{4-}$,[10a] $[Mo_5O_{15}(O_3PR)_2]^{4-}$,[10b,c] and $Mo_8O_{26}^{4-}$[10d−f] clusters have been reported.

Another property of tppz is its ability to mediate relatively large magnetic interactions between paramagnetic centers separated by more than 6.4 Å in the tppz-bridged metal complexes.[4b,11−14] Interestingly, the $[Fe(tppz)_2]^{2+}$ entity is a low-spin (LS) species,[4c,12] with the tridentate tppz molecule behaving as a strong-field ligand versus iron(II) in analogy with the parent terpy ligand.[15] Keeping in mind the greater mean spin-pairing energy for cobalt(II) relative to that for iron(II) for comparable six-coordinate complexes,[16] the possibility of the $[Co(tppz)_2]^{2+}$ species to undergo a thermally induced spin transition deserves to be explored. It is worthe noting that the majority of spin-crossover (SCO) compounds characterized so far deal with iron(II) and iron(III) compounds, whereas those with cobalt(II) have been investigated to a lesser extent.[15b]

Herein we present a preliminary magnetostructural study on the cobalt(II) complex of formula $[Co(tppz)_2](tcm)_2$ (**1**; tcm = tricyanomethanide anion), which exhibits a thermally induced spin transition with a change of the electron configuration $t_{2g}^6e_g^1$ (^2E_g, LS) ⇔ $t_{2g}^5e_g^2$ ($^4T_{1g}$, HS), the LS phase being achieved at $T \leq 200$ K.

The crystal structure of **1** has been solved at 293 K (Table S1 in the Supporting Information, SI). It consists of discrete $[Co(tppz)_2]^{2+}$ cations and tcm^- counteranions (Figure 1).

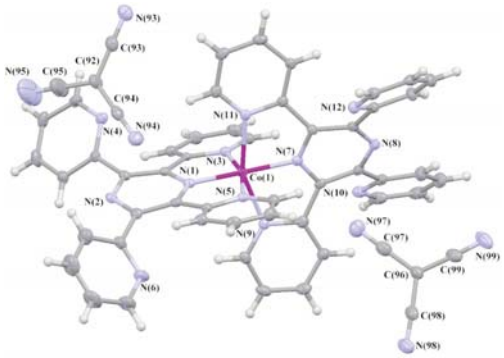

Figure 1. Perspective view of **1** (50% probability ellipsoids).

Each *mer*-tridentate tppz ligand coordinates to the cobalt(II) ion equatorially via two pyridyl donors and axially via the pyrazine, completing the coordination sphere. The value of the N(pyrazine)−Co−N(pyrazine) angle [179.56(8)°] is quasi-linear, whereas those of the remaining *trans* N−Co−N angles [156.80(7)° and 163.15(8)° for N(9)−Co(1)−N(11) and N(3)−Co(1)−N(5), respectively] reflect the steric constraints imposed by the rigidity of the tridentate tppz ligand. The dihedral angle between the least-squares planes defined by the coordinated pyridine and pyrazine rings of the two ligands is 86.35°, and the distortion parameter Σ, defined as the sum of the deviation from 90° of the 12 *cis* angles of the CoN_6 octahedron, equals 81.70°. The axial $Co-N_{pyrazine}$ bond lengths [1.865(2) and 1.936(2) Å] are shorter than the $Co-N_{pyridyl}$ ones [1.977(2)−

Received: May 22, 2014
Published: September 8, 2014

   dx.doi.org/10.1021/ic501195y | Inorg. Chem. 2014, 53, 10009−10011

2.160(2) Å; Table S2 in the SI), forming a compressed octahedral surrounding, as expected for a LS six-coordinate cobalt(II) ion significantly distorted by Jahn−Teller arising from the single e_g electron.[17] The structural parameters of **1** are consistent with a thermal-averaged mixture of HS and LS states for cobalt(II) SCO complexes (see Table S4 in the SI).

The whole ligands are appreciably twisted: the dihedral angles between the N(1)/N(2) pyrazine ring and each of its pyridyl substituents are 43.73(9)°, 45.94(10)°, 14.13(10)°, and 17.39(10)° arranged in order of rings containing N(4), N(6), N(5), and N(3) [to be compared with 23.52(11)°, 24.74(11)°, 31.31(11)°, and 35.00(10)° for the N(11), N(9), N(10), and N(12) rings in the tppz ligand containing the N(7)/N(8) pyrazine group]. The pyrazine rings from the two tppz ligands are significantly puckered, with maximum atomic deviations from a best mean plane being 0.0810(16) and 0.1313(17) Å at the C(3) and C(26) atoms, respectively. Low-energy conformations of free tppz molecules are predicted to have each pyridyl ring twisted from coplanarity with the pyrazine group roughly 50°.[4d] $\pi-\pi$-type interactions involving the pyridyl rings of the tppz ligands, which connect the $[Co(tppz)_2]^{2+}$ cations into a chain with cobalt(II) ions separated by 8.940 Å, contribute to stabilization of the structure {values of 3.8971(15) and 3.8366(16) Å for the Cg1[N(5)−C(20)−C(24)]···Cg2^{i}[N(3)−C(8)−C(12)] and Cg3[N(12)−C(39)−C(43)]···Cg4^{i}[N(10)−C(34)−C(38)] centroids, respectively; i, −1 + *x*, *y*, *z*; Figure 2}. Additionally, the tcm^- anions are linked to the

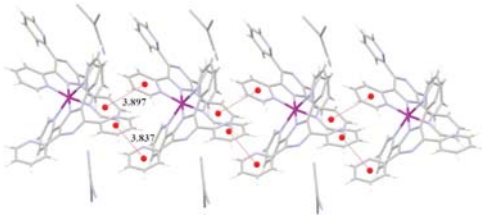

Figure 2. View of a fragment of the supramolecular chain in **1** arising from weak $\pi-\pi$-type interactions.

complex cation via very weak C−H···N-type interactions (Table S3 in the SI), leading to a three-dimensional supramolecular network. These intramolecular interactions seem to generate additional chemical pressure to stabilize the LS state of cobalt(II) in **1**. This is reflected by the low value of the *C* parameter (see below). A crucial role of lattice interactions in driving the SCO behavior has been evidenced previously.[15a,18]

The $\chi_M T$ versus *T* plot for **1** [χ_M is the magnetic susceptibility per cobalt(II) ion] is shown in Figure 3. $\chi_M T$ is almost constant in the temperature range 1.9−185 K, taking a value of ca. 0.42 cm^3 mol^{-1} K. This value is consistent with the $S = {}^1/_2$ ground state that follows the Curie−Weiss law with $g = 2.12$. When the sample is warmed, $\chi_M T$ smoothly increases, attaining a value of 0.85 cm^3 mol^{-1} K at 350 K. This behavior clearly indicates the occurrence of a very incomplete $^1/_2$ (LS) ⇔ $^3/_2$ (HS) conversion at 350 K. The magnetization (*M*) versus *H* plot for **1** at 2.0 K (see the inset of Figure 3) corresponds to what is expected for a spin doublet, with the value of *M* at 5 T (the maximum available field in our magnetometer) tending to a value somewhat above 1.0 μ_B

Analysis of the magnetic data of **1** through a theoretical model that considers one doublet state (^2E) and one quartet state ($^4T_1$) separated by an energy gap *E*, whose degeneracy is removed by a

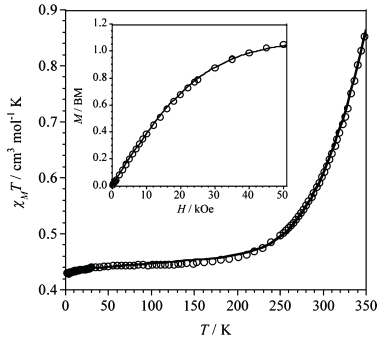

Figure 3. $\chi_M T$ versus *T* plot for **1**: (○) experimental; (—) best-fit curve through a model derived elsewhere.[19] The inset shows the *M* versus *H* plot for **1** at 2.0 K.

combination of spin−orbit coupling and first- and second-order Zeeman effects,[19] leads to the following two sets of best-fit parameters: $\gamma = -1.10(1)$, $\mu_E = 1.91\ \mu_B$, $\zeta = 510\ cm^{-1}$, $E = 2015(10)\ cm^{-1}$, and $C = 0.075(1)$ [or $\gamma = -1.49(1)$, $\mu_E = 1.86\ \mu_B$, $\zeta = 450\ cm^{-1}$, $E = 2070(10)\ cm^{-1}$, and $C = 0.0105(3)$]. γ is a term that lies between −1.5 (weak-field ligand) and −1 (strong-field ligand), μ_E is the effective magnetic moment for the ^2E state, ζ is the one-electron spin−orbit coupling constant, *E* is the energy gap between the ^4T and ^2E states, and *C* is the ratio of the vibrational partition functions in the HS and LS states. The calculated curves through both sets of values match very well the experimental data in the whole temperature range explored, and they compare well with those reported for other $Co^{II}N_6$ SCO systems.[20]

X-band electron paramagnetic resonance (EPR) measurements on a polycrystalline sample of **1** at low temperatures consists of a quasi-isotropic feature centered at 3220 G (Figure S2 in the SI; $T = 25$ K). This signal for a frozen dichloromethane solution of **1** at 4.0 K shows a hyperfine splitting of $A = 70$ G in the form of eight lines due to coupling to the $I = {}^7/_2$ nucleus of cobalt, with the *g* value being 2.12 and a frozen dichloromethane solution (Figure 4).

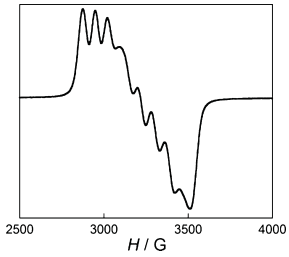

Figure 4. X-band EPR spectrum of a frozen dichloromethane solution of **1** at 4.0 K.

In summary, the tppz molecule having two potential tridentate sites in *trans* position is a strong-field ligand in its cobalt(II) complexes, as shown by the present magnetostructural investigation on the mononuclear compound **1**. Variable-temperature magnetic susceptibility measurements on a polycrystalline sample and EPR spectroscopy on both solid and frozen dichloromethane solutions of **1** revealed SCO behavior, in agreement with the previous results on the parent

dx.doi.org/10.1021/ic501195y | *Inorg. Chem.* 2014, 53, 10009−10011

$[Co(terpy)_2]^{2+}$, $[Co(4\text{-terpyridone})_2]^{2+}$, and $[Co(dpzca)_2]$ [terpy = 2,2′:6′,2″-terpyridine, 4-terpyridone = 2,6-bis[2-pyridyl-4(1*H*)-pyridone], and Hdpzca = bis(2-pyrazinylcarbonyl)amide] mononuclear species.[16c,21] The LS state in **1** is achieved at T = 185 K with $S = {}^1/_2$, and the HS configuration is far from being completely populated at 350 K, with the value of $\chi_M T$ at this temperature being only 0.85 cm^3 mol^{-1} K (to be compared with values of $\chi_M T$ in the range 2.5−3.0 cm^3 mol^{-1} K for full population of the HS state in the parent terpy- and 4-terpyridone-containing complexes). The influence of the counterion on the spin transition in **1** as well as the use of the $[Co(tppz)_2]^{2+}$ unit as a metalloligand to build SCO heterometallic species will be the subject of further works.

■ ASSOCIATED CONTENT

Supporting Information

Synthesis, crystallographic data (Tables S1−S3), CCDC 999841, structural data for CoN_6 SCO systems (Table S4), UV−vis electron spectrum (Figure S1), and X-band EPR spectrum on a solid sample (Figure S2). This material is available free of charge via the Internet at http://pubs.acs.org.

■ AUTHOR INFORMATION

Corresponding Authors

*E-mail: basia@ich.us.edu.pl.

*E-mail: Miguel.Julve@uv.es.

Notes

The authors declare no competing financial interest.

■ ACKNOWLEDGMENTS

This work was supported by the Polish National Science Centre (Grant 2012/07/N/ST5/02213), the MICINN (Spain; Project CTQ2010-15364), and the Generalitat Valenciana (Spain; Projects PROMETEO/2009/108 and ISIC/2012/002). Thanks are due to the Universitat de València for a predoctoral grant (T.G.), the Doktoris Project co-financed by the European Social Fund for a scholarship (J.P.G.) and the MICINN Ramón y Cajal Program for a postdoctoral contract (E.P.).

■ REFERENCES

(1) Goodwin, H. A.; Lions, F. *J. Am. Chem. Soc.* **1959**, *81*, 6415−6422.

(2) Graf, M.; Greaves, B.; Stoeckli-Evans, H. *Inorg. Chim. Acta* **1993**, *204*, 239−246.

(3) (a) Padgett, C. W.; Walsh, R. D.; Drake, G. W.; Hanks, T. W.; Pennington, W. T. *Cryst. Growth Des.* **2005**, *5*, 745−753. (b) Greaves, B.; Stoeckli-Evans, H. *Acta Crystallogr.* **1992**, *C48*, 2269−2271. (c) Bock, H.; Vaupel, T.; Näther, C.; Ruppert, K.; Havlas, Z. *Angew. Chem., Int. Ed. Engl.* **1992**, *31*, 299−301.

(4) (a) Machura, B.; Palion, J.; Mrozinski, J.; Kalinska, B.; Amini, M.; Najafpour, M. M.; Kruszynski, R. *Polyhedron* **2013**, *53*, 132−143. (b) Yuste, C.; Cañadillas-Delgado, L.; Ruiz-Pérez, C.; Lloret, F.; Julve, M. *Dalton Trans.* **2010**, *39*, 167−179. (c) Toma, L. M.; Armentano, D.; De Munno, G.; Sletten, J.; Lloret, F.; Julve, M. *Polyhedron* **2007**, *26*, 5263−5270. (d) Padgett, C. W.; Pennington, W. T.; Hanks, T. W. *Cryst. Growth Des.* **2005**, *5*, 737−744.

(5) (a) Maskus, M.; Abruña, H. D. *Langmuir* **1996**, *12*, 4455−4462. (b) Yuasa, J.; Fukuzumi, S. *J. Am. Chem. Soc.* **2006**, *128*, 15976−15977. (c) Yuasa, J.; Fukuzumi, S. *J. Am. Chem. Soc.* **2008**, *130*, 566−575. (d) Hadadzadeh, H.; Hosseinian, S. R.; Fatemi, S. J. A. *Polyhedron* **2009**, *28*, 2776−2784.

(6) (a) Fantacci, S.; De Angelis, F.; Wang, J.; Bernhard, S.; Selloni, A. *J. Am. Chem. Soc.* **2004**, *126*, 9715−9723. (b) Flores-Torres, S.; Hutchison, G. R.; Soltzberg, L. J.; Abruña, H. D. *J. Am. Chem. Soc.* **2006**, *128*, 1513−1522. (c) Carlson, C. N.; Kuehl, C. J.; Da Re, R. E.; Veauthier, J. M.; Schelter, E. J.; Milligan, A. E.; Scott, B. L.; Bauer, E. D.; Thompson, J. D.; Morris, D. E.; John, K. D. *J. Am. Chem. Soc.* **2006**, *128*, 7230−7241.

(7) (a) Rubino, S.; Portanova, P.; Girasolo, A.; Galvaruso, G.; Orecchio, S.; Stoco, G. C. *Eur. J. Med. Chem.* **2009**, *44*, 1041−1048. (b) Haghighi, F. H.; Hadadzadeh, H.; Darabi, F.; Jannesari, Z.; Ebrahimi, M.; Khayamian, T.; Salimi, M.; Rudbari, H. A. *Polyhedron* **2013**, *65*, 16−30.

(8) Alves, W. A.; Pfaffen, V.; Ortiz, P. I.; Córdoba de Torresi, S. I.; Torressi, R. M. *J. Braz. Chem. Soc.* **2008**, *19*, 651−659.

(9) Velázquez-Valenzuela, A.; Zhang, L.; Wang, L.; Cabot, P. L.; Brillas, E.; Tsay, K.; Zhang, J. *Electrochim. Acta* **2011**, *56*, 4744−4752.

(10) (a) Burkholder, E.; Zubieta, J. *Chem. Commun.* **2001**, 2056−2057. (b) Armatas, N. G.; Allis, D. G.; Prosvirin, A.; Carnutu, G.; O'Connor, C. J.; Dunbar, K.; Zubieta, J. *Inorg. Chem.* **2008**, *47*, 832−854. (c) Burkholder, E.; Golub, V.; O'Connor, C. J.; Zubieta, J. *Inorg. Chem.* **2003**, *42*, 6729−6740. (d) Hagrman, D.; Hagrman, P.; Zubieta, J. *Inorg. Chim. Acta* **2000**, *300*−*302*, 212. (e) Boukholder, E.; Zubieta, J. *Solid State Sci.* **2004**, *6*, 1421−1428. (f) Burkholder, E.; Zubieta, J. *Inorg. Chim. Acta* **2005**, *358*, 116−122.

(11) Graf, M.; Stoeckli-Evans, H.; Escuer, A.; Vicente, R. *Inorg. Chim. Acta* **1997**, *257*, 89−97.

(12) Campos-Fernández, C. S.; Smucker, B. W.; Clérac, R.; Dunbar, K. R. *Isr. J. Chem.* **2001**, *41*, 207−218.

(13) Hsu, G.-H.; Cheng, C.-W.; Cheng, S.-C.; Lin, S.-H.; Wei, H.- H.; Lee, C.-J. *Polyhedron* **2005**, *24*, 487−494.

(14) (a) Yuste, C.; Armentano, D.; Marino, N.; Cañadillas-Delgado, L.; Delgado, F. S.; Ruiz-Pérez, C.; Rillema, D. P.; Julve, M. *Dalton Trans.* **2008**, 1583−1596. (b) Carranza, J.; Sletten, J.; Brennan, C.; Lloret, F.; Cano, J.; Julve, M. *Dalton Trans.* **2004**, 3997−4005. (c) Carranza, J.; Brennan, C.; Sletten, J.; Clemente-Juan, J. M.; Lloret, F.; Julve, M. *Inorg. Chem.* **2003**, *42*, 8716−8727.

(15) (a) Halcrow, M. A. *Chem. Soc. Rev.* **2011**, *40*, 4119−4142. (b) García, Y.; Niel, V.; Muñoz, M. C.; Real, J. A. *Top. Curr. Chem.* **2004**, *233*, 229−257. (c) Baker, A. T.; Goodwin, H. A. *Aust. J. Chem.* **1985**, *38*, 207−214. (d) Goodwin, H. A. *Coord. Chem. Rev.* **1976**, *18*, 293−325.

(16) (a) Gütlich, P. *Eur. J. Inorg. Chem.* **2013**, 581−591. (b) Hayami, S.; Karim, M. R.; Lee, Y. H. *Eur. J. Inorg. Chem.* **2013**, 683−696. (c) Krikokapic, K.; Zerara, M.; Daku, M. L.; Vargas, A.; Enachescu, C.; Ambrus, C.; Tregenna-Piggott, P.; Amstutz, N.; Krausz, E.; Hauser, A. *Coord. Chem. Rev.* **2007**, *251*, 364−378.

(17) (a) Goodwin, H. A. *Top. Curr. Chem.* **2004**, *234*, 23−47. (b) Wu, S.-Q.; Wang, Y.-T.; Cui, A.-L.; Kou, H.-Z. *Inorg. Chem.* **2014**, *53*, 2613−2618. (c) Gass, I. A.; Tewary, S.; Rajaraman, G.; Asadi, M.; Lupton, D. W.; Moubaraki, B.; Chastanet, G.; Létard, J.-F.; Murray, K. S. *Inorg. Chem.* **2014**, *53*, 5055−5066.

(18) (a) Dupouy, G.; Marchivie, M.; Triki, S.; Sala-Pala, J.; Salaün, J.-Y.; Gómez-García, C. J.; Guionneau, P. *Inorg. Chem.* **2008**, *47*, 8921−8931. (b) Schweinfurth, D.; Weisser, F.; Dubrin, D.; Bogani, L.; Sarkar, B. *Inorg. Chem.* **2011**, *50*, 6114−6121. (c) Atmani, Ch.; El Hajj, F.; Benmansur, S.; Marchivie, M.; Triki, S.; Conan, F.; Patinec, V.; Handel, H.; Dupouy, G.; Gómez-García, C. J. *Coord. Chem. Rev.* **2010**, *254*, 1559−1569. (d) Novokov, V. V.; Anayev, I. V.; Pavlov, A. A.; Fedin, M. V.; Lyssenko, K. A.; Voloshin, Y. Z. *J. Phys. Chem. Lett.* **2014**, *5*, 496−500.

(19) Martin, R. L.; White, A. H. *Transition Met. Chem.* **1968**, *4*, 113−198.

(20) Vecchio-Sadus, A. M. *Transition Met. Chem.* **1995**, *28*, 38−45.

(21) (a) Kremer, S.; Henke, W.; Reinen, D. *Inorg. Chem.* **1982**, *21*, 3013−3022. (b) Figgis, B. N.; Kucharski, E. S.; White, A. H. *Aust. J. Chem.* **1983**, *36*, 1537−1561. (c) Galet, A.; Gaspar, A. B.; Muñoz, M. C.; Real, J. A. *Inorg. Chem.* **2006**, *45*, 4413−4422. (d) Echanescu, C.; Krivokapic, I.; Zerara, M.; Real, J. A.; Amstutz, N.; Hauser, A. *Inorg. Chim. Acta* **2007**, *360*, 3945−3950. (e) Kilner, C. A.; Halcrow, M. A. *Dalton Trans.* **2010**, *39*, 9008−9012. (f) Hayami, S.; Komatsu, Y.; Shimizu, T.; Kamihata, H.; Lee, Y. H. *Coord. Chem. Rev.* **2011**, *255*, 1981−1990. (g) Cowan, M. G.; Olguín, J.; Narayanaswamy, S.; Tallon, J. L.; Brooker, S. *J. Am. Chem. Soc.* **2011**, *134*, 2892−2894.

Inorganic Chemistry

Communication

pubs.acs.org/IC

Double Interpenetration in a Chiral Three-Dimensional Magnet with a (10,3)-a Structure

Thais Grancha,[†] Marta Mon,[†] Francesc Lloret,[†] Jesús Ferrando-Soria,*[,†] Yves Journaux,[‡] Jorge Pasán,[§] and Emilio Pardo*[,†]

[†]Departament de Química Inorgànica, Instituto de Ciencia Molecular (ICMOL), Universitat de València, 46980 Paterna, València, Spain

[‡]Institut Parisien de Chimie Moléculaire, Université Pierre et Marie Curie-Paris 6, UMR 7201, F-75252 Paris, France

[§]Laboratorio de Rayos X y Materiales Moleculares, Departamento de Física, Universidad de La Laguna, E−38201 Tenerife, Spain

Supporting Information

ABSTRACT: A unique chiral three-dimensional magnet with an overall racemic double-interpenetrated (10,3)-a structure of the formula $[(S)\text{-}(1\text{-PhEt})\text{-}Me_3N]_4[Mn_4Cu_6(Et_2pma)_{12}](DMSO)_3]\cdot 3DMSO\cdot 5H_2O$ (**1**; Et_2pma = *N*-2,6-diethylphenyloxamate) has been synthesized by the self-assembly of a mononuclear copper(II) complex acting as a metalloligand toward Mn^{II} ions in the presence of a chiral cationic auxiliary, constituting the first oxamato-based chiral coordination polymer exhibiting long-range magnetic ordering.

High-dimensional coordination polymers (CPs),[1] sometimes exhibiting fascinating and intriguing interpenetrated architectures,[2] attract the interest of chemists working in very diverse fields because of the broad variety of physical and chemical properties that they can exhibit.[3] The design of CPs exhibiting a spontaneous magnetization below a critical temperature (T_C)—achieved when suitably chosen paramagnetic ions are linked by appropriate organic ligands (or metalloligands) capable of efficiently transmitting the magnetic coupling between them—is especially appealing in the field of molecular magnetism.[4] In this regard, accurate control of the coordination network structure is required to get the desired long-range magnetic ordering, which is not always easy because of the many subtle factors that may affect the assembly process of the metal and organic building blocks.[5]

With the aim of synthesizing novel examples of heterospin magnets based on CPs, diverse rational self-assembly methods have been proposed that are based on the use of paramagnetic organic radicals or metal complexes as ligands toward other metal ions.[6a] The "complex-as-ligand" approach—where a paramagnetic preformed complex coordinates to free metal ions—has shown excellent results, affording better control of the net topology and the resulting magnetic properties.[6a] In particular, the use of oxamato-based metal complexes as precursors has led to different CPs with a broad diversity of architectures and magnetic properties.[6b]

In a previous work, we showed how the use of tetra-*n*-butylammonium salts of the dianionic mononuclear bis(oxamato)copper(II) complexes $(n\text{-}Bu_4N)_2[Cu^{II}L_2]^{2-}$, where L = *N*-2,6-dimethylphenyloxamate (Me_2pma) and *N*-2,6-diethylphenyloxamate (Et_2pma) (Scheme 1a), as bis(bidentate) metalloligands toward octahedral manganese(II) cations led to achiral, either two-dimensional (2D) or three-dimensional (3D), $Mn^{II}_2Cu^{II}_3$ extended anionic networks of 6^3-**hcb** and 10^3-**ths** net topologies, respectively, possessing a regular alternation of propeller-type Δ- and Λ-Mn^{II} enantiomers (Scheme 1b,c, respectively) and exhibiting long-range magnetic ordering at T_C = 10 K (2D) and 20 K (3D).[7]

Scheme 1. (a) Mononuclear Copper(II) Complex Anion and Chiral (*S*)-(1-PhEt)Me_3N Cation and (b−d) Postulated Structures of the Possible Resulting Metal−Organic Frameworks

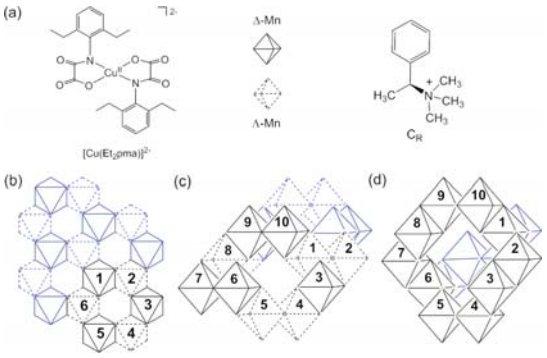

With the aim of synthesizing novel examples of chiral oxamato-bridged CPs with additional physical properties to the magnetic ones, which may potentially interact in a synergetic manner, we explore the possibility of achieving CPs with oxamato ligands crystallizing in chiral space groups, which has not been an easy task so far.[8a] So, in order to expand the range of physical properties shown by this class of multifunctional magnetic materials,[6b] we now focus on the use of enantiopure quaternary ammonium cations as chiral auxiliaries such as (*S*)-trimethyl-(1-phenylethyl)ammonium[8b] (Scheme 1a), which can tentatively induce the formation of chiral 3D $Mn^{II}_2Cu^{II}_3$ extended anionic

Received: July 31, 2015
Published: August 31, 2015

DOI: 10.1021/acs.inorgchem.5b01738
Inorg. Chem. 2015, 54, 8890−8892

networks of **srs** net topology possessing a segregated distribution of propeller-type Δ- or Λ-Mn^{II} enantiomers (Scheme 1d).

Herein we report the synthesis, crystal structure, and magnetic properties of a new example of chiral 3D oxamato-bridged heterobimetallic magnet of the formula $[(S)\text{-}(1\text{-PhEt})\text{-}Me_3N]_4[Mn_4Cu_6(Et_2pma)_{12}](DMSO)_3]\cdot 3DMSO\cdot 5H_2O$ (**1**). Interestingly, it includes a racemic mixture of double-interpenetrated[2b] 3D (Δ)-$Mn^{II}_2Cu^{II}_3$ and (Λ)-$Mn^{II}_2Cu^{II}_3$ extended anionic networks, with the source of chirality being provided by the presence of an enantiomerically pure (S)-(1-PhEt)Me_3N^+ countercation.

1 was obtained by reacting $[(S)\text{-}(1\text{-PhEt})\text{-}Me_3N]_2[Cu^{II}(Et_2pma)_2]\cdot 4H_2O$ and $MnCl_2$ (5:1 molar ratio) in a dimethyl sulfoxide (DMSO) solution. **1** crystallizes in the chiral space group $P2_12_12_1$ of the orthorhombic crystal system, and its absolute configuration was reliably assigned (Table S1 in the Supporting Information, SI).

The structure of **1** consists of two double-interpenetrated oxamato-bridged $Mn^{II}_2Cu^{II}_3$ anionic 3D networks with the same 10^3 **srs** net topology but opposite chirality, together with (S)-(1-PhEt)Me_3N^+ cations and free H_2O and DMSO molecules (Figures 1 and S1 and S2 in the SI). Both 3D networks are built

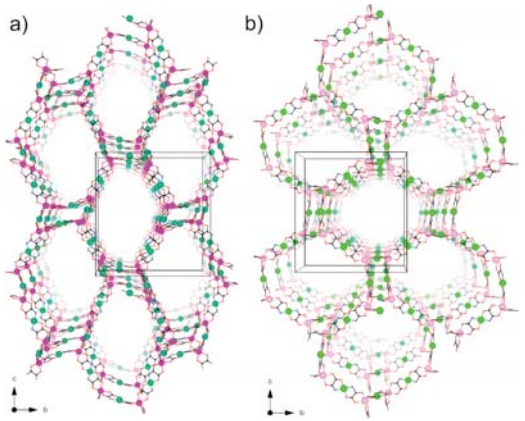

Figure 1. Perspective views of the two interpenetrated networks of **1**. The (Δ)-Mn^{II}-(P)-Cu^{II} (a) and (Λ)-Mn^{II}-(M)-Cu^{II} (b) atoms are depicted in dark and light purple and green colors, respectively. The aromatic rings of the oxamate ligand have been omitted for clarity.

from bis(oxamato)copper(II) entities acting as bis(bidentate) ligands through the *cis*-carbonyl O atoms toward tris(chelated) Mn^{II} ions (Figures 2 and S2 in the SI).

Each network possesses one crystallographically independent Mn atom and three crystallographically independent Cu atoms in the asymmetric unit cell [Mn(1), Cu(1), Cu(2), and Cu(3) in one network and Mn(2), Cu(4), Cu(5), and Cu(6) in the other one]. The Cu atoms are four- and five-coordinate in tetrahedrally distorted square-planar [Cu(1), Cu(3), and Cu(5)] and trigonally distorted square-pyramidal geometries [Cu(2), Cu(4), and Cu(6)], respectively. Their basal plane is formed, in all cases, by two amidate N atoms and two carboxylate O atoms from the *trans*-oxamato groups [Cu−N = 1.887(17)−1.972(17) Å and Cu−O = 1.891(18)−1.976(15) Å]. The apical position of the square-pyramidal Cu^{II} ions is occupied by a DMSO molecule [Cu−O = 2.32(2)−2.471(18) Å]. The values of the tetrahedricity parameter (δ) at the four-coordinate Cu^{II}

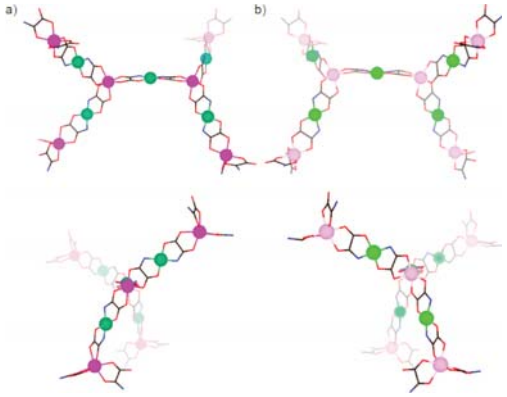

Figure 2. Front (top) and side (bottom) views of a fragment of the two interpenetrated networks of **1**. The (Δ)-Mn^{II}-(P)-Cu^{II} (a) and (Λ)-Mn^{II}-(M)-Cu^{II} (b) atoms are depicted in dark and light purple and green colors, respectively. The aromatic rings of the oxamate ligand have been omitted for clarity.

ions are in the range of 13.7−19.0° (δ = 0 and 90° for the ideal square plane and tetrahedron, respectively), while those of the trigonality parameter (τ) at the five-coordinate square-pyramidal Cu^{II} ions are in the range of 0.21−0.26 (τ = 0 and 1 for the ideal square and trigonal bipyramids, respectively). The Mn atoms possess a trigonally distorted octahedral geometry formed by six *cis*-carbonyl O atoms from the oxamato groups [Mn−O = 2.077(18)−2.30(2) Å]. The values of the trigonal twist angle (ϕ) at the six-coordinate Mn^{II} ions are in the range of 48.2−59.4° (ϕ = 60 and 0° for the ideal octahedron and trigonal prism, respectively).

Interestingly, each interpenetrated oxamato-bridged 3D $Mn^{II}_2Cu^{II}_3$ anionic network is present as one single enantiomer of opposite chirality, leading to an overall achiral racemic net structure (Figure S2 in the SI). There are previously reported 2-fold interpenetrating **srs** nets with opposite chirality.[9a] In these cases, the space group is centrosymmetric and the two interwoven 3D nets are related by an inversion center.[9] In **1**, this situation is precluded by the presence of the enantiopure chiral (S)-(1-PhEt)Me_3N^+ cations in the pores of the structure and, thus, no inversion centers are allowed. So, each of the two homochiral networks, built by repetition of the nonplanar $[(\Delta)\text{-}Mn^{II}_2\text{-}(P)\text{-}Cu^{II}_5]$ (Figure 2a) and $[(\Lambda)\text{-}Mn^{II}_2\text{-}(M)\text{-}Cu^{II}_5]$ (Figure 2b) structural motifs, respectively (with the values of the dihedral angles between the two $Mn^{II}Cu^{II}_3$ halves being 74.8 and 75.5°, respectively) is crystallographically unique.

The powder X-ray diffraction pattern of **1** is consistent with the calculated one (Figure S3 in the SI), confirming that the bulk sample is isostructural to the crystal selected for single-crystal X-ray diffraction.

Encouraged by the well-known efficiency of the oxamato ligands transmitting the magnetic coupling between neighboring metal atoms, we studied the magnetic properties of **1**. They are represented in the form of a $\chi_M T$ versus T plot [with χ_M being the direct-current (dc) molar magnetic susceptibility per Cu_3Mn_2 unit and T the temperature], supporting the occurrence of a 3D ferrimagnetic behavior (Figure 3a). At room temperature, $\chi_M T$ is equal to 7.97 $cm^3\ mol^{-1}\ K$. This value is slightly below that expected for the sum of three square-planar Cu^{II} ions ($\chi_M T$ = 0.40 $cm^3\ mol^{-1}\ K$ with $S_{Cu} = {}^1/_2$ and g_{Cu} = 2.1) and two octahedral high-spin Mn^{II} ions ($\chi_M T$ = 4.37 $cm^3\ mol^{-1}\ K$ with

DOI: 10.1021/acs.inorgchem.5b01738
Inorg. Chem. 2015, 54, 8890−8892

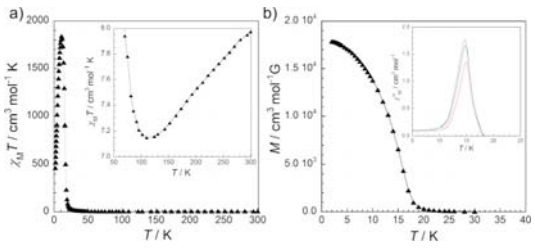

Figure 3. (a) Temperature dependence of $\chi_M T$ for **1** under an applied dc field of 0.1 kG ($T < 50$ K) and 10 kG ($T \geq 50$ K). The inset shows the minima in detail. (b) FCM for **1**, measured upon cooling within a field of 100 G. The inset shows the temperature dependence of χ_M'' with a 1.0 G oscillating field at different frequencies: 10 (red), 100 (blue), and 1000 (green) Hz. The solid lines are only guides for the eye.

$S_{Mn} = {}^5/_2$ and $g_{Mn} = 2.0$), suggesting the occurrence of a moderate *intra*molecular antiferromagnetic interaction between the Cu^{II} and Mn^{II} ions through the oxamate bridges. Upon cooling, $\chi_M T$ slowly decreases and attains a minimum at ca. 110 K (inset of Figure 3a), supporting the occurrence of a 3D ferrimagnetic behavior. Further cooling shows an abrupt increase of $\chi_M T$ below 25 K, to reach a maximum value of 1835 $cm^3\ mol^{-1}\ K$ at ca. 11 K.

In fact, **1** undergoes an abrupt paramagnetic-to-ferrimagnetic phase transition at T_C = 15 K, as revealed by the temperature dependence of the field-cooled magnetization (FCM; Figure 3b). The FCM curve, measured by cooling the sample within a small field of 100 G, increases sharply below 20 K, thereby suggesting the onset of a long-range ferrimagnetic transition. Indeed, the magnetic ordering is confirmed by the alternating-current (ac) magnetic properties in the form of the χ_M'' versus T plot (with χ_M'' being the ac out-of-phase susceptibility per Cu_3Mn_2 unit) at different frequencies (ν) of the 1 G oscillating field. So, χ_M'' becomes nonzero below 20 K, and nonfrequency-dependent maxima are observed at 15 K (inset of Figure 3b). The magnetic hysteresis loop at 2.0 K (Figure S4 in the SI) exhibits a very low value of the coercive field (H_c = 20 G), which is characteristic of soft magnets.[6]

In conclusion, a preformed mononuclear copper(II) complex with a chiral countercation has been used toward Mn^{II} ions to yield the first oxamato-based chiral 3D magnet. Although its structure consists of two enantiopure double-interpenetrated oxamato-bridged $Mn^{II}_2Cu^{II}_3$ anionic 3D networks with the same 10^3 **srs** net topology and opposite chiralities, **1** is chiral and crystallizes in a chiral space group as a consequence of the enantiopurity of the auxiliary (*S*)-(1-PhEt)Me_3N^+ counter-cations. Moreover, the presence of long-range ferrimagnetic ordering at 15 K, together with a chiral space group, opens the gate for the observation of interesting properties such as magnetically induced second-harmonic-generation[10a] or magnetochiral-dichroism[10b] effects. Our current efforts are devoted to the study of these properties in these types of materials.

■ ASSOCIATED CONTENT

Supporting Information

The Supporting Information is available free of charge on the ACS Publications website at DOI: 10.1021/acs.inorgchem.5b01738.

CIF file (CCDC 1416018) (CIF)

Experimental preparation, analytical and spectroscopic characterization of compound **1**, and additional figures (S1–S3) (PDF)

■ AUTHOR INFORMATION

Corresponding Authors

*E-mail: jesus.ferrando@uv.es.

*E-mail: emilio.pardo@uv.es.

Notes

The authors declare no competing financial interest.

■ ACKNOWLEDGMENTS

This work was supported by MINECO (Projects CTQ2013-46362-P and CTQ2013-44844-P) and the Generalitat Valenciana (Project PROMETEOII/2014/070). T.G. and M.M. thank the Universitat de Valencia and MINECO for predoctoral contracts. Thanks are also extended to the MICINN Ramón y Cajal Program (E.P.).

■ REFERENCES

(1) Abrahams, B. F.; Hoskins, B. F.; Michail, D. M.; Robson, R. *Nature* **1994**, *369*, 727–729.

(2) (a) Batten, S. R.; Robson, R. *Angew. Chem., Int. Ed.* **1998**, *37*, 1460–1494. (b) Han, L.; Qin, L.; Xu, L. P.; Zhao, W. N. *Inorg. Chem.* **2013**, *52*, 1667–1669.

(3) (a) Li, J.-R.; Kuppler, R. J.; Zhou, H.-C. *Chem. Soc. Rev.* **2009**, *38*, 1477–1504. (b) Gascon, J.; Corma, A.; Kapteijn, F.; Llabrés i Xamena, F. X. *ACS Catal.* **2014**, *4*, 361–378. (c) Train, C.; Gruselle, M.; Verdaguer, M. *Chem. Soc. Rev.* **2011**, *40*, 3297–3312. (d) Horike, S.; Umeyama, D.; Kitagawa, S. *Acc. Chem. Res.* **2013**, *46*, 2376–2384. (e) Ferrando-Soria, J.; Khajavi, H.; Serra-Crespo, P.; Gascon, J.; Kapteijn, F.; Julve, M.; Lloret, F.; Pasán, J.; Ruiz-Pérez, C.; Journaux, Y.; Pardo, E. *Adv. Mater.* **2012**, *24*, 5625–5629. (f) *Molecule-Based Magnetic Materials*; Turnbull, M. M., Sugimoto, T., Thompson, L. K., Eds.; ACS Symposium Series; American Chemical Society: Washington, DC, 1996; Vol. *644*.

(4) Kahn, O. *Molecular Magnetism*; VCH Publishers: New York, 1993.

(5) (a) Tabellion, F. M.; Seidel, S. R.; Arif, A. M.; Stang, P. J. *J. Am. Chem. Soc.* **2001**, *123*, 7740–7741. (b) Goesten, M. G.; Kapteijn, F.; Gascon, J. *CrystEngComm* **2013**, *15*, 9249–9257.

(6) (a) Pardo, E.; Ruiz-García, R.; Cano, J.; Ottenwaelder, X.; Lescouëzec, R.; Journaux, Y.; Lloret, F.; Julve, M. *Dalt. Trans.* **2008**, *21*, 2780–2805. (b) Grancha, T.; Ferrando-Soria, J.; Castellano, M.; Julve, M.; Pasán, J.; Armentano, D.; Pardo, E. *Chem. Commun.* **2014**, *50*, 7569–7585.

(7) Ferrando-Soria, J.; Grancha, T.; Julve, M.; Cano, J.; Lloret, F.; Journaux, Y.; Pasán, J.; Ruiz-Pérez, C.; Pardo, E. *Chem. Commun.* **2012**, *48*, 3539–3541.

(8) (a) Grancha, T.; Tourbillon, C.; Ferrando-Soria, J.; Julve, M.; Lloret, F.; Pasán, J.; Ruiz-Pérez, C.; Fabelo, O.; Pardo, E. *CrystEngComm* **2013**, *15*, 9312–9315. (b) Clemente-Leon, M. *Inorg. Chem.* **2008**, *47*, 6458–6463.

(9) (a) Carlucci, L.; Ciani, G.; Proserpio, D. M.; Sironi, A. *Chem. Commun.* **1996**, 1393–1394. (b) Alexandrov, E. V.; Blatov, V. A.; Kochetkov, A. V.; Proserpio, D. M. *CrystEngComm* **2011**, *13*, 3947–3958.

(10) (a) Train, C.; Nuida, T.; Gheorghe, R.; Gruselle, M.; Ohkoshi, S. *J. Am. Chem. Soc.* **2009**, *131*, 16838–16843. (b) Train, C.; Gheorghe, R.; Krstic, V.; Chamoreau, L.-M.; Ovanesyan, N. S.; Rikken, G. L. J. a; Gruselle, M.; Verdaguer, M. *Nat. Mater.* **2008**, *7*, 729–734.

DOI: 10.1021/acs.inorgchem.5b01738
Inorg. Chem. 2015, 54, 8890–8892

Metal–Organic Frameworks

International Edition: DOI: 10.1002/anie.201501691
German Edition: DOI: 10.1002/ange.201501691

Postsynthetic Improvement of the Physical Properties in a Metal–Organic Framework through a Single Crystal to Single Crystal Transmetallation**

Thais Grancha, Jesús Ferrando-Soria, Hong-Cai Zhou, Jorge Gascon,* Beatriz Seoane, Jorge Pasán, Oscar Fabelo, Miguel Julve, and Emilio Pardo**

In memory of Olivier Kahn

Abstract: *A single crystal to single crystal transmetallation process takes place in the three-dimensional (3D) metal–organic framework (MOF) of formula $Mg^{II}_2[Mg^{II}_4[Cu^{II}_2(Me_3mpba)_2]_3]\cdot 45\,H_2O$ (**1**; Me_3mpba^{4-} = N,N′-2,4,6-trimethyl-1,3-phenylenebis(oxamate)). After complete replacement of the Mg^{II} ions within the coordination network and those hosted in the channels by either Co^{II} or Ni^{II} ions, **1** is transmetallated to yield two novel MOFs of formulae $Co^{II}_2[Co^{II}_4[Cu^{II}_2(Me_3mpba)_2]_3]\cdot 56\,H_2O$ (**2**) and $Ni^{II}_2[Ni^{II}_4[Cu^{II}_2(Me_3mpba)_2]_3]\cdot 54\,H_2O$ (**3**). This unique postsynthetic metal substitution affords materials with higher structural stability leading to enhanced gas sorption and magnetic properties.*

The design and synthesis of metal–organic frameworks (MOFs) have experienced a rapid development during the past years.[1] Since the pioneering works on the structural chemistry of MOFs,[2] interest in this field has increased exponentially. In addition to the wide range of physical and chemical properties that MOFs can exhibit,[3] this unique class of molecular multifunctional materials provide an excellent playground to study complex supramolecular dynamic processes.[4]

An accurate control of the MOF structure through ligand design is crucial to achieve the desired properties. In this sense, MOFs with predetermined dimensionalities and specific topologies can be designed, to a certain extent, by a careful choice of metal ions and organic ligands. However, a total control of the MOF structure is not always possible because of the many subtle factors that may affect their assembly.[5] Alternative synthetic routes for the synthesis of MOFs with the desired physical properties, consisting of ligand chemical modification and/or metal substitution (transmetallation) of a preformed MOF without altering its structure, are very promising because of the possibility to better control the nature of the ligand spacers and the interacting metal nodes of the MOF structure.[6] Up to now, only a few examples showing a complete transmetallation within the coordination network of the MOF have been reported, with partial transmetallation within the pores being more frequently observed.[7] This is not surprising considering that controlling selective bond destruction and formation in the solid state has proved challenging.

Herein, we report a unique solid-state transmetallation in a new series of oxamato-based 3D MOFs with two exchangeable metal sites of general formula $M^{II}_2[M^{II}_4[Cu^{II}_2(Me_3mpba)_2]_3]\cdot n\,H_2O$ (**1**: M = Mg, $n = 45$; **2**: M = Co, $n = 56$; **3**: M = Ni, $n = 54$) where Me_3mpba^{4-} is the *N,N′*-2,4,6-trimethyl-1,3-phenylenebis(oxamate) ligand. Interestingly, the reported postsynthetic ion-exchange process is reflected in a significant improvement of the structural stability and the gas sorption and magnetic properties of the original precursor (**1**) to afford two novel examples of porous magnets (**2** and **3**) of the bimetallic oxamate family.[8]

1 was obtained as brownish green prisms by the direct reaction of aqueous solutions of the dicopper(II) complex $Na_4[Cu_2(Me_3mpba)_2]\cdot 4\,H_2O$[8b] and $Mg(NO_3)_2\cdot 4\,H_2O$ (1:2

[*] T. Grancha, Prof. Dr. M. Julve, Dr. E. Pardo
Instituto de Ciencia Molecular (ICMOL), Universitat de València
Paterna 46980, València (Spain)
E-mail: emilio.pardo@uv.es
Dr. J. Ferrando-Soria, Prof. Dr. H.-C. Zhou
Department of Chemistry, Texas A&M University
College Station, TX 77842-3012 (USA)
E-mail: jesus.ferrando@uv.es
Prof. Dr. J. Gascon, Dr. B. Seoane
Catalysis Engineering-Chemical Engineering Department
Delft University of Technology
Julianalaan 136, 2628 BL Delft (The Netherlands)
E-mail: j.gascon@tudelft.nl
Dr. J. Pasán
Laboratorio de Rayos X y Materiales Moleculares
Departamento de Física, Universidad de La Laguna
La Laguna 38201, Tenerife (Spain)
Dr. O. Fabelo
Institut Laue Langevin, Diffraction Group
Grenoble 38042 (France)

[**] This work was supported by the MINECO (Spain) (Projects CTQ2013-46362-P and CTQ2013-44844-P) and the Generalitat Valenciana (Spain) (Project PROMETEOII/2014/070). B.S. and J.G. acknowledge the financial support of the European Research Council under the European Union's Seventh Framework Programme (FP/2007-2013)/ERC Grant Agreement no. 335746, CrystEng-MOF-MMM. T.G. thanks the Universitat de València for a predoctoral contract. We acknowledge SOLEIL for provision of synchrotron radiation facilities and we would like to thank Pierre Fertey for assistance in using beamline CRISTAL. Thanks are also extended to the Ramón y Cajal Program (E.P.).

Supporting information for this article is available on the WWW under http://dx.doi.org/10.1002/anie.201501691.

molar ratio) at room temperature by slow diffusion in a H-shaped tube. **2** and **3** were obtained through a double cation-exchange reaction in the solid state by immersing crystals of **1** in saturated aqueous solutions of $M(NO_3)_2{\cdot}6H_2O$ (M = Co (**2**), Ni (**3**)) for several weeks. The whole exchange process was followed visually and no crystal dissolution was observed. Moreover, the final crystals had the same size and shape as those of the original ones. These facts rule out a possible dissolution–recrystallization mechanism for this system, and strongly suggest a solid-state process.[6d] The crystal structures of **1**–**3** could be determined by single-crystal X-ray diffraction using synchrotron radiation at the CRISTAL beamline in the Synchrotron SOLEIL (see Experimental Section, Supporting Information).

1–**3** crystallize in the same *P*4/*mmm* space group of the tetragonal system (see Table S1 in the Supporting Information). All three isostructural compounds consist of anionic 3D $M^{II}{}_4Cu^{II}{}_6$ (M = Mg (**1**), Co (**2**), Ni (**3**)) open-framework structures with hydrated M^{II} countercations occupying their cavities together with a varying amount of crystallization water molecules. The anionic 3D network of **1**–**3** can be described as an extended parallel array of oxamato-bridged $M^{II}{}_4Cu^{II}{}_6$ layers growing in the *ab* plane with a mixed square/octagonal ($4{\cdot}8^2$) net topology (Figure 1 and Figure S1). The layers are further interconnected through the two trimethyl-substituted *m*-phenylene spacers among the Cu^{II} ions, as earlier found in the related manganese(II) derivative of formula $Na^{I}{}_4\{Mn^{II}{}_4[Cu^{II}{}_2(Me_3mpba)_2]_3\}{\cdot}60H_2O$.[8b]

These features yield a common porous structure for **1**–**3** with a trimodal pore-size distribution along the *c* axis made up of one single type of square pores but two types of octagonal pores (Figure 1). These two types of octagonal pores result from the distinct orientation of the trimethyl-substituted phenylene spacers pointing into or out from the channels, which is reflected in their relative diameters of circa 1.5 and 2.0 nm. However, the occupation of the channels by the corresponding countercations is very different for the starting compound **1** and the transmetallated species **2** and **3**. In **1**, the hydrated Mg^{II} counterions are alternatively located in both the narrow and wide octagonal channels: half of them (Mg2) are weakly bound to the carboxylate oxygen atoms from the anionic network, whereas the remaining half (Mg3) are hydrogen bonded through the coordinated water molecules to the anionic network (Figure 1a and Figure S2a). In contrast, for **2** and **3**, the hydrated M^{II} counterions coming from the metal-ion-exchange process (M = Co (**2**), Ni (**3**)) can only be found in the largest octagonal channels (being hydrogen bonded to the coordination network) but also in the small square ones (Figure 1b and Figure S2b). The estimated values of the empty volume without the crystallization water molecules are 11074 (**1**), 11073 (**2**), and 11023 Å^3 (**3**), which represent up to circa 54.7 (**1**), 54.8 (**2**), and 55.4% (**3**) of potential empty space per unit cell volume (V = 20262 (**1**), 20216 (**2**), and 19911 Å^3 (**3**)).

To elucidate the mechanism of the transmetallation process, we monitored the exchange of Mg^{II} ions in **1** by M^{II} ions (M = Co (**2**), Ni (**3**)) through inductively coupled plasma atomic absorption spectroscopy (ICP-AES) and SEM using single crystals (Figure S3 and Figure 2). First aiming at clarifying the thermodynamics of metal-ion exchange, we studied the variation in metal stoichiometry within the MOF (Mg^{II}:Cu^{II} and M^{II}:Cu^{II}) at different M^{II} concentrations and long exchange times (14 days). Figure S3 reveals essentially the same ion-exchange pathway consisting of a continuous decrease of the Mg^{II} occupancy (and a concomitant increase of the M^{II} occupancy) with increasing [M^{II}] up to reaching saturation (at lower M^{II} concentrations for M = Co than for M = Ni). This overall behavior suggests a rather similar thermodynamic stability for both metal sites, that is, for those within the channels and those of the coordination

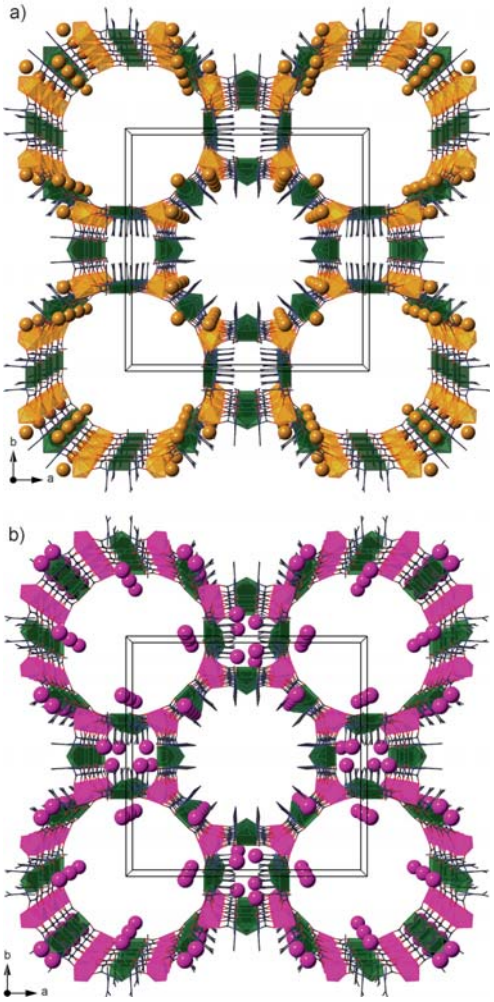

Figure 1. Perspective views of the anionic 3D $M^{II}{}_4Cu^{II}{}_6$ networks of a) **1** and b) **2**/**3** along the crystallographic *c* axis, showing the different site occupation of the channels by the M^{II} countercations (the coordinated and crystallization H_2O molecules are omitted for clarity). Polyhedra represent atoms in the coordination network and spheres represent atoms occupying the channels. Polyhedra colors: Cu = green; Mg = orange; Co/Ni = purple. Sphere colors: Mg = orange; Co/Ni = purple.

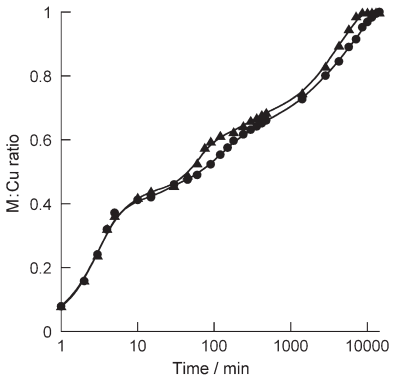

Figure 2. Kinetic profile of the ion exchange represented as the M^{II}:Cu^{II} ratio (M^{II} = Co^{II} (▲), Ni^{II} (●)) versus time plot (in semilogarithmic scale).

network. Second, the kinetics of the metal-ion exchange were monitored through the increase of the M^{II}:Cu^{II} ratio within the MOF, which was measured at specific time intervals (0–10 days) of immersion of the solid in saturated M^{II} aqueous solutions (Figure 2). A very fast exchange of around two out of six Mg^{II} ions takes place (in less than 5 min of exposure). This identical behavior for both Co^{II} and Ni^{II} substitutions, together with reaching the same M^{II}:Cu^{II} ratio, strongly suggest that this first step corresponds to the substitution of those metal ions hosted in pores. Afterwards, a slower substitution of the remaining four Mg^{II} ions by M^{II} ions takes place over the course of five (M = Co) and seven days (M = Ni), respectively, leading to complete transmetallation of the network. Interestingly, an intermediate saturation step (more obvious in the case of the Co^{II} derivative) can be observed at a M^{II}:Cu^{II} ratio of around 0.66 (Figure 2), which is likely related to cooperative effects in the occupation of the coordination network. These thermodynamic and kinetic results suggest an associative mechanism involved in the ion-exchange process.[6c] Additionally, the presence of weakly coordinated magnesium ions hosted in the channels (see structural section above) also supports that the Mg^{II} ions from the coordination network are replaced by those M^{II} ions previously situated in the channels located in close proximity to them. Preliminary studies suggest that the exchange process is reversible.

The powder X-ray diffraction (PXRD) patterns of freshly prepared samples of **1**–**3** (prepared from suspensions in water) are almost identical and they are consistent with the calculated ones (Figure S4). The correspondence of experimental and calculated structures confirms that the bulk samples are isostructural to the crystals selected for single-crystal X-ray diffraction, and that the open-framework structures remain unchanged after the transmetallation reaction. The water contents of **1**–**3** were independently determined by thermogravimetric analysis (TGA) under a dry N_2 atmosphere (Figure S5). All three compounds present a qualitatively similar behavior with a fast mass loss from room temperature followed by a "plateau" in the mass loss until decomposition begins. The estimated percentage weight loss values of 26 (**1**), 29 (**2**), and 28% (**3**) at 130 °C correspond to circa 45 (**1**), 56 (**2**), and 54 (**3**) water molecules, respectively.

To check the structural stability of the MOF structure upon removal of water molecules, variable-temperature PXRD studies were also carried out at 25, 70, 80, and 97 °C for **1**–**3** (Figure S6). **1** loses crystallinity very fast once removed from the water solution and further deteriorates when heating. Thus, its activated (dehydrated) phase shows a very poor crystallinity, suggesting a complete collapse of the open-framework structure of the original hydrated phase upon solvent removal (Figure S6a). **2** also loses crystallinity when exposed to air but the intensity of the peaks do not appreciably decrease when heated to 97 °C (Figure S6b). In contrast, the variable-temperature PXRD patterns of **3** show well-resolved peaks, which are located at the same positions and with similar intensities to those of the original hydrated phase, confirming the robustness of the MOF upon solvent removal (Figure S6c).

These PXRD results suggest that very different gas sorption properties should be observed for compounds **1**–**3**, as depicted by Figure 3. The N_2 adsorption isotherms at 77 K of **1**–**3** show a type I sorption behavior characteristic of microporous compounds (Figure 3a). The sorption capacities for each compound follow the trend **1** < **2** < **3**, as expected from the variable-temperature PXRD studies, with estimated Brunauer–Emmett–Teller (BET) surface areas of 444 (**1**), 613 (**2**), and 905 $m^2 g^{-1}$ (**3**).

To further confirm the effect of the metal-atom substitution on their gas sorption capacities, we also measured high-

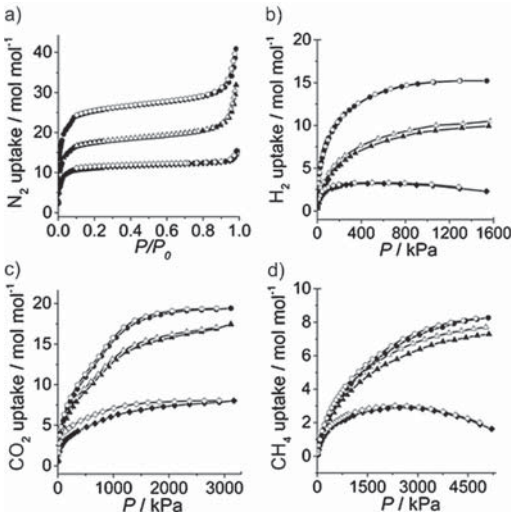

Figure 3. a) Low-pressure N_2 (77 K) and high-pressure b) H_2 (77 K), c) CO_2 (273 K), and d) CH_4 (273 K) sorption isotherms for the activated compounds **1** (◆), **2** (▲), and **3** (●). Filled and empty symbols indicate the adsorption and desorption isotherms, respectively. In (a–d), **1** is the bottom curve, **2** appears in the middle, and **3** at the top. Sorption units given in mol of adsorbate per mol of dehydrated MOF.

pressure H_2 (77 K), CO_2 (273 K), and CH_4 (273 K) adsorption isotherms of **1**–**3** (Figure 3b–d). Overall, a significant increase of the sorption capacities can be observed for the transmetallated species **2** and **3** (with a larger increase for Ni^{II} derivative **3**). The greater sorption capacity of **2** and especially **3** can be attributed both to the larger ion–quadrupole interactions because of the presence of Co^{II} and Ni^{II} ions and to the aforementioned increase of the structural stability in **2** and, more remarkably, in **3**. Although the gas uptakes follow, for all of the gases, the general trend **1** < **2** < **3**, the **2**:**1** and **3**:**1** adsorption ratios are quite different depending on the measured gas. These results suggest that this postsynthetic method for the preparation of MOFs is not only able to improve the adsorption capacity of a given material but also to tune its gas selectivity, opening the door for "à la carte" postsynthetic rational syntheses depending on the gases that should be separated.

The magnetic behavior of **1**–**3** was investigated through magnetic susceptibility measurements in both direct- (dc) and alternating-current (ac) fields. As expected, the exchange of the diamagnetic Mg^{II} ions (**1**) by paramagnetic Co^{II} (**2**) and Ni^{II} ions (**3**) (with $S_{Co} = 3/2$ and $S_{Ni} = 1$) has a dramatic influence in their dc magnetic properties (Figure S7). **1** behaves as well-isolated ferromagnetically coupled dicopper(II) units with a moderate ferromagnetic coupling between the two Cu^{II} ions. The Cu^{II} ions are coupled through the trimethyl-substituted phenylenediamidate bridges (with coupling constant $J = +14.0\ cm^{-1}$; this was fit using the Hamiltonian $H = -JS_1S_2$ with $S_1 = S_2 = S_{Cu} = 1/2$; solid line in the inset of Figure S7a).[9] In contrast, **2** and **3** show a typical ferrimagnetic behavior resulting from the strong antiferromagnetic coupling between the Cu^{II} and M^{II} ions through the oxamato bridge within each $M^{II}_4Cu^{II}_6$ layer (M = Co (**2**), Ni (**3**)), as previously found in the related manganese(II) derivative.[8b]

These overall ferro- (**1**) and ferrimagnetic (**2**, **3**) behaviors are further confirmed by the magnetization per formula unit (M) versus applied dc magnetic field (H) plots at 2.0 K (Figure S8). More importantly, a magnetic hysteresis loop is measured for both **2** and **3** at 2.0 K, with values of the coercive field of $H_c = 150$ (**2**) and 300 G (**3**) which are typical of soft magnets (inset of Figure S8).

The occurrence of a long-range 3D magnetic ordering in **2** and **3** is evidenced by the presence of a sharp frequency-independent maximum in the χ_M'' versus T plots (χ_M'' being the out-of-phase ac molar magnetic susceptibility per formula unit) at critical temperatures of $T_C = 22.5$ (**2**) and 25.0 K (**3**) (Figure 4). This is further confirmed by the M versus T plots (inset, Figure 4), which show an abrupt increase below circa 22.5 (**2**) and 25.0 K (**3**). These T_C values are somewhat higher than that earlier reported for the manganese(II) derivative ($T_C = 21.0$ K).[8b] Overall, this indicates that there exists an effective ferromagnetic interaction between the oxamato-bridged $M^{II}_4Cu^{II}_6$ ferrimagnetic layers. This interaction results from the weak ferromagnetic coupling between the Cu^{II} ions across the double 2,4,6-trimethyl-phenylenediamidate bridge within the Cu^{II}_2 pillaring units, as revealed by the magnetic behavior of **1**. Besides these "through-bond" interlayer interactions, the dipolar interactions with the paramagnetic

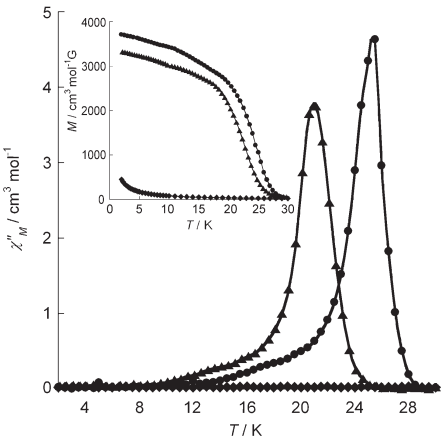

Figure 4. Temperature dependence of the ac current out-of-phase molar magnetic susceptibility (χ_M'') of **1** (◆), **2** (▲), and **3** (●) with a ±4.0 G field oscillating at 1000 Hz. Inset: temperature dependence of the magnetization (M) of **1** (◆), **2** (▲), and **3** (●).

high-spin M^{II} ions (M = Co (**2**), Ni (**3**)) hosted in the channels of the MOF may also play a non-negligible role on the long-range 3D magnetic ordering. This idea is supported by the higher T_C values of **2** and **3** when compared to the related manganese(II) derivative with diamagnetic sodium(I) ions as cationic hosts.[8b]

In summary, **1** exhibits a complete exchange of the Mg^{II} ions hosted in the channels and those constituting the heterobimetallic network after immersion in saturated aqueous Ni^{II} and Co^{II} solutions to afford **2** and **3**. Both the structural integrity of the framework and the crystallinity are maintained upon transmetalation of **1** to form **2** or **3**. Although the exchange of the metal counterions hosted in the channels has been observed previously in several MOFs acting as ion exchangers,[10] the reported exchange of the metal centers constituting the coordination framework has been rarely observed[7] and, in some cases, just in a partial manner.[11] More importantly, the postsynthetic transmetallation process of **1** affords materials with enhanced structural stability (which is especially relevant for **3**), as shown by a drastic improvement of the gas sorption properties. Finally, the substitution of the diamagnetic Mg^{II} ions in **1** by paramagnetic Ni^{II} and Co^{II} ions is responsible for the occurrence of a long-range magnetic ordering in **2** and **3**. Attempts to synthesize compounds **2** and **3** directly using slow diffusion methods were unsuccessful. These results demonstrate the clear advantages of postsynthetic methods to obtain MOFs with rationally predetermined architectures as well as improved, or even new, physical properties.

Keywords: gas sorption · magnetic properties · metal–organic frameworks · transmetalation · X-ray diffraction

How to cite: *Angew. Chem. Int. Ed.* **2015**, *54*, 6521–6525
Angew. Chem. **2015**, *127*, 6621–6625

[1] a) N. L. Rosi, M. Eddaoudi, J. Kim, M. O'Keeffe, O. M. Yaghi, *CrystEngComm* **2002**, *4*, 401 – 404; b) C. Janiak, *Dalton Trans.* **2003**, 2781 – 2804; c) D. Bradshaw, J. B. Claridge, E. J. Cussen, T. J. Prior, M. J. Rosseinsky, *Acc. Chem. Res.* **2005**, *38*, 273 – 282; d) S. Kitagawa, R. Matsuda, *Coord. Chem. Rev.* **2007**, *251*, 2490 – 2509; e) G. Férey, *Chem. Soc. Rev.* **2008**, *37*, 191 – 214; f) J. R. Long, O. M. Yaghi, *Chem. Soc. Rev.* **2009**, *38*, 1213 – 1214.

[2] a) B. F. Abrahams, B. F. Hoskins, D. M. Michail, R. Robson, *Nature* **1994**, *369*, 727 – 729; b) S. R. Batten, R. Robson, *Angew. Chem. Int. Ed.* **1998**, *37*, 1460 – 1494; *Angew. Chem.* **1998**, *110*, 1558 – 1595.

[3] a) D. Maspoch, D. Ruiz-Molina, J. Veciana, *Chem. Soc. Rev.* **2007**, *36*, 770 – 818; b) P. Dechambenoit, J. R. Long, *Chem. Soc. Rev.* **2011**, *40*, 3249 – 3265; c) E. Coronado, J. R. Galán-Mascarós, C. J. Gómez-García, V. Laukhin, *Nature* **2000**, *408*, 447 – 449; d) E. Pardo, C. Train, G. Gontard, K. Boubekeur, O. Fabelo, H. Liu, B. Dkhil, F. Lloret, K. Nakagawa, H. Tokoro, S.-I. Ohkoshi, M. Verdaguer, *J. Am. Chem. Soc.* **2011**, *133*, 15328 – 15331; e) G.-C. Xu, W. Zhang, X.-M. Ma, Y.-H. Chen, L. Zhang, H.-L. Cai, Z.-M. Wang, R.-G. Xiong, S. Gao, *J. Am. Chem. Soc.* **2011**, *133*, 14948 – 14951; f) E. Pardo, C. Train, H. Liu, L.-M. Chamoreau, B. Dkhil, K. Boubekeur, F. Lloret, K. Nakatani, H. Tokoro, S.-I. Ohkoshi, M. Verdaguer, *Angew. Chem. Int. Ed.* **2012**, *51*, 8356 – 8360; *Angew. Chem.* **2012**, *124*, 8481 – 8485; g) S.-I. Ohkoshi, K. Imoto, Y. Tsunobuchi, S. Takano, H. Tokoro, *Nat. Chem.* **2011**, *3*, 564 – 569; h) L. E. Kreno, K. Leong, O. K. Farha, M. Allendorf, R. P. Van Duyne, J. T. Hupp, *Chem. Rev.* **2012**, *112*, 1105 – 1125; i) C. Train, M. Gruselle, M. Verdaguer, *Chem. Soc. Rev.* **2011**, *40*, 3297 – 3312; j) C. Train, R. Gheorghe, V. Krstic, L.-M. Chamoreau, N. S. Ovanesyan, G. L. J. Rikken, M. Gruselle, M. Verdaguer, *Nat. Mater.* **2008**, *7*, 729 – 734.

[4] a) O. M. Yaghi, M. O'Keeffe, N. W. Ockwig, H. K. Chae, M. Eddaoudi, J. Kim, *Nature* **2003**, *423*, 705 – 714; b) J.-R. Li, R. J. Kuppler, H.-C. Zhou, *Chem. Soc. Rev.* **2009**, *38*, 1477 – 1504.

[5] M. G. Goesten, F. Kapteijn, J. Gascon, *CrystEngComm* **2013**, *15*, 9249 – 9257.

[6] a) S. M. Cohen, *Chem. Rev.* **2012**, *112*, 970 – 1000; b) M. Lalonde, W. Bury, O. Karagiaridi, Z. Brown, J. T. Hupp, O. K. Farha, *J. Mater. Chem. A* **2013**, *1*, 5453 – 5468; c) C. K. Brozek, M. Dincă, *Chem. Soc. Rev.* **2014**, *43*, 5456 – 5467; d) X. Cui, A. N. Khlobystov, X. Chen, D. H. Marsh, A. J. Blake, W. Lewis, N. R. Champness, C. J. Roberts, M. Schröder, *Chem. Eur. J.* **2009**, *15*, 8861 – 8873.

[7] a) S. Das, H. Kim, K. Kim, *J. Am. Chem. Soc.* **2009**, *131*, 3814 – 3815; b) Y. Kim, S. Das, S. Bhattacharya, S. Hong, M. G. Kim, M. Yoon, S. Natarajan, K. Kim, *Chem. Eur. J.* **2012**, *18*, 16642 – 16648; c) G. Mukherjee, K. Biradha, *Chem. Commun.* **2012**, *48*, 4293 – 4295; d) X.-J. Wang, P.-Z. Li, L. Liu, Q. Zhang, P. Borah, J. D. Wong, X. X. Chan, G. Rakesh, Y. Li, Y. Zhao, *Chem. Commun.* **2012**, *48*, 10286 – 10288; e) Z. Zhang, L. Zhang, L. Wojtas, P. Nugent, M. Eddaoudi, M. J. Zaworotko, *J. Am. Chem. Soc.* **2012**, *134*, 924 – 927; f) T.-F. Liu, L. Zou, D. Feng, Y.-P. Chen, S. Fordham, X. Wang, Y. Liu, H.-C. Zhou, *J. Am. Chem. Soc.* **2014**, *136*, 3 – 6.

[8] a) J. Ferrando-Soria, J. Pasán, C. Ruiz-Pérez, Y. Journaux, M. Julve, F. Lloret, J. Cano, E. Pardo, *Inorg. Chem.* **2011**, *50*, 8694 – 8696; b) J. Ferrando-Soria, P. Serra-Crespo, M. de Lange, J. Gascon, F. Kapteijn, M. Julve, J. Cano, F. Lloret, J. Pasán, C. Ruiz-Pérez, Y. Journaux, E. Pardo, *J. Am. Chem. Soc.* **2012**, *134*, 15301 – 15304; c) J. Ferrando-Soria, T. Grancha, M. Julve, J. Cano, F. Lloret, Y. Journaux, J. Pasán, C. Ruiz-Pérez, E. Pardo, *Chem. Commun.* **2012**, *48*, 3539 – 3541; d) J. Ferrando-Soria, T. Grancha, J. Pasán, C. Ruiz-Pérez, L. Cañadillas-Delgado, Y. Journaux, M. Julve, J. Cano, F. Lloret, E. Pardo, *Inorg. Chem.* **2012**, *51*, 7019 – 7021; e) J. Ferrando-Soria, H. Khajavi, P. Serra-Crespo, J. Gascon, F. Kapteijn, M. Julve, F. Lloret, J. Pasán, C. Ruiz-Pérez, Y. Journaux, E. Pardo, *Adv. Mater.* **2012**, *24*, 5625 – 5629; f) J. Ferrando-Soria, M. T. M. Rood, M. Julve, F. Lloret, Y. Journaux, J. Pasán, C. Ruiz-Pérez, O. Fabelo, E. Pardo, *CrystEngComm* **2012**, *14*, 761 – 764; g) J. Ferrando-Soria, R. Ruiz-García, J. Cano, S.-E. Stiriba, J. Vallejo, I. Castro, M. Julve, F. Lloret, P. Amorós, J. Pasán, C. Ruiz-Pérez, Y. Journaux, E. Pardo, *Chem. Eur. J.* **2012**, *18*, 1608 – 1617; h) T. Grancha, C. Tourbillon, J. Ferrando-Soria, M. Julve, F. Lloret, J. Pasán, C. Ruiz-Pérez, O. Fabelo, E. Pardo, *CrystEngComm* **2013**, *15*, 9312 – 9315.

[9] I. Fernández, R. Ruiz, J. Faus, M. Julve, F. Lloret, J. Cano, X. Ottenwaelder, Y. Journaux, M. C. Muñoz, *Angew. Chem. Int. Ed.* **2001**, *40*, 3039 – 3042; *Angew. Chem.* **2001**, *113*, 3129 – 3132.

[10] a) D. Denysenko, T. Werner, M. Grzywa, A. Puls, V. Hagen, G. Eickerling, J. Jelic, K. Reuter, D. Volkmer, *Chem. Commun.* **2012**, *48*, 1236 – 1238; b) T. Jacobs, R. Clowes, A. I. Cooper, M. J. Hardie, *Angew. Chem. Int. Ed.* **2012**, *51*, 5192 – 5195; *Angew. Chem.* **2012**, *124*, 5282 – 5285; c) R. Yao, X. Xu, X. Zhang, *Chem. Mater.* **2012**, *24*, 303 – 310.

[11] a) M. Kim, J. F. Cahill, H. Fei, K. Prather, S. M. Cohen, *J. Am. Chem. Soc.* **2012**, *134*, 18082 – 18088; b) C. K. Brozek, M. Dincă, *J. Am. Chem. Soc.* **2013**, *135*, 12886 – 12891; c) H. Fei, J. F. Cahill, K. Prather, S. M. Cohen, *Inorg. Chem.* **2013**, *52*, 4011 – 4016; d) M. Dincă, J. R. Long, *J. Am. Chem. Soc.* **2007**, *129*, 11172 – 11176; e) Z.-J. Zhang, W. Shi, Z. Niu, H.-H. Li, B. Zhao, P. Cheng, D.-Z. Liao, S.-P. Yan, *Chem. Commun.* **2011**, *47*, 6425 – 6427.

Received: February 21, 2015
Published online: April 14, 2015

Inorganic Chemistry

Article

pubs.acs.org/IC

Cation Exchange in Dynamic 3D Porous Magnets: Improvement of the Physical Properties

Thais Grancha,[†] Alvaro Acosta,[†] Joan Cano,[†,‡] Jesús Ferrando-Soria,*[,†] Beatriz Seoane,[§] Jorge Gascon,[§] Jorge Pasán,[⊥] Donatella Armentano,*[,∥] and Emilio Pardo*[,†]

[†]Departament de Química Inorgànica, Instituto de Ciencia Molecular (ICMOL), and [‡]Fundació General de la Universitat de València (FGUV), Universitat de València, 46980 Paterna, València, Spain

[§]Catalysis Engineering-Chemical Engineering Department, Delft University of Technology, Julianalaan 136, 2628 BL Delft, The Netherlands

[⊥]Laboratorio de Rayos X y Materiales Moleculares, Departamento de Física Fundamental II, Universidad de La Laguna, E−38201 Tenerife, Spain

[∥]Dipartimento di Chimica e Tecnologie Chimiche, Università della Calabria, Rende 87036, Cosenza, Italy

Supporting Information

ABSTRACT: We report two novel three-dimensional porous coordination polymers (PCPs) of formulas $Li_4\{Mn_4[Cu_2(Me_3mpba)_2]_3\}\cdot 68H_2O$ (**2**) and $K_4\{Mn_4[Cu_2(Me_3mpba)_2]_3\}\cdot 69H_2O$ (**3**) obtained—via alkali cation exchange in a single-crystal to single-crystal process—from the earlier reported anionic manganese(II)−copper(II) PCP of formula $Na_4\{Mn_4[Cu_2(Me_3mpba)_2]_3\}\cdot 60H_2O$ (**1**) [Me_3mpba^{4-} = *N*,*N*′-2,4,6-trimethyl-1,3-phenylenebis(oxamate)]. This postsynthetic process succeeds where the direct synthesis in solution from the corresponding building blocks fails and affords significantly more robust PCPs with enhanced magnetic properties [long-range 3D magnetic ordering temperatures for the dehydrated phases (**1**′−**3**′) of 2.0 (**1**′), 12.0 (**2**′), and 20.0 K (**3**′)]. Changes in the adsorptive properties upon postsynthetic exchange suggest that the nature, electrostatic properties, mobility, and location of the cations within the framework are crucial for the enhanced structural stability. Overall, these results further confirm the potential of postsynthetic methods (including cation exchange) to obtain PCPs with novel or enhanced physical properties while maintaining unaltered their open-framework structures.

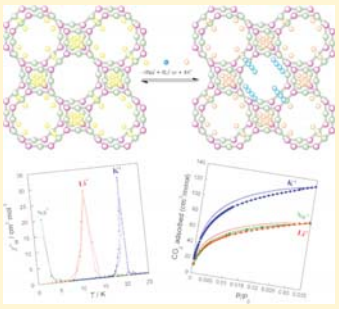

INTRODUCTION

The preparation of new examples of high-dimensional porous coordination polymers (PCPs), which are often called metal−organic frameworks (MOFs),[1−6] attracts the interest of many groups because of the great diversity of properties they can present.[7−12] PCPs are especially appealing for the design of the so-called multifunctional magnetic materials (MMMs),[13−15] where they combine magnetic properties with other essential properties in the field of nanotechnology.[16] For example, in the intercrossing area of MOF chemistry and molecular magnetism, the modulation of the magnetic properties of the host coordination framework is a hot topic. A rational route is the inclusion of particular guests such as neutral solvent molecules or gases and charged anions or cations through physi- or chemisorption processes, opening vast perspectives for this class of PCP-based porous magnets as magnetic sensors.

These rationally designed hybrid materials—consisting of metal ions or small coordination complexes linked by diverse organic or metallo-organic bridging ligands yielding two- (2D) or three-dimensional (3D) networks of varying topologies—show void channels as a remarkable common structural characteristic. In fact, the presence of these variable-size channels in their open-framework structure, which can be occupied by guest cations and anions or neutral solvent molecules, is ultimately responsible for their intriguing physical properties as well as for a fascinating host−guest chemistry.[17]

Total control of the PCP structure by using either hydro(solvo)thermal or rationally programmed soft-chemical methods is not always feasible, as many factors can interfere in the assembly process.[18] Alternatively, postsynthetic (PS) methods[19,20] can be helpful to gain control from a structural point of view and, thus, pave the way to the functionalization of a given PCP with the desired architecture, either to improve its properties or to incorporate new functionalities without altering its structure. Among the different possibilities that PS methods can offer (including transmetalation processes,[21,22] ligand exchange,[23] etc.), the exchange of guest molecules hosted in the pores of the PCPs[24,25] has emerged as the most straightforward way to improve properties such as magnetism,[26,27] gas adsorption,[28−37] catalysis,[38,39] drug delivery,[40] or luminescence.[41,42] Anionic oxamato-based coordination poly-

Received: August 18, 2015
Published: October 22, 2015

DOI: 10.1021/acs.inorgchem.5b01854
Inorg. Chem. 2015, 54, 10834−10840

mers[43−47] can be of potential interest in some or all of the aforementioned points.

RESULTS AND DISCUSSION

In an earlier communication, we reported the first porous magnet of the bimetallic oxamate family of formula $Na_4\{Mn_4[Cu_2(Me_3mpba)_2]_3\}\cdot 60H_2O$[45] (**1**) [$Me_3mpba^{4-}$ = *N*,*N*′-2,4,6-trimethyl-1,3-phenylenebis(oxamate)]. In this work, we report the crystal structures and magnetic and gas sorption properties of two novel porous magnets of formulas $Li_4\{Mn_4[Cu_2(Me_3mpba)_2]_3\}\cdot 68H_2O$ (**2**) and $K_4\{Mn_4[Cu_2(Me_3mpba)_2]_3\}\cdot 69H_2O$ (**3**). **2** and **3** are obtained via alkali cation exchange[28−42] from the previously reported ancestor **1** in a single-crystal to single-crystal (SC−SC) process (Scheme 1). Interestingly, this straightforward postsynthetic replacement of the Na^+ cations in **1** by Li^+ (**2**) or K^+ (**3**) cations enhances the robustness of the novel MOFs, and an overall improvement in both the gas sorption and the magnetic properties is observed.

Scheme 1. Cation Exchange Process for the Replacement of the Sodium(I) Ions (Yellow Spheres) in the Anionic Square/Octagonal Pillared Network of 1 with Lithium(I) (2) or Potassium(I) (3) Ions (Blue and Orange Spheres)

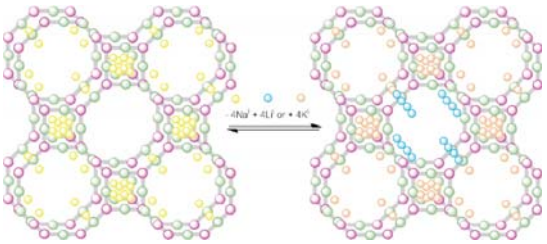

Synthesis and X-ray Crystal Structure. **1** was prepared as reported earlier[45] by slow diffusion in water of the preformed dicopper(II) complex $Na_4[Cu_2(Me_3mpba)_2]\cdot 4H_2O$ and $Mn(NO_3)_2\cdot 4H_2O$ (3:4 molar ratio) in an H-shaped tube at room temperature. **2** and **3** were obtained by immersing crystals of **1** in saturated aqueous solutions of $LiCl\cdot 6H_2O$ and $KCl\cdot 6H_2O$, respectively. Although ICP-AES measurements and SEM microscopy indicate that the majority of the cations are exchanged in a few minutes, preventing any possible kinetic analysis, the crystals were left in the saturated solutions for 24 h to ensure the complete replacement (see Experimental Section). Preliminary experiments point toward the reversibility of the process. The structures of **2** and **3** could be determined by X-ray diffraction on single crystals, revealing thus the occurrence of a unique SC−SC transformation upon alkali metal substitution in the solid state (see Experimental Section).

1−**3** are isostructural (Table S1, Supporting Information), and they consist of an anionic 3D $Mn^{II}_4Cu^{II}_6$ open-framework structure exhibiting a pillared square/octagonal layer structural architecture containing either small square channels or large octagonal pores along the *c* axis (Figure 1). The presence of two different types of narrow and wide octagonal pores (relative diameters of ca. 1.5 and 2.0 nm) arises from the different disposition of the trimethyl-substituted phenylene spacers directing inward or outward of the voids, respectively.

The hydrated charge-counterbalancing alkali M^I cations [M = Na (**1**), Li (**2**), and K (**3**)] exhibit a different distribution within the channels, along both the parallel and perpendicular

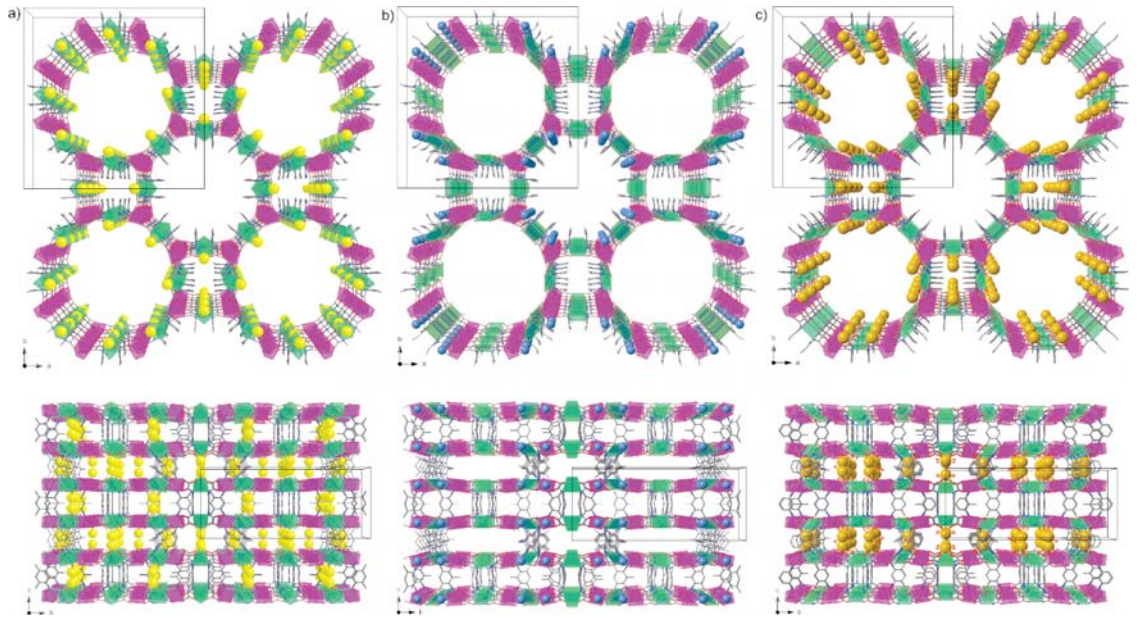

Figure 1. Perspective view of the 3D anionic network of **1** (a), **2** (b), and **3** (c) along the crystallographic *c* (top) and *a* (bottom) axes. Copper and manganese atoms from the covalent network are represented by green and purple polyhedra, respectively, whereas the sodium (**1**), lithium (**2**), and potassium (**3**) atoms occupying the channels are depicted as yellow, blue, and orange spheres, respectively (free and coordinated water molecules are omitted for clarity).

DOI: 10.1021/acs.inorgchem.5b01854
Inorg. Chem. 2015, 54, 10834−10840

directions most likely as a consequence of the variation in the ionic radii of these cations [0.68 (Li^+), 0.95 (Na^+), and 1.33 Å (K^+)]. While the small-sized Li^+ ions occupy only the narrow octagonal channels in **2**, the bigger Na^+ and K^+ occupy the square and wide octagonal channels in **1** and **3**, respectively (Figure 1a–c, top). Moreover, Li^+ ions are located in the intralayer space in **2**, whereas Na^+ and K^+ occupy the interlayer space in **1** and **3**, respectively (Figure 1a–c, bottom). This different location of the alkali metal ions must lie at the origin of the enhanced structural stability in **2** and **3** compared to **1**. Thus, although all M^I ions are weakly coordinated to the carboxylate- and/or carbonyl-oxygen atoms from the coordination network [M–O = 2.410(10)–2.883(12) (**1**), 1.925(14)–2.186(16) (**2**), and 2.683(11)–2.844(9) Å (**3**)], they coordinate in different positions. This fact, together with the different nature of the cations, plays a key role in the structural integrity or collapse upon solvent loss (Figures S1 and S2, Supporting Information).

Figures S1a and S2a show that Na1 and Na2 atoms, which are located in the larger octagonal pores, also full of water molecules, are simultaneously coordinated to the carboxylate-oxygen atoms from the two Me_3mpba ligands, forming the copper(II) basal plane. Upon water removal, this feature can originate a significant tetrahedral distortion of the square planar Cu^{II} ions, which would originate a reorientation of the organic linkers, ultimately leading to the structural collapse. This tetrahedral distortion of the copper(II) ions has already been reported for other oxamato-based PCPs.[44] In contrast, Li and K atoms in **2** and **3**, respectively, are coordinated to the carbonyl-oxygen atoms that form the coordination environment of the octahedral manganese(II) ions (Figures S1b,c and S2b,c). The possible distortions in the Mn^{II} octahedral geometry originated by displacements of the coordinated Li or K atoms when losing the water molecules would be much softer than those predicted for a square-planar to tetrahedral distortion and would not lead to a final structural collapse.

The estimated empty volumes without the highly disordered crystallization water molecules are slightly different for all three compounds [11997 (**1**), 13109 (**2**), and 12204 $Å^3$ (**3**)], and they represent up to 60%, 63.1%, and 55.8% for **1**, **2**, and **3**, respectively, of potential void per unit cell volume [V = 20075 (**1**), 20770 (**2**), and 21868 $Å^3$ (**3**)].

Thermogravimetric Analysis. The water contents of **1**–**3** are established by thermogravimetric analysis (TGA) under a dry N_2 atmosphere. A fast mass loss from room temperature to around 150 °C can be observed for all three compounds, followed by a *plateau* in the range ca. 150–300 °C, and then decomposition starts (Figure S3). The mass loss values of ca. 31% (**1**), 34% (**2**), and 35% (**3**) at 125 °C correspond to 60, 68, and 69 H_2O molecules per formula unit, respectively.

X-ray Powder Diffraction. The powder X-ray diffraction (PXRD) patterns of polycrystalline samples of the hydrated phases of **1**–**3** were measured in water suspensions to prevent the partial loss of water at room temperature (Figures 2 and S4–S6). Within each sample, the experimental PXRD pattern profiles are well consistent with the calculated ones (Figure 2), confirming the pureness of the bulk samples. Moreover, the comparison of the PXRD patterns of **1**–**3** further confirms that all three compounds are isostructural (Figure 2) and, thus, that the exchange process of the alkali metal does not modify the open-framework structures, as revealed by the single-crystal X-ray structures.

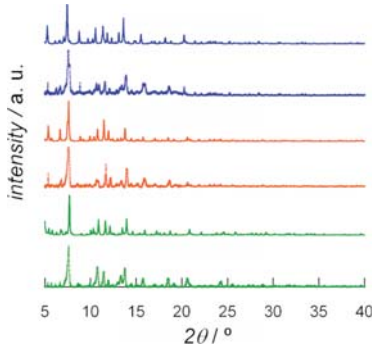

Figure 2. Experimental (—) and calculated (-O-) XRPD pattern profiles of the hydrated phases of **1** (green), **2** (red), and **3** (blue) measured as water suspensions in the 2θ range 5.0–40.0° at rt.

PXRD studies were then carried out for **1**–**3** in the temperature range 298–370 K to analyze the relative structural stability of each compound upon water loss (Figures 3 and S7–S10). The observed behavior is consistent with that predicted from the analysis of the crystal structures. After dehydration, variable-temperature PXRD patterns show a total loss of crystallinity for **1**, even at room temperature (Figure 3a). In contrast, the PXRD patterns of the activated phases of **2** and **3** show retention of crystallinity over the whole range of temperatures studied. Indeed, while **1** seems to amorphize upon removal of water, covalent networks of **2** and **3** remain crystalline, suggesting a very important role of the weak coordinative interactions with the diverse alkali countercations.

Gas Sorption Behavior. All samples of **1**–**3** were activated (dehydrated) at 80 °C under reduced pressure for 16 h prior to the sorption measurements (Figure 4), to give the dehydrated phases **1′**–**3′**.

The low-pressure N_2 adsorption isotherms at 77 K for **1′**–**3′** show remarkable differences. While the original **1′** displays hardly any adsorption of N_2, its lithium(I) (**2′**) and potassium(I) (**3′**) derivatives exhibit a much higher uptake (Figure 4a). For compounds **2′** and **3′**, the calculated Brunauer–Emmett–Teller (BET) surface areas [270 (**2**) and 200 m^2/g (**3**)] follow the trend expected according to the estimated volumes (see structural discussion above).

A similar trend to that of N_2 adsorption is observed for high-pressure H_2 isotherms measured at 77 K. In contrast, adsorption isotherms of CO_2 and CH_4 (both at 273 K) indicate that **1′** and **2′** have comparable porosities (see the almost overlapping CO_2 isotherms). We attribute these results to the amorphization of **1′** upon dehydration, which obviously leads to a less ordered structure with slightly smaller and less homogeneous pores that cannot be probed by N_2 at 77 K but are still accessible to smaller molecules such as CO_2. When comparing the adsorptive behavior of **2′** and **3′**, it is striking to observe that while the Li^+-containing sample displays a larger BET area, the K^+ sample shows a much higher affinity for H_2, CO_2, and CH_4. These results demonstrate that both the nature and location of the cation within the framework are of fundamental importance in the adsorptive properties of the material, in clear analogy to zeolites.[48]

Interestingly, these different uptake results for different adsorbates evidence that we are capable of achieving an important increase in the sorption capacity in a given material

DOI: 10.1021/acs.inorgchem.5b01854
Inorg. Chem. 2015, 54, 10834–10840

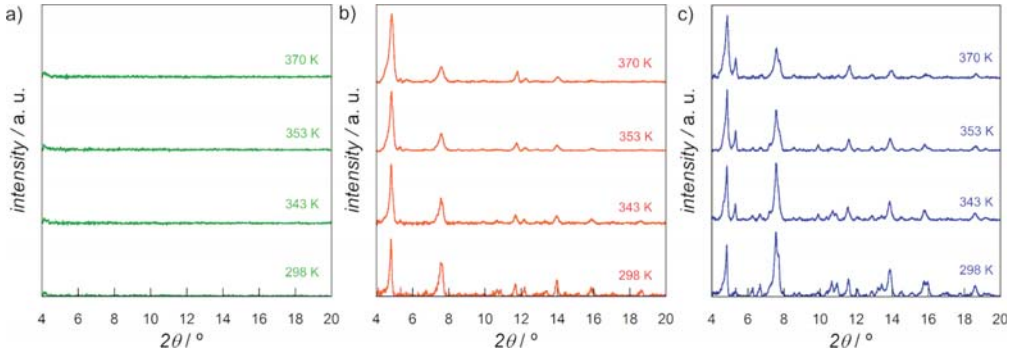

Figure 3. Variable-temperature XRD patterns of dehydrated **1** (a), **2** (b), and **3** (c) at 298, 343, 353, and 370 K.

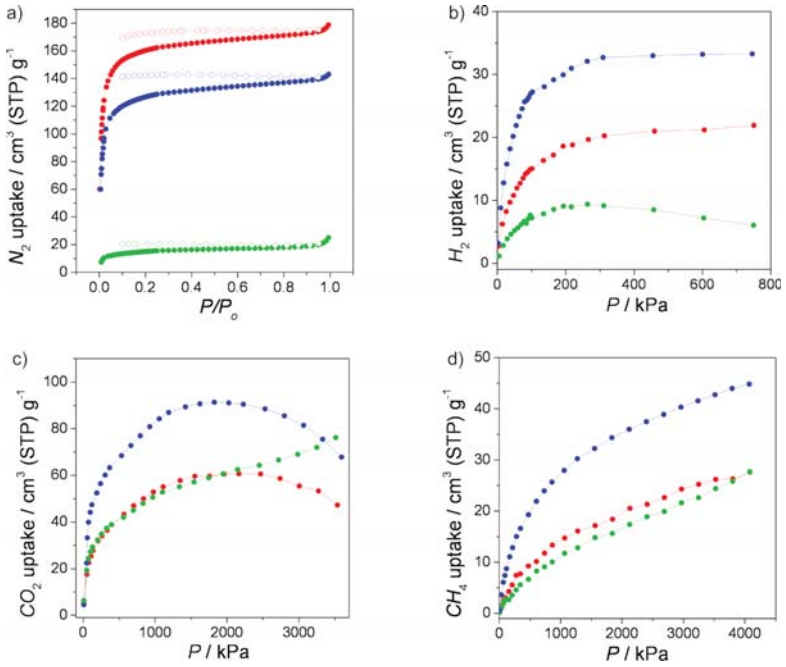

Figure 4. Low-pressure N_2 (a, 77 K) and high-pressure H_2 (b, 77 K), CO_2 (c, 273 K), and CH_4 (d, 273 K) sorption isotherms for **1′** (green), **2′** (red), and **3′** (blue). Filled and empty symbols indicate the adsorption and desorption isotherms, respectively. All samples were activated at 80 °C under reduced pressure for 16 h prior to carrying out the sorption measurements.

via cation exchange but, more importantly, and they reveal that we can also modify the gas selectivity.

Magnetic Properties. In order to analyze the effect of the alkali countercation replacement and the water loss along this series in the magnetic properties, we measured them in both the direct current (dc) and alternating current (ac) regimes (see Experimental Section), for both the hydrated samples **1**−**3** and their dehydrated phases **1′**−**3′**.

The $\chi_M T$ vs T plots (where χ_M is the dc molar magnetic susceptibility per $Cu^{II}_6Mn^{II}_4$ unit and T the temperature) for both **1**−**3** and **1′**−**3′** show the same qualitative general behavior (Figures S11 and S12). They exhibit a characteristic minimum indicative of a ferrimagnetic behavior as a consequence of the intralayer antiferromagnetic interactions between the Cu^{II} and high-spin Mn^{II} ions through the oxamato bridge, as previously found in other oxamato-based manganese(II)−copper(II)-layered compounds.

This common ferrimagnetic behavior of **1**−**3** was also suggested by the M vs H plots at 2.0 K (where M is the magnetization per $Cu^{II}_6Mn^{II}_4$ unit and H the applied dc magnetic field), which reveal, however, non-negligible differences between the hydrated and the dehydrated phases (Figure 5). The isothermal magnetization curves for **1**−**3** rapidly saturate at low field values, exhibiting maximum M values at 5 T, close to the calculated value of the saturation magnetization for the antiparallel spin alignment of the high-spin Mn^{II} (S_{Mn} = 5/2) and Cu^{II} (S_{Cu} = 1/2) ions [$M_s = (4g_{Mn}S_{Mn} - 6g_{Cu}S_{Cu})N\beta$ = 13.90 $N\beta$ with g_{Mn} = 2.0 and g_{Cu} = 2.1] (Figure 5a). In contrast, the isothermal magnetization curves for the dehydrated phases **1′**−**3′** do not saturate even at high fields,

DOI: 10.1021/acs.inorgchem.5b01854
Inorg. Chem. 2015, 54, 10834−10840

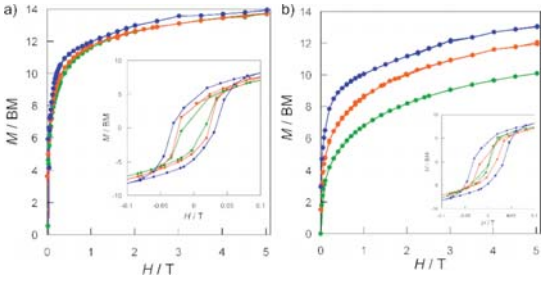

Figure 5. Field dependence of the magnetization (M) of **1**−**3** (a) and **1′**−**3′** (b). **1**, **1′** (green), **2**, **2′** (red), and **3**, **3′** (blue) at T = 2.0 K. The insets show in detail the hysteresis loops. The solid lines are only guides to the eye.

the maximum M values at 5 T being lower than the calculated saturation magnetization and dependent on the nature of the alkali countercation (Figure 5b). In addition, **1**−**3** show magnetic hysteresis loops with rather similar but low values of the coercive magnetic field around 400 G (inset of Figure 5a), whereas those of the dehydrated phases decrease from **3′** to **2′** and almost vanish for **1′** (inset of Figure 5b).

These differences in the magnetic behavior between **1**−**3** and **1′**−**3′** can be observed in the field-cooled magnetization (FCM) vs T plots (Figure S13). While the FCM curves of the hydrated phases show abrupt increases indicative of a long-range magnetic ordering at around 20.0 K for all three compounds (Figure S13a), those of the dehydrated phases shift continuously to lower temperatures following the trend **3′** > **2′** > **1′** (Figure S13b). This is further confirmed by the χ_M'' vs T plots (where χ_M'' is the out-of-phase ac molar magnetic susceptibility per formula unit) of **1**−**3** (Figure 6). Hence, a

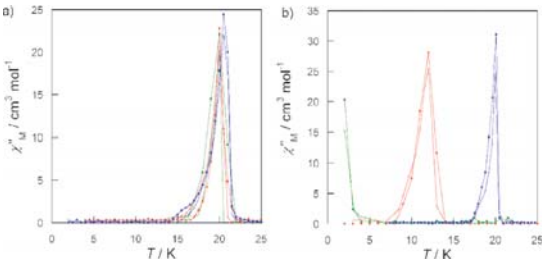

Figure 6. Temperature dependence of the ac out-of-phase molar magnetic susceptibility (χ_M'') of **1**−**3** (a) and **1′**−**3′** (b). **1**, **1′** (green), **2**, **2′** (red), and **3**, **3′** (blue) with a ±4.0 G field oscillating at 1000 (-●-) and 100 (-○-) Hz, respectively.

sharp frequency-independent peak occurs for **1**−**3** at a common critical temperature (T_C) value of 20.0 K (Figure 6a). Instead, the T_C values for the dehydrated phases decrease from 20.0 (**3′**) to 12.0 (**2′**) and then to below 2.0 K (**1′**) (Figure 6b).

Interestingly, the variation found in the long-range 3D magnetic ordering between **1**−**3** and **1′**−**3′** reflects the observed differences in the robustness of each compound upon water loss, as revealed by the PXRD studies. So, the T_C value shifts from 20.0 K to below 2.0 K for the sodium(I) derivative (**1′**), which is probably related to the aforementioned partial collapse of the network structure upon water removal. In contrast, the lithium(I) derivative (**2′**) exhibits a much softer decrease of the T_C value from 20.0 to 12.0 K, while the T_C value for the potassium(I) derivative (**3′**) remains unaltered, confirming thus the robustness of the network structure upon water removal.

CONCLUSIONS

In summary, we report a unique family of PCPs obtained in an SC to SC process via cation exchange. This process induces enhanced structural stability in the final materials, which is ultimately responsible for the severe improvement of both the magnetic and gas sorption properties upon solvent removal. In addition, the whole process has been followed by single-crystal X-ray diffraction, allowing comprehensive evidence, through structural insights, about the putative role of alkali metal ions on the structural stability of the materials and situating this work as one of the very first deep studies of cation-exchanged MOFs, reached with the help of single-crystal X-ray crystallography methods. Overall, the exchange of the sodium(I) countercations hosted in the channels by lithium(I) or potassium(I) results in more robust materials and affects dramatically their physical properties. On one hand, an important enhancement of the long-range 3D magnetic ordering temperatures for **2′** and **3′** has been observed. On the other hand, the nature and location of the cations within the framework determine the gas adsorption properties of the PCP. Our results give additional evidence that postsynthetic methods can be effectively used to modulate the physical properties of PCPs without altering their structures. Current efforts are dedicated to explore the ion exchange ability of these dynamic porous magnets toward toxic cations (radioactive and heavy metals) for future use of oxamato-based coordination polymers as detoxification agents.

EXPERIMENTAL SECTION

Materials. $Na_4[Cu_2(Me_3mpba)_2]\cdot 4H_2O$ was synthesized according to literature methods.[45] All chemicals were of reagent grade quality, and they were purchased from commercial sources and used as received.

Preparation of $M_4\{Mn_4[Cu_2(Me_3mpba)_2]_3\}\cdot nH_2O$ [1: M = Na^+ (*n* = 60); 2: M = Li^+ (*n* = 68); 3: M = K^+ (*n* = 69)]. X-ray quality bright green prisms of **1** were grown by slow diffusion of aqueous solutions prepared with stoichiometric amounts of $Na_4[Cu_2(Me_3mpba)_2]\cdot 4H_2O$ (0.011 g, 0.015 mmol) and $Mn(NO_3)_2\cdot 4H_2O$ (0.005 g, 0.020 mmol) in an H-shaped tube on standing at room temperature after 4 weeks. Well-formed pale green prisms of **2** and **3**, which were suitable for X-ray diffraction, were then obtained by immersing crystals of **1** for 24 h in saturated aqueous solutions of LiCl·$6H_2O$ and KCl·$6H_2O$, respectively. Yield: 0.010 g, 58%. Anal. Calcd (%) for $C_{78}H_{180}N_{12}O_{96}Na_4Cu_6Mn_4$ (3515.3): C 26.65, H 5.16, N 4.78. Found: C 26.59, H 5.11, N 4.78. IR (KBr): 1602 cm^{-1} (CO). **2**: Yield: 97%. Anal. Calcd (%) for $C_{78}H_{196}N_{12}O_{104}Li_4Cu_6Mn_4$ (3595.2): C 26.06, H 5.49, N 4.67. Found: C 26.19, H 5.71, N 4.66. IR (KBr): 1599 cm^{-1} (CO). **3**: Yield: 98%. Anal. Calcd (%) for $C_{78}H_{198}N_{12}O_{105}K_4Cu_6Mn_4$ (3741.8): C 25.04, H 5.33, N 4.49. Found: C 25.01, H 5.42, N 4.47. IR (KBr): 1600 cm^{-1} (CO).

Single-Crystal X-ray Diffraction. Single crystals of **2** and **3** were mounted on glass fibers, in a grease drop, and very quickly placed on a liquid nitrogen stream cooled at 100 K to avoid the degradation upon dehydration. Diffraction data were collected on a Bruker-Nonius X8APEXII CCD area detector diffractometer using graphite-monochromated Mo K_α radiation (λ = 0.710 73 Å). The data were processed through the SAINT[49] reduction and SADABS[50] multiscan absorption software. As previously reported, crystals of **2** and **3**, suitable for X-ray diffraction, were obtained by immersing crystals of **1** for 24 h in saturated aqueous solutions of LiCl·$6H_2O$ and KCl·$6H_2O$,

DOI: 10.1021/acs.inorgchem.5b01854
Inorg. Chem. 2015, 54, 10834−10840

respectively, after a crystal-to-crystal transformation accounting for a poor quality and a poor diffraction power of the samples with respect to **1** (Figure S14). In fact, a lower θ_{max} of diffraction was obtained (detected as Alerts A in the checkcifs of **2** and **3**), especially for **2**, even if many efforts were made to extract the best diffraction data from each sample. However, the solution and refinement parameters are suitable, compared with analogue MOF structures previously reported; thus we are convinced that the structures found are consistent.[51−54]

The structures were solved by the Patterson method and subsequently completed by Fourier recycling using the SHELXL-2013 software package.[55,56] In **2**, to increase the data/parameters ratio, only the metal atoms were refined anisotropically, while in **3** all non-hydrogen atoms were refined anisotropically except K^+ alkali metal, for which four positions have been refined, with 0.15 (K1a), 0.20 (K1b), 0.15 (K1c), and 0.5 (K2) occupancy factors, and disordered water molecules. The hydrogen atoms were set in calculated positions and refined as riding atoms. The high thermal vibration parameters (Alerts A and B in the checkcifs) displayed for atoms in the organic ligand are a consequence of contributions from different factors, including (a) the flexibility of the framework and consequential disorder, (b) the high residual electron density produced by the methyl groups that are dynamic components of the walls, (c) the use of some bond length and angle restraints during the refinements or fixed positions of some highly disordered atoms, and (d) above all the limitation in the data quality, coming from crystals obtained upon postsynthetic exchange. Furthermore, and as expected for such systems, the lattice water molecules were highly disordered and cannot be satisfactorily modeled (at the origin of the first-level Alerts A in **2** and **3**). The rare structures found from the ΔF map were refined with constraints, and their hydrogen atoms were generally neither found nor calculated. As a consequence, in both compounds **2** and **3** the contribution to the diffraction pattern from the highly disordered water molecules of crystallization (272 molecules of H_2O in **2** and 276 in **3** located in the voids of the lattice that amount to 60% percentage void volume of the unit cell) was subtracted from the observed data through the SQUEEZE method, implemented in PLATON.[57] The final formulation for each compound is consistent with the residual electron density and volume. The final full-matrix least-squares refinements on F^2, minimizing the function $\sum w(|F_o| - |F_c|)^2$, reached convergence with the values of the discrepancy indices given in Table S1. High R values (levels Alert A in checkcifs) are, most likely, mainly affected by the contribution of the highly disordered solvent to the intensities of the low-angle reflections. The final geometrical calculations and all the graphical aspects were carried out with CRYSTAL MAKER, WinGX, and POV-Ray programs.[58−60]

X-ray Powder Diffraction. Polycrystalline samples of **1**−**3** were prepared by introducing the corresponding sample into 0.5 mm borosilicate capillaries and then mounted and aligned on an Empyrean PANalytical powder diffractometer, equipped with a Cu Kα radiation (λ = 1.540 56 Å). For each sample, five measurements were collected at room temperature (2θ = 2−50°) and merged in a single diffractogram. The collected data were analyzed with the X'Pert HighScore Plus software.[61]

Variable-temperature PXRD studies were also carried out following the same procedure for solid polycrystalline samples of **1**−**3**. In this case, three repeated measurements were collected for each sample (2θ = 4−20°) at different temperatures (298, 343, 353, and 370 K) and merged in a single diffractogram. Each measurement was carried out after waiting 10 extra minutes once the corresponding temperature was stabilized. The chosen narrower angle interval (2θ = 4−20°) obeys equipment safety reasons when using the cryostat and given the lack of important peaks beyond that range.

Thermogravimetric Analysis. The TGA measurements were carried out on crystalline samples of **1**−**3** under a dry N_2 atmosphere with a Mettler Toledo TGA/STDA 851^e thermobalance operating at a heating rate of 10 °C min^{-1}.

Gas Sorption. Low-pressure N_2 adsorption isotherms at 77 K were measured on crystalline samples of **1**−**3** in a Tristar II 3020 Micrometrics equipment. Prior to the measurements, the adsorbent was outgassed at 80 °C under N_2 flow for 16 h. The BET model was used to estimate the surface areas.[62]

High-pressure adsorption isotherms of CO_2, CH_4, and H_2 (purity of 99.995%) were determined using the volumetric technique with an apparatus from BEL Japan (Belsorp HP). Samples of **1**−**3** (ca. 0.2 g) were placed in the sample container, and they were pretreated by increasing the temperature to 363 K at a rate of 10 K/min under vacuum and maintaining the temperature for 2 h prior to their analysis.

Magnetic Measurements. Variable-temperature direct current and alternating current magnetic susceptibility measurements were carried out with a Quantum Design SQUID magnetometer. Crystals of **1**−**3** were extracted from the mother liquor, and then they were immediately introduced at 110 K without vacuum under a continuous He flow to prevent any partial water loss prior to carrying out the magnetic measurements of these "fresh-hydrated" phases. Afterward, the polycrystalline samples of **1**−**3** were kept at 80 °C for 120 min under vacuum to yield the dehydrated phases **1**′−**3**′ prior to carrying out the magnetic measurements. The susceptibility data were corrected for the diamagnetism of both the constituent atoms and the sample holder.

■ ASSOCIATED CONTENT

Ⓢ Supporting Information

The Supporting Information is available free of charge on the ACS Publications website at DOI: 10.1021/acs.inorgchem.5b01854.

Preparation and physical characterization data of **2** and **3**, additional structural and magnetic data of **1**−**3** (Figures S1−S14), and crystallographic refinement details for **1**−**3** (Table S1) (PDF)

Crystallographic data for CCDC-1036928 (**2**) (CIF)

Crystallographic data for CCDC-1036929 (**3**) (CIF)

■ AUTHOR INFORMATION

Corresponding Authors

*E-mail: jesus.ferrando@uv.es.

*E-mail: donatella.armentano@unical.it.

*E-mail: emilio.pardo@uv.es.

Notes

The authors declare no competing financial interest.

■ ACKNOWLEDGMENTS

This work was supported by the MINECO (Spain) (Projects CTQ2013-46362-P and CTQ2013-44844-P), the Generalitat Valenciana (Spain) (Project PROMETEOII/2014/070), and the Ministero dell'Istruzione, dell'Università e della Ricerca (Italy). T.G. thanks the Universitat de València for a predoctoral contract. Thanks are also extended to the MICINN Ramón y Cajal Program (E.P.). B.S. and J.G. acknowledge the financial support of the European Research Council under the European Union's Seventh Framework Programme (FP/2007-2013)/ERC Grant Agreement no. 335746, CrystEng-MOF-MMM. We are especially thankful to Dr. Rafael Ruiz-García (Universitat de València) for unselfish help and continuous interest in this work.

■ REFERENCES

(1) Rosi, N. L.; Eddaoudi, M.; Kim, J.; O'Keeffe, M.; Yaghi, O. M. *CrystEngComm* **2002**, *4*, 401−404.

(2) Janiak, C. *Dalton Trans.* **2003**, 2781−2804.

(3) Bradshaw, D.; Claridge, J. B.; Cussen, E. J.; Prior, T. J.; Rosseinsky, M. J. *Acc. Chem. Res.* **2005**, *38*, 273−282.

(4) Kitagawa, S.; Matsuda, R. *Coord. Chem. Rev.* **2007**, *251*, 2490−2509.

DOI: 10.1021/acs.inorgchem.5b01854
Inorg. Chem. 2015, 54, 10834−10840

(5) Férey, G. *Chem. Soc. Rev.* **2008**, *37*, 191−214.
(6) Long, J. R.; Yaghi, O. M. *Chem. Soc. Rev.* **2009**, *38*, 1213−1214.
(7) Coronado, E.; Galán-Mascarós, J. R.; Gómez-García, C. J.; Laukhin, V. *Nature* **2000**, *408*, 447−449.
(8) Train, C.; Gheorghe, R.; Krstic, V.; Chamoreau, L.-M.; Ovanesyan, N. S.; Rikken, G. L. J. A.; Gruselle, M.; Verdaguer, M. *Nat. Mater.* **2008**, *7*, 729−734.
(9) Ohkoshi, S.-I.; Imoto, K.; Tsunobuchi, Y.; Takano, S.; Tokoro, H. *Nat. Chem.* **2011**, *3*, 564−569.
(10) Pardo, E.; Train, C.; Gontard, G.; Boubekeur, K.; Fabelo, O.; Liu, H.; Dkhil, B.; Lloret, F.; Nakagawa, K.; Tokoro, H.; Ohkoshi, S.; Verdaguer, M. *J. Am. Chem. Soc.* **2011**, *133*, 15328−15331.
(11) Kreno, L. E.; Leong, K.; Farha, O. K.; Allendorf, M.; Van Duyne, R. P.; Hupp, J. T. *Chem. Rev.* **2012**, *112*, 1105−1125.
(12) Pardo, E.; Train, C.; Liu, H.; Chamoreau, L.-M.; Dkhil, B.; Boubekeur, K.; Lloret, F.; Nakatani, K.; Tokoro, H.; Ohkoshi, S.; Verdaguer, M. *Angew. Chem., Int. Ed.* **2012**, *51*, 8356−8360.
(13) Maspoch, D.; Ruiz-Molina, D.; Veciana, J. *Chem. Soc. Rev.* **2007**, *36*, 770−818.
(14) Dechambenoit, P.; Long, J. R. *Chem. Soc. Rev.* **2011**, *40*, 3249−3265.
(15) Grancha, T.; Ferrando-Soria, J.; Castellano, M.; Julve, M.; Pasán, J.; Armentano, D.; Pardo, E. *Chem. Commun.* **2014**, *50*, 7569−7585.
(16) *Molecule-Based Magnetic Materials*; Turnbull, M. M., Sugimoto, T., Thompson, L. K., Eds.; ACS Symposium Series; American Chemical Society: Washington, DC, 1996; Vol. *644*.
(17) Yaghi, O. M.; O'Keeffe, M.; Ockwig, N. W.; Chae, H. K.; Eddaoudi, M.; Kim, J. *Nature* **2003**, *423*, 705−714.
(18) Goesten, M. G.; Kapteijn, F.; Gascon, J. *CrystEngComm* **2013**, *15*, 9249−9257.
(19) Brozek, C. K.; Dincă, M. *Chem. Soc. Rev.* **2014**, *43*, 5456−5467.
(20) Cohen, S. M. *Chem. Rev.* **2012**, *112*, 970−1000.
(21) Liu, T.-F.; Zou, L.; Feng, D.; Chen, Y.-P.; Fordham, S.; Wang, X.; Liu, Y.; Zhou, H.-C. *J. Am. Chem. Soc.* **2014**, *136*, 7813−7816.
(22) Grancha, T.; Ferrando-Soria, J.; Zhou, H.-C.; Gascon, J.; Seoane, B.; Pasán, J.; Fabelo, O.; Julve, M.; Pardo, E. *Angew. Chem., Int. Ed.* **2015**, *54*, 6521−6525.
(23) Fei, H.; Cahill, J. F.; Prather, K. a; Cohen, S. M. *Inorg. Chem.* **2013**, *52*, 4011−4016.
(24) Cui, X.; Khlobystov, A. N.; Chen, X.; Marsh, D. H.; Blake, A. J.; Lewis, W.; Champness, N. R.; Roberts, C. J.; Schröder, M. *Chem. - Eur. J.* **2009**, *15*, 8861−8873.
(25) Li, B.; Zhang, Y.; Ma, D.; Ma, T.; Shi, Z.; Ma, S. *J. Am. Chem. Soc.* **2014**, *136*, 1202−1205.
(26) Yao, R.; Xu, X.; Zhang, X. *Chem. Mater.* **2012**, *24*, 303−310.
(27) Zeng, M. H.; Yin, Z.; Tan, Y. X.; Zhang, W. X.; He, Y. P.; Kurmoo, M. *J. Am. Chem. Soc.* **2014**, *136*, 4680−4688.
(28) Dinca, M.; Long, J. R. *J. Am. Chem. Soc.* **2007**, *129*, 11172−11176.
(29) Yang, S.; Lin, X.; Blake, A. J.; Thomas, K. M.; Hubberstey, P.; Champness, N. R.; Schröder, M. *Chem. Commun.* **2008**, *7345*, 6108−6110.
(30) Himsl, D.; Wallacher, D.; Hartmann, M. *Angew. Chem., Int. Ed.* **2009**, *48*, 4639−4642.
(31) Nouar, F.; Eckert, J.; Eubank, J. F.; Forster, P.; Eddaoudi, M. *J. Am. Chem. Soc.* **2009**, *131*, 2864−2870.
(32) Yang, S.; Lin, X.; Blake, A. J.; Walker, G. S.; Hubberstey, P.; Champness, N. R.; Schröder, M. *Nat. Chem.* **2009**, *1*, 487−493.
(33) An, J.; Rosi, N. L. *J. Am. Chem. Soc.* **2010**, *132*, 5578−5579.
(34) Procopio, E. Q.; Linares, F.; Montoro, C.; Colombo, V.; Maspero, A.; Barea, E.; Navarro, J. A. R. *Angew. Chem., Int. Ed.* **2010**, *49*, 7308−7311.
(35) Nohra, B.; El Moll, H.; Rodriguez Albelo, L. M.; Mialane, P.; Marrot, J.; Mellot-Draznieks, C.; O'Keeffe, M.; Ngo Biboum, R.; Lemaire, J.; Keita, B.; Nadjo, L.; Dolbecq, A. *J. Am. Chem. Soc.* **2011**, *133*, 13363−13374.
(36) Yang, S.; Martin, G. S. B.; Titman, J. J.; Blake, A. J.; Allan, D. R.; Champness, N. R.; Schröder, M. *Inorg. Chem.* **2011**, *50*, 9374−9384.
(37) Lin, Z.-J.; Liu, T.-F.; Huang, Y.-B.; Lü, J.; Cao, R. *Chem. - Eur. J.* **2012**, *18*, 7896−7902.
(38) Fei, H.; Rogow, D. L.; Oliver, S. R. J. *J. Am. Chem. Soc.* **2010**, *132*, 7202−7209.
(39) Genna, D. T.; Wong-Foy, A. G.; Matzger, A. J.; Sanford, M. S. *J. Am. Chem. Soc.* **2013**, *135*, 10586−10589.
(40) An, J.; Geib, S. J.; Rosi, N. L. *J. Am. Chem. Soc.* **2009**, *131*, 8376−8377.
(41) An, J.; Shade, C. M.; Chengelis-Czegan, D. a; Petoud, S.; Rosi, N. L. *J. Am. Chem. Soc.* **2011**, *133*, 1220−1223.
(42) Qin, J.-S.; Zhang, S.-R.; Du, D.-Y.; Shen, P.; Bao, S.-J.; Lan, Y.-Q.; Su, Z.-M. *Chem. - Eur. J.* **2014**, *20*, 5625−5630.
(43) Ferrando-Soria, J.; Grancha, T.; Julve, M.; Cano, J.; Lloret, F.; Journaux, Y.; Pasán, J.; Ruiz-Pérez, C.; Pardo, E. *Chem. Commun.* **2012**, *48*, 3539−3541.
(44) Ferrando-Soria, J.; Ruiz-García, R.; Cano, J.; Stiriba, S.-E.; Vallejo, J.; Castro, I.; Julve, M.; Lloret, F.; Amorós, P.; Pasán, J.; Ruiz-Pérez, C.; Journaux, Y.; Pardo, E. *Chem. - Eur. J.* **2012**, *18*, 1608−1617.
(45) Ferrando-Soria, J.; Serra-Crespo, P.; de Lange, M.; Gascon, J.; Kapteijn, F.; Julve, M.; Cano, J.; Lloret, F.; Pasán, J.; Ruiz-Pérez, C.; Journaux, Y.; Pardo, E. *J. Am. Chem. Soc.* **2012**, *134*, 15301−15304.
(46) Ferrando-Soria, J.; Khajavi, H.; Serra-Crespo, P.; Gascon, J.; Kapteijn, F.; Julve, M.; Lloret, F.; Pasán, J.; Ruiz-Pérez, C.; Journaux, Y.; Pardo, E. *Adv. Mater.* **2012**, *24*, 5625−5629.
(47) Grancha, T.; Tourbillon, C.; Ferrando-Soria, J.; Julve, M.; Lloret, F.; Pasán, J.; Ruiz-Pérez, C.; Fabelo, O.; Pardo, E. *CrystEngComm* **2013**, *15*, 9312.
(48) Lozinska, M. M.; Mangano, E.; Mowat, J. P. S.; Shepherd, A. M.; Howe, R. F.; Thompson, S. P.; Parker, J. E.; Brandani, S.; Wright, P. A. *J. Am. Chem. Soc.* **2012**, *134*, 17628−17642.
(49) *SAINT*, version 6.45; Bruker Analytical X-ray Systems, Madison, WI, 2003.
(50) Sheldrick, G. M. *SADABS Program for Absorption Correction*, version 2.10; Analytical X-ray Systems: Madison, WI, 2003.
(51) Li, Q.; Zhang, W.; Miljanić, O. S.; Knobler, C. B.; Stoddart, J. F.; Yaghi, O. M. *Chem. Commun.* **2010**, *46*, 380−382.
(52) Furukawa, H.; Ko, N.; Go, Y. B.; Aratani, N.; Choi, S. B.; Choi, E.; Yazaydin, A. O.; Snurr, R. Q.; O'Keeffe, M.; Kim, J.; Yaghi, O. M. *Science* **2010**, *329*, 424−428.
(53) Smaldone, R. A.; Forgan, R. S.; Furukawa, H.; Gassensmith, J. J.; Slawin, A. M. Z.; Yaghi, O. M.; Stoddart, J. F. *Angew. Chem., Int. Ed.* **2010**, *49*, 8630−8634.
(54) Coskun, A.; Hmadeh, M.; Barin, G.; Gándara, F.; Li, Q.; Choi, E.; Strutt, N. L.; Cordes, D. B.; Slawin, A. M. Z.; Stoddart, J. F.; Sauvage, J. P.; Yaghi, O. M. *Angew. Chem., Int. Ed.* **2012**, *51*, 2160−2163.
(55) Sheldrick, G. M. *Acta Crystallogr., Sect. A: Found. Crystallogr.* **2008**, *64*, 112−122.
(56) *SHELXTL*-2013/4; Bruker Analytical X-ray Instruments: Madison, WI, 2013.
(57) Spek, A. L. *Acta Crystallogr., Sect. D: Biol. Crystallogr.* **2009**, *65*, 148−155.
(58) Palmer, D. *CRYSTAL MAKER*; Cambridge University Technical Services: Cambridge, 1996.
(59) Farrugia, L. J. *J. Appl. Crystallogr.* **1999**, *32*, 837−838.
(60) *POV-Ray*, version 3.6.2; Persistence of Vision Raytracer, Pty. Ltd., 2003.
(61) *X'Pert HighScore Plus*; PANalytical: The Netherlands, 2012.
(62) Brunauer, S.; Emmett, P. H.; Teller, E. *J. Am. Chem. Soc.* **1938**, *60*, 309−319.

DOI: 10.1021/acs.inorgchem.5b01854
Inorg. Chem. 2015, 54, 10834−10840

ChemPubSoc Europe

DOI: 10.1002/chem.201504176

CHEMISTRY
A European Journal
Full Paper

Multifunctional Materials | *Hot Paper*

Solid-State Molecular Nanomagnet Inclusion into a Magnetic Metal–Organic Framework: Interplay of the Magnetic Properties

Marta Mon,[a] Alejandro Pascual-Álvarez,[a] Thais Grancha,[a] Joan Cano,[a, b] Jesús Ferrando-Soria,[a] Francesc Lloret,[a] Jorge Gascon,[c] Jorge Pasán,[d] Donatella Armentano,*[e] and Emilio Pardo*[a]

Abstract: Single-ion magnets (SIMs) are the smallest possible magnetic devices and are a controllable, bottom-up approach to nanoscale magnetism with potential applications in quantum computing and high-density information storage. In this work, we take advantage of the promising, but yet insufficiently explored, solid-state chemistry of metal–organic frameworks (MOFs) to report the single-crystal to single-crystal inclusion of such molecular nanomagnets within the pores of a magnetic MOF. The resulting host–guest supramolecular aggregate is used as a playground in the first in-depth study on the interplay between the internal magnetic field created by the long-range magnetic ordering of the structured MOF and the slow magnetic relaxation of the SIM.

Introduction

Interest in metal–organic frameworks (MOFs)[1–4] has grown exponentially during the last few decades as a direct consequence of the thrilling properties that these materials may exhibit.[5] Owing to their rich host–guest chemistry,[6–8] MOFs have shown themselves as excellent playgrounds for the design of multifunctional materials.[9] However, although they have proven their efficiency as hosts for gases[6–8] and small molecules,[10–15] considerable work remains to be done in terms of molecular recognition[16] and/or encapsulation of more complex molecular systems, in analogy to molecular metal–organic cages (MOCs) in solution.[17] In this sense, recent developments in post-synthetic (PS) procedures on preformed MOFs can be a powerful tool[18] for the design of novel porous materials incorporating functional molecules in their porosity.[10–15]

Within the multidisciplinary field of molecular magnetism,[19] several research groups have engaged their efforts in the design of MOFs exhibiting a spontaneous magnetization below a critical temperature (T_C).[20–28] Among the functional guest molecules to be incorporated into MOFs, the so-called single-ion magnets (SIMs)[29] constitute very promising candidates. SIMs have gained special relevance, and different examples based on lanthanides[30–32] and actinides,[33–35] but also highly anisotropic transition-metal ions,[36–39] acting as molecular nanomagnets,[40] have been reported. The current challenge along this avenue of molecular magnetism is the further processing and addressing of these individual molecules over a variety of substrates for potential applications as high-density magnetic memories[40] and quantum-computing devices[41,42] in the emerging field of molecular spintronics.[43,44] Their advantages in the field of high-density information storage in comparison to traditional ferro- or ferrimagnetic materials are quite obvious as they exhibit molecular dimensions.

Inspired by the seminal work of Fujita[45–47] on the encapsulation of guest molecules in porous coordination networks through specific host–guest interactions, we present a synthetic strategy able to incorporate well-ordered SIMs within the pores of a magnetic MOF by means of a single-crystal to single-crystal (SC to SC) post-synthetic process.[48–50] By following this approach, long-range magnetic ordering from the magnetic MOF and slow magnetic relaxation of the incorporated SIM can be merged into a single solid, tentatively resulting in an interplay of both magnetic phenomena.

Herein, we report the solid-state incorporation by SC to SC transformation of such a big molecule as the Mn^{III} porphyrin of formula $[Mn^{III}(TPP)(H_2O)_2]ClO_4$ (TPP = 5,10,15,20-tetraphenylporphyrin)[51,52] into a manganese(II)–copper(II) 3D MOF of formula

[a] *M. Mon, A. Pascual-Álvarez, T. Grancha, Dr. J. Cano, Dr. J. Ferrando-Soria, Prof. Dr. F. Lloret, Dr. E. Pardo*
Instituto de Ciencia Molecular (ICMOL) Universitat de València
Paterna 46980 València (Spain)
E-mail: emilio.pardo@uv.es

[b] *Dr. J. Cano*
Fundació General de la Universitat de València (FGUV)
Paterna 46980 València (Spain)

[c] *Prof. Dr. J. Gascon*
Catalysis Engineering-Chemical Engineering Department
Delft University of Technology
Julianalaan 136, 2628 BL Delft (The Netherlands)

[d] *Dr. J. Pasán*
Laboratorio de Rayos X y Materiales Moleculares Departamento de Físic
Universidad de La Laguna La Laguna 38201
Tenerife (Spain)

[e] *Dr. D. Armentano*
Dipartimento di Chimica e Tecnologie Chimiche, Università della Calabria
87030, Rende, Cosenza (Italy)
E-mail: donatella.armentano@unical.it

Supporting information and ORCID(s) from the author(s) for this article are available on the WWW under http://dx.doi.org/10.1002/chem.201504176.

$Na_4\{Mn_4[Cu_2(Me_3mpba)_2]_3\}\cdot 60\,H_2O$ (**1**) [Me_3mpba^{4-} = *N*,*N*′-2,4,6-trimethyl-1,3-phenylenebis(oxamate)] earlier reported by some of us,[27] to yield the novel compound of formula $[Mn^{III}(TPP)]Na_3\{Mn_4[Cu_2(Me_3mpba)_2]_3\}\cdot 39\,H_2O$ (**MnTPP@1**). This unprecedented hybrid material exhibiting coexistence of a long-range magnetic order and a slow magnetic relaxation allows for an in-depth study on the interplay between the magnetic host matrix and the SIM guest.

Results and Discussion

MnTPP@1 was obtained by straight diffusion and reversible cation exchange in the solid state by soaking crystals of **1** in a saturated water/methanol (5:1) solution of $[Mn^{III}(TPP)(H_2O)_2]ClO_4$ (Figure 1a). After 24 h of immersion, the initially dark-brown solution became colorless (Figure 1b). This feature provides a clear indication of the successful insertion of the metalloporphyrin cationic units into the sodium-defective anionic MOF, which are likely retained within the pores of the MOF through electrostatic interactions. To ensure for complete substitution, the solution was replaced every 24 h over two weeks (see the Experimental Section, Supporting Information). The reversibility of the process can be evidenced by the recovery of the dark-brown color of the solution after the addition of an excess of NaCl (Figure 1c), which indicates a release of cationic metalloporphyrin units only in the presence of a substituting alkaline cation. The cation exchange process was monitored through ICP-AES and EDX analyses, which independently show that a partial substitution of only one of the three Na^+ cations per formula unit of **1** by the cationic $[Mn^{III}(TPP)(H_2O)_2]^+$ complexes takes place after 10 days under the saturation conditions (Figure 1d). To ensure for stoichiometric (1:1 $[Mn^{III}(TPP)(H_2O)_2]^+$/**1** molar ratio) substitution, the solution was replaced every 24 h over two weeks (see the Experimental Section, Supporting Information). The cation-exchanged crystals of **MnTPP@1** had the same size and shape as those of the original ones, ruling out a possible dissolution–recrystallization mechanism for this system and strongly suggesting a solid-state post-synthetic process.[53]

The PXRD patterns of water suspensions of freshly prepared samples of **1** and **MnTPP@1** are almost identical (Figure 2b, c)

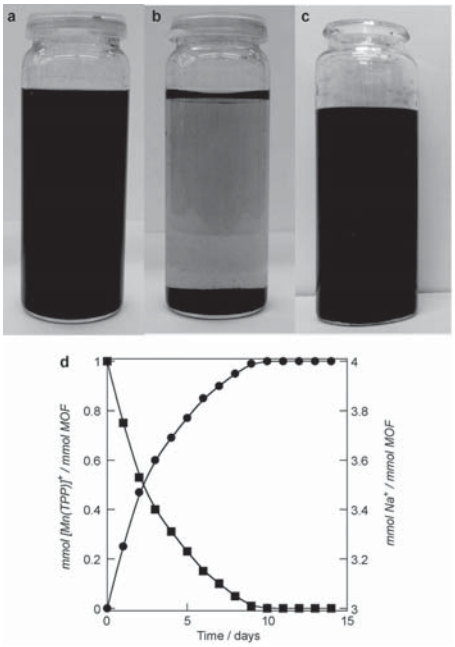

Figure 1. Photographs of the reversible cation-exchange reaction at the initial stage (a) and after 24 h (b). c) Photograph showing the reversibility after NaCl addition to a colorless aqueous **MnTPP@1** suspension. d) Kinetic profile of the cation-exchange process represented as the mmol $[Mn(TPP)]^+$/mmol MOF (●) and mmol Na^+/mmol MOF (■) ratios.

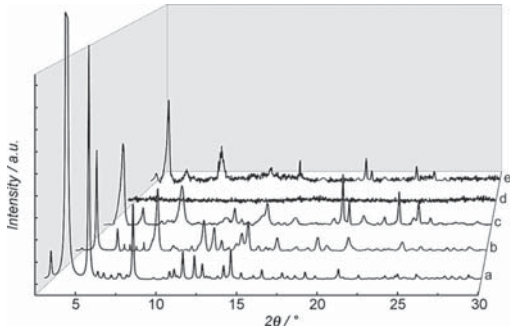

Figure 2. a) Calculated PXRD pattern profile of **1** (the out-of-scale highest peak at 3.4° was cut-off for the sake of clarity). Experimental PXRD pattern profiles of water-suspended and filtered polycrystalline samples of **1** (b and d) and **MnTPP@1** (c and e) in the 2θ range 2.0–30.0° at room temperature.

and they are consistent with the theoretical one for **1** (Figure 2a), thus confirming their isostructurality. However, **1** and **MnTPP@1** show very different structural stabilities when removed from the water solutions. Thus, the PXRD pattern of **1** exhibits no sign of crystallinity (Figure 2d), which suggests a complete collapse of the original hydrated phase upon solvent removal. In contrast, the PXRD pattern of **MnTPP@1** (Figure 2e) shows well-resolved peaks, which suggests that the presence of the porphyrine-based Mn^{III} complex induces structural stability to the open-framework structure of the parent MOF **1** thus preventing its collapse. The water content of **MnTPP@1** was determined by TGA under a dry N_2 atmosphere (Figure S1, Supporting Information). It shows a fast mass loss from room temperature followed by a pseudo plateau until thermal decomposition starts. The estimated weight loss of 18.5% at 150 °C corresponds to approximately 39 water molecules, which is in perfect agreement with the elemental analyses of **MnTPP@1**. The lower number of water molecules for **MnTPP@1** when compared to its ancestor **1** (39 vs. 60 H_2O) is likely explained by the occupation of the channels with the metalloporphyrin units.

Overall, the combination of the ICP-AES, EDX, elemental (see the Supporting Information), PXRD, and TGA analyses affords an unambiguous determination of the chemical composition and physical nature of **MnTPP@1**. Moreover, even if using single-crystal XRD methods to follow the insertion of such a big molecule within the MOF can be complicated because of the inherent disorder, our measurements (Figure S2, Supporting Information) allow structural insights into the presence of the guest molecule. Detailed information about the structural data and refinement can be found in the Supporting Information.

The crystal structure of **MnTPP@1** evidences that the 3D network remained crystalline during the inclusion process, even if the mononuclear Mn^{III} porphyrin guest was persistently disordered within the MOF host (Figures S3–S5, Supporting Information). However, density maps and structural analyses gave direct insights about the presence of mononuclear $[Mn(TPP)]^+$ cations. Moreover, taking into account the large number of water molecules hosted in the channels of **MnTPP@1**, each Mn^{III} cation most likely retains a D_{4h} symmetry inside the 3D net channels (Figure 3), whereby the Mn^{III} ion would possess a putative tetragonally elongated octahedral geometry with two water molecules occupying the axial positions, as in the crystal structure of the perchlorate salt of the complex precursor $[Mn^{III}(TPP)(H_2O)_2]ClO_4$.[52] The anionic $Mn^{II}_4Cu^{II}_6$ open-framework structure, exhibiting a pillared square/octagonal layer architecture, in which Mn^{II} and Cu^{II} ions are located on the vertices and midpoints of the edges, respectively, gave no evidence of remarkable changes in structural parameters (Table S1, Supporting Information) with respect to that previously reported for **1**,[27] acting as a perfect hosting matrix.

As in **1**, the robust infinite 3D network of **MnTPP@1** features three types of pores, different in size and shape, propagating along the *c* axis and enfolding up to 60% of the total lattice volume. It consists of regularly spaced, almost square-sized small pores (virtual diameter of ca. 0.4 nm) and two kinds of hydrophobic and hydrophilic octagonal-sized large pores (virtual diameters of ca. 1.5 and 2.2 nm, respectively; Figure 3a, left) resulting from the different disposition of the trimethyl-substituted phenylene spacers, pointing inwards or outwards of the voids (Figure S6, Supporting Information). Both octagonal channels are of an ideal size to hold the large cationic $[Mn^{III}(TPP)(H_2O)_2]^+$ complexes (Figure 3b,c). The van der Waals diameters comprising only the 24 atom-membered porphyrin core and the whole TPP ligand, including the four *meso* phenyl substituents, are 1.3 and 2.2 nm, respectively (Figure S6, Supporting Information). That being so, the four *meso* phenyl substituents are oriented almost perpendicular to the porphyrin core of the metalloporphyrin complexes in the smaller hydro-

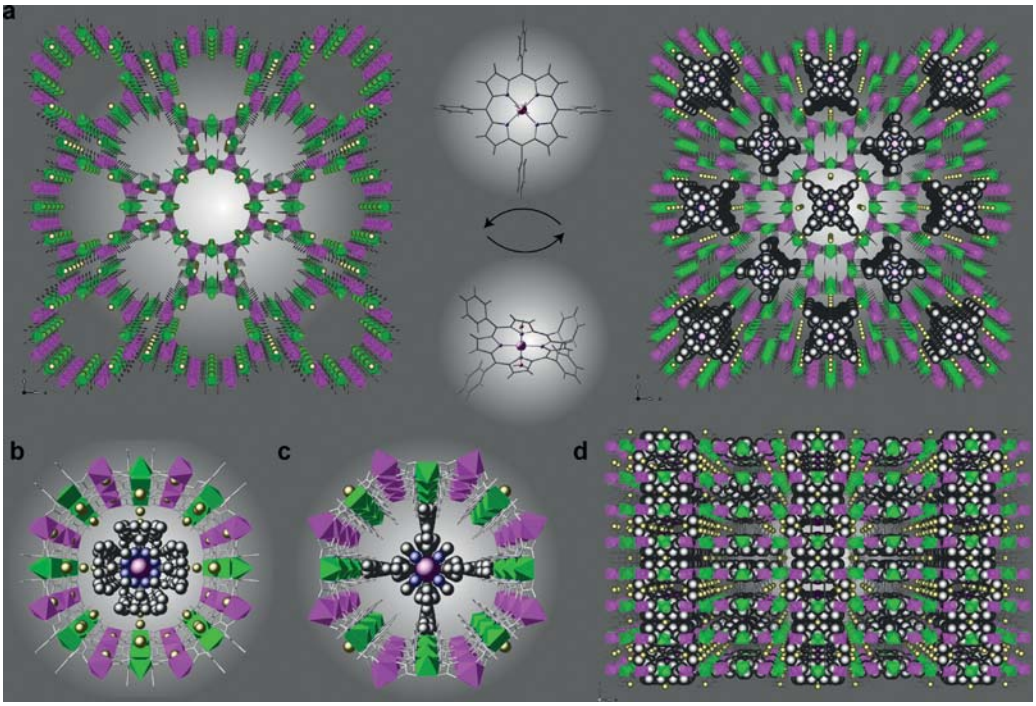

Figure 3. a) Perspective views along the crystallographic *c* axis of the bimodal square/octagonal-layered porous architecture of the starting anionic 3D MOF **1** (left) and the final hybrid material **MnTPP@1** (right); Perspective views along the crystallographic *c* axis of the hydrophilic (b) and hydrophobic (c) octagonal pores of the final hybrid material **MnTPP@1** filled by cationic $[Mn^{III}(TPP)(H_2O)_2]^+$ complexes; d) Perspective view along the crystallographic *b* axis of the final hybrid material **MnTPP@1**.

phobic pores of the MOF, most likely due to the reasonable steric constraints, to fit together in a lock and key fashion. Conversely, the poorer size fitting is likely at the origin of the higher disorder, both thermal and statistic, exhibited by the metalloporphyrin complexes filling the larger hydrophilic octagonal pores (Figure 3b and Figure S4a, Supporting Information). Hence, the size and shape of the cationic complexes prompted the two types of octagonal channels to reveal their distinct molecular recognition capabilities. In fact, the hydrophobic octagonal pores present all necessary features to allow for molecular recognition by means of π–π interactions between the four *meso* phenyl substituents of the TPP ligands and the ones belonging from the *m*-phenylene spacers of the MOF (Figure 3c).

Although the synthesis, X-ray crystal structure, and static magnetic properties of $[Mn^{III}(TPP)(H_2O)_2]ClO_4$ have already been reported,[51,52] its dynamic magnetic properties have not been studied. Indeed, this Mn^{III} porphyrin presents a field-induced slow magnetic relaxation similar to that shown by other SIMs based on highly anisotropic tetragonally elongated mononuclear Mn^{III} complexes recently reported by some of us.[54,55] In fact, the measurements of the alternating current (*ac*) magnetic susceptibility of $[Mn^{III}(TPP)(H_2O)_2]ClO_4$ showed slow magnetic relaxation effects under an external applied *dc* (direct current) magnetic field (Figures S7 and 4b, Supporting Information). However, no in- and out-of-phase *ac* signals indicative of SIM behavior were observed in the absence of an external applied *dc* magnetic field, (Figures S7a and 4b, top, Supporting Information). This feature is very common for SIMs[54,56,57] due to a fast quantum tunneling relaxation of the magnetization (QTM).[54] Thus, encouraged by the presence of $[Mn^{III}(TPP)(H_2O)_2]^+$ cations inside the channels of a magnetic MOF, we examined the magnetic properties of **MnTPP@1** in order to check for the influence of the magnetically ordered lattice of the MOF on the putative SIM behavior of the hosted molecule.

As for **1**,[27] the magnetic properties of **MnTPP@1** in the direct current (*dc*) regime show an overall ferrimagnetic behavior, which is evidenced by the presence of a minimum in the $\chi_M T$ versus T plots (χ_M being the *dc* molar magnetic susceptibility per formula unit) in Figure S8, Supporting Information. In both cases, the observed ferrimagnetic behavior is further confirmed by the M versus H plots (M being the molar magnetization per formula unit and H the applied *dc* magnetic field) at 2.0 K shown in Figures S9 and S10, Supporting Information. Interestingly, although both compounds exhibit magnetic hysteresis loops (inset of Figure S9, Supporting Information), the one for **MnTPP@1** is wider (coercive field, H_c, equal to 800 G and remnant magnetization, M_r, of about 5.0 BM) than that of **1** ($H_c = 100$ G and $M_r \approx 4.5$ BM). This feature anticipates the appearance of a long-range magnetic ordering for **MnTPP@1** at a higher temperature than for **1** (Figure 4a).[27]

A first evidence of the interplay between the magnetic properties of the SIM (guest) and the magnetic MOF (host) in

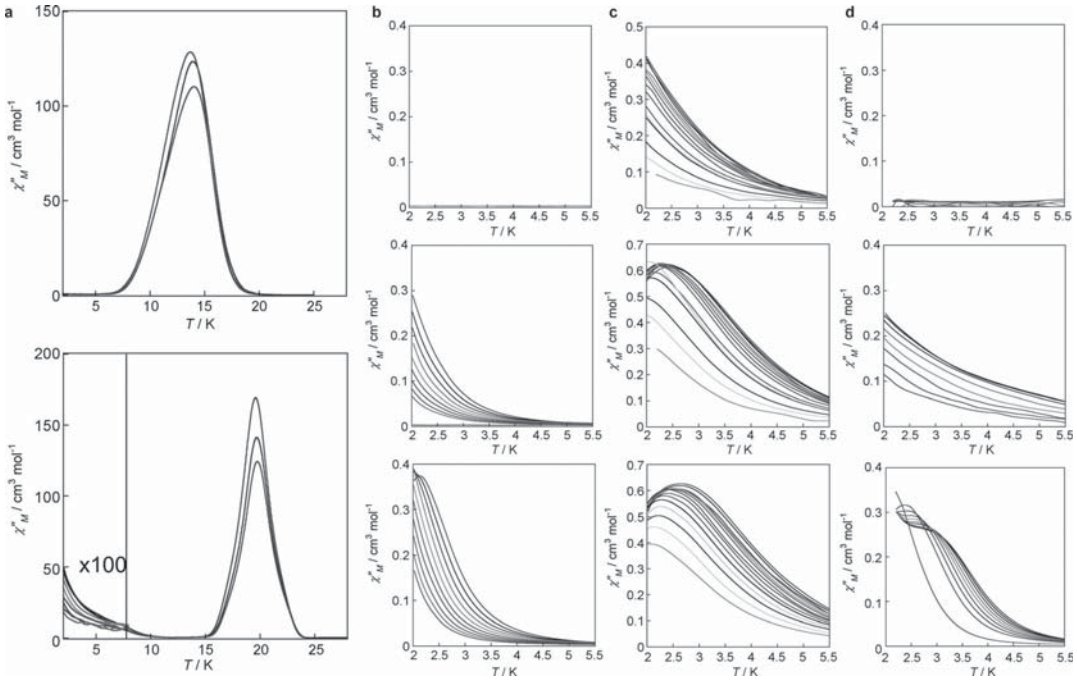

Figure 4. a) Temperature-dependence of the *ac* out-of-phase molar magnetic susceptibility (χ_M'') of **1** (top) and **MnTPP@1** (bottom) under a zero applied field. Temperature dependence of χ_M'' of $[Mn^{III}(TPP)(H_2O)_2]ClO_4$ (b), **MnTPP@1** (c), and **MnTPP@2** (d) in *dc* applied static fields of 0 (top), 1.0 (centre), and 2.5 kG (bottom) and under ±4.0 G oscillating field at frequencies in the range of 0.1–10 kHz.

MnTPP@1 was also anticipated by the magnetization curve as a function of the applied external magnetic field. As it is shown in Figure S9 and S10, Supporting Information, the magnetization for **1** increases faster than the corresponding for **MnTPP@1** in spite of the larger magnetization saturation of the last one. In fact, when increasing the external magnetic field, the magnetization values for **MnTPP@1** increase much more slowly than the calculated ones for the sum of **1** and $[Mn^{III}(TPP)(H_2O)_2]ClO_4$. This feature can be understood taking into account the occurrence of a very weak antiferromagnetic interaction (most likely dipolar in nature) between the magnetic moment of the SIM and that of the Mn^{II} sublattice of the ferrimagnetic network (antiparallel spins). The increase of the applied external field gradually overcomes this antiferromagnetic interactions leading to a parallel spin arrangement at higher fields.

Afterwards, we carried out magnetic susceptibility measurements for **MnTPP@1** in the alternating current (*ac*) regime in the form of the χ_M' and χ_M'' versus T plots (χ_M' and χ_M'' being the in-phase and out-of-phase *ac* magnetic susceptibilities per formula unit) (Figure S11, Supporting Information, and Figure 4a, bottom). In the absence of any external applied magnetic field, the presence of a frequency-independent sharp χ_M'' maximum (Figure 4a, bottom) at a critical temperature of $T_c = 20$ K confirms the occurrence of a long-range 3D magnetic ordering in **MnTPP@1**, which is slightly higher than that observed for **1** ($T_c = 15$ K,[27] see Figure 4a, top). More importantly, frequency-dependent χ_M'' signals appeared below 5 K, which indicates that the metalloporphyrin guest shows a slow magnetic relaxation in absence of any external applied magnetic field ($H_{dc} = 0$) (see Figure 4a bottom, c, top and Figure S11a, Supporting Information). This situation clearly contrasts with that found for $[Mn^{III}(TPP)(H_2O)_2]ClO_4$, in which the presence of a QTM yields a very fast relaxation of the magnetization at zero applied *dc* magnetic field (see Figure 4b top and Figure S7a in the Supporting Information).

This distinct dynamic magnetic behavior of $[Mn^{III}(TPP)(H_2O)_2]ClO_4$ and **MnTPP@1** strongly suggests that the internal field created by the remnant magnetization of the ferrimagnetic lattice is able to attenuate the QTM of the SIM. Otherwise, the presence of the metalloporphyrin cation guest also modifies the long-range magnetic ordering of the magnetic MOF host (T_c increases from 15 to 20 K) most likely due to the enhanced structural stability provided by the size of the guest compound. To the best of our knowledge, the occurrence of such an interplay between both magnetic phenomena within a single solid has never been reported.

In order to further confirm this unprecedented interplay between host long-range magnetic ordering and guest slow magnetic relaxation, we prepared an analogue of **MnTPP@1** by inserting the same Mn^{III} porphyrin into the isostructural magnesium(II) MOF derivative (without long-range magnetic order) of formula $Mg_2\{Mg_4[Cu^{II}_2(Me_3mpba)_2]_3\}\cdot 45\,H_2O$[50] (**2**). The resulting novel analogue of formula $[Mn^{III}(TPP)]Mg\{Mg_4[Cu_2(Me_3mpba)_2]_3\}\cdot 40\,H_2O$ (**MnTPP@2**) was characterized by chemical analyses and PXRD (Supporting Information, Figure S12), which evidences that it is isostructural to the parent compound **MnTPP@1**. Unlike **MnTPP@1** (Figure 4 b,c, top), the *ac* magnetic susceptibility measurements for **MnTPP@2** reveal the lack of any out-of-phase *ac* signal in the absence of any external magnetic field ($H_{dc} = 0$) (see Figure 4d, top). This fact confirms that the internal magnetic field in **MnTPP@1** plays a key role in the observation of slow magnetic relaxation effects under zero-*dc* external magnetic field by partially suppressing the QTM.

Under an external applied magnetic field ($H_{dc} \neq 0$), the Mn^{III} porphyrin presents a similar SIM behavior in $[Mn^{III}(TPP)(H_2O)_2]ClO_4$, **MnTPP@1**, and **MnTPP@2** as one can see in Figure 4 and Figures S7, S11, and S13. Overall, the values of the α parameter obtained from the Cole-Cole plots, together with those of the pre-exponential factor (τ_0) and the activation energy (E_a) from the Arrhenius plots, support single relaxation processes[58] for the SIM in all three compounds (see Table S2 and Figures S14–S16). These values are consistent with those previously reported for the very few and recent other Mn^{III} SIMs.[54,56,57] In addition, the very similar E_a values obtained for $[Mn^{III}(TPP)(H_2O)_2]ClO_4$, **MnTPP@1**, and **MnTPP@2** (Table S2, Supporting Information) clearly suggests that the Mn^{III} porphyrin cations possess the same tetragonally elongated octahedral geometry with two water molecules occupying the axial positions, a feature that was not definitively ascertained by the single-crystal X-ray diffraction study due to disorder problems.

Conclusion

In summary, we successfully transferred the solid-state host–guest chemistry to the magneto-chemistry of porous coordination polymers by reporting the single-crystal to single-crystal inclusion of a SIM within the pores of a magnetic MOF. Although a few examples showing the encapsulation of nanomagnets inside a MOFs[59,60] and also their organization in MOFs acting as SIM metal nodes, have been reported,[61–63] the present novel material—a rare example of supramolecular aggregate in which cooperating functional molecular systems are held together by noncovalent interactions—allows the observation, for the first time, of an internal field-induced slow magnetic relaxation behavior as a consequence of the attenuation of the QTM effects of the mononuclear complex by the internal field created by the long-range magnetic ordering of the 3D MOF. The significance of the reported results resides in the fact that most SIMs present a very fast relaxation of their magnetization in absence of an external magnetic field due to the occurrence of a very effective QTM. Thus, they could only be used for information storage under an applied magnetic field. Our results suggest a good strategy to attenuate (or even suppress) undesired QTM effects, pointing towards the addressing of SIMs inside a magnetic matrix as the best choice to observe slow magnetic relaxation effects without the need for an applied magnetic field.

Experimental Section

Preparation of 1, 2, MnTPP@1, and MnTPP@2

Compounds **1** and **2** were prepared as previously reported.[27,50] Well-formed dark-green prisms of **MnTPP@1** and **MnTPP@2** were obtained by immersing ca. 50 mg of crystals of **1** and **2**, respectively, for 2 weeks in water/methanol (5:1) solutions containing 5 mg of $[Mn^{III}(TPP)(H_2O)_2]ClO_4$.[51] Both solutions were replaced every 24 h during the 2 weeks, and then, gently washed with water/methanol (1:1) solutions to remove any trace of the mononuclear complex. Crystals of **MnTPP@1** were suitable for X-ray diffraction.

MnTPP@1: Elemental analysis calculated (%) for $C_{122}H_{166}Cu_6Mn_5N_{16}Na_3O_{75}$ (3781.6): C 38.75, H 4.42, N 5.93; found: C 38.75, H 4.32, N 5.97; IR (KBr): $\tilde{\nu}=1603\ cm^{-1}$ (CO).

MnTPP@2: Elemental analysis calcd (%) for $C_{122}H_{168}Cu_6MnN_{16}Mg_{5.5}O_{76}$ (3644.6): C 40.21, H 4.64, N 6.15; found: C 40.19, H 4.62, N 6.16; IR (KBr): $\tilde{\nu}=1602\ cm^{-1}$ (CO).

Single-crystal X-ray diffraction

Crystal data for **MnTPP@1**: $C_{122}H_{166}Cu_6Mn_5N_{16}Na_3O_{75}$, tetragonal, space group *P4/mmm*, $a=36.609(2)$, $c=15.3988(8)$, $V=20638(2)\ Å^3$, $T=90(2)$ K, $Z=4$, $\rho_{calcd}=1.217\ g\,cm^{-3}$, $\mu=0.984\ mm^{-1}$, of the 135649 reflections collected, 11352 are unique and 6710 observed with $I>2\sigma(I)$. Refinement of 412 parameters gave $R=0.1588$ and $R_w=0.4219$ for reflections with $I>2\sigma(I)$ and $R=0.2002$ and $R_w=0.4407$ for all reflections, with $S=1.479$.

CCDC 1414395 contains the supplementary crystallographic data for this paper. These data can be obtained free of charge from The Cambridge Crystallographic Data Centre.

X-ray powder diffraction

Solid polycrystalline samples as well as water-suspended polycrystalline samples of **1**, **2**, **MnTPP@1**, and **MnTPP@2** were introduced into 0.5 mm borosilicate capillaries prior to being mounted and aligned on a Empyrean PANalytical powder diffractometer, using $Cu_{K\alpha}$ radiation ($\lambda=1.54056$ Å). For each sample, five repeated measurements were collected at room temperature ($2\theta=2$–40°) and merged in a single diffractogram. The spinning option was disabled for the water-suspended samples due to the presence of water solvent within the capillaries which accounts for the slight asymmetry observed in some of the peaks.

Magnetic measurements

Variable-temperature (2.0–300 K) direct current (*dc*) magnetic susceptibility measurements under an applied field of 100 G ($T<30$ K) and 5.0 kG ($T\geq30$ K), and magnetization measurements at 2.0 K were carried out with a Quantum Design SQUID magnetometer. Variable-temperature (2.0–8 K) alternating current (*ac*) magnetic susceptibility measurements under ±5.0 G oscillating field at frequencies in the range of 1–10.0 kHz were carried out under different applied static fields in the range of 0–5.0 kG with a Quantum Design Physical Property Measurement System (PPMS). The magnetic susceptibility data were corrected for the diamagnetism of the constituent atoms and the sample holder. *Dc* and *ac* magnetic measurements were performed on powdered microcrystals and restraining the sample with *n*-eicosane in order to avoid any field-induced torqueing.

Acknowledgements

This work was supported by the MINECO (Spain) (Projects CTQ2013-46362-P, CTQ2013-44844-P and MDM-2015-0538), the Generalitat Valenciana (Spain) (Project PROMETEOII/2014/070) and the Ministero dell'Istruzione, dell'Università e della Ricerca (Italy). M.M., A.P.-A., and T.G. thank MINECO and the Universitat de València for predoctoral contracts. Thanks are also extended to the Ramón y Cajal Program and the "Convocatoria 2015 de Ayudas Fundación BBVA a Investigadores y Creadores Culturales" (E.P.). J.G. acknowledges the financial support of the European Research Council under the European Union's Seventh Framework Programme (FP/2007–2013)/ERC Grant Agreement no. 335746, CrystEng-MOF-MMM.

Keywords: magnetic ordering · metal–organic frameworks · multifunctional materials · quantum tunneling effects · single-ion magnet

[1] S. Kitagawa, R. Matsuda, *Coord. Chem. Rev.* **2007**, *251*, 2490–2509.
[2] G. Férey, *Chem. Soc. Rev.* **2008**, *37*, 191–214.
[3] J. R. Long, O. M. Yaghi, *Chem. Soc. Rev.* **2009**, *38*, 1213–1214.
[4] H. Furukawa, K. E. Cordova, M. O'Keeffe, O. M. Yaghi, *Science* **2013**, *341*, 1230444.
[5] C. Janiak, *Dalton Trans.* **2003**, 2781–2804.
[6] O. M. Yaghi, M. O'Keeffe, N. W. Ockwig, H. K. Chae, M. Eddaoudi, J. Kim, *Nature* **2003**, *423*, 705–714.
[7] S. Kitagawa, R. Kitaura, S. Noro, *Angew. Chem. Int. Ed.* **2004**, *43*, 2334–2375; *Angew. Chem.* **2004**, *116*, 2388–2430.
[8] J.-R. Li, R. J. Kuppler, H.-C. Zhou, *Chem. Soc. Rev.* **2009**, *38*, 1477–1504.
[9] T. Grancha, J. Ferrando-Soria, M. Castellano, M. Julve, J. Pasán, D. Armentano, E. Pardo, *Chem. Commun.* **2014**, *50*, 7569–7585.
[10] A. M. Fracaroli, H. Furukawa, M. Suzuki, M. Dodd, S. Okajima, F. Gándara, J. A. Reimer, O. M. Yaghi, *J. Am. Chem. Soc.* **2014**, *136*, 8863–8866.
[11] K. K. Tanabe, Z. Wang, S. M. Cohen, *J. Am. Chem. Soc.* **2008**, *130*, 8508–8517.
[12] A. Corma, M. Iglesias, F. X. Llabrés i Xamena, F. Sánchez, *Chem. Eur. J.* **2010**, *16*, 9789–9795.
[13] T. M. McDonald, J. A. Mason, X. Kong, E. D. Bloch, D. Gygi, A. Dani, V. Crocellà, F. Giordanino, S. O. Odoh, W. S. Drisdell, B. Vlaisavljevich, A. L. Dzubak, R. Poloni, S. K. Schnell, N. Planas, K. Lee, T. Pascal, L. F. Wan, D. Prendergast, J. B. Neaton, B. Smit, J. B. Kortright, L. Gagliardi, S. Bordiga, J. A. Reimer, J. R. Long, *Nature* **2015**, *519*, 303–308.
[14] M. J. Ingleson, J. Perez Barrio, J.-B. Guilbaud, Y. Z. Khimyak, M. J. Rosseinsky, *Chem. Commun.* **2008**, 2680.
[15] H. Deng, S. Grunder, K. E. Cordova, C. Valente, H. Furukawa, M. Hmadeh, F. Gandara, A. C. Whalley, Z. Liu, S. Asahina, H. Kazumori, M. O'Keeffe, O. Terasaki, J. Fraser Stoddart, O. M. Yaghi, *Science* **2012**, *336*, 1018–1023.
[16] Q. Li, W. Zhang, O. S. Miljanic, C.-H. Sue, Y.-L. Zhao, L. Liu, C. B. Knobler, J. F. Stoddart, O. M. Yaghi, *Science* **2009**, *325*, 855–859.
[17] M. Yoshizawa, J. K. Klosterman, M. Fujita, *Angew. Chem. Int. Ed.* **2009**, *48*, 3418–3438; *Angew. Chem.* **2009**, *121*, 3470–3490.
[18] H. Ledford, *Nature* **2015**, DOI 10.1038/nature.2015.17702.
[19] O. Kahn, *Molecular Magnetism*, VCH, Weinheim, **1993**.
[20] H. Tamaki, Z. J. Zhong, N. Matsumoto, S. Kida, M. Koikawa, N. Achiwa, Y. Hashimoto, H. Okawa, *J. Am. Chem. Soc.* **1992**, *114*, 6974–6979.
[21] S. Decurtins, H. W. Schmalle, P. Schneuwly, H. R. Oswald, *Inorg. Chem.* **1993**, *32*, 1888–1892.
[22] F. Lloret, G. De Munno, M. Julve, J. Cano, R. Ruiz, A. Caneschi, *Angew. Chem. Int. Ed.* **1998**, *37*, 135–138; *Angew. Chem.* **1998**, *110*, 143–145.
[23] E. Coronado, J. R. Galán-Mascarós, C. J. Gómez-García, V. Laukhin, *Nature* **2000**, *408*, 447–449.
[24] N. Roques, V. Mugnaini, J. Veciana, *Top. Curr. Chem.* **2009**, *293*, 207–258.
[25] P. Dechambenoit, J. R. Long, *Chem. Soc. Rev.* **2011**, *40*, 3249–3265.

[26] E. Pardo, C. Train, H. Liu, L.-M. Chamoreau, B. Dkhil, K. Boubekeur, F. Lloret, K. Nakatani, H. Tokoro, S. Ohkoshi, M. Verdaguer, *Angew. Chem. Int. Ed.* **2012**, *51*, 8356 – 8360; *Angew. Chem.* **2012**, *124*, 8481 – 8485.
[27] J. Ferrando-Soria, P. Serra-Crespo, M. de Lange, J. Gascon, F. Kapteijn, M. Julve, J. Cano, F. Lloret, J. Pasán, C. Ruiz-Pérez, Y. Journaux, E. Pardo, *J. Am. Chem. Soc.* **2012**, *134*, 15301 – 15304.
[28] M. H. Zeng, Z. Yin, Y. X. Tan, W. X. Zhang, Y. P. He, M. Kurmoo, *J. Am. Chem. Soc.* **2014**, *136*, 4680 – 4688.
[29] S. Gómez-Coca, D. Aravena, R. Morales, E. Ruiz, *Coord. Chem. Rev.* **2015**, *289 – 290*, 379 – 392.
[30] N. Ishikawa, M. Sugita, T. Ishikawa, S.-Y. Koshihara, Y. Kaizu, *J. Am. Chem. Soc.* **2003**, *125*, 8694 – 8695.
[31] N. Ishikawa, M. Sugita, W. Wernsdorfer, *Angew. Chem. Int. Ed.* **2005**, *44*, 2931 – 2935; *Angew. Chem.* **2005**, *117*, 2991 – 2995.
[32] A. Yamashita, A. Watanabe, S. Akine, T. Nabeshima, M. Nakano, T. Yamamura, T. Kajiwara, *Angew. Chem. Int. Ed.* **2011**, *50*, 4893 – 4896; *Angew. Chem.* **2011**, *123*, 4995 – 4998.
[33] J. D. Rinehart, J. R. Long, *J. Am. Chem. Soc.* **2009**, *131*, 12558 – 12559.
[34] N. Magnani, C. Apostolidis, A. Morgenstern, E. Colineau, J.-C. Griveau, H. Bolvin, O. Walter, R. Caciuffo, *Angew. Chem. Int. Ed.* **2011**, *50*, 1696 – 1698; *Angew. Chem.* **2011**, *123*, 1734 – 1736.
[35] V. Mougel, L. Chatelain, J. Pécaut, R. Caciuffo, E. Colineau, J.-C. Griveau, M. Mazzanti, *Nat. Chem.* **2012**, *4*, 1011 – 1017.
[36] W. H. Harman, T. D. Harris, D. E. Freedman, H. Fong, A. Chang, J. D. Rinehart, A. Ozarowski, M. T. Sougrati, F. Grandjean, G. J. Long, J. R. Long, C. J. Chang, *J. Am. Chem. Soc.* **2010**, *132*, 18115 – 18126.
[37] J. Vallejo, I. Castro, R. Ruiz-García, J. Cano, M. Julve, F. Lloret, G. De Munno, W. Wernsdorfer, E. Pardo, *J. Am. Chem. Soc.* **2012**, *134*, 15704 – 15707.
[38] E. Colacio, J. Ruiz, E. Ruiz, E. Cremades, J. Krzystek, S. Carretta, J. Cano, T. Guidi, W. Wernsdorfer, E. K. Brechin, *Angew. Chem. Int. Ed.* **2013**, *52*, 9130 – 9134; *Angew. Chem.* **2013**, *125*, 9300 – 9304.
[39] J. Martínez-Lillo, T. F. Mastropietro, E. Lhotel, C. Paulsen, J. Cano, G. De Munno, J. Faus, F. Lloret, M. Julve, S. Nellutla, J. Krzystek, *J. Am. Chem. Soc.* **2013**, *135*, 13737 – 13748.
[40] J. Gatteschi, D; Sessoli, R.; Villain, *Molecular Nanomagnets*, Oxford University Press, **2006**.
[41] M. N. Leuenberger, D. Loss, *Nature* **2001**, *410*, 789 – 793.
[42] M. Affronte, F. Troiani, A. Ghirri, A. Candini, M. Evangelisti, V. Corradini, S. Carretta, P. Santini, G. Amoretti, F. Tuna, *J. Phys. D* **2007**, *40*, 2999 – 3004.
[43] L. Bogani, W. Wernsdorfer, *Nat. Mater.* **2008**, *7*, 179 – 186.
[44] S. Sanvito, *Chem. Soc. Rev.* **2011**, *40*, 3336 – 3355.
[45] Y. Inokuma, T. Arai, M. Fujita, *Nat. Chem.* **2010**, *2*, 780 – 783.
[46] Y. Inokuma, M. Kawano, M. Fujita, *Nat. Chem.* **2011**, *3*, 349 – 358.
[47] Y. Inokuma, S. Yoshioka, J. Ariyoshi, T. Arai, Y. Hitora, K. Takada, S. Matsunaga, K. Rissanen, M. Fujita, *Nature* **2013**, *495*, 461 – 466.
[48] S. M. Cohen, *Chem. Rev.* **2012**, *112*, 970 – 1000.
[49] C. K. Brozek, M. Dincă, *Chem. Soc. Rev.* **2014**, *43*, 5456 – 5467.
[50] T. Grancha, J. Ferrando-Soria, H.-C. Zhou, J. Gascon, B. Seoane, J. Pasán, O. Fabelo, M. Julve, E. Pardo, *Angew. Chem. Int. Ed.* **2015**, *54*, 6521 – 6525; *Angew. Chem.* **2015**, *127*, 6621 – 6625.
[51] B. J. Kennedy, K. S. Murray, *Inorg. Chem.* **1985**, *24*, 1557 – 1560.
[52] M. N. Williamson, C. L. Hill, *Inorg. Chem.* **1987**, *26*, 4155 – 4160.
[53] X. Cui, A. N. Khlobystov, X. Chen, D. H. Marsh, A. J. Blake, W. Lewis, N. R. Champness, C. J. Roberts, M. Schröder, *Chem. Eur. J.* **2009**, *15*, 8861 – 8873.
[54] J. Vallejo, A. Pascual-Álvarez, J. Cano, I. Castro, M. Julve, F. Lloret, J. Krzystek, G. De Munno, D. Armentano, W. Wernsdorfer, R. Ruiz-Garcia, E. Pardo, *Angew. Chem. Int. Ed.* **2013**, *52*, 14075 – 14079; *Angew. Chem.* **2013**, *125*, 14325 – 14329.
[55] A. Pascual-Álvarez, J. Vallejo, E. Pardo, M. Julve, F. Lloret, J. Krzystek, D. Armentano, W. Wernsdorfer, J. Cano, *Chem. Eur. J.* **2015**, DOI 10.1002/chem.201502637.
[56] R. Ishikawa, R. Miyamoto, H. Nojiri, B. K. Breedlove, M. Yamashita, *Inorg. Chem.* **2013**, *52*, 8300 – 8302.
[57] G. A. Craig, J. J. Marbey, S. Hill, O. Roubeau, S. Parsons, M. Murrie, *Inorg. Chem.* **2015**, *54*, 13 – 15.
[58] J. A. Mydosh, *Spin Glasses: An Experimental Introduction*, Taylor & Francis, London, **1993**.
[59] M. Clemente-León, E. Coronado, C. J. Gómez-García, M. López-Jordà, A. Camón, A. Repollés, F. Luis, *Chem. Eur. J.* **2014**, *20*, 1669 – 1676.
[60] D. Aulakh, J. B. Pyser, X. Zhang, A. a. Yakovenko, K. R. Dunbar, M. Wriedt, *J. Am. Chem. Soc.* **2015**, *137*, 9254 – 9257.
[61] X. Zhang, V. Vieru, X. Feng, J.-L. Liu, Z. Zhang, B. Na, W. Shi, B.-W. Wang, A. K. Powell, L. F. Chibotaru, S. Gao, P. Cheng, J. R. Long, *Angew. Chem. Int. Ed.* **2015**, *54*, 9861; *Angew. Chem.* **2015**, *127*, 9999.
[62] A. E. Ion, S. Nica, A. M. Madalan, S. Shova, J. Vallejo, M. Julve, F. Lloret, M. Andruh, *Inorg. Chem.* **2015**, *54*, 16 – 18.
[63] J. J. Baldoví, E. Coronado, A. Gaita-Ariño, C. Gamer, M. Giménez-Marqués, G. Mínguez Espallargas, *Chem. Eur. J.* **2014**, *20*, 10695 – 10702.

Received: October 16, 2015
Published online on November 25, 2015

CRYSTAL GROWTH & DESIGN

Article

pubs.acs.org/crystal

Structural Studies on a New Family of Chiral BioMOFs

Thais Grancha,[†] Marta Mon,[†] Jesus Ferrando-Soria,*[,†] Donatella Armentano,*[,‡] and Emilio Pardo*[,†]

[†]Departament de Química Inorgànica, Instituto de Ciencia Molecular (ICMOL), Universitat de València, 46980 Paterna, València, Spain

[‡]Dipartimento di Chimica e Tecnologie Chimiche (CTC), Università della Calabria, Rende 87036, Cosenza, Italy

Supporting Information

ABSTRACT: The use of a family of dinuclear copper(II) complexes, prepared from enantiopure disubstituted oxamidato ligands derived from the natural amino acids L-alanine, L-valine, and L-leucine, as metalloligands toward barium(II) cations leads to the formation of three novel three-dimensional (3D) chiral metal−organic frameworks (MOFs). They exhibit different architectures, which serve as playground to study both how the chiral information contained in the starting enantiopure ligands is ultimately transmitted to the 3D structure and the effect of the size of the aliphatic residue of the amino acid on the final architecture.

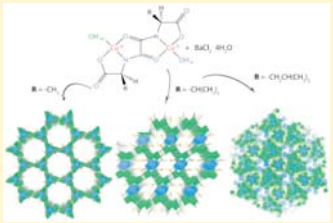

INTRODUCTION

The fruitful synergy of coordination chemistry and crystal engineering is elegantly exemplified by the exponential growth of the research on metal−organic frameworks (MOFs).[1−5] A great diversity of MOFs with both captivating high-dimensional structures and exciting chemical and physical properties have been obtained during the last decades.[6−19] They have found striking applications in such diverse fields as gas storage and separation,[20,21] transport and drug delivery,[22,23] magnetism,[24,25] molecular recognition,[26] or catalysis.[27] Besides the major achievements obtained so far, more work still needs to be done. This becomes particularly true on the quest for rational design strategies of chiral MOFs,[28] where the research is still scarce compared with nonchiral MOFs.

Apart from spontaneous resolutions,[29,30] the most extended strategy for obtaining chiral MOFs relies thus on the use of enantiopure ligands[31,32] or chiral induction agents,[33,34] which are often costly from both synthetic and economic points of view. More often than not, the common harsh reaction conditions, together with the many subtle parameters that can affect the assembly of MOFs, turn out to be of low efficiency. It is thus obvious that the controlled synthesis of enantiomerically pure MOFs is not an easy task, even more, envisaging to expand these methodologies to obtain novel families of chiral MOFs. Nevertheless, the unique possibilities and diverse functionalities of these materials make them attractive enough to face this challenge.

Metalloligand design strategy has proven to be efficient for the rational design of multifunctional MOFs of different dimensionalities.[35] Yet, this approach has been overlooked and poorly investigated for the rational design of chiral MOFs.[28] On this basis and following the footsteps of our previous results with oxamato derivatives,[36,37] we have now focused on a family of enantiopure disubstituted oxamidato ligands derived from natural amino acids[38−41] (Scheme 1, left). Bis(amino acid)-oxalamide ligands offer multiple coordination sites, through the carbonyl and the deprotonated amidate and carboxylate donor groups, as well as good perspectives as chiral inducer, due to the presence of the asymmetric α-carbon atom, paving thus the road for the rational design of water-resistant chiral *bio*MOFs. In fact, when acting as bis(tridentate) bridging ligands in their *trans* configuration, they form very stable dinuclear copper(II) complexes with one vacant equatorial position on each metal, which are likely occupied by water molecules in various protonation degrees depending on the pH medium (Scheme 1, right).[42,43]

Scheme 1. Chemical Structures of the Three Chiral Bis(amino acid)oxalamide Ligands (left), Highlighting the Potential Coordination Sites and Chiral Centers, and the Corresponding Dianionic Bis(hydroxo) Dicopper(II) Complexes (right)[a]

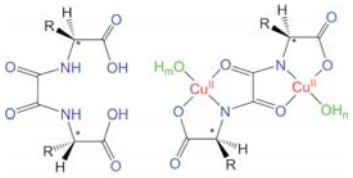

[a]The amino acid residues R are $-CH_3$ (alanine), $-CH(CH_3)_2$ (valine), and $-CH_2CH(CH_3)_2$ (leucine).

Received: July 15, 2016
Revised: July 28, 2016
Published: August 2, 2016

DOI: 10.1021/acs.cgd.6b01052
Cryst. Growth Des. 2016, 16, 5571−5578

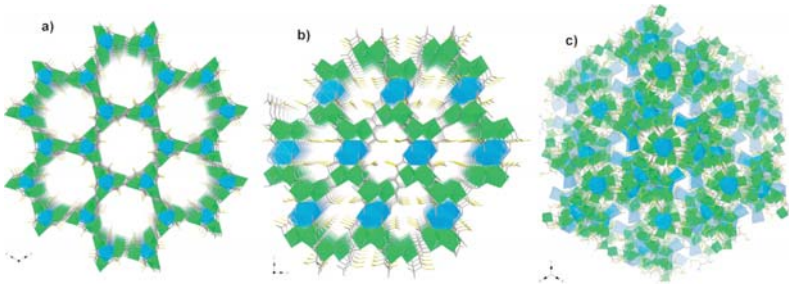

Figure 1. Perspective view of the structures of **1** (a), **2** (b), and **3** (c), showing the reduction of porosity, along the crystallographic *c* (**1**) and *b* (**2**) and the diagonal of the unit cell axis (**3**). Metal and ligand atoms are represented as polyhedra and sticks, respectively (Cu, green; Ba, blue). The amino acid residues R = $-CH_3$ (alanine), $-CH(CH_3)_2$ (valine), and $-CH_2CH(CH_3)_2$ (leucine) for **1**−**3**, respectively, have been depicted as yellow sticks. Hydrogen atoms and free water molecules are omitted for clarity.

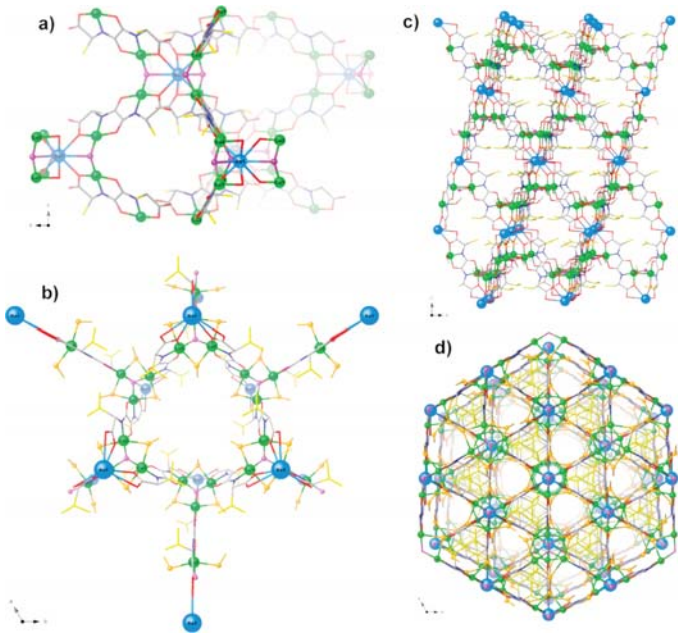

Figure 2. (a) Views of a fragment of **1** in the *bc* planes. (b) Views of a fragment of **2** in the *ab* planes underlining the triangular node built through methanol and hydroxo groups coordinating in a μ_2 and μ_3 mode, respectively. Views of sheets of **2** in the (c) *bc* and (d) *ab* planes (Cu, green; Ba, blue; methanol molecules, orange; hydroxo oxygen, purple; isopropyl chains, yellow; oxygen from ligands, red sticks; nitrogen, blue sticks).

RESULTS AND DISCUSSION

Synthesis and X-ray Crystal Structure. We report herein a novel family of water-stable three-dimensional (3D) chiral *bio*MOFs of formulas $\{Ba^{II}Cu^{II}_6[(S,S)\text{-alamox}]_3(OH)_2(H_2O)\}\cdot 30H_2O$ (**1**), $\{Ba^{II}Cu^{II}_6[(S,S)\text{-valmox}]_3(OH)_2(CH_3OH)_6\}\cdot 6H_2O$ (**2**), and $\{Ba^{II}Cu^{II}_4[(S,S)\text{-leumox}]_2(OH)_2(H_2O)_2\}\cdot 14H_2O$ (**3**), derived from the natural amino acids L-alanine, L-valine, and L-leucine, respectively [H_4-(*S*,*S*)-alamox = *N*,*N*′-bis[(*S*)-alanine]oxalyl diamide, H_4-(*S*,*S*)-valmox = *N*,*N*′-bis-[(*S*)-valine]oxalyl diamide, and H_4-(*S*,*S*)-leumox = *N*,*N*′-bis[(*S*)-leucine]oxalyl diamide, Scheme 1] exhibiting very different 3D architectures (Figure 1). This novel family of chiral *bio*MOFs arises as the perfect playground to study both how the encoded chiral information on the enantiopure ligands is ultimately translated to the 3D structure and the influence of the nature (size, shape, and hydrophobicity) of the aliphatic residue of the amino acid on the final architecture of the resulting *bio*MOF.

The present compounds were obtained as hexagonal (**1**, **2**) and cubic (**3**) prisms by slow diffusion of aqueous solutions of the corresponding bis(hydroxo)dicopper(II) complex precursor and $BaCl_2\cdot 4H_2O$ (3:1 molar ratio) in H-shaped tubes at room temperature, and their crystal structures were determined by single-crystal X-ray diffraction (see Supporting Information).

Compound **1** is isostructural to the previously reported calcium(II) analogue.[40] It crystallizes in the chiral $P6_3$ space group of the hexagonal system. Its structure consists of a chiral 3D barium(II)−copper(II) network, which is built up from *trans*-oxamidato-bridged dicopper(II) units, $\{Cu^{II}_2[(S,S)\text{-alamox}]\}$, acting as linkers between the Ba^{II} ions through carboxylate; further aqua/hydroxo groups (1:2 statistical

DOI: 10.1021/acs.cgd.6b01052
Cryst. Growth Des. 2016, 16, 5571−5578

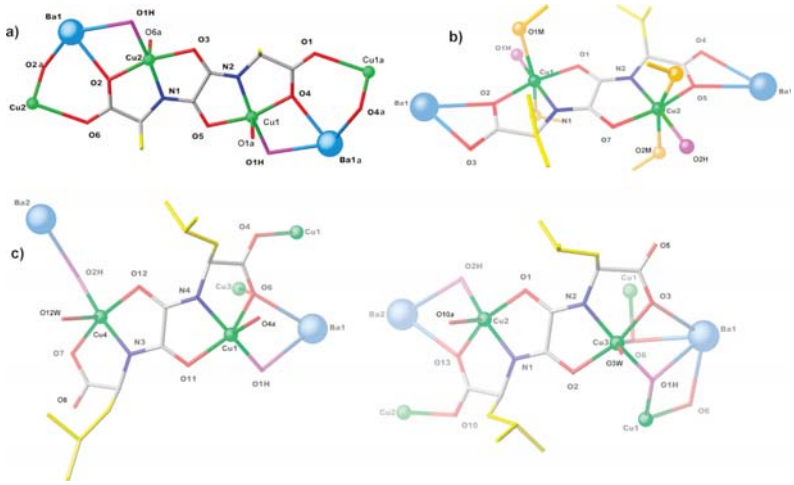

Figure 3. Details of coordination mode and environment of copper metal ions in **1** (a), **2** (b), and **3** (c) (Cu, green; Ba, blue; methanol molecules, orange; hydroxo oxygen, purple; isopropyl chains, yellow; oxygen from ligands, red sticks; nitrogen, blue sticks).

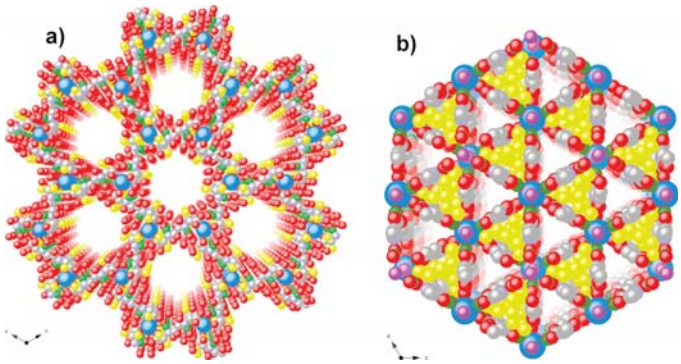

Figure 4. Portion of crystal structure of (a) **1** and (b) **2** along the *c* axis showing pore window featuring methyl groups (**1**) and isopropyl side chains (**2**) belonging to the amino acid residues of alanine- and valine-disubstituted oxamidato ligand, confined in the pores of the nets represented as space filling models (Cu, green; Ba, blue; O, red; hydroxo O, purple; C, gray; N, slate blue; isopropyl chains, yellow). Lattice water molecules and hydrogen atoms have been omitted for clarity.

distribution), acting as additional bridges between two neighboring dicopper(II) units and coordinated in a μ_3 fashion, support the whole system, unfolding an uninodal six-connected net (Figures 1, 2a, and 3a). The copper atoms, Cu(1) and Cu(2), are located at the edges of each hexagon. They adopt an elongated square pyramidal geometry, $CuNO_3O_{OH}$, formed by one amidate-nitrogen, one carbonyl-oxygen atom, one carboxylate-oxygen atom and one aqua/hydroxo group in the equatorial plane, and one carboxylate-oxygen atom from a neighboring dicopper(II) entity in the axial position (Figure 3a) [average values Cu−N = 1.915(10) Å; Cu−O_{OH} = 1.917(9) Å; Cu−O = 2.003(8) Å]. The barium atoms, Ba(1), regularly occupy the corners of each hexagon (Figure 1a). They exhibit a distorted monocapped square antiprismatic geometry, BaO_9, built by six carboxylate-oxygen atoms from six oxamidate groups and three aqua/hydroxo molecules (Figures S1a and S2a) [Ba−O = 2.662(9) Å; Ba−O_{OH} = 2.835(4) Å].

Overall, **1** can be described as a mixed oxamidate- and carboxylate(aqua/hydroxo)-bridged, honeycomb-like hexagonal 3D $Ba^{II}Cu^{II}_6$ open-framework showing relatively large hexagonal channels along the *c* axis (Figure 1a), which are occupied by crystallization water molecules (Figures 4a and 5). These channels have a virtual diameter of ca. 1.0 nm resulting from the alternating orientation of the methyl residues from the *trans*-(*S*,*S*)-alamox bridging ligands within adjacent channels. The estimated empty volume without the crystallization water molecules is 2209.2 $Å^3$, a value that represents up to ca. 58.5% of potential void per unit cell volume [V = 3777.1 $Å^3$].

Compound **2** crystallizes in the chiral R_3 space group of the trigonal system. Its structure consists of a chiral 3D barium(II)−copper(II) network, which is built up from *trans*-oxamidato-bridged dicopper(II) units, {Cu^{II}_2[(*S*,*S*)-valmox]}, acting as linkers between the Ba^{II} ions through carboxylate groups (Figures 1b, 2b, and 3b). The dicopper(II) units, above and below the barium atoms, are further interconnected through methanol and hydroxo groups coordinating in a μ_2 and μ_3 mode, respectively, yielding a fascinating triangular node (Figures 1b and 2b−d).

The two crystallographically independent copper atoms, Cu(1) and Cu(2), adopt an elongated distorted octahedral

DOI: 10.1021/acs.cgd.6b01052
Cryst. Growth Des. 2016, 16, 5571−5578

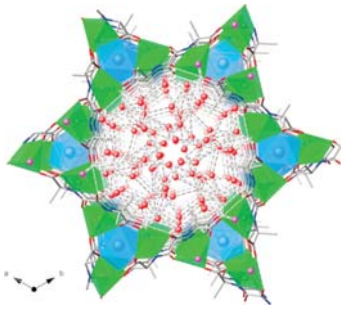

Figure 5. Perspective view of pores of **1** along the *c* axis showing pore window filled by hydrogen bounded water molecules (red spheres) sharing channels with methyl groups belonging to the amino acid residues of alanine disubstituted oxamidato ligand (hydrogen atoms have been omitted for clarity).

geometry, $CuNO_2O_{OH}O_{MeOH}$, built by one amidate-nitrogen, one carbonyl-oxygen atom, one carboxylate-oxygen atom, and one hydroxo group describing the equatorial plane and two methanol molecules occupying axial positions (Figure 3b) [average values Cu−N = 1.939(7) Å; $Cu-O_{OH}$ = 1.982(3) Å; $Cu-O_{MeOH}$ = 2.553(3) Å]. The barium atoms, Ba(1), present a distorted bicapped pentagonal antiprismatic geometry BaO_{12} built by 12 oxygen atoms of the six carboxylate groups from the valmox ligand (Figures S1b and S2b) [Ba−O = 2.955(7) Å].

The 3D network of **2** can be described as an extended array of anionic oxamidate-bridged Cu^{II}_3OH layers with a hexagonal net topology growing in the *ab* plane (Figure 2b,d), where the adjacent layers are displaced along the [110] direction leading to an *ABAB* pattern along the *c* axis, which are further interconnected through the barium atoms acting as pillars in an up and down disposition to give a uninodal six-connected net (Figure 2d).

As shown in Figures 2d and 4b, this 3D $Ba^{II}Cu^{II}_6$ open-framework shows two types of small corrugated hexagonal channels (Figures 1b, 2d, and 4b): hydrophilic ones occupied by crystallization water molecules (Figures S3) along the *c* axis or hydrophobic ones along the *b* axis in which the aliphatic chains (isopropylic valine residue) of the ligand are confined. In comparison with **1**, the empty volume of these channels have been reduced as consequence of the spatial orientation of the larger isopropyl residues and the carbonyl groups of the acidic part from *trans*-(*S*,*S*)-valmox bridging ligands (Figure 4b). In this sense, the estimated empty volume without the crystallization solvent molecules is 2822.7 $Å^3$, a value that represents up to ca. 47.2% of potential void per unit cell volume [V = 5974.2 $Å^3$].

Compound **3** crystallizes in the chiral $P2_13$ space group of the cubic system. Its structure consists of a chiral 3D barium(II)−copper(II) network, which is built up from *trans*-oxamidato-bridged dicopper(II) units, $\{Cu^{II}_2[(S,S)\text{-leumox}]\}$, acting as linkers between two of the three crystallographically independent Ba atoms [Ba(1) and Ba(2)] through carboxylate (Figure 3c); other Ba^{2+} ions [Ba(3)] are further grasped through a triple water bridge in a fascinating terminal $-Ba_2(\mu\text{-}H_2O)_3-$ cluster (Figures S1c, S2c, and 6); additional hydroxo groups acting as supplementary bridges between two neighboring dicopper(II) units and coordinated in a μ_3 fashion sustain the framework (Figures 1c, 3c, and 6). The four crystallographically not equivalent copper atoms, Cu(1), Cu(2), Cu(3), and Cu(4), are five-coordinated in a square pyramidal geometry, which is built by one amidate-nitrogen, one carbonyl-oxygen atom, one carboxylate-oxygen atom, and one hydroxo group in the equatorial plane and one carboxylate-oxygen atom from a neighboring dicopper(II) unit for Cu(1) and Cu(2), or one water molecule for Cu(3) and Cu(4), occupying the axial position (Figures 3c and 6) [average values Cu−N = 1.915(9) Å; $Cu-O_{OH}$ = 1.929(9) Å; $Cu-O_{eq}$ = 2.017(8) Å; $Cu-O_{ax}$ = 2.220(8) Å; $Cu-O_{water}$ = 2.392(7) and 2.550(8) Å].

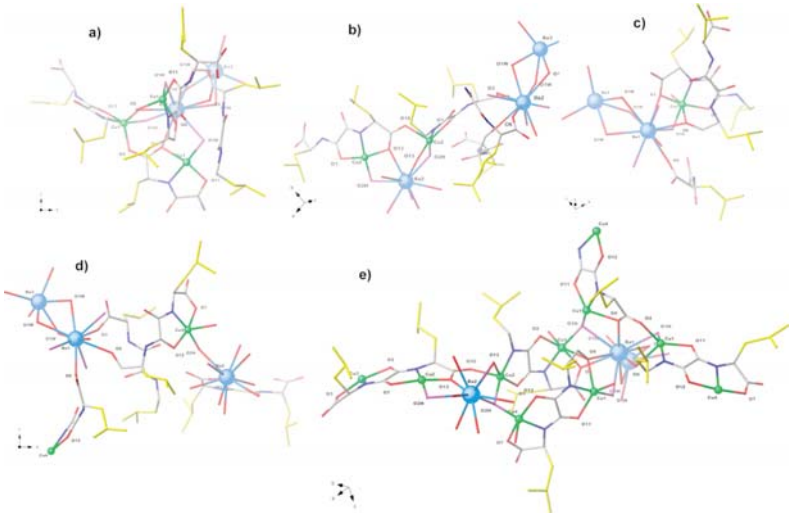

Figure 6. (a−d) Details of crystallographically not equivalent Cu(1), Cu(2), Cu(3), and Cu(4) copper metal ion connectivities in **3**. (e) Overall view of connectivities in a fragment of **3** (Cu, green; Ba, blue; hydroxo oxygen, purple; leucine side chains, yellow; oxygen from ligands, red sticks; nitrogen, blue sticks).

DOI: 10.1021/acs.cgd.6b01052
Cryst. Growth Des. 2016, 16, 5571−5578

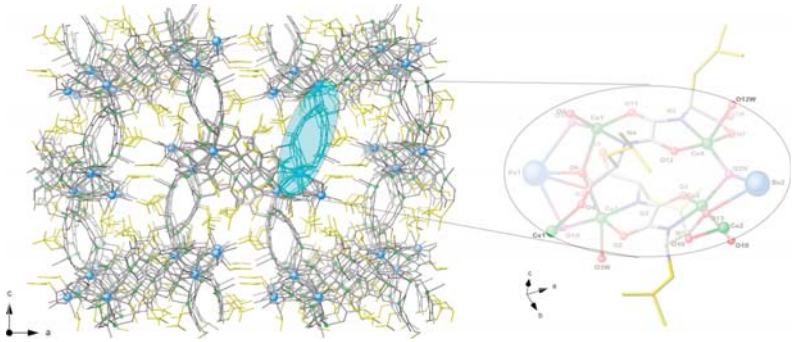

Figure 7. Perspective view of the 3D net structure of **3** along *b* axis. The inset shows a detail of tetranuclear copper rings regularly alternating in the structure.

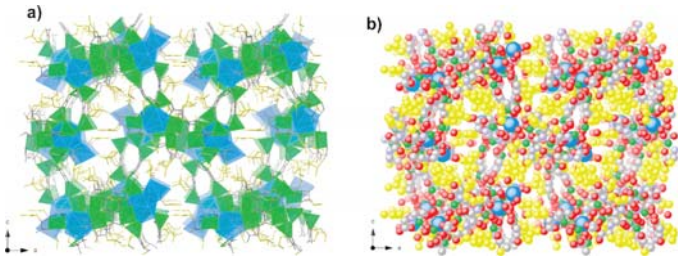

Figure 8. Perspective view of structure of **3** along *b* crystallographic axis as polyhedral (a) and space filling (b) models exhibiting isobutyl chains buried in hydrophobic channels.

The asymmetric coordination mode of the leumox ligand employing only one of the two "free" carbonyl-oxygen atoms to coordinate (Figure 3c) generates an intricate framework, where each crystallographically independent barium atom adopts different coordination geometry with Ba−O distances varying in the range 2.740(8)−3.030(14) Å. Their connectivities in the overall network have been represented in Figure 6 from Cu(1) to Cu(4), respectively. The Ba(1) atom is 12-coordinated, BaO_{12}, in a distorted bicapped pentagonal antiprismatic geometry, made by six carboxylate-oxygen atoms, hydroxo groups, and three water molecules (Figures S1c and S2c). The Ba(2) atom is ten-coordinated, BaO_{10}, in a bicapped square prismatic geometry formed by three carboxylate-oxygen atoms, three hydroxo groups, and four water molecules (Figures S1c and S2c). The Ba(3) atom is only hydrated being surrounded by six water molecules, three of them shared with Ba(2) atoms in a highly distorted trigonal prismatic geometry (Figures S1c, S2c, and 6).

The 3D structure of **3** can be described as a three-dimensional copper(II) network, which is built up from tetranuclear copper(II) rings, $\{Cu^{II}_4[(S,S)\text{-leumox}]_2\}$, in which two neighboring dicopper(II) units are linked through an hydroxo group acting as bridge together with a carbonyl oxygen atom from the ligand coordinated in a μ_3 fashion (see blue inset of Figure 7). Diverse solvated barium atoms are grasped by the net to ensure electroneutrality (Figure 7).

In comparison with **1** and **2**, the empty volume of these channels have been reduced as consequence of the spatial orientation of the larger isobutyl residues and the carbonyl groups of the acidic part from *trans*-(*S*,*S*)-leumox bridging ligands even if not as much as expected (Figure 8). In fact, the estimated empty volume without the crystallization solvent molecules is 7997.9 Å^3, a value that represents up to ca. 44.9% of potential void per unit cell volume [V = 17825.4 Å^3].

To better understand the frameworks of **1**−**3**, we have carried out a topological analysis by applying the concept of the simplified underlying net.[44−49] These analyses were performed using the computer program TOPOSPRO[50] and checked against the Reticular Chemistry Structural Resource (RCSR)[51] and EPINET databases.[52,53]

Network analysis of compound **1** reveals the uninodal six-connected **acs** net,[54] a hexagonal net of aligned, corner-sharing, trigonal prisms (Figure S4a) with point symbol of $(4^9{\cdot}6^6)$. Despite this net is among the 20 most frequent 3D underlying nets, a search using database of TOPOS shows that only few examples of **acs** nets with alkaline-earth metal ions have been reported.[55−58] In particular they all report structures of Mg^{2+} ions and formate as ligand, crystallized in chiral space groups. Interestingly no examples are known with amino acid derivative ligands. In turn, topological analysis of compound **2** reveals the most common **pcu** network,[49,51] of point symbol $(4^{12}{\cdot}6^3)$; a schematic view of the underlying uninodal six-connected net, obtained applying *simplification* procedures, is represented in Figure S4b. Only one example of **pcu** net containing alanine as ligand, with Pb(II) metal ions, has been reported,[59] whereas no examples are known with valine or leucine amino acids. Finally, the underlying net of compound **3** is the uninodal 3-connected net (Figure S4c) with point symbol of (10^3) and features **srs** ($SrSi_2$) topology according to the RCSR classification.[60] It is a common net but remarkably only five examples of 3D nets built with Cu^{2+},[61,62] Ni^{2+},[63] and Cd^{2+} ions[64] and amino acid derivate ligands can be found in the literature.

The unifying theme of the ligands used to build **1**−**3** is that they contain nonreactive and flexible side chains that are ideally

DOI: 10.1021/acs.cgd.6b01052
Cryst. Growth Des. 2016, 16, 5571−5578

suited for packing in the large structure. Furthermore, strictly speaking, the amino acids employed in our ligands, with aliphatic side chains such as alanine, valine, and leucine are all classified as hydrophobic. Anyway, alanine side chain being very short is not particularly hydrophobic. In our opinion this must be at the origin of the porous structure of compound **1** where either a large amount of water molecules or methyl group share the same channels. In contrast, the more hydrophobic valine side chain moves self-assembly in **2** in order to confine solvent and isopropyl groups in diverse pores. Leucine residues being hydrophobic, longer, and much more hindered than others prefers, as valine ones, to be buried in network hydrophobic cores, but this implies large space to reach the more stable folding. In this situation even expected metal ions binding from a bis(amino acid)oxalamide ligand may be affected and driven toward the more kinetically stable compound; in fact, side-chain packing may also be important to the kinetics of folding.

X-ray Powder Diffraction. Powder X-ray diffraction (PXRD) studies for **1**−**3** show a total loss of crystallinity for **2** and **3** (Figure S5), indicating that they amorphize when exposed to air. Their structures in which solvent act as active "ligand" are in total agreement with this behavior, especially for compound **2** where highly volatile methanol molecules, acting as bridge between neighboring copper atoms, built an effective node of the overall structure. In contrast, the covalent network of **1** remains crystalline. The PXRD patterns of **1**−**3** were then measured in water suspensions to prevent the partial loss of water at room temperature and the corresponding collapse of the structure in **2** and **3**. Figure 9 shows that the experimental PXRD patterns of **1**−**3** are consistent with the calculated ones confirming thus the pureness of the bulk samples.

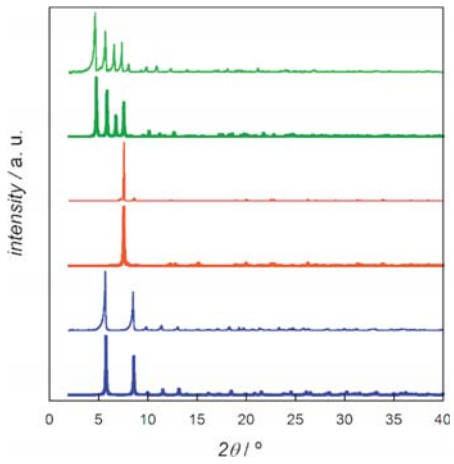

Figure 9. Experimental (solid lines) and calculated (bold lines) XRPD pattern profiles of the hydrated phases of **1** (blue), **2** (red), and **3** (green) measured as water suspensions in the 2θ range 5.0−40.0° at r.t.

Gas Sorption Behavior. The porosity of **1**−**3** was then evaluated by means of N_2 adsorption measurements at 77 K. Compounds **2** and **3** displayed hardly any adsorption of N_2 as could be expected from the structural collapse of the network shown by PXRD studies. In turn, high permanent porosity was observed for **1** (Figure 10) as a consequence of its remarkable stability and quite large channels. The isotherm shows a type I

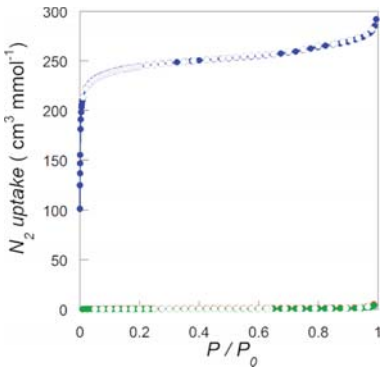

Figure 10. N_2 sorption isotherms at 77 K for the activated phases of **1** (blue), **2** (red), and **3** (green). Filled and empty symbols indicate the adsorption and desorption isotherms, respectively. All samples were activated at 80 °C under reduced pressure for 16 h prior to carry out the sorption measurements.

behavior with large uptake at low pressures (Figure 10). The Brunauer−Emmett−Teller (BET) surface area calculated was 966 m^2/g,[65] with a calculated pore size[66] of ca. 1.0 nm, which closely corresponds to that determined from the crystal structure. In addition, the CO_2 and CH_4 adsorption isotherms of **1** were also measured at 0 °C (Figure S5). The CO_2 and CH_4 loadings are 89.0 and 18.2 $cm^3\ g^{-1}$, respectively, at 900 mmHg, indicating a moderate CO_2/CH_4 gas selectivity (ideal selectivity of ca. 5, Figure S6).

CONCLUSIONS

The effectiveness of the metalloligand design strategy for the obtention of a family of chiral MOFs has been illustrated with the synthesis of three chiral *bio*MOFs from oxamidatecopper(II) complex precursors, which in turn were prepared using enantiopure amino acid derivatives as ligands, acting as metalloligands toward barium atoms. The encoded chiral information on the natural amino acids, L-alanine, L-valine, and L-leucine, have been efficiently transmitted to the final network by means of a metallosupramolecular design strategy. Very different structures for **1**−**3** have been obtained from, in principle, similar ligands, where the variation of the length on the hydrophobic aliphatic chains determine metal ion organization. Despite the similarity of the ligand, these results seem to suggest that self-assembly in **1**−**3** occurs in a hierarchical manner. Overall, the study of the influence of the length/size and shape of the aliphatic residue along this series of *trans*-oxamidato-bridged dicopper(II) units on the structural complexity of the 3D open-framework obtained have revealed a close relationship between them. This phenomena resembles the process of molecular recognition that takes place in polypeptides chains, where each amino acid residue is identified by different ligand connections acting as *fingerprints*.

ASSOCIATED CONTENT

Supporting Information

The Supporting Information is available free of charge on the ACS Publications website at DOI: 10.1021/acs.cgd.6b01052.

Experimental preparation; analytical and spectroscopic characterization of **1**, **2**, and **3** (PDF)

DOI: 10.1021/acs.cgd.6b01052
Cryst. Growth Des. 2016, 16, 5571−5578

Accession Codes

CCDC 1493129−1493131 contains the supplementary crystallographic data for this paper. These data can be obtained free of charge via www.ccdc.cam.ac.uk/data_request/cif, or by emailing data_request@ccdc.cam.ac.uk, or by contacting The Cambridge Crystallographic Data Centre, 12, Union Road, Cambridge CB2 1EZ, UK; fax: +44 1223 336033.

AUTHOR INFORMATION

Corresponding Authors

*E-mail: emilio.pardo@uv.es.
*E-mail: donatella.armentano@unical.it.
*E-mail: jesus.ferrando@uv.es.

Notes

The authors declare no competing financial interest.

ACKNOWLEDGMENTS

This work was supported by the MINECO (Spain) (Projects CTQ2013-46362-P, CTQ2013-44844-P and Excellence Unit "Maria de Maeztu" MDM-2015-0538), the Generalitat Valenciana (Spain) (Project PROMETEOII/2014/070), and the Ministero dell'Istruzione, dell'Università e della Ricerca (Italy). T.G. and M.M. thank the MINECO and the Universitat de València for predoctoral contracts. Thanks are also extended to the Ramón y Cajal Program and the "Convocatoria 2015 de Ayudas Fundación BBVA a Investigadores y Creadores Culturales" (to E.P. and J.F.-S.).

REFERENCES

(1) Kitagawa, S.; Kitaura, R.; Noro, S. *Angew. Chem., Int. Ed.* **2004**, *43*, 2334−2375.
(2) Férey, G. *Chem. Soc. Rev.* **2008**, *37*, 191−214.
(3) Long, J. R.; Yaghi, O. M. *Chem. Soc. Rev.* **2009**, *38*, 1213−1214.
(4) Furukawa, H.; Cordova, K. E.; O'Keeffe, M.; Yaghi, O. M. *Science* **2013**, *341*, 974.
(5) Eddaoudi, M.; Sava, D. F.; Eubank, J. F.; Adil, K.; Guillerm, V. *Chem. Soc. Rev.* **2015**, *44*, 228−249.
(6) Batten, S. R.; Robson, R. *Angew. Chem., Int. Ed.* **1998**, *37*, 1460−1494.
(7) Yaghi, O. M.; O'Keeffe, M.; Ockwig, N. W.; Chae, H. K.; Eddaoudi, M.; Kim, J. *Nature* **2003**, *423*, 705−714.
(8) Janiak, C. *Dalton Trans.* **2003**, 2781−2804.
(9) Bradshaw, D.; Claridge, J. B.; Cussen, E. J.; Prior, T. J.; Rosseinsky, M. J. *Acc. Chem. Res.* **2005**, *38*, 273−282.
(10) Férey, G.; Mellot-Draznieks, C.; Serre, C.; Millange, F.; Dutour, J.; Surblé, S.; Margiolaki, I. *Science* **2005**, *309*, 2040−2042.
(11) Kitagawa, S.; Matsuda, R. *Coord. Chem. Rev.* **2007**, *251*, 2490−2509.
(12) Tanabe, K. K.; Wang, Z.; Cohen, S. M. *J. Am. Chem. Soc.* **2008**, *130*, 8508−8517.
(13) Yang, S.; Lin, X.; Blake, A. J.; Walker, G. S.; Hubberstey, P.; Champness, N. R.; Schröder, M. *Nat. Chem.* **2009**, *1*, 487−493.
(14) Nohra, B.; El Moll, H.; Rodriguez Albelo, L. M.; Mialane, P.; Marrot, J.; Mellot-Draznieks, C.; O'Keeffe, M.; Ngo Biboum, R.; Lemaire, J.; Keita, B.; Nadjo, L.; Dolbecq, A. *J. Am. Chem. Soc.* **2011**, *133*, 13363−13374.
(15) Deng, H.; Grunder, S.; Cordova, K. E.; Valente, C.; Furukawa, H.; Hmadeh, M.; Gandara, F.; Whalley, A. C.; Liu, Z.; Asahina, S.; Kazumori, H.; O'Keeffe, M.; Terasaki, O.; Fraser Stoddart, J.; Yaghi, O. M. *Science* **2012**, *336*, 1018−1023.
(16) Ferrando-Soria, J.; Khajavi, H.; Serra-Crespo, P.; Gascon, J.; Kapteijn, F.; Julve, M.; Lloret, F.; Pasan, J.; Ruiz-Perez, C.; Journaux, Y.; Pardo, E. *Adv. Mater.* **2012**, *24*, 5625−5629.
(17) Cohen, S. M. *Chem. Rev.* **2012**, *112*, 970−1000.
(18) Grancha, T.; Ferrando-Soria, J.; Zhou, H.-C.; Gascon, J.; Seoane, B.; Pasán, J.; Fabelo, O.; Julve, M.; Pardo, E. *Angew. Chem., Int. Ed.* **2015**, *54*, 6521−6525.
(19) Nguyen, H. L.; Gandara, F.; Furukawa, H.; Doan, T. L. H.; Cordova, K. E.; Yaghi, O. M. *J. Am. Chem. Soc.* **2016**, *138*, 4330−4333.
(20) Li, J.; Sculley, J.; Zhou, H.-C. *Chem. Rev.* **2012**, *112*, 869.
(21) Peng, Y.; Krungleviciute, V.; Eryazici, I.; Hupp, J.; Farha, O.; Yildirim, T. *J. Am. Chem. Soc.* **2013**, *135*, 11887−11894.
(22) Horike, S.; Umeyama, D.; Kitagawa, S. *Acc. Chem. Res.* **2013**, *46*, 2376−2384.
(23) McKinlay, A. C.; Morris, R. E.; Horcajada, P.; Ferey, G.; Gref, R.; Couvreur, P.; Serre, C. *Angew. Chem., Int. Ed.* **2010**, *49*, 6260−6266.
(24) Dechambenoit, P.; Long, J. R. *Chem. Soc. Rev.* **2011**, *40*, 3249−3265.
(25) Grancha, T.; Ferrando-Soria, J.; Castellano, M.; Julve, M.; Pasán, J.; Armentano, D.; Pardo, E. *Chem. Commun.* **2014**, *50*, 7569−7589.
(26) Inokuma, Y.; Arai, T.; Fujita, M. *Nat. Chem.* **2010**, *2*, 780−783.
(27) Gascon, J.; Corma, A.; Kapteijn, F.; Llabrés i Xamena, F. X. *ACS Catal.* **2014**, *4*, 361−378.
(28) Bisht, K. K.; Parmar, B.; Rachuri, Y.; Kathalikattil, A. C.; Suresh, E. *CrystEngComm* **2015**, *17*, 5341−5356.
(29) Pardo, E.; Train, C.; Gontard, G.; Boubekeur, K.; Fabelo, O.; Liu, H.; Dkhil, B.; Lloret, F.; Nakagawa, K.; Tokoro, H.; Ohkoshi, S.; Verdaguer, M. *J. Am. Chem. Soc.* **2011**, *133*, 15328−15331.
(30) Wang, F.; Fu, H.-R.; Zhang, J. *Cryst. Growth Des.* **2015**, *15*, 1568−1571.
(31) Liu, Y.; Xi, X.; Ye, C.; Gong, T.; Yang, Z.; Cui, Y. *Angew. Chem., Int. Ed.* **2014**, *53*, 13821−13825.
(32) Ferguson, A.; Liu, L.; Tapperwijn, S. J.; Perl, D.; Coudert, F.-X.; Van Cleuvenbergen, S.; Verbiest, T.; van der Veen, M. A.; Telfer, S. G. *Nat. Chem.* **2016**, *8*, 250−257.
(33) Zhou, Z.; He, C.; Xiu, J.; Yang, L.; Duan, C. *J. Am. Chem. Soc.* **2015**, *137*, 15066−15069.
(34) Zhang, S.-Y.; Li, D.; Guo, D.; Zhang, H.; Shi, W.; Cheng, P.; Wojtas, L.; Zaworotko, M. J. *J. Am. Chem. Soc.* **2015**, *137*, 15406−15409.
(35) Dul, M.-C.; Pardo, E.; Lescouëzec, R.; Journaux, Y.; Ferrando-Soria, J.; Ruiz-García, R.; Cano, J.; Julve, M.; Lloret, F.; Cangussu, D.; Pereira, C. L. M.; Stumpf, H. O.; Pasán, J.; Ruiz-Pérez, C. *Coord. Chem. Rev.* **2010**, *254*, 2281−2296.
(36) Grancha, T.; Ferrando-Soria, J.; Castellano, M.; Julve, M.; Pasán, J.; Armentano, D.; Pardo, E. *Chem. Commun.* **2014**, *50*, 7569−7585.
(37) Grancha, T.; Tourbillon, C.; Ferrando-Soria, J.; Julve, M.; Lloret, F.; Pasán, J.; Ruiz-Pérez, C.; Fabelo, O.; Pardo, E. *CrystEngComm* **2013**, *15*, 9312−9315.
(38) Grancha, T.; Ferrando-Soria, J.; Cano, J.; Lloret, F.; Julve, M.; De Munno, G.; Armentano, D.; Pardo, E. *Chem. Commun.* **2013**, *49*, 5942−5944.
(39) Mon, M.; Ferrando-Soria, J.; Grancha, T.; Fortea-Pérez, F. R.; Gascon, J.; Leyva-Pérez, A.; Armentano, D.; Pardo, E. *J. Am. Chem. Soc.* **2016**, *138*, 7864−7867.
(40) Grancha, T.; Ferrando-Soria, J.; Cano, J.; Amorós, P.; Seoane, B.; Gascon, J.; Bazaga-García, M.; Losilla, E. R.; Cabeza, A.; Armentano, D.; Pardo, E. *Chem. Mater.* **2016**, *28*, 4608−4615.
(41) Mon, M.; Lloret, F.; Ferrando-Soria, J.; Martí-Gastaldo, C.; Armentano, D.; Pardo, E. *Angew. Chem., Int. Ed.* **2016**10.1002/anie.201606015R1.
(42) Lloret, F.; Julve, M.; Faus, J.; Ruiz, R.; Castro, I.; Mollar, M.; Philoche-Levisalles, M. *Inorg. Chem.* **1992**, *31*, 784−791.
(43) Lloret, F.; Julve, M.; Real, J. A.; Faus, J.; Ruiz, R.; Mollar, M.; Castro, I.; Bois, C. *Inorg. Chem.* **1992**, *31*, 2956−2961.
(44) Carlucci, L.; Ciani, G.; Proserpio, D. M. In *Making Crystals by Design*; Wiley-VCH Verlag GmbH & Co. KGaA: Weinheim, Germany, 2007; pp 58−85.
(45) Blatov, V. A.; Proserpio, D. M. *Modern Methods of Crystal Structure Prediction*; Oganov, A. R., Ed.; Wiley-VCH Verlag GmbH & Co. KGaA: Weinheim, Germany, 2010.

DOI: 10.1021/acs.cgd.6b01052
Cryst. Growth Des. 2016, 16, 5571−5578

(46) Hoffmann, F.; Fröba, M. In *The Chemistry of Metal-Organic Frameworks: Synthesis, Characterization, and Applications*; Wiley-VCH Verlag GmbH & Co. KGaA: Weinheim, Germany, 2016; pp 5−40.
(47) Blatov, V. A.; O'Keeffe, M.; Proserpio, D. M. *CrystEngComm* **2010**, *12*, 44−48.
(48) Alexandrov, E. V.; Blatov, V. A.; Kochetkov, A. V.; Proserpio, D. M. *CrystEngComm* **2011**, *13*, 3947−3958.
(49) O'Keeffe, M.; Yaghi, O. M. *Chem. Rev.* **2012**, *112*, 675−702.
(50) Blatov, V. A.; Shevchenko, A. P.; Proserpio, D. M. *Cryst. Growth Des.* **2014**, *14*, 3576−3586.
(51) O'Keeffe, M.; Peskov, M. A.; Ramsden, S. J.; Yaghi, O. M. *Acc. Chem. Res.* **2008**, *41*, 1782−1789.
(52) Blatov, V. A. *IUCr CompComm Newsletter* **2006**, *7*, 4−38.
(53) Blatov, V. A.; Proserpio, D. M. *Acta Crystallogr., Sect. A: Found. Crystallogr.* **2009**, *65*, 202−212.
(54) Sudik, A. C.; Cote, A. P.; Yaghi, O. M. *Inorg. Chem.* **2005**, *44*, 2998−3000.
(55) SIWZOP, SIWZOP01, SIWZOP02, SIWZOP03: Chen, S.; Shang, R.; Hu, K.-L.; Wang, Z.- M.; Gao, S. *Inorg. Chem. Front.* **2014**, *1*, 83−98.
(56) VESBAY: Liu, B.; Shang, R.; Hu, K.-L.; Wang, Z.-M.; Gao, S. *Inorg. Chem.* **2012**, *51*, 13363−13372.
(57) NIWPIU: Maczka, M.; Pietraszko, A.; Macalik, B.; Hermanowicz, K. *Inorg. Chem.* **2014**, *53*, 787−794.
(58) NIWZIE, NIWZIE01, NIWZIE02, NIWZIE03: Shang, R.; Xu, G.-C.; Wang, Z.-M.; Gao, S. *Chem. - Eur. J.* **2014**, *20*, 1146−1148.
(59) AJERUC: Reynolds, K.; Willett, R. D.; Twamley, B. *Acta Crystallogr., Sect. E: Struct. Rep. Online* **2003**, *59*, m402.
(60) Hyde, S. T.; O'Keeffe, M.; Proserpio, D. M. *Angew. Chem., Int. Ed.* **2008**, *47*, 7996−8000.
(61) QEMYEM: Facchin, G.; Torre, M. H.; Kremer, E.; Piro, O. E.; Castellano, E. E.; Baran, E. J. *Z. Naturforsch., B: J. Chem. Sci.* **2000**, *55*, 1157−1162.
(62) PEFSUQ: Lin, L.; Yu, R.; Yang, W.; Wu, X.-Y.; Lu, C.-Z. *Cryst. Growth Des.* **2012**, *12*, 3304−3311.
(63) EZUXIH: Li, H.-Y.; Huang, F.-P.; Jiang, Y.-M. *Inorg. Chim. Acta* **2011**, *377*, 91−98.
(64) HEBJUV: Kundu, T.; Sahoo, S. C.; Banerjee, R. *Cryst. Growth Des.* **2012**, *12*, 4633−4640.
(65) Brunauer, S.; Emmett, P. H.; Teller, E. *J. Am. Chem. Soc.* **1938**, *60*, 309−319.
(66) Cheng, L. S.; Ralph T, Y. *Chem. Eng. Sci.* **1994**, *49*, 2599−2609.

DOI: 10.1021/acs.cgd.6b01052
Cryst. Growth Des. 2016, 16, 5571−5578

ChemComm

COMMUNICATION

View Article Online
View Journal | View Issue

Cite this: *Chem. Commun.*, 2016, **52**, 7360

Received 2nd May 2016,
Accepted 12th May 2016

DOI: 10.1039/c6cc03667h

www.rsc.org/chemcomm

Spin-crossover complex encapsulation within a magnetic metal–organic framework†

Alexandre Abhervé,‡[a] Thais Grancha,‡[a] Jesús Ferrando-Soria,[a] Miguel Clemente-León,*[a] Eugenio Coronado,[a] João C. Waerenborgh,[b] Francesc Lloret[a] and Emilio Pardo*[a]

The solid-state incorporation of a mononuclear iron(III) complex within the pores of a magnetic 3D metal–organic framework (MOF) in a single crystal to single crystal process leads to the formation of a new hybrid material showing both a guest-dependent long-range magnetic ordering and a spin-crossover (SCO) behaviour.

Metal–organic frameworks (MOFs)[1–3] attract a lot of interest within the chemist community due to both, a wide diversity of fascinating porous architectures and the number of chemical and physical properties they can exhibit.[3] Closely related to their porous character and rich host–guest chemistry,[4,5] MOFs have also emerged as appealing candidates for the design of compounds combining more than one physical properties, the so-called multifunctional materials.[6–13] Hence, the presence of large channels, capable of hosting a functional molecule, allows a straight approach to add given physical properties to the material.

Multifunctional magnetic materials are of special interest within the multidisciplinary field of molecular magnetism.[14] In this area, the combination of a long-range magnetic ordering,[15] provided by a two- (2D) or three-dimensional (3D) metal–organic network with other appealing magnetic properties, such as those shown by the well-known single-molecule magnets (SMMs)[16] or spin-crossover (SCOs) compounds[17,18] for example, can lead to new advanced materials showing the coexistence of properties,[19] or even new magnetic properties,[20,21] which can be of interest in applications such as high-density magnetic memories[22] or quantum computing devices.[23,24] Several synthetic strategies can be followed to obtain these multifunctional magnetic materials. So far, direct self-assembly methods[25] have been the most widely used strategies to achieve this objective.[26–28] For example, Sieber *et al.* reported in a pioneering work,[29] the synthesis of a host–guest system of the formula $[Co(bpy)_3][LiCr(ox)_3]$ showing spin-crossover behaviour. More recently, post-synthetic (PS) procedures,[30,31] which can include transmetallation processes,[32] counter-ion[33] or ligand exchange,[34] *etc.*, on preformed MOFs, have emerged as powerful tools for the design of novel porous materials incorporating functional molecules or complexes.

In particular, PS methods have been proven effective recently for the insertion of a type of SMM, the so-called Single-Ion Magnets (SIMs), within the channels of a 3D magnetic MOF,[21] allowing an unprecedented study of the interplay between the SIM behaviour and the long-range magnetic ordering. However, as far as we know, no example of PS insertion of SCOs has been reported so far (Fig. 1).

Herein, we plan to extend the use of PS methods to other areas of molecular magnetism. So, aiming at the synthesis of hybrid materials showing both long range magnetic ordering and spin-crossover behaviour, we designed a synthetic strategy based on the solid-state incorporation *via* single-crystal to single-crystal (SC to SC) of a Fe(III) complex of the formula $[Fe^{III}(sal_2\text{-trien})]NO_3\cdot H_2O$ (H_2sal_2-trien = *N*,*N*′-disalicylidene-triethylenetetramine)[35] into the large pores (*ca.* 2.2 nm) of a manganese(II)–copper(II) 3D MOF of the formula $Na_4\{Mn_4[Cu_2(Me_3mpba)_2]_3\}\cdot 60H_2O$[36] (**1**) [$Me_3mpba^{4-}$ = *N*,*N*′-2,4,6-trimethyl-1,3-phenylenebis(oxamate)].[36,37] The strategy involves straight

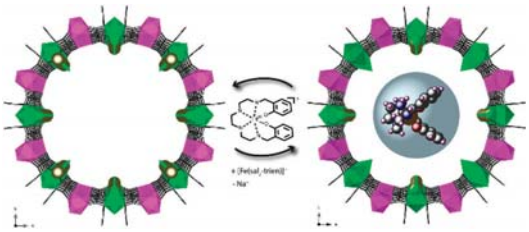

Fig. 1 Schematic representation of the SC to SC cation exchange process leading to the hybrid **Fe(sal$_2$-trien)@1**.

[a] *Departament de Química Inorgànica/Instituto de Ciencia Molecular (ICMol), Universitat de València, 46980 Paterna, València, Spain. E-mail: miguel.clemente@uv.es, emilio.pardo@uv.es; Fax: +34 3543273; Tel: +34 3544442*

[b] *Centro de Ciências e Tecnologias Nucleares, Instituto Superior Técnico, Universidade de Lisboa, 2695-066 Bobadela LRS, Portugal*

† Electronic supplementary information (ESI) available: Synthesis of compound **Fe(sal$_2$-trien)@1**. Physical techniques. Additional Fig. S1–S3. See DOI: 10.1039/c6cc03667h

‡ These authors have equally contributed to this work.

diffusion and cation-exchange to yield a novel compound of the formula $[Fe^{III}(sal_2\text{-trien})]Na_3\{Mn_4[Cu_2(Me_3mpba)_2]_3\}\cdot 43H_2O$ (**Fe(sal$_2$-trien)@1**).

Fe(sal$_2$-trien)@1 was obtained by soaking crystals of **1** in a saturated water solution of $[Fe^{III}(sal_2\text{-trien})]NO_3\cdot H_2O$. After 6 days of immersion, the crystals were filtered and washed with water (see the Experimental section, ESI†). The exchange of Na^+ cations by the cationic $[Fe^{III}(sal_2\text{-trien})]^+$ complexes was monitored through IR (Fig. S1, ESI†), SEM and ICP-AES. The cation-exchanged crystals had the same size and shape as those of the original ones, ruling out a possible dissolution–recrystallization mechanism for this system and strongly suggesting a solid-state process.[38]

The powder X-ray diffraction (PXRD) patterns of the water suspended samples of **1** and **Fe(sal$_2$-trien)@1** (Fig. 2b and c) are consistent with the calculated one for **1** (Fig. 2a), confirming their isostructurality. Very interestingly, both compounds show very different structural stabilities when exposed to air. Thus, **1** exhibits no crystallinity (Fig. 2d), which indicates a complete collapse of the original hydrated phase upon solvent removal, whereas the PXRD patterns of **Fe(sal$_2$-trien)@1** (Fig. 2e) show well-resolved peaks suggesting that the presence of the Fe(III) complex confers structural stability on the open-framework structure.

The retention of crystallinity was further confirmed by single-crystal X-ray diffraction. According to unit cell measurements, crystals of **Fe(sal$_2$-trien)@1** appear to be stable upon dehydration. Besides, a small increase in the size of the unit cell is observed for a single crystal of **Fe(sal$_2$-trien)@1**[39] compared with the crystal data of **1**.[36] Unfortunately, the structure could not be solved as the $[Fe(sal_2\text{-trien})]^+$ cation is crystallographically disordered.

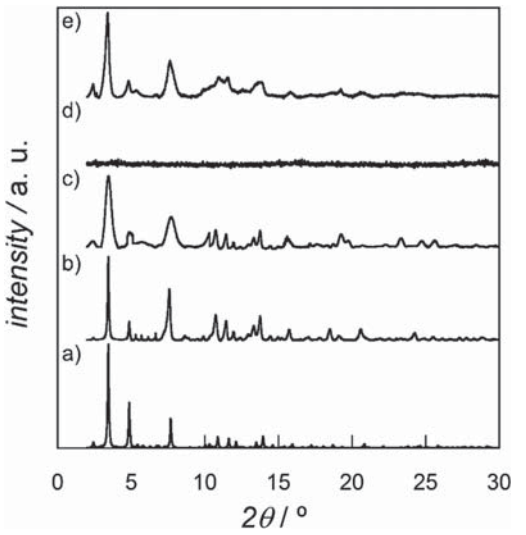

Fig. 2 (a) Calculated PXRD pattern profile of **1**. Experimental PXRD pattern profiles of water-suspended and filtered polycrystalline samples of **1** (b and d, respectively) and **Fe(sal$_2$-trien)@1** (c and e, respectively) in the 2θ range 2.0–30.0° at room temperature.

Thermogravimetric analysis (TGA) under a dry N_2 atmosphere for **Fe(sal$_2$-trien)@1** (Fig. S2, ESI†) shows a fast mass loss from room temperature to *ca.* 125 °C followed by a pseudo plateau until decomposition starts. The estimated weight loss of 31 (**1**) and 22% (**Fe(sal$_2$-trien)@1**) at 180 °C corresponds to 60 and 43 water molecules, respectively. The smaller number of water molecules for **Fe(sal$_2$-trien)@1** compared to its precursor **1** is in complete agreement with the occupation of the channels with the Fe(III) complexes.

Overall, the combination of the ICP-AES, IR, SEM/EDX, elemental, PXRD and TGA analyses (ESI†) allows for an unambiguous determination of the chemical composition of **Fe(sal$_2$-trien)@1**.

So, once the presence of mononuclear iron(III) complexes inside the channels of the magnetic MOF was confirmed, we examined the magnetic properties of this hybrid system in order to check for the possible spin-crossover transition of the hosted molecule. In fact, although the precursor used in this work, $[Fe^{III}(sal_2\text{-trien})]NO_3\cdot H_2O$, is low-spin (LS) and do not transit in the range of 2–300 K,[35] other salts of the complex have shown excellent spin crossover behaviours.[35,40]

The magnetic properties of **1** and **Fe(sal$_2$-trien)@1** were thus measured in both direct current (dc) and alternating current (ac) regimes (see the Experimental section) and they show relevant differences.

The $\chi_M T$ *vs.* T plots (χ_M is the dc molar magnetic susceptibility per $Cu^{II}_6Mn^{II}_4$ unit and T is the temperature) for both compounds are shown in Fig. 3a. In the low temperature region, **Fe(sal$_2$-trien)@1** shows a similar qualitative behaviour to that of **1**, the $\chi_M T$ values being slightly higher for **Fe(sal$_2$-trien)@1** due to the presence of one LS Fe^{III} centre (S = 1/2) per formula unit. Overall, they exhibit the same characteristic minimum indicative of a ferrimagnetic behaviour of the 3D network resulting from the antiferromagnetic coupling between the four high-spin (HS) Mn^{II} (S_{Mn} = 5/2) and the six Cu^{II} (S_{Cu} = 1/2) ions through the oxamato bridge, as previously found in other oxamato-based manganese(II)–copper(II) MOFs.[25] Interestingly, the increased value of the minimum temperature (T_{min}) for **Fe(sal$_2$-trien)@1** (inset of Fig. 3a) suggests a strengthening of the antiferromagnetic coupling, which is likely associated with the induced structural stability after the inclusion process (see the PXRD section) as reported previously.[21]

In both compounds, the observed ferrimagnetic behaviour is further confirmed by the *M versus H* plots (*M* being the molar magnetization per formula unit and *H* is the applied dc magnetic field) at 2.0 K (Fig. S3, ESI†). Thus, the isothermal magnetization curves exhibit a fast saturation in both compounds, and slightly slower for **1**. The maximum *M* values of 13.5 (**1**) and 14.3.0 $N\beta$ (**Fe(sal$_2$-trien)@1**) at 5.0 T are consistent with the expected ones considering an antiparallel alignment of the spins of 4 HS Mn^{II} (S_{Mn} = 5/2) and 6 Cu^{II} (S_{Cu} = 1/2) ions plus one LS Fe^{III} (S_{Fe} = 1/2) in the case of **Fe(sal$_2$-trien)@1**.

In contrast to what is seen in the low temperature region, important discrepancies in the 200–400 K range between **1** and **Fe(sal$_2$-trien)@1** are observed (Fig. 3a, inset). At room temperature, the $\chi_M T$ value for **Fe(sal$_2$-trien)@1** (17.08 cm^3 K mol^{-1}) is much

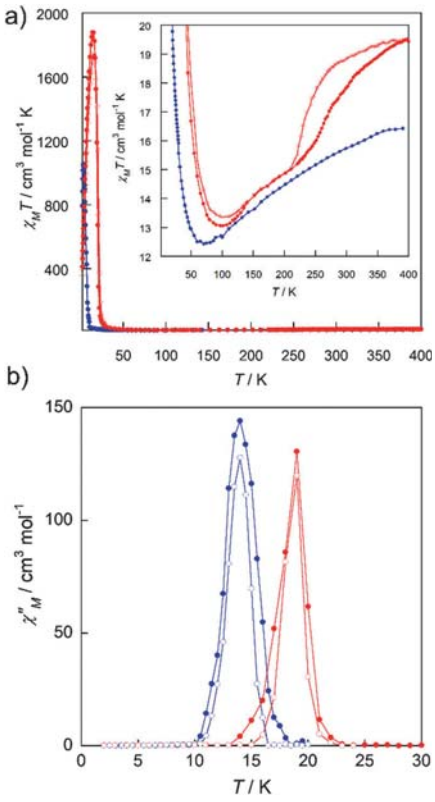

Fig. 3 $\chi_M T$ *versus* T plot for **1** (blue) and **Fe(sal$_2$-trien)@1** (red). The inset shows the minima and the high temperature region in detail, emphasising the thermal hysteresis loop. The full and empty circles represent the **Fe(sal$_2$-trien)@1** data recorded in the heating and cooling modes respectively.

higher than that expected for the sum of one low-spin Fe^{III} ion (0.4 cm^3 K mol^{-1}) plus the $\chi_M T$ value of **1** (15.73 cm^3 K mol^{-1}). This could be indicative of a HS $\leftrightarrow$ LS transition for the Fe^{III} centers. So, the thermal dependence of $\chi_M T$ **Fe(sal$_2$-trien)@1** was studied in the range of 200–400 K [in heating and cooling modes (full and empty red circles) in the inset of Fig. 3a, respectively]. Upon cooling from 400 K, $\chi_M T$ decreases very slowly down to *ca.* 250 K, below this temperature $\chi_M T$ decreases very sharply to 200 K (in contrast to **1**), which is characteristic of an $S = 5/2 \leftrightarrow 1/2$ SCO transition. In addition, the different behaviours of the heating and cooling modes after heating to 400 K could be explained by the loss of solvent molecules (even if *n*-eicosane was used to prevent this loss, ESI†) and/or subtle hysteresis effects. In the desolvated sample, the $\chi_M T$ value at ~300 K corresponds to the expected value for *ca.* 80% of Fe^{III} in the HS state indicating a partial SCO in total agreement with Mössbauer data (see below). Overall, the $\chi_M T$ values at 400 K indicate that although the salt of the complex used in this post-synthetic process ([Fe^{III}(sal$_2$-trien)]$NO_3 \cdot H_2O$) showed no SCO transition in the range of 2–300 K, its encapsulation within the pores of this MOF allows a SCO transition to occur, as observed for other salts of this Fe^{III} complex and for intercalation compounds.[26,28,40–42]

Finally, we carried out magnetic susceptibility measurements for **1** and **Fe(sal$_2$-trien)@1** in the alternating current (ac) regime in the form of the χ_M' and χ_M'' *versus* T plots (χ_M' and χ_M'' being the in-phase and out-of-phase ac magnetic susceptibilities per formula unit). Fig. 3b shows the presence of a frequency-independent sharp χ_M'' maximum at the critical temperatures of T_c = 14 K (**1**) and 19 K (**Fe(sal$_2$-trien)@1**) at the two different frequencies employed, confirming the occurrence of a long-range 3D magnetic ordering in both compounds. In addition, the higher T_c for **Fe(sal$_2$-trien)@1**, compared to that observed for **1** (Fig. 3b), reflects an increase of the intra-network magnetic coupling through the oxamate bridges induced by the presence of the iron complex within the pores of the MOF. In fact, when measuring **1** as an aqueous suspension (data not shown), T_c increases to 19 K.

In order to further confirm the $5/2 \leftrightarrow 1/2$ spin transition, we carried out Mössbauer spectroscopy measurements at 50 and 300 K for **Fe(sal$_2$-trien)@1** (Fig. 4 and Table S2, ESI†). These measurements, showing a predominant LS state at 50 K and a partial transition to the HS at 300 K (Fig. S4, ESI†), unambiguously indicate that the spin transition occurs. Furthermore, they confirm the insertion of the $[Fe(sal_2\text{-trien})]^+$ complexes.

In summary, the 3D magnetic MOF **1** exhibits a partial exchange of the Na^I cations hosted in their channels when being immersed in a saturated aqueous solution of [Fe^{III}(sal$_2$-trien)]$NO_3 \cdot H_2O$ to yield the novel hybrid compound **Fe(sal$_2$-trien)@1**, in a SC to SC process, maintaining the structural

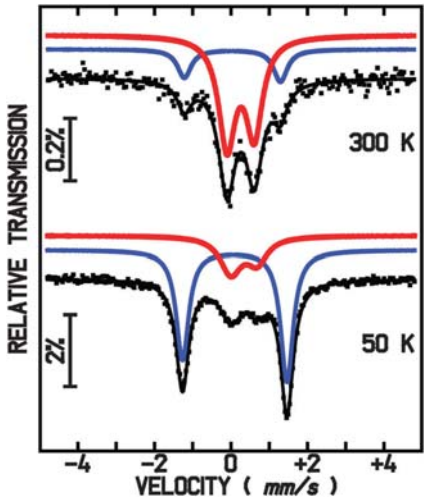

Fig. 4 Mössbauer spectra of a **Fe(sal$_2$-trien)@1** sample prepared at 300 K and cooled down to 50 K later. The lines over the experimental points are the sum of two doublets shown slightly shifted for clarity, corresponding to HS (red) and LS (blue) Fe^{III}. The estimated parameters for these doublets are collected in Table S2 (ESI†).

integrity of the framework. Interestingly, this post-synthetic process affords a novel material with enhanced structural stability, which is reflected in the strengthening of the ferrimagnetic behaviour and thus in the magnetic ordering temperature. More importantly, **Fe(sal$_2$-trien)@1** hosted in the pores shows a 5/2 $\leftrightarrow$ 1/2 spin transition behaviour, which is in contrast to what is seen in the starting precursor salt. Overall, our results, showing for the first time the PS encapsulation of a SCO complex within a magnetic 3D MOF, afford further evidence of the validity of post-synthetic methods to obtain multifunctional materials with rationally predetermined architectures and physical properties *via* the encapsulation of the desired molecule.

This work was supported by the European Commission (COST Action CA15128 MOLSPIN), the Spanish MINECO (Projects CTQ2013-46362-P, CTQ2013-44844-P, MAT2014-56143-R and Excellence Unit "Maria de Maeztu" MDM-2015-0538) and the Generalitat Valenciana (PROMETEO Program of excellence). A. A. and T. G. thank the Generalitat Valenciana and the Universitat de València for a predoctoral contract. Thanks are also extended to the Spanish Ramón y Cajal Program and the "Convocatoria 2015 de Ayudas Fundación BBVA a Investigadores y Creadores Culturales" (E. P.). C^{2}TN/IST author acknowledges the Portuguese Foundation for Science and Technology (FCT), contract UID/Multi/04349/2013.

Notes and references

1 G. Férey, *Chem. Soc. Rev.*, 2008, **37**, 191–214.
2 J. R. Long and O. M. Yaghi, *Chem. Soc. Rev.*, 2009, **38**, 1213–1214.
3 H. Furukawa, K. E. Cordova, M. O'Keeffe and O. M. Yaghi, *Science*, 2013, **341**, 974.
4 O. M. Yaghi, M. O'Keeffe, N. W. Ockwig, H. K. Chae, M. Eddaoudi and J. Kim, *Nature*, 2003, **423**, 705–714.
5 S. Kitagawa, R. Kitaura and S. Noro, *Angew. Chem., Int. Ed.*, 2004, **43**, 2334–2375.
6 E. Coronado, J. R. Galán-Mascarós, C. J. Gómez-García and V. Laukhin, *Nature*, 2000, **408**, 447–449.
7 D. Maspoch, D. Ruiz-Molina and J. Veciana, *Chem. Soc. Rev.*, 2007, **36**, 770–818.
8 C. Train, R. Gheorghe, V. Krstic, L.-M. Chamoreau, N. S. Ovanesyan, G. L. J. A. Rikken, M. Gruselle and M. Verdaguer, *Nat. Mater.*, 2008, **7**, 729–734.
9 C. Train, M. Gruselle and M. Verdaguer, *Chem. Soc. Rev.*, 2011, **40**, 3297–3312.
10 S.-I. Ohkoshi, K. Imoto, Y. Tsunobuchi, S. Takano and H. Tokoro, *Nat. Chem.*, 2011, **3**, 564–569.
11 P. Dechambenoit and J. R. Long, *Chem. Soc. Rev.*, 2011, **40**, 3249–3265.
12 L. E. Kreno, K. Leong, O. K. Farha, M. Allendorf, R. P. Van Duyne and J. T. Hupp, *Chem. Rev.*, 2012, **112**, 1105–1125.
13 T. Grancha, J. Ferrando-Soria, M. Castellano, M. Julve, J. Pasán, D. Armentano and E. Pardo, *Chem. Commun.*, 2014, **50**, 7569–7585.
14 O. Kahn, *Molecular Magnetism*, VCH Publishers, New York, 1993.
15 *Molecule-Based Magnetic Materials*, ed. M. M. Turnbull, T. Sugimoto and L. K. Thompson, American Chemical Society, Washington, DC, 1996, vol. 644.
16 R. Sessoli, D. Gatteschi, A. Caneschi and M. A. Novak, *Nature*, 1993, **365**, 141–143.
17 J. A. Real, E. Andres, M. C. Munoz, M. Julve, T. Granier, A. Bousseksou and F. Varret, *Science*, 1995, **268**, 265–267.
18 G. J. Halder, *Science*, 2002, **298**, 1762–1765.
19 M. Clemente-León, E. Coronado, C. Martí-Gastaldo and F. M. Romero, *Chem. Soc. Rev.*, 2011, **40**, 473.
20 M. Clemente-León, E. Coronado, C. J. Gómez-García, M. López-Jordà, A. Camón, A. Repollés and F. Luis, *Chem. – Eur. J.*, 2014, **20**, 1669–1676.
21 M. Mon, A. Pascual-Álvarez, T. Grancha, J. Cano, J. Ferrando-Soria, F. Lloret, J. Gascon, J. Pasán, D. Armentano and E. Pardo, *Chem. – Eur. J.*, 2016, **22**, 539–545.
22 J. Gatteschi, D. Sessoli and R. Villain, *Molecular Nanomagnets*, Oxford University Press, 2006.
23 M. N. Leuenberger and D. Loss, *Nature*, 2001, **410**, 789–793.
24 M. Affronte, F. Troiani, A. Ghirri, A. Candini, M. Evangelisti, V. Corradini, S. Carretta, P. Santini, G. Amoretti, F. Tuna, G. Timco and R. E. P. Winpenny, *J. Phys. D: Appl. Phys.*, 2007, **40**, 2999–3004.
25 M.-C. Dul, E. Pardo, R. Lescouëzec, Y. Journaux, J. Ferrando-Soria, R. Ruiz-García, J. Cano, M. Julve, F. Lloret, D. Cangussu, C. L. M. Pereira, H. O. Stumpf, J. Pasán and C. Ruiz-Pérez, *Coord. Chem. Rev.*, 2010, **254**, 2281–2296.
26 M. Clemente-León, E. Coronado, M. López-Jordà, G. Mínguez Espallargas, A. Soriano-Portillo and J. C. Waerenborgh, *Chem. – Eur. J.*, 2010, **16**, 2207–2219.
27 M. Clemente-León, E. Coronado, M. López-Jordà, C. Desplanches, S. Asthana, H. Wang and J.-F. Létard, *Chem. Sci.*, 2011, **2**, 1121.
28 M. Clemente-León, E. Coronado, M. López-Jordà, J. C. Waerenborgh, C. Desplanches, H. Wang, J.-F. Létard, A. Hauser and A. Tissot, *J. Am. Chem. Soc.*, 2013, **135**, 8655–8667.
29 R. Sieber, S. Decurtins, H. Stoeckli-Evans, C. Wilson, D. Yufit, J. A. K. Howard, S. C. Capelli and A. Hauser, *Chem. – Eur. J.*, 2000, **6**, 361–368.
30 S. M. Cohen, *Chem. Rev.*, 2012, **112**, 970–1000.
31 C. K. Brozek and M. Dincă, *Chem. Soc. Rev.*, 2014, **43**, 5456–5467.
32 T. Grancha, J. Ferrando-Soria, H.-C. Zhou, J. Gascon, B. Seoane, J. Pasán, O. Fabelo, M. Julve and E. Pardo, *Angew. Chem., Int. Ed.*, 2015, **54**, 6521–6525.
33 Z.-J. Lin, T.-F. Liu, Y.-B. Huang, J. Lü and R. Cao, *Chem. – Eur. J.*, 2012, **18**, 7896–7902.
34 H. Fei, J. F. Cahill, K. A. Prather and S. M. Cohen, *Inorg. Chem.*, 2013, **52**, 4011–4016.
35 E. Sinn, G. Sim, E. V. Dose, M. F. Tweedle and L. J. Wilson, *J. Am. Chem. Soc.*, 1978, **100**, 3375–3390.
36 J. Ferrando-Soria, P. Serra-Crespo, M. de Lange, J. Gascon, F. Kapteijn, M. Julve, J. Cano, F. Lloret, J. Pasán, C. Ruiz-Pérez, Y. Journaux and E. Pardo, *J. Am. Chem. Soc.*, 2012, **134**, 15301–15304.
37 T. Grancha, A. Acosta, J. Cano, J. Ferrando-Soria, B. Seoane, J. Gascon, J. Pasán, D. Armentano and E. Pardo, *Inorg. Chem.*, 2015, **54**, 10834–10840.
38 X. Cui, A. N. Khlobystov, X. Chen, D. H. Marsh, A. J. Blake, W. Lewis, N. R. Champness, C. J. Roberts and M. Schröder, *Chem. – Eur. J.*, 2009, **15**, 8861–8873.
39 a = 36.645(4) Å, c = 15.310(5) Å, V = 20559(3) Å^3, T = 120(2) K.
40 S. Dorbes, L. Valade, J. a Real and C. Faulmann, *Chem. Commun.*, 2005, 69.
41 S. Floquet, S. Salunke, M. Boillot, R. Clément, F. Varret, K. Boukheddaden and E. Rivière, *Chem. Mater.*, 2002, **14**, 4164–4171.
42 S. Floquet, M. Carmen Muñoz, E. Rivière, R. Clément, J.-P. Audière and M.-L. Boillot, *New J. Chem.*, 2004, **28**, 535.

JACS
JOURNAL OF THE AMERICAN CHEMICAL SOCIETY

Communication

pubs.acs.org/JACS

Selective Gold Recovery and Catalysis in a Highly Flexible Methionine-Decorated Metal–Organic Framework

Marta Mon,[†] Jesús Ferrando-Soria,[†] Thais Grancha,[†] Francisco R. Fortea-Pérez,[†] Jorge Gascon,[⊥] Antonio Leyva-Pérez,*[,‡] Donatella Armentano,*[,§] and Emilio Pardo*[,†]

[†]Departament de Química Inorgànica, Instituto de Ciencia Molecular (ICMOL), Universitat de València, 46980 Paterna, València, Spain

[⊥]Catalysis Engineering Department, Delft University of Technology, Julianalaan 136, 2628 BL Delft, The Netherlands

[‡]Instituto de Tecnología Química (UPV-CSIC), Universitat Politècnica de València-Consejo Superior de Investigaciones Científicas, Avda. de los Naranjos s/n, 46022 Valencia, Spain

[§]Dipartimento di Chimica e Tecnologie Chimiche (CTC), Università della Calabria, Rende 87036, Cosenza, Italy

Supporting Information

ABSTRACT: A novel chiral 3D bioMOF exhibiting functional channels with thio-alkyl chains derived from the natural amino acid L-methionine (**1**) has been rationally prepared. The well-known strong affinity of gold for sulfur derivatives, together with the extremely high flexibility of the thioether "arms" decorating the channels, account for a selective capture of gold(III) and gold(I) salts in the presence of other metal cations typically found in electronic wastes. The X-ray single-crystal structures of the different gold adsorbates **Au^{III}@1** and **Au^{I}@1** suggest that the selective metal capture occurs in a metal ion recognition process somehow mimicking what happens in biological systems and protein receptors. Both **Au^{III}@1** and **Au^{I}@1** display high activity as heterogeneous catalyst for the hydroalkoxylation of alkynes, further expanding the application of these novel hybrid materials.

The consumerism that modern societies have developed toward electronics devices has transformed the electronic waste into urban mines for noble metals. In particular, the recovery of gold from electronic scraps is extremely important from an economic and environmental perspective.[1] The high concentration of gold in electronic wastes has driven the quest of environmentally friendly methods for the recovery of gold from aqueous solutions. Although very few alternative methods to the highly contaminating cyanide leeching[2] have been proposed,[3,4] further advances focusing on increasing gold-selectivity and chemicals saving are mandatory.

Metal–organic frameworks (MOFs)[5−9] are porous materials showing a wide variety of thrilling chemical and physical properties and, consequently, find applications in very diverse fields.[10−15] Indeed, both MOF's porosity and their fascinating host–guest chemistry[14] lie at the origin of most of these properties. In the same way that other porous materials,[16,17] MOFs have proven their efficiency as vessels to capture and host small molecules[18] and, eventually, to separate mixtures of molecules according to their steric and stereochemical features as well as reactivity properties (functional substituent groups).[19−22]

Despite the fact that a few examples of selective metal capture by MOFs have been reported,[23] to the best of our knowledge, the important recovery of Au has not been studied. Aiming at expanding the scope of application of MOFs and taking advantage of the well-known strong affinity of gold for sulfur derivatives,[24,25] we have focused our efforts on the rational design of bioMOFs showing functional channels decorated with thio-alkyl chains derived from the natural amino acid[26] L-methionine (Scheme S1). Thus, we have synthesized a robust and water-stable 3D bioMOF of formula $\{Ca^{II}Cu^{II}_6[(S,S)\text{-methox}]_3(OH)_2(H_2O)\}\cdot 16H_2O$ (**1**). The presence of thioether groups within the accessible void space of this porous material encouraged us to evaluate its selectivity for the recovery of gold. Indeed, **1** exhibited a great affinity for Au^{3+} and Au^{+} salts (such as $AuCl_3$ and AuCl) in water, even in the presence of a wide variety of other metal cations regularly present in electronic wastes ("e-wastes") like Pd^{2+}, Ni^{2+}, Cu^{2+}, Zn^{2+} and Al^{3+}, yielding the novel compounds $(AuCl_3)_3@\{Ca^{II}Cu^{II}_6[(S,S)\text{-methox}]_3(OH)_2(H_2O)\}\cdot 9H_2O$ (**Au^{III}@1**) and $(AuCl)_2@\{Ca^{II}Cu^{II}_6[(S,S)\text{-methox}]_3(OH)_2(H_2O)\}\cdot 3H_2O\cdot 3CH_3OH$ (**Au^{I}@1**) (see Supporting Information (SI)).

Compound **1** was synthesized as green hexagonal prisms with a slow diffusion technique (see experimental section in the SI). Thereafter, in order to find out the maximum gold uptake capacity, we suspended 5 mg of **1** in 5 mL of a 0.02 M $AuCl_3$ H_2O/CH_3OH (1:1) solution to obtain **Au^{III}@1**. ICP-AES and SEM analyses indicated a maximum loading of 3 mmol of Au(III) per mmol of MOF after 1 h, which remained invariable after further time suspension. This indicates a total recovery of 598 mg of $AuCl_3$ per g of MOF in **Au^{III}@1**. The same procedure was repeated by soaking 5 mg of **1** in 5 mL of a 0.02 M AuCl aqueous solution. A maximum uptake of two mmol of AuCl per mmol of MOF was achieved after 3 h. The calculated total recovery of 300 mg of AuCl per g of MOF in **Au^{I}@1** is almost half-fold to that of **Au^{III}@1**.

The crystal structures of **1**, **Au^{III}@1** and **Au^{I}@1** could be determined by single-crystal X-ray diffraction (XRD) (see SI for structural details). They crystallize in the chiral $P6_3$ space group

Received: May 11, 2016
Published: June 13, 2016

DOI: 10.1021/jacs.6b04635
J. Am. Chem. Soc. 2016, 138, 7864−7867

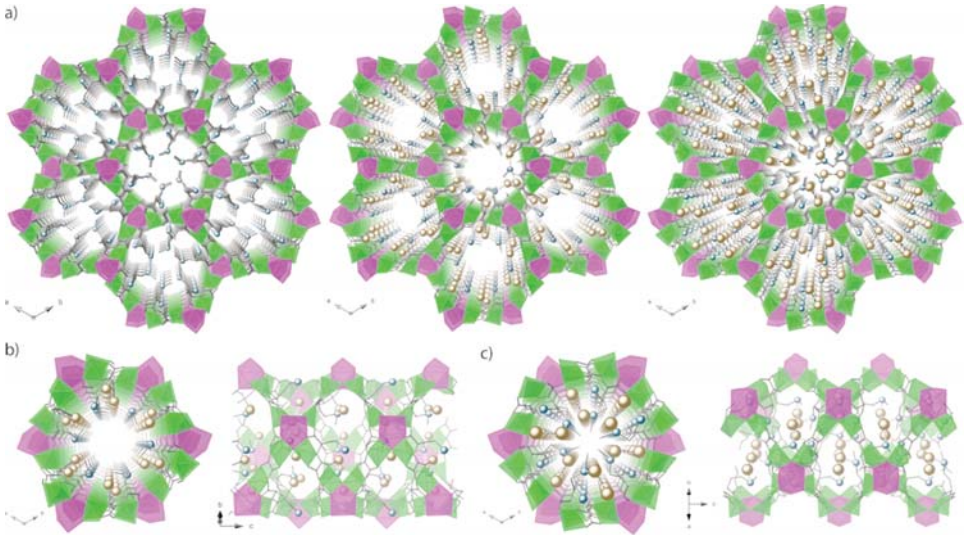

Figure 1. (a) Perspective views along the *c* axis of the porous structure of **1** (left), **Au^{III}@1** (center), and **Au^{I}@1** (right) determined by single-crystal XRD. Top (left) and lateral (right) views of one channel of **Au^{III}@1** (b) and **Au^{I}@1** (c). Copper and calcium atoms are represented by green and purple octahedra, respectively, whereas gold and sulfur atoms have been depicted as yellow and blue spheres. Free solvent molecules and Cl^- counterions are omitted for clarity.

and consist of honeycomb-like three-dimensional (3D) calcium(II)−copper(II) networks (Figure 1).

The network of **1** shows hexagonal channels of ∼0.3 nm as virtual diameter featuring highly flexible ethylenethiomethyl arms, belonging to the amino acid residues of methionine-disubstituted oxamidato ligand, which remain confined, together with lattice water molecules, in the pores of the MOF (Figure 1a, left and Figures S1 and S2a). The structures of **Au^{III}@1** and **Au^{I}@1**, determined by single-crystal XRD, confirm the preservation of the network of **1** even after gold capture. Delightfully, both of them host in the pores Au^{I} (**Au^{I}@1**) and Au^{III} ions (**Au^{III}@1**) clenched by methionine derivative arms (Figure 1b,c).

The gold(I) atoms in **Au^{I}@1** are two-coordinated, clutched by the sulfur atom from the two thioether arms and additional bridging chlorine atoms in a quite linear geometry of the S−Au−Cl type at the distended arm, whereas highly distorted, likely for steric constrains imposed by the network, at the more bent ones (Figures S2b and S3a). In contrast, the gold(III) atoms in **Au^{III}@1** are connected to the sulfur atom from only one of the two thioether arms and further bounded to three chloride atoms (two of them were not found from ΔF map, see crystallographic section in SI) in an expected distorted square planar coordination geometry (Figures S2b and S3b). The average Au−S bond distances of 2.75(7) (**Au^{I}@1**)/2.80(3) Å (**Au^{III}@1**) are somewhat longer than those reported so far for Au^{III}, whereas the Au−Cl ones of 2.50(7) (**Au^{I}@1**)/2.19(2) Å (**Au^{III}@1**) fall in the typical range of related gold(I) and gold(III) compounds found in the literature.[27−29] Aurophilic interactions[30] are present in **Au^{I}@1**, the shortest Au···Au separations being 3.04(2) Å (Figures S4 and S5).

As a striking structural uniqueness of this series of bioMOFs, they showed a permanent highly stable 3D net, featuring highly flexible arms able to arrange in different conformations of the thioether chains depending on the different chemical environments of the metal guests. The amino acid methionine side-chains remain available in the accessible voids of the bioMOF getting ready for metal ions recognition processes (Figure S6). The thioether "arms" are shown to adopt a stable conformation and target metals with high affinity, which is reminiscent of that seen in biological systems and protein receptors. They feature a sulfur available linkage which finally coordinates the desired metal assuming the favorite conformation. In fact, even if the honeycomb-like hexagonal 3D $Ca^{II}Cu^{II}_6$ network of **Au^{III}@1** and **Au^{I}@1** is basically the same of **1**, the thioether-containing arms exhibit a different conformation when holding the Au^{3+} and Au^{+} ions compared to the original material (see SI for structural details and Figures S1, S2, S6, and S7). Besides, only one of the two arms binds directly Au^{3+} in **Au^{III}@1**, the other being weakly bounded to Cl [S···Cl = 2.50(1) Å] and thus contributing through chlorine bridges to capture Au^{3+} in its second sphere of coordination (Figure S8) and forcing the folding of the flexible ethylenethiomethyl chains in a highly bent conformation of methyl groups and their overall arrangement pointing along *c* axis and not inward the pores (Figures S2c, S3b, and S6c). Hence, the virtual diameter of the channels is slightly increased after metal loading in **Au^{III}@1** (likely at the origin of disordered chloride atoms) in comparison to **1** and **Au^{I}@1** [∼0.3 (**1**), 0.2 (**Au^{I}@1**), and 0.6 nm (**Au^{III}@1**)], even if the estimated empty volumes without the crystallization solvent molecules decrease as expected in both **Au^{III}@1** and **Au^{I}@1** adsorbates [1101.4 (**1**), 776.2 (**Au^{I}@1**) and 609.8 Å^3 (**Au^{III}@1**) (Figures S1 and S7).

The experimental powder XRD (PXRD) patterns of **1**, **Au^{III}@1**, and **Au^{I}@1** are shown in Figure S9b,d,f, respectively. They are in agreement with the theoretical ones (Figure S9a,c,e), confirming the purity and homogeneity of the bulk samples. Solvent contents of both materials were estimated by thermogravimetric analysis under dry N_2 atmosphere (see Figure S10). Finally, Figure S11 shows the N_2 adsorption isotherms of **1**, **Au^{III}@1**, and **Au^{I}@1** at 77 K. They are consistent with the decrease in accessible void space in **Au^{III}@1** and **Au^{I}@1** estimated from the analysis of the crystal structure.

DOI: 10.1021/jacs.6b04635
J. Am. Chem. Soc. 2016, 138, 7864−7867

Aiming at evaluating the selectivity of **1** in gold(III) capture as well as the kinetics of the process, we then monitored the insertion of $AuCl_3$ within the pores of **1**, through ICP-AES and SEM, by soaking both powder and single-crystals of **1** in an equimolar aqueous solution of $AuCl_3$, $[Pd(NH_3)_4]Cl_2$, $NiCl_2$, $CuCl_2$, $ZnCl_2$, and $AlCl_3$ (see Figure 2 and SI). The kinetics of

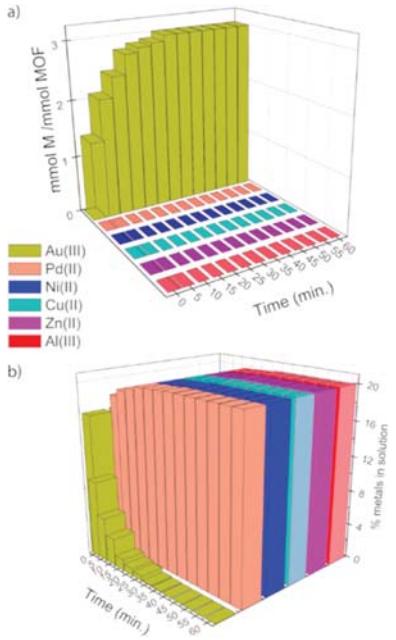

Figure 2. Kinetic profile of the selective gold(III) recovery by **1** represented as the mmol M/mmol MOF vs time (a) and the remaining % of metal cations in the aqueous solution vs time (b).

insertion was followed through both the increase of the mmol M/mmol MOF ratio (M = Au^{III}, Pd^{II}, Ni^{II}, Cu^{II}, Zn^{II} and Al^{III}) within the MOF (Figure 2a and Table S2) and the metal ratio (%) within the aqueous solution (Figure 2b and Table S3) at specific time intervals (0−60 min) of immersion of **1** in the aqueous solutions. A very selective and fast insertion of $AuCl_3$ within the MOF was observed, whereas all the other metal salts remained in solution. After only 5 min, a 67% of the maximum loading is achieved (Figure 2a). The maximum loading is finally reached after 30 min of soaking (3 mmol $AuCl_3$ per mmol MOF). In good agreement with solid data, ICP-AES and SEM indicate a continuous decrease of $[AuCl_3]$ within the aqueous solution, almost to a halt after 30 min of soaking (Figure 2b). Overall, the recovery efficiency of this material is close to 100%.

The same methodology was followed to test the selectivity of **1** in gold(I) capture by using the same equimolar aqueous solution but replacing $AuCl_3$ by partially dissolved AuCl (Figure S12). As expected, **1** also showed a great affinity and selectivity for AuCl in the presence of other metal salts. A maximum loading of 2 mmol of AuCl per mmol of MOF was achieved after 3 h, with a concomitant redissolution of the excess of suspended AuCl (Figure S12a and Table S4). The kinetic profile for the insertion of AuCl within the MOF indicates a somewhat slower process when compared to what happens to $AuCl_3$ (Figure S12b and Table S5). More likely, this fact can be attributed to the poor solubility of AuCl. Finally, both gold(III) and gold(I) salts were easily extracted from $\mathbf{Au^{III}@1}$ and $\mathbf{Au^{I}@1}$ by soaking them in a sulfur-containing solvent (i.e., dimethylsulfide), so that the resulting starting material (**1**) was completely reusable as confirmed by ICP and elemental analyses as well as the PXRD pattern of the material (**1′**) after the extraction process (Figure S13).

The extremely high loading of gold cations (15−20 wt %) supported on $\mathbf{Au^{III}@1}$ and $\mathbf{Au^{I}@1}$ is unprecedented in solids, as far as we know.[31] Thus, these new materials could be high-throughput heterogeneous catalysts in AuCl- and $AuCl_3$-catalyzed reactions, such as the hydroalkoxylation of alkynes[31,32] or the formation of related spiroketals, which have shown the highest turnover numbers in the field of homogeneous gold catalysis.[33−35]

Figure 3a shows that $\mathbf{Au^{III}@1}$ and $\mathbf{Au^{I}@1}$ catalyze the cyclization/ketalization of 4-pentyn-1-ol under standard con-

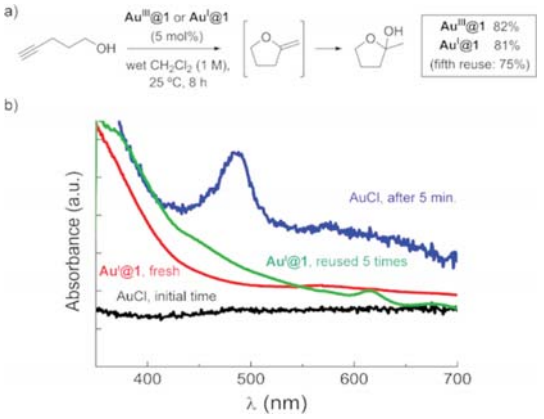

Figure 3. (a) Hydroalkoxylation of 4-pentyn-1-ol in wet CH_2Cl_2 catalyzed by $\mathbf{Au^{III}@1}$ and $\mathbf{Au^{I}@1}$. (b) Visible region of the UV−vis and RD measurements.

ditions (wet CH_2Cl_2 as a solvent, 1 M, room temperature) in good yield and selectivity, even after five reuses and without any leaching of gold detected by a filtration test (Figure S14). Kinetic experiments show that $\mathbf{Au^{III}@1}$ gives higher initial rates than $\mathbf{Au^{I}@1}$, in accordance with the higher Lewis acidity and wider porous size of the former. A first-order reaction with respect to the gold catalyst with a smooth langmuirian curve only saturated at yields >70% is also observed (Figure S15a).

Comparatively, the homogeneous reaction with AuCl shows an abrupt stopping of the conversion at around 60% yield, regardless the amount of gold salt employed (Figure S15b). This homogeneous reaction was followed by in situ UV−vis spectroscopy measurements (Figure 3b). A new band in the visible region at ∼500 nm denotes the generation of spherical plasmonic nanoparticles in just 5 min, which suggests that the reaction stops as consequence of the very fast agglomeration of AuCl in the form of catalytically inactive nanoparticles. In contrast, diffuse-reflectance spectroscopy measurements of the reused $\mathbf{Au^{I}@1}$ material show the absence of this plasmonic band (see also Figure S16), demonstrating the advantage of site isolation upon anchoring the Au salts to the thioether groups within the MOF structure. The small peak at ∼620 nm can be related to the reduction of a negligible amount of Au^{I} cations to plasmonic gold nanorods.[36]

DOI: 10.1021/jacs.6b04635
J. Am. Chem. Soc. 2016, 138, 7864−7867

In summary, we report an environmentally friendly, cheap, and easy-to-prepare in large-scale MOF whose channels are decorated with thioether groups. This material exhibits a high selectivity for $AuCl_3$ and AuCl, even in the presence of other metal cations regularly present in "e-wastes" such as Pd^{2+}, Ni^{2+}, Cu^{2+}, Zn^{2+}, and Al^{3+}, in a fully reversible process. The nature and kinetics of these postsynthetic selective processes have been evaluated. The structural stability of the 3D network of **1**, maintaining the crystallinity over the inclusion processes, allowed the resolution of the crystal structures of the corresponding final products $\mathbf{Au^{III}}$**@1** and $\mathbf{Au^{I}}$**@1**, permitting structural insights into the nature of the Au−S interaction and the flexibility and adaptability of the material. In addition, both compounds show excellent performance as reusable heterogeneous catalysts for the intramolecular hydroalkoxylation of alkynes. These results demonstrate the great versatility of MOFs in separation and further expand the scope of application of these unique class of porous materials.

■ ASSOCIATED CONTENT

Supporting Information

The Supporting Information is available free of charge on the ACS Publications website at DOI: 10.1021/jacs.6b04635.

Preparation and characterization of **1**, $\mathbf{Au^{III}}$**@1** and $\mathbf{Au^{I}}$**@1**. Experimental details of metal selectivity experiences. Additional Figures S1−S16. CCDC reference numbers 1478221−1478223 for **1**, $\mathbf{Au^{III}}$**@1** and $\mathbf{Au^{I}}$**@1** (PDF)
Crystallographic data (CIF)
Crystallographic data (CIF)
Crystallographic data (CIF)

■ AUTHOR INFORMATION

Corresponding Authors

*emilio.pardo@uv.es
*donatella.armentano@unical.it
*anleyva@itq.upv.es

Notes

The authors declare no competing financial interest.

■ ACKNOWLEDGMENTS

This work was supported by the MINECO (Spain) (Projects CTQ2013-46362-P, CTQ2013-44844-P, and Excellence Unit "Maria de Maeztu" MDM-2015-0538), the Generalitat Valenciana (Spain) (Project PROMETEOII/2014/070), and the Ministero dell'Istruzione, dell'Università e della Ricerca (Italy). M.M. and T.G. thank the MINECO and the Universitat de València for predoctoral contracts. Thanks are also extended to the Ramón y Cajal Program and the "Convocatoria 2015 de Ayudas Fundación BBVA a Investigadores y Creadores Culturales" (E. P., A. L.-P., and J. F.-S.). J.G. acknowledges the financial support of the European Research Council: FP/2007-2013 and ERC grant agreement no. 335746, CrystEng-MOF-MMM.

■ REFERENCES

(1) Hagelüken, C.; Corti, C. W. *Gold Bull.* **2010**, *43*, 209.
(2) Syed, S. *Hydrometallurgy* **2012**, *115−116*, 30.
(3) Liu, Z.; Frasconi, M.; Lei, J.; Brown, Z. J.; Zhu, Z.; Cao, D.; Iehl, J.; Liu, G.; Fahrenbach, A. C.; Botros, Y. Y.; Farha, O. K.; Hupp, J. T.; Mirkin, C. A.; Fraser Stoddart, J. *Nat. Commun.* **2013**, *4*, 1855.
(4) He, Y.-R.; Cheng, Y.-Y.; Wang, W.-K.; Yu, H.-Q. *Chem. Eng. J.* **2015**, *270*, 476.
(5) Férey, G. *Chem. Soc. Rev.* **2008**, *37*, 191.
(6) Long, J. R.; Yaghi, O. M. *Chem. Soc. Rev.* **2009**, *38*, 1213.
(7) Furukawa, H.; Cordova, K. E.; O'Keeffe, M.; Yaghi, O. M. *Science* **2013**, *341*, 1230444.
(8) Eddaoudi, M.; Sava, D. F.; Eubank, J. F.; Adil, K.; Guillerm, V. *Chem. Soc. Rev.* **2015**, *44*, 228.
(9) Cui, Y.; Li, B.; He, H.; Zhou, W.; Chen, B.; Qian, G. *Acc. Chem. Res.* **2016**, *49*, 483.
(10) Li, J.; Sculley, J.; Zhou, H. *Chem. Rev.* **2012**, *112*, 869.
(11) Horike, S.; Umeyama, D.; Kitagawa, S. *Acc. Chem. Res.* **2013**, *46*, 2376.
(12) McKinlay, A. C.; Morris, R. E.; Horcajada, P.; Férey, G.; Gref, R.; Couvreur, P.; Serre, C. *Angew. Chem., Int. Ed.* **2010**, *49*, 6260.
(13) Grancha, T.; Ferrando-Soria, J.; Castellano, M.; Julve, M.; Pasán, J.; Armentano, D.; Pardo, E. *Chem. Commun.* **2014**, *50*, 7569.
(14) Inokuma, Y.; Arai, T.; Fujita, M. *Nat. Chem.* **2010**, *2*, 780.
(15) Gascon, J.; Corma, A.; Kapteijn, F.; Llabrés i Xamena, F. X. *ACS Catal.* **2014**, *4*, 361.
(16) Cote, A. P.; Benin, A. I.; Ockwig, N. W.; O'Keeffe, M.; Matzger, A. J.; Yaghi, O. M. *Science* **2005**, *310*, 1166.
(17) Slater, A. G.; Cooper, A. I. *Science* **2015**, *348*, aaa8075.
(18) Ferrando-Soria, J.; Serra-Crespo, P.; de Lange, M.; Gascon, J.; Kapteijn, F.; Julve, M.; Cano, J.; Lloret, F.; Pasán, J.; Ruiz-Pérez, C.; Journaux, Y.; Pardo, E. *J. Am. Chem. Soc.* **2012**, *134*, 15301.
(19) Yang, S.; Ramirez-Cuesta, A. J.; Newby, R.; Garcia-Sakai, V.; Manuel, P.; Callear, S. K.; Campbell, S. I.; Tang, C. C.; Schröder, M. *Nat. Chem.* **2014**, *7*, 121.
(20) Alezi, D.; Peedikakkal, A. M. P.; Weseliński, Ł. J.; Guillerm, V.; Belmabkhout, Y.; Cairns, A. J.; Chen, Z.; Wojtas, Ł.; Eddaoudi, M. *J. Am. Chem. Soc.* **2015**, *137*, 5421.
(21) Foo, M. L.; Matsuda, R.; Hijikata, Y.; Krishna, R.; Sato, H.; Horike, S.; Hori, A.; Duan, J.; Sato, Y.; Kubota, Y.; Takata, M.; Kitagawa, S. *J. Am. Chem. Soc.* **2016**, *138*, 3022.
(22) Seoane, B.; Castellanos, S.; Dikhtiarenko, A.; Kapteijn, F.; Gascon, J. *Coord. Chem. Rev.* **2016**, *307*, 147.
(23) Yuan, S.; Chen, Y.-P.; Qin, J.; Lu, W.; Wang, X.; Zhang, Q.; Bosch, M.; Liu, T.-F.; Lian, X.; Zhou, H.-C. *Angew. Chem., Int. Ed.* **2015**, *54*, 14696.
(24) Häkkinen, H. *Nat. Chem.* **2012**, *4*, 443.
(25) Xue, Y.; Li, X.; Li, H.; Zhang, W. *Nat. Commun.* **2014**, *5*, 4348.
(26) Grancha, T.; Ferrando-Soria, J.; Cano, J.; Lloret, F.; Julve, M.; De Munno, G.; Armentano, D.; Pardo, E. *Chem. Commun.* **2013**, *49*, 5942.
(27) Blake, A. J.; Gould, R. O.; Greig, J. A.; Holder, A. J.; Hyde, T. I.; Schröder, M. *J. Chem. Soc., Chem. Commun.* **1989**, 876.
(28) Grirrane, A.; Álvarez, E.; García, H.; Corma, A. *Angew. Chem., Int. Ed.* **2014**, *53*, 7253.
(29) Yang, S.; Chai, J.; Song, Y.; Kang, X.; Sheng, H.; Chong, H.; Zhu, M. *J. Am. Chem. Soc.* **2015**, *137*, 10033.
(30) Schmidbaur, H. *Chem. Soc. Rev.* **1995**, *24*, 391.
(31) Corma, A.; Leyva-Pérez, A.; Sabater, M. J. *Chem. Rev.* **2011**, *111*, 1657.
(32) Trost, B. M.; Dong, G. *Nature* **2008**, *456*, 485.
(33) Hashmi, A. S. K. *Science* **2012**, *338*, 1434.
(34) Blanco Jaimes, M. C.; Böhling, C. R. N.; Serrano-Becerra, J. M.; Hashmi, A. S. K. *Angew. Chem., Int. Ed.* **2013**, *52*, 7963.
(35) Blanco Jaimes, M. C.; Rominger, F.; Pereira, M. M.; Carrilho, R. M. B.; Carabineiro, S. A. C.; Hashmi, A. S. K. *Chem. Commun.* **2014**, *50*, 4937.
(36) Pérez-Juste, J.; Pastoriza-Santos, I.; Liz-Marzán, L.; Mulvaney, P. *Coord. Chem. Rev.* **2005**, *249*, 1870.

DOI: 10.1021/jacs.6b04635
J. Am. Chem. Soc. 2016, 138, 7864−7867

CHEMISTRY OF MATERIALS

Article

pubs.acs.org/cm

Insights into the Dynamics of Grotthuss Mechanism in a Proton-Conducting Chiral *bio*MOF

Thais Grancha,[†] Jesús Ferrando-Soria,[†] Joan Cano,[†,‡] Pedro Amorós,[§] Beatriz Seoane,[∥] Jorge Gascon,[*,∥] Montse Bazaga-García,[⊥] Enrique R. Losilla,[⊥] Aurelio Cabeza,[⊥] Donatella Armentano,[*,▽] and Emilio Pardo[*,†]

[†]Departament de Química Inorgànica, Instituto de Ciencia Molecular (ICMOL), Universitat de València, 46980 Paterna, València, Spain

[‡]Fundació General de la Universitat de València (FGUV), Universitat de València, 46980 Paterna, València, Spain

[§]Institut de Ciència dels Materials (ICMUV), Universitat de València, E−46980 Paterna, Valencia, Spain

[∥]Catalysis Engineering Department, Delft University of Technology, Julianalaan 136, 2628 BL Delft, The Netherlands

[⊥]Depto. Química Inorgánica, Universidad de Málaga, Campus de Teatinos s/n, Málaga-29071, Spain

[▽]Dipartimento di Chimica e Tecnologie Chimiche, Università della Calabria, Rende 87036, Cosenza, Italy

Supporting Information

ABSTRACT: Proton conduction in solids attracts great interest, not only because of possible applications in fuel cell technologies, but also because of the main role of this process in many biological mechanisms. Metal−organic frameworks (MOFs) can exhibit exceptional proton-conduction performances, because of the large number of hydrogen-bonded water molecules embedded in their pores. However, further work remains to be done to elucidate the real conducting mechanism. Among the different MOF subfamilies, *bio*MOFs, which have been constructed using biomolecule derivatives as building blocks and often affording water-stable materials, emerge as valuable systems to study the transport mechanisms involved in the proton-hopping dynamics. Herein, we report a versatile chiral three-dimensional (3D) *bio*MOF, exhibiting permanent porosity, as well as high chemical, structural, and water stability. Moreover, the choice of this suitable bioligand results in proton conductivity, and allows us to propose a proton-conducting mechanism based on experimental data, which are displayed visually by means of quantum molecular dynamics simulations.

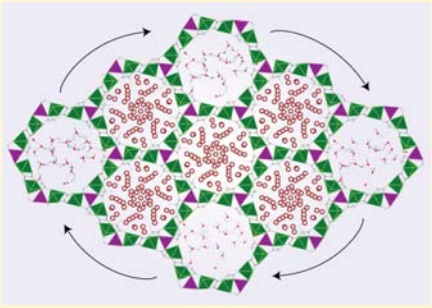

INTRODUCTION

Metal−organic frameworks (MOFs)[1−3] are extensively studied due to the large variety of physical and chemical properties that they can exhibit,[4,5] which are often related to their intrinsic porous character and rich host−guest chemistry. Besides, the design of highly robust, thermal- and water-stable (including also acid and basic media) MOF materials becomes highly relevant to facilitate good performance for potential applications.[6]

In this context, MOFs have recently become very relevant to achieve water-mediated proton[7−29] (H^+) or hydroxide (OH^-) ion[30]-conducting materials, which can find application in fuel cells.[8] This phenomenon is intimately related to the large amount of disordered water molecules, acting as proton carriers, hosted in their channels. Despite the relatively large number of MOFs showing excellent performance in proton conduction and recent advances into the understanding of the dynamics of proton transport in MOFs,[31] further work remains to be done to determine the real structure of the hydrogen-bonded network involved in proton conduction.

A quite recent step forward toward the design of original examples of MOFs consists of the use of biomolecules as ligands to construct high-dimensional coordination networks, called *bio*MOFs.[32,33] This subclass of materials offer, among other advantages, a more feasible moisture stability. Closely related to this last point, it has been established that water typically participates in molecular recognition and association in the solid state. Several studies further demonstrate that water thermodynamics is strictly dependent on the specific physicochemical properties of the confining environment.[34] Hence, the choice of a suitable bioligand may well succeed in the challenging task of affording water-stable *bio*MOFs with a large number of water molecules embedded within their pores.

Received: March 31, 2016
Revised: June 13, 2016
Published: June 13, 2016

DOI: 10.1021/acs.chemmater.6b01286
Chem. Mater. 2016, 28, 4608−4615

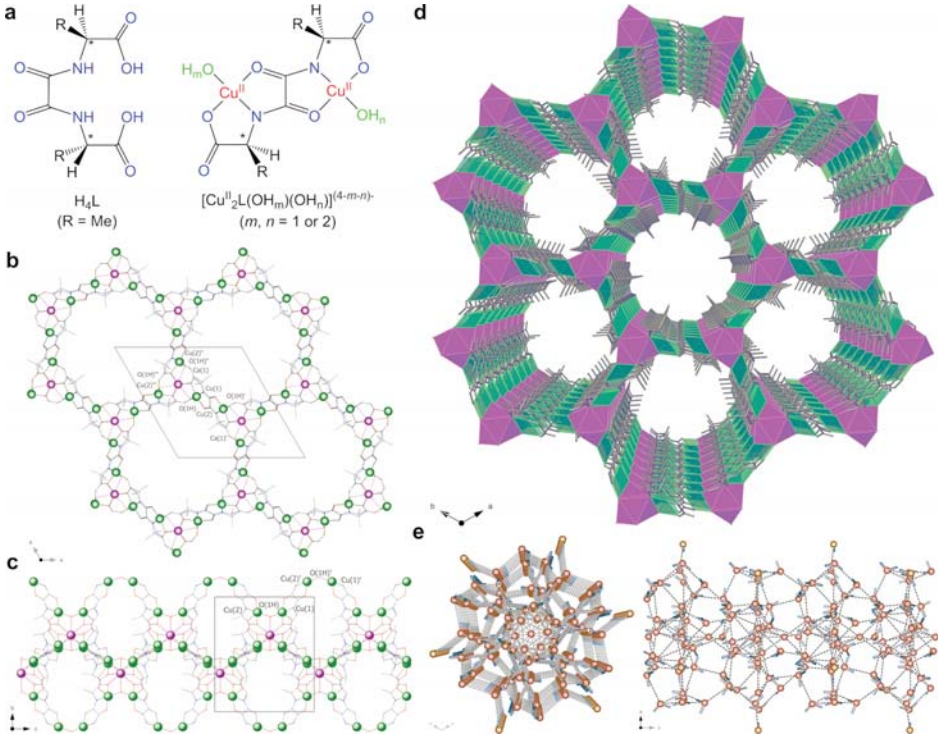

Figure 1. (a) Chemical structures of the chiral bis(amino acid)oxalamide ligands (left), highlighting the potential coordination sites and chiral centers and the corresponding dianionic bis(hydroxo) dicopper(II) complexes (right). Views of a fragment of **1** in the (b) *ab* and (c) *bc* planes, respectively, with the atom numbering scheme (symmetry code: (I) = $-x, -y + 1, z + {}^1/_2$; (II) = $-y + 1, x - y + 1, z$; (III) = $-x + y, -x + 1, z$). (d) Perspective view of the three-dimensional (3D) open framework of **1** along the *c*-axis (the crystallization water molecules are omitted for clarity). (e) Views along the crystallographic *c*-axis (left) and *a*-axis (right) of the array of hydrogen-bonded guest water molecules and hydroxide anions located in each hexagonal channel. Cu and Ca atoms are represented by green and purple spheres or polyhedra, respectively, whereas the ligands are depicted as sticks. The H atoms, when present, are represented as blue sticks, whereas the water molecules and hydroxide anions are depicted as red and orange spheres. Hydrogen bonds are represented by dotted lines.

This would occur in an *ordered* manner, through a process of molecular recognition, even more dynamic in the presence of proton conduction. However, despite these clear advantages and the growing interest in *bio*MOFs, no examples of these systems exhibiting proton conduction have been reported so far.

Previous results on disubstituted oxamidato ligands derived from natural amino acids are used as a basis[35−37] (see Figure 1a). Herein, we report a novel proton-conducting, chiral *bio*MOF, of formula $\{Ca^{II}Cu^{II}_6[(S,S)\text{-alamox}]_3(OH)_2(H_2O)\}\cdot 32H_2O$ (**1**) [H_4-(*S*,*S*)-alamox = *N*,*N*′-bis((*S*)-2-propanoic acid)oxamide, Figure 1a (left), with R = Me] exhibiting high chemical, thermal, and water stability (up to alkaline (pH 14) aqueous media). For the first time, the high-quality refinement of the crystal structure of **1**—showing the positions of the water molecules and their hydrogen atoms—allows to propose a conduction mechanism in a proton-conductive MOF, which is fully supported by structural and theoretical data.

RESULTS AND DISCUSSION

Synthesis and X-ray Crystal Structure. Compound **1** crystallizes in the chiral *P*63 space group of the hexagonal system. Its structure consists of a chiral 3D calcium(II)−copper(II) network, which is built up from trans oxamidato-bridged dicopper(II) units, $\{Cu_2[(S,S)\text{-alamox}]\}$, acting as linkers between the Ca^{II} ions through carboxylate; further aqua/hydroxo groups (1:2 statistical distribution), acting as additional bridges between two neighboring dicopper(II) units and coordinated in a μ^3 fashion, support the entire system, unfolding an uninodal six-connected net of ($4^9.6^6$) Schläfli symbol (see Figure 1 and Figure S1 in the Supporting Information).

Overall, **1** can be described as a mixed oxamidate- and carboxylate(aqua/hydroxo)-bridged, honeycomb-like hexagonal 3D $Ca^{II}Cu^{II}_6$ open framework showing relatively large hexagonal channels along the *c*-axis (Figure 1d), which are occupied by crystallization water molecules (see Figures 1e, as well as Figures S1 and S2 in the Supporting Information). These channels have a virtual diameter of ca. 1.0 nm, resulting from the alternating orientation of the methyl residues from the *trans*-(*S*,*S*)-alamox bridging ligands within adjacent channels. The estimated empty volume without the crystallization water molecules is 2089.1 Å^3, which is a value that represents up to ca. 58.0% of potential void per unit cell volume [V = 3604.1 Å^3] (Figure S3 in the Supporting Information). A striking structural feature of **1** is that all water molecules hosted in the pores are hydrogen-bonded, forming one-dimensional (1D) ribbons

DOI: 10.1021/acs.chemmater.6b01286
Chem. Mater. 2016, 28, 4608−4615

along the *c*-axis (see Figure 1e) that involve the aqua/hydroxo bridges of the network.

Thermogravimetric Analysis and Powder X-ray Diffraction. Thermogravimetric analysis (TGA) shows a mass loss at 473 K of 31.5% (Figure S4 in the Supporting Information) which corresponds to 30 H_2O molecules per formula unit, a value close to the 32 lattice molecules found in the crystal structure determined by single-crystal X-ray diffraction (SCXRD) at 90 K. The vapor water adsorption isotherm of **1** at 25 °C shows that the complete rehydration process, with the recovery of 32 mmol of water per mmol of *bio*MOF, can be only achieved under maximum relative humidity (see Figure S5 in the Supporting Information), which is in complete agreement with the proton conductivity measurements (see below).

Powder X-ray diffraction (PXRD) studies were carried out on a polycrystalline sample of **1** (Figure 2). PXRD patterns

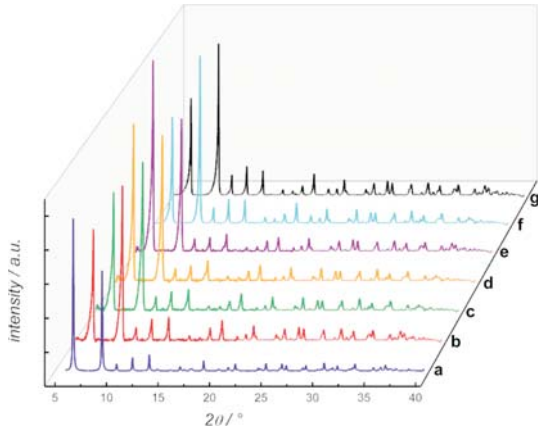

Figure 2. (a) Calculated PXRD pattern profile of **1** (pattern profile a). Variable-temperature XRD patterns of the activated phase of **1** at 298 K (pattern profile b), 343 K (pattern profile c), (d) 353 K (pattern profile d), and 370 K (pattern profile e). PXRD pattern profiles of **1** after proton conduction measurements (pattern profile f) and (pattern profile g) after 1 month of immersion in a pH 14 aqueous solution at room temperature (RT).

show the retention of crystallinity over the entire range of temperatures studied, confirming the structural robustness of the material upon water loss (Figures 2, pattern profiles b–e). In addition, the structural stability of this *bio*MOF was further verified both after proton conductivity experiments (pattern f in Figure 2) and also in basic aqueous media by immersion in a pH 14 aqueous solution for one month (pattern g in Figure 2).

The permanent porosity of **1** was demonstrated by means of N_2 adsorption at 77 K. The isotherm shows a type I behavior with large uptake at low pressures (Figure 3). The Brunauer–Emmett–Teller (BET) surface area calculated was 1015 m^2/g,[38,39] with a calculated pore size[40] of 1.1 nm, which closely corresponds to that determined from the crystal structure.

Proton Conductivity Measurements and Conducting Mechanism. Considering the strong interest observed recently in proton conductors,[7−29,31] together with the presence of an array of hydrogen-bonded water molecules along the hexagonal channels in **1** (see Figure 1e, as well as Figures S1 and S2), we performed ionic conductivity measurements.

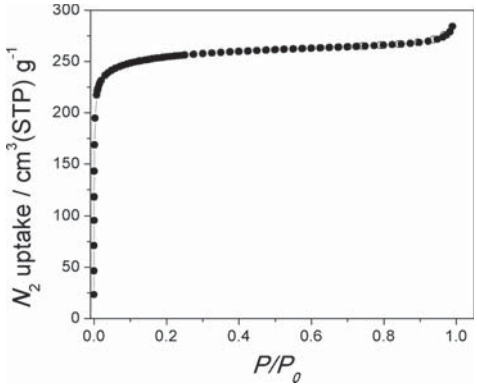

Figure 3. N_2 (77 K) adsorption isotherm for the activated compound **1**. Filled and empty symbols indicate the adsorption and desorption isotherms, respectively.

Impedance data in the form of a complex plane plot for **1** at 353 K and different relative humidity values (RH), after full equilibration of the measurements (Figure S6), are shown in Figure 4a. The data show an overlapped/deformed broad arc at high frequencies/low RH with an associated capacitances of ~(2–3) × 10^{-11} F cm^{-1}. With increasing RH, lower frequency effects are seen, in the form of an inclined spike with an associated capacitances of ~8–10 μF cm^{-1}, which indicates a partial-blocking electrode response consistent with proton migration. The structural stability of this MOF after post-impedance measurements was checked by X-ray diffraction and thermal analysis. The TG curves do not show changes in the water content for the different environmental conditions tested (Figure S4) suggesting the easy loss of two water molecules when exposed to air—further confirmed by crystal structure determined by SCXRD at room temperature (see the Supporting Information)—which can be only fully recovered within the humidity chamber. Furthermore, the PXRD patterns after the measurements are consistent with the theoretical one (Figure 2f).

The conductivity of **1** increases with the relative humidity (Figure 4a), which is characteristic of many water-mediated proton conductors. For instance, the conductivity at 353 K increases from 1.1 × 10^{-6} S cm^{-1} at 60% RH up to 8.6 × 10^{-4} S cm^{-1} at 95% RH. The proton conductivity for **1** measured at 297 K and 95% RH, 1.0 × 10^{-5} S cm^{-1}, is comparable with other carboxylate-based MOFs.[41] Figure 4b displays the overall pellet conductivities in traditional Arrhenius plots as a function of RH. These plots show a linear behavior with activation energies (E_a) of 0.42, 0.43, 0.42, and 0.34 eV for RH values of 60%, 70%, 80%, and 95%, respectively. These relatively small numbers are within the range typically attributed to a Grotthuss transfer mechanism via water molecules (0.1–0.5 eV).[42−46]

These results suggest that, even in the absence of free acid or basic groups in the framework, the presence of a hydrogen-bonded intricate chain involving both the free water and the coordinated hydroxo/water molecules is enough to develop moderate ionic conductivity. Although a vehicle mechanism[47] contribution cannot be discarded, this conductivity most-likely arises from the proton hopping through the hydrogen-bonded array of water molecules, as expected for a structure diffusion mechanism,[48,49] as reported previously in theoretical–experimental studies in pure water[50−52] or acid aqueous solutions.[53]

DOI: 10.1021/acs.chemmater.6b01286
Chem. Mater. 2016, 28, 4608–4615

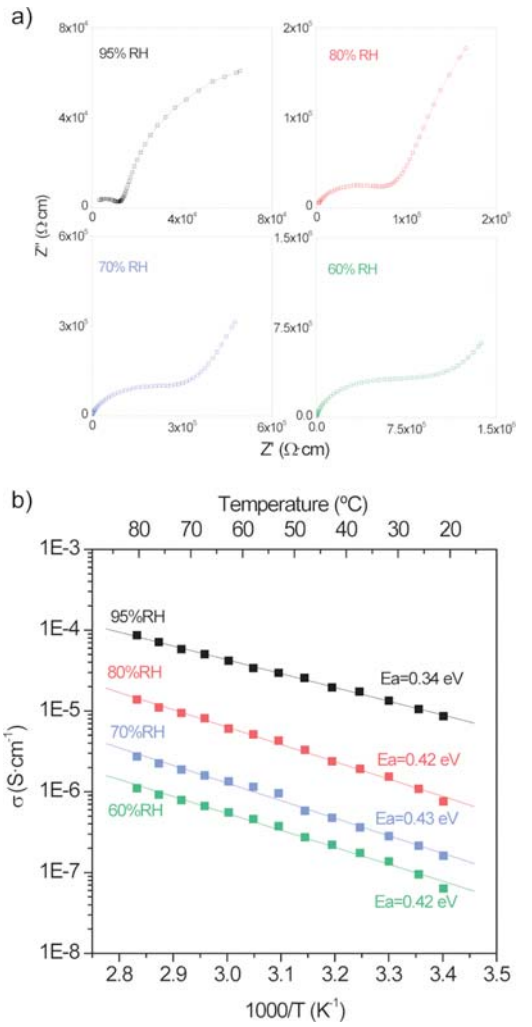

Figure 4. (a) Nyquist plots for compound **1** at 353 K under four different relative humidity (RH) values. Solid lines indicate the fitting to the equivalent circuit (RbQb)(RgbQgb)(Qe). (b) Protonic conductivity data of **1** versus reciprocal temperature (Arrhenius plot) at four selected RH values. Activation energies were highlighted.

It is clear that proton transport mechanisms in solids attract great interest, because of their relation to many natural processes[54] and its potential application in a wide variety of electrochemical and energy-conversion devices.[8] However, the vast majority of theoretical studies, with regard to the mechanism of proton conduction (most of them of theoretical nature), could only carried out so far in nonporous solids.[55−59] In contrast, despite the fact that MOFs show excellent results as proton-conducting materials—they exhibit large pores, which allows the movement of ions, as well as the presence of guest carrier molecules[24,60]—the first joint experimental/theoretical study dealing with the proton-conduction mechanism in a MOF was published only very recently.[31] This outstanding feature is undoubtedly related to the high disorder of the solvent molecules.

In a recent work,[28] Kitagawa et al. suggested that "only MOFs having small pores should be employed to construct *visible* proton-conducting pathways". This would be based on the reasonable assumption that disorder increases with increasing pore size. However, despite the large pores, water molecules hosted in the channels of **1** are particularly ordered and their positions—including those of their hydrogen atoms and, thus, the directionality of the hydrogen bond—could be undoubtedly allocated. With this information in hand, we are able to propose a clear conduction mechanism in a proton-conductive MOF, in clear agreement with the recent findings shown by Damasceno et al.[31]

Figure 1e shows the hydrogen-bonded pathways developing inside one hexagonal channel in **1**. At first sight, it is reasonable to suppose that several concerted tautomeric equilibriums should be followed in the channels (and in other proton-conducting MOFs). We focus just on a few of them to suggest a model consistent with the experimentally located hydrogen atoms. The observed pattern of atomic positions in the water-branched chain is reliable with a hopping of protons between neighboring and hydrogen-bonded water molecules, which is consistent with a Grotthuss-like mechanism.[48] The distances crossed by the H atoms in the hopping process range from 0.73(4) Å to 1.14(1) Å with corresponding O···O separations varying in the range of 2.686(10)−2.957(9) Å (detailed values in Table S1 in the Supporting Information).

The proposed mechanism is detailed as follows: Figure 5a represents the starting situation found in the crystal structure, whereas Figures 5b and 5c show the proposed intermediate stages with the proton hopping between neighboring molecules and their consecutive reorientation to finally recover the original situation (Figure 5d). Their orientations represent always a valid structure for the water net. We choose as the proton transfer starting point O2W, which can initiate two different pathways: toward O9W (path 1) or toward O1W (path 2). Afterward, the two pathways must follow the labeled way of path 1/path 2 or exhibit a possible deviation (path 1′ or path 2′), which is logical, given that an efficient concerted pathway requires multiple ways. Another important point is the occurrence of a hydrogen bond between hydroxo/water (O1H) and water molecule (O2W). The O2W···OH distance of 2.908(5) Å and the quite perfect directionality of the hydrogen bond (O−H···O2W angle of 171(14)°) seem to suggest that a proton transfer from O1H to the "initiator" O2W happens, indicating that a hydrogen of the hydroxo/water bridged molecule in **1** plays a role, as proton injector, in the proposed mechanism.

As shown in Figure 5, the proton transfer extents to the O10W and O11 disordered water molecules located in the center of the channels, suggesting that the entire network of water molecules participates in the conduction. We suggest that the translation movement of O10w and O11 waters along the *c*-axis around the center of the hexagonal voids (see structure refinement and Figure S7 in the Supporting Information) is consistent with proton transfer along the 1D channels and could be the key point for the proton conductivity. It is obvious to suggest that the insertion of acidic molecules, acting as proton injectors, would increase the proton conductivity value dramatically.

Theoretical Calculations. A detailed study of this type of material is not an easy task. Although some computational schemes, such as *ab initio* and density functional theory (DFT) methods, could offer a more realistic vision of this process, they

DOI: 10.1021/acs.chemmater.6b01286
Chem. Mater. 2016, 28, 4608−4615

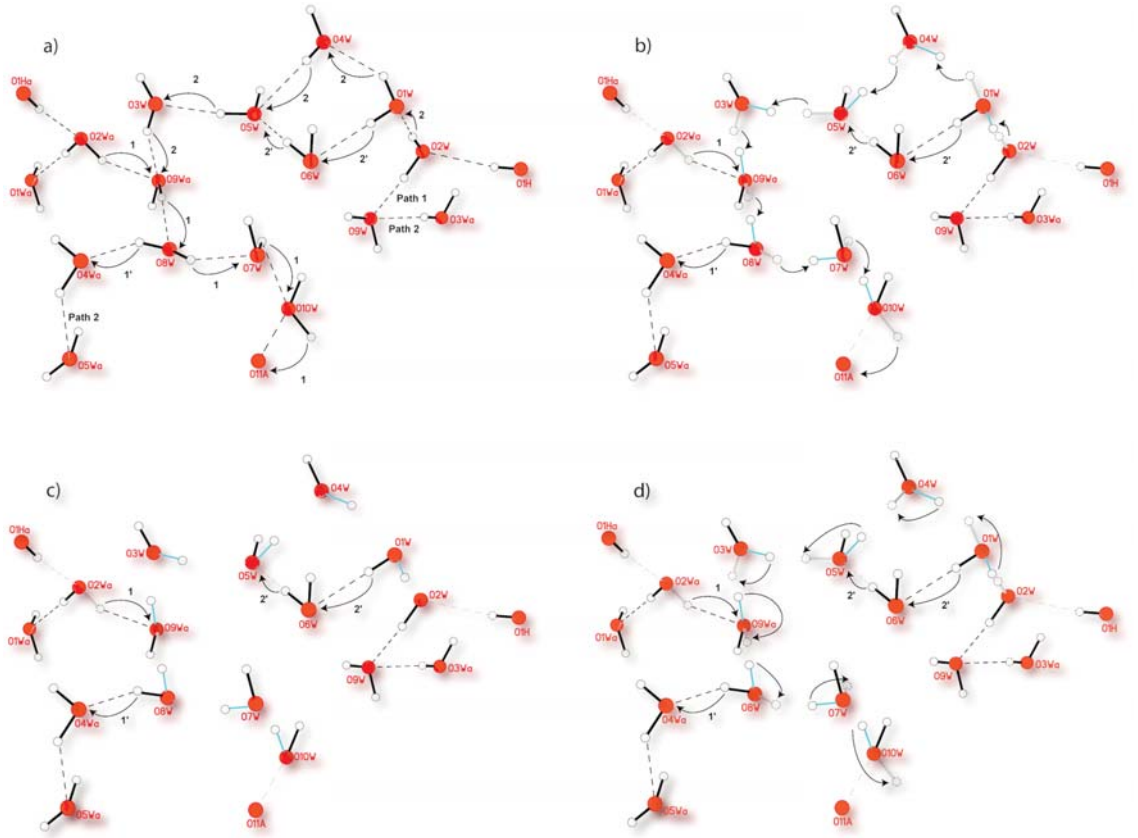

Figure 5. Complete cycle of the proton conduction showing the proton hopping between the hydrogen-bonded water/hydroxo molecules and the sequential reorientation: (a) starting real situation (data shown by crystal structure), (b, c) intermediate proposed stages where the proton hopping and the water molecules reorientation occur, and (d) recovery of the starting situation. The water molecules are represented by red filled spheres. The black, gray, and blue solid lines represent the initial (observed), the broken and the formed O−H bonds, respectively. The dotted circles and the continuous circles represent initial and final hydrogen positions, respectively. The dotted lines represent the hydrogen bonds. [Details on O···O distances: O1W···O4W, 2.870(8) Å; O1W···O6W, 2.957(9) Å; O2W···O9W, 2.752(9) Å; O2W···O1W, 2.866(6) Å; O2W···O1H, 2.908(5) Å; O3W···O5W, 2.776(6) Å; O3W···O9Wa, 2.825(10) Å; O4W···O5W, 2.801(9) Å; O4Wa···O8W, 2.775(12) Å; O5W···O6W, 2.740(9) Å; O7W···O8W, 2.780(11) Å; O7W···O10W, 2.885(10) Å; O8W···O9Wa, 2.754(12) Å; and O10W···O11A, 2.686(10) Å. Symmetry code: (a) = $-y, x - y, z$.]

have not been considered, because of the complexity and high CPU time consumption that is implied. Thus, using quantum molecular dynamics simulations, we have found an excellent compromise alternative. This methodology has been used to contrast the proposed structure diffusion mechanism on the basis of the experimental data. This simplified model provides us with a visual and dynamic picture of the proton hopping between neighboring water molecules within the hydrogen-bonded 1D arrays of water molecules hosted in the channels (see Videos S1−S6). Two different simulations were done on a fragment of the water channel, where O2W is considered as the starting point and therefore and additional hydrogen—coming from the $^1/_3$ water-bridged molecule O1H—was added. In the first simulation, the O11A water molecule was replaced by a hydroxo group in order to include, in a way, the attractive effect of the anode on the extra proton (see computational details, as well as Videos S1−S4). In the second one, no replacement was done to verify that the proton hopping occurs in a spontaneous manner (see Videos S5 and S6). Overall, the optimized structures shown in the videos are in agreement with the proposed structure diffusion (Grotthuss-type) mechanism[48] involving the cleavage and formation of O−H bonds, together with the hopping of the protons, followed by reorientation of the water molecules.

Even the limitations of the simplified model used, the dynamics simulation shown in Videos S1−S6 shed light on the same direction and contrast the possibility of the proposed pathways on the basis of the experimental data. In this sense, several remarkable features are clearly observed:

(i) The hopping of the protons occurs through a process of cleavage and formation of covalent O−H bonds involving the formation of relatively small charged water clusters: $H_5O_2^+$, $H_7O_3^+$, and $H_9O_4^+$, followed by a solvent reorganization process;[52]

(ii) The transfer of a hydrogen atom from the *initiator* O2W to the *terminal* O10W, after successive proton transfers and water molecules reorientation, follows the sequence: "O2W−

DOI: 10.1021/acs.chemmater.6b01286
Chem. Mater. 2016, 28, 4608−4615

O9W−O8W−O7W−O10W", as predicted in the proposed mechanism (path 1 in Figure 5); and

(iii) The proton, upon arriving to the *terminal* O10W, continues on its way, along the *c*-axis to O11A, suggesting that the proton hopping continues along the disordered water molecules through the center of the channels (see Figure S7). In the two theoretical simulations, the process requires 200 and 300 fs to finish.

CONCLUSIONS

In summary, we have reported the rational design of a unique chiral 3D *bio*MOF. This novel material exhibits permanent porosity, high chemical, structural and water/basic media stability, and proton conductivity. Compound **1**, hosting a large number of water molecules in their large pores in an *ordered* manner, allowed us to overcome the well-known difficulties[28] to achieve detailed experimental information on the pathways involved in the hopping of protons between neighboring water molecules in a MOF during proton conduction. We propose a precise Grotthuss-like mechanism, showing the different hydrogen-bonded pathways developing inside the channels of a proton-conductive MOF. Our results highlight the importance of design-by-synthesis as a very powerful tool to understand complex physicochemical phenomena of biological and industrial interest.

EXPERIMENTAL SECTION

Preparation of $\{Cu_6Ca[(S,S)\text{-alamox}]_3(OH)_2(H_2O)\}\cdot 32H_2O$ (1). Well-shaped hexagonal prisms of **1** suitable for X-ray structural analysis were obtained by slow diffusion in an H-shaped tube of aqueous solutions containing stoichiometric amounts of $(Me_4N)_2\{Cu_2[(S,S)\text{-alamox}](OH)_2\}\cdot 6H_2O$ (see the Supporting Information) (0.12 g, 0.18 mmol) in one arm and $CaCl_2$ (0.01 g, 0.06 mmol) in the other. They were isolated by filtration on paper and air-dried. Yield: 2.28 g, 67%; Anal.: calcd for $C_{24}Cu_6CaH_{92}N_6O_{53}$ (1734.4): C, 16.62%; H, 5.35%; N, 4.85%. Found: C, 16.87%; H, 5.21%; N, 4.85%; IR (KBr): ν = 1618 cm^{-1} (C═O).

Single-Crystal X-ray Diffraction. Crystal data for **1**: $C_{24}Cu_6CaH_{92}N_6O_{53}$, hexagonal, space group $P6_3$, a = 17.6943(10) Å, c = 13.2921(8) Å, V = 3604.0(5) $Å^3$, T = 90(2) K, Z = 2, ρ_{calc} = 1.598 g cm^{-3}, μ = 1.917 mm^{-1}, Flack parameter = 0.02(1), of the 34464 reflections collected, 5790 are unique and 4983 observed with $I > 2\sigma(I)$. Refinement of 332 parameters gave R = 0.0367 and R_w = 0.0966 for reflections with $I > 2\sigma(I)$ and R = 0.0452 and R_w = 0.1017 for all reflections, with S = 1.062. Further detailed information on the structural data can be found at the Supporting Information.

Proton Conductivity Studies. Electrical characterization for **1** was carried out on dense (~96%−98% theoretical density) cylindrical pellets (diameter ca. 5 mm and thickness ca. 1 mm) obtained by pressing ca. 40 mg of sample at 250 MPa, for 1 min. The pellets were pressed between porous C electrodes (Sigracet, No. GDL 10 BB, no Pt). The sample cell was placed inside a temperature- and humidity-controlled chamber (Espec, Model SH-222) and connected to an impedance analyzer (Agilent, Model HP4284A). AC impedance data were collected over the frequency range from 20 Hz to 1 MHz with an applied voltage of 1 V. The reproducibility of the experiments was evaluated by performing duplicate measurements in two different pellets. This may rule out extrinsic transport through the grain boundary associated with the pelletizing process,[61] although single-crystal measurements are necessary to discard interparticle conduction.

Proton conductivity measurements were carried out at different relative humidities (RH = 60%, 70%, 80%, and 95%) after equilibration by successive heating/cooling cycles from 21 °C to 80 °C at 0.2 °C/min. This procedure ensures stable conductivity values, being those fully reproducible after several cycles of measurements.

Impedance spectra were recorded upon cooling (0.2 °C/min) from 80 °C to 21 °C at 5 °C intervals. The stabilization time before each data acquisition was 5 min, with a maximum temperature variation of 0.1 °C.

Computing Details. Quantum molecular dynamics simulations were performed using the SIESTA program, version 3.2,[62] starting from an optimized structure. Only a hexagonal pore from the crystal structure of **1** with 64 H_2O molecules was chosen as a theoretical model to study the pathways involved in the proton conductivity. In order to simplify the model and to save computer processing unit (CPU) time, the walls of the channel were removed, i.e., only the water molecules were retained. In order to avoid a crumbling or large structural distribution of the system, the positions of the O atoms were highly constrained, whereas the H atoms remained free, allowing proton interchange between the neighboring molecules. The water molecule proposed as the starting proton donor into the experimental section was protonated (H_3O^+). Two different simulations were carried out (see Videos S1−S4 and Videos S5 and S6). In order to simulate the effect of the anode when the electric voltage was applied in the measurement of the proton conductance, a water molecule in a distant place was deprotonated in one of them (a hydroxo group is considered instead of a water molecule) (Videos S1−S4). Finally, preliminary calculations with no constraints of the O atoms also suggested a structure diffusion mechanism. Further detailed information on the structural data can be found in the Supporting Information.

ASSOCIATED CONTENT

Supporting Information

Videos S1−S6 showing the proposed proton conduction mechanism. The Supporting Information is available free of charge on the ACS Publications website at DOI: 10.1021/acs.chemmater.6b01286.

Additional preparations and physical characterization data of **1**; additional figures (Figures S1−S7); crystallographic refinement and hydrogen bonds details for **1** (Tables S1 and S2) (PDF)

Crystallographic data (CIF)

Cambridge Crystallographic Data Centre information for CCDC-1432054 (**1**) (PDF)

Video S1: Proton conduction mechanism from the quantum molecular dynamics simulations showing the proton hopping between the hydrogen bonded water molecules and the sequential reorientation; oxygen and hydrogen atoms are represented by red and pink spheres, respectively (the first 200 fs of the simulation are shown) (AVI)

Video S2: Proton conduction mechanism from the quantum molecular dynamics simulations showing the proton hopping between the hydrogen bonded water molecules and the sequential reorientation; oxygen and hydrogen atoms are represented by red and pink spheres, respectively (the first 200 fs of the simulation are shown) (AVI)

Video S3: Proton conduction mechanism from the quantum molecular dynamics simulations showing the proton hopping between the hydrogen bonded water molecules and the sequential reorientation; oxygen and hydrogen atoms involved in the conducting mechanism are represented by magenta and orange spheres, respectively (the first 200 fs of the simulation are shown) (AVI)

Video S4: Proton conduction mechanism from the quantum molecular dynamics simulations showing the proton hopping between the hydrogen bonded water

DOI: 10.1021/acs.chemmater.6b01286
Chem. Mater. 2016, 28, 4608−4615

molecules and the sequential reorientation; oxygen and hydrogen atoms involved in the conducting mechanism are represented by magenta and orange spheres, respectively (the first 200 fs of the simulation are shown) (AVI)

Video S5: Proton conduction mechanism from the quantum molecular dynamics simulations showing the proton hopping between the hydrogen bonded water molecules and the sequential reorientation; oxygen and hydrogen atoms are represented by red and pink spheres, respectively, and oxygen and hydrogen atoms involved in the conducting mechanism are represented by magenta and orange spheres, respectively (the first 300 fs of the simulation are shown) (AVI)

Video S6: Proton conduction mechanism from the quantum molecular dynamics simulations showing the proton hopping between the hydrogen bonded water molecules and the sequential reorientation; oxygen and hydrogen atoms are represented by red and pink spheres, respectively (the first 300 fs of the simulation are shown) (AVI)

AUTHOR INFORMATION

Corresponding Authors

*E-mail: j.gascon@tudelft.nl (J. Gascon).
*E-mail: donatella.armentano@unical.it (D. Armentano).
*E-mail: emilio.pardo@uv.es (E. Pardo).

Notes

The authors declare no competing financial interest.

ACKNOWLEDGMENTS

This work was supported by the MINECO (Spain) (Project Nos. CTQ2013-46362-P, CTQ2013-44844-P, MAT2013-41836-R, and Excellence Unit "Maria de Maeztu" MDM-2015-0538), the Generalitat Valenciana (Spain) (Project No. PROMETEOII/2014/070), Junta de Andalucía (Spain) (Project No. FQM-1656), and the Ministero dell'Istruzione, dell'Università e della Ricerca (Italy). T.G. thanks the Universitat de València for a predoctoral contract. Thanks are also extended to the Ramón y Cajal Program and the "Convocatoria 2015 de Ayudas Fundación BBVA a Investigadores y Creadores Culturales" (E.P.). B.S. and J.G. acknowledge the financial support of the European Research Council under the European Unioń s Seventh Framework Program (No. FP/2007-2013)/ERC Grant Agreement No. 335746, CrystEng-MOF-MMM.

REFERENCES

(1) Long, J. R.; Yaghi, O. M. The Pervasive Chemistry of Metal-Organic Frameworks. *Chem. Soc. Rev.* **2009**, *38*, 1213−1214.

(2) Férey, G. Hybrid Porous Solids: Past, Present, Future. *Chem. Soc. Rev.* **2008**, *37*, 191−214.

(3) Kitagawa, S.; Matsuda, R. Chemistry of Coordination Space of Porous Coordination Polymers. *Coord. Chem. Rev.* **2007**, *251*, 2490−2509.

(4) Maspoch, D.; Ruiz-Molina, D.; Veciana, J. Old Materials with New Tricks: Multifunctional Open-Framework Materials. *Chem. Soc. Rev.* **2007**, *36*, 770−818.

(5) Furukawa, H.; Cordova, K. E.; O'Keeffe, M.; Yaghi, O. M. The Chemistry and Applications of Metal-Organic Frameworks. *Science* **2013**, *341*, 974.

(6) Wang, K.; Lv, X.-L.; Feng, D.; Li, J.-R.; Chen, S.; Sun, J.; Song, L.; Xie, Y.; Li, J.-R.; Zhou, H.-C. Pyrazolate-Based Porphyrinic Metal−Organic Framework with Extraordinary Base-Resistance. *J. Am. Chem. Soc.* **2016**, *138*, 914−919.

(7) Okawa, H.; Shigematsu, A.; Sadakiyo, M.; Miyagawa, T.; Yoneda, K.; Ohba, M.; Kitagawa, H. Oxalate-Bridged Bimetallic Complexes {NH(prol)3}[MCr(ox)3] (M = Mn(II), Fe(II), Co(II); NH(prol)3-(+) = tri(3-Hydroxypropyl)ammonium) Exhibiting Coexistent Ferromagnetism and Proton Conduction. *J. Am. Chem. Soc.* **2009**, *131*, 13516−13522.

(8) Hurd, J. a; Vaidhyanathan, R.; Thangadurai, V.; Ratcliffe, C. I.; Moudrakovski, I. L.; Shimizu, G. K. H. Anhydrous Proton Conduction at 150 °C in a Crystalline Metal−organic Framework. *Nat. Chem.* **2009**, *1*, 705−710.

(9) Kitagawa, H. Metal-Organic Frameworks: Transported into Fuel Cells. *Nat. Chem.* **2009**, *1*, 689−690.

(10) Sadakiyo, M.; Yamada, T.; Kitagawa, H. Rational Designs for Highly Proton-Conductive Metal-Organic Frameworks. *J. Am. Chem. Soc.* **2009**, *131*, 9906−9907.

(11) Ohkoshi, S.; Nakagawa, K.; Tomono, K.; Imoto, K.; Tsunobuchi, Y.; Tokoro, H. High Proton Conductivity in Prussian Blue Analogues and the Interference Effect by Magnetic Ordering. *J. Am. Chem. Soc.* **2010**, *132*, 6620−6621.

(12) Taylor, J. M.; Mah, R. K.; Moudrakovski, I. L.; Ratcliffe, C. I.; Vaidhyanathan, R.; Shimizu, G. K. H. Facile Proton Conduction via Ordered Water Molecules in a Phosphonate Metal-Organic Framework. *J. Am. Chem. Soc.* **2010**, *132*, 14055−14057.

(13) Pardo, E.; Train, C.; Gontard, G.; Boubekeur, K.; Fabelo, O.; Liu, H.; Dkhil, B.; Lloret, F.; Nakagawa, K.; Tokoro, H.; Ohkoshi, S.; Verdaguer, M. High Proton Conduction in a Chiral Ferromagnetic Metal-Organic Quartz-like Framework. *J. Am. Chem. Soc.* **2011**, *133*, 15328−15331.

(14) Sahoo, S. C.; Kundu, T.; Banerjee, R. Helical Water Chain Mediated Proton Conductivity in Homochiral Metal−Organic Frameworks with Unprecedented Zeolitic *unh*-Topology. *J. Am. Chem. Soc.* **2011**, *133*, 17950−17958.

(15) Shigematsu, A.; Yamada, T.; Kitagawa, H. Wide Control of Proton Conductivity in Porous Coordination Polymers. *J. Am. Chem. Soc.* **2011**, *133*, 2034−2036.

(16) Colodrero, R. M. P.; Olivera-Pastor, P.; Losilla, E. R.; Aranda, M. a. G.; Leon-Reina, L.; Papadaki, M.; McKinlay, A. C.; Morris, R. E.; Demadis, K. D.; Cabeza, A. Multifunctional Lanthanum Tetraphosphonates: Flexible, Ultramicroporous and Proton-Conducting Hybrid Frameworks. *Dalton Trans.* **2012**, *41*, 4045−4051.

(17) Ponomareva, V. G.; Kovalenko, K. a; Chupakhin, A. P.; Dybtsev, D. N.; Shutova, E. S.; Fedin, V. P. Imparting High Proton Conductivity to a Metal-Organic Framework Material by Controlled Acid Impregnation. *J. Am. Chem. Soc.* **2012**, *134*, 15640−15643.

(18) Kim, S.; Dawson, K. W.; Gelfand, B. S.; Taylor, J. M.; Shimizu, G. K. H. Enhancing Proton Conduction in a Metal-Organic Framework by Isomorphous Ligand Replacement. *J. Am. Chem. Soc.* **2013**, *135*, 963−966.

(19) Ōkawa, H.; Sadakiyo, M.; Yamada, T.; Maesato, M.; Ohba, M.; Kitagawa, H. Proton-Conductive Magnetic Metal-Organic Frameworks, $\{NR_3(CH_2COOH)\}[M_a^{II}M_b^{III}(ox)_3]$: Effect of Carboxyl Residue upon Proton Conduction. *J. Am. Chem. Soc.* **2013**, *135*, 2256−2262.

(20) Umeyama, D.; Horike, S.; Inukai, M.; Kitagawa, S. Integration of Intrinsic Proton Conduction and Guest-Accessible Nanospace into a Coordination Polymer. *J. Am. Chem. Soc.* **2013**, *135*, 11345−11350.

(21) Sadakiyo, M.; Yamada, T.; Kitagawa, H. Proton Conductivity Control by Ion Substitution in a Highly Proton-Conductive Metal−Organic Framework. *J. Am. Chem. Soc.* **2014**, *136*, 13166−13169.

(22) Bao, S. S.; Otsubo, K.; Taylor, J. M.; Jiang, Z.; Zheng, L. M.; Kitagawa, H. Enhancing Proton Conduction in 2D Co-La Coordination Frameworks by Solid-State Phase Transition. *J. Am. Chem. Soc.* **2014**, *136*, 9292−9295.

(23) Bazaga-García, M.; Colodrero, R. M. P.; Papadaki, M.; Garczarek, P.; Zoń, J.; Olivera-Pastor, P.; Losilla, E. R.; León-Reina, L.; Aranda, M. A. G.; Choquesillo-Lazarte, D.; Demadis, K. D.; Cabeza, A. Guest Molecule-Responsive Functional Calcium Phosphonate

DOI: 10.1021/acs.chemmater.6b01286
Chem. Mater. 2016, 28, 4608−4615

Frameworks for Tuned Proton Conductivity. *J. Am. Chem. Soc.* **2014**, *136*, 5731−5739.
(24) Tadokoro, M.; Ohhata, Y.; Shimazaki, Y.; Ishimaru, S.; Yamada, T.; Nagao, Y.; Sugaya, T.; Isoda, K.; Suzuki, Y.; Kitagawa, H.; Matsui, H. Anomalous Enhancement of Proton Conductivity for Water Molecular Clusters Stabilized in Interstitial Spaces of Porous Molecular Crystals. *Chem.—Eur. J.* **2014**, *20*, 13698−13709.
(25) Maxim, C.; Ferlay, S.; Tokoro, H.; Ohkoshi, S.-I.; Train, C. Atypical Stoichiometry for a 3D Bimetallic Oxalate-Based Long-Range Ordered Magnet Exhibiting High Proton Conductivity. *Chem. Commun.* **2014**, *50*, 5629−5632.
(26) Nagarkar, S. S.; Unni, S. M.; Sharma, A.; Kurungot, S.; Ghosh, S. K. Two-in-One: Inherent Anhydrous and Water-Assisted High Proton Conduction in a 3D Metal-Organic Framework. *Angew. Chem., Int. Ed.* **2014**, *53*, 2638−2642.
(27) Phang, W. J.; Lee, W. R.; Yoo, K.; Ryu, D. W.; Kim, B.; Hong, C. S. pH-Dependent Proton Conducting Behavior in a Metal-Organic Framework Material. *Angew. Chem., Int. Ed.* **2014**, *53*, 8383−8387.
(28) Sadakiyo, M.; Yamada, T.; Honda, K.; Matsui, H.; Kitagawa, H. Control of Crystalline Proton-Conducting Pathways by Water-Induced Transformations of Hydrogen-Bonding Networks in a Metal-Organic Framework. *J. Am. Chem. Soc.* **2014**, *136*, 7701−7707.
(29) Tang, Q.; Liu, Y.; Liu, S.; He, D.; Miao, J.; Wang, X.; Yang, G.; Shi, Z.; Zheng, Z. High Proton Conduction at above 100 °C Mediated by Hydrogen Bonding in a Lanthanide Metal-Organic Framework. *J. Am. Chem. Soc.* **2014**, *136*, 12444−12449.
(30) Sadakiyo, M.; Kasai, H.; Kato, K.; Takata, M.; Yamauchi, M. Design and Synthesis of Hydroxide Ion-Conductive Metal-Organic Frameworks Based on Salt Inclusion. *J. Am. Chem. Soc.* **2014**, *136*, 1702−1705.
(31) Borges, D. D.; Devautour-Vinot, S.; Jobic, H.; Ollivier, J.; Nouar, F.; Semino, R.; Devic, T.; Serre, C.; Paesani, F.; Maurin, G. Proton Transport in a Highly Conductive Porous Zirconium-Based Metal-Organic Framework: Molecular Insight. *Angew. Chem.* **2016**, *128*, 3987−3992.
(32) McKinlay, A. C.; Morris, R. E.; Horcajada, P.; Férey, G.; Gref, R.; Couvreur, P.; Serre, C. BioMOFs: Metal-Organic Frameworks for Biological and Medical Applications. *Angew. Chem., Int. Ed.* **2010**, *49*, 6260−6266.
(33) Imaz, I.; Rubio-Martínez, M.; An, J.; Solé-Font, I.; Rosi, N. L.; Maspoch, D. Metal-Biomolecule Frameworks (MBioFs). *Chem. Commun.* **2011**, *47*, 7287−7302.
(34) Persch, E.; Dumele, O.; Diederich, F. Molecular Recognition in Chemical and Biological Systems. *Angew. Chem., Int. Ed.* **2015**, *54*, 3290−3327.
(35) Makarević, J.; Jokić, M.; Perić, B.; Tomišić, V.; Kojić-Prodić, B.; Žinić, M. Bis(Amino Acid) Oxalyl Amides as Ambidextrous Gelators of Water and Organic Solvents: Supramolecular Gels with Temperature Dependent Assembly/Dissolution Equilibrium. *Chem. - Eur. J.* **2001**, *7*, 3328−3341.
(36) Grancha, T.; Ferrando-Soria, J.; Cano, J.; Lloret, F.; Julve, M.; De Munno, G.; Armentano, D.; Pardo, E. Enantioselective Self-Assembly of Antiferromagnetic hexacopper(II) Wheels with Chiral Amino Acid Oxamates. *Chem. Commun.* **2013**, *49*, 5942−5944.
(37) Grancha, T.; Ferrando-Soria, J.; Castellano, M.; Julve, M.; Pasán, J.; Armentano, D.; Pardo, E. Oxamato-Based Coordination Polymers: Recent Advances in Multifunctional Magnetic Materials. *Chem. Commun.* **2014**, *50*, 7569−7585.
(38) Rouquerol, J.; Avnir, D.; Fairbridge, C. W.; Everett, D. H.; Haynes, J. H.; Pernicone, N.; Ramsay, J. D. F.; Sing, K. S. W.; Unger, K. K. Recommendations for the Characterization of Porous Solids. *Pure Appl. Chem.* **1994**, *66*, 1739−1758.
(39) De Lange, M. F.; Vlugt, T. J. H.; Gascon, J.; Kapteijn, F. Adsorptive Characterization of Porous Solids: Error Analysis Guides the Way. *Microporous Mesoporous Mater.* **2014**, *200*, 199−215.
(40) Cheng, L. S.; Yang, R. T. Improved Horvath—Kawazoe Equations Including Spherical Pore Models for Calculating Micropore Size Distribution. *Chem. Eng. Sci.* **1994**, *49*, 2599−2609.
(41) Horike, S.; Umeyama, D.; Kitagawa, S. Ion Conductivity and Transport by Porous Coordination Polymers and Metal-Organic Frameworks. *Acc. Chem. Res.* **2013**, *46*, 2376−2384.
(42) Colomban, P.; Novak, A. Proton Transfer and Superionic Conductivity in Solids and Gels. *J. Mol. Struct.* **1988**, *177*, 277−308.
(43) Munakata, H.; Chiba, H.; Kanamura, K. Enhancement on Proton Conductivity of Inorganic−organic Composite Electrolyte Membrane by Addition of Sulfonic Acid Group. *Solid State Ionics* **2005**, *176*, 2445−2450.
(44) Gosalawit, R.; Chirachanchai, S.; Shishatskiy, S.; Nunes, S. Krytox−Montmorillonite−Nafion Nanocomposite Membrane for Effective Methanol Crossover Reduction in DMFCs. *Solid State Ionics* **2007**, *178*, 1627−1635.
(45) Dai, C.-A.; Liu, C.-P.; Lee, Y.-H.; Chang, C.-J.; Chao, C.-Y.; Cheng, Y.-Y. Fabrication of Novel Proton Exchange Membranes for DMFC via UV Curing. *J. Power Sources* **2008**, *177*, 262−272.
(46) Hara, N.; Ohashi, H.; Ito, T.; Yamaguchi, T. Rapid Proton Conduction through Unfreezable and Bound Water in a Wholly Aromatic Pore-Filling Electrolyte Membrane. *J. Phys. Chem. B* **2009**, *113*, 4656−4663.
(47) Kreuer, K.; Rabenau, A.; Weppner, W. Vehicle Mechanism, A New Model for the Interpretation of the Conductivity of Fast Proton Conductors. *Angew. Chem., Int. Ed. Engl.* **1982**, *21*, 208−209.
(48) Agmon, N. The Grotthuss Mechanism. *Chem. Phys. Lett.* **1995**, *244*, 456−462.
(49) Marx, D. Proton Transfer 200 Years after von Grotthuss: Insights from *Ab Initio* Simulations. *ChemPhysChem* **2006**, *7*, 1848−1870.
(50) Tuckerman, M. E. On the Quantum Nature of the Shared Proton in Hydrogen Bonds. *Science* **1997**, *275*, 817−820.
(51) Marx, D.; Tuckerman, M. E.; Hutter, J.; Parrinello, M. The Nature of the Hydrated Excess Proton Inwater. *Nature* **1999**, *397*, 601−604.
(52) Hassanali, A.; Giberti, F.; Cuny, J.; Kühne, T. D.; Parrinello, M. Proton Transfer through the Water Gossamer. *Proc. Natl. Acad. Sci. U. S. A.* **2013**, *110*, 13723−13728.
(53) Vilčiauskas, L.; Tuckerman, M. E.; Bester, G.; Paddison, S. J.; Kreuer, K.-D. The Mechanism of Proton Conduction in Phosphoric Acid. *Nat. Chem.* **2012**, *4*, 461−466.
(54) Fujiyoshi, Y.; Murata, K.; Mitsuoka, K.; Hirai, T.; Walz, T.; Agre, P.; Heymann, J. B.; Engel, A. Structural Determinants of Water Permeation through Aquaporin-1. *Nature* **2000**, *407*, 599−605.
(55) Gordon, R. E.; Strange, J. H. Fast Hydrogen Ion Diffusion in Solid Hydrogen Uranyl Phosphate (HUP). *Solid State Commun.* **1979**, *31*, 995−997.
(56) Kreuer, K. D.; Rabenau, A.; Messer, R. Proton Conductivity in the Layer Compound $H_3OUO_2AsO_4{\cdot}3H_2O$ (HU As). *Appl. Phys. A: Solids Surf.* **1983**, *32*, 45−53.
(57) Capelli, S. C.; Falvello, L. R.; Forcén-Vázquez, E.; McIntyre, G. J.; Palacio, F.; Sanz, S.; Tomás, M. Proton Cascade in a Molecular Solid: H/D Exchange on Mobile and Immobile Water. *Angew. Chem., Int. Ed.* **2013**, *52*, 13463−13467.
(58) Ogawa, T.; Kamiguchi, K.; Tamaki, T.; Imai, H.; Yamaguchi, T. Differentiating Grotthuss Proton Conduction Mechanisms by Nuclear Magnetic Resonance Spectroscopic Analysis of Frozen Samples. *Anal. Chem.* **2014**, *86*, 9362−9366.
(59) Ogawa, T.; Aonuma, T.; Tamaki, T.; Ohashi, H.; Ushiyama, H.; Yamashita, K.; Yamaguchi, T. The Proton Conduction Mechanism in a Material Consisting of Packed Acids. *Chem. Sci.* **2014**, *5*, 4878−4887.
(60) Liang, X.; Zhang, F.; Feng, W.; Zou, X.; Zhao, C.; Na, H.; Liu, C.; Sun, F.; Zhu, G. From Metal−organic Framework (MOF) to MOF−polymer Composite Membrane: Enhancement of Low-Humidity Proton Conductivity. *Chem. Sci.* **2013**, *4*, 983−992.
(61) Tominaka, S.; Cheetham, A. K. Intrinsic and Extrinsic Proton Conductivity in Metal-Organic Frameworks. *RSC Adv.* **2014**, *4*, 54382−54387.
(62) Artacho, E.; Cela, J. M.; Gale, J. D.; García, A.; Junquera, J.; Martin, R. M.; Ordejón, P.; Sánchez-Portal, D.; Soler, J. M. SIESTA 3.2, 2012.

DOI: 10.1021/acs.chemmater.6b01286
Chem. Mater. 2016, 28, 4608−4615

Polyhedron 117 (2016) 710–717

Contents lists available at ScienceDirect

Polyhedron

journal homepage: www.elsevier.com/locate/poly

Oxotris(oxalato)niobate(V) as counterion in cobalt(II) spin-crossover systems

Willian X.C. Oliveira [a], Cynthia L.M. Pereira [a,*], Carlos B. Pinheiro [b], Klaus Krambrock [b], Thais Grancha [c], Nícolas Moliner [c], Francesc Lloret [c,1], Miguel Julve [c,1,*]

[a] Departamento de Química, Instituto de Ciências Exatas, Universidade Federal de Minas Gerais, Av. Pres. Antônio Carlos, 6627, Pampulha, 31270-901 Belo Horizonte, Minas Gerais, Brazil
[b] Departamento de Física, Instituto de Ciências Exatas, Universidade Federal de Minas Gerais, Av. Pres. Antônio Carlos, 6627, Pampulha, 31270-901 Belo Horizonte, Minas Gerais, Brazil
[c] Departamento de Química Inorgánica/Instituto de Ciencia Molecular (ICMol), Universitat de València, C/Catedrático José Beltrán 2, 46980 Paterna, València, Spain

ARTICLE INFO

Article history:
Received 13 May 2016
Accepted 11 July 2016
Available online 18 July 2016

Keywords:
Cobalt(II)
Niobium(V)
Spin-crossover
Heterobimetallic complex
Magnetic properties

ABSTRACT

This work is devoted to the investigation of the thermally induced spin-crossover behavior from a high-spin state (HS, $S = 3/2$) at higher temperatures to a low-spin phase (LS, $S = 1/2$) at lower temperatures of the six-coordinate cobalt(II) complex in the compound $[Co(terpy)_2]_3[NbO(C_2O_4)_3]_2{\cdot}3CH_3OH{\cdot}4H_2O$ (**2**). The crystal structure of **2** together with that of its counterion as tetraphenylarsonium(V) salt $(AsPh_4)_3[NbO(C_2O_4)_3]{\cdot}9H_2O$ (**1**) are also included. The spin-crossover process was followed by the thermal variation of the $\chi_M T$ product between 2.0 and 400 K under the warming mode, with the LS configuration being achieved at $T \leqslant 200$ K and the LS → HS interconversion being incomplete at 400 K. X-band EPR measurements both in solution and in the solid state were used to characterize the LS state. In order to substantiate the phenomenon in **2**, an analytical expression was presented based on the combination of the spin–orbit coupling and both first- and second-order Zeeman effects for a d^7 electronic configuration. The best-fit parameters were $C_{vib} = 0.0249$, $\lambda = -163$ cm^{-1}, $\alpha = 1.06$, $\Delta = 1532$ cm^{-1}, with a fixed value of $g_{LS} = 2.11$ determined from the fit of the EPR spectrum at 10 K.

1. Introduction

Although the coordination chemistry of niobium was subject of thorough research in the past based on their moderate cost, limited toxicity and large availability of oxidation states, the low stability of many of its salts in the presence of moisture and/or oxygen [1,2] and the light sensitivity of some of them [3], account for the living in the shadow of the niobium compounds of metal complexes of the 4d elements. Recently, the discovery of interesting properties exhibited when niobium is incorporated into alloys and steel strengtheners [4–6], electronic devices [7,8], porous metal-organic frameworks with highly gas adsorption [9], materials for catalysis [10–12] and heterometallic multifunctional magnetic systems [13–17], has renewed the interest in the coordination chemistry of this element. Thinking at the development of niobium-based molecular compounds, the oxalate-containing niobium(IV/V) complexes could be a suitable choice. However, although the paramagnetic $[Nb^{IV}(C_2O_4)_4]^{4-}$ species ($C_2O_4^{2-}$ = oxalate) has been isolated with univalent cations as counterions and their structures solved by X-ray diffraction [1], the easy oxidation and hydrolysis that it undergoes, makes very difficult its use as building block for metal assembling. The corresponding diamagnetic seven-coordinate niobium(V) complexes with an oxo group of general formula $[Nb^{V}O(C_2O_4)_x(H_2O)_y]^{(2x-3)-}$ ($x = y = 2$ or $x = 3$ and $y = 0$) which are relatively stable in common laboratory conditions, constitute good starting materials to build solid state architectures [18,19].

Herein we show how the use of the oxotris(oxalate)niobate(V) metalloligand as counterion allows the precipitation of the well known $[Co(terpy)_2]^{2+}$ cation (terpy = 2,2′:6′,2″-terpyridine), a well known spin crossover (SCO) species exhibiting a high-spin (HS, $S = 3/2$) ↔ low-spin (LS, $S = 1/2$) process [20,21]. As far as we know, this is the first time that an anionic metal complex is used as a precipitating agent towards the $[Co(terpy)_2]^{2+}$ cation, the charge balance of this cation being achieved by inorganic anions in previous reports [22,23]. The synthesis and crystal structure of

* Corresponding authors.
E-mail addresses: cynthialopes@ufmg.br, lopescynthia@yahoo.com.br (C.L.M. Pereira), Miguel.Julve@uv.es (M. Julve).

[1] Dedication: This contribution is dedicated to Prof. Dr. Juan Faus on the occasion of his retirement; he has been an outstanding teacher and very brilliant researcher and scientific father of several generations of coordination chemists at the University of Valencia.

http://dx.doi.org/10.1016/j.poly.2016.07.014
0277-5387/

the niobium-based salts $(AsPh_4)_3[NbO(C_2O_4)_3]\cdot 9H_2O$ (**1**) and $[Co(terpy)_2]_3[NbO(C_2O4)_3]_2\cdot 3CH_3OH\cdot 4H_2O$ (**2**) [$AsPh_4^+$ = tetraphenylarsonium(V) cation] together with the variable-temperature magnetic investigation and EPR study of **2** are presented in this work.

2. Experimental

2.1. Materials

$[Co(H_2O)_6](ClO_4)_2$, 2,2′:6′,2″-terpyridine (terpy), $AsPh_4Cl$, methanol, acetonitrile and dimethylsulfoxide were purchased from Sigma–Aldrich and used as received. The niobium salt $(NH_4)_3[NbO(C_2O_4)_3]\cdot 6H_2O$ was a gift from the Companhia Brasileira de Metalurgia e Mineração (CBMM) and it was also used without any further treatment.

2.2. Preparation of the complexes

2.2.1. $(AsPh_4)_3[NbO(C_2O_4)_3]\cdot 9H_2O$ (**1**)

Solid $AsPh_4Cl$ (2.50 g, 0.60 mmol) was added to an aqueous solution (10 cm^3) containing $(NH_4)_3[NbO(C_2O_4)_3]\cdot 6H_2O$ (1.00 g, 0.195 mmol). The resulting solution was kept under continuous stirring for 30 min at room temperature. The white solid that separated was filtered off, washed with small amounts of cold water and diethyl ether and dried in the open air. It was dissolved in 100 cm^3 of a H_2O–CH_3CN mixture (15:1 v/v) and left to evaporate at room temperature for five days. The white crystals were filtered off, washed with 2.0 cm^3 of cold acetonitrile and then with diethyl ether. Yield: 2.10 g (67%, 0.120 mmol). X-ray absorption microanalysis: 3:1 As/Nb molar ratio (5 spots). ^1H NMR ($CDCl_3$, 300 MHz): 7.69, 7.67 and 7.63 (m, 72H, H–Ph) ppm. ^{13}C (dmso-d_6, 200 MHz): 121.43, 131.36, 133.58, 134.75 ($AsPh_4^+$) and 166.71 ppm $C_2O_4^{2-}$ of $[NbO(C_2O_4)_3]^{3-}$. Elemental analysis for $C_{78}H_{78}O_{22}As_3Nb$ (1685.11 g mol^{-1}) – Exp. (Calc.): %C 55.57 (55.59), %H 4.49 (4.67)%. IR (KBr disk/cm^{-1}): 3481 [ν(O—H)], 3089, 3052 [ν(C—H)], 1710 and 1687 [ν_{as}(C=O)], 1483 [ν(C=C)], 1380 [ν_s(C=O)], 905 [ν(Nb=O)] and 683 [ν(As—C)].

2.2.2. $[Co(terpy)_2]_3[NbO(C_2O_4)_3]_2\cdot 3CH_3OH\cdot 4H_2O$ (**2**)

Solid $[Co(H_2O)_6](ClO_4)_2$ (10.0 mg, 21.8 μmol) was placed at the bottom of a 4.0 cm^3 test tube with 0.50 cm^3 of dmso. Then the tube was slowly filled with 2.50 cm^3 of a dmso–CH_3OH mixture (1:4 v/v) containing terpy (15.0 mg, 64.4 μmol). Finally, **1** (15.0 mg, 9.01 μmol) dissolved in 0.50 cm^3 of CH_3OH was placed on the top and the tube covered with parafilm®. X-ray quality deep brown crystals of **2** were grown in the text tube by slow diffusion at room temperature during 25 days. Yield: 3.20 mg (1.30 μmol, 29%). X-ray absorption microanalysis for **2**: 3:2 Co/Nb molar ratio. Elemental analysis for $C_{105}H_{86}N_{18}O_{33}Co_3Nb_2$ (2490.52 g mol^{-1}) – Exp. (Calc.): %C 51.55 (50.94), %H 3.02 (3.18), %N 10.49 (10.32), %Co 7.50 (7.30)%. IR (KBr disk/cm^{-1}): 3475 [ν(O–H)], 3062 and 2930 [ν(C–H)], 1715 and 1687 [ν_{as}(C=O)], 1641 [ν(C=N)], 1470 and 1448 [ν(C=C)], 1401 [ν_s(C=O)], 905 [ν(Nb=O] and 421 [ν(Co—N)].

2.3. Physical techniques

Elemental analysis (C, H and N) were carried out with a Perkin-Elmer 2400 analyser. The cobalt content was determined by atomic absorption with a Hitachi Z-8200 Polarized Atomic Absorption Spectrophotometer.

The infrared spectra for **1** and **2** were recorded on a Perkin-Elmer FTIR spectrophotometer using KBr pellets in the range 4000–400 cm^{-1} with an average of 32 scans and 2 cm^{-1} of spectral resolution. The molar ratio of the heavy atoms [As/Nb (**1**) and Co/Nb (**2**)] was determined by means of a scanning electron microscope Phillips ESEM XL30 (working tension of 20 kV), as the mean value of five different spots of the bulk. The samples were mounted in double faced tapes, free of heavy atoms.

The magnetic susceptibility measurements were carried out on crushed single crystals of **2** in the temperature range 2.0–400 K with a Quantum Design SQUID magnetometer and using applied magnetic fields of 0.5 T. Magnetization versus the magnetic field measurements for **2** were done at 2.0 K in the magnetic field range 0–5 T. Diamagnetic corrections of the constituent atoms of **2** were estimated from Pascal's constants. Experimental susceptibilities were also corrected for the magnetization of the sample holder (a plastic bag). In order to avoid any solvent loss in the sample preparation and vacuum process, the sample was prepared with single crystals of **2** immediately after collected from the test tubes, covered with icosane (49.73 mg) and introduced into a SQUID magnetometer at 200 K under a continuous helium flow. The sequence of the analysis was first cooling down the sample from 200 to 2.0 K, and then heating up until 400 K, which revealed to reach a desolvated compound up to 310 K. EPR measurements were carried out with a custom-built X-band spectrometer operating at about 9.38 GHz produced by a 500 mW Klystron (Varian). A commercial cylindrical resonant cavity (Bruker) was used. Magnetic fields were produced by an electromagnet (Varian) with a fully automated current source (Heizinger). Standard lock-in detection (EG&G) and field modulation of 100 kHz were also employed. The microwave frequency was stabilized by means of an automatic frequency control and measured with precision by a frequency-meter (PTS). Sample temperature of 10(1) K was achieved by an Oxford helium-flux cryosystem device.

2.4. Crystal data collection and refinement

X-ray diffraction data collection on single crystals of **1** and **2** were performed on an Oxford Gemini Ultra diffractometer at the LabCri from the Universidade Federal de Minas Gerais (**1**) and a Bruker-Saxi diffractometer (**2**) at the SCSIE from the Universitat de València by using Mo Kα radiation (λ = 0.71073 Å). The crystals were covered with mineral oil immediately after removed from crystallization tests for cryoprotection in order to avoid any solvent loss and mounted under a dinitrogen flux.

The measurements were performed at 120 (**1**) and 218 K (**2**). Data integration and scaling of the reflections were carried out with the Crysalis Pro software (171.37.34b) [24]. Final unit cell parameters were based on the fitting of the position of all reflections. Empirical absorption corrections were performed by using also the Crysalis Pro software based on the chemical formula [24]. The space group identification was done with XPREP [25]. The structures of **1** and **2** were solved via direct methods by using the SUPERFLIP program [26]. The positions of all atoms could be unambiguously assigned on consecutive difference Fourier maps. Refinements were performed by using SHELXL [25] based on F^2 through a full-matrix least-squares routine. Disordered phenyl rings, oxo and oxalate groups together with all solvent molecules of **1** were treated as isotropic atomic displacements. All non-hydrogen atoms and non-solvent molecules of **2** were refined with anisotropic atomic displacement parameters. All hydrogen atoms except those of the water molecules were located in difference Fourier maps and included as fixed contributions according to the riding model [27]. Values of C—H = 0.97 Å and U_{iso}(H) = 1.5 U_{eq}(C) for the methyl groups, C—H = 0.97 Å and U_{iso}(H) = 1.2 U_{eq}(C) for the aromatic carbon atoms and finally, O—H = 0.90 Å and U_{iso}(H) = 1.5 U_{eq}(O) for the OH group of the methanol molecules were adopted. Double split positions and rigid geometry were applied in the case of **1** for the disordered oxalate group from the $[Nb^VO(C_2O_4)_3]$ moiety and the arsenic atom together with two phenyl rings of the As3Ph_4^+ cation. The squeeze

technique was also applied in **1** in order to remove the spread electronic density in 468 Å^3 void (per unit cell, suppressing 121 electrons; see Fig. S1 in the Supporting Information) which is occupied with water molecules of crystallization. Three maxima of the electron density associated to the water molecules remained through the refinement in this process, since they are too close to the $[Nb^VO(C_2O_4)_3]^{3-}$ anion. These molecules were treated as isotropic atoms with freely refined occupancy. Double split positions were applied on the refinement of the oxygen atoms of the free water molecules in **2**. The crystal data and details of the structure refinement of **1** and **2** are listed in Table 1 whereas selected bond lengths and angles are given in Tables S1 (**1**) and S2 (**2**) of the Supporting Information.

3. Results and discussion

3.1. Synthesis and general characterization

Single crystals of **1** as white needles were obtained by slow evaporation of a water-acetonitrile solution of $(AsPh_4)_3[NbO(C_2O_4)_3]\cdot 9H_2O$. X-ray quality deep brown blocks of **2** were grown by slow diffusion of **1** and $[Co(H_2O)_6](ClO_4)_2$ in a MeOH–dmso mixed solvent containing the terpy ligand. The use of the niobium(V) precursor as tetraphenylarsonium salt (**1**) instead of the commercially available ammonium derivative is a key point in the synthesis of **2** because the protonation of the terpy ligand in the presence of an acid such as NH_4^+ competes with the formation of the $[Co(terpy)_2]^{2+}$ species.

The fact that there are no bands in the infrared spectrum of **1** in the range of 3300–3100 cm^{-1}, indicates the lack of N—H groups and consequently, the absence of NH_4^+ cations in that compound. The occurrence of stretching vibrations from aromatic C—H groups in the wavenumber range 3052–3089 cm^{-1} together with aromatic C=C and As—C vibrations at 1483 at 683 cm^{-1} respectively, are associated to the presence in **1** of the $AsPh_4^+$ cation. It can be considered as the confirmation of the success of the metathesis reaction where the ammonium was fully replaced by the tetraphenylarsonium in agreement with the structure of **1**. Two different C=O stretching vibrations which occur at 1710 and 1687 cm^{-1} support the presence in **1** of bidentate oxalate ligands. A medium intensity peak at 905 cm^{-1} in the infrared spectra of **1** is a diagnostic of the presence of the Nb^V=O group. Finally, the water molecules of crystallization of **1** are responsible for a strong absorption peak centered at 3481 cm^{-1}. Dealing with the infrared spectrum of **2**, absorption peaks at 1715, 1687 and 1641 cm^{-1} are attributed to the C=O (the two first ones) and C=N (the last one) vibrations of the oxalate and terpy ligands of the $[Nb^VO(C_2O_4)_3]^{3-}$ and $[Co(terpy)]^{2+}$ units. Additional peaks at 905 and 421 cm^{-1} are tentatively assigned to metal–ligand vibrations of Nb^V=O and Co—N, respectively. The lack of the As—C vibrations in **2** which are present in **1**, corroborates the full metathesis of the $AsPh_4^+$ cations by the $[Co(terpy)_2]^{2+}$ ions in agreement with the crystal structure of **2**. The O—H vibrations of the two types of the free solvent molecules (water and methanol) are responsible for a broad peak at 3475 cm^{-1} whereas several weak absorption peaks around 2930 cm^{-1} are attributed to the C—H stretching vibrations modes of the terpy ligand and the methanol molecules of crystallization (see IR spectra for **1** and **2** in Supporting Information as Figs. S2 and S3, respectively).

The thermal analysis of **1** under a dynamic dinitrogen atmosphere showed a first weight loss of 9.65% in an endothermic step between 25 and 120 °C which is associated to the evaporation of all the solvent molecules of crystallization (the calculated mass loss for the nine free water molecules is 9.62%). A weight loss of 84.1% which occurs between 220 and 650 °C, is probably due to the decomposition of organic matter. The residue is terminally stable heating up until 700 °C (the end of the analysis), and it corresponds to 6.91% initial mass, a value which agrees well with niobium(V) oxide (6.95% for 1/2 mol of Nb_2O_5). The thermal analysis of **2** was inconclusive, since this compound revealed to be unstable at room temperature by losing mainly free methanol molecules [see TG/DTA plot for **1** (Fig. S4) and the X-ray pattern comparison for **1** and **2** (Figs. S5 and S6) in the Supporting Information].

Table 1
Crystal data details of the structure determination for compounds **1** and **2**.

Compound	**1**	**2**
Empirical formula	$C_{78}H_{60}O_{14.72}As_3Nb$	$C_{105}H_{78}N_{18}O_{33}Co_3Nb_2$
Formula weight (g mol^{-1})	1550.51	2482.46
λ (Å)	0.71073	0.71073
T (K)	120	218(2)
Crystal size (mm^3)	0.35 × 0.11 × 0.06	0.37 × 0.36 × 0.34
Crystal system	triclinic	triclinic
Space group	$P\bar{1}$	$P1$
a (Å)	13.1324(5)	12.6164(4)
b (Å)	13.8387(6)	14.5974(4)
c (Å)	22.2474(8)	15.7892(5)
α (°)	79.468(3)	97.959(2)
β (°)	73.939(3)	99.271(3)
γ (°)	79.462(3)	107.584(3)
V (Å^3)	3782.2(3)	2681.10(15)
Z	2	1
μ (mm^{-1})	1.523	0.752
$F(000)$	1572	1261
ρ (mg m^{-3})	1.361	1.538
No. parameters	979	1408
Reflns collected	15461	21589
Reflections with $I > 2\sigma(I)$	11481	19624
Goodness-of-fit (GOF) on F^2	1.084	1.054
R^a, wR^b [$I > 2\sigma(I)$]	0.0506, 0.1277	0.0481, 0.1344
R^a, wR^b (all data)	0.0717, 0.1385	0.0548, 0.1396
Largest difference in peak and hole (e Å^{-3})	1.67, −2.55	1.33, −0.56

[a] $R = \sum||F_o| - |F_c||/\sum|F_o|$.
[b] $wR = [\sum(|F_o|^2 - |F_c|^2)^2/\sum|F_o|^2]^{1/2}$.

3.2. Crystal structures of *1* and *2*

The crystal structure of **1** was solved at 120 K and it reveals the complete replacement of the ammonium cations by the tetraphenylarsonium ions. Compound **1** crystallizes in the triclinic system, $P\bar{1}$ space group, with an asymmetric unit consisting of three crystallographically independent $AsPh_4^+$ cations (hereafter noted As1, As2 and As3) and one $[Nb^VO(C_2O_4)_3]^{3-}$ complex anion (see Fig. 1). The structure also contains free water molecules, but they are spread in a void of 260 Å^3.

The niobium(V) ion is seven-coordinate, six oxygen atoms from three bidentate oxalate ligands and one oxo group building a distorted pentagonal bipyramidal geometry around it. One of the axial positions is occupied by the oxo group (O1) whereas the other one is filled by an oxalate-oxygen (O13). The Nb^V—O_{oxo} double bond makes it shorter [Nb1—O1 = 1.853 Å] than the Nb—$O_{oxalate}$ single bond [Nb1–O13 = 2.029 Å]. The other niobium(V) to oxalate-oxygen bond lengths in the equatorial positions of the pentagonal bipyramid are very close to each other, their values varying in the narrow range 2.080 [Nb1—O10] to 2.145 Å [Nb1—O9]. Locally, there is a twofold axis over the niobium atom along the Nb1—O10 bond resulting in a disorder involving the oxo group and the out-of-equatorial plane oxalate group, with main group occupancy fitted to 55% of all structures. This disorder leads to a maxima of electron density over the pyramidal apical position slightly deviated from the related structures containing the $[Nb^VO(C_2O_4)_3]^{3-}$ unit [range of the values of the Nb=O and apical Nb—$O_{oxalate}$ bond distances are 1.70–1.72 and 2.10–2.25 Å, respectively] [18,19,28–32].

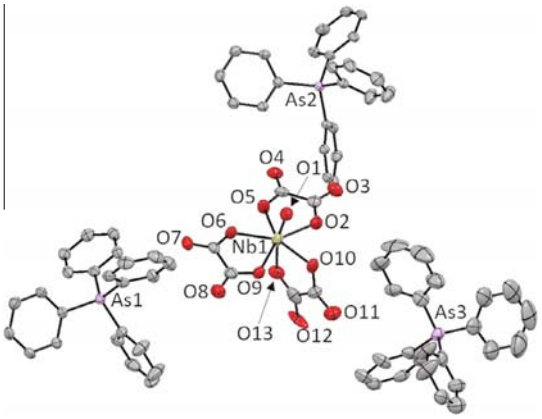

Fig. 1. Perspective view of the asymmetric unit of **1** with the atom numbering of the non-carbon atoms. The hydrogen atoms and the solvent molecules were omitted for clarity.

Each crystallographic independent arsenic(V) ion exhibits a tetrahedral environment being bonded to four phenyl carbon atoms. The values of the As—C bond distances are in the range expected varying from 1.905 to 1.912 Å. The fact that the As3—C bonds are slightly deviated from those concerning the other arsenic(V) ions in **1** is due to the disorder observed over this cation. Even splitting the position of the heavy atom As3 to treat the disorder, the decision to maintain a single position for the non-disordered phenyl rings creates this artifact.

The crystal packing of **1** relies mostly on C—H···π edge-to-face type of supramolecular interactions between the $AsPh_4^+$ cations with C···π distance in the range of 3.45(1)–4.18(2) Å [33], forming a 3D network, in a zigzag embrace with cages where the $[Nb^{V}O(C_2O_4)_3]^{3-}$ complexes and the water molecules can be found (see Fig. 2). Intriguingly, all but the disordered phenyl rings are involved in this kind of supramolecular interactions whereas it is more often to be found interacting by a mixture with π stacking, such as in the crystal packing of the trianionic transition metal complexes of formula $(PPh_4)_3[Ru(CN)_6]\cdot 2CH_2Cl_2\cdot 3CHCl_3$ [34] and $(AsPh_4)_3[Mn_3O(salox)\{Zn(N_3)_3Cl\}]$ [35] [PPh_4^+ = tetraphenylphosphonium cation and H_2salox = salicylaldoxime]. A prevalence of electrostatic interactions between the ions in **1** is observed due to the polar outer shell of the anions and the non-polar one for the cations which interacts by non-conventional C—H···O type interactions. This was observed looking at the part of the niobium(V) complex that is forced to interact with the cations which resulted to be disordered. In this respect, more than one possibility of interaction, and consequently at least two positions for these interacting atoms are allowed (which can be seen in Fig. S7 in the Supporting Information), probably because their interactions are weak and non-directional. The same is observed for the closest phenyl rings to the niobium(V) entities. The free water molecules are filling the void space, creating hydrophilic holes between the anions and they are also disordered, since there several possibilities of interaction between them and the disordered $[Nb^{V}O(C_2O_4)_3]^{3-}$ units.

The structure of complex **2** was solved at 218 K. It crystallizes in the non-centrosymmetric *P*1 space group, its chirality being caused by the packing of the solvent molecules. Three crystallographically independent $[Co(terpy)_2]^{2+}$ units (Co1, Co2 and Co3) occur in the asymmetric unit of **2** together with two $[Nb^{V}O(C_2O_4)_3]^{3-}$ entities (Nb1 and Nb2) plus three methanol and four water molecules. For the sake of simplicity, only the environments around Co1 and Nb1 of **2** will be described (see Fig. 3), the other two crystallographic independent units being very close. A perspective view of whole asymmetric unit is shown in Fig. S8 whereas selected bond lengths and angles around Co1, Co2, Co3, Nb1 and Nb2 are grouped in Table S2 in the Supporting Information).

As shown in Figs. 3 and S8, the three cobalt(II) ions are six-coordinate: six nitrogen atoms from two tridentate terpy ligands describe a distorted octahedral CoN_6 surrounding. The two niobium(V) ions (Nb1 and Nb2) are seven-coordinate with an oxo oxygen and six oxygen atoms from three different bidentate oxalate ligands describing distorted pentagonal bipyramid NbO_7. The values of the dihedral angle between the mean planes of the two chelating terpy ligands are 87.96, 89.06 and 88.55° at Co1, Co2 and Co3, respectively. The shortest distances between the crystallographically independent cobalt(II) ions occurs along the [2 1 1] direction and they are 8.728(1) (Co1···Co2), 8.597(1) (Co2···Co3) and 8.793(1) Å (Co1···Co3).

All cobalt atoms in **2** exhibit a very compressed trans N—Co—N axis involving the inner nitrogen atom of each terpy ligand (for instance, bond lengths of 1.873(6) [Co1—N2] and 1.930(6) Å [Co1—N5]). This structural feature obeys to the geometrical constraints of the tridentate terpy ligand, which subtends two fused five-membered chelate rings at the metal atom. Having this in mind, to compensate the Jahn–Teller compression effect, the axis formed by the outer nitrogen atoms of the terpy ligands have to be quite longer. So, the values of the bond distances in these directions are 2.008(5) (Co1—N1), 2.011(6) (Co1—N3), 2.150(7) (Co1—N6) and 2.161(6) Å (Co1—N4). The distortion parameter $\sum$, defined as the sum of the deviation from 90° of the twelve cis angles of the CoN_6 octahedron, is equal to 87.50°. The resulting compressed octahedral surrounding is as expected for a low-spin six-coordinate cobalt(II) ion distorted by the Jahn–Teller effect arising from the $t_{2g}^6e_g^1$ electronic configuration [36–38]. The structural parameters around Co1, Co2 and Co3 atoms in **2** at 218 K suggests a practically low-spin state for them (see Table 2 for SCO cobalt(II) complexes with terpy and related ligands).

The structure of the $[NbO(C_2O_4)_3]^{3-}$ anionic complex is very close to the previously reported for this entity in the complexes $[Ba_2(HC_2O_4)(H_2O)_3\{NbO(C_2O_4)_3\}]$ [28], $NH_4(Hdmphen)_2[NbO(C_2O_4)_3]$ [29] $[M_2(bipy)_3][NbO(C_2O_4)_3]$ [30] and $(Cat)_3[NbO(C_2O_2)_3]\cdot xH_2O$ [31,32] (dmphen = 2,9-dimethyl-1,10-phenanthroline; bipy = 2,2′-bipyridine and M = Co^{II}, Cu^{II} or Ni^{II}; Cat^+/x = Rb (I)/2 and NH_4^+/1). The coordination polyhedron around the niobium(V) ion is pentagonal bipyramidal with the double-bonded O1 oxygen atom and the O13-oxygen filling the axial positions and the O2O5O6O9O10 set of oxalate-oxygen atoms building the equatorial plane. The values of the axial Nb1—$O1_{oxo}$ and Nb1—$O13_{oxalate}$ bond lengths are 1.719(7) and 2.246(6) Å respectively, whereas the equatorial Nb1—$O_{oxalate}$ bond distances vary in the narrow range 2.110(6)–2.147(6) Å. The values of the angle subtended by the oxalate ligands at the Nb1 atom cover the range 70.66–73.37°. The niobium(V) ion of the $[NbO(C_2O_4)_3]^{3-}$ entities in **1** and **2** exhibits the same pentagonal bipyramidal NbO_7 coordination environment, but due to the disorder around the metal atom in the crystal structure of **1**, the apical Nb—O distances in this compound are slightly different from those in **2**. All other structural parameters, such as basal Nb—O bond distances, angles subtended at the metal ion by the chelating oxalate ligands and the dihedral angles between their mean planes are very close.

The crystal packing of **2** is ruled manly by π–π stacking interactions between the outer pyridyl groups of the $[Co(terpy)_2]^{2+}$ units, as shown in Fig. 4. The π–π contact distances cover the range 3.69 (1)–3.86(2) Å. A gap in the π–π stacking can also be seen in Fig. 4 between the cationic complexes of the Co3 and Co2 atoms along the [0 1 1] direction with the aromatic rings being separated by 5.24(2) Å. This leads to the packing of the 2D supramolecular

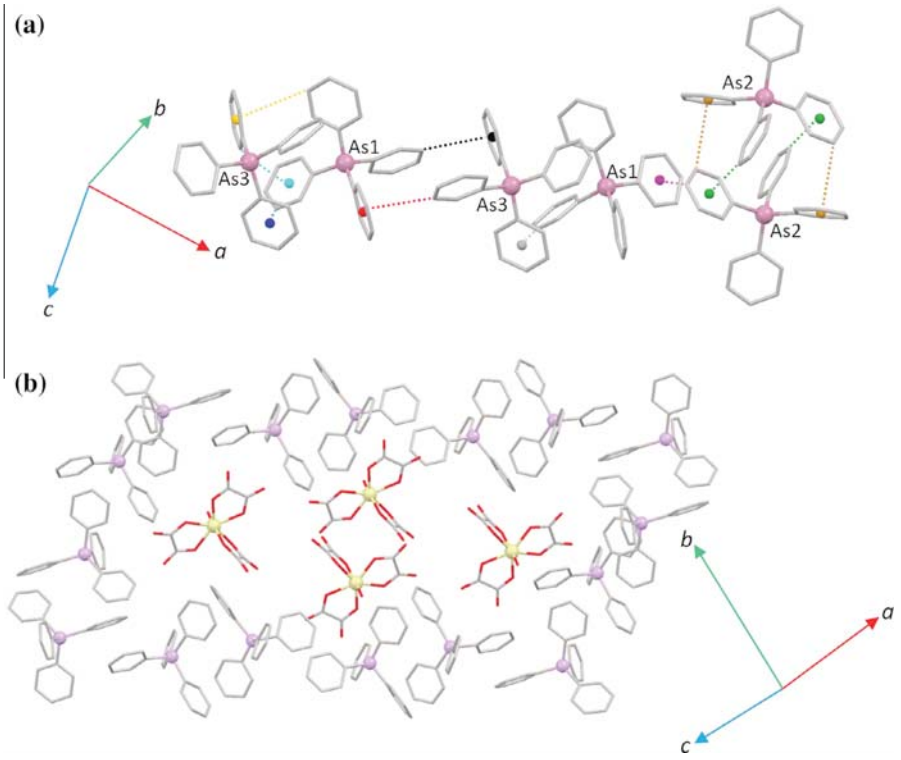

Fig. 2. (a) Crystal packing of the $AsPh_4^+$ cations by C—H···π edge-to-face interactions (doted lines) with respective values: 3.73(1) (orange), 3.77(2) (cyan), 3.85(1) (blue), 3.53 (1) (black), 3.90(3) (gray), 3.51(2) (magenta), 3.45(1) (brown) and 3.66(2) Å (green). (b) Cages formed by the packing of $AsPh_4^+$ cations filled with the niobium(V) complexes and water molecules. Crystallization solvent molecules and hydrogen were omitted for clarity. Color scheme follows that used in Fig. 1. Colour online.

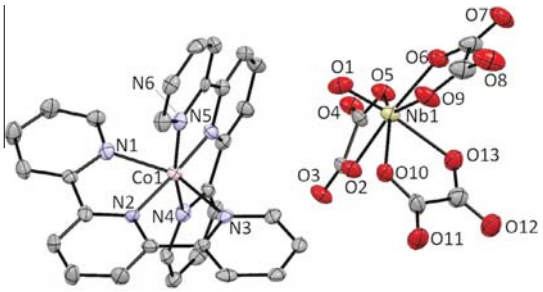

Fig. 3. Perspective view of the $[Co(terpy)_2]^{2+}$ and $[NbO(ox)_3]^{3-}$ entities of **2**. Hydrogen atoms and solvent molecules were omitted for clarity.

network down the [0 1 −1] direction creating voids that shelter the $[NbO(C_2O_4)_3]^{3-}$ anions and the solvent molecules (see Fig. S9 in the Supporting Information). The methanol and water molecules are located around the anionic oxotris(oxalate)niobate(V) entities being interlinked by hydrogen bonds.

3.3. Magnetic properties

The magnetic properties of **2** under the form of $\chi_M T$ against T plot [χ_M being the magnetic susceptibility per cobalt(II) ion] are shown in Fig. 5. $\chi_M T$ follows a Curie law in the temperature range 2.0–165 K with a value of ca. 0.41 $cm^3\ mol^{-1}$ K. Such a value is as expected for a spin doublet ($S = 1/2$ ground state with $g = 2.11$). Upon warming above 165 K, $\chi_M T$ continuously increases reaching a value of 1.46 $cm^3\ mol^{-1}$ K at 400 K. This behavior indicates the occurrence of an incomplete 1/2 (LS) ↔ 3/2 (HS) spin-crossover at 400 K. The plot of the magnetization versus the applied dc field of the sample at 2.0 K (see inset in Fig. 5) also supports a LS cobalt(II) species with the magnetization tending to saturate slightly above 1.0 Nβ under dc fields over 50 kOe.

X-band EPR measurements on a frozen dmso solution of **2** at 10.0 K shows a hyperfine splitting of $A = 80$ G in the form of eight lines due to the coupling of the $I = 7/2$ nucleus of cobalt(II), with a g value of 2.11(1) (Fig. 6). The same measurements performed on a polycrystalline sample of **2** at low temperatures consists of a quasi-isotropic feature centered at 3170 G (see Fig. S10 in the Supporting Information).

A better understanding of the spin-crossover in **2** can be achieved by the analysis of the removal of the degeneracy of the energy levels for the cobalt(II) ion, which consists of on an ^2E doublet and one $^4T_1$ quartet states, due to the combination of the spin–orbit coupling and both first- and second-order Zeeman effects (see Scheme 1).

The approach that we have used to treat the magnetic susceptibility data of complex **2** is based on the model proposed by Harris et al. [48] Taking into account the energy levels of the d^7 configuration in the crossover region for an idealized octahedral complex (Scheme 1) and following the Figgis' methodology [49] to estimate the effective magnetic moment for the $^4T_{1g}$ term, μ_{eff} ($^4T_{1g}$), and the application of the Van Vleck equation over the ^2E_g and $^4T_{1g}$ states, one obtains Eq. (1):

Table 2
Selected magneto-structural data for cobalt(II) complexes with terpy and related ligands.

Compound[a]	Spin state[b]	T X-ray (K)[c]	Co–N(central) (av. value in Å)	Co–N(distal) (av. value in Å)	∑ (in deg.)[d]	θ (in deg.)[e]	ϕ (in deg.)[f]	References
$[Co(terpy)_2]_3[NbO(C_2O_4)_3]\cdot 3CH_3OH\cdot 4H_2O$[g]	HS/LS	218	1.90	2.08	87.27	88.52	176.64	This work
$[Co(tppz)_2](tcm)_2$	HS/LS	293	1.90	2.07	81.70	86.35	179.60	[39]
$[Co(tppz)_2](PF_6)_2\cdot CH_3CN$	LS	110	1.88	2.05	85.70	79.84	180.00	[40]
$[Co(tppz)_2][BArF]_2\cdot CH_2Cl_2$	LS	110	1.96	2.07	87.00	90.00	180.00	[40]
$[Co(terpy)_2](ClO_4)_2\cdot 0.5H_2O$	HS/LS	243	2.02	2.14	109.58	90.00	180.00	[22]
$[Co(terpy)_2](BF_4)_2$	HS	270	2.04	2.15	119.99	89.55	178.22	[23]
	LS	30	1.92	2.09	89.02	88.68	178.37	
$[Co(C_{16}\text{-terpy})_2](BF_4)_2$	HS/LS	130	1.99	2.13	111.92	86.04	174.01	[41]
$[Co(C_{14}\text{-terpy})_2](BF_4)_2\cdot MeOH$	HS	190	2.03	2.15	119.31	84.89	173.68	[42]
	LS	10	1.88	2.05	91.63	85.83	175.76	
$[Co(terpyR_4)_2](PF_6)_2\cdot 3H_2O$	LS	123	1.86	1.94	75.71	89.16	178.99	[43]
$[Co(terpyR_8)_2](BF_4)_2\cdot 3H_2O$	LS	123	1.87	1.95	65.64	88.87	179.52	[43]
$[Co(tptpy)_2](BF_4)_2\cdot CH_3OH$	HS/LS(75%)	293	1.87	2.00	93.83	83.18	178.53	[44]
$[Co(qptpy)_2](BPh_4)_2\cdot 3.5dmf\cdot 2H_2O$	HS/LS(75%)	296	1.92	2.14	88.86	86.86	178.12	[44]
$[Co(4\text{-terpyridone})_2]X_2\cdot nS$								
$X = BF4^-/S = H_2O$	HS/LS	293	1.90	2.02	83.40	87.14	178.32	
$X = BF4^-/S = CH_3OH$	HS/LS	293	1.92	2.09	94.51	89.37	175.73	
$X = [SiF_6]^{2-}/S = CH_3OH$	LS	105	1.91	2.08	90.11	89.58	176.25	[45]
$X = [Co(NCS)_4]^{2-}/S = 0.5CH_3OH$	LS	293	1.86	1.95	65.28	88.02	179.54	
$X = I^-/S = 5H_2O$	LS	293	1.86	1.95	68.73	88.95	179.23	
$X = PF_6^-$	HS	293	2.03	2.16	122.93	88.60	173.17	
$[Co(HO\text{-}C_6\text{-terpy})_2](BF_4)_2\cdot H_2O$	LS	200	1.91	2.08	91.17	89.75	175.93	[46]
$[Co(HO\text{-}C_{12}\text{-terpy})_2](BF_4)_2$	LS	279	1.89	2.07	87.87	85.71	177.45	[46]
$[Co(dpzca)_2]$	HS	298	2.05	2.15	110.04	89.63	180.00	[47]
	LS	90	1.92	2.20	76.08	88.81	178.11	

[a] Abbreviations used: terpy = 2,2′:6′,2″-terpyridine; C_{16}-terpy = 4′-hexadecyloxy-2,2′:6′,2″-terpyridine; C_{14}-terpy = 40-tetradecyloxy-2,2′:6′,2″-terpyridine; $terpyR_8$ = 4″-octoxy-2,2′:6′,2″-terpyridine; $terpyR_4$ = 4″-butoxy-2,2′:6′,2″-terpyridine; tptpy = 4′-terphenylterpyridine; qptpy = 4′-quaterphenylterpyridine; tcm = tricyanomethanide; BArF = tetra(3,5-bis(triflurometyl)phenyl)borate; dmf = *N*,*N*′-dimethylformamide; HO–C_6-terpy = 4′-(6-hydroxyhexyl)-2,2′:6′,2″-terpyridine; HO–C_{12}-terpy = 4′-(6-hydroxydodecyl)-2,2′:6′,2″-terpyridine; Hdpzca = bis(2-pyrazylcarbonyl)imide.
[b] HS/LS = mixture of both spin states.
[c] Value of the temperature for the crystal structure measurement.
[d] Sum of the deviation from 90° of the 12 cis angles of the CoN_6 octahedron.
[e] Dihedral angle between the least squares planes of the two ligands.
[f] Value of the $N_{central}$–Co–$N_{central}$ angle.
[g] Mean values at the Co1, Co2 and Co3 atoms are given for this compound.

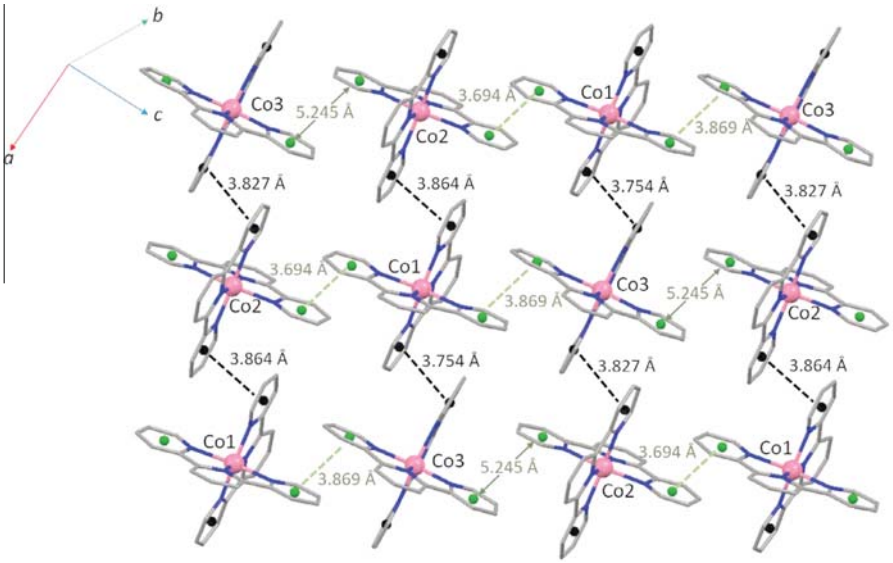

Fig. 4. A view of the 2D supramolecular network formed by π–π stacking interactions (dotted lines) among the $[Co(terpy)_2]^{2+}$ units.

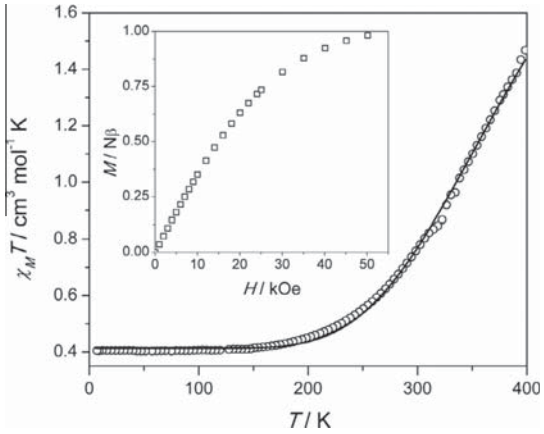

Fig. 5. $\chi_M T$ vs. T plot for **2** per cobalt(II) ion: (○) experimental; (–) best-fit curve through Eq. (1). The inset shows the M against H plot for **1** at 2.0 K.

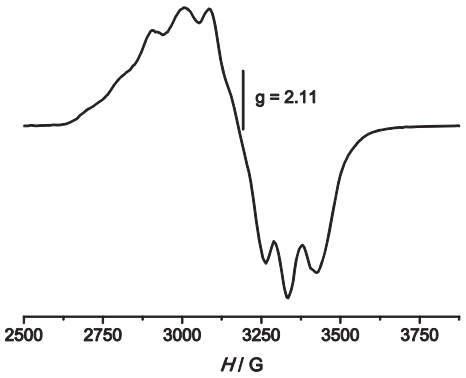

Fig. 6. X-band EPR spectrum of **2** in a frozen dmso solution at 10 K.

$$\mu_{\text{eff}}^2 = \frac{2\mu_E^2 C_{\text{vib}} + T_1\exp(y+2.5\alpha x) + T_2\exp(y+\alpha x) + T_3\exp(y-1.5\alpha x)}{2C_{\text{vib}} + \exp(y+2.5\alpha x) + 2\exp(y+\alpha x) + 3\exp(y-1.5\alpha x)} \quad (1)$$

being

$$T_1 = \frac{(5+\alpha)^2}{3} + \frac{20(2+\alpha)^2}{9\alpha x}$$

$$T_2 = \frac{2(11-2\alpha)^2}{15} - \frac{176(2+\alpha)^2}{225\alpha x}$$

$$T_3 = \frac{21(3-\alpha)^2}{5} - \frac{36(2+\alpha)^2}{25\alpha x} \quad (1a)$$

$$x = -\frac{\lambda}{kT} \qquad y = -\frac{E}{kT} \qquad \text{and} \qquad \alpha = \kappa A \quad (1b)$$

$$\mu_E^2 = 8\chi_E T = \frac{3g^2}{4} \quad (1c)$$

$$\mu_{\text{eff}}^2 = 8\chi_M T \quad (1d)$$

where μ_E is the effective magnetic moment for the ^2E_g state, assumed to be constant with the temperature [Eq. (1c)]. C_{vib} is the ratio of the vibrational partition functions in the HS and LS states. Since the metal–ligand bond distances are different in the HS and LS states (different vibrational frequencies), vibrational partition functions have to be introduced in Eq. (1) for the estimation of the relative population of the two states. In this sense, the C_{vib} parameter was introduced, where $C_{\text{vib}} = QE/QT$, QE and QT being he vibrational partition functions (for the ^2E_g and $^4T_{1g}$ states, respectively) defined by Golding et al. [50]. The other parameters are: λ is the spin–orbit coupling (about -180 cm^{-1} for the free ion); Δ is the energy gap between the ^2E_g (low spin) and $^4T_{1g}$ (high spin) states; κ is an orbital reduction parameter due to the covalency effects and A is another orbital reduction factor caused by the mixture of the ground triplet, $^4T_{1g}(4F)$ coming from ^4F term, with the excited one, $^4T_{1g}(4P)$ from the ^4P term. The value of A lies between 3/2 and 1 for the cases of weak and strong ligand field, respectively.

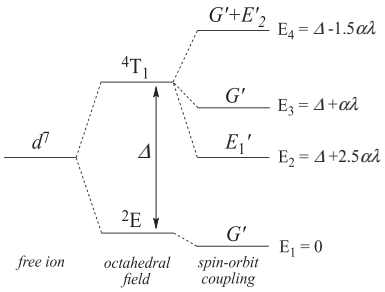

Scheme 1. Energy levels for an octahedral Co^{II} complex in the crossover region.

In the context of the proposed model, the best-fit parameters through Eq. (1) with fixed $g_{LS} = 2.11$ are: $C_{\text{vib}} = 0.0249$, $\lambda = -163$ cm^{-1}, $\alpha = 1.06$ and $\Delta = 1532$ cm^{-1}. The calculated curve matches well the experimental data in the whole temperature range investigated and the values of the best-fit parameters are in agreement with those reported for other $Co^{II}N_6$ SCO systems [39,48,51].

4. Conclusions

In summary, we show here the need to produce a non-Brønsted acid based niobium salt, in this case $(AsPh_4)_3[NbO(C_2O_4)_3]\cdot 9H_2O$ (**1**), from the commercial compound $(NH_4)_3[NbO(C_2O_4)_3]\cdot 6H_2O$ to prepare the $[Co(terpy)_2]^{2+}$ based salt $[Co(terpy)_2]_3[NbO(C_2O_4)_3]_2\cdot 3CH_3OH\cdot 4H_2O$ (**2**) containing $[NbO(C_2O_4)_3]^{3-}$ as counterion to avoid the protonation of the terpy ligand by the NH_4^+ cation in its complex formation with cobalt(II). Variable-temperature magnetic susceptibility measurements on a polycrystalline sample of **2** and EPR spectroscopy on both solid and dmso solutions of this complex revealed SCO behavior of the $[Co(terpy)]^{2+}$ unit of **2**. The LS state is achieved at $T \leqslant 200$ K and the HS configuration far from being fully populated at 400 K, with the value of $\chi_M T$ at this temperature being only 1.46 cm^3 mol^{-1} K (to be compared with values of $\chi_M T$ in the range 2.5–3.0 cm^3 mol^{-1} K in the parent terpy- and 4-terpyridone-containing complexes). We show here that the $[Nb^VO(C_2O_4)_3]^{3-}$ metalloligand appears as a suitable counterion to keep the SCO of the $[Co(terpy)_2]^{2+}$ unit. It deserves to be noted that only inorganic cations were used to achieve the charge balance of this SCO entity in the previous reports. This feature opens new perspectives towards multifunctional systems where for instance, one could try to combine the SCO behavior of the $[Co(terpy)_2]^{2+}$ cation with chiral, conducting or luminescent anionic metalloligands or well to check the systematic use of anionic metalloligands as counterions in other cationic SCO systems.

Acknowledgements

This work was supported by CAPES, CNPq, FAPEMIG (Brazil), MICINN (Spain) (Projects CTQ-2013-44844P and Unidad de

Excelencia María de Maetzu MDM-2015-0538), the Generalitat Valenciana (PROMETEOII/20147070) and the Brazilian-Spanish Project HB2014-00024. Thanks are due to Dr. Robson Monteiro and Dr. Rogério Ribas, Companhia Brasileira de Metalurgia e Mineração – CBMM for furnishing the starting oxalate-containing niobium(V) complex.

Appendix A. Supplementary data

CCDC 1454962 and 1418715 contains the supplementary crystallographic data for $(AsPh_4)_3[NbO(C_2O_4)_3]\cdot 9H_2O$ (**1**) and $[Co(terpy)_2]_3[NbO(C_2O_4)_3]_2\cdot 3MeOH\cdot 4H_2O$ (**2**). These data can be obtained free of charge via http://www.ccdc.cam.ac.uk/conts/retrieving.html, or from the Cambridge Crystallographic Data Centre, 12 Union Road, Cambridge CB2 1EZ, UK; fax: (+44) 1223-336-033; or e-mail: deposit@ccdc.cam.ac.uk. Supplementary data associated with this article can be found, in the online version, at http://dx.doi.org/10.1016/j.poly.2016.07.014.

References

[1] F.A. Cotton, M.P. Diebold, W.J. Roth, Inorg. Chem. 26 (1987) 2889.
[2] B.-L. Ooi, T. Shihabara, G. Sakane, K.-F. Mok, Inorg. Chim. Acta 266 (1997) 103.
[3] P.M. Kiernan, W.P. Griffith, J. Chem. Soc., Dalton Trans. (1975) 2489.
[4] X. Zheng, R. Bai, D. Wang, X. Cai, F. Wang, M. Xia, J. Yu, Rare Met. Mater. Eng. 40 (2011) 1871.
[5] V.K. Kharchenko, V.V. Bukhanovskii, Strength Mater. 44 (2012) 617.
[6] H. Mohrbacher, in: H. Mohrbacher, F. Siciliano (Eds.), International Symposium on Niobium Microalloyed Sheet Steel for Automotive Application; S. Hashimoto, S. Jansto, The Minerals, Metals & Materials Society, 2006.
[7] S.K. Park, Y.S. Han, Sol. Energy 110 (2014) 260.
[8] C. Granata, A. Vettoliere, M. Fretto, N. De Leo, V. Lacquaniti, J. Magn. Magn. Mater. 384 (2015) 117.
[9] C. Song, Y. Ling, Y. Feng, W. Zhou, T. Yildirim, Y. He, Chem. Commun. 51 (2015) 8508.
[10] A.M.R. Galletti, G. Pampaloni, Coord. Chem. Rev. 254 (2010) 525.
[11] T.L. Gianetti, R.G. Bergman, J. Arnold, Chem. Sci. 5 (2014) 2517.
[12] T. Murayama, J. Chen, J. Hirata, K. Matsumoto, W. Ueda, Catal. Sci. Technol. 4 (2014) 4250.
[13] B. Nowicka, T. Korzeniak, O. Stefanczyk, D. Pinkowiicz, S. Chorazy, R. Podgajny, B. Sieklucka, Coord. Chem. Rev. 56 (2012) 1946.
[14] S. Chorazy, R. Podgajny, W. Nitek, T. Fic, E. Görlich, M. Rams, B. Sieklucka, Chem. Commun. 49 (2013) 6731.
[15] D. Pinkowicz, R. Podgajny, B. Nowicka, S. Chorazy, M. Reczynsky, B. Sieklucka, Inorg. Chem. Front. 2 (2015) 10.
[16] R. Pradhan, C. Desplanches, P. Guionneau, J.-P. Sutter, Inorg. Chem. 42 (2003) 6607.
[17] S. Ohkoshi, K. Imoto, Y. Tsunobuchi, S. Takano, H. Tokoro, Nat. Chem. 3 (2011) 564.
[18] M. Juric, B. Peric, N. Brnicevic, P. Planinic, D. Pajic, K. Zadro, G. Giester, B. Kaitner, Dalton Trans. (2008) 742.
[19] M. Juric, P. Planinic, N. Brnicevic, in: T.M. Wong (Ed.), Niobium: Properties, Productions and Applications, Nova Science Publisher, Inc., 2011. Chapter 8, p. 1 and references therein.
[20] I. Krivokapic, M. Zerara, M.L. Daku, A. Vargas, C. Enachescu, C. Ambrus, P. Tregenna-Piggott, N. Amstutz, E. Krausz, A. Hauser, Coord. Chem. Rev. 251 (2007) 364. and references therein.
[21] K.S. Murray, in: M.A. Halcrow (Ed.), Spin-Crossover Materials. Principles and Applications, John Wiley & Sons, Chichester, United Kingdom, 2013, p. 35.
[22] H. Oshio, H. Spiering, V. Ksenofontov, F. Renz, P. Gütlich, Inorg. Chem. 40 (2001) 1143.
[23] C.A. Kilner, M.A. Halcrow, Dalton Trans. 39 (2010) 9008.
[24] Xcalibur CCD System, Agilent Technologies, CrysAlisPro Software System, Version 1.171.35.15, Agilent Technologies UK Ltd, Oxford, 2011.
[25] G.M. Sheldrick, Acta Crystallogr., Sect. A 64 (2008) 112.
[26] L. Palatinusz, G. Chapuis, SUPERFLIP – a computer program for the solution of crystal structures by charge flipping in arbitrary dimensions, J. Appl. Crystallogr. 40 (2007) 786.
[27] C.K. Johnson, in: F.R. Ahmed (Ed.), ORTEP, Crystallographic Computing, Copenhagen, Denmark, 1970, p 217.
[28] M. Juric, J. Popovic, A. Santic, K. Molkanov, N. Brnicevic, P. Planinic, Inorg. Chem. 52 (2013) 1832.
[29] W.X.C. Oliveira, C.L.M. Pereira, C.B. Pinheiro, J. Cano, F. Lloret, M. Julve, Chem. Commun. 51 (2015) 11806.
[30] M. Sestan, B. Peric, G. Giester, P. Planinic, N. Brnicevic, Struct. Chem. 16 (2005) 409.
[31] M. Juric, B. Peric, N. Brnicevic, P. Planinic, D. Pajic, K. Zadro, G. Giester, Polyhedron 26 (2007) 659.
[32] G. Mathern, R. Weiss, Acta Crystallogr., Sect. B 27 (1971) 1610.
[33] I. Dance, M. Scudder, Chem. Eur. J. 2 (1996) 481.
[34] M.J. Graham, J.M. Zadrozny, M. Shiddiq, J.S. Anderson, M.S. Fataftah, S. Hill, D.E. Freedman, J. Am. Chem. Soc. 136 (2014) 7623.
[35] P.L. Feng, C. Koo, J.J. Henderson, M. Nakano, S. Hill, E. del Barco, D.N. Hendrickson, Inorg. Chem. 47 (2008) 8610.
[36] H.A. Goodwin, Top. Curr. Chem. 234 (2004) 23.
[37] S.-Q. Wu, Y.-T. Wang, A.-L. Cui, H.-Z. Kou, Inorg. Chem. 53 (2014) 2613.
[38] I.A. Gass, S. Tewary, G. Rajaraman, M. Asadi, D. Lupton, B. Moubaraki, G. Chastanet, J.F. Létard, K.S. Murray, Inorg. Chem. 53 (2014) 5055.
[39] J. Palion-Gazda, A. Switlicka-Olszewska, B. Machura, T. Grancha, E. Pardo, F. Lloret, M. Julve, Inorg. Chem. 53 (2014) 10009.
[40] C.S. Campos-Fernández, B.W. Smucker, R. Clérac, K.R. Dunbar, Isr. J. Chem. 41 (2001) 207.
[41] S. Hayami, Y. Shigeyoshi, M. Akita, K. Inoue, K. Kato, K. Zsaka, M. Takata, R. Kawajiri, T. Mitani, Y. Maeda, Angew. Chem., Int. Ed. 44 (2005) 4899.
[42] S. Hayami, K. Murata, D. Urakami, Y. Kojima, M. Akita, K. Inoue, Chem. Commun. (2008) 6510.
[43] P. Nielsen, H. Toftlund, A.D. Bond, J.F. Boas, J.R. Pilbrow, G.R. Hanson, C. Noble, M.J. Riley, S.M. Neville, B. Moubaraki, K.S. Murray, Inorg. Chem. 48 (2009) 7033.
[44] Y.H. Lee, M.S. Won, J.M. Harrowfield, S. Kawata, S. Hayami, Y. Kim, Dalton Trans. 42 (2013) 11507.
[45] A. Galet, A.B. Gaspar, M.C. Muñoz, J.A. Real, Inorg. Chem. 45 (2006) 4413.
[46] Y. Komatsu, K. Kato, Y. Yamamoto, H. Kamihata, Y.H. Lee, A. Fuyuhiro, S. Kawata, S. Hayami, Eur. J. Inorg. Chem. 16 (2012) 2769.
[47] M.G. Cowan, J. Olguín, S. Narayanaswamy, J.L. Tallon, S. Brooker, J. Am. Chem. Soc. 134 (2011) 2892.
[48] C.M. Harris, T.N. Lockier, R.L. Martin, H.R.H. Patil, E. Sinn, I.M. Steward, Aust. J. Chem. 22 (1969) 2105.
[49] B.N. Figgis, Nature 182 (1958) 1568.
[50] R.M. Golding, W.C. Tennat, J.P. Bailey, M.A. Hudson, J. Chem. Phys. 48 (1968) 764.
[51] A.M. Vecchio-Sadus, Transition Met. Chem. 20 (1995) 38.

Inorganic Chemistry

Communication

pubs.acs.org/IC

Solvent-Dependent Self-Assembly of an Oxalato-Based Three-Dimensional Magnet Exhibiting a Novel Architecture

Marta Mon,[†] Thais Grancha,[†] Michel Verdaguer,[‡] Cyrille Train,[§] Donatella Armentano,*[,⊥] and Emilio Pardo*[,†]

[†]Departament de Química Inorgànica, Instituto de Ciencia Molecular, Universitat de València, 46980 Paterna, València, Spain

[‡]Institut Parisien de Chimie Moléculaire, Université Pierre et Marie Curie-Paris 6, UMR CNRS 8232, 75252 Paris Cedex 05, France

[§]Laboratoire National des Champs Magnétiques Intenses, Université Grenoble-Alpes, UPR CNRS 3228, B.P. 166, 38042 Grenoble Cedex 9, France

[⊥]Dipartimento di Chimica e Tecnologie Chimiche, Università della Calabria, 87036 Rende, Cosenza, Italy

Supporting Information

ABSTRACT: The old but evergreen family of bimetallic oxalates still offers innovative and interesting results. When $(Me_4N)_3[Cr(ox)_3]\cdot 3H_2O$ is reacted with Mn^{II} ions in a nonaqueous solvent, a novel three-dimensional magnet of the formula $[N(CH_3)_4]_6[Mn_3Cr_4(ox)_{12}]\cdot 6CH_3OH$ is obtained instead of the one-dimensional compound obtained in water. This new material exhibits an unprecedented stoichiometry with a binodal (3,4) net topology and the highest critical temperature (T_C = 7 K) observed so far in a manganese−chromium oxalate based magnet.

The synthesis of new two- (2D) or three-dimensional (3D) coordination polymers (CPs)[1] draws much attention from scientists working in different fields such as coordination chemistry, crystal engineering, and materials chemistry.[1] The interest in CPs of high dimensionality is associated with both structural and functional versatility.[2] The general use of preformed metal complexes as metalloligands[3] is an illustrative example of the so-called rational self-assembly methods. It allows for a somehow better control of both the structure and properties of the final CP, although the sensitivity to numerous parameters (solvent, temperature, counterions, etc.) leaves an open door toward structural variability.

Among the wide variety of organic ligands used to build up high-dimensional CPs, the oxalate ligand ($C_2O_4^{2-}$ = ox) merits special attention because of its large variety of coordination modes[4] and its efficiency in transmitting the exchange magnetic coupling between neighboring metal centers.[5] A careful look at the literature shows that the combination of tris(oxalate)-metalate(III) complexes together with a M^{II} ion in the presence of the appropriate templating countercation can lead to a wide range of bimetallic 2D and 3D CPs with different architectures and thrilling functionalities,[2b] as exemplified by the pioneering work of Okawa,[6a] Decurtins,[6b,c] and Coronado.[6d,e] Among other functions, they include chirality,[6f] slow magnetic relaxation,[6g] second harmonic generation,[6h] spin-crossover behavior,[6i] ferroelectricity,[6j] proton[6k,l] and electrical[6m] conductivity, and magnetic ordering.[6a−e,7]

In this work, we report the synthesis, crystal structure, and spectroscopic and magnetic properties of a new bimetallic 3D CP of the formula $(Me_4N)_6\{Mn_3[Cr(ox)_3]_4\cdot 6CH_3OH$ (**1**). Despite the existence of a good number of publications reporting bimetallic oxalate-based 2D and 3D CPs,[6,7] we show that it is still possible to discover novel architectures such as the binodal (3,4) network found in **1**. Moreover, **1** shows a long-range ferromagnetic ordering with the highest critical temperature (T_C) ever observed in a manganese−chromium oxalate based CP.[6,7a−d]

Large purple parallelepipeds of **1**, suitable for single-crystal X-ray diffraction, were grown by slow diffusion of pure methanolic solutions containing the preformed $(Me_4N)_3[Cr(ox)_3]\cdot 3H_2O$ and $Mn(NO_3)_2\cdot 4H_2O$ (see the Supporting Information). Instead, when a mixed H_2O/MeOH (1:1 volume ratio) solution under the same reaction conditions was used, a chain compound of the formula $Me_4N[Mn(H_2O)_3Cr(ox)_3]\cdot H_2O$ (**2**) was obtained.[4b] Hence, the solvent plays a key role in the molecular assembly process that leads to the formation of **1** and **2**. This is tentatively attributed to the change in the solvent polarity that modifies the hydrogen bonding and coordinating ability of the reactants. In particular, it is well-known that supramolecular interactions, such as hydrogen bonds between the water molecules and free carbonyl groups from oxalate, are enhanced in aqueous solution and favor a partial occupation of the coordination sphere of the metal ions by water molecules in **2** (Figure S1).[4b]

Compound **1** crystallizes in the polar *R*3*c* space group of the trigonal system (Table S1). The structure of **1** consists of an anionic 3D network, $\{Mn^{II}_3[Cr^{III}(ox)_3]_4\}^{6-}$, and tetramethylammonium countercations, which are hosted in the channels running along the [001] direction, together with disordered crystallization methanol solvent molecules (Figures 1, 2, and S2 and S3).

Within the anionic oxalate-bridged framework of **1**, each Cr^{III} ion is surrounded by three Mn^{II} ions, while each Mn^{II} ion is surrounded by four Cr^{III} ions, accounting for the final 4:3 Cr/Mn stoichiometry (Figure 1). Overall, the different connectivities of the Cr^{III} and Mn^{II} ions in **1**, acting as tri- and tetraconnectors,

Received: May 24, 2016
Published: July 7, 2016

DOI: 10.1021/acs.inorgchem.6b01256
Inorg. Chem. 2016, 55, 6845−6847

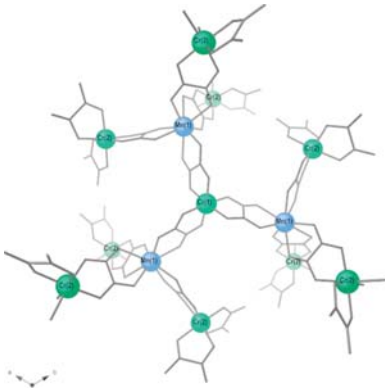

Figure 1. View of a fragment of the anionic network of **1**. Cr and Mn atoms are depicted as green and blue spheres, respectively, whereas ligands are represented by sticks.

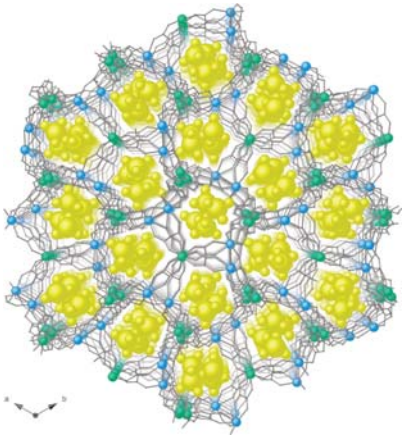

Figure 2. View along the *c* crystallographic axis of the bimetallic network of **1** showing the channels occupied by the tetramethylammonium cations (yellow spheres).

respectively, yield an unprecedented binodal (3,4) net with $(6^3)(6^3{\cdot}8^3)$ topology (Figure S2). The Cr^{III} ions are six-coordinated by three bis(bidentate) oxalate bridging ligands in a trigonally distorted CrO_6 octahedron [with an average Cr−O bond distance of 1.978(4) Å]. The Mn^{II} ions are eight-coordinated to four oxalate bridges from different $[Cr^{III}(ox)_3]^{3-}$ entities in a distorted MnO_8 square antiprism (Figure S3). Such a high coordination number for the Mn^{II} environment in **1** is rare for first-row transition-metal ions.[6k,l,7e,8] In fact, in the wide family of oxalate-bridged manganese−chromium CPs, the eight-coordination of the Mn^{II} ion is a key parameter in the observation of the original stoichiometries and topologies.[6k,l] In **1**, the Mn−O bond lengths cover a wide range of values with three short [2.177(5)−2.249(5) Å], two intermediate [2.305(4)−2.374(4) Å], two long [2.412(5)−2.414(5) Å], and one very long [2.662(5) Å] distances. This situation contrasts to that observed in previously reported oxalate-bridged manganese−chromium CPs,[6k,l] where the MnO_8 geometry is slightly less distorted, with bond lengths varying in the ranges 2.22−2.53 and 2.25−2.43 Å, respectively. Finally, the values of the Cr···Mn separations through the oxalate bridge are in the range 5.550(2)−5.674(2) Å (Figures 1 and S4).

The anionic heterobimetallic open framework of **1** shows receptor-type properties toward the Me_4N^+ cations through multiple and weak O(ox)···H−C host−guest interactions (Figures 2 and S5). Even if it was not possible to find a reasonable model for the disordered MeOH molecules (see the Supporting Information), structural analysis revealed an estimated volume of accessible solvent voids of 3500.2 $Å^3$, which represents up to 25.0% of the total unit cell volume (13997.0 $Å^3$). This feature should likely account for the cocrystallized methanol molecules embedded inside the rings, in good agreement with elemental analysis for **1**.

The solvent content of **1** was confirmed by thermogravimetric analysis (Figure S6). Moreover, the powder X-ray diffraction pattern of a polycrystalline sample of **1** is consistent with the calculated one (Figure S7), confirming the purity of the bulk material.

Figure 3a shows the thermal dependence of $\chi_M T$ for **1**, with χ_M being the molar magnetic susceptibility per Mn_3Cr_4 unit and T

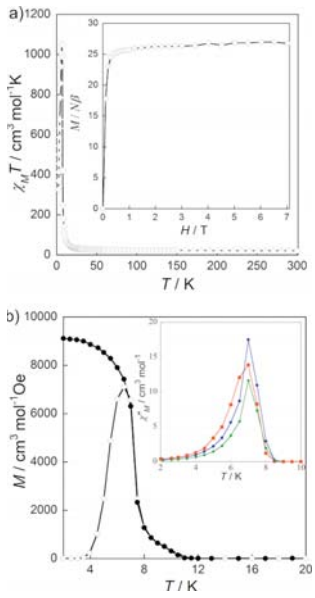

Figure 3. (a) Temperature dependence of $\chi_M T$ for **1** under an applied dc field of 100 G (T < 50 K) and 1 T ($T \geq$ 50 K). The inset shows the field dependence of M at 2.0 K. (b) FCM (●) and ZFCM (○) for **1** measured upon cooling and warming, respectively, within a field of 50 G. The inset shows the temperature dependence of χ_M'' at 100 (green), 1000 (red) and 10000 (blue) Hz.

the temperature. At room temperature, the $\chi_M T$ value is 21.13 $cm^3\ mol^{-1}$ K, which is slightly above that expected for the sum of three high-spin Mn^{II} ions ($S_{Mn} = {}^5/_2$) and four Cr^{III} ions ($S_{Cr} = {}^3/_2$), $\chi_M T$ = 20.59 $cm^3\ mol^{-1}$ K.[5] Upon cooling, $\chi_M T$ increases smoothly until ca. 15 K and then rises abruptly to reach a sharp maximum at about 7.0 K. Overall, the observed magnetic behavior is in agreement with a moderate intramolecular ferromagnetic coupling between the high-spin Mn^{II} ions and the Cr^{III} ions through the oxalate bridge, as was previously documented.[5]

DOI: 10.1021/acs.inorgchem.6b01256
Inorg. Chem. 2016, 55, 6845−6847

The observed ferromagnetic behavior is further confirmed by the M versus H plot (with M being the molar magnetization per Mn_3Cr_4 unit and H the applied direct-current magnetic field) at 2.0 K (inset of Figure 3a). The isothermal magnetization curve of **1** exhibits a very fast saturation, typical of a long-range ferromagnetic ordering, with the maximum M value of 26.8 Nβ at 7.0 T being close to that expected (M = 27 Nβ).[5] Finally, no hysteresis can be observed for **1** because it behaves as a soft magnet.[6,7]

The divergence of the field-cooled (FC) and zero-field-cooled (ZFC) magnetization curves at 7.0 K (Figure 3b) suggests the onset of a long-range ferromagnetic transition, which is ultimately confirmed by the sharp frequency-independent maxima at 7.0 K in the χ''_M versus T plots (inset of Figure 3b). Interestingly, although this ferromagnetic ordering has already been observed in other oxalate-based 2D and 3D manganese−chromium compounds, **1** exhibits a Curie temperature ($T_C \approx 7.0$ K) not only higher than that seen in other 3D manganese−chromium frameworks presenting large oxalate O−Mn distances and low-symmetry Mn^{II} ions ($T_C \approx 3.0$−4.0 K)[6e,k,7d] but also higher than those presented by the regular oxalato-based 2D manganese−chromium compounds ($T_C \approx 6$ K).[6a,c,d] This can be tentatively related to the fact that **1** exhibits the highest connectivity among all of the reported manganese−chromium networks.

In conclusion, we report the novel oxalate-based 3D magnet **1**, of the formula $[N(CH_3)_4]_6[Mn_3Cr_4(ox)_{12}]\cdot 6CH_3OH$, constructed by following a well-known metalloligand design strategy that relies on the use of the $[Cr^{III}(ox)_3]^{3-}$ complex as a ligand toward Mn^{II} ions in the presence of tetramethylammonium organic cations in a nonaqueous solvent. When the polarity of the solvent is changed, the coordination bonds are favored over hydrogen bonds during the self-assembly process, leading to the formation of a 3D coordination network originally in both stoichiometry and topology. In this network, the oxalate-bridged chains previously observed in **2** are further linked by newly formed oxalate bridges. Following its increased connectivity, this new high-dimensional open-framework magnet possesses the highest T_C reported so far for oxalate-bridged manganese(II)−chromium(III) magnets.

■ ASSOCIATED CONTENT

Supporting Information

The Supporting Information is available free of charge on the ACS Publications website at DOI: 10.1021/acs.inorgchem.6b01256.

Experimental preparation and characterization of **1**, Table S1, and Figures S1−S7 (PDF)
CCDC 1480930 (CIF)

■ AUTHOR INFORMATION

Corresponding Authors

*E-mail: donatella.armentano@unical.it (D.A.).
*E-mail: emilio.pardo@uv.es (E.P.).

Notes

The authors declare no competing financial interest.

■ ACKNOWLEDGMENTS

This work was supported by the MINECO (Spain; Projects CTQ2013-46362-P and CTQ2013-44844-P and Excellence Unit "Maria de Maeztu" MDM-2015-0538), the Ministero dell'Istruzione, dell'Università e della Ricerca (Italy), and CNRS (France). M.M. and T.G. thank the MINECO and the Universitat de València for predoctoral contracts. Thanks are extended to the Ramón y Cajal Program and the "Ayudas Fundación BBVA a Investigadores y Creadores Culturales" (to E.P.).

■ REFERENCES

(1) Batten, S. R.; Robson, R. *Angew. Chem., Int. Ed.* **1998**, *37*, 1460−1494.

(2) (a) Maspoch, D.; Ruiz-Molina, D.; Veciana, J. *Chem. Soc. Rev.* **2007**, *36*, 770−818. (b) Clemente-León, M.; Coronado, E.; Martí-Gastaldo, C.; Romero, F. M. *Chem. Soc. Rev.* **2011**, *40*, 473. (c) Grancha, T.; Ferrando-Soria, J.; Castellano, M.; Julve, M.; Pasán, J.; Armentano, D.; Pardo, E. *Chem. Commun.* **2014**, *50*, 7569−7585.

(3) Dul, M.-C.; Pardo, E.; Lescouëzec, R.; Journaux, Y.; Ferrando-Soria, J.; Ruiz-García, R.; Cano, J.; Julve, M.; Lloret, F.; Cangussu, D.; Pereira, C. L. M.; Stumpf, H. O.; Pasán, J.; Ruiz-Pérez, C. *Coord. Chem. Rev.* **2010**, *254*, 2281−2296.

(4) (a) Scott, K. L.; Wieghardt, K.; Sykes, A. G. *Inorg. Chem.* **1973**, *12*, 655−663. (b) Pardo, E.; Train, C.; Boubekeur, K.; Gontard, G.; Cano, J.; Lloret, F.; Nakatani, K.; Verdaguer, M. *Inorg. Chem.* **2012**, *51*, 11582−11593.

(5) Pardo, E.; Train, C.; Lescouëzec, R.; Boubekeur, K.; Ruiz, E.; Lloret, F.; Verdaguer, M. *Dalton Trans.* **2010**, *39*, 4951−4958.

(6) (a) Tamaki, H.; Zhong, Z. J.; Matsumoto, N.; Kida, S.; Koikawa, M.; Achiwa, N.; Hashimoto, Y.; Okawa, H. *J. Am. Chem. Soc.* **1992**, *114*, 6974−6979. (b) Decurtins, S.; Schmalle, H. W.; Schneuwly, P.; Oswald, H. R. *Inorg. Chem.* **1993**, *32*, 1888−1892. (c) Pellaux, R.; Schmalle, H. W.; Huber, R.; Fischer, P.; Hauss, T.; Ouladdiaf, B.; Decurtins, S. *Inorg. Chem.* **1997**, *36*, 2301−2308. (d) Clemente-León, M.; Coronado, E.; Galán-Mascarós, J.-R.; Gómez-García, C. J. *Chem. Commun.* **1997**, 1727−1728. (e) Coronado, E.; Galán-Mascarós, J. R.; Gómez-García, C. J.; Martínez-Agudo, J. M. *Inorg. Chem.* **2001**, *40*, 113−120. (f) Gruselle, M.; Train, C.; Boubekeur, K.; Gredin, P.; Ovanesyan, N. *Coord. Chem. Rev.* **2006**, *250*, 2491−2500. (g) Clemente-León, M.; Coronado, E.; Gómez-García, C. J.; López-Jordà, M.; Camón, A.; Repollés, A.; Luis, F. *Chem. - Eur. J.* **2014**, *20*, 1669−1676. (h) Train, C.; Nuida, T.; Gheorghe, R.; Gruselle, M.; Ohkoshi, S. *J. Am. Chem. Soc.* **2009**, *131*, 16838−16843. (i) Clemente-León, M.; Coronado, E.; López-Jordà, M.; Desplanches, C.; Asthana, S.; Wang, H.; Létard, J.-F. *Chem. Sci.* **2011**, *2*, 1121. (j) Pardo, E.; Train, C.; Liu, H.; Chamoreau, L.-M.; Dkhil, B.; Boubekeur, K.; Lloret, F.; Nakatani, K.; Tokoro, H.; Ohkoshi, S.; Verdaguer, M. *Angew. Chem., Int. Ed.* **2012**, *51*, 8356−8360. (k) Pardo, E.; Train, C.; Gontard, G.; Boubekeur, K.; Fabelo, O.; Liu, H.; Dkhil, B.; Lloret, F.; Nakagawa, K.; Tokoro, H.; Ohkoshi, S.; Verdaguer, M. *J. Am. Chem. Soc.* **2011**, *133*, 15328−15331. (l) Maxim, C.; Ferlay, S.; Tokoro, H.; Ohkoshi, S.-I.; Train, C. *Chem. Commun.* **2014**, *50*, 5629−5632. (m) Coronado, E.; Galán-Mascarós, J. R.; Gómez-García, C. J.; Laukhin, V. *Nature* **2000**, *408*, 447−449.

(7) (a) Carling, S. G.; Mathonière, C.; Day, P.; Malik, K. M. A.; Coles, S. J.; Hursthouse, M. B. *J. Chem. Soc., Dalton Trans.* **1996**, 1839−1843. (b) Mathonière, C.; Nuttall, C. J.; Carling, S. G.; Day, P. *Inorg. Chem.* **1996**, *35*, 1201−1206. (c) Coronado, E.; Galán-Mascarós, J.-R.; Gómez-García, C.-J.; Ensling, J.; Gütlich, P. *Chem. - Eur. J.* **2000**, *6*, 552−563. (d) Ballester, G.; Coronado, E.; Gimenez-Saiz, C.; Romero, F. M. *Angew. Chem., Int. Ed.* **2001**, *40*, 792−795. (e) Armentano, D.; De Munno, G.; Mastropietro, T. F.; Julve, M.; Lloret, F. *Chem. Commun.* **2004**, 1160−1161. (f) Armentano, D.; De Munno, G.; Mastropietro, T. F.; Julve, M.; Lloret, F. *J. Am. Chem. Soc.* **2005**, *127*, 10778−10779. (g) Corella-Ochoa, M. N.; Benet-Buchholz, J.; Martínez-Belmonte, M.; Galán-Mascarós, J. R. *Inorg. Chem.* **2015**, *54*, 4678−4687.

(8) (a) Rochon, F. D.; Melanson, R.; Andruh, M. *Inorg. Chem.* **1996**, *35*, 6086−6092. (b) Desjardins, S. R.; Wilcox, D. E.; Musselman, R. L.; Solomon, E. I. *Inorg. Chem.* **1987**, *26*, 288−300.

DOI: 10.1021/acs.inorgchem.6b01256
Inorg. Chem. 2016, 55, 6845−6847

Inorganic Chemistry

Article

pubs.acs.org/IC

Rational Synthesis of Chiral Metal–Organic Frameworks from Preformed Rodlike Secondary Building Units

Thais Grancha,[†] Xiaoni Qu,[†,‡] Miguel Julve,[†] Jesús Ferrando-Soria,[*,†] Donatella Armentano,[*,§] and Emilio Pardo[*,†]

[†]Departamento de Química Inorgánica, Instituto de Ciencia Molecular (ICMOL), Universidad de Valencia, 46980 Paterna, Valencia, Spain

[‡]College of Chemistry and Materials Science, Northwest University, Xi'an 710069, People's Republic of China

[§]Dipartimento di Chimica e Tecnologie Chimiche, Università della Calabria, Rende 87036, Cosenza, Italy

Supporting Information

ABSTRACT: The lack of rational design methodologies to obtain chiral rod-based MOFs is a current synthetic limitation that hampers further expansion of MOF chemistry. Here we report a metalloligand design strategy consisting of the use, for the first time, of preformed 1D rodlike SBUs (**1**) for the rational preparation of a chiral 3D MOF (**2**) exhibiting a rare **eta** net topology. The encoded chiral information on the enantiopure ligand is efficiently transmitted first to the preformed helical 1D building block and, in a second stage, to the resulting chiral 3D MOF. These results open new routes for the rational design of chiral rod-based MOFs, expanding the scope of these unique porous materials.

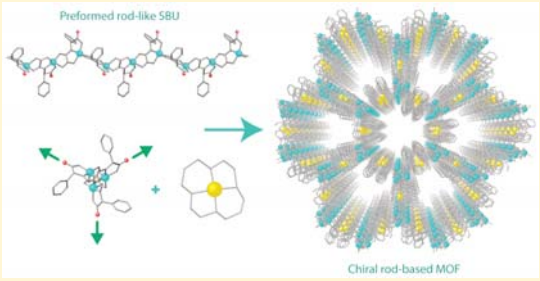

INTRODUCTION

Despite the many remarkable advances performed on metal–organic framework (MOF) chemistry,[1,2] the ability to precisely target structures on the basis of the size, shape, or chirality of the building blocks still needs further attention. This becomes especially relevant in the synthesis of both chiral MOFs and MOFs based on one-dimensional (1D) rodlike secondary building units (SBUs), as remarked recently by Yaghi et al.,[3] which represent two of the key challenges for the further development of MOF chemistry. Apart from the attractiveness of overcoming a synthetic milestone, the interest in developing synthetic strategies to target such systems stems from the plethora of properties they can accommodate. MOFs based on 1D rodlike SBUs[4] can show valuable properties for gas storage,[5] separations,[6] and catalysis[7] on the basis of their resistance to interpenetration and potential for isoreticular expansion.[8] Chiral MOFs[9] can show unique functionalities either based on chiral recognition processes[10] or derived from their noncentrosymmetric space groups.[11]

However, there is a methodological lacuna on the rational design of rod MOFs, targeting MOFs based on specific discrete SBUs, supermolecular building blocks (SBBs), and supermolecular building layers (SBLs).[12,13] The common preparation of rod MOFs have been based on trial and error experiments with symmetric homotopic linkers. Recently, some insights have been obtained into the controlled synthesis of rod MOFs with the use of a heterotritopic ligand,[3] where its asymmetric nature generates a preference for helical over straight rodlike SBUs and allow fine-tuning of the pitch of the helical SBUs in the resulting centrosymmetric MOF.

There are a reduced number of existing chiral MOFs in comparison to the huge variety of nonchiral MOFs reported so far. This is undoubtedly connected to the challenge that represents the synthesis itself. Apart from spontaneous resolution processes[14]—which mostly lead to conglomerates with a certain enantiomeric excess—the three most explored design strategies consist of (i) the presence of auxiliary induction agents,[15] (ii) the use of enantiopure ligands for their self-assembly with discrete SBUs,[16] and (iii) the use of chiral metalloligands.[17,18]

The common point of these three strategies relies on using discrete chiral subunits aimed at transmitting their encoded chiral information[19] to the final open-framework structure. The main drawback of the first two approaches, especially for the first, is that they often result in unsuccessful and poorly controlled processes. This is due to the fact that common assembly conditions are quite harsh and are affected by many subtle factors,[20] and they can lead to non-single-enantiomer chiral MOFs as a consequence of ligand racemization processes, formation of both enantiomers, or auxiliary chiral agent exclusion in the final structure. Despite these remarkable disadvantages, the ligand approach is still the most widely used. Conversely, the metalloligand approach, in addition to it being

Received: March 15, 2017
Published: May 5, 2017

DOI: 10.1021/acs.inorgchem.7b00681
Inorg. Chem. 2017, 56, 6551–6557

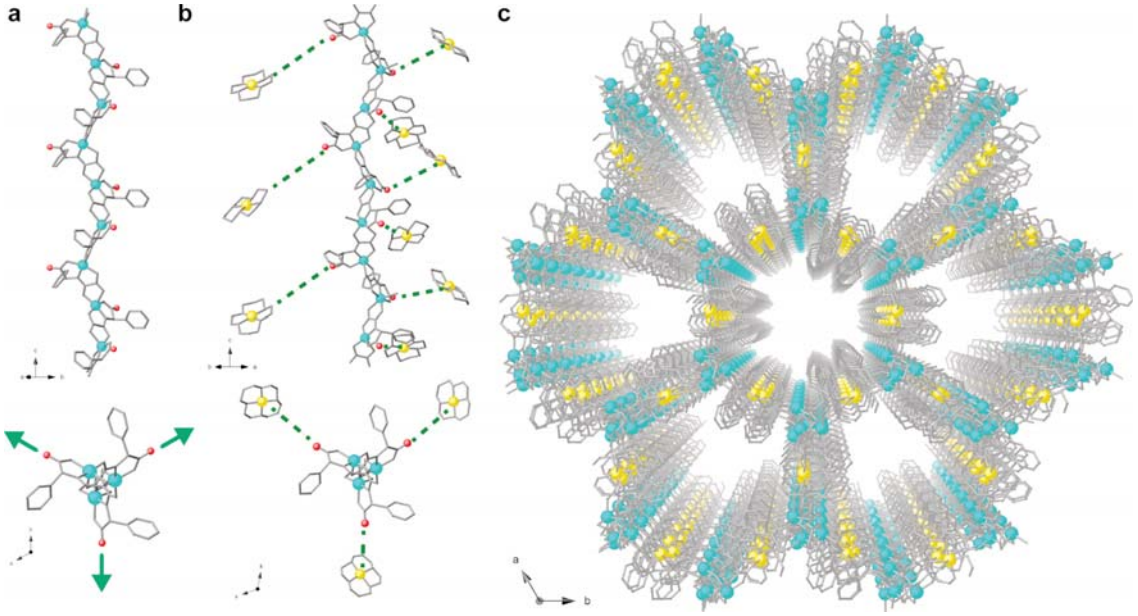

Figure 1. Chemical approach. (a) Perspective views of the precursor 1D compound **1** along the 111 (top) and 001 directions (bottom). Green arrows are depicted to emphasize the free carbonyl groups of the triconnector unit capable of further coordination. (b) Suggested self-assembling process consisting of the coordination of the free carbonyl groups of **1** toward $[Ni(cyclam)]^{2+}$ cations. Green dashed lines simulate the approach of $[Ni(cyclam)]^{2+}$ cations to the free carbonyl groups. (c) Perspective view of the 3D homochiral MOF **2**. The copper(II) and nickel(II) ions and the free carbonyl groups are represented by cyan, gold, and red spheres, respectively, whereas the ligands are depicted by gray sticks.

proven as an appealing route toward chiral assemblies, has been overlooked and, with some exceptions,[18] its study just has been practically limited to the small family of metallosalen complexes,[17] which, in addition, usually require of another ligand to build the chiral framework.

The present work aims to address simultaneously both challenges by using a metalloligand approach to build an enantiopure MOF made up of preformed helical 1D rodlike SBUs. Thus, we explore a novel rational synthetic strategy based on the use of an enantiopure ligand, derived from a amino acid, capable of building 1D chiral systems. This preformed chiral compound exhibits free carbonyl groups which can act as 1D rodlike building blocks toward square-planar metal complexes, yielding a chiral three-dimensional (3D) MOF (Figure 1). Although the deconstruction of well-known MOF structures showed infinite chains as building blocks,[4b] we show for the first time, to the best of our knowledge, the use of a preformed chiral 1D polymeric SBU for the construction of MOFs, which matches up with the SBUs of the final architecture.

RESULTS AND DISCUSSION

Here we report the synthesis of the enantiopure precursor 1D compound and the resulting chiral 3D MOF. First, the use of an oxamato-based derivative[18] of the amino acid D-phenylglycine (Scheme 1) led to one enantiopure chain of formula $Me_4N[Cu^{II}(R)\text{-pegma}]\cdot 2H_2O$ (**1**), where (*R*)-pegma = (*R*)-*N*-(ethyl oxoacetate)phenylglycine (Figure 1a). Then, the chiral 3D MOF of formula $[Ni(cyclam)][Cu^{II}(R)\text{-pegma}]_2\cdot 6H_2O\cdot 2i\text{-PrOH}$ (**2**) was obtained when the preformed compound **1** was reacted with the square-planar mononuclear cation $[Ni(cyclam)]^{2+}$ (Figure 1b,c).[21] Their chemical identities were

Scheme 1. Structural Formulas of D-Phenylglycine Methyl Ester (a) and HMeEt-(*R*)-pegma (b)[a]

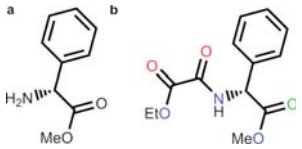

[a]Blue, red, and green colors represent the different coordination positions of the ligand.

established by the combination of EDX, elemental, PXRD, and TGA analyses (see the Supporting Information). In addition, the crystal structures of both **1** and **2** could be determined by single-crystal X-ray diffraction.

Crystal Structure. X-ray crystallography reveals that **1** crystallizes in the chiral space group $P3_1$ and consists of enantiomerically pure, oxamato-bridged Cu^{II} helical chains, Me_4N^+ cations, and H-bonded lattice water molecules (Figure 1a and Figure S1 in the Supporting Information). The single-stranded helices are arrayed in a right-handed (*P*) fashion, with a helical pitch of 14.43 Å (the *c* axis value).

Cu^{2+} metal ions adopt distorted-square-pyramidal coordination geometries, $CuNO_4$, with four oxygen atoms and one nitrogen atom from the (*R*)-pegma^{3-} ligand. Adjacent five-coordinate Cu^{II} metal ions are linked together by carboxylate and oxamidate groups of a dissymmetric (*R*)-pegma^{3-} ligand—exhibiting the alternating tridentate/bidentate bridging mode—to construct chains running along the [001] direction.

2 crystallizes in the trigonal chiral space group $P3_221$. The fundamental building unit of **2** contains right-handed Cu^{2+}

DOI: 10.1021/acs.inorgchem.7b00681
Inorg. Chem. 2017, 56, 6551−6557

chains of **1**, as simple helical SBUs, interconnected through unsaturated square-planar $[Ni(cyclam)]^{2+}$ ions, which hold chiral chains by coordinating free carbonyl groups from the phenyl-glycine amino acid residues pointing at the outside, to generate a 3D noninterpenetrating chiral porous network with 1D pseudohexagonal channels of 13 × 10 Å viewed along the [001] direction (Figures 1c and 2).

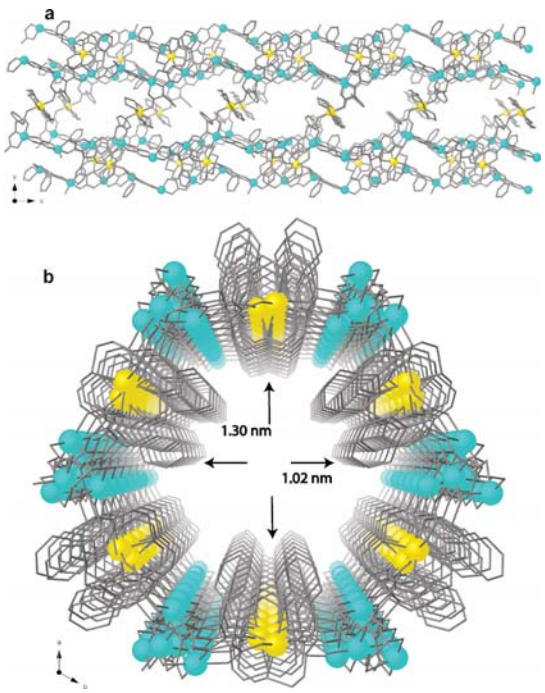

Figure 2. Representation of a pseudohexagonal nanotube-like channel of **2** of dimensions of 13 × 10 Å viewed along the [001] (a) and [100] (b) directions. Color scheme: Cu, cyan spheres; Ni, gold spheres; ligand, gray sticks.

In **2**, the $[Cu^{II}(R)\text{-pegma}]^-$ chain structure displays no evidence of remarkable changes in the structural parameters with respect to **1**. In both compounds, the five-coordinate Cu metal centers have similar Cu−O and Cu−N bond lengths (1.944(7)−2.263(7) and 1.899(8) Å (**1**) vs 1.928(6)−2.396(7) and 1.900(7) Å (**2**)). In fact, as in **1**, both Cu1 and Cu2 are sequentially linked by one bridging/bidentate carboxylate group and one bridging/tridentate oxalamino group, to form 1D motifs (Figures 1a and 3a). These trifold helical chains, all with the same handedness *P*, are brought together by $[Ni(cyclam)]^{2+}$ complexes acting as ditopic *metallolinkers* (Figure 3b,c). Thus, Ni^{2+} metal ions are coordinated by two oxygen atoms of two free carbonyl groups from consecutive phenyl-glycine amino acid residues (Ni−O bond lengths of 2.129(7) and 2.144(7) Å) and four nitrogen atoms of the cyclam ligand (Ni−N distances 1.96(2)−2.15(2) Å) in a distorted-octahedral geometry (Figure S2b in the Supporting Information).

It is notable that **2**, belonging to the rod MOF family, shows the property of "forbidden catenation".[8] The periodicity of the helical rods together with the directionality imposed by the

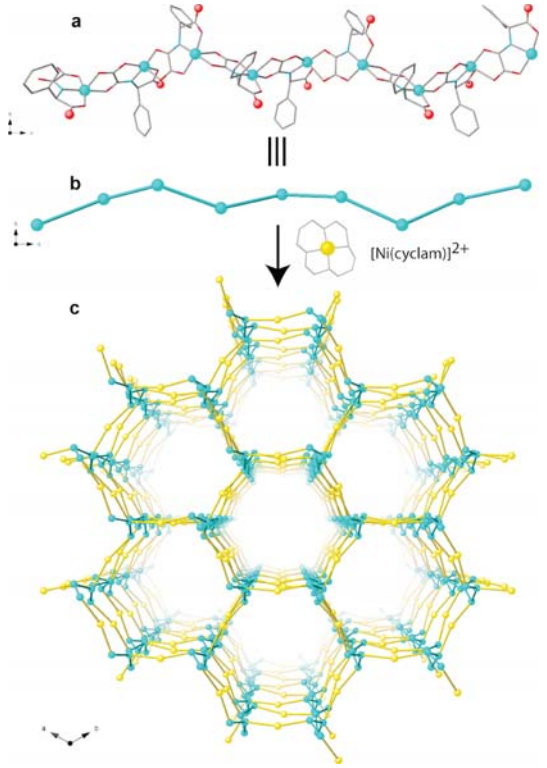

Figure 3. (a) View along the *a* crystallographic axes of $[Cu^{II}(R)\text{-pegma}]^-$ helical rod SBUs. (b) Schematic representation of trifold copper nodes. (c) View of the resulting underlying net of **2** showing **eta** topology, formed by rod, simple right-handed helical SBUs.

$Ni-O_{carboxylic}$ linkage constructs an impenetrable wall; thus, an interpenetration structure is prohibited, and a chiral architecture with hexagonal nanotube-like channels is formed. When van der Waals radii are taken into account, the pore's window diameter is 0.78 nm, which is filled by two isopropyl and six H_2O guest molecules per formula unit. Without guest molecules, the effective free volume of **2** is calculated by PLATON analysis (see the Supporting Information) to be 57.8% of the crystal volume (5692.4 $Å^3$ over the 9846.3 $Å^3$ of the unit cell volume).

Even if the structural description of a rod MOF is still rather subjective,[4b,22h] further insights into the structure of **2** can be gained by reducing multidimensional structures to simple rod geometries and associated underlying nets.[4b,8a,22] As shown in Figure 3, the $[Cu^{II}(R)\text{-pegma}]^-$ chains, constituting the rod-shaped SBUs, are already connected, as in **1**, to construct a 3_1 helix. As is known, the two ways to link 3-fold helices with one kind of vertex consist of either self-assembling of helices of the same hand to give **eta** nets or of a different hand to give **etb** nets.[4a,22e,g] In **2**, helices with structure as in **1**, all right-handed, are then linked linearly by $[Ni(cyclam)]^{2+}$ cationic complexes to generate a rare **eta** net (Figure 3 and Figure S3 in the Supporting Information),[23] which is the expected net, dependent on the rational approach we used to build an enantiopure rod-base MOF.

DOI: 10.1021/acs.inorgchem.7b00681
Inorg. Chem. 2017, 56, 6551−6557

Considering the sequential copper atoms of the rods as 3-fold connected nodes of extension and Ni^{II} metal ions as ditopic metallolinkers, the resulting structure of **2** is a 3-fold connected 3D chiral network, and its point symbol is 8^3.[4a,22e,g] Each copper atom (node) is three-coordinate, with two-coordination within the 3-fold helix and one to the metallolinker (Figure 3). Thus, the helical rod axes intersect a perpendicular plane in an **hcb** honeycomb pattern.[4b] On the other hand, the nature of the metallolinker employed to construct **2** allows us to consider the $[Ni(cyclam)(O)_2]^{2+}$ octahedra as nodes. In this case, their connections through $[Cu^{II}(R)\text{-pegma}]^-$ chains intersect a perpendicular plane to define the Kagomé pattern **kgm**[24] (point symbol 3.6.3.6), composed of hexagonal rings delimited by six triangular rings where the $[Cu^{II}(R)\text{-pegma}]^-$ helical rods reside (Figure 4).

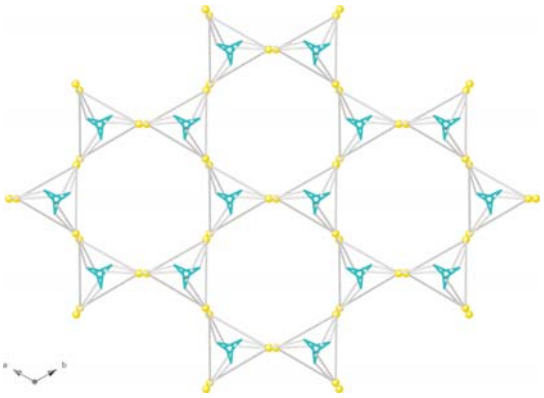

Figure 4. $[Ni(cyclam)O_2]^{2+}$ octahedra as nodes (gold spheres) in **2**, defining a Kagomé pattern, composed of hexagonal rings delimited by six triangular rings where the $[Cu^{II}(R)\text{-pegma}]^-$ helical rods (green sticks) reside.

Thermogravimetric Analysis and X-ray Powder Diffraction. The isostructurality of the bulk samples and the crystals selected for single-crystal X-ray diffraction was confirmed by powder X-ray diffraction (PXRD) experiments with a consistent experimental and calculated pattern (Figure 5). The solvent contents of **2** were assigned by thermogravimetric analysis (TGA) under a dry N_2 atmosphere (Figure S4 in the Supporting Information).

Gas Sorption Behavior. In order to further confirm the permanent porosity of the material, N_2 (77 K) and CO_2 (273 K) adsorption measurements were carried out (Figure S5 in the Supporting Information and Figure 6). Curiously, the N_2 isotherm shows a very poor uptake of ca. 1 mmol/g (Figure S5), which can be related to concomitant effects of the irregular shape of pores. In contrast, the CO_2 isotherm shows a large uptake of ca. 5 mmol/g at 1 atm (Figure 6), suggesting that the smaller and more polarizable CO_2 molecules can get into the pockets situated between the aromatic rings and interact with the many accessible copper(II) ions. The integrity of the framework after sorption measurements was proved by PXRD experiments, precluding the collapse of the framework after solvent evacuation and confirming the stability of **2** (Figure 5c).

Circular Dichroism. The enantiopure nature of both **1** and **2** was further confirmed by means of solution and solid circular dichroism (CD) spectra, respectively (Figure S6 in the Supporting Information). The similar positive Cotton effects in the visible region of the CD spectra can be attributed to copper(II) d−d transitions (the result of a chirality-induced effect on the copper centers by the enantiopure ligands), while those in the UV region can be assigned to metal-to-ligand charge-transfer (MLCT) and/or intraligand (IL) transitions.

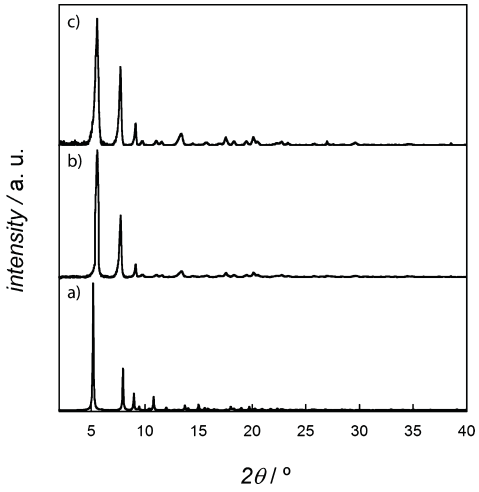

Figure 5. Calculated (a) and experimental (b) PXRD pattern profiles of **2** in the 2θ range 2.0−40.0° at room temperature. (c) PXRD pattern after sorption experiments.

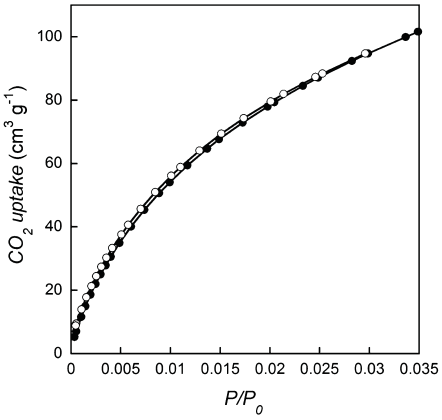

Figure 6. CO_2 adsorption isotherm for the activated compound **2** at 273 K. Filled and empty symbols indicate the adsorption and desorption isotherms, respectively.

CONCLUSIONS

In summary, we report the very first example of a design strategy to build chiral rod-based 3D MOFs from preformed helical 1D rodlike SBUs. This affords an efficient step-by-step transmission of the encoded chiral information from the enantiopure ligands to the helical 1D rodlike SBUs and then to the 3D MOF and, therefore, a better control of the nature and chiral properties of the resulting network. The validity of the proposed metalloligand approach to address simultaneously the challenge of synthesize chiral and rod-based MOFs in a

DOI: 10.1021/acs.inorgchem.7b00681
Inorg. Chem. 2017, 56, 6551−6557

controllable manner has been exemplified with the synthesis of **2**, which shows a rare **eta** net topology. These results open a new window to enlarge the scope of MOFs and allow foreseeing further synthetic efforts to expand this strategy by changing the nature of the rod and/or the metallolinker.

EXPERIMENTAL SECTION

Materials. All chemicals were of reagent grade quality. They were purchased from commercial sources and used as received. [Ni(cyclam)]Cl_2 was prepared as previously reported.[25] The preparation of the ligand is reported in the Supporting Information.

Preparation of Me_4N{Cu^{II}[(*R*)-pegma]}·$2H_2O$ (1). A methanolic solution (50 mL) of the proligand HMeEt-(*R*)-pegma (7.1 g, 26.8 mmol) was treated with a 25% methanolic solution of Me_4NOH (39.5 mL, 93.9 mmol). Another methanolic solution (10 mL) of $CuCl_2$ (3.61 g, 26.8 mmol) was then added dropwise while the reaction mixture was stirred. The resulting deep blue solution was filtered off to remove the small amount of solid particles and then concentrated to dryness in a rotary evaporator. The obtained blue powder was gently washed with acetone to remove the excess of Me_4NOH and dried under vacuum. This is the microcrystalline powder form of **1**. Yield: 8.64 g, 75%. Anal. Calcd for $C_{14}H_{22}CuN_2O_7$ (393.9): C, 42.69; H, 5.63; N, 7.11. Found: C, 42.63; H, 5.51; N, 7.14. IR (KBr): ν 1666 and 1610 cm^{-1} (C═O).

Well-formed elongated rectangular prisms of **1** were grown after several days of slow evaporation of a water/methanol solution (1/1 volume ratio) containing the solid. The crystals were collected by filtration and air-dried.

Preparation of [Ni(cyclam)][Cu^{II}(*R*)-pegma]$_2$·$6H_2O$·$2C_3H_8O$ (2). A multigram scale synthesis of **2** was carried out by the direct reaction of 1/1 water/isopropyl alcohol solutions (v/v) of compound **1** and [Ni(cyclam)]Cl_2: A 20 mL portion of the [Ni(cyclam)]Cl_2 solution (1.66 g, 5 mmol) was added dropwise over 10 mL of another solution containing compound **1** (3.94 g, 10 mmol). The resulting mixture was stirred for 1 h, and then the precipitated green polycrystalline powder was filtered off and air-dried. Yield: 4.6 g, 87%. Anal. Calcd for $C_{36}H_{64}Cu_2N_6NiO_{18}$ (1054.7): C, 41.00; H, 6.12; N, 7.97. Found: C, 41.11; H, 6.03; N, 7.84. IR (KBr): ν 1612 cm^{-1} (C═O).

Well-formed green cubic prisms of **2**, suitable for X-ray diffraction, were obtained by slow diffusion in an H-shaped tube of stoichiometric amounts of **1** in one arm and [Ni(cyclam)]Cl_2 in the other arm using the same water/isopropyl alcohol solvent. The crystals were collected by filtration and air-dried.

Single-Crystal X-ray Diffraction: X-ray Crystallographic Data Collection and Structure Refinement. Suitable crystals of **1** and **2** were selected and mounted on a MITIGEN holder in Paratone oil and very quickly placed in a liquid nitrogen stream at 90 K to avoid possible degradation upon dehydration. Diffraction data were collected on a Bruker-Nonius X8APEXII CCD area detector diffractometer using graphite-monochromated Mo Kα radiation (λ = 0.71073 Å). The data were processed through the SAINT[26] reduction and SADABS[27] multiscan absorption software. The structure was solved with the SHELXS structure solution program, using the Patterson method. The model was refined with version 2013/4 of SHELXL against F^2 on all data by full-matrix least squares.[28]

In both structures all non-hydrogen atoms were refined anisotropically except for a carbon atom of the Me_4N^+ cation (C(11)) in **1**, which is highly disordered (alert B in the checkcif, see below for details). In **2**, the use of some C−C and C−N bond length restraints during the refinements of highly disordered atoms belonging to the cyclam ligand has been reasonably imposed and related to its flexibility, making it a dynamic component of the framework. As a consequence of that disorder related to the cyclam moiety, alert A in the checkcifs was detected (see below for details).

In **1**, the hydrogen atoms of the water molecules were located on a ΔF map and refined with three restraints for each molecule (O−H and H···H distances) with thermal factors fixed to 0.06 Å^2, whereas those of the pegma ligands and Me_4N^+ cations were set in calculated positions and refined as riding atoms. In compound **2**, while the hydrogen atoms of the pegma, cyclam ligand, and isopropyl lattice molecules were set in calculated positions and refined as riding atoms. They were neither found nor located on lattice water molecules. Despite the fact that solvent molecules in **2** were highly disordered, they were somehow modeled. However, considering the quite large channels featured by this MOF, we thought that the better choice to reach the best model of the MOF net was to subtract the contribution to the diffraction pattern from the highly disordered water and isopropyl molecules located in the channels from the observed data through the SQUEEZE method, implemented in PLATON.[5] The residual agreement factors for reflections with $I > 2\sigma(I)$ before SQUEEZE are R1 = 0.0882 and wR2 = 0.2643 and after are R1 = 0.0480 and wR2 = 0.1140 (both CIF files have been supplied for the sake of clarity).

Testing the two enantiomeric models of the crystals **1** and **2** with a final refined Flack parameter of 0.05(1) shows that the handedness was uniquely determined.

A summary of the crystallographic data and structure refinement for the two compounds is given in Table S1 in the Supporting Information: CCDC 1520973−1520975 for **1**, **2_solvent**, and **2_squeezed**, respectively.

The final geometrical calculations on free voids and graphical manipulations were carried out with the PLATON[29] implemented in WinGX[30] and CRYSTAL MAKER[31] programs, respectively.

Level B alerts are suggested for the X-ray data of **1** by the PLATON/CIF check program: because of the disorder of Me_4N^+ cations, the U(eq) value for the nitrogen atom (N2; in Me_4N^+) is exceptionally large. For a similar reason, "**PLAT412** Type_2 Test for short nonbonding intra H···H contacts (involving XH3)" was also suggested. Effects such as dynamic disorder are at the origin of "**PLAT234** Type_4 Hirshfeld Rigid-Bond Test" and "**PLAT420** Type_2 Test for D-H without acceptor" related to the C8 and C9 terminal carbon atoms of the phenyl ring of the ligand and the oxygen atom of lattice water molecule O2W, respectively. "**PLAT035** Type_1 Check for _chemical_absolute_configuration" is suggested by default in relation to a value of Flack parameter (of 0.05(1)) that is not exactly zero but is very close and so is not relevant; as reported within the paper, the chemical absolute configuration of the overall structure is uniquely determined.

Two kinds of level A and B alerts are suggested for the X-ray data of **2** by the PLATON/CIF check program: because of the disorder of the cyclam moiety, U(eq) values for some carbon atoms are large and sometimes appreciably different in comparison with the average U(eq) values for non-hydrogen atoms bonded to them. For a similar reason, "**PLAT242** Type_2 Test for Unusually Low U(eq) as compared with bonded neighbors" and "**PLAT213** Type_2 Test ratio adp max/min in main residue(s)" were also suggested. As previously stated for **1**, as a level B alert, a check for chemical absolute configuration is suggested by default in relation to a value of Flack parameter (of 0.05(1)) that is not exactly 0; however, the chemical absolute configuration of the overall structure in **2** is undoubtedly determined.

X-ray Powder Diffraction. Polycrystalline samples of **2**, before and after the gas sorption experiments, were introduced into 0.5 mm borosilicate capillaries prior to being mounted and aligned on a Empyrean PANalytical powder diffractometer, using Cu Kα radiation (λ = 1.54056 Å). For each sample, five repeated measurements were collected at room temperature (2θ = 2−40°) and merged in a single diffractogram.

Thermogravimetric Analysis. The TGA measurements were carried out on a crystalline sample of **2** under a dry N_2 atmosphere with a Mettler Toledo TGA/STDA 851^e thermobalance operating at a heating rate of 10 °C min^{-1}.

Gas Sorption. Low-pressure N_2 and CO_2 adsorption isotherms at 77 and 273 K, respectively, were measured on crystalline samples of **1**−**3** on Tristar II 3020 Micrometrics equipment. Prior to the measurements, the adsorbent was outgassed at 80 °C under N_2 flow for 16 h.

DOI: 10.1021/acs.inorgchem.7b00681
Inorg. Chem. 2017, 56, 6551−6557

■ ASSOCIATED CONTENT

Supporting Information

The Supporting Information is available free of charge on the ACS Publications website at DOI: 10.1021/acs.inorgchem.7b00681.

Preparation and physical characterization data of the ligand, additional figures, and crystallographic refinement details for **1** and **2** (PDF)

Accession Codes

CCDC 1520973−1520975 contain the supplementary crystallographic data for this paper. These data can be obtained free of charge via www.ccdc.cam.ac.uk/data_request/cif, or by emailing data_request@ccdc.cam.ac.uk, or by contacting The Cambridge Crystallographic Data Centre, 12, Union Road, Cambridge CB2 1EZ, UK; fax: +44 1223 336033.

■ AUTHOR INFORMATION

Corresponding Authors

*E-mail for J.F.-S.: jesus.ferrando@uv.es; .
*E-mail for D.A.: donatella.armentano@unical.it.
*E-mail for E.P.: emilio.pardo@uv.es.

ORCID

Donatella Armentano: 0000-0002-8502-8074
Emilio Pardo: 0000-0002-1394-2553

Notes

The authors declare no competing financial interest.

■ ACKNOWLEDGMENTS

This work was supported by the MINECO (Spain) (Projects CTQ2013-46362-P and CTQ2016-75671-P and Excellence Unit "Maria de Maeztu" MDM-2015-0538), the Generalitat Valenciana (Spain) (Project PROMETEOII/2014/070), and the Ministero dell'Istruzione, dell'Università e della Ricerca (Italy). T.G. and X.Q. thank the Universitat de València and the China Scholarship Council for grants.

■ REFERENCES

(1) (a) Kitagawa, S.; Kitaura, R.; Noro, S. Functional porous coordination polymers. *Angew. Chem., Int. Ed.* **2004**, *43*, 2334−2375. (b) Furukawa, H.; Cordova, K. E.; O'Keeffe, M.; Yaghi, O. M. The chemistry and applications of metal-organic frameworks. *Science* **2013**, *341*, 1230444.

(2) (a) Long, J. R.; Yaghi, O. M. The pervasive chemistry of metal−organic frameworks. *Chem. Soc. Rev.* **2009**, *38*, 1213−1214. (b) Zhou, H.-C.; Long, J. R.; Yaghi, O. M. Introduction to Metal−Organic Frameworks. *Chem. Rev.* **2012**, *112*, 673−674. (c) Zhou, H.-C.; Kitagawa, S. Metal−Organic Frameworks (MOFs). *Chem. Soc. Rev.* **2014**, *43*, 5415−5418.

(3) Catarineu, N. R.; Schoedel, A.; Urban, P.; Morla, M. B.; Trickett, C. A.; Yaghi, O. M. Two Principles of Reticular Chemistry Uncovered in a Metal−Organic Framework of Heterotritopic Linkers and Infinite Secondary Building Units. *J. Am. Chem. Soc.* **2016**, *138*, 10826−10829.

(4) (a) Rosi, N. L.; Kim, J.; Eddaoudi, M.; Chen, B.; O'Keeffe, M.; Yaghi, O. M. Rod Packings and Metal−Organic Frameworks Constructed from Rod-Shaped Secondary Building Units. *J. Am. Chem. Soc.* **2005**, *127*, 1504−1518. (b) Schoedel, A.; Li, M.; Li, D.; O'Keeffe, M.; Yaghi, O. M. Structures of Metal−Organic Frameworks with Rod Secondary Building Units. *Chem. Rev.* **2016**, *116*, 12466−12535.

(5) (a) Caskey, S. R.; Wong-Foy, A. G.; Matzger, A. J. Dramatic Tuning of Carbon Dioxide Uptake via Metal Substitution in a Coordination Polymer with Cylindrical Pores. *J. Am. Chem. Soc.* **2008**, *130*, 10870−10871. (b) Yang, S.; Sun, J.; Ramirez-Cuesta, A. J.; Callear, S. K.; David, W. I. F.; Anderson, D. P.; Newby, R.; Blake, A. J.; Parker, J. E.; Tang, C. C.; Schröder, M. Selectivity and direct visualization of carbon dioxide and sulfur dioxide in a decorated porous host. *Nat. Chem.* **2012**, *4*, 887−894. (c) Mason, J. A.; Oktawiec, J.; Taylor, M. K.; Hudson, M. R.; Rodriguez, J.; Bachman, J. E.; Gonzalez, M. I.; Cervellino, A.; Guagliardi, A.; Brown, G. M.; Llewelyn, P. L.; Masciocchi, N.; Long, J. R. Methane storage in flexible metal−organic frameworks with intrinsic thermal management. *Nature* **2015**, *527*, 357−361.

(6) (a) Bourrelly, S.; Llewelyn, P. L.; Serre, C.; Millange, F.; Loiseau, T.; Férey, G. Different Adsorption Behaviors of Methane and Carbon Dioxide in the Isotypic Nanoporous Metal Terephthalates MIL-53 and MIL-47. *J. Am. Chem. Soc.* **2005**, *127*, 13519−13521. (b) Couck, S.; Denayer, J. F. M.; Baron, G. V.; Rémy, T.; Gascon, J.; Kapteijn, F. An Amine-Functionalized MIL-53 Metal−Organic Framework with Large Separation Power for CO_2 and CH_4. *J. Am. Chem. Soc.* **2009**, *131*, 6326−6327. (c) McDonald, T. M.; Mason, J. A.; Kong, X.; Bloch, E. D.; Gygi, D.; Dani, A.; Crocellà, V.; Giordanino, F.; Odoh, S. O.; Drisdell, W. S.; Vlaisavljevich, B.; Dzubak, A. L.; Poloni, R.; Schnell, S. K.; Planas, N.; Lee, K.; Pascal, T.; Wan, L. F.; Prendergast, D.; Neaton, J. B.; Smit, B.; Kortright, J. B.; Gagliardi, L.; Bordiga, S.; Reimer, J. A.; Long, J. R. Cooperative insertion of CO_2 in diamine-appended metal-organic frameworks. *Nature* **2015**, *519*, 303−308.

(7) (a) Fateeva, A.; Chater, P. A.; Ireland, C. P.; Tahir, A. A.; Khimyak, Y. Z.; Wiper, P. V.; Darwent, J. R.; Rosseinsky, M. J. A water-stable porphyrin-based metal-organic framework active for visible-light photocatalysis. *Angew. Chem., Int. Ed.* **2012**, *51*, 7440−7444. (b) Valvekens, P.; Vandichel, M.; Waroquier, M.; Van Speybroeck, V.; De Vos, D. An Amine-Functionalized MIL-53 Metal−Organic Framework with Large Separation Power for CO_2 and CH_4. *J. Catal.* **2014**, *317*, 1−10.

(8) (a) Rosi, N. L.; Eddaoudi, M.; Kim, J.; O'Keeffe, M.; Yaghi, O. M. Infinite Secondary Building Units and Forbidden Catenation in Metal-Organic Frameworks. *Angew. Chem., Int. Ed.* **2002**, *41*, 284−287. (b) Deng, H.; Grunder, S.; Cordova, K. E.; Valente, C.; Furukawa, H.; Hmadeh, M.; Gandara, F.; Whalley, A. C.; Liu, Z.; Asahina, S.; Kazumori, H.; O'Keeffe, M.; Terasaki, O.; Stoddart, J. F.; Yagi, O. M. Large-pore apertures in a series of metal-organic frameworks. *Science* **2012**, *336*, 1018−1023.

(9) Bisht, K. K.; Parmar, B.; Rachuri, Y.; Kathalikattil, A. C.; Suresh, E. Progress in the synthetic and functional aspects of chiral metal−organic frameworks. *CrystEngComm* **2015**, *17*, 5341−5356.

(10) Yoon, M.; Srirambalaji, R.; Kim, K. Homochiral Metal−Organic Frameworks for Asymmetric Heterogeneous Catalysis. *Chem. Rev.* **2012**, *112*, 1196−1231.

(11) Pardo, E.; Train, C.; Liu, H.; Chamoreau, L.-M.; Dkhil, B.; Boubekeur, K.; Lloret, F.; Nakatani, K.; Tokoro, H.; Ohkoshi, S.; Verdaguer, M. Multiferroics by Rational Design: Implementing Ferroelectricity in Molecule-Based Magnets. *Angew. Chem., Int. Ed.* **2012**, *51*, 8356−60.

(12) (a) Schoedel, A.; Cairns, A. J.; Belmabkhout, Y.; Wojtas, L.; Mohamed, M.; Zhang, Z.; Proserpio, D. M.; Eddaoudi, M.; Zaworotko, M. J. The asc Trinodal Platform: Two-Step Assembly of Triangular, Tetrahedral, and Trigonal-Prismatic Molecular Building Blocks. *Angew. Chem., Int. Ed.* **2013**, *52*, 2902−2905. (b) Schoedel, A.; Boyette, W.; Wojtas, L.; Eddaoudi, M.; Zaworotko, M. J. A Family of Porous Lonsdaleite-e Networks Obtained through Pillaring of Decorated Kagomé Lattice Sheets. *J. Am. Chem. Soc.* **2013**, *135*, 14016−14019.

(13) Guillerm, V.; Kim, D.; Eubank, J. F.; Luebke, R.; Liu, X.; Adil, K.; Lah, M. S.; Eddaoudi, M. A supermolecular building approach for the design and construction of metal−organic frameworks. *Chem. Soc. Rev.* **2014**, *43*, 6141−6172.

(14) Pardo, E.; Train, C.; Gontard, G.; Boubekeur, K.; Fabelo, O.; Liu, H.; Dkhil, B.; Lloret, F.; Nakagawa, K.; Tokoro, H.; Ohkoshi, S.; Verdaguer, M. High Proton Conduction in a Chiral Ferromagnetic Metal−Organic Quartz-like Framework. *J. Am. Chem. Soc.* **2011**, *133*, 15328−15331.

(15) (a) Bradshaw, D.; Prior, T. J.; Cussen, E. J.; Claridge, J. B.; Rosseinsky, M. J. Permanent Microporosity and Enantioselective

DOI: 10.1021/acs.inorgchem.7b00681
Inorg. Chem. 2017, 56, 6551−6557

Sorption in a Chiral Open Framework. *J. Am. Chem. Soc.* **2004**, *126*, 6106−6114. (b) Zhang, S.-Y.; Li, D.; Guo, D.; Zhang, H.; Shi, W.; Cheng, P.; Wojtas, L.; Zaworotko, M. J. Synthesis of a Chiral Crystal Form of MOF-5, CMOF-5, by Chiral Induction. *J. Am. Chem. Soc.* **2015**, *137*, 15406−15409.

(16) Ferguson, A.; Liu, L.; Tapperwijn, S. J.; Perl, D.; Coudert, F.-X.; Van Cleuvenbergen, S.; Verbiest, T.; van der Veen, M. A.; Telfer, S. G. Controlled partial interpenetration in metal-organic frameworks. *Nat. Chem.* **2016**, *8*, 250−257.

(17) (a) Song, F.; Wang, C.; Falkowski, J. M.; Ma, L.; Lin, W. Isoreticular Chiral Metal−Organic Frameworks for Asymmetric Alkene Epoxidation: Tuning Catalytic Activity by Controlling Framework Catenation and Varying Open Channel Sizes. *J. Am. Chem. Soc.* **2010**, *132*, 15390−15398. (b) Liu, Y.; Xi, X.; Ye, C.; Gong, T.; Yang, Z.; Cui, Y. Chiral Metal−Organic Frameworks Bearing Free Carboxylic Acids for Organocatalyst Encapsulation. *Angew. Chem., Int. Ed.* **2014**, *53*, 13821−13825.

(18) (a) Grancha, T.; Ferrando-Soria, J.; Cano, J.; Amorós, P.; Seoane, B.; Gascon, J.; Bazaga-García, M.; Losilla, E. R.; Cabeza, A.; Armentano, D.; Pardo, E. Insights into the Dynamics of Grotthuss Mechanism in a Proton-Conducting Chiral *bio*MOF. *Chem. Mater.* **2016**, *28*, 4608−4615. (b) Mon, M.; Ferrando-Soria, J.; Grancha, T.; Fortea-Pérez, F. R.; Gascon, J.; Leyva-Pérez, A.; Armentano, D.; Pardo, E. Selective Gold Recovery and Catalysis in a Highly Flexible Methionine-Decorated Metal−Organic Framework. *J. Am. Chem. Soc.* **2016**, *138*, 7864−7867. (c) Grancha, T.; Mon, M.; Ferrando-Soria, J.; Armentano, D.; Pardo, E. Structural Studies on a New Family of Chiral BioMOFs. *Cryst. Growth Des.* **2016**, *16*, 5571−5578. (d) Mon, M.; Lloret, F.; Ferrando-Soria, J.; Martí-Gastaldo, C.; Armentano, D.; Pardo, E. Selective and Efficient Removal of Mercury from Aqueous Media with the Highly Flexible Arms of a BioMOF. *Angew. Chem., Int. Ed.* **2016**, *55*, 11167−11172.

(19) Train, C.; Gruselle, M.; Verdaguer, M. The fruitful introduction of chirality and control of absolute configurations in molecular magnets. *Chem. Soc. Rev.* **2011**, *40*, 3297−3312.

(20) Cook, T. R.; Zheng, Y.-R.; Stang, P. J. Metal−Organic Frameworks and Self-Assembled Supramolecular Coordination Complexes: Comparing and Contrasting the Design, Synthesis, and Functionality of Metal−Organic Materials. *Chem. Rev.* **2013**, *113* (1), 734.

(21) Suh, M. P.; Moon, H. R. *Adv. Inorg. Chem.* **2006**, *59*, 39−79.

(22) (a) Carlucci, L.; Ciani, G.; Proserpio, D. M. In *Making Crystals by Design*; Wiley-VCH: Weinheim, Germany, 2007; pp 58−85. (b) Blatov, V. A.; Proserpio, D. M. *Modern Methods of Crystal Structure Prediction*; Oganov, A. R., Ed.; Wiley-VCH: Weinheim, Germany, 2010. (c) Hoffmann, F.; Fröba, M. In *The Chemistry of Metal-Organic Frameworks: Synthesis, Characterization, and Applications*; Wiley-VCH: Weinheim, Germany, 2016; pp 5−40. (d) Blatov, V. A.; O'Keeffe, M.; Proserpio, D. M. Vertex-, face-, point-, Schläfli-, and Delaney-symbols in nets, polyhedra and tilings: recommended terminology. *CrystEngComm* **2010**, *12*, 44−48. (e) Alexandrov, E. V.; Blatov, V. A.; Kochetkov, A. V.; Proserpio, D. M. Underlying nets in three-periodic coordination polymers: topology, taxonomy and prediction from a computer-aided analysis of the Cambridge Structural Database. *CrystEngComm* **2011**, *13*, 3947−3958. (f) Delgado-Friedrichs, O.; Foster, M. D.; O'Keeffe, M.; Proserpio, D. M.; Treacy, M. M. J.; Yaghi, O. M. What do we know about three-periodic nets? *J. Solid State Chem.* **2005**, *178*, 2533−2554. (g) O'Keeffe, M.; Yaghi, O. M. Deconstructing the Crystal Structures of Metal−Organic Frameworks and Related Materials into Their Underlying Nets. *Chem. Rev.* **2012**, *112*, 675−702. (h) Blatov, V. A. A method for topological analysis of rod packings. *Struct. Chem.* **2016**, *27*, 1605−1611.

(23) (a) Luisi, B. S.; Kravtsov, V. C.; Moulton, B. D. An (8,3)-a 3D Coordination Network and Concomitant Three-Connected Supramolecular Isomers. *Cryst. Growth Des.* **2006**, *6*, 2207−2209. (b) Chen, Z.-F.; Zhang, S.-F.; Luo, H.-S.; Abrahams, B. F.; Liang, H. $Ni_2(R^*COO)_4(H_2O)(4,4'\text{-bipy})_2$—a robust homochiral quartz-like network with large chiral channels. *CrystEngComm* **2007**, *9*, 27−29. (c) Tiliakos, M.; Katsoulakou, E.; Terzis, A.; Raptopoulou, C.; Cordopatis, P.; Manessi-Zoupa, E. The dipeptide H-Aib-l-Ala-OH ligand in copper(II) chemistry: Variation of product identity as a function of pH. *Inorg. Chem. Commun.* **2005**, *8*, 1085−1089.

(24) Barthelet, K.; Marrot, J.; Férey, G.; Riou, D. $V^{III}(OH)\{O_2C-C_6H_4-CO_2\}.(HO_2C-C_6H_4-CO_2H)_x(DMF)_y(H_2O)_z$ (or MIL-68), a new vanadocarboxylate with a large pore hybrid topology: reticular synthesis with infinite inorganic building blocks? *Chem. Commun.* **2004**, 520−521.

(25) Barefield, E. K.; Wagner, F.; Flerlinger, A. W.; Dahl, A. R. (1,4,8,11-Tetraazacyclotetradecane)Nickel(II) Perchlorate and 1,4,8,11-Tetraazacyclotetradecane. *Inorg. Synth.* **1976**, *16*, 220−225.

(26) *SAINT, version 6.45*; Bruker Analytical X-ray Systems, Madison, WI, 2003.

(27) Sheldrick, G. M. *SADABS Program for Absorption Correction, version 2.10*, Bruker Analytical X-ray Systems, Madison, WI, 2003.

(28) Sheldrick, G. M. A short history of SHELX. *Acta Crystallogr., Sect. A: Found. Crystallogr.* **2008**, *64*, 112−122. (b) *SHELXTL-2013/4*, Bruker Analytical X-ray Instruments, Madison, WI, 2013. (c) Sheldrick, G. M. Methods of space-group determination - a supplement dealing with twinned crystals and metric specialization. *Acta Crystallogr., Sect. A: Found. Adv.* **2015**, *71*, 3−8.

(29) (a) Spek, A. L. Structure validation in chemical crystallography. *Acta Crystallogr., Sect. D: Biol. Crystallogr.* **2009**, *65*, 148. (b) Spek, A. L. *Acta Crystallogr.* **1990**, *A46*, C34. (c) Van der Sluis, P.; Spek, A. L. BYPASS: an effective method for the refinement of crystal structures containing disordered solvent regions. *Acta Crystallogr., Sect. A: Found. Crystallogr.* **1990**, *46*, 194.

(30) Farrugia, L. J. WinGX suite for small-molecule single-crystal crystallography. *J. Appl. Crystallogr.* **1999**, *32*, 837.

(31) Palmer, D. *CRYSTAL MAKER*; Cambridge University Technical Services, 1996.

DOI: 10.1021/acs.inorgchem.7b00681
Inorg. Chem. 2017, 56, 6551−6557

Journal of Materials Chemistry A

PAPER

View Article Online
View Journal

Cite this: DOI: 10.1039/c7ta01179b

Tuning the selectivity of light hydrocarbons in natural gas in a family of isoreticular MOFs†

Thais Grancha,[a] Marta Mon,[a] Jesús Ferrando-Soria,*[a] Jorge Gascon,[b] Beatriz Seoane,[b] Enrique V. Ramos-Fernandez,[c] Donatella Armentano *[d] and Emilio Pardo *[a]

Received 7th February 2017
Accepted 4th May 2017

DOI: 10.1039/c7ta01179b

rsc.li/materials-a

Purification of methane from other light hydrocarbons in natural gas is a topic of intense research due to its fundamental importance in the utilization of natural gas fields. Porous materials have emerged as excellent alternative platforms to conventional cryogenic methodologies to perform this task in a cost- and energy-efficient manner. Here we report a new family of isoreticular chiral MOFs, prepared from oxamidato ligands derived from natural amino acids L-alanine, L-valine and L-leucine, where, by increasing the length of the alkyl residue of the amino acid, the charge density of the MOF's channels can be tuned (**1** > **2** > **3**), decreasing the adsorption preference towards methane over light hydrocarbons thus improving this purification process. The validity of our rational design strategy has been proved by a combination of single-component adsorption isotherms, adsorption kinetics of CH_4, C_2H_6, C_3H_8 and *n*-C_4H_{10}, and breakthrough experiments of binary CH_4/C_2H_6 and CH_4/C_3H_8 mixtures.

Introduction

Light hydrocarbons, C_1–C_4, are a basic feedstock for the chemical industry, generally obtained through steam cracking, but also present in natural gas and other less conventional gas fields.[1] The separation of the different light hydrocarbons present in natural gas is particularly important from industrial and ecological viewpoints.[2] In fact, the upgrading of natural gas is mandatory in order to fully exploit the highly abundant methane gas.[3] Currently, the purification of methane from the other light hydrocarbons in natural gas is performed by cryogenic liquefaction and fractional distillation, which represents the most cost- and energy-demanding step in the production of these important chemicals.[4] Hence, the development of new energy-efficient separation methodologies is highly desirable. Among the latest advances in implementing separation technologies,[5] adsorption on porous materials has emerged as a strong alternative to overcome the current energy penalties associated with the purification process of light hydrocarbons.[6]

Metal–Organic Frameworks (MOFs)[7–12] are a class of porous materials that provide countless applications in many fields due to the myriad of thrilling physical properties[13,14] they can offer, which are mainly associated with their porous character and rich host–guest chemistry.[15] However, in order to have the desired properties in a MOF, an accurate control of the MOF structure, and more precisely, of the size, shape and functionalization of the channels of the porous network is mandatory.[16–20] In this context, even if a total control of the structure is a challenge because of the many subtle factors that may affect the assembling process,[21] MOFs with predetermined dimensionalities and specific topologies[22,23] can somehow be designed by a careful choice of metal ions and design of organic ligands. In addition, due to their crystalline nature, X-ray crystallography allows shedding light and precisely determining their crystal structure and accordingly establishing structure-property relationships, which can be hardly done in other porous systems and explains the burgeoning growth of MOFs.[24,25]

Among the tuneable physical properties of MOFs, those regarding adsorption-based phenomena, such as gas adsorption[26,27] and separation[28,29] have attracted a lot of attention due to the global interest to move towards green economy and sustainable industrial development.[28,29] The former point can include the removal of non-desired species like toxic[30,31] and green-house[32–34] gases or the purification of desired hydrocarbons.[35–46] In particular, the most appealing strategies towards MOF-driven gas separation of light hydrocarbons consist either of a conscious design effort[46] or of the application of a post-

[a]Instituto de Ciencia Molecular (ICMOL), Universidad de Valencia, 46980 Paterna, Valencia, Spain. E-mail: jesus.ferrando@uv.es; Emilio.Pardo@uv.es

[b]Catalysis Engineering-Chemical Engineering Dept., Delft University of Technology, Julianalaan 136, 2628 BL Delft, The Netherlands

[c]Laboratorio de Materiales Avanzados, Departamento de Química Inorgánica-Instituto Universitario de Materiales, Universidad de Alicante, Alicante, Spain

[d]Dipartimento di Chimica e Tecnologie Chimiche, Università della Calabria, 87036 Rende, Cosenza, Italy. E-mail: Donatella.armentano@unical.it

† Electronic supplementary information (ESI) available: Preparation and physical characterization data. Crystallographic refinement details. Additional Fig. S1–S12 and Table S1. CCDC 1530549 and 1530550. For ESI and crystallographic data in CIF or other electronic format see DOI: 10.1039/c7ta01179b

synthetic methodology[47] in order to gain control and tune the size, shape and functionality of MOF's void channels.[16] Through these strategies, which rely on kinetic-based and/or thermodynamic-based mechanisms as well as on particular structural features, such as interpenetration or gate-opening effects, interesting light hydrocarbon separations have been performed.[48]

We show here the use of a rationally programmed method to build a new family of isoreticular MOFs,[49] consisting of the use of metalloligands with increasing length of their alkyl substituents. This method offers the possibility to finely tune the charge density of the MOF channels, by the concomitant pore size reduction and increase in the number of aliphatic residues, tailoring the kinetic adsorption selectivity of methane against other light hydrocarbons present in natural gas.[16–20] Thus, as a part of our recent research concerning the use of chiral oxamidato ligands derived from natural amino acids,[23,50–53] we report here the synthesis, crystal structures and gas sorption properties of a novel family of water-stable isoreticular chiral *bio*MOFs of general formula $\{Ca^{II}Cu^{II}_6L_3(OH)_2(H_2O)\}\cdot nH_2O$ [**1** (ref. 51): L = (*S*,*S*)-alamox = [bis[(L)-alanine]oxalyl diamide] (n = 32); **2**: L = (*S*,*S*)-valmox = [bis[(L)-valine]oxalyl diamide] (n = 13) and **3**: L = (*S*,*S*)-leumox = [bis[(L)-leucine]oxalyl diamide] (n = 11)] (see Scheme 1). These materials show very different gas sorption properties depending on the size of the aliphatic residue of the amino acid-based ligand (Scheme 1), which allows an exquisite control of the hydrophobicity of the channels and thus of the kinetic adsorption selectivity of methane from other components of natural gas.

Results and discussion

Preparation and X-ray crystal structures

2 and **3** were prepared as reported earlier for **1**.[51] Slow diffusion of aqueous solutions of the corresponding bis(hydroxo)dicopper(II) complex precursor, $(NMe_4)_2\{Cu_2L(OH)_2\}\cdot nH_2O$, and $CaCl_2\cdot 4H_2O$ (3 : 1 molar ratio) in a H-shaped tube at room temperature yielded blue/green elongated hexagonal prisms in all cases (see the ESI†).

The structures of **2** and **3** could be also determined by X-ray diffraction on single crystals. **1–3** are isomorphous and crystallize in the chiral $P6_3$ space group of the hexagonal system (Table S1†). Their structures can be described as chiral 3D calcium(II)-copper(II) networks with a uni-nodal six-connected acs net,[54,55] with the point symbol of $(4^9.6^6)$. Within the networks, the dicopper units, $[Cu^{II}_2L(OH)_2]$, connect the Ca^{II} ions through their carboxylate groups. Three aqua/hydroxo molecules (with 1 : 2 statistical distribution) coordinated in a μ_3 fashion, are also involved (Fig. 1, S1 and S2†). As a result, the Ca^{II} ions are nona-coordinated in a distorted monocapped square antiprism geometry.

The 3D $Ca^{II}Cu^{II}_6$ networks in **1–3** exhibit a honeycomb-like hexagonal architecture, giving rise to relatively large hexagonal channels along the *c* axis (Fig. 2). The Ca^{II} ions occupy the vertices of each hexagonal channel, with the adjacent Ca···Ca distance, constituting the edge of each ring, being 12.187(1), 12.122(4) and 12.076(4) Å for **1–3**, respectively. In turn, the square pyramidal or square Cu^{II} ions situate along the edges of the channels (Fig. 2 and S1†).

The most striking structural feature of this series of isoreticular compounds arises from the orientation of the amino acid residues pointing inwards the hexagonal channels and interstitial voids (Fig. 2, bottom and S1, S3–S8†). Methyl groups in **1** and isopropyl chains in **2** both show a medium to a regular distended conformation. In contrast, only one of the two isobutyl residues exhibits a distended conformation inwards the pores in **3** (Fig. S2†). Leucine residues being more hydrophobic and longer and so more hindered than other residues, most likely prefer to be buried in large space to reach the more stable folding, forcing one of the flexible isobutyl chains to adopt a highly bent conformation with their methyl groups pointing outward the pores (Fig. S2c†). For a structure-property relationship, it might be of interest to underline that the great framework flexibility, verified in particular in the longer amino acid side chains isopropyl (**2**) and isobutyl (**3**), undoubtedly will influence the diffusion of gases in the pores. Thus, it must be one of the synergic factors to take into account when aiming at achieving

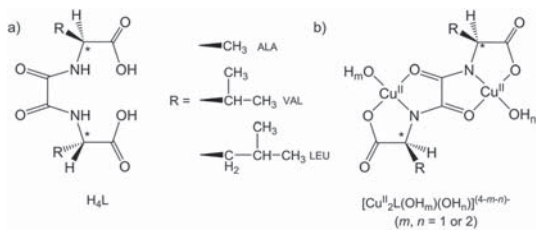

Scheme 1 (a) Chemical structures of the chiral bis(amino acid)oxalamide ligands emphasizing the increasing size of the amino acid residue in the series alanine, valine, and leucine and (b) the corresponding dianionic bis(hydroxo)dicopper(II) complexes.

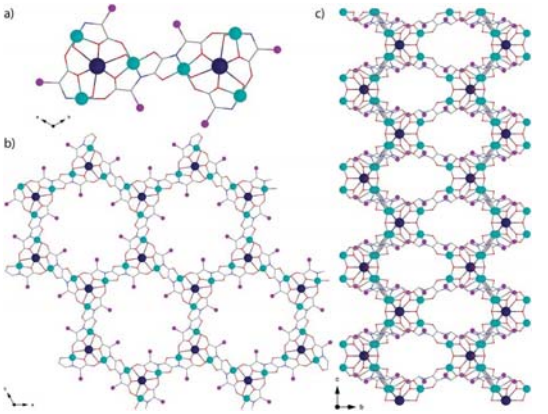

Fig. 1 (a) Common dicopper(II) building blocks in **1–3**. Views of **1–3** in the *ab* (b) and *bc* (c) planes, respectively. Copper and calcium atoms are represented by cyan and blue spheres, respectively, whereas the ligands are depicted as sticks (carbon: grey, oxygen: red and nitrogen: blue). The purple spheres represent the amino acid residues (see Scheme 1).

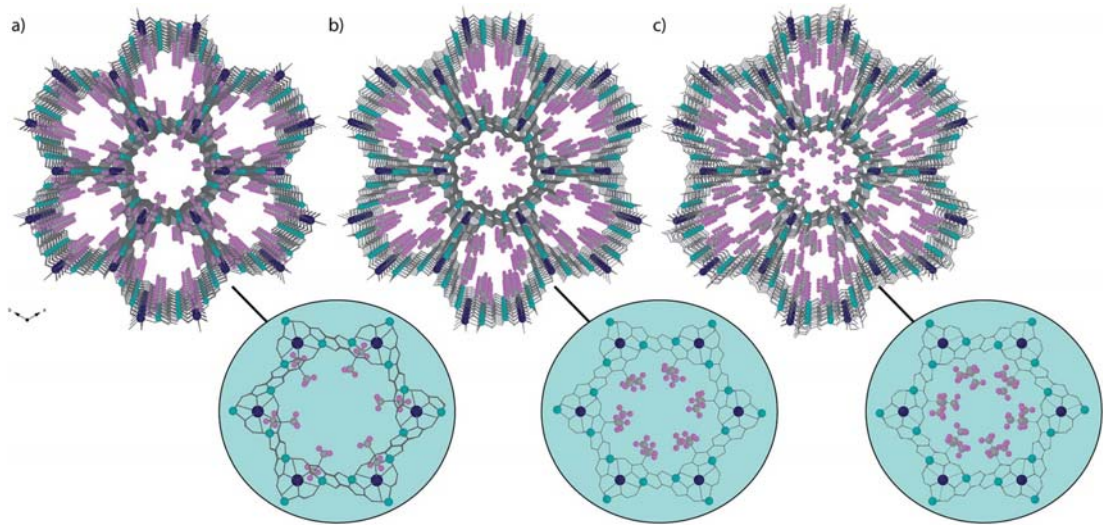

Fig. 2 (a) Perspective views along the crystallographic *c* axis of the porous structures of **1** (a), **2** (b) and **3** (c), determined by single-crystal X-ray diffraction, emphasizing the different alkyl groups in the boxed structures. Copper and calcium atoms are represented by cyan and blue spheres, respectively. The alkyl residues of the amino acids are shown as balls and sticks, whereas the remaining carbon, nitrogen and oxygen atoms from the ligand are shown as sticks. Free water solvent molecules are omitted for clarity.

a fine control on the selectivity and separation of, for example, methane in natural gas. In particular, the X-ray structure reveals a high thermal motion of the carbon atoms belonging to the leucine amino acid residues in **3**. This is enough to suppose a further optimization of the more stable side-chain conformation, thus enhancing efficient host–guest interactions or allowing also opportunistic hopping of these gases along the pores.

Because of the different sizes of the hydrophobic methyl (**1**), isopropyl (**2**) and isobutyl (**3**) groups, the resulting channels possess varying virtual diameters of *ca.* 1.0 (**1**), 0.75 (**2**) and 0.5 (**3**) nm (Fig. S3–S8†). Hence, in a static view, the pore-limiting diameters of the crystal structures are large enough to permit, in principle, the diffusion of different light hydrocarbons (*vide infra*) such as methane (CH_4), ethane (C_2H_6), ethylene (C_2H_4), propane (C_3H_8), propylene (C_3H_6) and butane (n-C_4H_{10}) which have related estimated kinetic diameters increasing from 3.8 Å for CH_4 up to 4.7 Å for n-C_4H_{10}.[28] The increasing degree of hydrophobicity together with the decreasing size of the pores account for the contents of free water molecules [32 (**1**), 13 (**2**) and 11 (**3**)]. This increasing charge density at the channels from **1** to **3** also suggests different functionalities of the channels and is reflected in the gas adsorption of light hydrocarbons (see below). Finally, the estimated empty volumes for **1–3** without the crystallization water molecules are 2089.1 (**1**), 1532.6 (**2**) and 1312.0 (**3**) $Å^3$, values which represent *ca.* 58.0, 43.4 and 37.5%, respectively, of potential void per unit cell volume [$V = 3604.1$ (**1**), 3529.7 (**2**) and 3501.0 (**3**) $Å^3$] (Fig. S3–S8†).

Thermogravimetric analysis and X-ray powder diffraction

The thermogravimetric analyses (TGA) under a dry N_2 atmosphere indicated the water contents of **1–3** (Fig. S9†). The mass loss values of *ca.* 31.5 (**1**), 15 (**2**), and 12% (**3**) at 150 °C are consistent with 32, 13, and 11 H_2O molecules per formula unit, respectively. Even if the larger pores in **1** undoubtedly influence the very large number of water molecules that its channels can accommodate, these results already suggest the very different hydrophobicity of the members of the family. Therefore, the number of crystallization water molecules filling the pores of **2** and **3** is drastically reduced compared to that of **1** as a consequence of their much larger alkyl chains and the resulting more hydrophobic environment.

The powder X-ray diffraction (PXRD) patterns of polycrystalline samples of **1–3** at room temperature (Fig. 3) confirm the pureness of the bulk samples with a consistent match between the experimental and calculated PXRD patterns.

Gas sorption properties

All samples of **1–3** were activated by immersion in methanol and then desolvated at 80 °C under reduced pressure for 24 h prior to the sorption measurements. Nitrogen adsorption isotherms at 77 K for **1–3** (Fig. 4) show fully reversible type I isotherms, characteristic of microporous materials with permanent microporosity, with estimated[56] Brunauer–Emmett–Teller (BET) surface areas [1015 (**1**), 561 (**2**), and 312 $m^2\ g^{-1}$ (**3**)] following the trend **1** > **2** > **3**, as expected from their decreasing pore size (estimated from the crystal structures). The analyses of the N_2 isotherm curves using the Horvath–Kawazoe model[57] reveal a microporous pore size distribution for **1–3** [1.08 (**1**), 0.68 (**2**), and 0.42 nm (**3**)], which are similar to those determined from the crystal structure and preclude assigning of the slight increase near saturation pressure to mesoporosity or N_2 condensation in the inter-particle space. In turn, it has been

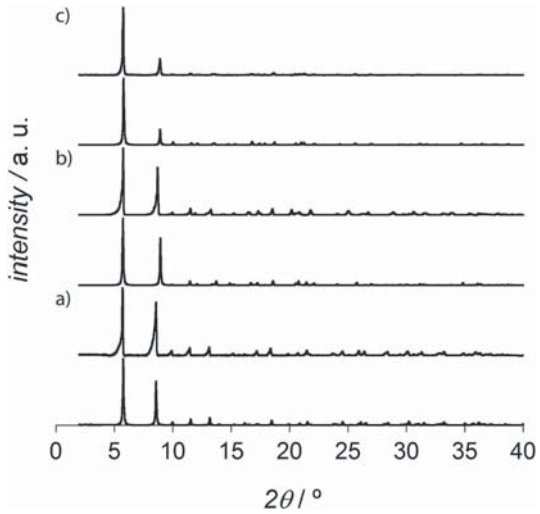

Fig. 3 Calculated (bottom) and experimental (top) XRPD pattern profiles of polycrystalline samples of **1** (a), **2** (b) and **3** (c) measured in the 2θ range 2.0–40.0° at r.t.

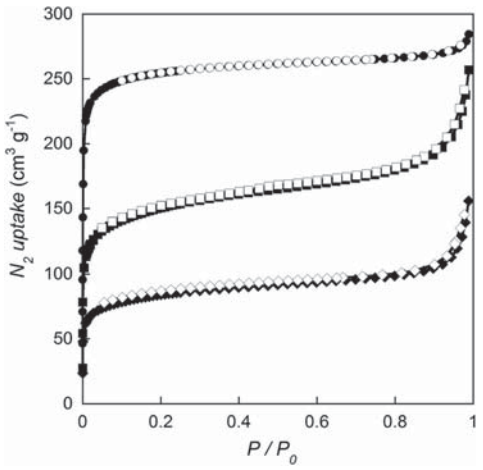

Fig. 4 N_2 sorption isotherms of the activated compounds **1** (○), **2** (□) and **3** (◇) at 77 K. Filled and empty symbols indicate the adsorption and desorption isotherms, respectively.

attributed to capillary condensation. The same behaviour was observed for the CO_2 adsorption isotherms, with a decrease in the gas uptake at 1 bar and 273 K [106.0 (**1**), 44.1 (**2**), and 22.3 $cm^3\ g^{-1}$ (**3**)] with increasing the length of the amino acid residue (Fig. S10†).

Once demonstrated the permanent microporosity of **1–3** as well as their different pore windows depending on the amino acid residue filling the cavities, we studied the performance of this family in the adsorption of different light hydrocarbons such as methane (CH_4), ethane (C_2H_6), ethylene (C_2H_4), propane (C_3H_8), propylene (C_3H_6) and butane (n-C_4H_{10}). So far, several adsorption studies have been carried out, for different MOFs, aiming at evaluating the adsorptive properties towards different olefins and paraffins.[35–46] This is commonly done by measuring single-component adsorption isotherms, as well as simulating mixed gas adsorption isotherms with the ideal adsorbed solution theory[58] or transient breakthrough[59] and/or, less frequently, by performing breakthrough experiments.[43,45,60–66] In particular, relevant to our study are the different reported MOFs performing separation of CH_4 from C_2, C_3 or C_4 hydrocarbons.[43,45,60–66] In these studies, they use bulky aromatic groups,[45] nitrogen donor moieties[43,65] and pendant C_3 alkoxy groups with various degrees of branching and saturation,[67] and/or coordinatively unsaturated metal sites[62] to increase the charge density of the channels, and consequently increase the interaction of C_{2+} hydrocarbons with the MOF's pores. However, **1–3** offer unique possibilities towards evaluating the real impact of the length of the alkyl side chains occupying the channels in the adsorption of different light hydrocarbons. Indeed, this is the first experimental study in which a family of isoreticular MOFs exhibiting different alkyl-functionalized pores is used to rationalize these adsorptive properties. Thus, the systematic variation of the length of the aliphatic residue will allow us to evaluate at the same time the influence of different parameters such as the pore window, hydrophobicity, kinetics and alkyl interactions in the adsorption, and consequently the selectivity towards light hydrocarbons in **1–3**.

Therefore, adsorption isotherms of light paraffins, CH_4, C_2H_6, C_3H_8 and n-C_4H_{10}, were first measured for **1–3** up to 1 bar at 273 K (Fig. 5). The adsorption capacities at 1 bar follow the same trend for **1–3**. An increase in adsorption capacities with the carbon chain length was observed, following the sequence $CH_4 \ll C_2H_6 < C_3H_8 < n$-$C_4H_{10}$, as a result of the enhancement of interactions with the side chain of the MOF. The only exception is n-C_4H_{10} in compound **1**, which adsorbs a slightly higher C_3H_8 amount at 1 bar. This could be related to a less efficient packing of n-C_4H_{10} with respect to C_3H_8 molecules together with the lack of stabilizing interactions between the alkyl chains of the gas and those of the walls of **1** (instead present in **2** and **3**), which starts to have a non-negligible effect on the adsorption process. In addition, the slope in the C_2H_6, C_3H_8 and n-C_4H_{10} adsorption isotherms, especially the latter two, becomes much steeper (Fig. 5), which is a clear marker of a stronger affinity between larger hydrocarbons and the pore surface in **1–3**. Interestingly, C_2H_6/CH_4 and C_3H_8/CH_4 adsorption ratios, in other words, ideal selectivities, at 1 bar (Fig. 5) also follow the sequence **1** (3.69 and 4.29) < **2** (4.45 and 5.57) < **3** (4.51 and 5.64), suggesting that the larger is the alkyl group decorating the MOF (**1** < **2** < **3**), the larger is the separation equilibrium between methane and the other hydrocarbons in the binary mixture.

The adsorption capabilities of **1–3** for olefins, C_2H_4 and C_3H_6 were also evaluated and are gathered, together with paraffins, in Fig. S11.† The C_2H_4 adsorption isotherms of all three compounds are identical to the C_2H_6 ones. In turn, the amounts of C_3H_6 adsorbed by **1–3** are significantly higher than those observed in the case of C_3H_8, which may be due to the stronger

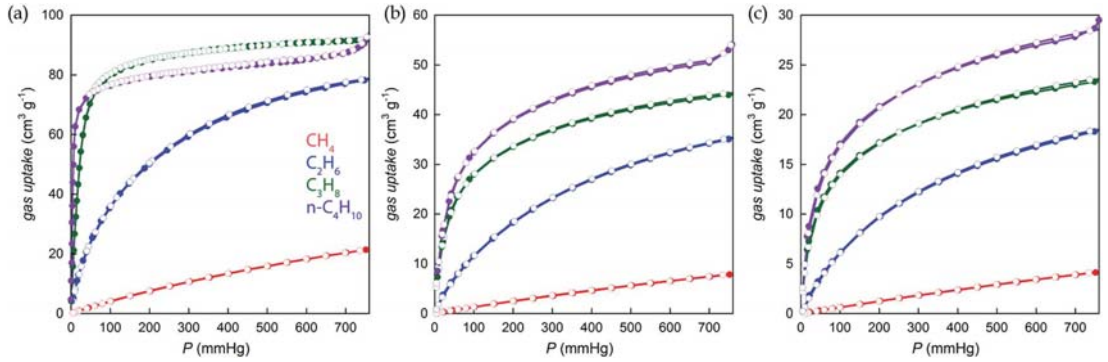

Fig. 5 CH_4 (red), C_2H_6 (blue), C_3H_8 (green) and C_4H_{10} (purple) adsorption isotherms of **1** (a), **2** (b), and **3** (c) at 273 K. Filled and empty symbols indicate the adsorption and desorption isotherms, respectively.

interaction of the π-bonding orbital of C_3H_6 with open metal sites and its smaller kinetic diameter.[39]

In view of the results shown in Fig. 5, and aiming at further confirming the effect of the increasing size of the alkyl chains in this new family of isoreticular MOFs on the adsorptive properties, kinetic adsorption of CH_4, C_2H_6, C_3H_8 and *n*-C_4H_{10} was performed (Fig. 6), which assesses how fast hydrocarbons are adsorbed. A non-negligible impact on the kinetic adsorption was observed for the different adsorbates as we move from **1** to **3**. The adsorbed amount of *n*-C_4H_{10} with respect to C_3H_8 changes from being almost equal for **1**, to be significantly higher in **2**, as a consequence of the higher number of aliphatic carbons able to interact with *n*-C_4H_{10}. However, these amounts tend to be similar in the case of **3**, probably due to the smaller window size of the MOF. It is noteworthy that the adsorbed amount of C_2H_6 with respect to CH_4 shows a considerable increase as we move in the series **1–3**. Thus, the larger the alkyl side chain in the surface of the pores (**1** < **2** < **3**), the lower the amount of CH_4 adsorbed by the MOF. This is especially relevant for **3**, which hardly adsorbs CH_4. These results (Fig. 6) further confirm the trend observed in the adsorption isotherms (Fig. 5) and even suggest higher mixture selectivities for methane with respect to other light hydrocarbons present in natural gas. Finally, the adsorption isotherm measurements collected in Fig. S11† also showed a certain selectivity for C_3H_6 *vs.* C_3H_8. Therefore, the kinetic adsorption of C_3H_6 was also evaluated and compared with that of C_3H_8. However, even if Fig. S12† shows a higher adsorption of C_3H_6 (especially for compound **2**), this small selectivity is not reflected on the time required to adsorb both gases in the kinetic experiments and does not allow the prediction of a successful separation and thus, breakthrough experiments were not carried out for these gases. The different experimental conditions used in the adsorption isotherms (long waiting times until reaching equilibrium) and the kinetic adsorption experiments (these experiment only measure the very beginning of the adsorption event) are at the origin of the apparent divergences observed on the adsorbed amounts between both experiments.

Overall, these results indicate that even if the pore window is key to explain the trend **1** > **2** > **3** in the adsorption capacities of this family, side-chain interactions between alkyl groups from both, gases and MOF walls, lie at the origin of their different selectivities. The very different uptake results for **1–3** clearly evidence that playing with the 'pore-limiting diameter' concept,

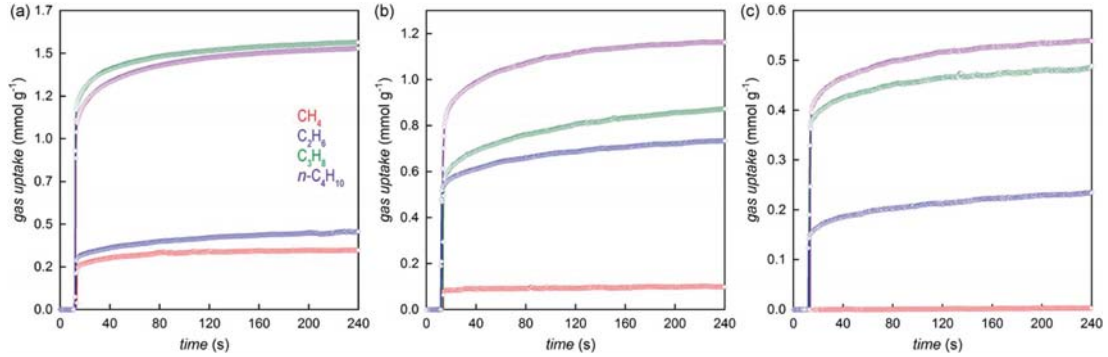

Fig. 6 Adsorption kinetic profiles of CH_4 (red), C_2H_6 (blue), C_3H_8 (green) and C_4H_{10} (purple) for compounds **1** (a), **2** (b) and **3** (c) at 273 K.

through the increase of the length of aliphatic side chains residing in the pores, does not only modify the sorption capacity of a given material but, more importantly, also affect the kinetics of adsorption, which is of paramount relevance in order to perform separations under standard-flow conditions in industries.

In light of the results above, to investigate the practical separation performance of this family as well as to confirm the validity of our approach to tune the MOF selectivities, breakthrough experiments were carried out at 298 K and 1 bar for binary mixtures of CH_4/C_2H_6 (75/25) and CH_4/C_3H_8 (75/25) using packed columns (*ca.* 1 g) of **1** and **3** (Fig. 7) as stationary phases and a total gas flow of 2 cm^3 min^{-1}. H_2 is used as the internal reference gas because it is not adsorbed under these conditions. In this way we can track the flow dispersion through the column.[68] CH_4 for sample **3** breaks at the same time as H_2, following the same profile (Fig. 7, bottom) and indicating non-uptake of CH_4 on this material. In contrast, C_2H_6 and C_3H_8 break much later, suggesting an almost infinite selectivity for the C_2H_6/CH_4 and C_3H_8/CH_4 separation. In case of **1**, CH_4 breaks later than H_2 (Fig. 7, top), suggesting a quantitative CH_4 adsorption and pointing towards a reduction of the selectivity for separating C_2H_6/CH_4 and C_3H_8/CH_4 mixtures. The lower slope of the breakthrough profile of **3** with respect to **1** can be attributed to the different flow regime through the bed. In the case of compound **1**, it is closer to a plug flow than in the case of compound **3**. In order to measure the non-ideality of the flows, we use H_2 as the internal reference since H_2 is not adsorbed under these conditions and the profile of the H_2 flow is due to the dispersion of the bed. As it can be seen in Fig. 7, the fluid-dynamics are different in both beds but the retention times are reliable as H_2 is used as the internal reference. Overall, as expected from the kinetic measurements, better separations of CH_4 from C_3H_8 and, especially, from C_2H_6 were observed for compound **3**. Yet, the differences in the C_3H_8–CH_4 and C_2H_6–CH_4 retention times were increased by *ca.* 5 and 30 min, respectively.

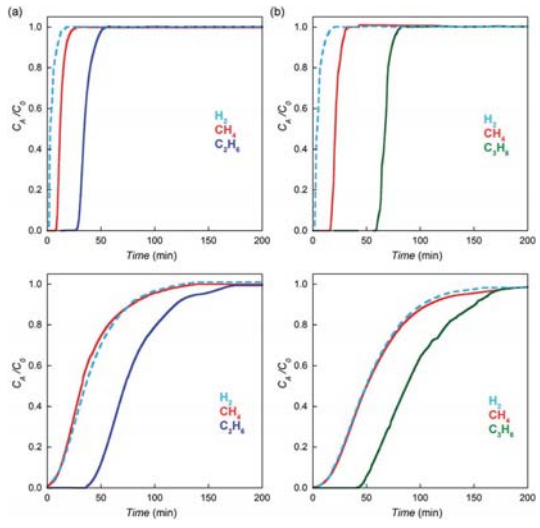

Fig. 7 Experimental column breakthrough curves of (a) CH_4/C_2H_6 (75 : 25, v/v) and (b) CH_4/C_3H_6 (75 : 25, v/v) gas mixtures measured at 298 K and 1 bar in a column using **1** (top) and **3** (bottom) as stationary phases. The total gas flow is 2 cm^3 min^{-1} in each case. H_2 was used as the reference gas.

Conclusions

In summary, we have reported a unique family of robust, cheap and easy to prepare on a large scale isoreticular MOFs. These porous materials, showing overall good results in gas adsorption and separation, were prepared rationally from oxamidato ligands derived from natural amino acids L-alanine, L-valine and L-leucine. Moreover, they offer the perfect playground to study how tuning of the length of the alkyl residues present in the channels of the MOFs modifies the gas adsorption capacities and selectivities towards different sized hydrocarbons. Overall, we observed that the higher was the length of the alkyl residue decorating the MOF walls, the lower was the affinity towards methane. As a consequence, we were able to control the kinetic adsorption selectivity of methane *versus* other light hydrocarbons present in natural gas, offering new rational ways for its purification.

Acknowledgements

This work was supported by the mineco (Spain) (Projects CTQ2013-46362-P, MAT2013-45008-P, MAT2016-81732-ERC, CTQ2016-75671-P and Excellence Unit "Maria de Maeztu" MDM-2015-0538), the Generalitat Valenciana (Spain) (Project PROMETEOII/2014/070, PROMETEOII/2014/004) and the Ministero dell'Istruzione, dell'Università e della Ricerca (Italy). T. G. and M. M. thank the Universitat de València and the mineco for predoctoral contracts. Thanks are also extended to the Ramón y Cajal Program (E. P. and E. V. R.-F. (RYC-2012-11427)). B. S. and J. G. acknowledge the financial support of the European Research Council under the European Union's Seventh Framework Programme (FP/2007-2013)/ERC Grant Agreement no. 335746, CrystEng-MOF-MMM.

Notes and references

1 S. Matar and L. F. Hatch, in *Chemistry of Petrochemical Processes*, Elsevier, 2001, pp. 1–28.
2 G. A. Olah and Á. Molnár, *Hydrocarbon Chemistry*, John Wiley & Sons, Inc., Hoboken, NJ, USA, 2003.
3 M. Beckner and A. Dailly, *Appl. Energy*, 2015, **149**, 69–74.
4 A. Van Miltenburg, W. Zhu, F. Kapteijn and J. A. Moulijn, *Chem. Eng. Res. Des.*, 2006, **84**, 350–354.
5 X. Y. Chen, H. Vinh-Thang, A. A. Ramirez, D. Rodrigue and S. Kaliaguine, *RSC Adv.*, 2015, **5**, 24399–24448.
6 H. Wu, Q. Gong, D. H. Olson and J. Li, *Chem. Rev.*, 2012, **112**, 836–868.
7 S. Kitagawa and R. Matsuda, *Coord. Chem. Rev.*, 2007, **251**, 2490–2509.
8 G. Férey, *Chem. Soc. Rev.*, 2008, **37**, 191–214.

9 J. R. Long and O. M. Yaghi, *Chem. Soc. Rev.*, 2009, **38**, 1213–1214.
10 O. K. Farha and J. T. Hupp, *Acc. Chem. Res.*, 2010, **43**, 1166–1175.
11 H. Furukawa, K. E. Cordova, M. O'Keeffe and O. M. Yaghi, *Science*, 2013, **341**, 974.
12 M. Pan, X.-M. Lin, G.-B. Li and C.-Y. Su, *Coord. Chem. Rev.*, 2011, **255**, 1921–1936.
13 T. Grancha, J. Ferrando-Soria, M. Castellano, M. Julve, J. Pasán, D. Armentano and E. Pardo, *Chem. Commun.*, 2014, **50**, 7569–7585.
14 Y. Cui, B. Li, H. He, W. Zhou, B. Chen and G. Qian, *Acc. Chem. Res.*, 2016, **49**, 483–493.
15 L. Fu, Y. Liu, M. Pan, X.-J. Kuang, C. Yan, K. Li, S.-C. Wei and C.-Y. Su, *J. Mater. Chem. A*, 2013, **1**, 8575.
16 M. Eddaoudi, *Science*, 2002, **295**, 469–472.
17 H. Furukawa, Y. B. Go, N. Ko, Y. K. Park, F. J. Uribe-Romo, J. Kim, M. O'Keeffe and O. M. Yaghi, *Inorg. Chem.*, 2011, **50**, 9147–9152.
18 R.-B. Lin, T.-Y. Li, H.-L. Zhou, C.-T. He, J.-P. Zhang and X.-M. Chen, *Chem. Sci.*, 2015, **6**, 2516–2521.
19 M. Kobalz, J. Lincke, K. Kobalz, O. Erhart, J. Bergmann, D. Lässig, M. Lange, J. Möllmer, R. Gläser, R. Staudt and H. Krautscheid, *Inorg. Chem.*, 2016, **55**, 3030–3039.
20 I. Spanopoulos, C. Tsangarakis, E. Klontzas, E. Tylianakis, G. Froudakis, K. Adil, Y. Belmabkhout, M. Eddaoudi and P. N. Trikalitis, *J. Am. Chem. Soc.*, 2016, **138**, 1568–1574.
21 M. G. Goesten, F. Kapteijn and J. Gascon, *CrystEngComm*, 2013, **15**, 9249–9257.
22 L. Carlucci, G. Ciani and D. M. Proserpio, in *Making Crystals by Design*, Wiley-VCH Verlag GmbH & Co. KGaA, Weinheim, Germany, 2007, pp. 58–85.
23 T. Grancha, M. Mon, J. Ferrando-Soria, D. Armentano and E. Pardo, *Cryst. Growth Des.*, 2016, **16**, 5571–5578.
24 W. M. Bloch, A. Burgun, C. J. Coghlan, R. Lee, M. L. Coote, C. J. Doonan and C. J. Sumby, *Nat. Chem.*, 2014, **6**, 906–912.
25 M. Mon, A. Pascual-Álvarez, T. Grancha, J. Cano, J. Ferrando-Soria, F. Lloret, J. Gascon, J. Pasán, D. Armentano and E. Pardo, *Chem.–Eur. J.*, 2016, **22**, 539–545.
26 S. Yang, J. Sun, A. J. Ramirez-Cuesta, S. K. Callear, W. I. F. David, D. P. Anderson, R. Newby, A. J. Blake, J. E. Parker, C. C. Tang and M. Schröder, *Nat. Chem.*, 2012, **4**, 887–894.
27 Y. Peng, V. Krungleviciute, I. Eryazici, J. T. Hupp, O. K. Farha and T. Yildirim, *J. Am. Chem. Soc.*, 2013, **135**, 11887–11894.
28 Z. R. Herm, E. D. Bloch and J. R. Long, *Chem. Mater.*, 2014, **26**, 323–338.
29 Z. Bao, G. Chang, H. Xing, R. Krishna, Q. Ren and B. Chen, *Energy Environ. Sci.*, 2016, **9**, 3612–3641.
30 E. López-Maya, C. Montoro, L. M. Rodríguez-Albelo, S. D. Aznar Cervantes, A. A. Lozano-Pérez, J. L. Cenís, E. Barea and J. A. R. Navarro, *Angew. Chem., Int. Ed.*, 2015, **54**, 6790–6794.
31 J. E. Mondloch, M. J. Katz, W. C. Isley III, P. Ghosh, P. Liao, W. Bury, G. W. Wagner, M. G. Hall, J. B. DeCoste, G. W. Peterson, R. Q. Snurr, C. J. Cramer, J. T. Hupp and O. K. Farha, *Nat. Mater.*, 2015, **14**, 512–516.
32 F. Luo, C. Yan, L. Dang, R. Krishna, W. Zhou, H. Wu, X. Dong, Y. Han, T.-L. Hu, M. O'Keeffe, L. Wang, M. Luo, R.-B. Lin and B. Chen, *J. Am. Chem. Soc.*, 2016, **138**, 5678–5684.
33 S. Yang, X. Lin, W. Lewis, M. Suyetin, E. Bichoutskaia, J. E. Parker, C. C. Tang, D. R. Allan, P. J. Rizkallah, P. Hubberstey, N. R. Champness, K. Mark Thomas, A. J. Blake and M. Schröder, *Nat. Mater.*, 2012, **11**, 710–716.
34 T. M. McDonald, J. A. Mason, X. Kong, E. D. Bloch, D. Gygi, A. Dani, V. Crocellà, F. Giordanino, S. O. Odoh, W. S. Drisdell, B. Vlaisavljevich, A. L. Dzubak, R. Poloni, S. K. Schnell, N. Planas, K. Lee, T. Pascal, L. F. Wan, D. Prendergast, J. B. Neaton, B. Smit, J. B. Kortright, L. Gagliardi, S. Bordiga, J. A. Reimer and J. R. Long, *Nature*, 2015, **519**, 303–308.
35 C. Gücüyener, J. van den Bergh, J. Gascon and F. Kapteijn, *J. Am. Chem. Soc.*, 2010, **132**, 17704–17706.
36 Y. He, R. Krishna and B. Chen, *Energy Environ. Sci.*, 2012, **5**, 9107.
37 D. Peralta, G. Chaplais, A. Simon-Masseron, K. Barthelet, C. Chizallet, A.-A. Quoineaud and G. D. Pirngruber, *J. Am. Chem. Soc.*, 2012, **134**, 8115–8126.
38 E. D. Bloch, W. L. Queen, R. Krishna, J. M. Zadrozny, C. M. Brown and J. R. Long, *Science*, 2012, **335**, 1606–1610.
39 Y.-S. Bae, C. Y. Lee, K. C. Kim, O. K. Farha, P. Nickias, J. T. Hupp, S. T. Nguyen and R. Q. Snurr, *Angew. Chem., Int. Ed.*, 2012, **51**, 1857–1860.
40 S. J. Geier, J. A. Mason, E. D. Bloch, W. L. Queen, M. R. Hudson, C. M. Brown and J. R. Long, *Chem. Sci.*, 2013, **4**, 2054.
41 C. Yu, M. G. Cowan, R. D. Noble and W. Zhang, *Chem. Commun.*, 2014, **50**, 5745.
42 B. Li, Y. Zhang, R. Krishna, K. Yao, Y. Han, Z. Wu, D. Ma, Z. Shi, T. Pham, B. Space, J. Liu, P. K. Thallapally, J. Liu, M. Chrzanowski and S. Ma, *J. Am. Chem. Soc.*, 2014, **136**, 8654–8660.
43 P.-Q. Liao, W.-X. Zhang, J.-P. Zhang and X.-M. Chen, *Nat. Commun.*, 2015, **6**, 8697.
44 A. H. Assen, Y. Belmabkhout, K. Adil, P. M. Bhatt, D.-X. Xue, H. Jiang and M. Eddaoudi, *Angew. Chem., Int. Ed.*, 2015, **54**, 14353–14358.
45 D.-X. Xue, Y. Belmabkhout, O. Shekhah, H. Jiang, K. Adil, A. J. Cairns and M. Eddaoudi, *J. Am. Chem. Soc.*, 2015, **137**, 5034–5040.
46 A. Cadiau, K. Adil, P. M. Bhatt, Y. Belmabkhout and M. Eddaoudi, *Science*, 2016, **353**, 137–140.
47 T. Grancha, J. Ferrando-Soria, H.-C. Zhou, J. Gascon, B. Seoane, J. Pasán, O. Fabelo, M. Julve and E. Pardo, *Angew. Chem., Int. Ed.*, 2015, **54**, 6521–6525.
48 X. Zhao, J. G. Bell, S.-F. Tang, L. Li and K. M. Thomas, *J. Mater. Chem. A*, 2016, **4**, 1353–1365.
49 M.-C. Dul, E. Pardo, R. Lescouëzec, Y. Journaux, J. Ferrando-Soria, R. Ruiz-García, J. Cano, M. Julve, F. Lloret, D. Cangussu, C. L. M. Pereira, H. O. Stumpf, J. Pasán and C. Ruiz-Pérez, *Coord. Chem. Rev.*, 2010, **254**, 2281–2296.
50 T. Grancha, J. Ferrando-Soria, J. Cano, F. Lloret, M. Julve, G. De Munno, D. Armentano and E. Pardo, *Chem. Commun.*, 2013, **49**, 5942–5944.

51 T. Grancha, J. Ferrando-Soria, J. Cano, P. Amorós, B. Seoane, J. Gascon, M. Bazaga-García, E. R. Losilla, A. Cabeza, D. Armentano and E. Pardo, *Chem. Mater.*, 2016, **28**, 4608–4615.
52 M. Mon, J. Ferrando-Soria, T. Grancha, F. R. Fortea-Pérez, J. Gascon, A. Leyva-Pérez, D. Armentano and E. Pardo, *J. Am. Chem. Soc.*, 2016, **138**, 7864–7867.
53 M. Mon, F. Lloret, J. Ferrando-Soria, C. Martí-Gastaldo, D. Armentano and E. Pardo, *Angew. Chem., Int. Ed.*, 2016, **55**, 11167–11172.
54 M. O'Keeffe, M. A. Peskov, S. J. Ramsden and O. M. Yaghi, *Acc. Chem. Res.*, 2008, **41**, 1782–1789.
55 A. C. Sudik, A. P. Côté and O. M. Yaghi, *Inorg. Chem.*, 2005, **44**, 2998–3000.
56 M. F. De Lange, T. J. H. Vlugt, J. Gascon and F. Kapteijn, *Microporous Mesoporous Mater.*, 2014, **200**, 199–215.
57 R. J. Dombrowski, C. M. Lastoskie and D. R. Hyduke, *Colloids Surf., A*, 2001, **187–188**, 23–39.
58 A. L. Myers and J. M. Prausnitz, *AIChE J.*, 1965, **11**, 121–127.
59 R. Krishna and J. R. Long, *J. Phys. Chem. C*, 2011, **115**, 12941–12950.
60 S. Horike, Y. Inubushi, T. Hori, T. Fukushima and S. Kitagawa, *Chem. Sci.*, 2012, **3**, 116–120.
61 J. Duan, M. Higuchi, S. Horike, M. L. Foo, K. P. Rao, Y. Inubushi, T. Fukushima and S. Kitagawa, *Adv. Funct. Mater.*, 2013, **23**, 3525–3530.
62 J. W. Yoon, J. S. Lee, S. Lee, K. H. Cho, Y. K. Hwang, M. Daturi, C.-H. Jun, R. Krishna and J.-S. Chang, *Chem.–Eur. J.*, 2015, **21**, 18431–18438.
63 A. M. Plonka, X. Chen, H. Wang, R. Krishna, X. Dong, D. Banerjee, W. R. Woerner, Y. Han, J. Li and J. B. Parise, *Chem. Mater.*, 2016, **28**, 1636–1646.
64 L. H. Wee, M. Meledina, S. Turner, G. Van Tendeloo, K. Zhang, L. M. Rodriguez-Albelo, A. Masala, S. Bordiga, J. Jiang, J. A. R. Navarro, C. E. A. Kirschhock and J. A. Martens, *J. Am. Chem. Soc.*, 2017, **139**, 819–828.
65 K. Liu, D. Ma, B. Li, Y. Li, K. Yao, Z. Zhang, Y. Han and Z. Shi, *J. Mater. Chem. A*, 2014, **2**, 15823–15828.
66 S. N. Talapaneni, D. Kim, G. Barin, O. Buyukcakir, S. H. Je and A. Coskun, *Chem. Mater.*, 2016, **28**, 4460–4466.
67 A. Schneemann, E. D. Bloch, S. Henke, P. L. Llewellyn, J. R. Long and R. A. Fischer, *Chem.–Eur. J.*, 2015, **21**, 18764–18769.
68 V. Safarifard, S. Rodríguez-Hermida, V. Guillerm, I. Imaz, M. Bigdeli, A. Azhdari Tehrani, J. Juanhuix, A. Morsali, M. E. Casco, J. Silvestre-Albero, E. V. Ramos-Fernandez and D. Maspoch, *Cryst. Growth Des.*, 2016, **16**, 6016–6023.

Inorganic Chemistry

Article

pubs.acs.org/IC

Spin Crossover in Double Salts Containing Six- and Four-Coordinate Cobalt(II) Ions

Joanna Palion-Gazda,*[,†] Barbara Machura,[†] Rafal Kruszynski,[‡] Thais Grancha,[§] Nicolás Moliner,[§] Francesc Lloret,[§] and Miguel Julve*[,§]

[†]Department of Crystallography, Institute of Chemistry, University of Silesia, Ninth Szkolna Street, 40006 Katowice, Poland

[‡]Department of X-ray Crystallography and Crystal Chemistry, Institute of General and Ecological Chemistry, Lodz University of Technology, 116 Żeromski Street, 90-924 Łódź, Poland

[§]Departament de Química Inorgànica/Instituto de Ciencia Molecular (ICMol), Universitat de València, C/Catedrático José Beltrán 2, 46980 Paterna, València, Spain

Supporting Information

ABSTRACT: The preparation and spectroscopic and structural characterization of three cobalt(II) complexes of formulas $[Co(tppz)_2](dca)_2$ (**1**), $[Co(tppz)_2][Co(NCS)_4]\cdot MeOH$ (**2**), and $[Co(tppz)_2][Co(NCO)_4]\cdot 2H_2O$ (**3**) [tppz = 2,3,5,6-tetrakis-(2-pyridyl)pyrazine and dca = dicyanamide] are reported here. Compounds **1**−**3** have in common the presence of the cationic $[Co(tppz)_2]^{2+}$ entity where each *mer*-tridentate tppz ligand coordinates to the cobalt(II) ion equatorially through two pyridyl donors and axially via the pyrazine, completing the six-coordination. The electroneutrality is achieved by the organic dca group (**1**) and the anionic tetrakis(thiocyanato-*κN*)cobaltate-(II) (**2**) and tetrakis(cyanato-*κN*)cobaltate(II) (**3**) complexes. Direct current (dc) magnetic susceptibility measurements of **1** in the temperature range 1.9−400 K show the occurrence of a thermally induced spin crossover behavior of the $[Co(tppz)_2]^{2+}$ unit from a high spin ($S = 3/2$) at higher temperatures to a low-spin ($S = 1/2$) at lower temperatures, with the low spin phase being reached at $T \leq 200$ K. X-band electron paramagnetic resonance (EPR) measurements in solution at low temperatures were used to characterize the low spin state. An analytical expression based on the combination of the spin−orbit coupling and both first- and second-order Zeeman effects for a d^7 electronic configuration was used to fit the magnetic data of **1**, the values of the best-fit parameters being $C_{vib} = 0.1367(9)$, $\lambda = -168(2)$ cm^{-1}, $\alpha = 1.12(1)$, $\Delta = 1626(15)$ cm^{-1}, and $g_{LS} = 2.12(1)$. The magnetic behavior of the four-coordinate cobalt(II) ions $[Co(NCS)_4]^{2-}$ (**2**) and $[Co(NCO)_4]^{2-}$ (**3**) with a $^4A_2$ ground state overlaps with the spin crossover of the $[Co(tppz)_2]_{2+}$ entity, the abrupt decrease of the $\chi_M T$ product below 15.0 K being due to zero-field splitting effects between the spin components $|\pm 1/2>$ and $|\pm 3/2>$. The combined analysis of the *dc* magnetic data and the Q-band EPR spectra in the solid state of **2** and **3** led to the following sets of best-fit parameters: $C_{vib} = 0.105(5)$, $\lambda = -170(4)$ cm^{-1}, $\alpha = 1.10(2)$, $\Delta = 1700(25)$ cm^{-1}, $g_{LS} = 2.10(1)$, $g_{HS} = 2.27(1)$, and $|D| = 3.80(2)$ cm^{-1} (**2**) and $C_{vib} = 0.100(1)$, $\lambda = -169(5)$ cm^{-1}, $\alpha = 1.10(3)$, $\Delta = 1500(30)$ cm^{-1}, $g_{LS} = 2.10(1)$, $g_{HS} = 2.28(1)$, and $|D| = 4.30(2)$ cm^{-1} (**3**). Some evidence of slowing of the relaxation of the magnetization has been found in the out-of-phase *ac* signal at very low temperatures under applied *dc* fields of 0.1−0.4 T for **3**, suggesting the occurrence of single-ion magnet behavior of its $[Co(NCO)_4]^{2-}$ anionic entity.

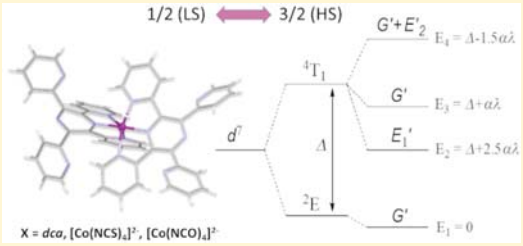

INTRODUCTION

In recent years, enormous efforts have been focused on the systematic examination of the magnetic behavior of cobalt(II) coordination compounds. These species may behave as single-molecule magnets (SMMs), single-ion magnets (SIMs), single-chain magnets (SCMs) or show spin-crossover (SCO). Three-,[1] four-,[2−12] five-,[13−20] six-,[21−42] seven-,[43−47] and eight-coordinate[48,49] zero-dimensional (0D) cobalt(II) complexes are known behaving as SMMs or SIMs. The choice of the cobalt(II) ion is based on its strong Ising-like magnetic anisotropy which is required to create an energy barrier for the magnetization reversal in SMMs, SIMs, and SCMs. Concerning the cobalt(II) SCO complexes,[50−65] a spin transition between low-spin (LS, $S = 1/2$) and high-spin (HS, $S = 3/2$) states is at the origin of their bistability, the conversion between these two states being triggered by various external stimuli such as temperature, pressure, light or X-ray irradiation, intense magnetic fields, or the inclusion of guest molecules. Depending on the nature of the ligands, crystal packing, solvent molecules, and noncoordinating counterions, the SCO behavior can be gradual or abrupt in the solid state.[61−65]

A great attention devoted to research in the field of molecular magnetism is attributed to possible applications of

Received: February 8, 2017
Published: May 22, 2017

DOI: 10.1021/acs.inorgchem.7b00360
Inorg. Chem. 2017, 56, 6281−6296

these SCO compounds in high-density magnetic information storage, chemosensors, or spintronic devices.[66−70] Rational design and synthesis of materials required for particular applications, however, remain a great challenge, and much more work is desirable in order to extend our knowledge on physicochemical relationships.

In the framework of the magnetostructural studies on the metal complexes with the 2,3,5,6-tetrakis(2-pyridyl)pyrazine (tppz) ligand (Scheme 1),[71−86] we report here the preparation, structural characterization, and variable-temperature magnetic and electron paramagnetic resonance (EPR) studies of three cobalt(II) complexes of formula $[Co(tppz)_2](dca)_2$ (**1**), $[Co(tppz)_2][Co(NCS)_4]\cdot MeOH$ (**2**), and $[Co(tppz)_2][Co(NCO)_4]\cdot 2H_2O$ (**3**) (dca = dicyanamide anion), where the diamagnetic organic dca group (**1**) and the paramagnetic metalloligands $[Co(NCS)_4]^{2-}$ (**2**) and $[Co(NCO)_4]^{2-}$ (**3**) act as counterions of the spin crossover unit $[Co(tppz)_2]^{2+}$. The results obtained are compared to those reported for the compound $[Co(tppz)_2](tcm)_2$ (tcm = tricyanomethanide anion) from a previous communication[83] and other related N_6-coordinated cobalt(II) complexes (Table S1).

Scheme 1. Structural Formula of 2,3,5,6-Tetrakis(2-pyridyl)pyrazine (tppz)

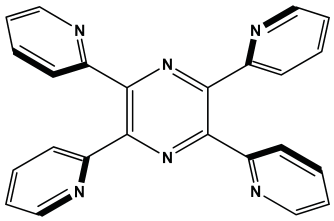

EXPERIMENTAL SECTION

Materials. The reagents used in the synthesis of the compounds were commercially available and were used without further purification.

*Preparation of the Complexes. [Co(tppz)$_2$](dca)$_2$ (**1**).* An aqueous solution (5 cm^3) of $NaN(CN)_2$ (0.180 g, 2 mmol) was added dropwise to another MeOH/MeCN (1:2 v/v) mixed solvent (15 mL) containing $CoCl_2\cdot 6H_2O$ (0.24 g, 1 mmol) and tppz (0.38 g, 1 mmol) under continuous stirring at room temperature for 12 h. The resulting deep-brown solution was allowed to evaporate in a hood at room temperature. X-ray quality crystals of **1** were grown from this solution after a week. They were collected by filtration and air-dried. Yield ca. 80% (based on tppz). Anal. Calc. for $C_{52}H_{32}CoN_{18}$ (**1**): C, 64.53; H, 3.33; N, 26.05. Found: C, 64.40; H, 3.28; N, 26.21%. IR (KBr, cm^{-1}): 2225(s) [ν_{as} + ν_s(C≡N$_{dca}$)], 2185(m) [ν_{as}(C≡N$_{dca}$)], 2125(vs) [ν_s(C≡N$_{dca}$)], 1595(m), 1567(sh), and 1529(w) [ν(C═N) and ν(C═C)]. UV−vis-NIR (solid, nm): 1396, 709, 562, 518, 479, 418, 349, and 284.

*[Co(tppz)$_2$][Co(NCS)$_4$] (**2**).* A solution of tppz (0.38 g, 1 mmol) in MeCN/MeOH (15 mL, 2:1, v/v) was added dropwise to a MeOH/H_2O (1:2 v/v) mixture (20 mL) containing $CoCl_2\cdot 6H_2O$ (0.24 g, 1 diamagnetic organic dca group (**1**) and the paramagnetic metalloligands $[Co(NCS)_4]^{2-}$ (**2**) and $[Co(NCO)_4]^{2-}$ (**3**) act as counterions of the spin crossover unit $[Co(tppz)_2]^{2+}$. The results obtained are compared to those reported for the compound $[Co(tppz)_2](tcm)_2$ (tcm = tricyanomethanide anion) from a previous communication[83] and other related N_6-coordinated cobalt(II) complexes (Table S1).

Table 1. Crystal Data and Structure Refinement for 1−3

	1·125 K	**1**·330 K	**2**	**3**
empirical formula	$C_{52}H_{32}CoN_{18}$	$C_{52}H_{32}CoN_{18}$	$C_{53}H_{36}N_{16}S_4Co_2O$	$C_{52}H_{36}Co_2N_{16}O_6$
formula weight	967.89	967.89	1159.08	1098.83
T, K	125.0(2)	330.0(2)	293.0(2)	293.0(2)
wavelength, Å	0.71073	0.71073	0.71073	0.71073
crystal system	orthorhombic	orthorhombic	monoclinic	orthorhombic
space group	*Pbcn*	*Pbcn*	$P2_1/c$	*Pbca*
unit cell dimensions, Å and deg	a = 8.9361(7)	a = 9.0081(4)	a = 14.1066(4)	a = 16.6555(5)
	b = 28.271(2)	b = 28.3969(14)	b = 17.7273(6)	b = 20.3398(8)
	c = 17.8978(14)	c = 18.0737(8)	c = 22.0434(14)	c = 29.6213(10)
			β = 106.716(4)	
V, Å^3	4521.6(6)	4623.3 (4)	5279.5(3)	10034.8(6)
Z	4	4	4	8
D_c, g cm^{-3}	1.422	1.391	1.458	1.455
absorption coefficient, mm^{-1}	0.441	0.431	0.843	0.729
F(000)	1988	1988	2368	4496
crystal size, mm	0.202 × 0.186 × 0.023	0.202 × 0.186 × 0.023	0.193 × 0.142 × 0.067	0.172 × 0.056 × 0.018
θ range for data collection [°]	3.34−25.05	3.32−25.05	3.58− 25.05	3.35−25.05
index ranges	$-10 \le h \le 10$	$-9 \le h \le 10$	$-16 \le h \le 16$	$-19 \le h \le 19$
	$-33 \le k \le 27$	$-33 \le k \le 25$	$-21 \le k \le 18$	$-24 \le k \le 24$
	$-21 \le l \le 16$	$-17 \le l \le 21$	$-22 \le l \le 26$	$-35 \le l \le 35$
reflections collected	13581	14846	13581	41166
independent reflections	3999 (R_{int} = 0.0652)	4089 (R_{int} = 0.0398)	9314 (R_{int} = 0.0451)	8860 (R_{int} = 0.055)
completeness to 2θ, %	99.7	99.7	99.7	99.7
min and max transm.	0.529 and 1.000	0.825 and 1.000	0.568 and 1.000	0.535 and 1.000
data/restraints/parameters	3999/0/323	4089/0/323	9314/0/687	8860/0/685
goodness-of-fit on F^2	1.167	1.057	1.077	1.110
final R indices [$I > 2\sigma(I)$]	$R1$ = 0.0764	$R1$ = 0.0539	$R1$ = 0.0459	$R1$ = 0.0599
	$wR2$ = 0.2079	$wR2$ = 0.1387	$wR2$ = 0.1127	$wR2$ = 0.1731
R indices (all data)	$R1$ = 0.0913	$R1$ = 0.0797	$R1$ = 0.0724	$R1$ = 0.0959
	$wR2$ = 0.2131	$wR2$ = 0.1520	$wR2$ = 0.1262	$wR2$ = 0.1925
largest diff. peak and hole, e Å^{-3}	0.74 and −0.47	0.50 and −0.49	0.39 and −0.53	1.20 and −0.57

DOI: 10.1021/acs.inorgchem.7b00360
Inorg. Chem. 2017, 56, 6281−6296

Table 2. Selected Bond Lengths (Å) and Angles (deg) for 1−3[a]

	1·125 K	1·330 K	2, Y = S	3, Y = O
		Bond Lengths		
Co(1)−N(1)	1.855(5)	1.870(3)	1.869(3)	1.877(3)
Co(1)−N(7)	1.917(5)	1.912(3)	1.927(3)	1.922(3)
Co(1)−N(3)	1.977(4)	2.003(2)	1.984 (3)	2.011(3)
Co(1)−N(5)	2.155(4)	2.128(2)	1.992(3)	1.997(3)
Co(1)−N(9)			2.126(3)	2.124(3)
Co(1)−N(11)			2.124(3)	2.102(3)
Co(2)−N(96)			1.958(3)	1.952(6)
Co(2)−N(97)			1.960(4)	1.946(5)
Co(2)−N(98)			1.956(4)	1.999(6)
Co(2)−N(99)			1.953(4)	1.970(6)
		Bond Angles		
N(1)−Co(1)−N(3)	82.10(11)	81.51(7)	81.47(9)	81.65(11)
N(1)−Co(1)−N(5)	101.16(10)	100.93(7)	81.55(9)	80.75(11)
N(1)−Co(1)−N(7)	180.0	180.0	176.30(9)	177.13(13)
N(1)−Co(1)−N(9)			104.65(9)	97.92(12)
N(1)−Co(1)−N(11)			96.71(9)	103.15(12)
N(3)−Co(1)−N(3)[a]	164.2(2)	163.01(14)		
N(3)−Co(1)−N(5)	90.41(15)	90.75(9)	162.91(9)	162.25(12)
N(3)[a]−Co(1)−N(5)	92.64(15)	92.46(9)		
N(3)−Co(1)−N(9)			95.98(10)	95.15(13)
N(3)−Co(1)−N(11)			86.99(9)	88.02(13)
N(5)−Co(1)−N(5)[a]	157.7(2)	158.14(14)		
N(5)−Co(1)−N(9)			86.45(9)	89.53(12)
N(5)−Co(1)−N(11)			96.91(9)	93.76(13)
N(7)−Co(1)−N(3)	97.90(11)	98.49(7)	98.54(9)	98.06(11)
N(7)−Co(1)−N(5)	78.84(10)	79.07(7)	98.53(9)	99.63(11)
N(7)−Co(1)−N(9)			79.04(9)	79.25(11)
N(7)−Co(1)−N(11)			79.60(9)	79.68(12)
N(9)−Co(1)−N(11)			158.64(8)	158.93(12)
C(99)−N(98)−C(98)	120.5(6)	123.2(7)		
N(97)−C(98)−N(98)	173.4(7)	170.1(7)		
N(99)−C(99)−N(98)	173.4(7)	170.6(8)		
N(96)−Co(2)−N(98)			108.97(15)	111.2(2)
N(97)−Co(2)−N(96)			106.55(15)	106.5(2)
N(97)−Co(2)−N(98)			113.60(15)	108.6(2)
N(99)−Co(2)−N(96)			110.58(15)	111.1(3)
N(99)−Co(2)−N(97)			105.89(17)	115.4(3)
N(99)−Co(2)−N(98)			111.28(16)	104.0(2)
N(96)−C(96)−Y(96)			178.7(4)	179.2(8)
N(97)−C(97)−Y(97)			178.9(4)	178.0(8)
N(98)−C(98)−Y(98)			178.8(4)	177.1(8)
N(99)−C(99)−Y(99)			178.8(4)	177.1(9)
C(96)−N(96)−Co(2)			174.8(4)	157.4(5)
C(97)−N(97)−Co(2)			171.2(4)	167.1(5)
C(98)−N(98)−Co(2)			168.0(3)	133.5(5)
C(99)−N(99)−Co(2)			173.9(3)	156.1(7)

[a]Symmetry transformations used to generate equivalent atoms: (a) = $-x + 1, y, -z + 1/2$.

mmol) and NH_4SCN (0.15 g, 2 mmol). The resulting solution was left under continuous stirring at room temperature for 12 h. The resulting deep-brown solution was allowed to evaporate in a hood at room temperature. X-ray quality crystals of **2** were obtained from solution after a week, collected by filtration and air-dried. Yield ca. 75% (based on tppz). Anal. Calc. for $C_{53}H_{36}N_{16}S_4Co_2O$ (**2**): C, 54.92; H, 3.13; N, 19.33; S, 11.06. Found: C, 54.74; H, 3.10; N, 19.52; S 11.21%. IR (KBr, cm^{-1}): 2069(vs) [$\nu(C{\equiv}N_{NCS}^-)$], 1588(m), 1567(sh) and 1525(w) [$\nu(C{=}N_{tppz})$ and $\nu(C{=}C_{tppz})$]. UV−vis-NIR (solid, nm): 1310, 708, 620, 507, 409 and 256.

*[Co(tppz)$_2$][Co(NCO)$_4$] (**3**).* A solution of tppz (0.38 g, 1 mmol) in MeCN/MeOH (15 mL, 2:1, v/v) was added to methanolic solution of $CoCl_2{\cdot}6H_2O$ (0.24 g, 1 mmol), under continuous stirring at room temperature for 15 min. The resulting deep-brown solution was filtered off and transferred to a long test tube containing the layers of an aqueous solution of NaOCN (0.13 g, 2 mmol) and a blank solution of $MeOH/H_2O$ (5 mL, 1:1, v/v). The tube was sealed and allowed to stand still for 2 weeks, during which time brown crystals of **3** had formed. They were collected by filtration and air-dried. Yield ca. 65% (based on tppz). Anal. Calc. for $C_{52}H_{36}Co_2N_{16}O_6$ (**3**): C, 56.84; H, 3.30; N, 20.40. Found: C, 56.66; H, 3.24; N, 20.58%. IR (KBr, cm^{-1}): 2197(vs) [$\nu(C{\equiv}N_{NCO}^-)$], 1590(m), 1568(sh) and 1527(w) [$\nu(C{=}N_{tppz})$ and $\nu(C{=}C_{tppz})$]. UV−vis-NIR (solid, nm): 1439, 727, 626, 507, 421, and 284.

DOI: 10.1021/acs.inorgchem.7b00360
Inorg. Chem. 2017, 56, 6281−6296

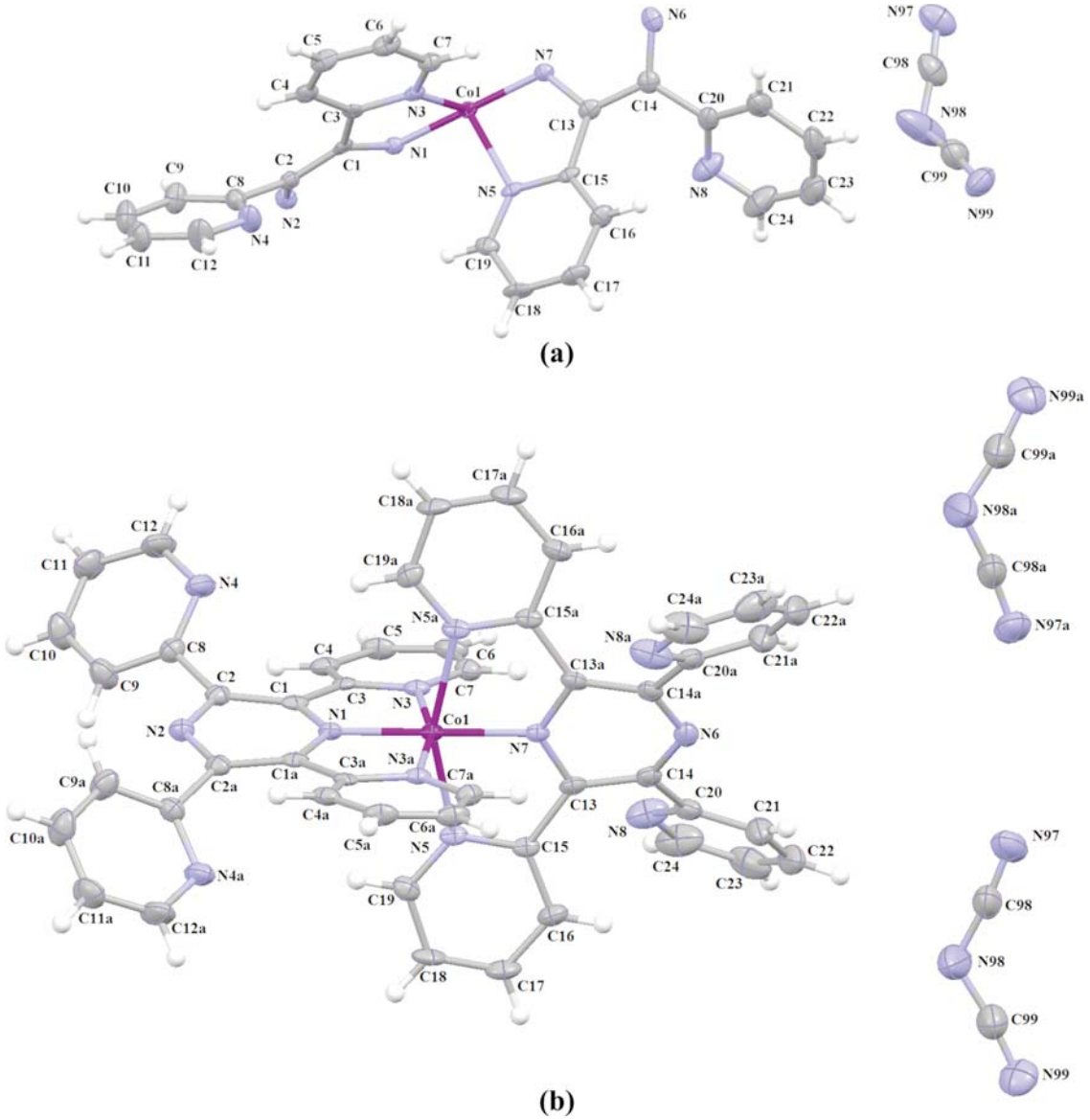

Figure 1. (a) A view of the asymmetric unit of **1·125 K** together with the atom numbering. (b) The molecular structure of **1·125 K**. Thermal ellipsoids are drawn at the 50% probability level [symmetry code: (a) = $-x + 1, y, -z + 1/2$].

Physical Techniques. IR spectra were recorded on a Nicolet iS5 spectrophotometer in the spectral range 4000−400 cm^{-1} with the samples in form of KBr pellets [Figures S1 (1), S2 (2), and S3 (3)]. The electronic spectra were obtained from solid state samples on Nicolet Evolution 220 *Nicolet iS50 FT-IR* spectrophotometers in the ranges 190−1100 and 700−1500 nm, respectively [Figure S4 (1−3)]. Powder X-ray diffraction (PXRD) measurements were performed on a PANalytical *Empyrean* X-ray diffractometer using Cu−Kα radiation (λ = 1.5418 Å), in which the X-ray tube was operated at 40 kV and 30 mA ranging from 5 to 80°. The experimental and calculated (with inclusion of the preferred orientation effects for compounds **2** and **3** and usage of March-Dollase parameter of 1.5) PXRD patterns for all three complexes [see Figures S5 (1), S6 (2), and S7 (3)] show a great coincidence of the positions of all peaks expected, each pattern confirming that the obtained structure from the single crystal is equal to the one of the bulk. The elemental analysis of sulfur was performed by the Carius method (sodium chloride being used as the sulfuric acid binder) and as benzidine sulfate (gravimetrically determined) after initial removing of excess of nitric acid by evaporation in an inert atmosphere. The C, H, and N contents were determined by using a PerkinElmer 240C elemental analyzer.

X-ray diffraction data on single crystals of **1**−**3** were collected by means of an Oxford Diffraction four-circle diffractometer Gemini A Ultra with Atlas CCD detector using graphite monochromated MoKα radiation (λ = 0.71073 Å) at room temperature. Diffraction data collection, cell refinement, and data reduction were performed using

DOI: 10.1021/acs.inorgchem.7b00360
Inorg. Chem. 2017, 56, 6281−6296

the CrysAlis^{Pro} software.[87] The structures were solved by the direct methods using SHELXS97 and refined by full-matrix least-squares on F^2 using SHELXL97.[88] All non-hydrogen atoms were refined anisotropically, and the hydrogen atoms were placed in calculated positions refined using idealized geometries (riding model) and assigned fixed isotropic displacement parameters, d(C−H) = 0.93 Å, U_{iso}(H) = 1.2 U_{eq}(C) (aromatic), and d(C−H) = 0.96 Å, U_{iso}(H) = 1.5 U_{eq}(C) (methyl and water). The methyl groups were allowed to rotate about their local 3-fold axis. Details of the crystallographic data collection, structural determination, and refinement conditions for **1**−**3** are given in Table 1, whereas the selected bond lengths and angles for these compounds are listed in Table 2.

RESULTS AND DISCUSSION

Descripton of the Structures. *[Co(tppz)$_2$](dca)$_2$ (1).* The single crystal X-ray structure of **1** was determined at 330 and 125 K in order to investigate the possible temperature-induced structural changes. The unit cell data and refinement conditions of **1** together with those of **2** and **3** are listed in Table 1, whereas the selected bond lengths and angles for **1**−**3** are given Table 2. As shown in Table 1, no structural phase transition occurs for **1** in the whole range of temperature. Only a very small increase in the cell volume (2.2%) along with very slight lengthening in all three cell axes was observed for this complex on going from 125 to 330 K.

The asymmetric unit of **1** contains one dca$^-$ counterion and half [Co(tppz)$_2$]$^{2+}$ cation, and the other half is generated by 2-fold rotation axis as the cobalt center and the N1, N2, N6, and N7 nitrogen atoms are located on the special position *c* of the *Pbcn* space group with the multiplicity four [Figures 1 (**1·125 K**) and S8 (**1·330 K**); see Supporting Information]. The cobalt(II) ion is octahedrally surrounded by six nitrogen atoms from two tridentate tppz ligands. Each tppz molecule coordinates to the cobalt(II) ion in a *mer* fashion, equatorially via pyridyl donors, and axially through pyrazine nitrogen atoms (abbreviated as N_{py} and N_{pz}, respectively). The same environment around the metal center was observed in the parent compound [Co(tppz)$_2$](tcm)$_2$.[83]

The major angular distortion of the [Co(tppz)$_2$]$^{2+}$ unit in **1** from the idealized octahedral geometry is attributed to geometrical constraints issued from the occurrence of two fused five-member chelate rings of the tppz ligand. The values of the N−Co−N angles for the nitrogen atoms in cis disposition vary in the ranges 78.84−101.16 (**1·125 K**) and 79.07−100.93° (**1·330 K**), whereas for those in trans configuration cover the ranges 157.7−180 (**1·125 K**) and 158.14−180° (**1·330 K**). The values of the dihedral angle between the least-squares planes defined by the coordinated pyridyl and pyrazine rings of the two tppz ligands are 88.43 (**1·125 K**) and 86.67° (**1·330 K**). The parameters Σ and Θ were also calculated in order to evaluate the octahedral distortion (eqs 1 and 2):

$$\Sigma = \sum_{i=1}^{12} |90 - \alpha_i| \quad (1)$$

$$\Theta = \sum_{i=1}^{24} |60 - \theta_i| \quad (2)$$

The more distorted the octahedron is, the higher the values of Σ and Θ are. Most importantly, these parameters have been proven to be spin-state dependent, and therefore they can be used to determine the spin state of the metal ion.[89]

The distortion parameter Σ [parameter defined as the sum of the deviation from 90° of the 12 cis angles of the CoN_6 octahedron, eq 1] equals 82.6 and 84.0° in **1·125** and **1·330 K**, respectively. No significant variation of these parameters occurs when cooling down. Also, the value of Θ [parameter defined as the sum of the 24 unique θ_i angles measured on the projection of two triangular faces of the octahedron along their common pseudo-3-fold axis, eq 2] only decreases slightly when going from 125 (Θ = 277°) to 330 K (Θ = 281°) (see Table 3).[89−91]

Table 3. Comparison of the Values of the Co−N Bond Lengths (Å) and Some Structural Distortion Parameters for 1·125 and 1·330 K

	1·125 K	1·330 K
Co−N_{pz}	1.855(5)	1.870(3)
	1.917(5)	1.912(3)
Co−$N^{av}_{(pz)}$	1.886	1.891
Co−N_{py}	1.977(4)	2.003(2)
	2.155(4)	2.128(2)
	1.977(4)	2.003(2)
	2.155(4)	2.128(2)
Co−$N^{av}_{(py)}$	2.066	2.0655
Co−N_{av}	2.006(4)	2.007(2)
Σ (deg)[a]	82.6	84.0
Θ (deg)[b]	277	281
dihedral angle (deg)[c]	88.43	88.67

[a]Σ is the sum of the deviation from 90° of the 12 cis angles of the CoN_6 octahedron. [b]Θ is the sum of the 24 unique N−Fe−N angles measured on the projection of two triangular faces of the octahedron along their common pseudo-3-fold axis. [c]Value of the dihedral angle between the least-squares planes defined by the coordinated pyridyl and pyrazine rings of the two tppz ligands.

Upon increasing the temperature, the average value of the Co−N bond lengths of **1** is almost constant within experimental error. The Co−N_{pz} bond distances are significantly shorter than those of the Co−N_{py} bonds, which may be ascribed to the Jahn−Teller distortion of the ^2E_g state of low-spin cobalt(II) ions. The lower number of antibonding e_g electrons in a LS metal ion $^2E_g(t_{2g}^6e_g^1)$ compared to a HS configuration $^4T_{1g}$ $(t_{2g}^5e_g^2)$ should result in stronger metal−ligand bonding and thus a less deformable coordination sphere. Because only one electron is transferred between the e_g and the t_{2g} orbitals, the thermal SCO in the cobalt(II) complexes is accompanied by small changes in the metal-donor atom bond lengths. A thorough analysis of the structural data, performed for the related N_6-coordinated Co(II) compounds (see Table S1; Supporting Information) shows that the average Co−N bond distances are 2.114 and 2.009 Å in HS and LS cobalt(II) complexes, respectively. With reference to SCO iron(II) compounds, where the change in the total spin is ΔS = 2, the Co−N bond lengths are less sensitive to the spin transition. Alternatively, the distortion parameters Σ and Θ seem to be distinctive of the cobalt(II) spin state. They are significantly larger in HS than in LS, and the following ranges of values were assumed in cobalt(II) coordination compounds: 61.10−99.10 (LS) and 110.80−134.70° (HS) for Σ and 185−319 (LS) and 353−403° (HS) for Θ. Taking into consideration the values of the Co−N bond lengths and distortion parameters Σ and Θ (Tables 2 and S1), it can be concluded that the central Co(II) ion in **1** has a quasi LS configuration in the temperature range investigated.

DOI: 10.1021/acs.inorgchem.7b00360
Inorg. Chem. 2017, 56, 6281−6296

As shown in Figures 2 (**1·125 K**) and S9 (**1·330 K**), the angular dicyanamide ligands with C(99)−N(98)−C(98) = 120.5(6)° and two nearly linear N−C−N units [mean value of N−C−N = 173.4(7)°] are involved in very weak C−H···N_{dca} and N_{dca}···π type interactions with the $[Co(tppz)_2]^{2+}$ complex cations [C(98)−N(97)···Cg(1)$^{h/i}$ = 3.312(6) Å; symmetry code: (h) = 1/2 + x, −1/2 + y, 1/2 − z; (i) = 3/2 − x, −1/2 + y, z]. Very small changes of this last contact are observed at 330 K [C(98)−N(97)···Cg(1)$^{h/i}$ = 3.339(6) Å] (see Tables S2 and S3; Supporting Information). The values of the shortest intermolecular cobalt···cobalt separation are 8.9361(7) (**1·125 K**) and 9.0081(4) Å (**1·330 K**).

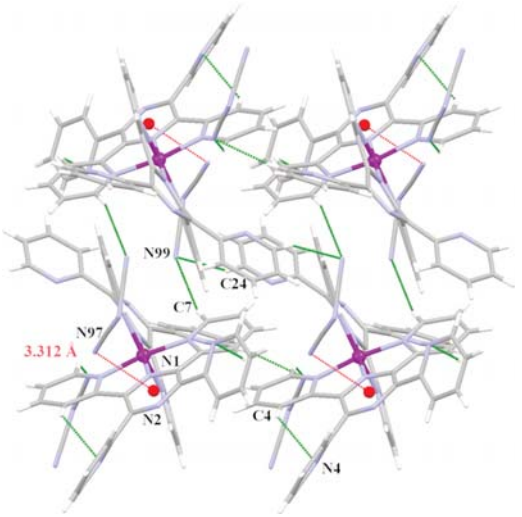

Figure 2. View of a fragment of the molecular packing of **1·125 K** showing C−H···N (green dotted line) and N_{dca}···π type (red dotted line) interactions between the dca^- groups and the pyrazine ring of the tppz ligands.

$[Co(tppz)_2][Co(NCS)_4]$·MeOH (**2**) *and* *$[Co(tppz)_2][Co(NCO)_4]·2H_2O$* (**3**). The crystal structures of **2** and **3** consist of $[Co(tppz)_2]^{2+}$ cations, $[Co(NCY)_4]^{2-}$ anions [Y = S (**2**) and O (**3**), and solvent molecules [MeOH (**2**) and H_2O (**3**)], interlinked by electrostatic forces, hydrogen bonds and π···π and Y···π type interactions (Tables S2−S4; Supporting Information). Most interestingly, compounds containing the tetrahedral $[Co(NCS)_4]^{2-}$ or $[Co(NCO)_4]^{2-}$ anions are relatively rare. A CSD search (Cambridge Structural Database, Version 5.37) revealed only 23 and 1 structures incorporating the $[Co(NCS)_4]^{2-}$ [55,92−113] or $[Co(NCO)_4]^{2-}$ [114] units, respectively.

Perspective views of the asymmetric units with the atom numbering of the compounds **2** and **3** are shown in Figures 3 and 4, respectively.

The cobalt(II) centers of the $[Co(NCS)_4]^{2-}$ and $[Co(NCO)_4]^{2-}$ complex anions have a distorted tetrahedral coordination environment defined by four nitrogen atoms from four terminal thiocyanate (**2**) or cyanate (**3**) ligands. Both pseudohalide groups are almost linear with values of the N−C−Y angles in the ranges 178.7(4)−178.9(4) (**2**) and 177.1(9)−179.2(8)° (**3**). In the case of $[Co(NCO)_4]^{2-}$, a significant bending is observed in the Co−N−C linkage [values of 133.5(5), 156.1(7), 157.4(5), and 167.1(5)°], while the Co−N−C angles of the $[Co(NCS)_4]^{2-}$ entity much less deviate from linearity [values ranging from 168.0(3) to 174.8(4)°]. Also, the distortion of the $[Co(NCS)_4]^{2-}$ unit from the ideal tetrahedral geometry in **2**, which is evidenced by the Co−N bond distances [1.953(4)−1.960(4) Å] and N−Co−N bond angles [105.89(17)−113.60(15)°], is smaller compared to that in $[Co(NCO)_4]^{2-}$ of **3** [Co−N bond lengths and N−Co−N angles in the ranges 1.946(5)−1.999(6) Å and 104.0(2)−115.4(3)°, respectively].

Additional information about the geometric distortion of $[Co(NCX)_4]^{2-}$ was obtained by performing continuous shape measurement (CShM) calculations,[115] which provide quantitative measures of the deviation of a given coordination sphere from the ideal geometry for which shape values equal zero. The calculated shape values with respect to the tetrahedron S(T_d)

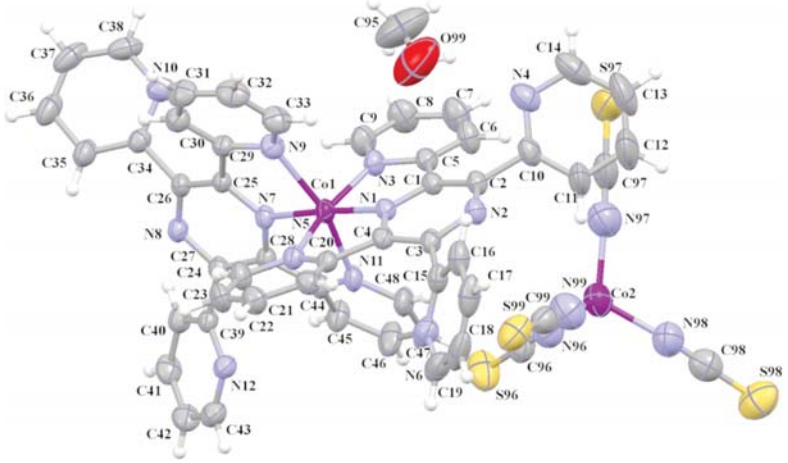

Figure 3. A perspective view of the asymmetric unit of **2** together with the atom numbering. The thermal ellipsoids are drawn at the 50% probability level.

DOI: 10.1021/acs.inorgchem.7b00360
Inorg. Chem. 2017, 56, 6281−6296

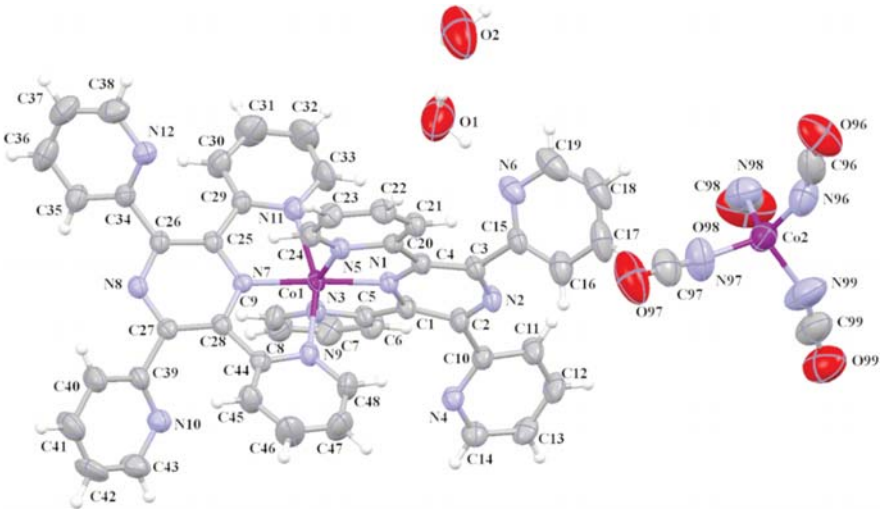

Figure 4. A perspective view of the asymmetric unit of **3** together with the atom numbering. The thermal ellipsoids are drawn at the 50% probability level.

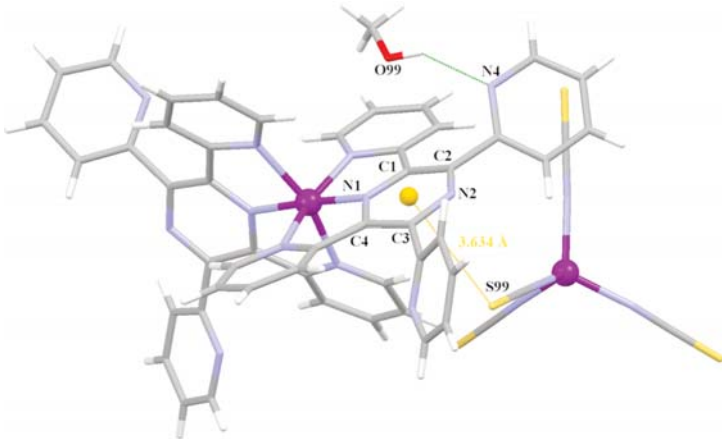

Figure 5. A view of the molecular structure of **2** showing the O(99)−H(99)···N(4) hydrogen bond and the S···π type interaction between the $[Co(tppz)_2]^{2+}$ complex cation and the $[Co(NCS)_4]^{2-}$ complex anion (yellow dotted line).

are 0.103 and 0.183 for $[Co(NCS)_4]^{2-}$ and $[Co(NCO)_4]^{2-}$, respectively, demonstrating that a larger distortion of the metal coordination sphere occurs in the tetrakis(cyanato-κN)-cobaltate(II) ion.

As in **1**, the tppz ligands in the $[Co(tppz)_2]^{2+}$ complex cations of **2** and **3** coordinate to the cobalt(II) ion in a *mer* fashion, equatorially via pyridyl donors (N_{py}) and axially through pyrazine nitrogen atoms (N_{pz}), to form a tetragonally compressed $[CoN_6]$ octahedral symmetry. An angular distortion of $[Co(tppz)_2]^{2+}$ is reflected in the N−Co−N angles: 79.04(9)−104.65(9) (**2**) and 79.25(11)−103.15(12)° (**3**) for the nitrogen atoms in cis disposition, and 158.64(8)−176.30(9) (**2**) and 158.93(12)−177.13(13)° (**3**) for those in trans arrangement. The values of the dihedral angle between the least-squares planes defined by the coordinated pyridyl and pyrazine rings of the two tppz ligands are 73.51 (**2**) and 79.19° (**3**). The values of the distortion parameter Σ are equal to 96.2 (**2**) and 88.8° (**3**), while those of Θ are 268 (**2**) and 285° (**3**). As discussed above for the structure **1**, the values of Σ and Θ may be distinctive of the spin state of the cobalt(II) ion. Their values for the $[Co(tppz)_2]^{2+}$ complex cations in **2** and **3** fall into the typical range of LS complexes (61.10−99.10 and 185−319° for Σ and Θ, respectively). Also, the values of the Co−N bond distances support that the cobalt(II) ions in $[Co(tppz)_2]^{2+}$ of **2** and **3** are practically low spin. Likewise in **1**, the cobalt−nitrogen bond lengths to the central pyrazine ring [1.869(2) and 1.927(2) (**2**) and 1.877(3) and 1.922(3) Å (**3**)] are shorter than those involving the outer pyridyl rings [1.984(2)−2.126(2) (**2**) and 1.997(3)−2.124(3) Å (**3**)]. The values of the average Co−N distance are 2.004 (**2**) and 2.005 Å (**3**).

The solvent molecules in the structures **2** and **3** are involved in hydrogen bonds. The OH group of the methanol molecule in **2** is hydrogen bonded to the N(4) atom of one

DOI: 10.1021/acs.inorgchem.7b00360
Inorg. Chem. 2017, 56, 6281−6296

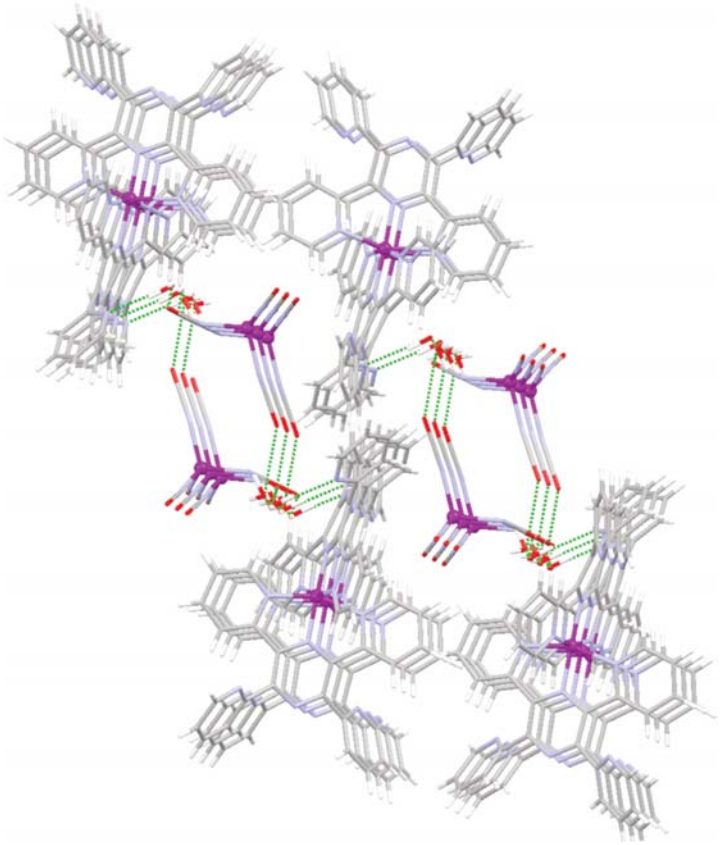

Figure 6. A view of a fragment of the supramolecular structure of **3** arising from the O—H···O and O—H···N hydrogen bonds.

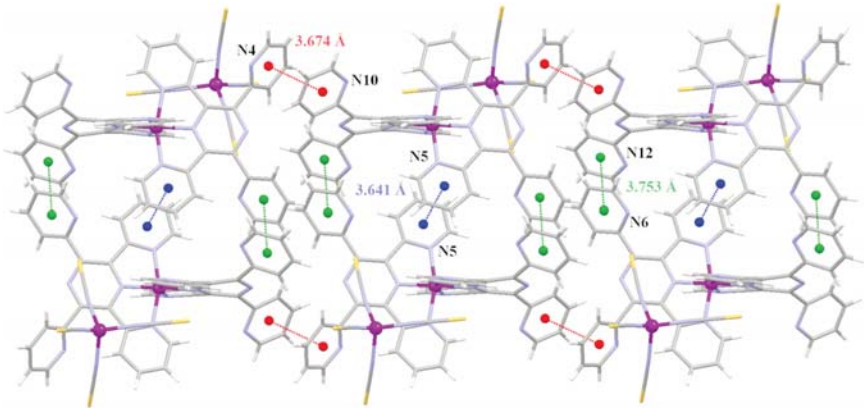

Figure 7. A view of the supramolecular double chain in **2** arising from weak $\pi\cdots\pi$ type interactions. The solvent molecules were omitted for clarity.

uncoordinated pyridyl ring of the tppz ligand [O(99)—H(99)···N(4) with D···A = 2.827(5) Å and D—H···A = 132.1°] (Figure 5), while the water molecules in **3** also form hydrogen bonds with the N(6) atom of one uncoordinated pyridyl ring of the tppz ligand [O(1)—H(1B)···N(6) with D···A = 2.945(7) Å and D—H···A angle = 166.2°] and an oxygen atom of the $[Co(NCO)_4]^{2-}$ anion [O(2)—H(2B)···O(97)[a] with D···A = 2.964(7) Å and D—H···A = 168.6°; symmetry code: (a) = 1/2 − *x*, −1/2 + *y*, *z*]. Moreover, one hydrogen bond involving only the water molecules occurs in **3** [O(1)—H(1A)···O(2) with D···A = 2.812(7) Å and D—H···A = 166.3°] (Figure 6).

In addition, the crystal structures of **2** and **3** are stabilized by intra- and intermolecular C—H···N and C—H···O type contacts

DOI: 10.1021/acs.inorgchem.7b00360
Inorg. Chem. 2017, 56, 6281−6296

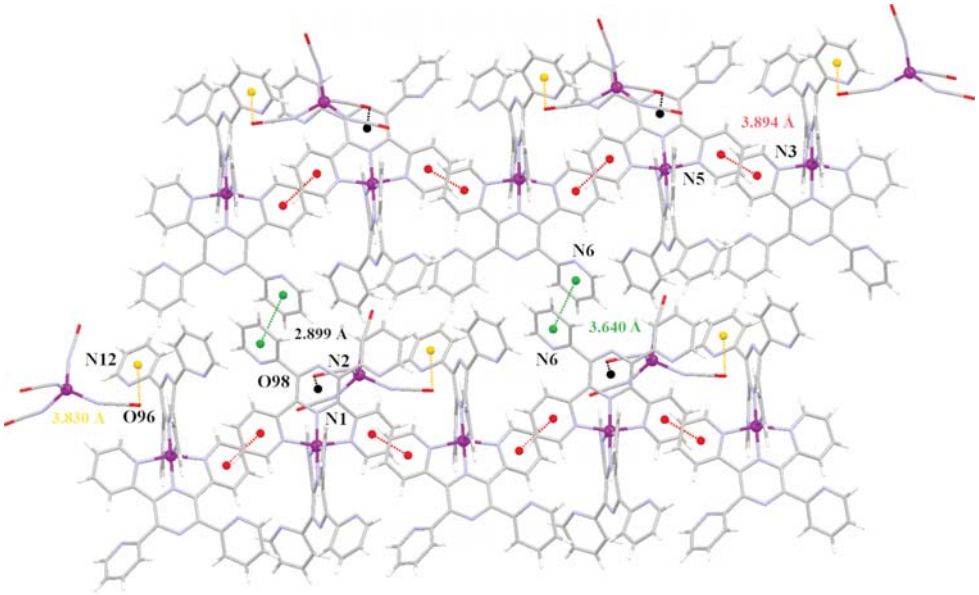

Figure 8. A view of the supramolecular 2D structure of **3** arising from weak $\pi\cdots\pi$ and O$\cdots\pi$ type interactions. The solvent molecules were omitted for clarity.

(Table S2) as well as through intermolecular $\pi-\pi$ stacking interactions between the pyridyl rings of the tppz ligand and S$\cdots\pi$ type or O$\cdots\pi$ type contacts, as shown in Figures 7 and 8. The metric parameters of the intermolecular contacts are gathered in Tables S2–S4. The shortest Co$\cdots$Co distances between $[Co(tppz)_2]^{2+}$ and $[Co(NCY)_4]^{2-}$ are 7.5141(7) (**2**) and 7.4020(9) Å (**3**) respectively, while the shortest Co$\cdots$Co distances between two $[Co(tppz)_2]^{2+}$ cations are equal to 8.1127(6) (**2**) and 8.3290(7) Å (**3**).

Magnetic Properties and EPR Spectra of 1–3. The $\chi_M T$ versus T plot for **1** [χ_M is the magnetic susceptibility per cobalt(II) ion] is shown in Figure 9. $\chi_M T$ follows a Curie law in the temperature range 1.9–170 K with a value of 0.42 cm^3 mol^{-1} K. This value is as expected for a spin doublet (S = 1/2 ground state with g = 2.12). Upon warming above 170 K, $\chi_M T$ smoothly increases to reach a value of 0.675 cm^3 mol^{-1} K at 400 K. This behavior is indicative of the occurrence of a very incomplete 1/2 (LS) ⇔ 3/2 (HS) conversion at 400 K. In this respect, $\chi_M T$ values in the range 2.5–3.0 cm^3 mol^{-1} K were observed for the complete population of the HS configuration of the cobalt(II) ion in the parent terpy- and 4-terpyridone-containing complexes.[50−58] The magnetization (M) versus H plot for **1** at 2.0 K corresponds to what is expected for a spin doublet with M at 5 T (the maximum available magnetic field in our magnetometer) tending to a value somewhat above 1.0 μ_B (see Figure S10 in the Supporting Information).

X-band EPR measurements on a frozen dmf solution of **1** at 4.0 K shows a quasi-isotropic spin doublet with an hyperfine splitting of A = 72 G in the form of eight lines due to the coupling to the I = 7/2 nucleus of the cobalt(II) with a g value of 2.13 (see inset of Figure 9).

The approach that we have used to treat the magnetic susceptibility data of **1** is based on the model proposed by Harris et al.[116] Having in mind the energy levels of the d^7 electronic configuration in the crossover region for an idealized

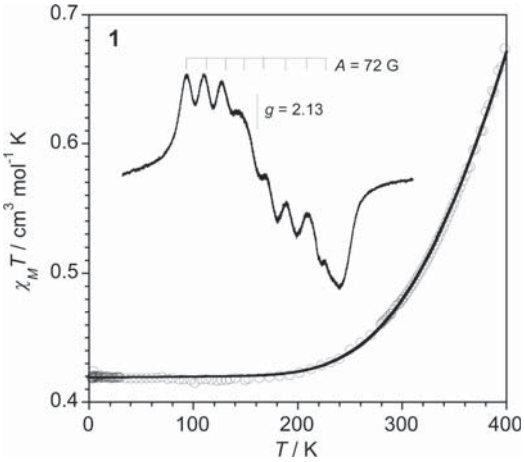

Figure 9. $\chi_M T$ against T plot for **1**: (○) experimental; (—) best-fit curve through eq 3 (see text). The inset shows the X-band EPR spectrum of **1** in a frozen dmf solution at 4.0 K.

octahedral complex (see Scheme 2) and following the Figgis' methodology[117] to estimate the effective magnetic moment for the $^4T_{1g}$ term, μ_{eff} ($^4T_{1g}$), and the application of the Van Vleck equation over the ^2E_g and $^4T_{1g}$ sates, one obtains eq 3

$$\chi_{ST}T = \left[1.5g_{LS}^2 C_{vib} + T_1 \exp(y + 2.5\alpha x) + T_2 \exp(y + \alpha x) + T_3 \exp(y - 1.5\alpha x)\right] / \left[16C_{vib} + 8\exp(y + 2.5\alpha x) + 16\exp(y + \alpha x) + 24\exp(y - 1.5\alpha x)\right] \quad (3)$$

DOI: 10.1021/acs.inorgchem.7b00360
Inorg. Chem. 2017, 56, 6281−6296

Scheme 2. Energy Levels for an Octahedral Cobalt(II) Complex in the Crossover Region

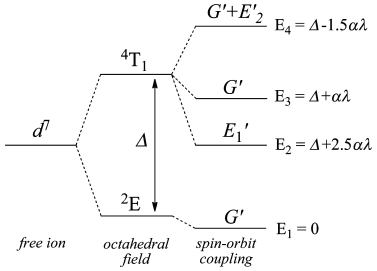

being

$$T_1 = \frac{(5+\alpha)^2}{3} - \frac{20(2+\alpha)^2}{9\alpha x}$$

$$T_2 = \frac{2(11-2\alpha)^2}{15} + \frac{176(2+\alpha)^2}{225\alpha x}$$

$$T_3 = \frac{21(3-\alpha)^2}{5} + \frac{36(2+\alpha)^2}{25\alpha x} \quad (3a)$$

$$x = -\frac{\lambda}{kT} \text{ and } y = -\frac{\Delta}{kT} \text{ and } \alpha - \kappa A \quad (3b)$$

In this equation, g_{LS} is the g-factor for the low-spin cobalt(II) ion (^2E_g state), λ is the spin−orbit coupling parameter (about −180 cm^{-1} for the free ion), Δ is the energy gap between the ^2E_g (low-spin) and $^4T_{1g}$ (high-spin) state (see Scheme 2), κ is an orbital reduction factor due to the covalency, and A is another orbital reduction factor caused by the mixture of the ground triplet, $^4T_{1g}(^4F)$ coming from the ^4F term, with the excited one, $^4T_{1g}(^4P)$ from the ^4P term. The value of A lies between 3/2 and 1 for the cases of weak and strong ligand field, respectively.

Given that the metal to ligand bond distances are different in the high- and low-spin species (different vibrational frequencies), vibrational partition functions have to be introduced in eq 3 for the estimation of the relative population of the two states. In this sense, the C_{vib} parameter was introduced therein where $C_{vib} = Q_E/Q_T$, Q_E, and Q_T being the vibrational partition functions (for the ^2E_g and $^4T_{1g}$ states, respectively) defined by Golding et al.[118] and Harris et al.[116]

In the context of the proposed model, the least-squares best-fit parameters through eqn 3 by using the *VPMAG* program[119] are g_{LS} = 2.12(1), C_{vib} = 0.1367(9), λ = −168 cm^{-1}, Δ = 1626 cm^{-1}, and α = 1.12(1). Assuming a value of A equal to 1.35 (intermediate value between weak and strong ligand field), one gets κ = 0.83. The calculated curve reproduces well the experimental data in the whole temperature range investigated, and the values of the best-fit parameters are in agreement with those previously reported for other $Co^{II}N_6$ SCO compounds.[59,83,116,120]

The magnetic properties of **2** and **3** under the form $\chi_M T$ against T plots [χ_M is the magnetic susceptibility per two cobalt(II) ions] are shown in Figures 10 and 11, respectively. The values of $\chi_M T$ at 300 K are 2.88 (**2**) and 2.97 cm^3 mol^{-1} K (**3**). Upon cooling, these values exhibit smooth decreases which are followed by Curie laws covering the temperature ranges 205−60 (**2**) and 180−45 K (**3**), and they further decrease to reach values of 2.09 (**2**) and 2.20 cm^3 mol^{-1} K (**3**) at 1.9 K. The thermal dependence of the $\chi_M T$ product in **2** and **3** obeys the coexistence of the $[Co(tppz)_2]^{2+}$ SCO unit and the paramagnetic $[Co(NCY)_4]^{2-}$ entity [Y = S (**1**) and O (**3**)] which are magnetically isolated. The decrease of $\chi_M T$ at low temperatures in both curves is essentially due to the zero-field splitting effects (D) of the $^4A_2$ ground-term of tetrahedral $[Co(NCY)_4]^{2-}$ unit, 2D being the energy gap between the |± 1/2> and |± 3/2> levels of the spin quadruplet. The M versus H plots for **2** and **3** at 4.0 K correspond to what is expected for the coexistence of a spin doublet and a spin quadruplet magnetically noninteracting, the value of M at 5 T tending to values somewhat above (**2**) and below (**3**) 4.0 μ_B [see Figures S11 (**2**) and S12 (**3**) in the Supporting Information].

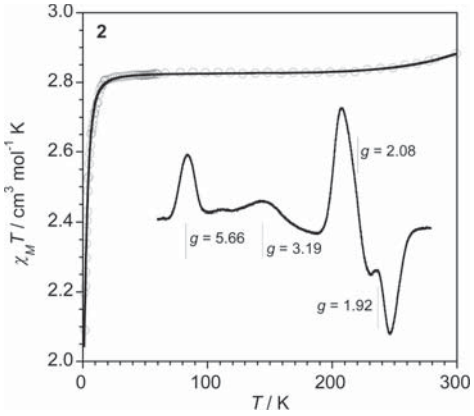

Figure 10. $\chi_M T$ versus T plot of **2**: (○) experimental; (—) best-fit curve through eq 4 (see text). The inset shows the Q-band EPR spectrum of a powdered sample of **2** recorded at 4.0 K.

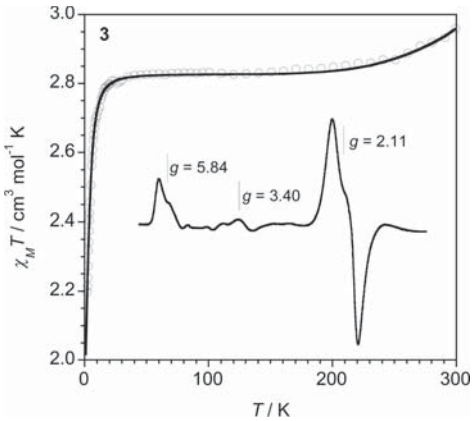

Figure 11. $\chi_M T$ versus T plot of **3**: (○) experimental; (—) best-fit curve through eq 4 (see text). The inset shows the Q-band EPR spectrum of a powdered sample of **3** recorded at 4.0 K.

Q-band EPR spectra of microcrystalline powder samples of **2** and **3** at 4.0 K (insets of Figure 10 and 11 respectively) are consistent with the presence of a low-spin cobalt(II) species [g_{LS} = 2.08 (**2**) and 2.11 (**3**)] and a tetrahedral high-spin cobalt(II) complex [g_{HS} values of 5.66, 3.19, and 1.92 (**2**) and 5.84 and 3.40 (**3**)].

DOI: 10.1021/acs.inorgchem.7b00360
Inorg. Chem. 2017, 56, 6281−6296

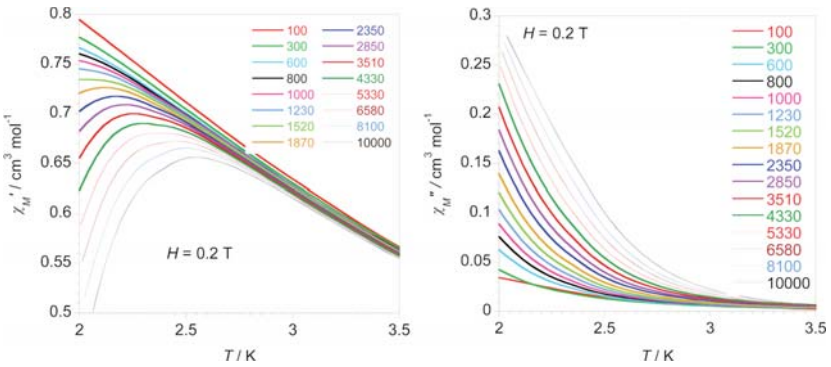

Figure 12. Frequency dependence of the (left) in-phase (χ_M') and (right) out-of-phase (χ_M'') components of the *ac* susceptibility for **3** under an applied static field of H_{dc} = 2000 G with a ±5.0 G oscillating field at frequencies in the range 100−10000 Hz.

Having in mind the coexistence in **2** and **3** of the $[Co(tppz)_2]^{2+}$ SCO unit and the four-coordinate $[Co(NCY)_4]^{2-}$ entity [Y = N (**2**) and O (**3**)], we analyzed the magnetic data of **2** and **3** through eq 4

$$\chi_M = \chi_{ST} + \chi_{HS} \quad (4)$$

with

$$\chi_{\parallel} = \frac{N\beta^2 g_{\parallel}^2}{4kT} \frac{1 + 9\exp(-2D/kT)}{1 + \exp(-2D/kT)}$$

$$\chi_{\perp} = \frac{N\beta^2 g_{\perp}^2}{4kT} \frac{4 + (3kT/D)[1 - \exp(-2D/kT)}{1 + \exp(-2D/kT)}$$

$$\chi_{HS} = \frac{\chi_{\parallel} + 2\chi_{\perp}}{3}$$

where the first term of eq 4 is corresponds to eq 3 and the second term accounts for the magnetic properties of the four-coordinate cobalt(II) unit which has been derived through the Hamiltonian of eq 5[121]

$$\mathbf{H} = D[\mathbf{S}_z^2 - 1/3S(S+1)] + g_{HS}\beta H\mathbf{S} \quad (5)$$

In this Hamiltonian we have neglected the rhombic components of the zero-field splitting to reduce the over-parameterization. Also for the same reason, we considered $g_{\parallel} = g_{\perp} = g_{HS}$ in the fitting process. The best-fit parameters through eq 4 are g_{LS} = 2.10(1), C_{vib} = 0.105(5), λ = −170(4) cm^{-1}, Δ = 1700(25) cm^{-1}, α = 1.10(2), g_{HS} = 2.27(1), and |*D*| = 3.80(2) for **2** and g_{LS} = 2.10(1), C_{vib} = 0.10(19), λ = −169(5) cm^{-1}, Δ = 1500(30) cm^{-1}, α = 1.10(3), g_{HS} = 2.28(1), and |*D*| = 4.30(3) cm^{-1} for **3**. Assuming a value of *A* = 1.35 for the SCO unit of **2** and **3**, the calculated value for κ is 0.82. The theoretical curves reproduce well the magnetic data in the whole temperature range investigated. The parameters obtained for the SCO unit in **2** and **3** are very close to those obtained for the same unit in **1**. The fact that the value of |*D*| for the tetrakis(*N*-thiocyanato)cobaltate(II) species in **2** is somewhat smaller than that of the tetrakis(*N*-cyanato)cobaltate)II) entity in **3** is due to the higher distortion of the ideal tetrahedral environment in the latter anionic complex as pointed out in the discussion of the respective structures.

Interestingly, compound **3** exhibits an incipient frequency-dependence of the out-of-phase signal (χ_M'') under external applied *dc* fields (H_{dc}) below 3.5 K down to the lowest temperature 2.0 K, as shown in Figure 12 (H_{dc} = 0.2 T) [see also Figures S13 (H_{dc} = 0.1 T) and S14 (H_{dc} = 0.4 T); Supporting Information)], a feature which is characteristic of SIMs behavior. Unfortunately, the expected maximum of χ_M'' due to the blocking could not be observed down to 2.0 K even to applying a *dc* magnetic field of 0.4 T [Figure S14 (right)].

However, under the assumption that the SIM has only one characteristic time, corresponding to a Debye relaxation process driven by one activation energy (E_a), the relaxation time (τ) may be written in terms of the Arrhenius law $\tau = \tau_0 \exp(E_a/k_BT)$. Taking into account that $\chi_M''/\chi_M' = 2\pi\nu\tau$ where ν is the experimental *ac* field exciting frequency, one obtains the relation $\ln(\chi_M''/\chi_M') = \ln(2\pi\nu\tau_0) + E_a/k_BT$, which allows to evaluate roughly the values of E_a and τ_o. This methodology has been applied successfully in other examples of SIMs and SMMs.[122−128] In the present case, the values obtained for E_a and τ_0 are 11.7 cm^{-1} and 2.2 × 10^{-9} s (Figure 13, H_{dc} = 0.2 T)

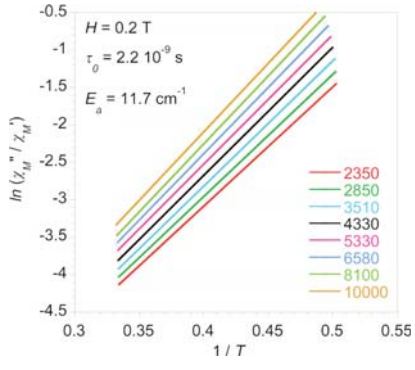

Figure 13. Natural logarithm of the χ_M''/χ_M' against $1/T$ for **3** under a *dc* field of 2000 G with a ± 5.0 G oscillating field at eight different frequencies.

and 12.0 cm^{-1} and 1.5 × 10^{-9} s (Figure S15, H_{dc} = 0.1 T; Supporting Information). The value of 2|*D*| (8.60 cm^{-1}) for **3** is somewhat below to that of E_a, the discrepancy between both values being most likely due to the rough approach used to evaluate the activation energy. The Cole−Cole plots of **3** in the temperature range 2.0−2.25 K at H_{dc} of 0.1 and 0.2 T [Figures S16(a) and S16(b), respectively; Supporting Information)]

DOI: 10.1021/acs.inorgchem.7b00360
Inorg. Chem. 2017, 56, 6281−6296

show only half of semicircles, precluding thus to go further in the analysis of these data. Finally, the fact that **2** does not exhibit the SIM behavior down to 2.0 K can be understood having in mind factors of the different ligand field strength and less distorted tetrahedral surrounding of the $[Co(NCS)_4]^{2-}$ unit (**2**) compared to $[Co(NCO)_4]^{2-}$ (**3**), the degrees of distortion being evaluated through continuous shape measurement calculations (see structural discussion).[115] Theoretical studies beyond the scope of the present work would be needed to understand the lack of SIM behavior for the $[Co(NCS)_4]^{2-}$ unit of **2**.

CONCLUSIONS

The comprehensive investigation on the structures and thermally induced SCO behavior of the $[Co(tppz)_2]^{2+}$ unit whose charge is counterbalanced by the diamagnetic organic dca group (**1**) and the paramagnetic $[Co(NCS)_4]^{2-}$ (**2**) and $[Co(NCO)_4]^{2-}$ (**3**) metalloligands has been carried out. The analysis of the structural data for the N_6-coordinated cobalt(II) compounds confirmed that the distortion parameters Σ and Θ can be distinctive of the cobalt(II) spin state. For compound **1**, a very incomplete 1/2 (LS) ⇔ 3/2 (HS) conversion occurs at 400 K. The most remarkable feature of **2** and **3** concerns the coexistence of the $[Co(tppz)_2]^{2+}$ SCO unit and the paramagnetic four-coordinate cobalt(II) ions $[Co(NCS)_4]^{2-}$ (**2**) and $[Co(NCO)_4]^{2-}$ (**3**) with a $^4A_2$ ground state. The coexistence in **3** of the SCO properties of the cation and the SIM behavior of the anion which is evidenced by the incipient frequency-dependent out-of-phase magnetic susceptibility signals under applied *dc* magnetic fields is also noteworthy. The best-fit parameters obtained for the SCO unit in **1**−**3** have comparable values, and the smaller value of *D* for the tetrakis(thiocyanato-*κN*)cobaltate(II) species in **2** compared to that of the tetrakis(cyanato-*κN*)cobaltate(II) entity in **3** is attributed to the higher distortion of the ideal tetrahedral environment in the latter anionic complex.

ASSOCIATED CONTENT

Supporting Information

The Supporting Information is available free of charge on the ACS Publications website at DOI: 10.1021/acs.inorgchem.7b00360.

Additional tables and figures as described in the text (PDF)

Accession Codes

CCDC 1529275−1529277 and 1529486 (**2**, **1·125 K**, **1·330 K**, and **3**, respectively) contain the supplementary crystallographic data for this paper. These data can be obtained free of charge via www.ccdc.cam.ac.uk/data_request/cif, or by emailing data_request@ccdc.cam.ac.uk, or by contacting The Cambridge Crystallographic Data Centre, 12 Union Road, Cambridge CB2 1EZ, UK; fax: +44 1223 336033.

AUTHOR INFORMATION

Corresponding Authors

*(J.P-G.) E-mail: jpalion-gazda@us.edu.pl.
*(M.J.) E-mail: miguel.julve@uv.es.

ORCID

Joanna Palion-Gazda: 0000-0003-1124-3182
Rafal Kruszynski: 0000-0003-1667-4379

Notes

The authors declare no competing financial interest.

ACKNOWLEDGMENTS

This work was supported by the Polish National Science Centre (Grant No. DEC-2012/07/N/ST5/02213), the Spanish MICINN (Projects CTQ2013-44844P, CTQ2016-75068P and Unidad de Excelencia Maria de MaetzuMD2015-0538), and the Generalitat Valenciana (PROMETEOII/2014/070). Thanks are due to the Universitat de València for a predoctoral grant (T.G.) and the DoktorisProject cofinanced by The European Social Fund for a scholarship (J.P.G.).

REFERENCES

(1) Eichhöfer, E.; Lan, Y.; Mereacre, V.; Bodenstein, T.; Weigend, F. Slow Magnetic Relaxation in Trigonal-Planar Mononuclear Fe(II) and Co(II) Bis(trimethylsilyl)amido Complexes—A Comparative Study. *Inorg. Chem.* **2014**, *53*, 1962−1974.

(2) Zadrozny, J. M.; Long, J. R. Slow Magnetic Relaxation at Zero Field in the Tetrahedral Complex $[Co(SPh)_4]^{2-}$. *J. Am. Chem. Soc.* **2011**, *133*, 20732−20734.

(3) Zadrozny, J. M.; Liu, J.; Piro, N. A.; Chang, C. J.; Hill, S.; Long, J. R. Slow magnetic relaxation in a pseudotetrahedral cobalt(II) complex with easy-plane anisotropy. *Chem. Commun.* **2012**, *48*, 3927−3929.

(4) Buchholz, A.; Eseola, A. O.; Plass, W. Slow magnetic relaxation in mononuclear tetrahedral cobalt(II) complexes with 2-(1H-imidazol-2-yl)phenol based ligands. *C. R. Chim.* **2012**, *15*, 929−936.

(5) Cao, D.-K.; Feng, J. Q.; Ren, M.; Gu, Y. W.; Song, Y.; Ward, M. D. A mononuclear cobalt(II)-dithienylethene complex showing slow magnetic relaxation and photochromic behavior. *Chem. Commun.* **2013**, *49*, 8863−8865.

(6) Saber, M. R.; Dunbar, K. R. Ligand effects on the magnetic anisotropy of tetrahedral cobalt complexes. *Chem. Commun.* **2014**, *50*, 12266−12269.

(7) Boča, R.; Miklovič, J.; Titiš, J. Simple Mononuclear Cobalt(II) Complex: A Single-Molecule Magnet Showing Two Slow Relaxation Processes. *Inorg. Chem.* **2014**, *53*, 2367−2369.

(8) Cucos, P.; Sorace, L.; Matei, I.; Maxim, C.; Shova, S.; Gheorghe, R.; Caneschi, A.; Hillebrand, M.; Andruh, M.; Tuna, F. Magnetic and Luminiscent Binuclear Double-Stranded Helicates. *Inorg. Chem.* **2014**, *53*, 7738−7747.

(9) Cao, D.-K.; Wei, R. H.; Li, X. X.; Gu, Y. W. Multifunctional mononuclear bisthienylethene-cobalt(II) complexes: structures, slow magnetic relaxation and photochromic behavior. *Dalton Trans.* **2015**, *44*, 5755−5762.

(10) Smolko, L.; Ĉernák, J.; Dušek, M.; Miklovič, J.; Titiš, J.; Boča, R. Three tetracoordinate Co(II) complexes $[Co(biq)X_2]$ (X = Cl, Br, I) with easy-plane anisotropy as field-induced single-molecule magnets. *Dalton Trans.* **2015**, *44*, 17565−17571.

(11) Ziegenbalg, S.; Hornig, D.; Görls, H.; Plass, W. Cobalt(II)-Based Single-Ion Magnets with Distorted. Pseudotetrahedral $[N_2O_2]$ Coordination: Experimental and Theoretical Investigations. *Inorg. Chem.* **2016**, *55*, 4047−4058.

(12) Rajnák, C.; Packová, A.; Titiš, J.; Miklovič, J.; Moncol', J.; Boča, R. A tetracoordinate Co(II) single molecule magnet based on triphenylphosphine and isothiocyanato group. *Polyhedron* **2016**, *110*, 85−92.

(13) Jurca, T.; Farghal, A.; Lin, P. H.; Korobkov, I.; Murugesu, M.; Richeson, D. S. Single-Molecule Magnet Behavior with a Single Metal Center Enhanced through Peripheral Ligand Modifications. *J. Am. Chem. Soc.* **2011**, *133*, 15814−15817.

(14) Habib, F.; Luca, O. R.; Vieru, V.; Shiddiq, M.; Korobkov, I.; Gorelsky, S. I.; Takase, M. K.; Chibotaru, L. F.; Hill, S.; Crabtree, R. H.; Murugesu, M. Influence of the Ligand Field on Slow Magnetization Relaxation versus Spin Crossover in Mononuclear Cobalt Complexes. *Angew. Chem., Int. Ed.* **2013**, *52*, 11290−11293.

DOI: 10.1021/acs.inorgchem.7b00360
Inorg. Chem. 2017, 56, 6281−6296

(15) Rajnák, C.; Titiš, J.; Fuhr, O.; Ruben, M.; Boča, R. Single-Molecule Magnetism in a Pentacoordinate Cobalt(II) Complex Supported by an Antenna Ligand. *Inorg. Chem.* **2014**, *53*, 8200−8202.
(16) Ruamps, R.; Batchelor, L. J.; Guillot, R.; Zakhia, G.; Barra, A.-L.; Wernsdorfer, W.; Guihéry, N.; Mallah, T. Ising-type magnetic anisotropy and single molecule magnetic behavior in mononuclear trigonal bipyramidal Co(II) complexes. *Chem. Sci.* **2014**, *5*, 3418−3424.
(17) Piñero Cruz, D. M.; Woodruff, D. N.; Jeon, I. R.; Bhowmick, I.; Secu, M.; Hillard, E. A.; Dechambenoit, P.; Clérac, R. Switching off the single-molecule magnet properties of the $[Co(Me_6tren)(OH_2)]^{2+}$ module by complexation with *trans*-$[Re(salen)(CN)_2]^-$. *New J. Chem.* **2014**, *38*, 3443−3448.
(18) Nedelko, N.; Kornowicz, A.; Justyniak, I.; Aleshkevych, P.; Prochowicz, D.; Krupiński, P.; Dorosh, O.; Ślawska-Waniewska, A.; Lewiński, J. Supramolecuar Control over Molecular Magnetic Materials: γ-Cyclodextrin-Templated Grid of Cobalt(II) Single-Ion Magnets. *Inorg. Chem.* **2014**, *53*, 12870−12876.
(19) Packová, A.; Miklovič, J.; Boča, R. Manifold relaxation processes in a mononuclear Co(II) single-molecule magnet. *Polyhedron* **2015**, *102*, 88−93.
(20) Shao, F.; Cahier, B.; Guihéry, N.; Rivière, E.; Guillot, R.; Barra, A.-L.; Lan, Y.; Wernsdorfer, W.; Campbell, V. E.; Mallah, T. Tuning the Ising-type anisotropy in trigonal bipyramidal Co(II) complexes. *Chem. Commun.* **2015**, *51*, 16475−16478.
(21) Vallejo, J.; Castro, I.; Ruiz-García, R.; Cano, J.; Julve, M.; Lloret, F.; De Munno, G.; Wernsdorfer, W.; Pardo, E. Field-Induced Slow Magnetic Relaxation in a Six-Coordinate Mononuclear Cobalt(II) Complex with a Positive Anisotropy. *J. Am. Chem. Soc.* **2012**, *134*, 15704−15707.
(22) Gómez-Coca, S.; Urtizberea, A.; Cremades, E.; Alonso, P. J.; Camón, A.; Luis, F.; Ruiz, E. Origin of slow magnetic relaxation in Kramers ions with non-uniaxial anisotropy. *Nat. Commun.* **2014**, *5*, 4300−4307.
(23) Herchel, R.; Váhovská, L.; Potočňák, I.; Trávníček, Z. Slow Magnetic Relaxation in Octahedral Cobalt(II) Field-Induced Single-Ion Magnet with Positive Axial and Large Rhombic Anisotropy. *Inorg. Chem.* **2014**, *53*, 5896−5898.
(24) Zhu, Y.-Y.; Yin, T.-T.; Liu, C.-W.; Gao, C.; Wu, Z. Q.; Zhang, Y.-Q.; Wang, B.-W; Gao, S. Field-induced slow magnetic relaxation in a hydrogen-bonded linked Co(II) 1D supramolecular coordination polymer. *Supramol. Chem.* **2015**, *27*, 401−406.
(25) Plenk, C.; Krause, J.; Rentschler, E. A Click-Functionalized Single-Molecule magnet Based on Cobalt(II) and Its Analogous Manganese(II) and Zinc(II) Compounds. *Eur. J. Inorg. Chem.* **2015**, *2015*, 370−374.
(26) Novikov, V. V.; Pavlov, A. A.; Nelyubina, Y. V.; Boulon, M.-E.; Varzatskii, O. A.; Voloshin, Y. Z.; Winpenny, R. E. P. A Trigonal Prismatic Mononuclear Cobalt(II) Complex Showing Single-Molecule Magnet Behavior. *J. Am. Chem. Soc.* **2015**, *137*, 9792−9795.
(27) Li, J.; Han, Y.; Cao, F.; Wei, R.-M.; Zhang, Y.-Q.; Song, Y. Two-field induced slow magnetic relaxation processes in a mononuclear cobalt(II) complex with a distorted octahedral geometry. *Dalton Trans.* **2016**, *45*, 9279−9284.
(28) Świtlicka-Olszewska, A.; Palion-Gazda, J.; Klemens, T.; Machura, B.; Vallejo, J.; Cano, J.; Lloret, F.; Julve, M. Single-ion magnet behavior in mononuclear and two-dimensional dicyanamide-containing cobalt(II) complexes. *Dalton Trans.* **2016**, *45*, 10181−10193.
(29) Zhang, Y.-Z.; Gómez-Coca, S.; Brown, A. J.; Saber, M. R.; Zhang, X.; Dunbar, K. R. Trigonal antiprismatic Co(II) single molecule magnets with large uniaxial anisotropies: importance of Raman and tunneling mechanisms. *Chem. Sci.* **2016**, *7*, 6519−6527.
(30) Roy, S.; Oyarzabal, I.; Vallejo, J.; Cano, J.; Colacio, E.; Bauza, A.; Frontera, A.; Kirillov, A. M.; Drew, M. G. B.; Das, S. Two Polymorphic Forms of a Six-Coordinate Mononuclear Cobalt(II) Complex with Easy-Plane Anisotropy: Structural Features, Theoretical Calculations, and Field-Induced Slow Relaxation of the Magnetization. *Inorg. Chem.* **2016**, *55*, 8502−8513.
(31) Palii, A. V.; Korchagin, D. V.; Yureva, E. A.; Akimov, A. V.; Misochko, W. Ya.; Aldoshin, S. M.; Shilov, G. V.; Talantsev, A. D.; Morgunov, R. B.; Tsukerblat, B. S. Single-Ion Magnet $Et_4[Co^{II}(hfac)_3]$ with Nonuniaxial Anisotropy: Synthesis, Experimental Characterization, and Theoretical Modeling. *Inorg. Chem.* **2016**, *55*, 9696−9706.
(32) Chandrasekhar, V.; Dey, A.; Mota, A. J.; Colacio, E. Slow Magnetic Relaxation in Co(III)-Co(II) Mixed-Valence Dinuclear Complexes with a $Co^{II}O_5X$ (X = Cl, Br, NO_3) Distorted-Octahedral Coordination Sphere. *Inorg. Chem.* **2013**, *52*, 4554−4561.
(33) Wu, D.; Zhang, X.; Huang, P.; Huang, W.; Ruan, M.; Ouyang, Z. W. Tuning Transverse Anisotropy in Co^{III}-Co^{II}-Co^{III} Mixed-Valence Complex toward Slow Magnetic Relaxation. *Inorg. Chem.* **2013**, *52*, 10976−10982.
(34) Zhu, Y.-Y.; Cui, C.; Zhang, Y.-Q.; Jia, J.-H.; Guo, X.; Gao, C.; Qian, K.; Jiang, S.-D.; Wang, B.-W.; Wang, Z. M.; Gao, S. Zero-field slow magnetic relaxation from single Co(II) ion: a transition metal single-molecule magnet with high anisotropy barrier. *Chem. Sci.* **2013**, *4*, 1802−1806.
(35) Colacio, E.; Ruiz, J.; Ruiz, E.; Cremades, E.; Krzystek, J.; Carretta, S.; Cano, J.; Guidi, T.; Wernsdorfer, W.; Brechin, E. K. Slow Magnetic Relaxation in a Co^{II}-Y^{III} Single-Ion Magnet with Positive Axial Zero-Field Splitting. *Angew. Chem., Int. Ed.* **2013**, *52*, 9130−9134.
(36) Ion, A.; Nica, S.; Madalan, A. M.; Shova, S.; Vallejo, J.; Julve, M.; Lloret, F.; Andruh, M. Two-Dimensional Coordination Polymers Constructed Using Simultaneously, Linear and Angular Spacers and Cobalt(II) Nodes. New Examples of Single-Ion Magnets. *Inorg. Chem.* **2015**, *54*, 16−18.
(37) Zhu, Y.-Y.; Zhu, M.-S.; Yin, T.-T.; Meng, Y.-S.; Wu, Z.-Q.; Zhang, Y.-Q.; Gao, S. Cobalt(II) Coordination Polymer Exhibiting Single-Ion-Magnet-Type Field-Induced Slow Relaxation Behavior. *Inorg. Chem.* **2015**, *54*, 3716−3718.
(38) Palion-Gazda, J.; Klemens, T.; Machura, B.; Vallejo, J.; Lloret, F.; Julve, M. Single ion magnet behaviour in a two-dimensional network of dicyanamide-bridged cobalt(II) ions. *Dalton Trans.* **2015**, *44*, 2989−2992.
(39) Zhu, Y.-Y; Zhang, Y.-Q.; Yin, T.-T.; Gao, C.; Wang, B.-W.; Gao, S. A Family of $Co^{II}Co^{III}$ Single-Ion Magnets with Zero-Field Slow Magnetic Relaxation: Fine Tuning of Energy Barrier by Remote Substituent and Counter Cation. *Inorg. Chem.* **2015**, *54*, 5475−5486.
(40) Liu, X.; Sun, L.; Zhou, H.; Cen, P.; Jin, X.; Xie, G.; Chen, S.; Hu, Q. Single-Ion-Magnet Behavior in aTwo-Dimensional Coordination Polymer Constructed from Co^{II} Nodes and a Pyridylhydrazone Derivative. *Inorg. Chem.* **2015**, *54*, 8884−8886.
(41) Vallejo, J.; Fortea-Pérez, F. R.; Pardo, E.; Benmansour, S.; Castro, I.; Krzystek, J.; Armentano, D.; Cano, J. Guest-dependent single-ion magnet behavior in a cobalt(II) metal-organic framework. *Chem. Sci.* **2016**, *7*, 2286−2293.
(42) Aravena, D.; Venegas-Yazigi, D.; Ruiz, E. Single-Molecule Magnet Properties of Transition-Metal Ions Encapsulated in Lacunary Polyoxometalates: A Theoretical Study. *Inorg. Chem.* **2016**, *55*, 6405−6413.
(43) Huang, X.-C.; Zhou, C.; Shao, D.; Wang, X.-Y. Field-Induced Slow Magnetic Relaxation in Cobalt(II) Compounds with Pentagonal Bipyramidal Geometry. *Inorg. Chem.* **2014**, *53*, 12671−12673.
(44) Habib, F.; Korobkov, I.; Murugesu, M. Exposing the intermolecular nature of the second relaxation pathway in a mononuclear cobalt(II) single-molecule magnet with positive anisotropy. *Dalton Trans.* **2015**, *44*, 6368−6373.
(45) Chen, L.; Chen, S.-Y.; Sun, Y.-C.; Guo, Y.-M.; Yu, L.; Chen, X.-T.; Wang, Z.; Ouyang, Z.-W.; Song, Y.; Xue, Z.-L. Slow magnetic relaxation in mononuclear seven-coordinate cobalt(II) complexes with easy plane anisotropy. *Dalton Trans.* **2015**, *44*, 11482−11490.
(46) Antal, P.; Drahoš, B.; Herchel, R.; Trávníček, Z. Late-First-Row Transition Metal Complexes Containing a 2-Pyridylmethyl Pendant-Armed 15-Membered Macrocyclic Ligand. Field-Induced Slow Magnetic Relaxation in a Seven-Coordinate Cobalt(II) Complex. *Inorg. Chem.* **2016**, *55*, 5957−5972.
(47) Chen, L.; Cui, H.-H.; Stavretis, S. E.; Hunter, S. C.; Zhang, Y.-Q.; Chen, X.-T.; Sun, Y.-C.; Wang, Z.; Song, Y.; Podlesnyak, A. A.;

DOI: 10.1021/acs.inorgchem.7b00360
Inorg. Chem. 2017, 56, 6281−6296

Ouyang, Z.-W.; Xue, Z.-L. Slow Magnetic Relaxation in Cobalt(II) Tetranitrate Complexes. Studies of Magnetic Anisotropy by Inelastic Neutron Scattering and High-Frequency EPR Spectroscopy. *Inorg. Chem.* **2016**, *55*, 12603−12617.
(48) Chen, L.; Wang, J.; Wei, J. M.; Wernsdorfer, W.; Chen, X.-T.; Zhang, Y.-Q.; Song, Y.; Xue, Z.-L. Slow Magnetic Relaxation in a Mononuclear Eight-Coordinate Cobalt(II) Complex. *J. Am. Chem. Soc.* **2014**, *136*, 12213−12216.
(49) Wei, J.-M.; Zhang, Y.-Q. Unexpectedly Strong Magnetic Anisotropy in a Mononuclear Eight-Coordinate Cobalt(II) Complex: a Theoretical Exploration. *Inorg. Chem.* **2015**, *54*, 1203−1205.
(50) Goodwin, H. A. Spin Crossover in Cobalt(II) Systems. *Top. Curr. Chem.* **2004**, *234*, 23−47.
(51) Krivokapic, I.; Zerara, M.; Daku, M. L.; Vargas, A.; Enachescu, C.; Ambrus, C.; Tregenna-Piggott, P.; Amstutz, N.; Krausz, E.; Hauser, A. Spin-crossover in cobalt(II) − imine complexes. *Coord. Chem. Rev.* **2007**, *251*, 364−378.
(52) Hayami, S.; Komatsu, Y.; Shimizu, T.; Kamihata, H.; Lee, Y. H. Spin-crossover in cobalt(II) compounds containing terpyridine and its derivatives. *Coord. Chem. Rev.* **2011**, *255*, 1981−1990.
(53) Kremer, S.; Henke, W.; Reinen, D. High-Spin-Low-Spin Equilibria of Cobalt(2+) in the Terpyridine Complexes $Co(terpy)_2X_2 \cdot nH_2O$. *Inorg. Chem.* **1982**, *21*, 3013−3022.
(54) Figgis, B. N.; Kucharski, E. S.; White, A. W. Crystal structure of Bis(2,2′.6′,6″-terpyridyl)cobalt(II) perchlorate c. 1.3 hydrate. *Aust. J. Chem.* **1983**, *36*, 1537−1561.
(55) Galet, A.; Gaspar, A. B.; Muñoz, M. C.; Real, J. A. Influence of the Counterion and the Solvent Molecules in the Spin Crossover System $[Co(4\text{-terpyridone})_2]X_p \cdot nH_2O$. *Inorg. Chem.* **2006**, *45*, 4413−4422.
(56) Enachescu, C.; Krikokapic, I.; Zerara, M.; Real, J. A.; Amstutz, N.; Hauser, A. Optical investigation of spin-crossover in cobalt(II) bis-terpy complexes. *Inorg. Chim. Acta* **2007**, *360*, 3945−3950.
(57) Kilner, C. A.; Halcrow, M. An unusual discontinuity in the thermal spin transition in $[Co(terpy)_2][BF_4]_2$. *Dalton Trans.* **2010**, *39*, 9008−9012.
(58) Cowan, M. G.; Olguín, J.; Narayanaswamy, S.; Tallon, J. L.; Brooker, S. Reversible Switching of a Cobalt Complex by Thermal, Pressure, and Electrochemical Stimuli: Abrupt, Complete, Hysteretic Spin Crossover. *J. Am. Chem. Soc.* **2012**, *134*, 2892−2894.
(59) Hayami, S.; Urakami, D.; Kojima, Y.; Yoshizaki, H.; Yamamoto, Y.; Kato, K.; Fuyuhiro, A.; Kawata, S.; Inoue, K. Stabilization of Long-Lived Metastable State in Long Alkylated Spin-Crossover Cobalt(II) Compound. *Inorg. Chem.* **2010**, *49*, 1428−1432.
(60) Oliveira, W. X. C.; Pereira, C. L. M.; Pinheiro, C. B.; Krambrock, K.; Grancha, T.; Moliner, N.; Lloret, F.; Julve, M. Oxotris(oxalate)-niobate(V) as counterion in cobalt(II) spin-crossover systems. *Polyhedron* **2016**, *117*, 710−717.
(61) Gütlich, P.; Garcia, Y.; Goodwin, H. A. Spin crossover phenomena in Fe(II) complexes. *Chem. Soc. Rev.* **2000**, *29*, 419−427.
(62) Real, J. A.; Gaspar, A. B.; Niel, V.; Muñoz, M. C. Communication between iron(II) building blocks and cooperative spin transition phenomena. *Coord. Chem. Rev.* **2003**, *236*, 121−141.
(63) Halcrow, M. A. Structure:function relationships in molecular spin-crossover complexes. *Chem. Soc. Rev.* **2011**, *40*, 4119−4192.
(64) Miller, R. G.; Narayanaswamy, S.; Tallon, J. L.; Brooker, S. Spin crossover with thermal hysteresis in cobalt(II) complexes and the importance of the scan rate. *New J. Chem.* **2014**, *38*, 1932−1941.
(65) Vieira, B. J. C.; Dias, J. C.; Santos, I. C.; Pereira, L. C. J.; da Gama, V.; Waerenborgh, J. C. Thermal Hysteresis in a Spin-Crossover Fe^{III} Quinolylsalicylaldimine Complex, $Fe^{III}(5\text{-Br-qsal})_2Ni(dmit)_2 \cdot$ solv: Solvent Effects. *Inorg. Chem.* **2015**, *54*, 1354−1362.
(66) Létard, J.-F.; Guionneau, P.; Goux-Capes, L. Towards spin crossover applications. In Gütlich, P., Goodwin, H. A., Eds.; Spin Crossover in Transition Metal Compounds III. *Top. Curr. Chem.* **2004**, *235*, 221−249.10.1007/b95429
(67) Linares, J.; Codjovi, E.; García, J. Pressure and Temperature Spin Crossover Sensors with Optical Detection. *Sensors* **2012**, *12*, 4479−4492.
(68) *Spin Crossover Materials: Properties and Applications*. Halcrow, M. A., Eds.; John Wiley & Sons, Ltd.: Chichester, U. K., 2013.
(69) Bartual-Murgui, C.; Akou, A.; Thibault, C.; Molnár, G.; Vieu, C.; Salmon, L.; Bousseksou, A. Spin-crossover metal-organic frameworks: promising materials for designing gas sensors. *J. Mater. Chem. C* **2015**, *3*, 1277−1285.
(70) Lefter, C.; Davesne, V.; Salmon, L.; Molnár, G.; DEmont, P.; Rotaru, C.; Bousseksou, A. Charge Transport and Electrical Properties of Spin Crossover Materials: Towards Nanoelectronic and Spintronic Devives. *Magnetochemistry* **2016**, *2*, 18.
(71) Graf, M.; Stoeckli-Evans, H.; Escuer, A.; Vicente, R. Significant antiferromagnetic exchange in copper(II) and nickel(II) dinuclear complexes of the substituted pyrazine ligand 2,3,5,6-tetra(2-pyridyl)-pyrazine (TPPZ): magnetic properties and crystal structure. *Inorg. Chim. Acta* **1997**, *257*, 89−97.
(72) Carranza, J.; Brennan, C.; Sletten, J.; Clemente-Juan, J. M.; Lloret, F.; Julve, M. Crystal Structures and Magnetic Properties of 2,3,5,6-Tetrakis(2-pyridyl)pyrazine (tppz)-Containing Copper(II) Complexes. *Inorg. Chem.* **2003**, *42*, 8716−8727.
(73) Carranza, J.; Sletten, J.; Brennan, C.; Lloret, F.; Cano, J.; Julve, M. Mono- di- and trinuclear 2,3,5,6-tetrakis(2-pyridyl)pyrazine (tppz)-containing copper(II) complexes: syntheses, crystal structures and magnetic properties. *Dalton Trans.* **2004**, 3997−4005.
(74) Hsu, G.-Y.; Chen, C.-W.; Cheng, S.-C.; Lin, S.-H.; Wei, H.-H.; Lee, C.-J. Structure and magnetic properties of one-dimensional metal complexes constructed from alternating dicyanamide linked through binuclear metal tetra-2-pyridylpyrazine subunits. *Polyhedron* **2005**, *24*, 487−494.
(75) Hadadzadeh, H.; Rezvani, A. R.; Yap, G. P. A.; Crutchley, R. J. Dinuclear copper(II) chloro complex of the ligand 2,3,5,6-tetra(2-pyridyl)pyrazine. *Inorg. Chim. Acta* **2005**, *358*, 1289−1292.
(76) Yuste, C.; Armentano, D.; Marino, N.; Cañadillas-Delgado, L.; Delgado, F. S.; Ruiz-Pérez, C.; Rillema, D. P.; Lloret, F.; Julve, M. Synthesis, crystal structures, and magnetic properties of tricyanomthanide-containing copper(II) complexes. *Dalton Trans.* **2008**, 1583−1596.
(77) Yuste, C.; Cañadillas-Delgado, L.; Ruiz-Pérez, C.; Lloret, F.; Julve, M. Dinuclear, tetranuclear and one-dimensional pyrazine-based copper(II) complexes: preparation, X-ray structure and magnetic properties. *Dalton Trans.* **2010**, *39*, 167−179.
(78) Machura, B.; Świtlicka, A.; Palion, J.; Kruszyński, R. Synthesis, spectroscopic characterization, X-ray structure, and DFT calculations of $[Cu(tppz)(SCN)_2]$. *Struct. Chem.* **2013**, *24*, 89−96.
(79) Callejo, L. M.; Madariaga, G.; Lezama, L.; Fidalgo, L.; De la Pinta, N.; Cortés, R. Trinuclear Nickel(II) Complex through a 2,3,5,6-Tetrakis(2-pyridyl)pyrazine Ligand with a Linear Exchange Pathway. *Inorg. Chem.* **2010**, *49*, 5353−5355.
(80) Toma, L. M.; Armentano, D.; De Munno, G.; Sletten, J.; Lloret, F.; Julve, M. 2,3,5,6-Tetrakis(2-pyridyl)pyrazine (tppz)-containing iron(II) complexes. Synthesis and crystal structures. *Polyhedron* **2007**, *26*, 5263−5270.
(81) Campos-Fernández, C. S.; Smucker, D. W.; Clérac, R.; Dunbar, K. R. Reactivity Studies of 2,3,5,6-Tetra(2-pyridyl)pyrazine (tppz) with First-Row Transition Metal ions. *Isr. J. Chem.* **2001**, *41*, 207−218.
(82) Luo, J.; Qiu, L.; Liu, B.; Zhang, X.; Yang, F.; Cui, L. Synthesis, Structure and Magnetic Properties of Two Cobalt(II) Dicyanamide (dca) Complexes with Heterocyclic Nitrogen Donors Tetra(2-pyridyl)pyrazine (tppz) and 2,4.6-Tri(2-pyridyl)-1,3,5-triazine (tptz): $[Co_2(tppz)(dca)_4] \cdot CH_3CN$ and $[Co_2(tptz)(dca)(H_2O)](dca)$. *Chin. J. Chem.* **2012**, *30*, 522−528.
(83) Palion-Gazda, J.; Świtlicka-Olszewska, A.; Machura, B.; Grancha, T.; Pardo, E.; Lloret, F.; Julve, M. High-Temperature Spin Crossover in a Mononuclear Six-Coordinate Cobalt(II) Complex. *Inorg. Chem.* **2014**, *53*, 10009−10011.
(84) Machura, B.; Palion, J.; Mroziński, J.; Kalińska, B.; Amini, M.; Najafpour, M. M.; Kruszynski, R. Manganese(II) complexes of tetra-(2-pyridyl)pyrazine − Syntheses, crystal structures, spectroscopic, magnetic and catalytic properties. *Polyhedron* **2013**, *53*, 132−143.

DOI: 10.1021/acs.inorgchem.7b00360
Inorg. Chem. 2017, 56, 6281−6296

(85) Demir, S.; Nippe, M.; Gonzalez, M. I.; Long, J. R. Exchange coupling and magnetic blocking in dilanthanide complexes bridged by the multielectron redox-active ligand tetra(2-pyridyl)pyrazine. *Chem. Sci.* **2014**, *5*, 4701−4711.
(86) Shatruk, M.; Phan, H.; Chrisostomo, B. A.; Suleimenova, A. Symmetry-breaking structural phase transitions in spin crossover complexes. *Coord. Chem. Rev.* **2015**, *289*−*290*, 62−73.
(87) *CrysAlisPRO*; Oxford Diffraction /Agilent Technologies UK Ltd: Yarnton, England, 2014.
(88) Sheldrick, G. M. *Acta Crystallogr., Sect. A: Found. Crystallogr.* **2008**, *64*, 112−122.
(89) Marchivie, M.; Guionneau, P.; Létard, J.-F.; Chasseau, D. Photo-induced spin transition: the role of the iron(II) environment distortion. *Acta Crystallogr., Sect. B: Struct. Sci.* **2005**, *61*, 25−28.
(90) McCusker, J. K.; Rheingold, A. L.; Hendrickson, D. N. Variable-Temperature Studies of Laser-Initiated $^5T_2 \rightarrow {}^1A_1$ Intersystem Crossing in Spin-Crossover Complexes: Empirical Correlations between Activation Parameters and Ligand Structure in a Series of Polypyridyl Ferrous Complexes. *Inorg. Chem.* **1996**, *35*, 2100−2112.
(91) Guionneau, P.; Marchivie, M.; Bravic, G.; Létard, J.-F.; Chasseau, D. Structural Aspects of Spin Crossover. Example of the $[Fe^{II}L_n(NCS)_2]$ Complexes. *Top. Curr. Chem.* **2004**, *234*, 97−128.
(92) Mathieu, F.; Weiss, R. Transition metal cryptates: the crystal and molecular structure of the cobalt(II) cryptate, $[Co(C_{16}H_{32}N_2O_5)][Co(SCN)_4]$. *J. Chem. Soc., Chem. Commun.* **1973**, 816a−816a.
(93) Chow, M.-Y.; Mak, T. C. W. A mononuclear cobalt(II) complex containing pyridine betaine and thiocyanate ligands: triaquabis-(pyridinioacetato-*O*) (thiocyanato-*N*)cobalt(1+) tetra(thiocyanato-*N*)cobaltate(2-). *Aust. J. Chem.* **1992**, *45*, 1307−1313.
(94) Burgess, J.; Fawcett, J.; Haines, R. I.; Singh, K.; Russell, D. R. Structure, solvatochromism, and solvation of *trans*-$[Co^{III}(cyclam)(NCS)_2](NCS)$ and the structure of $[Co^{II}(Me_4cyclam)(NCS)]_2[Co(NCS)_4] \cdot$ MeOH. *Transition Met. Chem.* **1999**, *24*, 355−361.
(95) Chatterton, N. P.; Goodgame, D. M. L.; Grachvogel, D. A.; Hussain, I.; White, A. J. P.; Williams, D. J. Influence of the Counterion ion the Formation of Polymeric Networks by Metal Complexes of Hexamethylenebis(acetamide). *Inorg. Chem.* **2001**, *40*, 312−317.
(96) Patra, G. K.; Goldberg, I.; Sarkar, A.; Chowdhury, S.; Datta, D. Metal ion complexes of the optically pure bi(4-phenyl-1,3-oxazoline) ligand. *Inorg. Chim. Acta* **2003**, *344*, 7−14.
(97) Banerjee, S.; Ray, A.; Sen, S.; Mitra, S.; Hughes, D. L.; Butcher, R. J.; Batten, S. R.; Turner, D. R. Pseudolaide-induced structural variations in hydrazine-based metal complexes: Syntheses, electrochemical studies and structural aspects. *Inorg. Chim. Acta* **2008**, *361*, 2692−2700.
(98) Li, R.; Brooker, S. An unexpected mixed-valence cobalt(II)/cobalt(III) complex of a pyrrole-containing tridentate Schiff-base ligand. *J. Inclusion Phenom. Mol. Recognit. Chem.* **2011**, *71*, 303−309.
(99) Adach, A.; Daszkiewicz, M.; Cieślak-Golonka, M. Cobalt(II) scorpionate-like complexes obtained from *in situ* synthesized ligand created in [Co(0)-1-hydroxymethyl-3,5-dimethylpyrazole-$VOSO_4$-NH_4SCN system. *Polyhedron* **2012**, *47*, 104−111.
(100) Qiu, Q.M.; Jin, Q.-H.; Sun, J.-J.; Liu, M.; Wang, J.-C.; Zhang, Y.-Y.; Zhang, C.-L. Synthesis and crystal structure of six-thiocyanato-connected transition metal complexes of 2,2′-biimidazole. *Polyhedron* **2012**, *44*, 215−220.
(101) Li, X.-Z.; Kong, X.-J.; Li, C.-Q.; Qu, H.; Zhu, L.-N.; Liao, D.-Z. Syntheses and structures of eight-semi-coordinate M(II) (M = Mn, Fe, Co, Ni, Cu, Zn) complexes and density functional theory study of bond dissociation energies for the M-O semi coordinate bonds. *Inorg. Chem. Commun.* **2013**, *27*, 114−118.
(102) Massoud, S. S.; Dubin, M.; Guilbeau, A. E.; Spell, M.; Vicente, R.; Wilfling, P.; Fischer, R. C.; Mautner, F. A. Azido- and thiocyanato-cobalt(II) complexes based pyrazole ligands. *Polyhedron* **2014**, *78*, 135−140.
(103) Tsunezumi, Y.; Matsumoto, K.; Hayami, S.; Fuyuhiro, A.; Kawata, S. Bis[tetrakis(pyridine-2-yl)methane-$\kappa^3N,N'N''$]cobalt(II) tetrakis(thiocyanato-κN)cobaltate(II) methanol monosolvate. *Acta Crystallogr., Sect. E: Struct. Rep. Online* **2014**, *70*, m96−m97.
(104) Caballero-Jiménez, J.; Habib, F.; Ramírez-Rosales, D.; Grande-Aztatzi, R.; Merino, G.; Korobkov, I.; Singh, M. K.; Rajaraman, G.; Reyes-Ortega, Y.; Murugesu, M. Inducing magneticcomunication in dinuclear Co(II) systems. *Dalton. Trans.* **2015**, *44*, 8649−8659.
(105) Huxel, T.; Klingele, J. Cobalt(II) complexes of a new imidazolium-tagged thiadiazole ligand with bis-(trifluoromethylsulfonyl)imide or tetraisothiocyanato cobalate as counterion. *Transition Met. Chem.* **2015**, *40*, 61−68.
(106) Rohrbaugh, W. J.; Jacobson, R. A. Tris(ethylenediamine)-cobalt(III) tetrakis(isothiocyanato)cobaltate(II) nitrate. *Acta Crystallogr., Sect. B: Struct. Crystallogr. Cryst. Chem.* **1977**, *33*, 3254−3256.
(107) Goodgame, D. M. L.; Grachvogel, D. A.; White, A. J. P.; Williams, D. J. Heterometallic Network Complexes of the Ambidentate Extended-Reach Linear Ligand 1-(4′-pyridyl)pyridine-4-one. *Inorg. Chem.* **2001**, *40*, 6180−6185.
(108) Sen, S.; Talukder, P.; Dey, S. K.; Mitra, S.; Rosair, G.; Hughes, D. L.; Yap, G. P. A.; Pilet, G.; Gramlich, V.; Matsushita, T. Ligating properties of a potentially teradentate Schiff base $[(CH_3)_2NCH_2CH_2N{=}CHC_6H_3(OH)(OMe)]$ with zinc(II), cadmium(II) cobalt(II), cobalt(III) and manganese(III) ions: synthesis and structural studies. *Dalton Trans.* **2006**, 1758−1767.
(109) Ghazzali, M.; Langer, V.; Öhrström, L. The role of intermolecular interactions in the assemblies of Fe^{II} and Co^{II} tetrakis-isothiocyanatometalates with tris(1,10-phenanthroline)-Ru^{II}: crystal structures of two dual metal assemblies featuring octahedral cationic and tetrahedral anionic modules. *J. Solid State Chem.* **2008**, *181*, 2191−2198.
(110) Bai, Y.; Zhang, G.-Q.; Dang, D.-B.; Ma, P.-T.; Niu, J.-Y. Synthesis, crystal structure and luminescence properties of one inorganic-organic hybrid compound $[FTMA]_2[Co(NCS)_4]$ (FTMA = ferrocenylmethyltrimethylammonium cation). *Spectrochim. Acta, Part A* **2011**, *79*, 570−573.
(111) Rodić, M. V.; Leovac, M. V.; Jovanović, L. S.; Vojinović-Ješić, L. S.; Divjaković, V.; Češljević, V. I. Transition metal complexes with thiosemicarbazide-based ligands: Part 59. Synthesis, structures and electrochemical properties of cobalt(III) complexes with 2-acetylpyridine S-methylisothiosemicarbazone. *Polyhedron* **2012**, *46*, 124−132.
(112) Vlahopoulou, G.; Escuer, A.; Font-Bardia, M.; Calvet, T. Synthesis and characterization of Co^{III}_3 inverse matallacrowns via use of 6-methyl-2-pyridylaldoxime. *Inorg. Chem. Commun.* **2012**, *16*, 78−80.
(113) Yin, Z.; Zhang, G.; Phoenix, T.; Zheng, S.; Fettinger, J. C. Assembling mono-, di- and tri-nuclear coordination complexes with a ditopic analogue of 2,2′:6′,2″-terpyridine: synthesis, structures and catalytic studies. *RSC Adv.* **2015**, *5*, 36156−36166.
(114) Ray, A.; Rosair, G. M.; Kadam, R.; Mitra, S. Three mono-di-trinuclear cobalt complexes of selectivity and non-selectivity condensed Schiff bases with N_2O and N_2O_2 donor sets: Syntheses, structural variations, EPR and DNA binding studies. *Polyhedron* **2009**, *28*, 796−806.
(115) Llunell, M.; Casanova, D.; Cirera, J.; Alemany, P.; Alvarez, S. *SHAPE*, version 2.1; Universitat de Barcelona: Barcelona, Spain, 2013.
(116) Harris, C. M.; Lockyer, T. N.; Martin, R. L.; Patil, H. R. H.; Sinn, E. Five and six-coordinated complexes of cobalt(II) with 2,2′:6′,2″-terpyridyl: Unusual structure and magnetism. *Aust. J. Chem.* **1969**, *22*, 2105−2116.
(117) Figgis, B. N. Magnetic Properties of Spin-Free Transition Metal Series Complexes. *Nature* **1958**, *182*, 1568−1570.
(118) Golding, R. M.; Tennant, W. C.; Bailey, J. P. M.; Hudson, A. NMR Study of Iron(III) *N*-Methyl-*N*-pnenyldithiocarbamate and its meta- and para-Fluorophenylderivatives. *J. Chem. Phys.* **1968**, *48*, 764−771.
(119) Cano, J. *VPMAG package, Revision 03*; University of València, 2004.
(120) Vecchio-Sadus, M. A. Electrosynthesis and magnetic behaviour of neutral cobalt(II) complexes of pyridine-2-carbaldehyde pyridin-2′-

DOI: 10.1021/acs.inorgchem.7b00360
Inorg. Chem. 2017, 56, 6281−6296

ylhydrazone (papyH) and its analogues. *Transition Met. Chem.* **1995**, *20*, 38−45.
(121) Kahn, O. *Molecular Magnetism*; VCH Publishers: Weinheim, Germany, 1993; p 17.
(122) Bartolomé, J.; Filoti, G.; Kuncser, V.; Schinteie, G.; Mereacre, V.; Anson, C. E.; Powell, A. K.; Prodius, D.; Turta, C. Magneto-structural correlations in the tetranuclear seroes of $\{Fe_3LnO_2\}$ butterfly core clusters: Magnetic and Mössbauer spectroscopic study. *Phys. Rev. B: Condens. Matter Mater. Phys.* **2009**, *80*, 014430.
(123) Martínez-Lillo, J.; Mastropietro, T. F.; De Munno, G.; Lloret, F.; Julve, M.; Faus, J. Enhancing the Magnetic Coupling of Oxalato-Bridged $Re^{IV}_2M^{II}$ (M = Mn, Co, Ni, and Cu) Trinuclear Complexes Via Peripheral Halide Ligand Effects. *Inorg. Chem.* **2011**, *50*, 5731−5739.
(124) Ishikawa, R.; Miyamoto, R.; Nojiri, H.; Breedlove, B. K.; Yamashita, M. Slow Relaxation of the Magnetization of an Mn^{III} Single Ion. *Inorg. Chem.* **2013**, *52*, 8300−8302.
(125) Grigoropoulos, A.; Pissas, M.; Papatolis, P.; Psycharis, V.; Kyritsis, P.; Sanakis, Y. Spin-Relaxation Properties of a High-Spin Mononuclear $Mn^{III}O_6$-Containing Complex. *Inorg. Chem.* **2013**, *52*, 12869−12871.
(126) Martínez-Lillo, J.; Mastropietro, T. F.; Lhotel, E.; Paulsen, C.; Cano, J.; De Munno, G.; Faus, J.; Lloret, F.; Julve, M.; Nellutla, S.; Krzystek, J. Highly Anisotropic Rhenium(IV) Complexes: New Examples of Mononuclear Single-Molecule Magnets. *J. Am. Chem. Soc.* **2013**, *135*, 13737−13748.
(127) Alexandru, M.-G.; Visinescu, D.; Marino, N.; De Munno, G.; Lloret, F.; Julve, M. $\{Co^{III}Mn^{III}\}_n$ corrugated chains based on heteroleptic cyanide metalloligands. *RSC Adv.* **2015**, *5*, 95410−95420.
(128) Dinca, A. S.; Vallejo, J.; Shova, S.; Lloret, F.; Julve, M.; Andruh, M. *Polyhedron* **2013**, *65*, 238−243.

DOI: 10.1021/acs.inorgchem.7b00360
Inorg. Chem. 2017, 56, 6281−6296